



The First Solar and Space Weather Euroconference

SP-463

The Solar Cycle and Terrestrial Climate

Santa Cruz de Tenerife, Tenerife, Spain 25-29 September 2000



European Space Agency Agence spatiale européenne

Proceedings of

The 1st Solar and Space Weather Euroconference

The Solar Cycle and Terrestrial Climate

25-29 September 2000 Instituto de Astrofísica de Canarias Santa Cruz de Tenerife, Tenerife, Spain

> European Space Agency Agence spatiale européenne

The conference was sponsored by:

European Commission. DG XII Science, Research and Development (TMR and INCO Programmes)

Dirección General de Enseñanza Superior e Investigaciones Científicas (Spanish Ministry of Science and Technology)

Cabildo Insular de Santa Cruz de Tenerife

Ayuntamiento de La Laguna

Ayuntamiento de Santa Cruz de Tenerife

CajaCanarias

European Space Agency

Observatoire de Paris

Instituto de Astrofísica de Canarias

With collaboration from:

Iberia

Banco Bilbao Vizcaya Argentaria (BBVA)

DISA, Corporación petrolifera S.A

SUN Microsystems Iberica S.A

Scientific Organising Committee

- B. Schmieder (Observatory of Paris, France, Co-chair)
- M. Vázquez (IAC, Spain, Co-chair)
- P.N. Brandt (KIS, Germany)
- G. Cauzzi (Observatory of Naples, Italy)
- E. Daily (ESA, The Netherlands)
- B. Fleck (ESA, The Netherlands)
- E. Friis-Christensen (Danish Space Research Institute, Denmark)
- M. Noguer (IPCC, UK)
- R. Marsden (ESA, The Netherlands)
- H. Wöhl (Freiburg, Germany)

Local Organising Committee

- M. Vázquez (Chair), J. de Araoz, E. Bejarano,
- L. Bellot Rubio, J.A. Bonet, A. Eff-Darwich,
- H. González Jorge, A. Jiménez, T. Karthaus,
- V. Martínez Pillet, I. Rodríguez Hidalgo

Cover image by G. Pérez Díaz (IAC)

Publication	Proceedings of The 1st Solar & Space Weather Euroconference 'The Solar Cycle and Terrestrial Climate' 25-29 September 2000, Santa Cruz de Tenerife, Tenerife, Spain (ESA SP-463, December 2000)
Edited by	A. Wilson ESA Publications Division
Published and distributed by	ESA Publications Division ESTEC, Noordwijk, The Netherlands
Printed in	The Netherlands
Price	130 Dutch Guilders / EUR 60
ISBN ISSN	92-9092-693-7 0379-6566
Copyright	© 2000 European Space Agency

CONTENTS

	Foreword	
М.	Vázquez & B. Schmieder	

xiii

Solar Variability

Chair: B. Schmieder

What Makes the Sun Tick? The Origin of the Solar Cycle K. Petrovay	3
The Solar Cycle is More than Skin Deep! R. Komm, R. Howe. & F. Hill	15
The Solar Cycle and the Tachocline: Theories and Observations T. Corbard et al.	21
Magnetic Sources of Solar Variability O.R. White	27
Variations in Total Solar Irradiance during the 11-year Solar Cycle G. Maris et al.	39
From Solar Minimum to Solar Maximum: Changes in Total and Spectral Solar Irradiance <i>G. de Toma & O.R. White</i>	45
Long-Term Changes in Solar Irradiance S. Solanki & M. Fligge	51
Total Solar Irradiance from VIRGO on SOHO C. Fröhlich & W. Finsterle	see Late Papers
Chair: P.N. Brandt	
Solar Variability in Ionizing Radiation (UV, X-rays) G. Schmidtke	61
Absolute UV Radiation, its Variability and Consequences for the Earth's Climate <i>G. Thuillier</i>	69

Mid-Term Variations in the Extreme UV Corona: the EIT/SOHO Perspective	79
J.F. Hochedez et al.	

Long-Term Variations in the Magnetic Fields of the Sun and Possible Implications for Terrestrial <i>M. Lockwood & S. Foster</i>	l Climate 85
Coronal Holes (Recorded from 1943) – a Source of the Solar-Induced Terrestrial Responses? J. Sykora et al.	95
Chair: G. Cauzzi	
The Dynamo Theory for the Maunder Minimum <i>G. Rüdiger</i>	101
Polar Ice as an Archive for Solar Cycles and the Terrestrial Climate J. Beer	see Late Papers
Irradiance or Luminosity Changes? S. Sofia & L.H. Li	107

Drift-Time Measurements of the Solar Diameter 1990-2000: New Limits on Constancy A.D. Wittmann & M. Bianda

Solar Surface Magnetism and the Increase of Solar Irradiance between Activity Minimum and Maximum 117 *M. Fligge et al.*

Mechanisms of Solar-Terrestrial Relations

Global Average Upper Ocean Temperature Response to Changing Solar Irradiance: Exciting the Internal Decadal Mode <i>W.B. White et al.</i>	125
Solar Forcing of El Niño and La Niña <i>T. Landscheidt</i>	135

Chair: B. Fleck

Comparative Study of the Atmospheric Effects Driven by Irradiance vs. Corpuscular Radiation	141
A Ludmány & T. Baranyi	
Sunshine, Clouds and Cosmic Rays	147
E. Pallé Bagó & C.J. Butler	

The Long-Term Terrestrial Record of Climate Change

CO ₂ and Astronomical Forcing of the Late Quaternary A. Berger & M.F. Loutre	155
Plio-Pleistocene Lacustrine Sedimentation in the Baza Basin (SE Spain) and its Relations with Climatic Shifts <i>L. Gibert et al.</i>	171

iv

The Solar Contribution to Climate Change

Chair: C. Fröhlich

Temperature Trends from Instrumental and Proxy Indicators for the Last Millennium <i>P.D. Jones & K.R. Briffa</i>	179
Is There a Correlation between Solar Cycle Lengths and Terrestrial Temperatures? Old Claims and New Results P. Laut & J. Gundermann	189
Description and First Results of the EC Project SOLICE (Solar Influences on Climate and the Environment) <i>ML. Chanin & J.D. Haigh</i>	195
Estimation of Natural and Anthropogenic Contributions to 20th Century Temperature Change S.F.B. Tett et al.	201
Natural Variability of Global Mean Temperatures: Contributions from Solar Irradiance Changes, Volcanic Eruptions and El Niño <i>A.P. van Ulden & R. van Dorland</i>	213
Chair: I. Rodríguez Hidalgo	
SPECIAL: An Interdisciplinary ESF Network on Space Weather and the Earth's Weather <i>N.B. Crosby & M.J. Rycroft</i>	219
PICARD: Solar Diameter, Irradiance and Climate L. Damé et al.	223
Non-Solar Sources of Global Warming	
Chair: V. Martinez Pillet	
Use of Climate Models for Climate Change Investigations K. Arpe et al.	233
Calculating the Climatic Impacts of Increased CO_2 : the Issue of Model Validation <i>W. Soon et al.</i>	243
THE IPCC Report 2001 J.T. Houghton	255

SOLSPA Summary

Summary and Perspectives	263
E.N. Parker	

Poster Papers: The Solar Cycle

Magnetic Power Spectra in the Solar Photosphere derived from Ground and Space based Observations V. Abramenko & V.B. Yurchyshyn	273
Cyclic Variation of Solar Large-Scale Convection P. Ambroz	277
The Variations of the Solar Activity and the Low Rigidity Cosmic Rays (1969-1998) A. Antalová et al.	281
MgIb ₂ Bright Features in the Solar Photosphere F. Berrilli et al.	285
Complexes of Activity – Basic Components of Activity Cycles (from the Bottom of the Convective Zone till the Interplanetary Space) V. Bumba et al.	289
Line-Depth and T _{eff} Variations with the Solar Cycle due to Possible Size-Changes of Photospheric Granulation <i>B. Caccin & V. Penza</i>	293
Gravitational Energy of Solar Oscillations and Climatic Changes D.K. Callebaut et al.	297
Hydrogen and Helium Nuclei of Galactic Origin in the Inner Heliosphere L. Del Peral et al.	301
The Solar Dynamo: Flux Pumping by Stratified Convection S.B.F. Dorch & Å. Nordlund	305
Investigating the Vertical Structure of the Solar Granulation with the Sodium D_2 Line <i>M.T. Eibe et al</i>	309
The Magnetic Network Contribution to Long-Term Irradiance Variations I. Ermolli et al	313
The Contribution of the Magnetic Regions to Irradiance Variations M. Fofi. et al.	317
Identification of Potential SEP Associated Flares from Interball RF15-I Hard X-ray Observations <i>S. Gburek et al.</i>	321
Comparison between Gradual and Impulsive Solar Energetic Particle Events Detected by EPHIN/SOHO Experiment <i>R. Gómez-Herrero et al.</i>	325
Galaxy-Sun-Earth Relations. The Dynamo of the Earth, and the Origin of the Magnetic Field of Stars, Planets, Satellites, and Other Planetary Objects <i>G.P. Gregori</i>	329
3-D Tomography of the Solar Photosphere A. Hanslmeier et al.	333
Variability of the CR/XBG-L Relationship during the Solar Cycle Evolution <i>M. Jakimiec et al.</i>	337

<i>p</i> -mode Frequency Shift as Solar Activity Index S.J. Jiménez-Reyes et al.	341
Variations of 3 GHz Daily Radio Flux during the Years 1995-2000 K. Jiricka et al.	345
On Measurements of Rapid Variations in Solar Flare Optical Radiation <i>P. Kotrc</i>	349
Phase Relations between Chromospheric and Transition Region Oscillations J.M. Krijger et al.	353
Fe I and Ca II K Lines in Quiet and Active Regions A. Kucera et al.	357
Radio Emission of Solar Chromosphere at Millimeter Wavelengths M.A. Loukitcheva & V.G. Nagnibeda	363
Polar Activity and Magnetic Field Reversal in Current Solar Cycle 23 V.I. Makarov et al.	367
Solar Activity Level on the Ascending Phase of the Solar Cycle 23 <i>G. Maris et al.</i>	371
Presentation of First Results from Multispectral Solar Patrol System and their Comparing with Some World Data <i>E. Marková et al.</i>	375
Local and Global Magnetic Oscillations in the Photosphere <i>P.F. Moretti et al.</i>	381
Solar Rotation and Activity Rate Z. Mouradian et al.	385
Persistent 22-year Cycle in Sunspot Activity: Evidence for a Relic Solar Magnetic Field K. Mursula et al.	387
Long-Term North-South Asymmetry in Solar Wind Speed: Evidence for a New Type of Century-Scale Solar Oscillation <i>K. Mursula & B. Zieger</i>	391
An Example of Isolated Active Region Energy Evolution: NOAA AR 7978 A. Ortiz et al.	395
On the Contrast of Faculae and Small Magnetic Features A. Ortiz et al.	399
Effects of Hysteresis of Some Solar Indices during the Past Three Solar Cycles 20, 21 and 22 A. Özgüç et al.	403
Granular Evolution from 2D (x, t)-Slices and from Tracking Granules W. Poetzi et al.	407
Behaviour of the Cosmic Ions Charge State under Acceleration in Their Sources <i>M.D. Rodriguez-Frias et al.</i>	411
Observation with EPHIN/SOHO of Electron during Quiet Time Periods <i>M.D. Rodriguez-Frias et al.</i>	415

The Intermittency of the Solar Intermediate-Term Periodicity (1969-1998) J. Rybák et al.	419
N-S Variation of the X-ray Flare Number during the Solar Cycle 22 B. Schmieder et al.	423
Mid-term Radiance Variation of Far-Ultraviolet Emission Lines from Quiet-Sun Areas U. Schühle et al.	427
Analysis of Three SEP Associated Flares J. Sylwester	431
EUV Irradiance Variations Measured with the SOHO Coronal Diagnostic Spectrometer <i>W.T. Thompson & P. Brekke</i>	435
Tilt Angle Variation through the 14th Sunspot Cycle L. Tóth & O.Gerlei	439
Study of Chromospheric Ca II Cloud-like Structures K. Tziotziou et al.	443
Regular and Random Components of Sunspot Activity during Active Sun and Great Minima: Model Simulation <i>I.G. Usoskin et al.</i>	447
What Can we Learn Studying Long-Term Magnetic Evolution of Solar Active Regions? L. van Driel-Gesztelyi et al.	451
Automatic Image Segmentation and Feature Detection in Solar Full-Disk Images A. Veronig et al.	455
On the Correlation between the Orientation of Moving Magnetic Features and the Large-Scale Twist of Sunpots <i>V. Yurchyshyn et al.</i>	459
Magnetic Topology in November 5, 1998 Two-Ribbon Flare as Inferred from Ground-Based Observations and Linear Force-Free Field Modeling <i>V. Yurchyshyn et al.</i>	463
Analysis of the Solar Magnetic Dipole Reversal during the Current Solar Cycle A.N. Zhukov & I.S. Veselovsky	467

Poster Papers: The Terrestrial Record of Solar Variability

Coherency between Solar Activity and Meteorological Parameters at 11 year Period <i>D. Altadill et al.</i>	473
On Solar-Terrestrial Correlation Studies: Pitfalls and Real Signals <i>R.E. Benestad</i>	477
The 11 year Solar Cycle and the Modern Increase in the δ^{13} C of Planktonic Foraminifera of a Shallow Water Mediterranean Sea Core (590-1979) G. Cini Castagnoli et al.	481
The Long-term Solar Cyclicity (210 and 90 years) and Variation of the Global Terrestrial Air Temperatures since 1868 V.A. Dergachev & O.M. Raspopov	485

viii

Long-term Variability of Solar Activity during the Holocene <i>V.A. Dergachev et al.</i>	489
The 1940's Temperature Decrease in Locations of Argentina <i>T. Heredia et al.</i>	493
Solar Wind near Earth: Indicator of Variations in Global Temperature <i>T. Landscheidt</i>	497
Characteristics of Intense Geomagnetic Storms and their Relation to Solar Active Phenomena C.H. Mandrini et al.	501
A Possible Origin of Long-Term Global Circulation Variations and 1920-1940 Years Warming <i>V. Mordvinov et al.</i>	505
Solar Variability Associated to Ionospheric. Stratospheric and Tropospheric Parameters <i>N. Ortiz de Adler & A.G. Elias</i>	509
Abrupt Climate Change around 2700-2800 years BP as Example of Existence of 2400 year Periodicity in Solar Activity and Solar Variability <i>O.M. Raspopov et al.</i>	513
35-year Climatic Bruckner Cycle – Solar Control of Climate Variability? O.M. Raspopov et al.	517
Physical Interpretation of Solar Cycle Length Connection to Global Surface Temperatures O.I. Shumilov et al.	521
Differences in the Zonal Behaviour of Solar Activity are Relevant for the Solar-Terrestrial Relations J. Sýkora et al.	525
Relationships between Ionospheric Disturbances and Changes of Sea Level Pressure over the Arctic L. Toth & S. Szegedi	529

Poster Papers: Non-Solar Sources of Climate Change

Evolution of Early Hominids in the Context of Climate Changes during the Plio-Pleistocene <i>E.Y. Bulygina & J.Gilbert Clols</i>	535
Retrieved Aerosol Parameters Needed in Climate Model Calculations H. González Jorge et al.	see Late Papers
CO ₂ Continuous Measurements at the Izaña GAW station P. Rípodas & R. Ramos	539
Atmospheric Aerosols Created by Varying Cosmic Ray Activity – One of the Key Factors of Non-Direct Solar Forcing of Climate <i>O.I. Shumilov et al.</i>	543
Influence of Cosmic Ray Intensity Modulated by Solar Activity and Volcanic Eruptions on the Climate <i>O.I. Shumilov et al.</i>	547
Estimation of a 'Clear' Sky Atmosphere using Ground and Satellite Measurements of the Solar Radiation <i>G. Tsiropoula & A. Argiriou</i>	551

Moon Dynamics and Climate Prediction *A. Ulla et al.*

Joint Organisation for Solar Observations (JOSO)

Data Handling in Solar and Geophysical Research Chair: M. Messerotti	
Solar and Geophysical Databases: the Tiles of a Planetary Meta-archive <i>M. Messerotti</i>	563
The Virtual Solar Observatory Concept F. Hill	569
Space Weather User Requirements of Solar Data N.B. Crosby	575
Meeting on the 1999 Solar Eclipse Chair: F. Clette	
The TECONet Project One Year after Totality F. Clette & JR. Gabryl	581
Comparison of Coronal Structures 11.8.1999 on the Long Observation Base <i>M. Belik et al.</i>	587
Radio Polarimetric Observations of the 11 August 1999 Solar Eclipse via the Trieste Solar Radio System <i>M. Messerotti et al.</i>	595
The Total Solar Eclipse of August 11, 1999 Observed at Bucharest Astronomical Institute in the 2.6 cm Radio Wavelength A. Oncica	601
Meeting on Observing Techniques and Recent Instrumental Development in Solar Physics Chair: G. Ceppatelli	
IBIS: A Purely Interferometric Instrument for Solar Bidimensional Spectroscopy <i>F. Cavallini et al.</i>	607
Solar Magnetometry with the Dutch Open Telescope R. Rutten et al.	611
The New Global High-Resolution H α Network: First Observations and First Results <i>M. Steinegger et al.</i>	617
Recent Developments in Solar Instrumentation at the Instituto de Astrofísica de Canarias I. Rodríguez-Hidalgo	623

Annual JOSO Meeting

Chair: B. Schmieder	
GREGOR: A 1.5m Telescope for Solar Research O. von der Lühe et al.	629
<i>Poster Papers: JOSO Meetings</i> Long-Term Observations of Solar Active Regions at the VNT <i>J.A. Bonet et al.</i>	635
Solar Patrol at Catania Astrophysical Observatory L. Contarino et al.	639
Optimal Windows to Determine Solar Granulation Image Quality C. Giammanco	643
Standardized Coordinate Systems for Solar Image Data W.T. Thompson	645

List of Participants

Late Papers

Total Solar Irradiance from VIRGO on SOHO C. Fröhlich & W. Finsterle	665
Polar Ice as an Archive for Solar Cycles and the Terrestrial Climate J. Beer	671
Retrieved Aerosol Parameters Needed in Climate Model Calculations H. González Jorge et al.	677

649

Foreword

FOREWORD

M. Vázquez & B. Schmieder Co-Chairs, Scientific Organising Committee

After the positive experiences with the Advances in Solar Physics Euroconferences held in Tenerife, Thessalonikii and Postdam, the same group of solar astronomers, under the umbrella of the Joint Organisation for Solar Observations (JOSO), proposed to the European Commission two further meetings with the name *Solar and Space Weather Euroconferences* (SOLSPA). The series is aimed at gathering, around selected topics of interest to solar physics, different communities of researchers involved in that field, observers, theoreticians and technical and industrial users in order to get the best overviews of those topics. We paid particular attention to the training of young people.

The topic of this first meeting was *The Solar Cycle and Terrestrial Climate*. One of the most important challenges to Mankind is to produce sustainable development while protecting the environment. A clear warning that something might go wrong is the increase in the mean temperature of the Earth over the last 150 years. Apart from an intrinsic variability, three external agents could be responsible for this: a) the increasing emission of greenhouse gases, such as carbon dioxide, produced by the burning of fossils fuels, b) the emission of different types of aerosols of natural and anthropogenic origins, and c) the increase in the mean level of magnetic activity on the Sun. Evaluating this last contribution was emphasised during the conference.

The venue was again Tenerife. CajaCanarias, the main savings bank of the province, generously supplied its Conference Centre in Santa Cruz de Tenerife, including the necessary personnel. The names of Antonio Pérez, Gustavo García, Alberto Sacramento and Arancha Martín should be mentioned here.

Around 200 colleagues from the fields of solar physics and climatology attended the meeting and contributed to a good atmosphere for discussion. Twenty-six countries were represented, most of them European. More than 40 young scientists participated in the conference, and we particularly appreciated those coming from Eastern Europe, whose presence was made possible through European Union support.

The conference took up four full days, with a busy agenda of scientific and social events, plus a fifth day devoted to visiting the Teide Observatory. The first part was devoted to the study of solar variability and how it could influence the terrestrial climate. The second part was dedicated to evaluating the different contributions of greenhouse gases, aerosols and solar activity to climate change, together with the presentation of some important projects. Finally, Prof. E. Parker summarised the scientific highlights of the meeting. During the final afternoon, there were different reports on the development of Solar Physics in Europe, and the

annual meeting of JOSO. The visit to the Teide Observatory allowed participants to see the new developments of the Canary Islands' solar telescopes.

One of the most memorable moments was the SolarMusic@Solspa2000 (Thursday evening). The first part was performed by three solar astronomers: Inés Rodríguez Hidalgo and András Ludmany at the piano and András Ludmany and Rob Rutten playing the flute transmitted their enthusiasm and professionalism to the audience. Then we heard with pleasure a Tenerife choir, *Carpe Diem*, conducted by Luis Correa and formed by a group of people involved in education. They offered Spanish and Latin-American songs, including an amusing one about Thales Theorem to celebrate the European Year of Mathematics. They finished with the University anthem, *Gaudeamus Igitur*.

There were numerous appearances in the media (newspapers, radio and TV), with a public lecture by Paal Brekke, on *The Sun through the Eyes of SOHO*.

The meeting was sponsored by the European Union under the TMR and INCO programmes. The Instituto de Astrofísica de Canarias provide significant financial support as well as important infrastructure facilities. Other support came from the Spanish Ministry of Science and Technology, the Observatoire de Paris and the companies Iberia, DISA, Banco Bilbao Vizcaya Argentaria (BBVA) and Sun Microsystems. The social events were possible thanks to the support of the Town Councils of La Laguna and Santa Cruz de Tenerife, the Cabildo Insular de Tenerife and the Instituto de Astrofísica de Canarias.

We wish to thank the European Space Agency for its willingness to publish these proceedings and for its great help to spread the contents of the meeting to the media at the international level. Andrew Wilson has carefully, and patiently, collected the papers for these proceedings. The papers were not refereed; the authors are responsible for the contents.

Finally, the organisers would like to express their gratitude to the members of the Local Organising Committee. The team of Judith de Araoz, Eva Bejarano and Tanja Karthaus deserves a special mention.

Solar Variability

WHAT MAKES THE SUN TICK?

The Origin of the Solar Cycle

K. Petrovay

Eötvös University, Department of Astronomy, Budapest, Pf. 32, H-1518 Hungary Phone: +36 20 3404907 Fax: +36 1 3722940 E-mail: kris@astro.elte.hu

Abstract. In contrast to the situation with the geodynamo, no breakthrough has been made in the solar dynamo problem for decades. Since the appearance of mean-field electrodynamics in the 1960's, the only really significant advance was in the field of flux tube theory and flux emergence calculations. These new results, together with helioseismic evidence, have led to the realization that the toroidal magnetic flux giving rise to activity phenomena must be stored and presumably generated below the convection zone proper, in what I will call the DOT (Dynamo-Overshoot-Tachoclyne) layer. The only segment of the problem we can claim to basically understand is the transport of flux from this layer to the surface. On the other hand, as reliable models for the DOT layer do not exist we are clueless concerning the precise mechanisms responsible for toroidal/poloidal flux conversion and for characteristic migration patterns (extended butterfly diagram) and periodicities. Even the most basic result of mean-field theory, the identification of the butterfly diagram with an α - ω dynamo wave, has been guestioned. This review therefore will necessarily ask more questions than give answers. Some of these key questions are

- Structure of the DOT layer
- α -quenching and distributed dynamo
- High-latitude migration patterns and their interpretation
- The ultimate fate of emerged flux

1. INTRODUCTION

The turn of the millennium invites us to look back and draw balances in all fields of human activity. Yet in solar dynamo theory we also have an added incentive to make such an assessment. In the theory of the geodynamo a significant breakthrough has been achieved in the past few years (Glatzmaier & Roberts 1995, Kuang & Bloxham 1997, Olson *et al.* 1999), leading to a surge of renewed activity in the field. One cannot but wonder if a similar breakthrough is within reach in the case of the solar dynamo. Unfortunately, as it will turn out from this review, the prospects are rather bleak, at least on a short term.

As for such a comparative assessment one needs a wider historical outlook this review will not be restricted to the developments that have taken place since the reviews of Weiss (1994) and Schmitt (1993). (Such developments were mostly limited to advances in the study of interface dynamos, cf. Sect. 3 below.) A wider historical overview, starting with the dawn of mean-field theory in the 1950s and 60s will thus be given in Section 2 below. Given the finite amount of space available, I will compensate for this wider temporal scope of the review by restricting attention strictly to the problem of the origin of the solar cycle, i.e. of the 22 year periodic variation of solar activity, and associated migration patterns (butterfly diagram). Solar activity variations on both shorter and longer timescales are ignored, as are the solar-type magnetic cycles in other stars, nonaxisymmetric phenomena such as active longitudes, and the problem of the long-time phase coherence of the cycle. This restriction is imposed out of necessity only, and in no way does it imply that these effects do not yield important clues even to the origin of the 22 year cycle itself. Clearly, a critical test of any theory of the solar cycle is whether it can be readily extended to predict these other phenomena as well.

After the historical overview, Section 3 will attempt to cut some order in the dazzling multitude of solar dynamo models by introducing a classification scheme. Three main model families can be clearly discerned: overshoot dynamos, interface dynamos and flux transport models, circulation-driven "conveyor belt" models being the most important subgroup of the latter class. Finally, Section 4 calls attention to some key areas where more intensive theoretical or observational efforts could lead to significant advance.

But first of all we should state clearly what are the basic observational facts to be interpreted by a solar cycle model. Once we apply our aforementioned restriction excluding long-term variations, stellar activity etc., the remaining list is quite short.

- The 11/22 year cycle period. Beside reproducing the value of the period, the crude agreement of this value with the timescale of pole-equator diffusion in the convective zone

Proc. 1st Solar & Space Weather Euroconference, 'The Solar Cycle and Terrestrial Climate', Santa Cruz de Tenerife, Tenerife, Spain, 25-29 September 2000 (ESA SP-463, December 2000)

also asks for an explanation. While such an order-of-magnitude equality can certainly be coincidental (cf. the coincidence of the solar rotation period with the convective turnover time in the deep convective zone), a natural explanation for it would clearly make any cycle model more attractive.

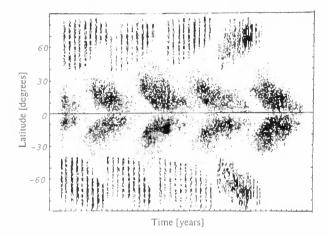


Figure 1: Extended butterfly diagram of solar activity: time-latitude distribution of sunspot groups (low-latitude branches) and polar faculae (high-latitude branches). After Makarov & Sivaraman (1989)

- The characteristic migration pattern (extended butterfly diagram). Our knowledge of latitudinal migration patterns of magnetic flux is summarized in the extended butterfly diagram of Figure 1. The tracers shown here track partly toroidal and partly poloidal fields.¹ While azimuthal field lines by definition cannot cross the surface, the observed properties of large-scale solar active regions² strongly suggest that they are tracers of a subsurface toroidal field, locally bulging out into the atmosphere. In this sense, photospheric magnetometry can give us information about the migration patterns of the toroidal field component as well. At low ($\leq 35^{\circ}$) latitudes both the poloidal and the toroidal field components migrate equatorward. At high latitudes, poloidal fields show a marked poleward migration, as indicated also by the migration pattern of a number of tracers such as quiescent prominences or the coronal green line. The migration pattern of high-latitude toroidal fields is less clear —a point we will return to in Section 4.2 below.

- The confinement of strong activity (large active regions) to low heliographic latitudes $|\Phi| \lesssim 35^{\circ}$.
- The phase dilemma(s). In its original sense (Stix 1976) the phase dilemma consists of the fact that at low latitudes the radial field (derived by azimuthal averaging of the magnetograms) is in an approximately π phase lag compared to the toroidal field at the same latitude. Another phase lag to be explained is the $\pi/2$ lag between the two branches of the butterfly diagram, i.e. that the polar field reversal occurs slightly after the sunspot maximum. Finally, the phase of torsional oscillations (cycle-related periodic oscillations of the rotational velocity in migrating belts) relative to the toroidal field is a third quantity constraining theories of the cycle.

2. HISTORY

2.1. Convection zone dynamos

It all started with Parker's (1955) classic paper that set down the foundations for solar $\alpha\Omega$ dynamo theory. In its trace, mean field electrodynamics was developed during the 1960's (Steenbeck *et al.* 1966. Krause & Rädler 1980). To give a reminder of the basics, described in so many other reviews (e.g. Cowling 1981, Belvedere 1985) the induction equation in a turbulent conductive medium reads

$$\partial_t \mathbf{B} = \nabla \times (\mathbf{U} \times \mathbf{B} + \vec{\mathcal{E}}) - \nabla \times \eta \nabla \times \mathbf{B}.$$
 (1)

where **B** is the mean magnetic field, **U** is the largescale flow velocity, ∂_t denotes time derivative, η is the magnetic diffusivity, and $\vec{\mathcal{E}}$ is the turbulent electromotive force arising as a result of the interaction between the turbulent velocity field **v** and the turbulent magnetic field. This latter is in turn the result of the action of **v** on the mean field **B**, so $\vec{\mathcal{E}}$ is a functional of **v** and **B**. Assuming scale separation $l \ll H_B$ where H_B is the length scale of the mean field and l is the scale of turbulence, $\vec{\mathcal{E}}$ can be expanded in the derivatives of **B**. For homogeneous and isotropic turbulence this yields

$$\mathcal{E} = \alpha \mathbf{B} - \beta \,\nabla \times \mathbf{B} \tag{2}$$

where α and β are now functionals of \mathbf{v} only. Substituting (2) into (1) we see that the role of β is formally identical to that of η . For this reason β is called *turbulent magnetic diffusivity*, and elementary considerations or even dimensional analysis yield $\beta \sim lv$.

¹Note that, owing to our assumption of axial symmetry, "toroidal" is now synonymous with "zonal" or "azimuthal", denoting the ϕ -component of a vector field in spherical coordinates, while "poloidal" is synonymous with "meridional", denoting the remaining components. This relieves us from giving a more generic definition of these terms.

 $^{^{2}}$ To be specific: their preferential East-West orientation following Hale's polarity rules. (The western, or leading magnetic polarity is identical on the same hemisphere and within the same cycle, and alternates between hemispheres and cycles)

As for turbulence the Reynolds number $\beta/\eta \gg 1$, in practice η can be omitted in equation (1). In contrast, the pseudoscalar α gives rise to a qualitatively new effect, the α -effect.

In the axisymmetric case considered here, using spherical coordinates θ , ϕ , r, **B** can be split as

$$\mathbf{B} = B\mathbf{e}_{\phi} + \nabla \times (A\mathbf{e}_{\phi})$$

where \mathbf{e}_{ϕ} is the azimuthal unit vector, B is the toroidal field component, and A is the (toroidal) vector potential of the poloidal field. We further assume that **U** is a pure rotation

$$\mathbf{U} = r \sin \theta \, \Omega \, \mathbf{e}_{\phi}$$

and introduce the shear vector

 $\hat{\rightarrow}$

$$\Omega = r\sin\theta\,\nabla\Omega$$

In the limit $r \sin \theta/H_B \to \infty$ the form of the vector operators simplifies to their form for the local Cartesian frame $\mathbf{e}_{x'} = \mathbf{e}_{\theta}$, $\mathbf{e}_{y'} = \mathbf{e}_{\phi}$, $\mathbf{e}_{z'} = \mathbf{e}_r$. Now we introduce a new frame xyz by rotating x'y'z' around \mathbf{e}_{ϕ} with an angle $-\pi/2 \leq \Delta\theta < \pi/2$ so that $\hat{\Omega}_x = 0$. With these assumptions and notations the poloidal and toroidal parts of equation (1) read

$$\partial_t A = \alpha B + \beta \, \nabla^2 A \tag{3}$$

$$\partial_t B = \hat{\Omega}_z \,\partial_x A - \alpha \nabla^2 A + \beta \,\nabla^2 B, \tag{4}$$

known as the classic dynamo equations.

It is clear from (3-4) that the role of the pseudoscalar α is to turn the poloidal and toroidal field components into each other which implies some kind of helical motion. The classic candidate for this, suggested by Parker (1955) is the passive advection of fields by helical convective motions. Later, alternative mechanisms for an α -effect were also proposed, based on a dynamic interaction of field and motions (see Section 4.3 below). A general property of these mechanisms is that α turns out to be positive in the bulk of the solar convective zone in the northern hemisphere, while it tends to be negative in the stably stratified layer below. (Being a pseudoscalar, α changes sign between hemispheres.)

The shear $\hat{\Omega}$, associated with differential rotation, in turn, winds up the poloidal field into a toroidal component. Without the α and Ω terms we would be left with a diffusively decaying field, so at least one of these terms is necessary for dynamo action in both equations. Depending on which, if any, of the dynamo terms in (4) is discarded, we distinguish α^2 , $\alpha\Omega$ and $\alpha^2\Omega$ dynamos. α^2 dynamos can be shown to give rise to non-oscillatory behaviour and toroidal and poloidal field amplitudes of the same order of magnitude which does not agree with the properties of the solar dynamo. Thus, in what follows we will concentrate on $\alpha\Omega$ dynamos, neglecting the second term on the r.h.s. of (4). (Note, however, that under more general conditions than those considered here, oscillatory α^2 dynamos can also be constructed, as pointed out recently by Schubert & Zhang 2000.)

Assuming that beside α and β , $\hat{\Omega}_z$ can also be regarded constant, the system (3-4) is homogenous and linear, admitting wavelike solutions of the form

$$B = B_0 \exp\left[i(\omega t - \mathbf{k}\mathbf{x})\right] \tag{5}$$

$$A = A_0 \exp\left[i(\omega t - \mathbf{k}\mathbf{x} + \delta)\right] \tag{6}$$

where $\omega = \omega_R + i\omega_I$ is a complex frequency while all other variables are real. ω_R , A_0 and B_0 can be taken to be non-negative without loss of generality. Introducing the (signed) Reynolds numbers

$$R_{\alpha} = \alpha / \beta k \qquad R_{\Omega} = \hat{\Omega}_z / \beta k^2 \tag{7}$$

as well as the dynamo number and the nondimensional frequency

$$D = R_{\alpha}R_{\Omega} \qquad \tilde{\omega} = \omega/\beta k^2 \tag{8}$$

and substituting the Ansatz (5-6) into (3-4) we find

$$(1+i\tilde{\omega})A_0 = k^{-1}R_{\alpha}B_0 e^{-i\delta}$$
(9)

$$(1+i\tilde{\omega})B_0 = -ik_x R_\Omega A_0 e^{i\delta} \tag{10}$$

The product of these latter equations is

$$(1+i\tilde{\omega})^2 = -iDk_x/k \tag{11}$$

As only k_x appears in (10), no unstable modes (self-excited field or "dynamo waves") exist with $k_x = 0$. Remembering the way we oriented our xaxis this implies that dynamo waves propagate along isorotational surfaces. But in which direction? The imaginary part of (11) reads

$$2\tilde{\omega}_R(1-\tilde{\omega}_I) = -Dk_x/k \tag{12}$$

As for unstable modes (self-excited field or "dynamo waves") $\omega_I \leq 0$, (12) yields the important result

$$k_x D < 0, \tag{13}$$

known as the **Parker–Yoshimura sign rule**. Thus, e.g. in the northern hemisphere equatorward propagation $(k_x > 0)$ implies D < 0. With a positive α , as is the case in the bulk of the convective zone, this implies $\partial_r \Omega < 0$, an outward decreasing rotational rate. This was indeed the general expectation for the solar internal rotational law in the 1960's and 1970's.

The solution of (11) is

$$\tilde{\omega} = i \pm (1 - i)(-Dk_x/2k)^{1/2} \tag{14}$$

For unstable modes obviously the plus sign applies. So the growth rate is

$$-\tilde{\omega}_I = (-Dk_x/2k)^{1/2} - 1 \tag{15}$$

Unstable modes thus exist when $|D| \ge 2$ in nondimensional units. As according to equation (8) |D| decreases with k, it is the **lowest** k modes, with a scale comparable to the solar radius R_{\odot} that have the highest growth rate and will dominate the solution. (Note that this implies that our formalism, derived for the limit $kr \sin \theta \to \infty$, is strictly speaking invalid for these modes —nevertheless it may still be used for general guidance.)

Note that when $\tilde{\omega}_I = 0$, $\tilde{\omega}_R = 1$ follows from (14): the period of the critical mode is thus just the diffusive timescale corresponding to R_{\odot} . Estimating α and $\hat{\Omega}_z$ on the basis of helical convection and the observed differential rotation, D proves to be order of unity for a convection zone dynamo, showing that the dynamo is indeed approximately critical, and thus naturally explaining the agreement of the cycle period with the diffusive timescale.

Finally, let us note that it is straightforward to work out from the above formulae that for an equatorward propagating wave, the phase of the radial field component relative to the toroidal field is $-3\pi/4$ if $\alpha > 0$ in the northern hemisphere and $\pi/4$ otherwise (Stix 1976).

Taken altogether, the above considerations showed that for the expected positive α -effect in the solar convective zone, assuming an inwards increasing rotational rate, one can correctly reproduce the cycle period, the equatorward branches of the butterfly diagram as a dynamo wave, and the low-latitude phase relationship. (The high-latitude poleward branch could obviously be reproduced by assuming $\partial_r \Omega > 0$ there, though this line was not pursued, relying on the Babcock-Leighton approach instead.) All this gave the impression that, missing details apart, the basic mechanism of the solar dynamo is well understood.

2.2. Crisis

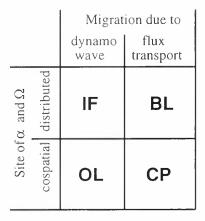
The first warning signs that something is amiss began to appear towards 1970, with the realization that most of the magnetic flux in the solar photosphere, and presumably below, is present in a strongly intermittent form, concentrated into strong flux tubes (Weiss 1964, Sheeley 1966, Stenflo 1973, Howard & Stenflo 1972). Flux tube theory developed in the 1970's and it became clear that for thicker flux bundles, owing to their lower surface/volume ratio, volume forces such as buoyancy, curvature and Coriolis forces dominate over the drag of the surrounding plasma flows acting on the surface. These tubes can then move largely independently of the surrounding flows, invalidating simple one-fluid descriptions like mean field theory. Thus, solar magnetic fields can be divided into two components: passive fields, consisting of thin flux fibrils, that move passively with the flow owing to the drag and are the subject of mean field theory; and active fields, consisting of thick flux bundles moving under the action of volume forces. And the characteristics of large active regions strongly suggested that they are essentially (fragmented) loops formed on toroidal flux bundles of 10^{22} Mx which clearly fall in the active category, outside the jurisdiction of mean field models.

What is more, Parker (1975) called attention to the fact that such flux bundles cannot be stored in the convective zone for a time scale comparable to the cycle period, being subject to buoyant instabilities that can rapidly remove the whole tube from the zone. The only place to store these tubes is near the bottom of the convective zone, especially in the stably stratified but still turbulent lower overshoot layer below it. Toroidal flux tubes lying here may still develop finite-wavelength buoyant instabilities that may give rise to loops erupting through the convective zone into the atmosphere, producing active regions. This scenario has gained firm foundations with the first nonlinear calculation of the emergence of such loops through the convective zone (Moreno-Insertis 1986), and such flux emergence models have by now evolved into an independent chapter of the global dynamo problem. In the present review we will not deal with this topic in detail (see the review by Moreno-Insertis 1994), even though flux emergence models are the only real "success story" of dynamo theory since the 1960's. While many details are still unclear, by now these models can reproduce sunspot proper motions and active region flux distributions to a quite convincing detail. A very robust main conclusion from the models, of great importance for the global dynamo, is that in order to reproduce the observed characteristics of active regions the toroidal flux tubes must have a field strength of about 10⁵ G —an order of magnitude higher than the turbulent equipartition field in the deep convective zone. Explaining the origin of such strong fields is a major challenge for dynamo theory.

Guided by these realizations, in the 1980's the first attempts were made to construct dynamos operating in the lower overshoot layer. The unknown profiles of α and the differential rotation, however, greatly impeded progress, allowing a far too wide parameter space to play with. Therefore, attempts were made to numerically simulate the whole convective zone, with a consistent picture of differential rotation, helical convection, and dynamo (Glatzmaier 1985). Nevertheless, the results (poleward propagating dynamo waves) were at odds with the observations, and when finally even the predicted differential rotation profile (constant on cylinders) was proven wrong by helioseismic measurements (constant on cones), the simulational approach was abandoned (cf. the remarks in Section 5).

On the other hand, the helioseismic determination of internal differential rotation gave new impetus to mean field dynamo theory. Those inversions clearly showed that most of the shear (the Ω -effect) is concentrated in a thin layer near the bottom of the convective zone, known as the tachocline. This was seen as further evidence that a thin layer situated about 200 000 km below the solar surface is of key importance for the working of the solar dynamo. Depending on the physical viewpoint we study it from, this layer is alternatively called dynamo layer, overshoot layer or tachocline. In the present review for simplicity I will refer to it as the DOT (Dynamo — Overshoot — Tachocline) layer.

Table 1: A classification scheme for solar dynamo models



3. MAIN FAMILIES OF MODELS

Solar mean field dynamo theory in the past decades gave rise to a bewildering variety of models. Nevertheless, all recent models (i.e. those using the helioseismic rotation law) can be classified into just four main types according to a plausible classification scheme (Table 1 and Figure 2). One classification parameter here divides the models according to whether they still interpret the butterfly diagram as a dynamo wave just like the orthodox convection zone dynamos did, or if they substitute that with some flux transport mechanism (meridional circulation or pumping). The other parameter in turn divides the models according to whether the α - and Ω effects are cospatial or "distributed", i.e. they take place in different (adjacent or very distant) parts of the model volume. The resulting four model types are as follows.

3.1. Cospatial wave models: OL dynamos

Widely known as "overshoot layer" or OL dynamos, these are perhaps the most conservative models that

simply replant the concepts of the convective zone dynamos of the 1960's and 70' into the DOT layer. As the helioseismic inversions show $\partial_r \Omega > 0$ at low latitudes, these models need to assume $\alpha < 0$ to get the right migration directions. This assumption is rather plausible in the DOT layer for several different physical mechanisms for α . The state-of-the-art in this approach is represented by the model of Rüdiger & Brandenburg (1995).

Successes:

 The butterfly diagram comes out right. The Parker-Yoshimura rule leads to polar and equatorial branches separated at the corotational latitude, as observed.

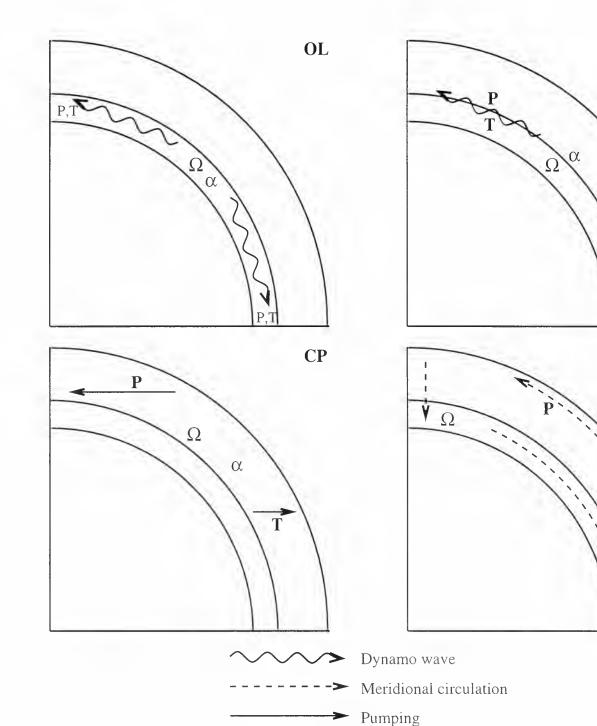
Difficulties:

- The low-latitude phase dilemma: as now $\alpha < 0$, the radial field is found to be nearly in phase with the toroidal field, instead of being in antiphase as observed.
- The cycle period tends to be too short for thin layer models. This is basically because the same amount of differential rotation is now concentrated in a much thinner layer, leading to much stronger shear and much higher dynamo numbers. This may be compensated by reducing α , e.g. by arguing that, as nonlinear effects act via a quenching of the α and Ω mechanisms, it is natural to expect that after saturation the dynamo will be effectively critical. Yet the degree to which the nonlinearity can increase the cycle period depends a lot on the assumptions made, and in general it does not seem sufficient (Rüdiger 1994). At any rate, certain "tricks", such as using an $\alpha^2 \Omega$ dynamo (Gilman et al. 1989) or introducing an intermittence factor (Rüdiger & Brandenburg 1995), can save the models, but then the crude coincidence of the period with the lateral diffusive timescale is coincidental.
- For an equatorial confinement of strong fields the α -effect needs to be arbitrarily confined to low latitudes. Nevertheless, such α distributions are indeed found in some calculations (cf. Schmitt 1993).

3.2. Distributed wave models: IF dynamos

Parker (1993) suggested a dynamo where the diffusivity discontinuously varies by many orders of magnitude across a surface. The α -effect operates on the high-diffusivity side of the interface, while the Ω effect (shear) is limited to the low-diffusivity side. He showed that under these conditions a dynamo wave can be excited, obeying the Parker-Yoshimura sign





IF

BL

Figure 2: Schematic illustration of the main features of main solar dynamo families. The sites of α and Ω effects and toroidal/poloidal field transport mechanisms and directions are shown in a meridional quadrate. The internal layers marked schematically are. from the inside outwards, the radiative, DOT and convective layers. **OL**: Overshoot layer dynamos; **IF**: Interface dynamos; **CP**: Cospatial pumping models; **BL**: Babcock-Leighton type models;

Buoyant emergence

rule. The attractive feature of this model is that the toroidal field generated on the low diffusivity side can be made arbitrarily strong by reducing the value of magnetic diffusivity there. Thus, the origin of 10^5 G fields could be explained.

Parker's analytic, plane parallel model has been extended to more realistic situations and incorporated in full solar dynamo models in a number of papers (Charbonneau & MacGregor 1997, Markiel & Thomas 1999). Unfortunately, the results are somewhat contradictory owing to numerical problems related to modelling the discontinuity. In this context we may perhaps note that the main physical difference of these IF models compared to the OL models is the spatial separation of α and Ω . The introduction of a discontinuity between them is an added feature that can simplify the analytic treatment but at the same time complicate the numerical calculations. A model where the diffusivity is continuously distributed, albeit with a sharp gradient, with α and Ω concentrated on the two sides of this gradient, may well be worth considering. Beside being more realistic, such a model might also avoid the numerical problems mentioned.

Successes:

- Strong toroidal fields can be readily explained.

Difficulties:

At the present stage, numerical difficulties prevail. An evaluation of the physical performance of the models will only be possible after these are resolved.

3.3. Cospatial transport models: CP dynamos

In an inhomogeneous medium, the proper expression of $\vec{\mathcal{E}}$ is more general than equation (2), the scalars α and β being substituted by tensorial expressions. A tensorial $\hat{\alpha}$ -term in (2) can then alternatively be written as

$\hat{\alpha}\mathbf{B} = \alpha\mathbf{B} + \hat{\alpha}_{S}\mathbf{B} - \vec{\gamma} \times \mathbf{B}$

where $\alpha = \text{Tr } \hat{\alpha}$, the last term is the vectorial product equivalent of the action of the antisymmetric part of $\hat{\alpha}$ on **B**, and $\hat{\alpha}_S$ is the symmetric and traceless part of $\hat{\alpha}$. Substituting (2) into (1) we see that the role of $-\vec{\gamma}$ is analoguous to that of **U**, i.e. it formally describes an advection of the magnetic field. This effect is called the (normal) *pumping* of the field along the inhomogeneity. The $\hat{\alpha}_S$ -term can be shown to give rise to a similar effect with the difference that the sign of the transport depends on the orientation of the field component perpendicular to the pumping direction (anomalous pumping; see Petrovay 1994 for a detailed discussion). It must be stressed that the descriptions using a tensorial alpha and those using pumping effects are formally equivalent. The advantage of the pumping formalism is that it helps one to get a physical "feeling" of the processes at work.

Depending on the particular inhomogeneity associated with the pumping, one can speak of density pumping, turbulent pumping etc. It was suggested by Krivodubskij & Kichatinov (1991) that, instead of appealing to a dynamo wave, the field migration patterns can also be interpreted by density pumping. directed towards the rotational axis for poloidal fields and away from it for toroidal fields. This pumping is supposed to operate throughout the convective zone, instead of being confined to the DOT layer. A more detailed model along these lines has recently been constructed by Kitchatinov et al. (1999). While the model reproduces well the phase relation for the torsional oscillations, it does not even address questions such as the origin of the deep-seated toroidal field. Thus, while the basic concept is interesting, at the present stage this "cospatial pumping" approach cannot be regarded as a serious aspirant for the explanation of the global dynamo.

3.4. Distributed transport models: BL dynamos

These are generally known as "Babcock-Leightontype" models (hence the BL code). While they indeed grew out of the semiempirical approach of Babcock (1961) and Leighton (1964) to the solar cycle. they did get a lot more radical in the 1990's. Indeed, in the era of convective zone dynamos, in the 1960's and 70's, the Babcock-Leighton approach was not seen as necessarily conflicting with the dynamo wave theory of the cycle. With a dynamo operating throughout the convective zone, the α -effect caused by the inclination of active region axes relative to E-W (which is the cornerstone of this approach) could be considered as helical convection caught in the act: and in his mathematical formulation of the model Leighton (1964) explicitly assumed that the toroidal field migration is the result of a dynamo wave. It was only the poleward migration of the poloidal field that was interpreted in terms of a lateral transport.

In subsequent versions of the model, meridional circulation plays the main role in transporting the poloidal fields to the poles near the surface. And from here it was just one step to close the circle and assume that the deep return flow of meridional circulation is responsible for the equatorward drift of the toroidal field. This step, made by Wang *et al.* (1991) was radical indeed: it represented the first break with the canonical interpretation of the butterfly diagram as a dynamo wave, generally accepted for three decades. The model essentially works like a conveyor belt: the poleward meridional circulation near the surface transports the poloidal fields towards the poles at high latitudes, giving rise to the poleward branch of the butterfly diagram. At the poles, the fields are advected down to the bottom of the convective zone where the shear converts them into toroidal fields that get amplified while advected towards the equator. Once these are strong enough, they are supposed to form buoyantly emerging loops at low latitudes that give rise to active regions, the Coriolis force lending an inclination to the loop planes, i.e. introducing an α -effect, and thus regenerating the poloidal field.

More recent versions of the model (Choudhuri et al. 1995, Dikpati & Charbonneau 1999) have developed it into an internally consistent modelling approach with the ambition of yielding a complete description of the solar cycle. As such, this family of models is at present the most serious competitor of the OL class.

Successes:

- The low-latitude confinement of strong activity comes out rather naturally. (The toroidal field is amplified by shear as it is advected equatorward.)
- A tolerable reproduction of the extended butterfly diagram (although the latitude where the two branches part tends to be too high). Note, however, that the original (one-dimensional) Babcock-Leighton models gave a much closer fit to the observed migration patterns, which was their main asset. In the extension to two dimensions, BL dynamos had to sacrifice this achievement.

Difficulties:

- The agreement of the corotational latitude with the latitude where the butterfly branches diverge must be considered coincidental (if reproduced at all).
- The α -effect is confined to the surface. This is probably unrealistic even for flux tube alpha, cf. the discussion in Section 4.3 below.
- The model, as all models relying on a flux tube alpha, is not self-exciting, as this α -effect works for strong fields only. It needs another dynamo mechanism to "kick it in".
- A serious problem is that the approach only works with an unrealistically low value for the turbulent diffusivity in the convective zone, $\beta \sim 10 \,\mathrm{km^2/s.}$ (This is needed to keep the two parts of the "conveyor belt" separated. In fact the main difference between the BL and IF models is that the separated seats of

 α and Ω communicate by diffusion in the IF models.) There is no justification for such a low value. On physical grounds, $\beta \sim 0.5 lv \simeq 500 \,\mathrm{km^2/s}$ is expected —indeed, even the one-dimensional Babcock–Leighton models predicted 600 km²/s. According to the controversial proposal of Vainshtein & Rosner (1991), on the other hand, the diffusivity should have been quenched by *many* orders of magnitude to values far lower than those used in the BL models. (Note that by now this question has been settled: diffusivity suffers no strong quenching in realistic, intermittent fields in three dimensions, Gruzinov & Diamond 1994, Petrovay & Zsargó 1998.)

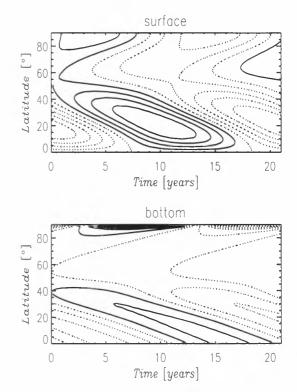


Figure 3: Steamy window: with realistic turbulent transport parameters, an arbitrary time-dependent poloidal field pattern imposed at the bottom of the convective zone is reflected, somewhat blurred, at the surface. After Petrovay & Szakály (1999)

One may wonder if the effect of the strong diffusive link can be reduced by some kind of selective field pumping that would keep the two field components apart. Petrovay & Szakály (1999) investigated this possibility in a model of poloidal field transport, incorporating all known transport effects (circulation, diffusion, turbulent pumping, density pumping). It turns out that diffusion is dominant. forging such a strong link between the DOT region and the surface that any migration pattern imposed at the bottom will be reflected at the top (Fig. 3). This seems to represent a serious difficulty for BL models.

4. KEY ISSUES

4.1. Structure of the DOT region

It is obvious from the above model descriptions that a thorough understanding of the structure and dynamics of the DOT layer is crucial for advance in solar dynamo theory. Unfortunately, at present we do not have a reliable model for this layer. As a complicated interplay of convection, rotation and magnetic fields is expected there, as a first step one would expect to develop models for just one aspect of the problem: a model for overshoot with no rotation and magnetic fields; a non-magnetic model for the tachocline with no overshoot; etc. Nevertheless, we lack even such simplistic models, and surprisingly little effort is made to construct them.

In the case of overshoot, the way to construct such a model is in principle well known: it consists in solving a conveniently truncated hierarchy of the Reynolds stress equations. Marik & Petrovay (2000) present preliminary results from a numerical study of this problem.

Helioseismic inversions show that the thickness of the tachocline is about $0.1 R_{\odot}$. This is puzzling, as even in the absence of turbulent diffusion, the Eddington-Sweet circulation should have mixed these layers enough in $4.6 \cdot 10^9$ years to extend the tachocline to much greater depths (Spiegel & Zahn 1992). It is most often assumed that the solution to this "thin tachocline problem" resides in anisotropic turbulence: an extremely strong horizontal anisotropy would indeed effectively smooth out horizontal gradients without contributing much to the vertical transport. But in view of strong nonlinear mode coupling in turbulence, such an extreme anisotropy seems dubious. Forgács-Dajka & Petrovay (2000) explore the alternative possibility that the necessary horizontal momentum transfer is due to an inverse A-effect: however, the necessary amplitude of Λ proves even more unrealistically large. Magnetic decoupling of the envelope from the radiative interior is a third explanation put forward by Rüdiger & Kitchatinov (1997).

4.2. High-latitude field patterns

In order to be able to decide between various dynamo models, one needs an issue on which they yield conflicting predictions that are relatively easy to test. One such case is the migration of the toroidal field at high latitudes. In dynamo wave (OL and IF) models at high latitudes all field components migrate polewards, following the Parker–Yoshimura rule. In contrast, the toroidal field in BL models typically shows

an equatorward migration, advected by the return flow of meridional circulation near the bottom of the convective zone. Thus, if a clear signature of migrating high-latitude toroidal fields were found. this could solve the problem in either way, depending on the direction of migration. It is often claimed (e.g. Harvey 1994) that high latitude ephemeral active regions show an equatorward migration. But a closer examination of such claims shows that they are based only on the fact that high latitude ephemeral regions as a whole tend to lie in the backwards extension of the low-latitude butterfly "wings" (just as polar faculae do), and not on a detailed study of migration patterns among high-latitude regions only. On the other hand, Callebaut & Makarov (1992) claim that at least 50% of polar faculae (well known for their poleward drift) correspond to dipoles with a preferential east-west orientation, thus forming part of the toroidal field. It has even been claimed that the highest-latitude part of the sunspot butterfly diagram also shows a poleward drift (Becker 1959). A clarification of this issue would clearly be important.

A related problem is the origin of ephemeral active regions in general. If they are used as magnetic tracers we would obviously like to know what kind of field do they trace?

4.3. Origin and profile of α

It is sometimes claimed that the origin of the α effect assumed is a basic difference between various dynamo models, so that excluding a certain α mechanism amounts to excluding a dynamo variety. In reality, our knowledge of all possible types of α effects is so scarce that wildly differing α -profiles can be derived for the same mechanism, depending on particular modelling assumptions. And vice versa: a given profile, used as input in a dynamo model, may be the consequence of various α -mechanisms.

More in-depth study of the possible α -mechanisms that can reduce this uncertainty could nevertheless really be used to constrain dynamo models in the future. For now, I will argue that, independently of its mechanism, α should be expected to be concentrated towards the bottom of the convective zone, or at least to pervade it uniformly (and not to be concentrated to the surface, as assumed in BL models). Let us see this for the three α -mechanisms that have been proposed.

- Cyclonic convection. In this classic variety of the α -effect, proposed by Parker (1955), α results from the effect of rotation on convection, so it increases with the Coriolis number, peaking near the bottom of the solar convective zone. Its sign is positive in the unstable layer and negative in the overshoot layer below.

- Magnetostrophic waves. This mechanism was proposed by Schmitt (1987) specifically to suggest an alternative α -mechanism for the overshoot layer that will not be suppressed by the strong toroidal fields there. It consists in growing helical waves and its sign is negative, as required by the dynamo wave models. More detailed calculations of its profile were performed by Ferriz Mas & Schüssler (1994), though the results may rely too heavily on the background stratification of the (incorrect) overshoot model used.
- Flux loop alpha. The magnetix flux loops emerging through the convective zone and creating the active regions are essentially largeamplitude nonlinear versions of the above mentioned unstable magnetostrophic waves, giving rise to a similar (but positive) α -effect. It is clear that after their decay, owing to their tilt, active regions contribute to the passive poloidal field. But is this contribution limited to the surface, or do the "feet" of the loop similarly decay, down to the bottom of the convective zone? This problem relates to the next subsection, but one expects that the eroding action of external turbulence (Petrovay & Moreno-Insertis 1997) will lead to the decay of the whole loop, thereby extending the α -effect down to its footpoints. In fact, our turbulent erosion calculations show that 90% of the magnetic flux in an emerging flux loop is lost before it reaches the surface! This lost flux, already submitted to the action of Coriolis force, should contribute to the poloidal field and to the α -effect far more than the actual active regions. And then we did not even mention the possibility of "failed active regions": flux loops that, their field strengths being too weak, never make it to the surface (Petrovay & Szakály 1993, Moreno-Insertis et al. 1995). All this strongly speaks for a flux loop α concentrated to the bottom of the convective zone.
- Unstable Rossby waves. Recently, Dikpati & Gilman (2000) considered a shallowwater model of the tachocline, analysing the behaviour of small perturbations of its geostrophic equilibrium state. They find that such large-scale perturbations are unstable if the subadiabaticity is low enough and they are characterized by a correlation between the vertical components of velocity and vorticity, i.e. by a non-vanishing mean helicity. In other words, these perturbations essentially behave like global-scale unstable Rossby waves, and owing to their mean helicity they can be expected to yield an α -effect.

4.4. The ultimate fate of emerged flux

This problem is interesting in its own right, as well as because of its importance for the α -effect problem. Once the active region has decayed, what happens to the "trunks" of the magnetic trees? Will they just stay there, "bleeding"? Will they reconnect and be drawn back below the convective zone? Or will they also decay? As indicated above, the turbulent erosion models (Petrovay & Moreno-Insertis 1997) seem to support the latter possibility. At any rate, thorough observational studies of the active region decay (cf. the review by van Driel-Gesztelyi 1999) may shed more light on this problem.

5. CONCLUSION: ...AND THE SIMULATIONS?

As we have seen, there is still no really convincing answer to the question "What makes the Sun tick?". Several conflicting approaches exist, none of which can fully explain the observed features of the solar cycle and all of which rely on some more or less arbitrary assumptions. In contrast to the optimistic outlook of about three decades ago, nothing seems safe now, not even the dynamo wave origin of the sunspot butterfly diagram. And the prospects do not seem to promise a spectacular change in this situation in the near future.

A number of previous reviews (e.g. Weiss 1994) expressed the view that the ultimate solution to the solar dynamo problem should be expected from numerical hydrodynamical simulations. So the reader may ask: why was the simulational approach hardly even mentioned in this review? Why is it that only mean field models were treated? The answer does not lie in the (undeniable) bias of the author but in the fact that in the past decade there simply have not been any numerical simulations constructed with the ambition of producing a global model for the solar cycle. As we indicated above, such attempts were made back in the 1980's; but, after their failure in reproducing the butterfly diagram and the internal rotation profile became clear, this line of research was completely abandoned. Those very few hydrodynamical simulations in the 1990's that had some direct bearing on the solar dynamo problem aimed at the modelling of smaller volumes inside the convective zone with the main purpose of studying the fine structure and transport of the magnetic field (Nordlund et al. 1992, Tobias et al. 1998, Dorch & Nordlund 2000).

The belief in the "miraculous healing power" of simulations may indeed have been too zealous before. After all, even in an ideal future where an infinite computing potential would make it feasible to make a 3D direct numerical simulation of the whole Sun for $4.6 \cdot 10^9$ years, the result would have no more direct benefit for us (apart from demonstrating that the laws of classical magnetohydrodynamics are indeed sufficient to describe solar phenomena) than offering a chance to determine any physical quantity at any internal point of our star with arbitrary precision. This feat, though far beyond the possibilities of contemporary observational solar physics, is still basically experimental work that, though important. in no way can substitute "real" theory.

And yet, the other extreme, represented by the present complete abandonment of the simulational approach, is just as lamentable as its opposite. This is especially so as the great advance in the geodynamo problem I referred to in the Introduction can mainly be attributed to the success of numerical simulations. The following pseudo-historical quote by Borges fits nicely the present situation in this respect.

Jorge Luis Borges:

On Rigour in Science

...In that Empire, the Art of Cartography achieved such Perfection that the map of a single Province occupied a whole City, and the map of the Empire, a whole Province. With time, these Gigantic Maps proved unsatisfactory and the Colleges of Cartographers set up a Map of the Empire that had the size of the Empire and coincided with it point by point. Less addicted to the Study of Cartography, the Following Generations considered this extensive Map useless and, not without Disrespect, they abandoned it to the Mercy of the Sun and of the Seasons. In the Western deserts broken Ruins of the Map still persist, inhabited by Animals and Beggars; in all the Country no other Relicts of the Geographic Disciplines remain.

> SUÁREZ MIRANDA: Viajes de varones prudentes, libro cuarto, cap.XLV, Lérida, 1658

Acknowledgements

This work was funded by the FKFP project no. 0201/97, and the OTKA project no. T032462.

References

Babcock, H. W. 1961, ApJ 133, 572

Becker, U. 1959, Z. für Astrophys. 48, 88

Belvedere, G. 1985, Sol. Phys. 100, 363

Callebaut, D. K., Makarov, V. I. 1992, Sol. Phys. 141, 381

Charbonneau, P., MacGregor, K. B. 1997, ApJ 486, 502

Choudhuri, A. R., Schüssler, M., Dikpati, M. 1995, A&A 303, L29

Cowling, T. G. 1981, ARA&A 19, 115

Dikpati, M., Charbonneau, P. 1999, ApJ 518, 508

Dikpati, M., Gilman, P. A. 2000, preprint

Dorch, B., Nordlund, A. 2000, astro-ph/0006358

Ferriz Mas, A., Schüssler, M. 1994, A&A 433, 852

Forgács-Dajka, E., Petrovay, K. 2000, in P. L. Pallé A. Wilson (Eds.), Helio- and Asteroseismology at the Dawn of the Millennium, ESA Publ., in press

Gilman, P. A., Morrow, C. A., De Luca, E. E. 1989, ApJ 338, 528

Glatzmaier, G. A. 1985, ApJ 291, 300

Glatzmaier, G. A., Roberts, P. H. 1995, Nature 377, 203

Gruzinov, A. V., Diamond, P. H. 1994, Phys. Rev. Lett. 72, 1651

Harvey, K. L. 1994, in R. J. Rutten C. J. Schrijver (Eds.), Solar Surface Magnetism, NATO ASI Series, Kluwer, Dordrecht, p. 347

Howard, R., Stenflo, J. O. 1972, Sol. Phys. 22, 402

Kitchatinov, L. L., Pipin, V. V., Makarov, V. I., Tlatov, A. G. 1999, Sol. Phys. 189, 227

Krause, F., Raedler, K.-H. 1980, Mean Field Magnetohydrodynamics and Dynamo Theory, Akademie-Verlag, Berlin

Krivodubskij, V. N., Kichatinov, L. L. 1991, in I. Tuominen, D. Moss, G. Rüdiger (Eds.). The Sun and Cool Stars: Activity, Magnetism, Dynamos, Proc. IAU Coll. 130, Springer, Berlin, p. 190

Kuang, W., Bloxham. J. 1997. Nature 389. 371

Leighton, R. B. 1964, ApJ 140, 1547

Makarov, V. I., Sivaraman, K. R. 1989. Sol. Phys. 123, 367

Marik, D., Petrovay, K. 2000, in P. L. Pallé A. Wilson (Eds.), Helio- and Asteroseismology at the Dawn of the Millennium. ESA Publ., in press

Markiel, J. A., Thomas, J. H. 1999, ApJ 523, 827

Moreno-Insertis, F. 1986, A&A 166, 291

Moreno-Insertis, F. 1994, in M. Schüssler W. Schmidt (Eds.), Solar Magnetic Fields, Proc. Freiburg Internat. Conf., Cambridge UP, p. 117

Moreno-Insertis, F., Caligari, P., Schüssler, M. 1995, ApJ 452, 894

Nordlund, Å., Brandenburg, A., Jennings, R. L., Rieutord, M., Ruokolainen, J., Stein, R. F., Tuominen, I. 1992, ApJ 392, 647

Olson, P., Christensen, U., Glatzmaier, G. 1999, J. Geophys. Res. 104, 10383

Parker, E. N. 1955, ApJ 122, 293

Parker, E. N. 1975, ApJ 198, 205

Parker, E. N. 1993, ApJ 408, 707

Petrovay, K. 1994, in R. J. Rutten C. J. Schrijver (Eds.), Solar Surface Magnetism, NATO ASI Series C433, Kluwer, Dordrecht, p. 415; also astro-ph/9703154

Petrovay, K., Moreno-Insertis, F. 1997, ApJ 485, 398

Petrovay, K., Szakály, G. 1993, A&A 274, 543

Petrovay, K., Szakály, G. 1999, Sol. Phys. 185, 1

Petrovay, K., Zsargó, J. 1998, MNRAS 296, 245

Rüdiger, G. 1994, in M. Schüssler W. Schmidt (Eds.), Solar Magnetic Fields, Proc. Freiburg Internat. Conf., Cambridge UP, p. 77

Rüdiger, G., Brandenburg, A. 1995, A&A 296, 557

Rüdiger, G., Kitchatinov, L. L. 1997, Astr. Nachr. 318, 273

Schmitt, D. 1987, A&A 174, 281

Schmitt, D. 1993, in F. Krause, K.-H. Rädler, G. Rüdiger (Eds.), The Cosmic Dynamo, IAU symp. 157, Kluwer, Dordrecht, p. 1

Schubert, G., Zhang, K. 2000, ApJ 532, L149

Sheeley, N. R. 1966, ApJ 144, 723

Spiegel, E. A., Zahn, J.-P. 1992, A&A 265, 106

Steenbeck, M., Krause, F., Rädler, K.-H. 1966, Zs. Naturforschung A 21, 369

Stenflo, J. O. 1973, Sol. Phys. 32, 41

Stix, M. 1976, A&A 47, 243

Tobias, S. M., Brummell, N. H., Clune, T. L., Toomre, J. 1998, ApJ 502, L177 Vainshtein, S. I., Rosner, R. 1991, ApJ 376, 199

van Driel-Gesztelyi, L. 1999, ASP Conf. Series 155, 202

Wang, Y.-M., Sheeley, N. R., Nash, A. G. 1991, ApJ 383, 431

Weiss, N. O. 1964, Phil. Trans. Roy. Soc. A 256, 99

Weiss, N. O. 1994, in M. R. E. Proctor A. D. Gilbert (Eds.), Lectures on Solar and Planetary Dynamos, Cambridge UP, p. 59

THE SOLAR CYCLE IS MORE THAN SKIN DEEP!

R. Komm, R. Howe, and F. Hill

National Solar Observatory, 950 N. Cherry Ave., Tucson, AZ 85719, U.S.A. tel: +1 520-318-8428 / fax: +1 520-318-8400 e-mail: komm@noao.edu / rhowe@noao.edu / hill@noao.edu

ABSTRACT

The solar rotation in the upper third of the convection zone shows a temporal variation that is clearly related to the solar cycle and resembles the so-called "torsional oscillation" known from measurement of the solar surface. Near the base of the convection zone, the equatorial rotation rate shows a temporal variation with a period of about 1.3 years. The strong correlation between the even-a coefficients, which sense the asphericity of the Sun, and the corresponding component of the surface magnetic field appears to be an effect of the solar surface. The total mode energy decreases substantially with increasing activity, while the total energy supply rate decreases only slightly. We speculate that the excess of the supplied energy might contribute to the irradiance variation.

Key words: Sun: activity; Sun: interior; Sun: oscillations.

1. INTRODUCTION

With helioseismic observations from the Global Oscillation Network Group (GONG) project and the Solar Oscillations Investigation (SOI) using the Michelson Doppler Imager (MDI) aboard the Solar and Heliospheric Observatory (SOHO) spacecraft covering about five years, we have data sets available which allow us to study the solar interior and its temporal variation with unprecedented detail. Here, we present a brief summary of recent results.

The acoustic modes are described in spherical harmonics characterized by the radial order n, the number of nodes in radial direction, the degree l, the number of node lines on the solar surface, and the azimuthal order m, the number of node lines through the poles. Each (n, l) multiplet contains (2l + 1)modes of different m. The degeneracy of these modes is lifted by symmetry-breaking processes such as rotation and asphericity. The frequencies ν_{nlm} of the modes within a multiplet are usually expressed as an expansion in orthogonal polynomials:

$$\nu_{nlm} = \nu_{nl} + \sum_{j=1}^{j_{max}} a_j(n,l) P_j^{(l)}(m) , \qquad (1)$$

where ν_{nl} is the central mode frequency, the $P_j^{(l)}(m)$ are orthogonal polynomials, for example Legendre or Clebsch-Gordan (see Ritzwoller & Lavely, 1991 and Schou et al., 1994), and $a_j(n,l)$ are the so-called *a*-coefficients. The odd-order coefficients describe the internal rotation of the Sun, while the even-order coefficients sense the asphericity of the solar structure, expressed in parameters such as sound speed or temperature.

The acoustic modes are thought to be stochastically excited by the release of acoustic energy from sources near the top of the turbulent convection zone (see, for example, Rast, 1999 and Stein & Nordlund, 1998). The mode area and width, as measured in a power spectrum, can be used to estimate the combined kinetic and potential mode energy and the rate at which energy is supplied to the modes.

In the following sections, we briefly describe the GONG and MDI data sets and the analysis techniques. We then focus on the temporal variations found in helioseismic observations. We discuss the temporal variation of the internal solar rotation, the variation of the even-a coefficients, and finally the variation of the mode energy and the energy supply rate.

2. DATA AND ANALYSIS

We used 45 GONG data sets processed through the GONG pipeline (Hill et al., 1996) covering the period 1995 May 7 to 1999 December 23. Each data set covers 108 days and consecutive data sets overlap by 36 days. The mode parameters for each mode, characterized by radial order n, spherical harmonic degree l, and azimuthal order m, were estimated from

^{*}Operated by AURA, Inc. under a cooperative agreement with the National Science Foundation

Proc. 1st Solar & Space Weather Euroconference, 'The Solar Cycle and Terrestrial Climate', Santa Cruz de Tenerife, Tenerife, Span, 25-29 September 2000 (ESA SP-463, December 2000)

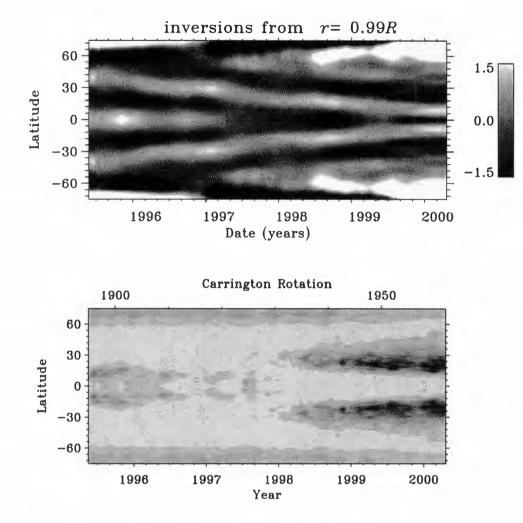


Figure 1. Top: Temporal and latitudinal variation of the residual rotation rate at radius $0.99R_{\odot}$ (after subtracting a temporal average) of the combined GONG and MDI data sets. Bottom: The magnetic flux from NSO Kitt Peak synoptic maps symmetrized around the equator (dark grey indicates high activity).

the 108-day power spectra using the standard GONG analysis (Anderson, Duvall, & Jefferies, 1990), which fits modes up to l = 150. We used only fits that passed the quality tests of the peak-fitting algorithm described in detail by Hill et al. (1998). The frequencies within each multiplet were then fitted to a polynomial series to obtain the *a* coefficients. The MDI data sets consist of 18 non-overlapping 72-day time series covering the period 1996 May 1 to 2000 April, 9, with two interruptions due to problems with the *SOHO* satellite. From the MDI data, the *a* coefficients were determined by directly fitting the multiplets in Fourier spectra up to l = 200 (Schou et al., 1994).

The odd-*a* coefficient sets were inverted using the twodimensional regularized least-squares (RLS) method and the two-dimensional subtractive optimally localized averages (OLA) method (Schou et al., 1998, and references therein), resulting in estimates of the rotation rate on, for example, a 51×49 point grid in radius and latitude. The grid points are spaced evenly in latitude, while the radial spacing depends on the sound speed and, as a consequence, the grid points are more closely spaced near the surface. To calculate rotation-rate residuals, we subtracted an error-weighted temporal mean, calculated for each grid point, from the inversion results.

The even-*a* coefficients were inverted for sound speed with a two-dimensional method (Antia & Basu, 1994) using only modes with frequencies between 1.5 to 3.5 mHz and even coefficients up to a_{14} . The higher order coefficients do not appear to be significant, at least for GONG data. This estimates the sound speed on a 16×10 grid in radius and latitude. We note that the inversion kernels are nearly the same for sound speed and magnetic field (see Figure 10 in Dziembowski et al., 2000). Thus, the inversion could have been done for either quantity or a combination of them, for a discussion see Antia et al. (2000) or Dziembowski et al. (2000).

To calculate the mode energy and the energy supply rate, we determined the mode width, Γ , and amplitude, A, for each (l, n) multiplet as a weighted average over all successfully fitted m values in the GONG data sets. We corrected for the effects of the spatial mask used in the reduction of GONG data and the gaps in the time series (Komm, Howe, & Hill, 2000a). The mode energy, E, is proportional

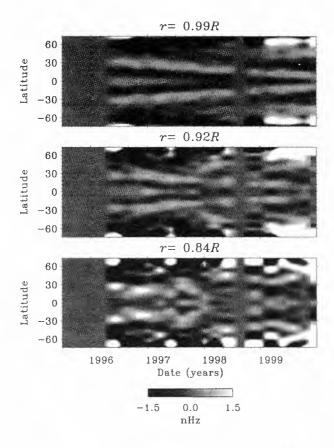


Figure 2. Top: Temporal and latitudinal variation of the residual rotation rate at three different depths $(0.99R_{\odot}, 0.92R_{\odot}, 0.84R_{\odot})$ of OLA inversions from the MDI data sets.

to mode width times amplitude, $E \propto A\Gamma$, and the energy supply rate, dE/dt, is proportional to mode energy times mode width or $dE/dt \propto A\Gamma^2$ (Goldreich, Murray, & Kumar, 1994; Christensen-Dalsgaard et al., 1996). The conversion factors used for GONG data are described in Komm, Howe, & Hill (2000b).

As in previous work, we used the magnetic flux (in Gauss) from the NSO Kitt Peak synoptic charts¹ as activity measure.

3. RESULTS

3.1. Temporal variation of the internal rotation

In this Section, we discuss the temporal variation of the residual rotation rate from near surface layers to the base of the convection zone. Figure 1 shows the temporal and latitudinal variation of the residual rotation rate at radius $0.99R_{\odot}$ (after subtracting a temporal average) of the combined GONG and MDI data sets. Bands of faster- and slower-thanaverage rotation move equatorward during the course of the solar cycle in a manner reminiscent of the so-called "torsional oscillation" pattern observed in Doppler measurements of the solar surface (Howard & LaBonte, 1980; Snodgrass, 1984; Ulrich, 1998). The rms-variation is less than 1% of the average rotation which agrees with surface measurements. The corresponding variation of the magnetic flux symmetrized around the equator (bottom panel) shows that the bands of faster-than-average rotation are located equatorward of the location of high magnetic activity in agreement with surface Doppler observations.

Figure 2 shows the temporal and latitudinal variation of the residual rotation rate at three different depths of inversions from the MDI data sets. The torsional oscillation pattern extends down to at least 8% ($r = 0.92R_{\odot}$) or the upper third of the convection zone; this pattern is not a surface phenomenon. The existence of this pattern in the upper part of the convection zone is by now well-established (Howe et al., 2000a; Howe, Komm, & Hill, 2000; Toomre et al., 2000; Antia & Basu, 2000).

In Figure 3, the residuals in equatorial rotation rate near the base of the convection zone show a periodic variation with a period of about 1.3 year (Howe et al., 2000b). The solid line represents the main component of an empirical mode decomposition (EMD) of the GONG data (Komm et al., 2000). The MDI data alone do not show the periodic behavior, which comes as no surprise since the current analysis of 72-day non-overlapping data sets does not provide sufficient temporal resolution. However, with one or two exceptions, the MDI data coincide with the EMD component (solid line). This unexpected periodicity might have implications for the understanding of solar magnetic activity, since the dynamo is expected to operate near the tachocline, the interface between convection zone and radiative interior.

3.2. Temporal variation of the sound speed

Figure 4 shows the temporal variation of the mean even a coefficients. The even-a coefficients show a good correlation with the corresponding components of the magnetic activity up to a_{14} . For higher order coefficients, the correlation breaks down, most likely due to the increasing difficulty in fitting higher order coefficients to noisy data. This correlation is by now well-established (Howe, Komm, & Hill, 1999; Antia et al., 2000; Dziembowski et al., 2000).

Antia et al. (2000) calculated two-dimensional inversions for sound speed using even-*a* coefficients from GONG and MDI data. After subtracting the temporal mean from of each grid point in latitude, the resulting residual sound speed shows no significant temporal variation at any subsurface depth $(0.99R_{\odot}$ or below) in contrast to the rotation residuals. Thus it appears that the temporal variation in the even *a*-coefficients arise from changes taking place in the surface layers.

¹ http://www.nso.noao.edu/nsokp/dataarch.html

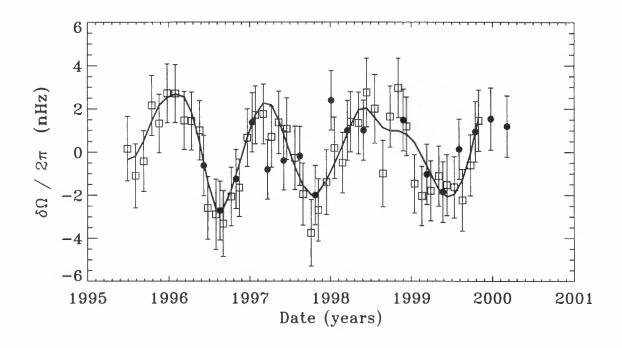


Figure 3. Variation with time of the residuals in equatorial rotation rate at radius $0.72R_{\odot}$. The symbols denote the data-inversion pairings: GONG-RLS (open squares), MDI-RLS (filled circles). The solid line represents the main component of an empirical mode decomposition of the GONG data.

3.3. Mode Energy and Energy Supply Rate

Figure 5 shows the mode energy at low- and highactivity levels (top panel), averaged over 20 and 11 data sets respectively. The mode energy decreases noticeably with increasing activity. The difference is about 13% on average near 3.0 mHz (bottom panel). Figure 6 shows that the energy supply rate decreases only slightly with increasing activity (top panel); the low- and high-activity subsets are almost indistinguishable. The decrease in supply rate from low to high activity is about 4% on average (bottom panel), except between about 3.0 and 3.6 mHz where the supply rate shows a zero change. The small variation of the energy supply rate might be compatible with a zero change (Chaplin et al., 2000).

To estimate the total amount of energy and energy supply rate in all p-modes, we fitted power laws to the average energy and supply rate. We then assumed that the fitted power laws are valid for all lvalues, used the high-l frequencies measured by Antia & Basu (1999), and calculated both quantities for modes between 1.5 and 4.5 mHz and l < 2540 (upper limit for this frequency range). In this way, we estimated a total energy of $3.0 \ 10^{34}$ erg and a total energy supply rate of $3.2 \ 10^{30} \text{ erg s}^{-1}$ (Komm, Howe, & Hill, 2000c). We repeated this procedure for the low- and high-activity subsets, shown in Figures 5 and 6, and found a decrease of about 8% in mode energy and a decrease of only 1% in energy supply rate with increasing activity. We speculate that the 7% excess energy might be transferred to the increasing number of flux tubes and thus might contribute to the irradiance variation. The estimated total supply rate is about the same size as the total (spectrally integrated) solar irradiance variation (Lean, 1997, and references therein), which means that p-modes might contribute about 5% to the observed irradiance variation.

4. SUMMARY

The internal solar rotation, derived from odd-a coefficients calculated from GONG and MDI data, shows clearly a variation with the solar cycle. The pattern of alternating bands of faster- and slower-thanaverage rotation extends over the upper third of the solar convection zone and agrees with the surface pattern known as torsional oscillations. The pattern disappears with increasing depth; no organized pattern is noticeable in the middle of the convection zone. At the base of the convection zone, the residuals of the equatorial rotation rate show a periodic behavior with a period of about 1.3 years. The torsional oscillation pattern in the upper convection zone has been established by several investigations, but the variation at the base of the convection zone has not been confirmed independently at the time of this presentation.

The sound speed of the solar interior, derived from even-a coefficients, shows no solar-cycle related variation or any other systematic temporal variation. It appears that the good correlation between the even-acoefficients and the corresponding coefficients of the magnetic activity is strictly a surface effect.

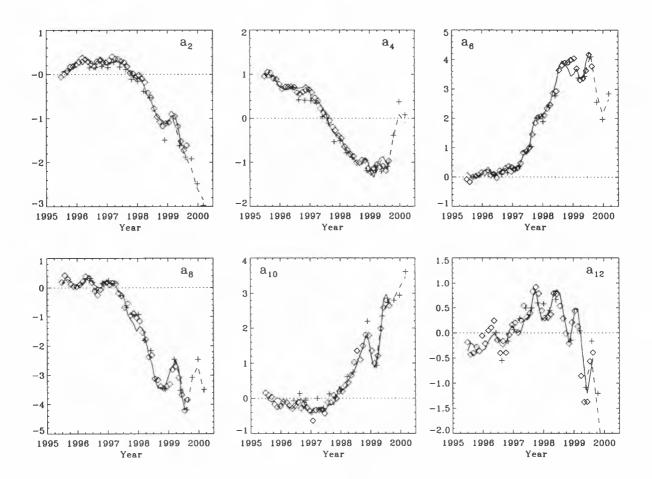


Figure 4. Temporal variation of the GONG (diamond) and MDI (cross) mean even a coefficients in units of 10^3 nHz. The error bars are about the size of the symbols for a_2-a_8 , almost twice as large for a_{10} , and about three times as large for a_{12} . The curves show the corresponding components of the magnetic flux, for GONG (solid) and MDI (dashed).

The mode energy decreases by about 13% from minimum to high activity, while the energy supply rate remains rather constant. This result leaves us with the puzzle that the energy supplied to the p-modes remains nearly constant during the solar cycle, while the energy contained in the modes decreases substantially. We speculate that the excess mode energy might contribute to the irradiance variation. This speculation has to be tested with new observations.

ACKNOWLEDGMENTS

This work was supported by NASA Grant S-92698-F. This work utilizes data obtained by the Global Oscillation Network Group (GONG) project, managed by the National Solar Observatory, which is operated by AURA, Inc. under a cooperative agreement with the National Science Foundation. The data were acquired by instruments operated by the Big Bear Solar Observatory, High Altitude Observatory, Learmonth Solar Observatory, Udaipur Solar Observatory, Instituto de Astrofísico de Canarias, and Cerro Tololo Interamerican Observatory. NSO/Kitt Peak data used here are produced cooperatively by NSF/NOAO, NASA/GSFC, and NOAA/SEL. The Solar Oscillations Investigation (SOI) involving MDI is supported by NASA grant NAG5-3077 to Stanford University. SOHO is a mission of international cooperation between ESA and NASA.

REFERENCES

- Anderson, E.R., Duvall, Jr., T.L., & Jefferies, S.M. 1990, ApJ, 364, 699
- Antia, II.M. & Basu, S. 1994, A&AS, 107, 421
 - ——. 1999, ApJ, 519, 400
 - ——. 2000, ApJ, (in press)
- Antia, H.M., Basu, S., Hill, H., Howe, R., Komm, R.W., & Schou, J. 2000, Helio- and Asteroseismology at the Dawn of the Millenium (Ed. A. Wilson), ESA SP-464, ESA Publications Division, Noordwijk, The Netherlands, (in press)
- Chaplin, W.J., Elsworth, Y., Isaak, G.R., Miller, B.A., & New, R. 2000, MNRAS, 313, 32
- Christensen-Dalsgaard, J. et al., 1996, Science, 272, 1286
- Dziembowski, W.A., Goode, P.R., Kosovichev, A.G., & Schou, J., 2000, ApJ,

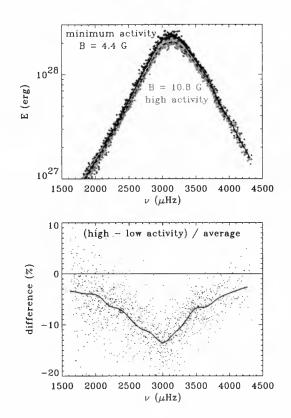


Figure 5. Mode energy, E, for two different levels of magnetic activity: low activity with $B \approx 4.4$ G (crosses, dashed line, average over 20 data sets) and high activity with $B \approx 10.8$ G (diamonds, solid line, average over 11 data sets). The solid and dashed line indicate rebinned values. The bottom panel shows the relative difference between high and low activity in percent of the average quantity.

- Goldreich, P., Murray, N., & Kumar, P. 1994, ApJ, 424, 466
- Hill, F., Stark, P.B., Stebbins, R.T., Anderson, E.R., Brown, T.M. et al. 1996, Science, 272, 1292
- Hill, F., Anderson, E., Howe, R., Jefferies, S.M., Komm, R.W., & Toner, C.G. 1998, Dynamics of the Interior of the Sun and Sun-like Stars (Eds. S.G. Korzennik & A. Wilson), ESA SP-418, ESA Publications Division, Noordwijk, The Netherlands, 1998, 231
- Howard, R.F. & LaBonte, B.J. 1980, ApJ, 239, L33
- Howe, R., Christensen-Dalsgaard, J., Hill, F., Komm, R., Larsen, R.M., Schou, J., Thompson, M.J., & Toomre, J. 2000a, ApJ, 533, L163
 2000b, Science, 287, 2456
- Howe, R., Komm, R., & Hill, F. 1999, ApJ, 524, 1084
- -----. 2000, Sol. Phys., 192, 427
- Komm, R., Hill, F., Howe, R., & Toner, C. 2000, Helio- and Asteroseismology at the Dawn of the Millenium (Ed. A. Wilson), ESA SP-464, ESA Publications Division, Noordwijk, The Netherlands, (in press)
- Komm, R., Howe, R., & Hill, F. 2000a, ApJ, 531, 1094

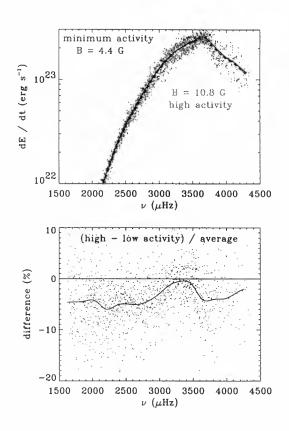


Figure 6. As Figure 5, but for the energy supply rate, which hardly varies with the solar cycle.

-----. 2000b, ApJ, 544, (in press)

- ——. 2000c, Helio- and Asteroseismology at the Dawn of the Millenium (Ed. A. Wilson), ESA SP-464, ESA Publications Division, Noordwijk, The Netherlands, (in press)
- Lean, J. 1997, ARA&A, 35, 33
- Rast, M.P. 1999, ApJ, 524, 462
- Ritzwoller, M.H. & Lavely, E.M., 1991, ApJ, 369, 557
- Schou, J., Christensen-Dalsgaard, J., & Thompson, M.J., 1994, ApJ, 433, 289
- Schou, J., et al., 1998, ApJ, 505, 390
- Snodgrass, H.B. 1984, Sol. Phys., 94, 13
- Stein, R.F. & Nordlund, A., 1998, ApJ, 499, 914
- Toomre, J., Christensen-Dalsgaard, J., Howe, R., Larsen, R.M., Schou, J., Thompson, M.J., 2000, Sol. Phys., 192, 437
- Ulrich, R.K. 1998a, Dynamics of the Interior of the Sun and Sun-like Stars (Eds. S.G. Korzennik & A. Wilson), ESA SP-418, ESA Publications Division, Noordwijk, The Netherlands, 1998, 851

THE SOLAR CYCLE AND THE TACHOCLINE: THEORIES AND OBSERVATIONS

T. Corbard¹, S.J. Jiménez-Reyes^{1,2}, S. Tomczyk¹, M. Dikpati¹, and P. Gilman¹

¹High Altitude Observatory, PO Box 3000, Boulder, CO 80307, USA ²Instituto de Astrofísica de Canarias, E-38701, La Laguna, Tenerife, Spain

ABSTRACT

We present some of the theories of what Petrovay (2001) called the DOT (Dynamo-Overshoot-Tachocline) layer emphasizing some predictions that may be tested by helioseismology. We first recall some constraint on these theories obtained by the previous latitudinal-average studies of the tachocline. Then, we investigate the latitudinal and temporal variations of the tachocline parameters by using our recent analysis of the 6 years of helioseismic observations with the LOWL instrument operating in Mano Loa, Hawaï since 1994. Within the observational uncertainties, our preliminary work yields no compelling evidence of variations or general trend of the tachocline parameters during the ascending phase of the current solar cycle (1994-2000).

Key words: Sun; Tachocline; Overshoot; Solar Cycle.

1. INTRODUCTION

The solar tachocline, so called after Spiegel & Zahn (1992), is defined as the layer at the base of the convection zone (hereafter, CZ) where important radial shear occurs. It is the transition zone where the angular velocity changes from its latitude-dependent value in the CZ to its constant and intermediate value in the radiative interior. We can emphasize three main reasons why this layer is of particular interest.

(i)Shear turbulence and/or meridional circulation inside the tachocline may provide a mechanism for mixing material between the CZ and the radiative interior (e.g. Brun et al. 1999; Schatzman et al. 2000) which is needed to understand, for instance, the burning of lithium and the depletion of helium and to reach a better agreement between solar models and helioseismic observations (e.g. Richard et al. 1996; Brun et al. 1999).

(ii) The tachocline may be the seat for angular momentum transport processes that could lead to the observed rigid rotation rate of the radiative interior. Hydrodynamical transport by unstable shear flow (e.g. Chaboyer et al. 1995) and transport by internal gravity waves in the tachocline (Kumar et al. 1999; Kim & MacGregor 2000) have been studied but they have not been found efficient enough to lead to an uniform internal rotation at the present age of the Sun. This probably requires also the presence of an internal magnetic field (Mestel & Weiss 1987; Charbonneau & MacGregor 1993; Gough & McIntyre 1998).

(iii) Finally, the tachocline is the best location for an oscillatory solar dynamo which is generally believed to be responsible for the solar magnetic cycle for the following reasons: (1) Its radial and latitudinal differential rotation has the ability to produce a toroidal field by shearing a pre-existing poloidal field. (2) The α -effect, the essential mechanism for producing poloidal field from toroidal field, is usually located in the CZ but the tachocline can also produce a strong α -effect by magnetic buoyancy instability (Ferriz-Mas et al. 1994) and/or by the unstable shallow-water modes (Dikpati & Gilman 2000a). (3) Because the tachocline (or part of it) may also be located in the slight sub-adiabatic overshoot layer, the toroidal fields can be stored for an extended period of time, and therefore can be amplified and acted on by the α -effect before they escape to the surface through buoyant rise or be disrupted completely by convective shredding.

We will first (Sect. 2) give some terminology about the different layers and their properties at the base of the CZ (also to be defined). Then, in Sect. 3, we present some models of the tachocline and their predictions that may be tested by helioseismology. Previous results obtained by forward modeling on the latitude-average properties of the tachocline are summarized in Sect 4. Then we use a new dataset from the LOWL instrument to investigate the latitudinal and temporal variations of the tachocline parameters during the ascending phase of the current solar cycle (Sect. 5).

2. LAYERS AT THE BASE OF THE CONVECTION ZONE: TERMINOLOGY, DEFINITIONS AND OBSERVATIONS

As mentioned above, there is, beside the tachocline, another layer defined at the interface between the superadiabatic CZ and the radiative interior: the overshoot layer. Different models exist for this layer. The first

Proc. 1st Solar & Space Weather Euroconference, 'The Solar Cycle and Terrestrial Climate', Santa Cruz de Tenerife, Tenerife, Spain 25-29 September 2000 (ESA SP-463, December 2000)



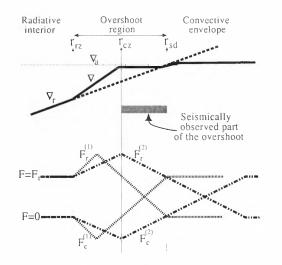


Figure 1. Schematic representation of the overshoot layer between the radiative zone boundary r_{rz} and the Schwarzschild boundary r_{sd} (i.e. where the temperature gradient equals both its adiabatic and radiative value $\nabla = \nabla_a = \nabla_r$). r_{cz} represents the seismically observed base of the CZ. Two different models of the convective (F_c) and radiative (F_r) flux variations are drawn for comparison. The total flux $F_t = F_c + F_r$ remains constant. The model (1) of Canuto (1997) allows a positive convective flux in the slightly sub-adiabatic and seismically observed part of the overshoot in contradiction with the Schwarzschild criterion while the model (2) of Zahn (1991) is such that $F_c \leq 0$ in all the overshoot layer.

particular radius, r_{sd} , corresponds to the Schwarzschild boundary which defines the beginning of the convectively unstable zone where the temperature gradient equal its adiabatic value $\nabla = \nabla_{ad}$. A second particular radius is where the temperature gradient is taking its radiative value ($\nabla = \nabla_r$) and the total flux is equal to the radiative flux $(F_t = F_r)$. This radius, r_{rz} , defines the radiative zone boundary. The region between r_{sd} and r_{rz} is what we here call the overshoot region (see Fig. 1). The 'base of the convection zone' r_{cz} , measured by helioseismology, corresponds to the location where the temperature gradient changes abruptly. If we allow a slightly subadiabatic zone below r_{sd} then helioseismology cannot distinguish between the slightly super-adiabatic CZ and the slightly sub-adiabatic overshoot layer (Christensen-Dalsgaard et al. 1995; Gilman 2000) and $r_{rz} < r_{cz} < r_{sd}$. Calibrations made by Basu (1997) lead to a value of $r_{cz} = 0.713 \pm 0.001 R_{\odot}$. Helioseismology can also place an upper limit for the slightly sub-adiabatic overshoot zone $[r_{cz}, r_{sd}]$. This upper limit is 0.05 pressure scale heights, about 2800Km or $\sim 0.004 R_{\odot}$ (Basu & Antia 1997). This is therefore a very thin layer. Another question concerning this layer is about the sign of the convective flux inside. If we follow the Schwarzschild criterion, we should have $F_c \leq 0$ as in Zahn (1991)'s model because this layer is (slightly) sub-adiabatic, but Ferriz-Mas (1996) and Canuto (1997) pointed out that, with a nonlocal mixing-length treatment of the CZ, this is not necessarily valid in the overshoot zone and we may well have $F_c > 0$ and $\nabla < \nabla_{ad}$ in spite of the Schwarzschild criterion. In that case the downward convective energy transport ($F_c < 0$) occurs only in the other (lower) part of the overshoot zone $[r_{rz}, r_{cz}]$, called the overshoot layer proper (Canuto 1997; Monteiro et al. 1998). In the same way, the zone with positive convective flux is sometimes called CZ proper (e.g. Ferriz-Mas 1996). These differences in the overshoot models may have some importance as it has been shown that flux tubes with equipartition field strength (~ 10⁴ G) can be stored in all the overshoot layer while the field strength of 10⁵ gauss required in order to explain the observed active regions at the surface (e.g. Schüssler et al. 1994), can only be stored where the convective flux is negative (Ferriz-Mas 1996).

3. THEORY: SOME MODELS OF THE TACHOCLINE AND THEIR PREDICTIONS

3.1. Purely hydrodynamic models

The first theory of the tachocline was developed by Spiegel & Zahn (1992). They mainly address the problem of the thickness of the tachocline, which we summarized as follows. The differential rotation $\Omega_1(\theta)$ at the top of the radiative interior induces a latitudinal temperature gradient and therefore a meridional circulation that would, without any stress acting on it, spread towards the interior in a thermal time-scale leading to a non rigid rotation rate in the interior and a very thick tachocline for the present Sun. We therefore need to invoke some stresses acting in the tachocline in order to prevent its progression towards the interior. Using a purely (i.e. non-magnetized) hydrodynamic model where the tachocline is treated as a boundary layer, Spiegel & Zahn (1992) suggest that a strong enough anisotropic turbulence could lead to a thin tachocline. They thus obtained a relation between the thickness of the tachocline w and the horizontal turbulent viscosity coefficient ν_h assumed to be much higher than its vertical counterpart.

$$\nu_h = 8.34 \ 10^6 \left(\frac{\Omega_0}{N}\right)^2 \left(\frac{r_{cz}}{w}\right)^4 \ \mathrm{cm}^2 \ \mathrm{s}^{-1} \qquad (1)$$

Nevertheless there remain two major questions with this approach. First, the latitudinal rotation profile inside the tachocline is likely to be linearly stable to 2D disturbances according to Rayleigh's criterion (Charbonneau et al. 1999b) and so it is probably not the process leading to the anisotropic turbulence assumed in the model. A solution to this problem may be found in a recent work of Dikpati & Gilman (2000a) showing that, if we allow radial deformations of the layer and use the so-called shallow water model as a first approximation of the full 3D problem, then the tachocline is found unstable in the slightly sub-adiabatic overshoot zone even in the purely hydrodynamic case (Fig. 2). The second difficulty with this hydrodynamic model is that, even if it leads to a latitudinal independent rotation at the base of the tachocline, it cannot explain the fact that there is also no significant radial gradient in the interior.

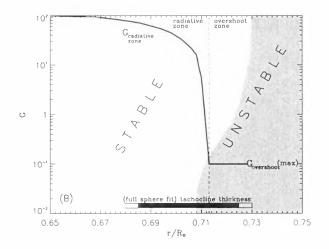


Figure 2. Stability diagram from the shallow water model (Dikpati & Gilman 2000a). The variation of $G \simeq 10^3 |\nabla - \nabla_{ad}|$ with radius is given by the solid line for schematic solar model. The stability zones and the tachocline thickness and location have been estimated from observations (Charbonneau et al. 1999a,b). The overshoot layer has arbitrarily been assigned a thickness of $0.015R_{\odot}$ and it is slightly sub-adiabatic with $|\nabla - \nabla_{ad}| \leq 10^{-4}$.

3.2. Magnetized models

Because it is very likely that the tachocline is magnetized, another mechanism that can lead to anisotropic turbulence in the tachocline is magnetic instability. It has effectively been shown (Gilman & Fox 1997, 1999; Dikpati & Gilman 1999) that there exists a joint instability between latitudinal differential rotation and toroidal magnetic fields. But two different kind of magnetic fields are usually invoked in the solar interior, namely primordial fields and dynamo generated fields. As we shall see, in both cases theories relate their properties to the shape of the tachocline.

(i) Dynamo generated magnetic fields. In virtually all dynamo theories (overshoot layer, interface or Babcok-Leighton dynamos, see the review of Petrovay (2001)), the shape and especially the thickness of the tachocline and the overshoot layer are key issues since they determine the strength of the magnetic field that can be stored and the process by which it is transformed. Using an MHD version of their shallow water model (Dikpati & Gilman 2000b) demonstrate that the presence of a magnetic field in the tachocline would induce a prolateness of the tachocline otherwise oblate. This can also be tested by helioseismology by measuring the central position of the radial shear at different latitudes. Such measurement of the prolateness would allow us to estimate the strength of the magnetic field depending on its geometry and localization inside the tachocline. The shape of the tachocline as obtained from this model is shown as a function of the toroidal field strength on Fig 3.

(ii) Primordial magnetic fields. Independently of any magnetic field that may be generated in the CZ, Gough &

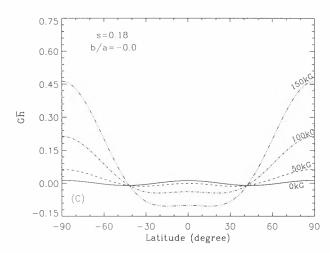


Figure 3. Shape of the top surface of the tachocline with a broad nonuniform toroidal magnetic field of different strength. G is the same quantity as in Fig. 2 and h is related to the width of the tachocline by $w \sim 0.035 R_{\odot}(1+h)$ Dikpati & Gilman (2000b).

McIntyre (1998) argue that we must also have a magnetic field in the radiative interior in order to explain the uniform (with no radial shear) rotation rate observed there. This large scale poloidal magnetic field would also confine the shear in a thin layer as a result of a balance between upward diffusion of the magnetic field and downward advection by the thermally driven tachocline circulation. They obtain the following relation between the thickness of the tachocline and the strength of the internal magnetic field:

$$|B_0| = 2.3 \ 10^3 \left(\frac{\Omega_0}{N}\right)^7 \left(\frac{r_{cz}}{w}\right)^9$$
 (Gauss). (2)

Such internal field is also required in the magnetic models of Rudiger & Kitchatinov (1997) and MacGregor & Charbonneau (1999) where the tachocline is identified with an MHD boundary layer located in the radiative interior. Assuming no magnetic coupling at the coreenvelope interface and that advective effects (as modeled by Spiegel & Zahn (1992)) dominate the viscous effects to prevent the inward spreading of the layer, MacGregor & Charbonneau (1999) obtain:

$$|B_0| \sim 3 \ 10^{-8} \left(\frac{r_c}{w}\right)^3$$
 (Gauss). (3)

This work also suggests that the primordial magnetic field is very likely to be decoupled from the tachocline i.e. entirely contained within the radiative interior. The interaction between a primordial time-independent magnetic field that would extend into the CZ and the timedependent dynamo-generated magnetic field had nevertheless been investigated by Boruta (1996) suggesting that this interaction would lead to an inversion and an amplification of the primordial field by an amount that depends again on the thickness of the tachocline. On the other hand, if the dynamo magnetic field is generated in the CZ, it has been shown to have only a weak influence on the dynamics of both the tachocline and the radiative interior (Hujeirat & Yorke 1998; Garaud 1999).

4. HELIOSEISMOLOGY: FORWARD MODELING AND THE LATITUDE-AVERAGE TACHOCLINE

Solar oscillation modes are identified by three integers: the spherical harmonics degree l and azimuthal order m, and the radial order n. The frequency splitting $\delta \nu_{nlm}$ induced by the rotation $\Omega(r, \mu)$ can be calculated by:

$$\delta\nu_{nlm} = \int_0^1 \int_0^1 K_{nlm}(r,\mu) \ \Omega(r,\mu) dr d\mu \tag{4}$$

where, r is the fractional solar radius, $\mu = \cos(\theta)$ and K_{nlm} are kernels calculated from a standard solar model.

Following Kosovichev (1996) we parameterize the rotation rate between 0.4 and 0.8 solar radius by an error function of the form:

$$\Omega(r,\theta) = \Omega_0 + \frac{\Omega_1(\theta) - \Omega_0}{2} \left(1 + erf\left(\frac{r - r_c(\theta)}{0.5 \ w(\theta)}\right) \right)$$
(5)

where Ω_0 represents the rigid rotation rate in the radiative interior, $\Omega_1(\theta)$ the rotation rate at the top of the tachocline, and $r_c(\theta), w(\theta)$ the central position and the width of the tachocline at the colatitude θ .

Several authors have inferred the latitude-average properties of the tachocline (i.e. r_c and w independent of θ) by looking for the parameters that give the best fit to the helioseismic observations, either by calibration (Kosovichev 1996; Basu 1997) or by genetic forward modeling (Charbonneau et al. 1999a). A weighted average of these results leads to a position $r_c = 0.704 \pm 0.002 R_{\odot}$ and a width $w = 0.052 \pm 0.010 R_{\odot}$. Therefore, it seems that, in a latitude-average, the tachocline is centered around $0.01R_{\odot}$ below r_{cz} and its upper third part is located in the nearly adiabatically stratified zone above r_{cz} . Nevertheless this results must be taken with caution because the decreasing radial resolution with latitude tends naturally to show a thicker tachocline at high latitudes thereby influencing the average thickness and position. The parameters obtained this way should therefore be regarded as upper limits for the tachocline properties. The latitudeaverage width is however probably the best estimate to use in the formulae obtained from the various theories of Sect. 3 which assume also a spherical symmetry.

In the hydrodynamic theory, Eq. 1 with a with of $0.05R_{\odot}$ leads to an horizontal turbulent viscosity coefficient of about 3 10⁶ cm² s⁻¹, several order of magnitude higher than the microscopic value. In the MHD theories the same value of the width leads to a primordial magnetic field strength of $|B_0| \sim 10^{-4}$ Gauss for both Eq. 2 and 3. This suggests that even a weak magnetic field is enough to keep the radiative interior rotating rigidly and to confine the radial shear to a thin layer compatible with observations. By analyzing the splitting coefficients from GONG observations, Basu (1997) set an upper limit of 0.3MG for a field located at the base of the CZ. From Eq. 2 this would correspond to a width of $0.0045R_{\odot}$ which cannot be excluded from observations. By shearing a poloidal field of 10^{-4} Gauss the theory of MacGregor & Charbonneau (1999) predicts the generation of a toroidal field of ~ 0.1 MG which is also compatible with the 0.3MG limit.

5. SEARCH FOR VARIATIONS WITH TIME AND LATITUDE USING INVERSION TECHNIQUES

5.1. Motivation

Theories predict variation with latitude of the shape of the tachocline. We have seen for example that, in the shallow-water model, the presence of a magnetic field would induce a prolate tachocline otherwise oblate. Both the magnetic model of Rudiger & Kitchatinov (1997) and the 2D hydrodynamic model of Spiegel & Zahn (1992) predict a thicker tachocline at the pole than at the equator (see also Elliott 1997). In the model of Gough & McIntyre (1998) the tachocline is thicker where the horizontal component of the magnetic field in the radiative interior is small. The poles should be therefore thicker but that may also be true for other latitudes. This means that the shape of the tachocline could also be a diagnostic for the geometry of the magnetic field. Some attempts have been made to infer latitudinal variations in the tachocline profile from observations (Antia et al. 1998; Charbonneau et al. 1999a), but no compelling evidence has been found yet. Even if, as shown in the previous section, the results tend to argue in favor of a prolate tachocline thicker at high latitudes than at the pole, this may very well be due to the limits in resolution associated with the datasets used.

Time variations are also expected mainly because of the changes of the magnetic field strength and geometry during the solar cycle. Some evolution of the large scale circulation inside the layer or the action of internal gravity waves may also induce temporal changes or oscillations in the tachocline parameters. Small amplitude oscillations, with a period of 1.3 year, have recently been found in the rotation profile close to the boundaries of the tachocline (Howe et al. 2000). These results are based on both GONG and MDI data but have not been confirmed by independent analysis (Antia & Basu 2000). If these oscillations are real, the 1.3 year period remains unexplained (see Gough 2000). Because of the observed magnetic cycle, we rather expect the tachocline variations to be on the time scale of the solar cycle (11 years). A first attempt at detecting long term temporal variations in the tachocline have been made by Basu & Schou (2000) using 11 sets of MDI observations covering 72 days each between July 1996 and April 1998. They found no clear changes in the width or position of the tachocline but gave some hints that the position may move slightly outwards with increased activity.

5.2. The observations: LOWL instrument

The LOWL instrument is a Doppler imager based on a Potassium Magneto-Optical Filter that has been operating on Mauna Loa, Hawaï since 1994 (see Tomczyk et al. (1995) for a detailed description). The spectra were processed using the LOWL pipeline, which has been recently improved (Jiménez-Reyes 2001). Annual time series for degrees from $\ell = 0$ up to 99 have been created by using spherical harmonic masks and a Fast Fourier Transform

has been applied to each one of the time series. The average duty cycle over one year of observations was around 20%. A detailed description of the fitting method can be found in Jiménez-Reyes et al. (2001).

5.3. Method: inversion and deconvolution

In general, inferring the internal rotation rate from observed splittings requires inverting the integral Eq. 4. In order to achieve this, we have used a 2D Least-Squares (LS) method (Corbard et al. 1997). Because the method is linear, the solution at any point (r_0, ν_0) is linear combination of observations $\langle \Omega(r_0, \nu_0) \rangle =$ $\sum c_{nlm}(r_0, \mu_0) \delta_{nlm}$. From Eq. 4 this is equivalent to taking a linear combination of the kernels K_{nlm} . The resulting kernel

$$\kappa(r_0, \mu_0, r, \mu) = \sum c_{nlm}(r_0, \mu_0) K_{nlm}(r, \mu)$$
 (6)

is called averaging kernel because it follows from the previous equations that the quantity $\langle \Omega(r_0, \mu_0) \rangle$ is an average of the rotation rate in a domain defined by $\kappa(r_0, \mu_0, r, \mu)$:

$$<\Omega(r_0,\mu_0)> = \int_0^1 \int_0^1 \kappa(r_0,\mu_0,r,\mu)\Omega(r,\mu)drd\mu$$
 (7)

The difficulties arise from the fact that Eq. 4 is an illposed problem with no unique solution. In this global LS method, we therefore need to introduce some a-priori knowledge on the rotation profile in order to *regularize* the solution and avoid strong oscillations. Nevertheless, this Regularized Least Squares (RLS) approach prevents us from recovering accurately sharp gradients as those expected in the tachocline because they do not conform to the global smoothness a-priori introduced. However we can then use our knowledge of the resolution in order to reach a better estimate of the tachocline width. The basic idea is to approximate Eq. 7 by a convolution equation (Charbonneau et al. 1999a; Corbard et al. 1998). If the the tachocline profile after inversion is approximated by an erf function of width w and if the radial part of averaging kernel is approximated by a Gaussian of standard deviation σ_r , then the 'true width' w_c can be obtained by:

$$w_c = \sqrt{w^2 - 8\sigma_r^2} \tag{8}$$

5.4. Results and Discussion

The results are shown in Fig. 4. The radial resolution obtained is about $0.12R_{\odot}$ at 60° and $0.10R_{\odot}$ at the equator. The angular resolution achieved with LOWL data is about 20° at the equator. Because the radial shear doesn't exist at about 30° and because the angular resolution decrease at high latitudes, we limit our analysis to two latitudes: the equator and 60°. Therefore, in the following, prolateness refers to the difference between the central position of the layer at these two latitudes.

Because the inferred width at the equator is always lower than the resolution we cannot use our simple model

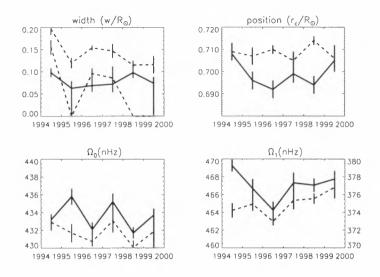


Figure 4. Inferred tachocline parameters as a function of time from LOWL observations. The full and dashed lines correspond respectively to fit at the equator and at 60° . For the width (upper left), the lower dashed line is obtained after deconvolution using Eq. 8. The scale on the right of the lower right panel corresponds to the fit at 60° (dashed line).

for deconvolving. This indicates that the width of the tachocline at the equator is probably lower than the local spacing of the grid used for the inversion i.e. $0.02R_{\odot}$. The same happens at 60° for 1995, 1998 and 1999. There is therefore no strong evidence of a systematically thicker tachocline at 60°. Moreover the errors reported on the plot are formal errors as obtained from the fits but Monte Carlo simulations have been carried out which suggest that the uncertainties on the inferred widths after the whole inversion process are between ± 0.02 and $\pm 0.03R_{\odot}$.

The center of the tachocline is always found deeper at the equator than at 60° . The variation of this prolateness with time is shown in Fig. 5. The maximum of prolateness found is about $0.02R_{\odot}$ and no prolateness is found the first and last years. These differences and their fluctuations are nevertheless very small and are also very sensitive to the inversion parameters chosen and especially the amount of regularization used. The lower panel of Fig. 5 illustrates this point by showing that, with a more regularized inversion, the maximum prolateness is about $0.03R_{\odot}$ and a minimum is no longueur found for 1994.

Generally speaking, we do not find from this analysis evidence of any general trend or significant oscillation in the tachocline parameters during the ascending phase of the actual solar cycle. In particular we do not find an outward trend for the central position as suggested by Basu & Schou (2000). Nevertheless, a prolateness of the layer is observed every year which allow us to, at least, exclude an oblate tachocline. The amount of prolateness found between the equator and 60° is however of the same order of magnitude than the uncertainties on the width of the layer. We can therefore only set an upper limit for the prolateness which is around $0.03R_{\odot}$. This is in good

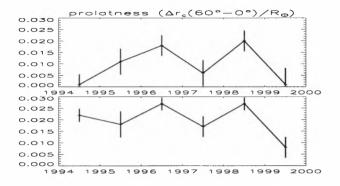


Figure 5. Difference between the central position inferred at 60° and at the equator, as a function of time. The upper plot corresponds to the results of Fig. 4 while the lower plot corresponds to inversion using stronger regularization.

agreement with previous estimates of Antia et al. (1998) ($0.004 < \Delta_{rc}/R_{\odot} < 0.023$) and Charbonneau et al. (1999a) ($\Delta_{rc} \simeq 0.023R_{\odot}$). Using the shallow-water model and shape curves as shown in Fig. 3, this would correspond to a toroidal magnetic field strength of about 0.1MG if it is located in the overshoot layer or about 0.6MG if it is located in the radiative interior. If the toroidal field is concentrated in bands migrating towards the equator during the ascending phase of the cycle, one would expect, from the shallow water model, a decreasing prolateness for the period of LOWL observations. This general trend cannot be excluded but is not observed from our preliminary analysis of LOWL data.

ACKNOWLEDGMENTS

T. Corbard and S.J. Jiménez-Reyes are very thankful to the organizers of the meeting for providing financial support. T. Corbard acknowledge support from NASA grant S-92678-F.

REFERENCES

- Antia H.M., Basu S., 2000, ApJ, 541, 442
- Antia H.M., Basu S., Chitre S.M., 1998, MNRAS, 298, 543
- Basu S., 1997, MNRAS, 288, 572
- Basu S., Antia H.M., 1997, MNRAS, 287, 189
- Basu S., Schou J., 2000, Solar Phys., 192, 481
- Boruta N., 1996, ApJ, 458, 832
- Brun A.S., Turck-Chièze S., Zahn J.P., 1999, ApJ, 525, 1032
- Canuto V.M., 1997, ApJ, 489, L71
- Chaboyer B., Demarque P., Pinsonneault M.H., 1995, ApJ, 441, 865
- Charbonneau P., MacGregor K.B., 1993, ApJ, 417, 762
- Charbonneau P., Christensen-Dalsgaard J., Henning R., et al., 1999a, ApJ, 527, 445

- Charbonneau P., Dikpati M., Gilman P.A., 1999b, ApJ, 526, 523
- Christensen-Dalsgaard J., Monteiro M.J.P.F.G., Thompson M.J., 1995, MNRAS, 276, 283
- Corbard T., Berthomieu G., Morel P., et al., 1997, A&A, 324, 298
- Corbard T., Berthomieu G., Provost J., Morel P., 1998, A&A, 330, 1149
- Dikpati M., Gilman P.A., 1999, ApJ, 512, 417
- Dikpati M., Gilman P.A., 2000a, ApJ, in press
- Dikpati M., Gilman P.A., 2000b, ApJ, submitted
- Elliott J.R., 1997, A&A, 327, 1222
- Ferriz-Mas A., 1996, ApJ, 458, 802
- Ferriz-Mas A., Schmitt D., Schuessler M., 1994, A&A, 289, 949
- Garaud P., 1999, MNRAS, 304, 583
- Gilman P.A., 2000, Solar Phys., 192, 27
- Gilman P.A., Fox P.A., 1997, ApJ, 484, 439
- Gilman P.A., Fox P.A., 1999, ApJ, 510, 1018
- Gough D., 2000, science, 287, 2434
- Gough D.O., McIntyre M.E., 1998, Nat, 394, 755
- Howe R., Christensen-Dalsgaard J., Hill F., et al., 2000, science, 287, 2456
- Hujeirat A., Yorke H.W., 1998, New Astronomy, 3, 671
- Jiménez-Reyes S.J., 2001, in progress, Ph.D. thesis, La Laguna University
- Jiménez-Reyes S.J., Corbard T., Palle P.L., Tomczyk S., 2001, In: SOHO 10/ GONG 2000 Workshop, Helioand Asteroseismology at the Dawn of the Millennium, vol. SP-464, ESA Publications Division, Noordwijk, The Netherlands
- Kim E.J., MacGregor K.B., 2000, ApJ, submitted
- Kosovichev A.G., 1996, ApJ, 469, L61
- Kumar P., Talon S., Zahn J., 1999, ApJ, 520, 859
- MacGregor K.B., Charbonneau P., 1999, ApJ, 519, 911
- Mestel L., Weiss N.O., 1987, MNRAS, 226, 123
- Monteiro M.J.P.F.G., Christensen-Dalsgaard J., Thompson M.J., 1998, In: Korzennik S.G., Wilson A. (eds.) Structure and Dynamics of the Interior of the Sun and Sun-like Stars, vol. SP- 418, 495–498, ESA Publications Division, Noordwijk, The Netherlands
- Petrovay K., 2001, this proceeding
- Richard O., Vauclair S., Charbonnel C., Dziembowski W.A., 1996, A&A, 312, 1000
- Rudiger G., Kitchatinov L.L., 1997, Astronomische Nachrichten, 318, 273
- Schatzman E., Zahn J.P., Morel P., 2000, A&A, submitted
- Schüssler M., Caligari P., Ferriz-Mas A., Moreno-Insertis F., 1994, A&A, 281, L69
- Spiegel E.A., Zahn J.P., 1992, A&A, 265, 106
- Tomczyk S., Streander K., Card G., et al., 1995, Solar Phys., 159, 1
- Zahn J.P., 1991, A&A, 252, 179

MAGNETIC SOURCES OF SOLAR VARIABILITY

Oran R. White

High Altitude Observatory U.S. National Center for Atmospheric Research* Box 3000 Boulder, CO 80307-3000 USA Tel: 970 533 7318 / Fax: 970 533 7318 Email: orw@hao.ucar.edu

ABSTRACT

Solar magnetic activity causes fluctuations in the Sun's radiative output as well as in the solar wind. Here I present a broad, brief description of the sources of these fluctuations. Because of the energetic dominance of the Sun's radiative output in the terrestrial atmosphere, I concentrate on the different types of solar radiative variability of the Sun as observed from the Earth. This leads to discussion of the different magnetic structures observed in the solar atmosphere and their thermodynamic conditions. Emphasis will be on the solar photosphere where the bulk of the Sun's radiant energy originates. Magnetic properties of the solar corona leading to fluctuations in the solar wind will be discussed briefly. I want the reader to see how the variability across the solar spectrum comes from differences in physical conditions from the deepest visible layers to the outermost regions we see. It is in these regions where coronal holes and coronal mass ejections produce solar wind variations needed to explain cosmic ray modulation. The change in the nature of the Sun's variability from the photosphere to the corona comes directly from changes in topology of magnetic fields as we move out from the photosphere to the corona.

Key words: solar irradiance; activity; solar cycle.

1. INTRODUCTION

Variability in both the Sun's radiative output and solar wind is important in current studies of the solar-terrestrial interaction. Time series of the Sun's radiative variability outside the wavelength region from 300 nm to 1000 μ m are distinctly different from that in this spectral region visible from the surface of the Earth. These differences arise from magnetic structures observed in the solar atmosphere and their thermodynamic conditions. The observed variability comes from two basic solar properties: 1) the evolution of solar surface structure during the 11-yr Schwabe cycle and 2) the transit of these structures across the solar disk due to the 27-day rotation of the Sun. Figure 1a shows the magnetic field distribution in the photosphere on August 8, 2000 for comparison with the Sun's appearance in visible light (1b) and the EUV (1c). Such patterns change with the emergence and decay of magnetic regions containing sunspots, but their visibility and aspect changes as they rotate across the solar disk visible from the Earth. Figure 1c shows the EUV solar image on the same date. Clearly, the EUV radiation originates in a much more extended atmosphere than the radiation at visible wavelengths.

The solar photosphere is very important because the bulk of the Sun's radiant energy between 160 nm and 1 mm wavelength originates there. At wavelengths below 160 nm, the radiation comes from the higher temperature solar chromosphere and corona. Typical values for electron temperature and density of the photosphere are 6000° K and 10^{11} /cm³ compared to values of $2 \times 10^{6^{\circ}}$ K and 10^{7} /cm³. In these lower density layers, we see magnetic fields in the form of fine loops and flux ropes as they emerge from sunspot regions. This change in magnetic topology is the key concept in understanding both radiative variability as function of wavelength and variability in the structure of the solar wind.

Section 2 describes the wavelength dependence variability from the X-ray region to the visible and onto the very long wavelengths. In Section 3, coronal structure and variability of the solar wind will be discussed. Section 4 summarizes our progress in modeling the variable solar atmosphere. In Section 5, I present current questions and conclusions from this survey.

^{*}The National Center for Atmospheric Research is sponsored by the U.S. National Science Foundation

Proc. 1st Solar & Space Weather Euroconference, 'The Solar Cycle and Terrestrial Climate', Santa Cruz de Tenerife, Tenerife, Spain, 25-29 September 2000 (ESA SP-463, December 2000)

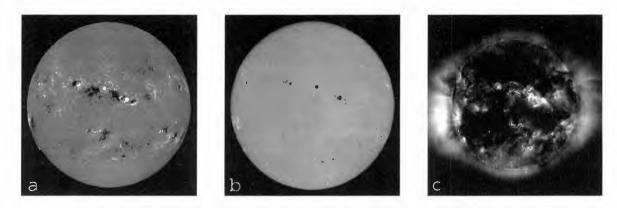


Figure 1. The Sun on 8 August 2000. a. Solar Magnetogram from the U.S. National Solar Observatory, positive magnetic polarity (white) and negative polarity (black), b. White Light Image from the SOHO/MDI experiment, and c. FeXV 19.5 nm EUV image from the SOHO/EIT experiment.

2. THE SPECTRUM OF SOLAR IRRADIANCE VARIABILITY

2.1. The Schwabe Cycle in TSI, Solar Magnetism, and Sunspot Counts

In considering climate effects of the Sun, the total solar irradiance (TSI) is energetically the dominant solar input. Figure 2 shows the Fröhlich-Lean composite TSI record (Fröhlich-Lean 1997) together with the sunspot number record and our record of the Sun's average magnetic field strength from 1976 to 2000. This epoch of modern daily observation is our basic source of nearly continuous measurements of solar magnetic fields, radiation, and surface structure; therefore, it is our baseline for estimating both past and future changes in solar radiation. George Ellery Hale and his colleagues at Mt. Wilson Observatory first measured solar magnetic fluxes early in the 20th century. Daily measurement of solar magnetism over the full solar disk, however, did not commence until the 1950s when the necessary electronic systems for measuring the longitudinal Zeeman effect in spectroheliograms became available. The total irradiance (Figure 2 upper panel) obviously follows the 11-year Schwabe cycle of solar magnetic activity as traced in sunspot counts (Figure 2 middle panel). However, the sharp downward excursions are due to the passage of individual spots as they cross the solar disk. Thus, we see the obvious confrontation of bright and dark features on the solar disk in producing both a $\sim 0.1\%$ brightening at the time of maximum sunspot count as well as short-lived darkenings superimposed on it. The net effect is an increase in the solar irradiance in phase with the magnetic activity cycle of the Sun.

The average solar magnetic field shown in Figure 2 lower panel follows this same cyclic pattern. Strong magnetic fields emerge from the solar interior in sunspots and their faculae. Sunspots are dark, cool regions where these strong fields pierce the visible photosphere. In contrast, their associated faculae appear as brighter regions against the neighboring quiet Sun. As a sunspot region evolves and fades, the faculae disperse into a magnetic network outlining large supergranulation cells (30 Mm diameter) on the quiet solar surface. Thus, it appears that the faculae and their remnants are the source of the increase in TSI at solar maximum despite the presence of the dark spots.

Figure 2 clearly shows the strong correlation between the irradiance and the average magnetic field on solar cycle time scales, but the correlation weakens on comparison of daily values. As the stronger correlation between TSI and sunspot number suggests, the short term irradiance changes depend more on field concentrations in the photosphere than on the mean global field strength.

The cyclic behavior of the Sun's strong surface magnetic field reflects the cyclic variation of the solar dynamo located at a depth of one quarter of a solar radius. Weak magnetic fields are generated from a local surface dynamo process in the quiet Sun and also organize into the network mentioned in the previous paragraph. The role of these weak fields in the Sun's radiative variability is not known at this time.

2.2. Radiative Variability at Different Wavelengths in the Solar Spectrum

The TSI measures the radiant energy from all wavelengths from the radio spectrum to X-rays, but the very short and long wavelengths (EUV and radio) show quite different signatures of solar variability compared to that for the visible spectrum from 300 nm to 1000 μ m. Figure 3 shows this difference between total irradiance and two spectral irradiances in the period from 1993 to 1995 in the descending phase of solar cycle 22. The two spectral irradiances are in the Ly α line of neutral hydrogen at 121.6 nm and in the 1-2 nm x-ray band. The Ly α data are from UARS/SOLSTICE, courtesy of Gary Rottman, and the x-ray fluxes are from the YOHKOH/SXT, courtesy of Loren Acton. A time series for the important EUV region from 10 nm to 90 nm cannot be shown due to the lack of observation from 1978 to 1999.

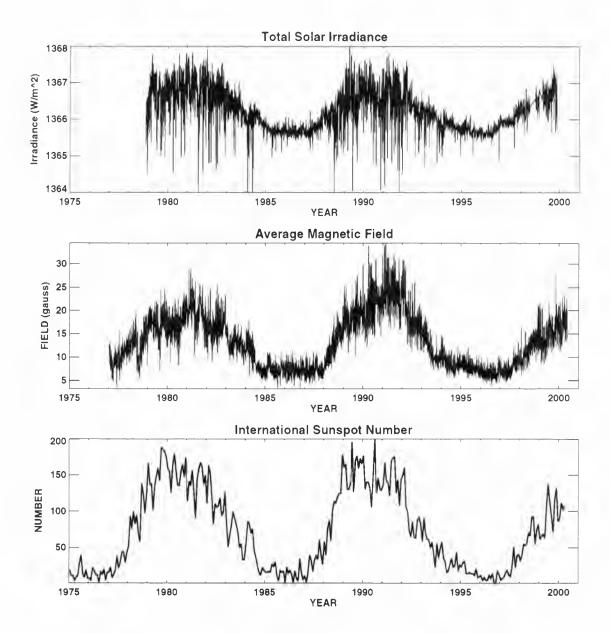


Figure 2. The 11-year Schwabe Cycle in Total Solar Irradiance (upper), Average Solar Magnetic Field (middle), and Average International Sunspot Number (lower).

The Ly α time series is typical of the Sun's UV variability: clear episodes of 27-day rotational modulation due to bright active regions as they transit the solar disk superposed on the rise and fall of the solar cycle. In contrast, variability of the x-ray record is much stronger and more transient in time. During quiet periods such as in the second quarter of 1994 in Figure 3, these UV and X-ray records and the TSI show the 27-day rotational modulation pattern. When the Sun was much more active at the beginning of 1994, these three records are quite different, i.e., more TSI decreases due to sunspots, a strong but regular 27-day modulation in Ly α , and a sharp, sustained increase in the X-ray flux. Amplitudes of these fluctuations differ by orders of magnitude in these three wavelengths, i.e., 0.1% in TSI, 15% in Ly α , and 10X in soft X-rays.

Therefore, the solar spectrum is also a spectrum of radiative variability in which the extremes in wavelength (X-ray and radio) show stronger, more transient fluctuations than the spectrum from 90 nm to 1 cm wavelength. This mid range spectrum from the Lyman continuum edge at 91.2 nm to the far IR at 1 cm varies more slowly and carries 99.9% of the radiant energy. Despite the energetic dominance of the UV-Visible-IR wavelength range, radiation at wavelengths below 90 nm drives heating and molecular balance above the neutral troposphere in the Earth's thermosphere. See Solanki & Unruh (1997).

In the next section, this spectrum of variability will be connected to the appearance of the Sun in wavelength ranges corresponding to the Total, UV, EUV, and X-ray irradiances.

2.3. The Physical Nature of Sources of Radiative Variability

The appearance of the Sun at visible, UV, EUV, and X-ray wavelengths in Figure 4 shows how the differences in time series of irradiances (Figure 3) arise from differences in the distribution of bright and dark features on the visible face of the Sun.

In the photospheric spectrum, 300 nm to 1000 μ m, we see small dark spots and faint vein-like faculae on a bright disk covered with very small granulation cells (Figure 4 upper panel). Areas of spots and faculae are small fractions of the total disk area. Thus, the bulk of the TSI comes from this nearly feature-less, bright disk. The spots and faculae associated with strong magnetic fields modulate the apparent solar output at the 0.1% level because of their small areas relative to total disk area.

At UV wavelengths below 180 nm and in some deep absorption lines such as CaII K 393.3 nm, the facular regions appear to fill with brighter fine structures than at visible wavelengths, i.e. as in Figure 4 middle panel. They are called plages. In the UV, the Sun still appears as a disk with a sharp edge; therefore, the bulk of UV radiation originates in thin layers immediately above the photosphere. At these shorter wavelengths, sunspots are covered by the UV emitting layers and become less visible. We now see the cause of differences between TSI and UV time series in Figures 3 upper panel and 3 middle panel: movement of plages across the disk as the Sun rotates produces the 27-day modulation in the UV irradiance. The transition from faculae to plage in magnetic regions occurs because we "see" higher layers due to an increase in opacity of the solar chromosphere at these wavelengths.

In the EUV and X-ray spectra below 30 nm, images 4b and 4c show dark coronal holes, bright active regions, and emission structures extending beyond 0.2 solar radii outside the disk. This distribution of bright and dark features results in X-ray variability in Figure 3 lower panel that is so different from that shown in the visible spectrum (Figure 2 upper panel) and UV (Figure 2 middle panel). Furthermore, sequences of these short wavelength images show transient brightenings due to solar flares and jet-like eruptions. Fluctuations in coronal radiations show higher frequencies than the longer wavelengths due to these transient events. Production of highly ionized FeXV and 2 nm X-rays requires electron temperatures of \sim 2 \times 10^{6° K compared with 6000° and 10,000° in the photosphere and chromosphere, respectively. Thermodynamically, EUV and X-ray emissions come from a tenuous, high temperature plasma capable of varying quite rapidly due to dynamic fine structures tied to the magnetic field lines.

The field lines arching into the corona are firmly rooted in the high density photosphere where the gas pressure is the controlling force. In the corona, the situation is reversed: magnetic tension and pressure dominate because the gas pressure is so low.

To appreciate the complexity of the magnetic structure of the corona, high resolution images are necessary. Figure 5 shows such an image at 17.1 nm from the TRACE experiment. The field lines connect to smaller regions in the atmosphere and then expand out into the low density corona. Furthermore, the emission appears to be concentrated along the field lines. This image shows the extreme inhomogeneity of the solar corona. Foreground structures are obviously transparent to emission from features in the background, i.e., the medium is optically thin. The transparency and inhomogeneity of the coronal plasma rules out simple layer models for estimating irradiances.

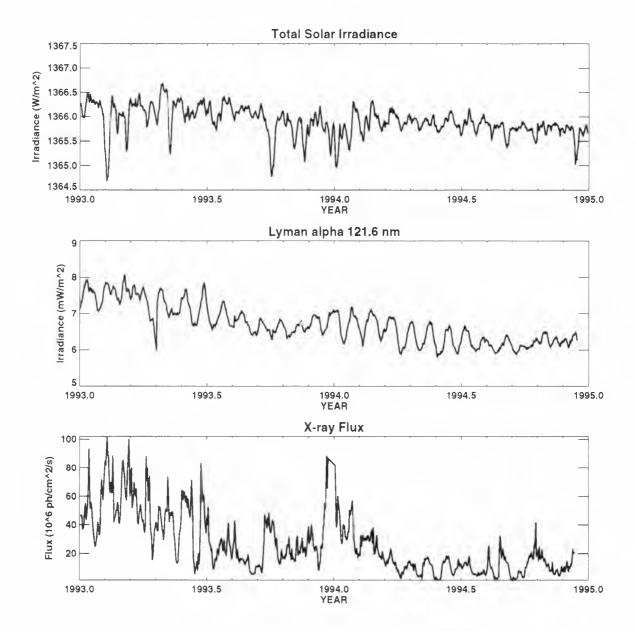
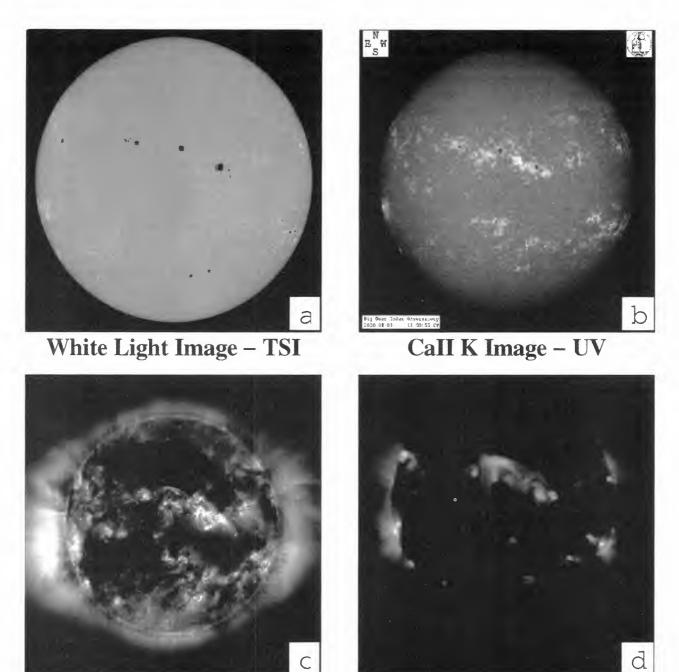


Figure 3. Comparison of TSI Variability with UV and X-ray Variability 1993-1995: TSI all wavelengths (upper), Ly α – UV 121.6 nm (middle), 1-2 nm X-ray (lower).



32



FeXV 19.5 nm Image – EUV

1-2 nm Image – X-ray

Figure 4. Appearance of the Sun in different "Irradiances." a. TSI – VIRGO/MDI white light image, b. UV lines – BBSO CaII K image, c. EUV – VIRGO/EIT image, d. X-ray – YOHKOH/SXT image.

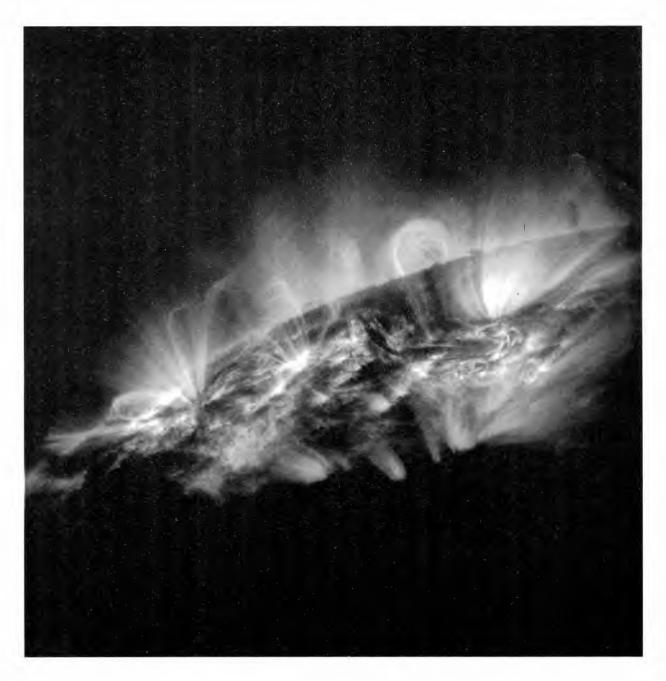


Figure 5. Image of Coronal Magnetic Structure illuminated by EUV emission from the FeXII 17.1 nm – EUV. Data on 08/19/1999 from the TRACE experiment.

3. CORONAL STRUCTURE AND VARIABILITY OF THE SOLAR WIND

3.1. Coronal Holes and Solar Wind Stream Interaction Regions

In coronal holes, the magnetic field lines are open into the interplanetary medium. This magnetic topology results in higher speed plasma flows relative to the flows from sunspot regions where the field lines close back to the photosphere and impede the solar wind outflow. As the Sun rotates, the higher speed outflow overtakes the slower wind and produces shocks in a thin boundary layer on the leading edge of the spiral wind stream. Such discontinuities scatter incoming energetic particles and thereby modulating the cosmic ray flux at the Earth. These interaction regions associated with coronal holes concentrate in spiral patterns near the solar magnetic equator and extend far into the heliosphere.

3.2. Coronal Mass Ejections, Flux Ropes, and Prominences

Ejections of coronal plasma are more dynamic events introducing structure into the solar wind. When ejected in a direction to intercept the Earth, they produce geomagnetic activity. CMEs appear to be expulsions of long, horizontal magnetic flux ropes associated with solar prominences. The solar image in Figure 6 shows prominences seen against the solar disk as dark filaments. A filament is a condensation of neutral hydrogen in the low corona that appears dark because it absorbs the radiation from below. They follow long channels that may extend nearly around the Sun. Such channels are observed to pass through sunspot regions as well as lie in quiet regions outside sunspot formation latitudes closer to the poles. Prominences show continuous internal flows and appear to be relatively stable for long periods of time. When observed "end-on" at the limb, filaments lie at the bases of helmet streamers in the corona. Current models show the condensation lying inside a large diameter magnetic flux rope with a helical field. The buoyant flux rope is held down in the corona by the hydrogen condensation. This configuration can be destabilized by violent events such as flares or more subtle changes in field topology in quiet regions. Such destabilization then allows the flux rope to rise through the corona and pass into the heliosphere, carrying with it the hydrogen condensation and magnetized plasma. Such an ejection is seen in the three coronagraph images in Figure 7. I emphasize that the filament eruption is only one part of the CME process. Excellent examples of CMEs can be seen in images from the Large Angle and Spectrometric Corongraph (LASCO) on SOHO.

Both coronal holes and mass ejections have characteristic cyclic signatures that follow the Schwabe cycle. Their aggregate effect produces fluctuations in the heliospheric plasma that can modulate the cosmic ray flux. We then have a terrestrially important variation in energetic particle fluxes that arises from coronal phenomena that have little direct connection to variations in the Sun's radiative output. Nevertheless, they correlate through the underlying cause, the solar magnetic cycle.

4. MODELING SOLAR VARIABILITY

Computations of the solar output and its variability are needed to replace missing data, past or present. Such estimates also can be made from models of structures observed in the solar atmosphere. Because of complexity of the magnetized solar atmosphere, a full "forward" computation of the Sun's output is not possible at the present time.

4.1. Radiative Variability

Estimates of solar radiation come from regression transformations and irradiances computed from model atmospheres. Regressions between two or more observables give a linear transfer function to estimate one variable from the other, i.e.,

$$\operatorname{Irrad}(\lambda_1, t) = a + b\operatorname{Irrad}(\lambda_2, t) . \tag{1}$$

A typical example is the use of the 10.7 cm radio flux to estimate UV irradiances. See Tobiska et al. (2000). A more successful approach is mult-variant regressions of an observed irradiance on a set of solar activity indices such as sunspot index, facular index, CaII K index, MgII index. For example,

$$\operatorname{Irrad}(\lambda, t) = a_{\lambda} + b_{\lambda} \operatorname{I}_{\text{sunspot}} + c_{\lambda} \operatorname{I}_{\text{faculae}} + d_{\lambda} \operatorname{I}_{\text{network}}$$
(2)

These indices contain information on the darkness of spots and the brightness of faculae and plages. This multi-variant scheme is the common method for estimating the TSI using data from daily solar images (Frohlich et al. 1988; Chapman et al. 1996).

Given a set of physical models of sunspots, faculae, quiet atmosphere, etc., and the theory for the production and transfer of radiation; radiation emerging from them can be computed and summed to give an irradiance, i.e.,

Irrad
$$(\lambda, t) = \Sigma_{\text{disk}} I_{\text{structure}}(\lambda, x, y)$$
 (3)

where emergent intensity $(\int S(\tau) \exp(-\tau) d\tau)$ from each structure is is computed and then summed over the full solar image. This synthesis approach has been used successfully by Solanki, et al. (1997) and Fontenla et al. (1999) to compute the solar spectrum and its variability.

Since the solar photosphere is the dominant source of radiative energy from the Sun, modeling it as a composite stellar atmosphere is a viable approach. Since

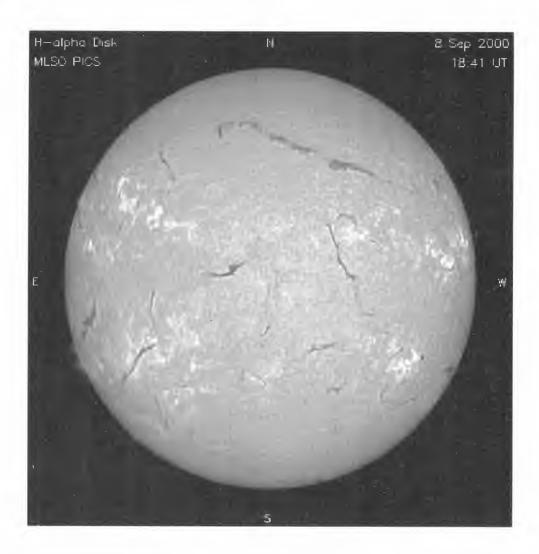


Figure 6. Solar Image in the HI 656.3 nm line, 08/09/2000. The dark filaments are prominences seen against the disk. They are the loci of magnetic flux ropes that produce CMEs. From the Mauna Loa Solar Observatory (HAO).

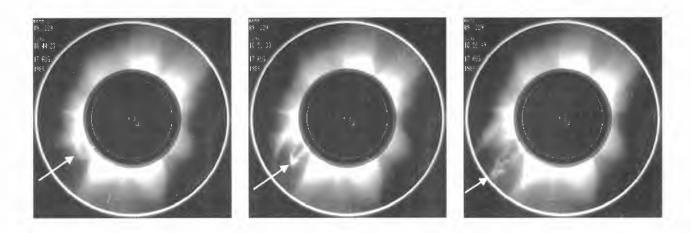


Figure 7. Images of the corona recorded on 08/17/1989 at 18:44 UT, 18:51 UT, and 18:54 UT. The sequence shows a prominence eruption and expulsion of coronal plasma in lower left quadrant. From the Mk3 coronagraph at the Mauna Loa Solar Observatory (IIAO).

the depth of the photosphere is so small relative to the solar radius, we use the plane parallel atmosphere approximation in solving the radiative transfer equations in the photosphere and low chromosphere. This condition fails as we go into the corona as demonstrated in Figure 5 where the EUV emission occurs in the thin flux tubes from active regions. Therefore, the increasing inhomogeneity and spatial extent of the solar atmosphere as we observe into the corona forces the use of multi-variant schemes (Equation 2) for estimating irradiances in the EUV. The transient nature of EUV and X-ray variability makes prediction difficult.

Given the reality of a highly structured solar atmosphere, the best method for determining radiative variability is to continue measuring it from space. But research to determine the physical conditions in sunspots, faculae, plages, prominences, and coronal holes must be continued as a basis for realistic prediction of solar change.

5. PLASMA VARIABILITY

The coronal structure and its extension into the heliosphere presents similar problems in estimating plasma variability. This is complicated further by the transient CME events associated with prominence eruptions. Theoretical models of magnetic flux ropes and prominences now exist (Low 1996; Rust & Kumar 1996), but they have not been applied to operational prediction of CMEs. The physics of solar wind stream interaction regions is understood, but their aggregate effect throughout the heliosphere is difficult to model. Observations of the speed, density, and magnetic field of the solar wind are now available from many spacecraft. These measurements give empirical boundary conditions for computation of heliospheric structure and its effect on spacecraft environment and cosmic ray fluxes. Such a computational approach is now underway in the Solar, Heliospheric, and Interplanetary Project (http://sec.noaa.gov/shine).

6. CONCLUSIONS AND QUESTIONS

We now know the degree of variability of the TSI during the last 22 years, and magnetic activity appears to be the principal source of the observed variations. However, we are not yet able to measure any long-term change in the quiet Sun because of uncertainties in the measurements and the shortness of the record. We also have a good picture of variability at wavelengths below 300 nm. Variability of the spectrum above 160 nm cannot be detected in data from current space experiments, except in the cores of strong absorption lines. Current atmospheric models do give spectral irradiances in the visible close to the observed values. Our record of UV, EUV, and X-ray variability will continue to improve as new instruments are flown in space to measure both irradiances and images showing the radiation sources. Many questions remain in our study of solar variability and its origins, though.

A very fundamental questions is: Does the Suns luminosity change? Irradiance measurements only define the Suns radiation in the direction of the Earth; therefore, they cannot determine the radiative output at all directions from the Sun. As in all stellar measurements, we assume that the luminosity is obtained from an irradiance by assuming spherical symmetry in the radiation field. Only advanced stellar atmosphere computations with magnetic fields can address this question.

Another puzzle is the formation of flux ropes needed for prominences and CMEs. Such magnetic flux ropes are observed, but how are they formed and maintained during the solar cycle, particularly at high latitudes. Equally important is the question of destabilization of these ropes to produce CMEs.

Foukal's observations of dark faculae at 1.6 microns is now questioned by new, high resolution observations (Foukal et al. 1989; Wang et al. 1998). Observation of dark faculae requires the temperature of faculae to crossover that of the quiet photosphere. This, in turn, gives a decrease in irradiance over broad ranges in the spectrum. If the temperature crossover does not exist, then the net effect of faculae is to increase the irradiance at all wavelengths.

The solar atmosphere is obviously not a quiet stellar envelope when observed at short wavelengths. High resolution observations of the chromosphere and corona show small scale transient fluctuations. The existence of such fluctuations questions the reality of statistical equilibrium in both excitation and ionization in our attempts to synthesize the spectrum.

7. RELEVANT CONFERENCES, INTERNET SITES, BOOKS

The literature on solar magnetic fields and their effects is extensive and increasing rapidly due to more use of the Internet. The following Web sites are sources for all of the solar images in this brief review:

- http://www.bbso.njit.edu/
- http://mlso.hao.ucar.edu/
- http://lasco-www.nrl.navy.mil/ http://umbra.nascom.nasa.gov/EIT
- http://penumbra.nascom.nasa.gov/TRACE/Data/
- http://umbra.nascom.nasa.gov/yohkoh_archive.html
- http://sohowww.nascom.nasa.gov/data/

Instructive papers on the subject can be found in the following conference proceedings:

The Solar Cycle, Proceedings of U.S. NSO 12th Sum-

mer Workshop, K.L. Harvey (ed.), Astronomical Society of the Pacific Conference Series, vol. 27, 1992

- The Solar Engine and Its Influence on Terrestrial Atmosphere and Climate, E. Nesme-Ribes (ed.), NATO ASI Series 1: Global Environmental Change, vol. 25, Springer-Verlag, 1993
- The Sun as a Variable Star: Solar and Stellar Irradiance Variations, Proceedings of the 143rd IAU Colloquium, J.M. Pap, C. Fröhlich, H.S. Hudson, and S.K. Solanki (eds.), Cambridge University Press, 1994
- The Sun as a Variable Star: Solar and Stellar Irradiance Variations (Contributed Papers), Proceedings of the 143rd IAU Colloquium, J.M. Pap, C.
 Fröhlich, H.S. Hudson, and W.K. Tobiska (eds), Solar Physics, vol. 154, no. 1, 1994
- Histoire Solaire et Climatique, E. Nesme-Ribes and G. Thuillier, Belin, Paris, 2000
- La Historia del Sol y El Cambio Climatico, M. Vazquez Abeledo, McGraw Hill, Madrid, 1998

ACKNOWLEDGMENTS

I am indebted to Gary Rottman and Tom Woods for access to the UV data from UARS/SOLSTICE and to Loren Acton for the YOHKOH/SXT x-ray flux data. The open data policies from the VIRGO, MDI, and EIT experiments on SOHO and the TRACE experiment made this pictorial presentation possible. Assistance from Cindy Worster, Randy Meisner, and Giuliana de Toma in preparing the final manuscript was invaluable. I am indebted to Peter Fox for solving last minute problems in production of this paper. This work is supported in part by NASA grant NAG5 7838.

REFERENCES

- Frohlich, C., Lean, J.L., 1997. In: New Eyes to See the Sun and Stars, IAU Symposium 185
- Chapman, G.A., Cookson, A.M., Dobias, J.J., 1996, Journal Geophysical Research, 101, 13541
- Solanki, S.K., Unruh, Y.C., 1997, A&A, 18, 4
- Fligge, M., Solanki, S.K., Unruh, Y.C., 2000, A&A, 353, 380
- Fontenla, J., White, O.R., Fox, P.A., et al., 1999, ApJ, 518, 480
- Foukal, P., Little, R., Graves, J., et al., 1990, ApJ, 353, 712
- Wang, H., Spirock, T.,Goode, P.R., et al., 1998, ApJ, 495, 957W
- Low, B.C, 1996, Sol. Phys., 167, 217L
- Rust, D.M. and Kumar, A., 1996, ApJ, 464L, 199R

Tobiska, W.K, Woods, T., Eparvier, F. et al., in press, "The SOLAR2000 empirical solar irradiance model and forecast tool," J. Atm. Solar Terr. Phys.

VARIATIONS IN TOTAL SOLAR IRRADIANCE DURING THE 11-YEAR SOLAR CYCLE

Georgeta Maris, Miruna-Daniela Popescu, Adrian Oncica

Astronomical Institute of the Romanian Academy St. Cutitul de Argint 5, RO-75212 Bucharest 28, Romania Fax: +40 1 337.33.89; tel.: +40 1 335 80 10 E-mail: gmaris@roastro.astro.ro

ABSTRACT

Our aim is to perform a study about the connections between the variations of the total solar irradiance (TSI) and the solar activity phenomena during the 11-year solar cycle. We use the TSI data registered by a lot of experiments (from ERB/NIMBUS 7 to VIRGO/SOHO) and the solar indices related to sunspot, radio flux on 10.7 cm, coronal green line and solar flare activity. A comparison between the solar cycles 21, 22 and the ascending phase of the 23rd cycle is made. Moreover, we tried to review the links between the global solar magnetic fields and the neutrino flux fluctuations, for understanding the solar interior role in the surface activity.

1. INTRODUCTION

The Sun is the primary source of energy responsible for governing both the weather and the climate of Earth. The proofs that our Sun is not a constant star are very well documented. For that reason alone, the idea that variations in the solar radiation output could be responsible for terrestrial changes in the Earth environment comes immediately in everybody's mind. "Global warming" has become a very hot and serious subject for a wide range of scientific communities, as it can have extensive social, ecological and economic implications. How much is the Sun responsible for this, and how much other natural or human-made processes, is still an open debate.

Much meteorological and climatic data suggest that there are significant responses in Earth's atmosphere and oceans to the variability of the Sun: drought cycles, variations in global sea surface temperatures, variations in stratospheric temperatures at specific locations and in the storms across the oceans, variations in the year-toyear tree growth as determined by tree-ring studies, and long-term climate variations. All of them show remarkable correlation with various forms of solar variability over time spans ranging up to 100,000 years. The generally accepted most likely mechanism for connecting the solar variability with the global climate is the variation of the total solar irradiance (TSI), which if it is large enough must undoubtedly affect climate.

Counting the TSI as a product of the solar interior processes with the atmosphere phenomena, some considerations about the solar interior role in the surface solar activity are made (section 2). In section 3, the TSI variations in correlation with some solar activity indices are analyzed during the maximum, the minimum and the ascending phase of the 11-year solar cycles 21-23. The results are discussed in comparison with the ones obtained for the whole TSI space registered period (since 1978). Short Fourier analyses of the longest series of indices (R. F 10.7 and TSI) are presented in section 4.

2. THE ROLE OF THE SOLAR INTERIOR IN THE SURFACE ACTIVITY

In order to understand the surface manifestation of the Sun's activity, one has to begin from the physical processes inside the Sun. because although the bulk of the solar energy is radiated into space from the photosphere, cromosphere and corona, it is generated in the central core. The only physical measurable quantity that can give us some information about what happens in the opaque interior of the Sun - is the solar neutrino rate. With the purpose to determine the solar neutrino fluxes of different energies, there are five detectors that take neutrino flux measurements since 1970: Homesake. GALLEX. SAGE. Kamiokande and SuperKamiokande. There are many attempts to establish if there is a correlation of the neutrino flux with the solar 11-year cycle. These studies are now in progress, the analysis of GALEX data showing an anti-correlation, while the SuperKamiokande data show a correlation with the activity cycle (Grandpierre 1999).

Proc. 1st Solar & Space Weather Euroconference, 'The Solar Cycle and Terrestrial Climate', Santa Cruz de Tenerife, Tenerife, Spain, 25-29 September 2000 (ESA SP-463, December 2000)

Even if it is controversial, we present here a few results found in the literature, for underlining the importance of the attempt to correlate all the processes that take place at all the layers of the Sun, from its core to the corona and its extension to the interplanetary space.

The phenomenon that links all the aspects of the solar variability is a common source, the magnetic activity of the Sun. Magnetic fields weave through the outer third of the Sun's interior - the convection zone - and penetrate the solar surface, extending outward through the solar atmosphere. This is why a connection between the global solar magnetic field and neutrino fluxes is an important approach. An anti-correlation between these two quantities was found. As the solar diameter rises up when the magnetic pressure decreases, a correlation between the solar size and measured neutrino fluxes was visible and even highly significant (Gavryuseva and Gavryusev 1999). Moreover, an important correlation was observed between the neutrino flux and the numbers of flares shifted by 27 days backward (Klochek et al. 2000). This is explained by the fact that the time necessary for the magnetic fields to emerge from the bottom of the convective zone to the Sun's surface is about 27 days (Moreno-Insertis et al. 1994). That correlation agrees with the idea that the interaction between neutrinos and solar magnetic fields occurs at the bottom of the convective zone (McNutt 1997).

3. TSI VARIATION ANALYSIS

The Sun's total (spectrally integrated) radiative output is the variability best quantified observationally. Overlapping cross-calibrated measurements made by active cavity radiometers since November 1978

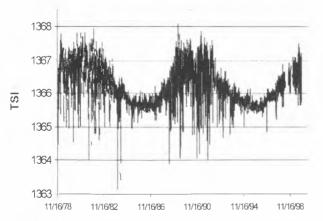


Figure 1. A composite record of total solar irradiance compiled from detailed cross-calibrations of various radiometric measurements from 1978 to 1999, adjusted to the absolute scale of Space Absolute Radiometric Reference (SARR).

compose a total irradiance database with sufficient longterm precision to identify an 11-year cycle (Willson 1994. Lee III et al. 1995) (see fig. 1).

The difference between the minimum and maximum amplitude of the total irradiance cycle may be as much as 0.15% and precedes the phase of solar activity (Schatten 1988).

This total irradiance variations have been explained in terms of a combination of decreases due to sunspot blocking and increases due to bright faculae and plages (Foukal and Lean. 1990) both of which are positively correlated with solar magnetic activity. The two effects tend to cancel each other, and the net positive correlation of the total solar irradiance is explained as a slight excess of facular brightening over sunspot darkening (Reid 2000).

3.1. Extreme Phases Studies of the Solar Cycles

By following the evolution of the solar activity phenomena throughout a cycle of 11 year we can distinguish the following phases of the cycle: minimum, ascending phase, maximum, descending phase. The cycle phases differ by duration and are characterized by different levels of solar activity. For this reason studies of correlations between various manifestations of the solar activity in each phase represent a very interesting topic of the solar physics.

The Romanian Solar Group at AIRA (the Astronomical Institute of the Romanian Academy) held by G. Mariş is implied in studies of the link between TSI and certain solar activity indices. in the maximum and minimum phase period for solar cycles. The study covers the solar cycles 21-23 (the maximum phase of the SC 21 (1979-1980). the minimum of SC 22 (1985-1987). the maximum of SC 22 (1989-1990). (Mariş and Dinulescu 1995. Mariş and Dinulescu 1997) the minimum of SC 23 (1996-1997) and the ascending phase of SC 23. The authors consider that the dependence between TSI and various solar activity indices should be analyzed separately for different phases of the solar cycle. taking into consideration the evolution of the solar magnetic field in a way specific to each phase of the cycle.

From the solar activity indices we have chosen:

R - the daily sunspot relative number (the Wolf number) (Sunspot Bulletin, SIDC-Brussels), defined as:

$$\mathbf{R} = \mathbf{k} \ (10\mathbf{g} + \mathbf{f}),$$

were g is number of sunspot groups. f is total number of spot on the visible hemisphere and \mathbf{k} reduces the observed values to the standard sunspot number:

F - the radio flux on 10.7 cm (2800 MHz), daily values expressed in units of 10^{22} Wm⁻²Hz⁻¹ (Solar-Geophysical Data, NGDC-Boulder, Colorado) (SGD).

In the previous papers there were used also other indices in our analysis. We review here some of them:

 I_c - the coronal index in green line, 530.3nm (Tatranska Lomnica Observatory):

 $I_f A$ - the daily flare total areas index defined by Mariş and Dinulescu (1997) as:

$$I_f A = \sum A_i$$

where $\sum A_i$ is the sum of the flare areas in one day, expressed in millionths of solar disk.

SFN - the daily scaled flare number defined by Pap and Vrsnak (1989) as:

$$SFN = \sum k_i N_i$$

were \mathbf{k}_i is the scaling coefficient with values ranging between 0.5 and 50, by the importance class of the flares, and \mathbf{N}_i is the daily number of flares in a particular class of importance, calculated by us for the period studied:

The correlation between TSI and the above mentioned solar indices has been analyzed (using the linear regression method) in the extreme phases of the solar cycles (maximum and minimum) as well as for the subdivision of these periods, as follows:

- a) in the *maximum phases* of the solar cycles 21 (1979-1980), 22 (1989-1990) and 23 (1999-2000);
- b) in the *minimum period of solar activity* for the cycles 21-22 (1985-1987) and 23 (1996-1997);
- c) for *annual periods*: 1979; 1980; 1985; 1986; 1987; 1989; 1990;
- d) on *Carrington rotations*. from rotations 1758 to 1796 and 1809 to 1836;
- c) in *deeps of irradiance* (D1: 27 Feb. 2 May 1980;
 D2: quarterlyIV.1980; D3: quarterly II, 1989; D4: quarterly III, 1990).

In the tables below we present the correlation coefficients between TSI and the solar activity indices used for the minimum (table 1) and respectively maximum phase (table 2) of the last three cycles.

Table 1. The correlation coefficients between TSI and the solar activity indices during the **minimum phase** between the solar cycles 21 - 22.

Interval	R	F 10.7	I _C	$I_{f}A$	SEN
*85 - *87	+0.091	± 0.224	+0.435	-0.086	-0.022
1985	-0.233	-0.228	+0.285	-0.320	-0.252
1986	-0.199	-0.199	-0.189	+0.335	-0.177
1987	+0.202	-0.384	+0.684	+0.042	-0.077
D '86	-0.350	-0.228	+0.435	-0.281	-0.244

<i>Minimum SC</i> 22 - 23:	
(Feb. 1996 - Feb. 1997	r (TSI, R) = -0.121
	r(TSI, F 10.7) = -0.119

No correlation is observed between TSI and any of the analyzed indices during the minimum phases (SC 21-22: 1985-87 and SC 23: 1996-97 – see table 1).

Unlike the maximum solar periods, where a large number of well-defined "deeps" is registered. in the analyzed minimum only one significant "deep". 3 September - 31 December 1986 could be selected. The TSI registered a pronounced decrease over several days. followed up by a slow reversion to the previous values; this demonstrates once more the complexity of high energy phenomena at the scale of the entire solar atmosphere which by determining each other bring about unforeseen consequences in the TSI variation. On the "deeps" analyzed in the maximum phases, the absolute values of the correlation coefficients were without exception higher than those of the "deep" analyzed in the minimum (Maris and Dinulescu. 1995). The "deep" of the minima emphasizes a more pronounced anti-correlation between TSI and R than in the annual intervals or throughout the entire interval considered, the same tendency being maintained also for the flare activity evaluated through IfA and SFN. While between TSI and F10.7 there is a rather anti-correlation. between TSI and I_c there is a slightly positive correlation: this fact demonstrates, on the one hand, an anti-phase variation between the TSI and the UV radiation (well approximated by the F 10.7 index) from the low corona, and, on the other hand, an almost linear dependence between TSI and the green emission of the upper corona (estimated by the I_c index).

Given the intrinsic relationship between the solar differential rotation and the generation of the toroidal magnetic fields that determine the small-scale magnetic activity in the solar atmosphere (the activity regions). we have presented in detail the analysis of the linear correlation on the Carrington solar rotations. Out of the total 39 solar rotations analyzed. in 61% of the cases the correlation index oscillates between positive and negative values indicating the correlation or anticorrelation, respectively, between TSI and various manifestations of the solar activity in the photosphere. chromosphere and corona. In 13% of the rotations, the correlation coefficient between TSI and the considered indices remains negative, which means that there is a variation of the analyzed phenomena in anti-phase. The correlation coefficient has a strange behaviour in 26% of the rotations studied, when it remains positive for all the analyzed phenomena. The positive correlation is explained by the absence of spots groups in the photosphere (R = 0) in the longer periods specific to the solar activity minimum, which determines the quasitotal absence also of the flare phenomena from the chromosphere ($I_f A = 0$, SFN = 0).

A slight anti-correlation between TSI and R is observed for the deep of irradiance (D'86), due to the blocking effect of the sunspots. A slight positive value of the correlation coefficient appears for the year 1987. This is because the 1987 year is already the beginning of the ascending phase of SC 22 and, as we will see also for the ascending phase of SC 23, it may be a confirmation of a diminish of the sunspots blocking effect.

Between TSI and F 10.7. there are the same trends as for the above indices, with a slight negative value in the deep D'86 and an increase of the UV radiation contribution to TSI for the beginning of the ascending phase of SC 22 (1987).

The correlation coefficients between TSI and the coronal index I_C has an increased value for the year 1987, while for the flare indices only one slight positive value is found for the year 1986. This proves that the cruptive area (I_tA) brought some contribution, through its emissivity from X-rays to visible light, to the total solar radiation output.

Table 2. The correlation coefficients between TSI and the solar activity indices on the **maximum phases** of the SCs 21 and 22.

Interval	R	F 10.7	Ic	$I_{\rm f}A$	SFN
1979	-0.528	-0.497	0.176	-0.302	-0.264
1980	-0.412	-0.566	-0.006	-0.465	-0.385
1989	-0. 419	-0.375	-0.467	-0.117	-0.094
1990	-0.280	-0.182	-0.249	-0.139	+0.236
D ₁ '80	-0.450	-0.666	-0.696	-0.584	-0.558
D ₂ '80	-0.506	-0.831	-0.022	-0.588	-0.519
D '89	-0.655	-0.399	-0.606	-0.190	+0.117
D '90	-0.761	-0.339	-0.718	-0.252	-0.191

The study of the maximum phases shows an anticorrelation between TSI – R and TSI – F 10.7 (see table 2) due to the fact that in this phase the blocking effects of the sunspots are dominating and the active regions contribution in the radio flux manifests in a stronger way. The negative values become more evident in the deeps of irradiance. In the deeps of SC 21 (D₁ '80 and D₂ '80) the anti-correlation of the radio flux and eruptive areas is more powerful, while in the deeps of SC 22 (D '89 and D '90) we have higher values for the coronal index.

3.2. The Current Solar Cycle Analysis

The ascending trend of all the three indices (TSI. R and F 10.7) can observe in the figure below. for the period 1996-1999 (the ascending phase of the current cycle). For the last 100 days in the graphs a different shape between TSI curve and the other two curves is evident that corresponds to the beginning of the maximum

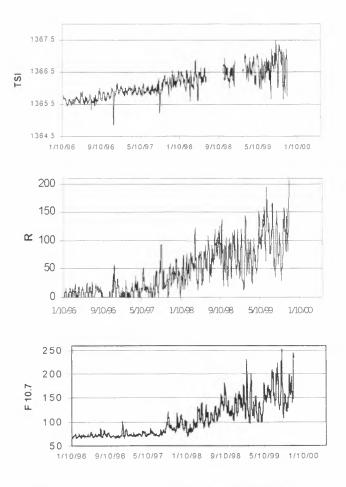


Figure 2. The total solar irradiance (TSI), the daily sunspot relative number (R) and, the radio flux on 10.7 cm (F 10.7) for the ascending phase of the SC 23.

phase of the solar cycle, where the blocking effect is acting more efficiently.

The correlation coefficients between TSI and the solar
activity indices during the ascending phase of SC 23:
Oct. 1996 – Nov. 1999: $r(TSI, R) = +0.415$
r (TSI, F 10.7) = +0.530

For the ascending phase of the present solar cycle one can see a positive value of the correlation coefficients both between TSI and R as well as TSI and F 10.7. This tendency remains the same over the entire period Nov. 1978 – Nov. 1999 (evidently, the correlation is slightly lower, but it remains positive).

The correlation coefficients between TSI and the solar
activity indices during the period 1978 1999:
Nov. 1978 – Nov. 1999: r (TSI, R) = + 0.367
r (TSI, F 10.7) = +0.400

The period Nov. 1978 – Nov. 1999 begins a year before the maximum of SC 21 and contains two fazes of maximum, two of minimum, two ascendant and two descendent phases, therefore, two complete cycles of 11 year. The positive value of r (TSI, R) and r (TSI, F 10.7) for two complete cycles is quite unexpected. It seems that the tendency manifested on the ascending phase of SC 23 imposes a general trend for a longer period. One can see the same tendency for the year 1987, that can be considered the beginning of the ascending phase of SC 22 (see table 1).

4. SPECTRAL ANALYSIS OF TSI, R AND F 10.7

On the series of data we applied the estimated power spectral density using Welch's averaged periodogram method. The data are divided into overlapping sections, each of which is detrended and windowed by a Hanning window. The results are presented in figure 3. We choose to focus only on the interval between ten and a hundred days because here we expect to find the relevant information. For R and F 10.7 a peak at about 28 days can be observed. For TSI, a deep at about 28 days appears, superposed over a larger plateau between 25 and 40 days. The same plateau could be observed in the R power spectral density. An harmonic component at about 14 days is seen in R and TSI data and practically absent in F 10.7 data.

The coherence function, defined as: $|P_{xy}|^2 / (P_{xy}, P_{yy})$ shows the little coherence of TSI data with R and F10.7, respectively, except for a surprising feature around 60 days. The sunspot – radio coherence function reaches a peak of over 90% at 28 days and keeps its value higher of 90% over the entire spectrum.

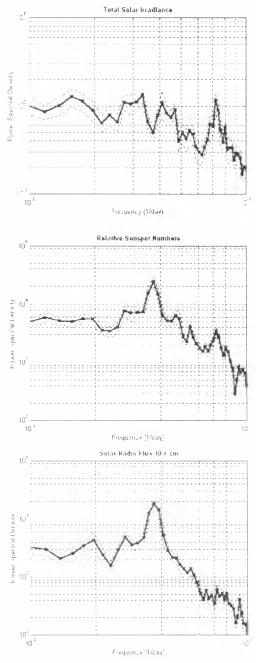


Figure 3: The power spectral density of TSI, R and 17:10⁻⁷

5. CONCLUSIONS

This correlation TSI - R is due to the fact that R is a numerical index, it gives no information about the sunspots importance (area). During the maximum

phases, there are big sunspots that define very energetic active regions that have usually big flares; these highly emissive regions give the 0.15 % rise of the total

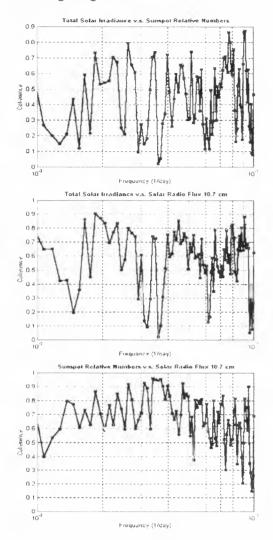


Figure 4. The coherence function: TSI v.s R, TSI v.s. F10.7, and R v.s. F10.7.

radiation output observed during the maximum activity periods. The situation is completely different during the minimum, when the sunspots blocking effect is weaker because there are no big sunspot groups and no important emissive events. Here, the correlation coefficients are decreasing to zero.

The positive correlation between TSI and R or F10.7 during the ascending phase, remains a matter of a further study as well as a deeper Fourier analysis applied on the studied indices. The correlation between TSI and some solar activity indices also ask for other

indices that would characterize better the physical properties of the involved phenomena.

The strange correlation between very important global characteristics of the solar power engine should be regarded as an evidence of the connection between the processes taking place inside the Sun and its outer layers.

ACKNOWLEDGEMENTS

Two of us (G. M. and M.-D. P.) are grateful to the organizers of the First SOLSPA Euroconference for financial support to attend the meeting.

REFERENCES

- Foukal P., Lean J., 1990. Science 247, 556
- Gavryuseva E.A. and Gavryusev V.G. 1999 in: Long and Short Term Variability in Sun's History and Global Change, ed. Schroder W., p. 89

Grandpierre A. 1999. A & A. 348, 993

- Klochek N.V., Nikonova M.V., Sotnikova R.T. 2000, JENAM Poster Session
- Lee III. R. B., Gibson, M. A., Wilson, R. S., Thomas, S., 1995, J. Geophys. Res., 100, 1667

Maris, G., Dinulescu, S., 1995, Rom. Astron. J. 5, 121

- Mariş, G., Dinulescu, S., 1997, Rom. Astron. J. 7, 11
- McNutt, L. Jr., 1997. Preprint SRA-97-06
- Moreno-Insertis, N., Schussler, M., Caligary, P., 1994, in: Rutten R.J. and Schrjiver C.J. (eds.) Solar Surface Magnetism, p. 407
- Pap. J., Vrsnak, B., 1989, LAU Colloquium 104, Poster Papers, Haisch, B. M. and Rodono, M. (eds.).
 Catania Astrophysical Obs., Special Publ., p. 243
- Reid, G.C., 1995, Rev. Geophys., 33, Suppl., 103
- Schatten, K.H., 1988, Geophys. Res. Lett. 1, 121
- Willson R.C. 1994 in: Pap J.M., Frohlich C., Hudson H.S., Solanki S.K., (eds.) *The sun as a Variable Star*, IAU Colloq, 143, p. 4, Cambridge, Cambridge Univ. Press

¹LASP, University of Colorado, Boulder, COLORADO, USA ²HAO, National Center for Atmospheric Research, Boulder, COLORADO, USA

Giuliana de Toma¹ and Oran R. White²

FROM SOLAR MINIMUM TO SOLAR MAXIMUM: CHANGES IN TOTAL AND SPECTRAL SOLAR IRRADIANCE

ABSTRACT

The rising phase of solar cycle 23 from the time of minimum in 1996 to its high activity phase in 2000, is significantly different from the previous two cycles. Cycle 23 is magnetically weaker with sunspot and facular area almost a factor of two lower than in cycle 22. The evolution of total solar irradiance (TSI) relative to solar magnetic flux and activity indices is different for the rising phase of this cycle. While most activity indices are consistently lower for cycle 23, current measurements of TSI from SOHO/VIRGO and UARS/ACRIMII indicate an increase similar to the one observed during the past solar cycle. Models of TSI based on facular excess and sunspot photometry gave good TSI estimates for cycle 22, but they give TSI estimates below the observed values for cycle 23. This difference raises questions about TSI observations themselves, TSI estimates based on ground-based observations and the sources of solar radiative variability. We review the recent measurements of solar magnetism, solar activity and radiative variability from both ground-based and space observatories to give a comprehensive overview of the rising phases of both solar cycle 22 and 23.

Key words: Sun: activity, Sun: irradiance, Methods: data analysis.

1. INTRODUCTION

The solar activity cycle has been observed in sunspots for centuries, but measurements of solar irradiance and solar magnetic flux cover only two and a half cycles, i.e. cycles 21–23. Solar cycles 21 and 22 were very active cycles, but cycle 23 has been a weak cycle so far. Other cycles, such as solar cycles 9 and 17, similar to cycle 23 existed in the past, but this is the first time that a relatively weak cycle is observed with a modern array of instruments. In this paper, we analyze the rising phase of solar cycle 23, from the time of solar minimum in 1996 into its maximum phase in summer of 2000. We will describe the evolution of the solar irradiance and magnetic flux during this time and compare it to the analogous period for cycle 22. In particular, we will discuss the measurements of total solar irradiance (TSI) during the two cycles and their relationship to magnetic flux observations. Since its beginning in 1996, solar cycle 23 has been magnetically less active, with sunspot area and total magnetic flux systematically below the values for the two previous cycles. In contrast, the SOHO/VIRGO and UARS/ACRIMII experiment show an increase in TSI in 1999 larger then expected from empirical models based on sunspot and facular observations. If this "anomalous" behavior of TSI is real, it raises the question if magnetic activity in the form of sunspots, faculae, and enhanced network is the only source of solar radiative variability. Given the importance of variations in the Sun's radiative output for the Earth's environment, this question is relevant not only to understand the solar activity cycle, but also the solar influence on the Earth's system.

2. THE RISE OF SOLAR CYCLE 23: 1996–2000 PERIOD

Solar minimum between solar cycle 22 and 23 occurred in 1996. Minimal solar activity was reached in the spring and fall of 1996. These two periods had equally low solar activity and were separated by a small burst of activity of the declining cycle 22. The time of solar minimum is not a single point in time, but rather an extended period, usually lasting a couple of years, when the old and new cycles coexist and the average level for magnetic activity remains low. It is often useful for practical purposes to define the onset of a new cycle more precisely. The time of minimum for solar cycle 23 was chosen in October 1996 (Joselyn et al., 1997; de Toma, White, & Harvey, 2000). Activity remained very low until the summer of 1997, when, in two solar rotations, there was an increase in the emergence of magnetic flux in the solar atmosphere. Several new active regions appeared between August and September 1997, and there was a relatively small, but clear, increase in most indices of solar activity (Figures 2-3). Activity continued to rise in the years 1997-1999, but the

Proc. 1st Solar & Space Weather Euroconference, 'The Solar Cycle and Terrestrial Climate', Santa Cruz de Tenerife, Tenerife, Spain, 25-29 September 2000 (ESA SP-463, December 2000)

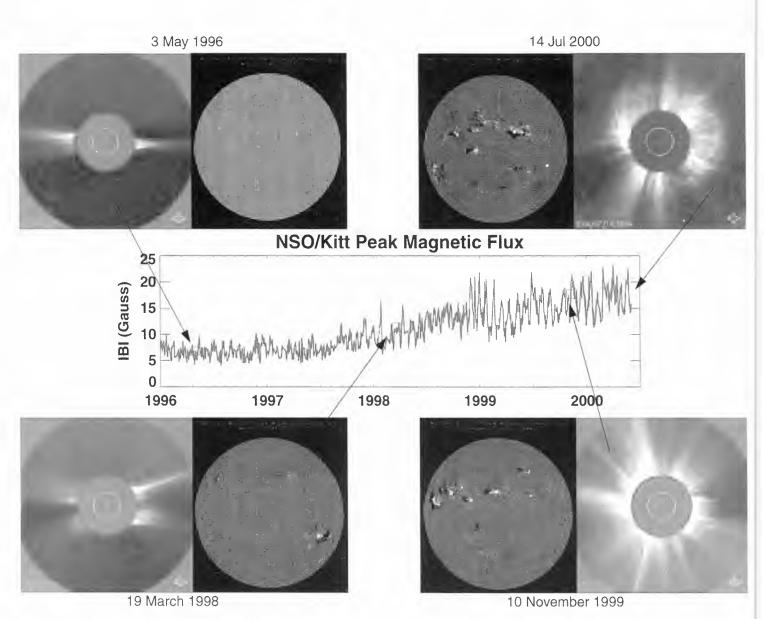


Figure 1: Evolution of the solar corona (SOHO/LASCO) and of the photosperic magnetic field (NSO/Kitt Peak) during the rising phase of solar cycle 23. At the time of solar minimum in the Spring of 1996, there are not active regions on the solar disk and only the magnetic network is visible. At the same time, the corona is weaker and coronal streamers are confined at equatorial latitudes. In March 1998, the cycle has reached a moderate activity level. We notice an increase in the coronal emission, and two bands of active regions associated with the new cycle 23 which have formed at midlatitudes. As the cycle evolves, there is an increase in the magnetic flux emergence, and the corona assumes a more symmetric shape. The November 1999 images are at high activity: the corona is very symmetric, with streamers visible at many latitudes, and large activity complexes are seen in the Northern hemisphere of the Sun. The LASCO image on July 14, 2000 shows a coronal mass ejection (CME) event which was preceded by a large flare. The CME induced an interplanetary shock wave and caused a large (class G5) geomagnetic storm the following day. This was the largest solar particle event so far in cycle 23.

	1986	1989	1990	1996	1999	2000*
Magnetic Flux	7.200	18.898	21.057	6.743	15.014	17.075
HeI 1083nm index	46.139	76.578	74.960	42.732	68.773	74.231
Mg II 280nm index	.264	.282	.279	.264	.274	
F10.7 radio flux	74.0	213.4	189.8	72.0	153.5	181.3
Sunspot Number	13.4	157.6	142.6	8.6	93.3	118.8
Sunspot Area	73.7	1828.07	1333.83	55.25	862.50	1425.08
Facular Area		28552.0	23369.2	1444.5	12496.6	18275.7
TSI (Nimbus 7/ERB)	1371.414	1372.299	1372.641			
TSI (SOHO/VIRGO v2.5)				1365.634	1366.608	
TSI (SOHO/VIRGO v3.0)				1366.038	1366.850	1366.918
TSI (SOHO/DIARAD)				1366.162	1366.976	1367.241

Table 1. Solar Activity Indices and Total Solar Irradiance: Yearly Values

*Averages for the year 2000 are based on the period January-June 2000, and are still preliminary

rise was fairly slow, characterized by small, simple, and short-lived sunspots and sunspot groups and by a relatively low flare activity. The highest values for sunspot number and the 10.7 cm radio flux were reached in November of 1999 and again in March and July 2000. The first half of 2000, as we approached solar maximum, was characterized by higher solar activity and an increasing number of CMEs and flare events, often associated to geomagnetic storms like the storms on April 7, June 8 and July 15, 2000. The latter was a very strong geomagnetic storm, which followed an intense flare eruption and full-halo CME on July 14 (Figure 1), and has been the largest solar radiation storm so far in cycle 23. Geomagnetic storms have also been associated to coronal holes at equatorial latitudes, as on Feruary 24 and August 28, 2000. In the spring-summer of 2000 sunspot number and 10.7 cm radio flux fluctuated a lot going from relatively high values, as on May 16 (ssn = 189and F10.7 = 264.5) and on July 18 (ssn = 228 and F10.7 = 270.5), to low values, as on May 6 (ssn = 50) and F10.7 = 129.1). However, the average values for sunspots, radio flux, as well as, magnetic flux remain moderate and systematically below the values observed in the two previous cycles, as illustrated by Table 1 and Figures 2–3.

As the cycle progresses, the distribution of photospheric magnetic fields and the shape of the solar corona change significantly (Figure 1). A number of observations, such as the distribution of coronal streamers and of coronal holes, the topology of the unipolar magnetic fields in the polar regions, and the latitudinal distribution of sunspot regions, all indicate that in summer of 2000 we are reaching the maximum phase of solar cycle 23. Observations of the solar corona from SOHO/LASCO (Figure 1) and MLSO/MK4 show the corona has an almost symmetric configurations, typical of solar maximum. Coronal holes and helmet streamers, have been reaching equatorial latitudes since winter of 2000. In summer of 2000, the unipolar magnetic field in the polar region is weak, i.e. about 0.2×10^{22} Mx in the North and -0.2 10²² Mx in the South, according to NSO/Kitt Peak data, but has not reversed yet. Sunspots are appearing over a large range of latitudes from about 3 to 38 deg. in both hemispheres.

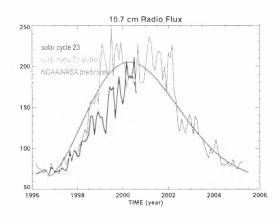


Figure 2. Comparison of the observed values of the 10.7 cm radio flux for solar cycle 23, with the NOAA/NASA solar prediction made in 1997, and with the previous cycle. Solar cycle 22 data have been shifted to match the time of minimum between cycle 21 and 22 in September 1986 with the recent minimum in October 1996.

Some active regions are occurring below 10 deg. and a few within 5 deg. from the equator.

Solar cycle 23 has been so far much weaker than expected by the NOAA/NASA predictions made in September 1997 shown in Figure 2. Cycle 23 has shown a relatively slow rise during his ascending phase in 1997–1999, and has not reach the level of activity seen in cycle 22 and 21 yet.

2.1. Comparison of Solar Cycle 22 and 23

In Figure 3, we present the time series for the composite TSI (Fröhlich & Lean, 1997), the NSO/Kitt Peak magnetic flux data, and some common indices of solar activity. They include chromospheric indices such as the Mg II core-to-wing ratio at 280 nm and He I equivalent width at 1083 nm, the coronal 10.7 cm radio flux, and the sunspot number. Average values during low and high activity for cycles 22 and 23 are given in Table 1, where we report annual averages at solar minimum and two and three years after minimum. Analysis of these observations shows that cycle 23 has been less vigorous magnetically than

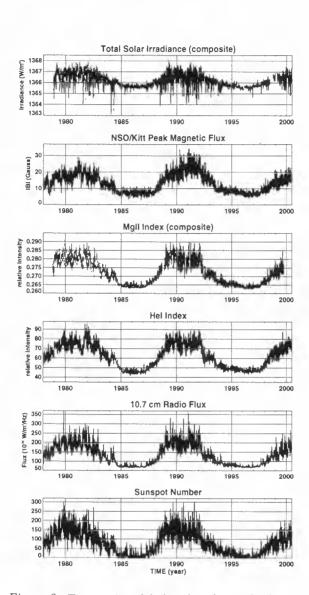


Figure 3. Time series of daily values for total solar irradiance (composite), NSO/Kitt Peak magnetic flux data, Mg II 280 nm index (composite), the He I 1083 nm index, the 10.7 cm radio flux, and the sunspot number from 1978 to the present. The rising phase of cycle 23 is quite different from cycle 21 and 22. Cycle 21 and 22 were strong cycles with a fairly rapid rise from minimum to maximum activity. So far cycle 23 has been a weaker cycle. On average, sunspot number, 10.7 radio flux, magnetic flux, and the Mg II and He I indices are lower for cycle 23 than for the two previous cycles. In 2000, during the maximum phase of cycle 23, sunspot number and area fluctuated a lot reaching at times unusually low values. In contrast, the observed values for TSI in late 1999 and 2000 are almost at the same level observed during the previous cycle maximum in 1989.

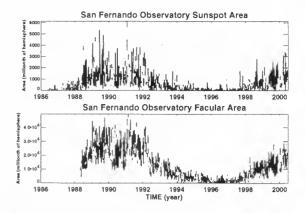


Figure 4. Sunspot and facular areas derived from images taken at San Fernando Observatory in the blue continuum at 672.3 nm and in the Ca II k line at 393.4 nm, respectively.

cycles 21 and 22. The photospheric magnetic flux, most activity indices, as well as UV irradiance have lower values for this cycle. In particular, we note the lower values for sunspot number and area for this cycle. Observations at San Fernando Observatory of sunspot and facular area are a factor of two lower than in solar cycle 22 (Figure 4, and Table 1). This is consistent with the magnetic flux measured at NSO/Kitt Peak, and with the weaker effect of sunspot passages on TSI. However, the relative increase in TSI from minimum to maximum is about the same for both cycle 22 and 23.

3. TOTAL SOLAR IRRADIANCE

In Figure 5, we note the decrease in the effect of sunspot disk passages on TSI during the rise of cycle 23 compared to the corresponding phase of cycle 22, as expected from the photometric observations of sunspots which indicate a decrease in the number of large spots and spot groups. Despite the weaker effect of sunspots on TSI, the relative increase in TSI in 1999–2000 is similar to the one observed during the maximum phase of cycle 22. Empirical models based on sunspots and faculae, which well represented TSI observations during the last solar cycle, fail to explain completely the observed rise in TSI during the present cycle.

3.1. Observations and Models

Measurements of TSI from SOHO/VIRGO v2.5 showed an early increase in TSI starting at the end of 1996 and continuing in 1997. At the end of 1999, the observed increase in TSI was already 1 Wm^{-2} , and comparable to the increase observed in TSI by Nimbus-7/ERB during the maximum of solar cycle 22 (Figure 5). UARS/ACRIMII observations, currently available up to 1999, seemed to confirm the trend in the SOHO/VIRGO observations. In contrast, the magnetic flux remained low until September 1997, and only in the fall of 1997 started to show the effects of increased solar activity. Observations of chromospheric irradiances also showed very little

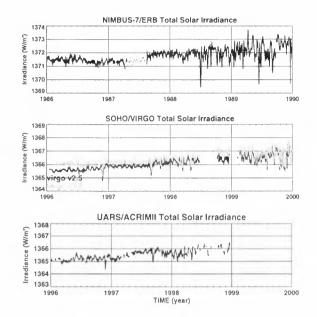


Figure 5. Total solar irradiance as measured by Nimbus-7/ERB, SOHO/VIRGO and UARS/ACRIMII during the rising phase of solar cycle 22 and 23. The difference in the absolute values of the observations is due to differences in the absolute calibration of the instruments. The average increase in total solar irradiance during the first three years of cycle 22 and 23 are similar, but the modulation of total solar irradiance induced by sunspot passages across the solar disk is much weaker for cycle 23.

or no increase until the summer of 1997, in agreement with the magnetic flux evolution.

To better understand the TSI observations, we have used empirical model of TSI based on the photometric indices derived at San Fernando Observatory (Chapman, Cookson, & Dobias, 1996; Chapman et al., 1997). Images in the CaII K line at 393.4 nm are used to estimate bright features in the form of plages/faculae and network, while images in the red continuum at 672.3 nm are used to estimate the photospheric contribution of sunspots. The indices are derived from the residual images, i.e. after the quiet Sun center-to-limb variation has been subtracted, and the intensity is normalized to the disk center intensity (Walton & Preminger, 1999). All the pixels are added together with the appropriate contrast and therefore, include both dark and bright features. The CaII index is dominated by bright structures and the red continuum index by sunspots. These indices, which give the contrast pixel by pixel, are superior to other commonly used photometric indices, which assume the contrast for spots and faculae, i.e. PSI (Fröhlich, Pap, & Hudson, 1994) and PFI (Lean et al., 1988 and references therein).

In Figure 6, we present the TSI model based on the San Fernando photometric indices and its fit to observations. The model is computed for the period 1988–1996 and extrapolated forward in time. Models estimates are in excellent agreement with observations for solar cycle 22: the correlation coefficient is 0.935 and accounts for 87% of the variance of the data. The model predicts an increase of about $0.5 \,\mathrm{Wm^{-2}}$ from 1996 to the end of 1999, and un-

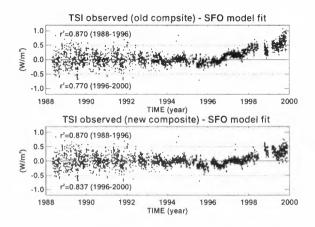


Figure 6. Residuals between total solar irradiance composite as derived from satellite observations and modeled irradiance using San Fernando indices. The model is based on a fit to observations for the period 1988-1996and extrapolated forward in time. Both version v2.5 (top panel) and v3.0 (bottom panel) of the VIRGO data are compared with model estimates. The model is in better agreement with version v3.0 than with v2.5, but for both versions the observed increase in 1999 is larger than the modeled increase.

derestimates the observations from SOHO/VIRGO v2.5 by about a factor of two. The disagreement between model estimates and SOHO/VIRGO v2.5 starts in 1996 and continues to the present time (de Toma et al., 2000b). Results similar to ours have been obtained by Fröhlich (1999) using an empirical model based on different facular and sunspot proxies. The disagreement between observations and models of TSI has led to a revision of the SOHO/VIRGO observations. VIRGO data are the weighted average of measurements from two radiometers, PMO6 and DIARAD (Fröhlich & Anklin, 2000) on board the SOHO spacecraft. Anomalies have been found in both radiometers after the instruments are powered off. A new version of the VIRGO data, v3.0, have been released on September 4, 2000. The VIRGO v3.0 data (Figure 5) are significantly different from the v2.5 data. For version v3.0, the increase from minimum to maximum is reduced from $1 \,\mathrm{Wm^{-2}}$ to $0.8 \, \mathrm{Wm^{-2}}$. A different sensitivity correction from the one used in VIRGO v3.0 is applied to the DI-ARAD data from the DIARAD team. The latest DIARAD data also show a TSI increase in late 1999 of $0.8 \,\mathrm{Wm^{-2}}$, in agreement with VIRGO version v3.0 (Table 1). A comparison between SOHO/VIRGO v3.0 observations and the model estimates is shown in the bottom panel of Figure 6. Models estimates and observations have an higher correlations in 1996– 2000 for the VIRGO data v3.0 than for v2.5 and there is very good agreement up to 1997. However, starting in 1998 the observations show a faster increase. In figure 7, we present a second set of models for the rising phase of cycle 22 and 23, where we fit Nimbus-7/ERB and SOHO/VIRGO v3.0 separately during the period 1986-1999, and 1996-1999. In this case, we used the MgII index to estimate facular and network contribution, since the San Fernando CaII K images we used before to estimate

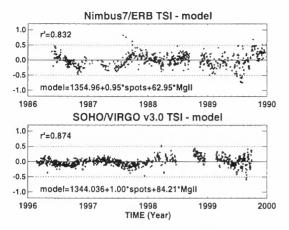


Figure 7. In the two panels we show the residuals between model fits and observations from Nimbus-7/ERB, and SOHO/VIRGO v3.0 for the rising phase of solar cycle 22 and 23. The models use the San Fernando index for sunspots and the Mg II index for faculae to estimate total solar irradiance. Good correlation between data and models is found for both cycle 22 and 23, but the model equations are significantly different. To fit the observed rise in total solar irradiance during cycle 23, a higher coefficient for the facular term is needed.

faculae and network started only in 1988 and does not cover the rising phase of cycle 22. We find very good agreement between models and observations for both Nimbus-7/ERB and SOHO/VIRGO data, with correlation coefficients of 0.91 and 0.93, respectively. However, to account for the faster rise in TSI during this cycle, the coefficient in the linear regression for our facular index, in this case the Mg II index, is almost 33% larger for cycle 23 than for cycle 22.

Empirical models based on sunspots and faculae have been largely used in the past to model TSI (Foukal & Lean, 1988; Chapman et al., 1996; Lean et al., 1998). Results for solar cycle 22 have given very good fits to observations, leading to the assumption that "dark" spots and "bright" faculae and network are responsible for most of the observed variability in TSI (Chapman et al., 1996; Lean et al., 1998). We now find that is not possible to fit cycle 22 and 23 with the same model. It is very important to determine if the current measurements of TSI are correct, and if the difference between the two cycles is real. We emphasize the challenge to measure TSI with an accuracy of 200ppm, which is necessary to understand the TSI differences we see.

4. CONCLUSIONS

We are now in the maximum phase of solar cycle 23. This is usually an extended period of time, that lasts 2 or 3 years. The periods of highest activity during the rise of cycle 23 were in November 1999, and July 2000.

So far, cycle 23 has been magnetically weaker than the two previous cycles, this is confirmed by a number of observations including: sunspot area and number, magnetic flux, coronal 10.7 cm radio flux, and the chromospheric Mg II and He I indices. TSI evolution during this cycle is not completely consistent with magnetic flux and the other indices of solar activity. TSI values in late 1999 are larger then expected by empirical models based on cycle 22 observations. To fit TSI observations well during cycle 23, an increase in the facular contribution to TSI of about 33% relative to cycle 22 is necessary, according to our model estimates.

If the measures of TSI are correct, the faster increase in TSI suggests that the sources of radiative variability may be different for this cycle. It is very important to investigate this discrepancy between the two cycles further to better understand the sources of TSI variability. This is crucial not only to the understanding of the Sun itself, but to the understanding of the solar influence on the Earth's atmosphere and climate. However, measurements of one complete cycle (cycle 22) and parts of cycles 21 and 23 are not enough to understand fully if and how the solar atmosphere may have changed between cycles 22 and 23. It is thus very important to continue the TSI measurement programs through cycle 23 and in the future.

ACKNOWLEDGMENTS

We thank Dr. Gary Chapman and Dr. Stephen Walton for making available to us the San Fernando photometric indices and for the useful discussions on TSI models. We are grateful to Dr. Karen Harvey for her helpful comments on solar cycle evolution. We thank Dr. Jack Harvey for providing the magnetic flux and He I 1083 nm data. NSO/Kitt Peak data used here are produced cooperatively by NSF/NOAO, NASA/GSFC, and NOAA/SEL. This work has been supported by the NASA grant NAG5-7838.

REFERENCES

Chapman G.A., Cookson A.M., Dobias J.J., 1996 JGR, 101, 13541

Chapman G.A., et al., 1992, JGR, 97, 8211

de Toma G., White O.R., Chapman G.A., Walton S.R., Harvey, K.L., 2000b, submitted to ApJ

de Toma G., White O.R., Harvey K.L., 2000 ApJ 529, 1101 $\,$

Foukal, P., Lean, J., 1988, ApJ, 328, 347

Fröhlich C., Anklin M., 2000, in the 7th International Conference on New Developments and Applications in Optical Radiometry, in press

Fröhlich C., 1999, Adv. Space Res., 24, n.2, 157

Fröhlich C., Lean J.L., 1997, in New Eyes to See the Sun and Stars, IAU Symposium 185

Fröhlich, C., Pap, J., Hudson, H.S, 1994, Sol. Phys. 152, 111

Joselyn, J., et al., 1998, EOS 78, 205

Lean, J.L., Cook, J., Marquette, W., and Johannesson, A., 1998, ApJ, 492, 390

Walton S.R., Preminger D.G., 1999, ApJ, 514, 959

LONG-TERM CHANGES IN SOLAR IRRADIANCE

Sami K. Solanki¹ and Marcel Fligge²

¹Max-Planck-Institut für Aeronomie, 37191 Katlenburg-Lindau, Germany ²Institute of Astronomy, ETH Zentrum, CH-8092 Zurich, Switzerland

ABSTRACT

Measurements of solar irradiance with the necessary precision to reveal the sun's intrinsic variability started in 1978. These measurements have revealed dips in solar brightness due to the passage of sunspots across the solar disc on a solar rotation time scale and a remarkable increase of the solar irradiance at solar activity maximum. In order to uncover a possible connection between solar irradiance variations and climate, however, it is necessary to extend the irradiance record to earlier times with the help of models.

A brief introduction is given to the results of irradiance measurements and to our current understanding of the underlying physical causes, followed by an overview of the efforts to reconstruct irradiance or the underlying magnetic field at earlier times. The secular variation of solar irradiance, in particular the magnitude of the irradiance increase since the Maunder minimum, is critically discussed.

1. INTRODUCTION

There is considerable circumstantial evidence that solar variability influences the Earth's climate. For example, indicators of solar activity (14 C concentration) and of climate (glaciers) show a clear correlation over the last 7000 years (Eddy 1977). Also, the solar cycle length shows an excellent correlation with northern hemisphere land temperatures since approximately 1860 (Friis-Christensen and Lassen 1991), although more recently the two records have diverged (see Sect. 5).

In order to determine whether there really is a significant solar contribution to global climate change or whether these are just chance correlations we need to first determine the variation of solar quantities that actually could affect the Earth's climate, since parameters such as the solar cycle length are at best proxies of the relevant physical variables. In a second step it is then necessary to study the reaction of the Earth's atmosphere with the variability of the solar parameters. The present review concentrates on the first step.

Three main routes by which the Sun could influence climate have been identified:

- 1. Variations of the total solar irradiance, i.e. the brightness of the Sun as measured above the Earth's atmosphere, integrated over all wavelengths. This quantity represents to very high accuracy the total radiative input to Earth.
- 2. Variations of the Sun's spectral irradiance, i.e. changes in the Sun's brightness at a certain wavelength or within a given wavelength range. The UV radiation influences atmospheric chemistry, in particular the production and destruction of ozone (e.g. Haigh 1994, 1996). A different rate of change of UV relative to total irradiance can have a significantly different effect on the radiative heating of the Earth's atmosphere (Larkin et al., 2000).
- 3. Variations in the heliospheric magnetic field (which is anchored in the Sun's interior). Such variations, coupled with corresponding changes in the solar wind, influence the number and the energy spectrum of the cosmic rays reaching the Earth (Potgieter 1998, Simpson 1998) These in turn have been linked to global cloud cover by Svensmark and Friis-Christensen (1997), Svensmark (1998), Marsch and Svensmark (2000).

This review concentrates on the long-term variations of total and spectral irradiance, where long-term implies a time scale of centuries. Thus, changes on the solar evolution time scale (10^9 years) and the thermal time scale of the convection zone (10^5 years) will not be touched upon. Also, variations on the time scale of solar rotation up to that of the solar cycle are dealt with relatively briefly. More details on these shorter term variations are presented by Fligge et al. (2000a, these proceedings). In addition to the irradiance we also briefly touch upon changes in the underlying magnetic field, which has an influence on the cosmic ray flux.

Proc. 1st Solar & Space Weather Euroconference, 'The Solar Cycle and Terrestrial Climate', Santa Cruz de Tenerife, Tenerife, Spain, 25-29 September 2000 (ESA SP-463, December 2000)

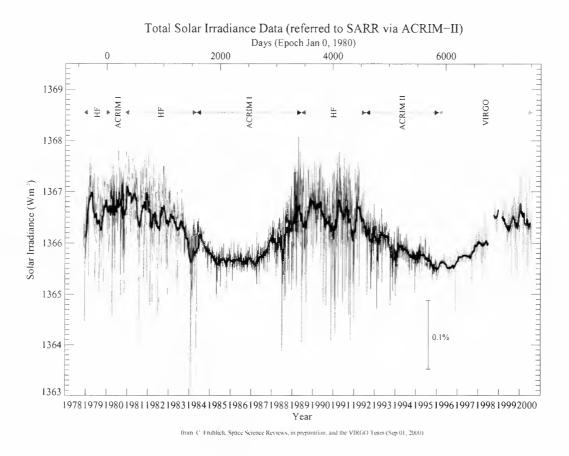


Figure 1. The total solar irradiance vs. time. Plotted is a composite of measurements made between 1978 and 2000 by various instruments. Figure kindly provided by C. Fröhlich.

2. PHYSICAL CAUSES OF SOLAR IRRADIANCE VARIATIONS

Measurements with sufficient accuracy to reveal total solar irradiance (TSI) variations at a level of 0.1% have been regularly carried out since 1978 (see Fröhlich 2000 for a review). A number of instruments have been involved, each with its own absolute irradiance calibration. The absolute values obtained by the various instruments may differ somewhat, but they exhibit very similar relative changes. A consistent time series combining the outputs of the various instruments (i.e. a composite) was constructed by Fröhlich and Lean (1998, cf. Fröhlich 2000, 2001). This composite is plotted in Fig. 1 and now covers a full solar cycle and one half each of two others.

Unfortunately, this period is not sufficiently long to search for signs of solar influence on climate due partly to the large intrinsic short-term variability of the climate system. Also, the cycles covered so far (Nos. 21, 22, 23) are too similar to directly allow us to extrapolate to earlier times, when the Sun was either more active (cycle 19) or, as was usually the case, less active.

In the case of solar spectral irradiance the observational evidence is even less complete. Almost all the measurements are restricted to the UV. Knowledge of the variability in the visible is limited to the results of VIRGO on SOHO (and is only reliable on short time scales) and no direct measurements exist of irradiance variability at wavelengths greater than 1 micron.

In order to learn how total or spectral irradiance varied in the past we need to obtain a physical understanding of the causes of irradiance variability. To help reconstruct past irradiance we also need to uncover proxies of irradiance that have been measured for as long a time as possible (a quantitative reconstruction from first principles is not currently possible). In addition, the variability and activity level of Sun-like stars needs to be studied. The investigation of a sufficiently large sample of Sun-like stars may help to determine the full range of solar variability within a short period compared to that required to gain the same knowledge from the study of the Sun alone. All these (complementary) approaches have been taken by various investigators.

On time scales of the solar cycle and less the major source of both spectral and total irradiance variability is the magnetic field at the solar surface. For sunspots this was already clear in the early 1980's (e.g. Hudson et al. 1982, Foukal 1981). A theoretical explanation for why the Sun darkened globally due to (local) spots at its surface had also been provided (Spruit 1982). The dip in TSI due to the passage of a sunspot group across the solar surface is illustrated in the upper panel of Fig. 2, while the lower panel exhibits the brightening due to the passage of a region composed mainly of faculae.

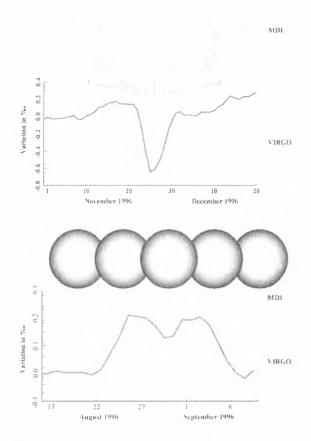


Figure 2. Traces of the total solar irradiance recorded by the VIRGO instrument on SOHO (thick solid curves) in November and December 1996 (upper panel) and in August and September 1996 (lower panel). Above each trace MDI full disc continuum images for five days within these periods are marked. Note the passage of two small spots (upper panel) and of the faculae (lower panel).

The role of bright faculae and the network has taken a considerably longer time to work out. Due to the network's distribution over the whole solar disc, the small size of individual elements and the weakness of an individual element's signature in almost every proxy, it was particularly difficult to include in the analysis, and even today poses the largest problem. Early work (e.g. Foukal and Lean 1986, 1988) employed chromospheric proxies of faculae and the network. More recently, Fligge et al. (2000b, 2001, cf. Solanki and Fligge 2001) have directly determined the fraction of the irradiance variations caused by the magnetic field using a combination of magnetograms and atmospheric models of the various types of magnetic features. They have shown that over 95% of the measured irradiance variability is caused by magnetic fields at the solar surface (see Fligge et al. 2000a. these proceedings, for details).

This work, together with that of Fröhlich and Lean (1998), suggests that also the irradiance variations over past solar cycles can be determined from the surface distribution of the magnetic field, if appropriate records of the field distribution or of proxies thereof are available.

Since the spectra of sunspots and faculae can be calculated over a broad range of wavelengths (covering over 99% of the contribution to the TSI and its variation) with sufficient accuracy to reproduce the best observations (Unruh et al. 1999) it is straightforward to model also changes in the spectral irradiance on time scales of a solar cycle or less, once the total irradiance has been reconstructed (Solanki and Unruh 1998, Unruh et al. 1999, Fligge et al. 2000b). the results of the models are in surprisingly good agreement with the available data.

3. RECONSTRUCTIONS OF PAST CYCLIC IRRADIANCE VARIATIONS

Proxies of the magnetic flux distribution are indeed available in the form of the Zürich Sunspot Relative Number (R_z , since 1700), the Group Sunspot Number (R_g , since 1610), sunspot and facular areas (A_s , A_f , since 1874), Ca II plage areas (A_p , since 1915), etc. None of these is a perfect proxy for either the sunspot or facular contribution to the TSI, whereby the sunspot contribution is more reliably represented than that of the faculae. This has to do with the clearer signal produced by sunspots.

Nevertheless, these data can be employed to reconstruct the cyclic component of the irradiance back to the Maunder minimum. It should be noted that in this Section we do not discuss any possible secular trend, so that the irradiance curves shown here indicate only a part of the total change of the irradiance. The various reconstructions of this type differ in the length of time that they cover, the data they are based on and the underlying assumptions regarding the details of the reconstruction (Foukal and Lean 1990, Lean et al. 1995, Solanki and Fligge 1998, 1999. Lockwood and Stamper 1999). In Fig. 3 we plot the reconstruction due to Solanki and Fligge (1999) from 1700 to 1998. As more and increasingly better data are available, the quality of the reconstruction improves. Thus between 1700 and 1749 only yearly values of the sunspot number are reliably available, between 1750 and 1817 only monthly and between 1818 and 1874 daily values are available, while from 1874 onwards other proxies in addition to daily sunspot number can also be used. The increasing quality of the reconstruction is clearly visible in the figure; whereas in the early part of the reconstruction only the outline of the cycle is reproduced, from 1818 onwards the reconstruction can separate, even if only partially, between the contributions of faculae and sunspots.

It is possible to separate between these distinct contributions on the basis of a single data record by taking into account the fact that the sunspot and facular contributions have different time scales. Finally, from 1874 onwards the contributions from these two sources can be clearly separated due to the availability of separate data records (note that for the faculae a set of five proxies are used in order to obtain



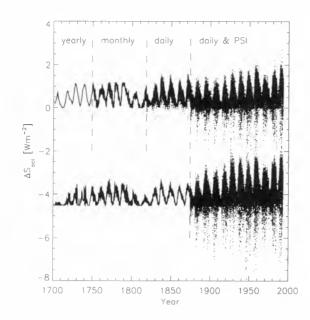


Figure 3. Reconstructed cyclic component of solar total irradiance since 1700. See text for details. (From Solanki and Fligge 1999).

results that are as robust as possible. Solanki and Fligge 1999).

A number of assumptions need to be made for such a reconstruction. For example, the properties of sunspots and faculae are assumed to be independent of time. Thus there is little room in such models for the factor of 2-3 enhanced cyclic brightness variability seen in Sun-like stars by Lockwood et al. (1992). Earlier modelling (Schatten 1993) appeared to support the possibility of such strong cycles within the context of our understanding of solar surface features. However, more recent and more careful modelling (Radick et al. 1998, Knaack et al. 2001) has shown that the behaviour of these stars cannot be reconciled with that of the Sun unless their surface features differ significantly from those on the Sun. Could this imply that the Sun is currently in an atypical state, so that we may not use measurements of current irradiance variations to reconstruct the past? However, there is new evidence for a bias among the observations of Lockwood et al. (1992) in the selection of stars (Radick 2001), which suggests that the behaviour of the Sun in the last 2-3 cycles is not atypical and may be used as a guide for the reconstruction of TSI at earlier times.

The magnitude and source of the cyclic component of irradiance variations is thus well known. Further improvements of the reconstructions of this component of the complete irradiance variation are needed, and indeed possible. but these are expected to improve things quantitatively (e.g. improve the separation between sunspots and faculae prior to 1874) but not qualitatively.

Once the spectral irradiance changes over a given cycle can be reproduced by a model (see Sect. 2) it is possible to determine them all the way back to the Maunder minimum. The remarks made above regarding the TSI reconstructions apply equally to the spectral irradiance. Here the uncertainty is larger due to the weaker constraints set by observations during the space era.

4. SECULAR IRRADIANCE VARIATIONS: INCREASE IN THE IRRADIANCE LEVEL SINCE THE MAUNDER MINIMUM

Let us now turn to the possible secular change in irradiance. There is some evidence that the cyclic irradiance variations discussed above lie on top of a slowly changing irradiance background. Such a secularly changing background is important for a possible influence of solar irradiance variations on climate since. if we average over 11 years, the net increase in TSI due to the cyclic component alone corresponds to only 0.6 W m⁻² (i.e. roughly 0.04%) since the Maunder minimum.

There are basically two lines of evidence for secular changes in solar irradiance, both of them somewhat indirect.

4.1. Stellar evidence

As the Sun's magnetic activity waxes and wanes not only does its irradiance vary but also the brightness in the cores of prominent spectral lines such as Ca II H and K in the violet part of the solar spectrum. White et al. (1992) found from a comparison of the Ca II emission of 102 field stars (measured by Baliunas and Jastrow 1990) with the Sun that the range of the Ca II emission from the Sun lies considerably higher than for most of the stars in this sample.

Thus the Sun is more active than these stars even during the minima of its last few activity cycles. Baliunas and Jastrow (1990) concluded that the stars with the lowest Ca flux levels are in a Maunder minimum state. Since the Ca II core emission is produced mainly in faculae and the network and there are no faculae at activity minimum, the lower emission seen in these stars must be due to a reduced network. White et al. (1992) actually found that the emission must be reduced to below the level achieved by simply removing all the network emission (although there is considerable uncertainty about this). If correct, this would imply that other mechanisms than purely magnetic ones are responsible for the reduced Ca II flux at Maunder minimum.

Lean et al. (1992) and Zhang et al. (1994) used the correlation between variations of Ca II and of irradiance (respectively irradiance due to faculae) over the solar cycle to extrapolate the irradiance back to the Maunder minimum level. They obtained that the Sun was less bright by 0.24% (Lean et al. 1992),

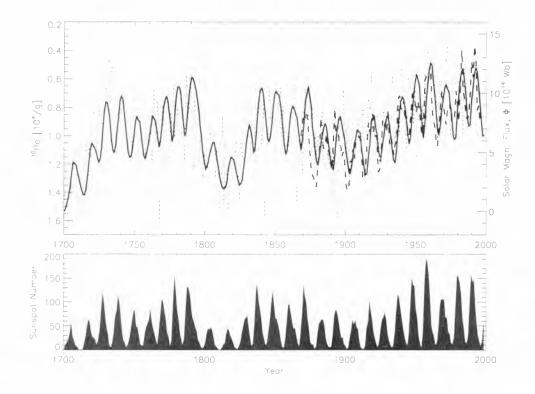


Figure 4. Evolution of the open magnetic flux at the solar surface since the end of the Maunder Minimum in 1700 as predicted by a model of the surface evolution of the Sun's magnetic field (upper panel, solid curve). For comparison, the flux of the interplanetary magnetic field (Lockwood et al., 1999) reconstructed from the geomagnetic an-index (dashed curve) and the ¹⁰Be concentration in ice cores (Beer et al., 1990) (dotted curve and left-hand, inverted scale) are also plotted. The interplanetary flux values have been multiplied by a factor of 2 in order to obtain the total unsigned flux. The ¹⁰Be record has been plotted without any smoothing or filtering. For comparison, the lower panel shows the corresponding time sequence of the sunspot number, R (see Solanki et al., 2000 for details).

respectively by 0.2-0.6% compared to the present (Zhang et al. 1995).

One problem with the Baliunas and Jastrow (1990) result is that for the stars in their sample there is no good way to distinguish between stars of solar age in a Maunder minimum state and older. less rapidly rotating stars with generally lower activity levels. Newer observations of the old open cluster M67 show that there are indeed some stars with an activity level below that of the Sun (Radick 2001).

From the stellar side there is thus some (although not quite definite) evidence for the decrease in network magnetic flux and hence of the irradiance. Also, there is considerable uncertainty regarding the magnitude of the irradiance change between the Maunder minimum and a present day activity minimum. This is partly seen in the large range of possible values given by Zhang et al. (1995) in their admittedly simple analysis. Additional uncertainty is caused by the fact that it is now unclear which stars in the sample of Baliunas and Jastrow (1990) represent true Maunder minimum stars.

Schmitt (1997) has argued on the basis of a complete volume sample of stars observed in X-rays that there is no evidence for stars exhibiting much smaller magnetic activity than parts of the Sun (vis. coronal holes). According to him therefore the Sun would still have considerable magnetic flux during the Maunder minimum and would thus not be much less bright at than during a current minimum. This suggests that either the network fields do not weaken significantly in the Maunder minimum relative to the present-day minimum, or another source of X-rays opens up there, or that stars in a Maunder minimum state are extremely rare (and the lower Ca II emission in many Sun-like stars has other, unknown, causes). It should be noted, however, that X-ray flux depends at least as strongly on magnetic field topology (open or closed flux) as on the total amount of magnetic flux.

4.2. Heliospheric evidence

Evidence for secular trends in solar activity comes from the interplanetary magnetic field reconstructed from the aa-index of geomagnetic activity (Lockwood et al. 1999). They find that the interplanetary magnetic flux at the minimum of solar activity has roughly doubled since 1900. The reconstructed interplanetary field is plotted in the upper frame of Fig. 4 (dashed curve). The secular trend is even stronger than the cyclic signal in the interplanetary field. This behaviour is mirrored by the ¹⁰Be concentration in Greenland ice (Beer 2000), which is represented by the dotted curve in Fig. 4. ¹⁰Be is produced by the interaction of cosmic rays with constituents of the upper atmosphere. Since the cosmic ray flux is modulated by the heliospheric magnetic field and by the solar wind, the ¹⁰Be concentration (like that of ¹⁴C) is a measure of the heliospheric effect of solar activity.

Lockwood and Stamper (1999) have argued that since the irradiance over a solar cycle correlates rather well with the interplanetary flux that therefore the secular trend in the latter must also be reflected in the TSI. This is an interesting approach, although one needs to keep in mind the following. The heliospheric magnetic field is the extension of the open magnetic flux on the solar surface. The open flux is only a small fraction (a few percent at solar maximum) of the total magnetic flux. A model has been proposed by Solanki et al. (2000), which reproduces both the reconstructed interplanetary field (Lockwood et al. 1999) and the ¹⁰Be record with high accuracy. The model is represented by the solid curve in Fig. 4. The model produces a secularly varying open flux by requiring that this flux has a lifetime of years (in contrast to the major part of the magnetic flux emerging at the solar surface, which disappears again within days or, at the most, months). Such a long lifetime of a small fraction of the total flux has been confirmed by Wang et al. (2000). Unfortunately, due to the much shorter lifetime of most of the magnetic flux we cannot use the same or a similar model to explain a secular trend in the total magnetic flux. This implies that another cause must be found for any significant secular trend in the irradiance.

4.3. Other approaches

An alternative approach regarding the magnitude of a possible secular trend since the Maunder minimum is to try to set limits on it. A lower limit is obviously close to zero (there is as yet no definitive evidence that a trend exists). Setting an upper limit is far less straightforward and is never quite free of assumptions. Besides stars and the interplanetary field there are basically two ways in which such limits can be set.

4.3.1. Comparison of reconstructed irradiance with measurements

By requiring that part of the reconstructed irradiance record since 1978 should match the observed irradiance, an upper limit can be set on the irradiance change since the Maunder minimum. It is an upper limit, since cycles 21, 22 and 23 are relatively similar. The composite record of measured irradiance plotted in Fig. 1 is consistent with no secular trend (excepting the controversial analysis of Willson 1997), and cannot be reconciled with large secular trends. Solanki and Fligge (1998) used this technique to set an upper limit of 5 W m⁻² since the Maunder minimum (Solanki and Fligge 1998, 1999).

4.3.2. Limit derived from magnetograms

One can in principle set an upper limit on any secular change in irradiance due to changes in the magnetic flux by considering a magnetogram at solar activity minimum. If we know the irradiance enhancement due to each magnetic feature and obtain the flux in the magnetic features at activity minimum (i.e. in the network), then we can estimate the brightness of the Sun in the absence of the network. This technique, which assumes that the secular variations are entirely magnetic in origin, has never been applied. It requires extremely deep magnetograms (tests have shown that the resulting increase in irradiance since the Maunder minimum increases linearly with decreasing noise level) and a very good knowledge of the brightness of network elements.

In summary, there is circumstantial evidence for a secular trend in solar irradiance. However, none of this evidence is clear-cut or straightforward, so that the absence of such a trend cannot be ruled out. Even more difficult than determining the magnitude of the secular irradiance variations is to discover their detailed time dependence.

5. FUNCTIONAL FORM OF THE SECULAR IRRADIANCE CHANGE

For studies of the influence of solar variability on climate it is not sufficient to know by how much the irradiance has changed since the Maunder minimum, one also requires the exact time dependence of its variation. So far three approaches have been taken.

Lean et al. (1995) have assumed that the background irradiance is proportional to the amplitude of the solar cycle (specifically the amplitude of the group sunspot number) and have reconstructed the irradiance accordingly.

Hoyt and Schatten (1993) on the other hand propose a trend corresponding closely to cycle length, although a number of other indicators also enter into it. Baliunas and Soon (1995) have presented evidence that the amplitudes of stellar cycles (seen in Ca II H + K) scale with the length of the stellar cycle. Such a relation is also known for the Sun (although with a relatively low correlation coefficient of 0.4 or less).

In the absence of a clear-cut preference for one or the other of these possible trends Solanki and Fligge (1998, 1999), cf. Fligge and Solanki (2000), have

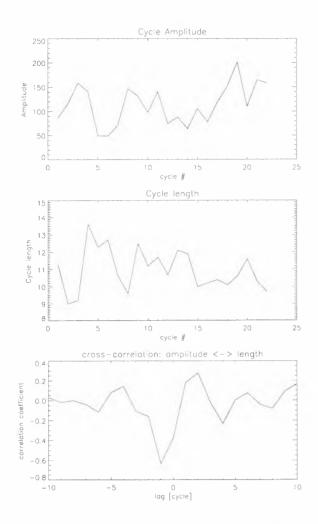


Figure 5. (a) Record of cycle amplitude derived from the sunspot relative number record. (b) Cycle length (obtained following the procedure given by Friis-Christensen and Lassen 1991). (c) Crosscorrelation function of the two quantities.

presented two reconstructions, one based on a secular trend following the cycle amplitude, the other following cycle length.

Finally, Lockwood and Stamper (1999) have employed the secular trend of the interplanetary magnetic field to determine the secular behaviour of the irradiance. Specifically, they correlate the measured irradiance with the measured interplanetary fields (over cycles 21 and 22) and apply the same correlation to the interplanetary magnetic field at earlier epochs to obtain the irradiance. As shown by Solanki et al. (2000) the trend in the interplanetary field is determined by both the cycle amplitude and length (with the amplitude playing a somewhat bigger role). As pointed out in Sect. 4.2, so far no a priori physical reason for the irradiance to follow the interplanetary magnetic field has been found, although a connection should not be ruled out.

The cycle length and amplitude records are more closely related than suggested by the correlation coefficient, which typically is on the order of 0.3-0.4. The cross-correlation *function* between the two

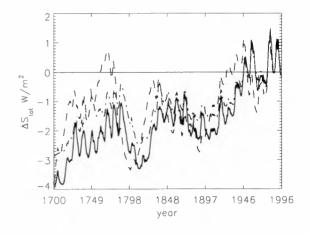


Figure 6. Reconstructed total solar irradiance vs. time. Plotted are the reconstructions due to Hoyt and Schatten (1993; dashed), Lean et al. (1995; dashdotted), Solanki and Fligge (1998; solid). The plotted curves include both a cyclic and an estimated secular component.

quantities has a maximum amplitude when the two records are out of phase by roughly one cycle, with the cycle length leading the cycle amplitude. This is illustrated in Fig. 5. This explains why Friis-Christensen and Lassen (1991) found a good correlation with air temperature over land masses, while Reid (1987) noted that sea surface temperatures had risen faster than solar activity.

The complete change in irradiance is given by the combination of the cyclic variability (described in Sect. 3) and the secular variation (note that in the model of Lockwood and Stamper 1999 these two contributions are not modelled separately).

The total solar irradiance as reconstructed by Hoyt and Schatten (1993; dashed), Lean et al. (1995; dash-dotted) and Solanki and Fligge (1998, 1999; solid) is plotted in Fig. 6. Note that the reconstruction following cycle length and amplitude are not too different since approximately 1850, but deviate considerably prior to that.

In Fig.7 the irradiance curves since 1978 resulting from the various models are compared with the measurements (as presented by Fröhlich 2000). Considerable differences between the curves are seen, and not all models exhibit a satisfactory agreement with the data. The models of Solanki and Fligge (1998, 1999) turn out to reproduce this set of data very well.

If we make the assumption that the secular irradiance change is due to changes in the magnetic network alone, then it it possible to not only estimate the evolution of the TSI but also that of the spectral irradiance. Fligge and Solanki (2000) and Lean (2000) have both used the models of Unruh, Solanki and Fligge (1999) to reconstruct the spectral irradiance since the Maunder minimum (Lean et al. 1995 previously carried out a simpler reconstruction of in-

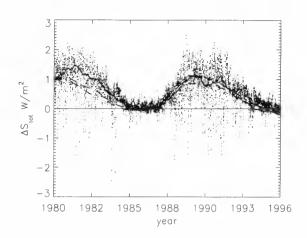


Figure 7. Measured (dotted curve) and reconstructed total solar irradiance vs. time. The plotted models are due to Hoyt and Schatten (1993, dashed curve), Lean et al. (1995, dash-dotted curve) and Solanki and Fligge (1999, solid curve).

tegrated UV irradiance). Fligge and Solanki (2000) employed the TSI changes modelled by Solanki and Fligge (1999), while Lean (2000) chose those of Lean et al. (1995). Accordingly Fligge and Solanki (2000) obtain two different secular trends, one following the cycle amplitudes, one the cycle length. The reconstructed irradiance at wavelengths shortward of 300 nm is plotted in the upper part of Fig. 8, while the irradiance longward of 700 nm is displayed in the lower part of Fig. 8. Note the order of magnitude larger variation in the UV, where however the influence of sunspots is far weaker compared to the IR.

In addition to the assumption underlying the TSI reconstruction the spectral irradiance models have the additional uncertainty that they assume the spectrum of the network elements to be the same as of active region faculae. The results of Topka et al. (1997) and Ortiz et al. (2000) suggest, however, that this is not the case. Hence, there are grounds for improving and extending the models of long-term spectral irradiance measurements.

6. CONCLUSIONS

An overview has been given of our present knowledge of solar irradiance variations since the Maunder minimum. The results as well as the assumptions underlying them and the uncertainties are discussed. In spite of the significant progress of the last years considerable uncertainties remain, some of which become visible in the difference between the various reconstructed records of past irradiance. Before these are sorted out the exact role played by solar irradiance in determining climate will remain unclear.

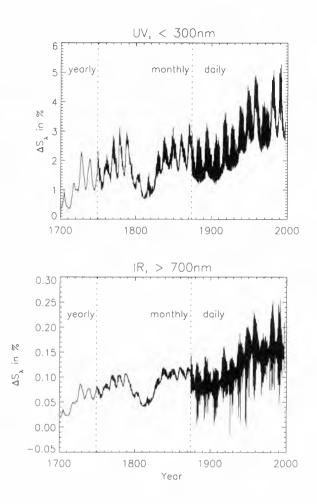


Figure 8. Reconstruction of the increase (in percent) of spectral solar irradiance since the Maunder minimum. Top: for the ultraviolet at $\lambda < 300$ nm, Bottom: for the infrared at $\lambda > 700$ nm. (From Fligge and Solanki 2000).

REFERENCES

- Baliunas S. and Jastrow R. (1990): Evidence for long-term brightness changes of solar-type stars. *Nature* 348, 520–523.
- Baliunas S., Soon W.H. (1995): Are Variations in the Length of the Activity Cycle Related to Changes in Brightness in Solar-Type Stars? Astrophys. J. 450, 896-901.
- Beer J. (2000): Long Term, Indirect Indices of Solar Variability. Space Science Reviews, in press.
- Eddy J.A. (1977): Climate Change 1, 173-190.
- Fligge M. and Solanki S.K. (2000): The solar spectral irradiance since 1700. Geophys. Res. Lett. 27, 2157–2160.
- Fligge M., Solanki S.K., Meunier N. and Unruh Y.C. (2000a): Solar surface magnetism and the increase of solar irradiance between activity minimum and maximum. ESA Publications SP-463, in press.
- Fligge M., Solanki S.K. and Unruh Y.C. (2000b): Modelling irradiance variations from the surface distribution of the solar magnetic field. Astron. Astrophys. 353, 380-388.

- Fligge M., Solanki S.K., Meunier N. and Unruh Y.C. (2001): Astron. Astrophys., in preparation.
- Foukal P. (1981): Sunspots and changes in the global output of the sun. The Physics of Sunspots, 391– 423.
- Foukal P. and Lean J. (1986): The influence of faculae on total solar irradiance and luminosity. Astrophys. J. 302, 826–835.
- Foukal P. and Lean J. (1988): Magnetic modulation of solar luminosity by photospheric activity. Astrophys. J. 328, 347–357.
- Foukal P. and Lean J. (1990): An empirical model of total solar irradiance variation between 1874 and 1988. Science 247, 556–558.
- Friis-Christensen E. and Lassen K. (1991): Length of the solar cycle: An indicator of solar activity closely associated with climate. *Science* **254**, 698– 700.
- Fröhlich C. (2000): Observations of Irradiance Variability. Space Science Reviews, in press.
- Fröhlich C. and Lean J. (1998): The Sun's total irradiance: Cycles. trends and related climate change uncertainties since 1976. *Geophys. Res. Lett.* 25, 4377–4380.
- Haigh J.D. (1994): The role of stratospheric ozone in modulating the solar radiative forcing of climate. *Nature* **370**, 544–546.
- Haigh J.D. (1996): The Impact of Solar Variability on Climate. Science 272, 981–984.
- Hoyt D.V. and Schatten K.H. (1993): A discussion of plausible solar irradiance variations, 1700-1992. J. Geophys. Res. 98, 18895–18906.
- Hudson H.S., Silva S., Woodard M. and Willson R.C. (1982): The effects of sunspots on solar irradiance. Sol. Phys. 76, 211–219.
- Knaack R., Fligge M., Solanki S.K. and Unruh Y.C. (2001): The influence of an inclined rotation axis on solar irradiance. *Astron. Astrophys.*, in preparation.
- Larkin A., Haigh J.D. and Djavidnia S. (2000): The effect of solar UV irradiance variations on the earth's atmosphere. *Space Science Reviews*, in press
- Lean J. (2000): Evolution of the Sun's Spectral Irradiance Since the Maunder Minimum. *Geophys. Res. Lett.* 27, 2425–2428.
- Lean J., Beer J. and Bradley R. (1995): Reconstruction of solar irradiance since 1610: Implications for climate change. *Geophys. Res. Lett.* 22, 3195– 3198.
- Lean J., Skumanich A. and White O. (1992): Estimating the sun's radiative output during the Maunder Minimum. *Geophys. Res. Lett.* 19, 1595– 1598.
- Lockwood G.W., Skiff B.A., Baliunas S.L. and Radick R.R. (1992): Long-term solar brightness changes estimated from a survey of sun-like stars. *Nature* **360**, 653–655.

- Lockwood M. and Stamper R. (1999): Long-term drift of the coronal source magnetic flux and the total solar irradiance. *Geophys. Res. Lett.* **26**, 2461.
- Lockwood M., Stamper R. and Wild M.N. (1999): A doubling of the Sun's coronal magnetic field during the past 100 years. *Nature* **399**, 437–439.
- Marsch N.D., Svensmark H. (2000): Low cloud properties influenced by cosmic rays. *Phys. Rev. Lett.*, in press.
- Ortiz A., Solanki S.K., Fligge M., Domingo V. and Sanahuja B. (2001): On the contrast of faculae and small magnetic features. *Astron. Astrophys.*, in preparation.
- Potgieter M.S. (1998): The Modulation of Galactic Cosmic Rays in the Heliosphere: Theory and Models. Space Science Reviews 83, 147–158.
- Radick R. (2001): In: Recent Insights into the Physics of the Sun and the Heliosphere: Highlights from SOHO and other Space Missions. Kluwer. Dordrecht, P. Brekke et al. (Eds.), IAU Symp. 203, in press.
- Radick R., Lockwood G.W., Shift B.A. and Baliunas S.L. (1998): Patterns of Variation among Sun-like Stars. Astrophys. J. 118, 239.
- Reid G.C. (1987): Influence of solar variability on global sea surface temperatures. Nature 329, 142– 143.
- Schatten K.H. (1993): Heliographic latitude dependence of the Sun's irradiance. J. Geophys. Res. 98, 18,907-18,910.
- Schmitt J.H.M.M. (1997): Coronae on solar-like stars. Astron. Astrophys. 318, 215.
- Simpson J.A. (1998): Recurrent Solar Modulation of the Galactic Cosmic Rays and the Anomalous Nuclear Component in Three Dimensions of the Heliosphere. Space Science Reviews 83, 7–19.
- Solanki S.K. and Fligge M. (1998): Solar irradiance since 1874 revisited. *Geophys. Res. Lett.* 25, 341– 344.
- Solanki S.K. and Fligge M. (1999): A reconstruction of total solar irradiance since 1700. *Geophys. Res. Lett.* 26, 2465–2468.
- Solanki S.K. and Fligge M. (2001): How much of the solar irradiance variations is caused by the magnetic field at the solar surface? *Adv. Space Res.* in press.
- Solanki S.K. and Unruh Y.C. (1998): A Model of the Wavelength Dependence of Solar Irradiance Variations. Astron. Astrophys. 329, 747–753.
- Solanki S.K., Schüssler M. and Fligge M. (2000): Secular evolution of the Sun's large-scale magnetic field since the Maunder Minimum. *Nature*. in press.
- Spruit H.C. (1982): Effect of spots on a star's radius and luminosity. Astron. Astrophys. 108, 348–355.
- Svensmark H. (1998): Influence of Cosmic Rays on Earth's Climate. Phys. Rev. Lett. 81, 5027–5030.

- Svensmark H. and Friis-Christensen E. (1997): Variation of cosmic ray flux and global cloud coverage
 A missing link in solar-climate relationships. J. Atmos. Terr. Phys. 59, 1225–1232.
- Topka K.P., Tarbell T.D. and Title A.M. (1997): Properties of the Smallest Solar Magnetic Elements. II. Observations versus Hot Wall Models of Faculae. Astrophys. J. 484, 479.
- Unruh Y.C., Solanki S.K. and Fligge M. (1999): The spectral dependence of facular contrast and solar irradiance variations. *Astron. Astrophys.* **345**, 635–642.
- Wang Y.-M., Sheeley N.R. and Lean J. (2000): Understanding the evolution of the Sun's open magnetic flux. *Geophys. Res. Lett.* 27, 621–624.
- White O.R., Skumanich A., Lean J. and Livingston W.C. (1992): The sun in a noncycling state. Publ. Astron. Soc. Pac. 104, 1139-1143.
- Willson R.C. (1997): Total solar irradiance trend during solar cycle 21 and 22. *Science* **277**, 1963– 1965.
- Zhang Q., Soon W.H., Baliunas S.L., Lockwood G.W., Skiff B.A. and Radick R.R. (1994): A method of determining possible brightness variations of the Sun in past centuries from observations of solar-type stars. Astrophys. J. 427, L111-L114.

SOLAR VARIABILITY IN IONIZING RADIATION (UV, X-RAYS)

G. Schmidtke

Fraunhofer-Institute of Physikal Measurement Techniques (IPM) Heidenhofstr. 8, D-79110 Freiburg, Germany Phone: +49(0)761/8857-176, Fax: -224, e-mail: gerhard.schmidtke@ipm.fhg.de

Abstract: This topic refers to the interaction of the solar XUV radiation with the earth's upper atmosphere: The highly variable photon flux from the sun is absorbed in the terrestrial thermospheric-ionospheric (T/I) region thus controlling most of the processes in the altitude region from about 90 km to 600 km.

In the terrestrial T/I altitude regions molecular nitrogen and molecular and atomic oxygen are the primary neutral constituents. These constituents absorb the XUV solar photons <102.7 nm (photoionization limit of molecular oxygen) generating the daytime ionosphere. By interaction of the photoelectrons with the T/I constituents (neutral particles, electrons and ions) most of the energy is converted into heating. T/I temperatures are lowest at the turbopause at about 90 km and highest at the exosphere at about 1000 km.

The solar XUV spectrum from 110 nm to 1 nm is generated in the lower chromosphere through the corona at temperature levels ranging from some 10.000 K up to about 100.000.000 K with corresponding spectral emissions from neutral atoms and moderate to highly ionized atoms. With the exception of the hydrogen Lyman-continuum spectral line emissions dominate the XUV spectrum.

In view of an active sun with flares, solar rotations and cycles XUV absorption and subsequent processes lead to a vivid picture of our fascinating terrestrial atmospheric T/I altitude region. It is still under investigation also in the frame of the international TIGER Program of ISCS/SCOSTEP.

1. Introduction

With reference to the title, there are two aspects with respect to 'ionizing radiation', the nature of the solar XUV spectrum and the nature of the terrestrial T/I altitude region.

There is no clear definition of the XUV spectral region, yet. However, dealing with the terrestrial T/I altitude region, the spectral region of 110 nm to 16 nm is of primary interest, because the main energy transfer from the sun to the upper atmosphere is going on in this part of the spectrum.

Since the photoionization-absorption cross sections of the T/I gases exceed $10*10^{-22}$ m², the XUV radiation is fully absorbed by a T/I gas layer of <1 mm thickness at NTP. The main gas constituents are atomic oxygen and molecular nitrogen and oxygen. The photoionization limits are at 102.7 nm (corresponding to ~12.1 eV) for molecular oxygen, at 91.1 nm for atomic oxygen and at 79.6 nm for molecular nitrogen (see bars in Figure 1).

The absorption of XUV photons by the T/I particles initiates a complex series of subsequent processes that includes the generation of photoelectron-ion pairs (supplying the ionosphere), electron-particle-collisions, excitation of molecules, electron heating, dissociation of molecules, ion-molecule reactions, secondary ionization, escaping radiation, etc.. Most of the energy finally is converted to T/I heating. The temperature distribution shows lowest values at he turbopause at about 90 km and highest at the exosphere exceeding 600 km (see below in Fig. 8).

The physics of the solar atmosphere is even more complex as compared to the T/I region. With (kinetic) temperatures ranging from some 10.000 K (lower chromosphere) up to about 100.000.000 K (transition region and corona), an equivalent energy range from some eV (1 eV corresponds to ~1240 nm) to ~10.000 eV (~0.1 nm) is covered. In this hot plasma spectral emissions from neutral atoms (H I, He I, C I, O I,...) and moderate to highly ionized atoms (He II, C II, C III, O II, O III, O IV,..., Ne VII, Ne VIII,..., Mg IX,...,Si XI,..., Fe X, Fe XI, Fe XII,..., Fe XVI,...) are generated. With the exception of the hydrogen Lyman-continuum (91 nm to 70 nm) spectral line emissions dominate the XUV spectrum.

In Figure 1 the bars (lower part of the Figure) cover the XUV spectral ranges where T/I atoms/molecules are ionized. The upper part of Fig. 1 shows the ASSI Solar EUV Reference Spectrum (Schmidtke et al., 1992) as it is used in intervals in thermospheric/ionospheric (T/I) physics, for example for computations and modelling. The spectrum was measured on November 10, 1988 during moderate solar activity conditions with a value of the Covington index of $F_{10.7} \approx 150$ (a description of this index see below).

Proc. 1st Solar & Space Weather Euroconference, 'The Solar Cycle and Terrestrial Climate', Santa Cruz de Tenerife, Tenerife, Spain, 25-29 September 2000 (ESA SP-463, December 2000)

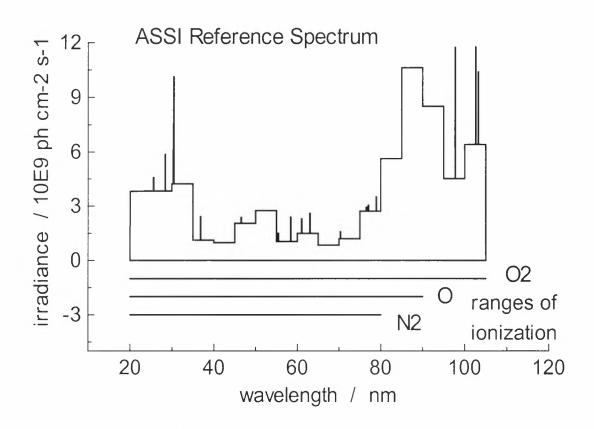


Fig. 1: Intercomparison of the solar XUV radiation with the spectral ranges (bars) of the ionized terrestrial species O₂, O and N₂ due to absorption of XUV photons

2. Measuring techniques

Based on the most spread techniques as used in the laboratory, first measurements of the solar XUV spectra below 120 nm were conducted by Johnson et al. (1958) launching rockets with film spectrographs. This way solar emission continua and spectral lines down to 97.7 nm have been investigated. However, the capability of photographic recording is limited by the straylight background from longer wavelengths: Since the Schumann-Runge film is also sensitive to visible light, more than seven orders of magnitude of energy in the VIS as compared to solar emissions near 100 nm have to be kept off the film. Additional disadvantages of the film are the low absolute accuracy, a low dynamic range of less than two orders of magnitude and a very low temporal resolution of minutes. Also the film recovery is difficult and costly for rockets and it is almost impossible for satellites.

The photoelectric techniques as used by Hinteregger (1963) has proven superior to the film techniques. Depending on the photo-sensitive material, XUV detectors are not sensitive to the VIS radiation. The photon recordings can even be transferred to ground via telemetry providing a time resolution down to small fractions of a second.

Sensitivity of photoelectric, proportional and Geiger counting devices has improved to an extend such that single-photon counting is close to reality, especially at shorter wavelengths (below 10 nm) that is more sensitive than film by orders of magnitude.

Since more than three decades photoelectric techniques is applied in rocket and satellite space missions to determine the solar XUV irradiance. In order to understand the results better, some of the problems involved applying these techniques are to be explained: Due to the strong absorption of XUV photons, the reflecting grating spectrometers and the photon detectors must be 'open' - to be operated under vacuum conditions. The common problems associated with vacuum exposed optics are surface changes of the optical components causing decreases or even increases of their sensitivity. Two processes cause these changes, (1) the interaction of the high energetic XUV photons with the upper layers of the optical surfaces and (2) the out-gassing from the vacuum exposure during the mission.

(1): For example, previously deposited contaminants can be removed from the optical surfaces by either evaporation in the space environment or scrubbing by XUV photons. As a consequence, the overall instrumental sensitivity increases or decreases depending on the efficiency of the lower surface layers. (2): In the vacuum environment the upper layers of the optical surfaces may be removed. In addition, contaminants of lower efficiencies to XUV photons are often deposited on the surfaces during the mission causing a decrease of the efficiency. Hydrocarbons are the most likely source of these contaminants. If the hydrocarbon molecules are polymerized into a film by solar XUV radiation, the instrumental efficiency may drop dramatically.

The effects causing efficiency changes are of complex nature, and even worse, both tendencies, increasing and decreasing sensitivity changes, are competing with each other with time and with wavelength range. They can neither be traced or measured individually nor be modelled. For these reasons it is not possible to correct the recorded photometric XUV data to distinguish solar irradiance changes from instrumental efficiency changes. The only way to derive accurate solar XUV flux numbers is to repeatedly determine the instrumental efficiency during the mission. This was not yet done in the past. It is planned for the first time for the ISS-SOLAR mission of the SOL-ACES (Wienhold et al., 2000) experiment with true in-flight calibration capability.

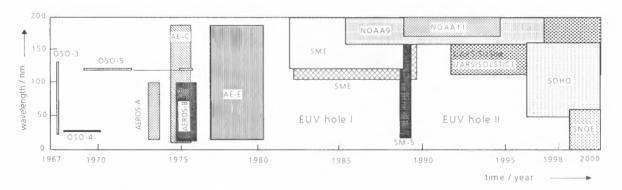
These problems have to be taken into account when results from solar XUV measurements are discussed.

3. Solar XUV variability

Solar XUV radiation is recorded using satellites repeatedly since 1967 as shown in Figure 2. (The wavelength range is extended toward longer wavelengths up to 200 nm, because there are quite a few missions covering both wavelength ranges > 110 nm and < 110 nm.) Considering the XUV spectral range, due to the technological difficulties as explained above, there is a serious lack on XUV data with respect to time and spectral coverage as well as to sufficient radiometric accuracy (< 20 %). For example, up to now there is no XUV data set covering a full solar cycle. While there have been satellite missions during the solar cycle 20, there is a large XUV 'hole' thereafter.

Still, the recorded data provide a rough picture on the variability of the solar XUV fluxes depending on the solar activity. Out of the large variety of solar processes, there are three types of activity of special interest for T/I aeronomy: Solar flares, emissions from active regions as 'modulated' by solar rotations and solar cycles. These types of activity represent periods of less than an hour, of about 27 days and of ~11 years, respectively. As a general rule, coronal emissions from active regions increase significantly stronger with solar activity than those of chromospheric origin – with the exception of resonance emissions from Be-like ions such as Mg IX and Si XI.

To get some hints about the magnitude of variability that occurred in the past, examples of the three noted types of activity are presented.



Time / wavelength coverage of solar flux measurement from satellites by spectrometers

Fig. 2: Time/wavelength coverage of solar XUV/UV spectrophotometric measurements from satellites

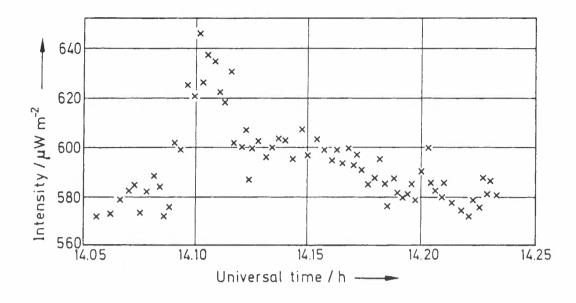


Fig. 3: Increased intensity of the He II 30.4 nm emission line as recorded during a 2B solar flare on 15 June 1973 aboard AEROS-A satellite (Schmidtke, 1978)

As to flares: In Fig. 3 the increased emission of the ionized helium atom at 30.4 nm amounts to about 25 % intensity changes during a relatively short period of ~15 min for a 2B type flare on 15 June 1973. This emission is chosen, because it is about representative for the integral flux change of the spectral range from 110-1 nm. Though coronal emissions exceed this increase by far, the bulk of the XUV flux is of chromospheric origin being well represented by the helium 30.4 nm line.

XUV changes with solar rotation of ~27 days primarily depend on the state of solar activity of the corresponding solar cycle that differs from one to the next one. Strongest variability is observed at the peak of the cycle activity with recorded total flux increases up to 40 %. In Fig. 4 photon fluxes of the spectral lines of He II (30.4 nm), C III (97.7 nm), H I (102.5 nm), O VI (103.2 nm), O V (63.0 nm), He I (58.4 nm) and Fe XVI (33.5 nm) fairly well represent a typical solar rotation at higher activity levels. Largest amplitudes are noted for coronal emissions (see Fe XVI line at 33.5 nm).

In the lower part of Fig. 4 the Covington index is marked for comparison. The index is equal to the numerical value (in units of 10^{-22} W m⁻² Hz⁻¹) of the solar radio noise at 2800 Hz, i.e. at a wavelength of 10.7 cm.

This 10.7 cm flux is primarily generated in the chromospheric/coronal transition region by thermal bremsstrahlung mechanisms. It is well correlating with the higher ionized solar XUV emissions such as Fe X-XII at medium and high solar activity. Correlation is less satisfying for the bulge of chromospheric

emissions. At solar minimum it may even anti-correlate with solar XUV emissions (Schmidtke, 1984). Still, this index is widely used as a proxy to represent the XUV energy flux for example in T/I modelling (see also Figures 7 and 8) because of the lacking availability of solar XUV data with adequate time coverage and radiometric accuracy.

It is still rather difficult to quantify solar XUV variability with solar cycle due to the lack on corresponding recordings with time as well as due to the lacking calibration capability of space instrumentation during the past satellite missions – as required to achieve high radiometric accuracy of the data. For this reason only rough estimates can be presented.

The large data set as available from the EUVS experiment aboard Atmospheric Explorer-E (AE-E) can demonstrate solar cycle 20 variability for the given period (Hinteregger, 1981). The ratio of solar flux changes with wavelength from the beginning of the AE-E mission (close to solar minimum of cycle 21) toward the solar maximum shows (see Fig. 5) decreasing values toward longer wavelengths. Again, the strongest changes appear with coronal emissions at shorter wavelengths: The variability of highly ionized emissions from iron atoms even exceeds one order of magnitude during the given fraction of the solar cycle 20 from July 1976 to January 1979, whereas typical chromospheric emissions from hydrogen and helium increase by factors of two to three during the same period.

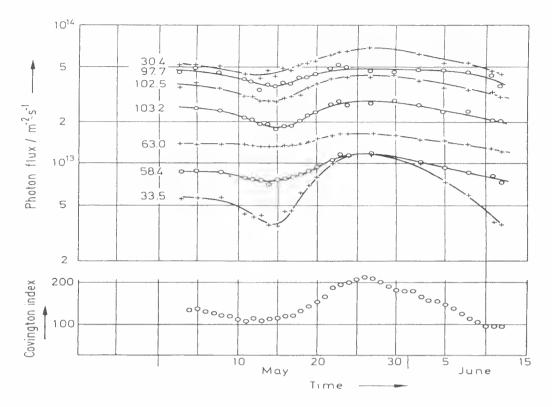


Fig. 4: Variability with solar rotation of a few solar emission lines (Hall and Hinteregger, 1970) and F_{10.7} (solar noise) index for comparison during May/June 1969.

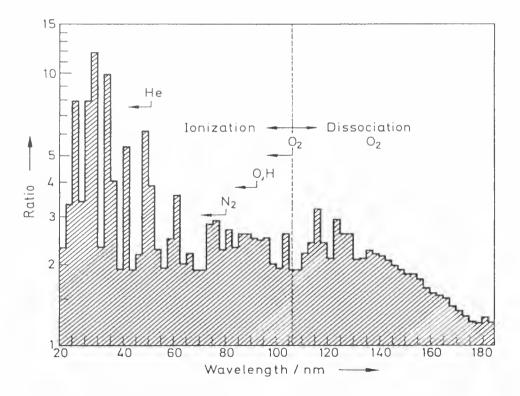


Fig. 5: Rate of change of XUV emissions: Ratio of flux levels in July 1976 (close to solar minimum) and January 1979 (close to solar maximum) as recorded by the EUVS experiment (Hinteregger, 1981).

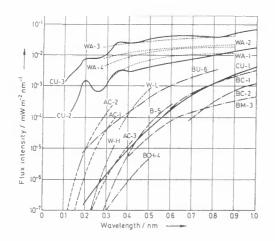


Fig. 6: Solar continuum spectra obtained with

proportional counter and Bragg spectrometers by various authors demonstrating strong variability in the wavelength region <1 nm (Kreplin (1977).

In this Figure reference is also given to the interaction of the XUV radiation with the terrestrial environment as marked by 'Ionization <---> Dissociation' etc..

The total amount of variability with solar cycle is still under discussion. As supported by ionospheric observations (Rawer, 1984) an increase of the total XUV flux by a factor of two (\pm 100 %) with solar cycle is a reasonable estimate. The most variable solar radiation energy (see Fig. 6) is recorded at wavelengths <1 nm. However, as compared with the XUV radiation from 110-1 nm the contribution to the energy budget of the T/I altitude region is negligible (< 0.1 mW m⁻²).

4. Thermospheric/ionospheric implications of XUV solar flux changes

The orders of magnitude of the total solar output with respect to the involved XUV energy should be noted first: The total energy of the solar radiation is of the order of 1366 W m⁻². The strongest EUV emission line, that is the one of hydrogen Lyman-alpha (H I at 121.6 nm), is only contributing about 5.5 mW m⁻², and the energy from the total XUV spectral range below 110 nm (110-1 nm) amounts to about 3.5 mW m⁻². Taking into account a variability with solar cycle of 100 % (see above), solar XUV energy changes are about 3.5 mW m⁻². This is a fraction of $2.6*10^{-6}$ with respect to the 'solar constant' (total solar radiation energy at the top of our atmosphere at 1 solar-earth distance unit).

A basic energy flux of the order of 3.5 mW m^{-2} and a variable flux component of up to the same order of magnitude - this is the main contribution to the energy which drives most of the processes of our upper atmosphere (in the thermospheric/ionospheric altitude region).

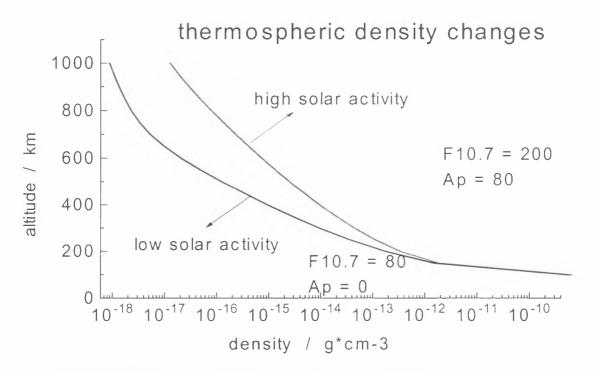


Fig. 7: XUV induced thermospheric density changes computed with the MSIS model. (Solar quiet and high activity conditions are chosen with F_{10.7}=80 / A_p=0 and F_{10.7}=200 / A_p=80, respectively.)

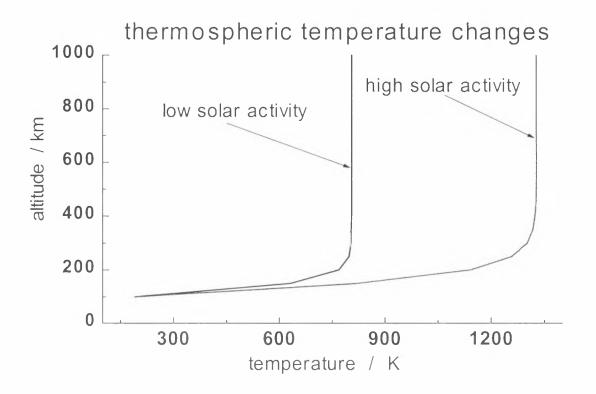


Fig. 8: XUV induced thermospheric temperature changes computed with the MSIS model. (Solar quiet and high activity conditions are chosen with F_{10.7}=80 / A_p=0 and F_{10.7}=200 / A_p=80, respectively.)

The interaction of the solar XUV radiation with the terrestrial environment is primarily triggered by the absorption of the photons by the T/I particles (O₂, N₂ and O) leading to ionization and to a series of secondary processes with energy conversion into heating and escaping radiation. The most important parameters characterizing the T/I state are the density and temperature. To get an overview of possible T/I implications as induced by solar XUV changes total upper atmospheric density (Fig. 7) and temperature changes (Fig. 8) from solar minimum to maximum conditions are presented as is computed using the MSIS model. Solar quiet and high activity conditions are chosen with $F_{10,7}=80$ / $A_p=0$ and $F_{10,7}=200$ / $A_p=80$. respectively (The index Ap is representing the geomagnetical activity as induced by the solar wind.). Thermospheric parameters are set at equatorial levels.

Provided the XUV changes are fairly represented by these numbers which amount to a factor of two (that is a reasonable approach, see above) the corresponding total thermospheric density changes increase with altitude to a maximum of a factor of ten (at the level of the exosphere >600 km) as given in Fig. 7. At the same level of altitude the temperature is increased from about 800 K to 1300 K. The presented numbers should be considered as about maximum possible changes of the given T/I parameters as induced by the solar XUV variability on a longterm scale of a solar cycle. On shorter time scales any smaller changes might occur.

5. Problems and outlook

Due to the given technological difficulties there are still serious problems to be solved and open questions to be answered. The most urgent aims to meet should be to

- conduct future measurements with true in-flight calibration and
- provide full time coverage of two subsequent solar cycles.

A combination of sophisticated XUV spectrophotometers (SOHO CELIAS/SEM and SUMER; TIMED/SEE; ISS/SOL-ACES) and low-cost broadband sensors (SNOE; GOES; PHOTON) would provide a reasonable technological base for this purpose.

It is the primary goal of the international SCOSTEP ISCS TIGER Program to support activities in this context. 68

6. References

Hall, L. A., and H. E. Hinteregger: J. Geophys. Res. 75, 6959 (1970).

Hinteregger, H. E., in C. de Jager (ed.): The Solar Spectrum, D. Reidel Publ. Co., Dordrecht, Holland, 179 (1963).

Hinteregger, H. E.: Advances in Space Res. 1, 39 (1981).

Johnson, F. S., H. H. Malitson, J. D. Purcell, and R. Tousey: Astrophys. J. 127, 80, 1958.

Kreplin, R. W.: The solar output and ist variation. Boulder, CO: Colorado Assiciated University Press, 287 (1977). Rawer, K.: Encyclopedia of Physics XLIX/7: Geophysics III, Part VII, 256 (1984).

Schmidtke, G.: Planet. Space Sci. 26, 347 (1978).

Schmidtke, G., in Rawer, K.: Encyclopedia of Physics XLIX/7: Geophysics III, Part VII, 31 (1984).

Schmidtke, G., T. N. Woods, J. Worden, G. J. Rottman, H. Doll, and C. Wita: Geophys. Res. Lett. 19, 2175, 1992.

Wienhold, F. G., J. Anders, B. Galuska, U. Klocke, M. Knothe, W. J. Riedel, G. Schmidtke, R. Singler, U. Ulmer and H. Wolf: Phys. Chem. Earth (C) 25, 473 (2000).

Worden, J., T. N. Woods, G. J. Rottman, G. Schmidtke, H. Tai, H. G. Doll and S. C. Solomon: Opt. Eng. 35, 554 (1996).

ABSOLUTE UV RADIATION, ITS VARIABILITY AND CONSEQUENCES FOR THE EARTH'S CLIMATE

Gérard Thuillier

Service d'Aéronomie du CNRS, Bp 3 91 371 Verrières-le-Buisson, France Ph : 33 1 64 47 42 91; Fx : 33 1 69 20 29 99; e-mail : gerard.thuillier@aerov.jussieu.fr

Abstract:

The UV solar radiation is a key input for the physics of the Earth'stratosphere by its action on the photochemistry, temperature and dynamics. In the Earth'climate records, different time scale are found. For the shortest, a possible candidate inducing such variations may be the Sun. However, total solar irradiance change may be small regarding its direct radiative effect on the Earth'temperature. Positive retroactions are invoked to amplify the radiative solar induced effects. UV may be considered and several mechanisms will be briefly reviewed. Therefore, for stratosphere as well as Climate, absolute UV irradiance and variability are needed. We shall reviewed the present results in term of accuracy and availability, and shall consider the expected results from the coming missions.

I Scientific rationale Physics of Earth'atmosphere and climate

The solar ultraviolet has a double importance for the Earth atmosphere. First, it plays a major role in the temperature, photochemistry and Dynamics of the middle atmosphere. Second, being originating from the solar photosphere and chromosphere, this last part induces variability in time of the spectral UV irradiance.

UV produces atomic oxygen by photodissociation of molecular oxygen. Atomic oxygen by recombination with molecular oxygen, generates ozone which has strong absorption bands in the middle UV and is at the origin of the temperature increase of the stratosphere. Consequently, between 120 and 300 nm, the solar radiation is fully absorbed in the Earth'atmosphere by ozone and molecular oxygen. Therefore, UV being the dominant source of energy in the middle atmosphere, it plays a major role in the stratosphere thermal structure and Dynamics (Hood, 1999).

Variability in the visible domain is very small except in the core of some Fraunhofer lines (e.g. Ca lines). Below 400 nm, the observed variability is increasing for decreasing wavelength. At 200 nm, from solar minimum to solar maximum activity, the change is 8%. However, the existence of the catalytic reactions induce significant changes in the middle atmosphere (Hood, 1999). As UV varies according solar activity, ozone presents a similar variation with the solar cycle (Hood and Mc Cormack, 1992). Furthermore, other minor species participate in a cycle of complex catalytic reactions. As we shall see below, the initial motivation (and still up to date) was the ozone possible destruction through catalytic reactions involving chlorine. As all these processes are strongly wavelength dependent, accurate UV solar irradiance and its variation, are requested for atmospheric Physics, in particular to identify the origin of the natural/anthropogenic ozone variation.

Is the Earth'climate concerned by solar activity? This is an important question which occupies a central position in the present debate about the Earth'atmosphere warming. When the reconstructed temperature of the last millennium is displayed together with the reconstructed solar activity (Eddy, 1976, Lean, 1997a), a correlation clearly appears. A typical example is the Maunder minimum together with the particularly cold period of second half of the XVIIth century. This is strongly supported by several other results such as, for example the relation between the temperature change and the length of the solar cycle (Friis-Christensen and Lassen, 1991, and Lassen and Friis-Christensen, 1995), the sea-surface temperature from 1860 and the sunspots number (Reid, 1991). However, a correlation is not a demonstration of a physical link, but a way to make investigation. Natural climate variability independent of solar forcing may exist, but will be not considered here.

Several semi empirical modelling were made using as inputs, the solar activity, the greenhouse gas concentration and the volcanic aerosols for the last century (Schlesinger and Ramankutty, 1992; Kelly and Wigley, 1992). Volcanic aerosols have effects not extending more than a few years depending of the quantity of injected materials in the troposphere and their altitude. Greenhouse gas concentration have a continuous increase and do not follow the temperature decrease as experienced in the 1900's and in 1940-1970 for example. These last variations are better represented when the solar activity is taken into account. In the Milankovitch'astronomical theory of climate, the amount of energy received by the Earth is slowly changing with time due to the change of the Earth'orbital parameters. The amount of change per decade is not great, but applied with persistence. Furthermore, positive retroactions act as amplifiers of the initial change. Such as are the albedo and thermohaline circulation. In the Milankovich'theory,

Proc. 1st Solar & Space Weather Euroconference, 'The Solar Cycle and Terrestrial Climate', Santa Cruz de Tenerife, Tenerife, Spain, 25-29 September 2000 (ESA SP-463, December 2000)

the total solar irradiance is changing by effect of Sun-Earth distance change while no change is made as a function of wavelength. During the Schwabe cycle, the total solar irradiance changes by 0.1% (cycle 21-22), but could be greater during the Maunder minimum (0.3% as quoted by Lean, 1997a). Applying this amount in a GCM model, Sadourny (1995) simulated the cold period which occurred during the Maunder minimum with the right amplitude of temperature change. However, it remains to explain thow such a total irradiance change applied during some solar cycles is able to produce the observed effect. In other words, what is the mechanism generating this rapid response of the atmosphere ?

When considering the Solar activity/Earth'climate link, we have to consider changes as a function of wavelength applied over short time as compared to duration encountered in the glacial-interglacial transition for example. Consequently, positive retroactions as amplifiers are searched. Thermohaline circulation due to low velocity of water circulation cannot be part of processes. But, the Earth' atmosphere is a likely candidate. Indeed, clouds covers plays a very important role in climate processes and its relation with cosmic rays as recently shown by Svensmark and Friis-Christensen (1995), opens the field of positive retroactions.

In many cases, climate evolution due to solar activity, are simulated by changing the total solar irradiance, that is to say affecting equally all wavelengths and considering a constant amount of ozone. This last assumption is not the reality as shown by Hood and Mc Cormack (1992). For solar cycle 22, the total solar irradiance changes of 0.1 % of which about one third, can be attributed to the 200-400 nm domain (Lean et al., 1997b). The remaining is likely distributed in the visible and IR solar continuum. The incident photons after scattering and reflection, are absorbed in the troposphere and Earth'surface (visible and IR domain), while those below 300 nm are fully absorbed. Its is also a wavelength domain where catalytic reactions are strongly acting. This is why UV and ozone are presently considered as a potential driver in the Sun/Earth'climate relationship.

Ozone change may have several effects (Soon, 1996; Haigh, 1994 and 1999; Shindell, et al., 1999), such as

- on the stratosphere temperature due to ozone absorption in UV and IR at 9.6 μm, ozone being also a greenhouse gas,
- on Dynamics down to the upper troposphere,

- on waves propagation.

In the above works, stratosphere photochemistry is included leading to amplify the radiative solar activity effects by changing the stratosphere and troposphere Dynamics. This is likely to occur at low latitudes by changing the troposphere-stratosphere temperature gradient which drives the strength of the Hadley cell and the propagation of the planetary waves. Ozone may be also involved in some biosphere mechanism through plankton and carbon dioxide cycle. All these processes are under evaluation and the key input is the UV solar irradiance and its variation.

II Strategy of measurements and missions

In the seventies, UV observations were carried out from balloons and rockets. Comparisons of the results showed discrepancies up to 20% above 200 nm reaching in some cases a factor two between Ly α and 200 nm (Heath and Thekaekara, 1977).

The importance of accurate solar data being well acknowledged, the NASA Office of Space Science wrote in 1978, a recommendation for the coming space missions which should :

" include long-term observations of solar irradiance at ultraviolet wavelengths, the global distribution and time variation of atmospheric trace species and the dynamics behaviour of the upper atmosphere."

The analysis of the reported discrepancies leads to consider potential sources:

i) calibration source accuracy,

- ii) procedure of calibration,
- iii) ageing of the instruments exposed to Sun radiation,
- iv) material deposition during ground operation,
- v) material deposition in orbit.

Comparison of international standards made regularly have insured that there is no significant discrepancy in the national standards used for calibrating the instruments (Köhler et al., 1996). Procedure of calibration were checked in details through an initiative of the National Institute of Standards and Technology (NIST): in the case of the ATLAS missions, three sunspectrometers being part of the mission, the same source was provided to PI teams for estimating its spectral irradiance by running a home calibration. Comparison of the results to the original data allowed to detect weaknesses of the procedures and derive appropriate corrections.

Materials exposed to space has been also subject of laboratory investigations as well as exposition to space environment, samples being retrieved to ground afterwards. Several missions of that type were performed bringing important information about the stability of glasses characteristics in presence of UV, EUV, X rays and contamination from the platform itself (LDEF missions, Clark et al., 1984).

Indeed, an important source of degradation in space is the material deposited on the first optical surface during ground and space operations. These material are generally destroyed by the hard solar radiation. By polymerisation of the hydrocarbon compounds, light elements disappear while carbon or similar particles remain on the entrance optics. Cleanliness of rooms, thermal vacuum chambers and associated equipments, is the major concern. Low outgassing materials used in the construction of the spacecrafts and instruments was also strongly recommended and checked during the design phase by the space agencies.

Another step for avoiding instruments ageing and for monitoring its responsivity was made in the instrument design. Entrance optics were kept under tight covers during the ground operations and if possible, during the first weeks in orbit where most of the outgassing is occurring. Furthermore, incorporating in flight calibration sources or equivalent system has allowed significant increase in the instrument performance as we shall show below.

A further step for increasing the scientific return of the solar space observations, was in the field of the scheduled operations and capability of instrument retrieval. This led to the following strategy :

- i) Two or more instruments in orbit
- ii) Use of short term mission with instrument retrieval allowing to make a post-flight calibration
- iii) Instruments intercomparison before flight and after if possible.

This strategy as well as the new concepts as shown above were not fully applied immediately. However, better results were obtained concerning the absolute solar irradiance and its variability by the Solar Mesosphere Explorer (Rottman, 1988) and by the SpaceLab I and SpaceLab II which provided data in agreement within 4 % RMS (Labs et al., 1985; Vanhoosier et al., 1988). The main results of this strategy will be obtained with the NOAA, Upper Atmosphere Research Satellite (UARS), the ATLAS missions, ERS2 and SOHO satellites, as we shall show below.

III Irradiance measurements

3.1 instruments and missions

We have considered here only missions after 1985.

For the measurement of the stratospheric ozone vertical profiles, the scattered light as a function of wavelength was observed on board the NIMBUS 7 satellite by the SBUV spectrometer (Cebula et al., 1998a). Daily spectral data were also obtained by deploying a diffuser plate to direct the solar light towards the instrument. Before the completion of that mission (1987), NOAA-9 and NOAA-11, both carrying the SBUV/2 spectrometers, were launched in 1985 and 1988 respectively. SBUV instruments are made of two Ebert-Fastie double monochromators. A similar instrument took place eight time on the Space Shuttle (SSBUV) for checking the SBUV absolute photometric scale. The SBUV instruments are calibrated with secondary standards provided by National Institute for Standards and Technology (NIST).

On board UARS, the SOLSTICE (Rottman et al., 1993) and SUSIM (Brueckner et al., 1993) instruments were placed. The first consists in three double gratings spectrometers having the capability to observe both the Sun and a set of stars (mainly O and B) for which the stability is well acknowledged, and which are used for calibration. The SUSIM instrument, existing in two models (one on UARS, another on ATLAS) consists in two double gratings spectrometers. whose in flight calibration is made by use of four deuterium lamps. The ground calibration was done using the SURF radiation run by NIST for both instruments.

The ATLAS missions have a payload made of several instruments dedicated to the Earth'atmosphere and solar observations For these measurements, the SSBUV, SOLSPEC (Thuillier et al., 1997, 1998) and SUSIM instruments were placed on board the Space Shuttle. SSBUV as SBUV is made of two double gratings spectrometers, while SOLSPEC uses three of them and contains deuterium and tungsten lamps for in flight relative calibration. SOLSPEC was calibrated with the Heidelberg Observatory blackbody (Mandel et al., 1998) which temperature is measured by a pyrometer calibrated by the Physikalisch-Technische Bundesanstalt (PTB) of Berlin. It also used the NIST lamps for absolute scale checking. The three ATLAS missions had a 10-day duration.

ERS2 was launched in May 1995 and carried the GOME instrument dedicated to ozone monitoring. For that, it needs the absolute solar irradiance which is measured by the same instrument made of four double gratings monochromators. GOME was calibrated by tungsten ribbon lamps provided by NIST.

SOHO carries several instrumen's. Among them, SUMER is a high resolution spectrometer using two detectors (one is used for comparison). This high resolution instrument (0.0042 nm) is also a high spatial resolution instrument. Full Sun information was obtained by scanning the slit perpendicular to its long axis. The instrument was calibrated using a secondary standard calibrated against the synchrotron radiation (BESSY I of PTB).

Tables I and II summarize the missions and the instruments characteristics.

3.2 comparisons of the recent results

For comparing two dataset from different instruments, the wavelength scale and slit functions should be identical, otherwise, their ratio may vary of an amount which is not related to their photometric scales. To avoid that effect, running mean over typically 2 to 5 nm is made. However, nearby deep Fraunhofer lines or strong emission lines, large oscillations of their ratio may be generated.

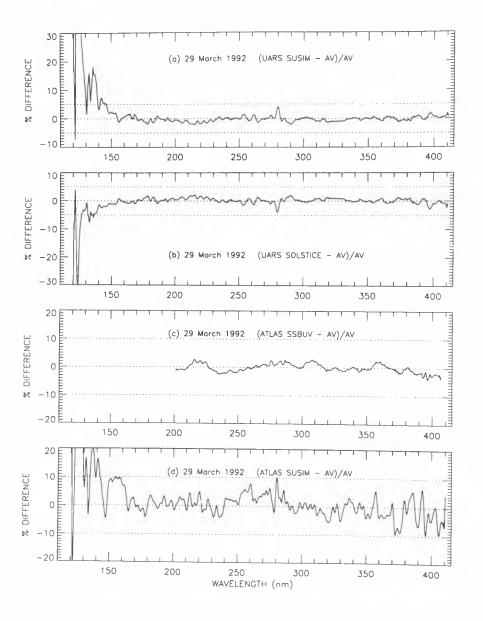


Figure 1 : Ratio at 3 nm resolution of the SOLSTICE-SUSIM/UARS and SSBUV-SUSIM/ATLAS 1 for 29 March 1992 (Woods et al., 1996).

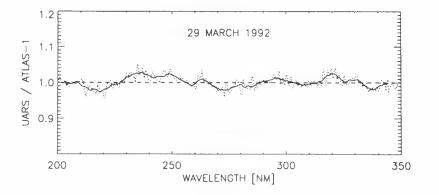


Figure 2 : Ratio of the mean UARS spectrum (Woods et al., 1996) to the ATLAS 1 mean spectrum (Cebula et al., 1996) at 1.1 and 5 nm resolution.

SUMER and SOLSTICE have in common the 120-156 nm domain. For comparing with SOLSTICE, SUMER radiance data were transformed into irradiance. An agreement of 15 % between the two data sets is found which is within the combined uncertainties of each data set (Wilhlem et al., 1999).

The SBUV/2 instruments on board NOAA 9 and 11 spacecrafts use, for observing the Sun, a diffuser plate. Its reflectivity experienced a long-term change. For the NOAA 11 mission, the solar irradiance measured decreased especially at 200 nm of 4% and 18 % in a year and five years respectively. This effect was decreasing at greater wavelength (5% at 300 nm and close to zero at 400 nm after 5 years). Using eight Shuttle flights with the SSBUV instruments appropriate corrections were made (Cebula et al., 1998a) providing absolute spectral irradiance having an accuracy of 2.3 % (2 σ) at 180 nm with better number for greater wavelengths. This allows to derive the longterm change, 7 % at 200 nm from 1989 to 1994, which was found in agreement (within 1%) with the long-term change inferred from the Mg II index (based on the solar rotation) as proxy of solar activity (see next section).

For the time of ATLAS 1 and 2, Woods et al. (1996) compared the four data sets from UARS (SOLSTICE, SUSIM) and from ATLAS (SSBUV, SUSIM). Between 120 and 400 nm, the SUSIM to SOLSTICE irradiance ratio was calculated at 3 nm resolution. Below 150 nm, this ratio exhibits strong oscillations due to the presence of intense chromospheric lines. Above, the ratio remains within $\pm 2\%$ around unity, and in the domain 300-350 nm very close to unity. When comparing with the mean of the four spectra measured on 29 March 1992 (ATLAS 1), with each individual spectrum, SOLSTICE and SUSIM/UARS remain in good agreement, SSBUV presents deviations from the mean not exceeding 2 %, but SUSIM/ATLAS shows differences especially between 250 and 300 nm and above 350 nm (figure 1). The same work was done for the 15 April 1993 (ATLAS 2) with similar conclusions. However, SUSIM /ATLAS presents a difference with respect to the mean below 300 nm, which is increasing shortwards and reaching 7% at 220 nm.

The solar irradiance measured at the same time on 29 March 1992 by the three spectrometers SSBUV, SOLSPEC and SUSIM on board ATLAS 1 were compared by Cebula et al. (1996). The three spectra being averaged, deviation from the mean are opposed for SOLSPEC and SUSIM at 250 nm and close to zero for SSBUV. Comparing the mean ATLAS 1 spectrum with the mean UARS spectrum, the deviation was less than 1 % (figure 2). Further comparisons made by Thuillier et al. (1998) for ATLAS 1 and 2 measurements between the three instruments observing at the same time confirm the conclusions of Woods et al. (1996) (figure 3).

GOME placed on ERS2, provides solar irradiance which were compared with the data obtained during the 8th Shuttle flight (January 1996) of SSBUV in the domain 310-410 nm. From the unity, the ratio of the two datasets deviate no more than 5% with a mean value of 2%. However, this ratio presents periodic variation as a function of wavelength showing obvious etalon pattern due to some optical component (Weber et al., 1998). The long-term instrument stability has not been kept and a decrease of irradiance from July 1995 has been observed increasing towards the short wavelength (15 % at 245 nm in January 1996).

3.3 the UV variability

With instrument perfectly stable, solar variability is naturally obtained. Whatever the means used to retrieve the instruments characteristics, this is done with a certain precision which can masked the solar variability in certain domain where it is particularly small, but still of scientific interest.

A usual proxy of solar activity is the radio flux at F10.7 cm. It is emitted in the solar atmosphere transition region and therefore is not characterising accurately the UV which originate from the chromosphere. The Mg II index has been proposed by Heath and Schlesinger (1986). In the core of the Mg II Fraunhofer line, the h and k chromospheric components are noticeable on a high resolution spectrum as shown on Figure 4 (top). With a low resolution instrument, a smooth Mg II absorption line is recorded (figure 4, bottom). The Mg II index is obtained by making the ratio between the solar continuum and the core. For that, the Mg II absorption line is sampled at some specific wavelengths allowing to calculate the Mg II index. Its advantage is to be nearly independent of the instrument absolute responsivity, that is to say not ageing dependent. However, it dependents of the slit function of the spectrometer making the observations. This is why, for establishing a long series, it is mandatory to dispose of overlapping observations by two successive missions. This has been done up to now.

The SBUV instruments has provided the longest series initiated by NIMBUS 7 and continued by NOAA 9 and 11 providing data from 1978 to 1994. Figure 5 shows the long-term variation after setting the Mg II index on a unique scale (DeLand and Cebula, 1993). The Schwabe cycle is clearly shown as well as the effect of the solar rotation in particular at solar maximum. After taking into account the specific slit functions of the SBUV, and the SOLSTICE and SUSIM instruments on board UARS, de Toma et al. (1997), and Cebula and DeLand (1998b) showed that the corresponding Mg II indices were consistent and have a linear dependence. This has allowed to extend the NOAA series by adding SOLSTICE data after October 1994 when NOAA 11 was no more observing (Viereck and Puga, 1999). Furthermore, GOME on board ERS2, provides Mg II

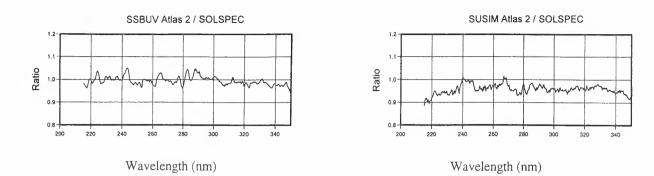


Figure 3 : Ratio at 5 nm resolution of the SSBUV and SUSIM to SOLSPEC irradiances for 15 April 1993 (mission ATLAS 2, Thuillier et al., 1998)

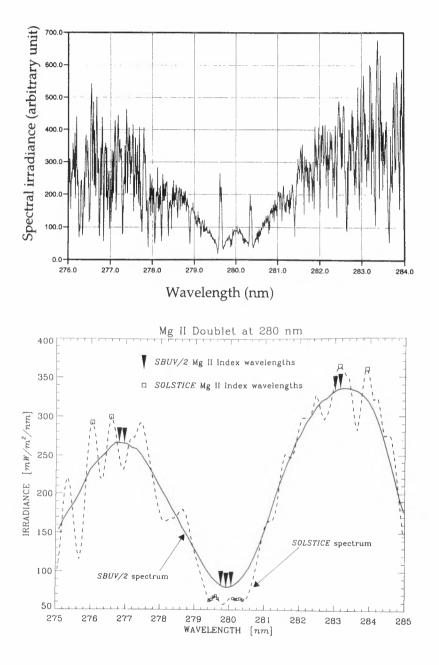


Figure 4 : The high resolution solar spectrum (top) around the Mg II Fraunhofer line observed by the UVSP spectrometer on board SMM (Kurucz, 1996). The same spectral domain (bottom) as observed by SBUV/2 and SOLSTICE (Cebula and DeLand, 1998b).

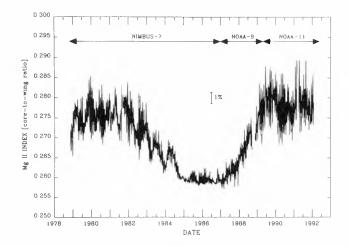


Figure 5 : The normalised Mg II index (DeLand and Cebula, 1993).

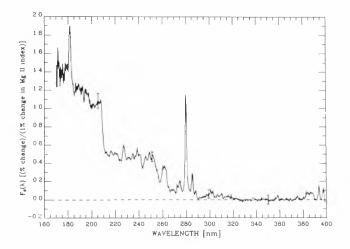


Figure 6 : The scale factor providing the spectral variability normalised by the Mg II index (DeLand and Cebula, 199

indices which are in agreement with those measured at the same time by SOLSTICE on board UARS (Weber et al., 1998).

The Mg II index allows to derive the irradiance variability as a function of wavelength. The observed variability at a given wavelength has been evaluated as a function of the Mg II index change generated by the solar rotation. This leads to Figure 6 which provides the percentage of change (scale factors) as a function of wavelength normalised on a constant Mg II index percentage change. As these results are based on variability due to the solar rotation, it is important to investigate if they are also usable over a long-term, i.e. the Schwabe cycle. This is discussed in details by DeLand and Cebula (1998) who conclude positively. The scale factor of Figure 6 was established from the SBUV/2 data, then not covering the domain below 175 nm. This was made down to Ly α by Lean et al. (1992) over four solar rotation, and Chandra et al. (1995) over both short and long times scales who suggested the domain below 175 nm to be underpredicted by the scale factor. However, this being kept in mind, the scale factor allows to derive the variability at any wavelength at any date for which the Mg II index is available.

IV Next missions and conclusions

The importance of UV in Earth' atmospheric Physics and Climate is well acknowledged. As a consequence strong requirements in term of accurate solar irradiance data and its variability have been made.

The comparisons shown above of solar irradiance measured by several instruments having different design, and different method and source of absolute calibration, agree within 4 to 5 % in the UV with certain domain quoted at 2 %. The most consistent results are found for the UARS spectrometers. It is also noticeable that comparisons of mean spectra (e.g., mean UARS and mean ATLAS spectra) show better agreement than comparison of two individual spectra. This suggests errors not even distributed as a function of wavelength.

Solar spectral irradiance variability as described by the Mg II index, provides consistent results when observed by different instruments after appropriate processing and comparisons allowed by overlapping missions. The series extends now over 22 years. The solar spectral irradiance variability obtained from the solar rotation is consistent with the long-term observed changes. This allows to use that solar proxy for simulating effects of solar activity change in the Earth'atmosphere and climate.

For the future, we note the following:

UARS, originally designed to operate during 18 months, is still working with, however a limited payload. including the two spectrometers SOLSTICE and SUSIM running nominally. UARS is expected to operate up to 2003.

The ENVISAT 1 platform will carry two spectrometers, MERIS (Medium Resolution Imaging Spectrometer) and SCIAMACHY (SCanning Imaging Absoption SpectromMeter for Atmospheric CHartographY, Bovensmann et al., 1999). They study the land surface and middle atmosphere by observing the backscattered light. They will be also able to carry solar spectral observations as GOME. ENVISAT 1 will be launched by mid 2001.

The next operation will be the SOlar Radiation and Climate Experiment (SORCE, Rottman et al., 1997, 2000) investigation which is designed to operate from mid 2002 on board a free-flying satellite for a 6-year duration. It will carry four instruments:

i) TIM monitoring the total solar irradiance,

- ii) SOLSTICE observing the spectral irradiance from 120 to 320 nm,
- iii) SIM measuring the spectral irradiance from 200 to 2000 nm,
- iv) XPS observing several XUV bands from 1 to 35 nm.

On board the International Space Station (ISS), a solar pallet (SP) will be operated for a duration of three years. It will be launched in 2004. It consists in three instruments which description is given by Thuillier al. (1999):

i) SOVIM measuring the total solar irradiance (TSI),

- ii) SACES observing from 17 to 220 nm,
- iii) SOLSPEC observing from 180 to 3000 nm.

These two missions have basically the same scientific aims: measurement of the total and spectral solar irradiance and how is partitioned the variability per spectral domains within the total solar irradiance, for Atmospheric and Climate Physics. They are obviously closely related in term of spectral domains. However, the main difference may be found in the different calibration principles used by SACES, SOLSTICE and SOLSPEC. Furthermore, ISS-SP will extent more in the IR domain while SORCE will extent more in EUV.

For these missions, it is expected to relate UARS with SORCE, and SORCE with the Space Station experiments and ENVISAT 1. This will allow continuity and useful comparisons for both spectral and total solar irradiance data provided by instruments of different concepts and calibrations. Anticipated accuracy is about 3% or better. An advantage of the ISS is the retrieval of the instruments for a post-mission laboratory check. We finally note that the strategy of overlapping missions will be still applied. This will insure that TSI, UV and EUV absolute irradiance and their variability will be accurately measured as required for the understanding of the solar variability role in Atmospheric and Climate Physics.

REFERENCES

Bovensmann, H, Burrows, J. P., Buchwitz, M., Frerick, J., Noel, S., Rozanof, V. V., Chance, K. V., and Goede, A. P. H., SCIAMACHY : mission objectives ans measurements modes, J. Atm. Sci., 56, 127-150, 1999.

Brueckner, G. E., Eldow, K. L., Floyd IV, L. E., Lean, J. L., and VanHoosier, M. E., J. The Solar Ultraviolet Spectral Irradiance Monitor (SUSIM) experiment on board the Upper Atmosphere Research Satellite (UARS), J. Geophys. Res. 98, 10695-10711, 1993

Cebula, R.P., Thuillier, G., Vanhoosier, R. M., Hilsenrath, E., Hersé, M., Simon, P. C., Observations of the solar irradiance in the 200-350 nm interval during the ATLAS 1 mission: A comparison among three sets of measurements-SSBUV, SOLSPEC, and SUSIM, Geophys. Res. Let., 23, 2289-2292. 1996.

Cebula, R. P., DeLand, M. T., NOAA 11 solar backscattered ultraviolet, model 2 (SBUV/2) instrument solar spectral irradiance measurements in 1984-1994, 1. Observations and long-term calibration J. Geophys. Res., 103, 16235-16249, 1998a.

Cebula, R. P., DeLand, M. T., Comparison of the NOAA 11 SBUV/2, UARS SOLSTICE, and UARS SUSIM Mg II solar activity proxy indices, Sol. Phys., 177, 117-132, 1998b.

Clark, L. G., Kinard, W. H., Carter, D. J. Jr, and Jones, J. L., The Long Duration Exposure Facility mission 1 Experiments, NASA SP-473, 1984.

Chandra, S. J., Lean, J., White, O. R., Prinz, D. K., Rottman, G. J., and Brueckner, G. E., Solar UV irradiance variability during the declining phase of the solar cycle 22, Geophys. Res. Lett., 22, 2481-2484, 1995.

DeLand, M. T. and Cebula, R. P., Composite Mg IIsolar activity index for solar cycles 21 and 22, J. Geophys. Res., 98, 12809-128823, 1993.

DeLand, M. T., Cebula, R. P., NOAA 11 solar backscattered ultraviolet, model 2 (SBUV/2) instrument solar spectral irradiance measurements in 1984-1994, 2. Results, validation, and comparisons, J. Geophys. Res., 103, 16251-16273, 1998.

de Toma, G., White, O. R., Knapp, B. G., Rottman, G. J., and Woods, T. N., Mg II core-to wing index: comparison of SBUV/2 and SOLSTICE time series, J. Geophys; Res., 102, 2597-2610, 1997.

Eddy, J., The Maunder minimum, Science, 192, 1189-1202, 1976.

Friis-Christensen, E., and Lassen, K., Length of the solar cycle: an indicator of solar activity closely associated to climate, Science, 254, 698-700, 1991.

Haigh, J. D., The role of stratopheric ozone in modulating the solar radiative forcing of climate, Nature, 370, 544-546, 1994.

Haigh, J. D., Modelling the impact of solar variability on climate, J. Atm. Sol. Terr. Phys., 61, 63-72, 1999. Heath, D., and Schlesinger, B. M., The Mg II 280 nm doublet as a monitor of changes in solar ultraviolet irradiance, J. Geophys. Res., 8672-8682, 1986. Heath, D., and Thekaekara, M. P., The solar spectrum between 1200 and 3000 A, in The solar output and its variation, Ed. O. R. White, Colorado Associated University Press, Boulder, p. 193-212, 1977.

Hood, L. L., Effects of short-term solar UV variability on the stratosphere, J. Atm. Sol. terr. Phys., 61, 45-51, 1999.

Hood, L.L., et Mc Cormack, J.P., Components of interannual ozone change based on NIMBUS 7 TOMS data, Geophys. Res. Lett., 19, 2309-2312, 1992.

Kelly, P., and Wigley, Solar cycle length, greenhouse forcing and global climate, Nature, 360, 460-462, 1992.

Kölher, R., Goebel, R., and Pello, R., Results of an international comparison of spectral responsivity of silicon photodetectors, *Metrologia* **32**, 463-468, 1996. Kurucz, R., private communication, 1996

Labs, D., Neckel, H., Simon, P. C., and Thuillier, G., Solar Phys., Ultraviolet solar irradiance measurements from 200 to 358 nm during the SpaceLab I, **107**, 203, 1987.

Lassen, K., and Friis-Christensen, E., Variability of solar cycle legth during the past five centuries and the apparent association with terrestrial climate, J. Atm. Terr. Phys., 57, 835-845, 1997.

Lean, J., Vanhoosier, M. E., Brueckner, G. E., Rottman, G. J., SUSIM/UARS observations of the 120 to 300 nm flux variations during the maximum of the solar cycle: inference for the 11-year cycle, Geophys. Res. Lett., 19, 2203-2206, 1992.

Lean, J., The sun's variable radiation and its relevance for the Earth, Annu. Rev. Astron. Astrophys., 35, 33-67, 1997a

Lean, J., Rottman, G. J., Kyle, H. L., Woods, T. N., Hickey, J. R., and Puga, L. C., Detection and parametrization of variations in solarmid-and nearultraviolet radiation (200-400 nm), J. Geophys. Res., 102, 29939-29956, 1997b.

Mandel, H., Labs, D., Thuillier, G., Hersé, M., Simon, P.C., Gillotay, D., Calibration of the SOLSPEC spectrometer to measure the solar irradiance from space, Metrologia, 35, 697-700, 1998.

Reid, G. C., Solar irradiance variations and global ocean temperatures, J. Geomag. Geoelectr., 43, 795-801, 1991.

Rottman, G., Observations of solar UV and EUVvariability, Adv. Space Res., 8, 53-66, 1988.

Rottmann, G. J., Mount, G., Lawrence, G., Woods, T., Harder, J., and Tournois, S., Solar spectral Irradiance measurements: visible to near infrared, Metrologia, 35, 9707-712, 1997.

Rottman, G. J., SORCE, 2000, on web site http://lasp.colorado.edu/sorce

Rottman, G. J., Woods T. N., and Sparn, T. P., Solar Stellar Irradiance Comparison Experimeny: instrument design and operation, J. Geophys. Res. 98, 10667-10678, 1993.

Sadourny, R., Maunder minimum and Little ice age: impact of a long-term variation of the solar flux on the energy and water cycle, NATO ASI series, vol. 22, Ed. J. C. Duplessy and M. T. Spyridakis, Springer-Verlag, Berlin Heidelberg, 1994.

Schlesinger, M. E., and Ramankutty,, N., Implications for global warming of intercycle solar irradiance variations, Nature, 360, 330-333, 1992.

Shindell, D., Rind, Balachrandran, N., Lean, J., and Lonergan, P., Solar variability, ozone and climate, Science, 284, 305-308, 1999.

Soon, W. H., Posmentier, E. S., and Baliunas, S. L., Inference of solar irradiance variability from terrestrial temperature changes, 1880-1995: an astronomical application of the sun-climate connection, Astrophys. J., 472, 891-902, 1996.

Svensmark, H., and Friis-Christensen, E., Variation of cosmic ray flux and global cloud coverage - a missing link in solar-climate relationships, J. Atm. Solar Terres. Phys., 59, 1225-1232, 1997.

Thuillier, G., Hersé, M., Simon, P.C., Labs, D., Mandel, H. and Gillotay, D., Observation of the UV solar spectral irradiance between 200 and 360 nm during the ATLAS I mission by the SOLSPEC spectrometer, Sol. Phys., 171, 283-302, 1997.

Thuillier, G., Hersé, M., Simon, P.C., Labs, D., Mandel, H., and, Gillotay, D., Observation of the solar spectral irradiance from 200 to 870 nm during the ATLAS I and 2 Missions by the SOLSPEC Spectrometer, Metrologia, 35, 689-695, 1998

Thuillier G., Fröhlich C., and Schmidtke, G., Spectral and total solar irradiance measurements on board the international Space Station, in Utilisation of the International Space Station, Second european Symposium, ESA-SP433, 605-611, 1999

VanHoosier, M. E., Bartoe, J. F., Brueckner, G. E., and Prinz, D. K., Absolute solar spectral spectral irradiance 120-400 nm(results from the Solar Uktraviolet Spectral Irradiance Monitor- Experiment on board SpaceLab 2), *Astro. Lett. and Commun.* 27, 163-168, 1988.

Weber, M., Burrows, J. P., and Cebula, R. P., GOME solar UV/VIS irradiance measurements between 1995 and 1997 - First results on proxy solar activity studies. Solar Phys., 177, 63-77, 1998.

Viereck, R. A., and Puga, L. C., The NOAA Mg II core-to-wing solar index: construction of a 20-year time series of chromospheric variability from multiple satellites, J. geophys. Res., 104, 9995-10005, 1999.

Wilhelm, K., Woods, T. N., Schüle, U., Curdt, W., Lemaire, P., and Rottman, G. J., The solar ultraviolet spectrum from 120 nm to 156 nm: a radiometric comparison between SUMER/SOHO and SOLSTICE/UARS, Astron. Astrophys., 352, 321-326, 1999.

Woods, T.N., Prinz, D.K., Rottman, G.J., London, J., Crane, P. C., Cebula, R.P., Hilsenrath, E., Brueckner, G. E., Andrews, M. D., White, O. R., VanHoosier, M. E., Floyd, L.E., Herring, L. C., Knapp, B. G., Pankratz, C. K., and Reiser, P. A., Validation of the UARS solar ultraviolet irradiances: Comparison with the ATLAS I and 2 measurements, J. Geophys. Res., 101, 9541-9569, 1996.

Platform	instruments	launch date	operation
NOAA 9	SBUV/2	3/1985	ended 5/1997
NOAA 11	SBUV/2	9/1988	ended 10/1994
UARS	SOLSTICE, SUSIM	9/ 1991	working
ATLAS 1-2-3	SSBUV, SOLSPEC, SUSIM	3/92, 3/93, 11/93	completed
ERS2	GOME	5/95	working
SOHO	SUMER	12/1995	working

Table I : Platforms, missions and instruments used for UV measurements from 1988.

Instrument	range (nm)	bandpass (nm)
SBUV	170-410	1.1
SOLTICE-UARS	119-420	0.1-0.2
SUSIM-UARS	115-410	0.15-1.1-5
SUSIM-ATLAS	115-410	0.15-5
SSBUV-ATLAS	160-405	0.15
SOLSPEC-ATLAS	200-2500	1 nm below 850 nm
GOME-ERS2	240-790	0.2 to 0.4
SUMER-SOHO	46.5-161	0.0042

Table II : Spectral characteristics of the instruments.

79

MID-TERM VARIATIONS IN THE EXTREME UV CORONA : THE EIT / SOHO PERSPECTIVE

Jean-François Hochedez, Frédéric Clette, Erwin Verwichte, David Berghmans, Pierre Cugnon

Royal Observatory of Belgium, Solar Physics Department, Circular Avenue 3., B-1180 Brussels Belgium hochedez@oma.be, Tel: +32 2373 0302, Fax: +32 2374 9822, http://sol.oma.be

ABSTRACT

Since the start of the SoHO mission, EIT -the Extreme ultraviolet Imaging Telescope- offers a global view of the solar corona over the whole rising phase of the current activity cycle. Such a dataset is unprecedented. We give here the current results of an on-going investigation over the entire EIT archive. In this process, numerous classes of magnetic regions of all sizes as well as dynamical events will be identified in the images. The change in their properties (location. size, topology, lifetime, integrated flux) and their mutual relationships will then be monitored over the rise of magnetic activity towards the current maximum. In the Fe XV images (2 MK), the on-disk and off-disk intensity distributions have been evaluated, and their evolution is described. We developed an image processing technique that extracts the smallest detectable features. The cosmic ray hits are statistically disentangled from the solar point-like phenomena. and the trends in both rates are assessed.

1. INTRODUCTION

The expanding solar atmosphere is one of the main sources of interactions between the Sun and the Earth environment. The coronal instruments aboard the Solar and Heliospheric Observatory (SoHO) -a joint NASA/ESA mission- were primarily designed to elucidate the physical mechanisms responsible for accelerating the solar wind and for heating the corona. Although earlier missions (Skylab, SMM, Yohkoh) improved the understanding of the largest energy releases, a new generation of more sensitive instruments was needed to explore the so-called "Quiet Sun" regions that account for the largest volume in the hot and thin corona. Among SoHO coronal experiments. EIT, the Extreme-ultraviolet Imaging Telescope (Delaboudinière et al. 1995, Moses et al. 1997) uses innovative normalincidence mirrors to provide global high-resolution views of the on-disk corona (its field of view is 45 min). It is able to image the faint emission of the corona in four ion lines corresponding approximately to 80 000 K (He II, 30.4 nm), 1 MK (Fe IX/X, 17.1 nm), 1.6 MK (Fe XII, 19.5 nm), and 2 MK (Fe XV, 28.4 nm). Since January 1996 -before the minimum of cycle 23- it has ensured a near continuous monitoring, except for a couple of interludes (133 days from June 25, 1998 when contact with the SOHO spacecraft was temporarily lost. and 42 days from December 22, 1998).

Scanning the EIT / SoHO archive -systematically and automatically- paves the way to investigations in many different fields of solar physics. The need is also inherent to such a huge data set :

- There is no simple way to render on a screen the complete information of even a single image (typical images are 1024 × 1024 pxl × 14 bits / pxl). Their global and individual wealth seems thus better suited to an algorithmic approach that synthesises the parameters of interest. facilitating further interpretations. Yet, the visual inspection is not to be underestimated. In some algorithms, it drives the choice of parameters that would otherwise be arbitrary.
- Identification of all kinds of local or global events is possible with the use of advanced pattern recognition schemes. Once time series are available, statistical tools can be applied to help defining normal conditions or cross-correlating behaviours.

Consequently, it is expected that from such an analysis well-known solar objects and events are extracted, of which properties and mutual relationships at all available space and time scales can be followed. This scale issue is known to be linked to many significant questions of solar physics.

Comparable synoptic surveys have been undertaken with success by other space and ground-based imager teams : SXT / Yohkoh (*e.g.* Hara, 2000), HXT / Yohkoh (*e.g.* Sakao, 2000), LASCO / SoHO (*e.g.* Rich, Derc, Howard, 2000), MDI / SoHO (*e.g.* Turmon, Pap, Mukhtar, Bogart, 1999). Wilcox Solar Observatory, Mauna Loa Solar Observatory, NSO, and naturally by all dedicated instruments providing extended time series (*e.g.* Sunspot Index Data Centre, GOES, NOAA, CELIAS, COSTEP & ERNE / SoHO).

As for EIT, some studies were already carried out fruitfully for a few specific parameters. The Sun centre coordinates and radius are monitored, leading to the description of the height structure of the chromosphere and transition region over the years (Auchère *et al.* 1998). The average signal is also plotted to assess the global EUV flux from the corona, but so far, it served to estimate the degradations undergone by the telescope, particularly by its CCD.

The evolution of the atmospheric structuring informs about the causally linked regions, namely the higher corona above, and the convection zone below :

Proc. 1st Solar & Space Weather Euroconference, 'The Solar Cycle and Terrestrial Climate', Santa Cruz de Tenerife, Tenerife, Spain, 25-29 September 2000 (ESA SP-463, December 2000)

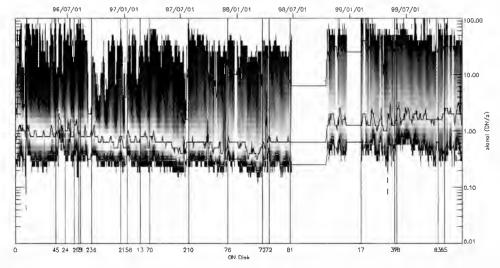
- Radiometric solar UV measurements are prerequisites to terrestrial climate models. The flares, the coronal mass ejections (CMEs), the coronal holes, or the He II flux density are all observed with the EIT in a unique way. Each embodies one impact of the corona on the Earth. Furthermore, the scientific results of our scanning process will be input to new Space Weather models (Poedts, 1999). The corona is the source of the subsequent heliospheric processes.
- The definition and correlation of new activity indices assess meaningfully the solar and stellar variability.
- In order to understand the dynamo and the solar variability, it is important to describe accurately the differential rotation. By comparing diverse tracers such as bright points, new insights are gained (Brajša *et al*, 2000).

Table 1 shows the status of the EIT collection as of September 2000. It amounts to a total of approximately 170 000 images. At the time when these lines are written, it is realistic to assume that EIT observations will cover the full cycle 23 until some successor prolongs the monitoring. However, almost five years of daily scrutiny have already passed, and the time is ripe to tackle the archive as a whole.

Wavelength	Number of images fffr (Full Field, Full Re solution)	Nb. of images ffhr (Full Field, Half Re solution)
17.1 nm Fe IX/X	5 581	2 479
19.5 nm Fe XII	61 858	38 437
28.4 nm Fe XV	5 596	1 415
30.4 nm He II	9 563	3 307

Table 1. Status of the EIT archive as of September2000. The full field is 45' wide, full resolution gives 1024×1024 pixels, half resolution gives 512×512 pixels.

Given the extent of the archive, we first focussed on the Fe XV bandpass (2 MK) as it allows dealing with



smaller, more regular data series. By nearing the temperature ranges, potential comparisons with Yohkoh / SXT are hence legitimated. This paper deals therefore with the 2 MK corona only.

Two kinds of analysis can be envisioned : photometric and morphological studies. Both have been undertaken for their expected benefits are different.

2. PHOTOMETRIC STUDIES

The *a priori* easiest quantitative parameters to extract from EUV solar images are of photometric nature. This approach consists, for example, in recognizing active regions (AR) by their brightness, or in tracking the global emission of the corona. It suffers unfortunately from various instrumental and operational drawbacks. The main ones owe to the badly estimated loss of sensitivity that is only partly recovered through recurrent bakeouts of the detector. Other corrections must compensate for the variable location *viz.* distance of SoHO with respect to the Sun.

However, the photometric approach is usually very instructive as shown hereafter. It is also the required first step toward on-flight calibrations and the desirable radiometric advances.

All the analysed full-field 28.4 nm images went through the following steps :

- The image is corrected for the electronic offset, the grid shadow, the pre-flight flatfield, and converted to logarithmic scale.
- The image is split into "on-disk" (< 95% R_O), "off-disk" (> 105% R_O), and "limb" (in-between).
- The intensity histograms are computed on-disk and off-disk. As it exhibits singularities, the limb region is excluded from this study.
- The histograms of the log intensities were shifted to take into account the variable exposure time, the filter configuration and the binning.

After the recovery of SoHO, not all data were hitherto processed yet.

Figure 1. The on-disk intensity distributions of EIT Fe XV images from January 1996 to December 1999. Each vertical slice is a median distribution over two days. The vertical lines indicate the bakeout periods with their durations below. The lowest significantly represented, the most represented and the highest significantly represented intensities are plotted. Intensities and occurrences have log scales.

In Figure 1, the histograms are nicely modulated if there are only one or two active regions, during *e.g.* 1996. From July 1997 onwards, the picture is more intricate. The most represented signal appears to vary between 0.5 and 3 DN/s. It seems strongly affected by the repeated efforts to recover the sensitivity of the detector by means of bakeouts (heating it from its working temperature of -60°C up to +15°C during tens to hundreds of hours). Although the pre-flight photometric calibration of the EIT has been finalized (Dere *et al.* 2000), it is impossible to infer radiometric quantities as long as the degradations are not corrected for.

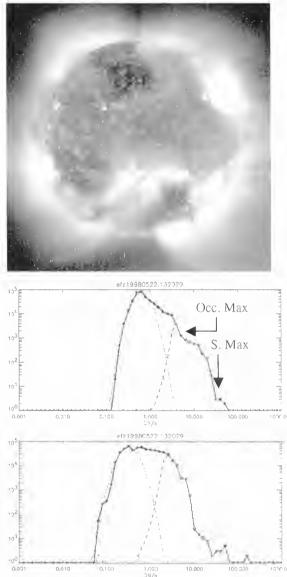


Figure 2. One EIT Fe XV image with its on-disk and off-disk histograms. The lognormal fit appears as a parabola, the power laws as straight lines. "Occ.Max" is the maximum number of occurrences in the active region area. "S.Max" is the brightest signal reached.

Nonetheless, the shape of the distributions contains information. In (Pauluhn *et al.* 2000), quiet Sun EUV distributions are better fitted by a lognormal than by other functions. We therefore fitted the Quiet Sun component of the Fe XV on-disk histograms with a lognormal expression :

$$d(x) = \frac{N_0}{x} e^{\frac{-(\ln(x) - \mu)^2}{2\sigma^2}}.$$
 Eq. 1

which turns out to be a parabola in a log-log scale. Indeed, it is apparent (See Figure 2) that the observed distributions exhibit a parabolic shape at the lower intensities. The active regions (AR) of higher intensities produce a power law distributed tail. Interestingly, the coronal holes do not generate a perceptible mismatch between the on-disk histograms and the fitting functions.

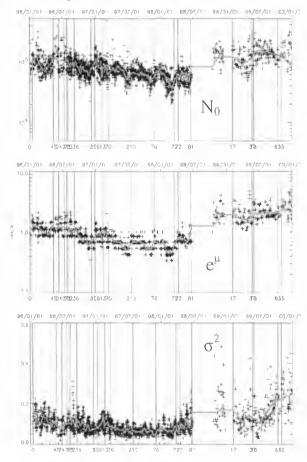


Figure 3. Parameters of the lognormal corresponding to a fit of the on-disk "quiet Sun" intensity distributions. From top to bottom : $N \cdot e^{u}$ and σ^{2} of Eq. 1.

Due to the normalization, the N_o, e^u and σ^2 parameters are not independent. It is still worth noting that the first two increased chiefly during the SoHO vacation, whereas σ^2 rose later, after mid 1999, e^u relates to the quiet Sun brightness, but it contains contributions from additive features in the line of sight (*e.g.* the canopy), and from the instrument sensitivity drift since the flatfield degradation is not corrected for, σ^2 may give a more direct access to the quiet Sun evolution, even if it also encompasses elevated structures, or their absence (like above coronal holes).

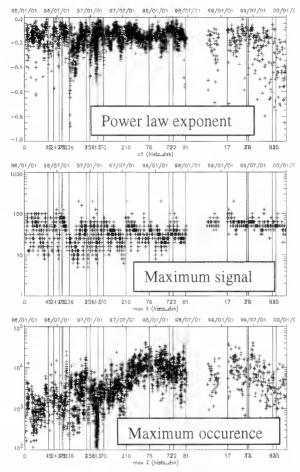


Figure 4. Parameters of the power law corresponding to a fit of the on-disk "active Sun" intensity distributions. From top to bottom : slope, maximum signal and maximum number of occurrences (S.Max and Occ.Max respectively of Figure 2)

From a first look at the graphs in Figure 4 we can make the following observations :

- The exponent of the power law does not change much over the course of the four years under study.
- The maximum signal (S.Max) saturates at ~80 DN/s. It is not instrumental, and relates rather

to the size and the filling factor of the brightest objects in the corona.

• The maximum number of occurrences (Occ.Max). related to the area covered by active regions (ARs). increased by one order of magnitude through 1997. and has roughly stabilized since then.

This confirms that the increase in EUV flux with rising activity would originate in the expansion of ARs. Their average brightness seems conversely to be fairly constant, and their maximum brightness to be controlled by the filling factors, and by the instrument resolution.

Although the field of view has not been restricted to a ring yet, and has been kept externally square instead, it is instructive to look at the off-disk histograms in the same manner as the on-disk ones (Figure 5 and Figure 2). A couple of artefacts are noticed in Figure 5 :

- A visible light leak suddenly occurred in 1996 and was finally cancelled via the use of an additional aluminium filter early 1998. High off-disk signals were recorded meanwhile in a rather limited area.
- The electronic offset is not perfectly known. By subtracting an incorrect value, one introduces errors affecting mainly low intensities. Short exposure times thus enhance this problem (*e.g.* July 1996)

The active regions, observed once per solar rotation in the on-disk figure, are now seen twice, at the East and at the West limb. The median EUV flux has increased exponentially from early 1996 to late 1999. As far as the instrumental degradation is concerned, this means that an intensity level of less than 1 DN/s has not degraded the imager appreciably, since the recovering effect of the bakeouts are barely seen. Physically, it is interpreted as the cumulative emission of the canopy that develops with the magnetic cycle. This observation will be subject to further quantitative analysis.

The flux has increased by a factor 8 in the considered period, while the sunspot number increased by 20 times, and the 10.7 cm radio flux by a factor 2.3 in the same interval.

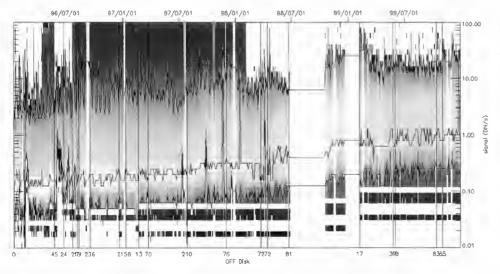


Figure 5. The off-disk intensity distributions of EIT Fe XV images from January 1996 to December 1999. Each vertical slice is a median distribution over two days. The vertical lines indicate the bakeout periods with their durations below. significantly The lowest represented. the most represented and the highest significantly represented are plotted. intensities Intensities and occurrences have log scales.

3. MORPHOLOGICAL STUDIES

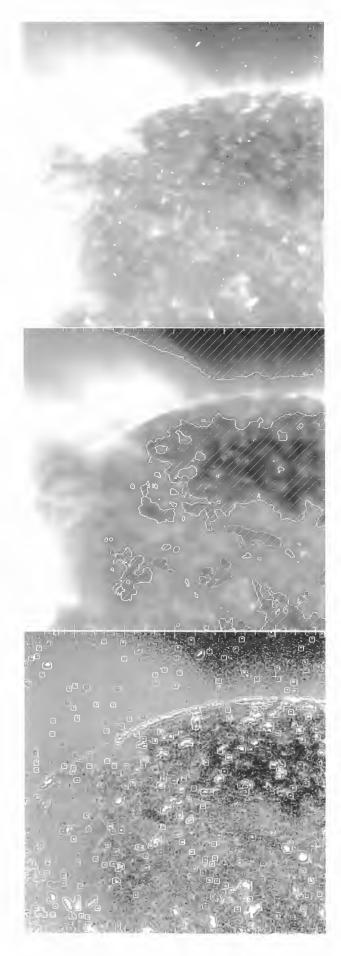
A complementary line consists in the use of advanced pattern recognition techniques. Although it pushes the current methods to their limits, it proves feasible to segment EUV solar structures. The principal current constraints originate in the high CPU requirements that contradict somewhat the purpose of scanning the whole archive, and in the programming standards not compatible with the otherwise prevalent IDL language, expanded by the SSW (Solar SoftWare library). Besides the increased confidence provided by sophisticated tools, this approach allows deciphering subtle phenomena like the morphology, the dynamics, or the complexity of ARs. As a first application, we report about the small features in the EIT Fe xv images.

We developed and programmed a non-linear filtering method that replaces each pixel by a "best estimate value" built from the 5×5 neighbourhood. It is named "Minimum Plane Fit" (MPF) as a plane is futed through the lowest pixels of the neighbourhood, and the central pixel is interpolated. It proves to efficiently extract the small bright objects as illustrated in Figure 6.

Small features are then counted whether on-disk or offdisk, and as a function of the level of the background on top of which they occur. Its threshold has been set at 35 DN. It is the boundary between the photon-noise and the read-noise dominated regimes. Given the typical exposure times (~100 s), it also roughly corresponds to the coronal holes maximal brightness. Features are extracted if the raw signal exceeds the filtered one by more than 2.5σ , sigma being the quadratic sum of the read noise and the Poissonian photon noise. In the following, one event accounts for one pixel belonging to a feature. Darker off-disk (> $1.05 \times R_{\odot}$) regions cannot exhibit any solar point-like source. This is where the cosmic ray hit rate is estimated to be quite steady around a value of 4.10^{-5} evt/pxl/s (Figure 7). In contrast. on-disks densities of small bright features are not much a function of exposure time. They can thus be associated with small solar structures. The cosmic hits rate contributes at most to half of the observed density 4.10^{-5} evt/pxl/s × ~100 s = 4.10^{-3} evt/pxl < 10^{-2} Eq. 2 10⁻² is the minimum density of pixels involved in ondisk ($< 0.95 \times R_{\odot}$) small features as seen in Figure 8.

The extracted entities that are not cosmic hits appear to be bright points or magnetic loop footpoints.

Figure 6. Extraction of point-like features in an EIT image. The upper picture is a raw Fe XV image in log scale. The middle one has been MPF-filtered. The areas below 35 DN happen to correspond to coronal holes. They are encircled and hatched. The bottom picture is the difference image. Small features are highlighted by contours based on the 2.5 σ criterion and dilated for clarity. They match cosmic hits, bright points or magnetic loop footpoints in the original image. In this paper, the limb region is always excluded.



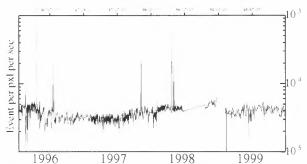


Figure 7. Cosmic ray hits rate measured in the EIT Fe XV images. The average value is approximately 4.10^{-5} event/pxl/s. The flux is modulated by the solar rotation. The sudden peaks correspond to proton events or telemetry inconsistencies.

The remarkable result is the regular decrease of the density of solar point-like features from 0.04 evt/pxl early 1996 down to 0.01 evt/pxl late 1999 in the darker parts of the on-disk images (*i.e.* coronal holes). These tiny features are visually identified as bright points.

In the more intense part of the solar disk, the density of small objects is higher since many magnetic loop footpoints are included in the count. Still, there is a decline from 0.12 evt/pxl to 0.03 evt/pxl. These results would confirm observations from SXT (Nakakubo, Hara, 2000) but could possibly be fully or partly attributed to instrumental effects such as Point Spread Function, or Charge Collection Efficiency degradations. The analysis is now going on in order to characterize the events photometrically and geometrically.

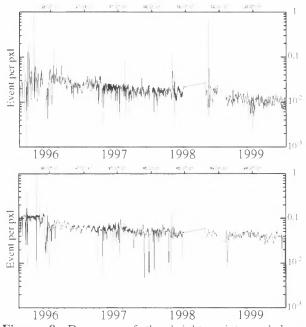


Figure 8. Decrease of the bright points and loop footpoints densities for the darker (upper graph) and brighter (lower graph) Fe XV solar disk. The excesses come from proton showers or telemetry faults, the troughs issue from absorbing prominences that augment the area but not the bright points rate.

CONCLUSIONS

Several trends have been found in the 2 MK corona from January 1996 to December 1999. The flux has exponentially increased by a factor 8 due to the expansion of active regions. The density of point-like solar sources has decreased from 0.04 to 0.01 evt/pxl in the coronal holes, and from 0.12 to 0.03 evt/pxl elsewhere. Sophisticated tools are currently being developed in collaboration with image analysis teams. The results will extend with further investigations, the examination of the three other wavelengths, and the continuation and improvements of the synoptic monitoring. It is expected that this study will lead simultaneously to a deepening of the EIT instrument understanding, and to new insights in solar physics.

ACKNOWLEDGEMENTS

The authors acknowledge the support from PRODEX, and from the Belgian government through the OSTC. SOHO is a project of international cooperation between ESA and NASA.

REFERENCES

- Auchère, F., & *al*, 1998, The prolate solar chromosphere. A&A 336, L57
- Brajša, R., & al, 2000, An Analysis of the Solar Rotation Velocity by Tracing Coronal Features, IAU Symposium 203
- Delaboudinière, J.-P., & al, 1995. EIT : Extreme-Ultraviolet Imaging Telescope for the SOHO Mission, Solar Physics, 162, p.291
- Dere, K., & *al*, 2000, The pre-flight photometric calibration of the extreme-ultraviolet imaging telescope EIT, Solar Physics, 195, p.13
- Hara, H., 2000, Yohkoh Soft X-ray Observations in One Solar Activity Cycle, IAU Symposium 203
- Moses, D, & al, 1997, EIT Observations of the Extreme Ultraviolet Sun. Solar Physics, 175, Issue 2, p.571
- Nakakubo, K., Hara, H., 2000, Variation of X-Ray Bright Point Number Over the Solar Activity Cycle. Advances in Space Research, 25, Issue 9, p.1905
- Pauluhn, A., & *al*, 2000, Statistics of quiet Sun extreme ultraviolet intensities, to appear in A&A
- Poedts, S., 1999, OSTC project, CPA, Leuven
- Rich, N., Dere, K., Howard, R., 2000, Synoptic maps from the LASCO and EIT experiments on SoHO. AGU 6/2000
- Sakao, T., 2000, One Solar Cycle of Yohkoh/HXT Flare Observations, IAU Symposium 203
- Turmon, M., Pap, J., Mukhtar, S., Bogart, R., 1999. Automatically finding solar active regions using SOHO/MDI photograms and magnetograms. AGU 12/1999
- The slides related to this paper can be found at : http://homepage.oma.be/hochedez/Solspa_Talk.htm

LONG-TERM VARIATIONS IN THE MAGNETIC FIELDS OF THE SUN AND POSSIBLE IMPLICATIONS FOR TERRESTRIAL CLIMATE

M. Lockwood^{1, 2}, and S. Foster²

¹ Rutherford Appleton Laboratory, Space Science Department, Chilton, Oxfordshire, England, U.K. ² Southampton University, Department of Physics and Astronomy, Southampton, Hampshire, U.K.

ABSTRACT

Recent studies of the variation of geomagnetic activity over the past 140 years have quantified the "coronal source" or "open" magnetic flux F_s that leaves the solar atmosphere and enters the heliosphere and have shown that it has risen, on average, by 34% since 1963 and by 140% since 1900. This variation is reflected in studies of the heliospheric field using isotopes deposited in ice sheets and meteorites by the action of galactic comic rays. The variation has also been reproduced using a model that demonstrates how the open flux accumulates and decays, depending on the rate of flux emergence in active regions and on the length of the solar cycle. The cosmic ray flux at energies > 3 GeV is found to have decayed by about 15% during the 20th century (and by about 4% at >13 GeV). We show that the changes in the open flux do reflect changes in the photospheric and sub-surface field which offers an explanation of why open flux appears to be a good proxy for solar irradiance extrapolation. Correlations between F_{sy} solar cycle length, L, and 11-year smoothed sunspot number, R_{11} , explain why the various irradiance reconstructions for the last 150 years are similar in form. Possible implications of the inferred changes in cosmic ray flux and irradiance for global temperatures on Earth are discussed.

Key words: Solar variability; climate change; heliospheric field; solar irradiance; cosmic rays

1. INTRODUCTION

1.1. Solar Irradiance Variations

There has been a growing interest in long-term variations of the Sun. What was once termed the "solar constant" has been shown to vary with the sunspot cycle and thus is now generally referred to as the "total solar irradiance", S. The amplitude of this variation is of order 0.1% [Willson, 1997; Fröhlich and Lean, 1998]. Irradiance variations are mainly caused by the combined effect of darkening by sunspots with the brightening of associated faculae and of the network. Of the two, the brightening is the dominant effect [Chapman et al., 1997], but both are associated with the magnetic field at the solar surface [Fligge et al., 1998]. Variations of the irradiance on this 11-year timescale have not been considered to be greatly significant for Earth's climate because their effects are smoothed by the heat capacity of the oceans [Wigley and Raper, 1990]. However, continuous and homogeneous sunspot observations have been made since 1749, and sunspot numbers show longer-term, secular variations (on timescales of order 100 years and greater) in addition to the 11-year solar activity cycle [Gleissberg, 1944; Pulkkinen et al., 2000]. Any associated changes in the total solar irradiance on these longer timescales would be significant for global climate change because they would not be smoothed. Thus an understanding of the ratio of the amplitudes of the variations on 11-year and longer timescales is of great importance. Using various proxy data, attempts have been made to extrapolate the recently observed total solar irradiance variation back in time [Hoyt and Schatten, 1993; Lean et al., 1995; Solanki and Fligge, 1998; 1999; Lockwood and Stamper, 1999; Lean, 2000] and these reconstructions have been used to evaluate its rôle in the rise of average surface temperatures on Earth [Lean et al., 1995; Lockwood et al., 1999b; Tett et al., 1999].

1.2. Cosmic Rays

The Earth is shielded from galactic cosmic rays by the heliosphere. A number of processes are active, although their relative importance is still a matter of debate. However, the heliospheric magnetic field is the key component of this shield [Moraal et al., 1993; Pot-gieter, 1995], such that the cosmic ray fluxes seen at Earth are very highly anticorrelated with the local heliospheric field (the interplanetary magnetic field, IMF) [Cane et al., 1999]. The field is dragged out of the sun by the continuous, but highly variable, solar wind and fluctuates with the level of magnetic activity on the sun. This results in the fluxes of those cosmic rays that do penetrate the shield and reach the Earth, showing a clear solar cycle variation, with a strong anticorrelation with sunspot numbers.

Cosmic rays are a key part of the global electric circuit that is driven primarily by thunderstorms [*Bering et al.*, 1998]. They generate air ions in the subionospheric gap which allows current to flow between the tops of thunderclouds and the ionosphere and also between the ionosphere and the ground in association with the fairweather electric field. It is not known what sort of modulation to this circuit could be brought about by the changes in cosmic ray fluxes, not what the implications of this might be.

Svensmark and Friis-Christensen [1997] and Svensmark [1998] have reported a solar cycle variation in the global fraction of terrestrial cloud cover seen from space. These authors proposed that this is because

Proc. 1st Solar & Space Weather Euroconference, 'The Solar Cycle and Terrestrial Climate', Santa Cruz de Tenerife, Tenerife, Spain, 25-29 September 2000 (ESA SP-463, December 2000) cloud cover is directly influenced by the galactic cosmic rays incident on Earth. The cloud data used by Svensmark and Friis-Christensen [1997] and Svensmark [1998] were compiled from a variety of sources. Concerns about this compilation of diverse and uncalibrated cloud data were pointed out by a number of authors (see review by Soon et al. [2000]) and the correlation was made weaker when data for after 1992 became available [Kristjánsson and Kristiansen, 2000]. There was also no clear dependence on cloud type, as would have been expected. Another criticism has been that the polar regions were excluded from the study because cloud cover there could not always be distinguished from the ice caps. However, subsequent work has shown that there is a strong correlation for one subset of the cloud cover, as seen at infrared wavelengths [N. Marsh and H. Svensmark, private communication, 1999; Marsh and Svensmark, 2000]. These observations are possible at all latitudes (for both day and night), and so true full-globe averages could be used. The data are the "D2" set compiled and inter-calibrated by the International Satellite Cloud Climate Project (ISCCP) [Rossow et al., 1996]. The strong correlation with cosmic ray fluxes is for clouds that are inferred to be at low altitudes and so is associated mainly with stratus and stratocumulus cloud types. The correlations are strongest for maritime regions at midlatitudes and are poor in areas dominated by other phenomena such as the El Niño-Southern Oscillation (ENSO). The correlations are compelling, especially with the higher energy of cosmic rays (but not so high in energy that the amplitude of the solar cycle variation becomes negligible). The correlation coefficient for 12-month smoothed data exceeds 0.85.

Several more cycles of data are required before we can be confident that the solar cycle variation of cloud cover is not just a chance occurrence. The mechanism or mechanisms that could result in a correlation between cosmic ray fluxes and the global cloud cover are highly controversial and are certainly not yet understood, although clear possibilities are emerging [*Svensmark*, 2000, this volume]. If present, such a mechanism would mean that long-term changes in the heliospheric field were of great importance.

1.3. Geomagnetic Activity

As well as modulating the solar irradiance and the heliospheric field (discussed above in sections 1.1 and 1.2), solar activity causes geomagnetic activity through energy extracted from the solar wind flow by Earth's magnetosphere. This has been monitored in a continuous and homogeneous manner since 1868 using antipodal observing stations in southern England and Australia. The level of activity was quantified by *Mayaud* [1972], who developed the *aa* index, using the range of the fluctuations of the horizontal component of the field observed in 3-hour intervals at these stations. The *aa* index was designed to be very well correlated with other planetary indices of geomagnetic activity; for example, the variations in annual means of *aa* and the planetary Ap index are almost identical since the start of the Ap data series in 1932 [Mayaud, 1972; Ahluwalia, 1997]. This is true for both the solar cycle and the longer-term variations. The long-term changes in *aa* are also highly correlated with related phenomena, such as the occurrence of low-latitude aurorae [Pulkkinen et al., 2000]. The *aa* data sequence shows a systematic long-term rise in geomagnetic activity since 1900, a variation which shows some intriguing similarities to the observed rise in global mean surface temperatures [Cliver et al., 1998b]. Clilverd et al. [1998] have analyzed in detail a variety of potential causes for this rise in aa and eliminated most of them. For example, the long-term drift of the geomagnetic field has caused a systematic shift in the magnetic latitudes of the stations: The Northern Hemisphere station used to generate aa has drifted about 4° equatorward in magnetic coordinates since 1868, whereas that in the Southern Hemisphere has drifted about 2° poleward. However, the data show that the activity at both stations has risen in an almost identical manner and thus the rise is not caused by this effect. Stamper et al. [1999] studied interplanetary data from solar cycles 20, 21, and 22 (1963-1996) in a search for the cause of the rise in aa. They used the theory of solar wind power extraction by Earth's magnetosphere [Vasyluinas et al., 1982] to show that the largest of several contributions to the long-term change in aa was a rise in the magnitude of the interplanetary magnetic field around the Earth. Lockwood et al. [1999a] also used this theory to, effectively, separate the effects of nonrecurrent geomagnetic activity (for example, induced by coronal mass ejections) and recurrent geomagnetic activity (due to fast solar wind streams) and thereby developed a procedure to compute the magnitude of the interplanetary field at Earth B_E from the *aa* data.

1.4. Solar Cycle Length

There is another important indicator of long-term solar change derived from a continuous measurement sequence. This is the solar cycle length L, derived from the sunspot numbers R. Gleissberg [1944] noted that there was a long-term (of order 80-100 years) quasiperiodic behavior in R and that this was related to L. He employed a long-timescale secular filter to smooth the values of L, which were determined from the times of adjacent minima and maxima of R. In recent years a variety of other methods to determine L have been developed. For example: Hoyt and Schatten [1993] determined from each annual mean of R the fraction of the cycle that had been completed and then measured the delay to the same point in the next cycle; Fligge et al. [1999] have employed Morlet wavelets; Mursula and Ulich [1998] have used median activity times; Friis-Christensen and Lassen [1991] used a method and filter that were similar to Gleissberg's; and Lockwood [2000] has used an autocorrelation technique.

These various techniques produce variations in L that are similar but with distinct differences. The variation found by *Friis-Christensen and Lassen* [1991] anticor-

relates both with global average temperatures on Earth and the *aa* geomagnetic index. This is because it falls more gradually over the last 100 years than, for example, the variations deduced by *Lockwood* [2000] and *Fligge and Solanki* [1998] that show more step-like falls, followed by periods of more constant L.

The irradiance constructions of *Hoyt and Schatten* [1993] and *Solanki and Fligge* [1998; 1999] depend on L. These reconstructions are quite similar to those from other methods, and some possible reasons why L is a valuable proxy are discussed in section 4.

1.5. Coronal Source Flux

The coronal source surface is where the magnetic field becomes approximately radial. It is a roughly spherical surface at a heliocentric distance r of about $2.5R_s$ (where R_s is a solar radius; that is, the photosphere is at $r = 1R_s$). This surface can be considered as the boundary that separates the solar corona from the heliosphere. The magnetic flux threading the coronal source surface is called the open solar flux or the coronal source flux, F_s .

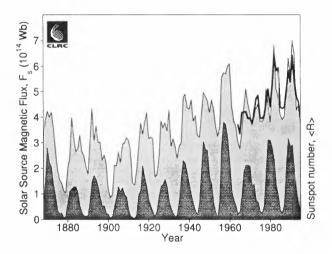


Figure 1: Variation of annual means of the coronal source flux F_s as derived from the aa index by the method of Lockwood et al. [1999a] (thin line bounding grey shaded area) and from interplanetary measurements of the radial component of the interplanetary magnetic field near Earth (thick line). The dark area gives the variation of the smoothed sunspot number.

On annual timescales, the interplanetary magnetic field (IMF, the heliospheric field in the ecliptic plane), obeys the Parker spiral orientation with a garden hose angle γ that is approximately constant at a given r [Gazis, 1996; Stamper et al., 1999]. Thus the IMF's radial component near Earth $B_{rE} = B_E \cos{(\gamma)}$ can also be estimated from the *aa* geomagnetic activity data using the method of Lockwood et al. [1999a]. This has significance for the heliosphere away from the ecliptic plane because the Ulysses spacecraft has shown that sheet, rather than volume, currents dominate, to the extent that latitudinal

gradients of the average radial heliospheric field are small [Balogh et al., 1995; Lockwood et al., 1999b]. This means that the radial field B_r , at a heliocentric distance r and at any latitude, is approximately equal to $(r/R_1)^2 B_{rE}$, where $R_1 = 1$ AU. Because, on average, the Parker spiral theory of the heliospheric field applies and because this does not predict significant flux crossing the current sheet at $r < R_1$, the total magnetic flux leaving the Sun and entering the heliosphere (the coronal source flux) is $F_s = (1/2)(4\pi R_1^2) < |B_{rE}|$. The method of Lockwood et al. [1999a] for deriving annual means of F. from the aa index assumes that both Parker spiral theory and the uniformity of B_r were valid at all times since 1868. The method was developed using data from solar cycles 21 and 22 and then tested against independent interplanetary measurements from cycle 20 [Lockwood and Stamper, 1999]. Their results are shown in figure 1. The lightly shaded area is the coronal source flux estimated from the aa index; the thick line is the corresponding value derived from the mean radial field $\langle B_{rE} \rangle$ measured by spacecraft near $r = R_1$. The area shaded black gives the variation of smoothed sunspot number for comparison. Figure 1 shows that the average F_s has risen by 34% since 1964 and by 140% since 1900

2. LONG TERM CHANGES IN THE PHOTOSPHERE

The changes in the total open flux of the sun relate specifically at the source surface $(r \approx 2.5R_s)$ and could result from changes that are restricted to the corona $(1R_s < 1R_s)$ $r \leq 2.5R_s$), with little implication for the total flux emerged through the photosphere (which contains both open and closed solar flux and is of order is of order $10F_s$ [Wang et al., 2000b]), nor possibly even for the distribution of that flux over the solar surface. As discussed above, changes in the total solar irradiance, on timescales of 20 years or less, are well explained by magnetic phenomena in and below the solar photosphere $(r \approx 1R_s)$ and so the implications for irradiance of the drift in open flux are not immediately clear. However, Lockwood and Stamper [1999] obtained a correlation of the coronal source flux F_s with solar irradiance measurements of 0.84. In fact, they correlated the data from the various monitors separately and used the regression fits to intercalibrate the instruments. If the intercalibration of the instruments by Fröhlich and Lean [1998] is adopted, this correlation falls to 0.79. From this correlation, Lockwood and Stamper derived a longterm irradiance variation that is strikingly similar to that of Lean et al. [1995]. This agreement is even closer for the revised reconstruction presented recently by Lean [2000]. Lean used a method which employs sunspot numbers added to a long-term drift with a waveform given by 11-year running means of sunspot numbers, and with an amplitude based on a comparison of the Maunder minimum and noncyclic Sun-like stars. The extrapolation by Lockwood and Stamper is also quite similar to the reconstruction by Solanki and Fligge [1998], who add contributions by the active regions (based on sunspot numbers, R) to a quiet sun (network) variation (based on cycle length, L).

The possibility that F_s could be used as a valid single proxy for irradiance variation reconstruction (as opposed to a composite of added terms) is also suggested by the fact that the changes in F_s , as shown in Figure 1, do have some marked similarities to some changes seen in the solar photosphere; thus they appear to reflect changes in the magnetic field there and in the subsurface layers. Figure 1 shows that the peak sunspot number Rat the maximum of the solar cycles has risen in association with F_s . Figures 2a and 2b show that this is also true for have the solar-cycle averages of sunspot number R_{11} [Lockwood et al., 1999b]. Figure 2c shows that there is also some similarity to the variation of solar cycle length, L, as deduced by the autocorrelation technique of Lockwood [2000]. (To aid comparison, Figure 2c shows {12.5 - L}, note that 12.5 years is merely a convenient reference value and has no significance). In addition, careful inspection reveals that there has been a small upward drift of the minima in R (figure 1).

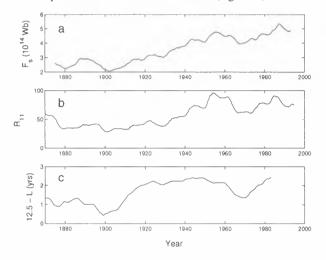


Figure 2: (a) The 11-year running means of the coronal source flux F_s , derived from the aa index of geomagnetic activity (see Figure 1); (b) 11-year running means of the sunspot number, R_{11} ; (c) (12.5 – L), where L is the length of the solar cycle in years and is derived from autocorrelation functions of sunspot number R, using the method of Lockwood [2000].

Foster and Lockwood [2000] have shown that there is also a strong correlation between annual means of F_s and the standard deviations of sunspot latitudes. They employed the observations of sunspot groups that were made at Greenwich between 1874 and 1981 and extended this sequence using the observations made in a compatible way at Mt. Wilson after 1967. Figure 3 shows that the spread of sunspot latitudes increases with a very similar waveform to F_s , although the long-term (~100-year) drift is a smaller fraction of the solar cycle variation than it is for F_s . In other words, the photosphere shows more spots, spread over a greater area of its surface, when F_s is higher. Thus the variations in F_s do appear to be a symptom of changes in the surface field. These findings indicate that there have been considerable changes in the processes that generate and distribute photospheric and coronal magnetic fields.

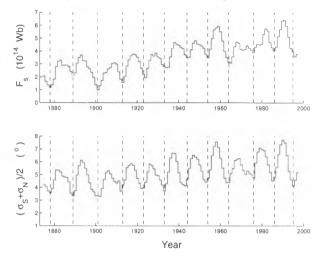


Figure 3: (a) The variation of annual means of the coronal source flux, F_s , as shown in Figure 1, compared with (b) the average of the standard deviations of sunspot group latitudes, $(\sigma_N + \sigma_S)/2$, as deduced by Foster and Lockwood [2000] from Greenwich and Mount Wilson sunspot group observations. σ_N and σ_S are the standard deviations for the Northern and Southern solar hemispheres, respectively, and are effectively the width of the wings in the butterfly diagram.

The magnetic field at the photosphere includes both open flux (that threads the coronal source surface) and the larger closed flux (that does not) and is generated by dynamo processes in the solar interior, in particular at the base of the convection zone (at around $r = 0.7R_s$). This field emerges in active regions (as bipolar magnetic regions, or BMRs) [Harvey and Zwaan, 1993] at a total rate which increases with the number of sunspots. Most of the flux associated with BMRs is annihilated by diffusion toward the neutral line between regions of opposite field polarity, but some is added to the fields associated with the supergranulation network. This field is transported over the solar surface by the differential rotation in the outer Sun, by convection associated with supergranules, and by meridional poleward flow in the surface layers. As the centers of the two polarity regions of a BMR separate in the differential rotation, the magnetic field loops rise through the coronal source surface, and the coronal source flux increases. Open flux (that threads the coronal source surface) accumulates near the poles, where it forms the large coronal holes seen at the subsequent sunspot minimum [Wang et al., 2000a].

Recent theoretical modelling by *Solanki et al.* [2000] predicts a rôle for both cycle length and emergence rate in the long-term variation of coronal source flux shown in Figure 1. These authors used the sunspot number to quantify *E*, the rate of flux emergence through the photosphere in BMRs. The basic equation is the continuity of open network flux:

$$\mathrm{d}F_s/\mathrm{d}t = \gamma E - F_s/\tau_N \tag{1}$$

where E is the rate of flux emergence through the photospheric active regions, τ_N is the time constant for destruction of open network flux and $\gamma = (1 + \tau_t / \tau_a)^{-1}$ and thus depends on the time constants for flux annihilation in active regions τ_a and for transfer of flux from active regions to the network τ_i . Solanki et al. [2000] estimate γ to be 0.015 and derive a best fit with a time constant τ_N of 4 years. Because this τ_N is sufficiently large, the cycle length L will influence the amount of residual open network flux because shorter cycles will mean that this decay does not progress as far as during longer cycles. This prediction is confirmed by Figure 4, which contrasts the variation of $\{12.5 - L\}$ (bottom graph) with the rate of increase in the coronal source flux, dF_s/dt from the variation of F_s shown in figure 1 (top graph). Because 20-year intervals were used to evaluate

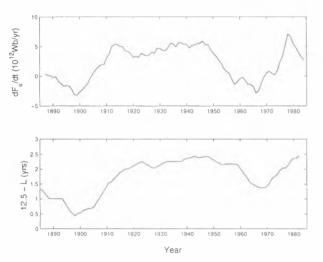


Figure 4: (top) Rate of increase in the coronal source flux (dF_s/dt). Running means over 20-year intervals are presented. (bottom) The variable [12.5 - L], where L is the length of the solar cycle, in years, derived from the autocorrelation function of sunspot number R using 20year intervals (as in Figure 2c).

L, running means of dF_s/dt over 20-year intervals are presented. A clear similarity is evident. In particular, when *L* is a maximum (minima in {12.5 - *L*}), dF_s/dt is negative. Some lag is present in Figure 4, but considering that these are smoothed data sets, this is probably not significant. This relationship between the cycle length *L* and dF_s/dt was inherent in the modelling of the F_s data sequence by *Solanki et al.* [2000]. Thus Figure 4 confirms their conclusion that cycle length *L* and the rate of flux emergence (related to sunspot number *R*) in

active regions are both key elements in the long-term accumulation of open solar flux (when average sunspot numbers R_{11} are high and/or when cycle lengths L are low) and its decay (when R_{11} is low and/or when cycle lengths L are large).

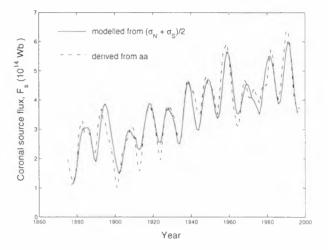


Figure 5: The variations of the coronal source flux F_{ss} derived from geomagnetic activity by Lockwood et al. [1999a] and as shown in Figure 1 (dot-dash line); and as predicted using the model of Solanki et al. [2000], as adapted by Foster and Lockwood [2000] (solid line).

Figure 5 shows the observed variation of F_s and a bestfit model prediction using the Solanki et al. model and equation (1). In this plot, the emergence rate *E* has been quantified in a slightly different way, using the spread of sunspot latitudes (figure 3) and the best-fit τ_N is 3.8 years. [*Foster and Lockwood*, 2000], but the result is almost exactly the same as presented by *Solanki et al.* [2000]. It can be seen that the agreement is excellent. Thus we have a new understanding of how variations in the flux emergence rate and solar cycle length have produced the observed long-term drift in the coronal source flux.

3. LONG-TERM VARIATIONS IN COSMIC RAYS

Because of their large gyroradii and complex paths, cosmic rays sample much greater regions of the heliosphere than do near-Earth satellites. Thus we would expect a strong anticorrelation of the coronal source flux F_s with cosmic ray fluxes. The products of galactic cosmic ray bombardment of the atmosphere have been detected using neutron monitors continuously since 1953. Cosmic rays are also shielded by the geomagnetic field, such that the range of energies studied depends on the latitude of the observing station. For example, for the mid-latitude station at Climax, USA, primary cosmic ray particles of energy exceeding 3 GeV can be detected, whereas for the lower-latitude stations at Huancayo, Peru and Haleakala, Hawaii the greater shielding by the geomagnetic field means that only primaries of energy exceeding 13 GeV can be detected. The two stations at Huancayo and Hawaii provide a homogene90

ous data sequence, the data series being continued at Hawaii, after monitoring ceased at Huancayo in 1993.

Lockwood [2000] has shown that there is a strong anticorrelation between the fluxes of cosmic rays and the coronal source F_s deduced from the *aa* geomagnetic index by Lockwood et al. [1999a]. The correlation coefficients for count rates at Climax (C) and Huancayo/Hawaii (H) are $c_c = -0.874$ and $c_H = -0.897$. The best-fit, least squares linear regressions are $C/10^3 = 5.22$ $-0.278F_s$ and $H/10^3 = 1.866 - 0.345F_s$. The correlations show that $c_c^2 = 76.4\%$ and $c_H^2 = 77.3\%$ of the variations in the cosmic ray fluxes seen at Climax and Huancayo/Hawaii, are explained by the strength of the heliospheric field alone. Other factors, such as drifts that depend on the polarity of the heliospheric field [Ahluwalia and Wilson, 1996; Usoskin et al., 1998] and the solar wind flow [Sabbah, 2000], collectively contribute a maximum of $(1 - c_{C}^{2}) = 23.6\%$ and $(1 - c_{H}^{2}) =$ 22.7% to the variations.

Using the high correlations and the corresponding leastsquares regression fits between C and F_s and between H and F_s , along with the data sequence of F_s shown in Figure 1, the cosmic ray fluxes can be extrapolated back to 1868. The results are shown in Figure 6, the solid line being for the Climax data (>3 GeV), and the dashed line being for the Huancayo/Hawaii data (>13 GeV). In both cases, the count rates have been normalised to the average value seen during solar cycle 21. The plot indicates that the average fluxes of cosmic rays above 3 GeV were approximately 15% higher in 1900 than they are now, whereas the fluxes at energies above 13 GeV were higher by about 4%.

Also shown in Figure 6 is the variation of cosmic ray fluxes since 1937 deduced from a collection of ionisation chambers at high latitudes, and near sea level [Ahluwalia, 1997] (solid line joining dots). The sites employed are Cheltenham (1937-1956), Fredericksberg (1956-1972) and Yakutsk (1954-1994). The geomagnetic energy cutoffs at these stations are 2.2 GeV, 2.2 GeV and 1.7 GeV, respectively, but fluxes are limited by the higher atmospheric cutoff of about 4 GeV in each case. The muons detected relate to somewhat higher energy primary cosmic rays than for the neutron monitors discussed above, and the median energy observed by these ionisation chambers is 67 GeV. To provide a single sequence, considerable intercalibration factors have been applied to the data from these ionisation chambers [Ahluwalia, 1997], and thus long-term drifts may not be accurately represented. Of particular concern is that so little overlap in data (1954-1956) exists for full annual means from Cheltenham and Yakutsk. Nevertheless, there are strong similarities for the variation for >13 GeV predicted from the F_s values (the correlation coefficient is 0.811). In terms of the percentage change, both the solar cycle variations and the longerterm drifts seen by the ionisation chambers are smaller (indicating that they are responding to higher-energy primary cosmic rays that are less influenced by the he-

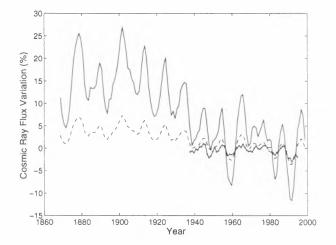


Figure 6: Inferred variation of cosmic ray fluxes since 1868. The solid line is an extrapolation using F_s , based on the correlation with counts C by the cosmic ray neutron detector at Climax (geomagnetic energy cutoff of 3 GeV). The dashed line is based on the correlation with the counts H by the cosmic ray neutron detectors at Huancayo/Hawaii (geomagnetic energy cutoff 13 GeV). The line joining dots is the variation deduced from three ionization chambers by Ahluwalia [1997], which respond to a median energy of 67 GeV. In all cases, the variation is relative to the average value seen during solar cycle 21. After Lockwood [2000].

liospheric shield). Analysis of global carbon-14 production [*Struiver and Quay*, 1980] implies that the combined ionisation chamber data may underestimate a slight downward drift in the cosmic ray fluxes in the period 1937-1970 [*O'Brien*, 1979].

The high anticorrelations between cosmic ray fluxes and the coronal source flux imply that there should be a strong anti-correlation between F_s and the abundance of the ¹⁰Be isotope in ice cores, produced by cosmic ray bombardment. The ¹⁰Be isotope is formed as a spallation product in the upper atmosphere when galactic cosmic rays impact oxygen and nitrogen nuclei. This isotope is deposited in ice sheets by precipitation over a subsequent extended period. Thus a lag is expected. Lockwood [2000] found a strong anticorrelation of F_s with the ¹⁰Be isotope abundance (derived from the Dye-3 Greenland ice core [Beer et al., 1998]) for annual means from 1868-1985. The peak correlation coefficient is at a lag of 1 year and is -0.64. The best-fit, least squares linear regression is $[^{10}Be$ in atoms $g^{-1}] = 10^4$ $(1.323 - 0.133F_s)$. Figure 7 compares the extrapolated variation of cosmic ray flux (at >13 GeV) since 1868 (solid line, as shown in Figure 6), with the ¹⁰Be isotope record, scaled using the regressions given above. In both cases, the variation is relative to the average value seen during solar cycle 21. The long-term trend is reproduced in both data sets although the solar cycle variations are not identical. This is consistent with the results of *Fligge et al.* [1999], who found that cycle lengths derived from the 10 Be isotope data were not fully reliable, presumably because the extended response

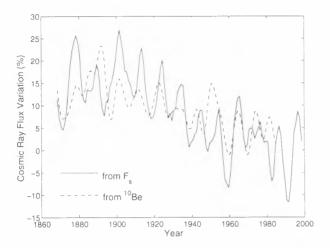


Figure 7: Variation of cosmic ray flux since 1868. The solid line is an extrapolation using F_{s} , based on the correlation with fluxes at >3 GeV shown in Figure 6. The dashed line is based on the ¹⁰Be isotope record, scaled using the correlations with F_{s} . In both cases, the variation is relative to the average value seen during solar cycle 21.

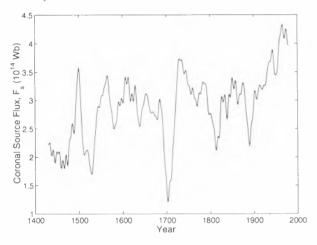


Figure 8. Extrapolated coronal source flux F_s from the ¹⁰Be isotope data, using the regression analysis of data since 1868.

function is variable (due to a spread of isotope deposition timescales caused by climate variability) and the difficulties in dating the ice.

We can use the full data sequence of the ¹⁰Be isotope data, along with the regression with F_s for data since 1868, to estimate the coronal source flux back to near 1400. This extrapolation is shown in Figure 8: These data are 11-year running means in which the solar cycles have been smoothed out. Comparison with Figure 2 shows that the drift in average F_s since 1868 is very well reproduced. The plot shows that variations in F_s seen since 1900 are similar in amplitude to those seen at prior times. Particularly rapid changes are seen late in the "Maunder minimum" of sunspot activity (roughly 1645-1715) [e.g., *Cliver et al.*, 1998b], with F_s falling to its lowest value of 1.2×10^{14} Wb near 1700, toward the end of this period. This corresponds to a value of about one quarter of present-day values. That F_s should reach a minimum at the end, rather than in the middle, of the Maunder minimum is consistent with the model of *Solanki et al.* [2000]. This is because the F_s would decay throughout the minimum because the flux emergence

Other studies similarly confirm the drift of F_s discussed here. For example, *Bonino et al.* [1995] use the Titanium isotope ⁴⁴Ti, produced in meteorites by galactic cosmic rays and having a half life of about 96 years, to deduce a rise in the heliospheric field throughout the 20th century: the rise found is four times larger than would be deduced from sunspot numbers using the anticorrelation with cosmic ray fluxes seen since 1953.

rate in active regions was exceptionally low.

4. CONCLUSIONS AND IMPLICATIONS

Recent work has revealed that there have been important long-term (here meaning ~100 year) changes in the magnetic field in the solar atmosphere. Some of this field permeates the coronal source surface and enters the heliosphere. Because of the work by Solanki et al. [2000], an understanding of these changes is becoming available to us, in terms of the emergence of flux in active regions, its transfer to the network, and the balance between loss of open network flux and its accumulation in coronal holes. In particular, this gives us an understanding of why the length of the solar cycle has important implications. Shorter solar cycles facilitate a rise in the coronal source flux; longer cycles allow it to decay. However, the accumulation of the coronal source flux is also strongly dependent on the rate of flux emergence in active regions. In general, the peak and cycle-averaged sunspot numbers are larger when cycles are shorter. Thus shorter cycles can also be associated with larger flux emergence rates and there is less time available for the open flux to decay. Together, these effects mean that the net effect is that shorter cycles correlate with increasing coronal source flux.

The change in the coronal source flux was revealed by studies of the long-term drift in geomagnetic activity [*Lockwood et al.*, 1999a; b]. Because this work was based on the quantitative theory of solar wind-magnetosphere coupling, the change in the open solar flux has been quantified and found to be considerable (a factor of 2.4 change since 1900). The variation is confirmed by studies of isotopes produced by cosmic ray bombardment in ice cores and meteorites. Cross-correlation allows us to calibrate these changes and so extrapolate the solar changes further back in time. For example, the ¹⁰Be isotope in ice cores shows us that by the end of the Maunder minimum the coronal source flux had fallen to about a quarter of present-day values.

In addition to influencing the transfer of energy from the solar wind to the magnetosphere, the rise in F_s will have caused the cosmic ray flux incident on the Earth to have fallen. In this paper, we have estimated that the cosmic ray fluxes above 3 GeV were 15% higher, on average,

around 1900 than they are now. The corresponding figure for >13 GeV particles is about 4%. The potential implications of this are not yet understood.

4.1. Potential Effects of Cosmic Ray Variations

Cosmic rays generate air ions in the subionospheric gap which allows current to flow in the global electric circuit. This connects thunderclouds with the ground via lightening, by closing the loop via the ionosphere [*Bering et al.*, 1998]. It is not yet known what sort of modulation to this circuit is caused by the changes in cosmic ray fluxes, nor what influence this might have.

The apparent correlation between cosmic rays and global cloud cover will remain just that until we have sufficient data to confirm or disprove its significance. That having been said, the strong correlation for the global low-altitude cloud cover, [Marsh and Svensmark, 2000] is very self-consistent and interesting and would be very important indeed were it to reflect a genuine and active mechanism. Potential mechanisms that might explain how cosmic ray products grow in size to allow water droplets to condense are now beginning to emerge. Given that we now know that cosmic ray fluxes have declined systematically over the past 100 years with the increasing heliospheric field, it is now very important to investigate these mechanisms, both experimentally and theoretically.

4.2. Solar Irradiance Reconstructions

Lockwood and Stamper [1999] found a correlation of the coronal source flux F_s with solar irradiance measurements and used this to generate a reconstruction of past variation of irradiance. Figure 9 contrast this to other reconstructions of the irradiance. A fair degree of agreement can be seen between the various variations inferred, despite the fact that they are based on different assumptions and proxies. Figure 2 offers a simple practical reason as to why these solar irradiance reconstructions are similar. The coronal source flux F_s , which was used as a proxy for total irradiance by Lockwood and Stamper [1999], is highly correlated with the 11-year running means of sunspot number, which Lean et al. [1995] and Lean [2000] use to give the waveform longterm drift. The coronal source flux is also related to the cycle length (Figures 2 and 4), which was used as a proxy for total irradiance by Hoyt and Schatten [1993] and to give the quiet sun variation by Solanki and Fligge [1998]. Thus these methods are not as independent as they initially seem, in terms of the waveform of the irradiance variation that they predict on 100-year timescales. However, the amplitude of the long-term drifts derived are also similar, and this is not derived the same way for the three cases. By linking emergence rate through the photosphere in active regions (covered by sunspots and faculae), solar cycle length and the coronal source flux, the work of Solanki et al. [2000] may offer the origins of a theoretical explanation of the agreement between the reconstructions of Lean et al. and Solanki and Fligge with the extrapolation by Lock-wood and Stamper.

4.3. The Effects of inferred Solar Irradiance Variations

The concept that significant climate change is caused by

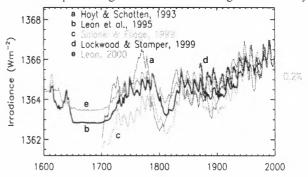


Figure 9: A comparison of the various solar irradiance reconstructions (courtesy Judith Lean).

changes in the solar irradiance is certainly not new [e.g. Blanford, 1891]. The observed solar cycle variation in irradiance is small, S varying between 1367.0 Wm⁻² and 1368.3 Wm⁻², a variation of just under 0.1%. The most conservative of the estimates of the drift in the 11-year running mean of the irradiance, S_{11} , are by Lockwood and Stamper [1999] and Lean [2000] for which $\Delta S_{11} =$ 1.65 ± 0.23 Wm⁻² over the last century, a rise of 0.12 ± 0.02%. Allowing for Earth's albedo, a, and spherical geometry this gives a change in the radiative forcing at the top of the atmosphere of $\Delta Q = \Delta S_{11}(1-a)/4 \approx$ 0.29 ± 0.04 Wm⁻², where a is here taken to be 0.3 [see discussion of the concept of Q by Hansen et al., 1997]. The effect of any change in S on global mean surface temperatures will be complex because it will be made up of contributions that are much stronger at some wavelengths than at others and because a variety of other effects (for example, changes in anthropogenic greenhouse gases, tropospheric sulphate aerosols and volcanic dust in the stratosphere, ozone absorption of UV etc.) will also be active and will interact with each other in complex feedback loops [Rind and Overpeck, 1993; Hansen et al., 1997]. This estimate of ΔQ due to solar change is similar to the estimate in the last IPCC (Intergovernmental Panel on Climate Change). By way of comparison, the IPCC's ΔQ estimates for the same interval due to CO₂, other greenhouse gasses, and aerosols are roughly 1.5 Wm⁻², 1.1 Wm⁻², and -1.3 Wm⁻², respectively [e.g. Wigley et al., 1997].

In order to make a simple evaluation of the effect of the solar irradiance change, we can adopt an estimate of the "climate sensitivity", dT/dQ, where T is the global mean of the surface temperature. Using an estimate of the climate sensitivity of $dT/dQ = 0.85 \pm 0.15^{\circ}C/Wm^{-2}$ [*Rind and Overpeck*, 1993], we predict a temperature rise of $\Delta T = -0.16+(0.147\pm0.026)\times([S \text{ in }Wm^{-2}]-1365)$. This represents a consensus view of the Earth's climate sensitivity, being the average of values from several large numerical models of the coupled atmosphere-

ocean circulation system, with an uncertainty set by the range of the estimates. From this we infer that the sun's brightness change, on its own, could have caused a temperature rise of 0.24 ± 0.04 °C since 1900.

Lockwood et al. [1999b] illustrate how the inferred variations from irradiance changes, ΔT , are highly correlated with the observed global average of the surface temperature, ΔT_o [e.g. Parker et al., 1994] the correlation coefficient being 0.93 and at a lag of $\delta t = 2$ years, which is consistent with the heat storage effect of the oceans [Wigley and Raper, 1990]. However, great care must be taken not to over-interpret this correlation. It would imply a climate sensitivity of dT/dQ =2.2°C/Wm⁻², in order to explain the observed temperature rise ΔT_o in terms of solar irradiance variations alone. This is a higher value than any of the published estimates from modelling studies (one of the largest is dT/dQ = 1.7°C/Wm⁻², by Nesme-Ribes et al. [1993]) and roughly twice the consensus value. Multi-variable analysis that accounts for several mechanisms, including anthropogenic effects, natural climate variability and volcanoes does reveal correlations are improved if some solar drift is included [Wigley et al., 1997; Tett et al., 19971.

Lockwood et al. [1999b] and Lean et al. [1995] compared the inferred temperature rise ΔT (for the consensus prediction of the climate sensitivity) with that observed ΔT_o we find no significant difference for the period 1870-1910. On the other hand, the change in solar luminosity alone can account for only about 50% of the rise in ΔT_o over the period 1910-1960 but leas than 31% of the rapid rise in ΔT_o over 1970-present. In the same interval, industrially-produced CO₂ in the atmosphere increased from about 280 to 355 ppmv. The implications are that that the onset of an man-made contribution to global warming was disguised by the rise in the solar irradiance and that the anthropogenic effect may have a later, but steeper, onset than previously thought. Such an effect is consistent with the predictions for combined greenhouse and aerosol pollutants [Wigley et al., 1997; Hansen et al., 1997]. Recently, Tett et al. [1999] have used a set of simulations made by a coupled atmosphere-ocean global circulation model to deduce a shift from solar forcing to anthropogenic effects as this century has progressed.

Acknowledgments: The author is grateful for discussions with a number of scientists, in particular: S. Solanki, N. Marsh, H. Svensmark, Y.-M. Wang, G. Cini Castognoli and J. Lean. He is also grateful to J. Beer, who supplied the ¹⁰Be isotope ice core data, and to the World Data Center system. This work was supported by the U.K. Particle Physics and Astronomy Research Council.

REFERENCES

Ahluwalia, H.S., Galactic cosmic ray intensity variations at a high-latitude sea-level site 1937-1994, *J. Geophys. Res.*, 102, 24,229-24,236, 1997

- Ahluwalia, H.S., and M.D. Wilson, Present status of the recovery phase of cosmic ray 11-year modulation, J. Geophys. Res., 101, 4879-4883, 1996.
- Balogh, A., E.J. Smith, B.T. Tsurutani, D.J. Southwood, R.J. Forsyth, and T.S. Horbury, The heliospheric field over the south polar region of the Sun, *Science*, 268, 1007-1010, 1995.
- Beer, J., S. Tobias, and N. Weiss, An active Sun throughout the Maunder minimum, Sol. Phys., 181, 237-249, 1998.
- Bering, E.A., A.A. Few, and J.R. Benbrook, The global electric circuit, *Phys. Today*, *51*, 24-30, 1998.
- Blanford, H.F., The paradox of the sunspot cycle in meteorology, *Nature*, 43, 583-587 (1891)
- Bonino, G., G. Cini Castognoli, N. Bhabdari and C, Taricco, Behavior of the heliosphere over prolonged solar quiet periods by ⁴⁴Ti measurements in meteorites, *Science*, 270, 1648-1650.
- Cane, H.V., G. Wibberenz, I.G. Richardson, and T.T. von Rosenvinge, Cosmic ray modulation and the solar magnetic field, *Geophys.Res.Lett.*, 26, 565-568, 1999.
- Chapman, G.A., A.M. Cookson, and J.J. Dobias, Solar variability and the relation of facular to sunspot areas during cycle 22, Astrophys. J., 842, 541-545, 1997.
- Clilverd, M.A., T.D.G. Clark, E. Clarke, and H. Rishbeth, Increased magnetic storm activity from 1868 to 1995, J. Atmos. Sol.-Terr. Phys., 60, 1047-1056, 1998.
- Cliver, E.W., V. Boriakoff, and K. Bounar, Geomagnetic activity and the solar wind during the Maunder minimum, *Geophys. Res. Lett.*, 25, 897-900, 1998a.
- Cliver, E.W., V. Boriakoff, and J. Feynman, Solar variability and climate change: Geomagnetic activity and global surface temperature, *Geophys. Res. Lett.*, 25, 1035-1038, 1998b.
- Fligge, M., S.K. Solanki, Y.C. Unruh, C. Fröhlich and C. Wehrli, A model of solar total and spectral irradiance variations, *Astron. Astrophys.*, 335, 709-718, 1998.
- Fligge, M., S.K. Solanki, and J. Beer, Determination of solar cycle length using the continuous wavelet transform, Astron. Astrophys, 346, 313, 1999.
- Foster, S. and M. Lockwood, Long-Term Changes in the Solar Photosphere Associated with Changes in the Coronal Source Flux, *Geophys. Res. Lett.*, submitted, 2000
- Friis-Christensen, E., and K. Lassen, The length of the solar cycle, an indicator of solar activity closely associated with climate, *Science*, 192, 1189-1202, 1991.
- Fröhlich, C., and J. Lean, The Sun's total irradiance: Cycles, trends and related climate change uncertainties since 1976, *Geophys. Res. Lett.*, 25, 4377-4380, 1998.
- Gazis, P.R., Solar cycle variation of the heliosphere, *Rev. Geophys.*, 34, 379-402, 1996.
- Gleissberg, W., A table of secular variations of the solar cycle, J. Geophys. Res., 49, 243-244, 1944.
- Hansen, J., M. Sato, and R. Ruedy, Radiative forcing and climate response, J. Geophys. Res., 102, 6831-6864, 1997.
- Harvey, K.L., and C. Zwaan, Properties and emergence of bipolar active regions, *Sol.* Phys., 148, 85-118, 1993.

- Hoyt, D., and K. Schatten, A discussion of plausible solar irradiance variations 1700-1992, 18895-18906, 1993.
- Kristjánsson, J.E., and J. Kristiansen, Is there a cosmic ray signal in recent variations in global cloudiness and cloud radiative forcing?, J. Geophys. Res., 105, 11,851-11,863, 2000.
- Lean, J., Evolution of the Sun's spectral irradiance since the Maunder minimum, *Geophys. Res. Lett., in press*, 2000.
- Lean, J., J. Beer, and R. Bradley, Reconstruction of solar irradiance since 1610: Implications for climate change, *Geophys. Res. Lett.*, 22, 3195-3198, 1995.
- Lockwood, M., Long-Term Variations in the Magnetic Fields of the Sun and the Heliosphere: their origin, effects and implications, J. Geophys. Res., in press, 2000
- Lockwood, M., and R. Stamper, Long-term drift of the coronal source magnetic flux and the total solar irradiance, *Geophys Res. Lett.*, 26, 2461-2464, 1999.
- Lockwood, M., R. Stamper, and M.N. Wild, A doubling of the sun's coronal magnetic field during the last 100 years, *Nature*, 399, 437-439, 1999a.
- Lockwood, M., R. Stamper, M.N. Wild, A. Balogh, and G. Jones, Our changing Sun, Astron. Geophys, 40, 4.10-4.16, 1999b.
- Marsh, N., and H. Svensmark, Cosmic rays, clouds and climate, *Space Sci. Rev.*, in press, 2000.
- Mayaud, P.N., The *aa* indices: A 100-year series characterising the magnetic activity, *J. Geophys. Res.*, 77, 6870-6874, 1972.
- Moraal, H., Cosmic ray modulation studies in the outer heliosphere, Nucl. Phys. B, 33A, B,, proc. suppl., 161-178, 1993.
- Mursula, K., and T. Ulich, A new method to determine the solar cycle length, *Geophys. Res. Lett.*, 25, 1837-1840, 1998.
- Nesme-Ribes, E., E.N. Ferrierer, R. Sadournay, H. LeTreut, and Z.X. Li, Solar dynamics and its impact on solar irradiance and the terrestrial climate, J. Geophys. Res., 98, 18923-18935, 1993.
- O'Brien, K., Secular variations in the production of cosmogenic isotopes in the Earth's atmosphere, J. Geophys. Res., 84, 423-431, 1979.
- Parker, D.E., P.D. Jones, A. Bevan, and C.K Folland, Interdecadal changes of surface temperatures since the late 19th century, J. Geophys. Res., 99, 14,373-14,399, 1994.
- Potgieter, M.S., The long-term modulation of galactic cosmic raysnin the heliosphere, Adv. in Space Res, 16(9), 191-203, 1995
- Pulkkinen, T.I., H. Nevanlinna, P.J. Pulkkinen, and M. Lockwood, The Earth-Sun connection in time scales from years to decades to centuries, *Space Sci. Rev.*, in press, 2000.
- Rind, D. and J. Overpeck, Hypothesized causes of decade-to-decade climate variability: climate model results, *Quaternary Sci. Rev.*, 12, 357-374 (1993)
- Rossow, W.B., A.W. Walker, D.E. Beuschel, and M.D. Roiter, International Satellite Cloud Climatology Project (ISCCP): Documentation of new datasets, WMO/TD 737, World Met. Org., Geneva, 1996.

- Russell, C.T., and R.L. McPherron, The magnetotail and substorms, Space Sci. Rev., 15, 205-225, 1973.
- Sabbah, I., The role of interplanetary magnetic field and solar wind in modulating both galactic cosmic rays and geomagnetic activity, *Geophys. Res. Lett.*, 27, 1823-1826, 2000.
- Solanki , S.K. and M. Fligge, Solar irradiance since 1874 revisited, *Geophys. Res. Lett.*, 25, 341-344, 1998.
- Solanki, S.K. and M. Fligge, A reconstruction of total solar irradiance since 1700, *Geophys. Res. Lett.*, 26, 2465-2468, 1998.
- Solanki, S.K., M. Schüssler, and M. Fligge, Secular evolution of the Sun's magnetic field since the Maunder minimum, *Nature*, in press, 2000.
- Soon, W., S. Baluinas, E.S.Posmentier, and P. Okcke, Variations of solar coronal hole qarea and terrestrial lower tropospheric air temperature from 1979 to mid-1998: Astronomical forcings of changes in Earth's climate?, New Astron., 4, 563-579, 2000.
- Stamper, R., M. Lockwood, M.N. Wild, and T.D.G. Clark, Solar causes of the long term increase in geomagnetic activity, J. Geophys Res., 104, 28,325-28,342, 1999.
- Stuiver, M., and P.D. Quay, Changes in atmospheric carbon-14 attributed to a variable Sun, *Science*, 207, 11, 1980.
- Svensmark, H., Influence of cosmic rays on Earth's climate, *Phys. Rev. Lett.*, 81, 5027-5030, 1998.
- Svensmark, H., and E. Friis-Christensen, Variation of cosmic ray flux and global cloud coverage: A missing link in solar-climate relationships, J. Atmos. Sol. Terr. Phys., 59, 1225-1232, 1997.
- Tett, S., P.A. Stott, M.R. Allen, W.J. Ingram and J.F.B. Mitchell, Causes of twentieth century temperature change, *Nature*, 388, 569-572, 1999.
- Usoskin, I.G., H. Kananen, K. Mursula, P. Tanskanen, and G.A. Kovaltsov, Correlative study of solar activity and cosmic ray intensity, *J. Geophys. Res.*, 103, 9567-9574, 1998.
- Vasyliunas, V.M., J.R. Kan, G.L. Siscoe, and S.-I. Akasofu, Scaling relations governing magnetospheric energy transfer, *Planet Space Sci.*, 30, 359-365, 1982.
- Wang, Y.-M., N.R. Sheeley Jr., and J. Lean, Understanding the evolution of Sun's magnetic flux, *Geophys. Res. Lett.*, 27, 621-624, 2000a.
- Wang , Y.-M., J. Lean, and N.R. Sheeley Jr., The longterm evolution of the Sun's open magnetic flux, *Geophys. Res. Lett.*, 27, 505-508, 2000b.
- Wigley, T.M.L., and S.C.B. Raper, Climatic change due to solar irradiance changes, *Geophys. Res. Lett.*, 17, 2169-2172, 1990.
- Wigley, T.M.L., P.D. Jones, and S.C.B. Raper, The observed global warming record: what does it tell us? *Proc. Natl. Acad. Sci.*, USA, 94, 8314-8320, 1997
- Willson, R.C., Total solar irradiance trend during cycles 21 and 22, *Science*, 277, 1963-1965, 1997.

M. Lockwood, World Data Centre C-1 for Solar-Terrestrial Physics, Space Science Department, Rutherford Appleton Laboratory, Chilton, Didcot, Oxfordshire OX11 0QX, England, U.K. (m.lockwood@rl.ac.uk)

"CORONAL HOLES" (RECORDED FROM 1943) – A SOURCE OF THE SOLAR–INDUCED TERRESTRIAL RESPONSES ?

J. Sýkora¹, O. G. Badalyan², and V. N. Obridko²

¹Astronomical Institute, 05960 Tatranská Lomnica, Slovak Republic: sykora@ta3.sk ²IZMIRAN, 142190 Troitsk, Russia; badalyan@izmiran.troitsk.ru; obridko@solter.troitsk.ru

ABSTRACT

The low brightness regions identified in distribution of the Fe XIV 530.3 nm coronal emission seem to be a natural proxy of coronal holes. Patrol measurements of this "green coronal line" intensity are on hand from about 1940. Our paper summarizes shortly all the previous findings demonstrating close affinity of the green corona low brightness regions and coronal holes and outlines new possibilities to prove this affinity. Among these, our original calculations of the magnetic field topology and the magnetic field strength in the corona allow to explore the coronal holes widely. The long-term regularities found in distribution of the coronal green line brightness provide a promising way how to predict the parameters of solar activity a cycle ahead.

Key words: solar corona; coronal emission; coronal holes; solar cycle; prediction.

1. INTRODUCTION

Physical conditions allowing excitation of the Fe XIV 530.3 nm coronal green line (CGL) imply that intensity of this emission needs to decrease greatly within the regions of low plasma density and temperature. At the same time, coronal holes (CH) are convincingly characterized by a considerably reduced values of both these physical parameters. Except of that. CH represent magnetically open regions which. shortly after their discovery by the Skylab satellite in 1973, were identified as an important source of the solar wind and geophysical disturbances (e.g., Zirker, 1977). Re-tracing all the open magnetic field lines from the source surface $(2.5R_{\odot})$ back to the photosphere shows that CH could be the only source of the interplanetary magnetic field responsible for heliospheric magnetic conditions and for modulation of cosmic rays (Soon et al., 2000 and the references therein). In this connection, frequency of CH appearance and evolution of the total area occupied by CH during solar cycle are of particular interest. Evidently, extensive investigation of the long-term evolution of CH seems crucial for a better understanding of causes and effects in the solar-terrestrial physics chain and for possible practical exploitation of the results revealed.

One of the physically hopeful ways in this direction is to carry out extensive time-space analysis of the CGL radiation. Using full set of existing patrol measurements of the CGL intensity, performed by a small world-wide network of high-altitude coronal observatories, we have created a homogeneized original database representing a matrix of 72 values (one measurement at each 5° of the solar position angle) of the CGL intensity (expressed in the so-called absolute coronal units – a.c.u. in the next) for each day in the period 1943-1993. Thus, the space resolution of the data is one day (about 13°) in the solar longitude and 5° in the solar latitude. For the period 1994–1999 only the semi-anually averaged data are at our disposal. More complete description of the observations and data reduction can be found in Sýkora (1992a), Sýkora and Parisi (1998) and Badalyan et al. (2001). Our database was already exploited partially to demonstrate the CGL/CH reletion (see the next Section) and some new approaches to explore it are envisaged.

2. A SHORT REVIEW OF THE PREVIOUS RESULTS

An attempt to give a complete summary of the previous studies of CH by using measurements of the CGL intensity is as follows:

(a) Primarily, it should be emphasized that Waldmeier (1956; 1981) applied the term "koronaloch" (which stands for coronal hole in German) long before the CH discovery by *Skylab*. He used it for the regions of minimum CGL brightness identified in his polar maps of corona.

Proc. 1st Solar & Space Weather Euroconference, 'The Solar Cycle and Terrestrial Climate', Santa Cruz de Tenerife, Tenerife, Spain, 25-29 September 2000 (ESA SP-463, December 2000)

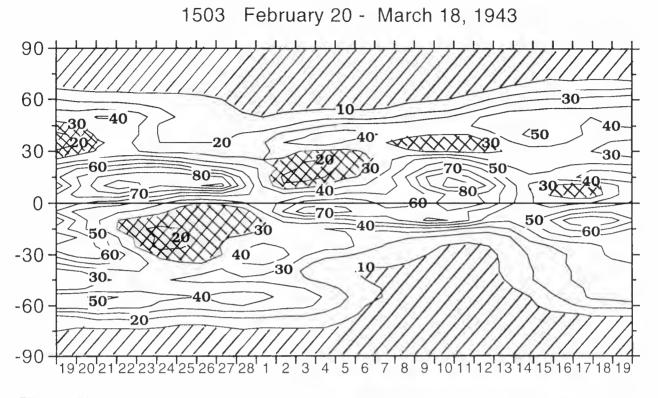


Figure 1. This is an example of the CGL intensity synoptic map from the beginning period of our database. The extensive polar and much smaller low-latitude GCLBR are hatched in this map. (Bartels numbering of rotations is adopted within the present paper).

(b) Fairly good space identity of the brightness minima seen in the CGL synoptic charts and CH recorded by *Skylab* was demonstrated by Letfus et al. (1980).

(c) Later, the long-term distribution of the green corona low brightness regions (GCLBR) was correlated with the solar wind parameters and the geophysical K_{p^-} and aa-indices (Sýkora, 1992b). In this paper GCLBR were investigated within the zone of $\pm 60^{\circ}$ of solar latitude, in contradistinction to all other paper quoted in this Section where only polar CH we investigated. It was found that:

- Number of GCLBR varies considerably during the solar cycle being approximately in anti-correlation with the sunspot cyclicity.

Positive correlation exists between size and frequency of GCLBR situated in the zones $\pm (20 - 40)^{\circ}$ on one side and the velocity and duration of the solar wind streams on the other side.

– Quite a similar result was obtained when correlating GCLBR with the K_p - and aa-indices. This indicates that the middle-latitude zones at both the solar hemispheres are particularly relevant for the geophysical responses.

(d) In the paper by Bavassano et al. (1994) it was shown that the extensive polar regions of very low green corona brightness (alias polar CH) do exist and infiltrate to the lower solar latitudes during fairly broad periods around the solar cycle minima. (e) Also Dorotovič (1998) confirmed a clear negative correlation of the total area occupied by the low brightness of green corona around the solar poles and the sunspot cycle curve.

Summarizing all the known results coming from the long-term distribution and evolution of the CGL brightness one is persueaded on quite a similar behaviour and properties of the regions with low CGL emission and those revealed for CH in a huge number of studies. This conclusion allows to assume that the CH phenomenon can be hopefully explored starting already from about 1940 and using the proper synoptic charts of the CGL brightness.

3. HOW TO ADVANCE ON THE STUDY OF THE GCLBR (ALIAS CH) ?

Some of the findings enumerated in the preceding Section should be, of course, more precised and quantified. This requires semewhat new approach to the exploitation of our database. At present, we are able to draw the CGL intensity synoptic charts for the whole period 1943–1993 and to identify the "raw" low brightness regions within them. An example of such a map is shown in Figure 1. The extensive polar and much smaller low-latitude GCLBR are hatched in this map. One can see that the boundaries of the polar and low-latitude GCLBR were adopted different (10 and 30 a.c.u., respectively). This very tenta-

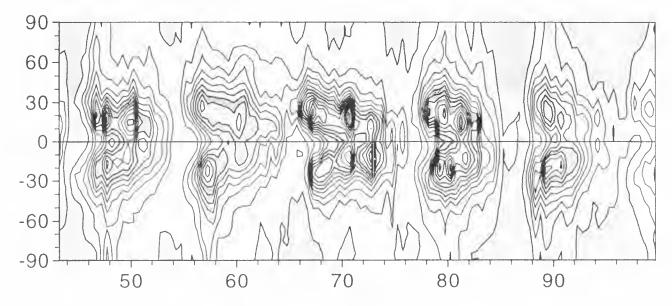
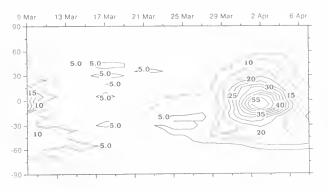


Figure 2. Time latitude distribution of the CGL intensity during the last five solar activity cycles (the isophotes are drawn with step of 10 a.c.u, ranging from 10 to 140).





1821 October 9 - November 4, 1989

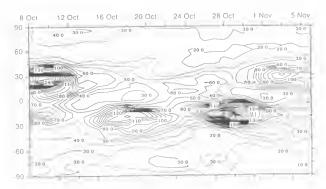


Figure 3. The CGL synoptic charts typical for the minima (above) and maxima (below) of the solar cycles. The scale in the upper map is even double. Four huge active regions are present on the 1821 map (in one of them the CGL intensity reached 240 a.c.u.), in contrast to one moderately active region with 55 a.c.u. on the 1773 map.

tive choice of the boundaries and necessity of their more precise definition may be understood from the following explanation.

The CGL intensity is derived from observations performed at the solar limb. Understandably, the principal factor "befogging" a true intensity at a given point of the solar corona comes from integration of the light signal along the line of sight. In case of the CGL observations this integration is along an interval of heliographic longitudes corresponding to about 3-day solar rotation (about 40° of latitude). Over such an interval the coronal regions of different brightness are integrated and averaged. Activity, and therefore, the coronal brightness varies greatly with the solar cycle (Figure 2 and a number of Figures in Sýkora et al., 2000). Understandably, degree of smoothing the real CGL intensities changes substantially also with the solar latitude (Figure 3 demonstrates a typical difference in appearance of the CGL synoptic charts drawn for minimum and maximum phases of solar cycle). All the mentioned circumstances should be carefully considered and incorporated into the reliable definition of GCLBR which subsequently will allow the relevant time-space analysis of them on the solar surface.

4. CORONAL HOLES FROM THE MAGNETIC FIELD MEASUREMENTS

Recently we have tried to check the CGLBR/CH affinity by another way. A software was developed allowing us to calculate an averaged magnetic field strength in the corona all around the solar disk and in dependence on the distance from the disk centre. These calculations are based on the distribution of the full magnetic field vector measured in the

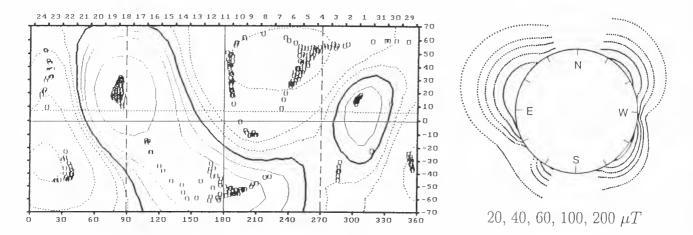


Figure 4. This is an example how the limb positions of CH well enough correlate with the bubbles displayed by the isolines of the magnetic field strength. (The vertical dashed lines approximately indicate the solar limb on the 11 August 1999 eclipse day).

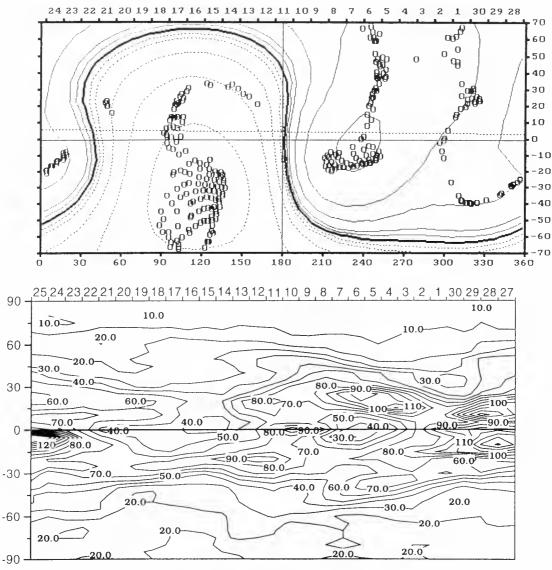




Figure 5. Positions of CH (upper map) well enough agree with those of GCLBR (lower map) during the 11 July 1991 eclipse.

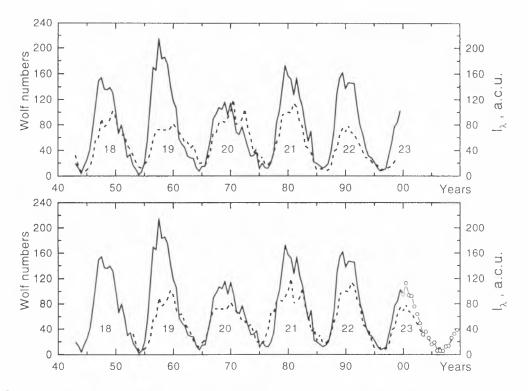


Figure 6. Cyclic variations of the mean semi-annual Wolf numbers (solid lines) and coronal green line intensities I_{λ} (dashed lines) for the period of 1943–1999 (activity cycles 18–23). On the lower panel, the values of I_{λ} are shifted forward by 10 years. The open circles in this lower panel indicate our forecast of the Wolf numbers for solar cycle 23 and 24.

photosphere. We have found (Sýkora et al., 2001) increased magnetic field strength and stretching of the isogausses above the magnetically open regions (cf. CH). An example of such a relation is demonstrated in Figure 4 where the magnetic field strength and positions of CH are compared for the 11 August 1999 solar eclipse day. The "swellings in the system of isogausses (i.e., the regions of the increased magnetic field strength) well correlate with the positions of CH situated at the limb of the NE- and NWquadrants and CH situated not far behind the limb of the SW-quadrant. In Figure 4 CH are represented by the clusters of small open circles. Following from the method of calculation, these are regions where the open magnetic field lines of force are rooted in the photosphere. A similarly good correspondence was found in case of other our eclipse observations (Sýkora et al., 2001).

The above finding led us to an idea to compare positions of the magnetically open regions (cf. CH), seen in the magnetic synoptic charts, with the positions of the GCLBR. identified in the synoptic charts of the CGL brightness. Experimentally this is done for the period of 11 July 1991 eclipse observation (Figure 5). Appart from uncertainties coming from the limb observations, quite a good correspondence is found between the GCLBR and CH positions. This repeatedly stimulates us to study CH behaviour by backward analysis of GCLBR.

5. PREDICTION OF THE SOLAR CYCLES 23 AND 24 FROM THE CGL BRIGHTNESS

During the all-sided analysis we have found interesting to compare a long-term course of the global CGL brightness, calculated for the Sun as a star, with behaviour of the known sunspot cycle curve. Surprisingly, some reasons were found to utilize characteristics of the global CGL brightness in the present cycle for prediction of the sunspot cycle parameters a cycle ahead (for a full reasoning of this prediction technique see Badalyan et al., 2001).

The upper panel of Figure 6 shows variations of the CGL intensity I_{λ} in the equatorial zone during the past five 11-year cycles of solar activity. The dashed line represents I_{λ} values in the latitudinal zone from $\pm 20^{\circ}$ to $\pm 20^{\circ}$, i.e., without separation between the two hemispheres. The Wolf number curve is drawn by a solid line. One can notice some peculiarities in the behaviour of I_{λ} a lower cycle 19 in comparison with cycle 20, and less extensive variations in I_{λ} from cycle to cycle in comparison with the Wolf numbers.

Even a superficial inspection of both curves in the upper panel of Figure 6 suggests that cyclic variations in the Wolf numbers follow the green line variations with a delay of one cycle. To verify this impression, we shifted the I_{λ} values forward by 10 years (the mean length of cycles 18-22) when plotting the lower panel of Figure 6. It is evident that the shifted CGL curve does agree better with the Wolf number

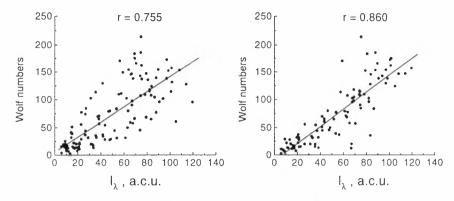


Figure 7. Regression dependence between the Wolf numbers and CGL intensities in the equatorial zone $\pm 20^{\circ}$ for the whole 1943–1999 period are shown. Values of I_{λ} in the left part were not shifted while, the values in the right part were shifted forward by 10 years. The corresponding correlation coefficients are indicated.

curve. This conclusion was corroborated numerically by calculating the correlation coefficients.

The left panel in the lowest part of Figure 7 represents the regression dependence between the Wolf numbers and the 'non-shifted' CGL intensities for the entire period of 1943-1999 (the points correspond to the upper panel in Figure 6); and the right panel shows the same dependence for I_{λ} shifted forward by 10 years (the points correspond to the lower panel in Figure 6). A comparison of the left and right panels makes it evident that the correlation is considerably higher on the right panel than on the left one, the correlation coefficients being $r = 0.860 \pm 0.027$ and $r = 0.755 \pm 0.040$, respectively.

We have analysed correlation relations in the pairs of consecutive cycles. The correlation coefficients appeared to be always higher if I_{λ} was shifted forward by about a cycle. Thus, the analysis performed shows that the CGL brightness correlates with the Wolf numbers much better when shifted forward by about 10 years, i.e., for a cycle approximately. In general, characteristics of the CGL brightness within the solar equatorial zone seem to be are closely related to the Wolf numbers of the following cycle. At the same time, the cyclic curves of the Wolf numbers and CGL brightness shifted by ~ 10 years coincide well enough, even in some details. This effect is especially pronounced at the descending branches of the solar cycles.

The above regularities allow us to predict the Wolf number curve in any cycle on the basis of the CGL brightness curve in the preceding cycle. Our calculations provide the maximum semi-annual value of Win cycle 23 equal to 106-118 and the epoch of maximum in the first half of 2000. Hence, the present cycle is not as high as was expected and predicted several years ago, nor as low as forecasted by some authors. The end of the cycle is expected in 2006-2007. Proceeding from the current CGL brightness (the second half of 1999), we can predict a low cycle 24 with the maximal W not exceeding 50 (similarly to the cycles 5 and 6) and the epoch of maximum in 2010-2011. Thus, as inferred by our results, we are on the eve of a deep minimum of solar activity similar to that at the beginning of the 19th century.

ACKNOWLEDGMENTS

The authors greatly appreciate the support of the VEGA Grant 02/5007/98 of the Slovak Academy of Sciences and the Grant No. 99-02-18346 of the Russian Foundation for Basic Research.

REFERENCES

- Badalyan O.G., Obridko, V.N., Sýkora J., 2001, Solar Phys., in press
- Bavassano B., Storini M., Felici A., et al., 1994, COSPAR Colloq. Series 5, 285
- Dorotovič I., 1998, Thesis, Slovak Centr. Obs., Hurbanovo
- Letfus V., Kulčár L., Sýkora J., 1980, in Solar and Interplanetary Dynamics, eds. M. Dryer and E. Tandberg-Hanssen, Reidel, Dordrecht, 49
- Soon W., Baliunas S., Posmentier E.S., et al., 2000, New Astronomy 4(8), 563
- Sýkora J., 1992a, Contrib. Astron. Obs. Skalnaté Pleso 22, 55
- Sýkora J., 1992b, Solar Phys. 140, 379
- Sýkora J., Badalyan O.G., Obridko V.N., 2001, Adv. Space Res., in press
- Sýkora J., Badalyan O.G., Storini M., 2000. in this volume
- Sýkora J., Parisi M., 1998, Astron. Astrophys. Trans. 16(1), 75
- Waldmeier M., 1956, Z. Astrophys. 38, 219
- Waldmeier M., 1981, Solar Phys. 70. 251
- Zirker J.B., 1997, Coronal Holes and High Speed Wind Streams, Colorado Associate Univ. Press. Boulder

THE DYNAMO THEORY FOR THE MAUNDER MINIMUM

Günther Rüdiger

Astrophysikalisches Institut Potsdam, Germany

ABSTRACT

We study the nonlinear interplay between dynamoinduced magnetic fields and differential rotation in stellar convection zones. The magnetic back reaction is threefold: Lorentz force, α -quenching and Λ -quenching. If only the Malkus-Proctor feedback is used, the dynamo shows an interesting non-periodic behaviour which, however, disappears when α -quenching is included. If also a strong Λ -quenching is allowed to modify the differential rotation, the dynamo resumes its exotic performance with periodically changing cycle periods and fluctuating magnetic parities. The Elsasser number has been set to unity whereas the magnetic Prandtl number must be smaller than unity. For too small magnetic Prandtl numbers (e.g. for Pm = 0.01), however, the grand minima seldom occur.

I. INTRODUCTION

It seems that Earth and Sun realize two different forms of magnetic dynamos. While the solar magnetic activity exhibits a distinct periodicity with a period of 11 years, the terrestrial magnetic field is 'permanent'. Indeed, two different sorts of dynamos in spherical geometry have been constructed with the desired properties. The socalled α^2 -dynamo yields stationary solutions while the $\alpha\Omega\text{-dynamo}$ yields oscillatory solutions (under certain assumptions even with the correct period. Observation and theory are rather in agreement. There are, however, striking differences in the time behaviour: the solar activity is not strictly periodic and the Earth dynamo is not strictly permanent. There exist known variations of the solar cycle between 9 and 13 yrs, also known is the Maunder minimum for the Sun. The power spectrum of the solar cycle does not form a delta function. The quality $\omega/\Delta\omega$ of the 11-year cycle seems to be of order of 5 (Wittmann, 1978; Hoyng, 1993).

The activity cycle of the Sun is not exceptional: The observation of chromospheric Ca-emission of solar-type stars yielded activity periods between 3 and 20 yr (Noyes et al., 1984; Baliunas and Vaughan, 1985; Saar and Baliunas, 1993). A few of these stars do not show any significant activity. This suggests that even the existence of grand minima is a typical property of cool main-sequence

stars like the Sun. From ROSAT X-ray data, Hempelmann et al. (1996) find that up to 70% of the stars with a constant level of activity exhibit only a low level of coronal X-ray emission. HD 142373, e.g., with its X-ray luminosity of only $\log F_{\rm X} = 3.8$, is a typical candidate. We conclude that during a grand minimum not only the magnetic field in the activity belts is weaker than usual, but the total magnetic field energy is reduced.

A wavelet analysis of sunspot data by Frick et al. (1997) indicates a decrease of the short-term cycle period at the end of, or even through (if periods are detectable) a grand minimum. The latitudinal distribution of the few sunspots observed during the Maunder minimum was highly asymmetric (Ribes and Nesme-Ribes, 1993; Nesme-Ribes et al., 1994). Short-term deviations from the north-south symmetry in regular solar activity are readily observable (Verma, 1993), yet a 30-year period of asymmetry in sunspot positions as seen during the Maunder minimum (cf. Spörer, 1889) remains a unique property of grand minima and should be associated with a parity change of the driving internal magnetic fields.

After Wittmann (1978) and very recently Beer et al. (1998), there is empirical evidence for the persistence of the solar cycle throughout the Maunder minimum, of course with a drastically reduced amplitude.

2. MEAN-FIELD ELECTRODYNAMICS

There are so far two concepts for dynamo-induced grand minima of cyclic magnetic activity. The first one is based on the idea that, due to the stochastic character of the turbulence, its statistical properties and hence the α effect and all related phenomena vary with time (Choudhuri, 1992; Hoyng et al., 1994; Schmitt et al., 1996; Otmianowska-Mazur et al., 1997). The second one works with the inclusion of the magnetic feedback to the internal solar rotation (Weiss et al., 1984). Kitchatinov et al. (1994) and Tobias (1996, 1997) even introduced the conservation law of angular momentum in the turbulent convection zone including magnetic feedback in order to produce grand minima of the dynamo cycle. In the present paper, we for the first time present a 2D mean-field theory in spherical polar coordinates on the basis of a solar overshoot dynamo model (Rüdiger and Brandenburg, 1995)

Proc. 1st Solar & Space Weather Euroconference, 'The Solar Cycle and Terrestrial Climate', Santa Cruz de Ténerife, Tenerife, Spain, 25-29 September 2000 (ESA SP-463, December 2000)

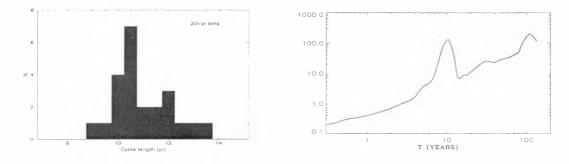


Figure 1. LEFT: The distribution of the solar cycle length does not approach a Dirac function, the 'quality' of the cycle only gives values of about 5. RIGHT: The wavelet spectrum of the sunspot-number time series shows two peaks for both 10 yr and 100 yr (Frick et al., 1997).

together with a theory of differential rotation based on the Λ -effect concept (Küker et al., 1993).

We assume axial symmetry of the hydromagnetic state of the star and ignore meridional flows. Then the mean velocity and magnetic field in spherical coordinates reads B =

$$\left(\frac{1}{r^2\sin\theta}\frac{\partial A(r,\theta,t)}{\partial\theta},-\frac{1}{r\sin\theta}\frac{\partial A(r,\theta,t)}{\partial r}\;,\;B(r,\theta,t)\right),$$

with A the poloidal-field potential and B the toroidal field.

The field equations for the convection zone include the effects of diffusion, α -effect, toroidal field production by differential rotation, and the Lorentz force. They are detailed described in Rüdiger and Arlt (2000).

The domain of the computations covers the outer parts of the Sun down to a fractional solar radius, x = r/R, of 0.5. The convection zone extends from x = 0.7 to x = 1. The α -effect works only in the lower part from x = 0.7to x = 0.8 while turbulent diffusion of the magnetic field, turbulent viscosity, and the Λ -effect are present in the whole convection zone. Below x = 0.7, both the magnetic diffusivity and the viscosity are two orders of magnitude smaller than in the convection zone. The boundary conditions are specified as $Q_{r\phi} = \partial/\partial r = B = 0$ at r = R and $Q_{r\phi} = A = B = 0$ at the inner boundary. As usual, Q_{ij} is the one-point correlation tensor of the velocity fluctuations (see Eq. (3) below).

3. THE INTERNAL SOLAR ROTATION

The main observational features of the internal solar rotation are given in Fig. 2, i.e.

- surface equatorial acceleration of about 30%,
- strong polar sub-rotation and weak equatorial superrotation,
- reduced equator-pole difference in Ω at the lower convection-zone boundary.

The characteristic Taylor-Proudman structure in the equatorial region and the characteristic disk-like structure in

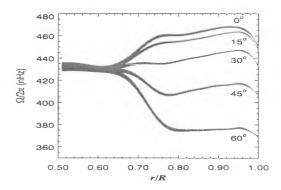


Figure 2. The internal rotation of the Sun after the inversion of SOHO data.

the polar region are comprised by the results. In the search for *stellar* surface differential rotation, chromospheric activity has been monitored for more than a decade. There is not yet a very clear picture. For example, the rotation pattern of the solar-type star HD 114710 might easily be reversed compared with that of the Sun (Donahue and Baliunas, 1992) if the same butterfly diagram is applied.

In close correspondence to dynamo theory we develop the theory of differential rotation in a mean-field formulation starting from the conservation of angular momentum.

$$\frac{\partial}{\partial t} \left(\rho r^2 \sin^2 \theta \Omega \right) + \frac{\partial}{\partial x_i} \left(\rho r \sin \theta Q_{i\phi} \right) = 0, \quad (2)$$

where the Reynolds stress is derived from the correlation tensor

$$Q_{ij} = \langle u'_i(\mathbf{x}, t) u'_j(\mathbf{x}, t) \rangle \tag{3}$$

of the rotating turbulence field.

The correlation tensor involves both dissipation ('eddy viscosity') as well as 'induction' (Λ -effect):

$$Q_{ij} = \Lambda_{ijk}\Omega_k - \mathcal{N}_{ijkl}\Omega_{k,l}.$$
 (4)

Both effects are represented by tensors and must be computed carefully. For anisotropic and rotating turbulence

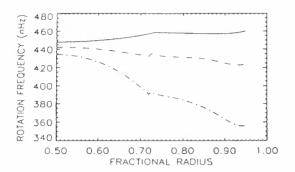


Figure 3. Theory of the solar internal rotation by Kitchatinov and Rüdiger (1995). The rotation frequency is given for the equator (solid), mid-latitudes (dashed) and poles (dashed-dotted).

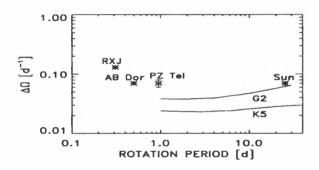


Figure 4. Theory of the stellar internal rotation in comparison with observations. Obviously, there is a missing process in the theory for very fast rotation.

the zonal fluxes of angular momentum can be written as

$$Q_{r\phi} = -\nu_{\Gamma} r \sin \theta \frac{\partial \Omega}{\partial r} + \nu_{T} \left(V^{(0)} + \sin^{2} \theta V^{(1)} \right) \Omega \sin \theta,$$

$$Q_{\theta\phi} = -\nu_{T} \sin \theta \frac{\partial \Omega}{\partial \theta} + \nu_{T} H^{(1)} \Omega \sin^{2} \theta \cos \theta \qquad (5)$$

(see Rüdiger, 1989). All coefficients are found to be strongly dependent on the Coriolis number $\Omega^* = 2\tau_{\rm corr} \Omega$ with $\tau_{\rm corr}$ as the convective turnover time. Moreover, the most important terms of the Λ -effect correspond to higher orders of the Coriolis number. The Coriolis number exceeds unity almost everywhere in the convection zone except the surface layers. That is true for all stars – in this sense all main-sequence stars are rapid rotators. *Theories linear in* Ω *are not appropriate for stellar activity physics*.

The Coriolis number Ω^* is smaller than unity at the top of the convection zone and larger than unity at its bottom. At that depth we find minimal eddy viscosities (' Ω quenching') and maximal $V^{(1)} = H^{(1)}$. Since the latter are known as responsible for pole-equator differences in Ω , we can state that the differential rotation is produced in the deeper layers of the convection zone where the rotation must be considered as rapid ($\Omega^* \leq 10$).

The solution of (2) with the turbulence quantities after (5) is given in Küker et al. (1993) and Kitchatinov and Rüdiger (1995) using a mixing-length model by Stix and Skaley (1990). With a reasonable mixing-length ratio we find the correct equatorial acceleration of about 30 %.

There is a clear radial sub-rotation $(\partial \Omega / \partial r < 0)$ below the poles while in mid-latitudes and below the equator the rotation is basically rigid (Fig. 3). In this way the bottom value of the pole-equator difference is reduced and the resulting profiles of the internal angular velocity are close to the observed ones. Fig. 4 presents the results of an extension of the theory to a sample of main-sequence stellar models (spectral types G2 – the Sun – and K5) given in

$$\delta \Omega \simeq \text{const.}$$
 (6)

should be not too rough. Recent observations plotted in Fig. 3 seem to confirm this surprising and unexpected result where in all cases the constant value approaches 0.08 day^{-1} .

Kitchatinov and Rüdiger (1999). So we find that for one

and the same spectral type the approximation

4. THE DISTRIBUTED DYNAMO

Our equations are normalized with $r = R\tilde{r}$, $t = R^2/\eta_{\rm T}\tilde{t}$, $\Omega = \Omega_0\tilde{\Omega}$ as well as with $A = R^2B_{\rm eq}\tilde{A}$ and $B = B_{\rm eq}\tilde{B}$. $B_{\rm eq}$ is the turbulence-equipartition field defined below. After insertion of the relations into the dynamo equation

$$\frac{\partial B}{\partial t} = \operatorname{rot}(\langle u \rangle \times \langle B \rangle + \mathcal{E}).$$
(7)

Here only a non-uniform rotation will be imposed on the mean flow, $\langle \mathbf{u} \rangle$; any meridional flow shall be introduced later. The turbulent electromotive force, $\boldsymbol{\mathcal{E}} = \langle \mathbf{u}' \times \mathbf{B}' \rangle$, contains induction α_{ij} and dissipation η_{ijk} , i.e.

$$\mathcal{E}_i = \alpha_{ij} \langle B_j \rangle + \eta_{ijk} \langle B_j \rangle_{,k} + \dots$$
 (8)

Both tensors are pseudo-tensors. While for η_{ijk} an elementary isotropic pseudo-tensor exists (" ε_{ijk} "), the same is not true for α_{ij} . An odd number of Ω 's is, therefore, required for the α -tensor, which is only possible with an odd number of another preferred direction, (say) g. The α -effect can thus only exist in stratified, rotating turbulence. The first formula reflecting this situation.

$$\alpha = c_{\alpha} \frac{l_{\text{corr}}^2 \Omega}{H_{\rho}} \cos \theta, \tag{9}$$

was given by Krause (1967) with H_{ρ} being the density scale height. Evidently, α is a complicated effect, where the effective α might really be very small; the unknown factor c_{α} in (9) may be much smaller than unity. The strength of this effect was computed in recent analytical and numerical simulations for both convectively unstable as well as stable stratifications.

Finally we arrive at the system of dimensionless equations

$$\frac{\partial\Omega}{\partial t} = \frac{\mathrm{Pm}}{r^4} \frac{\partial}{\partial r} \left(r^3 \left(r \frac{\partial\Omega}{\partial r} - V^{(0)} \Omega \right) \right) + \frac{\mathrm{Pm}}{r^2 \sin^3 \theta} \frac{\partial}{\partial \theta} \left(\sin^3 \theta \frac{\partial\Omega}{\partial \theta} \right) +$$

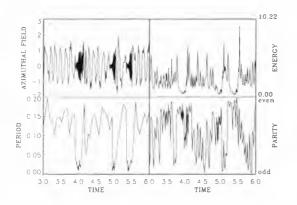


Figure 5. The time dependence of the dynamo basics for the magnetic Malkus-Proctor feedback only (i.e. without both α -quenching and Λ -quenching, Pm = 0.1, E = 1). TOP: Toroidal magnetic field (left) and magnetic energy (right). BOTTOM: Cycle time (left) and magnetic parity (right).

$$+\frac{\mathrm{E}}{r^{2}\sin\theta}\left(\frac{1}{r}\frac{\partial A}{\partial\theta}\frac{\partial(rB)}{\partial r}-\frac{1}{\sin\theta}\frac{\partial A}{\partial r}\frac{\partial}{\partial\theta}(\sin\theta B)\right),\tag{10}$$
$$\frac{\partial A}{\partial t}=\frac{\partial^{2}A}{\partial r^{2}}+\frac{\sin\theta}{r^{2}}\frac{\partial}{\partial\theta}\left(\frac{1}{\sin\theta}\frac{\partial A}{\partial\theta}\right)+r\sin\theta C_{\alpha}\alpha B,\tag{11}$$

$$\frac{\partial B}{\partial t} = \frac{1}{r} \frac{\partial^2}{\partial r^2} (rB) + \frac{1}{r^2} \frac{\partial}{\partial \theta} \left(\frac{1}{\sin \theta} \frac{\partial}{\partial \theta} (\sin \theta B) \right) + \frac{C_{\Omega}}{r} \frac{\partial \Omega}{\partial r} \frac{\partial A}{\partial \theta} + \frac{C_{\Omega}}{r} \frac{\partial \Omega}{\partial \theta} \frac{\partial A}{\partial r} - - \frac{C_{\alpha}}{r \sin \theta} \frac{\partial}{\partial r} \left(\alpha \frac{\partial A}{\partial r} \right) - \frac{C_{\alpha}}{r^3} \frac{\partial}{\partial \theta} \left(\frac{\alpha}{\sin \theta} \frac{\partial A}{\partial \theta} \right).$$
(12)

The model is defined by five dimensionless numbers, namely the magnetic Reynolds numbers of differential rotation and α -effect, $C_{\Omega} = \Omega_0 R^2 / \eta_{\rm T}, C_{\alpha} = \alpha_0 R / \eta_{\rm T}$, the magnetic Prandtl number $Pm = \nu_T / \eta_T$, the Elsasser number $E = B_{eq}^2/\mu_0 \rho \eta_T \Omega_0$, and the strength of the Λ effect, $V^{(0)}$. Here α_0 is the dynamo-alpha amplitude. The equipartition value of the magnetic field is given by $B_{\rm eq} = \sqrt{\mu_0 \rho \langle u'^2 \rangle}$, where $\langle u'^2 \rangle$ is the mean intensity of the turbulent velocity field. With the eddy diffusivity. $\eta_{\rm T} = c_\eta \langle u'^2 \rangle \tau_{\rm corr}$, the Elsasser number reads $E = 2/(c_n \Omega^*)$. The Coriolis number $\Omega^* = 2\tau_{corr}\Omega_0$ is a measure of the basic rotation. In the α -effect, $\alpha = \alpha_0 \cos\theta \sin^2\theta$, the factor $\sin^2\theta$ has been introduced to restrict magnetic activity to low latitudes and $\alpha_0 \simeq l_{\rm corr} \Omega_0$. In general the C_Ω exceeds C_α (' $\alpha \Omega$ dynamo'). Our dynamo works with $C_{\alpha} = -10$ and $C_{\Omega} = 10^5$. $V^{(0)}$ is positive in order to produce the required super-rotation, its amplitude is 0.37.

5. RESULTS AND DISCUSSION

Figures 5–8 demonstrate the action of different effects. The graphs shows the variation of the toroidal magnetic field at a certain point (r = 0.75 which is the center of

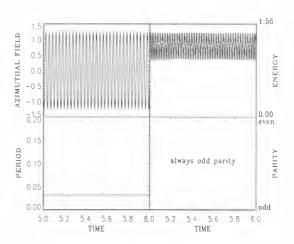


Figure 6. The same as in Fig. 5 but with α -quenching and without Λ -quenching ($\lambda = 0$). TOP: Toroidal magnetic field (left) and magnetic energy (right). BOTTOM: Cycle time (left) and magnetic parity (right).

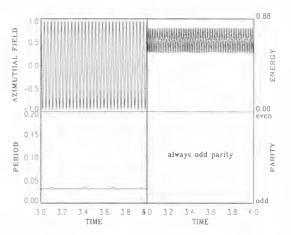


Figure 7. The same as in Fig. 6 but with Λ -quenching $(\lambda = 1)$. TOP: Toroidal magnetic field (left) and magnetic energy (right). BOTTOM: Cycle time (left) and magnetic parity (right).

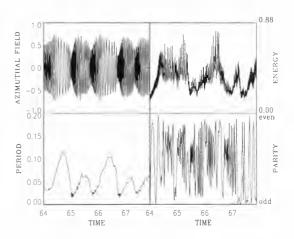


Figure 8. The same as in Fig. 6 but for strong Λ -quenching ($\lambda = 25$). TOP: Toroidal magnetic field (left) and magnetic energy (right). BOTTOM: Cycle time (left) and magnetic parity (right).

the dynamo zone, $\theta = +30^{\circ}$), the total magnetic energy, the variation of the cycle period, and the parity $P = (E_{\rm S} - E_{\rm A}/(E_{\rm S} + E_{\rm A}))$, derived from the decomposition of the magnetic energy into symmetric and antisymmetric components. All times and periods are given in units of a diffusion time $R^2/\eta_{\rm T}$. Field strengths are measured in units of $B_{\rm eq}$.

Fig. 5 shows the results of a model with the Malkus-Proctor effect as the only feedback on rotation and may be compared with the results in Tobias (1996), although a number of assumptions are different between Tobias' Cartesian approach and our spherical model. It shows a quasi-periodic behaviour with interruptions in activity like grand minima. This model, however, neglects the feedback of strong magnetic fields on the α -effect and the differential rotation.

The same model, but with local α -quenching

$$\alpha \propto \frac{1}{1 + (B/B_{\rm eq})^2},\tag{13}$$

is used for Fig. 6 where *B* is the absolute value of the magnetic field. A one-period solution appears, since magnetic fields are suppressed before the nonlinearity due to the Malkus-Proctor feedback disturbs the oscillatory behaviour of the $\alpha^2 \Omega$ -dynamo. The period of a mere $\alpha^2 \Omega$ -dynamo with α -quenching is 0.023 in units of Figs. 5–8.

Similarly to the suppression of dynamo action, a quenching of the A-effect causing the differential rotation is applied by

$$V^{(0)} \propto \frac{1}{1 + \lambda (B/B_{\rm eq})^2}.$$
 (14)

As shown in Fig. 7, only a decrease in maximum field strength and total magnetic energy results for $\lambda = 1$; the periodic behaviour remains the same, i.e. the effect of the Λ -quenching is too small to alter the differential rotation significantly. However, an increase of λ leads to grand minima – an example for $\lambda = 25$ is given in Fig. 8. In agreement with the sunspot data, a minimum of the cycle period occurs shortly after the grand minimum. The solar cycle period varies between 9 and 13 yr, but it is unknown for the time of the Maunder minimum. The amplitude of the periodicity fluctuations is much higher in the Malkus-Proctor model. Although these variations are weaker in the full model shown in Fig. 8, they are still stronger than those observed. In all cases we studied, the magnetic Prandtl number is Pm = 0.1. For Pm = 1, however, grand minima do not appear in models as in Fig. 5 and 8.

The non-periodic solutions in Figs. 5 and 8 show strong variations of the parity between purely symmetric and antisymmetric states. It should be noted that the dynamo zone is filled with several (usually 5-6) magnetic-field belts migrating towards the equator. Slight shifts of this belt-structure against the equator result in strong variations in the parity. Averaged over time, dipolar and quadrupolar components of the fields have roughly the same strength; all periodic solutions (e.g. Figs. 6 and 7) have purely dipolar structure.

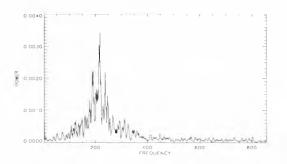


Figure 9. Power spectrum of the magnetic-field amplitude variations for the 'Malkus-Proctor' model of Fig. 5. The frequency is given in arbitrary units.

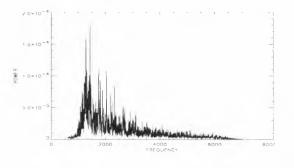


Figure 10. The same as in Fig. 9 but for the model with strong Λ -quenching given in Fig. 8.

The periodicities of the magnetic field can be analysed with spectra of very long time series. Figs. 9 and 10 show the spectra of the Malkus-Proctor model and the strong-A-quenching model, resp. The long-term variations of the field will be represented by a set of close frequencies whose difference is the frequency of the grand minima. The Malkus-Proctor model shows a number of lines close to the main cycle frequency. The difference between the two highest peaks can be interpreted as the occurrence rate of grand minima. However, the shape of the spectrum indicates that the magnetic-field appears rather irregularly. The spectrum of the model with all feedback terms and strong Λ -quenching is given in Fig. 10 and shows a similar behaviour with highest amplitudes near the main cycle frequency of the magnetic field. The average frequency of the grand minima is represented by the distance of the two highest peaks.

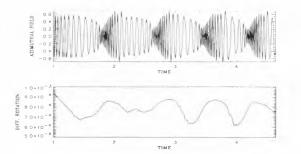


Figure 11. Correlation between magnetic field oscillations and variations of the differential rotation measure $(\partial \Omega / \partial r)^2$, averaged over the latitude θ .

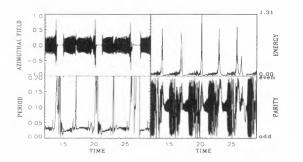


Figure 12. The same as in Fig. 8 but for Pm=0.01. The grand minima are much more seldom than for Pm=0.1.

Fig. 11 shows the variation of the radial rotational shear averaged over θ , $\langle (\partial \Omega / \partial r)^2 \rangle$, versus time, compared to the magnetic field taken from Fig. 8. A minimum in differential rotation is accompanied by a decay of the magnetic field and followed by a grand minimum. The differential rotation is being restored during the grand minimum since the suppressing effect of magnetic Λ -quenching is reduced.

6. SUMMARY

We can summarise the results as follows: When only considering large-scale Lorentz forces on the differential rotation, one gets irregular grand minima with strong variations in cycle period (by a factor of 10). If the suppression of dynamo action (α -quenching) is included, the dynamo returns to oscillations with one frequency. If a strong feedback of small-scale flows on the generation of Reynolds stress (Λ -quenching) is added, grand minima occur at a reasonable rate between 10 and 20 cycle times. The cycle period varies by a factor of 3–4. The northern and southern hemispheres slightly differ in their temporal behaviour. This is a general characteristic of mixed-modes dynamo explanations of grand minima.

In any case, magnetic Prandtl numbers smaller than unity are required for the existence of grand minima. However, the magnetic Prandtl number directs the intermittency of the activity cycle. For small values of Pm the occurrence of grand minima again becomes more and more exceptional (Fig. 12).

REFERENCES

- Baliunas S. L. and Vaughan A. H., 1985, ARA&A , 23, 379
- Beer J., Tobias S. M. and Weiss N. O., 1998, Solar Phys. 181, 237
- Choudhuri A. R., 1992, A&A 253, 277
- Donahue R.A. and Baliunas S.L., 1992, ApJ 393, L63
- Frick P., Galyagin D., Hoyt D. V., Nesme-Ribes E., Schatten K. H., Sokoloff D. and Zakharov V., 1997, A&A 328, 670
- Hempelmann A., Schmitt J. and Stępien K., 1996, A&A 305, 284

- Hoyng P., 1993, A&A 272, 321
- Hoyng P., Schmitt D. and Teuben L. J. W., 1994, A&A 289, 265
- Kitchatinov L. L., Rüdiger G. and Küker M., 1994, A&A 292, 125
- Kitchatinov L.L. and Rüdiger G., 1995, A&A 299, 446
- Kitchatinov L.L. and Rüdiger G., 1999, A&A 344, 911
- Krause F., 1967, Eine Lösung des Dynamoproblems auf der Grundlage einer linearen Theorie der magnetohydrodynamischen Turbulenz. Thesis, Universität Jena
- Küker M., Rüdiger G. and Kitchatinov L. L., 1993, A&A 279, 1
- Malkus W. V. R. and Proctor M. R. E., 1975, J. Fluid Mech. 67, 417
- Nesme-Ribes E., Sokoloff D., Ribes J. C. and Kremliovsky M., 1994, The Maunder minimum and the solar dynamo. In: Nesme-Ribes E. (ed.) NATO ASI Series, The Solar Engine and Its Influence on Terrestrial Atmosphere and Climate. Springer-Verlag, Berlin, p. 71
- Noyes R. W., Weiss N. O. and Vaughan A. H., 1984, ApJ 287, 769
- Otmianowska-Mazur K., Rüdiger G., Elstner D. and Arlt R., 1997, GAFD 86, 229
- Ribes J. C. and Nesme-Ribes E., 1993, A&A 276, 549
- Rüdiger G., 1989, Differential rotation and stellar convection: Sun and solar-type stars, Gordon and Breach Science Publishers, New York
- Rüdiger G. and Brandenburg A., 1995, A&A 296, 557
- Rüdiger G. and Arlt R., 2000, The physics of the solar cycle. In: Ferriz-Mas A., Jimenez N. (eds.) Advances in nonlinear dynamos. The Fluid Mechanics of Astrophysics and Geophysics, v. 8 (acc.)
- Saar S. H. and Baliunas S. L., 1993, Recent advances in stellar cycle research. In: Harvey K. L. (ed.) The Solar Cycle Workshop. ASP Conference Series 27, p. 150
- Saar S. H. and Baliunas S. L., 1993, The magnetic cycle of κ Ceti (G5V). In: Harvey K. L. (ed.) The Solar Cycle Workshop. ASP Conference Series 27, p. 197
- Schmitt D., Schüssler M. and Ferriz-Mas A., 1996, A&A 311, L1
- Spörer G., 1889, Verhandl. Kgl. Leopold.-Carol. Deutschen Akad. Naturf. 53, 283
- Stix M. and Skaley D., 1990, A&A 232, 234
- Tobias S. M., 1996, A&A 307, L21
- Tobias S. M., 1997, A&A 322, 1007
- Verma V. K., 1993, ApJ 403, 797
- Weiss N. O., Cattaneo F. and Jones C. A., 1984, GAFD 30, 305
- Wittmann A., 1978, A&A 66, 93

IRRADIANCE OR LUMINOSITY CHANGES?

Sabatino Sofia¹ and Linghuai H. Li^{1,2}

¹Department of Astronomy, Yale University, New Haven, CT 06520, USA ²Purple Mountain Observatory, Chinese Academy of Science, Nanjing, Jiangsu 210008, China

ABSTRACT

Whereas a variation of the solar luminosity, L, will inevitably cause a similar change of the total solar irradiance, S, the opposite is not true. In fact, the bulk of the days to months variations of S can be explained entirely in terms of the passage of active regions across the solar disk. In this case, L remains essentially unchanged.

For the total irradiance variation observed over the solar cycle, the issue is more uncertain. One view explains this modulation primarily as a combined action of active regions and magnetic network. These components would be superposed to an otherwise unchanging photosphere, the other view suggests that the activity cycle modulation of S is primarily produced by a variation of L (both in terms of R and $T_{\rm eff}$) caused by structural reajustments of the interior of the Sun induced by a changing magnetic field. We will present evidence in support of this second interpretation, and a model for it. We will also present the S variations over the last 5 centuries implied by our model.

Key words: Solar interior; magnetic field; irradiance.

1. INTRODUCTION

There is no question that

- The hours to months variations of the total irradiance are primarily (totally?) due to active regions.
- The spots depress the irradiance.
- The faculae add to the irradiance.
- The contrasts are sufficiently high to be measured with some confidence.
- The temporal behavior during one rotation is exactly as expected.

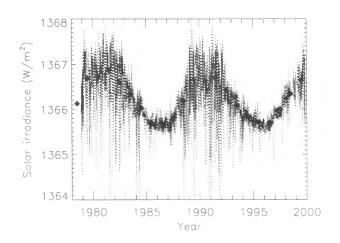


Figure 1. A composite solar irradiance record from the end of 1978 to the present (Fröhlich & Lean, 1998) and the yearly mean of solar irradiance.

However, it is not the case for the 11-year cycle, as shown in Figure 1 (Fröhlich & Lean, 1998).

- It is usually **assumed** that the magnetic network causes most of the modulation.
- The measured network contrast is insufficient to account for the entire variation (Ermolli et al., 2000).
- The precision of the irradiance measurements is less certain because instrument degradation is more significant than that in short timescales.
- Proxies of the network are designated, and their magnitude is adjusted to minimize residuals with observations.

From this viewpoint, it is assumed that the background photosphere remains unchanged during the entire cycle.

Of course, an alternative possibility is that most (if not all) of the 11 year variability is due to a change in the "luminosity" without the effects of the magnetic network. In order for that to happen, the following are true:

Proc. 1st Solar & Space Weather Euroconference, 'The Solar Cycle and Terrestrial Climate', Santa Cruz de Tenerife, Tenerife, Spain, 25-29 September 2000 (ESA SP-463, December 2000)

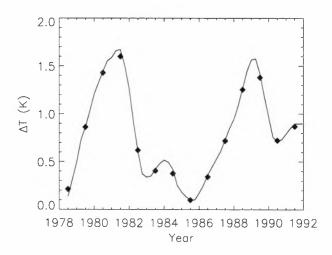


Figure 2. The measured solar photospheric temperature variations from 1978 to 1992 (Gray & Livingston, 1997) and the yearly mean.

- The photospheric temperature must change.
- The internal solar structure must change.
- The solar radius must change.

We propose here the explanation that the 11-year modulation of the total irradiance is due to structural adjustments of the solar interior in response to a variable internal magnetic field.

2. EVIDENCE IN SUPPORT OF SOLAR STRUCTURE VARIATIONS

2.1. Variations of solar effective temperature

The solar effective temperature was measured by Gray & Livingston (1997) from ratios of spectral line depths of

 $CI(\lambda 5380)/FeI(\lambda 5379)$

and

$CI(\lambda 5380)/TiII(\lambda 5381)$

The excitation potentials of these lines are different from each other.

$$CI = 7.68 \text{ eV},$$

Fe I= 3.69 eV,
Ti II= 1.57 eV.

The consistency of results indicates that the $T_{\rm eff}$ they measure is photospheric temperature. The spectroscopic temperature variations of the sun measured by Gray and Livingston (1997) over the period from 1978 to 1992, are shown in Figure 2. The zero point is chosen arbitrarily.

2.2. Variations of solar oscillations

Solar-cycle effects on solar oscillation frequencies were determined by Libbrecht and Woodard (1990). Recently, Bhatnagar et al. (1999) presented a correlation analysis of GONG p-mode frequencies with nine solar activity indices for the period from 1995 August to 1997 August. A decrease of 0.06 μ Hz in frequency during the descending phase of solar cycle 22 and an increase of 0.04 μ Hz in the ascending phase of solar cycle 23 are observed. These results provide the first evidence for change in p-mode frequencies around the declining phase of cycle 22 and the beginning of new cycle 23. This analysis further confirms that the temporal behavior of the solar frequency shifts closely follow the phase of the solar activity cycle. Besides, the analysis given by Howe et al. (1999) suggests that the solar cycle related variation of the oscillation frequencies is not due to contamination of observed Doppler shifts by the surface magnetic fields.

2.3. Radius variations

Ground-based measurements of the solar radius exist over three centuries, but the results are controversial and inconsistent. When a homogenized data base covering observations over the last three centuries is used, Basu (1998) found a statistically significant positive correlation between solar radius and sunspot numbers. Measurements of the solar radius made with the Danjon astrolabe at Santiago, Chile, and with the magnetograph of the solar telescope of Mount Wilson Observatory during the period 1990-1995, show similar variations in time and with a similar trend as the variation of sunspot numbers (Noël, 1997).

The space-based MDI-SOHO limb observations (Emilio et al., 2000) also show that the cycle variation of the solar radius is in phase with sunspot numbers. However, the estimated upper limit for the cycle variation is $\delta r_{\rm cycle} = 21 \pm 3$ milliarcsec.

All the above are inconsistent with an unchanging solar interior and suggest changes within the solar interior.

3. METHOD

Several years ago, Endal et al. (1985) proposed that a variable internal magnetic field should affect all the global parameters of the sun. Subsequently, Lydon & Sofia (1995) carefully systematized the formulation of the problem, and wrote a code to do exploratory calculations. They found that sensible internal magnetic fields variations would perturb he internal structure of the sun, and consequently affect all global solar parameters.

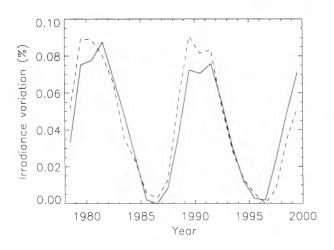


Figure 3. Comparison between the measured (solid curve) and calculated (dashed curves) solar irradiance variations.

The formulation and the code was further generalized by Li and Sofia (2000), and it is still being enriched at the present time. Elements of the new code are:

- Include the magnetic energy per unit mass χ , and the ratio of magnetic pressure to magnetic energy, $\gamma 1$, as two additional variables in stellar structure and evolution.
- Take into account influence of magnetic fields on radiative opacities.
- Take into account all time-dependent contributions to the equations of stellar structure (we need short timescales).
- Modify the radiative loss assumption of a convective element to include local turbulence effects associated with small-scale magnetic fields.
- Use real equations of state on computing first and second order derivatives associated with magnetic fields.
- Use the most up-to-date stellar evolution codes (YREC7) since the effects we wish to determine are very small.

4. RESULTS

We use this code to show that the entire 11-year variations of the total irradiance (3) and $T_{\rm eff}$ (see Figure 4) could be produced by a magnetic field of strength (20-47 kG) and location ($r = 0.96R_{\odot}$) equal to that determined from helioseismology (Antia et al., 2000), as shown in Figure 5. Figure 6 shows the corresponding internal structure adjustment of the sun. The calculated cycle change of the solar radius is about 0".02, which is in agreement with the MDI/SOHO observation (Emilio et al., 2000).

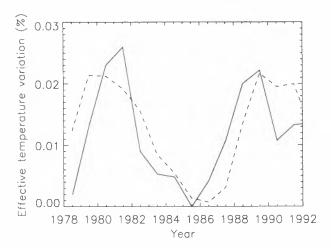


Figure 4. Comparison between the measured (solid curve) and calculated (dashed curve) solar photospheric temperature variations.

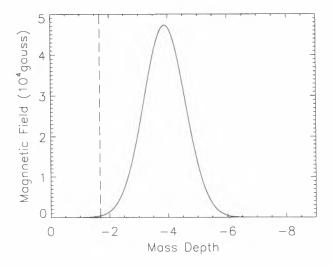


Figure 5. Distribution of the inferred magnetic field in the solar interior in 1989 according to the measured irradiance and photospheric temperature cyclic variations given in Figures 1 and 2. The vertical line indicates the base of the convection zone.

From this fit we find that the maximum magnetic field in the solar interior, B_m , is related to R_Z via

$$B_m = B_0 \{ 190 + [1 + \log_{10}(1 + R_Z)]^5 \}, \quad (1)$$

where R_Z is the yearly-averaged sunspot number, $B_0 = 90$ G. The profile of the magnetic energy per unit mass χ is described by a gaussian function

$$\chi = \chi_m \exp[-\frac{1}{2}(M_D - M_{\rm Dc})^2/\sigma^2],$$
 (2)

where $M_{\rm Dc} = -4.25$ specifies the location and $\sigma = 0.5$ specifies its width. B_m is used to determine χ_m . The mass depth M_D is defined as

$$M_D = \log_{10}(1 - M_r/M_{\odot})$$

Using Eqs. (1) and (2), we can extrapolate the solar irradiance back during the period when the annual

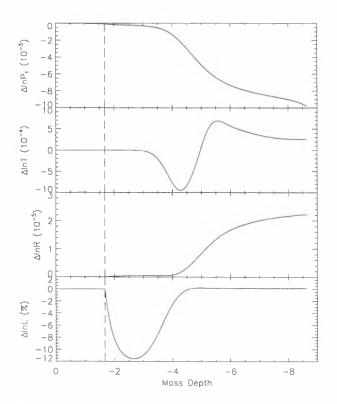


Figure 6. The structural changes caused by the magnetic field distributions given in Figure 5: relative pressure, temperature, radius and luminosity changes from top to bottom. The vertical line indicates the base of the convection zone.

sunspot numbers are available (Schove, 1983; Hoyt & Schatten , 1998), as shown in Figure 7.

As we can see from Fig. 7, the maximum variability of the solar radius is about 2×10^{-5} , or 0.02 arc s. Although this variation is in agreement with the most recent determination of the cycle radius variations obtained from the MDI experiment on SOHO (Emilio et al., 2000), it is much smaller than the radius changes determined from historical data over the last 2 centuries. In our view, the most reliable historical data sets from which solar radius changes can be determined are the duration of total eclipses measured near the edges of totality. From them, changes of the order of 0.5 arc s have been detected. In particular, a change of 0.34 arc s between 1715 and 1979 (Dunham et al., 1980), a change of 0.5 arc s between 1925 and 1979 (Dunham et al., 1980), and no change between 1979 and 1976 (Sofia et al., 1983), were detected. If such changes are real, what could cause them? What are the corresponding solar irradiance changes?

If we use the magnetic field location required to produce the 11 year cycle variability, we find that it is impossible to produce a 0.5 arcsec radius variation even if we apply an unreasonablely strong magnetic field. However, our model shows that the deeper the location of a magnetic field and the more intense the magnetic field, the larger the resulting radius change.

We thus compute the magnetic field required to pro-

duce the detected radius change between 1715 and 1979 as a function of mass depth, as displayed in the top panel in Fig. 8. It is well known that a strong magnetic field will cause a change of location of the boundary between the convective and the radiative region (Lydon & Sofia, 1995). The second panel from the top in this figure shows how the convection boundary R_{CZ} varies with the applied magnetic field (solid curve), and how the location of the maximal magnetic field, R_B , varies with the mass depth (dashed curve). The shadowed region indicates the half-width of the required magnetic field. Of particular relevance are the values corresponding to the base of the convection zone, as indicated by the dot-dashed line in this figure, since all conventional dynamo models locate the process precisely at that depth. There, the magnetic field required to cause a 0.34 arcsec change of the solar radius is 1.3 million G, and the resulting luminosity variation is 0.12 percent (the third panel of Fig. 8), which is almost equally due to the variation of effective temperature (the bottom panel) and radius, since the radius variation contributes $2 \times \Delta \ln R = 0.07\%$. These values are interesting for producing significant climate change if the solar variations are sufficiently long lasting, and for not grossly contradicting what we know about the Sun, excepting a value for the magnetic field that is larger than we are comfortable with, but it is not in conflict with helioseismology (Antia et al., 2000; Sofia & Li, 2000).

5. CONCLUSIONS

From what we present above, we reach the following conclusions:

- The total irradiance variation, and the photospheric temperature variation observed over the 11-year activity cycle can be explained in terms of the variation of an internal solar magnetic field of 20-47 kG located at $r = 0.96R_{\odot}$.
- The above result is in agreement with helioseismological data, and with the variations of the solar radius measured with MDI/SOHO.
- The extrapolation of this process to the past 2-3 centuries produces a change in luminosity of only 0.1%, and a radius change of only 0.02 arcsec.
- If radius variations of order 0.5 arcsec do occur, a larger (1.3 MG) variation of a field located below the base of the convection zone is required.
- The combined effect of both phenomena can yield a ΔL of 0.2% over many decades.

ACKNOWLEDGMENTS

This work was supported in part by a NASA grant and Li was supported by Natural Science Foundation

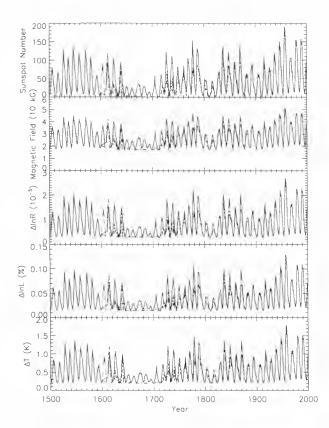


Figure 7. Solar variability in the past five centuries (solid curve corresponds to the Zürich sunspot number R_Z) and in the past four centuries (dashed curve conrresponds to the group sunspot number R_G). kG stands for kilo-Gauss. L for total solar luminosity, T for solar effective temperature, R for solar radius.

of China (project 19675064).

REFERENCES

- Fröhlich, C. & Lean, J. 1998, in IAU Sympsium 185: New Eyes to See Inside the Sun and Stars, ed. F.L. Deubner, (Dortrecht: Kluwer Academic Publ.), 89
- Ermolli, I., Berrilli, F., Florio, A. 2000, this proceedings
- Gray, D.F. & Livingston, W.C. 1997, ApJ, 474, 802
- Libbrecht, K. G., Woodard. M. F. 1990, Nature, 345. 779
- Bhatnagar, A., Jain. K., Tripathy, S. C., 1999, ApJ 521, 885
- Howe, R., Komm, R., Hill, F., 1999. ApJ 524, 1084
- Basu, D. 1998, Solar Phys., 183, 291
- Noël, F. 1997, A&A, 325, 825
- Emilio, M., Kuhn. J.R., Bush, R.I. & Scherrer. P. 2000, ApJL, in press
- Endal, A.S., Sofia, S. & Twigg, L.W. 1985, ApJ, 290, 748
- Lydon, T.J. & Sofia, S. 1995, ApJ Suppl., 101, 357
- Li, L. H., Sofia, S., submitted to ApJ (see astroph/0007203).

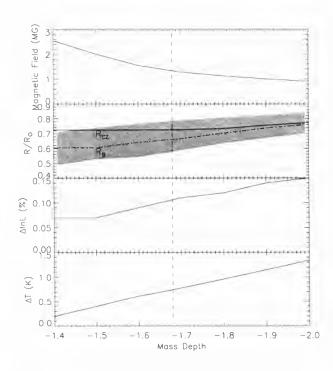


Figure 8. Solar variability corresponding to the probable change in the solar radius between 1715 to 1979. R_{CZ} is the location of the base of the convection zone, while R_B is the location of maximal magnetic field. MG stands for Million Gauss. The mass depth is defined as $\log(1 - M/M_{\odot})$ by the mass coordinate M. The smaller the mass depth, the closer to the surface of the model sun.

- Antia, H.M., Chitre, S.M., & Thompson, M.J. 2000, A&A, in press
- Schove, D. J., Sunspot cycles (Stroudsburg: Hutchinson Ross Publ., 1983), 10
- Hoyt, D. V., Schatten, K. H. 1998 Solar Phys. 181. 491
- Dunham, D. W., Safia, S., Fiala, A. D., Herald, D., Muller, P. M. 1980, Science, 210, 1243
- Sofia, S., Dunham, D. W., Dunham, J. B., Fiala, A. D. 1983, Nature, 304, 522
- Sofia, S. & Li, L. H., 2000, submitted to JGR

DRIFT-TIME MEASUREMENTS OF THE SOLAR DIAMETER 1990-2000: NEW LIMITS ON CONSTANCY

Axel D. Wittmann¹, Michele Bianda²

¹ Universitäts-Sternwarte, D-37083 Göttingen, Germany (wittmann@uni-sw.gwdg.de)

² Istituto Ricerche Solari, CH-6605 Locarno-Monti, Switzerland (mbianda@cscs.ch)

ABSTRACT

Drift-time measurements of the solar diameter have been made with two optically identical solar Gregory telescopes (aperture 45 cm) at Izaña/Tenerife and Locarno/ Switzerland. In contrast to some other authors the solar semidiameter R derived from these measurements does not show longterm variations in excess of about ± 0.0003 "/yr and does not show cycle-dependent variations in excess of about \pm 0.05". Our mean value for the solar semidiameter at unit distance is $R=(960.63\pm0.02)$ " from 7583 visual transit observations made at Izaña in 1990-2000, and R=(960.66±0.03)" from 2470 visual transit observations made at Locarno in 1990-1998. This applies to visual wavelengths of about 550 nm. At Izaña semidiameters were also measured photoelectrically from CCD transits at wavelengths of 486 nm and 583 nm; these are typically smaller by about 0.6" or 440 km.

I. INTRODUCTION

Since it was found that even the solar irradiation 'constant' is cycle-dependent (Willson et al., 1986; Willson and Hudson, 1988; Hudson, 1988) and varies in phase with the sunspot relative number (largest at solar maximum, smallest at solar minimum), the study of global properties of the sun, its outcrops of activity, and its influences on the earth and its climate has gained increased interest among scientists. Although solarterrestrial relations are essentially one-way (there is no significant influence of the earth on the sun), the global properties of the sun, such as its energy output, activity cycle, differential rotation, diameter variations, oscillations. etc., are of utmost importance for life on earth and its future, and, therefore, merit close investigation.

2. MEASUREMENTS

Here we report about measurements of the solar diameter which were made with two optically identical solar Gregory-type vacuum telescopes (D = 45 cm, f = 25.0 m) at Izaña/Tenerife (latitude 28.30°, altitude 2413 m) and Locarno-Monti/Switzerland (latitude 46.18°, altitude 506 m). The latter telescope is an almost identical re-build of the telescope formerly operated at IRS/Locarno by the Göttingen University Observatory. The technique we employed is drift-scan timing, which is the equivalent of classical transit timing (as employed, e.g., at Greenwich in 1750-1939), but at arbitrary hour angle using an equatorially-mounted solar telescope (for details see Wittmann, 1977; Wittmann et al., 1981). The principle of the method is to measure the time is takes the solar disk to pass, due to diurnal rotation at the equatorial rate of ~15 "/s, across a fiducial mark representing a fixed hour angle (with the telescope at rest at that angle). The transit of both limbs (west limb preceeding, east limb following) is observed and timed either visually using a white-light projected image or electronically using a monochromatic CCD image and a fast frame grabber (see Wittmann, 1997). Both methods have their pros and cons, but from practical experience we conclude that a carefully-made visual observation is worth about eight or ten single CCD pictures. Figure 1 shows two typical transit sequences taken by CCD (visual transits can't be shown, but are looking quite similar): The first 8 frames of each series show the passage of the W-limb, the last 8 frames show the passage of the E-limb. The header of each frame carries an accurate timing mark (UT), which is also shown in Figure 1.

3. **REDUCTION**

The measured drift times T, which depend on the geocentric distance r, the geocentric declination δ , and the proper motion d α /dt of the sun, were reduced to the equator ($\delta = 0$) and to unit distance (r = 1 au) using the formalism described by Wittmann and Neckel (1996). Our final results are tabulations of the measured drift time T (s) and of the semidiameter R (") at unit distance as function of date (e.g. JD) and time (e.g. UT).

Using numerical techniques of superposed epoch analysis and maximum entropy power spectral analysis we have analyzed our data in order to detect periodicities or other systematic variations, but - with perhaps one exception (a rotation-coupled modulation of shape at the limit of detectability, cf. Mikhailutsa et al., 2000) - we did not find such variations. We can neither detect a significant (i.e., larger than ± 0.06 ") dependence on heliographic latitude in our observations, which - due to the seasonal change of the position angle of the sun's axis cover a latitude range of only $\pm 26^{\circ}$ around the equator.

4. **RESULTS**

Figure 2 shows the solar semidiameter measured at Locarno in 1990-1998 (top) and at Tenerife in 1990-2000 (bottom). Due to the priority of other observational projects at Locarno, the measurements there have last been made on November 7, 1998.

Proc. 1st Solar & Space Weather Euroconference, 'The Solar Cycle and Terrestrial Climate', Santa Cruz de Tenerife, Spain, 25-29 September 2000 (ESA SP-463, December 2000)

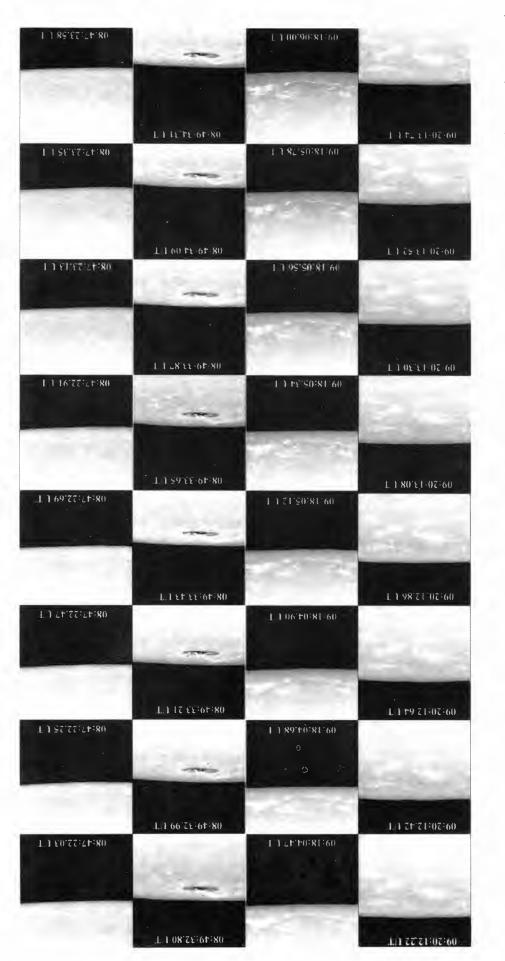


Figure 1: Drift scan observations made at the GCT on 11 August 1997 (486 nm, top two panels) and on 04 April 2000 (583 nm, bottom two panels; note the increased facular activity). Each CCD frame, of which 32 are shown here, has an angular size of 92×92 ." The upper two panels show, from left to right, the passage of the W-limb at 8:47 UT and the passage of the E-limb (with a sunspot) at 8:49 UT (T=130.85 s, R=959.81"). The lower two panels show the passage of the W- limb at 9:18 UT and the passage of the E-limb at 9:20 UT (T=128.62 s, R=960.09").

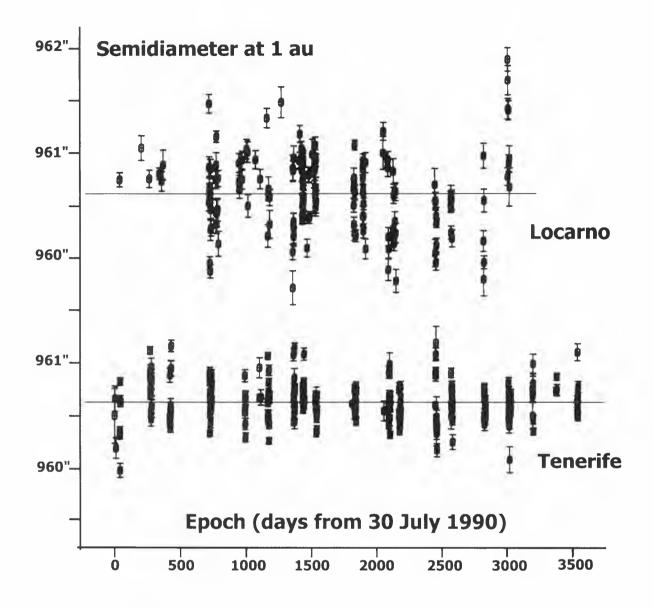


Figure 2: Semidiameter results from Locarno (1990-1998, top) and Tenerife (1990-2000, bottom). The daily mean values of the solar semidiameter (148 for Locarno, 232 for Izaña) are plotted as a function of time. One-sigma error levels are indicated by error bars (which, however, due to the relatively small dispersion of the diagram, mostly blend with their neighbors). Time is reckoned in days from 30 July 1990 0 UT. so that, e.g., 04 April 2000 0:00 UT is 3536.0 days from the initial epoch. The horizontal clustering of points reflects the distribution of the observing campaigns over the years (no drift observations were made during the winter season, when the conditions use to be fairly bad at both sites).

Table 1. Annual mean semidiameters (seconds of arc). N is the number of observations

Year	N	Wittmann	N	Noel	N	Bianda	N	Laclare
1990	363	960.48 ± 0.04	124	961.06 ± 0.07	48	960.74 ± 0.13	353	959.38 ± 0.02
1991	1002	960.71 ± 0.02	104	960.78 ± 0.06	92	960.83 ± 0.09	266	959.44 ± 0.02
1992	570	960.67 ± 0.02	160	960.63 ± 0.06	322	960.57 ± 0.04	293	959.40 ± 0.02
1993	802	960.63 ± 0.02	292	960.49 ± 0.03	266	960.74 ± 0.05	347	959.39 ± 0.01
1994	1176	960.68 ± 0.02	248	960.24 ± 0.03	655	960.66 ± 0.03	267	959.47 ± 0.02
1995	481	960.66 ± 0.02	230	960.08 ± 0.03	320	960.57 ± 0.04	273	959.48 ± 0.02
1996	879	960.59 ± 0.02	246	959.85 ± 0.03	265	960.43 ± 0.05	313	959.47 ± 0.02
1997	643	960.62 ± 0.03	240	960.00 ± 0.03	276	960.39 ± 0.05	392	959.52 ± 0.02
1998	1012	960.60 ± 0.02	316	960.27 ± 0.03	226	961.01 ± 0.08	357	959.52 ± 0.01
1999	359	960.68 ± 0.04	400	960.47 ± 0.03				
2000	296	960.67 ± 0.04	258	960.41 ± 0.03				
	7600	0.00.000	0(10	0(0.00 + 0.01	0.470	0.00.00.004	20(1	0.50 45 + 0.00
Mean:	1583	960.63 ± 0.02	2618	960.39 ± 0.01	2470	960.66 ± 0.04	2861	959.45 ± 0.02

Table 1 shows a comparison of annual mean values of the solar semidiameter as observed by A.D. Wittmann at Izaña/Tenerife until 10 April 2000, M. Bianda at Locarno until 7 November 1998, F. Noel at Santiago de Chile until 11 August 2000, and by F. Laclare at Calern until 25 September 1998 (the latter data were taken from the tabulation in the web pages of Observatoire de la Côte d'Azur).

Whereas some authors have found significant variations of the solar diameter during the 11-yr cycle (Delache et al., 1988; Delache et al., 1993; Jimenez et al., 1994; Ulrich and Bertello, 1995; Laclare et al., 1996; Noel, 1997; Noel, 1998; Rozelot, 1998; Noel 1999; Noel, 2000), we do not detect longterm variations, in particular cycle-dependent variations, in excess of about ± 0.0003 "/yr, and we do not detect short-term variations, in particular seasonal variations, in excess of about ± 0.05 " (cf. Figure 2). This is in agreement with, e.g., Brown and Christensen-Dalsgaard (1998), who have not found long-term variations in excess of $\pm .05$ " in the HAO series of automated photoelectric transit measurements (Brown et al., 1982) during 1981-1987. Although Wittmann et al. (1993) have detected a sudden change in their diameter data, this is most probably due to the change of circumstances and the first interruption of the Locarno series in 1982.

ACKNOWLEGEMENTS

The GCT at Izaña is operated by Universitäts-Sternwarte Göttingen (USG) at the Spanish Obervatorio del Teide of the Instituto de Astrofisica de Canarias (IAC). The GCT at Locarno is operated by Fondazione IRSOL (Locarno). Special thanks are due to Eduardo Alge (Locarno) for making additional drift scan measurements in 1990-1996. We wish to thank Fernando Noel (Santiago de Chile) for many personal communications and for generously providing us with his most recent results prior to publication.

REFERENCES

Brown, T.M., Elmore, D.F., Lacey, L., Hull, H., 1982, Appl. Opt. 21, 3588.

Brown, T.M, Christensen-Dalsgaard, J., 1998, ApJ. 500, L195.

Delache, Ph., Laclare, F., Sadsoud, H., 1988, in: Chri-

stensen-Dalsgaard, J., Frandsen, S. (eds.), Advances in

Helio- and Asteroseismology, pp. 223-226, Dordrecht.

Delache, Ph., Gavryusev, V., Gavryuseva, E., Laclare, F.,

Régulo, C., Roca Cortés, T., 1993, ApJ. 407, 801.

Hudson, H.S., 1988, Ann. Rev. Astron. Astrophys. 26, pp. 473-507.

Jimenez, A., Hernandez, P., Claret, A., Palle, P.L., Régulo, C., Roca Cortés, T., 1994, ApJ. 435, 874.

Laclare.F., Delmas,C., Coin,J.P., Irbah,A., 1996, Solar Phys. 166, 211.

Mikhailutsa, V.P., Wittmann, A.D., Bianda, M., 2000,

- Astron. Astrophys. Transact. 18 (in press).
- Noel, F., 1997, Astron. Astrophys. 325, 825.

Noel, F., 1998, Astron. Astrophys. Suppl. Ser. 132, 219.

Noel, F., 1999, Astron. Astrophys. 343, 1001.

Noel, F., 2000, in: Proc. 5th Summer School on Solar

Astrophysics, Snt. Pierre d'Oleron, France (in press).

Rozelot, J.P., 1998, Solar Phys. 177, 321.

Ulrich, R.K., Bertello, L., 1995, Nature 377, 214.

Willson, R.C., Hudson. H.S., Fröhlich, C., Brusa, R.W., 1986, Science 234, 1114.

Willson, R.C., Hudson, H.S., 1988, Nature 332, 810.

Wittmann, A., 1977, Astron. Astrophys. 61, 225.

Wittmann, A., Bonet, J.A., Wöhl, H., 1981, in: Cram, L.E.,

- Thomas, J.H. (eds.), The Physics of Sunspots, pp. 424-433,
- National Solar Observatory, Sunspot, NM.

Wittmann, A.D., Alge, E., Bianda, M., 1993, Solar Phys. 145, 205.

Wittmann, A.D., Neckel, H., 1996, Solar Phys. 163, 1. Wittmann, A.D., 1997, Solar Phys. 171, 231.

SOLAR SURFACE MAGNETISM AND THE INCREASE OF SOLAR IRRADIANCE BETWEEN ACTIVITY MINIMUM AND MAXIMUM

Marcel Fligge¹, Sami K. Solanki², Nadège Meunier³, and Yvonne C. Unruh⁴

¹Institute of Astronomy, ETH Zentrum, CH-8092 Zurich, Switzerland

²Max-Planck-Institut für Aeronomie, D-37191 Katlenburg-Lindau, Germany

³W. W. Hansen Experimental Physics Laboratory, Annex A207, Stanford University, Stanford, CA 94305-4085 ⁴Institute for Astronomy, University of Vienna, Türkenschanzstrasse 17, A-1180 Wien, Austria

ABSTRACT

We present model reconstructions of solar total and spectral irradiance variations based on the assumption that solar irradiance changes are entirely produced by solar surface magnetic features.

The model makes use of calculations of sunspot and facular contrasts as a function of wavelength and limb angle. The distribution of magnetic features on the solar surface is extracted from averaged MDI magnetograms.

We reconstruct the irradiance measured by VIRGO between 1996 and 2000, i.e. from the onset of solar cycle 23 right into its maximum. Preliminary results show that the model is able to reconstruct both short-term (days to weeks) and long-term (years) solar irradiance variations simultaneously. No further component of non- or only indirectly magnetic origin is necessary to explain the observed irradiance changes.

Key words: Solar Irradiance; Faculae; Sunspots; Active Network.

1. INTRODUCTION

Solar irradiance variations are closely related to the evolution of the magnetic field at the solar surface (Foukal & Lean. 1988; Lean et al., 1998; Fligge et al., 2000; Fligge & Solanki, 2001). The appearance and evolution of active regions on the solar surface leaves distinct fingerprints in modern irradiance records which can easily be measured with space-borne instruments (Hudson et al., 1982; Willson & Hudson, 1988; Fröhlich, 2000). Sunspots and active regionfaculae, hence, are generally considered to be the dominant contributors to solar irradiance changes on time-scales of days to weeks (Fröhlich & Pap, 1989; Fligge et al., 1998, 2000).

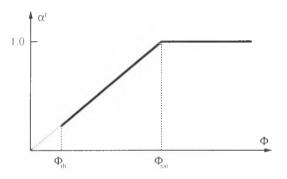


Figure 1. Relationship used to convert magnetic flux Φ measured within a pixel of a magnetogram into a corresponding facular filling factor α^{f} . The facular filling factor α^{f} increases linearly from $\Phi_{\rm th}/\Phi_{\rm sat}$ at the threshold flux, $\Phi_{\rm th}$, to 1.0 at the saturation flux, $\Phi_{\rm sat}$.

The origin of the longer-term increase of solar irradiance between activity minimum and maximum is less clear, however, and still widely debated. Small-scale magnetic elements composing the active network can be expected to contribute substantially to the observed irradiance increase during activity maximum (Foukal & Lean, 1988; Solanki & Fligge, 2001). However, other sources of non-magnetic or only indirectly magnetic origin have also be proposed, based on, e.g., the theory of r-mode oscillations (Wolff & Hickey, 1987a,b) or photometric measurements of the solar limb reported by Kuhn et al. (1988) and Kuhn & Libbrecht (1991).

In the following, we present a model of solar irradiance variations that is entirely based on temporal changes of the surface distribution of the solar magnetic field. Within a single run the model reproduces both, solar irradiance changes on time-scales of days to weeks as well as the long-term increase of solar irradiance on the solar cycle time-scale. The model has only a single free parameter to be fixed by fitting the VIRGO (Variability of IRradiance and Gravity Oscillations, Fröhlich et al., 1995). This provides further evidence that it is indeed the magnetic field at

Proc. 1st Solar & Space Weather Euroconference, 'The Solar Cycle and Terrestrial Climate', Santa Cruz de Tenerife, Tenerife, Spain, 25-29 September 2000 (ESA SP-463, December 2000)

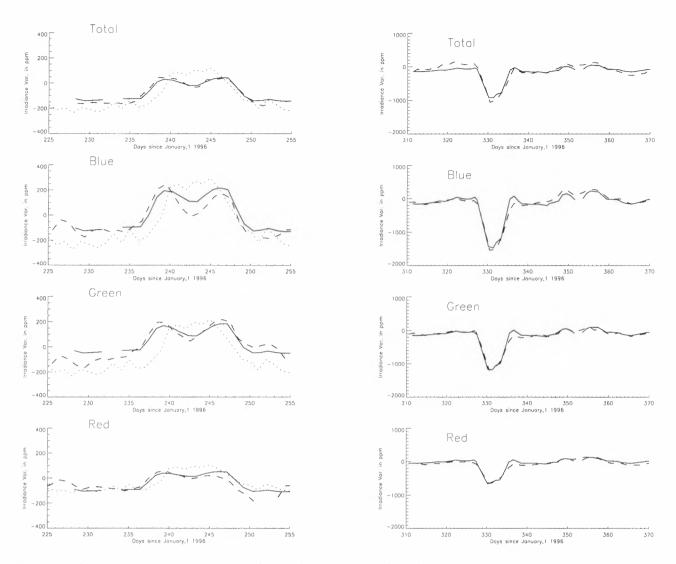


Figure 2. Comparison between measured (dashed) and modeled (solid) solar total and spectral irradiance variations for the time between 15 August and 15 September 1996 (left panel) and 6 November 1996 and 6 January 1997 (right panel), respectively. Plotted are (from top to bottom) the total irradiance, and the spectral irradiance variations measured in the blue, green and red color channels of VIRGO, respectively. Our model reproduces the double-peaked structure originating from the CLV of the facular contrast (left panel). However, some deviations from the measurements remain unexplained. For comparison, the dotted curve in the left panel shows a reconstruction which neglected the CLV of the facular contrast. The dimming of solar irradiance due to the passage of sunspots (right panel) is also well reproduced. (From Fligge et al., 2000)

the solar surface which is responsible for by far the largest fraction of the observed irradiance variations – at least on time-scales accessible by modern measurements.

2. THE IRRADIANCE MODEL

The irradiance model described below rests upon the following basic assumptions. Firstly, we assume that irradiance variations are entirely caused by the magnetic field at the solar surface. This premise implies that no additional component of non-magnetic or only indirectly magnetic origin is necessary to explain the observed irradiance changes. Secondly, it is sufficient to divide the solar surface into only the following components, i.e. quiet Sun, sunspots (for which umbral and penumbral regions are treated separately, however) and faculae. In particular, active region faculae and the active network features are described by the same model atmosphere. Finally, the atmospheric models used to calculate the intensity spectra of each individual component do not change in time. Temporal variations are exclusively due to the changing surface coverage of the Sun by the individual components.

Within the framework of this model, two basic ingredients are necessary to reconstruct solar irradiance variations. Firstly, we need a detailed description of the distribution of the magnetic field on the solar surface and its evolution in time. This can be gained from a careful analysis of a time series of full-disc magnetograms.

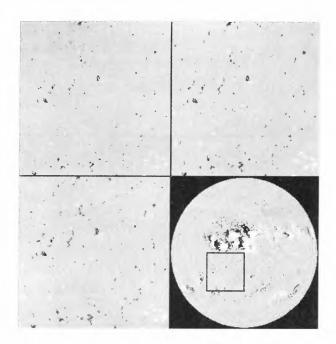


Figure 3. Extraction of the active network from MDI magnetograms averaged over 1-min (upper left), 5-min (upper right) and 20-min (lower left), respectively. The frame in the full-disc magnetogram (lower right) marks the considered network region.

Secondly, the intensity I of each individual component as a function of wavelength λ and position $\mu\,=\,\cos\theta$ (where θ is the heliocentric angle) on the solar disc must be known. These are calculated using Kurucz' spectral synthesis code ATLAS9 (Kurucz. 1992) from plane-parallel model atmospheres of the quiet Sun, sunspot umbrae. sunspot penumbrae and faculae. We use the standard model atmosphere FAL-C (Fontenla et al., 1993) for the quiet Sun and an appropriate radiative equilibrium model (Kurucz, 1991) for the sunspots (cf. Severino et al., 1994; Solanki, 1997). The umbra is represented by a model atmosphere of $T_{eff} = 4500$ K while $T_{eff} = 5400$ K has been chosen for the penumbra. The employed facular model is a slightly modified version of FAL-P of Fontenla et al. (1993) for which details are given by Unruh et al. (1999).

The intensity of a pixel (i, j) on the solar surface at wavelength λ and time t can then be written as a sum over the contributions from the individual components, i.e.

$$I_{i,j}(\lambda;t) = \sum_{x=u,p,f} \alpha_{i,j}^{x}(\Phi;t) \cdot I^{x}(\mu(i,j),\lambda) \quad (1)$$

+
$$(1 - \sum_{x=u,p,f} \alpha_{i,j}^{x}(\Phi;t)) \cdot I^{q}(\mu(i,j),\lambda),$$

where $I^{u.p.s.q}(\mu, \lambda)$ stands for the intensity spectrum of the umbral, penumbral. facular and quiet Sun component, respectively.

The filling factors $\alpha_{i,j}^{u.p.f.q}(\Phi;t)$, i.e. the fractional

coverage of any pixel (i, j) by one of the components, are extracted from full-disc magnetograms by converting the measured magnetogram signal Φ into the corresponding filling factor α (where $\Phi = \phi/\mu$ and ϕ is the magnetogram signal). For sunspots (umbra and penumbra) we set $\alpha_{i,j}^p = \alpha_{i,j}^p = 1$ since they are well resolved by the used MDI full-disc magnetograms. Faculae are more loosely packed and we expect $\alpha_{i,j}^f < 1$ for the weaker features. The applied conversion scheme for faculae is shown in Fig. 1. Starting at Φ_{th} , i.e. the threshold value given by the noise level of the magnetograms, the filling factor increases linearly to $\alpha^f = 1$ at Φ_{sat} . The Φ_{th} , the only free parameter in our model, is determined by requiring that the model should reproduce the observed irradiance variations.

Finally, the irradiance is calculated by integrating the intensity over the whole solar disc, i.e. by summing up the contributions from the individual pixels.

3. RESULTS

3.1. Short-term variability

The model has first been used to reconstruct solar irradiance variations over a time period of, respectively, one and two month during activity minimum when the influence of single active regions on solar irradiance can be studied particularly well. The results, presented in Fig. 2, are compared to VIRGO measurements of the total as well as spectral irradiance variations at 862 nm. 500 nm and 402 nm. During the first time period from mid August to mid September 1996 (left panel of Fig. 2) a faculae dominated active region crossed the solar disc. The observed irradiance record (dashed line) shows a distinct double peak which is well reproduced by our model (solid line) in all four spectral regions. The double peak is due to the pronounced center-to-limb variation (CLV) of the facular brightness whose contrast increases strongly towards the solar limb. For comparison, a second reconstruction (dotted line) based on a disc-integrated proxy for the facular emission (i.e. Mg II core-to-wing ratio) fails completely to reproduce the double peak.

The second period from the beginning of November 1996 to the beginning of January 1997 is plotted in the right panel of Fig. 2. This time, a spot dominated active region moved across the solar disc. Again, the reconstruction reliably reproduces the spot-induced depletion of the solar irradiance.

3.2. Long-term variability

When reconstructing irradiance changes on timescales of the solar cycle great care must be taken in order to include also subtle changes of the active



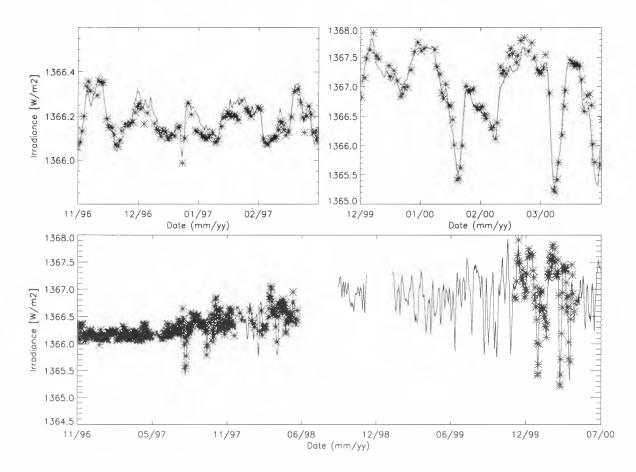


Figure 4. Reconstruction (stars') of total solar irradiance for roughly 700 individual days between the end of 1996 and mid 2000, i.e. from the onset of solar cycle 23 right into its maximum. The irradiance record measured by VIRGO is represented by the solid line. The two panels on the top show a zoom-in to the beginning (left panel) and the end (right panel) of the complete dataset (lower panel), respectively. The model is able to reproduce both, short-term variations on time-scales of days to weeks as well as the longer-term increase of solar irradiance between activity minimum and maximum.

network. The 1- σ noise level of ordinary 1-min magnetograms of MDI is of the order of 20 Gauss. This is not good enough to enable a reliable detection of all or at least most of the network features. Therefore, it is necessary to average over series of 5 or 20 consecutive magnetograms in order to increase the signal-to-noise ratio. Before averaging, the individual 1-min magnetograms have been corrected for differential rotation.

The effect of the averaging on the detection of the active network is presented in Fig. 3. The magnetograms on the upper left (1-min). upper right (5-min) and lower left (20-min), respectively, are enlargements of the frame plotted in the full-disc magnetogram in the lower right. As can be seen, more and more network features become visible when going to longer averages or, equivalently, longer integration times.

Based on these magnetograms, we then reconstructed solar irradiance variations for roughly 700 individual days between the end of 1996 and mid 2000 using exactly the same model atmospheres and input parameters as for the short-term reconstructions described in Sect. 3.1. The results are presented in Fig. 4. The VIRGO measurements are given by the solid line while the reconstructed values are marked by stars.

The lower panel shows the reconstruction over the whole time period. As you can see, the increase between the onset of solar cycle 23 at the end of 1996 and the first half of 2000 when solar activity reached its maximum is very well reproduced. This becomes even more striking when looking at the two enlargements on the top of Fig. 4. The left panel is a zoom-in to the beginning of the selected time period, i.e. near the activity minimum. while the panel on the right is a zoom-in during the time of maximum activity. The quality of the reconstruction is impressive given the simplicity of the employed model and the fact that it possesses only a single free parameter.

The model allows the calculation of solar spectral irradiance variations from 160 nm to 160 000 nm with varying spectral resolution (resolving power better than 200 in the visible). Unfortunately, the longterm sensitivity of VIRGO's sunphotometers is not stable enough to allow a comparison of the reconstructed and measured spectral irradiance records over such a long period. Nevertheless, we present

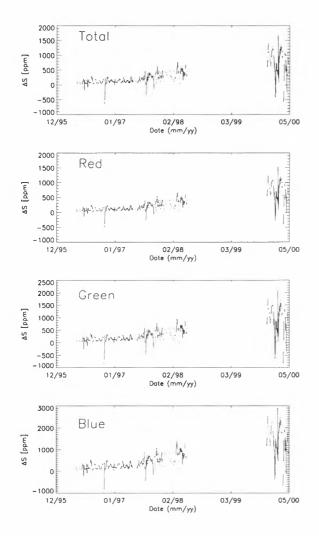


Figure 5. From top to bottom: Reconstructed irradiance variations for the total solar irradiance as well as for the three spectral channels measured by VIRGO which are centered around 862 nm, 500 nm and 402 nm. The irradiance increase between activity minimum and maximum is most pronounced in the blue channel which shows an increase that is about twice as large as the one in the total.

in Fig. 5 the reconstructed irradiance records for the four spectral regions measured by VIRGO, i.e. the total irradiance as well as the irradiance in the three spectral channels centered around 862 nm, 500 nm and 402 nm, respectively. The blue channel shows the steepest rise, reflecting the increase of solar spectral irradiance variability towards shorter wavelengths. While the total and the red channel show comparable variations the increase is the blue is about twice as large as in the total (note the different scaling of the axis').

4. CONCLUSIONS

We have presented a model of solar irradiance variations which is entirely based on the changing solar surface magnetic field. The model is able to reproduce both total and spectral solar irradiance changes on time-scales of days up to the length of the solar cycle. In particular, no additional component is necessary to reproduce the long-term increase of solar irradiance between activity minimum and maximum beside the contributions from sunspots and small magnetic features forming faculae and the active network. In particular, there is no need to distinguish between the contribution of the network and of faculae.

REFERENCES

- Fligge M., Solanki S.K., 2001, J. Astrophys. Astr., in press
- Fligge M., Solanki S.K., Unruh Y.C., Fröhlich C., Wehrli C., 1998, Astron. Astrophys., 335, 709
- Fligge M., Solanki S.K., Unruh Y.C., 2000, Astron. Astrophys., 353, 380
- Fontenla J.M., Avrett E.H., Loeser R., 1993, Astrophys. J., 406, 319
- Foukal P., Lean J., 1988, Astrophys. J., 328, 347
- Fröhlich C., 2000, Space Science Revies, in press
- Fröhlich C., Pap J.M., 1989, Astron. Astrophys., 220, 272
- Fröhlich C., Romero J., Roth H., et al., 1995, Sol. Phys., 162, 101
- Hudson H.S., Silva S., Woodard M., Willson R.C., 1982, Sol. Phys., 76, 211
- Kuhn J.R., Libbrecht K.G., 1991, Astrophys. J., Lett., 381, L35
- Kuhn J.R., Libbrecht K.G., Dicke R.H., 1988, Science, 242, 908
- Kurucz R.L., 1991, In: Crivellari L., Hubeny I., Hummer D.G. (eds.) Stellar Atmospheres - Beyond Classical Models, 441–448, Kluwer, Dordrecht
- Kurucz R.L., 1992, Revista Mexicana de Astronomia y Astrofísica, 23, 187
- Lean J.L., Cook J., Marquette W., Johannesson A., 1998, Astrophys. J., 492, 390
- Severino G., Gomez M.T., Caccin B., 1994, In: Rutten R.J., Schrijver C.J. (eds.) Solar Surface Magnetism, 169–177, Kluwer, Dordrecht
- Solanki S.K., 1997, In: ASP Conf. Ser. 118: 1st Advances in Solar Physics Euroconference. Advances in Physics of Sunspots, 178
- Solanki S.K., Fligge M., 2001, Adv. Space Res., submitted
- Unruh Y.C., Solanki S.K., Fligge M., 1999, Astron. Astrophys., 345, 635
- Willson R.C., Hudson H.S., 1988, Nature, 332, 810
- Wolff C.L., Hickey J.R., 1987a, Sol. Phys., 109, 1
- Wolff C.L., Hickey J.R., 1987b, Science, 235, 1631

Mechanisms of Solar-Terrestrial Relations

GLOBAL AVERAGE UPPER OCEAN TEMPERATURE RESPONSE TO CHANGING SOLAR IRRADIANCE: EXCITING THE INTERNAL DECADAL MODE

Warren B. White¹, Michael D. Dettinger¹, Daniel R. Cayan¹

Scripps Institution of Oceanography, University of California San Diego 9500 Gilman Drive, La Jolla, CA, 92037, USA Tel: 858-534-4826 Fax: 858-534-7452 E-mail: <u>wbwhite@ucsd.edu</u> Tel: 858-534-44507 Fax: 858-534-7452 <u>dcayan@ucsd.edu</u> Tel: 858-822-1507 Fax: 858-534-7452 mddettin@usgs.gov

Global-average upper ocean temperatures Abstract: anomalies of $\pm 0.05^{\circ}$ K fluctuate in fixed phase with decadal signals in the Sun's irradiance of ± 0.5 Watts m⁻² over the past 100 years (White et al., 1997), but its amplitude is 2 to 3 times that expected from the transient Stefan-Boltzmann radiation balance (White et al., 1998). Examining global patterns of upper ocean temperature and lower troposphere winds find the internal interannual mode of variability in Earth's ocean-atmosphere-terrestrial system with global-average upper ocean temperature anomalies of ±0.05°K occurring naturally, independent of changing solar irradiance (White et al., 2000). Yet coherence and phase statistics indicate that the observed internal decadal mode in Earth's ocean-atmosphereterrestrial system is excited by the decadal signal in the Sun's irradiance. To understand the thermodynamics of this association we conduct a global-average upper ocean heat budget utilizing upper ocean temperatures from the SIO reanalysis and air-sea heat and momentum fluxes from the COADS reanalysis, finding the source of decadal global warming to be the reduction in trade wind intensity across the tropics, decreasing global average latent heat flux out of the ocean. We demonstrate that this reduction in trade wind intensity in the Pacific Ocean is governed by a delayed action oscillator mechanism in the oceanatmosphere system differing little from that used to explain the El Niño-Southern Oscillation (Graham and White, 1998). We operate an intermediate coupled model of this delayed action oscillator, normally driven by white noise, by superimposing the Stefan-Boltzmann upper ocean temperature response to decadal changes in the Sun's irradiance. We find the latter, with weak amplitude of ±0.02°K and non-random phase, able to excite a decadal signal in this delayed action oscillator, yielding a damped resonance response of ±0.1°K in the equatorial

Pacific Ocean, with dissipation provided by longwave radiation to space.

1. Background

White, Lean, Cayan, and Dettinger (1997; hereafter known as WLCD) examined time sequences of global and basin average upper ocean temperature based upon the examination of the Global Ice and Sea Surface Temperature (GISST) sea surface temperature data set from 1900 to 1994 (Folland and Powell, 1994) and the National Oceanographic Data Center (NODC) vertical temperature profile data set from 1955 to 1994 (White, 1995), together with time sequence of changes in the Sun's irradiance estimated over the past century by Lean et al. (1995). Using power spectra and multi-channel singular spectrum analysis, they found spectral peaks for decadal (9 to 13 years) and interdecadal (18 to 25 years) period scales in both the Sun's irradiance and global-average sea surface temperature records significantly correlated with each other over the 95 years from 1900 to 1994. Subsequently, WLCD band-pass-filtered these upper ocean temperature datasets with half-power points at 8 and 15 year periods for the decadal signal and at 15 and 30 year periods for the interdecadal signal, finding global and basin averages ranging over $\pm 0.05^{\circ}$ K ($\pm 0.07^{\circ}$ K) on decadal (interdecadal) period scales, with estimated standard errors of $\pm 0.01^{\circ}$ K, associated with changes in the Sun's irradiance ranging over ± 0.5 W m⁻² (± 0.3 W m⁻²) (see Figure 1a and Figure 1b). These global average temperature signals were observed to lag corresponding signals in the Sun's irradiance by 30° to 45° of phase in an apparent response to changes in the Sun's surface radiative forcing of about ± 0.1 Watts m⁻² averaged over the Earth's surface.

Examination of the NODC temperature profile dataset by WLCD allowed solar-related signals in globalaverage upper ocean temperature on decadal and

Proc. 1st Solar & Space Weather Euroconference, 'The Solar Cycle and Terrestrial Climate', Santa Cruz de Tenerife, Tenerife, Spain, 25-29 September 2000 (ESA SP-463, December 2000)

interdecadal period scales to be observed penetrating from 40 to 120 m into the upper ocean into the upper portion of the main pycnocline, with shallower (deeper) penetration in the tropics (extratropics) (see Figure 2). Below these relatively shallow depths, global-average temperature changes were uncorrelated with changes in the Sun's irradiance, with deeper penetration appearing to be resisted by vertical stratification within the main body of the main pycnocline separating the upper ocean from the deep ocean. So the excess heat storage associated with changes in the Sun's solar radiative forcing on decadal and interdecadal period scales was found trapped in the upper layer of the global upper ocean above the main pycnocline, presumably balanced there by radiative-plus-turbulent heat loss to the overlying atmosphere.

Subsequently, White, Cayan, and Lean (1998) demonstrated that changes in global average sea surface temperatures (SST's) are geophysically irrelevant when considering the Earth's global-average oceanic response to changes in the Sun's surface radiative forcing; that is, SST's change for reasons independent of changing net heat flux divergence, as for example from vertical mixing at the base of the near-surface mixed layer. Instead they recognized the importance of selecting an upper ocean temperature variable that represents changes in the diabatic heat storage (DHS) of the upper ocean above the main pycnocline (Moisan and Niiler, 1998). Subsequently, they computed basin average, tropical average, and global average upper ocean DHS changes directly from the available NODC temperature profile dataset, associating them with changes in the Sun's surface radiative forcing on decadal and interdecadal period scales. They constructed gridded fields of DHS changes, and corresponding depth average temperature (DAT) changes from the sea surface to the top of the main pycnocline, from 20°S to 60°N from 1955 to 1996.

White et al. (1998) found decadal and interdecadal DAT anomalies larger than expected from the perturbation form of the Stefan-Boltzmann radiation balance for the Earth's surface (i.e., 0.3°K per W m⁻²) in response to observed changes in the Sun's surface radiative forcing of ± 0.1 Watts m⁻² on decadal and interdecadal period scales (Wigley and Raper, 1990; Reid, 1991). Moreover, by examining the transient global average heat budget of the upper ocean, with the Stefan Boltzmann radiation balance for the Earth's surface providing the steady state limit, White et al. (1998) found the global upper ocean temperature incapable of coming into radiation equilibrium with solar forcing on decadal timescales. They found the observed global average DAT response 2 to 3 times that expected of the transient Stefan-Boltzmann radiation response. Moreover, the phase lag between peak solar forcing and global average DAT anomalies was observed to be much less (that is, approaching 0°) that

expected from the transient radiation balance. These differences in both amplitude and phase indicated that global warming in the upper ocean on decadal period scales is larger than can be expected from changes in the Sun's surface radiative forcing. This suggested to White *et al.* (1998) that some internal positive feedback intensifies the upper ocean temperature response to changes in the Sun's irradiance.

2. Data and Methods

This work utilizes gridded fields of SST and SLP anomalies from the GISST data set over the globe (i.e., from 40°S to 60°N) constructed at the Hadley Center in the United Kingdom from 1900 to the 1995 (Folland and Powell, 1994). It also utilizes the diabatic heat storage (DHS) anomalies from 20°S to 60°N constructed from NODC vertical temperature profile data set at the Scripps Institution of Oceanography (SIO) in California from 1955 to 1998 (White, 1995). It makes use of gridded fields of SST anomalies and air-sea heat flux (Q) anomalies from 40°S to 60°N constructed by the National Centers for Environmental Prediction (NCEP) in the Washington D.C. from 1955 to 1998 (Kalnay et al., 1996). It also utilizes the Comprehensive Ocean-Atmosphere Data Set (COADS) Q anomalies from 20°S to 60°N from 1995 to 1998 (Woodruff et al. 1993; Slutz et al., 1995). These anomalies are band-pass filtered for decadal signals of 7 to15 year period (Kaylor, 1982), with the GISST SST data sets filtered from 1900 to 1994, the SIO, NCEP, and COADS data sets filtered from 1955 to 1998, with the same filter applied to anomalies in the Sun's irradiance estimated over the past century by Lean et al. (1995) over both record lengths.

2. Possible Scenarios for the Intensification of the Upper Ocean Temperature Response to the Decadal Signal in the Sun's Irradiance

Feedback scenarios for this observed intensification of the global average DAT response to changes in the Sun's irradiance appear at first glance to be obvious. For example, we might expect Sun-induced global warming to increase the moisture content in the troposphere, reducing latent heat from the sea surface and blocking longwave back radiation to space. Or we might expect Sun-induced global warming to decrease global average cloud cover, with anomalous extratropical subsidence dominating anomalous tropical cumulus convection, allowing more solar radiation to penetrate to the sea surface. Yet White et al. (1998) unveiled a situation more complex than this, finding internal modes of decadal and interdecadal variability in the Earth's ocean-atmosphere-terrestrial system phase locked to decadal and interdecadal signals in the Sun's irradiance (Figure 4).

White and Cayan (1998) went on to provide the first global description of upper ocean temperature, sea level pressure, and surface winds of the internal interdecadal signal, finding it characterized by global symmetries about the equator and between ocean basins. They constructed a delayed action oscillator model that could account for these symmetries and could produce 18 to 23 year quasiperiodic signals in the absence of interdecadal forcing by the Sun's irradiance. Last year, White et al. (2000a) found global average DAT anomalies of ±0.1°K associated with the El Niño-Southern Oscillation (ENSO) occurring independently of changes in the Sun's irradiance on interannual period scales (Figure 3), yet as large as those observed on decadal and interdecadal period scales. Recently, Tourre et al. (2000) found biennial, interannual, decadal, and interdecadal signals over the Pacific basin in covarying SST and SLP anomalies displaying patterns and evolution very similar to one another (Figure 5a and Figure 5b), suggesting that each signal arises from similar ocean-atmosphere coupling mechanisms, already fairly well understood on interannual period scales (Neelin et al., 1998). These results suggest that natural internal modes of variability occur within the Earth's ocean-atmosphereterrestrial system on biennial, interannual, decadal, and interdecadal period scales and that they are naturally associated with global-average SST and DAT warming and cooling. Thus, the task of understanding the intensification of global-average SST and DAT responses to changes in the Sun's irradiance becomes one of understanding how decadal and interdecadal modes of Earth's internal ocean-atmosphere-terrestrial system are excited by the decadal and interdecadal signals in the Sun's irradiance.

3. Excitation of Earth's Internal Decadal Mode by Decadal Signals in the Sun's Irradiance

We begin by examining the global-average upper ocean heat budget of the decadal signal to determine how global-average DHS anomalies are generated intrinsically, in the absence of decadal changes in the Sun's irradiance. This tells us whether turbulent air-sea heat fluxes or radiative air-sea heat fluxes dominate global warming and cooling of the upper ocean on decadal period scales. We focus on the tropical global-average DHS anomalies from 20°S to 20°N because they account for 85% of the global warming from 40°S to 60°N. We compare the anomalous global-average DHS tendency with global-average total air-sea heat flux (Q_T) anomalies and their components, the shortwave-minus-longwave radiative fluxe $(Q_{sw} - Q_{1w})$ anomalies and the sensible-plus-latent turbulent fluxes (Q_H + Q_E) anomalies, finding the latter dominating the former in Q_T (that is, $Q_{sw} - Q_{LW} - Q_H - Q_E$) and explaining the anomalous global-average DHS tendency (Figure 6a). Now we partition the latent heat flux anomaly (Q_E) into its two component parts; that is, the part due to changes in the background wind (Q_{EW}) and that due to changes in the gradient between specific humidity of the air and the saturated specific humidity at the sea surface (Q_{EE}), finding both contributing about equally to Q_E (**Figure 6b**). This indicates that anomalous global-average DHS warming (cooling) occurs in response to a decrease (increase) in the trade wind intensity across the global tropical ocean and to an increase (decrease) in moisture content in the overlying air column.

Now we seek to determine how these changes in trade wind intensity and moisture content over the global tropical ocean can occur within the context of an oceanatmosphere coupled system. White et al. (2000b) recently determined that the decadal signal in the ocean-atmosphere system in the Pacific Basin, observed earlier in Figure 5a and Figure 5b, obeys the same delayed action oscillator mechanism as the interannual signal, described previously by Graham and White (1988). To demonstrate this, we display time-distance diagrams of pycnocline depth anomaly propagating cyclonically around the tropical North Pacific Ocean from off the equator onto the equator for biennial, interannual, and decadal signals (Figure 7). This propagation of off-equatorial signals onto the equator (that is, westward propagating Rossby waves off the equator reflecting at the western boundary and initiating eastward propagating Kelvin waves on the equator) provides the delayed negative feedback required to produce quasi-periodic behavior in the coupled system. This reflection process works by changing the sign of the equatorial pycnocline depth anomalies, which in turn change the sign of the SST anomalies, which in turn change the sign of the anomalous trade wind forcing of off-equatorial pycnocline depth anomalies, which take another a half cycle to propagate westward and back onto the equator to initiate a delayed negative feedback. The fact that this delayed action oscillator can be seen operating on decadal period scales (right, Figure 7), with off-equatorial Rossby waves driven by the same changes in the trade winds that also account for Pacific tropical warming and cooling, indicates that the later derives from the former. So our task becomes one of establishing whether the decadal signal in the Sun's irradiance can excite this decadal signal in the delayed action oscillator model of the Pacific basin.

A conceptual model for this delayed action oscillator was constructed by Graham and White (1988), yielding the quasi-periodic behavior of El Niño. Subsequently Graham *et al.* (1990) found the gravestmode Rossby wave with peak amplitude near 8° latitude generating the quasi-periodic El Niño of 2 to 4 year period scale, while higher-mode Rossby waves, with peak amplitudes between 15° and 20° latitude and propagating westward with speeds much less than at 7° latitude, yield a quasi-periodic decadal signal of 10 to 12 year period scale (Figure 8). Now we utilize white noise to drive the delayed action oscillator model of Graham and White (1988) for 5000 years, finding a broad band of variability ranging from 2 to 10 years in the frequency spectrum, with peak variability near 4 year period scale (a, Figure 9). Now, if we augment this white noise with a small decadal signal in equatorial SST of 0.02°K, consistent with that expected from the transient Stefan-Boltzmann response to the decadal signal in the Sun's irradiance, then we find it preferentially exciting this decadal mode of variability of 11 year period in the delayed action oscillator model (a, Figure 9). This decadal response is in phase with the weak solar forcing, yielding significant squared coherence with it (b, Figure 9). Furthermore, the amplitude of this decadal signal, filtered from 7 to 15 years, is larger than the initial forcing of ±0.02°K, achieving equatorial SST anomalies of \pm 0.1°K (c, Figure 9). This suggests that the observed decadal signal in Figure 5a and Figure 5b arises from excitation of the delayed action oscillator mechanism in the real ocean by the relatively weak heating of the upper layer of the tropical Pacific Ocean by the decadal signal in the Sun's irradiance.

4. Discussion and Conclusions

Since scientists became aware of discrete biennial, interannual, decadal, and interdecadal signals in the global ocean-atmosphere system (for example, Mann et al., 1995), the search for the origin of each signal has been vigorous. Any number of coupled models have been developed to explain these signals, each believed to arise naturally as intrinsic modes in Earth's ocean-atmosphereterrestrial system. Yet in the search for the source of global-average upper ocean temperature changes (White et al., 1997, 1998), decadal and interdecadal signals in the Earth's ocean-atmosphere-terrestrial system were found to be phase locked to decadal and interdecadal signals in the Sun's irradiance. Moreover, White et al. (1998) found global-average upper ocean temperatures on decadal and interdecadal period scales larger than expected from the transient Stefan-Boltzmann response to changes in the Sun's irradiance, while White et al. (2000a) found the interannual signal yielding changes in global-average upper ocean temperature of similar magnitude, independent of changes in the Sun's irradiance. These results suggest the task of establishing how the Earth responds to decadal and interdecadal variability the Sun's irradiance is one of determining how Earth's internal decadal and interdecadal modes of variability are excited by this changing solar irradiance.

Here we find the decadal signal in the Pacific Ocean associated with the delayed action oscillator mechanism used to explain the quasi-periodicity of El Niño. Thus we drive an intermediate model of the delayed action oscillator with equatorial SST anomalies of $\pm 0.02^{\circ}$ K derived from the direct forcing of the decadal signal in the Sun's irradiance. In the absence of this regular solar forcing, white noise forcing produces a broad band of El Niño variability, with peak amplitude ranging from 3-to-5 year period. But with the addition of solar forcing, an additional signal is generated in the model at 11 year period, with an SST signature 2 to 3 times larger than that imposed on it by the solar forcing. This supports the hypothesis that the decadal signal in the Sun's irradiance excites the internal decadal mode in the Earth's ocean-atmosphere system and explains its quasi-periodicity.

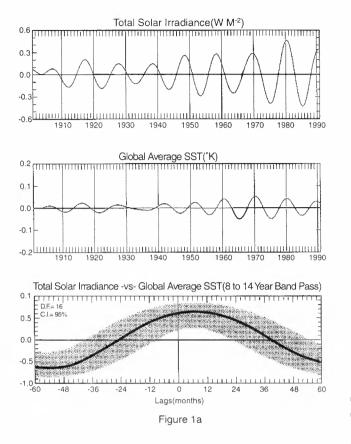
5. References

- Folland, D.K. and D.P. Powell, 1994. The Standard GISST Data Sets: Version 1 and 2. Climate Res. Tech. Note 56, Hadley Center, Met. Office, Bracknell, Berkshire, Eng., 50-51.
- Graham, N.E. and W.B. White, 1988. The El Niño cycle: a natural oscillator of the Pacific ocean-atmosphere system. *Science*, **240**, 1293-1302.
- Graham, N.E., W.B. White, and A. Pares-Sierra, 1990. Low frequency ocean-atmosphere interactions in the tropical Pacific. *In* Air-Sea Interaction in the Tropical Western Pacific. *Ed.* C. Jiping and J. Young, China Ocean Press, Beijing. 457-484.
- Kalnay and co-authors, 1996. The NCEP/NCAR 40-year reanalysis project. *Bull. Amer. Meteor. Soc.*, 77, 437-471.
- Kaylor R.E., 1977. Filtering and Decimation of Digital Time Series U.M.D., Tech. Rpt. Note, BN 850.
- Lean, J.L., J. Beer, and R. Bradely, 1995. Reconstruction of solar irradiance since 1610: implications for climate change. *Geophys. Res. Letters*, **22**, 3195-3198.
- Mann, M.E., J. Park, and R.S. Bradley, 1995. Global interdecadal and century-scale climate oscillations during the past five centuries, *Nature*, **378**, 266-270.
- Moisan, J.R. and P.P. Niiler, 1998. The seasonal heat budget of the North Pacific: net heat flux and heat storage rates (1950-1990). J. Phys. Oceanogr., 28, 401-421.
- Neelin, J.D., D.S. Battisti, A.C. Hirst, F.-F. Jin, Y. Wakata, T. Yamagata, S. Zebiak, 1998. ENSO theory. J. Geophys. Res., 103, 14,261-14, 290.
- Reid, G.C., 1991. Solar total irradiance variations and the global sea surface temperature record. *J. Geophys. Res.*, **96**, 2835-2844.
- Slutz, R.J., S.J. Lubker, J.D. Hiscox, S.D. Woodruff, R.L. Jenne, D.H. Joseph, P.M. Steurer, and J.D. Elms, 1985. Comprehensive Ocean-Atmosphere Data Set; Release 1, NOAA Environmental Research Lab., Boulder, CO, 268 pp.

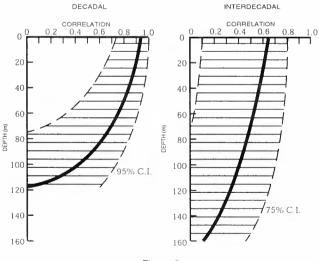
- Tourre Y.M., B. Rajagopalan, Y. Kushnir, M. Barlow, and W.B. White, 2000. Patterns of coherent decadal and interdecadal time scale variability in the Pacific Ocean during the 20th century. *Geophys. Res. Lett.* (in press).
- White, W.B., 1995. Design of a global observing system for basin-scale upper ocean temperature changes. *Progress in Oceanogr.*, **36**, 169-217.
- White, W.B., J. Lean, D.R. Cayan, and M. Dettinger, 1997. A response of global upper ocean temperature to changing solar irradiance. J. Geophys. Res., 102, 3255-3266.
- White, W.B. and D.R. Cayan, 1998. Quasi-periodicity and global symmetries in interdecadal upper ocean temperature variability. *J. Geophys. Res.*, **103**, 21335-21354.
- White, W.B., D.R. Cayan and J. Lean, 1998. Global upper ocean heat storage response to radiative forcing from changing solar irradiance and increasing greenhouse

gas/aerosol concentrations. J. Geophys. Res., 103, 21355-21366.

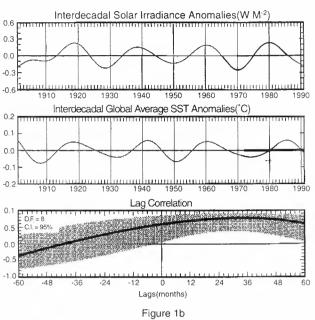
- White, W.B., D.R. Cayan, M.D. Dettinger, and G. Auad, 2000a. Sources of global warming in upper ocean temperature during El Niño. *J. Geophys. Res.*, (in press).
- White, W.B., Y.M. Tourre, B. Rajagopalan, Y. Kushnir, M. Barlow, 2000b. A delayed action oscillator mechanism shared by biennial, interannual, and decadal signals in the Pacific basin. J. Climate (in review).
- Wigley, T.M.L. and S.C.B. Raper, 1990. Climate change due to solar irradiance changes. *Geophys. Res. Letters*, 17, 2169-2172.
- Woodruff, S.D., S.J. Lubker, K. Wolter, S.J. Worley, and J.D. Elms, 1993. Comprehensive Ocean-Atmosphere Data Set Release 1a; 1980-92. *Earth Systems Monitor*, 4, 1-8.

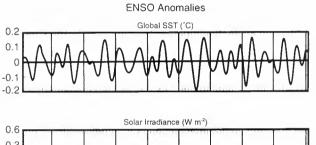


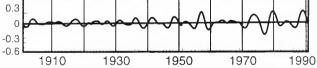
CORRELATIONS: TEMPERATURE -vs- SOLAR IRRADIANCE WITH DEPTH

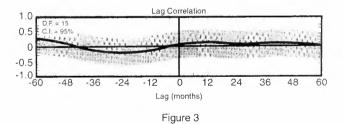


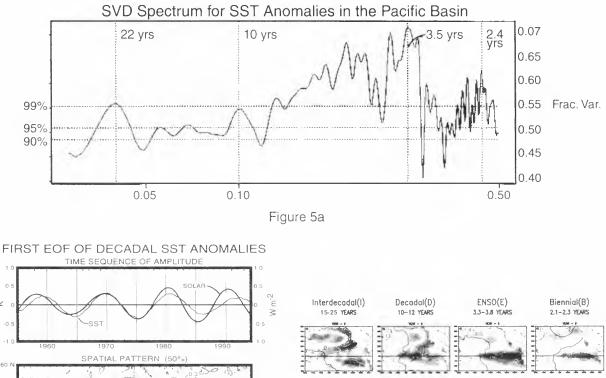


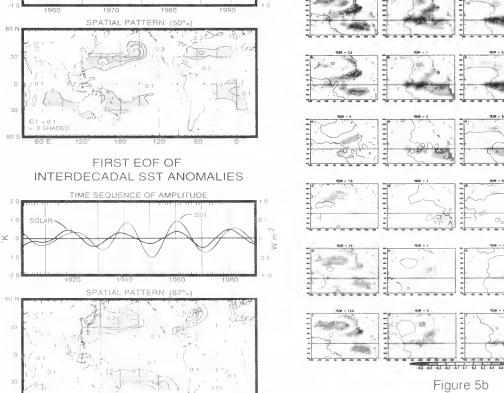












¥

60

Figure 4

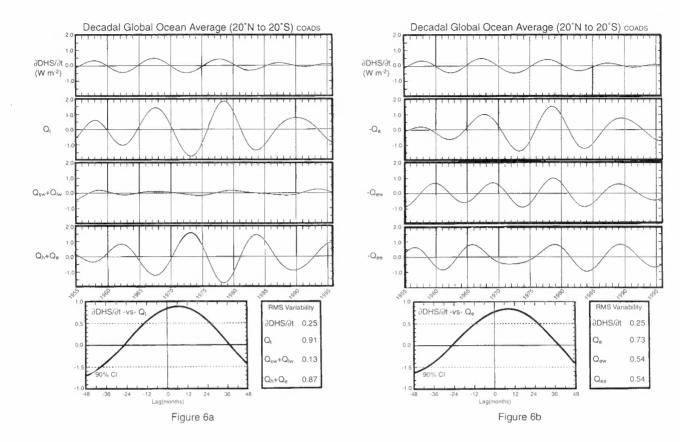
Part Part

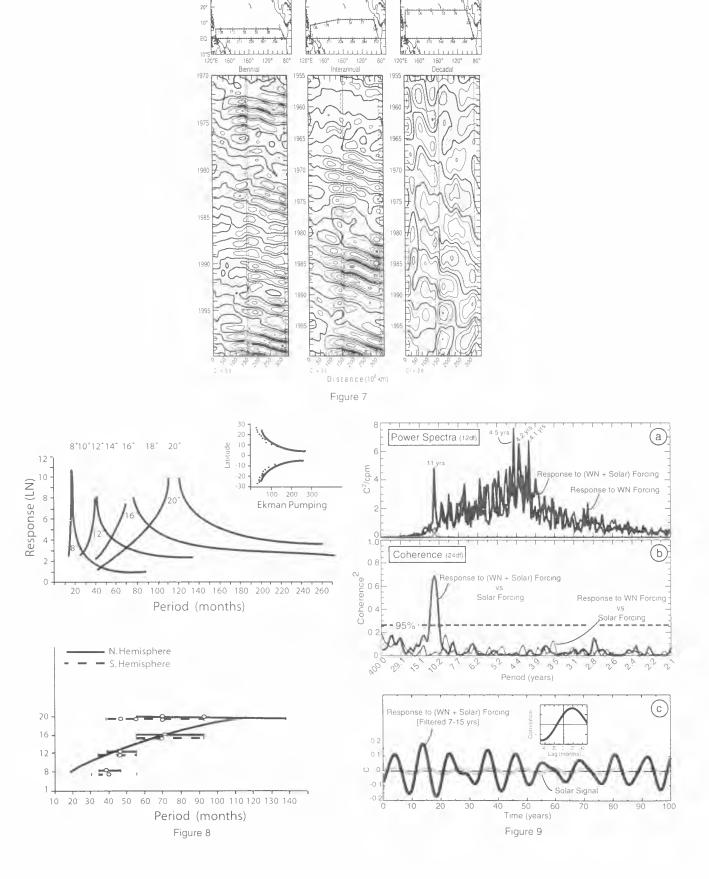
1111-1

11111

1111111







18°C Isotherm Depth Anomalies

30

Ą

SOLAR FORCING OF EL NIÑO AND LA NIÑA

Theodor Landscheidt

Schroeter Institute for Research in Cycles of Solar Activity, 11227 Cabot Trail, Belle Côte, Nova Scotia B0E 1C0, Canada. Tel. (902) 235-2281. E-mail: theodor.landscheidt@ns.sympatico.ca.

Abstract-Global temperature anomalies are dominated by ENSO events which are viewed to be the most spectacular example of a free internal oscillation of the climate system not subjected to external forcing. It is shown, however, that El Niño, La Niña, and the Southern Oscillation are subjected to strong solar forcing. They are closely connected with special phases in the rise to maximum and the fall to minimum of the 11-year sunspot cycle which coincide with significant accumulations of energetic solar eruptions. This pattern made it possible to forecast the last two El Niños and the extension of La Niña beginning in 1998. On this basis, the next El Niño is to be expected around 2002.9 (± 0.4). An alternating preponderance of El Niño and La Niña is shown to be linked to the 22-year Hale cycle constituted by 11-year magnetic reversals in sunspot activity. La Niña prevailed in the cycle 1954-1976 and El Niño in the cycle 1976-1996 $(P < 10^{-9})$. This alternating pattern can be traced back to the Hale cycle beginning in 1889. A predominance of La Niña may be expected in the current 22-year cycle.

Introduction

Anomalous warming (El Niño) or cooling (La Niña) of surface water in the eastern equatorial Pacific occurs at irregular intervals (2 to 7 years) in conjunction with the Southern Oscillation, a massive seesawing of atmospheric pressure between the southeastern and the western tropical Pacific. The coordinated El Niño/Southern Oscillation phenomenon (ENSO), also including La Niña, is the strongest source of natural variability in the global climate system. Anomalies in the global temperature – positive or negative deviations from a defined mean temperature – are primarily driven by ENSO events (Peixoto and Oort, 1992). Only when explosive volcanic activity intervenes, global temperature is modulated by its cooling effect.

So it is plausible that there are strong links to weather in other world regions. As this might be the key to longrange seasonal forecasts, there is strong interest in precursors that could make it possible to predict ENSO events. The NOAA tripwire open ocean buoy array including deep ocean moorings and surface drifters gives climatologists an early warning of 3 to 12 months of an impending El Niño. Daily observations of changes in sea surface temperature (SST), surface wind, upper ocean thermal structure, and ocean currents enable researchers to develop models that can be tested by experimental forecasts.

It seems to be very difficult, however, to design models that extend the 12-month limit set by the observation of precursors. Zane and Zebiak of the Lamont-Doherty Earth Observatory made the first successful forecast of an El Niño in early 1986, one year ahead of the event, but their model did not predict the strong El Niño in 1997. At present, there exist no physical or statistical models that can skillfully predict ENSO events at lead times longer than 12 months (Neelin and Latif, 1998). According to Neelin and Latif (1998) weather noise and deterministic chaos, representing the internal variability of the climate system, set the fundamental limits to the lead time. This emphasis on the exclusively internal character of ENSO events is in accordance with the tenet of climatology that ENSO phenomena are the most spectacular example of a free internal oscillation of the climate system not subjected to external forcing (Peixoto and Oort, 1992). If it could be shown that this tenet is not tenable because there is external forcing, this would have far reaching consequences for the global warming debate.

Correlation between ENSO events and sunspot cycle

If there were external forcing, deterministic chaos, discussed by Neelin and Latif, would not prevent long-range forecasts. Lorenz has emphasized that sensitive dependence on initial conditions and ensuing limited predictability are only valid for processes within the climate system.

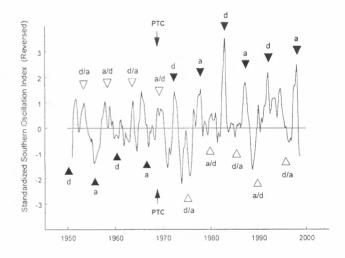


Figure 1. Close correlation between extrema in the SOI, indicating ENSO events, and phases a and d within the ascending and declining partof the 11-year sunspot cycle. The phase reversal after 1968 is associated with a predictable perturbation in the Sun's dynamics explained in the text.

External periodic or quasiperiodic energy flow can force its rhythm on atmosphere and oceans. Long-term climate effects due to varying solar irradiance, if strong enough, would be a case in point. Investigations into connections between irradiance variations in the course of the 11-year sunspot cycle and changing climate are usually focused on maxima and minima in sunspot activity. It is easy to see that these extrema show no direct relationship with ENSO events. Fig. 1 demonstrates, however, that a close correla-

Proc. 1st Solar & Space Weather Euroconference, 'The Solar Cycle and Terrestrial Climate', Santa Cruz de Tenerife, Tenerife, Spain, 25-29 September 2000 (ESA SP-463, December 2000)

tion emerges when other phases of the sunspot cycle are examined.

The curve shows slightly smoothed standardized monthly data of the SOI, the Southern Oscillation Index (Climate Prediction Center, 1998). It measures the pressure gradient across the tropical Pacific which, in turn, is an indicator of equatorial wind variations. Low negative SOI values, indicating El Niños, go along with weaker than normal trade winds over the central Pacific, warmer than normal sea surface temperatures (SST) over the eastern equatorial Pacific, and a reduced westward pressure gradient with changing wind stress values. High positive SOI values indicate La Niña conditions, just the opposite of the El Niño scenario. In Fig. 1 the data are reversed so that strong positive peaks point to El Niños and negative deviations to La Niñas.

After 1970, on the right of the two arrows marked by PTC, all filled triangles point to El Niños and all empty triangles to negative deviations. All of these triangles mark special phases in the 11-year sunspot cycle. This cycle is not symmetric. Reliable observations available since 1750 show that the mean rise to the sunspot maximum (4.3 years) is considerably steeper than the decline to the sunspot minimum (6.7 years). The mean ratio of the rising part to the whole 11-year cycle is 0.39. Nature often repeats patterns on different scales. The phases indicated by triangles form such a fractal. The filled triangles mark points a and d which divide the ascending and the descending part of the sunspot cycle such that the ratio 0.39, found in the whole cycle, is again established in the respective parts.

A maximum entropy frequency analysis of monthly SOI data (1950-1998) shows that the ratio 0.39 stands out in the frequency pattern. Phase d falls at 2.6 years after the zero phase of the declining part. This period nearly coincides with a sharp outstanding frequency peak at 2.5 years which is significant beyond the 1% level. This was confirmed by a Panofsky and Brier χ^2 -test applied to the Blackman-Tukey power spectrum of the SOI data. Phase a is also emphasized by these tests.

Midpoints between phases a and d (a/d and d/a), marked by empty triangles, are farthest away from points a and d. So it is consistent that they indicate the opposite effect, La Niña instead of El Niño in the range after 1970. Before 1970 everything is reversed. Empty triangles, indicating a/d and d/a, consistently point to El Niños, and filled triangles, marking a and d, to La Niñas. As this conspicuous pattern is linked to the Sun's activity, which again is based on the Sun's dynamics, an explanation of the phase reversal, too, should be found in the Sun's dynamics.

Perturbations in Sun's motion and phase reversals

Babcock's solar dynamo model links the Sun's varying activity to its differential rotation on its axis. It takes into

account the Sun's spin momentum, but not its orbital angular momentum related to its irregular oscillation about the centre of mass of the solar system, first described by Newton. This orbital momentum can reach 25% of the spin momentum and varies forty-fold within a few years (Landscheidt, 1999). If there were transfer of angular momentum from the Sun's orbit to the spin on its axis, this would make a difference of up to 7% in its equatorial rotational velocity (Blizard, 1982). Such acceleration or deceleration has actually been observed. This seems to be indicative of a case of spin-orbit coupling of the spinning Sun and the Sun revolving about the centre of mass involving transfer of angular momentum. Coupling could result from the Sun's motion through its own ejected plasma (Landscheidt, 1999). The low corona can act as a brake on the Sun's surface (Dicke, 1964). Change in the Sun's rotation on its axis could have a crucial effect on the unstable tachocline where the turbulent convective zone meets the more stable radiative zone and variations in rotation are observed to be a regular phenomenon (Howe et al., 2000). This is just the region where the Sun's varying activity is supposed to have its roots.

It has been shown that there are cycles in the Sun's motion which are associated with solar activity and climate change (Landscheidt, 1983, 1987, 1988, 1990, 1998 a, 1998c). On this basis, I correctly predicted, for example, energetic solar eruptions, strong geomagnetic storms, the end of the Sahelian drought, and drought conditions around 1999 in the United States 1 to 4 years before the events. The forecast of solar eruptions and geomagnetic storms, checked by astronomers and the Space Environment Center, Boulder, covered six years and reached a hit rate of 90%.

Fig. 2 shows how the rate of change of the Sun's orbital angular momentum (L) – the torque dL/dt driving the Sun's motion about the centre of mass of the solar system – constitutes a torque cycle of varying length. The initial

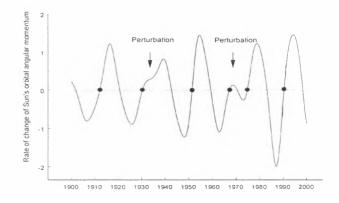


Figure 2. Time rate of change dL/dt of the orbital angular momentum in the Sun's irregular motion about the centre of mass of the solar system. Filled circles mark the initial phases of a cycle in dL/dt. Arrows indicate perturbations in the sinusoidal course of dL/dt that are associated with phase reversals in related solar-terrestrial cycles.

phases of this cycle are marked by filled circles. Perturbations in the sinusoidal course of the torque cycle, indicated by arrows, occurred around 1933 and 1968. Such events recur at quasi-periodic intervals and mark initial phases of a perturbation cycle with a mean length of 35.8 years. Observation shows that such perturbations, which are predictable, release phase reversals in cycles of climate phenomena connected with the Sun's activity.

Forecast of ENSO events

The perturbation in the torque cycle that occurred in 1968 falls just at the phase reversal in the correlation pattern presented in Fig. 1. It is marked by arrows and the acronym PTC (Perturbation in torque cycle). The next PTC will occur in 2007. The pattern in Fig. 1 made it possible to predict the last two El Niños (Landscheidt, 1995) and the extension of La Niña beginning in 1998. In the first week of January 1999 I predicted that La Niña should prevail till 2000.1 and beyond. This proved correct though the lead time was as long as 13 months. End of March 1999 I extended the lead time to 15 months by predicting that La Niña would last till 2000.5. This again turned out correct. The successful forecast of the last El Niño was made more than two years before the event. At present there exist no physical or statistical models that can skillfully predict ENSO events at lead times longer than 12 months (Neelin and Latif, 1998), though daily precursor observations are continuously taken into account. In many cases the forecasts of specialized institutes change every few months. As I predicted in January 1999, the maximum phase of the next El Niño is to be expected around 2002.9 (\pm 0.4). This is an even longer lead time. If such long-range forecasts of ENSO events in the tropcical Pacific could be shown to be dependable, this might be the key to long-range forecasts of seasonal weather in other world regions linked to ENSO.

Energetic solar eruptions and ENSO events

Why is it that just phases a and d within the ascending and descending part of the 11-year sunspot cycle are related to ENSO events? Fig. 3 gives a potential answer. It shows the distribution of highly energetic X-ray flares within the respective ascending and descending part of the sunspot cycle. The sample covers all flares $X \ge 6$ observed by satellites between 1970 and 1998. These data are available at the National Geophysical Data Center, Boulder. The rising and falling parts of different length were normalized to have equal length 1. Then they were superimposed to make it easy to recognize identical phases. Intense X-ray flares, nearly always accompanied by heavy coronal mass ejections, are geophysically more effective than flares categorized into classes of optical brightness (Joselyn, 1986). As many as 19 of the 34 investigated X-ray flares concentrate on the short interval of 0.23 on the unit scale, marked by a horizontal bar at the top left. Only 15 of the flares fall at the remaining large interval covering a range of 0.77 on the unit scale.

The normalized position of points a and d is marked by a filled triangle. The climate effect, observed at a and d lags the solar eruptions, the conceivable cause, though only by 8 months on average. Statistically, the flare accumulation is

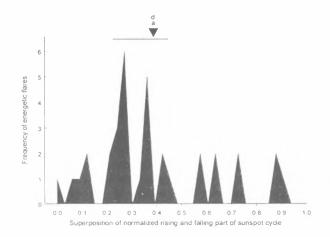


Figure 3. Distribution of intense X-ray flares (X \ge 6), observed 1970-1998, in relation to phases a and d in the ascending and declining part of the 11-year sunspot cycle. The climatological effect, linked to phases a and d, lags the significant accumulation of flares, the conceivable cause.

highly significant. Even when compared with the distribution of mean counts of grouped optical flares, bootstrap resampling and randomization tests show that the probability of a false rejection of the sceptic null hypothesis is much smaller than 0.01. Highly energetic cosmic ray flares observed between 1942 and 1970 corroborate this result. All events listed by Sakurai (1974) were included in the sample except the weakest events with a cosmic ray increase $\leq 2\%$. The distribution shows a strong accumulation in the same range.

Potential physical background

At present there are no strict physical arguments that could explain in detail how solar activity causes ENSO events. It is possible, however, to develop working hypotheses that suggest potential mechanisms. Intense X-ray flares are nearly always accompanied by strong proton events and coronal mass ejections which cause the highest velocities in the solar wind and create shock waves that compress and intensify the magnetic fields which modulate the intensity of galactic cosmic rays. There are indications that this has a strong effect on cloud cover over the oceans. The overall effect of clouds is that they cool the planet more than they heat it. The global mean long-wave and short-wave cloud forcing are both larger than the trace gas forcing by a factor of 15 to 20. The short-wave effect (albedo) shifts the system to a cooler climate, while the long-wave effect (absorption) causes a warmer climate. The Earth Radiation Budget Experiment (ERBE) data show that in the present climate the short-wave forcing is stronger and generates a net cooling of at least -17 W/m^2 (Ramanathan et al., 1989).

Svensmark and Friis-Christensen (1997) have shown that global cloud cover over the oceans, observed by satellites, is linked to variations in the flux of galactic cosmic rays modulated by the solar wind (r = 0.95). This effect, attributed to cloud seeding by ionized secondary particles, was observed to induce a change in cloud cover by more than 3% within 3 1/2 years. The corresponding change in radiative forcing is in the range 0.8 to 1.7 W m⁻². This is significant, as the total radiative forcing by CO₂ accumulated in the atmosphere since pre-industrial times has been estimated to be 1.5 W m⁻². According to Svensmark (1998) cosmic ray forcing explains nearly all of the temperature change in the period 1980-1995. Measurements of cosmic ray flux registering myons instead of neutrons go back to 1937. When Svensmark (1998) compared these data with temperature in the Northern Hemisphere, his former results were corroborated. Short-term observations show the same response. According to Pudovkin and Veretenenko (1995), Forbush decreases - sudden deep drops in cosmic ray flux within 2 days after energetic flares - coincide with local shrinking of cloud cover by 3%.

It is assumed that the secondary ions produced by cosmic rays serve as condensation nuclei with hygroscopic properties that enhance the formation of clouds. Pruppacher and Klett (1997) have provided evidence that this is occuring in thunderstorms, but it is not clear to which extent cloud development is affected. The underlying microphysical processes are not yet understood in detail. They should be analysed by laboratory experiments. Svensmark is planning such experiments in cooperation with CERN. Unexpected support for a link between cosmic ray flux and cloud cover comes from the observation that Neptune's whitish methane clouds increase in surface coverage at intervals of about 11 years when the cosmic ray flux is intense because the sunspot cycle is in a minimum (Baliunas and Soon, 1998).

As the regions of the tropical Pacific around Indonesia and northern Australia, where ENSO events are triggered by instabilities in the sea surface pressure, have dense and extensive cloud layers reaching altitudes of 22 km at geomagnetic latitudes close to -20°, allowing relatively strong cosmic ray effects, it is not unimaginable that there is a physical link between energetic solar eruptions and variations in surface pressure gradients that release instabilities in the ENSO regions. Energetic solar eruptions could indirectly shrink the dense cloud layers around the centre of the large low pressure cell in the western tropical Pacific via a weaker cloud seeding effect of cosmic rays. The increasing insolation would disturb sea surface pressure enough to trigger instability in the pessure balance of the Southern Oscillation that could be amplified by concomitant feedback processes in the atmosphere-ocean system.

This would explain a close correlation between cosmic ray intensity, cloud cover, and Southern Oscillation Index found by Kuang, Jiang, and Yung (1998) for the period 1983 - 1991. Revealingly, in their graphical presentation (Fig. 2a) the SOI lags cloud cover which again lags cosmic rays. This points to a causal relationship. Isolated Forbush decreases, mentioned already, are associated with immediate decreases in cloudiness by 3% that last a week and longer. Even such short-term effects could be sufficient to release or sustain conditions for the development of El Niños, especially when they trigger tropical cyclones (Ramage, 1986).

I do not pretend that the proposed hypothetical mechanism is actually working. Others are imaginable. Flares increase the Sun's UV radiation by at least 16%. Ozone in the stratosphere absorbs this excess energy which causes local warming and circulation disturbances. General circulation models developed by Haigh (1996), Shindell et al. (1999), and Balachandran et al. (1999) confirm that circulation changes initially induced in the stratosphere can penetrate into the troposphere and influence temperature,

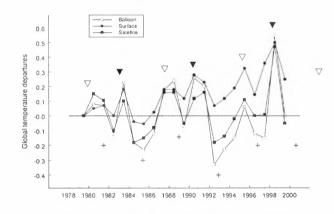


Figure 4. Global temperature anomalies based on satellite, balloon sonde, and surface observations. Filled triangles mark initial phases of the torque cycle in the Sun's motion and empty triangles asymmetric phases in between explained in the text. Plus signs indicate midpoints between the respective phases. The correlation pattern made it possible to predict the last two extrema in the departures. The next positive extremum is to be expected around 2002.9. A minimum in the departures should be reached around 2000.7.

air pressure, Hadley circulations and storm tracks by changing the distribution of large amounts of energy already present. As ENSO events are linked to trade winds and trade winds to Hadley cells that may be affected by flare induced circulation change in the stratosphere, it seems plausible that energetic solar eruptions may be an essential link in the causal chain triggering ENSO events, especially if there is a barrage of solar eruptions covering weeks. It may be objected that these working hypotheses lack detail and precision. However, we do not even know exactly how individual ENSO events come into existence.

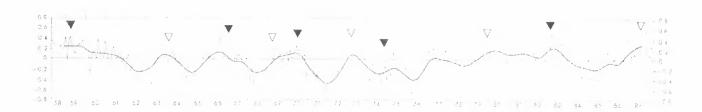


Figure 5. Monthly-mean temperature anomalies in °C averaged over the Northern Hemispheric mass between surface and 25-km height (After Peixoto and Oort, 1992). Filled triangles mark initial phases of the torque cycle in the Sun's motion about the centre of mass of the solar system. Empty triangles indicate phases that reflect the ratio 0.61 of the declining part of the sunspot cycle to the whole 11-year cycle. Maxima of the anomalies closely follow the strong variations in the width of intervals between consecutive crucial phases in the torque cycle.

The lack of elaborate theory does not impair the heuristic importance of the results, especially as they were corroborated by successful forecast experiments. Epistemologically, the stages of gathering data, finding patterns, and setting up working hypotheses necessarily precede the development of precise theories.

Torque cycle and temperature anomalies

The torque cycle in the Sun's motion, presented in Fig. 2, adds to the dependability of ENSO forecasts as it is closely connected with extrema in global temperature anomalies which are primarily driven by ENSO events. Fig. 4 from the World Climate Report presents a case in point. It shows global temperature anomalies based on satellite, balloon sonde, and surface observations. They are referenced to a common zero point in 1979, the beginning of satellite measurements. Black triangles mark initial phases of the torque cycle that have been shown to coincide with accumulations of energetic solar eruptions (Landscheidt, 1976). Empty triangles indicate the mean ratio 0.61 of the declining part of the sunspot cycle to the whole 11-year cycle. Phases 0.61 and 0.39 are mirror images of each other in relation to the symmetry centre of the cycle. Plus signs mark midpoints between the respective phases. Temperature consistently lags the crucial phases in the torque cycle by a few months, thus pointing to a causal relationship. The close correlation made it possible to correctly forecast a negative extremum for 1997.0 and a positive one for 1998.6 (Landscheidt, 1998b). The next minimum is to be expected around 2000.7 and the following maximum around 2002.9. Forecasts of maxima should turn out to be more precise than forecasts of minima.

Figure 5 after Peixoto and Oort (1992) shows Northern Hemisphere temperature anomalies for the troposphere and the low stratosphere. It extends the correlation back to 1958 so that it covers four decades. It is conspicuous how closely maxima in the anomalies follow the strong variations in the width of intervals between consecutive active phases in the torque cycle. Southern Hemisphere temperatures corroborate this connection.

Alternating preponderance of El Niño and La Niña

The true sunspot cycle is the magnetic Hale cycle with a mean length of 22 years. The magnetic polarities of preceding and following sunspots in each hemisphere reverse in each 11-year cycle so that their return to the original magnetic state is linked to the initial phase of the Hale

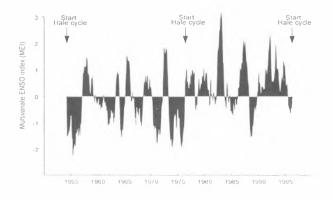


Figure 6. Preponderance of La Niña in the Hale cycle 1954-1976 and of El Niño in the following magnetic sunspot cycle ending 1996. The ENSO data are based on the MEI (Wolter and Timlin,1998). The highly significant alternating pattern can be traced back to 1900. If the pattern holds, a predominance of La Niña may be expected in the current Hale cycle.

cycle. Fig. 6 shows a close relationship between the Multivariate ENSO Index (MEI) based on the main observed variables over the tropical Pacific (Wolter and Timlin, 1998), and the Hale cycle. The preponderance of La Niña in the Hale cycle 1954 - 1976 and of El Niño in the following cycle is obvious. This alternating pattern can be traced back to 1900, as far as monthly SOI data are available. The connection can be evaluated quantitatively by investigating to which degree the SOI means in consecutive Hale cycles deviate from each other and whether their positive and negative signs form a consistent alternating pattern. A bootstrap analysis based on the t-test yields $P < 10^{-9}$ for the two Hale cycles shown in Fig. 6. The distributions in the preceding Hale cycles back to the initial phase 1889, too, yield highly significant results, though on a

lower level ($P < 10^{-3}$). This could be due to deteriorating quality of observational data.

If the pattern holds, a preponderance of La Niña is to be expected during the Hale cycle that began in 1996. So far, there were two La Niñas and one El Niño. A predominance of La Niñas, lasting 22 years, would have a strong effect on global temperature comparable to the cool period in the sixties and early seventies when temperatures were falling in spite of a steep increase in anthropogenic CO₂.

Outlook

The results presented here, though tested by forecast experiments, are only first tentative steps in a new direction. There are many unsolved problems, and not only theoretical ones. Phase reversals linked to perturbations in the torque cycle, as presented in Fig. 1, can be traced back to the beginning of instrumental records. They are a heuristic actuality. Yet how can it be explained that there is a complete reversal in the effect though we are dealing with the same phases in the sunspot cycle and unchanged conditions in the climate system? Obviously we need to understand first what happens in the Sun's convection zone when perturbations in the torque cycle occur. Is there a bistable oscillator that switches to another mode when a perturbation in the torque cycle disturbs the established equilibrium? Another haunting observation is that not only strong solar eruptions, but also extended lulls in flare activity can affect ENSO events. I think that these problems can only be solved by a joint interdisciplinary effort of open-minded scientists.

REFERENCES

- Balachandran, N. K., Rind, D., and Shindell, D. T., 1999: Effects of solar cycle variability on the lower stratosphere. J. Geophys. Res. 104, 27321-27339.
- Baliunas, S. and Soon, W., 1998. World Climate Report 3, No. 15, 10.
- Blizard, J., 1982: Bull. Am. Astron. Soc. 13, 896.
- Climate Prediction Center, NOAA, Data and indices, 1998: http://nic.fb4.noaa.gov.
- Dicke, R. H., 1964: Nature 202, 432.
- Haigh, J. D.,1996: On the impact of solar variability on climate. Nature 272, 981-984.
- Howe, R., Christensen-Dalsgaard et al., 2000: Dynamic variations at the base of the solar convection zone. Science 287, 2456-2460.
- Joselyn, J. A., 1986: SESC methods for short-term geomagnetic predictions. In: Simon, P. A. et al., eds.: Solar-terrestrial predictions. Boulder, NOAA, 405.
- Kuang, Z., Jiang, Y., and Yung, Y. L., 1998: Cloud optical thickness variations during 1983-1991: Solar cycle or ENSO? Geophys. Res. Lett. 25, 1415-1417.
- Landscheidt, T., 1976: Beziehungen zwischen der Sonnenaktivität und dem Massenzentrum des Sonnensystems. Nachrichten der Olbersgesellschaft Bremen 100, 3-19.
- Landscheidt, T., 1983: Solar oscillations, sunspot cycles, and climatic change. In: McCormac, B. M., ed.: Weather and climate

responses to solar variations. Boulder, Colorado Ass. Univ. Press, 293-308.

- Landscheidt, T., 1987: Long-range forecasts of solar cycles and climate change. In: Rampino, M. R., Sanders, J. E., and Koenigsson, L., eds.: Climate: History, periodicity, and predictability. New York, van Nostrand Reinhold, 421-445.
- Landscheidt, T. 1988: Solar rotation, impulses of the torque in the Sun's motion, and climatic variation. Climatic Change 12, 265-295.
- Landscheidt, T., 1990: Relationship between rainfall in the Northern Hemisphere and impulses of the torque in the Sun's motion. In: Schatten, K. H. and Arking, A.: Climate impact of solar variability. NASA Conference Publication 3086, 259-266.
- Landscheidt, T., 1995: Die kosmische Funktion des Goldenen Schnitts. In: Richter, P. H., ed.: Sterne, Mond und Kometen. Bremen, Hauschild, 240-276.
- Landscheidt, T., 1998a: Global Warming or Little Ice Age? In: Bate, R., ed.: Global Warming - The continuing debate. Cambridge, the European Science and Environment Forum, 129-158.
- Landscheidt, T., 1998b: Forecast of global temperature, El Niño, and cloud coverage by astronomical means. In: Bate, R., ed.: Global Warming - The continuing debate. Cambridge, the European Science and Environment Forum, 172-183.
- Landscheidt, T., 1998c: Solar activity: A dominant factor in climate dynamics. Energy and Environment 9, No. 6, 683-720.
- Landscheidt, T., 1999: Extrema in sunspot cycle linked to Sun's motion. Solar Physics 189, 415-426.
- Neelin, J. D. and Latif, M., 1998: El Niño dynamics. Physics Today, December 1998, 32-36.
- Peixoto, J. P. and Oort, A. H., 1992: Physics of climate. New York, American Institute of Physics, 415-433.
- Pruppacher, H. R., Klett, J. D., 1997: Microphysics of clouds and precipitation. Kluwer Academic Publishers.
- Pudvokin, M. and Veretenenko, S., 1995: Cloudiness decreases associated with Forbush-decreases of galactic cosmic rays. J. Atmos. Terr. Phys. 57, 1349-1355.
- Ramage, C. S., 1986: Scient. American, June 1986, 59-61.
- Ramanathan, V., Barkstrom, B. R., Harrison, E. F., 1989: Climate and the Earth's radiation budget. Physics Today, May 1989, 22-23.
- Sakurai, K., 1974: Physics of solar cosmic rays. Tokyo, University of Tokyo Press, 149.
- Shindell, D., Rind, D., Balachandran, N., Lean, J., and Lonergan, P., 1999. Solar cycle variability, ozone, and climate. Science 284, 305-309.
- Svensmark, H. and Friis-Christensen, E., 1997: Variation of cosmic ray flux and cloud coverage. J. Atmos. Terr. Phys. 59,1225-1232.
- Svensmark, H., 1998: Influence of cosmic rays on Earth's climate. Phys. Rev. Lett. 81, 5027-5030.
- Wolter, K. and Timlin, M. S., 1998: Measuring the strength of ENSO. Weather 53, 315-324.

COMPARATIVE STUDY OF THE ATMOSPHERIC EFFECTS DRIVEN BY IRRADIANCE VS. CORPUSCULAR RADIATION

A. Ludmány and T. Baranyi

Heliophysical Observatory Debrecen, H-4010 Debrecen, P.O.Box 30. Hungary phone/fax: (36-52) 311-015; e-mail: ludmany@tigris.klte.hu / baranyi@tigris.klte.hu

ABSTRACT

The overwhelming majority of the literature dealing with the solar-climatic effects treats the problem in terms of irradiance variations. The present contribution yields an overview of the rival paradigm: the role of the variations of plasma streams, and also demonstrates the necessity of distinction between the two possible energy channels. They can be confused in certain cases which may mislead the interpretation of the possible underlying mechanisms. The efficiency factors of the two solar energy channels are discussed, it is demonstrated that the corpuscular channel cannot be neglected, but in some respects it can be at least as important as the irradiance impacts. A reasonably convincing set of evidences has been published in our earlier papers a new kind of semiannual fluctuation as well as three polarity rules exhibited by atmospheric phenomena with respect to solar magnetic field polarities. The possible role of these polarities is discussed in terms of the interplanetary magnetic field components. This is partly controlled by the solar main magnetic dipole field, on the other hand it is also governed by the magnetic field topology of the CME's front region preserving the helicity of the originating active region.

INTRODUCTION

Lots of publications are devoted to the problem of the Sun-climate relations. Although this was the favourite topic of the early solar-terrestrial investigations, the progress was relatively small for a long time in this field. The possible reasons were also thoroughly investigated in several studies which revealed several components of the problem. The most remarkable feature of the early studies was a pure empirical approach, the authors simply looked for the signatures of the 11-year cycle in the time serii of any surface phenomena, or they studied their correlations with the Wolf numbers. It was a common property of most solarclimatic studies (admitted or not) that the irradiance variations were assumed to be responsible for the atmospheric impact. The use of the Wolf-numbers was an obvious choice in most cases because it is the longest homogeneous solar dataset. Two indirect meanings can be attributed to it. On one hand it simply represents the level of the solar activity which is an obvious simplification because a scalar quantity cannot give account about all relevant properties of the evolution of the magnetic features. On the other hand, as recent results show, the solar irradiance follows quite reliably the 11-year solar cycle (Fröhlich and Lean, 1998), so long-term investigations based on the Wolf-number concern the irradiance impacts. It was a popular index and very useful in providing evidences for the connections between solar phenomena and the lower atmosphere, although several methodological problems made some earlier studies contradictory (Pittock, 1978; Herman and Goldberg, 1978) and several findings cannot be explained with irradiance effects (Tinsley, 1996).

The starting assumption of our project was of paradigmatic nature. If one chooses some physical quantities to study, the basis of the choice is generally some preliminary conjecture about the unknown mechanism, a personal prejudice, if you like. The possibility of the role of corpuscular streams apparently used to be neglected without any satisfactory explanation. Thus it appeared appropriate to examine the impact and role of plasma effects to get closer to the underlying mechanisms. The monthly mean of Wolfnumber may have a high correlation with some parameters of the plasma stream, so a plasma effect on the lower atmosphere might be detected by using it, but the interpretation would be mislead because the Wolfnumber suggests irradiance effect. Thus it is highly necessary to distinguish between these two paradigms.

TWO CHANNELS OF SOLAR ENERGY

If plasma effects in the lower atmosphere were mentioned at all, they were commented as highly improbable because of the small amount of energy carried by plasma streams. It may be illuminating to compare the characters of the radiative and plasma effects. The following properties can be decisive in the efficiency of a solar impact.

Full amount of transported energy. In this respect the irradiance, no doubt, predominates overwhelmingly. The energy fluxes carried by the two medias at the mean Sun-Earth distance are:

electromagnetic: $1.36 \times 10^6 erg \cdot cm^{-2} \cdot s^{-1}$

corpuscular: $\sim 10^{-1} erg \cdot cm^{-2} \cdot s^{-1}$

which is a difference of seven orders of magnitudes, apparently a quite convincing electromagnetic predominance. However, this only means that the stationary energy budget of the atmosphere installed by

Proc. 1st Solar & Space Weather Euroconference, 'The Solar Cycle and Terrestrial Climate', Santa Cruz de Tenerife. Tenerife. Spain, 25-29 September 2000 (ESA SP-463. December 2000)

the quiet Sun is basically determined by the electromagnetic flux.

Relative variance. This is a much more relevant indicator in the present context, the consequence of activity phenomena. If the stationary regime is set then the terrestrial response will depend on the deviation of the solar fluxes from the quiet values. The variation of the full elextromagnetic flux - the solar constant - is about a few thousandths of the stationary value whereas that of the flux carried by corpuscular streams may be hundreds of percents. The density increase of the corpuscular flux may be one order of magnitude and the velocity may have a fivefold growth. The electromagnetic variability is the highest in the short wavelength range, but this does not affect too much the full energy output and it affects mainly the upper atmospheric ionization. This means that if we consider the events of solar activity, the corpuscular channel cannot be neglected.

Temporal run. The efficiency of corpuscular phenomena is even more remarkable if we consider as to how well defined are the events temporally. The difference is also significant. The main ingredients of the solar constant variability are the faculae and spots. It takes several days for both of them to alter the solar constant by a few thousandths of the stationary value even in the most rapidly developing active regions or by turning in the visible hemisphere. At the same time it takes less than one hour for the plasma velocity and density to reach the mentioned increase. Thus the difference of temporal factors is about two orders of magnitude.

Spatial concentration. A further aspect is the distribution of the atmospheric energy input. The electromagnetic radiation is evenly distributed on the global surface whereas the corpuscular streams are confined to the terrestrial magnetic fields and they reach the lower layers in specific restricted areas in the auroral oval, so their distribution is highly inhomogeneous.

The above properties mean that, although the absolute value of the energy carried by the plasma streams is much lower than that of the irradiance, the plasma effects are much more concentrated in space and time and they deviate much more from the stationary value. This means that, at least on a short time scale, the plasma effects may be expected more efficient than those of irradiance. In other terms, on a longer timescale the total solar irradiance is responsible for the overall energy budget of the atmosphere, but on a shorter timescale the solar activity phenomena act mainly by means of the plasma streams. In this latter case the result is obviously no global temperature variation but some modification of the global atmospheric circulation. If a big amount of energy is input into a restricted volume within a short time then the expected result may be an alteration of the circulation patterns.

This expectation is corroborated by the finding which was only referred to for a while as a signature of plasma effects in the lower atmosphere. A specific variation of the vorticity area index (VAI) has been detected at those times when the Earth crossed interplanetary sector boundaries (Wilcox et al., 1973, Tinsley et al. 1994). This result showed that events of the interplanetary plasma may in fact have impact onto the lower atmosphere by means of reconnection processes.

CONDITIONS OF ATMOSPHERIC RESPONSES

Our strategy was to base the studies on as long datasets as possible. This meant that practically all physical quantities should have been described by some proxy data which were being recorded for a reasonably long time. Solar wind velocity data were represented by the geomagnetic aa-index (Mayaud, 1972); the atmospheric response was represented by surface temperature data (Vose et al., 1992); polarities of the solar main dipole field were determined by Makarov and Sivaraman (1986) on the basis of prominence positions; and finally, distinction was made between the solar sources of specific geomagnetic events on the basis of the timeprofile analysis by Legrand and Simon (1989). These datasets allowed the analysis starting from the year 1868. The investigations revealed a very complex behaviour indicating a definite sensitivity of the atmosphere to the magnetic field topologies of solar plasmas. A brief overview of the findings is as follows.

1. A semiannual fluctuation was the first signature detected (Baranyi and Ludmány, 1992). We wanted to check the conjecture of Bucha (1976) about a winter predominance of corpuscular effects on the basis of Hungarian data and an equinoctial preference was found: the aa-index - temperature correlations are higher at equinoxes than around solstices.

2. The polarity-dependence of the semiannual fluctuation was the second signature (Baranyi et al. 1995, Baranyi and Ludmány, 1995a). On an extended material (a number of European meteorology stations) the semiannual fluctuation was only detected in those years when the solar dipole field was parallel with that of the Earth (figure 1.).

3. The dependence on solar sources is perhaps the most intriguing and complex feature. It was found (Baranyi and Ludmány, 1995b) that the sense of the atmospheric response given to the specific geomagnetic event depended on the solar location of the source ejecting the given plasma stream. In particular, plasma effects originating from the polar regions as well as from the activity belts, release opposite atmospheric changes. This feature also depends on the magnetic cycle. If the years of opposite solar main dipole field polarities are separated, then the senses of the atmospheric responses are exchanged. When the main dipole is parallel with that of the Earth then the correlation of temperature data is positive with events from the activity belts and it is negative with those coming from the polar coronal holes, and these senses are exchanged in antiparallel years (figure 2.).

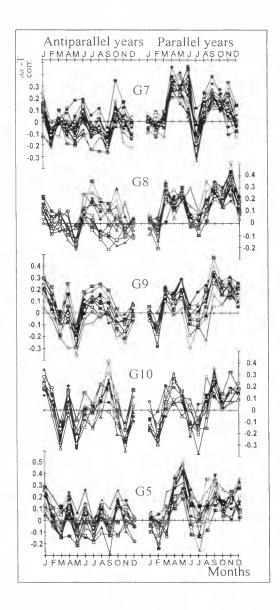


Figure 1: The polarity-dependent semiannual fluctuation. Annual variation of the efficiency of plasma effects at 58 European stations (taken from Baranyi and Ludmány, 1995a, names of the stations see therein), where the effect was recognizable. Regions of the groups of stations: G7: Great Britain, G8: France, G9: Germany-Austria, G10: Middle Europe, G5: Southern Scandinavia.

4. The sense of the terrestrial response is also sitedependent (Baranyi et al, 1998), opposite responses were found on the hemispheres separated by the magnetic meridian (the plane of rotational and magnetic axes).

It should be stressed that the above regularities are found on the datasets of 712 northern meteorological stations. It is not surprising that they are not valid everywhere. Stations exhibiting these rules constitute specific patterns, they are confined to powerful circulation features like the Icelandic Low. This is one of the most characteristic property of this set of rules

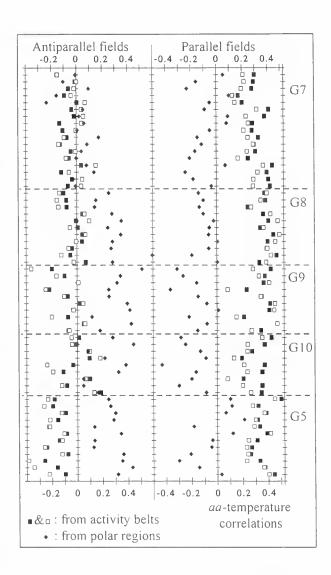


Figure 2: The polarity and source-dependent atmospheric response at the same 58 stations as in figure 1 (more details in Baranyi and Ludmány, 1995b)

also corroborating the corpuscular background because the corpuscular streams do not act globally and homogeneously, as mentioned in the previous section, but they reach the lower layers in relatively narrow regions and they can only contribute to or modify the existing circulation processes.

Studies based on the irradiance assumption were unable to interpret the disappearance of a correlation if it was checked on a different time-interval or geographic site, and an occasional sign reversal of a correlation was even more confusing. However, such phenomena are natural consequences of the highly complicated vectorial behaviour of the plasma effects, as the above properties demonstrate. This also means that a satisfactory description of the solar-tropospheric relations cannot be given by using only the scalar parameter of the irradiance.

VARIATIONS IN THE IMF

It is remarkable that the listed regularities reflect a systematic behaviour. To treat them in a consistent scenario, it is worth considering the possible role of the components of the interplanetary magnetic field as the solar plasma can interact with the terrestrial environment by magnetic field reconnections.

The first feature, the semiannual fluctuation may seem to be a consequence of the well known semiannual behaviour of the geomagnetic activity, but it is not. The latter is the enhancement of the geomagnetic disturbances around the equinoxes and the above reported fluctuation is the enhancement of the tropospheric response, i.e. the correlation. Nevertheless, they may have a common reason, the Russell-McPherron effect (Russell and McPherron, 1973), in which the Bz komponent plays a central role, as the By component of the inward as well as outward directed interplanetary magnetic field projects a negative Bz component in the magnetospheric system in March and September respectively. The main difficulty with the interpretation was that the above reported semiannual fluctuation takes place in those years when the dipole fields of the solar and terrestrial main magnetic fields are parallel and they are absent when the solar dipole field turns over, although one would expect the opposite effect by assuming reconnection interactions. The explanation can only be given by considering the rest of the listed regularities.

It is suitable to distinguish between the poloidal and toroidal components of the solar activity which are simultaneously present with varying weights and polarities (Legrand and Simon, 1991). The above results suggest that the roles of these two contributors are different in controlling the IMF components. The poloidal component of the IMF is provided by the solar wind from the quiet Sun and its variations (the recurrent variability) are given by the fast streams from the polar coronal holes, whereas the toroidal component is represented by the ejected plasma clouds. Variations of both components release different geomagnetic disturbances, this made possible to Legrand and Simon (1989) to distinguish between them, but the main ingredient, the Bz component should be negative by any geomagnetic events. An important difference between poloidal and toroidal events is in the way of producing negative Bz component.

The Bz components of the quiet solar wind and the fast recurrent streams in the Geocentric Solar Equatorial System (GSE) flucuate around zero at the distance of the Earth, the Bz component of these streams in the Geocentric Solar Magnetospheric System (GSM) is mainly realized through the projection effects of the By component which is highly significant because of the spiral structure. On the other hand the plasma clouds from active regions (causing the so called fluctuating geomagnetic activity) have intrinsic Bz component in the GSE. There is a growing number of evidences that significant plasma ejections originate mostly from distorted flux ropes, the helically kinked fields are the most probable sources of CMEs (Rust and Kumar, 1996; Canfield et al., 1999). In turn, the CMEs can transport the frozen-in helical topology of the source region (Bieber and Rust, 1995; Bothmer and Schwenn, 1999) thus the forefront of the inflating CME usually has significant Bz-values, which may also be increased by the inflation of the cloud for simple geometrical reasons (Felix Pereira and Girish, 1998). It should be added that by recent observations the magnetic field of the CME may be more complex than a single kinked flux rope (Kahler et al., 1999) but a dominant Bz component is generally present.

The 2-3 regularities (figure 2) can only be interpreted by some key factors which act reversely in the poloidal and toroidal events. This assumption has also been checked on the semiannual fluctuation in such a way that a further restriction was made on the datasets (Baranyi and Ludmány, 1997). Only those years were taken into account in both (parallel and antiparallel) orientations when no recurrent disturbances were observed, i.e. no effects from the polar coronal holes reached the terrestrial atmosphere and all disturbances could have been attributed to events from the activity belts. The sense of the semiannual fluctuation also alternated in the correlation with the streams from the activity belt showed negative extrema in antiparallel years.

The above considerations show that the differences between the IMF properties of the poloidal and toroidal events are quite well analysed (see also Gonzalez et al., 1996; Gonzalez et al., 1999) and it is apparently not surprising that they result in different atmospheric responses. The most unexpected feature of the 2 figure is that these two processes exchange their roles by the reversal of the solar dipole polarity. To reveal the key factor(s) of this exchange several properties of the incident streams have been examined in the parallel and antiparallel years but the obtained differences cannot be regarded to be decisive without further examinations excepting one factor, the By component. Though these results should be regarded to be preliminary as yet, it may be appropriate to mention here that the most conspicuous difference is exhibited by the occurrence probabilities of the oppositely directed By components. More details of this comparisons will be published elsewhere.

It is worth mentioning that the By component is a key factor in the modulation of global electric circuit and atmospheric circulation (Tinsley, 2000). Furthermore, the asymmetric behaviour of By may also be responsible for the above mentioned 4.feature, the E-W asymmetry of the atmospheric response.

CONCLUSIONS

Recent results support the common opinion that the irradiance is a key factor in long-term solar-climatic processes (Soon et al., 2000). However the present results and several here cited reports demonstrate that in short-term processes the importance of the plasma effects is not negligible, in some respects it may be decisive, for instance in affecting the atmospheric circulation patterns. The reported regularities and considerations may help in revealing the relevant factors and conditions from the solar surface until the atmosphere. Besides the mentioned global electric circuit, recent publications report some possible impacts, as the modification of the local pressure (Tóth and Szegedi, 2000) as well as the dominant pressure system and distribution of temperature and pressure deviations (Bohníček et al., 1999).

ACKNOWLEDGEMENTS

This work was supported by the Hungarian Science Foundation under contract OTKA T025640.

REFERENCES

- Baranyi, T. and Ludmány, A. (1992): Semiannual fluctuation and efficiency factors in sun-weather relations. *J.Geophys. Res.* Vol. 97, No.A10, 14923-14928, 1992.
- Baranyi, T. and Ludmány, A. (1994): Distinction between the climatic effects of the solar corpuscular and electromagnetic radiation. *Sol. Phys.* Vol. 152, 297-302, 1994.
- Baranyi, T., Ludmány, A. and Terdik, G. (1995): Semiannual fluctuation depending on the polarity of the solar main magnetic dipole field. *J.Geophys.Res.* Vol. 100, No. A8, 14801-14805, 1995.
- Baranyi, T. and Ludmány, A. (1995a): Role of the solar main magnetic dipole field in the solar-tropospheric relations. Part I. Semiannual fluctuations in Europe. *Ann.Geophys.* Vol. 13, 427-436, 1995.
- Baranyi, T. and Ludmány, A. (1995b): Role of the solar main magnetic dipole field in the solar-tropospheric relations. Part II. Dependence on the types of solar sources. *Ann.Geophys.* Vol. 13, 886-892, 1995.
- Baranyi, T. and Ludmány, A. (1997): Some polarity conditions in corpuscular events. *Sol. Phys.* Vol. 173, 383-389, 1997.
- Baranyi, T., Ludmány, A. and Coffey H. (1998): 22 year solar modulation of Earth's northern hemisphere temperatures. *Geophys. Res. Lett.* Vol 25, 2269-2272, 1998.
- Bieber J.W. and Rust D.M. (1995) The escape of magnetic flux from the Sun. *Astrophys.J.* Vol. 453, 911-918, 1995.

- Bohníček J., Hejda P., Bucha V., Pýcha J. (1999):
 Possible geomagnetic activity effects on weather.
 Ann. Geophys. Vol. 17, 925-932, 1999.
- Bothmer V. and Schwenn R. (1998): The structure and origin of magnetic clouds in the solar wind. *Ann.Geophys.* Vol. 16, 1-24, 1998.
- Bucha, V. (1976): Changes in the geomagnetic field and solar wind - causes of changes of climate and atmospheric circulation. *Stud. Geophys. Geod.* Vol. 20, 346, 1976.
- Canfield R.C., Hudson, H. and McKenzie D.E. (1999): Sigmoidal Morphology and Eruptive Solar Activity *Geophys.Res.Lett.* Vol. 26, No.6. 627-630, 1999.
- Felix Pereira B. and Girish T.E. (1998): Variation in the directions of north-south component of IMF in the GSE system near earth and Parker's model. *Geophys. Res. Lett.* Vol. 25, No.10, 1613-1616, 1998.
- Fröhlich C. and Lean J. (1998): The Sun's Total Irradiance: Cycles, Trends and Related Climate Change Uncertainties since 1976. *Geophys. Res. Lett.* Vol. 25, No.23, 4377-4380, 1998.
- Gonzalez W.D., Tsurutani B.T. and Tang F. (1996): The Solar and Interplanetary Causes of Geomagnetic Activity and Quiet. *ASP Conf. Series* Vol. 95, 453-461, 1996.
- Gonzalez W.D., Tsurutani B., Gonzalez A.L.C. (1999): Interplanetary origin of geomagnetic storms. *Space Science Reviews* Vol. 88, 529-562, 1999.
- Herman J.R. and Goldberg R.A. (1978): Sun, Weather and Climate. NASA SP-426, Washington, 1978.
- Kahler S.W., Crooker N.U. and Gosling J.T. (1999): A magnetic polarity and chirality analysis of ISEE3 interplanetary magnetic clouds. *J.geophys.Res.* Vol. 104, No.A5, 9911-9918, 1999.
- Legrand, J.P. and Simon P.A. (1991), A two component solar cycle, *Solar*. *Phys.* Vol. 131, 187-209, 1991.
- Legrand J.P. and Simon P.A. (1989): Solar cycle and geomagnetic activity: A review for geophysicists. Part I. The contribution to geomagnetic activity of shock waves and of the solar wind. *Ann. Geophys.* Vol. 7, 565-578, 1989.
- Ludmány A. and Baranyi T. (1998): An indirect hint to the torsion of magnetic fields above active regions. *JOSO Ann.Rep.1997*, 88-89, 1998.
- Makarov, V.I. and Sivaraman, K.R. 1986, *Bull. Astr. Soc. India* Vol. 14, 163, 1986.
- Mayaud, P.N. (1972): The aa-indices: a 100-year series characterizing the magnetic activity. *J.geophys.Res.* Vol. 77, 6870, 1972.
- Pittock, A.B. (1978): A critical look at long term sunweather relationships. *Rev. Geophys.* Vol. 16, 400, 1978.
- Rostoker, G. and Sharma, R.P. (1980): Correlation of high latitude tropospheric pressure with the structure of the interplanetary magnetic field. *Canad.J.Phys.* Vol. 58, 255, 1980.
- Rust D.M. and Kumar A. (1996): Evidence for helically kinked magnetic flux ropes in solar eruptions. *Astrophys.J.* Vol.464, L199-L202, 1996.

Russell C.T. and McPherron R.L. (1973): Semi-annual variation of geomagnetic activity. *J.geophys.Res.* Vol. 78, 92, 1973.

Soon W., Posmentier E. and Baliunas S. (2000): Climate hypersensitivity to solar forcing? *Ann.Geophys.* Vol. 18, 583-588, 2000.

Tinsley, B.A., Hoeksema, J.T. and Baker, D.N. (1994): Stratospheric volcanic aerosols and changes in airearth current density at solar wind magnetic sector boundaries as conditions for the Wilcox tropospheric vorticity effect. J.Geophys.Res., Vol.99, 16805, 1994.

Tinsley, B.A. (1996): Correlations of Atmospheric Dynamics with Solar Wind Changes of Air-Earth Current Density into Cloud Tops. J.Geophys. Res.-Atmospheres., Vol.101, 29701, 1996.

Tinsley, B.A. (2000): Influence of Solar Wind on the Global Electric Circuit, and Inferred Effects on Cloud Microphysics, Temperature, and Dynamics in the Troposphere. *Space Science Reviews* in press 2000.

Tóth L. and Szegedi S. (2000) this proceedings.

Vose, R.S., Schmozer, R.L., Steurer, P.M., Peterson, T.C., Heim, R., Karl, T.R. and Eischeid, J.K. eds. (1992): The Global Historical Climatology Network: Long-Term Monthly Temperature, Precipitation, Sea Level Pressure and Station Pressure Data, *Environmental Sciences Division Publ.* No. 3912. Oak Ridge National Laboratory, Oak Ridge, Tennessee.

Wilcox, J.M., Scherrer L., Svalgaard W.O., Roberts W.O. and Olson R.H. (1973): Solar magnetic structure: influence on stratospheric circulation. *Science*, Vol. 180, 185, 1973.

SUNSHINE, CLOUDS AND COSMIC RAYS.

E. Pallé Bagó and C.J. Butler

Armagh Observatory, College Hill, BT61 9DG. Armagh, N. Ireland

ABSTRACT

Our analysis of the new ISCCP (International Satellite Cloud Climatology Project) D2 cloud data reveals that there is a correspondence between the low cloud cover and the galactic cosmic ray flux. Using several proxies for solar activity and the radiative forcing for the ISCCP cloud types, we estimate the possible impact that such a solar-terrestrial connection may have on climate and find that much of the warming of the past century could be quantitatively accounted for by the direct and indirect effects of solar activity. We have also analysed the behaviour of the available proxies for cloud cover existing for the last century, searching for the cloud cover decrease predicted by the low cloud- cosmic ray flux correlation. The sunshine records and the synoptic cloud records both indicate that the total cloud cover over the oceans has increased during the past century but the evidence for a low cloud decrease is unclear.

Key words: Sunshine, Clouds, Cosmic Rays, Climate.

I. INTRODUCTION

The extent to which the recent global warming has an anthropogenic origin (e.g. via the enhanced greenhouse effect) as opposed to a natural origin (e.g. through volcanic activity or solar variability) is of crucial importance for our understanding of how the Earth's climate has varied in the past and how it may vary in future. Detailed fits of global and hemispherical temperatures since the mid-19th century with empirical models involving the enhanced greenhouse effect and solar variability require at least one parameter linked to solar activity for a satisfactory fit in the mid-20th century (Kelly & Wigley, 1992; Soon et al., 1996).

A possible modulation of the Earth's albedo by changes in cloudiness resulting from changes in the flux of galactic cosmic rays was proposed by Svensmark & Friis-Christenssen (1997). This mechanism looked particularly promising after a strong correlation between cloud factor over mid-latitude oceans and cosmic ray flux was found by these authors for the period 1984-1991. They suggested that cosmic rays promote the formation of terres-

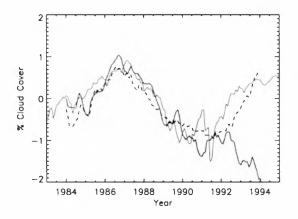


Figure 1. Total cloud cover (solid thick line) and low cloud cover (broken line) over the SFC areas as obtained with the D2 dataset from infrared (low clouds) and visual plus infrared (total cloud) observations. The solid thin line represents the Climax Cosmic Ray Flux scaled for comparison. (from Palle and Butler, 2000a)

trial clouds through ionization of particles in the troposphere. As both the flux and the energy spectrum of cosmic rays are known to be modulated by the interplanetary magnetic field, which in turn is strongly influenced by the magnetic field of the Sun, it is feasible that cosmic rays provide the link whereby solar activity affects the global climate (Svensmark, 1998). Here we will analyse recent evidence to support this link.

2. CORRELATION BETWEEN COSMIC RAY FLUX AND CLOUD FACTORS

Our first objective was to ascertain whether or not previous reports (Svensmark & Friis-Christenssen, 1997; Svensmark, 1998), that the total cloud cover over midlatitude oceans, excluding the tropics, (hereafter SFC zones) correlates strongly with cosmic ray flux, are substantiated by a new improved satellite cloud data set (IS-CCP D2). In Figure 1 we plot the total cloud cover over this latitude range together with the cosmic ray flux, suitably scaled for overlap. We note that a close correspondence between the cosmic ray flux and total cloud cover is maintained from 1983 till 1991, the period previously

Proc. 1st Solar & Space Weather Euroconference, 'The Solar Cycle and Terrestrial Climate', Santa Cruz de Tenerife, Tenerife, Spain, 25-29 September 2000 (ESA SP-463, December 2000)

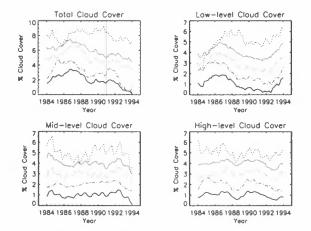


Figure 2. The 12-month running mean of the total, lowlevel, mid-level and high-level cloud cover for the period 1983-1995 covered by the ISCCP D2 dataset. Five different series are represented in each panel, ordered from bottom to the top as follows: Cloud cover over the whole Earth, the tropics ($\pm 22^{\circ}.5$), mid-latitudes ($\pm 22^{\circ}.5 \Rightarrow \pm$ 60°), the SFC zones (ocean areas excluding the tropics) and poles ($\pm 60^{\circ} \Rightarrow \pm 90^{\circ}$). Cloud cover is measured as the fraction of the sky covered by clouds. The amplitude of the cloud cover variation is real, but the mean value is shifted for plotting purposes. (from Palle and Butler, 2000a)

studied by Svensmark and Friis-Christenssen (1997), but that subsequent to this, the curves diverge. Thus, when we include the data from 1992 to 1994, we find that the new D2 data series does not confirm the previous findings in respect to the total cloud cover. Instead the correlation with the galactic cosmic ray flux now appears more strongly correlated with the low cloud cover.

In Figure 2 we show the mean monthly cloud factors for selected regions (described on the caption) for low, medium and high altitude clouds (2, 4.5 and 10 km mean altitude respectively), each smoothed with a twelvemonth filter to eliminate seasonal effects. We note the following: (1) the good correlation between total cloud factor and cosmic ray flux from 1983-91 breaks down after 1991; (2) the high level and mid-level clouds show no systematic variation over the period 1983-94; (3) the lowlevel clouds for all latitude zones excluding the poles are well correlated with the cosmic ray flux over the period 1983-94.

3. ESTIMATING CLOUD FORCING

The role of clouds in climate is still not well understood; they have two opposite effects. On the one hand they tend to cool the climate by reflecting short-wave solar radiation back to space, and on the other to warm the climate by trapping the long-wave radiation emitted from the Earth's surface. The balance of these two effects is in part determined by the cloud height; on average low clouds are believed to cool and high clouds to warm the climate (Ockert-Bell & Hartmann, 1992; Ramanathan et al., 1989). Provided the above correlation is

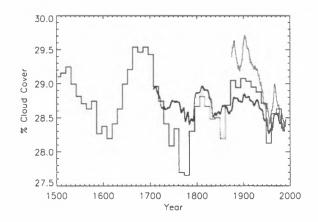


Figure 3. The 11-year smoothed reconstructed cloud cover for the whole Earth derived from the Zurich Sunspot number (middle line) and the aa index (top line). In addition we plot the reconstructed cloud cover factor for the whole Earth derived from the 11-year mean Heliocentric potential (longer line).

maintained over long periods, a reduced low-cloud factor would be expected during high solar activity, and the increased solar activity in recent decades would translate into a global decrease in the low, cooling clouds thereby contributing to global warming (Svensmark, 1998).

In order to make a prediction of the low cloud factor, earlier in the 20th century and in the 19th century when cosmic ray fluxes are unavailable, we have also determined the regression relations between the Sunspot Number, the <aa> index and the low cloud factor as determined from the ISCCP-D2 data. For even longer periods, extending back before the 19th century, we use the Heliocentric Potential, an interplanetary magnetic field index calculated by O'Brien (1979) which is based on the carbon isotope concentration in tree-rings.

From the regression between the various activity indices and the low cloud factor over the interval 1983-1994, we can make a prediction of the change in average low cloud factor since the late 19th century. The results indicate a decrease in low cloud factor by about 1% over the past one hundred years (see Figure 3), leading to a reduced albedo and positive radiation forcing in recent decades. Together with the increased forcing from the increase in solar irradiance, this leads to a total solar activity induced change in the global mean temperature of ~ 0.5°C which is close to the observed increase of 0.55°C since 1900 (Lean & Rind, 1998; Jones & Briffa, 1992).

Similarly, we can compute from the change in 14 C levels. (via the Heliocentric Potential), the effect of activity induced cloudiness on temperatures in the late 17th and early 18th centuries during the Maunder Minimum. We derive a cloud induced global cooling of 0.5° during this period compared to modern temperatures. This together with a cooling of 0.32°C from an inferred reduced solar irradiance of ~0.25% at that time (Rind & Overpeck, 1993) implies a combined cooling of 0.82°C, reasonably close to the value of ~ 1.0°C believed to have occurred at this time.

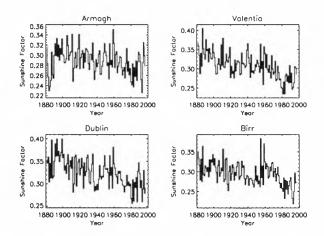


Figure 4. Total annual sunshine hours for the four Irish sites (1881-1998).

The details of these calculations are given in Palle & Butler (2000a). They are subject to several assumptions, including: (1) the correlation between low cloud and cosmic ray flux is maintained over long time scales; (2) other cloud types remain constant; (3) that there is no additional change in the cloud factor from global warming, i.e. no feedback.

4. OTHER CLOUD DATA AND CLOUD PROXIES

The above analysis, working from the observed correlation of low cloud factor with cosmic rays and solar activity indices, has serious implications for our understanding of the causes of climate change in the past century as it suggests that most of the global warming during this period can be attributed to the combined direct (irradiance) and indirect (low cloud factor) effects of solar activity. However the actual amount of the variation in cloud factor predicted is small ($\sim 1\%$) and could easily be swamped by other factors. In this respect we note that the above correlation applies only to low clouds whereas a comprehensive forcing computation would require knowledge of the variability of clouds at all levels. It is important, therefore, to examine any other evidence we can find that could give us actual measured cloud factors over the past century.

Since satellite-based cloud records do not extend for more than a couple of decades and calibration problems between the existing datasets do not allow a straight forward comparison, we have examined cloud proxy records and synoptic cloud observations, both measured from ground stations, to study the cloud cover behaviour on time scales longer than a decade.

One such relevant cloud proxy is sunshine duration. Daily records of the duration of bright sunshine have been obtained at four stations in Ireland since May 1880 using a standard *Campbell-Stokes* sunshine recorder (Observers Handbook, 1982). Two are located in the east of Ireland; at Armagh Observatory and The Ordnance Survey Office, Phoenix Park, Dublin; one in the extreme west at valentia Island/Cahirciveen, Co Kerry; and the fourth, in the



Figure 5. Adapted from Norris (1999). Yearly global mean departure (thick dash) and zonal mean departures (thin) from long-term mean daytime total cloud cover over the ocean. Zonal means are for 10° -lat bands between $60^{\circ}N$ and $40^{\circ}S$. Units are percent sky cover. Three-year running mean smoothing was applied.

midlands, at Birr Castle, Co Offaly.

The most prominent feature of the data, for all four sites. is a gradual decline in the total annual sunshine hours over much, if not all, of the 118 year period during which records have been obtained (see Figure 4). The effect is particularly conspicuous at the most westerly site of Valentia Island/Cahirciveen, on the County Kerry coast, where the number of sunshine hours has dropped by $\sim 20\%$ since the end of the last century. If we plot the seasonal averages, the gradual decrease is seen in all stations in most seasons. Similar results were reported by Stanhill (1998) using records of sunshine duration over Israel, though over a shorter time than the Irish records.

The sunshine data has been shown to be a very good proxy for total cloud cover over monthly to yearly time scales, at least over the Irish region (Pallé & Butler, 2000b). Unfortunately the sunshine records are related only to the total cloud factor and do not give us any information on cloud type. It can also be argued that the sunshine records are a local measurement and that the observed trends are not necessarily similar for other areas. However, Pallé & Butler (2000b) compared the variability of the ISCCP D2 satellite cloud records over Ireland and other areas of the globe and found that the Irish cloud variability is very similar to the whole North Atlantic region and in general to all mid-latitude oceanic regions, over the period comprised by the data (July 1983- August 1994). Thus it seems that the sunshine factor over Ireland could be particularly useful in indicating wider trends.

If the Irish sunshine data are indeed relevant to the global trend they would indicate a rise in the total cloud factor since the late 19th century, whereas the low cloud - cosmic ray correlation would predict a fall in low cloud factor over the same period. One explanation could be that high cloud has increased in this period to a greater extent than low cloud has decreased. As, on average, high clouds warm and low clouds cool the climate, increased high cloud and decreased low cloud would both give an additional positive radiative forcing increment to the solar irradiance forcing thereby leading to further enhanced global warming. Table 1. Sunshine records and synoptic cloud data compilations from the ground. Satellite cloud measurements from different satellite measurements are also displayed, however the short duration of those records makes them unsuitable for long-term studies. References: ¹Palle and Butler, 2000b; ²Stanhill, 1998a; ³Stahle et al., 1991; ⁴Sun and Groissman, 2000; ⁵Norris, 1999; ⁶Sun and Groissman, 2000; Karl et al., 1995; Liepert, 1997; DCSCVC, 1998 and therein; ⁷Stanhill, 1998b and therein; Liepert, 1997; ⁸Kernthaler et al., 1999; ⁹Palle and Butler, 2000a; ¹⁰Kristjansson and Kristiansen, 2000; ¹¹Menzel et al., 1996.

Dataset	Total Cloud Cover	Low Clouds	High Clouds	Period
Ground Data				
¹ Sunshine in Ireland (decrease)	Increase	_	_	1881-1998
² Sunshine in Israel (decrease)	Increase	_	_	1979-1995
³ Sunshine (?) Central USA (tree-rings)	Stable	_	-	1700-1980
⁴ Synoptic Clouds over FUSSR	Increase	Decrease	Increase	1936-1990
⁵ Synoptic Cloud over Oceans	Increase	Increase		1952-1995
⁶ Synp. Cloud (Austr, N.Am, India, Europe,)	Increase	_	Increase	1900-1990
⁷ Ground-based solar radiation (various)	Increase	_	_	1960-2000
Satellite Data				
⁸ ISCCP C2	Stable	_	Increase	1983-1991
⁹ ISCCP D2	Stable	CRF-Decrease	Stable	1983-1994
¹⁰ DMSP (water clouds over Oceans)	Increase	_		1988-1998
¹¹ HIRS (only Cirrus)	-	_	Increase	1989-1996

A second set of records we explore are the synoptic cloud observations. Synoptic observations of total cloud cover are taken in many observatories worldwide. The procedure for the measurements is simple, at certain times of the day, the observer notes the number of ocktas (1/8 th of the sky) covered by clouds. A totally overcast sky is registered 8 and a clear sky 0. At some stations, coverage by different cloud types is also recorded.

Observations of synoptic cloud cover over the oceans from volunteer ships since 1952 have been compiled and analysed by Norris (1999). Norris found that the global mean cloud cover over the oceans has increased by 1.9% (sky cover) between 1952 and 1995 (see Figure 5). Global mean low cloud cover is observed to increase by 3.6% during the same period. Trends in zonal mean cloud cover in 10° -lat bands between 60° N and 40° S were all found to be positive. Several possible artifacts were examined but it was considered unlikely that they could explain the observed interdecadal variability. Norris (1999) concludes, however, that the trends cannot be accepted as real until they have been corroborated by related meteorological parameters and satellite-based measurements.

Sun & Groissman (2000), have studied synoptic cloud cover variations over the former USSR from 1936 to 1990. They find high cloud to be increasing and low cloud decreasing with the total cloud increasing over this period. Though for a continental, as opposed to a maritime climate region, these findings are pretty much in line with the sort of trends suggested earlier by the Irish sunshine data and the cosmic ray - low cloud correlation. Though the total cloud trends are similar, it is difficult to reconcile the results by Norris (1999) and by Sun & Groissman (2000) on low clouds, other than to point out that they refer to very different regions. However, it should be noted that the Sun & Groissman trends are very statistically significant whereas those by by Norris are prone to many systematic effects such as might arise from a change in the latitude of preferred shipping lanes.

Similar reports to those of Norris (1999) and Sun and Groissman (2000), using cloud synoptic observations are described in Table 1. They all show an increasing trend in total cloud cover. No other general studies (involving more than one particular station) about specific synoptic cloud type variability are known to the authors.

In Table 1 we refer also to the reduction in ground solar radiation levels reported at a world-wide range of sites during the last 40 years (Stanhill, 1998 and references therein), suggesting a total cloud cover increase. However, such radiation decreases have not been always accompanied by an increase in cloud cover and its possible that changes in cloud type or atmospheric or cloud transparency could be responsible.

Thus it appears that the 'historical' cloud datasets (sunshine and synoptic cloud) indicate a general increase in the total cloud cover during the last century or at least in recent decades. The evidence for low cloud trends is less clear though it does not rule out a decrease in line with the prediction from solar activity levels.

A compilation of cloud satellite measurement is given in Table 1, however the short time span of the datasets (the longest is the ISCCP D2 covering little more than 11 years), makes them unsuitable for such long-term studies. Cloud types reported as stable as in the case of ISCCP C2 and D2 are in fact quite variable and a definite trend can not be clearly established. In fact the only two clear trends are the increasing trends found for DMSP (Defence Meteorological Satellite Project) satellites, detecting liquid clouds over the oceans, and the cirrus clouds detected by the HIRS (High-resolution Infrared Radiation Sounder). The decreasing trend in the low cloud cover from the ISCCP D2 is inferred only on basis of the possible cosmic ray influence. However the satellite measurements do not dispute the general conclusions reached using the 'historical' data.

5. WHAT IS CAUSING THE TOTAL CLOUD INCREASE?

We have seen in the previous section how the available proxies for clouds seems to indicate that total cloud cover has been increasing over the last century. But what are the reasons for the change? Certainly a connection between energetic particles entering the atmosphere and the cloud formation would explain a decrease, but not the opposite trend.

Could the long term trend in total cloud result from a mean air and sea surface temperature increase? An increase in cloud formation might be expected from an increase in evaporation rates following the rise in seasurface temperatures which have accompanied global warming (Reid, 1987). Little is known about the effects that a change in temperature will have on clouds. Global circulation models predict a cloud amount decrease when climate warms (Cess, 1996) which has not been seen. A progressive moistening of the atmosphere has been seen (Wentz and Schabel, 2000). However, since the relative humidity has remained constant, an increase in the water content of the atmosphere would not necessarily lead to an increase in cloud factor.

An increase in tropospheric aerosols could also give rise to increased cloud formation. However Norris (1999) stated that the 10°-lat bands trends in synoptic cloud observations between 60°N and 40°S, are generally larger for the Southern Hemisphere and Tropics than trends in the mid-latitude Northern Hemisphere. For Norris (1999), this argues against attribution of increased cloud cover to increased anthropogenic aerosols, and suggests that it is possible that global cloud cover is responding to some other global parameter, perhaps global temperature. Pallé & Butler (2000b) found a correlation between the sunshine records over Ireland and the solar cycle length. Since the sunspot cycle length was shown to be strongly related to the NH air temperature (Friis-Christenssen & Lassen, 1991), they concluded that in the vicinity of Ireland, it seems likely that decreased sunshine hours (increased cloudiness) results from the increased temperatures associated with global warming

Another effect to take into consideration is the effect of increased aircraft traffic. In many of the sites where a decrease in total solar irradiance has been found, an increasing trend of cirrus cloud formation has also been detected. A shift from stratiform to higher frequencies of convective clouds has also been observed (Liepert, 1997; Stanhill, 1998). Finally, another possibility could be natural weather variability associated with shifts in weather patterns.

6. CONCLUSIONS

There appears to be a significant correspondence between the low cloud cover as seen from modern satellite data and the galactic cosmic ray flux. However the extent of this dataset is short and gives space for many uncertainties when trying to establish the long-term behaviour of the cloud cover. The potential effect of such a relationship has been explored and the authors demonstrated that, if it were true, it would be of dramatic importance to the climate.

In order to assess the validity of the prediction over long time scales, some proxies have been compared. Sunshine records and the synoptic cloud cover over many areas of the Earth seem to agree that the total cloud cover has been increasing over the last century. This is in the opposite direction to the trend predicted for low clouds by the cosmic ray - low cloud correlation. The reliability of the datasets though is uncertain, but the agreement in the trends suggest that they are real, and maybe caused by the temperature rise which has occurred during the last century or other causes not related with energetic particles entering the atmosphere. It seems then that the overall picture of the cloud variability during past times can be far more complicated than suspected. The importance of such changes will depend on the variability of the different cloud types and on the geographical distribution of those changes. However, both mechanisms, a long term trend and a direct cosmic ray influence, present a challenge to present and future global circulation models and will have a crucial role on our understanding of the climate change. Until the cloud behaviour on temporal and geographical scales is understood, via long and reliable datasets, global circulation models and predictions will be seriously handicapped.

ACKNOWLEDGMENTS

We would like to thank Dr. K. O'Brien for discussions and M. Murphy for assistance with computing. The sunshine data for Dublin, Birr and Valentia Island/Cahirciveen were kindly provided by D. Fitzgerald of Met Eireann, Dublin. Research at Armagh Observatory is grant-aided by the Department of Culture, Arts and Leisure for Northern Ireland.

REFERENCES

Cess R.D. et al.(34), 1996. J. Geophys. Res. 101, 12791-12794.

- DCVDVC: Decade-to-Century-Scale Climate Variability and Change. National Research Council, 1998 *National Academy Press* Washington D.C., International Standard Book Number:0-309-06098-2, p 17.
- Friis-Christenssen E., Lassen K. 1991. *Science* **254**, 698-700.
- Jones P.D., Briffa, K.R., 1992. The Holocene 2, 165-179.
- Karl T.R., Jones P.D., Knight R.W., Kukla G., Plummer N., Razuvaev V.N., Gallo K.P., Lindesay J.A., Charlston R.J., 1995. *Natural Climate Variability on Decadeto-Century Time Scales*. National Research Council: Washington D.C., 80-95.
- Kelly P.M., Wigley T.M.L., 1992. Nature 360, 328-330.
- Kernthaler S.C., Toumi R., Haigh J.D., 1999. *Geoph. Res.* Letters 26, num. 7, 863-865.
- Kristjansson J.E., Kristiansen J., 2000. J. Geophys. Res. 105, 11851-11863.
- Lean J., Rind D., 1998. Journal of Climate 11, 3069-3094.
- Liepert B.G., 1997. International Journal of Climatology 17, 1581-1593.
- Menzel W.P., Wylie D.P., Strabala K.I., 1996. *IRS96*, *Current problems in Atmospheric radiation*. Smith and Stamnes(Eds) ISBN 0-937194-39-5, pp 719-725.
- Norris J.R., 1999. Journal of Climate 12, 1864-1870.
- O'Brien K., 1979. J. Geophys. Res. 84, 423.
- Observers Handbook, 4th Edition. 1982. UK Meteorological Office (Eds). Her Majesty's Stationery Office, London, p 153.
- Ockert-Bell M.E., Hartmann D.L., 1992. Journal of Climate 5, 1157-1171.
- Pallé E., Butler C.J., 2000a. Astronomy & Geophysics 41, Issue 4, 18-22.
- Pallé E., Butler C.J., 2000b. International Journal of Climatology (in press)
- Ramanathan, V., Cess, R.D., Harrison, E.F., Minnis, P., Barkstrom, B.R., Ahmad, E., Hartmann, D., 1989. Science 243, 52.
- Reid G.C., 1987. Nature 129, 142-143.
- Rind, D., Overpeck, J., 1993. Quat. Sci. Rev. 12, 357-374.
- Soon, W.H., Posmentier, E.S., Baliunas, S.L., 1996. Astrophysical Journal 472, 891-902.
- Stahle D.W., Cleaveland M.K., Cerveny R.S., 1991. International Journal of Climatology 11, 285-295.
- Stanhill G., 1998. International Journal of Climatology 18, 347-354.
- Stanhill G., 1998. International Journal of Climatology 18, 1015-1030.
- Sun B., Groissman P.Y., 2000. International Journal of Climatology 20, 1097-1111.
- Svensmark, H., Friis-Christenssen, E., 1997. J. Atmos. Solar-Terrest. Phys. 59, 1225-1232.
- Svensmark, H., 1998. Phys. Rev. Lett. 81, 5027-5030.
- Wentz F.J., Schabel M., 2000. Nature 403, 414-416.

The Long-Term Terrestrial Record of Climate Change

CO2 AND ASTRONOMICAL FORCING OF THE LATE QUATERNARY

A. Berger and M.F. Loutre

Université catholique de Louvain Institut d'Astronomie et de Géophysique G. Lemaître 2 Chemin du CyclotronB-1348 Louvain-la-Neuve, Belgium Tel. +32 10-47 32 97 / fax: +32 10-47 47 22 e-mail: <u>berger@astr.ucl.ac.be</u> / <u>loutre@astr.ucl.ac.be</u>

ABSTRACT

The LLN 2-D Northern Hemisphere climate model has been used to reconstruct the long-term climatic variations over the Quaternary Ice Age. Sensitivity analyses to the astronomically-driven insolation changes and to the CO₂ atmospheric concentration have been performed. In particular, an atmospheric CO2 concentration decreasing linearly from 320 ppmv at 3 Myr BP (Late Pliocene) to 200 ppmv at the Last Glacial Maximum was used to force the model in addition to the insolation. Under such condition, the model simulates the intensification of glaciation around 2.75 Myr BP, the late Pliocene-early Pleistocene 41-kyr cycle, the emergence of the 100-kyr cycle around 900 kyr BP, and the glacial-interglacial cycles of the last 600 kyr. Experiments have shown that both isotopic stages 11 and 1 request a high CO₂ to reach the interglacial level. The insolation profile at both stages and modeling results tend to show that stage 11 might be a better analogue for our future climate than stage 5e. Although the insolation changes alone act as a pacemaker for the glacial-interglacial cycles, CO₂ changes help to better reproduce past climatic changes and, in particular, the air temperature and the southern extent of the ice sheets. However CO₂ alone is unable to generate any glacialinterglacial cycle. Using the calculated insolation and a few scenarios for CO₂, the climate of the next 130 kyr has also been simulated. It shows that our interglacial will most probably last particularly long (50 kyr). This conclusion is reinforced if we take into account the possible intensification of the greenhouse effect which might result from man's activities over the next centuries.

1. INTRODUCTION TO THE MILANKOVITCH THEORY

The current Ice Age, which the Earth entered 2 to 3 million years ago, is called the Quaternary Ice Age. It is characterized by multiple switches of the global climate between glacials (with extensive ice sheets) and interglacials (with a climate similar to or warmer than today by a few degrees Celsius). Over the last million years, the waxing and waning of ice sheets occurred in a more or less regular way. Reconstructions of long-term climatic variations, like the ice volume and sea level, show a sawtooth shape with a 100-kyr quasi-cycle over which shorter quasi-cycles of roughly 41 and 21 kyr are

superimposed (Berger, 1988). The last cycle goes from the Eemian interglacial times, centered roughly 125 kyr BP, to the present-day Holocene interglacial which peaked 6 kyr BP. It includes the Last Glacial maximum (LGM) which occurred 20 kyr ago. In the Northern Hemisphere, the LGM differed strikingly from the present in the huge land-based ice sheets, reaching approximately 2 to 3 km in thickness and amounting to about 43 x 10⁶ km³ of ice more than today. This value is consistent with the global land-based ice volume maximum reconstruction exceeding today's grounded ice sheets by 52.5 x 10^6 km³ (Yokoyama et al., 2000) and a volume of Antarctic ice exceeding the present-day value by $\sim 10 \text{ X } 10^6 \text{ km}^3$. This last value corresponds to an equivalent global sea-level change of ~ 25 m (although this value might be a little bit too large, Bentley, 1999). Due to these ice sheets, sea level was indeed lower than today by roughly 130 m (Yokoyama et al., 2000) and the global average surface air temperature was ~ 5° C below present. CO₂ levels were about half of their present-day value and aerosol loading may have been higher than present (Petit et al., 1997).

But the 100-kyr cycle, so dominant a feature of the late Pleistocene record, does not exhibit a constant amplitude over the past 3 million years. Many spectral analyses (from Pestiaux and Berger, 1984 to Bolton et al. 1998) showed that this periodicity disappears before 1 Myr BP roughly, the climatic variability being dominated by the 41-kyr cycle during the Late Pliocene and early Pleistocene.

These kinds of broad climatic features are those explained by the astronomical theory of paleoclimates. Proponents of this theory claim that the changes in the Earth's orbital and rotational parameters have been sufficiently large as to induce significant changes in the seasonal and latitudinal distributions of irradiation received from the Sun and so, to force glacials and interglacials to recur in the manner deduced from geological records. In this process, feedbacks due to changes in the albedo, the water vapour and other greenhouse gases play a fundamental role.

The incoming solar radiation received over the Earth has an annual periodic variation due to the Earth's elliptic translation motion around the Sun. But in addition, the seasonal and latitudinal distributions of this

Proc, 1st Solar & Space Weather Euroconference, 'The Solar Cycle and Terrestrial Climate', Santa Cruz de Tenerife, Tenerife, Spain, 25-29 September 2000 (ESA SP-463, December 2000)

solar radiation are changing in time due to the so-called long-term variations in three astronomical elements (Berger, 1996a, 1996b). These are the eccentricity e, a measure of the shape of the Earth's orbit around the Sun, the obliquity ε , the tilt of the equator with respect to the plane of the Earth's orbit, and the climatic precession, $e\sin\widetilde{\omega}$, a measure of the Earth-Sun distance at the summer solstice.

According to theoretical calculations (Berger, 1978), the eccentricity of the Earth's orbit varies between near circularity (e = 0) and slight ellipticity (e = 0.07) at a period which mean is about 100 kyr. The most important terms in the series expansion occur however at 404, 95, 124, 99, 131 and 2,380 kyr (in decreasing order of amplitude). The tilt of the Earth's axis varies between about 22° and 25° at a period of nearly 41 kyr. As far as precession is concerned, the equinoxes and solstices shift slowly around the Earth's orbit relative to the perihelion, with a mean period of 21 kyr (it is measured by the longitude, $\widetilde{\omega}$, of the moving perihelion). This period results actually from the existence of two periods which are close to each other: 23 and 19 kyr. In the insolation formulas used to study past and future astronomical forcing of climate, the amplitude of sin $\widetilde{\omega}$ is modulated by eccentricity in the term $e\sin\widetilde{\omega}$.

The combined influence of changes in e, ε , and $e \sin \widetilde{\omega}$ produces a complex pattern of insolation variations. A detailed analysis of the changes in daily solar radiation (Berger et al., 1993a) shows that it is principally affected by variations in precession, although the obliquity plays an important role for high latitudes, mainly in the winter hemisphere.

The orbital hypothesis of climatic change was first quantitatively formulated by the astronomer Milutin Milankovitch in the 1920s. He argued (Milankovitch, 1941) that insolation changes in the high northern latitudes during the summer season were critical to the formation of continental ice sheets. During periods when insolation in the summer was reduced, the snow of the previous winter would tend to be preserved, a tendency that would be enhanced by the high albedo of the snow and ice areas. Eventually, the effect of this positive feedback would lead to the formation of persistent ice sheets.

A simple linear version of the Milankovitch model predicts therefore that the proxy record of climate variations would contain the frequencies of the astronomical parameters that are responsible for changing the seasonal and latitudinal distributions of the incoming solar radiation. It happens that investigations since the late 1970s have indeed demonstrated that the 19-, 23- and 41-kyr periodicities actually occur in long records of the Quaternary climate (Hays et al., 1976; Imbrie et al., 1992). However, the same investigation identified also the largest climatic cycle as being 100 kyr. As the 100-kyr eccentricity cycle is very weak in the insolation (Berger et al., 1993a), it cannot be related to the orbital forcing by any simple linear mechanism (Imbrie et al., 1993).

Over the last 25 years, a number of modelling efforts have attempted to explain the relationship between astronomical forcing and climatic change (Berger, 1995). Most of these modelling studies have focused on the origin of this 100-kyr cycle. Although these models are based on parameters which are considered to be physically plausible, they are all simplified. What these models do confirm is that the response to orbital forcing is non-linear and that it involves internal processes and feedback mechanisms. Whether the external orbital forcing drives the internal processes, phase-locks the oscillations of an internally driven system, or acts as a pacemaker for the free oscillations of an internally driven system remains, however, an open question.

As a consequence, the discussion of how the climate system responds to orbital forcing calls for the construction of a physically realistic model of the timedependent behaviour of the coupled climate system, including the atmosphere, the oceans, the cryosphere, the lithosphere and the biosphere. At that time-scale, plate tectonics, mantle convection, mountain building and Sun evolution are kept constant.

2. LLN 2-D MODEL

It was suggested earlier (Berger, 1979) that the timeevolution of the latitudinal distribution of the seasonal pattern of insolation is the key factor driving the behaviour of the climate system while the complex interactions between its different parts amplify this orbital perturbation. That dynamical behaviour of the seasonal cycle suggests that time-dependent coupled climate models might be able to test whether or not the astronomical forcing can drive the long-term climatic variations. Such time-dependent climate models must therefore be forced only by the astronomical variations of insolation for each latitude and day, the so-called boundary conditions used in equilibrium atmospheric general circulation model experiments (ice-sheet size and area, sea-surface temperature, albedo, etc.) being all generated by the climate model itself.

Such climate models have been constructed in Louvainla-Neuve. Only the Northern Hemisphere version of the LLN 2-D models will be discussed here. This climate model links the Northern Hemisphere atmosphere, ocean mixed layer, sea-ice, ice sheets and continents (Gallée et al., 1991). It is a latitude-altitude model. In each latitudinal belt, the surface is divided into at most seven oceanic or continental surface types, each of which interacting separately with the subsurface and the atmosphere. The oceanic surfaces are ice-free ocean and sea-ice cover, while the continental surfaces are the snow-covered and snow-free lands and the Northern Hemisphere ice sheets.

The atmospheric dynamics is simulated by a two-level quasi-geostrophic model written in pressure coordinates and zonally averaged. Although the model domain is limited to the Northern Hemisphere a cross-equatorial heat flux is allowed. Precipitations over the ice sheets are corrected to take into account the surface slope, the elevation and the continentality of these ice sheets. For the calculation of the radiative fluxes, the vertical temperature profile in the troposphere is determined from the static stability parameter and the pressure. The vertical variation of specific humidity is deduced from the zonally averaged surface temperature and relative humidity. Annual mean and monthly distribution of the zonal cloudiness are prescribed. The calculation of the solar radiation takes into account absorption by H₂O, CO₂ and O₃, Rayleigh scattering, absorption and scattering by cloud and aerosol layers, and reflection by the surface. The longwave radiation scheme follows a formulation used in GCM's. The atmosphere interacts with the other components of the climate system through vertical fluxes of momentum, heat and water vapour. The model explicitly incorporates detailed surface energy balance and snow and sea-ice budgets.

The vertical profile of the upper ocean temperature is computed by a mixed-layer model. The oceanic transport and its influence on the sea-surface temperature are simulated through a diffusive parameterization of the meridional convergence of heat. Sea ice is represented by a thermodynamic model including leads and a parameterization of lateral accretion.

A special attention is paid to the albedo of snow, of vegetation in the tundra/taiga regions, of sea water and of sea ice. More details on the model are given in Gallée et al. (1991) and also in Berger et al. (1990) for the ice sheet – lithosphere model, in Berger et al. (1989) for the upper ocean and in Berger et al. (1994) for the radiative convective scheme.

Simulation of the present climate shows that the model is able to reproduce the main characteristics of the atmospheric general circulation and the seasonal cycles of the oceanic mixed layer, of the sea ice, and of the snow cover (Gallée et al., 1991).

This atmosphere-ocean model is asynchronously coupled to a model of the three main Northern Hemisphere ice sheets and their underlying bedrock in order to simulate the long-term climatic changes. The coupled climate model is then forced by the astronomically-derived insolation and by the atmospheric CO_2 concentration, because the model does not contain any carbon cycle yet. Results from some experiments made with this model over the last glacialinterglacial cycles will be discussed here.

3. SENSITIVIY OF THE LLN 2-D MODEL TO CO₂

Since the publication of Hays et al. (1976), the major question remains whether or not the astronomicallyinduced changes in solar radiation received on the Earth are able to generate the climatic changes reconstructed independently by geologists.

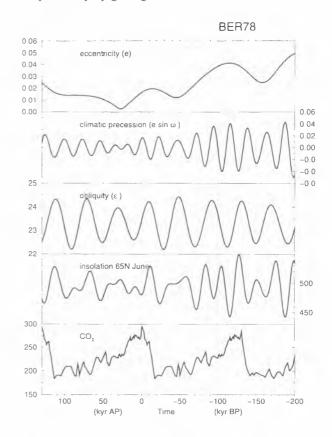


Figure 1. Long term variations of eccentricity, precession, obliquity, summer solstice insolation at 65°N (Berger, 1978) and atmospheric CO₂ concentration (Jouzel et al., 1993 for the past) from 200 kyr BP to 130 kyr AP.

To test this astronomical hypothesis, all external forcings (including CO_2), except the insolation changes (Figure 1), have to be kept constant. Experiments were therefore performed with three selected constant CO_2 concentrations - low (210 ppmv), high (290 ppmv) and medium (250 ppmv) – which corresponds to an average concentration for, respectively, glacial, interglacial and intermediate times (Berger et al., 1998b). Most of the time, during the last 200 kyr at least, CO_2 is varying around 225 ppmv (between 200 and 250 ppmv), higher values being reached only during the interglacials (Petit et al., 1999). The pre-industrial value, representative of our Holocene interglacial is ~ 280 ppmv, but the

present-day level (year 2000 A.D.) is already 368 ppmv, more than 30 % above the interglacial levels and about twice as much as during the glacial maximum.

The conclusions that we can draw from such experiments (Figure 2) are the following.

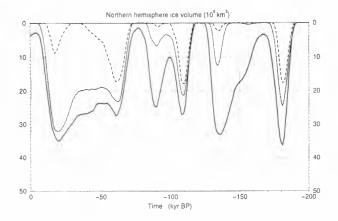


Figure 2. Simulated ice volume of the Northern Hemisphere using the LLN 2-D NH climate model forced by insolation and a constant CO_2 concentration over the last 200 kyr (210 ppmv in full line, 250 ppmv in dotted line and 290 ppmv in dashed line).

(i) A frequent melting of the ice sheets occur under a high CO_2 concentration (290 ppmv and even 250 ppmv).

(ii) Only the CO₂ concentration of 210 ppmv provides a simulation which might be compared to the geological reconstructions, the two other experiments leading to an amplitude of the ice volume variations which is far less than in geological reconstructions. When CO₂ is kept at its glacial value (210 ppmv), the amplitude of the ice volume change is about 35×10^6 km³, but the amount of ice remains always lower than $20 \times 10^6 \text{ km}^3$ when the CO₂ concentration is 290 ppmv. Actually, it appears that the CO₂ level of 210 ppmv is low enough to allow the albedo-temperature and water vapor-temperature feedbacks to start playing their fundamental role in amplifying the direct climatic impact initiated by the orbitally-induced insolation changes. The analysis of the spectra of the Northern Hemisphere ice volume simulated under a 210, 250 and 290 ppmv forcing confirms that the coherency with the SPECMAP data (Imbrie et al., 1984) is significant (at the 5 % level) in the precession, obliquity and eccentricity bands only for 210 ppmv (Figure 3). However, a major deficiency remains in the results of the 210 ppmv experiment: the Northern Hemisphere ice sheets melt too often during some interglacials while there is evidence that the Greenland ice sheet survived over the last 2 to 3 glacialinterglacial cycles at least (Dansgaard et al., 1993). It was shown (Gallée et al., 1993) that this shortcoming does not prevent the ice sheets to grow again leading to a 100 kyr quasi-cyclicity similar to the one seen in the geological data.

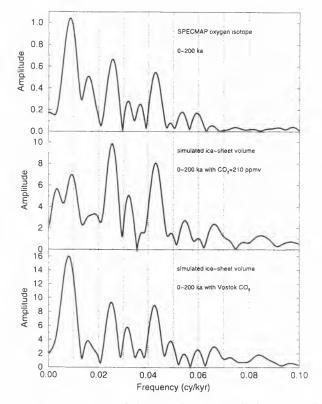


Figure 3. Spectra of the SPECMAP stacked curve, of the ice volume simulated by the LLN 2-D Northern Hemisphere climate model forced by insolation and a constant CO_2 concentration of 210 ppmv (see Figure 2 full line) and of the ice volume simulated by the LLN 2-D Northern Hemisphere climate model forced by insolation and the Vostok CO_2 reconstruction by Jouzel et al. (1993) from 200 kyr BP to present (Figure 4 full line).

(iii) The response of the climate system is far from being linear in CO₂. Relatively large volumes of ice are created for the three CO₂ levels at 181, 109 and 61 kyr BP, with each time the 250 ppmv curve being situated half-way between the 210 and 290 ppmv ones (at these three dates the differences between the results of these 2 extreme CO₂-concentration experiments are respectively 20 and twice 10 x 10^{6} km³). This is not the case for the other ice maxima. At 136 and 90 kyr BP, large ice sheets appear only for 210 ppmv, the differences between the 210 and 290 ppmv cases amounting to respectively 30 and 25 x 10⁶ km³. At these two dates, the 250 ppmv simulation is definitely closer to the 290 ppmv one. In contrast, at 20 kyr BP, the difference between the low and the high CO₂ experiments amounts also to more than 25 x 10^6 km³, but the 250 ppmv simulated ice maximum of 30 X 10⁶ km³ is here very closely tied to the 210 ppmv one. This very large difference in the response of the model for the 250 ppmv CO₂ level seems to indicate the existence of critical CO₂ concentrations (which are time dependent)

around which the climate system may be responding either like the high or like the low CO_2 level.

The different behaviour of the model to CO_2 around 20 kyr BP, as compared to what happens around 136 and 90 kyr BP is actually related to the state in which the climate system is before these ice maxima: the Earth is in a glacial during isotopic stages 4 to 2, whereas the climate before the other two maxima is interstadial, the amount of ice being rather low when the insolation starts to decrease and to induce the entrance into glaciation. Therefore at 136 and 90 kyr BP, a lower CO_2 – as compared to the LGM case – is requested to enter into glaciation, preventing the 250 ppmv forcing to build sufficiently large ice sheets.

(iv) The similar behaviour of the response of the model under a 250 and a 290 ppmv forcing during all interstadials (except stage 3) confirms that its sensitivity to CO_2 is different in a cold-glaciated Earth than during a warm – ice free Earth. This implies that during interglacials (like the Holocene), an ice age can be triggered, in our model, only by a rather low CO_2 concentration (below 250 ppmv at least).

(v) At the ice volume minima dated 166, 75 and 4 kyr BP in the 210 ppmv experiment, the ice sheets disappear under the 290 and 250 ppmv CO₂ concentrations and are very small for 210 ppmv. They disappear also for the three concentrations between 200 and 190 kyr BP and between 125 and 118 kyr BP. All these 5 situations correspond to a 65° N June insolation which peaks above 525 Wm⁻² a few thousands of years earlier. The behaviour at 100 kyr BP, where the ice sheets disappear only for 290 ppmv, is different from what happened at 75 and 4 kyr BP, although the insolation minimum located at 116 kyr BP was much deeper than in the 75 and 4 kyr BP cases, having led to an appreciable amount of ice at 110 kyr BP.

(vi) In a similar way, the situation between 165 and 135 kyr BP can be associated with the situation between 50 and 20 kyr BP. Both intervals going from a minimum to a maximum of ice are exceptionally long (30 kyr) compared to the more traditional 10 kyr associated to the precession cycle. This is definitely related to the small oscillations in the insolation occurring between 170 and 140 kyr BP and between 65 and 30 kyr BP. Associated to a quite small and slowly varying eccentricity, the very weak precessional signal is unable to drive the climate system into a cycle. These cases are quite interesting for the future climate as similar situations occur quite often in the insolation of the next 100,000 years.

4. RESPONSE OF THE LLN MODEL TO CO₂ CHANGE ONLY

The atmospheric CO₂ concentration is, in a complex way, related to climate. It is actually not a forcing, but a feedback, and thus it bears on the features of the climatic change. The question was raised whether these CO2 variations alone could be responsible for the glacial-interglacial cycles (Loutre and Berger, 2000a). In the experiments designed to try answering these questions, the insolation was kept constant through time and the atmospheric CO₂ concentration reconstructed from the Vostok ice core was used as the only external forcing (Jouzel et al., 1993). Cool to hot orbits were selected corresponding for example to an insolation at 65°N in June ranging from 403.2 Wm⁻² to 602.3 Wm⁻² (the present day value being 477.6 Wm⁻²). The results obtained using the LLN 2-D NH climate model is totally different from those obtained from the twin experiment (described in section 3) where a constant CO₂ but a real variable insolation are used. Either the orbit is cold enough and the ice volume increases to a maximum volume which thereafter remains constant, or the orbit is too warm preventing the model to generate any ice sheet. As a consequence, according to the LLN 2-D NH climate model, the long-term variations of the atmospheric CO₂ concentration taken from the Vostok reconstruction is, when considered as the only external forcing, unable to drive the climate system into any glacial-interglacial cycle for the ice volume. This is, however, not the case for the temperature which exhibits the CO₂ peaks in its spectrum. These experiments confirm not only the fundamental role played by the astronomical forcing on climatic cycles, but also the important influence of the atmospheric CO₂ concentration on temperature.

5. RESPONSE OF THE LLN MODEL TO THE INSOLATION AND CO₂ FORCINGS

As there is no carbon cycle coupled to our model yet, we can only study how the response of the LLN 2-D model to the orbitally induced forcing is modified when using a variable CO_2 instead of a fixed one. We assume as a first step, that using CO_2 as an external forcing instead of an internally generated parameter has no significant impact on the long-term variations of climate, although it may influence the short-term response as a feedback.

Broadly speaking the response of the model under the Vostok CO_2 (Jouzel et al., 1993) and the insolation (Berger, 1978) forcings reproduce quite well the geological record over the last 200 kyr (Berger and Loutre, 1996; Berger et al., 1998b) (Figure 4). However, our simulations are only providing variations of the Northern Hemisphere continental ice volume. In the comparisons, we must therefore keep in mind that we do not have any reconstruction of the Southern Hemisphere

ice volume (mainly Antarctica) and that a large number of hypotheses subtend the model.

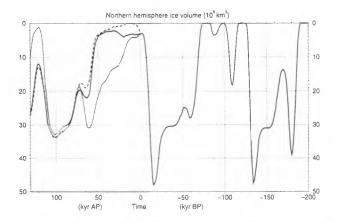


Figure 4. Simulated ice volume of the Northern Hemisphere using the LLN 2-D Northern Hemisphere climate model forced by insolation and CO_2 , from 200 kyr BP to 130 kyr AP. The atmospheric CO_2 concentration of Figure 1 leads to the full line. The dotted line results from a simulation where CO_2 is kept equal to 210 ppmv over the next 130 kyr and the dashed curve provides the results of the 750 ppmv scenario. Ice volume increases downward (Loutre and Berger, 2000b).

When compared to the stacked, smoothed oxygenisotope record of SPECMAP (Imbrie et al., 1984; Martinson et al., 1987), one can see that the overall timing is quite well reproduced, but discrepancies in the magnitude of the ice volume can be observed. The largest one is probably the too large ice melting simulated by the model around 170 kyr BP, although the ice volume maximum at 182 kyr BP seems to be well captured by the model. The large values of insolation around 175 kyr BP induce this important melting of the Northern Hemisphere ice sheets. Either it is an important deficiency of the model or we have to look for a significant change in the Southern Hemisphere continental ice at that time. At the end of stage 6, the simulated glacial maximum occurs at 135 kyr BP while the δ^{18} O ice volume maximum occurs at 151 kyr, but we must accept that this last remains large from 156 to 133 kyr BP. The model simulates very well the transitions between isotopic stages 6 and 5 and between the isotopic substages 5e (Eemian interglacial) and 5d. This is due mainly to the insolation changes, but it is reinforced by important changes in the CO₂ concentration and all the feedbacks in the model. Although the timing of what may correspond to isotopic substages 5c, 5b and 5a are quite well reproduced (a coincidence which is certainly reinforced by the astronomical tuning of the SPECMAP curve), the amount of ice is here again much less than in SPECMAP. This discrepancy is more or less similar to the one occurring at isotopic substage 6.5, 170 kyr ago. Moreover, the δ^{18} O ice volume minimum around 90 kyr

BP lasted for about 10 kyr, contrarily to the simulations, and the simulated ice volumes at stages 5a and 4 are lagging behind the δ^{18} O curve (between 3 kyr and 8 kyr).

At 70 kyr BP, the ice sheets start to form quite rapidly to lead to a first ice volume maximum at 59 kyr BP. This is followed by a weak melting of ~ 5 x 10^6 km³ leading to a minimum in the simulated ice volume at 50 kyr BP. The ice sheets are then starting to grow again, slowly to about 30 kyr BP and then more rapidly to the Last Glacial Maximum where they amount to 47×10^6 km³ of ice at 15 kyr BP. Stage 3 is therefore more or less well reproduced although, as for the 170 kyr BP interstadial, there is not enough ice according to SPECMAP. The simulated Last Glacial Maximum is lagging behind SPECMAP by 4 kyr, a lag which is related to the late CO₂ minimum in the Vostok curve.

Finally, the model simulates a deglaciation from 15 kyr to 3 kyr BP leaving only the Greenland ice sheet in the Northern Hemisphere with roughly 3 x 10^6 km³ of ice. Since 3 kyr BP, the ice volume is shown to increase slightly reaching 3.2×10^6 km³ today which represents about the present value. In parallel our simulated climate is slightly cooling since the peak of the Holocene. A similar observation is clearly visible, but over the whole last 10,000 years, in the Greenland temperature record published by Johnsen et al. (1995, see their Figure 2).

As far as the ice volume maxima are concerned, SPECMAP shows two extremes located at the Last Glacial Maximum (~ 20 kyr BP) and at stage 6 (~ 151 kyr BP), with the LGM being slightly the largest. There are also two secondary maxima, roughly of the same size: isotopic substage 6.6 (183.3 kyr BP) and stage 4 (60.4 kyr BP). The simulation using Jouzel et al. CO_2 reconstruction mimicks pretty well these maxima, except for the late arrival of stage 6 and an ice volume larger at stage 6.6 than at stage 4.

It is interesting to note that the simulated Northern Hemisphere ice sheets are melting totally three times: between 126 and 117 kyr BP, 100 and 97 kyr BP and 83 and 74 kyr BP. Although this is not realistic (the Greenland ice sheet having survived; Dansgaard et al., 1993), it can be explained by the large insolation occuring at these times (as already mentioned in section 3) and the large CO_2 concentration between 130 and 115 kyr BP which continues to play an important role in the behaviour of the ice sheets over the next 30 to 40 kyr.

Being given all hypotheses used in the modeling experiments, the results may be considered as surprisingly good. Using the reconstructed CO_2 concentrations from deep-sea or ice cores improves the

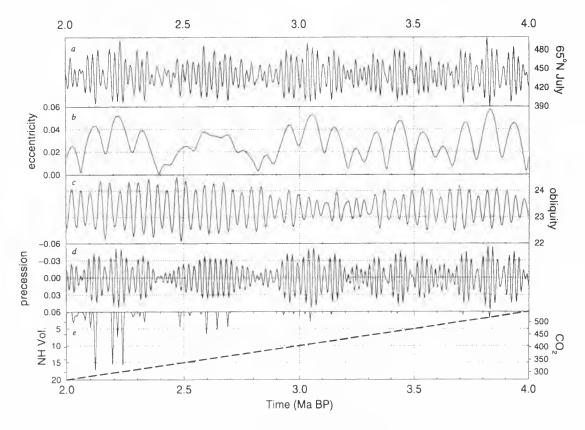


Figure 5. The Earth's orbital elements and the resultant insolation variation from 4 to 2 Myr; (a) the 65°N July insolation (Wm^{-2}), (b-d) the Earth's orbital parameters (Loutre and Berger, 1993) and (e) simulation from 3,940 to 2 Myr (solid line), with CO₂ linearly decreasing from 540 ppmv at 4 Myr to 270 ppmv at 2 Myr (bold dashed line).

constant CO_2 simulations (Figure 2) and their spectra (Figure 3), if SPECMAP is used as a standard for comparison. These experiments confirm that variations in the Earth's orbit and related insolation act as a pacemaker of ice ages (Hays et al., 1976) and that CO_2 variations shape the 100 kyr cycle and mainly improve the simulated surface air temperature (Gallée et al., 1992; Loutre et al., 1994).

A deeper analysis of these experiments also confirm the importance of the processes governing the response of the modelled climate system to insolation and/or CO_2 changes. These are essentially related to the albedo- and water vapor feedbacks (Berger et al., 1993b), to the taiga-tundra direct and indirect impacts on high latitudes surface albedo (Berger, 1998), to the altitude and continental effects on the precipitations over the ice sheets, to the ageing of snow due to the recrystallization process and its impact on the albedo, to the lagging lithospheric response to the ice sheets loading (Crucifix et al., 2000) and to the mechanical destabilisation of the ice sheets through the rapid melting of their southern front as compared to the northern one (Berger et al., 1992, 1993c).

Based upon this validation of the LLN 2-D model over the last two climatic cycles, experiments dealing with the early and middle Pleistocene were made.

6. THE ENTRANCE INTO THE QUATERNARY ICE AGE

The first significant ice sheets in the Northern Hemisphere develop about 3 Myr BP when the Eurasian Arctic and North-eastern Asia entered into glaciation. Attempts have been made to explain this significant intensification of Northern Hemisphere glaciation 3 million years ago. In particular, Maslin et al. (1995) proposed that it was forced by the gradual increase in the amplitude of obliquity from 3.5 to 2.5 Myr BP and a sharp rise in the amplitude of precession and thus of insolation. Li et al. (1998b) discussed further the possible additional influence of a progressive CO₂ linear decrease from 540 ppmv to 270 ppmv between 4 and 2 Myr as suggested by Saltzman and Verbitsky (1993). This 540 ppmv concentration of CO₂ is closed to that deduced by Cerling (1992). In such a case, the model simulates very small short-lasting ice sheets before 3 Myr BP (Figure 5, panel e), but it is only after 2.7 Myr BP that the simulated ice sheets start to exceed 3 x 10° km³.

Actually there are three intervals between 3 and 2 Myr BP during which the ice sheets can develop (3.2 and 2.9, 2.75 and 2.45 and 2.35 and 2.1 Myr BP). They correspond to three time intervals where the insolation



162

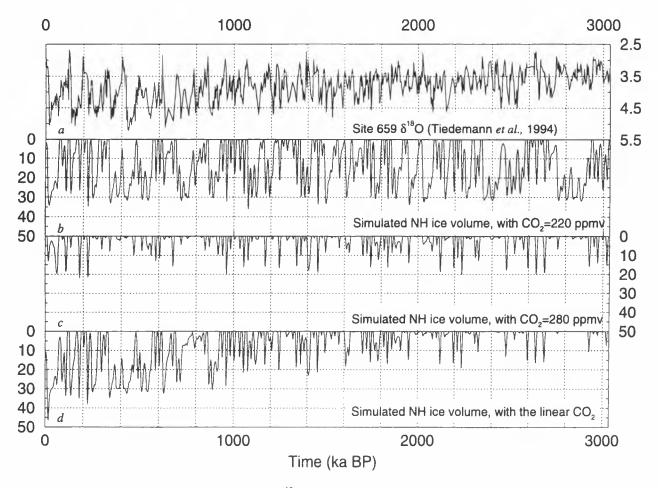


Figure 6. Comparison between (a) the Site 659 $\delta^{18}O$, in $\%_{o}$ (Tiedemann et al., 1994), and (b) the simulated Northern Hemisphere ice-sheet volumes, in 10^{6} km³, under constant atmospheric CO₂ concentrations 220 ppmv, (c) 280 ppmv, and (d) a linearly decreasing CO₂ concentration going from 320 ppmv at 3 Myr BP to 200 ppmv at the Last Glacial Maximum.

(in particular in July at 65°N) varies with a large amplitude (Figure 5, panel a). This large amplitude of the insolation variation is related to the strong 400-kyr period which characterizes this whole one million-year interval. Moreover, from 3.5 to 2.5 Ma, the amplitude of obliquity gradually increases. Sensitivity experiments using different CO₂ changes show that low summer insolation can lead to the development of the late Pliocene Northern Hemisphere ice sheets only when the CO₂ concentration is sufficiently low to allow winter snow to persist from year to year. For our model, this threshold seems to be around 380 ppmv which is reached somewhere between 2.9 and 2.7 Myr BP. But the deepest summer insolation minima (of the order to 400 Wm⁻² at 65°N in July) required for the ice sheets to grow occur only when the amplitude of precession (and eccentricity) variations is large explaining why significant glaciation can not be initialized until 2.75 to 2.55 Myr BP. The same deep minima are also requested for generating the other corresponding glacial maximum advances at 2.33, 2.24, 2.22 and 2.13 Myr BP.

As a consequence, the Late Pliocene ice ages correspond to time of high eccentricity. Indeed during the warm Late Pliocene, the Northern Hemisphere ice sheets could develop only during very cold summer. It is the opposite to what happens during the Late Pleistocene where the interglacials are related to high eccentricity. Significant Northern Hemisphere ice sheets exist most of time during this cold Late Pleistocene and only high summer insolation can start to melt the ice sheets and lead to an interglacial.

7. THE LAST 3 MYR

The relative success obtained with the LLN 2-D climate model lead to test whether it can sustain its possibility to simulate long-term climatic changes and their characteristics over a very long period, the last 3 million years (Berger et al., 1999). The model was therefore forced by the calculated astronomically-derived insolation of Loutre and Berger (1993) and by different CO_2 scenarios. Such different atmospheric CO_2 scenarios were used because of a lack of CO_2 reconstruction over this remote past. With constant CO_2 concentrations, the simulated ice volume (Figure 6b and c) does not show the gradual increase which is recorded in the marine sediments (e.g. Figure 6a). By using a linearly decreasing CO_2 concentration going from 320 ppmv at 3 Myr BP to 200 ppmv at the Last Glacial Maximum, the simulated changes are in broad agreement with those obtained from the sedimentary records.

From 3 to 2 Myr BP, the intensification of glaciation at about 2.7 Myr BP is simulated, but spectral analysis of the ice volume for this whole period is difficult because of the long time intervals with no ice. From 2 to 1 Myr BP, the simulation has a spectrum similar to the spectrum of the δ^{18} O record, 41 kyr being the dominant period (Figure 7), but the duration of the warm intervals is still longer in the simulation. In timing, the simulated glaciations generally correlate to coolings in the $\delta^{18}O$ record. For example, the remarkable glaciations at 1.95 Myr, 1.78 Myr and 1.74 Myr (Figure 6d) clearly correspond to the distinct coolings in the δ^{18} O data. However, the relative magnitude of the simulated glaciations is sometimes different from the data. For instance, the glaciation at 1.21 Myr is a minor one in the simulation, and corresponds to a major cooling in the data. This deficiency can possibly be related to the rough representation of CO2 in the simulation, but also to the structure of the model.

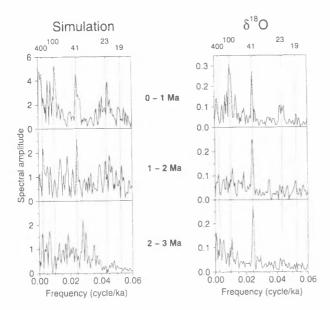


Figure 7. Comparison between the spectra of the simulated Northern Hemisphere ice volume represented in Figure 6d, and of the Site 659 $\delta^{18}O$ data (Tiedemann et al., 1994).

From 1 Myr BP to the present, the simulation again has a spectrum similar to the geological one: it is now dominated by the 100-kyr period instead of by the 41kyr one. Moreover, besides the similar timing for the ice waxings and wanings, the comparison in the relative amplitude between the simulation and δ^{18} O record becomes better, particularly over the last 600 kyr. For example, the ice sheets are melted (as discussed, this complete melting is not realistic but does not prevent the model from reproducing the climatic cycles) around 100, 200, 300, 500, 600 and 700 kyr BP, corresponding to the interglacials recorded in the data. The simulated glacial maxima at 888, 717, 628, 542, 432, 342, 251, 135 and 15 kyr BP can be compared to the glacial maxima in the δ^{18} O record, but a difference in the relative magnitude still exists, especially for the glacial maximum around 79 kyr BP and at stage 6. The simulated ice volume at stage 2 (46 x 10^6 km³, Figure 6) is similar to that in the 200 kyr experiment using the Vostok CO₂ (48 x 10⁶ km³, Berger and Loutre, 1996). But at isotopic stages 11 and 1 too much ice is simulated due to the quite low CO2 values of the linearly decreasing scenario. Using the fluctuating CO₂ concentrations reconstructed by Li et al. (1998a) for the last 600 kyr, the ice volume simulation for the two stages is improved.

In both the simulation and δ^{18} O record, the amplitude of the climatic variations generally increases with time. A key factor to explain the emergence of the 100-ka period at ~ 1 Myr BP is related to the warm climate characterizing the Earth before 1 Myr BP. Under a relatively high atmospheric CO₂ concentration, the Northern Hemisphere ice sheets were too small ; any moderate insolation maxima could melt them and therefore stop the glaciation process. After $\sim 1 \text{ Myr BP}$, larger ice sheets started to exist during most of the time because of lower CO₂ concentrations. Under such conditions, moderate insolation maxima could reduce the ice volume slightly, but only the largest insolation maxima, occurring under high eccentricity, high obliquity and Northern Hemisphere summer at perihelion (minimum climatic precession), could lead to significant meltings of the ice sheets and therefore to interglacials, making the ~ 100 -kyr periodicity the most remarkable feature of climate over the time interval from 1 Myr BP to present.

8. THE LAST 400 KYR

Four CO2 reconstructions were actually used for simulating the past 575 kyr (Berger and Loutre, 2000). The first one is based on a multiple regression between the deep-sea record from Ontong Java Plateau in the western equatorial Pacific and the ice core CO₂ from Antarctica (Berger W. et al., 1996). The second one is generated from a regression between the Vostok CO2 concentration and the SPECMAP oxygen isotope values calculated over the last 218 kyr and extended over the past 575 kyr (Li et al., 1998a). The same procedure was applied for the third one, using the low latitude stacked δ^{18} O record from marine core MD 900963 of site 677 (Bassinot et al., 1994) instead of the SPECMAP record. Finally, the reconstructed CO₂ concentration from Vostok over the last four glacial-interglacial cycles was used (Petit et al., 1999). As this Vostok record extends only to 414 kyr BP, the CO₂ from Li et al. (1998a) was used from 575 to 440 kyr BP and a linear interpolation between 440 and 414 kyr BP ensured the transition towards the Vostok record. The broad features of the results obtained from these different CO₂ scenarios are pretty well similar, except that the maximum of stage 11 is larger and lasts longer in Vostok than in the other scenarios. This feature of the Vostok record, if confirmed, leads to a CO2 concentration which has lasted high longer than the proxy δ^{18} O record tend to show. This quite long CO₂ maximum has a significant impact on the length of the simulated stage 11, a result similar to what might happen to our stage 1 if the future CO₂ level is kept high over a sufficiently long period of time. The major difference between ice volume simulated with the 4 scenarios arises indeed during isotopic stages 11 and 10. From 400 to 350 kyr BP the ice volume simulated with Vostok remains lower than 5 $\times 10^6$ km³ over the whole interval, while in the other experiments, it remains at its minimum for only 10 kyr and then increases to reach a value of 31×10^6 km at 350 kyr BP.

Actually, in the Vostok experiment, the small amplitude in the insolation change and the steady high atmospheric CO_2 concentration from 405 to 340 kyr BP prevent ice sheets to grow. This has an impact on the following glacial, the amount of ice $(22 \times 10^6 \text{ km}^3)$ being much smaller than in the other experiments. This confirms the importance of the past history of the climate system in a transient experiment as underlined by Berger et al. (1998b). All scenarios lead to very similar ice volume variations afterwards : over the last 325 kyr, the different glacial-interglacial cycles are pretty well the same both in amplitude as well as in timing.

In particular, from stage 5 onwards there is no real significant difference between all the experiments. This can be expected from the rather good agreement between the different CO₂ reconstructions, except during the early part of stage 5. Indeed, Vostok CO2 not only remains high during 5e, but it does not show any substantial change in the following 15 kyr neither, despite a distinct cooling over the Antarctic ice sheet. Not until 6 kyr after the major cooling of stage 5d does a substantial decline in CO₂ occur, another 5 kyr being required to return to an approximate phase relationship of CO₂ with temperature variations. This behaviour of the Vostok record is totally different from what happens in the CO₂ scenari obtained from a linear extrapolation using the marine record. There, the CO₂ remains high during a much shorter time, mirroring the marine isotopic curves. However, this difference does not lead to any significant difference between the respective simulated ice volumes, contrary to what happened at stage 11. The reason is that during isotopic stage 5, insolation is characterized by a large amplitude of its variations preventing the system to respond significantly to different CO₂ forcings. This kind of behaviour has also been discussed in length by Berger et al. (1998b) and Loutre and Berger (2000b) for the last and next glacial-interglacial cycles.

This similarity in the CO_2 concentration of stage 5 and stage 11 (long lasting maximum) and the difference in their insolation behaviour stress again the importance of better understanding these relatively long interglacials during which high values of CO_2 are sustained, whether the ice volume remains rather low (stage 11) or not (stage 5) during the whole stage. Recent experiments (Raynaud et al., 2000) are showing in particular that the chronology of Vostok CO_2 at stage 11 can have a significant impact on the length of the simulated stage 11 ice volume, a result which confirms the results obtained from the scenari mentioned above.

9. THE NEXT GLACIAL-INTERGLACIAL CYCLE

9.1. Insolation

The major feature of the insolation over the next tens of thousands of years is the small amplitude of its variations. This is because we are approaching a minimum of the 400-kyr eccentricity cycle. Eccentricity is indeed modulating the climatic precession parameter which controls most of the long-term variations of the daily insolation received from the Sun (Berger et al., 1993a).

As an example, the amplitude of the long-term variations of the mid-month insolation at 65° N in June is less than 30 Wm⁻² from 0 to 50 kyr AP. This is far less than the amplitude during stage 5 which reaches 110 Wm⁻² during 5e. As far as the insolation is concerned the Eemian can therefore hardly be considered as an analogue for the next thousands of years.

Actually, the insolation variation from 5 kyr BP to 60 kyr AP is really exceptional. Over the last 3 Myr, only five intervals were found to be highly correlated (correlation coefficient higher than 0.8) to this period of reference (Berger and Loutre, 1996). The most recent of these intervals goes from 405 to 340 kyr BP. The average insolation is about the same for all these intervals (~ 487 Wm⁻²) and the standard deviation ranges between 12 and 16 Wm⁻², against 9 Wm⁻² for the interval 5 kyr BP to 60 kyr AP.

Moreover, the precessional cycles over these intervals are very similar, all shorter than the traditional value of 21 kyr. The average is roughly 13 kyr and from 30 to 44 kyr AP, the eccentricity becomes so low that one cycle almost disappears. This feature is related to the inverse relationship which characterizes the frequency and amplitude modulations of precession: at the 400-kyr time scale the lowest amplitude corresponds to the shortest period, a relationship which is even more dramatic between 447 and 471 kyr AP (Berger et al., 1998a).

Assuming that the insolation is the pacemaker of the long-term climatic variations, the best and closest analogue for our near future is consequently from 405 to 340 kyr BP, an interval which corresponds more or less to stage 11 in the stacked marine δ^{18} O record from SPECMAP (Imbrie et al., 1984). If the main driving forces of the climate system are changes in the astronomical parameters and in CO₂, we would argue that if one forcing (the astronomical one) is not changing any more like during stage 11, stage 1 and the near future, the importance of the other (CO₂) will be magnified.

9.2. Simulated Climate

As there is no interactive CO₂ cycle yet in the LLN model, it was decided to use the past CO₂ variations reconstructed by Jouzel et al. (1993) as a first approximation for the future (Berger and Loutre, 1996; Loutre and Berger, 2000b). This reconstructed time series was shifted toward the future by 131 kyr, in such a way that the CO₂ value at the initial stage of the integration coincides with the present-day value of the reconstruction. However, the atmospheric CO₂ concentration is, in some complicated ways, related to climate; this scenario can therefore introduce some incoherence between the orbitally-forced climatic changes and the CO₂ forcing, a remark which is strengthened by the fact that the insolation over the last glacial-interglacial cycle is not an analogue for the future.

Under such a natural scenario, the ice volume simulated by the LLN 2-D model, starting with the present-day Greenland ice sheet, leads first to an interglacial which is exceptionally long (Figure 4). The peak of this interglacial lasts ~ 55 kyr (from 5 kyr BP to 50 kyr AP), which is rather unusual when compared to the more traditional 10 to 20 kyr found in geological records (Kukla et al., 1972, 1997). This characteristic is related to the small changes in insolation described above and a CO₂ concentration which remains larger than 270 ppmv over the next 20 kyr. In a warm world - like in the late Pliocene - Li et al. (1998b) have shown that a high eccentricity is requested to force high latitudes summer insolation to become particularly low during the negative phase and minimum of precession and so, to initiate a glacial. This is exactly the reverse of what is observed during the late Pleistocene glacial world where a high eccentricity is usually associated to an interglacial (Hays et al., 1976). This means that, if for one reason or another, the CO₂ atmospheric concentration remains high at the geological time scale, the future of the Holocene might look much more like the late Pliocene (or even earlier warm periods like the Pliocene, the Paleocene-Eocene boundary and the Mid-Cretaceous although the significantly different geography at these remote times prevent to use them as "analogues" for the next hundreds of thousands of years – Crowley, 1990).

Starting 50 kyr AP, there is a global trend of growing ice sheets with a short reversal which lasts roughly 10 kyr. The first maximum of ice occurs at 63 kyr AP with 22 x 10^6 km³, a maximum which is partly due to the important decrease of CO₂ which started at 57 kyr AP. It is followed by a secondary minimum at 71 kyr AP with 20 x 10^6 km³ of ice and a maximum of 33 x 10^6 km³ at 100 kyr AP, before deglaciation starts.

9.3. Stage 11, an analogue for the future

We will focus now on three intervals going from 405 to 340 kyr BP, 130 to 65 kyr BP and 5 kyr BP to 60 kyr AP corresponding roughly to isotopic stages 11,5 and 1 respectively. Let us point out that the lower boundary taken here for the first time interval (405 kyr BP) fits much better with Termination V of Shackleton et al. (1990) (415 kyr BP) than with the 423-427 kyr range in the age models of SPECMAP.

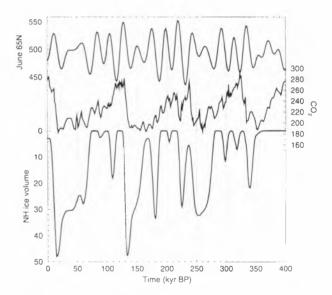


Figure 8. Northern Hemisphere ice volume simulated by the LLN 2-D climate model forced by insolation and atmospheric CO₂ concentration. (top) summer solstice insolation at 65°N (Berger, 1978); (middle) the atmospheric CO₂ concentration reconstructed from Vostok ice core over the last 414 kyr BP (Petit et al., 1999). For the future, the reconstructed time series from Vostok (Jouzel et al., 1993) was shifted toward the future by 131 kyr, in such a way that the CO₂ value at the initial stage of the integration coincides with the present-day value of the reconstruction. (bottom) the response of the model to the insolation and CO₂ forcings.

Since these three periods correspond to interglacials, it is not surprising that their simulated Northern Hemisphere ice volume is small (Figure 8). During stage 11, it varies only slightly at least until 350 kyr BP making this simulated interglacial exceptionally long. During stage 5 it experiences large variations, the amplitude reaching more than 15 x 10^6 km³ during the abortive glaciation of stage 5d, 110 kyr ago. For stage 1 and the future, it is very stable again with a pattern very similar to stage 11.

The simulated annual hemispheric mean surface temperature confirms that stage 11 is a much better analogue for the future than stage 5.

10. THE POSSIBLE HUMAN IMPACT

Let us first note that, according to the reconstructed CO₂ concentration over the last two glacial-interglacial cycles, 290 ppmv is reached only during very limited times. Most of the time, the CO₂ concentration is situated around 225 ppmv (between 210 and 250 ppmv). A constant CO₂ concentration of interglacial level (~ 280 ppmv) is therefore already a very strong forcing of the climate system and it is even more the case for the present-day concentration of ~ 370 ppmv. This is why two other long-term CO2 scenarios were constructed during which high CO₂ values will be kept over a few hundreds of years (Loutre and Berger, 2000b). They are based upon the IPCC scenarios leading respectively to a stabilized CO₂ concentration of 750 and of 550 ppmv between the XXIInd and the XXIIIrd centuries (Houghton et al., 1996). Currently it is assumed that the CO₂ concentration will increase from the unperturbed level (assumed to be 296 ppmv in the model) to 750 or 550 ppmv over the next 200 years, will decrease to 300 ppmv over the following 450 or 300 years, will reach linearly the 1 kyr AP concentration of the natural scenario of section 9 and will then follow this scenario up to 130 kyr AP.

The responses of the Northern Hemisphere ice sheets to these scenarios are very different. In the 550 ppmv experiment, a slight melting of the Northern Hemisphere ice occurs only over the next 1,000 years and it is very difficult to see any difference with the results from the natural scenario based upon the Vostok data. For 750 ppmv, the impact is far more pronounced, a complete melting of the Greenland ice sheet being simulated between roughly 10 and 14 kyr AP. These results seem to indicate that there is a threshold value of CO₂ above which the Greenland ice sheet disappears in the LLN 2-D model. On another hand, with the same CO₂-Vostok forcing the model simulates an ice-free Northern Hemisphere at the peak of the Eem (not recorded in the Greenland ice core, Dansgaard et al., 1993) but not at the Holocene. This weakness of the model reveals a high sensitivity to the insolation

forcing, but does not affect qualitatively the overall reconstruction of the glacial-interglacial cycles.

A detailed analysis of the contribution of the individual ice sheets to the total northern hemisphere ice volume shows that it is dominated by the Greenland ice sheet up to 50 kyr AP. At this date, the Eurasian ice sheet starts to grow significantly, followed by the Northern American ice sheet a few thousands of years later. As in other experiments made by Loutre and Berger (2000b), the human burst of CO₂ during the XXth to XXIInd centuries seems to be sufficient to lead to a melting of the Greenland ice sheet in the LLN model. This is occurring under a constant CO₂ concentration larger than 290 ppmv (with a melting from 30 to 55 kyr AP) and even in the 750 ppmv scenario where the CO₂ concentration is supposed to reach back 300 ppmv as soon as at 650 yr AP and from this time onwards, to return to the natural scenario (the total melting then occur between 8 and 15 kyr AP).

The simulated ice volume in the 750 ppmv scenario are almost the same as in the natural scenario after 40 kyr AP. After 100 kyr AP, the natural, the 550 and the 750 ppmv scenarios lead to more or less similar results. It seems therefore that 40 kyr at least are required for the climate system to be no longer sensitive to what could happen over the next few centuries.

11. CONCLUSIONS

Being given that the LLN model is a model of intermediate complexity, all the results obtained so far must be confirmed by more sophisticated ones. In particular, a coupled carbon cycle must be added and the Northern Hemisphere version extended to the whole Earth. The question remains indeed to know which latitudes are reacting the first to the insolation changes because we are not anymore sure that the triggering insolation lies in the high northern latitudes in summer as assumed by Milankovitch (1941). Some authors suggest that the tropics respond first (McIntyre and Molfino, 1996; Berger and Loutre, 1997; Rutherford and D'Hondt, 2000) or that the Southern Hemisphere leads the Northern Hemisphere (Pépin et al., 2001). In this latter case, we may assume that the large oceanic volume there would damp considerably the initial direct response of this Southern Hemisphere to any local insolation change and delay significant changes up to the time that the same kind of insolation anomaly starts to influence the Northern Hemisphere. Any partial transfer of the Southern Hemisphere climate response to Northern Hemisphere would prepare this the hemisphere to respond quicker to the coming local insolation change. Moreover, this hemisphere with its large continental masses would response much more rapidly. The amplitude of the climatic change would finally be sufficient to become the major forcing of the Southern Hemisphere which would definitely behave

more or less in phase with the Northern one. It will remain however that the local insolation anomalies would modulate the occurring climatic changes even to an extend that both hemispheres might not necessarily be in phase, temporarily at least. Such a transient behaviour of climate at different latitudes will be tested soon using the global version of the LLN 2-dimension model.

REFERENCES

- Bassinot F.C., Labeyrie L.D., Vincent E., Quidelleur X., Shackleton N.J. and Y. Lancelot (1994) The astronomical theory of climate and the age of the Brunshes-Matuyama magnetic reversal, *Earth and Planetary Science Letters*, 126(1-3), 91-108.
- Bentley M.J. (1999) Volume of Antarctic Ice at the Last Glacial Maximum, and its impact on global sea level change, *Quaternary Science Reviews*, 18(14), 1569-1595.
- Berger A. (1978) Long-term variations of daily insulation and Quaternary climatic changes, J. Atmos. Sci., 35(12), 2362-2367.
- Berger A. (1979) Insolation signatures of Quaternary climatic changes, *II Nuovo Cimento*, 2C(1), 63-87.
- Berger A. (1988) Milankovitch theory and climate, *Rev. Geophys.*, 26(4), 624-657.
- Berger A. (1995) Modelling the response of the climate system to astronomical forcing. In: "Future Climates of the World, A Modelling Perspective", A. Henderson-Sellers (ed.), pp. 21-69, vol. 16 World Survey of Climatology (H.E. Landsberg, ed.), Elsevier, Amsterdam.
- Berger A. (1996a) Orbital variations. In: "Encyclopedia of Climate and Weather", S. Schneider (ed.), pp. 557-564, Oxford University Press, New York.
- Berger A. (1996b) Orbital parameters and equations. In: "Encyclopedia of Climate and Weather", S. Schneider (ed.), pp. 552-557, Oxford University Press, New York.
- Berger A. (1998) The role of CO₂, sea-level and vegetation during the Milankovitch forced glacial-interglacial cycles, in: "*Geosphere-Biosphere Interactions and Climate*", L. Bengtsson (ed.), November 1998.
- Berger A., Fichefet T., Gallée H., Tricot C., Marsiat I., and J.P. van Ypersele (1989) Astronomical forcing of the last glacial-interglacial cycle. In: "Our Changing Atmosphere", P. Crutzen, J.Cl. Gérard and R. Zander (eds), pp. 353-382, Université de Liège, Institut d'Astrophysique, Cointe-Ougrée.
- Berger A., Fichefet Th., Gallée H., Marsiat I., Tricot Ch., and J.P. van Ypersele (1990) Physical interactions within a coupled climate model over the last glacial-interglacial cycle, *Transac*-

tions of the Royal Society of Edinburgh: Earth Sciences, 81 part 4, 357-369.

- Berger A., Fichefet Th., Gallée H., Tricot Ch., van Ypersele J.P. (1992) Entering the glaciation with a 2-D coupled climate model, *Quaternary Science Reviews*, 11 n°4, 481-493.
- Berger A., Loutre M.F. and C. Tricot (1993a) Insolation and Earth's orbital periods, *J. Geophys. Res.*, 98(D6), 10,341-10,362.
- Berger A., Tricot C., Gallée H. and M.F. Loutre (1993b) Water vapour, CO₂ and insolation over the last glacial-interglacial cycles, *Phil. Trans. R. Soc.*, *London*, B341, 253-261.
- Berger A., Gallée, H., Tricot, Ch. (1993c) Glaciation and deglaciation mechanisms in a coupled 2-D climate - ice sheet model, *J. of Glaciology*, 39 n° 131, 45-49.
- Berger A., Tricot C., Gallée H., Fichefet T. and M.F. Loutre, 1994. The last two glacial-interglacial cycles simulated by the LLN model. In: "Long Term Climatic Variations, Data and Modelling", J.Cl. Duplessy and M.T. Spyridakis (eds), NATO ASI Series, vol. 22. pp. 411-452, Springer-Verlag Berlin Heidelberg.
- Berger A., and M.F. Loutre (1996) Modelling the climate response to astronomical and CO₂ forcings, *C.R. Acad. Sci. Paris*, 323 (IIa), 1-16.
- Berger A., and M.F. Loutre (1997) Intertropical latitudes and precessional and half-precessional cycles, *Science*, 278(5342), 1476-1478.
- Berger A., Li X.S., and M.F. Loutre (1999): Modelling Northern Hemisphere ice volume over the last
 3 Ma, *Quaternary Science Reviews*, 18(1), 1-11.
- Berger A., Loutre M.F. and J.L. Mélice (1998a) Instability of the astronomical periods over the last and next millions of years, *Paleoclimates Data and Modelling*, 2(4), 239-280
- Berger A., Loutre M.F. and H. Gallée (1998b) Sensitivity of the LLN climate model to the astronomical and CO_2 forcings over the last 200 kyr, *Climate Dynamics*, 14, 615-629.
- Berger A. and M.F. Loutre (2000), Climate 400,000 years ago, a key to the future ? In: "Marine Isotope Stage 11: an extreme interglacial ?",
 A. Droxler, R. Poore, L. Burckles and L. Osterman (eds), American Geophysical Union.
- Berger W.H., Bickert T., Yasuda M.K., and G. Wefer (1996) Reconstruction of atmospheric CO₂ from ice-core data and the deep-sea record of Ontong Java plateau: the Milankovitch chron., *Geol. Runds.*, 85, 466-495.
- Bolton E.W., Maasch K.A. and J.M. Lilly (1995) A wavelet analysis of Plio-Pleistocene climate indicators: a new view of periodicity evolution, *Geophysical Research Letters*, 22(20), 2753-2756.

- Cerling T.E. (1992) Use of carbon isotopes in paleosols as an indicator of the $p(CO_2)$ of the paleoatmosphere, *Global Biogeochemical Cycles*, 6(3), 307-314.
- Crowley T.J. (1990) Are there any satisfactory geologic analogs for a future greenhouse warming ? *Journal of Climate*, 3(11), 1282-1292.
- Crucifix M., Loutre M.F., Lambeck K., and A. Berger (2000), Effect of isostatic rebound on modelled ice volume variations during the last 200 kyr, *Earth and Planetary Science Letters* (accepted).
- Dansgaard W., Johnsen S.J., Clausen H.B., Dahl-Jensen D., Gundestrup N.S., Hammer C.U., Hvldborg C.S., Steffensen J.P., Svelnbjörnsdottir A.E., Jouzel J. and G. Bend (1993) Evidence for general instability of past climate from a 250kyr ice-core record. *Nature*, 364, 218-220.
- Gallée H., van Ypersele J.P., Fichefet Th., Tricot C. and
 A. Berger (1991) Simulation of the last glacial cycle by a coupled sectorially averaged climate
 ice-sheet model. I. The Climate Model, J. Geophys. Res., 96, 13,139-13,161.
- Gallée H., van Ypersele J.P., Fichefet Th., Marsiat I., Tricot C. and A. Berger (1992) Simulation of the last glacial cycle by a coupled, sectorially averaged climate - ice-sheet model. II. Response to insolation and CO₂ variation, J. Geophys. Res., 97(D14), 15,713-15,740.
- Gallée H., Berger A. and N.J. Shackleton (1993) Simulation of the climate of the last 200 kyr with the LLN 2D-model. In: "*Ice in the Climate System*", R. Peltier (ed.), NATO ASI Series I, Global Environmental Change vol. 12 (Springer Verlag, Berlin) pp. 321-341.
- Hays J.D., Imbrie J. and N.J. Shackleton (1976) Variations in the Earth's orbit: pacemaker of the ice ages, *Sciences*, 194, 1121-1132.
- Houghton J.T., Meira Filho L.G., Callander B.A., Harris
 N., Kattenberg A. and K. Maskell (eds) (1996)
 "Climate Change 1995 the Science of Climate Change". Contribution of WGI to the Second Assessment Report of the Intergovernmental Panel on Climate Change. Cambridge University Press, Cambridge, 572p.
- Imbrie, J., Hays, J., Martinson, D.G., McIntyre, A., Mix, A.C., Morley, J.J., Pisias, N.G., Prell, W.L., Shackleton, N.J. (1984) The orbital theory of Pleistocene climate : support from a revised chronology of the marine ¹⁸O record. In : *"Milankovitch and Climate"*, A. Berger, J. Imbrie, J. Hays, G. Kukla, B. Saltzman (Eds), pp. 269-305, D. Reidel Publ. Company, Dordrecht, Holland.
- Imbrie J., Boyle E.A., Clemens S.C., Duffy A., Howard W.R., Kukla G., Kutzbach J., Martinson D.G., McIntyre A., Mix A.C., Molfino B., Morley J.J., Peterson L.C., Pisias N.G., Prell W.L.,

Raymo M.E., Shackleton N.J. and J.R. Toggweiler (1992) On the structure of major glaciation cycles, *Paleoceanography*, 7(6), 701-738.

- Imbrie J., Berger A., Boyle E.A., Clemens S.C., Duffy A., Howard W.R., Kukla G., Kutzbach J., Martinson D.G., McIntyre A., Mix A.C., Molfino B., Morley J.J., Peterson L.C., Pisias N.G., Prell W.L., Raymo M.E., Shackleton N.J. and J.R. Toggweiler (1993) On the structure and origin of major glaciation cycles. 2. The 100,000-year cycle, *Paleoceanography*, 8(6), 699-735.
- Johnsen S.J., Dahl-Jensen D., Dansgaard W., and N. Gundestrup (1995) Greenland palaeotemperatures derived from GRIP bore hole temperature and ice core isotope profiles, *Tellus*, 47B(5), 624-629.
- Jouzel J., Barkov N.I., Barnola J.M., Bender M., Chappellaz J., Genthon C., Kotlyakov V.M., Lorius Cl., Petit J.R., Raynaud D., Raisbeck G., Ritz C., Sowers T., Stivenard M., Yiou F. and P. Yiou (1993) Vostok ice cores: extending the climatic records over the penultimate glacial period, *Nature*, 364(6436), 407-412.
- Kukla G., Matthews R.K. and M.J. Mitchell (1972) Present interglacial: how and when will it end? *Quaternary Research*, 2(3), 261-269.
- Kukla G., McManus J.F., Rousseau D.D. and I. Chuine (1997) How long and how stable was the last interglacial ? *Quaternary Science Reviews*, 16(6), 605-612.
- Li, X.S., Berger, A., Loutre, M.F. (1998a) CO₂ and Northern Hemisphere ice volume variations over the middle and late Quaternary. *Climate Dynamics*, 14(7-8), 537-544.
- Li, X.S., Berger, A. Loutre, M.F., Maslin, M.A., Haug, G.H., and Tiedemann R. (1998b) Simulating late Pliocene Northern Hemisphere climate with the LLN 2-D model, *Geophys. Res. Lett.*, 25(6), 915-1918.
- Loutre M.F. and A. Berger (1993) Sensibilité des paramètres astro-climatiques au cours des 8 derniers millions d'années, *Scientific Report* 1993/4, Institut d'Astronomie et de Géophysique G. Lemaître, Université catholique de Louvain, Louvain-la-Neuve.
- Loutre M.F., Berger A., Dutrieux A. and H. Gallée (1994) The response of the LLN climate model to the astronomical forcing over the last glacial-interglacial cycle, *Terra Nostra*, *Schriften der Alfred-Wegener-Stiftung*, 1/94, 11-15.
- Loutre M.F. and A. Berger (2000a) No glacialinterglacial cycle in the ice volume simulated under a constant astronomical forcing and a variable CO_2 , *Geophysical Research Letters*, 27(6), 783-786.

- Loutre M.F. and A. Berger (2000b) Future climatic changes: are we entering an exceptionally long interglacial? *Climatic Change*, 46(1-2), 61-90.
- Loutre M.F. and A. Berger (2000c) Stage 11 as an analogue for the present interglacial, *Global and Planetary Change* (submitted).
- Martinson D.G., Pisias N.G., Hays J.D., Imbrie J., Moore T.C. and N.J. Shackleton (1987) Age dating and the orbital theory of the ice ages: development of a high-resolution 0 to 300,000year chronostratigraphy, *Quat. Research*, 27(1), 1-29.
- Maslin M.A., Haug G.H., Sarnthein M., Tiedemann R., Erlenkeuser H., and R. Stax (1995) Northwest Pacific Site 882: The initiation of Northern Hemisphere Glaciation. *Proc. ODP, Sci. Repts.* 145, 315-329, College Station, TX (Ocean Drilling Project).
- McIntyre A. and B. Molfino (1996) Forcing of Atlantic equatorial and subpolar millennial cycles by precession, *Science*, 274(5294), 1867-1870.
- Milankovitch M.M. (1941) "Kanon der Erdbestrahlung und seine Anwendung auf des Eizeitenproblem", R. Serbian Acad. Spec. Publ. 132, Sect. Math. Nat. Sci., pp. 633. (Canon of insolation and the ice-age problem, English translation by Israel Program for Scientific Translation, Jerusalem, 1969).
- Pépin L., Raynaud D., Barnola J.M., and M.F. Loutre (2000), Hemispheric roles of climate forcings during glacial-interglacial transitions as deduced from the Vostok record and LLN-2D model experiments. *Journal of Geophysical Research* (special issue) (accepted).
- Pestiaux P. and A. Berger (1984) An optimal approach of the spectral characteristics of deep-sea climatic records, In: "Milankovitch and Climate", Berger A. et al. (eds), 1, pp. 417-445, Reidel Publ. Company, Dordrecht, Holland..

- Petit J.R., Basile I., Leruyuet A., Raynaud D., Lorius C., Jouzel J., Stievenard M., Lipenkov V.Y., Barkov N.Y., Kudryashov B.B., Davis M., Saltzman E., and V. Kotlyakov (1997) Four climate cycles in Vostok ice core, *Nature*, 387(6631), 359-360.
- Petit J.R., Jouzel J., Raynaud D., Barkov N.I., Barnola J.M., Basile I., Benders M., Chappellaz J., Davis M., Delaygue G., Delmotte M., Kotlyalkov V., Legrand M., Lipenkov V.Y., Lorius C., Pépin L., Ritz C., Saltzman E., and M. Stievenard (1999), Climate and atmospheric history of the past 420,000 years from the Vostok ice core, Antarctica, *Nature*, 399(6735), 429-436.
- Raynaud D., Loutre M.F., and C. Ritz (2000), The Vostok record in the context of Marine Isotope Stage (MIS) 11, CO₂ forcing and stability of East Antarctica. *AGU Monograph* (submitted).
- Rutherford S. and S. D'Hondt (2000) Early onset and tropical frocing of 100,000-year Pleistocene glacial cycles, *Nature*, 408, 72-75.
- Saltzman B. and M.Y. Verbitsky (1993) Multiple instabilities and modes of glacial rhythmicity in the Plio-Pleistocene: a general theory of late Cenozoic climatic change, *Climate Dynamics*, 9, 1-15.
- Shackleton N.J., Berger A. and W.R. Peltier (1990) An alternative astronomical calibration of the lower Pleistocene timescale based on ODP site 677, Trans. of the Royal Society of Edinburgh: Earth Sciences, 81, 251-261.
- Tiedemann R., Sarnthein M. and N.J. Shackleton (1994) Astronomic time scale for the Pliocene Atlantic δ^{18} O and dust flux records of Ocean Drilling Program site 659, *Paleoceanography*, 9(4), 619-638.
- Yokoyama Y., Lambeck K., De Deckker P., Johnston P., and L.K. Fifield (2000) Timing of the Last Glacial maximum from observed sea-level minima, *Nature*, 406(6797), 713-716.

PLIO-PLEISTOCENE LACUSTRINE SEDIMENTATION IN THE BAZA BASIN (SE SPAIN) AND ITS RELATION WITH CLIMATIC SHIFTS

L. Gibert¹, C.Ferrandez-Canyadell², G.Scott³

1 Dept. Enginyeria Minera i Recursos Naturals. Universitat Politecnica de Catalunya. Farinera 2, 08211 Castellar del Vallès, Barcelona. (Spain). gbeotas@hotmail.com 2 Department of Stratigraphy and Paleontology Faculty of Geology, University of Barcelona Martí Franquès s/n, E-08028 Barcelona (Spain).cferran@geo.ub.cs 3 Berkeley Geochronology Center. 2455 Ridge Road, Berkeley CA 94709 (USA). gscott@bgc.org

ABSTRACT

The study of sedimentary cycles in the lacustrine Baza basin (SE Spain) allows the reconstruction of the evolution of climate during the lower Pliocene to upper Pleistocene. Several temporal orders of sedimentary cycles have been identified in the basin, recording fluctuations in the lake level owing to different magnitudes of climate changes. The shorter cycles (millimetric) span some years and the largest cycles (tens of meters) span a hundred thousand years or more. The sedimentary cycles are of two different rock types and sedimentary features. One rock type represents periods of falling (or low) lake levels, and the other type subsequent periods of rising (or high) lake levels. Two main types of cycles can be distinguish within the basin. Cyclity in marginal areas was recorded by the alternation of subaquatic and subaereal deposits caused by the expansion and contraction of the lake. In contrast, the cyclicity in the central areas of the basin was recorded in continuous subaquatic deposits caused by oscillation of the lake level that changed the salinity and circulation in the paleolake. These central area deposits have the potential to contain a complete record of climate cyclity for most of the last 4 million years.

INTRODUCTION

lacustrine environments are Shallow sensitive indicators of climate. Lakes in enclosed basins are especially susceptible to changes in the amount of rainfall and evaporation, which produce changes in both the size of the lake and the salinity of the water. Periods of increased rainfall produce an expansion of the lake, so that marginal areas previously under subaereal conditions are covered with lacustrine sediments. Dry atmospheric periods produce a contraction of the lake so that marginal lacustrine sediments can be exposed to subaerial conditions and deposits. This cyclical process can occur at different time scales, creating different order sedimentary cycles in the marginal areas of the lake. A modern example of the climatic sensitivity of shallow lakes is Lake Chad located between the Sahara desert and the tropics. During the last Ice Age, the lake covered 1.000.000

square kilometres. In 1966 the lake was only 25,000 square kilometers, but shrank to 1200 square kilometers during the drought of Sahel in 1992.

Climate changes are reflected by a more subtle signal in the central area of a lake. This depositional environment can remain under water even in dry periods, but the salinity can change. During periods when the rainfall/evaporation balance is negative. dissolved salts (e.g. chlorides, sulphates and carbonates) concentrate in the water and may precipitate. This produces a sequence of deposits containing different types of salts reflecting their different concentrations in the drying lake water. When a wetter climate returns the salinity of the water decreases and the formation of saline deposits comes to a halt. As a result of this cyclic process, different orders of sedimentary cycles appear (millimeter to centimeter) which represent climate oscillations of different length (annual to thousand years). Lacustrine cyclostratigraphy can be a direct reflection of the paleoclimate evolution of a region. In theory, all temporal scales of cyclicity can be found in lacustrine deposits. In practice however, analyses of lacustrine cyclostratigraphy are restricted by two primary difficulties. First is the problem of finding a long and continuous sedimentary record (with a developed chronology) that is well exposed for study. The second difficulty is relating the sedimentary effects to the causes in the climate.



Figure 1: Geological location of the Baza basin in the Betic Range (SE Spain).

Proc. 1st Solar & Space Weather Euroconference, 'The Solar Cycle and Terrestrial Climate', Santa Cruz de Tenerife. Ténerife. Spain. 25-29 September 2000 (ESA SP-463, December 2000)

CYCLOSTRATIGRAPHY OF THE BAZA BASIN

The Baza basin is located in the Betic range, in SE Spain (Figure 1). It was connected with the sea until the end of the Miocene (Vera et al 1994). The basin became isolated from the sea owing to general tectonic uplift, then a large lacustrine system of more than 1000 km2 was established. This situation of internal drainage persisted until the upper Pleistocene (about 100kyr) when stream piracy from the Guadalquivir Basin began draining the Baza basin (Calvache and Viseras 1997). Losing its endorreic character, the Baza basin's lacustrine sedimentation was replaced by erosion. Nowadays, large outcrop areas expose a lacustrine sedimentary record for most of the last four million years (Plio-Pleistocene). The Baza basin expose different types of sedimentary cycles related with different scales of fluctuations of paleolake level in different sedimentary environments. Two main groups of paleolake environments are being studied: those occurring in the marginal zones where subaereal conditions can be common: and those located in more central areas where the lake appears to have been permanent and the sedimentary record is probably continuous. Within both environments, cycles of several orders of magnitude can be differentiated (figure 2).

Cycles in marginal zones

In the marginal areas of the lake, oscillations of the water level are recorded as alternations of sediments which represent subaquatic and subaereal conditions. One type of deposit corresponds to an expansion of the lake, while another deposit of subaereal sediments or features (mainly edaphyc) corresponds to a retreat of the lake. Based on their lithology, two types of cycles are distinguished in these marginal areas: fluviolacustrine cycles and successions of palaeosols.

Fluvio-lacustrine cycles

Fluvio-lacustrine cycles consist of a lower reddish detrital unit and an upper white carbonate-rich unit. Reddish detrital units correspond to deposition in a fluvial plain, occurring when the lake retreats, whereas the upper units are lacustrine sediments formed in an expansive phase of the lake. Two orders of magnitude of fluvio-lacustrine cycles can be differentiated in the basin. Cycles of first order of magnitude are more than 20 m thick and represent durations of between 0.5 and 1 my. They have a great lateral continuity, even towards the centre of the basin indicating the low bathimetric coefficient of the lake. The best examples of these cycles are found in the NE sector of the basin. Fluvio-lacustrine cycles of a smaller order occur along the western margin, where the lacustrine sediments of the Baza basin interfinger with the fluvial deposits of the adjacent Guadix basin. These cycles are thinner

(between 5 and 15m) and span shorter periods of time. The high frequency of this second order cyclicity points to a climate origin. Longer cycles could also be the result of tectonic uplift or collapse, which would produce a relative change of the lake level and sediment supply.

Successions of palaeosols

Palaeosols are common, representing subareal exposure during lower water level episodes along the fluctuating lake margin. Lacustrine deposits alternate with palaeosols, representing the return of higher lake levels. Frequently, examples of palaeosols are found within the carbonate-rich units of the longer fluviolacustrine cycles. Sometimes these sequences contain more than 20 successive palaeosols. Fully developed palaeosols have a large lateral continuity, and are useful for local correlation around the lake margin. Different pedological features can be seen, such as a hardpan at the top of a palaeosol horizon. The span of time that these palaeosol cycles represent is assumed to be between 20,000 and 100,000 years, (figure 3).

Cycles in central areas

In the central area of the basin, a permanent body of water dominated the sedimentation. The water chemistry changed from slightly saline in wet periods to strongly saline in dry times. This is reflected in the sediments by the formation of evaporitic cycles where salts (mainly sulphates, such as gypsum) alternate with clays and marls. Different orders of magnitude of evaporitic cycles, millimetric to metric in thickness, can be distinguish apparently responding to different orders of fluctuation in the lake level.

A second type of cycle, consisting of alternating dark and light clays is found in the most central parts of the lake. These cycles represent the alternation of oxicanoxic conditions on the lake floor, which were probably related to changes in the stratification of the water column (figure 4).

Evaporitic cycles

Evaporitic cycles consist of laterally continuous alternations of centimeter scale layers of clay with calcium sulphates. Changes in lithology directly reflect changes in the salinity of the lake water, which are related to climate variations. During dry periods the incoming water supply was reduced and evaporation was high, producing an increased concentration of salts in the lake and their precipitation. This type of deposition ends when wet conditions return, with dilution of the salty water and the arrival of detrital deposits (clay). On a longer time scale, larger (metric) units can be distinguished by alternating packets dominated by one of the two components (either sulphate or clay). Likewise, within the centimetric evaporitic cycles are similar but smaller (millimetric) alternations of salt and clay. Thus, cycles of three orders can be distinguished in these sediments. corresponding to changes of different magnitude and duration in the composition of the lake water (figure 5).

Figure 2

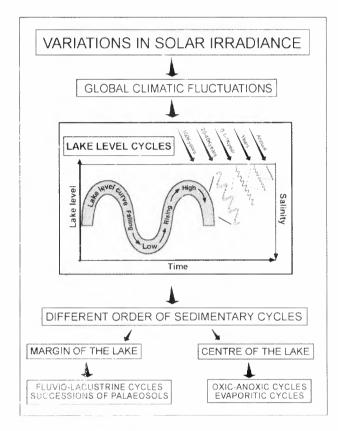


Figure 2 shows the relationships between variations in total solar irradiance on the Earth and lacustrine sedimentary cycles.

Oxic-anoxic cycles

Occurring only in the most central areas of the lake are layers (0.5-1 m thick) of black organic shale covered by lighter colour layers of clay and gypsum. Sulphates are present throughout the entire cycle, forming smaller scale (centimetric and millimetric) evaporitic cycles. Typically covering this lighter unit is a hard limestone layer poor in gypsum.

These light/dark cycles can be related to changes not only in the lake level, but, in the stratification of the water column (figure 4). The black shale units correspond to periods of high lake level in which water becomes stratified. Anoxic conditions dominate on the lake bottom thus retarding the decay of accumulating organic matter. In addition, these less saline waters may be periods of higher biologic productivity. Then during periods of low lake levels, a more complete circulation of waters in the lake would terminate the stratification and the restricted anoxic conditions. These new conditions of high salinity and oxygen produce gypsum-rich layers of lighter colour. During periods of transgression of the lake there would be a return to lower salinity conditions, thus forming the hard limestones (figure 6).

Figure 3

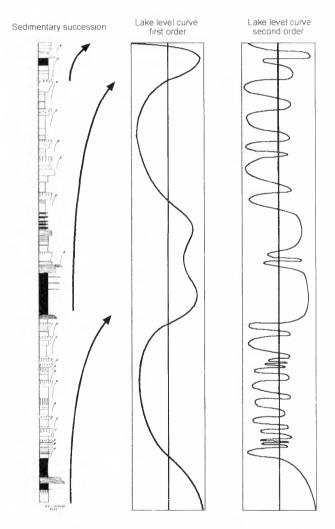


Figure 3. Plio-Pleistocene sequence of 70m from the marginal area of the Baza basin, with two superimposed orders of sedimentary cycles, and the relative lake level curves deduced from them. Long cycles (large arrows) correspond to fluvio-lacustrine cycles of first order. Short cycles (small arrows) correspond to successions of palaeosols representing oscillations in the lake of higher frequency (second order).

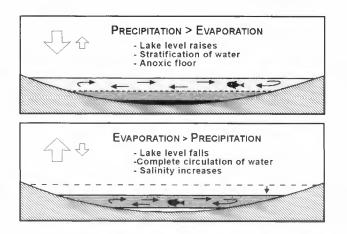


Figure 4

Figure 4. Oxic-anoxic cyclicity in the central areas of the Baza basin. In periods with positive hydric balance the waters might become stratified, with a layer of more dense (saline) water on the lake floor. Circulation of water only occurs in the upper layers, thus producing an anoxic floor which facilitates the preservation of organic matter. Anoxic conditions disappear when the water stratification is broken by a fall in the water level, which produces a general increase in salinity and water circulation, with the formation of evaporites and clays.

Orders of ciclicity

Sedimentary cycles of different order, with thickness from 20 m to less than 1 mm can be distinguished in the lacustrine sediments of the Baza basin. Fluviolacustrine cycles (as thick as 20 meters) in the marginal areas represent the first order cycle. These cycles have kilometric lateral continuity and probably represent a duration of 0.5 and 1 my. Successions of palaeosols occur within these fluvio-lacustrine cycles, and represent the second order cyclity. These second order cycles correspond to lake level fluctuations on the order of 20-100 ky. Cycles of third order are the evaporitic and oxic-anoxic cycles (0.5 to 1.5 m) in the central areas, representing periods of about 20 ky. Evaporitic deposits of centimetric scale correspond to the 4th order, representing periods of 100 to 1000 years. And finally, millimetric evaporite beds are the 5th order, representing climate or weather changes on the order of years or even seasons.

DISCUSION AND CONCLUSIONS

The last four million years of the Earth's climate history are characterised by different orders of continuous climate shifts with superimposed effects. Climate cycles can be related to changes in the total solar irradiance which arrive at the Earth's surface. Small changes in solar irradiation can affect other factors, such as volume of ice sheets and ocean

currents, which might accentuate or geographically expand a climate shift. Variations in total insolation are due to two basic factors: changes on the Earth orbital parameters (Milankovich cycles) and variations in Solar activity (Maunder minimums, 11y Solar cycle and possibly others of longer duration). Climate changes directly affects sedimentary processes of lakes. Among other events, these changes modifying the chemical concentrations in the water column, the morphology and structure of sediments, as well as the erosion and deposition rate through the catchment. Climate fluctuations are thus recorded in sediments and can be recognized from lithologic, sedimentologic and cyclostratigraphy studies. Shallow lacustrine systems are one of the most sensitive depositional environments to record climate changes. One restriction in using cyclostratigraphy is the problem of discontinuous depositional records. However, at least in the central zones, the Baza basin appears to provide a continuous stratigraphic lacustrine record from the lower Pliocene to the upper Pleistocene. This preliminary examination shows the recognition of climate changes at various scales, represented by sedimentary cycles of different orders corresponding to variations of different magnitude in the lake level. Further studies on the spectral analysis of the cycles, the isotopic composition of the precipitated sediments, and both absolute and relative dating in the Baza basin will provide a basis to reconstruct the evolution of climate during the Plio-Pleistocene in this region.



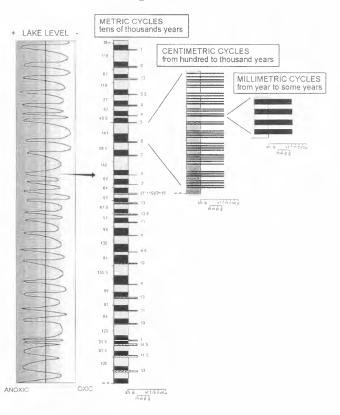


Figure 5. Cycles of three different order (metric to millimetric) recognised in a stratigraphic section of 26 m from the central zone of the Baza basin, together with the curve of the relative lake level elaborated from the cycles of higher order.

Figure 6



RISSING Decreasing gypsum and increasing carbonate

LOW Increasing gypsum and carbonate, decreasing the organic content

HIGH Laminated black shale increasing gypsum upwards

Figure 6. Oxic-anoxic cycle showing a lower black unit (period of high lake level) covered by a lighter one rich in gypsum (low lake level) which is covered by a rich carbonatic layer (transgressive period).

Acknowledgements: we want to thank to J.Serra, E. Maestro and J.Gibert for their constructive discussions.

REFERENCES

- De Boer P.L. and Smith D.G. Orbital Forcing and Cycling Sequences. International Association of Sedimentologist, Special Publication n°19. Blackwell Scientific Publications.
- Calvache, ML., Viseras, C. 1997 Long-Term control mechanisms of stream piracy processes in southeast Spain. Earth surface processes and land forms, Vol22: 93-105.
- Gibert L. Maestro E. Gibert J. 1997 Neogene-Quaternary lacustrine alluvial cycles in the Baza basin (SE Spain). 15th International Sedimentological Congress . Alicante (Spain), pp. 378-380.
- Nicole van Vugt ed. 2000 Orbital forcing in late Neogene lacustrine basins from the Mediterranean. Geologica Ultraiectina n°189.
- Read J.F. Kerans C. Weber L.J. F Sarg, J. Wright F.M. 1995. Milankovitch Sea-level Changes, Cycles, and reservoirs on Carbonate Platforms in Greenhouse and Ice-House Worlds. Society for Sedimentary Geology (SEPM) Short course n° 35.
- Vera J.A., Rodriguèz, J., Guerra, A. And Viseras, C. 1994. LA cuenca de Guadix-Baza, Documents et trabaux de l'IGAL, 14: 1-17.

The Solar Contribution to Climate Change

TEMPERATURE TRENDS FROM INSTRUMENTAL AND PROXY INDICATORS FOR THE LAST MILLENNIUM

P.D. Jones and K.R. Briffa

Climatic Research Unit University of East Anglia, Norwich NR4 7TJ, U.K. Phone: +44 1603 592090 / Fax: +44 1603 507784 Email: <u>p.jones@uea.ac.uk</u>

ABSTRACT

Instrumental temperature estimates for the land and marine regions of the world show a warming of the annual mean since 1861 of 0.6°C. The warming has not occurred linearly, but in two periods, 1915-40 and since 1975. The 1990s is the warmest decade since comparable records began in the 1860s and 1998 the warmest year. Overall, the warming is of the same magnitude in both hemispheres. Earlier instrumental temperatures are available in some regions of the world, particularly Europe. Here, temperatures during the late-17th century were about 1°C cooler than 1990s levels, values confirmed by totally independent measurements from boreholes. Longer series, of various combinations of proxy temperature indicators (from natural and written archives of the past), show the 20th century was the warmest century in the last millennium. The coolest centuries were the 17th and the 19th, with the coldest decades, 1601-10, 1691-1700 and 1811-20, each being about 0.7°C below the 1961-90 average. About half the decadal-scale variance can be explained by changes in solar irradiance and volcanism. Anthropogenic factors (greenhouse gases) need to be invoked to explain the dramatic increases during the 20th century.

INTRODUCTION

Although it can be argued that precipitation has a greater impact on many natural ecosystems and on various sectors of the economy, temperature is generally considered to be the fundamental indicator of the state of the climate system. Past periods of climate history are generally referred to by how warm or cold they were compared to present levels. The purpose of this paper is to review the sources of information on temperature changes over the last millennium. Three main periods of varying data quality are recognized: the instrumental period since the mid-19th century when thermometric records were relatively widespread, although never completely global; the early instrumental period (1700-1850) when records were available from a limited number of locations, principally European; and finally, the remainder of the millennium, when information about past temperature levels must be gleaned from written (historical evidence) and natural (e.g. tree rings, ice cores, corals, lake and marine sediments) archives.

INSTRUMENTAL PERIOD (1850 onwards)

The period since the middle of the 19th century represents a time within which sufficient numbers of temperature measurements enable the development of extensive grid-box datasets of monthly surface temperatures allowing the estimation of large-scale averages. Researchers in the UK and USA have developed datasets combining station temperature records from land regions and sea surface temperatures over ocean areas. To enable these to be easily combined, all the basic data need to be expressed as anomalies from a common reference period (1961-90). The use of anomalies minimizes a whole array of problems related to absolute temperatures: differences between neighbouring land and marine locations, differing elevation, varying observation times and different methods of calculating monthly-mean temperatures at land stations. Before combination, it is essential to ensure that all records (both land and marine) are homogeneous over their entire length of record. All issues related to the development of the surface temperature database are discussed in Jones et al. (1999) and references therein.

Figure 1 shows annual temperature averages for the Northern Hemisphere (NH), Southern Hemisphere (SH) and Globe for 1856-1999, derived from the Jones *et al.* (1999) $5^{\circ} \times 5^{\circ}$ grid-box dataset. Similar series have been derived by other groups (Peterson *et al.*, 1998 and Hansen *et al.*, 1999). Both hemispheres experienced a long-term warming of about 0.6° C since 1861 (or 1901), most of which occurred in two phases from about 1915 to 1940 and since 1975.

Jones *et al.* (1997) have estimated the standard errors due to sampling changes (both sparse coverage and complete lack in some regions) since the mid-19th century. Individual annual estimates are accurate to $\pm 0.1^{\circ}$ C (95% confidence limits) since 1951 and about twice this figure during the 19th century. On the basis of these results it can be argued that the two periods of warming are the only significant excursions to have occurred over the last 150 years. Another important conclusion of the Jones *et al.* (1997) study is that on an annual timescale, there are only about 50 statistically independent observations over the Earth's surface.

Proc. 1st Solar & Space Weather Euroconference, 'The Solar Cycle and Terrestrial Climate', Santa Cruz de Tenerife, Tenerife, Spain, 25-29 September 2000 (ESA SP-463, December 2000)

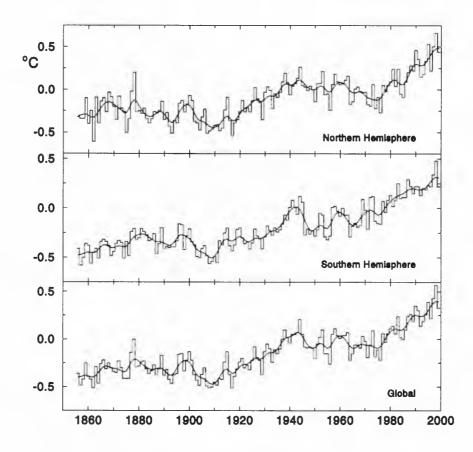


Figure 1: NH, SH and global averages for land and marine regions, 1861-1999. Data are expressed as anomalies from 1961-90 and the smooth line highlights variations on decadal timescales.

A limited spatial sampling, as is available for much of the later half of the 19th century can provide a reliable estimate of the global average, though sampling errors are greater. Extending this to earlier times, proxy climatic networks can also be expected to produce meaningful hemispheric estimates, provided the palaeoclimatic material is both a good proxy for temperature and reasonably well distributed over most of the hemispheric surface.

EUROPEAN INSTRUMENTAL TEMPERATURES (1700 onwards)

Instrumental records in many regions are often considerably longer than generally available in digital databases or in National Meteorological Service (NMS) archives. Early sources in most countries are poorly documented, particularly for periods during the nineteenth century, before the foundation of the NMS. In Europe, the situation is excenuated and long instrumental records can be derived for upwards of 50 locations in western and northern Europe back to about 1780 (Jones, 2001), in some cases in excess of 100 years more than recognized by the NMS. Some of these long records have been known for many years, but for others the potential has only just begun to be realised (Moberg *et al.*, 2000; Yan *et al.*, 2000). Daily records of temperature and pressure have recently been derived from eight sites in an EU-funded project (IMPROVE) back to the mid-to-late 18th century. All the results will be published soon in a special issue of *Climatic Change* and all the data made available on a CD. The development of these series is painstaking, as not only is digitization of all the sub-daily records necessary, but homogeneity assessment is vital using all the metadata information that can be found with the original ledgers. The work is not very fashionable when compared to developing natural proxy series, but properly undertaken, many more aspects of climate change can be assessed with the long daily time series.

Figure 2 shows annual, winter (DJF) and summer (JJA) temperature averages for three regions of Europe (Central England, Fennoscandia and Central Europe). Central England is the well-known record developed by Manley (1974) and updated by Parker *et al.* (1992). Fennoscandia is a six site average of temperatures from Uppsala, Stockholm, Trondheim, St. Petersburg, Vardo and Archangel'sk. The Swedish and St. Petersburg records are discussed more by Moberg *et al.* (2000) and Yan *et al.* (2000). Central Europe is the average of five sites (Vienna, Kremsmünster, Innsbruck, Hohenpeissenberg and Berlin), of which, the Austrian records are discussed by Auer *et al.* (1999). All three regional records show long-term annual warming since the late 18th century, but decades such as the 1730s, 1760s and

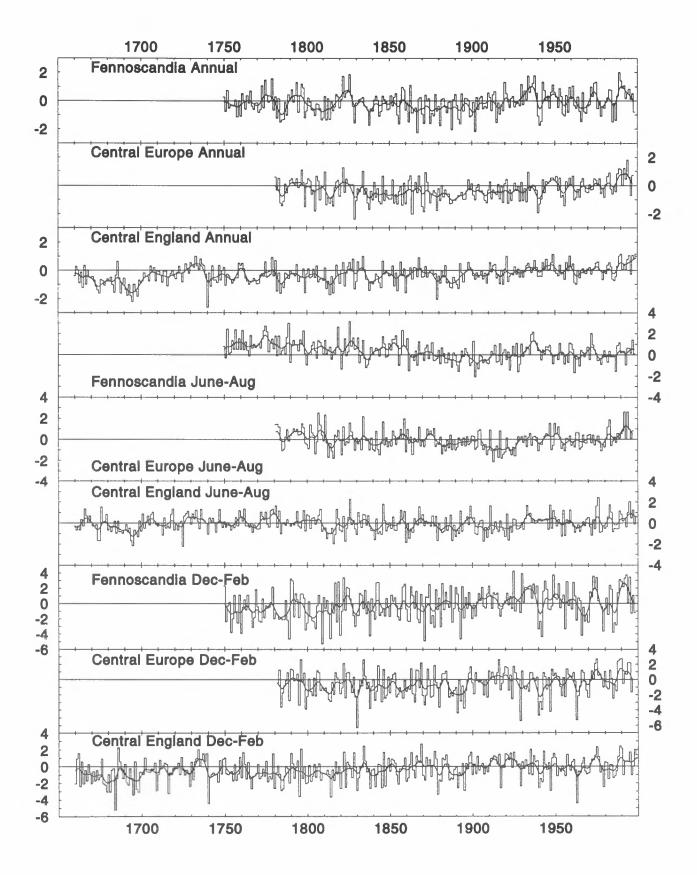


Figure 2: Annual, summer (JJA) and winter (DJF) averages of temperatures for Fennoscandia, Central Europe and Central England (see text for the stations used in the first two regions). The smooth line highlights variations on decadal timescales, and the temperatures are expressed as anomalies from the 1961-90 period.

1820s were only marginally cooler than present-day levels. The coolest decades were in the late-19th century (the start of the hemispheric and global series in Figure 1) and some earlier decades such as the 1810s, 1830s, 1740s and much of the period before 1710. The coldest year in western Europe in all instrumental records that extend back that far was 1740. Long-term warming is clear in the winter season, but summers in the late 18th century were slightly milder or at similar levels compared to today. The differential seasonal response indicates a reduction in continentality (lower summer/winter temperature differences in the 20th century).

The long European records clearly show that the coldest period of the last 350 years, the late 17th century, was only about 1°C below present day levels. Totally independent estimates of temperatures over the past 500 years have recently been reconstructed using a network of boreholes (Huang *et al.*, 2000). This technique measures temperature at different depths in a borehole, inverting the record to get a smoothed indication of surface temperatures (with decadal resolution over the last few decades but on century and longer timescales before the 20th century). Borehole records need to be selected carefully; ideally to avoid fluid in the strata and other inhomogeneities that would prevent a constant flow of heat from depths.

Figure 3 compares borehole-estimated temperatures with annual temperature averages for Central England (average of 26 boreholes) and Central Europe (120). It is clear that on the 50-year timescale, the agreement is extremely good, particularly the correspondence in temperature levels in the late-17th and 18th centuries. Huang et al. (2000) have developed six continental curves, but the spatial coverage of the holes is far from ideal in some continents. The European locations (146) are all in western Europe or the British Isles, ideal for the comparisons in Figure 3, but not appropriate for providing good spatial coverage in other parts of Europe. Averages for the other continents also have poor spatial coverage but indicate greater warming (particularly in North America) between 1500 than present. Changes in land use have been postulated as a cause of some of the intercontinental differences (see, e.g., Skinner and Majorowicz, 1999). Major changes in European land use took place many centuries earlier than the 16th century. For parts of North America, major land clearances and conversion to agriculture in the 19th century would have led to an apparent cooler land surface, a signal which would migrate down the hole. Much of eastern North America, for example, appears forested today but much of this is regrowth during the 20th century. To fully develop the borehole database requires land-use histories, to be certain today's land surface was similar in the past.

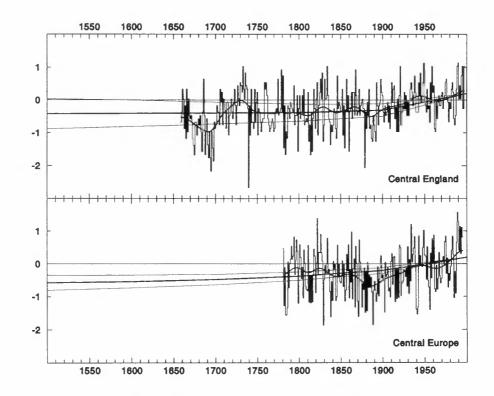


Figure 3: Annual averages of temperatures for Central England and Central Europe compared to borehole averages (from Huang et al., 2000) for the same regions. The wavy-smooth line is a 50-year Gaussian filter fit through the annual instrumental temperature series. The borehole record is the smoother line from 1500 to 2000, whose associated two standard errors of estimate are the thinner pair of lines. Temperatures are anomalies from the 1961-90 period.

PROXY RECORDS FOR THE MILLENNIUM

Proxy (non-instrumental) records are of two types: evidence from written documentary sources (principally from Europe and the Far East) and natural archives (physical and biological such as tree rings, ice cores, corals and lacustrine and marine sediments). The study of each of these is a discipline in itself and few are expert in the minutiae of each (Bradley, 1999, however, provides an excellent introductory synthesis of many of the disciplines). Developments in each archive highlight different backgrounds of the the discipline. Dendroclimatology tends to be the most statistical and historical climatology the least, but this is a simplification to illustrate their different strengths and weaknesses. Proxy climate records are developed specifically with a view to extending instrumental records, and all require calibration with instrumental data, ideally on the year-to-year timescale. Despite possible limitations, their most important features are often taken to be their long timescale (low-frequency) variations.

Within dendroclimatology recently, emphasis (e.g. Cook et al., 1995 and Briffa, 2000) has been placed on problems associated with the interpretation of lowfrequency aspects of climate forcing (distinguishing climate effects from biologically-induced processes that affect tree growth). These papers, however, should neither be taken as evidence that all tree-ring based reconstructions have problems, nor, and more importantly, that other proxy records are immune. Instead, these studies signal the need to recognize a problem that has yet to be fully realised or addressed in the other proxy disciplines. Historical records have inherent high-pass filters associated with the life span of historical observers. Coral growth may change due to an increase or lessening of light levels at different depths in the ocean, or exhibit slow changes associated with coral geometry; and some ice core records must be corrected for the compressive thinning of layers with depth (Briffa, 1995). Even isotopic measurements in ice cores must be calibrated against instrumental records, to confirm the validity of theoretical relationships with temperature (see, e.g., Dahl-Jensen et al., 1999, with respect to past temperatures over Greenland).

The key aspect of all proxy climate reconstruction is calibration, relating the parameter to a temperature measure, and retaining a part of the instrumental record to verify that the relationship still holds during an independent period. The longer the calibration and verification period, the more confident the user can be of the proxy's reliability as a past recorder of climate. In some regions, the short length of instrumental records means that formal calibration and verification is greatly restricted (e.g. the Antarctic, parts of the Arctic and the Tropics), but it should still be attempted, not assumed. The relatively long correlation decay lengths of surface temperature mean that even in central Greenland, long records can be inferred from coastal sites and used in assessments. Longer instrumental records often exist in colonial archives for tropical islands where coral records are to be found. Palaeoclimatologists generally spend relatively little time collecting instrumental data for calibrating their data. Searches may often allow instrumental records to be extended by several decades. but the workers in many disciplines probably consider themselves insufficiently qualified to follow this course of action. Documentary evidence has a clear problem with calibration as the types of sources used (annals, diaries etc.) are not generally available after instrumental records became widespread in Europe. Documentary series extended to the present with 'indexed' instrumental data may, therefore, give apparently excellent calibration/verification results (because the comparisons are essentially like with like). making them appear considerably better than reconstructions with natural archives.

Multiproxy assemblages

The last twenty years or so have seen dramatic advances in many palaeoclimatic fields, providing evidence about the past from more diverse archives and locations. More recently, several groups have attempted to produce large-scale averages of many of the various local records using a variety of simple and complex approaches. The first of the modern era was Bradley and Jones (1993), who averaged decadal means from 17 locations over the NH. Each series was equally weighted by standardization over the common period of 1861-1960 (10 decades). The resulting average was rescaled from sigma units to °C using instrumental averages for the summer season over the NH. Less spatially extensive studies in the 1960s and 1970s were more subjective, involving inferences from curve matching and experience, although the more objective study of Williams and Wigley (1981) was a notable exception.

Since 1998, four compilations of proxy evidence have been published, providing annual-timescale values for much of the last millennium, some as just hemispheric averages, others producing year-by-year maps showing temperature patterns over much of the NH. A fifth series for the Arctic region has been developed by Overpeck et al. (1997) but is not considered here. Jones et al. (1998) averaged together ten diverse proxy records for the NH, giving equal weight to each by standardising each series over a common reference period of 1901-50. Crowley and Lowery (2000) used a few of the same reconstructions (21 in total), but attempted to improve the spatial coverage by incorporating some that were only decadally resolved. Again, all were equally weighted and the average re-scaled to the variance of the hemispheric temperature series. More complex regression-based weighting has been employed by

Mann *et al.* (1998, 1999) and Briffa *et al.* (2000) (see also Briffa, 2000). Both also use considerably more proxy series, necessitating many different combinations to accommodate the reduced proxy availability during earlier parts of the millennium. Briffa *et al*'s (2000) reconstruction is entirely based on nearly 400 maximum latewood density series (with growth trends removed by a new technique designed to preserve long-timescale climate signals) made up from data extracted from thousands of individual conifer trees and calibrated for eight mid-to-high latitude regions of the NH. Mann *et al*'s (1998, 1999) reconstructions are the most complex and spatially detailed as they calibrate spatial patterns of temperature variability to spatial patterns in the array of about 100 proxy climatic series they use.

All four reconstructions are not independent of each other as they all use some common series to varying degrees. Only two (the Fennoscandian and Polar Urals tree-ring reconstructions. Briffa et al., 1992, 1995) are, however, included in all four. All data used are a mix of raw proxy measurements and series calibrated to instrumental temperatures, generally over the late 19th and 20th centuries. The basic assumptions in all proxy climate reconstruction are relevant, i.e. uniformitarianism in the temporal response of the proxy to the temperature forcing and consistency in the expression of the forcing response (the fact that the statistical quality does reduce further back in time can be used to expand regression-based standard errors for the earlier years). Jones et al. (1998) and Crowley and Lowery (2000), however, assume all contributing series are of equal importance. The other two, to varying degrees, use regression so also tacitly assume that interrelationships between the proxies are consistent with those in calibration periods. Mann et al. (1998, 1999) also make extensive use of early instrumental data for the 18th and 19th centuries, principally European series, but also from some coastal locations in Asia and North America. It could be argued that early instrumental sources are best left unused, enabling them to extend verification periods where they are available.

The final principal difference between the series is that Mann et al. (1998, 1999) and Crowley and Lowery (2000) have been calibrated/fitted against calendar year temperature averages, while Jones et al. (1998) and Briffa et al. (2000) are fitted against summer (June to August), and extended summer (April-September, i.e., growing season temperatures), respectively. Most proxy climate reconstructions (particularly trees and ice cores, see Bradley, 1999) have generally been shown to be responsive to summer conditions, but as the extended summer is part of the calendar year regression with annual temperatures will indicate reasonable relationships, even if winter temperatures have little influence on the proxies.

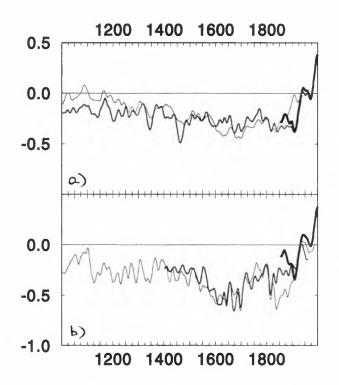


Figure 4: Multiproxy combinations of annual-timescale temperature reconstructions for the millennium (all series smoothed with a 30-year Gaussian filter), a) the annual series of Mann et al. (1999-medium) and Crowley (2000-thin) and b) the 'summer' series of Jones et al. (1998-medium) and Briffa et al. (2000-thin). In a) the thickest line is a similarly smoothed record of NH land and marine temperatures for the calendar year and in b) as a) but for the April to September average. The zero line is the 1961-90 reference period average.

Figure 4 shows the four NH series for the millennium, together with instrumental averages since 1861. Two separate plots compare the calendar year and the growing season series. All four series show similar lowfrequency features, but exhibit several disagreements in the shorter-timescale details. Table 1 shows correlations between the entire lengths of the series, for the raw and high-frequency (residuals from a 30 year filter) data. In all, the 20th century is the warmest of the millennium, with either the 17th or the 19th centuries the coldest. All the series show slight cooling throughout much of the millennium, until the dramatic rise during the 20th century. The warmth and the warming that has taken place are unprecedented over the last 1000 years. Extending each with instrumental records (as many of the proxy series used were collected as far back as the 1970s), the 1990s are the warmest decade and 1998 the warmest year of the millennium, though it should be borne in mind that the proxy records have probably not captured all the variance exhibited in the instrumental data.

Table 1. Correlations between the four millennial reconstructions of NH temperatures. Raw correlations above the diagonal and high-frequency (residuals from a 30-year Gaussian filter) below. The lengths of record used are J (Jones *et al.*, 1998, 1000-1981), B (Briffa *et al.*, 2000, 1402-1960), C (Crowley, 2000, 1000-1965) and M (Mann *et al.*, 1999, 1000-1981). All the correlations use the longest possible periods of overlap.

	J	В	С	М
J	-	0.62	0.51	0.47
В	0.75	-	0.52	0.36
С	0.76	0.79	-	0.51
М	0.76	0.43	0.70	-

Explaining the changes during the Millennium

Both Mann *et al.* (1998) and Crowley (2000) have extended their analyses by considering what external forcing factors could have caused the changes evident in the series in Figure 4. Crowley's (2000) analysis was more extensive using an Energy Balance Model (EBM) of the climate system with time series of natural (solar and volcanic) and anthropogenic (carbon dioxide, other trace gases and sulphate aerosols) forcing factors. The differences between the various series in Figure 4 reflect some of the uncertainties in our knowledge of past temperature (see Mann et al., 1999, for more discussion), but our knowledge of the past histories of the forcing factors is also far from perfect. Greenhouse forcing is well understood because the gases are well mixed and records of trapped air in ice cores show little change until the late 19th century. Proxy records of past solar output changes abound but there is no universally accepted series. Crowley (2000) reconstructed two solar variability series using ¹⁰Be and ¹⁴C proxies spliced to the Lean et al. (1995) reconstruction of solar irradiance from the 17th century. Volcanic forcing is even more uncertain. Also, because it is transitory, influencing climate for a few years following major eruptions, it has often been ignored in many climate change studies. even though it has been clearly shown to be a major factor in some proxy climate reconstructions (e.g. Briffa et al., 1998). Crowley (2000) extended the well-used

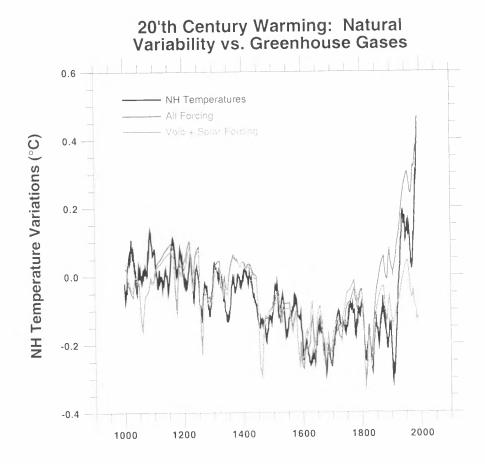


Figure 5: Comparison of the Crowley (2000) multiproxy average for the NH with EBM simulations using natural forcings only and natural forcings plus anthropogenic factors (greenhouse gases and sulphate aerosols).

Sato *et al.* (1993) series using two ice-core volcanic records (see also Robock and Free, 1996), but this would seem to be far from ideal. Despite the known uncertainties in the two forcing series and the annual estimates of hemispheric temperatures, comparisons with the EBM simulated temperatures (Crowley, 2000) show that between 41 and 64% of the pre-1850 decadal-scale variance can be explained by solar irradiance and volcanism. Figure 5 shows comparisons between the millennial reconstruction and the EBM results.

CONCLUSIONS

Temperatures measured over the instrumental period since 1861 show about a 0.6°C warming globally, with the 1990s the warmest decade and 1998 the warmest year. Longer instrumental records from Europe show cooler temperatures in the late 17th and early 19th century, about 1°C cooler than today. Not all decades were significantly colder than today. The 1730s, 1760s and 1820s were only marginally cooler than the 1930s and 1990s over western and northern Europe. The degree of warming over Europe since the late 17th century is confirmed by independent studies using a network of boreholes.

Temperature estimates for earlier periods in the millennium must be derived from proxy indicators in natural and written archives. Four different compilations of the available evidence show that temperatures have cooled from the first four centuries of the millennium to their coldest values in the 17th and 19th centuries. The 20th century has seen dramatic warming and, when averaged, is the warmest of the millennium. The compilations use some of the same proxy sources, but the basic data is combined in different ways with different basic aims. The coldest decades of the millennium in the 17th century (probably 1601-10 and 1691-1700) were about 0.7°C cooler than the 1961-90 base period, 1°C below the warmest decade of the 1990s. Recent work by Crowley (2000) shows that between 41 and 64% of the decadal-scale variance of the NH temperatures pre-1850 can be explained by changes in solar irradiance and volcanism. The dramatic temperature rise in the 20th century appears to be only adequately explained by anthropogenic forcing of the climate.

ACKNOWLEDGEMENTS

This work has been supported by the U.S. Department of Energy (Grant No. DE-FG02-98ER62601). The authors thank Tom Crowley for the series plotted in Figure 5 and Mike Mann and Tom Crowley for the series plotted in Figure 4.

REFERENCES

- Auer, I., Böhm, R., Schoener, W. and Hagen, M. (1999): ALOCLIM - Austrian-Central European Long-term Climate - The creation of a multiple homogenised long-term climate data set. Proc. Second Seminar for Homogenization of Surface Climatological Data, Budapest, November 1998, 25pp.
- Bradley, R.S. (1999): *Paleoclimatology: reconstructing climates of the Quaternary*, Harcourt/Academic Press, San Diego, 610pp.
- Bradley, R.S. and Jones, P.D. (1993): 'Little Ice Age' summer temperature variations: their nature and relevance to recent global warming trends. *The Holocene*, Vol. 3, pp.367-376.
- Briffa, K.R. (1995): Interpreting high-resolution proxy climatic data – The example of dendroclimatology, In Analysis of Climate Variability; Applications of Statistical Techniques (H. von Storch and A. Navarra, Eds.) Springer, Berlin, pp.77-94.
- Briffa, K.R. (2000): Annual climate variability in the Holocene: interpreting the message of ancient trees. *Quaternary Science Reviews*, Vol. 19, pp.87-105.
- Briffa, K.R., Jones, P.D., Bartholin, T.S., Eckstein, D., Schweingruber, F.H., Karlen, W., Zetterberg, P. and Eronen, M. (1992): Fennoscandian summers from AD 500: temperature changes on short and long timescales. *Climate Dynamics*, Vol. 7, pp.111-119.
- Briffa, K.R., Jones, P.D., Schweingruber, F.H., Shiyatov, S.G. and Cook, E.R. (1995): Unusual twentieth-century summer warmth in a 1,000year temperature record from Siberia. *Nature*, Vol. 393, pp.156-159.
- Briffa, K.R., Jones, P.D., Schweingruber, F.H. and Osborn, T.J., 1998: Influence of volcanic eruptions on Northern Hemisphere summer temperatures over the last 600 years. *Nature* 393, 450-455.
- Briffa, K.R., Osborn, T.J., Schweingruber, F.H., Harris, I.C., Jones, P.D., Shiyatov, S.G. and Vaganov, E.A. (2000): Low-frequency temperature variations from a northern tree-ring density network. J. Geophys. Res. (submitted).
- Cook, E.R., Briffa, K.R., Meko, D.M., Graybill, D.S. and Funkhouser, G. (1995): The 'segment length curse' is long tree-ring chronology development for palaeoclimatic studies. *The Holocene*, Vol. 5, pp.229-237.
- Crowley, T.J. (2000): Causes of climate change over the past 1000 years. *Science*, Vol. 289, pp.270-277.
- Crowley, T.J. and Lowery, T. (2000): How warm was the Medieval Warm Period? A comment on "Man-made versus Natural Climate Change". *Ambio*, Vol. 39, pp.51-54.

- Dahl-Jensen, D., Mosegaard, K., Gundestrup, N., Clow, G.D., Johnsen, S.J., Hansen, A.W. and Balling, N. (1998): Past temperatures directly from the Greenland Ice Sheet. Science, Vol. 282, pp.268-271.
- Hansen, J., Ruedy, R., Glascoe, J. and Sato, M. (1999): GISS analysis of surface temperature change. J. Geophys. Res., Vol. 104, pp.30997-31022.
- Huang, S., Pollack, H.N. and Shen, Po-Yu. (2000): Temperature trends over the past five centuries reconstructed from borehole temperatures. *Nature*, Vol. 403, pp.756-758.
- Jones, P.D. (2001): Early European Instrumental Records, In Climate and Climatic Impacts: The last 1000 years (P.D. Jones, T.D. Davies, A.E.J. Ogilvie and K.R. Briffa, Eds.) Kluwer Academic/Plenum Publishers (in press).
- Jones, P.D., Osborn, T.J. and Briffa, K.R. (1997): Estimating sampling errors in large-scale temperature averages. J. Climate, Vol. 10, pp.2548-2568.
- Jones, P.D., Briffa, K.R., Barnett, T.P. and Tett, S.F.B. (1998): High-resolution palaeoclimatic records for the last millennium: Interpretation, integration and comparison with general circulation model control run temperatures. *The Holocene*, Vol. 8, pp.455-471.
- Jones, P.D., New, M., Parker, D.E., Martin, S. and Rigor, I.G. (1999): Surface air temperature and its changes over the past 150 years. *Rev. Geophys.*, Vol. 37, pp.173-199.
- Lean, J., Beer, J. and Bradley, R. (1995): Reconstruction of solar irradiance since 1610: implications for climatic change. *Geophys. Res. Letts.*, Vol. 22, pp.3195-3198.
- Manley, G. (1974): Central England temperatures: monthly means 1659 to 1973. *Q. J. Roy. Met. Soc.*, Vol. 100, pp.389-405.
- Mann, M.E., Bradley, R.S. and Hughes, M.K. (1998): Global-scale temperature patterns and climate forcing over the past six centuries. *Nature*, Vol. 392, pp.779-787.
- Mann, M.E., Bradley, R.S. and Hughes, M.K. (1999): Northern Hemisphere temperatures during the past millennium: Inferences, uncertainties and limitations. *Geophys. Res. Letts.*, Vol. 26, pp.759-762.
- Moberg, A. et al. (2000): Day-to-day variability trends in 160-to-275 year long European instrumental records. J. Geophys. Res. (in press).
- Parker, D.E., Legg, T.P. and Folland, C.K. (1992): A new daily Central England temperature series. *Int. J. Climatol.*, Vol. 12, pp.317-342.
- Peterson, T.C., Karl, T.R., Jamason, P.F., Knight, R. and Easterling, D.R. (1998): The first difference method: maximising station density for the calculation of long-term global temperature change. J. Geophys. Res., Vol. 103, pp.25967-25974.

- Robock, A. and Free, M. (1996): The volcanic record in ice cores for the past 2000 years. In *Climate Variations and Forcing Mechanisms of the last* 2000 years (P.D. Jones, R.S. Bradley and J. Jouzel, Eds.), Springer, Berlin, pp.533-546.
- Sato, M., Hansen, J.E., McCormick, M.P. and Pollack, J. (1993): Stratospheric aerosol optical depths (1850-1990). J. Geophys. Res., 98, pp.22987-22994.
- Skinner, W.R. and Majorowicz, J.A. (1999): Regional climatic warming and associated twentieth century land-cover changes in north-western North America. *Climate Research*, Vol. 12, 39-52.
- Williams, L.D. and Wigley, T.M.L. (1983): A comparison of evidence for Late Holocene summer temperature variations in the Northern Hemisphere. *Quaternary Research*, Vol. 20, pp.286-307.
- Yan, Z., Jones, P.D., Moberg, A., Bergstrom, H., Davies, T.D. and Yang, C. (2000): Recent trends in weather and seasonal cycles - An analysis of daily data from Europe and China. J. Geophys. Res. (submitted).

IS THERE A CORRELATION BETWEEN SOLAR CYCLE LENGTHS AND TERRESTRIAL TEMPERATURES? OLD CLAIMS AND NEW RESULTS.

Peter Laut' and Jesper Gundermann"

^{*} Technical University of Denmark. Building 377, DK-2800 Lyngby, Denmark. tel: +45 45-255481 / fax: +45 45-255480 / e-mail: ifakpl@pop.dtu.dk

¹ Danish Energy Agency, Amaliegade 44, DK-1256 Copenhagen K, Denmark.

tel: +45 33-926718 / fax: +45 33-926837 / e-mail: jgu@ens.dk

ABSTRACT

The present analysis was triggered by continuing claims in the Danish public climate debate (1) that terrestrial temperatures are almost exclusively determined by solar activity, (2) that the human influence until now has been negligible and (3) that there is no need to reduce manmade greenhouse gas emissions. To support these claims usually reference is made to the "strikingly good agreement" between solar cycle lengths and Northern Hemisphere land temperatures which was described by E. Friis-Christensen and K. Lassen in two articles [Science 1991 and J. Atmos. Sol. Terr. Phys. 1995] and attracted word wide attention. Especially some central figures in the two articles have been widely referred to both in the public discussion and in scientific litterature. The Danish Energy Agency asked us to clear up if these claims were justified. This question is, of course, of vital importance for national energy policies. Our present work demonstrates that an alternative analysis of the underlying physical data leads to figures which do not support the claims mentioned above.

INTRODUCTION

The topic of my presentation is the correlation between terrestrial temperatures and solar cycle lengths, and I will especially focus upon the claim that the global warming of the last hundred years has been caused by changes in solar activity - in some way expressed by a corresponding variation of solar cycle lengths - and that the influence from man-made greenhouse gasses must have been quite insignificant. My starting point will be the next two figures:

Figure 1 comes from an article published in *Science* in 1991 by *Friis-Christensen and Lassen* [1991]. One curve (*) shows Northern Hemisphere land temperatures and the other (+) solar cycle lengths (minimum-minimum and maximum-maximum). The first 20 points on the solar curve are heavily smoothed, so called "12221-filtered" values. That means that every point is a weighted average of five solar cycle lengths (with weights ¹/₈, ¹/₄, ¹/₄, ¹/₈) and hence represents a time interval of about 55 years.

These 20 points form a kind of S-shape which is seen to agree quite well with the S-shape of the temperature curve. The last four points belong to a different kind of species, since they are only partially filtered or not filtered at all. They seem to establish an agreement between the solar cycle lengths and the recent global warming. This apparent agreement has played an important role in the public Danish climate debate. Many people see it as a kind of proof that the recent global warming is caused by solar activity alone, virtually without any contributions from man-made greenhouse gasses, and they argue that the planned reductions of man-made greenhouse gas emissions therefore are meaningless. We shall later return to this figure, but first have a look at Figure 2 which is an update of Figure 1 by the same authors. It shows the same parameters for a longer time period (The solar cycle lengths are here exclusively minimum-minimum lengths). It was published in 1995 in The Journal of Atmospheric and Solar-Terrestrial Physics [Lassen and Friis-Christensen 1995]. As you can see this figure also shows a good agreement of the two curves, particularly over the last 100 years of global warming. This figure has also been used to argue that the correlation is so good that it simply does not leave room for any human influence. These two figures have become standard references in the public Danish climate debate, and they are reproduced in books, newspaper articles and on television.

Some time ago the *Danish Energy Agency* asked us to analyse the underlying physical data and find out if it really is true that these physical data support the view that the human influence upon the recent global warming must be negligible. In view of the current international efforts to reduce greenhouse gas emissions we found it an important task to try to answer this question.

A RE-ANALYSIS

We therefore acquired the physical data underlying Figure 2 and obtained Figure 3. Our figure looks rather different from Figure 2 even though the physical data employed are exactly the same, including the smoothing of the temperature curve. The main difference is that the temperature curve rises well above the solar curve over the

Proc. 1st Solar & Space Weather Euroconference, 'The Solar Cycle and Terrestrial Climate', Santa Cruz de Tenerife, Tenerife, Spain, 25-29 September 2000 (ESA SP-463, December 2000)

last 100 years, so that our figure cannot be used to argue that solar activity is the one dominant cause of the recent global warming.

There are two main reasons for this discrepancy. The first is that Friis-Christensen and Lassen in their Figure 2 have put two different temperature series together [Groveman and Landsberg 1979a-c, Jones et al. 1986, Jones 1988] without performing the necessary zero point correction, even though the two series are defined by different reference periods. In this way the right hand part of the temperature curve is lowered in such a way that about one third of the observed global warming disappears on their figure. The gap between the two temperature series and a certain overlap can be seen on Figure 2 around year 1860. The other main reason for the discrepancy between our figure and Figure 2 is that on Figure 2 the solar curve has been placed too high as compared to a straightforward linear regression fit. Thereby a good agreement of the solar curve with the right hand side of the temperature curve is obtained (i.e. with the reduced global warming) at the expense of the left hand side of the figure, where the solar curve is seen to "hover" well above the temperature curve. It should be added that a minor part of the discrepancy is due to the fact that our linear regression coefficients have been determined on the basis of preindustrial data alone in order to secure that they would reflect solar rather than human influences.

We then acquired the physical data underlying Figure 1 from the Science article. These are shown on Figure 4, with the two new cycle lengths which since have been observed (points 5 and 6) and the corresponding 12221filtered values (points 1' and 2'). It is seen that the raw, nonfiltered solar cycle lengths (\blacklozenge) are oscillating violently, while the filtered cycle lengths (+) form a much smoother curve. Therefore, nonfiltered and filtered data should not be joined into one curve. This can be seen from the following argument: If one, e.g., takes the points of the filtered curve until about 1960 and then adds the next two low lying nonfiltered points (x and y), one will obtain a curve showing a dramatic global cooling. And taking the filtered curve a little longer until about 1970 and adding the two nonfiltered points marked 3 and 4 one will obtain a curve showing a dramatic global warming. That was actually how the good agreement of the solar curve with the recent global warming in the Science article was obtained.

AN UPDATE

At last we performed an updated analysis (Figure 5). Here the old *Groveman-Landsberg* temperature reconstruction has been replaced by the more recent reconstruction published by *Mann et al.* [1998] and combined with a

modern instrumental temperature record issued by the Hadley Centre (Combined land air and sea surface temperature anomalies for the Northern Hemisphere 1951 -1998, at http://www.meto.gov.uk/sec5/CR div/Tempertr/ lsst vals nh.html). Again we see that the nonfiltered solar cycle lengths (\blacklozenge) oscillate violently in contrast to the smooth curve of filtered cycle lengths (thick line). The rectangular frame on the right hand side of Figure 5 shows the relative short time period covered by the Science-91 figure. We recognize the S-shape of the solar curve and the S-shape of the temperature curve. Here, however, they are not scaled to fit. That is because the linear regression here has been performed for the entire expanded time period. If we narrow down the range of the linear regression to the "time slice" of the Science figure, the linear regression will scale up the flat S-shape of the solar curve into the steep Sshape of the temperature curve, and we obtain again the good agreement of the Science figure.

We did not try to determine the percentage of a possible solar influence connected with solar cycle lengths, because this cannot be done by curve fitting alone.

Lassen and Friis-Christensen [2000] also have prepared an update recently (Figure 6). The temperature curve here is the reconstruction of Mann et al. [1998]. Again the agreement is seen to be good, particularly in the period of global warming. However the good agreement has been achieved by methods which may be questioned: (1) The authors have doubled the number of solar data points over the period of global warming - and thereby also doubled the mathematical weight of this particular period in the linear regression - and thereby improved the agreement of the solar cycle lengths with the temperature curve selectively in the period of global warming at the expense of all other periods. (2) The authors have introduced 'weight factors' to the individual data points in order to take "into account an estimated uncertainty in both variables". However, they do not disclose the numerical values they have chosen for these weight factors, and therefore it is not possible directly to check their calculations. Nevertheless, we have tried to reproduce their figure and have found that this could be done. When we skip all solar data prior to the year 1800 and then perform a straightforward linear regression upon the remaining data we obtain a figure which is practically identical with Figure 6. This shows that their data handling must be equivalent to discarding the first 230 years of the solar record. We found that intriguing. One could have argued that, if the data prior to 1800 are so uncertain as to justify weight factors which are effectively zero, the data must also be too uncertain to deserve being displayed on Figure 6, and hence should have been omitted entirely.

The doubling of data points, which is mentioned above, is

obtained by adding maximum-maximum solar cycle lengths to the otherwise minimum-minimum cycle lengths of figure 2, and such data are only available for the period of global warming.

At last we performed a simple linear regression covering the entire time period using the same data as *Friis-Christensen and Lassen* (but omitting the maximummaximum cycle lengths in order to secure equal weights for all time periods) and obtained Figure 7, where much of the good agreement again has disappeared.

CONCLUSION

Our conclusion is that the impression, created by the articles of *Friis-Christensen* and *Lassen*, that the recent global warming has been caused predominantly by changes in solar activity, is not supported by the physical data they have used.

REFERENCES

- Friis-Christensen, E., and K. Lassen, Length of the solar cycle: An indicator of solar activity closely associated with climate, *Science*, 254, 698-700, 1991.
- Groveman, B. S., and H. E. Landsberg, Simulated Northern Hemisphere temperature departures 1579-1880, *Geophys. Res. Lett.*, *6*, 767-769, 1979a.
- Groveman, B. S., and H. E. Landsberg, Reconstruction of Northern Hemisphere temperature: 1579-1880, *Publ. 79-181*, Univ. of M., College Park, Md., 1979b.
- Groveman, B. S., and H. E. Landsberg, Data appendices to publication 79-181, *Publ. 79-182*, Univ. of M.,

College Park, Md., 1979c.

- Jones, P. D., Hemispheric surface air temperature variations: Recent trends and an update to 1987, *J. Clim.*, *1*, 654-660, 1988.
- Jones, P. D., S. C. B. Raper, R. S. Bradley, H. F. Diaz, P. M. Kelly, and T. M. L. Wigley, Northern Hemisphere surface air temperature variations: 1851-1984, J. Clim. Appl. Meteorol., 25, 161-179, 1986.
- Lassen, K., and E. Friis-Christensen, Variability of the solar cycle length during the past five centuries and the apparent association with terrestrial climate, *J. Atmos. Sol. Terr. Phys.*, 57(8), 835-845, 1995.
- Lassen, K., and E. Friis-Christensen, Reply to the article "Solar cycle lengths and climate: A reference revisited" by P. Laut and J. Gundermann, J. Geophys. Res., In print, 2000.
- Lassen, K., and P. Thejll, Northern Hemisphere temperatures and the solar cycle lengths theory: New data, *Annual meeting of The European Geophysical Society*, Nice, April 2000.
- Laut, P., and J. Gundermann, Solar cycle length hypothesis appears to support the IPCC on global warming, *J. Atmos. Sol. Terr. Phys.*, 60(18) 1719-1728, 1998.
- Laut, P., and J. Gundermann, Solar cycle lengths and climate: A reference revisited, *J. Geophys. Res., In print,* 2000.
- Mann, M. E., R. S. Bradley, and M. K. Hughes, Globalscale temperature patterns and climate forcing over the past six centuries, *Nature*, 392, 779-787, 1998.
- McNish, A. G., and J. V. Lincoln, Prediction of sunspot numbers, *Trans. Am. Geophys. Union, 30*, 673-685, 1949.

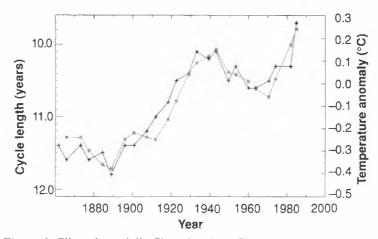


Figure 1: Filtered, partially filtered and nonfiltered solar cycle lengths (+) compared with Northern Hemisphere land temperatures (*). This figure from *Friis-Christensen and Lassen* [1991] has - in the public debate - been used to argue that the recent global warming is entirely due to changes in solar activity.

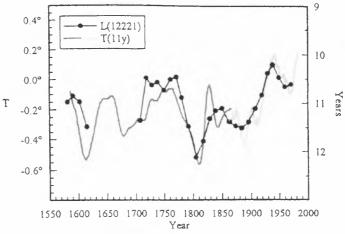


Figure 2: Filtered and partially filtered solar cycle lengths (solid circles) compared with a temperature reconstruction by Groveman and Landsberg [1979] (left) and temperature anomalies by Jones et al. [1986, 1988] (right). The two temperature series are joined together without zero point adjustment, even though they are defined by different reference periods. As a consequence the right hand side temperature curve has been placed too low, whereby one third of the global warming disappears on the graph. The solar curve has been placed too high as compared to a straightforward linear regression fit. Thereby a good agreement with the lowered temperature curve to the *right* (i.e. the recent global warming) has been obtained, but at the expense of the left hand side of the temperature curve, where the points of the solar curve predominantly lie above the temperature curve. This figure from Lassen and Friis-Christensen [1995] has also been used in the public debate to argue that the agreement with the recent global warming is so good that no room is left for any significant human influence.

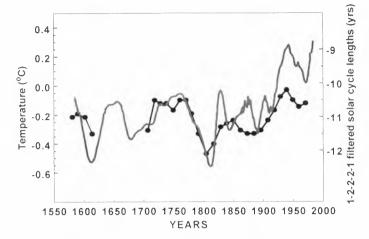


Figure 3: Presentation of the same physical data as in Figure 2, but here (a) the two temperature series are displayed in the *same scale*, i.e. with a zero point correction taking account of their different reference periods, and (b) the constants of the linear regression are exclusively based on values *before* the recent period of global warming (i.e. before 1870) in order to avoid interference of possible solar and man-made effects. The temperature curve here rises clearly above the solar curve. Therefore it cannot be used to argue, that the human influence must be negligible.

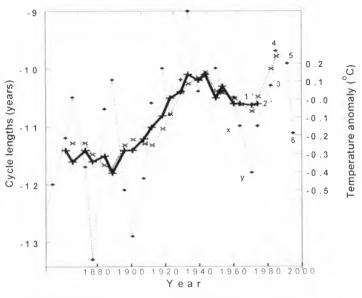


Figure 4: The physical data underlying Figure 1. Points 1'. 2', 3 and 4 are the last four points on Figure 1 (the *filtered* points 1' and 2', however, now replace the corresponding *partially filtered* points on Figure 1). Points 5 and 6 are the two solar cycle lengths which have been observed in the mean time. *Thick line* (\blacklozenge) : 12221-filtered cycle lengths. *Dotted line* (\blacklozenge) : Observed, nonfiltered solar cycle lengths. *Thin line* (\bigstar) : Northern Hemisphere land temperatures. Notice the violent variation of nonfiltered cycle lengths and the smooth variation of filtered cycle lengths. The good agreement with the recent global warming in the Science-91 article of *Friis-Christensen* and *Lassen* was obtained by the addition of the nonfiltered points 3 and 4 to the smoothed curve. The smoothed curve does not show any trace of global warming.

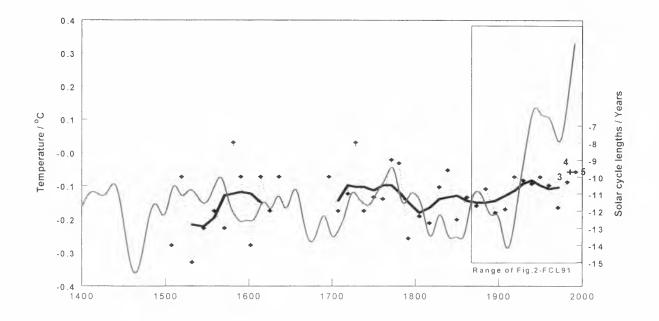


Figure 5: (a) The solid line shows smoothed Northern Hemisphere temperatures 1400-1990, obtained by combining the reconstruction of *Mann et al.* [1998] with a series issued by the *Hadley Centre* [2000]. (b) The thick line shows the 12221-filtered minimum-minimum solar cycle lengths as given in *Lassen and Friis-Christensen* [1995] with the most recent value added. The scaling of these cycle lengths is obtained by linear regression. (c) The dotted line (\blacklozenge) shows the individual nonfiltered minimum-minimum cycle lengths with the last two points marked 3 (which corresponds to point 3 on Figure 4) and 5 (which has since been observed). (d) The nonfiltered maximum-maximum cycle length which is also shown on Figure 4 as point 4 is here marked by ' \blacklozenge '. (e) The range of Figure 1 is marked by the rectangle. The S-shapes of the two curves can be recognized, but are not scaled to fit since the linear regression here covers the whole solar data set.

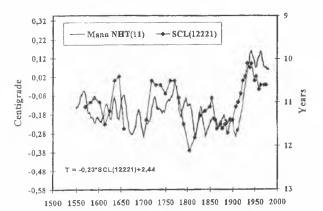


Figure 6: Update from *Lassen and Friis-Christensen* [2000]. The number of data points over the period of global warming has been doubled and a special weighting has been introduced, which virtually reduces the influence of data points in the period 1570-1800 to zero. Thereby an agreement with the global warming has been obtained. The temperature curve is an 11-yr average of the reconstruction of Mann et al. [1998].

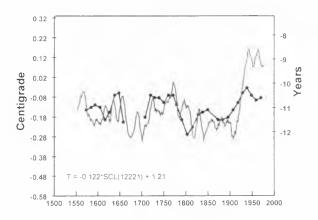


Figure 7: The same data as in Figure 6, but without the doubling of data points over the period of global warming. Here the linear regression has been extended over the whole solar data set and all cycle lengths enter with equal weights.

DESCRIPTION AND FIRST RESULTS OF THE EC PROJECT SOLICE (SOLAR INFLUENCES ON CLIMATE AND THE ENVIRONMENT)

Marie-Lise Chanin,

Service d'Aéronomie, BP 3, 91370, Verrières-le-Buisson, France, Tel: 33 69 20 07 94, Fax: 33 69 20 29 99, email : marie-lise.chanin@aerov.jussieu.fr

Joanna D. Haigh

Imperial College of Science, Technology and Medicine, London SW7 2BZ, UK Tel: 44 171 594 7671, Fax: 44 171 594 7900, email: j.haigh@ic.ac.uk

Abstract

Recent statistical studies of observational records suggest that solar effects do play a significant part in natural climate variability. However, a physical mechanism to account for the apparent solar effects has not been fully developed. Variations in solar ultraviolet radiation (UV) are much greater than that in total irradiance and, because this UV is absorbed in the middle atmosphere causing additional ozone formation, it is possible that stratospheric processes may excite a response in the climate of the lower atmosphere. In the SOLICE project we adopt a co-ordinated plan of modelling and observational studies designed to produce new assessments of the impact of solar variability on climate and to address some of the key questions concerning the mechanisms whereby these take place.

Introduction: Mechanisms for solar-climate links

The most simple way in which a change in solar output can impact the Earth's climate system is through the change in the wavelength-integrated irradiance reaching the Earth, generally referred to as the Total Solar Irradiance (TSI). Many studies have explored the direct relationship between solar irradiance and climate by correlating time series of TSI or various proxies of solar activity (e.g. solar cycle length) with surface temperature. Alternatively, model studies have examined the impact of including solar forcing in addition to other forcing such as greenhouse gases and tropospheric aerosol amounts. These studies suggest that the direct effect of solar variation is not negligible but do not explain the amplitude of the apparent response in, for example, the 30hPa geopotential height. Considering that the amplitude of solar variability is the largest in the UV part of the spectrum and the fact that UV irradiance change affects both the radiative forcing and the mean meridional circulation, we intend to examine in detail in this project whether this could induce indirectly a change in the atmosphere and in the climate compatible with the observations. Let us summarise below the two main ways whereby it could enhance or modify the impacts of changing TSI.

a) Radiative Forcing

Variations in stratospheric composition and thermal structure resulting from UV changes may have an impact on tropospheric climate through changes in radiative forcing (Haigh, 1994). Thus, in addition to a direct increase in downward short-wave irradiance at the tropopause, higher solar activity can cause an increase in downward infrared flux by heating the stratosphere and also a radiative forcing due to ozone changes. However, the sign of the ozone effect is not well established. The direct solar radiative forcing between minimum and maximum periods of solar activity over the 11-year activity cycle is about 0.3 Wm ². The additional forcing due to ozone increases and lower stratospheric warming has been calculated by different authors (including Haigh, 1994) with quite different results ranging from -0.13 to +0.05 Wm⁻². This disparity in both sign and amplitude may reflect the different approaches used in specifying and/or calculating ozone changes and the stratospheric temperature response

b) Mean meridional circulation and wave-mean flow interaction

Changes in the ozone in response to the solar cycle also have the potential to change circulation patterns via the changes in temperature. For example, changes in the latitudinal temperature gradients will lead to changes in zonal and meridional wind distributions at all levels of the atmosphere. Haigh, (1999) found a sensitivity of the strength and width of the Hadley circulation to typical changes in ozone: during a solar maximum the subtropical jets moved polewards and the associated Hadley circulation was found to weaken and broaden. Shindell et al., (1999) on the other hand, although reporting a similar poleward movement of the subtropical jets, found the strength of the Hadley circulation to increase. The difference may be due to the way in which the ozone changes are

Proc. 1st Solar & Space Weather Euroconference, 'The Solar Cycle and Terrestrial Climate', Santa Cruz de Tenerife, Tenerife, Spain, 25-29 September 2000 (ESA SP-463, December 2000)

imposed and the extent to which they alter the static stability of the tropical lower stratosphere. In the stratosphere temperature changes will lead both to meridional circulation changes and also to changes in zonal wind strength, which will then alter the pattern of planetary wave propagation

Observations of the middle atmosphere response to solar forcing.

The enhancement of shorter wavelength radiation during periods of greater solar activity means that the largest direct radiative heating of the atmosphere is felt at higher altitudes. More specifically increased levels of ultraviolet radiation in the wavelength range 175-320 nm heat the stratosphere and mesosphere due to absorption by ozone and oxygen. The temperature response to the 11-year solar cycle has been observed in the last decades in the whole middle atmosphere and above using a number of different techniques. From the thermosphere to the troposphere, one can mention : incoherent radar, sodium trails, rockets, Rayleigh lidar, SSU satellites, and, for the lower part of the stratosphere and the troposphere, radiosondes (e.g.: Labitzke and van Loon 1997). Most of those results have been reviewed in Chanin et al., (1989) and more recently by Chanin and Ramaswamy in the recent WMO-UNEP Scientific Assessment of Ozone Depletion, 1998 (WMO, 1999). The horizontal structure of the response is obtained by the global maps obtained from radiosondes and SSU, whereas the other sets of data provided a description of the vertical structure of the response at different latitudes. The analysis of all the available data indicates that the solar signature on atmospheric temperature is highly variable in amplitude (from 50K to a fraction of 1K) and in sign, both with latitude and altitude. The facts that the response changes its sign with altitude with a vertical wavelength of the order of 20-30 km and that its amplitude depends on the sign of the quasi-biennial oscillation (QBO) have been interpreted as indicating a role of planetary waves in amplifying the direct solar signal. (Chanin et al., 1989), but no clear mechanism was put forward to explain this result. The change of ultraviolet spectral irradiance should also affect the ozone concentration. However the ozone changes are less well documented, even though there are some results from ozone measurements obtained by ground-based and satellite which suggest a variation of about 2% in global total ozone between periods of minimum and maximum activity over the Sun's 11 year cycle.

However until recently the models could not reproduce the latitude and altitude structure of the observations of both the temperature and ozone changes, very likely because they were only twodimensional (2D) (Brasseur 1993, Haigh 1994). If the agreement between temperature data and 2D models at the tropics is quite satisfactory, this is not at all the case at mid and high latitudes, as the models do not predict the change of sign of the correlation. Similarly the 2D photochemical-transport models predict a variation of around 2% change in global total ozone in response to changes in ultraviolet spectral irradiance, as measured by satellite instruments. However, the models do not reproduce the latitude and altitude structure observed in the satellite data and tend to overestimate the response in the middle stratosphere and underestimate it in the lower stratosphere. It is well known that 2D models cannot satisfactorily represent changes in three-dimensional planetary-scale wave transport of ozone and this may be the cause of the discrepancies. It should also be recognised that the satellite data cover less than two solar cycles and it is possible that other effects have been aliased onto the solar signal.

Results of recent modelling studies

More recently, the impact of the heating of the middle atmosphere on the dynamics has been recognised in several 3D modelling studies. Kodera et al. (1991), Kodera (1995), Balachandran and Rind (1995) and Shindell et al., (1999) used climate models and data analysis to study the response of the winter polar stratosphere to solar ultraviolet changes. They showed that anomalies in mean zonal wind, introduced into the mid-latitude upper stratosphere in early winter by changes in the latitudinal distribution of solar heating, could modify the interaction with the mean flow of vertically propagating planetary waves such that the zonal wind anomaly propagated downwards and polewards through the winter. They also modelled the extra-tropical response to the QBO of tropical lower stratospheric winds and proposed that the QBO could modulate the solar effect such that the downward and poleward propagation of a westerly wind solar anomaly would be more likely to take place during the east phase of the QBO. This is consistent with the observations of Labitzke and van Loon (e.g. 1997) which showed much stronger correlation between 30hPa geopotential height and 10.7cm solar index in winter when the data were sorted by the phase of the QBO. It may also explain the planetary wave structure observed in the other dataset (Chanin et al, 1989). In Kodera's studies, the westerly wind anomaly penetrates down to the troposphere so that his work may explain some of the observations of apparent climatic response to solar variability in the lower atmosphere in winter.

Variations in solar UV also affect stratospheric ozone concentrations. Haigh (1996, 1999) and Shindell et al (1999) have shown that the inclusion of solar-induced ozone variations significantly enhances the ability of GCMs to reproduce the observed solar effects.

These recent results have built the ground on which the SOLICE project is based.

Objectives of SOLICE

The main objectives of the study are to:

- Assess the effects of solar variability on climate, including regional and seasonal effects, using a range of general circulation models (GCMs).
- Assess the impact of solar variability on stratospheric ozone, radiative forcing of climate and surface UV using coupled chemistry-climate models.
- Investigate the internal variability of the stratosphere and the impact of the quasi-biennial oscillation on solar effects using GCMs and mechanistic models.
- Provide 3D measures of the solar signal in temperature, geopotential height and ozone using a unified methodology and data extending over the next solar maximum.
- Carry out a detailed intercomparison and analysis of model and observational results to advance understanding of the mechanisms behind solarclimate links.
- Contribute to international model intercomparisons and trend assessments such as those under the remit of the SPARC project.

Participants in SOLICE

- Imperial College of Science, Technology and Medicine, London, UK (ICSTM) : Dr. J. D. Haigh, Overall coordinator,
- Free University of Berlin, Germany (FUB): Prof. K. Labitzke
- UK Meteorological Office (UKMO) : Dr. J. Austin
- University of Oslo, Norway (UIO): Prof. I. S. A. Isaksen
- Service d'Aéronomie du CNRS, France (CNRS): Dr. M.-L. Chanin
- Aristotle University of Thessaloniki, Greece (AUTH): Prof. C. Zerefos
- Council for the Central Laboratory of the Research Councils, UK (CCLRC), Rutherford Appleton Laboratory (RAL): Dr. L. J. Gray
- University of Arizona, Tucson, USA (LAPL): Prof. L. L. Hood
- Goddard Institute for Space Sciences, USA (GISS): Dr. D. T. Shindell

Description of the Project

A co-ordinated programme of numerical modelling and data analysis is planned.

a) Numerical Modelling

In order to achieve these objectives we propose a study involving several co-ordinated modelling and

data activities. Long (twenty year) simulations of the effects of enhanced solar spectral irradiance, and of solar-induced stratospheric ozone increases, on the climates of two different general circulation models (GCMs), extending throughout the troposphere and middle atmosphere, will be produced and the results analysed to assess the role of troposphere-stratosphere interactions in amplifying the solar effects. By imposing appropriate accelerations in the tropical lower stratosphere the same models will be used to assess the impact of the quasi-biennial oscillation (QBO) on these results. The natural internal variability of the stratosphere and its sensitivity to changes in solar irradiance and the QBO will be assessed using a stratosphere-mesosphere model, which will allow multiple long runs for sensitivity studies.

The modelling studies will incorporate series of experiments with models of various types designed to investigate different aspects of the interaction of solar radiation with the chemical and dynamical structure of the lower and middle atmosphere. These will include the first ever simulations of the effect of variations in solar spectral irradiance, on both 27-day and 11-year timescales, on stratospheric ozone using general circulation models (GCMs) with coupled stratospheric chemistry. GCMs will also be used to study links between the stratosphere and tropospheric climate including the effects of solar-induced changes in stratospheric climate on wave propagation and how this is modulated by the quasi-biennial oscillation (QBO). The modulation of sea surface temperatures by solar variations and the effect on climate will be studied using a GCM with a coupled ocean in the context of other GCM climate simulations. Chemical transport models will allow detailed investigations of solar impact on stratospheric chemistry and a 3D dynamical model of the middle atmosphere will be used to investigate the internal variability of the stratosphere, its response to solar variability and how this is impacted by the QBO.

b) Updating of data sets

The data studies will involve the development of a unified method for the analysis of global threedimensional fields of temperature and ozone in the context of the response of these fields to other factors including the OBO and volcanic eruptions. We propose to update the analysis of the solar signature in the longest available data sets of atmospheric parameters from the ground to the mesosphere. This large altitude region is considered to include both direct responses on ozone and molecular oxygen but also signatures associated with possible downward propagating effects and feedback. The parameters considered are temperature, geopotential heights, ozone and winds. This choice is made for the following reasons: temperature results partly from radiative equilibrium and plays a central role in chemistry and dynamics; geopotential heights reflect the temperature of the

underlying column; ozone is a key parameter in the atmospheric radiative balance and its density is directly related to UV solar changes. Those three parameters have already been analysed in term of solar influence in the past, but these studies suffer from inhomogeneities in the calculation of the solar relationship (temporal and spatial average, QBO phases, different analysis method etc.). And finally, wind measurements are also of great interest as they can answer some of the questions related to the dynamical contribution and have not yet been investigated by many authors in a systematic manner. Almost all the existing data sets will continue to acquire new data during the coming years (except SSU). This period will be of major interest as a new solar maximum is due which we hope will be free of any disturbance by major volcanic eruptions, as was the case during the last two solar maxima.

The unified analysis method will include the use of a linear regression model and EOF analysis. The linear regression model used will include seasonal components (annual and semi-annual), a trend, a function related to solar activity (10.7 cm solar flux), a function of the QBO, a function of ENSO, and a function related to stratospheric aerosol optical depth (AOD) The addition of the EOF analysis represents a valuable complementary analysis technique as EOFs are derived from the data itself without need of any a priori assumptions or external functions. These methods are being implemented, but the reanalysis is delayed to include the solar maximum into the data set. Only the set of data used by Labitzke and van Loon (1997) has been updated. It confirms the high correlation between 30hPa geopotential height and the 10.7cm solar index over nearly four solar cycles between 1958 and 1999.

c) Intercomparison between data and models

Comparison of the results of the modelling and data studies will be made to validate the models and the model results will then be analysed to elucidate details of the mechanisms whereby solar variability affects climate. The results will also be used to calculate solar radiative forcing parameters, taking proper account of the response of stratospheric ozone, and to estimate the regional impacts of solar variability.

Selected First Results

The first SOLICE results to date have been obtained by Larkin et al., (2000) from GCM runs using different assumptions concerning changes in solar irradiance and solar-induced ozone. The results presented in figures 1 and 2 show the sensitivity to the assumptions made. This is a key issue at the early stage of the project, as these conclusions need to be taken account by the other groups before doing the 20 years runs.

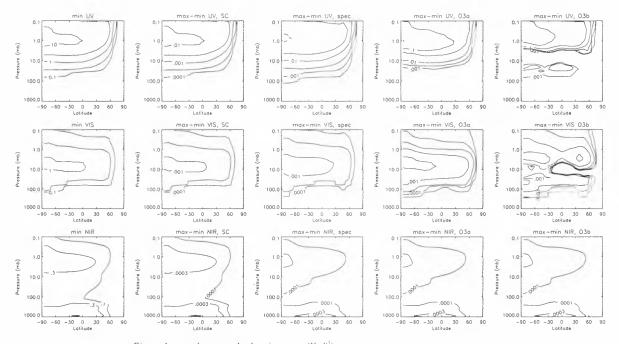


Figure 1 : zonal mean solar heating rates (K d^{-1})

First column solar minimum values.

Columns 2-5 show difference between solar max_and solar min_assuming;

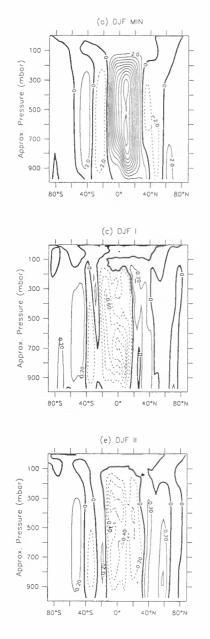
Column 2: 0.08% in TSI uniform across spectrum.

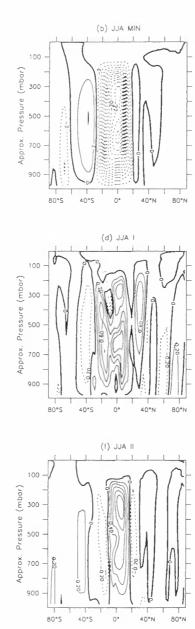
Column 3: 0.08% in TSI with spectral distribution. Column 4: As col.3 plus ozone increase from 2D model.

Column 5: As col.3 plus ozone increase from SBUV/TOMS.

Contours are shown at 1x10n and 3x10n with the range of n varying between frames

The figure 1 shows the zonal mean solar heating rates (K d^{-1})) for solar minimum and for the difference Max-Min, and this for different spectral ranges: (220-320nm, 320-690nm, 690-10000nm), different spectral distribution of the TSI (0.08% in TSI uniform across spectrum and 0.08% in TSI with spectral distribution, and different distributions of the ozone increase: ozone increase from 2D model and ozone increase from SBUV/TOMS. The conclusions from these runs show that one should include in the models the spectral distribution of irradiance change (which gives almost an order of magnitude increase in stratospheric heating rates) and also include ozone changes (which gives another factor of about 3 in the stratosphere and shows that the structure of heating rate change depends on the structure of the ozone change). The issue is that the vertical and latitudinal structure of the ozone change are not well known and therefore





should be better extracted from the data if possible before the runs are performed.

The figure 2 shows the mean meridional circulation for 2 seasons (DJF and JJA) for solar minimum and for the difference solar maximum-solar minimum with 2 different imposed ozone changes: 2D model ozone changes and TOMS/SBUV ozone changes. The solar minimum case shows large winter Hadley cell with positive (clockwise) values in DJF and opposite in JJA. One can also see weaker summer hemisphere Hadley cell and mid-latitude Ferrel cells. The conclusions from these second sets of runs are that in both experiments the winter cells weaken, and there is some indication that summer cells do likewise and that Ferrel cells get push polewards. This has implications for local changes in climate, especially in mid-latitudes where vertical air motion changes significantly.

Figure 2 mean meridional circulation for 2 seasons (left DJF, right JJA). Top solar row: minimum run. Second row: difference between solar min. and solar max. in experiment with 2D model ozone changes. Third row: as above but with TOMS/SBUV ozone changes.

Contribution of SOLICE to the international Project SPARC/WCRP

The SPARC Project (Stratospheric Processes and their Role in the Climate) has been asked by the World Climate Research Programme (WCRP) to study further the issue of the solar influence in climate. This is being done within the modelling component of SPARC: GRIPS. SOLICE has already contributed to the international intercomparison of the response of different models to solar forcing. The first set of models includes the Imperial College, GISS and MRI models. The results of the intercomparison indicates very clearly the influence of the structure of ozone distribution between solar maximum and solar minimum on the short wave heating rate difference and therefore on the mean temperature difference between solar max and solar min. However the zonal-mean wind difference between solar maximum and solar minimum has similar features for the 3 models.

Conclusion

After this project is over, more definitive statements will be possible concerning (a) whether and how variations in solar irradiance affect the circulation of the middle atmosphere and the lower atmosphere (including the Hadley circulation) and how these are inter-related, (b) how and to what extent solar variations affect planetary wave propagation in the middle atmosphere and (c) the sensitivity of climate studies to the inclusion of various factors such as interactive ozone and the QBO. As a result of these model intercomparisons it will be possible to make well based statements on which factors need to be included in GCMs for realistic simulations of climate and climate change.

New model results of the impact of solar variability on atmospheric chemistry and climate and new analysis, including data from the next solar maximum, of the solar signal in observations of temperature and ozone are expected in the next 3 years from SOLICE

It should contribute to advance our understanding of the mechanisms whereby solar variability affects climate and lead to a new assessment of the solar radiative forcing of climate.

An assessment of the impacts of solar variability on seasonal and regional variations in climate and on surface UV should also be obtained. This research effort carried out in cooperation with SPARC should contribute to international detection/attribution studies.

References

Balachandran, N. K. and Rind, D. 1995 Modeling the effects of UV variability and the QBO on the troposphere-stratosphere system. Part I: The middle atmosphere. J. Clim., 8, 2058-2079.

Brasseur, G. 1993 The response of the middle atmosphere to long-term and short-term solar variability: A.two-dimensional model. *J. Geophys. Res.*, **98**, 23079-23090.

Chanin M..-L., Ph Kechkut, A. Hauchecorne and K. Labitzke, 1989. The solar activity-QBO effect in the lower thermosphere, Ann. Geophys. 7, (5), 463-470.

Chanin M.-L. and Ramaswamy V. 1999, in Chapter 5 of WMO-UNEP Scientific Assessment of Ozone Depletion-1998, WMO Report N°44.

Haigh J. D, 1994 The role of stratospheric ozone in modulating the solar radiative forcing of climate. *Nature*, 370, 544-546..

Haigh J. D., 1996. The impact of solar variability on climate. *Science*, 272, 981-984,

Haigh J. D., 1999. A GCM study of climate change in response to the 11-year solar cycle. *Quart. J.Roy.Meteorol.Soc.*, 125, 871-892, 1999.

Kodera, K., 1995, On the origin and nature of the interannual variability of the winter stratospheric circulation in the northern hemisphere. *J. Geophys. Res.*, 100, 14077-14087.

Kodera, K., Chiba, M. and Shibata, K., 1991 A general circulation model study of the solar and QBO modulation of the stratospheric circulation during the Northern Hemisphere winter. *Geophys. Res. Lett.*, 18, 1209-1212.

Labitzke, K. and van Loon, H. 1997 The signal of the 11-year sunspot cycle in the upper troposphere-lower stratosphere. *Space Sci. Rev.*, 80, 393-410.

Larkin, A., J.D. Haigh, and S. Djavidnia, 2000: The effect of solar UV irradiance variations on the Earth's atmosphere. *Space Science Reviews*, in press

Shindell, D., Rind, D., Balachandran, N., Lean, J. and Lonergan, P. 1999 Solar cycle variability, ozone, and climate. *Science*, 284, 305-308.

ESTIMATION OF NATURAL AND ANTHROPOGENIC CONTRIBUTIONS TO TWENTIETH CENTURY TEMPERATURE CHANGE

Simon F. B. Tett, Gareth S. Jones, Peter A. Stott, David C. Hill[†], John F. B. Mitchell, Myles R. Allen^{†‡},

William J. Ingram, Tim C. Johns, Colin E. Johnson,

Andy Jones, David L. Roberts, David M. H. Sexton and Margaret J. Woodage

Hadley Centre for Climate Prediction and Research,

The Met. Office, London Road, Bracknell, Berkshire RG12 2SY, UK.

[†]Space Science and Technology Dept., Rutherford Appleton Laboratory,

Chilton, OX11 0QX, UK

[‡]Dept. of Physics, Clarendon Laboratory, University of Oxford, Oxford, OX1 3PU, UK

ABSTRACT

This is a shortened version of a paper with the same title and authors in preparation for J. Geophys. Res.

Using a coupled atmosphere/ocean general circulation model we have simulated the climatic response to natural and anthropogenic forcings from 1860 to 1997. The model, HadCM3, requires no flux adjustment, and has an interactive sulphur cycle, a simple parametrisation of the effect of aerosols on cloud albedo (first indirect effect) and a radiation scheme which allows explicit representation of well-mixed greenhouse gases. Simulations were carried out in which the model was forced with: changes in natural forcings (solar irradiance and stratospheric aerosol due to explosive volcanic eruptions); well-mixed greenhouse gases; tropospheric anthropogenic forcings (tropospheric ozone, well-mixed greenhouse gases and the direct and first indirect effects of sulphate aerosol); anthropogenic forcings (tropospheric anthropogenic forcings and stratospheric ozone decline).

Using an "optimal detection" methodology to examine temperature changes near the surface and throughout the free atmosphere we find that we can detect the effects of changes in well-mixed greenhouse gases, other anthropogenic forcings and natural forcings. Thus these have all had a significant impact on temperature. We estimate the linear trend in global-mean near-surface temperature from well mixed greenhouse gases to be 0.9 ± 0.24 K/century, offset by cooling from other anthropogenic forcings of 0.4 \pm 0.26 K/century giving a total anthropogenic warming trend of 0.5 ± 0.15 K/century. Over the entire century natural forcings give a linear trend close to zero. Observed surface temperature changes are generally consistent with our simulations but the simulated tropospheric response, since the 1960s, is about 50% too large.

Our analysis suggests that the early 20th century warming can best be explained by a combination of warming due to increases in greenhouse gases and natural forcing, some cooling due to other anthropogenic forcings, plus a substantial, but not implausible, contribution from internal variability. In the second half of the century we find that the warming is largely caused by changes in greenhouse gases, with changes in sulphates and, perhaps, volcanic aerosol offsetting approximately one-third of the warming. Warming in the troposphere, since the 1960s, is probably mainly due to anthropogenic forcings with a negligible contribution from natural forcings.

I. INTRODUCTION

Several authors (e.g. Santer et al. (1996); Hegerl et al. (1997); North & Stevens (1998); Tett et al. (1999); Hegerl et al. (2000); Stott et al. (2000)) have carried out studies in which they claimed to have detected significant changes in temperature either at the surface or in the free atmosphere. On decadal timescales or longer they attributed changes over the last 30-50 years to anthropogenic rather than natural effects whether externally forced or due to internal variability. Most of these studies used a variant of the optimal fingerprinting algorithm(Hasselmann 1993; North et al. 1995; North & Kim 1995; Hasselmann 1997; Hegerl & North 1997; Allen & Tett 1999).

Tett et al. (1999) (T99 from hereon) and Stott et al. (2000) (S00 from hereon) computed responses from the Atmosphere/Ocean General Circulation Model (AOGCM) HadCM2(Johns et al. 1997) to solar, volcanic, greenhouse and the direct anthropogenic sulphate forcing. They compared the responses with observations of surface temperature using a spatiotemporal methodology and concluded that natural causes alone could not explain observed changes in surface temperature from 1946–1996. HadCM2 included an ocean model with a resolution of $2.5^{\circ} \times 3.75^{\circ}$ and

Proc. 1st Solar & Space Weather Euroconference, 'The Solar Cycle and Terrestrial Climate', Santa Cruz de Tenerife, Tenerife, Spain, 25-29 September 2000 (ESA SP-463, December 2000)

needed a flux adjustment¹ to keep the control simulation stable and its climate close to the current climate. It represented all greenhouse gases as equivalent CO_2 , and the direct effect of sulphates as changes in surface albedo.

Barnett et al. (1999) compared simulations from several different models with observations and found that there were cases in which simulated linear trends in northern summer temperature were inconsistent with observations. Most of those models used a simple parametrisation of the effects of sulphate aerosols similar to that used in HadCM2. However they found that the amplitude of the "sulphate" component computed from a single simulation of ECHAM4 (a model with a representation of the indirect effect of aerosols and an interactive sulphur cycle) was, in one case, inconsistent with observations. If this result were confirmed by other models, which include physically based parametrisations of the direct and indirect effect of sulphates, then the hypothesis that sulphates alone have significantly offset greenhouse gas warming would be unlikely to be true.

The aim of this paper is to examine the contributions of natural and anthropogenic forcings to temperature change during the 20th century using a new AOGCM, HadCM3(Gordon et al. 2000; Pope et al. 2000). HadCM3 has 19 atmospheric levels with a resolution of $2.5^{\circ} \times$ 3.75° and the ocean component has 20 levels with a resolution of $1.25^{\circ} \times 1.25^{\circ}$. In addition to an increase in oceanic resolution it includes many improvements on HadCM2 which have removed the need for a flux adjustment. HadCM3 represents the radiative effects of CO_2 , N_2O , CH_4 , and some of the (H)(C)FCs individually. The direct effect of sulphate aerosol is now simulated using a fully interactive sulphur cycle scheme that models the emissions, transport, oxidation and removal of sulphur species. The first indirect effect of sulphate aerosol(Twomey 1974), which was not represented at all in HadCM2, is now modelled using a relatively simple, non-interactive technique.

The control simulation is stable for multi-century integrations and the temperature variability near the surface, though not in the free atmosphere, compares well with observations(Collins et al. 2000b). HadCM2 and HadCM3 show similar global-mean temperature responses to increases in greenhouse gases during the 20th and the 21st centuries but HadCM3 shows less tropical warming than HadCM2 due to changes in details of the physics parametrisations(Williams et al. 2000).

The rest of the paper is organised as follows. First we describe the simulations and observations. We then describe the simulated responses and compare them with observations. Next we describe the detection and attribution methodology. In section 5 we show the results of the analyses and in section 6 we conclude.

2. SIMULATIONS

The control simulation for HadCM3 (CONTROL) has constant, near pre-industrial², forcing and we use the first 1200 years of the simulation in our analysis. Four ensembles with different external forcings were carried out using HadCM3. Each ensemble consisted of four simulations. The ensembles are:

- **GHG** The simulations were forced with historical changes in well-mixed greenhouse gases.
- **TROP-ANTHRO** The simulations were forced with changes in well-mixed greenhouse gases (as GHG), anthropogenic sulphur emissions and their implied changes to cloud albedos, and tropospheric ozone.
- **ANTHRO** As TROP-ANTHRO except from 1974 stratospheric ozone decline was included.
- **NATURAL** The simulations were forced with the solar irradiance timeseries of Lean et al. (1995) and a timeseries of stratospheric aerosol due to explosive volcanic eruptions (Sato et al. 1993). Both forcing timeseries have been extended to 1997.

Four sets of initial conditions to start the GHG, ANTHRO and NATURAL ensembles were taken from states in CON-TROL separated by 100 years. Note that, for example, the first GHG and NATURAL simulations use the same initial conditions. All simulations except TROP-ANTHRO start in 1/Dec/1859 and the twelve anthropogenic simulations ended on 30/Nov/1999. The NATURAL simulations were integrated to 30/Nov/1997. Initial conditions for TROP-ANTHRO were taken from ANTHRO on 1/Dec/1974.

2.1. Observed datasets and data processing

We compare the results of the model simulations with an updated version of the surface temperature dataset of Parker et al. (1994) and with the HadRT2.1s radiosonde temperature dataset – an updated version of Parker et al. (1997). Radiosonde data from the Indian subcontinent (60° E – 90° E, 0 – 30° N) was removed because of apparent problems with its quality and the remaining data corrected for known changes in instruments by comparison with co-located MSU data(Parker et al. 1997).

Annual averages of both the surface and radiosonde datasets were computed from monthly-mean temperature anomalies. At each location we required there to be at least eight months of observations; otherwise we discarded the annual-mean value.

The annual-mean surface observations were decadally averaged, with periods ending in 1997. For each decade

¹Flux adjustments are artificial fluxes of heat and water which vary in space and throughout the seasonal cycle but are constant from year to year and in all the HadCM2 simulations.

 $^{^2}$ The concentrations (ppbv) used for the well-mixed greenhouse gases are: CO₂: 289600, CH₄: 792.1 N₂O: 285.1. The (H)(C)FCs all had zero concentrations.

we required that there be at least 5 years of data; otherwise the decadal-mean value was discarded. In our analysis of surface temperature we consider changes on 100-year timescales using decadal data with the 100-year average removed. Locations in the observations at which less than five decades were present were omitted. This data was then filtered, using spherical harmonics, to remove scales below 5,000 km (T99, S00). Harmonics were further weighted by $1/\sqrt{2l} + 1$ (*l* is the total spherical harmonic wavenumber) to give each spatial scale included equal weight(Stott & Tett 1998). Simulated data was decadally averaged, bilinearly interpolated in latitude and longitude to the observational grid. Simulated data was discarded where there were no observational data and then processed in the same way as the observations were.

When computing global-mean timeseries we first bilinearly interpolated (latitude and longitude) simulated annual-mean near-surface temperature data to the observational grid, discarding simulated data where there were no observational data. As the observed data are anomalies relative to 1961–90 we computed the 1961–90 climate mean for each simulation and the observations, removed it and computed global-means. In order to show changes relative to the beginning of the century we removed the global mean time-average for 1881–1920 from each timeseries.

Annual-mean simulated data from throughout the atmosphere was trilinearly (pressure, longitude and latitude) interpolated to the three-dimensional observed grid and discarded where there was no observed data. We then processed the simulations and observations by first removing the 1971–1990 mean, zonally averaging (requiring that there be four longitudes with data present in any zonal band) and then computing the difference between 1985–1995 and 1961–1980. Unlike T96 and AT99 simulated data had the observational mask applied and the 1971–90 normal removed before zonal averaging. This change in processing had little impact on the signals and tended to reduce slightly the variability of the annualaverage zonal-mean temperatures(Collins et al. 2000b).

Changes in surface temperature observed over the century show warming (Fig. 1(a)) over most of the world with, in general, land warming more than the ocean, central Eurasia and Canada warming most and cooling occurring in parts of the North Atlantic to the south of Greenland and Iceland.

The free atmosphere changes show cooling (Fig. 1(b)) in the stratosphere and warming in the troposphere. The cooling extends down to 500 hPa above the Arctic — far below the reanalysis tropopause. The tropospheric warming is uneven with a maximum warming of 0.6K occurring at about 50° N and almost no warming at 30° N. Differences between the observations shown here and that of T96 (see their Fig. 2D) are due to the continued development of the radiosonde dataset and removal of data from the Indian sub-continent.

3. MODEL AND OBSERVED TEMPERATURE RESPONSES

Annual means of global-mean temperature from the ensemble averages (Fig. 2) show that the simulated responses are all inconsistent with the observations. From the 1920s until the 1950s GHG warms less than the observations. From the 1940s onwards it begins to warm and by the end of the 20th century has warmed more, over the century, than the observations. Addition of sulphates and ozone to GHG, giving ANTHRO, delays the simulated warming until the 1960s. From then till the end of the century ANTHRO, TROP-ANTHRO and the observations warm at approximately the same rate. The small differences between ANTHRO and TROP-ANTHRO suggest that stratospheric ozone changes have little impact on near-surface temperature despite the large differences in radiative forcing (not shown). We believe that this small response is due to the stratospheric ozone forcing being concentrated over Antarctica.

Natural forcings, in our simulations, produce a general warming from the 1910s, until the eruption of Agung in 1963. After this the observations warm while the subsequent eruptions of El Chichón and Pinatubo cool NATU-RAL.

The patterns of simulated response from the 20th century are shown in Fig. 3. All three anthropogenic ensembles (GHG, TROP-ANTHRO and ANTHRO) produce more warming over land than over the sea. GHG has the most warming of these ensembles and warms more than the observations. In the GHG ensemble the Arctic warms most while the North Atlantic and large regions of ocean in the southern hemisphere warm considerably less than the global average (Fig. 3(a)). AN-THRO and TROP-ANTHRO are in reasonable agreement with the observations (Fig. 1(a)), and both warm less than GHG especially in the mid-latitudes of the northern hemisphere where the sulphate cooling will be large. NATURAL shows no distinctive signal, probably because there is little change in natural forcing between the start and end of the century.

We now examine temperature changes throughout the atmosphere between the decade 1985-1995 and the twenty year period 1961–1980. All three anthropogenic ensembles have similar warming in the troposphere, greatest warming in the upper tropical troposphere and warm more in the northern hemisphere than the southern (Fig. 4). The upper tropical troposphere and southern hemisphere warm more in GHG than in TROP-ANTHRO while high northern latitudes warm less. The latter could be due to the effects of tropospheric ozone or to internal climate variability. Neither simulation cools the stratosphere or upper troposphere as much as the observations (Fig. 1(b)). Inclusion of stratospheric ozone decline in ANTHRO produces large stratospheric cooling (of up to 6K over Antarctica), especially in high latitudes, which brings this ensemble into better agreement with the observations (Fig. 1(c)). Unlike the anthropogenic simulations NATURAL warms in the tropical stratosphere, probably due to the 1991 Pinatubo eruption, but has little temperature response in the troposphere.

The boundary between cooling and warming is close to the tropopause in all ensembles except over Antarctica in ANTHRO (Fig. 4). In this ensemble the cooling over Antarctica extends down to 500 hPa and the tropopause rises, its pressure falling by 50 hPa. The data over Antarctica is insufficient to tell if this occurred in reality. However, the observed Arctic cooling down to 500 hPa is not present in any of the ensembles.

Qualitative comparison of our ensembles with the observations suggests that ANTHRO is the most similar to the observations (compare Fig 4(c) with Fig 1(b)). As all the anthropogenic ensembles are quite similar in the troposphere it appears that increases in greenhouse gases and stratospheric ozone decline are the most important contributors to temperature changes in the free atmosphere.

4. DETECTION AND ATTRIBUTION METHODOLOGY

One of the main problems in attributing climate change to possible causes arises from the difficulties in estimating the radiative forcing and climate response due to different forcings. In particular, there are large uncertainties in the overall magnitude of the climate response to a given forcing due, for example, to uncertainties in climate sensitivity or the rate of ocean heat uptake(Kattenberg et al. 1996). The size of the forcing associated with many of the factors other than well mixed greenhouse gases, notably aerosols, is also uncertain(Shine et al. 1995). To reduce the impact of these uncertainties, we use a methodology first proposed by Hasselmann (1979) which has been shown to be a form of multivariate regression (AT99). This assumes that the observations (\mathbf{y}) may be represented as a linear sum of simulated signals (X) and internal climate variability (u):

$$\mathbf{y} = \mathbf{X}\boldsymbol{\beta} + \mathbf{u} \tag{1}$$

where β_i is the scaling factor, or amplitude, that we apply to the *i*th signal (**x**_i) to obtain the best fit to the observations. In this paper the signals are ensemble averages from the simulations described earlier. Any errors in the *magnitude* of the forcing and climate responses are allowed for through scaling the model responses (**x**_i) by the signal amplitudes (β_i). Errors in the *patterns* of forcing and response are not taken into account by this procedure. The values of β which give the best fit (the best-estimate value $\tilde{\beta}$) to observations, using the standard linear regression approach are (AT99):

$$\tilde{\boldsymbol{\beta}} = (\mathsf{X}^T \mathsf{C}_N^{-1} \mathsf{X})^{-1} \mathsf{X}^T \mathsf{C}_N^{-1} \mathbf{y} = \mathsf{F}^T \mathbf{y}$$
(2)

where C_N is the covariance matrix of natural variability ($\mathcal{E}(\mathbf{u}\mathbf{u}^T)$) estimated, in our case, from simulations of coupled-atmosphere ocean GCMs. We do not normally have enough data to accurately estimate the inverse covariance matrix (C_N^{-1}) so we estimate its inverse from a truncated representation of it based on its leading eigenvectors. Simulated and observed data are also filtered by projection onto these eigenvectors.

Both the observations and signals include internal climate variability (noise) which leads to uncertainty in $\tilde{\beta}$. We estimate uncertainty ranges (the 5–95% range unless stated otherwise) in $\tilde{\beta}$ using its covariance matrix (AT99 and Mardia et al. (1979)):

$$\tilde{\mathsf{V}}(\tilde{\beta}) = \mathsf{F}^T \mathsf{C}_{N_2} \mathsf{F},\tag{3}$$

where C_{N_2} is an estimate of $\mathcal{E}(\mathbf{u}\mathbf{u}^T)$ using data which is statistically independent of that used to estimate C_N .

We perform two related tests:

- detection This tests the null-hypothesis that the observed response to a particular forcing or combination of forcings is zero. We do this by computing the two-tailed uncertainty range about $\tilde{\beta}$ using $\tilde{V}(\tilde{\beta})$ and testing whether it includes zero. Rejection of this null and a positive value of $\tilde{\beta}_i$ implies detection.
- **amplitude-consistency** This tests the null-hypothesis that the amplitude of the observed response is consistent with the amplitude of the simulated response. We do this by computing the two-tailed uncertainty range about $\tilde{\beta}$ using $\tilde{V}(\tilde{\beta})$ and testing whether it includes unity. In this test we inflate $\tilde{V}(\tilde{\beta})_{ij}$ by a factor of $\sqrt{(1+1/m_i)}\sqrt{(1+1/m_j)}$ to compensate for sampling noise in the signals, where m_i and m_j are the ensemble sizes. Failure of this test means that the simulated signal amplitude is inconsistent with the observations. When we report consistency with unity, we mean that it is neither greater than nor less than unity at a given confidence level.

Unless otherwise stated, results are reported as significant if the relevant null-hypothesis can be rejected at the 5% level. All reported uncertainty ranges are 5-95%.

The best estimate of the temperature trend (or any other linear diagnostic such as changes in global-mean temperature), due to a forcing factor, is the product of the signal amplitude and the trend computed from the appropriate ensemble-average. The covariance matrix used to compute uncertainties is computed by multiplying $\tilde{V}(\tilde{\beta})_{ij}$, inflated to compensate for signal-noise, by the trends of the 1th and jth ensembles.

Covariance matrices are estimated from intra-ensemble variability (i.e. variability within the ensemble) and from CONTROL. To obtain these estimates we process data in exactly the same manner as we do the observations and simulations giving the **u** in eqn. (1). In all our analysis segments were overlapped by ten years. When computing covariance matrices from intra-ensemble variance we remove the ensemble average and scale each realisation of **u** (segment) by a factor of $\sqrt{(m-1)/m}$ where *m* is the number of ensemble members.

In Section 5 we analyse changes in near-surface temperature on 100-year timescales (century) and on 50-year timescales (50-year), and changes in zonal-mean temperature throughout the atmosphere (free-atmosphere). The two near-surface analyses examine changes in time and in space while the free-atmosphere analysis looks at spatial changes over a thirty-five year period (Section 2.1).

For both the 50-year and the free-atmosphere analysis we use intra-ensemble variability from the GHG, ANTHRO and NATURAL ensembles to estimate C_N and data from CONTROL to estimate C_{N_2} . Any significant differences between C_N and C_{N_2} would reduce the power of the optimisation algorithm (i.e. increase uncertainty ranges) but would not introduce a bias in the estimated signal amplitudes.

For the century analysis we believe that nine realisations of century timescale variability from the intra-ensemble variability of HadCM3 is not enough to generate a sufficiently reliable estimate of C_N . Therefore we use control and intra-ensemble variability from five ensembles of HadCM2 (S00) to estimate C_N while C_{N_2} is estimated using HadCM3 CONTROL and intra-ensemble variability from the GHG, ANTHRO and NATURAL ensembles.

4.1. Consistency

We test that the best-estimate combination of signals is consistent with our linear statistical model (Eqn 1) by computing the residual sum of squares:

$$R^{2} = \sum_{i=1}^{\kappa} \frac{(y_{i} - \sum_{j=1}^{n} X_{ij} \tilde{\beta}_{j})^{2}}{C_{N_{2}ii}}.$$
 (4)

where *i* is an index over the ranked eigenvectors of C_N , *j* is an index over signals and κ is the number of eigenvectors used to filter signals and observations (see subsection 4.3 for details).

In the case of noise-free signals R^2 is Fdistributed (AT99). As an *ad hoc* correction for noise in the signals we scale R^2 by 1/(1 + s), and assume that it is still F-distributed, where s is:

$$s = \sum_{i=1}^{n} (\tilde{\beta}_i / m_i)^2$$

and m_i is the number of ensemble members in the 1th ensemble. The justification for this *ad hoc* scaling is that the expected difference between the observations and the best-estimate response would be larger by a factor of $\sqrt{1+s}$ due to the noise in the simulations. In the case of signals (and observations) with high signal-to-noise ratio we verified this scaling by Monte-Carlo tests.

4.2. Estimated degrees of freedom for covariance matrices

In order to compute uncertainties and truncations we need an estimate of the degrees of freedom (dof) of the covariance matrices we compute. These matrices are computed from various different datasets and their dof is the sum of the dof of the individual datasets. For CONTROL the estimated dof, assuming maximally overlapped segments, is the number of non-overlapping segments multiplied by 1.5 (Allen & Smith (1996); S00) and rounded down to the nearest integer. For each ensemble the estimated dof is the number of non-overlapping segments in a single simulation multiplied, again, by 1.5, rounded down to the nearest integer and then multiplied by m - 1 (to account for removal of the mean).

The estimated dof for the two covariance matrices used in our analysis are shown in Table 1. Note that the estimated dof of $\tilde{V}(\tilde{\beta})$ is that of C_{N_2} .

The estimated degrees of freedom for the century analysis (see Table 1) may be over-optimistic as the individual HadCM2 ensemble members were all initialised from the same 1700-year control. Furthermore the last three simulations of each of the two solar ensembles were initialised by applying small random perturbations to the first solar simulation in each ensemble. Similarly the three HadCM3 ensembles were all initialised from the same HadCM3 control. 100-year segments may not be completely independent of one another. Uncertainty in the dof of C_{N_2} is relatively unimportant: halving the dof used in our statistical tests increases the uncertainty ranges by 3%. The estimated dof of C_N is used to determine the maximum allowable truncation (see below) and so we explore the sensitivity of our results to truncation.

4.3. Truncation

If C_N is an order $n \times n$ matrix, then where possible, we perform all analysis at the smaller of its dof and n. If the consistency test passes at the 10% level all further analysis is carried out at this truncation (κ). All data is then filtered by projection onto the leading κ eigenvectors of C_N . If the test fails at this truncation then we carry out the analysis at the largest truncation at which the test passes at the 10% level and explore the reasons for the test failure.

Our estimated dof are somewhat arbitrary as are the criteria we use to determine truncation. Therefore we explore the sensitivity of our results to truncation.

4.4. Degeneracy

We used the same three tests as T99 and S00 to test for signal degeneracy or co-linearity (see pages 243–248 of Mardia et al. (1979)). We wish to err on the side of including too many signals as by not including a signal in an analysis we assume that its amplitude is zero. Therefore the largest value from the three tests determined the number of signals we considered.

If two signals are degenerate, the usual consequence is that neither is individually detectable, since a range of linear combinations are equally consistent with the data including those which assign zero amplitude to one signal or the other. However, specific combinations of these signals may easily be detectable.

4.5. Transformations

We assume that the three anthropogenic signals (GHG, ANTHRO and TROP-ANTHRO) are linear combinations of the following physically-based signals:

- G Response to well-mixed greenhouse gases alone.
- O_T Response to stropospheric ozone changes.
- O_S Response to stratospheric ozone decline.
- *O* Response to both stratospheric and tropospheric ozone changes.
- S Response to sulphates (indirect and direct)

namely,

$$\begin{array}{rcl} \mathsf{GHG} & = G \\ \mathsf{ANTHRO} & = G + S + O & = GSO \\ \mathsf{TROP-ANTHRO} & = G + S + O_T & = GSO_T \end{array}.$$

The amplitudes and covariance matrices of these physically based signals are given by a linear transformation of the original amplitudes and of $\tilde{V}(\tilde{\beta})$. For example, suppose we model the observations as a linear superposition of the GHG and ANTHRO simulations:

$$\mathbf{y} = \mathbf{x}_{\mathsf{GHG}}\beta_{\mathsf{GHG}} + \mathbf{x}_{\mathsf{ANTHRO}}\beta_{\mathsf{ANTHRO}}$$

 β_{GHG} in this equation is not simply the estimated amplitude of the greenhouse response. It is the *additional* greenhouse response we need to add to the best-fit AN-THRO simulation to obtain the best overall fit to the observations. In this case the amplitude of the greenhouse and "other anthropogenic" signals is:

$$\tilde{\beta}_G = \tilde{\beta}_{\text{Anthro}} + \tilde{\beta}_{\text{GHG}} \tilde{\beta}_{SO} = \tilde{\beta}_{\text{Anthro}}.$$

In this example, the variance in $\tilde{\beta}_G$ is equal to the sum of the variances in $\tilde{\beta}_{GHG}$ and $\tilde{\beta}_{ANTHRO}$.

4.6. Signal-to-noise

Amplitude uncertainty ranges, and particularly the upper bound, estimated from signals with a low signal-to-noise ratio are likely to be incorrect(Allen & Stott 2000). We use the following summary statistic for the Jth signal to give us some guidance when this may be occurring:

$$(\text{SNR})^2 = \frac{m_j}{\kappa} \sum_{i=1}^{\kappa} \frac{X_{ij}^2}{C_{N_{2ii}}}$$

where κ is the truncation. When the "signal" \mathbf{x}_j is pure Gaussian noise $(SNR)^2$ has an expected value of 1 and is distributed as $F(\kappa, \nu_2)$ where ν_2 is the dof of C_{N_2} .

5. DETECTION AND ATTRIBUTION OF OBSERVED TEMPERATURE CHANGES

5.1. Changes in near-surface temperature on century timescales

We now examine changes in near-surface temperature from 1897–1997 using both spatial and temporal information. For most of the 20th century TROP-ANTHRO and ANTHRO are identical and therefore we use the latter in subsequent analyses. We transform the amplitudes of GHG and ANTHRO to obtain amplitudes of G (greenhouse gases) and SO (sulphates and ozone) as described in Section 4. Tests for degeneracy suggest that we can reliably estimate the amplitude of G, SO and NATURAL signals simultaneously. Thus all further analysis is done using this combination of signals.

The filtered observations (see Section 4) contain more than 96% of the observed variance (Table 1) and the residuals are consistent with those expected from CON-TROL at all truncations. All three signals are detected demonstrating that all have had a significant impact on changes in near-surface temperature over the 20^{th} century. Furthermore, the amplitudes are all consistent with unity—the model is consistent with observations on decadal timescales and on continental to global spatial scales.

Signal-to-noise ratio is large for the anthropogenic signals but small for NATURAL (Table 1) suggesting it is significantly noise-contaminated. Though our detection of NATURAL is probably robust, its estimated amplitude ranges, and in particular the upper range, are sensitive to this noise contamination(Allen & Stott 2000).

We reconstruct the global-mean temperature changes from the best-estimate signal amplitudes and simulated responses (Fig. 5). Well-mixed greenhouse gases and other anthropogenic effects (largely the indirect effect of sulphate aerosols) almost balance giving a total anthropogenic warming of approximately 0.1K from the beginning of the 20th century to the 1960s. Thereafter anthropogenic effects warm the planet by approximately 0.5K. From the 1950s onwards natural and anthropogenic nongreenhouse gas forcings each cause a cooling of about 0.1K. Together they offset about 0.2K of the estimated 0.6K warming due to greenhouse gases over the same period.

While Fig. 5 shows the best-estimate combination of signals, it is even more important to consider uncertainty ranges. These are most easily summarised in terms of linear trends (Fig. 6 over selected periods (the entire century, 1897-1947 and 1947-1997 – see Section 4 for details.) Over the 20th century anthropogenic forcings cause a warming trend of 0.5 ± 0.15 K/century. The trend due to greenhouse gases is 0.9 ± 0.24 K/century while the remaining anthropogenic factors cool at a rate of 0.4 ± 0.26 K/century. Over the century natural forcings contribute little to the observed trend.

During the early century greenhouse gases and natural forcings cause warming trends of about 0.2 to 0.3 K/century while other anthropogenic factors produce negligible cooling trends (Fig. 6). Over the last half of the century greenhouse gases warm the climate at a rate of 1.7 ± 0.43 K/century with natural forcings (largely volcanic aerosol) and other anthropogenic factors (mainly the indirect effect of sulphate aerosols) both causing an estimated cooling trend of about 0.3 ± 0.2 K/century. Thus, since 1947 changes in aerosol concentrations (anthropogenic and natural) have offset at least a third of the greenhouse gas warming.

5.2. Free atmosphere changes

We now examine the difference between the 10-year zonal-mean from 1986–1995 and the 20-year zonal-mean for 1961–1980 as in AT99.

Earlier we showed that the changes in the free atmosphere simulated by TROP-ANTHRO and GHG are similar. We therefore do not use GHG in this analysis, examining combinations of TROP-ANTHRO, ANTHRO and NATU-RAL. This assumes that the relative amplitudes of the G and SO_T responses are as in TROP-ANTHRO. To separate the impact of stratospheric ozone decline from all other anthropogenic effects we transform the amplitude of the TROP-ANTHRO and ANTHRO signals to give amplitudes of GSO_T (all anthropogenic forcings except stratospheric ozone decline) and O_S (stratospheric ozone decline on climate)—see subsection 4.5 for details.

In the three-signal case the maximum truncation of C_N is seven. For truncations beyond this the ratio of the residual to control variance is three to five times too large (Fig. 7(a)). At truncation seven the filtered observations contain 48% of the observed mass-weighted variance (Table 1) compared to 71% at truncation 36 (the truncation we believe the largest we can reasonably consider given the estimated dof of C_N — Table 1).

The SNR for the two anthropogenic signals is reasonably high (Table 1), while the SNR for the natural signal is less than one. We also find that the amplitude of at most two signals can reliably be simultaneously estimated. There are three reasons why we neglect natural effects in further analysis of the free-atmosphere changes. First, the simulated response to natural forcings (Fig. 4(d)) is small. Second, we did not detect NATURAL in any combination including it. Thirdly no linear amplification of it alone is consistent, using the F-test of subsection 4.1, with the observations. Thus we consider the GSO_T and O_S signals.

Failure to detect NATURAL does not rule out the possibility of a significant natural influence on climate. The simulated signal is weak and noise noise contaminated and so our failure to detect it does not strongly rule out the possibility of some process which preferentially amplifies the response to solar or volcanic forcing. Furthermore there remains the possibility that natural effects may have an influence on shorter timescales. For example the stratospheric warming associated with volcanoes and possible links between changes in the upper tropospheric circulation and the solar cycle e.g. Salby & Callaghan (2000); Hill et al. (2000).

The GSO_T and O_S case has residual variance consistent with CONTROL for all truncations less than or equal to seven (Fig. 7(a)). Detection of GSO_T , but not of O_S , occurs at those truncations (Fig. 7(b)). While the amplitude of O_S is consistent with unity the same is not true of GSO_T which has a best-estimate value of 0.65. This suggests that the simulated tropospheric response is about 50% stronger than the observed response.

Above truncation seven the residual variance is approximately three to five times larger than that of CON-TROL (Fig. 7(a)) and we now consider why this might be. The observations filtered by these leading seven eigenvectors do capture the gross features of the tropospheric warming (Fig. 8(a)). However, at this truncation, the filtered observations do not show the observed stratospheric cooling (Fig. 1(b)) as seen more clearly in the difference between the raw and the filtered observations (Fig. 8(b)). The raw observations are cooler in the stratosphere and approximately 0.1K warmer throughout large regions of the troposphere than the filtered observations. Therefore our failure at truncations greater than seven is probably due to the simulated stratospheric variability being too small though gross signal error cannot be ruled out. At truncation seven the best-estimate warming from GSO_T is similar to the filtered observations (Fig. 8(a)) in the troposphere.

6. SUMMARY AND CONCLUSIONS

We have presented results from a set of simulations of HadCM3. It has a physically based interactive sulphur cycle, a simple parametrisation of the first indirect effect of sulphate aerosols(Twomey 1974) and a better radiation scheme than its predecessor, HadCM2, allowing explicit representation of well-mixed greenhouse gases. HadCM3 has higher resolution in the ocean than HadCM2 and additional changes were made to the atmospheric component of the model. These changes have removed the need for flux adjustments to keep the model stable for multi-century integrations

We forced the model with "historical" changes in greenhouse gas concentrations, sulphate emissions, tropospheric and stratospheric ozone, solar irradiance changes and changes in volcanic stratospheric aerosol in four ensembles each of four simulations.

We found that the effects of well-mixed greenhouse gases, other anthropogenic effects (largely the indirect effect of sulphate aerosols), and natural causes (solar irradiance changes and volcanic eruptions) could be detected in the record of surface temperature change during the entire 20th century. The best-fit combination of simulations was consistent with observations.

We found that the early 20th century warming can be explained by a response to natural forcings, a large warming, relative to other factors, from internal climate variability with the effect of greenhouse gases largely being balanced by other anthropogenic forcings.

The late century warming was largely explained by greenhouse gases offset by the effect of volcanic aerosol and the indirect effect of anthropogenic aerosols. Over the entire century natural forcings make no net contribution as they warm early in the century and cool from the 1960s on. Greenhouse gases warm at a rate of 0.9 ± 0.24 K/century while other anthropogenic forcings cool at a rate of 0.4 ± 0.26 K/century giving a total anthropogenic warming of 0.5 ± 0.15 K/century.

We detected the effect of other anthropogenic forcings on the radiosonde record of temperature change in the free atmosphere from 1961-95 but with a simulated tropospheric response about 50% too large. We found no evidence of a climatic effect from stratospheric ozone decline nor a natural effect on the free troposphere. Analysis on shorter timescales might detect the influence of volcanic eruptions and the solar cycle.

The most crucial caveat in our work is that the variability we use to compute uncertainty limits is derived from simulations. Analysis of the free atmosphere suggests that the simulated stratospheric variance is too small by as much as a factor of five. Collins et al. (2000a) compared the variability of simulated summer near-surface temperatures from CONTROL with a proxy temperature dataset from circa 1400 to 1950. These results suggest that the internal variance of HadCM3 is two to three times smaller than the variance estimated from the proxy data but at least some of the differences may be due to neglect of naturally forced climate variability. After inflating the simulated variance by a factor of five we still detected the effect of greenhouse gases though not other factors.

Before 1979 there is little direct measurement of the changes in solar irradiance and thus considerable uncertainty in its timeseries. For example we could have used the timeseries of Hoyt & Schatten (1993) rather than Lean et al. (1995). There is also some uncertainty in the forcing from explosive volcanic eruptions. Lacis et al. (1992) quote a forcing from volcanoes of 30 W/m^2 (without stratospheric adjustment) per unit aerosol optical depth. We find a forcing of 20 W/m² per unit aerosol optical depth once we include stratospheric adjustment. In the century analysis we found no evidence that the model's response to natural forcings was incorrect but found several 50-year periods when it was. As we only carried out simulations with total natural forcing we were not able to explore differential error in the solar and volcanic forcings.

European surface observations indicate that the model has about half the anthropogenic sulphate aerosol concentrations observed. Non-sulphate aerosols such as black carbon have not been taken into account. Since black carbon exerts a positive forcing and there should be a strong correlation between the spatial and temporal distributions of sulphur and black carbon emissions from fossil fuel combustion, this may mitigate the effect of the underestimated direct sulphate forcing. Furthermore, the bulk of the negative radiative forcing (offsetting the effect of the well-mixed greenhouse gases) is due to the first indirect effect of sulphate aerosol on cloud albedo, the magnitude of which is extremely uncertain(Schimel et al. 1995) as is the impact of underestimating anthropogenic sulphate aerosol concentrations on it. We have not included the second indirect effect which increases cloud lifetime(Albrecht 1989) which could be of similar importance to the first indirect effect.

In our simulations stratospheric ozone decline produced a strong negative forcing but a weak near-surface temperature response. If we neglect this forcing we find that the simulated response to greenhouse gases is significantly overestimated in the 1937–87 and 47–97 periods.

We have not considered the effects of other forcings such as changes in land-surface properties and mineral dust which could have effected climate. Nor have we considered the effect of observational error on our results which may be significant for the radiosonde data(Gaffen et al. 2000). Finally we have not explicitly considered the effect of noise in the signals. In the century analysis the natural signal has a low signal-to-noise ratio so that its estimated amplitude is biased towards zero and the computed uncertainty ranges are probably too small. Work is in progress to investigate the effects of such contamination. Nevertheless our results strongly suggest that anthropogenic forcings have been the dominant cause of temperature changes over the last 30 to 50 years.

ACKNOWLEDGMENTS

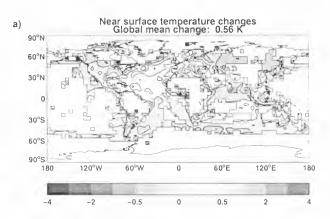
Financial support to carry out the simulations and fund SFBT, PAS, GSJ, DCH, AJ, CEJ, DLR, DMHS and MJW was provided by U.K. Dept. of Environment Transport and the Regions contract PECD 7/12/37. JFBM, WJI and TCJ were all supported by the U.K. Public Met. Service Research contract. MRA was supported by a Research Fellowship from the U.K. Natural Environment Research Council. Supplementary support was provided by European Commission contract ENV4-CT97-0501 (QUARCC). The help and encouragement of Geoff Jenkins during the work reported here is gratefully acknowledged as is the contribution of the many colleagues who developed HadCM3.

REFERENCES

- Albrecht B.A., 1989, Science, 245, 1227
- Allen M.R., Smith L.A., 1996, J. Climate, 9, 3373
- Allen M.R., Stott P.A., 2000, Cli. Dyn, in preparation
- Allen M.R., Tett S.F.B., 1999, Cli. Dyn., 15, 419
- Barnett T.P., Hasselmann K., Chelliah M., et al., 1999, BAMS, 2631–2659

- Collins M., Osborn T.J., Tett S.F.B., Briffa K.R., Schweingruber F.H., 2000a, J. Clim., (Submitted)
- Collins M., Tett S.F.B., Cooper C., 2000b, Clim. Dyn., (In press)
- Gaffen D., Sargent M., Habermann. R., Lanzante J., 2000, J. Clim., 13, 1776
- Gordon C., Cooper C., Senior C.A., et al., 2000, Climate Dyn., 16, 147
- Hasselmann K., 1979, In: Shaw D.B. (ed.) Meteorology over the tropical oceans, 251–259, Royal Meteorological Society
- Hasselmann K., 1993, J. Clim., 6, 1957
- Hasselmann K., 1997, Cli. Dyn., 13, 601
- Hegerl G.C., North G.R., 1997, J. Clim., 10, 1125
- Hegerl G.C., Hasselmann K., Cubasch U., et al., 1997, Cli. Dyn., 13, 613
- Hegerl G.C., Stott P.A., Allen M.R., et al., 2000, Cli. Dyn., (in press)
- Hill D., Gillett N., Allen M., Stott P., Tett S., 2000, J. Geophys. Res., (In Prep.)
- Hoyt D.V., Schatten K.H., 1993, J. Geophys. Res., 98, 18895
- Johns T.C., Carnell R.E., Crossley J.F., et al., 1997, Cli. Dyn., 13, 103
- Kattenberg A., Giorgi F., Grassl H., et al., 1996, In: Houghton J.T., Meira Filho L.G., Callander B.A., et al. (eds.) Climate Change 1995. The Science of Climate Change, chap. 6, 285–358, Cambridge University Press, Cambridge
- Lacis A., Hansen J., Sato M., 1992, GRL, 19, 1607
- Lean J., Beer J., Bradley R., 1995, Geophys Res Lett, 22, 3195
- Mardia K.V., Kent J.T., Bibby J.M., 1979, Multivariate Analysis, Academic Press
- North G.R., Kim K.K., 1995, J. Clim., 8, 409
- North G.R., Stevens M.J., 1998, J. Clim., 11, 563
- North G.R., Kim K.K., Shen S.S.P., Hardin J.W., 1995, J. Clim., 8, 401
- Parker D., Gordon M., Cullum D., et al., 1997, Geo. Res. Lett., 24, 1499
- Parker D.E., Jones P.D., Folland C.K., Bevan A., 1994, J. Geophys. Res, 99, 14373
- Pope V.D., Gallani M.L., Rowntree P.R., Stratton R.A., 2000, Climate Dyn., 16, 123
- Salby M., Callaghan P., 2000, 13, 2652
- Santer B.D., Taylor K.E., Wigley T.M., et al., 1996, Nature, 382, 39
- Sato M., Hansen J.E., McCormick M.P., Pollack J.B., 1993, J. Geophys. Res., 98, 22987
- Schimel D., Alves D., Enting I., et al., 1995, In: Houghton J.T., Filho L.G.M., Callander B.A., et al. (eds.) Climate Change 1995. The Science of Climate Change, chap. 2, 65–131, Cambridge University Press, Cambridge

- Shine K.P., Fouquart Y., Ramaswamy V., Solomon S., Srinivasan J., 1995, Climate Change 1994, chap. 4 Radiative Forcing, 168–203, CUP
- Stott P.A., Tett S.F.B., 1998, J. Clim., 11, 3282
- Stott P.A., Tett S.F.B., Jones G.S., et al., 2000, Cli. Dyn., (to appear)
- Tett S.F.B., Stott P.A., Allen M.R., Ingram W.J., Mitchell J.F.B., 1999, Nature, 399, 569
- Twomey S.A., 1974, Atmos. Environ., 8, 1251
- Williams K.D., Senior C.A., Mitchell J.F.B., 2000, J. Climate, submitted



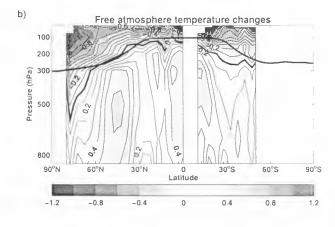


Figure 1. Observed temperature changes

a): Observed changes in near-surface temperature (1977– 97 minus 1881–1920). A contour interval of 1K is used from -4K to 4K with additional contours at ± 0.5 K and ± 0.25 K.

b): Observed changes in zonal-mean temperature (1985– 95 minus 1961–80). A contour interval of 0.1K is used with every second contour labelled from -1.2K to 1.2K. The black line denotes the zonal-mean position of the tropopause from the NCEP/NCAR reanalysis for the period 1985–95 using data provided by the NOAA-CIRES Climate Diagnostics Center, Boulder, Colorado, from http://www.cdc.noaa.gov/.

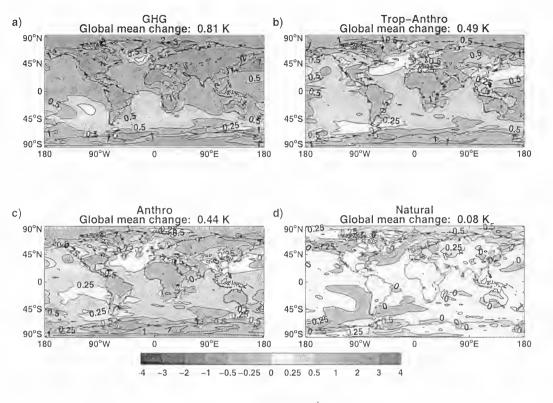


Figure 3. Simulated 20th century temperature changes.

Temperature difference (K) between the 20-year average 1977–1997 and the 40-year average 1881–1920 for the four ensembles, GHG (a), TROP-ANTHRO (b), ANTHRO (c), and NATURAL (d). Note these plots show the *raw* model data (i.e. without the observed mask). All other details are as Fig.1(a).

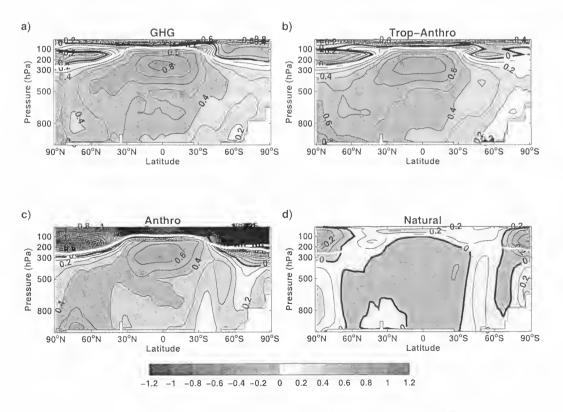


Figure 4. Simulated zonal-mean temperature differences

Differences (K) between 1985–1995 and 1961–1980 for the four ensembles: GHG (a), TROP-ANTHRO (b) ANTHRO (c) and NATURAL (d). White lines show the position of the mean tropopause in CONTROL while the dashed white line in (c) shows the mean position of the tropopause in a atmosphere only simulation with 1990 stratospheric ozone. The maximum difference between the two lines is approximately 50 hPa. All other details are as Fig. 1 (b).

Case	Period	Trunc.	% Var.	GHG	T-A	ANTHRO	NATURAL	ν_1	ν_2
Surface	1897–97	40	96.4	5.85	3.77	3.35	1.17*	40	27
(century)	1897–97	20	91.3	7.45	4.50	3.93	1.43	40	27
Free Atmos.	1961–95	7†	48.0	—	6.11	5.90	0.97*	36	42

Table 1. Signal properties

Shown for each analysis are the truncation used (third column), and the fraction of the observed variance (after processing) after filtering in the truncated eigenvector space (fourth column). By processing we mean, for example, projection onto spherical harmonics and weighting by $\sqrt{(1/2l+1)}$ for the surface analyses and, zonal-meaning and mass weighting for the free atmosphere analysis.[†] denotes cases in which the truncation used is less than the largest possible.

The centre columns show the signal-to-noise ratio (SNR—see Section 4.6 for details) of the simulated signals. T-A (TROP-ANTHRO) is identical to ANTHRO before 1975. SNR values shown with a * are where the value is not significantly different, at the 90% level, from unity (that expected by chance) suggesting significant noise contamination of that simulated signal.

Shown in the right-hand columns are the estimated dof of $C_N(\nu_1)$ and $C_{N_2}(\nu_2)$.

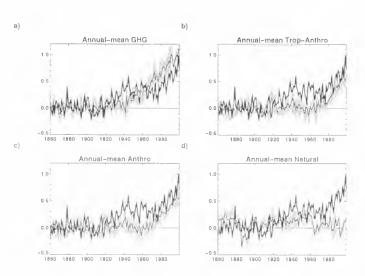


Figure 2. Global-mean near-surface temperature changes

Near-surface changes in global-mean temperature, relative to the 1881–1920 mean for the observations (thick black line) and the ensemble-mean of the GHG(a), TROP-ANTHRO(b), ANTHRO(c) and NATURAL(d) simulations (thin black line). The maximum and minimum range from the individual simulations is shown in gray.

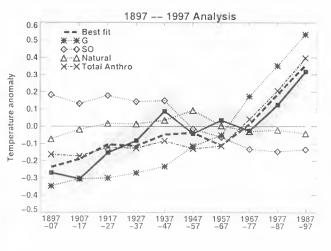


Figure 5. 100-year best-estimate reconstruction of nearsurface temperature changes

Reconstruction of temperature variations for 1897–1997. Observed (solid line with squares), best-estimate (heavy dashed line) changes and best-estimate contributions from *G* (dotted line with asterisks), *SO* (dotted line with diamonds), NATURAL (dotted line with triangles). Also shown is the best-estimate total anthropogenic contribution (dot-dashed line with crosses). All timeseries were reconstructed from data in which the 100-year mean had first been removed. The grey region centred on the observations shows the uncertainty range due to internal variability (two sigma decadal variability computed from C_{N_2}).

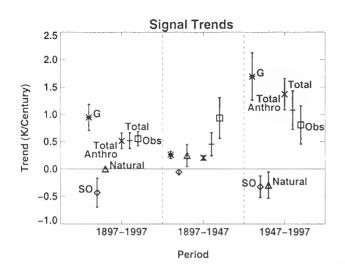


Figure 6. Linear trends from century analysis

Best-estimate linear trend and uncertainty ranges (K/century) for G (asterisk), SO (iamond), NATURAL (triangle), total anthropogenic trend (x), total trend (+) and observed trends (square). Symbols show best-estimate trend whilst error bars show the 5-95% uncertainty range inflated to allow for four member ensembles.

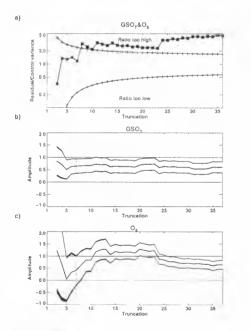


Figure 7. Sensitivity to truncation for free atmosphere analysis.

The ratio of the residual to the CONTROL variance (solid line with asterisks), using a logarithmic scale, is plotted in (a). Note that CONTROL variance has been inflated (see Section 4 for details). The vertical dotted line shows truncation seven – the largest truncation for which the residual and CONTROL variance are consistent.

Shown as a function of truncation are the bestestimate amplitudes (solid line), 5–95% "detection" uncertainties (light-gray shading), 5–95% "amplitudeconsistency" uncertainties (thin black shading) for GSO_T (b) and O_S (c).

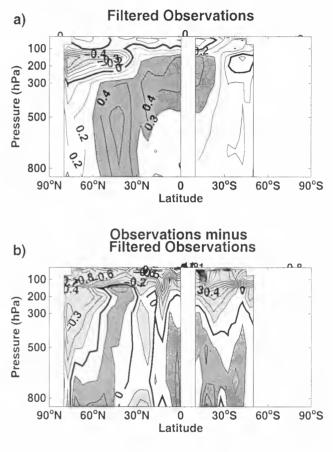


Figure 8. Filtered observations

a: Observed changes in zonal mean temperature filtered by projection onto the leading seven eigenvectors of C_N . A contour interval of 0.1 is used with dark (light) shading for values above (below) 0.3K (-0.3K) and the zero contour drawn bold.

b: Raw observations minus (a) (i.e. what the filtering removes). A contour interval of 0.1K is used with dark (light) shading for values above (below) 0.1K (-0.1K). The zero contour is drawn bold.

NATURAL VARIABILITY OF GLOBAL MEAN TEMPERATURES: CONTRIBUTIONS FROM SOLAR IRRADIANCE CHANGES, VOLCANIC ERUPTIONS AND EL NINO

Aad P. van Ulden and Rob van Dorland

Royal Netherlands Meteorological Institute (KNMI) PO Box 201, 3730 AE De Bilt, The Netherlands Tel: +31 30 2206447 e-mail: aad.van.ulden@knmi.nl/rob.van.dorland@knmi.nl

ABSTRACT

The contributions of solar irradiance changes, volcanic eruptions and the El Niño-Southern Oscillation (ENSO) to global mean temperature variations from 1882 to 1999 are analysed. The ENSO-signal is modeled in terms of the pressure anomalies in Darwin (Australia). The response to solar and volcanic forcings is modeled using an energy-balance climate model. It appears that fast temperature variations (periods 2y-20y) are primarily due to ENSO and to volcanic forcings. The 11y solar activity cycle is poorly correlated with temperature and plays a minor role.

Long term variations in solar irradiance and in volcanic forcing provide a plausible explanation for the observed global warming in the first half of the 20th century. When the total natural signals are subtracted from the observed temperatures an exponential temperature trend remains, which resembles the computed trend, using a plausible estimate of the anthropogenic radiative forcing.

INTRODUCTION

Global mean temperatures show a broad spectrum of variability, ranging from quasi-biennial oscillations to a long-term warming trend over the past century. Major sources of global climate variability are: The El Niño-Southern Oscillation (ENSO), major volcanic eruptions, variations in solar activity and anthropogenic emissions of greenhouse gases and aerosols.

ENSO is a manifestation of the non-linear interactions between the atmosphere and the Pacific Ocean, which lead to variations in global patterns of temperature, cloudiness and precipitation (e.g. Halpert and Ropelewski, 1992). ENSO has a significant impact on global mean temperatures as well (e.g. Jones, 1988). The state of ENSO is well documented by observations of surface air pressure over the Pacific. ENSO has a broad spectrum of variability with most of its variance on interannual to decadal time-scales.

Major volcanic eruptions create stratospheric dust clouds, consisting of sulphate aerosols. These aeosols enhance the reflection of solar radiation, and produce negative radiative forcings, which are clearly visible in ground-based and satellite-based radiation measurements (Robock, 2000; Minnis et al., 1993). Temperature records show, that volcanic dust clouds warm the stratosphere and cool the earth surface (Robock, 2000). The lifetime of volcanic dust clouds is relatively short (ca 2 years), but the temperature response is both damped and prolonged by the thermal inertia of the oceans. Moreover, sequences of major eruptions may give rise to significant variance on decadal and interdecadal time-scales (North and Stevens, 1998; Rowntree, 1998). Since 1960 the volcanic forcing is relatively well known, but further back in time the reconstructions are quite uncertain, allthough the dates of major eruptions are well documented and some proxi-data are available.

Variations in solar activity also produce radiative forcings. Since 1979 accurate satellite observations of total solar irradiance (TSI) are available, which show that the radiative output of the sun varies in phase with its 11-year activity cycle (Frölich and Lean, 1998). Parameterizations of this activity cycle provide plausible forcings prior to 1979 (Lean et al., 1995; Solanki and Fligge, 1998). There is ample evidence for the existence of longterm variations in solar activity as well. The corresponding TSI-variations are quite uncertain (Lean et al., 1992; Baliunas and Soon, 1995; Hoyt and Schatten, 1993; Lean et al., 1995; Solanki and Fligge, 1998; Harrison and Shine, 1999; van Ulden and van Dorland, 1999).

The anthropogenic influence on climate includes both positive radiative forcings (mainly due to greenhouse gases) and negative forcings (mainly due to aerosols). The net anthropogenic forcing is quite uncertain, mainly due to uncertainties in the role of anthropogenic aerosols. (IPCC, 1994; Hansen et al., 1998).

Apparently, interdecadal variations in all radiative forcings are uncertain. Therefore many researchers have attempted to infer the magnitude of interdecadal radiative forcings from temperature observations. The possibilities to do so are limited. In the first place, the instrumental temperature record is not much longer than a century. Thus a limited number of independent decadal datapoints is available. In the second place, the temperature response to radiative forcings is not accurately known, both with respect to the equilibrium climate sensitivity and to the attenuation and delay of the response by the thermal inertia of the oceans. This prohibits in fact any simple direct attribution of observed interdecadal temperature variations to one or more of the possible forcing mechanisms.

In this paper we take a somewhat different approach. We use the information contained in the fast temperature

Proc. 1st Solar & Space Weather Euroconference, 'The Solar Cycle and Terrestrial Climate', Santa Cruz de Tenerife, Tenerife, Spain, 25-29 September 2000 (ESA SP-463, December 2000)

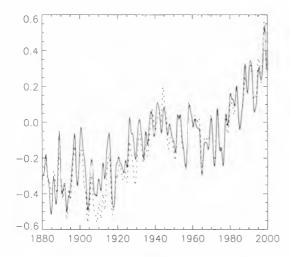


Figure 1. Global mean temperatures relative to 1961-1990.[K].. The dotted line is the reconstruction of the combined global air-sea temperature T_{Jones} by Jones (1994; updated by Jones). The solid line is a linear combination of the global mean air temperature by Vinnikov et al. (1990) (weight 2/3) and the global sea surface temperature by Kaplan et al. (1998) (weight 1/3). This record is denoted by T_{VmKap} . Both records are smoothed in order to remove the annual cycle and higher frequencies. We see that after 1950 the two combined records are very similar. In the first half of the 20th century the differences are larger, which may be attributed to differences in correction procedures and interpolation methods.

signals on interannual to decadal time-scales. These fast variations are primarily due to ENSO, to volcanic forcings and to the 11y solar cycle, which are relatively well documented, while the very uncertain slower changes in anthropogenic and solar forcings are less important. This allows the inference of the scaling factors for ENSO and for radiative forcings with some confidence. The scaling factors for the fast signals are then used to estimate the possible contributions of ENSO, volcanic activity and solar activity to interdecadal temperature changes. The total natural signals are then subtracted from the original temperature records and the resulting residual time series is analysed.

DATA SETS

The data sets are shown and specified in the figures 1-3.

APPROACH

The temperature signal of ENSO is assumed to be a linear function of the pressure anomaly ΔP_{Darwin} .

$$\Delta T_{\rm ENSO}(t) = S_{\rm ENSO} \Delta P_{\rm Darwin}(t - \tau_{\rm ENSO})$$
(1)

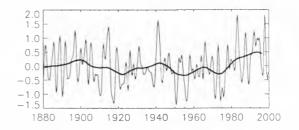


Figure 2. ENSO index [mbar]. The index used is the pressure anomaly observed in Darwin (Source: Bureau of Meteorology Australia). Shown are 1y and 10y moving averages.

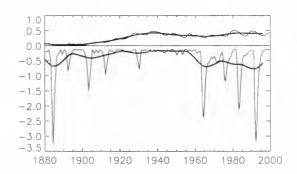


Figure 3. Natural radiative forcings $[Wm^{-2}]$. The positive forcing is the solar forcing, based on Solanki and Fligge B (1998), in which the long term variations are based on variations in the solar cycle length. This reconstruction is matched in 1979 with the observations collected by Frölich and Lean (1998).

The negative forcing is the volcanic forcing. We constructed this forcing using the ice-core indices by Robock and Free (1995) for the years up to 1959. The period 1960-1978 is based on surface radiation data by Dyer and Hicks (1968) and Dyer (1974), on observations of stratospheric sulphate by Sedlacek et al. (1983) and on lunar eclips data by Keen (1983, 1993). The period since 1979 is based on satellite data as analysed by GISS (Sato et al., 1993). For the ice-core data and lunar-eclips data we assumed a background optical depth $\tau = 0.05$. The ice-core data were scaled to match the other data for the period 1963-1966, which includes the Agung eruption. The radiative forcing is computed from the optical depth using $F_{volc}=26\tau$ (Lacis et al., 1992; Rowntree, 1998).

Shown are 1y and 10y moving averages.

, where t is the time, S_{ENSO} a scaling factor (Kmbar⁻¹) and τ_{ENSO} a time-lag. The temperature response to radiative forcings is modeled using the atmosphere-ocean energy-balance model by Hoffert et al. (1980). This model describes the radiative response of the troposphere and the attenuation and delay of the temperature response by the thermal inertia of the

oceanic mixed layer and the deep ocean. The actual temperature response to volcanic forcing $\Delta T_{Vole}(t)$ is assumed to be proportional to the modeled response $\Delta T_{VoleModel}(t)$ and described by:

$$\Delta T_{Volc}(t) = S_{Rad} \Delta T_{VolcModel}(t) / S_{Model}$$
(2)

where S_{Model} is the equilibrium climate sensitivity used in the energy balance model and S_{Rad} the actual climate sensitivity to be determined from regression with temperature observations. In this paper we use $S_{Model} =$ 0.6 KW⁻¹m², an oceanic mixed layer depth of 50m and the oceanic diffusion coefficient and upwelling velocity proposed by Hoffert et al. (1980).

The reponse to solar forcings is treated in the same way and given by:

$$\Delta T_{Sun}(t) = S_{Rad} \Delta T_{SunModel}(t) / S_{Model}$$
(3)

The total natural signal is described by:

$$\Delta T_{\text{Natural}} = \Delta T_{\text{ENSO}} + \Delta T_{\text{Volc}} + \Delta T_{\text{Sun}}$$
(4)

In this equation we have 3 adjustable parameters: the ENSO scaling factor S_{ENSO} , the ENSO time delay τ_{ENSO} and the climate sensitivity to radiative forcing S_{Rad} . We will estimate these 3 parameters from linear regression with observed temperatures.

ANALYSIS OF THE FAST SIGNALS

The regression is performed for the fast signals, which are obtained by subtracting running decadal means from running annual means. This procedure acts as a bandpass filter with half-power values at 2 y and 20 y. The regression coefficients are obtained by maximizing the explained variance. The regression period is 1951-1995. The regression coefficients are shown in table 1.These coefficients are also used for the period 1882-1950.

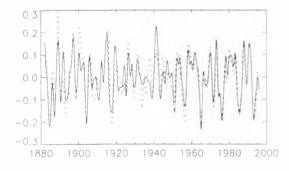


Figure 4. Fast temperature signals [K]. Solid line: fast component of T_{VinKap} ; Dotted line: fast component of $\Delta T_{natural}$

Table 1. Regression coefficients for the fast signals

1951-1995	τ _{ENSO} (y)	S _{ENSO} (Kmbar ⁻¹)	S_{Rad} (KW ⁻¹ m ²)
T _{Jones}	0.30	0.134	0.55
$T_{\rm VinKap}$	0.33	0.145	0.66

Table 2. Regression results for the fast signals (2y-20y)

	σ _{TENSO} (K)	σ _{TVolc} (K)	1 5 11 11	Expl. Var.	Residual Standard Error (K)
T _{Jones}					
1951-1995	0.071	0.068	0.007	82 %	0.039
1882-1950	0.075	0.041	0.005	20 %	0.078
1882-1995	0.073	0.054	0.006	47 %	0.064
T _{VinKap}					
1951-1995	0.076	0.082	0.008	88 %	0.034
1882-1950	0.078	0.048	0.005	61 %	0.061
1882-1995	0.077	0.062	0.007	72 %	0.052

In figure 4 we show the fit of the sum of the natural signals to T_{VinKap} We see a good fit for the whole period 1882-1995.

Information on the quality of the fits is given in table 2. Table 2 shows that in the period 1951-1995, most of the fast variations in T_{Jones} and T_{VinKap} are explained by the three natural signals. The standard deviation of the ENSO-signal is about equal to that of the volcanic signal, while the solar signal is an order of magnitude smaller. For the period 1882-1950 the results for the two temperature reconstructions show marked differences. For T_{VinKap} again a significant fraction of the variance is explained, while this is not the case for T_{Jones} It appears that this is primarily caused by a mismatch between T_{Jones} and ENSO in the period around WWII. This is illustrated in figure 5.

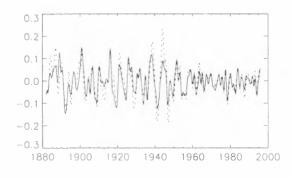


Figure 5. Residuals of the fast temperature signals [K]. Dotted line: $T_{Jones} - \Delta T_{natural}$; solid line: $T_{TinKap} - \Delta T_{natural}$.

THE SOLAR CYCLE

In this section we analyse the role of the 11y solar activity cycle. To this end we apply a band-pass filter with half power values at 5y and at 20y. In figure 6 we show for this period band the ENSO-corrected temperature signal $\Delta T_{VinKap} - \Delta T_{ENSO}$, together with the volcanic signal and the solar signal. We see that all major volcanic events are also visible in the ENSOcorrected temperatures. We also see that periods between 9y and 10y dominate both the temperature variations and the volcanic signals in this band. For the whole period 1882-1995, the correlation between the two signals is 0.87. The dominance of periods between 9y and 10y is clearly due to the intervals between major volcanic eruptions. On the other hand, the solar signal has a correlation of only 0.04. Only in the period 1950 -1980, the solar signal is highly correlated with temperature. In this period the solar cycle happens to be in phase with the volcanic forcing. In other periods the solar cycle is either uncorrelated, or negatively correlated with both temperature and the volcanic signal. These results do not support the existence of a strong solar forcing in phase with the 11-y activity cycle, as proposed by Svensmark and Friis-Christensen (1997).

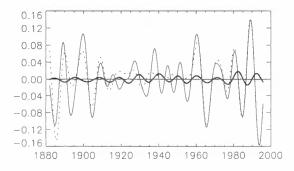


Figure 6. Temperature signals in the "solar band" [K]. Solid line: $T_{VinKap} - \Delta T_{ENSO}$; dotted line: ΔT_{Volc} ; Thick line: ΔT_{Sun} .

ANALYSIS OF TOTAL SIGNALS

Using the regression coefficients for T_{VinKap} from table 1 and (1) - (3), we have computed the full natural signals, including both the fast and the slow components. These are shown in figure 7.

In figure 8 we show the sum of these natural components together with T_{VinKap} . We see that the difference between the two curves is small until about 1950 and increases thereafter.

This is even more clear in figure 9, which shows the difference between the observed temperatures and the

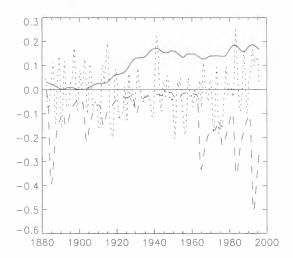


Figure 7. Natural temperature signals [K] .(1y running means) Solid line: ΔT_{Sun} ; dotted line: ΔT_{ENSO} ; broken line: ΔT_{Volc} .

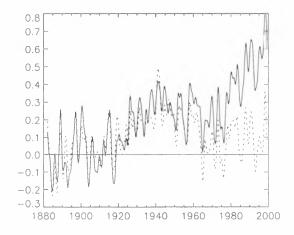


Figure 8. Temperature signals [K] (1y running means). Solid line: T_{VinKap} ; dotted line: $\Delta T_{Natural}$.

natural signals. It appears that the residual temperature shows a warming trend, which increases exponentially in time.

For T_{Jones} we obtain very similar results, allthough in this case the residual scatter is larger (not shown). The residual global warming cannot be explained by the natural signals included in this study, but it resembles the global warming, which we computed with our energy-balance climate model using a plausible reconstruction of the anthropogenic radiative forcing (see figure 9).

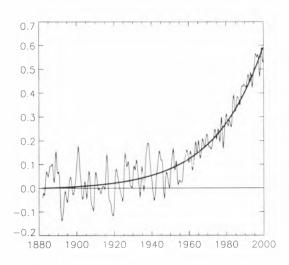


Figure 9. Residual temperature (1y running mean). Thin line: $T_{VinKap} - \Delta T_{Natural}$; smooth line: computed response to an exponential radiative forcing with an e-folding time of 25y (corresponding to an annual increase of about 4%). The magnitude of this forcing is about 1.1 Wm^{-2} in 1990. This estimate falls within the range of net anthropogenic forcings given in IPCC (1995).

CONCLUSIONS

Volcanic forcings and ENSO explain much of the observed variations in global mean temperature with periods of 2y to 20y. The present analysis does not support a strong solar forcing in phase with the 11y activity cycle.

Decreasing volcanic activity and increasing solar activity provide a plausible explanation for the observed temperature rise in the first half of the 20th century.

The high volcanic activity in the period 1963-1993 explains the observed cooling in the 1960s and has reduced the global warming in the period 1970–1995.

The residual global warming in the second half of the 20^{th} century can be explained by a plausible anthropogenic radiative forcing.

ACKNOWLEDGEMENTS

The authors are gratefull to all the providers of data.

REFERENCES

- Baliunas, S and W. Soon (1995): Are variations in the length of the activity cycle related to changes in brightness in solar-type stars ?, Astrophys. J., 450, 896-901, 1995.
- Dyer, A.J. (1974): The effect of volcanic eruptions on global turbidity, and an attempt to detect long-

term trends due to man. Q. J. R. Met. Soc., 100, 563-571, 1974.

- Dyer, A.J. and B.B. Hicks (1968): Global spread of volcanic dust from the Bali eruption of 1963. Q. J. R. Met. Soc., 94, 545-554, 1968.
- Frölich, C. and J. Lean (1998): The sun's total irradiance: cycles, trends and related climate change uncertainties since 1976, *Geophys. Res* . *Lett.*, 25, 23, 4377-4380, 1998.
- Haigh, J.D. (1999): A GCM study of climate change in response to the 11-year solar cycle, Q. J. R. Meteorol. Soc., 125, 871-892, 1999.
- Halpert, M.S. & C.F. Ropelewski, Surface temperature patterns associated with the Southern Oscillation, J. Climate, 5, 577-593, 1992.
- Hansen, J., M. Sato, A. Lacis, R. Ruedy, I. Tegen and E. Matthews (1998): Climate forcings in the industrial era, *Proc. Natl. Acad. Sci. USA*, 95, 12753-12758, 1998.
- Harrison, R. G. and K. P. Shine (1999): A review of recent studies of the influence of solar changes on the earth's climate, *Hadley Centre Technical Note* 6, Met. Office, Bracknell, UK, 64p, 1999.
- Hoffert, M.I., A.J. Callegari and C.-T. Hsieh, (1980): The role of deep sea heat storage in the secular response to climate forcing. J. Geophys. Res., 85, 6667-6679, 1980.
- Hoyt, D.V. & K.H. Schatten, A discussion of plausible solar irradiance variations, 1700-1992, J. Geoph. Res. 98, A11, 18,895-18,906, 1993.
- IPCC-1994: Climate Change 1994: Radiative Forcing of Climate Change, Cambridge Univ. Press, 1995.
- IPCC-1995: Climate Change 1995: The Science of Climate Change, Cambridge Univ. Press, 1996.
- Jones, P. D.(1988) The influence of ENSO on global temperatures, *Climate Monitor*, 17, 3, 80-89, 1988.
- Jones, P.D.(1994): Hemispheric surface air temperatures: a reanalysis and update to 1993, *J. Climate* 7, 1794-1802, 1994.
- Kaplan, A., M. A. Cane, Y. Kushnir, A. C. Clement, M. B. Blumenthal and B. Rajagopalan (1998): Analyses of global sea surface temperature 1856-1991, J. Geophys. Res., 103, C9, 18567-18589, 1998.
- Keen, R. (1983): Volcanic aerosols and lunar eclipses. *Science*, 222,1011-1013, 1983.
- Keen, R. (1993): Lunar eclips observations. Bull. Global Volcanism Network, 18, 15-16.
- Lacis, A., J. Hansen & M. Sato (1992): Climate forcing by stratospheric aerosols, *Geophys. Res. Lett.*, 19, 1607-1610, 1992.
- Lean, J., W. Livingston, A. Skumanich, and O. White (1992): Estimating the sun's radiative output during the Maunder Minimum, *Geophys. Res. Lett.* 19, 1591-1594, 1992.
- Lean, J., J. Beer and R. Bradley (1995): Reconstruction of solar irradiance since 1610:

Implications for climate change, *Geophys. Res. Lett.* 22, 23, 3195-3198, 1995.

- Minnis, P., E.F.Harrison, G.G. Gibson, F.M. Denn, D.R. Doelling and W.L. Smith, Jr.(1993):Radiative forcing by the eruption of Mt. Pinatubo deduced from NASA's Earth Radiation Budget Experiment data, *Science*, 259, 1411-1415, 1993.
- North, G.R. & M.J. Stevens (1998): Detecting climate signals in the surface temperature record, *J. Climate*, 11, 563-577, 1998.
- Robock, A. (2000): Volcanic Eruptions and climate, *Rev. Geophys.*, 38, 191-219, 2000.
- Robock, A. and M.P. Free (1995): Ice cores as an index of global volcanism from 1850 to the present. J. Geophys. Res., 100, D6, 11,549-11,567, 1995.
- Rowntree, P.R. (1998): Global average climate forcing and temperature response since 1750, *Int. J. Climatol.*, 18, 355-377, 1998.
- Sato, M., J.E. Hansen, M.P. Mc Cormick & J.B. Pollack (1993): Stratospheric aerosol optical depths, 1850-1990, J. Geophys. Res. 98, 22987-22994, 1993.
- Sedlacek, W.A., E.J. Mroz, A.L. Lazrus and B.W. Gandrud (1983): A decade of stratospheric sulfate measurements compared with

observations of volcanic eruptions. *J. Geophys. Res.*, 88,C6, 3741-3776, 1983.

- Solanki, S.K. and M. Fligge, Solar irradiance since 1874 revisited, *Geophys. Res. Lett.*, 25, 341-344, 1998.
- Svensmark, H. and E. Friis-Christensen, Variation of cosmic ray flux and global cloud coverage- a missing link in solar-climate relationships, J. Atmos. and Solar-Terr. Phys., 59, 1225-1232, 1997.
- Soon, W.H., E.S. Posmentier and S.L. Baliunas (1996): Inference of solar irradiance variability from terrestrial temperature changes, 1880-1993: an astrophysical application of the sun-climate connection, *Astrophys. J.*, 472: 891-902, 1996.
- Van Ulden, A.P. & R. van Dorland (1999): An assessment of the influence of variations in solar activity on climate, Report 410 200 041, Dutch National Research Programme on Global Air Pollution and Climate Change, Royal Netherlands Meteorological Institute, de Bilt, the Netherlands, 1999
- Vinnikov, K. Ya., P. Ya. Groisman, and K.M. Lugina (1990): Empirical data on contemporary global climate changes (temperature and precipitation), J. Clim., 3, 662-677, 1990.

SPECIAL: AN INTERDISCIPLINARY ESF NETWORK ON SPACE WEATHER AND THE EARTH'S WEATHER

N. B. Crosby and M. J. Rycroft

International Space University, Strasbourg Central Campus - Parc d'Innovation, Boulevard Gonthier d'Andernach, 67400 Illkirch-Graffenstaden, France

ABSTRACT

The phenomena in space that may cause space weather induced effects in the Earth's environment and their possible association with meteorological observations, both on short- and long-term scales, is a controversial topic. Highly energetic cosmic ray, solar and magnetospheric charged particles may have direct or indirect effects on the layers of the atmosphere with which they come into contact. The aim of the interdisciplinary European Science Foundation (ESF) Network study on "Space Weather and the Earth's Weather: Electrodynamic and Charged Particle Effects on the Stratosphere and Troposphere" is to improve the scientific understanding of this topic within the Sun-Earth scenario. Its ultimate objective is to generate global, regional and local models to relate electrical changes in the atmosphere to the distribution of the highly energetic particles, and thereafter to examine and quantify the relationship between such changes with the properties of the global atmospheric electric circuit and also the distribution of cloud and rainfall. This paper presents the scientific background behind the Network and its objectives: the current acronym for the Network is SPECIAL - Space Processes and Electrical Changes Influencing Atmospheric Layers.

Key words: atmospheric electricity; atmospheric weather; space weather; scientific network.

1. INTRODUCTION TO THE ESF NETWORK

Scientists have for a long time discussed whether or not solar activity could have any direct and/or indirect consequences on atmospheric weather (shortterm) and the Earth's climate (long-term). The lack of consistent and statistically significant physical evidence to support this hypothesis has been the key problem. In recent years, with the emergence of the subject of space weather, it has been suggested that perhaps the physical phenomena that induce unwanted space weather effects on satellites and humankind's technological systems may also have potential effects on the planet's meteorology (weather and/or climate). Perhaps these are two sides of the same coin, as it is both the same charged particles as well as the same part of geospace (from the ground up to the magnetopause) that we are investigating. If this is indeed the case, scientific results in these fields may prove beneficial for both communities (meteorology and space weather).

In this paper we shall present some information on a newly established scientific Network which was planned to look into the possibility of this connection: its original title was "Space Weather and the Earth's Weather: Electrodynamic and Charged Particle Effects on the Stratosphere and Troposphere". The acronym SPE-CIAL (Space Processes and Electrical Changes Influencing Atmospheric Layers) has been chosen recently for easy identification of the Network and SPECIAL has its own web page located at http://sgo.fi/SPECIAL.

SPECIAL is a European Science Foundation (ESF) Scientific Network (http:// www.esf.org). The scientific networks of ESF are increasingly interdisciplinary and, as shown in this paper, ideal for a subject such as SPECIAL. The duration of the SPE-CIAL network is three years, beginning in September 1999 and ending in summer 2002, although it may be extended somewhat or even develop into a fully fledged research programme.

In the following, the scientific background behind SPECIAL and its objectives are summarized in Section 2. In the final section the multi-beneficial aspects of SPECIAL are presented; contact information for future activities of the Network are also given.

2. SCIENTIFIC BACKGROUND TO SPECIAL AND ITS OBJECTIVES

Highly energetic charged particles (e.g. solar protons, cosmic rays and magnetospheric particles) can

Proc. 1st Solar & Space Weather Euroconference. 'The Solar Cycle and Terrestrial Climate', Santa Cruz de Tenerife, Tenerife, Spain, 25-29 September 2000 (ESA SP-463, December 2000)

interact with the Earth's middle and lower atmosphere. A change in their fluxes, due to the solar activity cycle, may either directly or indirectly have consequences on the surroundings. It may modify the chemistry of the middle atmosphere and change the ionization in the air which could lead to condensation nuclei for water droplets. Furthermore, it may modify the electric field distribution and/or the electric current flowing between the Earth's surface and the ionosphere. In turn, the current may deposit charge layers on cloud droplets and sulphate aerosols which may significantly affect cloud physical processes under non-thunderstorm conditions. It is getting the global picture of all these linked phenomena that is important, and the aim of SPECIAL is indeed to improve the scientific understanding of this topic within the Sun-Earth scenario. A list of references to important works related to SPECIAL is available on the Web (see http://www2.sgo.fi/SPECIAL/Bibliography.html).

The objectives of SPECIAL in this respect can be divided into four parts: 1.) quantifying the atmospheric response, 2.) generating and testing hypotheses concerning the quantified effects, 3.) eventually generating numerical models, and 4.) in parallel, planning new instruments/facilities to observe specific phenomena.

To quantify the atmospheric response unequivocally will rely on two different approaches, A.) one based on studying particular events in detail and B.) the other using statistics. The former approach uses detailed analyses of meteorological (e.g. pressure, temperature, cloud distribution, etc.) observations made during particularly strong and clearly defined "space weather" events (November 1993, January 1997 and May 1998) that already have been studied in great detail. Statistics are the tool in the second approach; rigorous statistical analyses of meteorological and other data sets (e.g. ionospheric, magnetometer, ...) are to be performed. This is done, for example, by using the superposed epoch analysis method of analysis and comparing with the same number of randomly chosen key dates to estimate the significance of the result. The ultimate goal of both approaches is to give us a better understanding of the physical mechanisms involved in the processes.

The second objective of SPECIAL concerns the quantified effects of the solar wind and energetic charged particles on the atmosphere that have been found, generating hypotheses on these results and furthermore testing these hypotheses. Eventually, the next objective is generating numerical models on global, regional and local scales on the following three issues:

- The response of the global electric circuit, the ionospheric potential, the air current density, the probability of occurrence of sprites, etc.
- Changes to both the tropospheric and stratospheric chemistry

• Changes to cloud nucleation, cloud microphysics, the distribution of aerosols and clouds, rainfall, etc..

In all these three issues the spatial and temporal variations of the properties of the galactic, solar and magnetospheric charged particles entering the atmosphere are to be taken into account.

In parallel to the carrying out of the above investigations, the planning of new instruments and facilities is being considered. Examples include considering the feasibility of observing, by various techniques, sprites in Europe (e.g. in Alsace, Pyrenees, or Turkey) and from the International Space Station or a dedicated satellite. Also the feasibility of establishing a high altitude observatory for measuring atmospheric electricity and related parameters with well-understood instruments (e.g. in Tenerife, La Réunion, or Antarctica) is being studied.

A related project carried out as part of the World Climate Research Programme is SPARC (Stratospheric Processes And their Role in Climate). Its main themes are:

- Stratospheric indicators of climate change (e.g., temperature, ozone and water vapour changes)
- Stratospheric processes and their relation to climate (e.g. stratosphere-troposphere exchange and the quasi biennial oscillation)
- Modelling of stratospheric effects on climate (e.g., model climatologies, reference data sets and sudden warmings).

Thus SPARC and SPECIAL are complementary to each other. Table 1 gives, simply, the physical mechanisms whereby changes on the Sun can affect the properties of the Earth's atmosphere, from the troposphere up to the thermosphere. It is evident that A and C are primarily within the SPARC domain, whereas B is central to SPECIAL; C also plays a role in SPECIAL.

3. MULTI-BENEFICIAL ASPECTS OF SPECIAL AND ITS FUTURE ACTIVITIES

3.1. Earth Weather / Space Weather

As mentioned previously SPECIAL concerns a subject that may be multi- beneficial, not only to the meteorological (weather/climate) communities, but also to the space weather community. It is well known that energetic charged particles may cause unwanted problems on both technological and biological systems in space as well as on Earth. Technical examples include the malfunctioning of operational satellites in Earth orbit, disturbances to global Table 1. Summary of the mechanisms which could be responsible for causing changes in the Earth's ionosphere and thermosphere, mesosphere and stratosphere due to changing conditions on the Sun. in interplanetary space, in the magnetosphere and in the troposphere. Whilst A and C are considered mainly by SPARC (Stratospheric Processes And their Role in Climate, http://www.aero.jussieu.fr/~sparc/), a project of the World Climate Research Programme, B is central to SPECIAL and C should not be forgotten.

PHYSICAL AGENTS FOR SOLAR VARIABILITY EFFECTS ON THE EARTH'S ENVIRONMENT

- A. SOLAR RADIATION X-rays, smaller fluxes but larger variations UV, larger fluxes but smaller variations
- B. CHARGED PARTICLES
 Plasma (thermal). ≥ eV
 Magnetospheric. ≥ keV
 Solar protons. ≥ MeV
 galactic cosmic rays. ≥ GeV
- C. WAVES Gravitational tides Planetary scale waves Gravity waves

positioning systems in space and electric power grid systems on ground, as well as corrosion of conducting pipelines. Hazards to astronauts and to the crew and passengers aboard high-flying aircraft are also of increasing concern. SPECIAL deals with the weather that occurs in the troposphere and environmental factors (such as aerosols, ions and radon released from the ground), the climate (the coupled troposphere/stratosphere system) and climate changes. This paper suggests that it may be the same population of energetic particles that causes "changes" both from the space weather and meteorological points-ofview, implying that common factors may exist and should be investigated.

3.2. Past and Future SPECIAL Activities

The first meeting of SPECIAL was held from 2 to 4 December 1999 at the ESF in Strasbourg, France: 26 people attended this meeting. The main objective of this meeting was to discuss and chart the way forward. To do this, three informal groups were established in the following topics:

- Atmospheric electrodynamics and effects of the global electric circuit on the troposphere
- Solar wind and energetic charged particle effects on the atmosphere
- Effects of lightning on the middle atmosphere (Schumann resonances, ULF phenomena and sprites, etc.).

The purpose of splitting into three groups was for easier discussions, having a manageable number of persons in each group. The coordination of the work of these groups during the next six months was established and presented at the end of the meeting. This meeting has been the driver of the future meetings of SPECIAL.

An informal meeting about SPECIAL was held at the EGS General Assembly in Nice in April 2000. The Next Formal Meeting of SPECIAL is scheduled for 8 - 11 November 2000, at the Max-Planck-Institute für Aeronomie in Katlenburg-Lindau, Germany.

For more information about SPECIAL and/or inquiries about becoming involved in this network, which are welcomed, please contact the authors:

M. J. Rycroft (Michael J. Rycroft @ukgateway.net). Chairman of the ESF Network Coordination Committee SPECIAL, and/or N. B. Crosby (ncrosby @wanadoo.fr). Scientific secretary of SPE-CIAL, C. Werner who is the ESF liaison can be contacted at cwerner@esf.org for practical/logistical matters concerning the Network.

ACKNOWLEDGMENTS

The authors would like to thank all the members of the SPECIAL Network for their fruitful work and enthusiasm. Special thanks go to Dr. Thomas Ulich for creating and updating the SPECIAL web-page (http://sgo.fi/SPECIAL).

PICARD: SOLAR DIAMETER, IRRADIANCE AND CLIMATE

Luc Damé¹, David Cugnet¹, Michel Hersé¹, Dominique Crommelynck², Steven Dewitte², Alexandre Joukoff², Isabelle Ruedi³, Werner Schmutz³, Christoph Wehrli³, Christian Delmas⁴, Francis Laclare⁴, Jean-Pierre Rozelot⁴

 ¹Service d'Aéronomie du CNRS, BP 3, F-91371 Verrières-le-Buisson Cedex, France Tel: +33 1 64474328, Fax: +33 1 69202999, e-mail: luc.dame@aerov.jussieu.fr
 ²Institut Royal Météorologique, 3 av. Circulaire, B-1180 Bruxelles, Belgium
 ³PMOD, World Radiation Center, Dorfstrasse 33, CH-7260 Davos Dorf, Switzerland
 ⁴CERGA, Observatoire de Calern, F-06460 St Vallier de Thiey, France

ABSTRACT

The PICARD microsatellite mission will provide 3 to 4 years simultaneous measurements of the solar diameter, differential rotation and solar constant to investigate the nature of their relations and variabilities. The 110 kg satellite has a 42 kg payload consisting of 3 instruments: SODISM, which will deliver an absolute measure (better than 4 milliarcsec) of the solar diameter and solar shape, SOVAP, measuring the total solar irradiance, and PREMOS, dedicated to the UV and visible flux in selected wavelength bands. Now in Phase B, PICARD is expected to be launched by 2005. We review the scientific goals linked to the diameter measurement with interest for Earth Climate, Space Weather and Helioseismology, present the payload and instruments' concepts and design, and give a brief overview of the program aspects.

INTRODUCTION

Since the solar energy is one of the major driving inputs for terrestrial climate and since it exists some correlations between surface temperature changes and solar activity, it appears important to know on what time scale the solar irradiance and other fundamental solar parameters, like the diameter, vary in order to better understand and assess the origin and mechanisms of the terrestrial climate changes.

Global effects, such as diameter changes, large convective cells, the differential rotation of the Sun's interior and the solar dynamo at the base of the convective zone, can probably produce variations in the total irradiance or, at least, correlate with these variations associated, during maximum, with the changing emission of bright faculae and the magnetic network. The aim of these correlations is double: on one side prediction and on the other explanation of the past history of climate, like the Maunder minimum period.

To establish long-term links and trends between solar variability and climate changes, it is necessary to achieve not only high precision but also absolute measurements, what the diameter measurements of PICARD shall bring. Further, this high precision allows "instantaneous" monitoring of the diameter changes, i.e., with a proper orbit for the microsatellite, oscillations and, in particular, the gravity modes.

SCIENTIFIC OBJECTIVES

Why the diameter?

From 1666 to 1719, Jean Picard and his student Philippe de la Hire measured the solar diameter, observed the sunspots and determined the Sun rotation velocity. Fortunately, these measurements covered the Maunder minimum and some time after. The data were reexamined by Ribes et al. (1987) who, after removing the seasonal variation of the solar diameter, obtained the annual means at 1 AU. These values, averaged for the Maunder minimum period, and after while the Sun recovered a significant activity, show a definitive difference of the order of 0.5 to 1 arcsec, corresponding to a larger Sun diameter during the Maunder minimum. As expected, few sunspots were observed. Moreover, Picard's data also showed a slow down of the Sun rotation velocity at equator and significantly more sunspots in the south Sun hemisphere than in the north.

Diameter and Earth's climate

The solar constant measurements performed in space by the radiometers since 1978 were modeled using the sunspots number and faculae. This allowed to reconstruct the solar constant variation till 1610 (Lean, 1997). This showed that the solar constant experienced a significant decrease during the Maunder minimum. The temperature in the northern hemisphere has been also reconstructed for the same period. The cooling of this period is known as the Little Ice Age. The similarity of the temperature and solar constant variations strongly suggests the Maunder minimum as the cause of the Little Ice Age. To assess this suggestion, climate models were run by Sadourny (1994) that showed the Maunder minimum as the possible cause of the Little Ice Age. Volcanic eruptions (major ones) also play a certain role, but their effects do not extent more than a few years.

As during the Maunder minimum where, as suggested by Picard's data, the Sun radius experienced a significant change, the modern data of Sun diameter measurements and sunspots number, set together by Laclare <u>et al.</u> (1996), reveal a relation between the Sun radius and solar constant variations corresponding to an increase of the Sun radius for a decrease of the solar constant (cf. Fig. 1). Therefore, in order to establish experimentally without ambiguity the Sun constant and diameter relationship, we propose to operate from space by measuring simultaneously both quantities from the same platform

Proc. 1st Solar & Space Weather Euroconference, 'The Solar Cycle and Terrestrial Climate', Santa Cruz de Tenerife, Tenerife, Spain, 25-29 September 2000 (ESA SP-463, December 2000)

and in non-magnetic lines or continua. The importance of the measurements for climatology is straightforward taking into account the Little Ice Age and the Maunder minimum events.

Prediction and precision

The total solar irradiance measure made by radiometers from space over the last 20 years, is excellent in relative terms (10⁻⁵) but poor in absolute. The amplitude of the variation over the cycle (0.1 %) is small and is about the same than the uncertainty on the absolute value from one instrument to the other. Prediction tendency of climate change from such data is not straightforward and adjustment of data sets of different origins an art (cf. Fröhlich and Lean, 1998). On the contrary, and if the relation irradiance-diameter is established by PICARD, the diameter measure which is precise, reproducible and absolute to 4 mas (or even better when the HIPPARCOS data will be recalibrated by FAME or GAIA) and which, accordingly to Laclare et al. (1996), has an amplitude over the solar cycle of 0.4 arcsec or so, provides a proper - and quantified sampling of the activity change over the cycle. Furthermore, the diameter measure will be done in the visible but also in the UV at 230 nm a wavelength band much more variable (6 to 8%) with the solar cycle and well known for its role in the chemistry of ozone, incidentally one of the possible links between solar activity and Earth climate.

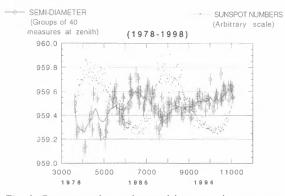


Fig. 1: Opposing phase observed between the sunspots number and the semi-diameter measured at CERGA's Astrolabe (1978–1998).

Note that we measure the solar radius using the inflexion point of the radial intensity curve, a measure less sensitive to the instrumental photometry and point spread function (diffraction, jitter, *etc.*). In practice an average profile is first obtained and fitted using a smooth function (double hyperbolic tangent with 7 parameters). Then, each individual radius corresponding to a limb pixel is determined using two parametric deviations from this profile, intensity and limb displacement, applying the appropriate corrections for diffraction, jitter, diffusion and the integration and purely geometrical effects of the CCD A precision of 10 mas is achieved, mostly corresponding to the photon noise limit. Because centering is essential, the whole process is, in fact repeated so that the generation of the averaged limb profile recentering is not affected by solar activity (identified) and the limb shape deformations. Cumulating these individual radius measure by hundreds, allow to achieve a precision better than a mas on the global but also specific radius (polar, equatorial or of higher orders).

Lyman alpha monitoring

Lyman alpha irradiance has been monitored since 1977 and more recently by UARS since 1991. The SORCE satellite will be launched in late 2002 and it will also monitor Lyman alpha irradiance. Since these irradiance monitoring experiments observe the Sun as a star, there is no information about the physical causes of the observed irradiance changes. To identify the causes of changes in Lyman alpha, one needs to compare the full disk irradiance data with images. PICARD will provide high spatial resolution (1 arcsec) and continuous (every 45 minutes) Lyman alpha images which will complement the SORCE measurements. These images will make possible to better account for the observed Lyman alpha changes and also for a better reconstruction of the longterm Lyman alpha data set. Lyman-alpha irradiance is important for the ozone changes and for the formation of the ionospheric D-region in the Earth's atmosphere. Its understanding should result in significant progress in atmospheric science and aeronomy.

Oscillations

Another major objective of PICARD is to attempt the detection of the gravity modes (g-modes) of the Sun. These modes are of prime importance to understand the structure and dynamics of the solar core which cannot be studied by using solar pressure modes (p-modes) alone. So far the g-modes have not been discovered by any set of instruments onboard the SOHO spacecraft (Appourchaux et al., 2000). The 1-o upper limit of g-modes amplitude at around 200 µHz is typically 1 mm/s or 0.1 ppm (Fröhlich et al., 1998). Given a velocity amplitude of 1 mm/s at 200 µHz, the displacement of the solar surface would be of about 1.6 m p-p which is equivalent to a variation of solar radius of about 2 µarcsec. This level could be marginally detected by PICARD although not the method used for detecting the g-modes. Nevertheless, it is worth noticing that MDI/SOHO was able to without an optimized telescope and imaging scheme as we have — to observe a 10 µarcsec high frequency pmode (5 min.) solar limb oscillation signal (Kuhn et al., 1997).

With PICARD we want to detect intensity fluctuations at the solar limb that will perturb the equivalent solar radius signal. Appourchaux and Toutain (1998) reported to have detected p-modes using the limb data of the LOI instrument. In some case the amplification with respect to full-disk integrated data is about 4, i.e. it means that a p-mode with an amplitude of 1 ppm in full disk is observed with an amplitude of 4 ppm at the limb (cf. Damé et al., 1999). Analyses of Toutain et al. (1999) and Toner et al. (1999) confirmed such an amplification factor of 5. If we hope that the same amplification factor holds for the g-modes, we may detect them faster with the limb data of PICARD than with SOHO ones. A pessimistic derivation gave 20 years for the detection of the first few g-modes with SOHO (Fröhlich <u>et al.</u>, 1998). With PICARD we can seriously envisage detecting them in less than 2 years with the amplification factor above.

PICARD PAYLOAD

To carry the proposed measurements PICARD has 3 instruments: SODISM, the "SOlar Diameter Imager and Surface Mapper", for the measure of the diameter and differential rotation (this is, therefore, a whole Sun imager), SOVAP (SOlar VAriability PICARD), for the measure of the total absolute solar irradiance (correlation with SODISM measurements) and PREMOS (PREcision MOnitoring of Solar variability), a package of 3 set of 4 UV and visible Sun photometers. Fig. 2 presents an artist view of PICARD's microsatellite. SODISM is realized by the Service d'Aéronomie du CNRS, France, with a contribution from the Space Science Department of ESTEC, SOVAP by the Royal Meteorological Institute of Belgium, and PREMOS by the World Radiation Center of Switzerland.

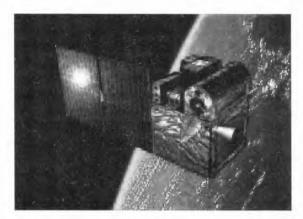


Fig. 2: Artist view of PICARD microsatellite: 60x60x80 cm³ in size. Shown are the 3 instruments: SO-DISM, telescope and guiding, right, SOVAP, differential radiometer, center, and PREMOS (flux monitors) left, near the solar panels. In the back, one can see the electronics box supporting two S-band antennae and a solar pointer (acquisition maneuvers).

SODISM

SODISM is a simple telescope of useful diameter 110 mm. It forms a complete image of the Sun on a large, back thinned, CCD of 2048 x 2048 useful pixels. The pixel, 13.5 μ m, corresponds to 1.05 arcsec (at 1 AU) and the effective spatial resolution is also about an arcsec (at the limb). SODISM observes in 4 wavelengths bands the whole Sun (230 nm, 548 nm, 160 nm and Lyman alpha) and 2 calibration channels (cf. Table 1) accessible through the use of 2 cascading filter-wheels, each with 5 positions.

Operational modes

The main observing wavelength is 230 nm (8 nm bandwidth). It corresponds to a mostly flat UV continuum formed in the high photosphere. It is the best possible choice of wavelength since it is sensitive to UV variations (about half of the MgII index variability for instance), it corresponds to the ozone bands (and by chemical interaction in the stratosphere, the UV may affect the stratospheric dynamics and, consequently, the clouds coverage — which may be one of the paths of the Sun influence on the Earth's climate) and the limb darkening in this continuum is limited.

UV nominal mode	230 nm
Visible	548 nm
Active regions	160 nm
Prominences and ionosphere	Lyman alpha
CCD Flat Field	"Diffusion"
Scaling factor	"Star field"

Table I: Observing and calibration modes of SO-DISM/PICARD.

In addition, SODISM/PICARD observes 548 nm which is near the center wavelength of the 100 nm bandpass used by Francis Laclare CERGA's group for the solar diameter measurement with the Astrolabe (and, in the near future, with the new DORAYSOL instrument). The 160 nm and Lyman alpha filters are used for identification of active regions and prominences. This is essential to prevent activity manifestations to affect the "quiet" radius determination. This possibility to avoid, in the diameter computation, the pixels at the limb affected by faculae, active regions, prominences, sunspots or pores, is an essential feature of SODISM/PICARD since activity, therefore, does not add noise to the diameter measure (active solar pixels are not accounted).

The diffusion plates are simply used to monitor the CCD response and sensitivity (Flat Field). The CCD itself is a complete state-of-the-art system (EEV 4280 2048x4096 pixels back thinned and with frame transfer) hopefully developed in parallel of our program for the asteroseis-mology satellite program COROT.

Finally, specific to PICARD — and providing an AB-SOLUTE diameter reference better than 4 mas (milliarcsec)— is the "Star field" channel. It provides access to stellar fields in which (with a limit magnitude of 6 or so) stars' triplets (and more: field with 5 and 6 stars also available) of the HIPPARCOS reference catalog are imaged, allowing to scale our diameter measure and, if required, to identify and to follow any structural change in the focus or CCD dimensions which could affect the diameter measure.

Optical concept

SODISM has a sound optical concept allowing to achieve a near distortion free and dimensionally stable image of the solar limb. It has a symmetry of revolution (no complex optics — filters at normal incidence nothing else than the two mirrors and a filter set in the optical path) and a single telescope-detector-guiding telescope support structure for common referencing and stability. The telescopes mirrors are made of SiC without coatings (reflectivity of 35-40 % in the UV and yet 20 % in the visible). Advantage is indeed that the photometry will not change by aging and degradation of coatings since there are no coatings. Further, the primary and secondary mirrors will help to remove 96 % of the visible solar flux, preserving the filters from degradation and, due to the high conductivity of SiC, this flux will be evacuated to external radiators.

Mechanical/thermal stability

To provide a stable measurement of semi-diameters to a couple mas over the two to six years duration of the mission, SODISM/PICARD mechanical stability has to be excellent intrinsically and controlled. The design selected achieves mechanical and thermal stability because of the choice of a single monolithic structure — a tube of carbon-carbon — to link the SiC mirrors of the telescope and to the detector. As well the guiding telescope is in the same structure, its mirrors and the 4quadrant detector being directly placed in the carboncarbon tube. This new type of structure (developed for example by ALCATEL SPACE, cf. Bailly et al., 1997) allows to reduce the thermal regulation to half a degree for a relative change of the diameter < 1 mas (1 thousand of a pixel). The isotropic property of carbon-carbon and a detailed knowledge of the experiment (interferometric calibration), will help to further gain, by modelisation, a factor 100 to 1000 on the short term diameter variations (useful for the solar limb oscillations). This means that couples of µarcsec could be inferred, allowing a direct monitoring of limb oscillations. Note that, beside focusing, the only other systematic error which affects the diameter directly is the size of the detector (silicium has an expansion coefficient of $\sim 2 \ 10^{-6}$ and requires, to keep errors below \pm 0.5 mas, a \pm 0.1 °C temperature regulation).

Fig. 3 shows the structure design of the SO-DISM/PCARD telescope, with the carbon-carbon tubes, the INVAR plates and SiC mirrors. Note also the small titanium feet which account for the dilatation of the platform (instrumental plateau base plate in aluminum but with a carbon skin).

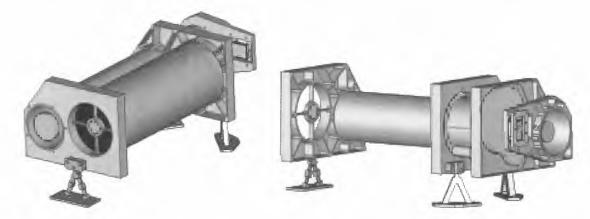


Fig. 3: Mechanical structure of the SODISM/PICARD telescope (350 mm between the primary and secondary mirror and 150 mm between the primary and the CCD surface: total length without cover of 550 mm). Note the 3 Invar plates linked together with the 550 mm long carbon-carbon tube of Ø100 mm. The primary mirror is mounted on 3 piezoelectrics driven by a guiding telescope directly placed inside the C-C tube. The CCD (cooled to -40°C), is uncoupled from the Invar plate by a Cordierite support.

Measurements	Solar diameter, differential rotation and full Sun UV and visible imaging
Number of channels	6 (230, 548, 160 nm, Ly α, "Flat Field" & "Star Field")
Telescope focal length — solar image	2650 mm — Ø25 mm
Telescope optics	Primary Ø120 mm (used: 110 mm); Secondary Ø34 mm (used: 25 mm)
EEV-4280 back thinned CCD detector	2048x4096 13.5 µm square pixels (frame transfer: 2048x2048 pixels used)
Guider acquisition range	1.2°
Guider nominal pointing range	$\pm 30''$
Guider servo bandwidths	0 to a few Hz (platform); a few Hz to 50 Hz (fine guiding on the primary)
Quad-cell image displacement sensitivity	Better than 0.01 arcsec
Piezo displacement range	$\pm 6 \mu m (\pm 1 arcmin)$
Pointing precision maximum residual jitter	0.1" (1 tenth of a pixel)
Absolute solar shape precision	Better than 4 mas (6 stars HIPPARCOS enhanced calibration in 2003)
Relative semi-diameter precision	Better than 1 mas

Table 2: Characteristics of SODISM.

Pointing

Image guiding and stabilization is provided by a telescope with similar optical properties than the main telescope and directly implemented in the carbon-carbon structural tube. The 4-quadrant detector assembly is fine guiding the piezoelectrics which activate the primary mirror of the telescope. Fine guiding is used so that the image of the Sun on the CCD does not move by more than 0.1 arcsec, i.e. 1 tenth of a pixel (about 1 tenth of the Airy disk as well at 230 nm). The 4-quadrant detector will also provide (by access to the low frequency part of the control signal) accurate guiding to the microsatellite itself. In that case the coarse guiding of the stellar sensor is overruled by our sensor when the Sun acquisition is effective in the nominal $\pm 0.6^{\circ}$ field of view. The 4-quadrant detector is provided by ESTEC and similar to the one used with success on SOHO by the LOI/VIRGO instrument.

Ground program: PICARDSOL

The Engineering Model of SODISM will be used in CERGA, France, in conjunction with the newly working DORAYSOL and the longstanding (25 years of observations) Astrolabe of Francis Laclare. As such, and for the first time, the same instrument will be used in space and on ground to measure the solar diameter, deduce atmospheric bias and state on ground instruments possible accuracy. It is expected that the ground instrument will operate for more than a solar cycle. A new generation seeing monitor, measuring the coherence length and temporal coherence (MISOLFA), will also be used in conjunction with PICARDSOL and DORAYSOL to better assess atmospheric effects on the ground diameter measure (in order to validate the past historical measurements).

SOVAP

To measure the solar constant, PICARD will use a SOVA I type radiometer, SOVAP, the "P" standing for PICARD. SOVA 1 is a differential absolute solar radiometer developed at the RMIB, Royal Meteorological Institute of Belgium (Crommelynck and Domingo, 1984). The RMIB radiometers have been flown in Space 8 times from 93 to 98. SOVAP radiometric core is formed by two blackened cavities constructed side by side on a common heat sink. In between each cavity and the heat sink a heat flux transducer is mounted. The difference between the two transducers' outputs gives a differential heat measurement, in which the common part of the thermal surrounding radiation seen by the two cavities is eliminated. By the symmetrical construction and good insulation thermal asymmetry is minimized. SOVAP characteristics are summarized in Table 3.

PREMOS

This instrument is provided by the World Radiation Center, Davos, Switzerland. It consists in 4 "filter radiometers", based on the same principle than a radiometer (equilibrium of the flux inside a cavity) but with the preselection of a known and reduced spectral bandwidth. These photometers are observing in the UV and the visible, at the same wavelengths, 230 and 548 nm than SODISM and in two other UV wavelengths: 311 and 402 nm. 3 sets of these 4 photometers are used one being a reference — in order to monitor aging effects. The 230 nm channel has a dual function: it estimates the UV flux in this ozone sensitive bandwidth, and it indicates a possible degradation of SODISM's CCD sensitivity.

Measured quantity	Total irradiance (Wm ⁻²)
Number of channels	2
Number of reference voltages	6
Cavity type	Cylindrical, diffuse black
Diameter precision aperture	1 cm
Slope angle	2.5°
Solar sampling period	3 minutes
Duty cycle	50 %
Instrument noise	$< 0.1 \text{ Wm}^{-2}$

Table 3: Characteristics of SOVAP (default measurement mode).

Measured quantity	Spectral irradiance at 230,			
	311, 402 and 548 nm (Wm ⁻²)			
Number of photometers	12 (3 sets of 4)			
FWHM bandwidth	8 nm at 230, 311 and 548 nm			
	5 nm at 402 nm			
Cavity type	Cylindrical, diffuse black			
Full view angle	2.5°			
Slope angle	0.7°			
Diameter precision aperture	3 mm			
Accuracy of aperture area	< 10 ⁻³			
Cross-Talk	$< 10^{-5}$			

Table 4: Characteristics of PREMOS.

THE PICARD MISSION

The PICARD's system uses most of the basic components of the CNES microsatellite product line, namely, the ground segment (MIGS) made of the "Centre de Contrôle Microsatellites" (CNES Toulouse), a band S station (and most probably a complementary station at high latitude) and the flight microsatellite segment. These components will be qualified by the first microsatellite mission of the product line, namely, the mission DEMETER. The PICARD system is operated mostly the same way than DEMETER and, in this way, confirms the generic character wanted and developed for the microsatellite product line.

Orbit

The PICARD's mission requires, ideally, an orbit with constant viewing of the Sun or, at minimum, with limited or short duration eclipses. The expected mission lifetime is 3 to 4 years with a possible extension to 6 years. Launch opportunities are essentially Sun Synchronous Orbits (SSO) with local time 6h/18h (little or no eclipses). Several scenarios are still under consideration for the PICARD flight which is not expected before 2005 (the launch date and expected life time are important since the diameter/constant relationship will defini-

tively be better determined during the near linear part of the rising cycle than at minimum when the "constant" is mostly "constant"...). If 4 years can be envisaged based on the experience of the first microsatellites, and since our payload is not expected to degrade (telescope with SiC mirrors, etc.), a launch in 2005 is then possible.

Brief or non-eclipsing Sun-synchronous viewing orbits are essential in order to achieve both the thermal stability for the absolute long term diameter measurement and the near continuous sampling for the long periods gmodes oscillations. At present launch is planed with a dedicated Dnepr russian rocket on a 750 km SSO orbit.

Pointing needs

The pointing needs on the PICARD satellite (for the scientific measure) is a pointing in the Z axis (telescope axis), towards the Sun, and with a precision of $\pm 0.01^{\circ}$. This performance will be achieved by the attitude control system using an ecartometry information from the

payload (from the SODISM guiding telescope: pointing differences between the telescope and the Sun center direction). This, by itself, illustrates nicely the optimization capacity offered by the microsatellite system.

Pointing needs also imply a specific configuration of the stellar sensors (two heads) to preserve a permanent stellar pointing calibration along the orbit (stellar calibration need for the SODISM telescope scaling factor).

Characteristics

To the exception of the attitude control system, the microsatellite platform for PICARD is very similar of the one of DEMETER. Globally, the adaptations are reasonable (in cost and complexity) and confirm the right choice of recurring technologies in the initial microsatellite product line.

Table 5 summarizes the essential characteristics of the present PICARD's microsatellite. The performances are derived, mostly, from the microsatellite product line. To the exception of the power allowance, somewhat critical, these are well along the payload needs (cf. Table 6).

Characteristics	PICARD Microsatellite
Size (cm^3) [L x W x H]	60 x 75 x 80
Mass (kg)	Platform (with lest): 68 kg
	Payload: 42 kg max
	Total 110 kg (for 120 kg nominal: 10 kg margin)
Power (w)	Platform: 30 W (average on an orbit)
	Payload: 42 W (average on an orbit)
	Total: 72 W
Pointing accuracy	3 axis stabilized, 0.1°
Pointing stability (platform)	0.01°
Pointing stability (SODISM)	0.1" (active pointing control on the primary mirror)
Mass Memory	1 Gbits
Telemetry flow	400 Kbits/s (1.5 Gbits/day)
TC (commands)	10 Kbits (immediate or delayed)
Orbit restitution	1 km
Onboard datation	< 0.5 s (TU difference)

Table 5: Performances of PICARD microsatellite.

Characteristics	PICARD Payload	SODISM	SOVAP	PREMOS	Electronics boxes (2)
Mass (kg)	41.8	17.9	5.8	4.1	10 & 4
Size (cm ³)	60x60x30 18x19x19*	60x27x28	35x15x15	30x9x20	<16x26x26 <18x19x19*
Power (W)	32.9	18.4	10.1	4.4	NA
Thermal Control (W)	9.0	9.0		_	NA
Average Telemetry (Mbits/day)	1510	1500	5	5	NA

* this electronic's box is placed under the microsatellite platform

Table 6: Characteristics of PICARD model payload.

Table 6 summarizes the mass, power and nominal telemetry characteristics of the PICARD mission. Note that the PICARD Mission Center will normally be operated by the RMIB and that, most probably, antennae (S band) in Toulouse and Kiruna will be used for telemetry needs (about 1.5 Gbits per day). Depending on the data compression scheme selected, a higher telemetry rate (1.9 Gbits per day) could require a third antenna.

ACKNOWLEDGEMENTS

We are thankful to the CNES Microsatellite Division and Direction des Programmes and in particular to B. Tatry, C. Bouzat, J.-Y. Prado, F. Dulac and N. Papineau for their support to the mission, and would like to acknowledge the PICARD project and scientific teams (10 collaborators, 27 Co-Investigators) whom are doing a remarkable work towards a successful PICARD's mission.

REFERENCES

- Appourchaux, T. <u>et al.</u>, Observational Upper Limits to Low-Degree Solar g-Modes, Ap. J. 538(1), 401-414 (2000).
- Appourchaux, T. and Toutain, T., in Sounding Solar and Stellar Interiors, IAU Symposium 181 (Poster Volume), Eds. J. Provost and F.X. Schmider, 5 (1998).
- Bailly, B. <u>et al.</u>, High Stability Carbon/Carbon Telescope Structure, Proc. ICSO'97, CNES International Conference on Space Optics, Ed. G. Otrio, S4, 1–11 (1997).
- Crommelynck, D. and Domingo, V., Solar Irradiance Observations, Science 225, 180-181 (1984).
- Damé, L. et al., PICARD: Simultaneous Measurements of the Solar Diameter, Differential Rotation, Solar Constant and their Variations, in Symposium on Helioseismology and Solar Variability, Adv. in Space Research 24(2), 205–214 (1999).
- Fröhlich, C. and Lean, J., The Sun's total irradiance: Cycles, trends, and related climate change uncertainties since 1976, Geophysical Research Letters 25(23), 4377 (1998).
- Fröhlich, C. and the Phoebus Group, in Structure and Dynamics of the Sun and Solar-like Stars, Proceedings of the SOHO 6 / GONG 98 workshop, Boston, USA, ESA SP-418, 67 (1998).
- Kuhn, J.R. <u>et al.</u>, Precision Solar Astrometry from SOHO/MDI, in Sounding Solar and Stellar Interiors, IAU Symposium 181, Eds. J. Provost and F.X. Schmider, 103–110 (1997).
- Laclare, F., Delmas, C., Coin, J.P. and Irbah, A., Measurements and Variations of the Solar Diameter, Solar Physics 166, 211–229 (1996).
- Lean, J., The Sun's Variable Radiation and its Relevance for Earth, Annu. Rev. Astron. Astrophys. 35, 33–67 (1997).
- Ribes, E., Ribes, J.C. and Barthalot, R., Evidence for a Larger Sun with a Slower Rotation during the Seventeenth Century, Nature 326, 52–55 (1987).
- Sadourny, R., Sensitivity of Climate to Long-term Variations of the Solar Output, in The solar engine and its influence on terrestrial atmosphere and climate, Ed. E. Nesme-Ribes, NATO ASI Series I, vol. 25, 479–491, Springer Verlag (1994).
- Toner, C.G., Jefferies, S.M. and Toutain, T., Increasing the Visibility of Solar Oscillations, Ap. J. 518(2), L127-L130 (1999).
- Toutain, T., Berthomieu, G. and Provost, J., Light perturbation from stellar nonradial oscillations: an application to solar oscillations, A. & A. 344, 188-198 (1999)

Non-Solar Sources of Global Warming

USE OF CLIMATE MODELS FOR CLIMATE CHANGE INVESTIGATIONS

K. Arpe, U. Cubasch and R. Voss

Max-Planck Institute for Meteorology, Bundesstr. 55, 20146 Hamburg, Germany e-mail: arpe@dkrz.de

ABSTRACT

Problems to get adequate observational data for model validation are discussed. Nevertheless it can be shown that the climate models used at Max-Planck Institute for Meteorology (ECHAM) give realistic estimates for the present climate. Model simulations for future or past climates show that the temperature increase in the last decades can be explained by forcings from changes in the greenhouse gas concentrations. Simulations with changing solar radiation show as well an increase in the 2m temperature during the last decades but with a too small amplitude. It is shown that observations and simulations with different models support each other which provides some confidence in the results of our simulations, despite of deficiencies in observational data and in model formulations.

1. INTRODUCTION

Large changes of the climate of the earth have been observed in the last centuries and thousands of years on different time scales. Generally it is very difficult to assign such climate changes to specific causes by means of diagnostic studies, an exception may be the climate changes due to changes of the orbital parameters (e.g. Berger, 1978) due to their distinct frequencies. By means of climate simulations with numerical models it is possible to investigate impacts of single external forcings which can help understanding observed climate changes.

A main problem in using model simulations for understanding climate changes lies in the imperfection of the climate models, though errors in the mean fields may not be relevant for impact studies. Another problem lies in insufficient observational data for validating model results and for forcing the climate models. Therefore, international regional and global programs and observational campaigns have been initiated in recent years such as the Global Energy and Water Cycle Experiment (GEWEX) and its subprogramms. Enhanced observations, data collection and coordinated research will lead to both a better understanding of physical processes within the energy and hydrological cycle and an additional database for validating atmospheric models.

In Section 2 we shall demonstrate uncertainties of observed or analysed data on different scales in time and space and suggest data sources for validation. Only data sets which are produced in the environment of numerical weather forecasts provide the complete range of data on all scales in time and space needed for validating climate models. Therefore the use of, and problems associated with, such numerical analysis especially with the recently produced reanalysis data will be addressed.

In Section 3 it will be shown how far the atmospheric model ECHAM4 (Roeckner et al., 1996a) is able to simulate the present day climatology when prescribing observed sea surface temperatures (SSTs). The ability of this model to simulate the large scale circulation and its variability has been shown in several publications (e.g. Bengtsson et al., 1996) and improvements due to the more recent model version are described by several publications, e.g. Roeckner et al. (1996a). Therefore, we shall restrict our study here to the quantities relevant to this investigation. Climate change studies deal mostly with 2m temperatures while this study will address more the hydrological cycle, because it reflects much more the ability of the model to simulate the real atmosphere.

Coupled ocean-atmosphere general circulation models (CGCMs) have been used to simulate the climate of the next century by assuming different scenarios of greenhouse gases according to suggestions by the Intergovernmental Panel on Climate Change (IPCC, 1995). They have also been used to investigate the climate of previous centuries using variable radiation of the sun as estimated by Lean (1997) or by Hoyt and Schatten (1993). Before interpreting such scenario runs, one needs to know how far the models are able to reproduce the mean climatology and the temporal variability of meteorological parameters under present climate conditions. Due to limited computer resources, long-term CGCM simulations can presently be performed only at a relatively low resolution, typically up to a horizontal grid resolution of 2.5° or a T42 spectral resolution (T42 means that any horizontal variability which is shorter than a wavelength of 360°/42 on any great circle cannot be represented). Smaller scale processes like convection have to be parameterized which may result in another model limitation.

In Section 4 the realism of the coupled model will be investigated. Roeckner et al. (1996b) have shown that their coupled model is able to reproduce among others the ENSO phenomenon satisfactorily which is the most dominant interannual variability of the ocean-atmosphere system. This is a requisite for more detailed investigations of climate change.

Results from scenario simulations of the next century based on changing greenhouse gas forcings are shown in Section 5 and compared with scenario simulations using variable solar radiation, which are described Section 6.

Proc. 1st Solar & Space Weather Euroconference, 'The Solar Cycle and Terrestrial Climate', Santa Cruz de Tenerife, Tenerife, Spain, 25-29 September 2000 (ESA SP-463, December 2000)

The resolution in coupled models may be insufficient to distinguish between regions which may have distinctly different climatologies due to orographic effects. The investigation will therefore concentrate on large-scale signals and on regions with strong signals.

2. OBSERVATIONAL DATA

For validating models observational data are required which are averaged in time and space over a grid which is comparable to the scales in the models. Especially for the hydrological cycle this requirement is hardly met. Precipitation data are used to demonstrate problems with observational data for model validation.

Area mean precipitation estimates over land are mostly based on observations at a few stations which are analysed to obtain area means (Rudolf et al., 1992). Currently the highest feasible resolution for an analysis of precipitation on a global scale is a month in time and 2.5° in space. Because of these limitations in data sets based on direct observations, precipitation data from analysis schemes which are used for numerical weather forecasts are useful alternatives. Such schemes use a very large range of observations (wind, temperature, pressure, humidity etc.) from all possible platforms but not 2m temperatures, precipitation or evaporation. The latter quantities are predicted in an atmospheric model which is run within the analysis cycle to provide a first guess for the next analysis time step. In this study we shall rely often on the data from the ECMWF reanalysis (ERA) for the period 1979 to 1993 (Gibson et al., 1997) and from the NCEP reanalysis (NRA) for the period 1958 to 1997 (Kalnay et al., 1996). They are called reanalyses as they have been done recently using the same state-of-the-art scheme for the whole period. The data are not affected by

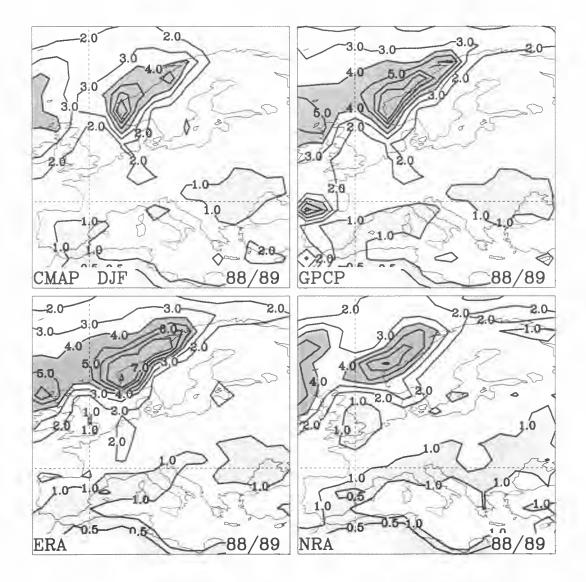


Figure 1: Precipitation during winter 1988/89 as estimated from precipitation related observations (CMAP and GPCP) and simulated in the reanalyses from ECMWF and NCEP(ERA and NRA). Contours at 0.5,1,2,3,4,5,6,7,10 mm/d. Shading for values > 1mm/d and > 4mm/d.

any changes in the analysis schemes in contrast to data from numerical analyses within operational forecasting systems. Variabilities in time arise mainly from atmospheric variabilities but also from changes in quality and distribution of the observational data. Especially the introduction of new observational data, e.g. reports from commercial aircrafts and observations from satellites may introduce artificial trends.

Comparisons of these reanalysis data with observational data or estimates based on precipitation related observations in figure 1 show the limitations of reanalysis data. Estimates of precipitation over Europe for DJF 1988/1989 by CMAP (Xie and Arkin, 1997) and GPCP (Huffmann et al.,1996) are compared with ERA and NRA. A main problem with precipitation analyses based solely on observations results from having a too sparse network. In mountainous areas the observations are often carried out in valleys while most of the precipitation of area means of precipitation. However, the overall similarities in the different estimates provide some confidence in their usefulness, as long as one is not interested in detailed structures.

The quantity used more often in climate change studies is the surface temperature. Also this quantity has quite a few problems e.g. in connection with representativeness and there is also a height dependence of temperature. Because of this lack of representativeness the observed 2m temperatures are not used in ERA. Observational data also suffer from systematic and random errors.

3. MODEL SIMULATIONS

In this study results of numerical experiments with the GCM ECHAM4 (Roeckner et al., 1996a) are used. In the simulations discussed in this section, the atmospheric model was forced with observed sea surface temperatures, SSTs, including sea ice boundaries (Rayner et al., 1996). Observed changes in the greenhouse gas concentration were applied as well.

Atmospheric climate models presently used are able to simulate the main large-scale atmospheric features satisfactorily. Redistribution of incoming solar energy is the key process in the climate system and is closely connected with the global hydrological cycle. The radiation budget of the earth is characterized by an exchange between the earth as a whole including the oceans and the atmosphere and the outer space while we can regard the earth as a closed system with respect to water.

Important components are radiative processes in the free atmosphere including interactions with clouds, generation of precipitation in convective and large scale processes, evaporation at the surface of continents and oceans and condensation of water vapour in the atmosphere. The latter leads to the generation of clouds and further to precipitation in the form of rain and snow. Over land the precipitation is on occasions accumulated as snow, used by vegetation, evaporated again into the atmosphere, stored in the upper layers of the soil or finally discharged by the rivers into the oceans. Present models represent all these processes but do not account for very slowly varying components of the energy and hydrological cycle e.g. the change of inland ice and the changes of water reservoirs in the deep ground which are caused e.g. by the use for irrigation in arid regions.

Limitations in modelling the climate result from a coarse resolution in time and space and from a need to parameterize small scale processes, e.g. the evaporation and condensation of water. These limitations result partly from restrictions in computer resources and partly from our incomplete knowledge of the processes. It has been found that the models can reproduce large-scale features better than small-scale features in space and in time.

On a large-scale and in long-term means over the oceans evaporation exceeds precipitation so that the oceans lose water to the atmosphere. Over the continents, however, precipitation exceeds evaporation and the atmosphere is losing water to the land. Transport from oceans to continents by the atmosphere and back through rivers leads to a closed water budget. It is shown in Table 1 that the ECHAM4 model is able to simulate the global hydrological cycle within the margin of observational uncertainty. The model data are taken from several simulations with the ECHAM4 T42 model which were forced with varying observed SSTs for the period 1979 to 1994.

Table 1 shows clearly that a fundamental quantity such as the global long-term mean of precipitation is only known with an accuracy of about 10%. This corresponds to an uncertainty in the global energy budget of about 10 W/m² for the atmosphere as well as for the surface of the earth, because precipitation contributes efficiently to the energy exchange between the earth and the atmosphere.

On continental scales (Table 2) the differences between simulations and observations are larger, as might be expected. The precipitation over Africa and North America seems to be overestimated by the model.

Table 1: Comparison of simulated and observed (estimated) water transports. Observed (estimated) values are given in brackets. The ranges given for the observations results from 10 different climatologies but only the minimum and maximum values are given. The model results are gained with the ECHAM4 T42 model. Units: 10¹⁵ kg/year.

precipitation (P)	evaporation(E)
oceans 408 [380 to 426]	445 [410 to 441]
continents 113 [109 to 121]	76 [71 to 95]
global 521 [489 to 547]	E = P

Table 2: Comparison of simulated and observed (estimated) precipitation over different continents. The ranges given for the observations result from 3 different climatologies but only the minimum and maximum values are given. The model results are gained with the ECHAM4 T42 model. Units: 10¹⁵ kg/ year.

	model	observations
Africa	24.5	19.1 to 21.9
N. America	17.2	11.0 to 15.2
S. America	27.5	26.1 to 29.7
Asia	28.2	23.9 to 30.7
Australia	4.1	3.0 to 4.1
Europe	6.7	5.5 to 7.1

In figure 2 long-term averages of 2m temperatures and precipitation during the winter season (December to February, DJF) is shown as observed or simulated. The temperatures are simulated cooler over northern Russia and warmer over the Mediterranean Sea than estimated by Legates and Willmott (1990) and there is more precipitation in the simulations in a belt from southern Italy to Turkey and over Russia than in the GPCP analysis. It is not easy to decided which of these fields are more correct but several indications suggest that these are model biases.

The ability of the ECHAM4 model to simulate the interannual variability of a precipitation related quantity is shown in figure 3 by time series of the river discharge of the Paraná river as observed at Posadas or calculated from precipitation minus evaporation in the catchment area of the Paraná in the simulations. The absolute values are in this respect not relevant but one can see that the model is reacting realistically to the SST forcing especially in connection with ENSO. The El Niño event 1982/1983 shows a very strong peak in the river dis-

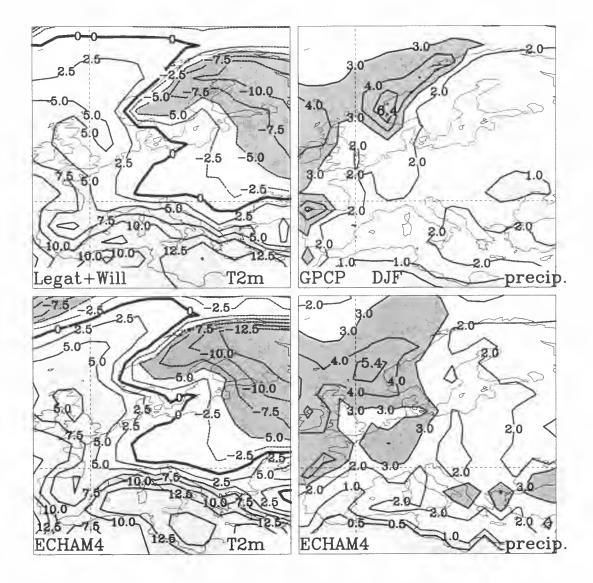


Figure 2: Long-term mean 2m temperatures and precipitation for winter as estimated from observations by Legates and Willmott (1990) and by GPCP and as simulated by the ECHAM4 T42 model when forced with observed SSTs

charge. The correlation between both time series is 0.53. One can recognize in figure 3 as well a steady increase during the 90 years, an observation which will be take up again below.

4. COUPLING THE OCEAN AND THE ATMOSPHERIC MODEL

The CGCM used in this study is based on the ECHAM4 T42 AGCM, which was mentioned already above and on the OPYC-3 ocean model (Roeckner et al., 1996b). Because of systematic errors in both models there is still a flux correction needed but improvements in both models made it possible to restrict this correction to annual means of water and heat. A short description of the models and of the coupling method is given by Roeckner et al. (1996b). Also simulations with the older ECHAM3/ LSG coupled model are used in this study. See Cubasch et al. (1997) and Voss et al. (1998) for more details in the solar forcing runs.

It takes a long time for ocean models to adjust to atmospheric forcings even when starting from an initial field which is close to the observed climatological mean. For this spin-up period the ocean was forced with present day atmospheric data which were either observed or gained from an AGCM with observed SSTs, because the comprehensive data needed for the spin-up are only available for recent periods. Also during the phasing-in

of the coupling between the oceanic and the atmospheric models, present day data were used for controlling both models. Moreover, in the so-called control experiment (CTL), the concentrations of greenhouse gases like carbon dioxide, methane etc, and the solar forcing are fixed at the observed 1990 values so that the simulated CTL climate does represent modern climate.

Roeckner et al. (1996b) demonstrate that their CGCM, in the CTL mode, is able to simulate most large-scale features of the atmosphere and the ocean. They also show a realistic simulation of the ENSO phenomenon.

5. SCENARIO SIMULATIONS: GREENHOUSE GAS IMPACTS

In the greenhouse gas scenario experiment (GHG), the concentrations of the greenhouse gases are prescribed as a function of time. Between 1860 and 1990, the concentration changes are prescribed as observed and from 1990 onward, according to IPCC scenario IS92a (IPCC, 1995). Because of the lack of pre-industrial ocean data, the GHG experiment was initialized with data of the CTL experiment. The associated shift in greenhouse gas concentrations is taken into account by enhancing the observed/projected concentrations of these gases in an appropriate way. Although this approach allows for a correct computation of the radiative forcing, it does not account for the warm bias in the initial state. This initial

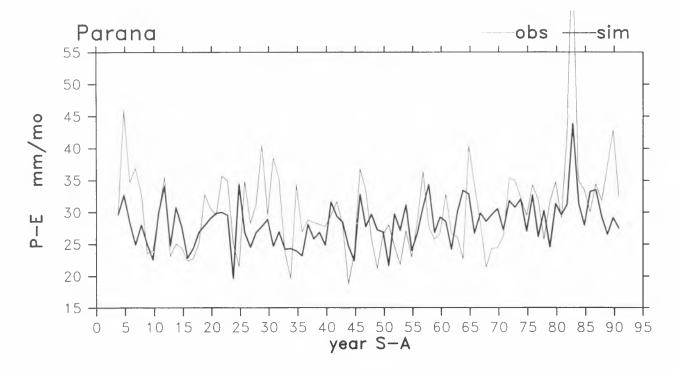


Figure 3: River discharge of the Paraná river, observed at Posadas, and simulated precipitation minus evaporation in the Paraná catchment basin. Annual means for the September to August period.

warm bias, compared to the observations, is maintained throughout the simulation and, therefore, does not affect climatic trends.

Figure 4 shows 2m temperature and precipitation distributions over Europe for winter for the present and in 100 years time in the scenario simulations with the coupled atmosphere ocean model (GHG run). One recognizes a dramatic increase of 2m temperatures in northern Europe of up to 9K. Such an increase can be found all over the northern continents, especially large over northern Siberia. This is also the area where one finds the strongest signal in the observations (Jones, 1994). This enhanced warming in most northern latitudes in winter can be found in simulations by different centres, e.g. Hadley Centre. It might be connected with a decrease of sea ice and snow cover, which has been observed in recent years and which is also simulated by the model. During JJA (not shown) temperature increases are more concentrated to the centres of the continents and have smaller amplitudes.

The patterns of precipitation of the GHG run for the present day climate (1970-1990) are very close to those of the AGCM (ECHAM4 in figure 2). There is a largescale overestimation of precipitation in the AGCM and GHG of the present day climate when compared with GPCP data (see figure 2), however, with realistic distributions of maxima and minima. The impact of the increase of greenhouse gases is an increase of precipitation in northern Europe and a decrease in southern Europe. The increase in northern latitudes can be found almost everywhere around the world not only in simulations at MPI but also in those by the Hadley Centre. Investigations of observations suggests that such a trend has already started in recent decades in northern Europe but the signal is very weak, because a very large interannual and interdecadal variability of this quantity (Arpe and Roeckner, 1999). Trends of temperature and precipitation in observations during the last century are investigated by Schönwiese and Rapp (1997). They show that already in the past an increase of temperature in eastern Europe together with a precipitation increase in northern latitudes occur with similar patterns as predicted for the coming century in figure 4 though with smaller amplitudes.

The decrease of precipitation over the Mediterranean is specific for this area. An uncertainty arises for this area from a systematic error in many models which is a shift of the Azores anticyclone towards Spain in connection with reduced precipitation. This is also an area where a validation with observational data is hampered by the fact that precipitation events occur more sporadic than in northern Europe. Another systematic change with increased greenhouse gases is a concentration of precipitation along the ITCZ, i.e. more precipitation along a narrow band and decreased precipitation in adjacent regions (not shown).

In figure 3 it was shown that one of the big river catchment basins show an increase of river discharge during the last century which is well simulated by the atmospheric model forced with observed SSTs. This increase is similarly simulated by the GHG run.

6. SCENARIO SIMULATIONS: SOLAR FORCING

Increasing the solar radiation has a similar effect as the greenhouse increase: it disturbs the energy balance at the surface which leads as a linear response to an increase of the surface temperature. A main difference is that the greenhouse gas is affecting all latitudes in a similar way while an increase of solar radiation will have no direct impact in polar night areas and increasing impacts towards the equator. This leads to increased baroclinicity, i.e. increases of temperature mainly equator-wards of the main frontal systems. One might expect more impacts on the summer hemisphere. This reasoning applies for the direct impact, but because of the dominate role of the ocean, non-linear interactions and very long time scales this direct impact may not be visible in trend analyses. Voss and Cubasch (2000) indeed show in their figure 2 the main impact in the subtropics and in their figure 3 a stronger impact in the summer hemisphere. However, Rind et al. (1999) associate the larger impact in the tropics and subtropics to a positive feedback with water vapour.

In figure 5 a comparison of northern hemisphere annual mean 2m temperature anomalies during the last centuries is made. A 19 year running mean has been applied to emphasis the long term variability. Biases between the curves are less of concern as each of the data sets may have used different periods of reference for calculating the climatological means. Estimates of observations are those by Mann et al. (1998) and by the Climate Research Unit (CRU, Jones, 1994). The main feature in the estimates based on observations is a strong increase in the 1920s and 1930s and a further increase in the 1980s and 1990s. This general increase during the last century is followed by the GHG model simulation (mainly CO2 increase), also with an increase of 0.7K during the last century. The simulations forced by varying solar radiation, estimated by Lean (1997) - LE- or by Hoyt and Schatten (1993) -HS- show an increase as well but much less than observed or simulated by the GHG run.

All these simulations were carried out with the ECHAM3/LSG T21 model version (Voss et al., 1998) which is now succeeded by the ECHAM4/OPYC T42 version (Roeckner et al., 1996b) for operational use because of its better performance, which was used in the previous sections. There are no simulations available with varying solar radiation with this more recent model

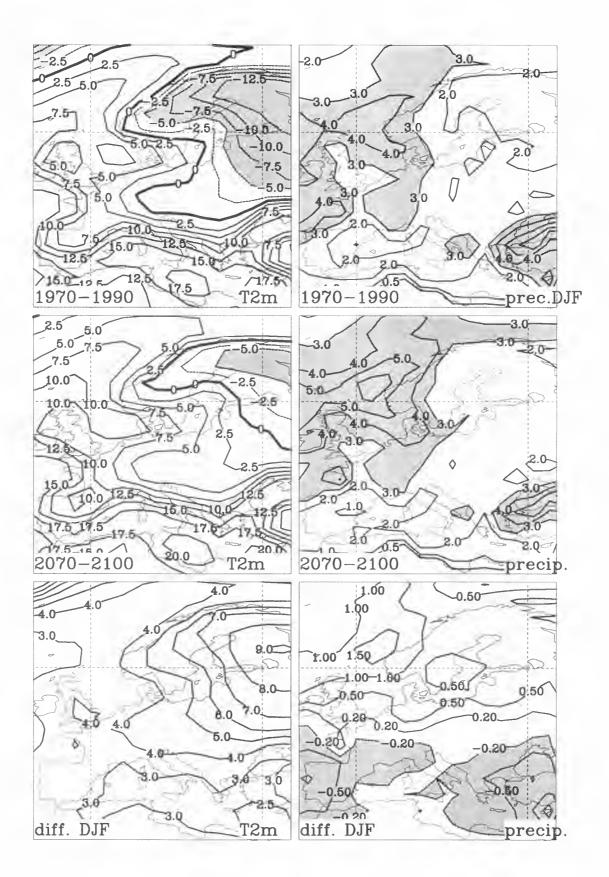


Figure 4: 2 m temperature and precipitation during winter in simulations with the coupled ocean-atmosphere model ECHAM4/OPYC T42 for the present (1970-1990), in 100 years time (2070-2100) and the differences.

version, but GHG simulations show a stronger response than that shown here which is then compensated by an inclusion of forcings from anthropogenic aerosols leading to an even better agreement with observations than that shown in figure 5.

The HS and LE simulations show a clear variability forced from the solar radiation although the solar constant varies in the experiments only between 1363 and 1367 W/m². The estimates from observational data from Mann et al. (1998) show a variability similar to the simulations only for the period 1750 to 1850. This discrepancy may partly result from uncertainties in the estimates of the solar forcing, obvious from the large difference in the forcing estimates by Lean (1997) or by Hoyt and Schatten (1993).

7. CONCLUSION

Model simulations show that the temperature increase in the last decades can be explained by forcings from changes in the greenhouse gas concentrations. Simulations with changing solar radiation show as well an increase in the 2m temperature during the last decades but with a too small amplitude.

This study suffers from a wide range of deficiencies. The model is run only with a low resolution T21 or T42 and many processes had to be parameterized. The forcings for the model are also not well known and not all known forcings are considered in this study, e.g. the one by aerosols. The simulations have been validated with data which are only known with a large margin of uncertainty.

We found that observations and simulations with different models support each other and this provides some confidence in the results of our simulations, despite the uncertainties mentioned above.

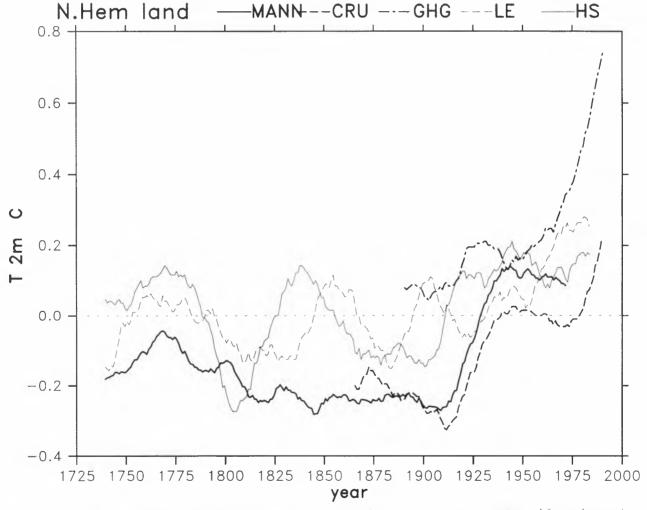


Figure 5: Northern hemisphere annual mean 2m temperature anomalies over continents as estimated from observations by Jones (CRU) and Mann (MANN) and as simulated with the coupled ocean-atmosphere model ECHAM3/LSG T21 assuming different forcings: variable solar radiation as estimated by Lean (1997) -LE- or be Hoyt and Schatten (1993) -HS- or variable greenhouse gases - GHG. A running mean over 19 years has been applied.

ACKNOWLEDGEMENT

This study has been made possible by the technical support of the German Climate Computing Centre (DKRZ). Computing resources were as well provided by the ECMWF special project scheme. The work was supported by the German Ministry for Education, Science Research and Technology (BMBF) and EC project under the Framework IV (EV5V-CT92-0123).

REFERENCES

- Arpe, K. and E. Roeckner, 1999: Simulation of the hydrological cycle over Europe: Model validation and impacts of increasing greenhouse gases. Advances in Water Resources, 23, 105-119.
- Berger, A., 1978: Long-term variations of daily insolation and quaternary climate change. J. Atmos. Sci., 2362-2367.
- Bengtsson, L., Arpe, K., Roeckner, E. and U. Schulzweida, 1996: Climate predictability experiments with a general circulation model. Clim. Dyn. 12, 261-275.
- Cubasch, U., Voss, R., Hegerl, G.C., Waskewitz, J. and T.J. Crowley, 1997: Simulation of the influence of solar radiation variations on the global climate with an ocean-atmosphere general circulation model. Clim. Dyn. 13, 757-767.
- Cubasch U. and R. Voss, 2000: The influence of total solar irradiance on climate. Space Science Reviews, in press.
- Gibson, J.K., Kållberg, P., Uppala, S., Hernandez, A., Nomura, A. and Serrano, E., 1997: ECMWF Reanalysis Project Report Series: 1. ERA description. Available from ECMWF, 71p.
- Hoyt, D.V. and K.H. Schatten, 1993: A discussion of plausible solar irradiance variations, 1700-1992.J. Geophys. Res., 98, 18895-18906.
- Huffman, G.J., Adler, R.F., Arkin, P.A., Chang, A., Ferraro, R., Gruber, A., Janowiak, J., Joyce, R.J., McNab, A., Rudolf, B., Schneider, U. and P. Xie, 1996: The Global Precipitation Climatology Project (GPCP) combined precipitation data set. Bull. Amer. Meteor. Soc., 78, 5-20.
- IPCC, Climate change 1995, the science of Climate Change. Houghton, J.T., Meira Filho, B.A., Callendar, B.A., Harris, N., Kattenberg, A. & Maskell, K. (eds), Cambridge University Press, Cambridge (1996), 572pp.
- Jones, P.D., 1994: Hemispheric surface air temperature variations: a reanalysis and an update to 1993. J. Climate 7, 1794-1802.
- Kalnay, E., Kanamitsu, M., Kistler, R., Collins, W., Deaven, D., Gandin, L., Iredell, M., Saha, S., White, G., Woollen, J., Zhu, Y., Chelliah, M., Ebisuzaki, W., Higgins, W., Janowiak, J., Mo, K.C., Ropelewski, C., Leetmaa, A., Reynolds, R. and Jenne, R., 1996: The NCEP/NCAR Reanalysis Project. Bull. Amer. Meteor. Soc., 77, 437-471.

- Lean, J., 1997: The sun's variable radiation and its relevance to earth. Annu. Rev. Astron. Astrophys., 35, 33-67.
- Legates D.R. and C.J. Willmott, 1990: Mean seasonal and spacial variability in gauge-corrected, global precipitation. International J. of Climatology, 10, 111-127.
- Mann, M.E., Bradley, R.S. and M.K. Hughes. 1998: Global-scale temperature patterns and climate forcing over the past six centuries. Nature, 392, 779-787.
- Rayner, N.A., Hearten, E.B., Parker, D.E., Folland, C.K. and Hacked, R.B. Version 2.2 of the global sea-ice and sea surface temperature data set, 1903-1994. (*Climate Research Technical Note CRTN74, Bracknell, UK*, 1996)
- Rind, D., Lean, J. and R. Healy, 1999: Simulated timedependent climate response to solar radiative forcing since 1600. J. Geophys. Res., 104, D2, 1073-1990.
- Roeckner, E. et al. The atmospheric general circulation model ECHAM-4: Model description and simulation of present-day climate (*Max-Planck-Institute for Meteorology, Hamburg, Report no.* 218, 1996a)
- Roeckner, E., Oberhuber, J.M., Bacher, A., Christoph, M. and I. Kircher, 1996b: ENSO variability and atmospheric response in a global coupled atmosphere-ocean GCM, Clim. Dyn., 12, 737-754.
- Rudolf, B., Hauschild, H., Reifl, M. and U, Schneider. 1992: The calculation of area mean precipitation totals on a 2.5 grid by an objective analyses method. Meteorol. Zeitschrift, N.F. 1, 32-50.
- Schönwiese C.-D. and J. Rapp, 1997: Climate Trend Atlas Europe. Based on Observations 1891-1990. Kluwer, Dordrecht, 228 pp.
- Voss, R., Sausen, R. and U. Cubasch, 1998: Periodically synchronously coupled integrations with the atmosphere-ocean general circulation model ECHAM3/LSG. Climate Dynamics 14, 249-266.
- Voss, R. and U. Cubasch, 2000: Climate response to variations of the solar irradiance since 1700 in coupled AOGCM simulations. Submitted to J. Atmos. and Solar-Terrestrial Physics.
- Xie, P. and P. Arkin, 1997: Global Precipitation: A 17-Year Monthly Analysis Based on Gauge Observations, Satellite Estimates and Numerical Model Outputs. Bull. Amer. Meteor. Soc., 78, 2539-2558.

Correspondence and requests for materials should be addressed to Klaus Arpe, Max-Planck Institute for Meteorology, Bundesstr. 55, D-20146 Hamburg, Germany, e-mail: arpe@dkrz.de.

CALCULATING THE CLIMATIC IMPACTS OF INCREASED CO2: THE ISSUE OF MODEL VALIDATION

Willie Soon^{*}, Sallie Baliunas^{*}, Kirill Ya.Kondratyev,[⊕], Sherwood B. Idso,[♯], and Eric Posmentier^{*} (wsoon@cfa.harvard.edu)

*Harvard-Smithsonian Center for Astrophysics, Cambridge, Massachusetts

and Mount Wilson Observatory, Mount Wilson, California

[⊕]Research Centre for Ecological Safety, Russian Academy of Sciences, St. Petersburg, Russia

⁴US Water Conservation Laboratory, Phoenix, Arizona

*Long Island University, Brooklyn, New York

ABSTRACT

It is commonly believed that increases in man-made greenhouse gases could cause large increases in surface and lower atmospheric temperatures with disastrous global and regional environmental consequences. Because the expected human-made climate forcings are relatively small when compared to various other natural (both internal and external) background and forcing factors, we focus on the important question of climate model validation. We review common deficiencies in general circulation model calculations of atmospheric temperature, surface temperature, precipitation and their complex space-time variability associated with the multiply interacting climate components and feedbacks. These deficiencies also impact our understanding of how Earth's climate responses to external forcing agents such as the natural variations of incoming radiant and particle energies linked to changes in the Sun. We also review examples of expected climatic effects of anthropogenic CO2 forcing.

1. Some Difficulties in Simulating Climate Variables

Consider the nominal, globally-averaged number of 2.5 W m^{-2} that is associated with the total radiative forcing by all anthropogenic greenhouse gases (GHGs). Or, a doubling of CO₂ concentration¹ uniformly mixed throughout the atmosphere that adds about 4 W m⁻² to the troposphere-surface system.

In order to appreciate the scientific difficulties associated with finding climatic changes induced by the an-

thropogenic CO₂ forcing, one may start by analyzing the energy budget of the climate system. First, consider the "artificial flux adjustments",² some as large as 100 W m⁻² locally, utilized by certain GCMs to minimize unwanted drift in the ocean-atmosphere coupled system (e.g., Murphy 1995; Glecker & Weare 1997; Cai & Gordon 1999; Yu & Mechoso 1999). Next, consider the uncertain global energy budgets that vary by at least 10 W m⁻² in the empirically deduced fluxes of shortwave and longwave radiation, and latent and sensible heat within the surface-atmosphere system (see Table 1 of Kiehl & Trenberth 1997).

These artificially-modified and uncertain energy balance components impose severe constraints on our ability to find the climatic imprint of a mere 4 W m⁻² associated with anthropogenic CO₂ forcing over 100 to 200 years. Those uncertainties explain why all current GCM studies of the climatic impacts of increased atmospheric CO₂ are expressed in terms of *relative change* based on control, or unforced, experiments that are known a priori to be incomplete in their forcing and feedback physics.³ More important, it is premature to conclude — based only on the rate of change of forcing (e.g., 4 W m⁻² for anthropogenic CO₂ versus the 0.4 W m⁻² for July insolation changes at 60°N by the Earth's

Proc. 1st Solar & Space Weather Euroconference, 'The Solar Cycle and Terrestrial Climate', Santa Cruz de Tenerife, Tenerife, Spain, 25-29 September 2000 (ESA SP-463, December 2000)

¹The quantitative details and the rate at which this forcing is imposed upon our atmosphere ranges from the observed rate of increase of CO_2 concentration over the past 30 years of about 0.4% per year to the more inflated increment of 1% to 4% (!) per year in some GCM experiments, but that is not the primary concern of our discussion now.

²In addition to the heat flux adjustment considered here, nonphysical flux adjustments for freshwater, salinity and wind stress (momentum) are also applied in many contemporary GCMs.

³In Soon *et al.* (1999), we briefly summarized the problems associated with, for example, models' underestimation or incorrect prediction of natural climate change on decade to century timescales. Some of the problems may be connected to difficulties in dealing with many of the suspected climate forcings, such as volcanic eruptions, stratospheric ozone variations, sulfate aerosol changes and solar particle and light variations. Another strongly coupled predicament is the inability of short climate records to capture the essential range of natural variability that would provide confidence in probability assessments of potential climatic changes on decades to centuries.

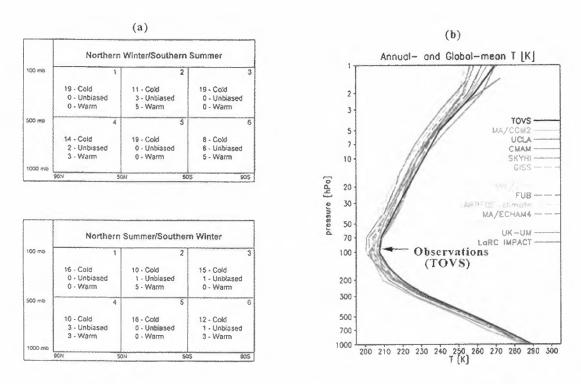


Fig. 1.— (a) Illustration of the cold-temperature bias problem in the troposphere in simulations produced by 14 different GCMs. Indicated in each box are the model temperature biases relative to observations [From Johnson 1997]. Regions 1, 3 and 5 gave unanimous verdicts for the models' cold bias. (b) Note that the cold-bias problem (most GCMs curves lie to the left of the observed temperature line labeled TOVS) extends into the stratosphere. [From Pawson *et al.* 2000]

orbital variations in about 100 years as contrasted by Houghton 1991) — that the climatic effects of man-made CO_2 will overwhelm the more *persistent* effects of a positional change in the Earth's rotation axis and orbit. The latter type of climate change is suspected to be the cause of historical glacial and inter-glacial climate oscillations, while the potential influence of added CO_2 can only be guessed from our experiences in climate modeling.

Historical evidence also indicates that large, abrupt climatic change occurs naturally and not uncommonly (e.g., Alley 2000). In historical records, phase differences seen between atmospheric CO_2 and proxy-temperature indicate that atmospheric CO_2 sometimes follows rather than leads temperature and biosphere changes (e.g., Priem 1997; Dettinger & Ghil 1998; Fischer *et al.* 1999; Indermühle *et al.* 1999). Our point is that in order to have the anthropogenic or natural CO_2 forcing as the cause or trigger for rapid climate change, various complex climatic feedback and amplification mechanisms must operate. Most of those mechanisms for rapid climatic change are neither sufficiently known nor understood (e.g., Marotzke 2000; Stocker & Marchal 2000). [Apparently, a fast trigger like increased atmospheric methane from rapid release of trapped methane hydrates in permafrosts and on continental margins may be a key ingredient for amplification or feedback leading to large climatic change (Kennett *et al.* 2000).]

If natural and largely uncontrollable factors that yield rapid climate change are common, are humans capable of actively modifying climate for the better? Such a question has been posed and cautiously answered in the negative, e.g., by Kellogg & Schneider (1974). Given current concerns about rapid climate change, several geoengineering proposals are being revived and debated in the literatures (e.g., Schneider 1996; Govindasamy & Caldeira 2000). We argue that even if climate is hyper-sensitive to small perturbations in radiative forcing, the task of understanding climate processes must still be first accomplished before any effective actions can be taken.

1.1. Temperature

How well do GCMs actually simulate atmospheric temperatures? As emphasized by Johnson (1997), it has been known since IPCC (1990) that all GCMs suffer from the "general coldness problem," particularly in the lower tropical troposphere and upper polar troposphere (regions 1, 3 and 5 in Figure 1a). This problem exists in 104 out of 105 possible outcomes from 35 different simulations by 14 climate models. Boer *et al.* (1992) have labeled such common deficiencies as 'systematic,' 'tenacious,' 'insensitive,' 'universal,' and 'essential.'

What causes the systematic errors? Johnson (1997) suggested that temperature responses of GCMs could suffer from extreme sensitivity to systematic aphysical entropy sources introduced by spurious numerical diffusion, Gibbs oscillations and inadequacy of sub-grid-scale parameterizations. The analysis of Egger (1999) seems to support this suggestion and calls for the evaluation of high order statistical moments like entropies to check on the quality of numerical schemes in climate models.

The coldness problem also extends to the stratosphere (Figure 1b), where Pawson *et al.* (2000) showed that the cold bias is more uniformly distributed. Therefore, they suggest that this particular problem is most likely associated with underestimation of radiative heating rates (i.e., too little absorption of solar radiation by ozone in the near infrared) or too much longwave emission in the middle atmosphere. Other needed critical improvements relate to the physical representation of gravity wave momentum deposition in the stratosphere and mesosphere, as well as problems associated with the generation of gravity waves in the troposphere (McIntyre 1999).

How about surface temperatures? Notable here is the recent evaluation by Bell *et al.* (2000) of the interannual changes in surface temperature of the control (unforced) experiments from 16 different coupled ocean-atmosphere GCMs of the CMIP.⁴ Bell *et al.* found that the majority of the GCMs significantly underestimate the observed, detrended global surface temperature variability over the oceans (Figure 2's panel b) while overestimating the variability over land (Figure 2's panel c). The most decisive illustration of the biased results from all GCMs comes from the ratio of the over-land to over-ocean temperature variability in panel (d) of Figure 2. The authors mention factors such as external forcing agents (CO₂, solar variability and volcanic eruption) and GCMs' underestimation of ENSO⁵ variability as possible causes of the systematic discrepancy between observed and GCM-predicted interannual temperature changes. They eventually pin the discrepancy to non-physical representations of land surfaces that lead to low soil moisture (which yields artificially greater land temperature variability) than more realistic land surface schemes. Bell et al. also point out another problem faced by many GCMs: too much variability in the model's surface temperatures both over land and sea at high latitudes. Here, excessive interannual variability in the coverage of snow and sea ice in the GCMs is noted.

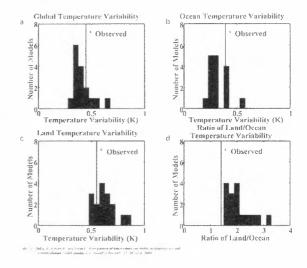


Fig. 2.— Comparisons of detrended 1959-1998 observed surface temperature variability with the unforced results from 16 different GCMs of the CMIP. (Temperature variability is calculated from the r.m.s. standard deviation of the 40 annually averaged data.) The statistically significant difference in the observed and GCM ratios of the land/ocean variability (panel d) has been shown to be associated with the unphysical parameterization of land surface processes. [From Bell *et al.* 2000]

The result of Bell et al. (2000) is not surprising,

⁴Coupled Model Intercomparison Project.

⁵El Niño-Southern Oscillation

246

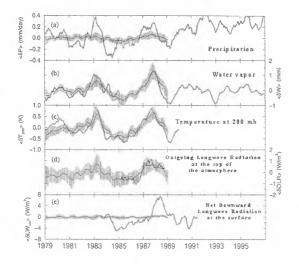


Fig. 3.— Comparison of the observed (thick solid line) tropical-mean interannual variations of (a) precipitation $[\langle \delta P \rangle]$, (b) total precipitable water vapor $[\langle \delta W \rangle]$, (c) temperature at 200 mb $[\langle \delta T_{200} \rangle]$, (d) outgoing longwave radiation (OLR) at the top of the atmosphere $[\langle \delta OLR \rangle]$, and (e) the net downward longwave radiation at the surface $[\langle \delta LW_{sfc} \rangle]$ with the ensemble-mean of 30 AMIP GCM results (the thin solid curve overlaid with vertical lines showing the range of one intermodel standard deviation of the ensemble mean). Contrast the good agreement for simulated water vapor, temperature and OLR but the *internally inconsistent* results for precipitation and net surface longwave radiation. (All climate simulations were forced with observed SST). [From Soden 2000]

as physical modeling of land processes are particularly difficult with so many unknown factors and their large ranges of uncertainties. For example, Pitman et al. (1999) documented that for tropical forest, the annually averaged simulations varied by 79 W m^{-2} for the sensible heat flux and 80 W m^{-2} for the latent heat flux in 16 different GCMs. Over grassland, the range was 34 W m^{-2} and 27 W m^{-2} respectively. The models' simulations of temperature varied by 1.4 K for tropical forest and 2.2 K for grassland. Another important concern is the tradeoff between increasing realism in model representations of land processes and the risk of crossing the threshold of undesired complexity. There are new types of drift in climate variables now recognized in GCMs with explicit treatments of land surface variables like soil moisture or snow water mass (e.g., quantified in terms of systematic and incremental drifts in Dirmeyer 2000).

1.2. Precipitation

Soden (2000) documented another important but puzzling behavior in the current generation of GCMs. In this case, the systematic problem comes from the inability of the ensemble of some 30 different atmospheric GCMs in the $AMIP^6$ to produce the interannual changes in the precipitation observed over the Tropics (averaged over 30°N and 30°S). Figure 3 highlights the important comparison of the agreement for the GCM simulations of the amount of water vapor, tropospheric temperature at 200 mb and outgoing longwave radiation (OLR) versus the disagreement for precipitation and net downward longwave radiation to the surface. This comparison emphasizes that the agreements are fortuitous because the atmospheric GCMs were forced with observed sea surface temperatures (SSTs), while the modeled interannual variabilities of the hydrologic cycles are seriously underestimated by a factor of three to four. From the hint of the relatively constant value of the downward longwave flux reaching the surface (Figure 3's panel e), Soden (2000) points to possible systematic problems in current GCM representations of low-lying boundary layer clouds. The study, however, cannot exclude possible errors in the precipitation data from satellites and thus calls for improved precipitation products.

Another problem in hydrology is the the unphysical, negative specific humidity (!) associated with the steep topography of the Northern Hemisphere extra-tropics (see Rasch & Williamson 1990; Schneider *et al.* 1999).

1.3. Clouds

As an illustration of the representation of clouds in GCMs, we show in Figure 4 the parameterization of the large-scale formation of cloud cover that is used in one state-of-the-art GCM (Yang *et al.* 2000). Cloud cover is very sensitive to relative humidity, U, and to both U_s, the saturated relative humidity within the cloud, and U₀₀, the threshold relative humidity at which condensation begins. The creators of this GCM discuss, for example, how the formula is used to tune

⁶Atmospheric Modeling Intercomparison Project.

Table 1: Observations and predictions of seasonal and annual Northern Hemisphere (NH) equator-to-pole surface temperature gradients (in $^{\circ}C$ per 5 $^{\circ}$ latitude; EPG) and ocean-land surface temperature contrasts (in $^{\circ}C$; OLC). [From Jain *et al.* 1999]

	EPG			OLC		
	Annual	Summer (JJA)	Winter (DJF)	Annual	Summer (JJA)	Winter (DJF)
NH observations	-3.1	-2.0	-3.9	0.3	-5.5	6.5
GCM unforced	-2.9	-1.7	-3.8	3.8	-3.8	11.4
GCM CO ₂ -forced	-2.7	-1.6	-3.6	3.3	-4.4	10.9

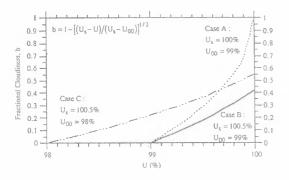


Fig. 4.— On the large sensitivity of parameterized cloud cover (contrasted by cases A, B and C) to relative humidity, U, and to values of U_S, the saturated relative humidity within the cloud and U_{00} , the threshold relative humidity at which condensation begins. [From Yang *et al.* 2000]

the formation of clouds by 20-30% through large-scale condensation at high latitudes or near polar regions in order to match what is observed.

Yao & Del Genio (1999) reported that even for a scenario with the most sophisticated and realistic large-scale cloud formation and moist convection schemes, their GCM model results are still about 6° C warmer than the observed temperature at the South Pole and about 2° C cooler elsewhere in both polar regions. The model is also noted to be too warm at sea-ice margins but too cold in the poorly observed southern midlatitudes. Finally, Yao & Del Genio explained that their model results are within 1° C at other latitudes (i.e., the tropics) because "the implied ocean heat transports are defined to be consistent with observed sea surface temperatures."

Clearly, the parameterization of cloud formation processes remains a major challenge in the climate modeling enterprise.

2. Expected Outcomes of CO₂ Forcing

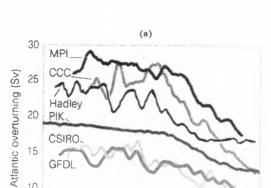
Given the difficulties and unknowns in parameterizations of important climatic processes and variables, what do models predict for an increased CO_2 forcing scenario? Let's look at three examples.

First, is the change in CO_2 forcing expected to alter the character of the seasonal temperature cycle? If so, how do predictions compare to what has been observed. at least over the last few decades?

Jain *et al.* (1999) examined this question by considering three parameters for the Northern Hemisphere (NH) surface temperature: (a) the mean temperature's amplitude and phase; (b) the equator-topole surface temperature gradient (EPG); and (c) the ocean-land surface temperature contrast (OLC).

A comparison between observed and modeled EPG and OLC climatologies is summarized in Table 1. The results show that changes expected from the added CO_2 forcing are typically smaller than the differences between the unforced GCM and observed values in EPG and OLC. So, detecting differential CO_2 effects in seasonal differences in EPG and OLC is not straightforward.

Jain *et al.* (1999) also found significant differences between observed interannual and decadal trends for both EPG and OLC and results from CO₂-forced climate



Hadley

CSIRO.

GFDL

1900

20 PIK

15

10

5

1850

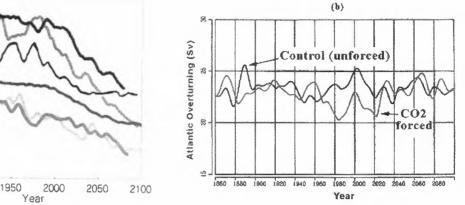


Fig. 5.— Predicted large changes (20-50% reductions in overturning rate by 2100 A.D.) in the thermohaline circulation (THC) under [a] a CO₂-forced scenario for six different coupled climate models [from Rahmstorf 1999] and [b] a state-of-the-art MPI GCM with improved spatial resolution of tropical ocean [from Latif et al. 2000]. The quantity shown is the maximum North Atlantic overturning flowrate in Svedrups $(10^6 \text{ m}^3 \text{ s}^{-1})$ at a depth of about 2000 m. Apparently, with an improved representation of the air-sea interactions in the Tropics, the major weakening (or even collapse under stronger and persistent forcing) of the THC predicted by earlier GCMs no longer holds true.

experiments. For example, the CO₂-forced run predicts a statistically significant increase in amplitude (and delay in phase) for the seasonal cycle of OLC, but no such change is observed. Worst yet, even the unforced experiment yielded a statistically significant increase in the amplitude of the OLC seasonal cycle, which makes the search for a CO_2 -forced signal in this parameter almost impossible. Furthermore, it was found that the amplitude of the annual cycle of the NH surface temperature decreases in a way consistent with CO₂forced experiments. But the observed trend in seasonal phase shows an advance of the seasons, contradicting the delay predicted by the models. Jain et al. offered three explanations for the disagreement: model flux corrections, significant impact of low-frequency natural variability and sampling limitation in observational data. Therefore, seasonal cycles are probably not useful "fingerprints" for the impact of anthropogenic CO_2 .

Next, consider clouds. Given the complexity of representing relevant processes for clouds, can one find a probable CO₂-forced imprint in them?

First, as Yao & Del Gino (1999) have commented, it is misleading to claim that under a CO₂-induced warming climate with more evaporation, an increasing cloud cover is expected, because cloud cover depends more closely on relative humidity than specific humidity. Under CO_2

doubling experiments with different parameterization schemes, Yao & Del Gino (1999) predicted a decrease in global cloud cover but showed that there is an increase in middle- and high-latitude continental cloudiness. They also cautioned that because "a physical basis for parameterizing cloud cover does not yet exist," all predictions about cloud changes should be viewed critically.

Other authors, like Senior (1999), have emphasized the importance of including parameterizations of interactive cloud radiative properties and called for a common diagnostic output like the water path length within the cloud in control (unforced) experiments. Rotstayn (1999) implemented detailed microphysical processes of a prognostic cloud scheme in a GCM and found a large difference in the climate sensitivity from an experiment with a diagnostic treatment of clouds. A stronger water vapor feedback was noted in the run with the prognostic cloud scheme than in the run with the diagnostic scheme, which in turn caused a strong upward shift of the tropopause upon warming. Rotstayn found that an artificial restriction on the maximum heights of high clouds in the diagnostic scheme largely explained the differences in the climatic responses. It is in the midst of this incremental learning that we conclude there are no reliable predictions of expected responses of clouds to increased CO_2 in the air.

Third, consider the oceans. Under an increased atmospheric CO₂ forcing, one commonly predicted transient response is the weakening of the North Atlantic thermohaline circulation (THC) owing to the net increase in freshwater fluxes (e.g., Dixon *et al.* 1999; Rahmstorf & Ganopolski 1999; Russell & Rind 1999; Wood *et al.* 1999; see Figure 5a). In one GCM experiment, Russell & Rind (1999) explained that despite a global warming of 1.4° C near the time of CO₂ doubling, large regional coolings of up to 4° C occurred in both the North Atlantic Ocean (56-80°N, 35°W-45°E) and South Pacific (near Ross Sea, 60-72°S, 165°E-115°W),⁷ because of reduced meridional poleward heat transfer over the North Atlantic and local convection over the South Pacific.

More important, and somewhat surprising, Latif et al. (2000) have just reported a new stabilization mechanism that results in no THC weakening (see Figure 5b). Their MPI⁸ state-of-the-art coupled ocean-atmosphere GCM resolved the tropical oceans at a meridional scale of 0.5° rather than the more typical scale of 2-6°, and made the MPI GCM better adapted for studying the ENSO phenomenon. When forced under an increasing CO₂ scenario, it produced no weakening of the THC. Latif et al. showed that anomalously high salinities in the tropical Atlantic (initiated by excess freshening over the equatorial Pacific) were advected poleward to the sinking region of the THC, and the effect is apparently sufficient to compensate for local increases in freshwater influx. Hence, with the additional stabilizing degree of freedom from the tropical oceans, the THC remains unchanged in the CO₂-forced experiment. Thus, there is no credible expectation of a "disastrous" change in the oceanic circulation over the North Atlantic under a CO₂-forced climate.

Many questions remain open regarding what one can conclude from the current generation of GCMs about the CO2-induced modifications of Earth's climate. The climatic impacts of increases in atmospheric CO₂ are not robustly ascertained. In fact, even the range of modeled global warming remains large and not physically well constrained (e.g., Forest et al. 2000). For example, the aggregate of various GCMs gives a global climate sensitivity that ranges from 1.5 to 4.5°C (e.g., p. 34 of IPCC 1996) for an equilibrium response to a doubling of atmospheric CO_2 concentration. Räisänen (1999) optimistically emphasized that many of the seemingly qualitative inter-model disagreements in CO2-forced climate responses (including differing signs of predicted response in variables such as precipitation and soil moisture) could be attributed largely to differences in the internal variabilities of different climate models. On the other hand, Forest et al. (2000) utilized the MIT statistical-dynamical climate model to quantify the probability of expected outcomes by performing a large number of sensitivity runs, i.e., by varying the cloud feedback and the rate of heat uptake by the deep ocean. They found that the IPCC's range of equilibrium climate sensitivity of 1.5 to 4.5°C corresponds roughly to only an 80% confidence interval under a particular optimal value of global-mean vertical thermal diffusivity below the ocean's mixed layer. The 95% probability range for the climate sensitivity is quantified by Forest et al. to be 0.7 to 5.1°C. In the final analysis, Forest et al. (2000) gave the more relevant result for transient responses to a doubling of atmospheric CO₂ to be an increase in global temperature between 0.5 and $3.3^\circ\mathrm{C}$ at the 95%confidence level.

Attribution of causes of recent climatic change. Other more specific attempts to "fingerprint" CO_2 forcing by comparing observed and modeled changes in the structure of vertical temperature profiles⁹ have

⁷See, however, a later paper by Russell *et al.* (2000), where the predicted regional changes over the Southern Ocean are admitted to be unreliable because of the model's excessive sea ice variability. The high-latitude southern ocean is also well-documented to suffer from large climate drift (Cai & Gordon 1999). For example, within 100 years of coupling the atmosphere to the ocean, the Antarctic Circumpolar Current intensifies by 30 Sv (from 157 to 187 Sv), despite the use of flux adjustment. Cai & Gordon identified the instability of convection pattern in the Southern Ocean to be the primary cause of the problem.

⁸Max Planck Institut für Meteorologie at Hamburg.

⁹Here, we also wish to add that the commonly misapplied claim of surface or tropospheric warming together with (lower) stratospheric cooling as a "fingerprint" of CO_2 is in fact false. Such a pattern of change is a natural behavior of the atmosphere associated with potential vorticity anomalies in the upper air's flow structure (see e.g., Hoskins *et al.* 1985; Liu & Schuurmans 1990). This note is relevant because it precludes any affirmative statements being made about the unique detection of anthropogenic CO_2 "fingerprints" unless more is understood about natural atmospheric variability.

revealed more insights into areas for improved model physics, such as the unrealistically coherent coupling between the tropical lapse rate and mean temperature for variability over timescales of 3 to 10 years (e.g., Gillett et al. 2000). Recent efforts, such as that of Bengtsson et al. (1999), have highlighted the inconsistency between the differing observed surface and tropospheric temperature trends and the simulated GCM trends that include forcing factors like the combined anthropogenic GHGs, anthropogenic sulfate aerosols (both direct and indirect effects), stratospheric aerosols from Mount Pinatubo eruption, as well as changes in the distribution of tropospheric and stratospheric ozone. In addition, Roeckner et al. (1999) discuss how adding other forcing components, like direct and indirect aerosol effects, to the GHG forcing has led to a somewhat unexpected weakening in the intensity of the global hydrologic cycle.

Nonlinear dynamical perspective on climate change. A somewhat different interpretation of recent climate change is also possible (Corti et al. 1999; Palmer 1999). In an analysis of the Northern Hemisphere's 500-mb geopotential heights, the authors show that the record since the 1950s could essentially be projected in terms of the modes of four naturally occurring, shorter-term, atmospheric circulation regimes.¹⁰ Then, climate variability, viewed as vacillations among these quasi-stationary weather regimes, can be quantified by changes in the probability density function associated with each regime. Indeed, Palmer and colleagues proposed that the impact of anthropogenic CO₂ forcing may be revealed as a projection onto modes of these natural circulation patterns and weather regimes. But there is no guarantee that the underlying structure of the weather regimes would remain the same under the perturbation of a different or stronger forcing.

Next, the authors showed that recent observed changes could be interpreted primarily as the increasing probability associated with the Cold-Ocean-Warm-Land circulation pattern (COWL regime as earlier studied by Wallace *et al.* 1995 or regime labeled cluster A in Corti *et al.* 1999), perhaps consistent with the projection of anthropogenic CO₂ forcing. In this view, the authors proposed to resolve the contentious discrepancy between the rising trend in surface temperature versus the relative constancy of the lower tropospheric temperature (i.e., as summarized in the report of NRC 2000). The rationale employed was that most of the recent hemispheric-mean temperature change is associated with the COWL pattern. And since the COWL pattern is primarily a surface phenomenon, one can therefore expect to find a stronger anthropogenic CO₂-forced temperature imprint at the surface than in the troposphere. Away from the surface, the land-sea contrast weakens significantly, so that no imprint of anthropogenic thermal forcing anomalies persist there.

None of the current GCMs has yet simulated such a pattern of observed change. The strongest anthropogenic CO₂ pattern of response in GCMs is still expected in the middle to high troposphere, simply because of the dominance of direct radiative effects. How the surface and the column of air in the troposphere are coupled is not well understood. This particular problem is likely to modify conclusions of much recent exploratory research efforts to partition roles between various natural (volcanic, solar and internal unforced climate variability) and anthropogenic forcings (CO2, sulphate aerosols and ozones) that adopted either instrumental or proxy surface temperatures as their sole evidential constraints (Lean et al. 1995; Soon et al. 1996; Overpeck et al. 1997; Mann et al. 1998; Tett et al. 1999; Andronova & Schlesinger 2000; Crowley 2000).

A further question left unanswered by Corti et al. (1999) is why increased CO_2 should lead to an increase in the residence frequency of the COWL regime. Any of several warming influences may contribute to the positive bias of COWL because the main physical cause of the pattern is the differential heat capacity between land and sea. In this respect, it is important to point out that the COWL pattern is a robust feature of unforced climate experiments under various air-sea coupling schemes tested by Broccoli et al. (1998). But as emphasized by those authors, even though a direct comparison of observations with model-derived unforced patterns and changes "has implications for the detection of climate change, [they] do not intend to attribute the recent warming of Northern Hemisphere land to specific causes." Broccoli et al. thus concluded that separating forced and unforced changes in observational records is difficult and ambiguous.

¹⁰Identified in Corti *et al.* (1999) as Cold-Ocean-Warm-Land, Pacific North American Oscillation, North Atlantic Oscillation and Arctic Oscillation circulation patterns.

Interpreting climate change under such a non-linear dynamical perspective imposes a strong requirement that GCMs accurately simulate natural circulation regimes and their associated variabilities down to regional and synoptic scales.¹¹ This particular requirement is especially difficult to fulfill, because the global radiative forcing of a few W m⁻² expected from anthropogenic CO_2 is so small compared to the uncertain energy budgets of various components of the climate system as well as flux errors in model parameterizations of physical processes. Consequently, significant challenges in numerical weather and climate modeling remain.

New observational scheme. To obtain more confidence in climate modeling, a substantial advancement in observational capability is needed. Improved precision, accuracy, and global coverage are all important requirements. For example, Schneider (1994) has estimated that a globally averaged accuracy of at least 0.5 W m⁻² in net solar-IR radiative forcing is needed in order to realistically resolve the present unacceptably large range of estimates of climate sensitivity. In this respect, Goody et al. (1998) have recently proposed the complementary scheme of interferometric measurements of spectrally resolved thermal radiance and radio occultation measurements of refractivity (with help from GPS¹² satellites) that can achieve global coverage with an absolute accuracy of 1 cm^{-1} in spectral resolution and 0.1 K in thermal brightness temperature. The sensitivity of 0.1 K is needed to quantify expected warming from increased greenhouse gases in one decade, while the resolution of 1 cm⁻¹ is needed to aim towards recognizing differences in possible spectral radiance fingerprints among several causes (see e.g., Figures 6 and 7 of Goody et al. 1998). With the promised high vertical resolution of about 1 km, the complementary thermal radiances and GPS refractivity measurements may lead to a better understanding of clouds. These observational schemes offer hope, not only to critically test climate model predictions, but to provide for early detection of anthropogenic CO₂ effects before they may become too large.

4. Social Comments

This talk has been largely an apology for our lack of understanding of Earth's climate system. To date, we do not know whether man-made CO_2 has caused, or will cause, the climate to change for better or for worse. There is clear evidence for beneficial effects of enhanced CO_2 on plants (Idso & Idso 1994); but the complete aspects of CO_2 impacts on society are not so easily evaluated. There are widely differing views on plausible theoretical expectations of anthropogenic CO_2 effects, ranging from dominant radiative imprints in the upper and middle troposphere (based on GCMs results) to nonlinear dynamical responses. At the current level of understanding, a disastrous global and regional environmental change from increasing atmospheric CO_2 is neither a quantifiable nor a scientific proposition.

As for a second opinion on our evaluation of climate models' systematic errors, the thoughts of Bryson (1993) are applicable: "A model is nothing more [sic.] than a formal statement of how the modeler believes that the part of the world of his concern actually works. It may be simple or complex. ... Because of the size and complexity of the climate system, no set of equations, and thus no mathematical model, has yet been devised to describe or simulate adequately the complete behavior of the system. ... it may be many years before computer capacity and human knowledge [sic.] are adequate for a reasonable simulation. This is not to say that present computer simulations are useless-they are simply not terribly good yet. For example, the average error of the largest, most complex GCM simulations of the present rainfall is well over 100 percent. The temperature errors are impressively large also-up to twenty degrees Centigrade for Antarctica, ten degrees in the Arctic, and two to five degrees elsewhere. The main models in use all have similar errors, but this is hardly surprising, since they are all essentially clones of each other."

Thus, the problems in our inability to simulate present-day climate change are substantial. The perspective from nonlinear dynamics — which suggests that "confidence in a model used for climate simulation will be increased if the same model is successful when used in a forecasting mode" (IPCC 1990, as quoted in Palmer 1999) — also portends a most difficult task ahead.

¹¹This requirement has led Palmer to say that this possible shift in detection strategy towards very local patterns of change is "the very antithesis of the global greenhouse effect."

¹²Global Positioning System.

Oreskes *et al.* (1994) has further reminded us all that because natural systems are never closed and model results are always non-unique, it is *impossible* to have a verified and validated numerical climate model. Therefore, the proper role of a model is to *challenge* existing formulations (i.e., a climate model is built to test proposed mechanisms of climate change) rather than to *predict* unconstrained scenarios of change by adding CO_2 to the atmosphere.

Available documentary evidence tells us that climate change significantly influences human activity. It is thus high time for us to address the scientific question of whether the reverse influence could really be detectable on a global extent, especially from the increased anthropogenic CO_2 in our air. As a start, it would certainly be helpful for all climate scientists and many more from other fields of research, including economists, social scientists and law-makers interested in public policy, to begin working together to distinguish between what one may consider climate uncertainties versus what one should admit as climate unknowns.

Acknowledgments

This work was supported by the National Aeronautics and Space Administration (Grant NAG5-7635). W. Soon thanks Manolo Vázquez, chairperson of this first Solar and Space Weather (SOLSPA) Euroconference organizing committee, for the kind invitation and travel support. E. S. P. acknowledges the support of the Long Island University Faculty Research Released Time program.

References

Alley, R., Ice-core evidence of abrupt climate changes, Proc. Natl. Acad. Sci. (USA), 97, 1331-1334, 2000.

Andronova, N. G., and Schlesinger, M. E., Causes of global temperature changes during the 19th and 20th centuries, *Geophys. Res. Lett.*, 27, 2137-2140, 2000.

Bell, J., Duffy, P., Covey, C., Sloan, L., and the CMIP investigators, Comparison of temperature variability in observations and sixteen climate model simulations, *Geophys. Res. Lett.*, 27, 261–264, 2000.

Bengtsson, L., Roeckner, E., and Stendel, M., Why is the global warming proceeding much slower than expected? *J. Geophys. Res.*, 104, 3865-3876, 1999.

Boer, G. J., Arpe, K., and 12 co-authors, Some results from an intercomparison of the climates simulated by 14 atmospheric General Circulation Models, *J. Geophys. Res.*, 97, 12771-12786, 1992.

Broccoli, A. J., Lau, N.-C., and Nath, M. J., The Cold Ocean-Warm Land pattern: Model simulation and relevance to climate change detection, *J. Clim.*, 11, 2743–2763, 1998.

Bryson, R. A., Environment, environmentalists, and global change: A skeptic's evaluation, *New Lit. Hist.*, 24, 783-795, 1993.

Cai, W., and Gordon, H. B., Southern high-latitude ocean climate drift in a coupled model, J. Clim., 12, 132-146, 1999.

Corti, S., Molteni, F., and Palmer, T. N., Signature of recent climate change in frequencies of natural atmospheric circulation regimes, *Nature*, 398, 799-802, 1999.

Crowley, T. J., Causes of climate change over the past 1000 years, *Science*, 289, 270-277, 2000.

Dettinger, M. D., and Ghil, M., Seasonal and interannual variations of atmospheric CO_2 and climate, *Tellus*, 50B, 1–24, 1998.

Dijkstra, H. A., and Neelin, J. D., Imperfections of the thermohaline circulation: Multiple equilibria and flux correction, J. Clim., 12, 1382–1392, 1999.

Dirmeyer, P. A., Climate drift in a coupled landatmosphere model, *J. Hydrometeorol.*, 1, in press, 2000.

Dixon, K. W., Delworth, T. L., Spelman, M. J., and Stouffer, R. J., The influence of transient surface fluxes on North Atlantic overturning in a coupled GCM climate change experiment, *Geophys. Res. Lett.*, 26, 2749-2752, 1999.

Egger, J., Numerical generation of entropies, *Mon. Wea. Rev.*, 127, 2211-2216, 1999.

Fischer, H., Wahlen, M., Smith, J., Mastroianni, D., and Deck, B., Ice core records of atmospheric CO_2 around the last three glacial terminations, *Science*, 283, 1712–1714, 1999.

Forest, C. E., Allen, M. R., Stone, P. H., and Sokolov, A. P., Constraining uncertainties in climate models using climate change detection techniques, *Geophys. Res.*

Lett., 27, 569-572, 2000; see also Forest, C. E., Allen, M. R., Sokolov, A. P., and Stone, P. H., Constraining climate model properties using optimal fingerprint detection methods, *Clim. Dyn.*, submitted April 5, 2000.

Gillett, N. P., Allen, M. R., and Tett, S. F. B., Modelled and observed variability in atmospheric vertical temperature structure, *Clim. Dyn.*, 16, 49-61, 2000.

Glecker, P. J., and Weare, B. C., Uncertainties in global ocean surface heat flux climatologies derived from ship observations, *J. Clim.*, 10, 2764-2781, 1997.

Goody, R., Anderson, J., and North, G., Testing climate models: An approach, *Bull. Am. Meteor. Soc.*, 79, 2541-2549, 1998.

Govindasamy, B., and Caldeira, K., Geoengineering Earth's radiation balance to mitigate CO₂-induced climate change, *Geophys. Res. Lett.*, 27, 2141–2144, 2000.

Hoskins, B. J., McIntyre, M. E., and Robertson, A. W., On the use and significance of isentropic potential vorticity maps, *Q. J. Roy. Meteorol. Soc.*, 111, 877–946, 1985.

Houghton, J. T., The predictability of weather and climate (The Bakerian Lecture 1991), *Phil. Trans. R. Soc. Lond. A*, 337, 521-572, 1991.

Idso, K. E., and Idso, S. B., Plant responses to atmospheric CO_2 enrichment in the face of environmental constraints: A review of the past 10 years' research, *Agric. for Meteorol.*, 69, 153–203, 1994.

Indermühle, A., and 11 co-authors, Holocene carboncycle dynamics based on CO_2 trapped in ice at Taylor dome, Antarctica, *Nature*, 398, 121–126, 1999.

Intergovernmental Panel on Climate Change (IPCC), *Climate Change: The IPCC Scientific Assessment*, edited by J. T. Houghton *et al.*, 365 pp., Cambridge Univ. Press, 1990.

Intergovernmental Panel on Climate Change (IPCC), *Climate Change 1995: The Science of Climate Change*, edited by J. T. Houghton *et al.*, 572 pp., Cambridge Univ. Press, 1996.

Jain, S., Lall, U., and Mann, M. E., Seasonality and interannual variations of Northern hemisphere temperature: Equator-to-pole gradient and ocean-land contrast, J. Clim., 12, 1086-1100, 1999. Johnson, D. R., "General coldness of climate models" and Second Law: Implications for modeling the Earth system, *J. Clim.*, 10, 2826-2846, 1997.

Kellogg, W. W., and Schneider, S. H., Climate stabilization: For better or for worse? *Science*, 186, 1163-1172, 1974.

Kennett, J. P., Cannariato, K. G., Hendy, I. L., and Behl, R. J., Carbon isotopic evidence for methane hydrate instability during Quaternary interstadials *Science*, 288, 128–133, 2000.

Kiehl, J. T., and Trenberth, K. E., Earth's annual global mean energy budget, *Bull. Am. Meteor. Soc.*, 78, 197-208, 1997.

Latif, M., Roeckner, E., Mikolajewicz, U., and Voss, R., Tropical stabilization of the thermohaline circulation in a greenhouse warming simulation, *J. Clim.*, 13, 1809–1813, 2000.

Lean, J., Beer, J., and Bradley, R., Reconstruction of solar irradiance since 1610: Implications for climate change, *Geophys. Res. Lett.*, 22, 3195–3198, 1995.

Liu, Q., and Schuurmans, C. J. E., The correlation of tropospheric and stratospheric temperatures and its effect on the detection of climate changes, *Geophys. Res. Lett.*, 17, 1085–1088, 1990.

Mann, M. E., Bradley, R. S., and Hughes, M. K., Global-scale temperature patterns and climate forcing over the past six centuries, *Nature*, 392, 779–787, 1998.

Marotzke, J., Abrupt climate change and thermohaline circulation: Mechanisms and predictability, *Proc. Natl. Acad. Sci. (USA)*, 97, 1347-1350, 2000.

McIntyre, M. E., How far have we come in understanding the dynamics of the middle atmosphere? in *The 14th European Space Agency (ESA) Symposium on European Rocket and Balloon Programmes and Related Research*, (ed. B. Kladeich-Schürmann: ESA Publication), 581-590, 1999.

Murphy, J. M., Transient response of the Hadley Centre coupled ocean-atmosphere model to increasing carbon dioxide. Part I: Control climate and flux adjustment, J. *Clim.*, 8, 36-56, 1995.

National Research Council (NRC), Reconciling observation of global temperature change, 104 pp., National Academy Press, 2000. Oreskes, N., Shrader-Frechette, K., and Belitz, K., Verification, validation, and confirmation of numerical models in the Earth sciences, *Science*, 263, 641–646, 1994.

Overpeck, J., and 17 co-authors, Arctic environmental change of the last four centuries, *Science*, 278, 1251–1256, 1997.

Palmer, T. N., A nonlinear dynamical perspective on climate prediction, J. Clim., 12, 575-591, 1999.

Pawson, S., and 39 co-authors, The GCM-Reality Intercomparison Project for SPARC (GRIPS): Scientific issues and initial results, *Bull. Am. Meteor. Soc.*, 81, 781-796, 2000.

Pitman, A. J., and 25 co-authors, Key results and implications from phase 1(c) of the Project for Intercomparison of Land-surface Parameterization Schemes, *Clim. Dyn.*, 15, 673-684, 1999.

Priem, H. A., CO₂ and climate: A geologist's view, *Space Sci. Rev.*, 81, 173-198, 1997.

Rahmstorf, S., Shifting seas in the greenhouse? *Nature*, 399, 523-524, 1999.

Rahmstorf, S., and Ganopolski, A., Long-term global warming scenarios computed with an efficient coupled climate model, *Clim. Change*, 43, 353–367, 1999.

Räisänen, J., Internal variability as a cause of qualitative intermodel disagreement on anthropogenic climate changes, *Theor. Appl. Climatol.*, 64, 1-13, 1999.

Rasch, P. J., and Williamson, D. L., Computational aspects of moisture transport in global models of the atmosphere, *Q. J. Roy. Meteorol. Soc.*, 116, 1071–1090, 1990.

Roeckner, E., Bengtsson, L., Feichter, J., Lelieveld, J., and Rodhe, H., Transient climate change simulations with a coupled atmosphere-ocean GCM including the tropospheric sulfur cycle, J. Clim., 12, 3004–3032, 1999.

Rotstayn, L. D., Climate sensitivity of the CSRIO GCM: Effect of cloud modeling assumptions, J. Clim., 12, 334-356, 1999.

Russell, G. L., and Rind, D., Response to CO₂ transient increases in the GISS coupled model: Regional coolings in a warming climate, *J. Clim.*, 12, 531-537, 1999.

Schneider, E. K., Kirtman, B. P., Lindzen, R. S., Tropospheric water vapor and climate sensitivity, J. Atmos. Sci., 56, 1649-1658, 1999.

Schneider, S. H., Geoengineering: Could -or should- we do it? *Clim. Change*, 33, 291-302, 1996.

Schneider, S. H., Detecting climatic change signals: Are there any "Fingerprints"? *Science*, 263, 341–347, 1994.

Senior, C. A., Comparison of mechanisms of cloudclimate feedbacks in GCMs, *J. Clim.*, 12, 1480–1489, 1999.

Soden, B. J., The sensitivity of the tropical hydrological cycle to ENSO, *J. Clim.*, 13, 538-549, 2000.

Soon, W., Baliunas, S., Robinson, A. B., and Robinson, Z. W., Environmental effects of increased atmospheric carbon dioxide, *Clim. Res.*, 13, 149–164, 1999.

Soon, W. H., Posmentier, E. S., and Baliunas, S. L., Inference of solar irradiance variability from terrestrial temperature changes, 1880-1993: An astrophysical application of the Sun-climate connection, *Astrophys. J.*, 472, 891-901, 1996.

Stocker, T. F., and Marchal, O., Abrupt climate change in the computer: Is it real? *Proc. Natl. Acad. Sci.* (USA), 97, 1362-1365, 2000.

Tett, S. F. B., Stott, P. A., Allen, M. R., Ingram, W. J., and Mitchell, J. F. B., Causes of twentieth-century temperature change near the Earth's surface, *Nature*, 399, 569-572, 1999.

Wallace, J. M., Zhang, Y., and Renwick J. A., Dynamic contribution to hemispheric mean temperature trends, *Science*, 270, 780-783, 1995.

Wood, R. A., Keen, A. B., Mitchell, J. F. B., and Gregory, J. M., Changing spatial structure of the thermohaline circulation in response to atmospheric CO₂ forcing in a climate model, *Nature*, 399, 572–575, 1999.

Yang, F., Schlesinger, M. E., and Rozanov, E., Description and performance of the UIUC 24-layer stratosphere/troposphere general-circulation model, J. Geophys. Res., 105, 17925-17954, 2000.

Yao, M.-S., and Del Genio, A. D., Effects of cloud parameterization on the simulation of climate changes in the GISS GCM, *J. Clim.*,12, 761-779, 1999.

Yu, J.-Y., and Mechoso, C. R., A discussion on the errors in the surface heat fluxes simulated by a coupled GCM, *J. Clim.*, 12, 416–426, 1999.

THE IPCC REPORT 2001

John Houghton

Co-chair, Working Group I, Intergovernmental Panel on Climate Change (IPCC),

IPCC unit, Hadley Centre, Meteorological Office, Bracknell, RG12 2SY, UK

Tel: +44-(0)1344-856888 Fax: +44-(0)1344-856912 Email: ipccwg1@meto.gov.uk

Abstract

The IPCC was founded in 1988 with the aim of providing assessments of all aspects of global climate change especially the influence of human activities on such change. It aims to involve as many scientists as possible in these assessments and also to involve governments in ensuring that their presentation is relevant and clear. A Third Assessment Report (TAR) is in preparation and will be published next year. Particular attention will be given in this report to all known contributions to radiative forcing, to the simulation of the climate of the 20th century, to the details of the carbon cycle, to advances in climate modelling, to the form of he climate response to increased radiative forcing from greenhouse gases and to possible major influence of such forcing on the ocean circulation. Two of the most important likely impacts of climate change will result from the rise in sea level and the more intense hydrological cycle. The internationally agreed Framework Convention on Climate Change (FCCC) has the Objective of stabilising greenhouse gas concentrations in the atmosphere. This will require large reductions in projected emissions of gases such as carbon dioxide with important implications for the world's energy industry.

The IPCC

First I want to explain a little about the IPCC and its assessment reports. The IPCC was founded in 1988 jointly by the World Meteorological Organisation (WMO) and the United Nations Environment Programme (UNEP) with the aim of providing assessments of all aspects of global climate change especially the influence of human activities on such change. Three working groups were set up, Working Group I to address the science of climate change and Working Groups II and III to address the impacts of climate change and the relevant policy options.

The IPCC's first comprehensive assessment report on Climate Change was published in 1990 and was widely accepted by the scientific community and by governments. It was influential in the establishment and formulation of the Framework Convention on Climate Change agreed by most world governments at the 'Earth Summit' in Rio de Janeiro in 1992. A Second Assessment Report (the SAR) was agreed in 1995 and published in 1996 and during the 1990s a number of reports have also been published dealing with various aspects of climate change.

Let me make two points about the IPCC reports. First, we have tried to involve as many scientists from as many countries as possible in the IPCC process. We are fortunate that many of the leading scientists in the world in the various scientific disciplines associated with climate change have worked with the IPCC and despite the large demands made by the IPCC process they are still involved as the IPCC prepares its Third Assessment Report (TAR). The involvement of scientists occurs not only in the preparation and writing of the reports but also in the review process. Each report goes through a double review. a review by scientific experts and a review by governments in both of which many hundreds of scientists are involved. It is the resulting ownership by the world scientific community that ensures that the IPCC reports are accurate and authoritative.

Secondly, let me explain further about the involvement of governments. For each report there is a policymakers' summary, agreed in its detailed wording at an intergovernmental meeting where delegates from a hundred countries or more are typically present. Representatives of the scientific authors are also present to ensure that nothing is changed that affects the integrity of the science. What the government delegates do is to ensure that the summary is relevant to their policy needs and stated clearly in unambiguous language. It is interesting that each time we have been through this process the policymakers' summary has come out of it improved in its accuracy and clarity. The fact that government delegates are involved means that the world's governments also feel some ownership of the reports, something that is very important when policy options are being considered.

The IPCC TAR is now in preparation and will be available early next year. The second review process is nearing completion although there is still debate about some of the wording in the chapters. As the chapters are still in the process of change, I

Proc. 1st Solar & Space Weather Euroconference, 'The Solar Cycle and Terrestrial Climate', Santa Cruz de Tenerife, Tenerife, Spain, 25-29 September 2000 (ESA SP-463, December 2000)

cannot tell you exactly what is in the assessment. However, in the paragraphs that follow I will briefly present some of the issues that are being addressed especially those where there has been a concentration of scientific work since the SAR was produced five years ago.

Contributions to radiative forcing

Radiative forcing in the context of the work of the IPCC is defined as the change in the net radiation in watts per square metre at the top of the troposphere that occurs as a result of factors that perturb the climate system. The contributions to radiative forcing that arise from changes in the concentrations of greenhouse gases can be calculated from their radiative properties that, for all the important gases, are well known.

Much less well known are the contributions to radiative forcing from small particulates present in the atmosphere known as aerosols that originate from both natural and anthropogenic sources. The most important anthropogenic aerosols are sulphate particles arising from sulphur dioxide emissions. These remain in the lower atmosphere for a few days before being washed out and so are mainly present near industrial regions. Since they scatter solar radiation back to space their direct effect is a negative radiative forcing. Because such particles can act as condensation nuclei they can also influence the properties of clouds, tending to increase the number of droplets and decrease their mean size. Since clouds with a higher number of smaller droplets tend to be more reflective this indirect effect can lead also to a negative radiative forcing. Other anthropogenic aerosols arise from biomass burning; depending on their composition they can possess positive or negative radiative forcing.

Over the past few years a lot of studies of the likely effects of aerosols have been pursued. Estimates of their radiative forcing to date and its distribution are subject to large uncertainty; this is especially the case with the indirect forcing component. In the future it is expected that, because of pollution control measures in many countries, the concentration of sulphates will tend to fall. The radiative forcing due to the likely emissions of anthropogenic aerosols is estimated to be much smaller than that from. greenhouse gases

The possible contribution to radiative forcing from changes in solar radiation is of particular interest to the SOLSPA conference. Estimates of the range of possible changes in the total solar output during recent centuries have been made on the basis of recent observations especially from space instruments and on models of the sun's likely behaviour. The IPCC SAR provided an estimate of solar radiative forcing since 1850 in the range 0.1 –0.5 W m⁻², which can be compared with about 2.4 W m⁻² from greenhouse gases during the same period. The SAR also concluded that any solar radiative forcing during the 21^{st} century is likely to be

much smaller than the forcing due to anthropogenic changes in greenhouse gases. An important point to make is that radiative forcing through changes in total solar radiation or through changes in greenhouse gas concentrations are similar in kind. It is not allowable therefore for changes in solar radiation and changes in greenhouse gases to considered as competing mechanisms for climate change, as is often blindly done by the media. Radiative forcing due to solar radiation changes and due to changes in greenhouse gases or aerosols need to considered together, as has now been done by a number of authors when modelling the climate of the 20th century.

Over the past five years a number of papers have been published on the possible importance of mechanisms through which the climate effects of variations in solar radiation may be enhanced. One mechanism concerns the influence of variations in solar ultraviolet radiation on atmospheric ozone leading to changes in stratospheric structure and circulation. Another mechanism is associated with the possibility that variations in solar cosmic radiation could lead to variations in cloudiness through varying the number of ions acting as condensation nuclei. Other papers at the conference have described these effects in more detail. Although the possibility of such effects is interesting and should be explored, the studies so far do not provide clear demonstration as to how such enhancement mechanisms might operate nor evidence that the possible forcings associated with them are at all comparable with the forcing from the anthropogenic increase of greenhouse gases.

The climate record of the 20th century

Many attempts have been made to model the climate, especially the temperature, of the 20th century. Most of these find a best fit by including in addition to greenhouse gas increases, aerosol cooling (particularly important in accounting for the lack of warming in the 1950-80 period), volcanic eruptions and solar forcing (especially important in helping to account for the rise in global average temperature in the first 40 years of the century). None of these studies provide a perfect fit, nor would one be expected because of the substantial natural variability of climate arising, for instance, from interactions and exchanges between different components of the climate system.

A question of very great interest is whether anthropogenic climate change has been detected. The IPCC Second Assessment Report of 1995 concluded that 'the balance of evidence suggests a discernible human influence on climate.' Many detection and attribution studies since then have confirmed and tended to strengthen this statement.

The carbon cycle

The exchange of carbon with the terrestrial biosphere has been an area of particular interest in recent years. A major question has been whether, over the past few decades, the terrestrial biosphere has been, on average, a source or a sink. Also what is likely to occur in the future? Data that has helped to elucidate this has come from accurate measurements of the atmospheric oxygen concentration. As carbon dioxide dissolves in the ocean all of the carbon dioxide goes in and there is no change in atmospheric oxygen. However, if carbon dioxide is fixed through the growth of trees or vegetation on land, the carbon is taken up by the vegetation and the oxygen returns to the atmosphere. Different variations occur in the atmospheric oxygen concentration therefore depending on whether the carbon dioxide is removed into the ocean or into the land biosphere.

During the 1980s on average globally, vegetation tended to be a source of carbon dioxide; during the 1990s vegetation has tended to be a sink. The land biosphere in tropical regions, despite deforestation, has almost been in carbon balance during the 1990s, possibly because of carbon dioxide fertilisation and also because of the increased use of nitrogen fertilisers. Regarding the future, some carbon models are suggesting that the land biosphere is likely to continue to act as a sink during the first part of the 21st century but then, later in the century, because of the negative influence of climate change the situation could reverse and the terrestrial biosphere become a substantial source of carbon dioxide. More understanding of all the processes involved is required before we can make more definite statements.

Modelling of climate change

Models are absolutely key to our understanding of climate change because they are the only tool we have of adding together the wide range of non linear processes that occur within the total climate system. The performance of models is continually improving and confidence in projections made with them has increased substantially. Just let me mention one area of improvement and one encouraging result.

The area of improvement is that of atmosphere ocean coupling. Until recently, in order for the 'model climate' to be realistic artificial corrections were applied to fluxes of energy or momentum at the atmosphere-ocean interface. Due to model developments, such corrections are no longer required in the most advanced models. It has been encouraging to note that results from these advanced models have in general confirmed the projections of climate change made with the earlier models that included substantial flux corrections.

A further encouraging model result has the successful simulation of major features in the pattern of climate change that resulted from the eruption of the Pinatubo volcano in 1991. This provides some credibility to the use of models to simulate climate change due to perturbations arising from human activities.

Patterns of climate response

There is a large demand amongst policy makers for information about the changes in climate that are likely to occur on a regional scale. Although a lot of effort has gone into the development of models appropriate to this scale, there is as yet inadequate consistency between such models –which means that there is much uncertainty in the detail of climate change on these smaller scales.

Associated with this interest in the regional scale is increasing attention to the likely patterns of climate response to greenhouse gas forcing. Because the circulation patterns in the atmosphere and the ocean are highly complex, it cannot be expected that the response of the climate to external forcing would be uniform heating everywhere. It is much more likely that the response will be linked to some of the major patterns of climate variability such as the North Atlantic Oscillation (NAO) or the El Nino. The El Nino is the most well know of these patterns. Its origin is in the south Pacific where about every five years the sea surface temperature shows a strong positive anomaly off the coast of Peru. Linked with this are climate extremes such as droughts and floods in many of the continents especially in Australia, Africa and the Americas. An important question is whether this major climatic regime will alter as a result of increasing greenhouse gases. Many scientists think that it very likely will, a suggestion that tends to be supported by the very unusual El Ninos that have occurred in the 1990s.

The thermohaline circulation

A final area of current scientific interest I want to mention is a link between long term climate change and the ocean circulation, called the thermohaline circulation (THC). A region where the THC is linked to circulation in the deep ocean is that of the north Atlantic. between Greenland and Scandanavia. Water there has travelled from the tropical regions during which much evaporation has occurred. It is therefore very salty and also cold. It is therefore more dense than average and tends to sink to the bottom. It there becomes the source of water for the 'conveyor belt', as it is sometimes called, the deep ocean circulation that is going on kilometres down in the ocean, linking the oceans together and conveying heat and fresh water around the world.

In a warmer world there is increased precipitation especially at high latitudes. Increased rainfall over the north Atlantic region will make the water less salty, therefore less dense. It will therefore not sink so readily and the THC will weaken. Climate models simulate this effect; some cut off the circulation completely within about 200 years of increasing greenhouse gases, others just weaken it. Further, there is evidence from paleoclimate history of the THC being cut off a number of times in the past.

The THC has a particular influence on the climate of north west Europe; if it weakens that part of Europe will be colder than it would otherwise be. The models all indicate less warming than average in this region –although none show it actually becoming colder. This influence of changes in the THC on the climate of Europe and the rest of the world needs much further study.

The impacts of climate change

The IPCC has recently produced a new set of possible emission scenarios (the SRES scenarios) for the 21st century. Estimates of the increase in global average temperature from 1990 to 2100 for these scenarios falls in the range 1 to 5°C. What would be the main impacts of the associated climate change? These will vary from country to country. Some impacts will be positive; for instance, increased temperature at high latitudes will lengthen the growing season and increased carbon dioxide will in some regions stimulate crop growth. However, because humans and ecosystems have adapted to the current climate, a large change of climate in most places will lead to negative impacts. This is particularly because the rate of climate change projected for this century assuming continuing growth of greenhouse gas emissions is most likely larger than has been experienced on earth during the last 10,000 years. Let me just mention two of the main impacts.

The first is the rise in sea level with a best estimate of about half a metre by the end of the 21st century. The main reason for this is the thermal expansion of sea water; melting of glaciers also makes a significant contribution. Because the ocean takes many centuries to warm throughout its depth, approximately this rate of expansion will continue for many centuries. Areas particularly affected will be low lying river deltas (such as in Bangladesh, southern China and Egypt) and many islands in the Indian and Pacific oceans. Many millions of people in these areas will be displaced. Other nations will have to bear substantial cost to build up their sea defences.

A second major impact of global warming is on the hydrological cycle. A warmer world is a wetter world – more evaporation and more water vapour in the atmosphere. That means more precipitation on average; it also means more energy in the atmospheric circulation because the major energy source for that circulation is the latent heat release from the condensation of water vapour. A more intense hydrological cycle means that heavy rainfall tends to be heavier; it also means that in some dry areas their low rainfall will tend to be reduced. That is because the air that participates in down draughts over dry regions, because of its greater energy, will have risen higher where it becomes colder and drier.

All models show this result which implies a greater frequency and intensity of both droughts and floods. These will tend to occur especially, but not only, in sub tropical regions where countries are least able to cope with them. Droughts and floods are, in fact by and large, the most damaging disasters that occur in the world, leading to more deaths, misery and economic loss than other disasters. Very serious examples of both have occurred in Africa and elsewhere this year.

The mitigation of climate change

Because of the likely serious impacts arising from the climate change due to increasing greenhouse gases, all the main nations of the world signed the Framework Convention on Climate Change (FCCC) at the Earth Summit in Rio de Janeiro in1992.

Article 3 of the FCCC commits the Parties to the Convention to:

'take precautionary measures to anticipate, prevent or minimize the causes of climate change and mitigate its adverse effects. Where there are threats of serious or irreversible damage, lack of full scientific certainty should not be used as a reason for postponing such measures, taking into account that policies and measures to deal with climate change should be cost-effective so as to ensure global benefits at the lowest possible cost.'

Article 2 of the FCCC puts action regarding Climate Change in the context of Sustainable Development. It states:

'The ultimate objective of this Convention....is to achieve...stabilisation of greenhouse gas concentrations in the atmosphere at a level that would prevent dangerous anthropogenic interference with the climate system. Such a level should be achieved within a time frame sufficient to allow ecosystems to adapt naturally to climate change, to ensure that food production is not threatened and to enable economic development to proceed in a sustainable manner.'

Since carbon dioxide is the most important of the greenhouse gases, the FCCC Objective requires the stabilisation of the carbon dioxide concentration to be addressed by reducing its emissions from fossil fuel sources or by increasing the sinks which remove carbon-dioxide from the atmosphere (eg by reducing deforestation and increasing aforestation). Because of the long life of carbon dioxide in the atmosphere, for stabilisation of its atmospheric concentration to be achieved within the next

century, substantial reductions in emissions to well below today's levels will be needed.

At the Conference of the Parties to the FCCC held in Kyoto in December 1997 action was agreed by developed countries to reduce their greenhouse gas emissions by the year 2010. This is seen as a first stage in meeting the Convention's Objective.

Can the world's energy industry contemplate the changes required? In a detailed study published in 1993 by the World Energy Council (WEC) of energy generation and use next century, an 'ecologically driven' scenario is described associated with which there would be a profile of carbon dioxide emissions which would lead to stabilisation of atmospheric carbon dioxide concentration. The WEC show how this can be achieved -particularly by strong drives to increase energy efficiency and to develop the use of energy sources with much lower carbon dioxide emissions. Under this scenario by 2020, developing countries, as they industrialise, are projected to roughly double their energy use and their carbon dioxide emissions, while developed countries are projected to reduce their energy use by about 10% and their carbon dioxide emissions by about 30%. Estimates of the annual cost of realising such a scenario suggest figures of 1% or less of Global World Product (GWP) which is considerably less than most of the estimates which economists have made of the damage likely to result from climate change impacts.

Achievement of such a scenario will not be easy. Commitment is required from governments, industry and from all of us as individuals to take seriously the challenge of environmental stewardship. Further, the matter is an urgent one. As the WEC points out 'the real challenge is to communicate the reality that the switch to alternative forms of supply will take many decades, and thus the realisation of the need and the commencement of the appropriate action must be *now* (their italics).'

Bibliography

'Climate Change 1995; The Second IPCC Assessment of Climate Change' published in three volumes by CUP, April 1996

'Special Report on Emissions Scenarios', published for the IPCC by CUP, 2000

J.T.Houghton 'Global Warming; the complete briefing' Second Edition, Cambridge University Press 1997

'Energy for Tomorrow's World', World Energy Council, 1993

SOLSPA Summary

SUMMARY AND PERSPECTIVES

E. N. Parker

Dept. of Physics, University of Chicago 933 East 56th Street Chicago, Illinois 60637 USA tel: (708) 798-3497 e-mail: parker(a)odysseus.uchicago.edu

ABSTRACT

This conference brings together atmospheric scientists and solar physicists to review contemporary knowledge on global warming and its causes. The dynamical atmosphere of our planet is a complicated nonlinear, and only quasi-stable, engine, responding strongly to the varying internal stimuli of volcanic cruptions, anthropogenic greenhouse gases, and local deforestation, and to external stimuli of varving solar brightness, from IR to UV, and perhaps even to The scientific challenge is to cosmic ravs. understand the peculiar variability of the Sun and the complex physics of the terrestrial response. This knowledge and understanding is essential for the difficult political and economic task of shaping the optimum human response. It appears from the presentations at the conference that understanding has come a long way, with the Sun driving global warming in the early part of the last century and greenhouse gases taking over in the second half. It is also evident that we have a lot of work ahead to understand the physics of cloud formation etc. if we are to construct broadly predictive global climate models.

INTRODUCTION

This meeting has been extraordinary in combining solar physics and atmospheric science to pursue the problem of terrestrial climate and global warming. We heard reviews of recent advances in our understanding of the solar dynamo and the origins of solar activity. We heard reviews of advances in the history of terrestrial climate and in the dynamical nature of climate. It is my impression that we are beginning to get some idea of the causes of the general warming of climate since about 1880, on which more will be said later. It is also my impression that there is a lot of work in both the laboratory and in the field that has yet to be done before we understand precisely why things behave as they do, on which more will be said later.

It is not my intention in this summary to repeat what we all have heard from the speakers and what we have read in the posters during the week. That information is sketched in the book of abstracts. So I apologize ahead of time to the many authors whose diverse and individual contributions I will not mention explicitly. Your individual works are part of the whole, and it is my purpose to give my impressions and understanding of what we have learned during the course of the meeting. I am still in the process of digesting the flood of results presented here, and I would appreciate it if any serious omissions or errors of mine are pointed out to me. I want the written version of this presentation to be as useful as possible for the eventual reader.

COSMIC RAYS AND SOLAR ACTIVITY

It is convenient to begin with the role played by the terrestrial atmosphere and the galactic cosmic rays in exploring the history of solar activity and climate change. You are aware that ¹⁴C is produced in the atmosphere by cosmic rays bombarding ^{14}N . The ^{14}C is unstable, with a half life of about 5000 years. The rate of production of ¹¹C at any given time in the past. and the relative abundance compared to the common-¹²C incorporated into vegetation at that time, is determined by the intensity of the cosmic rays at that time, of course. That is to say, the creation of ¹⁴C is followed by oxidation into CO₅, which then dwells in the atmosphere for perhaps 20-50 years before it is absorbed into the oceans: etc. along with the CO2 made with ¹²C. It follows that a sample of wood of known age provides a determination of the cosmic ray intensity a few years before the wood was grown. Using tree ring dating of old samples of wood, and taking advantage of the bristle cone pine growing in the mountains of western United States, the record has been extended back 7000 years and more. The variations of the cosmic ray intensity over time can be seen and provide direct information on the general level of solar activity. For the fact is that the gusty solar wind produced in the years of high solar activity is more effective in sweeping away the galactic cosmic rays from the inner solar system than is the steady solar wind produced in the periods of low activity. The result is a substantial decrease in the cosmic ray intensity at Earth with increasing

Proc. 1st Solar & Space Weather Euroconference, 'The Solar Cycle and Terrestrial Climate', Santa Cruz de Tenerife, Tenerife, Spain, 25-29 September 2000 (ESA SP-463, December 2000)

magnetic activity at the Sun. Note that the familiar 11-year activity cycle does not show up in the ^{14}C production because the ^{14}C has a longer dwell time in the atmosphere than the 11 years, thereby smearing the production rate over about 30 years. Variations over periods longer than 20 years are often 10 percent or more and show up clearly.

SOLAR VARIABILITY

Now in 1894 Walter Maunder pointed out that the record of sunspots, based on observations since 1611 when Galileo and others first applied the telescope, indicated that sunspots were scarce through the 70 years from about 1645 to 1715. The available records over that period were spotty, but indicated a striking scarcity of sunspots, with most of the small number of spots confined to the southern hemisphere of the Sun. No one seems to have paid much attention to the phenomenon, subsequently called the Maunder Minimum. The origin of sunspots was not known. In fact it was more than 10 years before Hale showed that sunspots are a magnetic phenomenon. So no one knew what it might mean, and it was all too easy to shrug off the Maunder Minimum as poor observational work. Evidently both scientists and theologians abhor a mystery. However, when we recall that sunspots can be seen with the naked eve when the Sun is dimmed to a red disk in a smoky sky, and even the most rudimentary telescope renders a modest spot conspicuous, it is hard to dismiss the scarcity of sunspot detection over the period 1645-1715. And what can it all mean?

The subject seems not to have been taken up again until Jack Eddy became interested in the early seventies. As a result of his scholarly researches the phenomenon became even more mysterious. And his professional appointment was terminated because his work was deemed irrelevant. To make a long story short, he explored the historical records and soon determined that the Maunder Minimum was a real event, during which time sunspots were greatly reduced in number. He remarked that he found an entry in Cassini's log that Cassini had seen a sunspot that day. Cassini went on to say that he had been looking for sunspots for ten years, without success until that moment. Once eddy had established the reality of the Maunder Minimum, he asked the question of how common was this kind of thing? Once in four centuries of telescopic observation gave no certain estimate. So Eddy turned to ¹⁴C, which showed 10 distinct century-long epochs of enhanced cosmic ray intensity in the last 7000 years. He noted that there was no evident time pattern to the recurrences of such prolonged minima in solar

activity. Curiously, the 15^{th} century exhibited a similar prolonged period of reduced activity, and it was named the Spörer Minimum after an early researcher in solar activity. The minimum before that was in the 4^{th} century BC, etc. Then the late 19^{th} century is now also recognized as a brief faltering in the normal level of solar activity.

Along with the periods of reduced solar activity, Eddy identified 8 periods of reduced ¹⁴C production, indicating century-long periods of enhanced solar activity. The most recent was the 12th century, and he named it the Medieval Maximum. It now appears that the generally high level of solar activity of the second half of the twentieth century is the equal of any of the other periods of enhanced activity, so the Twentieth Century Maximum makes the 9th in the last 7000 years.

Now sunspots are a product of magnetic field. generated in the convective zone of the Sun (the outer 2/7 of the solar radius, with a depth of 2×10^{5} km) presumably by a combination of the differential rotation and the cyclonic convective cells in the convective zone. This generation of magnetic field by fluid flow is called a dvnamo. The magnetic fields that give rise to sunspots are also responsible for coronal heating, flares, coronal mass ejections, etc. so that the conspicuous but benign sunspot is simply an indicator of the general magnetic activity around the Sun, and of the associated gusty solar wind and decreased cosmic rav intensity, of course. Helioseismology has been able to map the angular velocity $\Omega(\mathbf{r}, 0)$ throughout the solar interior. The result was not anticipated, nor can it yet be explained after the fact. In a first approximation the angular velocity is found to be essentially independent of radius throughout the convective zone, depending only on latitude in the same way that the visible surface of the Sun varies with latitude, with the rotation period observed to be 25 days at the equator. increasing smoothly to about 30 days at the poles. The radiative interior (the inner 5/7 of the solar radius) rotates rigidly with a period of about 27 days. The result is a thin layer of strong shear at the base of the convective zone, called the *tachocline*. The effect of this shear is to stretch out in the azimuthal direction any radial magnetic field, thereby producing a growing azimuthal magnetic field, which in turn is the cause of the sunspots when the azimuthal field floats up and emerges through the surface.

Petrovay and Rüdiger reviewed the present state of dynamo theory, indicating the present theoretical uncertainties in the form of the dynamo. An essential part of the dynamo operation is diffusive dissipation. for without it there is no generation of net magnetic flux. The theoretical dynamo requires an effective diffusion coefficient $\eta \sim 10^{11} - 10^{13}$ cm^2/s Observations of the spreading of magnetic field across the surface of the Sun indicate a similar range of diffusion. The turbulent convection that makes up the convective zone would diffuse a puff of smoke at a rate somewhere in this range, mixing and extending an initial cloud into a long thin scrpentine filament that is soon dispersed by ordinary thermal molecular diffusion. So it was taken for granted for many years that the diffusion of magnetic field necessary for a working dynamo was automatically taken care of by the turbulent convection. However, the magnetic fields beneath the surface of the Sun now appear to be much too intense to submit to the expected stretching into the long thin scrpentine filaments. The tension along the field would increase enormously as the initial volume is elongated, very soon resisting further stretching. So the physics of the "turbulent diffusion" of magnetic field in the Sun, or elsewhere in the astronomical universe, is not at all clear. Observations indicate only that some sort of rapid diffusion occurs. The solar dynamo evidently is able to provide field on an 11-year basis, and that indicates effective dissipation of magnetic field. So Nature knows how to do it, but we do not. However the rapid diffusion of magnetic field through the convective zone is not the only mystery.

The magnetic field appearing at the visible surface of the Sun is found to be in a fibril state, consisting of widely separated flux tubes with characteristic diameters of 10^2 km and field intensities of $1-2x10^3$ Gauss. There is no detectable magnetic field in the interfibril spaces, and the mean field observed by the magnetograph (which does not resolve the individual fibrils) is simply a measure of the mean separation of the fibrils. Thus, where the magnetograph shows 15 Gauss, it follows that the fibrils occupy about 10^{-2} of the surface area.

There is indirect evidence that the magnetic field is in a fibril state throughout the convective zone. For instance, the dynamics of the buoyant rise of azimuthal flux bundles from the base of the convective zone, where they are created, to the surface, where they appear as a nearly east-west bipolar magnetic region, indicates that the flux bundles started with intensities of 5×10^4 Gauss or more. Weaker fields would be overwhelmed by the Coriolis force, neither appearing at the surface at low latitudes, nor showing the observed nearly east-west orientation. Unless one assumes that the lower convective zone is uniformly filled with field of $5x10^4$ Gauss, one concludes that the flux bundles of $5x10^4$ Gauss represent separated fibrils.

It should be noted, then, that it is not understood why the field is in such an extreme fibril state, rather than spread out smoothly into a continuum. The magnetic energy of the fibril state is much larger than if the field were spread out smoothly. On the other hand, the fibril state interferes less with the free convective transport of heat in the field-free fluid between the fibrils. In that respect the fibril state may represent a minimum total energy - magnetic plus thermal. But the physics of the creation of the fibril field is not at all clear.

In summary, it is not unfair to say that the dynamics of the convection and nonuniform rotation, and the associated generation of the 11 and 22-year magnetic cycle of the Sun pose recognized problems, about which we know a great deal, but which are unsolved. We cannot show why the Sun is obliged by the laws of nature to exhibit magnetic activity in the way that it does. Hopefully the next decade or two will see us in a position of better understanding. For the present problem of terrestrial climate change we proceed with the observational facts of solar magnetic activity.

TERRESTRIAL CLIMATE

With the history of solar activity in hand, Eddy's next move was to point out the remarkable tendency for such climate parameters as the mean annual temperature in the northern temperate zone to track the level of solar activity. Temperatures in Europe and China showed declines of 1-2 C below the average during the Maunder Minimum, which stands out clearly in agricultural records of the times, particularly toward the northern limits of agriculture. For instance the rice farmers in the Yellow River Valley were reduced from two to only one rice crop each year. One can imagine what that did to the economy and the well being of the citizens. The Greenland Vikings succumbed to the cold weather during the Spörer Minimum, and the 15th through the 17th century has become known as the Little Ice Age.

The temperatures during the Medieval Maximum were elevated by comparable amounts above the norm, and high latitude agriculture flourished while arid regions, such as what is now southwestern United States, suffered severe and lengthy droughts.

For climate farther in the past Eddy turned to the advance and retreat of glaciers, and the climate record was then not so precise, of course. Even so, it showed climate variations consistent with the varying activity levels of the Sun.

The physical mechanism that coupled the climate to solar activity was unknown. The fact was simply that, for reasons unknown, the terrestrial climate in the northern hemisphere responds to the decadal average level of solar activity. The 11-year variation of activity itself does not appear in the climate record in any obvious way, although it was pointed out that drought in the high plains of western United States shows a remarkable tendency to appear at the deep solar minimum arising every 22 years. It was noted, too, that, as one might expect, the oceanic southern hemisphere does not show any significant response to the level of solar activity. Atmospheric electricity was considered as a possible connection between the solar modulated cosmic ray intensity, and it was known that the temperature of the upper stratosphere varied with the level of solar activity. However, it was not possible to show at that time whether these processes had any sensible effect on the mean annual temperature in the troposphere.

Curiously, Eddy's startling discoveries were largely ignored in the appropriate scientific communities. They did not fit into the conventional wisdom, so they were judged either a statistical fluke or unimportant, or both. I tried at one point to inform a NASA review committee, of which I was a member, that Eddy's researches opened up a whole new field of inquiry. I was immediately informed by a distinguished member of the committee that, if I knew as much about the atmosphere as he. I would realize that solar activity cannot possibly have an effect on terrestrial climate. I presume he thought of solar activity purely in terms of the coming and going of sunspots, which in themselves are entirely harmless. It reminded me of the famous pronouncement by Kelvin in 1896 that there is no way that the Sun can cause the observed variations of the magnetic field of Earth that make up the geomagnetic storm, in spite of the overwhelming observational evidence that magnetic storms are closely associated (with a 1-2 day lag) with large flares on the Earth-facing portions of the solar disk. Kelvin ignored the possibility of particle emission from the Sun, already suggested as the cause of the magnetic storms. He assumed instead that space is absolutely empty-a hard vacuum- so that a magnetic fluctuation seen at Earth is really just a fluctuation in the magnetic field at the Sun, that field extending out into space in the form a dipole.

I tell these anecdotes because they illustrate the eternal human difficulty in dealing with the most

elementary effects. We grapple with the problem today, on which more will be said later.

As the reader is aware, the big break came with the launching of the first absolute radiometer into space in 1978. There were voices crying that the brightness of the Sun is obviously constant, except perhaps for brief transients caused by dark sunspots appearing on the solar disk. So it was declared that the precision space measurements were a waste of effort at a time when "important" measurements were needed in space. NASA made the decision to go ahead anyway, and you know the astonishing results, which were displayed and discussed in this meeting. The varying solar brightness has subsequently been shown, from detailed observations, to be largely a consequence of the bright faculae that occur widely in the magnetic regions on the surface of the Sun. The faculae may sometimes be accompanied by sunspots, and sometimes momentarily dominated by the formation of a large spot, but on the whole the broad faculae dominate the mean brightness of the Sun. The role of the faculae raises the question of the energy supply up to the surface that is necessary to sustain the faculae.

The radiometers showed that the bolometric brightness of the Sun declined by 0.15 percent following the 1979 maximum into the 1986 minimum. Subsequently the brightness increased by about 0.1 percent to the maximum in 1990, declining again to the minimum of 1996, etc. Our speakers showed us the observed variations on several graphics. The brightness variations are small, and one wonders how much the brightness might have declined during the prolonged Maunder Minimum, when it was measured that the mean annual temperature in the northern temperate zone declined 1-2C. The sensitivity of the terrestrial temperature to the varying brightness of the Sun is not something that is known from first principles even today.

One would like to have the Sun repeat the Maunder Minimum for us so that the proper instrumentation might be brought to bear on the problem, and there is little doubt that in the next millennium the Sun will do just that. However, so long a wait is not useful in the present situation. Fortunately there is the possibility of monitoring other stars with the same spectrum (atomic abundances), mass, and age $(4.6 \times 10^9 \text{ years})$ as the Sun.

In the sixties O.C. Wilson at the Mt. Wilson and Palomar Observatories began monitoring the activity of a variety of stars, based on the sensitivity of the central core structure of certain chromospheric lines to the state of magnetic activity of the star. The spectroscopic effect was established and calibrated for the Sun, even if the precise physics of the effect is not properly understood. Most solar type stars, and many others as well, exhibit cycles of magnetic activity with periods as short as 6 years, and some much longer. On the other hand, it should be noted that one solar type star was found to be in a Maunder Minimum phase, with a steady low level of activity since the beginning of the survey. Another was observed to slide into a Maunder Minimum phase after having gone through a couple of cycles. Sally Baliunas and coworkers took over the survey when Wilson retired and have continued to the present day. When the varying brightness of the Sun became known, they devised instruments to monitor the brightness of these stars, using the mean brightness of their stellar sample as the absolute standard. In that way they are able to detect variations in brightness of 0.1 percent or less in the individual stars. They found brightness variations similar to the variations of Sun. and, in some cases, substantially larger variations in association with strong activity cycles. They found an approximate universal linear relation between the amplitude of the brightness variation ΔL and the level of magnetic activity, with the Sun somewhat less vigorous in its variations than most of the other solartype stars. Using this relation, an extrapolation to conditions appropriate to the Maunder Minimum suggested that the Sun was fainter by 0.4 ± 0.2 percent at that time. One cannot help noting that a decline of 1 C in the northern temperate zone yields a fractional change $\Delta T/\Gamma \cong \Delta L/L$. Noting that Earth does not behave as a simple black body. for which $\Delta T/T = \Delta L/4L$, this suggested that the brightness variation ΔL might be the major cause of the cold climate of the Little Ice Age, with $|\Delta T| \sim 1-2C$. On the other hand, the response of climate involves more than simple radiative heating and cooling, with the response of the atmosphere to solar brightness (which extends over IR, visible, and UV and affects different levels of the atmosphere in different ways) depending on such things as varying cloud cover, atmospheric electricity, temperature of the stratosphere, etc. That is why the question of the complex response to solar activity has been discussed so extensively in the present conference.

This is an appropriate point, then, to comment on the cosmic ray effects in the atmosphere in addition to forming ¹⁴C. That is the production of ions and electrons by the bombarding cosmic ray protons and heavier nuclei. They produce energetic secondary electrons and mu mesons that penetrate down through the atmosphere, creating electrons and ions all the

way to the ground. Svensmark has suggested that these atmospheric ions may enhance the formation of water drops, thereby explaining the close association of low cloud cover with the cosmic ray intensity, which is modulated in the heliosphere by the 11-year solar cycle. It is an interesting and potentially important idea. I am very curious to see how it will check out. Jasper Kirkby described to us the experiments planned at CERN to test the physics of cloud formation by relativistic particles, and we look forward to the outcome of those laboratory experiments.

We should be aware, too, of the possibility of significant climatic effects through the variation of atmospheric electricity. This intriguing concept has been around for many years and still remains unresolved, so far as I am aware. The idea begins with the fact that the terrestrial ionosphere is charged positive to about 3x10° volts relative to ground by tropical thunderstorms. The charge leaks down from the ionosphere through the troposphere because of the small number of free electrons and ions created in the atmosphere by the cosmic rays. With the electrical conductivity of the atmosphere controlled by the cosmic ray intensity, the vertical electric field shows a significant 11-year modulation. It is not unreasonable to expect that the nucleation of acrosols, water droplets, and ice crystals is affected by this electric field, leading to another connection of cloud cover to cosmic ray intensity and solar activity.

Indeed, the physics of cloud formation appears in every aspect of the climate variation, including direct heating by sunlight. I would hope that with the important issues that need to be decided in connection with climate variation and global warming, an all out effort can be launched to understand this vital aspect of atmospheric science. There is a lot of laboratory work to be done under carefully controlled conditions, e.g. the CERN experiment, on the nucleation of aerosols, ice crystals, and water drops, as well as the related field work to study the application of the laboratory results

The climate variations of the past millenium have been vastly extended by Jürg Beer, who reported briefly on some of the results obtained from his arctic ice cores, which extend the arctic record back 10^5 years. Of particular interest is the occasional drop in atmospheric temperature, in a couple of decades, followed by a decline in atmospheric CO₂. The phenomenon is plausibly related to a change in ocean circulation. Although one might then ask what caused the circulation to change abruptly. It should be noted that Baliumas's monitoring of solar-type stars shows one star whose brightness declined about 0.4 percent over a period of only 5 years, in association with a abrupt decline in its activity. The cause of such a transient is unknown, but it raises the question of whether the Sun might occasionally play a similar trick. One wonders what the response of the terrestrial climate might be in that case.

Contrary to what is politically correct these days, I sometimes wonder if the Sun plays a role, along with the Malenkovich effects. in the coming and going of the ice ages. With our very limited knowledge and understanding of the long term variations of the Sun, it is no less plausible to suggest a change in the circulation mode within the Sun than it is to appeal to an equally mysterious change in ocean circulation here on Earth. Who knows?

Collectively the questions about the Sun, with its influence on terrestrial climate, demand vigorous investigation of the potential for diverse variations of magnetic activity and brightness. If we are politically and economically concerned about the present global warming, in part a consequence of the variations of the Sun, then we should quickly launch a program to explore the limits of solar variation. Specifically, we should monitor a thousand solar-type stars, so that in 10 years time we have the equivalent of 10,000 years of history of short term variations of a star like the Sun. Needless to say, we will remain ignorant of long term variations until many years of dedicated The technology for monitoring have passed. automatic monitoring has been developed and tested. and the whole project would be quite cheap by current standards. And of the utmost importance. In fact, since returning home from this conference I have learned that a ground based project of automated monitoring of 160 solar type stars is currently underway at Tennessee State University. and there are plans for a space mission to monitor a vastly larger number of such stars. Dedicated long term monitoring is the only way that we can expand our present limited knowledge. I hope that NASA, the National Science foundation, the Department of Defense, ESA, and the other funding agencies can understand that.

GLOBAL WARMING

Consider the global warming of the twentieth century. Its beginning may be traced to the modest Dalton Minimum, when the activity of the Sun fell briefly to relatively low levels in the decades around 1880. Solar activity increased from that point in time to somewhere around 1950 or 1960 and has been more or less steady at that elevated level ever since.

We note that since about 1980 the high level of solar activity has begun to show some small signs of declining Then we recall that this Twentieth Century Maximum is comparable in strength and duration to the Medieval Maximum of the 12th century, and the associated global warming has been comparable to the estimated warming in the 12th century, viz. some 1-2 C. Tett, et al, and van Alden and van Dorland presented extensive analyses of the warming.

Now the accumulation of anthropogenic greenhouse gases, e.g. CO₂, began more than a century ago. However, up to about 1950 the modest accumulation could hardly have had any great effect on terrestrial climate. It appears, then, that the warming from 1880 up to 1950 or 1960 was driven largely by the increased activity and brightness of the Sun. Thus it is equally apparent, with no further increase in solar activity, that the warming after about 1970 should be attributed mainly to the accumulating greenhouse gases, which have increased at an ever increasing rate If some one can think of other since 1950. contributing effects, we should listen carefully. It is important, too, to understand that in a strongly nonlinear system like the atmosphere, the contribution to global warming by any one effect may be substantially altered as conditions change as a consequence of other effects.

This raises a number of specific questions, of course. For instance, does the warm climate of 1960 respond to increasing greenhouse gases in the same way that the cold climate of 1880 might have responded. We note that today's increased surface sea water temperatures are absorbing atmospheric CO₂ at a reduced rate, so the accumulation in the atmosphere is more efficient. One wonders what will be the situation in the next hundred years when the oceans are even warmer. Then one wonders how the anticipated very warm dynamical atmosphere of the future might respond to a specified change in solar brightness. It is not obvious that we can expect the same relation between $\Delta T/T$ and $\Delta L/L$. How then does ΔL affect the different levels of the dynamical atmosphere, with some of the IR absorbed relatively high in the atmosphere, the visible largely at the ground, and the UV absorbed at the top of the What was this vertical distribution stratosphere. when the atmosphere was relatively cold in 1880 and what might it be when the atmosphere becomes relatively hot, as we may reasonably expect by the year 2050 or 2100? How, then, will the climatic effect of a given addition of CO₂ change in the warmer atmosphere? The record of terrestrial ΔT over the last thousand years indicates the remarkable sensitivity of ΔT to ΔL , and we really need to understand how that comes about so that we can anticipate what may occur in the future. As already noted, it means that the indirect effects, e.g. cloud cover, UV heating of the stratosphere, atmospheric electricity, as well as the possibility of effects not yet identified, must be investigated, quantified, and included or discarded. The ultimate goal is a comprehensive understanding of the physics of each process, which can be combined into an ultimate ideal comprehensive dynamical global climate model to provide a means for exploring the consequences of any given stimulus.

GLOBAL CLIMATE MODELS

At the present time the global climate models are able to incorporate a remarkable number of effects, thanks to the hard work and ingenuity of those who construct them. The models have reached a point where they can evaluate the consequences of individual effects, thereby helping us understand some of the physical implications of each component of the models. These studies make it clear that the ultimate ideal model, providing a reliable quantitative response to any given stimulus, is still some way in the future. Besides refinement of existing models. and the need for bigger faster computing, there is much physics is yet to be understood, e.g. the formation of clouds, and the formation and distribution of acrosols. Indeed, the list of essential effects to be included in a quantitative global climate model is daunting. Some of the more obvious effects are:

1. Vertical inhomogeneity including stratospheric coupling to the troposphere.

2. Global wind patterns

3. Ocean circulation patterns.

4.Ocean surface water temperatures

5.Cloud cover patterns expected from the above and from the given cosmic ray intensities.

6.Atmospheric heating as a function of altitude and latitude.

7. Transient effects, e.g. volcanic cruptions.

8.Ozone variations.

9.Deflection of winds by surface typography, e.g. mountain ranges, cold oceans, etc.

An expert in the field could add many more to the list. It is obvious that some effects, e.g. cloud cover.

cannot be introduced into the interactive dynamics until the physics is understood properly. Then we note that both the vertical and horizontal resolution of the global model must be greatly improved if the principal effects are to be included in a quantitatively realistic way. Resolution is limited by computer power and we look forward to its continuing development. The physics yet to come from the laboratory is the other major thrust of the development of the ultimate global model.

It is not necessary here to spell out the economic and political implications of global warming. The problems, if they can be dealt with at all before catastrophe, require the most complete quantitative description and understanding that science can provide. Carelessness on the scientific side can undermine any national or international efforts to control the burning of fossils fuels and the adoption of alternative - and probably more expensive - energy sources. It is cause for concern, therefore, to find that some individuals working in the field, and some administrators controlling the research funds, have already made up their minds as to the outcome of the science. On the one hand, the communication of scientific results has been suppressed, with threats of terminating research funds, and, on the other hand, premature recommendations have been passed upward from the scientific to the political community. New effects and results have been made unwelcome and stifled to the best ability of Why an individual, and established groups. particularly one who has made the effort to obtain legitimate scientific credentials, should prefer a preconceived conviction to an open inquiring mind is beyond my comprehension. But it is an observational fact. Our ability to handle the scientific challenge of climate change will be a subject of future historical research and writing. The eyes of future generations will be upon us. There has never been an individual scientific problem that will have so much impact as the global warming inquiry on the long term well being of the human race. I have included anecdotes in the text to illustrate some of the more outstanding contemporary problems. There are many that I have not included, and I anticipate that there will be many more before our task is done. If we are all aware of the human problem in the scientific investigation. I am sure that we can carry the scientific problem through to successful and honorable completion.

Poster Papers

The Solar Cycle

MAGNETIC POWER SPECTRA IN THE SOLAR PHOTOSPHERE DERIVED FROM GROUND AND SPACE BASED OBSERVATIONS

V. I. Abramenko¹, V. B. Yurchyshyn²

¹Crimean Astrophysical Observatory, 334413, Nauchny, Crimea, Ukraine, *e-mail* avi@crao.crimea.ua ²Big Bear Solar Observatory, New Jersey Institute of Technology, Big Bear City, CA 92314, USA

ABSTRACT

We study the magnetic power spectra of active and quiet regions by using Big Bear Solar Observatory and SOHO/MDI measurements of the longitudinal magnetic fields. The MDI power spectra were corrected with Modulation Transfer Function. We obtained reliable magnetic power spectra in the high wave numbers range, up to $k = 4.6 \text{ Mm}^{-1}$, which corresponds to spatial scale of l = 1.4 Mm. We show that the spectral discontinuity at high wave number $k = 3 \text{ Mm}^{-1}$ largely depends on the spatial resolution of the data and it appears at higher wave numbers as the resolution of the data improves. The spectral discontinuity in the raw spectra is located at wave numbers about 3 times smaller than the wavenumber, corresponding to the resolution of the data, and at wave numbers about 2.0-1.5 times smaller in the case of the noise-and-resolution corrected spectra. The magnetic power spectra for active and quiet region are different: the active region power spectrum is described as $\sim k^{-1.7}$ while in quiet sun region the spectrum behaves as $\sim k^{-1.3}$. We suggest, that the difference can be due to small-scale dynamo action in the quiet sun photosphere. Our estimations show that the dynamo can generate more than 6% of the observed magnetic power.

Key words: Sun: magnetic fields, magnetic power spectrum

1. INTRODUCTION

Many phenomena in the solar atmosphere result from direct and continuous interaction of the magnetic fields with photospheric plasma flows. It has been shown that the supergranulation velocity field is responsible for the well-known net-like structure of the photospheric magnetic fields and the chromospheric network (Leighton 1964; Simon and Leighton 1964).

One way to explore the interaction between the magnetic fields and plasma motions is by investigating the nature of the photospheric magnetic fields in terms of their magnetic power spectrum. The magnetic power spectrum revealss ongoing dynamics and represents the hierarchical distribution of the magnetic power at different spatial scales and can be described as $E(k) \sim k^{\mu}$, where $\mu < 0$ within some range of wave numbers called the inertial range (Monin and Yaglom 1975). Spectral discontinuities, which divide the power spectrum in spectral subranges may indicate the presence of different energy transfer mechanisms and/or energy input at certain spatial scales. Thus, the morphology of the magnetic power spectra is of vital importance for understanding the observed distribution of the photospheric magnetic fields and for elaborating theoretical models of photospheric turbulence.

In the past, the magnetic power spectra have been investigated in several studies (Nakagawa and Priest 1973; Nakagawa and Levine 1974; Knobloch and Rosner 1981; Lee at al. 1997) in which only ground based measurements of the magnetic fields have been used.

We use here ground and space based measurements of the longitudinal magnetic fields to obtain reliable magnetic power spectra at high wave numbers and to study their structure.

2. OBSERVATION

Our data include Big Bear Solar Observatory (BBSO) and SOHO/MDI measurements of the magnetic fields in active and quiet regions. Observations of AR NOAA 8375 were made on November 4 1998, when the active region was located at the center of the solar disk. The BBSO videomagnetogram obtained at 17:25 UT in the Ca I 6103Å spectral line with a pixel size of 0".76 × 0".60. The SOHO/MDI magnetogram of the same active region was recorded at 16:32 UT with a pixel size of 0".6 × 0".6 in the Ni I 6767Å spectral line. The BBSO magnetogram was carefully co-aligned with the MDI magnetogram and rescaled. We also used magnetograms of two quiet regions. The first one is the BBSO magnetogram (390" × 300") recorded on September 20 1998 at 16:52 UT near the center of the solar disk far away from

Proc. 1st Solar & Space Weather Euroconference, 'The Solar Cycle and Terrestrial Climate', Santa Cruz de Tenerife, Tenerife, Spain, 25-29 September 2000 (ESA SP-463, December 2000)

active region magnetic fields. Since the MDI magnetogram has a large field of view $(420'' \times 420'')$, the second quiet region magnetogram is a part of the MDI magnetogram of size $350'' \times 150''$ just to the south of AR NOAA 8375.

3. CALCULATIONS OF MAGNETIC POWER SPECTRA

From the Fourier transform of the observed distribution of the magnetic fields, we calculated the magnetic power spectrum defined as (Monin and Yaglom 1975):

$$E(k) = \int_{|\vec{k}|=k} |U(\vec{k})|^2 \cdot dS(\vec{k}),$$
(1)

where $|U(\vec{k})|$ is Fourier Transformation of the data and $dS(\vec{k})$ is an element of the length of circle $|\vec{k}| = k$. Applying the mean value theorem to the integral (1) we can calculate E(k) as follows

$$E(k_m) = 2\pi k_m \sum_{k_m - \frac{dk}{2} \le |\vec{k}| \le k_m + \frac{dk}{2}} |U(\vec{k})|^2 / N(k_m),$$
(2)

where the sum is taken over $N(k_m)$ nodal points inside the area of an annulus enclosed by two circles of radii $k_m - dk/2$ and $k_m + dk/2$. The width of the annulus is defined as $dk = n\sqrt{\Delta k_x^2 + \Delta k_y^2}$, where n = 2. Wavenumber k and linear scale l are related by expression l [Mm] = $2\pi/k$, because we specified Δx and Δy are measured in Mm.

In order to avoid strong contributions to the power spectrum coming from the sunspot and as well as the associated leakage of the magnetic power from low to high wave numbers, we blocked out the sunspot and calculated the active region magnetic power spectra (Fig. 1).

At high wave numbers the spectra are flat, which indicates the presence of noise (Figure 1). Under the assumption that the spectral power of noise does not depend on the wavenumber, we subtract the power level of noise from all the spectra (Fig. 1, 2).

The next step was to reduce distortion of the MDI power spectra due to the finite spatial resolution of the MDI telescope. Using the diffraction limit of the telescope, 1".25, we calculated Gaussian Modulation Transfer Function (MTF) which relates raw spectrum E(k) and intrinsic power spectrum $\tilde{E}(k)$ (Margenau 1964)

$$E(k) = \tilde{E}(k) \cdot |MTF|^2(k).$$
(3)

We used (3) to obtain MDI noise-and-resolution corrected spectra (denoted as AR MDI/M^C in Figure 1 and QS2 MDI/M^C in Figure 2).

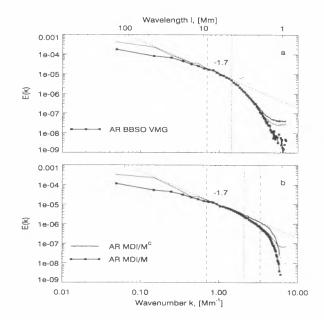


Figure 1. Top panel: BBSO active region power spectra: raw spectrum (thin line), "spot-corrected" spectrum (thick line) and spot-and-noise corrected spectrum (thick line with asterisks). Bottom panel: MDI active region power spectra: raw spectrum (thin line), spot-and-noise corrected spectrum (AR MDI/M, thick line with asterisks), spectrum corrected with Modulation Transfer Function (AR MDI/M^C, thick line). The verticals indicate the beginning and the end of linear intervals on which power indices were defined.

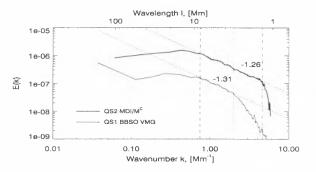


Figure 2. Quiet region BBSO power spectrum (QS1 BBSO VMG, thin line), and MDI power spectrum corrected with Modulation Transfer Function (QS2 MDI/ M^C , thick line). The dashed vertical indicates the beginning of linear intervals on which power indices were defined. The dotted vertical shows the end of the linear interval in the QS1 BBSO VMG spectrum, while the dash-dot line indicates the end of the interval in the QS2 MDI/ M^C specrum.

4. THE SPECTRA ANALYSIS

In each corrected spectrum we defined linear intervals and their slopes for three different ranges of wave numbers: low, intermediate and high wavenumbers (Figure 3)

The position of the spectral discontinuity (break) between the low and intermediate ranges (low wavenumber break) in all the spectra is approximately the same and corresponds to scales of 8 - 12 Mm (Figure 3, see also Muller 1988). This break appears, apparently, because we lack large-scale magnetic structures in the magnetograms. Note, that we analyze here only "spot-corrected" spectra. The power spectrum, which include the contribution of the sunspot do not show any particular feature at scales around 10 Mm (see Figure 2, thin line).

The high wavenumber break in the spectra between the intermediate and high wavenumber ranges deserves special attention. Unlike the low wavenumber break, the position of the high wavenumber break is not stable and it occurs at higher wave numbers as the data quality improves (see Figures 3, 4).

We compare our spectra with previous results by Nakagawa and Priest (1973) and Lee at al. (1997). In Figure 4 we show three quiet region power spectra calculated from observational data obtained with different instruments, seeing conditions and spatial resolution. For each spectrum we define the ratio between wavenumber k_r , which corresponds to the resolution limit of the data and wavenumber k^* , where the high wavenumber break appears in the spectrum.

Nakagawa and Priest presented an uncorrected magnetic power spectrum (denoted as NP 1973 in Figure 4) with the high wavenumber break at $k^* = 0.63$. The spectrum was obtained from the Kitt Peak longitudinal magnetogram with spatial resolution of 5''.0. which corresponds to $k_r = 1.73 \text{ Mm}^{-1}$ (note, that $k = 2\pi/l$). For this spectrum the we found the ratio $k_r/k^* = 2.75$. Lee at al.(1997) reported a high wavenumber break at $k^* = 3.0 \text{ Mm}^{-1}$ in the MTFcorrected spectrum obtained from BBSO data with spatial resolution of about 1".8 ($k_r = 4.9 \text{ Mm}^{-1}$). These values give the ratio k_r/k^* of 1.63 (the spectrum, denoted as Lee et al. in Figure 4). In the present paper, for the MDI quiet region corrected spectrum (QS2 MDI/M^C in Figure 4) we found the ratio $k_r/k^* = 6.88/4.57 = 1.50$, where $k_r = 6.88$ Mm⁻¹ corresponds to the diffraction limit of the MDI telescope, 1''.25.

We also defined the ratio for the active region spectra (see Fig. 3). For the raw BBSO active region spectrum the ratio $k_r/k^* = 4.33/1.43 = 3.03$ is defined by the 2" atmospheric limit of resolution. For the raw MDI active region spectrum the ratio is $k_r/k^* = 6.88/2.10 = 3.28$, while the ratio decreased to $k_r/k^* = 6.88/3.35 = 2.10$ for the corrected spectrum (AR MDI/M^C in Figure 4).

One sees that the high wavenumber break is largely defined by the spatial resolution of the data and it appears at higher wave numbers as the resolution of the data improves. In the case of the raw spectra, the break is positioned at wavenumbers of about 3 times smaller than the wavenumber corresponding to the resolution of the data, and at wave numbers

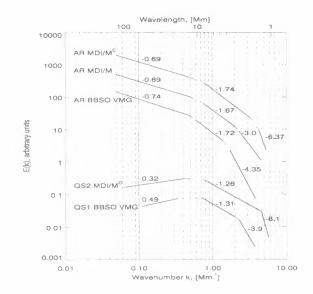


Figure 3. A schematic representation of all the magnetic power spectra obtained in the present study.

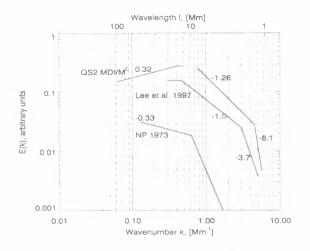


Figure 4. A schematic representation of the quiet region MDI magnetic power spectra obtained in the present study and quiet region magnetic power spectra calculated in previous works by Nakagawa and Priest (denoted in the figure as NP 1973) and by Lee and co-authors, denotes in the figure as Lee et al. 1997.

about 1.5-2.0 times smaller in the case of corrected spectra.

5. CONCLUSIONS AND DISCUSSION

Using high resolution BBSO and MDI measurements of the photospheric magnetic fields we have obtained, for the first time, reliable magnetic power spectra in the high wavenumber range up to $k = 4.6 \text{ Mm}^{-1}$ that corresponds to spatial scale l = 1.4 Mm.

The power spectra for active and quiet region magnetic fields differ considerably and can be described as $\sim k^{-1.7}$ for the active region magnetic field and as $\sim k^{-1.3}$ for the quiet region field.

The spectral behavior of the magnetic power spectra derived from the ground and space based measurements is substantially the same in the inertial intervals that changes according to spatial resolution of the data.

We found that the spectral discontinuity (break) at high wave numbers is largely determined by the spatial resolution of the data and it appears at higher wave numbers as the resolution of the data improves. The break in the raw spectra is located at wave numbers about 3 times smaller than the wavenumber corresponding to the resolution limit of the data, and at wave numbers about 2.0-1.5 times smaller in the case of the noise-and-resolution corrected spectra.

It has been known that the magnetic power spectrum, like the velocity power spectrum, shows a spectral discontinuity at wavenumber $k \cong 3.0 \text{ Mm}^{-1}$ (Lee at al. 1997 and references therein). The spectral discontinuity was interpreted to be the manifestation of the granulation structure in the magnetic field pattern and it represents a distinct scale of spectral energy transfer (Muller 1988; Lee et al. 1997). On the other hand, our results indicate that the wavenumber $k = 3.0 \,\mathrm{Mm^{-1}}$ is not a special scale, and the magnetic power spectra with a slope of μ may be extended into high wave numbers range far beyond the limit of the spatial resolution of the present day measurements. In other words, using the existing measurements of the magnetic fields, we do not reach the spatial scales where dissipative processes become significant.

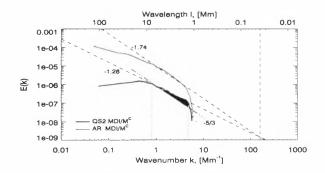


Figure 5. The active region (AR MDI/M^C, thin line) and quiet region (QS2 MDI/M^C, thick line) MDI corrected power spectra. Dashed lines show the best linear fit to the spectra in the inertial ranges. They cross each other at a spatial scale of about 40 km. The shaded area between the -5/3 dash-dot-dot-dot line and the -1.26 dashed line corresponds to the lower limit of magnetic power apparently generated by small-scale dynamo action in the quiet sun photosphere.

The main assumption of Kolmogorov's theory is that in fully developed isotropic turbulence the driving force is acting only at large scales L and there are

essentially no contributions coming from wave numbers larger than L^{-1} (Frisch 1995). In this case, kinetic energy cascades from large to small spatial scales showing spectral behavior with a power index of -5/3. We show that the power spectrum for the quiet region magnetic fields is considerably less steep and it has power law index of -1.3. If we assume that local small-scale dynamo operates in quiet sun region (Petrovay and Szakály 1993; Cattaneo 1999), than additional energy brought by the dynamo will be redistributed along the spectrum (Monin and Yaglom 1975) and this will decrease the value of the spectral index. We estimate the lowest relative amount of power generated by the small-scale dynamo under the assumption that the dynamo does not affect the magnetic power spectrum at wave numbers smaller than $L^{-1} = 0.77 \text{ Mm}^{-1}$. A total observed magnetic power in the inertial range was calculated as the area confined by the line $\sim k^{-1.26}$ on the top and zero power level on the bottom and verticals k = 0.77 and k = 4.57 (shaded area in Figure 5). The shaded area can be treated as additional power generated by the small-scale dynamo action. The additional power is about 6.4% of the total observed magnetic power in the inertial range. Numerical modeling of turbulent convection showed that up to 20% of magnetic energy can be generated by solar granulation and supergranulation by means of the local small-scale dynamo acting in the photosphere (Cattaneo 1999).

We expect that future improvement of the spatial resolution of the data will extend magnetic power spectra to much higher wave number which will result in an increase of the estimated magnetic power generated by the small-scale dynamo.

This work was supported by NSF-ATM (97-14796) and NASA (NAG5-4919) grants. We thank Drs H. Wang, M. Woodard and J. Lee for careful reading of the manuscript and useful comments.

REFERENCES

- Cattaneo, F. 1999, ApJ, 515
- Frisch, U. 1995, "Turbulence, The Legacy of A.N. Kolmogorov", Cambridge University Press
- Knobloch, E., Rosner, R. 1981, ApJ, 247, 300
- Lee, J.W., Chae, J.C., Yun, H.S., Zirin, H. 1997, Solar Phys., 171, 269
- Leighton, R.B. 1964, ApJ, 140, 1547
- Monin, A.S., Yaglom, A.M. 1975, "Statistical Fluid Mechanics", vol. 2, ed J.Lumley (ed), MIT Press, Cambridge, MA
- Muller, R. 1988, in: "Solar and Stellar Granulation", Rutten, R., Severino, G. (eds), NATO ASI Ser. C, 263, 101
- Nakagawa, Y., Prist, E.R. 1973, ApJ, 179, 949
- Nakagawa, Y., Levine, R.H. 1974, ApJ, 190, 441
- Petrovay, K., Szakaly, G. 1993, Astron. Astrophys., 274, 543
- Simon, G.W., Leighton, R.B. 1964, ApJ, 140, 1120

CYCLIC VARIATION OF SOLAR LARGE-SCALE CONVECTION

Pavel Ambrož

Astronomical Institute, 251 65 Ondřejov, The Czech Republic

ABSTRACT

The inferred values of the solar large-scale velocities, derived from the transport of background magnetic flux, were investigated during three last solar cycles nos. 21, 22 and 23. Large-scale horizontal turbulent flow was detected and the structure of vertical flow was estimated. Cyclic changes of the velocity patterns were tested and the representative variations of RMS velocity values, zonal and meridional velocities were confirmed. Specific variations of the inferred horizontal divergence, possibly relating with variable vertical transport of magnetic flux through the convection zone, are discussed.

Key words: Sun; activity cycle; large-scale velocity.

1. INTRODUCTION

Large-scale velocity field, analyzed in the present contribution, is inferred from consecutive pairs of the synoptic measurements made regularly during the last 24 years on the Wilcox Solar Observatory (WSO) of Stanford University. The synoptic data arrays, containing the values of the magnetic flux distribution, were reconstructed from the sets of harmonic coefficients. In our calculations the coefficients with maximal principal index up to l = 19 were used. The corresponding values for 320 Carrington rotations were computed in each from 2664 grid points per rotation in solar photosphere. Increment of the grid points is 5 heliographic degrees in both, zonal and meridional directions. Such data contain only the large-scale component of the magnetic flux; the intense magnetic features are effectively filtered.

The magnetic flux over the whole photosphere varies in time not only in the magnitude, but also in the spatial distribution. The lifetime of individual magnetic regions is usually long from 6 to 12 Carrington Rotation Periods (one CRP is 27.275 days). As showed in the previous studies (Ambrož, 1987, 2000), the position and the shape of magnetic regions change during their lifetime. Relative displacements can be inferred, when the Local Correlation Tracking Method (November, 1986) is applied on the two consecutive magnetic synoptic arrays. Displacement during one CRP can be transformed into the horizontal velocity vectors, computed in all the grid points in the photosphere. The velocity is interpreted as a speed of the local horizontal transport of magnetic phenomena inside of the selected window, computed relative to the Carrington reference system. Besides of the zonal and meridional velocity fields also the values of the horizontal divergence of the horizontal velocity can be derived. Each from the mentioned fields is composed from the axially symmetric (zonal averaged) values and from nonaxially symmetric component of the field. In our present study only the dependence of the axially symmetric component of the velocity on the latitude and time, is studied.

2. LONG-TERM EVOLUTION OF THE VELOCITY PATTERNS

The contour plot of the total magnetic flux distribution (usually known as the butterfly diagram), presented in Figure 1 is derived from WSO measurements. On the horizontal axis the Carrington rotation numbers are plotted. The butterfly patterns relate from left to right with the activity cycle nos. 21, 22 and 23. Values derived polewards from 70 degrees of the latitude on both hemispheres (dotted lines) are invalid for our study. The lowresolution measurements from Stanford give only one value in this zone and the reconstructed data can be considered as artifacts. All the data, available polewards from latitude 50 degrees, were from this reason ignored for further calculations.

The contour plot in Figure 2 of the mean meridional velocity show the very distinct dependence of the mean meridional velocity on the phase of the 11-year activity cycle. The bright regions show the mean meridional transport toward the solar north pole and in the dark regions is mean velocity oriented to the south. The patterns change during the cycle, however the principal N-S symmetry is preserved during the whole studied time interval. During the phase of enhanced activity the mean poleward transport is suppressed and the equatorward velocities dominate. Just after the cycle maximum the poleward transport from equator to the latitude limit 30 or 40 degrees is formed.

The plot of the net horizontal divergence is shown in Figure 3. The dark regions represents the mean negative divergence (convergence) and the bright regions corresponds with the positive values. The divergence data

Proc. 1. Solar & Space Weather Euroconference, 'The Solar Cycle and Terrestrial Climate', Santa Craz de Tenerife, Tenerife, Spain, 25-29 September 2000 (ESA SP-463, December 2000)

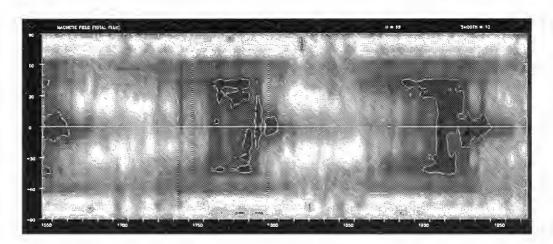


Figure 1. Contour plot (butterfly diagram) of the total magnetic flux during last three activity cycles nos. 21, 22 and 23. See description in the text.

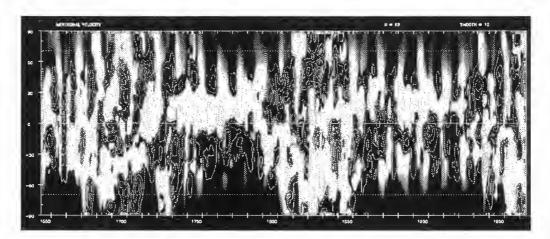


Figure 2. Contour plot of the averaged meridional velocity. Format is similar as in Fig. 1. For details see in the text.

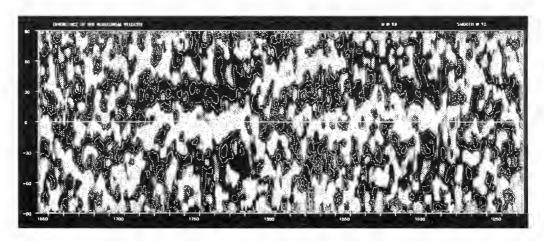


Figure 3. Contour plot of the net values of the horizontal divergence. Format is similar as in Fig. 2.

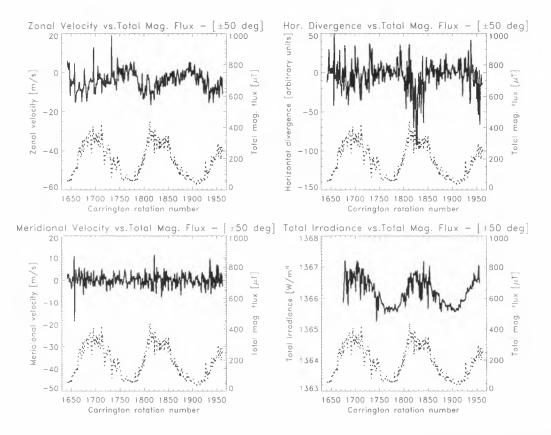


Figure 4. Plots of the mean values of the zonal and meridional velocities, horizontal divergence, total solar irradiance and total magnetic flux during last 24 years.

structure varies during the 11-year activity cycle. During the initial and maximal phase of the cycle the both regions are highly diversified and the average net divergence values are low or nearly zero. In this initial phase the close equatorial zone is covered by negative divergence. In higher latitudes, poleward from 30 degrees of latitude the positive values dominate. In the declining phase of the cycle and in the minimum have the divergence regions compact structure with positive values around the equator and the two negative divergence belts between 20 and 40 degrees on both hemispheres. During the period of minimum the negative regions are maximally developed and the equatorial positive region nearly vanishes. Such rule is observed for all three available solar cycles.

Plots of the net mean values of the zonal and meridional velocities, horizontal divergence and the total solar irradiance relative to the total magnetic flux are presented in Figure 4. Mean zonal velocity (upper left) is plotted by full line and the values are computed for each Carrington rotation in the zonal belt within 50 degrees of the latitude during the whole interval from year 1976 to 2000. The dotted line shows variation of the mean magnetic flux. The both curves are nearly inverse; the extremes of the velocity are located about 16 CRP before the total magnetic flux curve. The curve of the net meridional velocity (bottom left) is very noisy with highest amplitudes during the cycle maximum period. The net horizontal divergence (upper right) shows the extreme negative values in the maximum of the cycles. The plot of the total solar irradiance shows high correlation with the curve of the total magnetic flux. The composite data of the total solar irradiance was adopted from Fröhlich and Lean (1998).

Plots of the derived cross-correlation functions are presented in Figure 5. They demonstrate the cross correlation functions calculated from the zonal velocity (upper left), meridional velocity (bottom left), horizontal divergence (upper right) and total solar irradiance (bottom right) relative to the total magnetic flux. Discussion of the individual cases is presented in the final section of this paper.

3. DISCUSSION AND CONCLUSIONS

Zonal and meridional transports, as well as the horizontal divergence are studied via the net arithmetic means for each from 320 Carrington rotations. The obtained velocity patterns show regularities in the global distribution of all three values, however each of them have an original distribution and do not show direct common relationship with the structure of the total magnetic flux. The sets of the global values from the broad equatorial belt for all studied Carrington rotations vary with the mean period of 11-year cycles of activity. Each velocity parameter reflects their relationship to the set of the total magnetic flux values differently.

The variations of the zonal velocity show clear phase shift (-16 CRP) relative to the maximum of total magnetic flux and the mean amplitude of the variations is lower than 10 m/s. The meridional displacement oscillates around the zero value with highest mean amplitude around 3 m/s

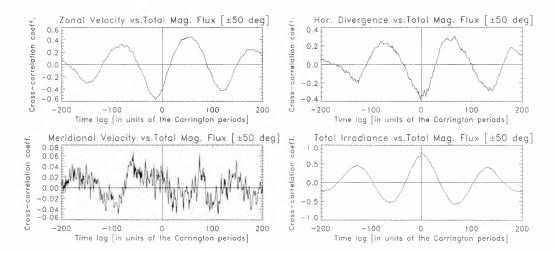


Figure 5. Plots of the cross-correlation functions between the total magnetic flux and the zonal and meridional velocities, horizontal divergence and the total solar irradiance.

during the cycle maximum. The net horizontal divergence is substantially different from zero only during the period of the enhanced magnetic flux, but their values are expressed only in arbitrary relative units. The both, zonal and meridional velocity cyclic variations do not close correlate with the total magnetic flux curve. The cross correlation minimum of the zonal velocity is, however, located 16 CRP before the magnetic flux. The meridional velocity plot is substantially different from the both previous curves and is characterized by an amplitude modulation of the short noisy spikes. The cross correlation coefficient with the zero time lags is nearly equal to zero. Contribution of the both zonal and meridional velocities to the total horizontal velocity is characterized by mean RMS velocity values for each Carrington rotation. The cross correlation maximum also precedes the magnetic flux curve for 16 CRP. The horizontal transport is probably causally bounded with the occurrence of the magnetic flux. The horizontal divergence relates with the magnetic flux without the time difference, however the obtained anticorrelation is still fully unclear. On the other hand, the total solar irradiance shows the positive cross correlation with zero displacement relative to the total magnetic flux.

The horizontal transport, reported in the present paper, shows the still unexpectedly dramatic moving structures of the large-scale magnetic fields in solar photosphere. The changes in the different phases of the 11-year cycle of solar activity document the large-scale long term cyclically changing dynamic regime in the solar convection zone. We suppose that the changes of the global regime of the convection during the activity cycle is able to modify also the total solar output.

ACKNOWLEDGEMENTS

The Wilcox Solar Observatory data used in present study was obtained via the WWW site http://quake.stanford.edu/~wso with courtesy of J.T. Hoeksema. Author is grateful also to X. Zhao for kind help during the period of data preparation. The Wilcox Solar Observatory is supported by NASA, NSF, and ONR. We acknowledge receipt of the composite dataset of the total solar irradiance version 15 from PMOD/WRC, Davos, Switzerland. Present work was made under support of grant of GA/AVČR No. A3003806 and S1003006 and the Key Project AVČR No. K1-003-601.

REFERENCES

- Ambrož, P.: 1987, Bull. Astron. Inst, Czechosl. 37, 110.
- Ambrož, P.: 2000, Solar Phys. (in print).
- Fröhlich, C. and Lean, J.: 1998, in F. L. Deubner (ed.), IAU Symposium 185: New Eyes to See Inside the Sun and Stars, Kluwer Academic Publ., Dortrecht, The Netherlands, p. 89.

November, L. J.: 1986, Applied Optics 25, 392.

THE VARIATIONS OF THE SOLAR ACTIVITY AND THE LOW RIGIDITY COSMIC RAYS (1969 – 1998)

Anna Antalová¹, Karel Kudela¹, and Ján Rybák²

¹Institute of the Experimental Physics, Slovak Academy of Sciences, Watson str. 47, 04353 Košice, The Slovak Republic ²Astronomical Institute, Slovak Academy of Sciences, 05960 Tatranská Lomnica, The Slovak Republic

ABSTRACT

The wavelet power spectra were calculated and compared for the whole solar disk time series: the Mt. Wilson Magnetic Plage Strength Index (MPSI) and the Mt. Wilson Sunspot Index (MWSI) as well as the low rigidity Calgary cosmic rays (CR). The intermediate- and the longterm periodicities are established during a 6-year interval of the respective cycle (2 years before and 4 years after the cycle maximum). The periodicities longer than 100 days are dominant in the post-maximum years. The 260-day period of the MPSI has dual structure, the peaks are in 1979 and in 1981–1982 post-maximum years. We found, that the well known long-term cosmic ray periodicity 1.5 – 1.7 year is present in the low rigidity Calgary cosmic rays, in 1983.5 and in 1991.0 years.

1. INTRODUCTION

In prior papers, the significant variations were found among various solar events (e.g., the long-duration X-ray flares, Antalová, 1994, 1999), the solar wind speed (Richardson et al., 1994), the geophysical data (Mendoza et al., 1999) and the cosmic rays (Valdés-Galicia, Pérez-Enriquez and Otaola, 1996, Kudela et al., 1999). SOHO/MDI and GONG helioseismic data (Komm, Howe and Hill, 2000) reveals very important period around 1.3 year (about 474 days). It is more-less confirmed that the intermediate- and the long-term solar variability periods are related to the solar magnetic flux. In this paper we present the wavelet power spectra (WPS) of the solar and the low rigidity cosmic ray data (from Calgary) for the cycles No. 21 and No.22.

2. THE DATA SETS

Wavelet power spectra have been computed for the following parameters:

(a) Mt. Wilson Magnetic Plage Strength Index (MPSI). For each magnetogram taken at the 150–Foot Solar Tower, the Mt. Wilson Magnetic Plage Strength

Index (MPSI) value and the Mt. Wilson Sunspot Index (MWSI) value are calculated. To determine MPSI the absolute values of the magnetic field strengths is summed for all pixels where the absolute value of the magnetic field strength is between 10 and 100 gauss. This number is then divided by the total number of pixels (regardless of magnetic field strength) in the magnetogram.

(b) Mt. Wilson Sunspot Index (MWSI). The MWSI values are determined in much the same manner as the MPSI, though summation is only done for pixels where the absolute value of the magnetic field strength is greater than 100 gauss. Data are daily means from more then just one measurement (if available). The MPSI and MWSI data were taken from www.mtwilson.edu/Science/UCLA/.

(c) **CR** – the low rigidity Calgary cosmic rays – Calgary latitude 51° 05' N. Calgary longitude 114° 08' W, vertical cutoff 1.09 GV, count rate approximately 2×10^4 per 5–min (Venkatesan et al., 1989).

3. METHOD OF PROCESSING

The common tool of the frequency investigation of the data series - the Fourier Transform (FT) - does not allow the extraction of any temporal information of the data series. Different sines and cosines, into which FT decomposes data series, cannot be localized in time according to the uncertainty principle as these trigonometric functions are calculated for sharp frequencies (Bracewell, 1965). Therefore FT is not appropriate for the study of data series which show significant temporal variability.

The wavelet transform is a suitable tool to analyze time series that contain non-stationary power at many different frequencies (Daubechies, 1990). Its functions - wavelets - are localized in both time and frequency, characterized by non-dimensional time parameter η and frequency ω_0 .

As we are dealing with a simple oscillatory data series, the Morlet wavelet - a plane sine wave of amplitude windowed in time by a Gaussian function, has been selected for searching of power in different frequencies over the whole time length of the series.

Proc. 1st Solar & Space Weather Euroconference, 'The Solar Cycle and Terrestrial Climate', Santa Cruz de Tenerife, Tenerife, Spain, 25-29 September 2000 (ESA SP-463, December 2000)

Describing our data series as x_n with an fixed temporal spacing δt and the data index n = 0, 1, ..., N the Morlet wavelet can be prescribed as the following function $\psi_0(\eta) = \pi^{-1/4} e^{i\omega_0 \eta} e^{-\eta^2/2}$. For this selected wavelet the non-dimensional frequency ω_0 has been set to 6 fixing the length of all wavelets according to their scale s. The continuous wavelet transform of a discrete time series x_n is defined (Torrence and Compo, 1998) as the convolution of data series with a scaled in frequency s and translated in time η wavelet $\psi_0(\eta)$ as

$$W_n(s) = \sum_{n'=0}^{N-1} x_{n'} \psi^* \left[\frac{(n'-n)\delta t}{s} \right]$$
(1)

where the sign ψ^* denotes the complex conjugative of the wavelet ψ . The wavelet transform W_n is so a projection of the data series onto the selected wavelets of different scale s at different time. Varying the scale s and translating along the time index n picture of varying (if existing) amplitude for different scales can be determined over the whole time interval of the data series.

In order to compare directly the WT at each scale s the wavelet functions were normalized to have unit energy at each scale. As the wavelet Morlet function ψ_0 and its wavelet transform $W_n(s)$ are complex the wavelet power spectrum $|W_n(s)|^2$ was calculated to visualize the time-frequency behaviour of the data series amplitudes.

A convenient set of scales has been selected following the formula $s_j = s_0 2^{j \cdot \delta j}$ for j = 0, 1, ..., J where s_0 is the smallest computed scale and J specifies the largest one. Parameter δj specifies the scale resolution. For broader period range (16-2048 days) these parameters has been set as $s_0 = 16$ and J = 336, for the narrower one (18-38 days) parameter s_0 has been changed 2. For both ranges the scale resolution δj was fixed to 48 scales per octave.

The WT computational algorithm of Torrence and Compo (1998) has been used in this study. As it is based intrinsicly on the FT of the data sets of the finite length the data sets had to be padded with zeroes in order to bring the total length of the data sets N to the next higher power of 2. This padding with zeroes decreases the amplitudes of the wavelet power spectrum $|W_n(s)|^2$ as still more and more zeroes entered the temporary data set increasing the scale s of the transform. Therefore the coin of incidence was introduced here as the e-folding time of the wavelet power spectrum $|W_n(s)|^2$ areas covered by this coin of incidence (indicated in our plot by cross-hatched regions) the amplitudes has been reduced in their magnitude.

In order to setup the significance levels of the derived wavelet power spectrum the null hypothesis has been formulated according to Torrence and Compo (1998) assuming that the time series has a mean power spectrum, given by normalized FT power spectrum of the red noise univariate lag-1 autoregressive process. If a wavelet power spectrum is well above the background mean power spectrum (global spectrum), then it can be assumed to be real with a certain confidence level. The 95% confidence level, used in this study, implies that 5% of the wavelet power should be above this level for each scale. In this study the global wavelet spectrum $\overline{W}^2(s) = 1/N \sum_{n=0}^{N-1} |W_n(s)|^2$ has been used as an estimate of the background mean power spectrum against which the significance of the local WPS features has been tested according to findings of Percival (1995) and Kestin et al. (1998). In Table 1 we give the global power spectra periods of our data series.

4. RESULTS AND DISCUSSION

Our investigated period is still very short to be able to draw general conclusions about the time-frequency behaviour of the long-term solar periodicities during solar cycles. Nevertheless, the following conclusions can be drawn on periods given in Table 1.

- The time period WPS show the significant statistical differences of the MPSI and the MWSI data comparing to the low rigidity Calgary cosmic rays, in studied years. We found the large differences between WPS of the increasing and the declining parts of the last two cycles. We present quantitative evidence that in the maximum epoch of the last two solar cycles, there is no continual duration of the long-term periodicities, but there are multifrequency dual peaks of the solar cycle maxima. Time location of WPS impulses coincide with preand post- maximum years (Gnevyshev gap, Storini and Pase, 1995; Bazilevskaya et al., 1998, Rybák, Antalová and Storini, 2000).
- The 21-st solar cycle characteristics: The 21-st solar cycle is unique in the density of the occurrence of 150-day periodicity in all solar parameters. The 154-day periodicity (Rieger et al., 1985) was expected in the solar and the heliospheric (Cane, Richardson and von Rosenvinge, 1998) data and really such period is present (together with other larger periods) in the XBG (in late 1980, 1982.7), the SXR-flare indices (in late 1980, 1982.7, see Rybák, Antalová and Storini, 2000), in the MPSI and the MWSI (there is significant multi-period peak with periods greater than 128-days, mainly in post-maximum years). In the CR, the 154-day period is present in 1981.4, 1982.7, 1986.1, 1990.0, and 1991.6 years.
- What concerns of the quasi-biennial period, which is generally but erroneously believed that is better expressed in the even than in the odd cycles, we obtain following result. The occurrence of the quasibiennial period is remarkable high during the 21-st cycle in the MPSI (877-days, 2.4-year) and the MWSI (around 900 days, 2.5 year) data. The quasibiennial period, in the occurrence of the LDE flares is not related to the 21-st cycle (as the MPSI and MWSI), but to the 22-nd solar cycle maximum (see Table 1, LDE -2.3 year, IMP-2.2 year). This is very important difference between the 21-st and the 22-nd cycles.

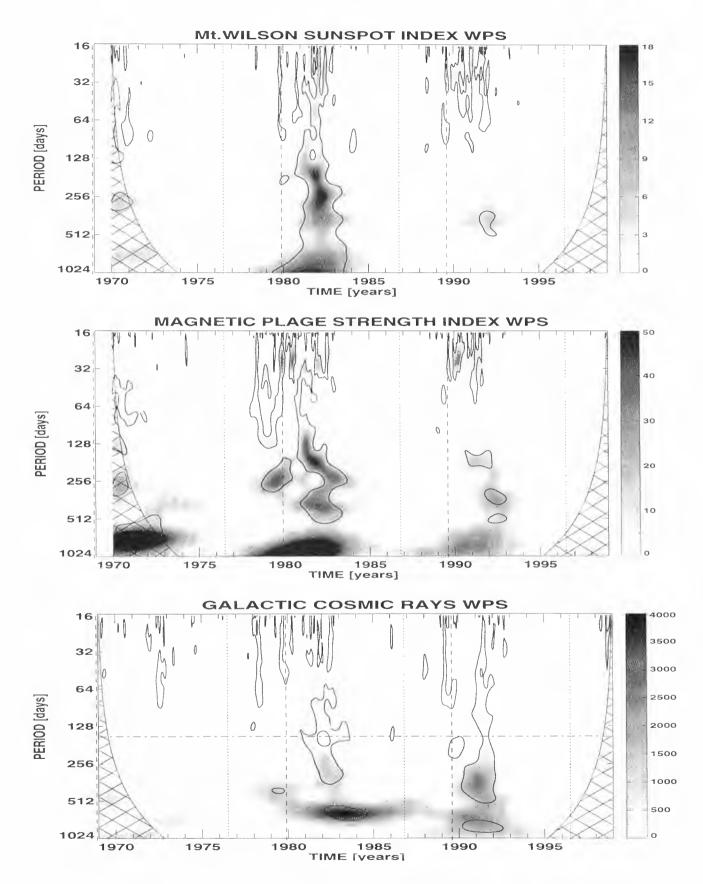


Figure 1. The wavelet power spectrum (WPS) of the Mt. Wilson Magnetic Plage index, the Mt. Wilson Sunspot index and the Calgary Cosmic Ray data series. The time spacing parameter of the series is 1 day, the scale resolution is 48 scales per octave. The thick solid curve stem for the 95% confidence level of the spectrum. The coin of incidence is marked by the cross-hatched regions. The solar activity cycle maxima and minima are signed by dashed and dotted vertical lines respectively according to the Wolf's sunspot index. 150-day period is marked by the point-dashed horizontal line (in bottom panel).

Table 1. The synodic recurrence, the intermediate-term and the long-term periods obtained from wavelet global power spectrum analysis. In the head-line are given expected periods, from Wolff's g-beats (Wolff, 1974). LT (1)- stay for the long-term periods lower than 1000-days, LT (2)- for the long-term periods greater than 1000-days.

IP(days)	27.0-	53-	83-	155-	270-	323-	LT (1)-	LT (2)-
MPSI	27.5				268	396-1.1y	877–2.4y	
MWSI	26.4	53		164	263	414-1.2y		
XBG	28.0		83	155	301		568–1.5y	1333–3.7y
LDE	31.5	48	80	146	223	770–2.1y	850-2.3y	1412-3.9y
IMP	38.2		83	157	268		810-2.2y	
CR						400-1.1y	647–1.7y	

- The expected the 1.7 year (647-days) period of the cosmic rays (Valdés-Galicia, Pérez-Enríquez and Otaola, 1996) is found in the 21-st cycle: the 1983.5 peak in CR and in XBG; the 1982.5 peak in the LDE flares. In the 22-nd cycle, the CR-peak is present in 1991; but its dominant periods are 400- and 800-days.
- We found the occurrence of the 1.1 1.5 year periodicity in the following data: in the MPSI (period 396–days, 1.1-year), the MWSI (414 days, 1.2 year), XBG (568–days, 1.5 year) and in the low rigidity Calgary CR (in 1991, the period is 1.1 year).
- Synodic recurrence. As is well known, the synodic recurrence of the cosmic rays is indicator of quasistable heliospheric conditions (Vernova et al., 1995) and reflects the repetition of *the all 27-day CR profile* as ' time unit'. We found the synodic recurrence of CRs mainly in 1978, 1979, 1982 and also in 1986, 1989, 1991 and in 1998.

ACKNOWLEDGMENTS

This contribution was carried out within the scope of the Slovak VEGA Grant 2/7229/20 and 2/5137/20. A. Antalová thanks the warm hospitality of the Instituto de Astrofisíca de Canarias during the 1-st SOLSPA Euroconference and expresses her gratitude to European Union for financial support.

The computations were performed using the modified wavelet software, original of which was provided by C. Torrence and G. Compo (Program in Atmospheric and Oceanic Sciences, University of Colorado, Boulder, U.S.A.) available at URL: paos.colorado.edu/research/wavelets/.

This study includes data from the synoptic program at the 150-Foot Solar Tower of the Mt. Wilson Observatory. The Mt. Wilson 150-Foot Solar Tower is operated by UCLA, with funding from NASA, ONR and NSF, under agreement with the Mt. Wilson Institute.

REFERENCES

Antalová, A., 1994, Adv. Space Res. 14, 721

- Antalová, A. 1999, Proc. of the 9-th European Meeting on Solar Physics, ESA SP-448, 743
- Bazilevskaya, G.A., Krainev, M.B., Makhmutov, V.S., Sladkova, A.I, Storini, M. and Flückiger, E., 1998, in Proc. 16-th ECRS, Alcala, Spain, 83
- Bracewell, R.N., 1965, *The Fourier Transform and Its* Application, McGraw-Hill, New York
- Cane, H.V., Richardson, I.G. and von Rosenvinge, T.T., 1998, Geophys. Research Letters 25, 4437
- Daubechies, I., 1990, *IEEE Transactions on Information* Theory 36, 961
- Komm, R., Howe, R. and Hill, F., 2000, in these Proceed.
- Kudela, K., Yasue, S., Munakata, K. and Bobik, P., 1999, 26-th ICRC, Vol. 7, 163
- Kumar, P. and Foufoula-Georgiou, E., 1997, Reviews of Geophysics 35, 385
- Mendoza, B., Lara, A., Maravilla, D. and Valdés-Galicia. J.F., 1999, Solar Phys. 185, 405
- Percival, D.P., 1995, Biometrika 82, 619
- Richardson, J.D., Paularena, H.I., Belcher, J.W. and Lazarus, A. J., 1994, Geophys. Res. Letters 21, 1559
- Rieger, E., Share, G.H., Forrest, D.J., Kanbach, G., Reppin, G., Chupp, E.L., 1985, Nature, **312**, 623
- Rybák, J., Antalová, A. and Storini, M., 2000, in these Proceedings
- Solar Geophysical Data, 1969 1976, Parts I and II; 1994, No. 602, part II
- Storini, M. and Pase, S., 1995, STEP GBRSC News 5, Special issue, 255
- Torrence, C. and Compo, G.P., 1998, Bulletin of the American Meteorological Society 79, 61
- Valdés-Galicia, J.F., Pérez-Enríquez, R. and Otaola, J.A., 1996, Solar Phys. 167, 409
- Venkatesan, D., Mathews, T., Graumann, H. and Sharman, P., 1989, Calgary Cosmic Ray Intensity Records-Super Neutron Monitor, The Calgary University
- Vernova, E.S., Tyasto, M.I., Baranov, D.G. and Grigorian, M.S. 1995, in the 24-th ICRC, Roma, Vol. 4, 564Wolff, C.L., 1974, Astrophys. J. 193, 721

MgIb₂ BRIGHT FEATURES IN THE SOLAR PHOTOSPHERE

F. Berrilli^{1,2}, R. Bruno², G. Consolini², A. Florio¹ and E. Pietropaolo^{3,2}

¹Dipartimento di Fisica, Universita` di Roma 'Tor Vergata' Viale della ricerca scientifica 1, I-00133 Roma, Italy tel: +39 06-7259-4430 / fax: +39 06-2023507 e-mail:berrilli@roma2.infn.it

²IFSI/CNR Area di Ricerca 'Tor Vergata', I-00133 Roma, Italy

³Dipartimento di Fisica, Universita` dell'Aquila Via Vetoio, 1-67010 L'Aquila, Italy

ABSTRACT

The magnetic network is a key component of solar irradiance and of the energy transport toward the corona. These network structures are associated in the photosphere with bright magnetic elements, whose dynamics is determined by granulation.

The association between small magnetic elements and bright points in the photosphere, which are cospatial with magnetic network (e.g. Muller et al., 2000, or Baudin et al., 1997), allow us the selection of magnetic regions of interest for a spectroscopic study.

The photospheric magnetic network contribution to the Total Solar Irradiance (TSI) and its variations is a still open problem even if it has been discussed in different papers (e.g. Unruh, Solanki and Fligge, 1999, or Schuhle et al., 2000). Recently, by analyzing full-disk RISE-PSPT observations, it has been evaluated the photospheric network contrast and the role of related variations to the TSI (Ermolli, Berrilli and Florio, 1999).

In this paper we present an analysis of properties of photospheric vertical velocity and broad band intensity fields associated to bright MgIb₂ elements. The observations of a central quiet granulation field were obtained with the THEMIS-IPM using the Fel 557.6 nm and MgIb₂ 517.3 nm lines.

OBSERVATIONS

Different sequences of broad band (5 nm FWHM around 557 nm) and monochromatic images were performed at the THEMIS telescope (Observatorio del Teide, Tenerife) in 1999 July. We analyzed the data series performed the July 8th (from 7:21 UT to 8:04 UT), with the IPM monochromator (Cavallini, 1998). The telescope set-up limited the spatial resolution to

~0.4 arcsec (about 300 km on the Sun). A square portion (34 arcsec \times 34 arcsec) of the quiet Sun at the disk center, was imaged with the broad band camera and through the IPM monochromator at different spectral points around 517.3 nm (MgIb₂ line) and 557.6 nm (Fe I line), with 2.1 pm FWHM. The image scale was set at 0.134 arcsec/pixel.

Two 12-bit binned CCD cameras (Berrilli et al., 1997) recorded the frames. Each monochromatic image was acquired with an exposure time of 0.3 s and the total interval between successive images was 2.5 s.

After the corrections for dark current, flat field and telescope tracking loss a sub-portion of (30 arcsec \times 30 arcsec) made up the final images. Velocity fields were computed using Doppler shift, evaluated with a Gaussian shape non-linear best fit of the line profile. Before the analysis of the granulation pattern and the study of the convective velocity fields, the acoustic modes pattern has been removed from the images. We applied a subsonic filter (Title et al., 1989) with a cut-off velocity of 6 km s⁻¹.

IMAGES ANALYSIS

To identify the small scale magnetic fields areas we use the strong correlation between magnetogram signal and brightness in the Mglb₂ blue wing. Although the granulation dynamics produces a rapid evolution of the bright points, we restrict our analysis on the average properties of photospheric fields.

To extract $MgIb_2$ features we average over the 40 minutes sequence obtained in the wing (- 30 pm) of Mg line and we produce the image shown in Fig.1.

The corresponding broad band image is obtained averaging all the 570 broad band frames, while the velocity image is obtained from the average of the 32 photospheric vertical velocity fields coming out from the Fel 557.6 spectral frames.

Proc. 1st Solar & Space Weather Euroconference, 'The Solar Cycle and Terrestrial Climate', Santa Cruz de Tenerife, Tenerife, Spain, 25-29 September 2000 (ESA SP-463, December 2000)

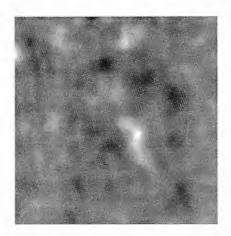


Figure 1: Average image in Mg wing $(\lambda_0 - 30pm)$ obtained from a set of 32 frames.

MgIb₂ BRIGHT FEATURES EXTRACTION

In order to identify active regions in average Mglb₂ image, we adopted the following procedure. Firstly we studied the features of his intensity distribution function. As shown in figure 2 the distribution has a bimodal character that can be easily obtained as a superposition of two gaussian distributions. This is an evidence of two distinct populations that can be associated with quiet and active regions. Then, on the basis of this bimodal character we define a threshold I_{th} as the intensity value corresponding to the intersection of two gaussian curves: I_{th} = 0.65.

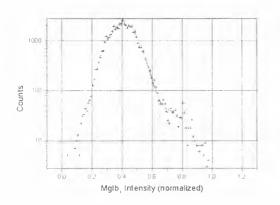


Figure 2: Distribution of $Mglb_2$ intensities (crosses) with the two superimposed gaussian distributions (solid lines).

In figure 3 we show the image obtained adopting the aforementioned threshold. The image shows some scattered bright regions that would be correlated to average broad band intensity and velocity fields. In detail we selected 4 intense bright regions (labeled A-D in figure 3).

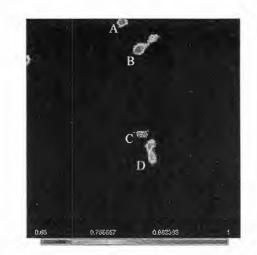


Figure 3: Image of selected MgIb₂ active regions

DISCUSSION

In Table 1 we report the statistical properties of $Mglb_2$ blue wing intensities, broad band intensities, and vertical photospheric velocities, associated to bright $Mglb_2$ regions.

The velocity average values confirm the role of granular convection on the transport of magnetic elements.

It seems that a slight positive contrast in broad band intensity images is related to active regions, in contrast to the fact that these regions are associated to downflows, usually dark in white light images.

Table 1: 1st column, active region label; 2nd column, MgIb₂ average normalized intensity; 3rd column, average broad band contrast (Γ_{bb}), defined as <1_{region}>/<I_{frame}>; 4th column, average vertical velocity of active region obtained from 557.6 spectra (negative values are up-flows, while positive ones are downflows).

Active area	Mg Intensity	Γ_{bb}	<v> ms⁻¹</v>
А	0.80±0.08	1.02±0.02	-1±30
В	0.76±0.08	0.99±0.02	$+150\pm40$
С	0.72±0.05	1.01±0.01	+ 79±50
D	0.75±0.06	1.01±0.02	$+98\pm70$

On the other hand the distributions of figure 4 underline the importance of studying the properties of active regions individually, while the granulation dynamics produces a temporal dependence of the features. So it is clear that experimental (better spatial and temporal resolution) and theoretical (dynamical models) improvements are necessary to tackle the problem of bright points in the photospheric network.

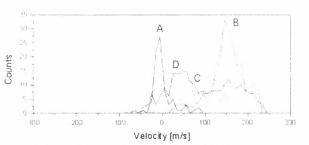


Figure 4: Vertical velocity distributions associated to the selected active regions. Negative values are upflows, while positive ones are down-flows.

ACKNOWLEDGEMENTS

This work is based on observations obtained with the Italian Panoramic Monocromator mounted at the THEMIS-CNRS/INSU-CNR telescope at the Spanish Observatorio del Teide (Tenerife) of the Instituto de Astrofísica de Canarias. We thank the THEMIS staff for the efficient support in the observations. Special thanks are due to C. Briand, G. Ceppatelli and G. Mainella for the IPM operation support.

BIBLIOGRAPHY

- Baudin F., Molowny-Horas R. and Koutchmy S.: Granulation and magnetism in the solar atmosphere, *A&A.*, Vol. 326, pp. 842-850, 1997.
- Berrilli F., Caccin B., Cantarano. S. and Egidi A.: Image acquisition system for the Italian Panoramic Monochromator of the THEMIS telescope, *Il Nuovo Cimento C*, Vol. 20, pp. 967, 1997.
- Cavallini F.: The Italian Panoramic Monochromator, A&AS, Vol. 128, pp. p.589-598, 1998.
- Ermolli I., Berrilli F. and Florio A.: Solar irradiance variations associated to quiet network, *ESA SP*-448, Vol. 1, pp. 275, 1999.
- Muller R., Dollfus A., Montagne M., Moity J., Vigneau J.: Spatial and temporal relations between magnetic elements and bright points in the photospheric network, *A&A*, Vol. 359, pp.373-380, 2000.
- Schühle U., Wilhelm K., Hollandt J., Lemaire P., Pauluhn A.: Radiance variations of the quiet Sun at far-ultraviolet wavelengths, A&A, Vol. 354, pp.L71-L74, 2000.
- Title A. M., Tarbell T. D., Topka K. P., Ferguson S. H., Shine R. A. and the SOUP Team: Statistical properties of solar granulation derived from the SOUP instrument on Spacelab 2, *ApJ*, Part 1, Vol. 336, Jan. 1, pp. 475-494, 1989.
- Unruh Y. C., Solanki S. K. and Fligge M.: The spectral dependence of facular contrast and solar

irradiance variations, *A&A*, Vol.345, pp.635-642, 1999.

COMPLEXES OF ACTIVITY - BASIC COMPONENTS OF ACTIVITY CYCLES (FROM THE BOTTOM OF THE CONVECTIVE ZONE TILL THE INTERPLANETARY SPACE)

V. Bumba (bumba@asu.cas.cz), M. Klvaňa (mklvana@asu.cas.cz) Astronomical Institute, Academy of Sciences of the Czech Republic, 251 65 Ondřejov, Czech Republic A. GARCIA (adriana@ci.uc.pt) Observatório Astronómico Universidade de Coimbra, 3000 Coimbra, Portugal

Abstract

Previous, as well as new results demonstrate the importance of the development of complexes of activity for the dynamics of the global, as well as local solar activity and magnetic field distribution in time and space. These basic activity elements connecting individual active regions grow successively for more than one year in close relation with the longitudinal activity distribution. Their magnetic fields and activity gradually become complicated. They often develop in series of several complexes, consecutively appearing in the same area of the solar surface. The evolution of such a series culminates in the formation of large, complex active regions, producing powerful flares, and eruptions of chromospeheric and coronal matter into space. Then, in three to four rotations, its primarily very complicated magnetic field, occupying a large portion of the solar surface, quickly simplifies, and several rotations later, a coronal hole develops.

1. Introduction

We would like to demonstrate how we conceive the basic element of solar activity, as regards its development in time, as well as its positioning in the solar atmosphere. We believe that this element, combining mostly in a specific way a certain number of individual active regions, originating in the same source, conjoins and cumulates their activity power. And this physically interconnected family of active regions, if they appear in almost the same area several times repeatedly, can reach a very high degree of geoactivity. Its successive growth through the photosphere, chromosphere and corona into interplanetary space depends not only on the power of the source, but also on the age and density of the remnants of the previous activity in the area, on the quantity, live history, succession of and mutual relations between the successively supplied new magnetic fluxes of its active regions.

The appearance of such forms of activity is not accidental. It is given by the stage of development of the activity cycle and the degree of the resulting dynamics of photospheric convective and other movements, and the global magnetic field distribution. Probably, there also exist regularities in the intensity and organization of the internal, deeper lying sources of magnetic and kinetic energy, initiating the studied activity in the higher layers of the solar atmosphere.

This is the reason why we summarize our experience obtained by studying the formation and evolution of various elements of the eleven-year activity cycle, or activity impulses demarcated in time and area, or complexes of solar activity during the last four elevenyear activity cycles.

2. Introduction of a simple complex of activity

Bumba and Howard (1965a, b) demonstrated that the development of a single active region is not enough to make a permanent change in the pattern of even weak background fields. To achieve the slow transitions from one form to another we see in the background fields, it is necessary to maintain a certain density of activity over a large area. A larger density of activity is observed to occur in clusters of active regions. During the years of maximum activity it is difficult to separate these clusters of activity from each other, but in the descending phase of the cycle and closer to minimum it is relatively easy to follow the development and evolution of these complexes of activity, as we have called such clusters, due to their complicated formation and highly extended volume of the solar atmosphere they occupy. Evidently, they represent the basic unit of solar activity in time and space connecting the individual active regions into one activity impulse. Its formation can be observed in the following way:

Over a certain longitude range one may see no new active regions - only old fields - for several rotations. Then in one rotation, one or more new active regions form. On subsequent rotations, new active regions form and the area occupied by fields expands in both latitude and longitude. In general, the first sunspot groups to form are the largest of the complex and later ones are smaller. The larger is the complex of activity, the larger are its first spot groups and the longer is the lifetime of the complex. The expansion of the boundaries of a complex of activity measured once on each rotation is linear with time in longitude, with a velocity of the order of 100 msec⁻¹. In latitude there seems to be a limit of about 40° in the maximum extension, beyond which the expansion is extremely small (a few tens of meters per second). Some of these complexes of activity have associated with them features in the green-line coronal isophote maps which show approximately the same expansion and lifetimes (Bumba and Sýkora, 1974).

Proc. 1st Solar & Space Weather Euroconference. 'The Solar Cycle and Terrestrial Climate', Santa Cruz de Tenerife, Tenerife, Spain, 25-29 September 2000 (ESA SP-463, December 2000)

3. Studies of evolution of the proton-flare region and other large complex activity formation

3.1 Process of proton-flare region formation and desintegration as a successive evolution of several complexes of activity in the same area of the solar atmosphere

We have studied the evolution and formation of various complex activity events. Already during the declining part of the 19th solar activity cycle, we found that the active regions producing flares which were followed by a particle emission, observed as cosmic rays or PCA events, correlated with a specific configuration of the background magnetic field (Bumba, 1972). During the 20th solar cycle, several active centers that were the source of the largest particle events, such as the proton-flare region of November 1969, January 1971, September 1971, August 1972 and July 1974 were examined with regard to the behavior of their local and background magnetic field distribution. Again the same type of relation to practically the same form of large-scale magnetic features was observed (Bumba et al., 1972; Bumba and Sýkora, 1972a, b; Bumba, 1973a, b).

The formation of such a characteristic large-scale magnetic field body is a continuous process which consists of individual magnetic field patterns successively transforming form one stage to the next due to the successive appearance of new magnetic fluxes in newly appearing complexes of activity, or individual active regions only. It consists of weakening, dissipation and shape changes of the old fields, their mutual interaction with newly emerged fields and subsequent weakening, or strenghtening of the resulting fields, etc. In the case of August 1972 and July 1974, we saw that it was possible to decompose the entire very complex process into individual stages, the evolution of each of which was subject to the regularities, observed by a simple complex of activity evolution.

In the magnetically complicated situation described, new sunspot groups continued to form and grow until the maximum phase was reached during the rotation in which the proton flare occurred, and then their development and new appearance practically stopped.

In its maximal phase, the large-scale magnetic field characteristic body, giving birth to the proton-flare regions, very often occupies one half of the solar surface, and all visible layers of the solar atmosphere. It probably extends far into the outer corona.

Just after the proton flares occur, not only the main proton-flare region disintegrates, but the whole complex magnetic field body disintegrates as well. Instead of the enlargement of the field area and gradual weakening of its intensity, the field dissipation is much faster and practically in situ, the field disappearing in various places of the region simultaneously. This means that the magnetic field dissipation process, which in the normal single active region takes place over many rotations $(5\div 6)$ during which the field is transported away from its place of formation and gradually weakens, is accelerated at least twice or three times.

The same phenomenon observed on the scale of a proton-flare region seems to occur also on the scale of the whole visible disk when 3 or 4 rotations are sufficient for the large-scale background field to be fully reorganized, to disintegrate and nearly totally dissipate. Normally about 12 or more rotations are needed for the evolution of the large-scale magnetic field body. However, in these special cases, 3 or 4 rotations are enough to completely disturb the result of the long-lasting complicated development. We emphasize that there is no photospheric or chromospheric activity (i.e. no flares are observed) during this period of disintegration.

3.2 Processes of evolution of series of activity complexes, accompanied by mighty activity events, studied later

Successive entanglement of the magnetic fields Once again in activity cycles 21 and 22 (Bumba et al., 1996a; Bumba et al., 1998; Bumba and Klvaňa, 1997), we observed the long-term successive evolution of the large-scale magnetic field patterns reaching their climax in the formation of large complex active regions that produced numerous energetic white-light and protonemitting flares (Bumba & Sýkora 1974; Bumba 1982; Bumba et al., 1987; Bumba & Geszstelyi, 1988a, b), and newly, also coronal mass ejections (for example, Jordan et al., 1997). Again, in each case, the time scale of the process was of the order of one year or more, and in all cases, the local magnetic fields were transformed step by step from a relatively simple configuration at the beginning into the very complex one during the maximum stage. A number of processes were involved in this transformation: the appearance of new magnetic flux in active regions or in activity complexes; the dissipation and changes in the structure of older magnetic fields; the mutual interaction of all fields and their subsequent weakening as well as strenghtening; etc. In this complexity, all processes were found to be time antisymmetric, i.e. the growth phase was about 6 times longer than the declining phase. Similarly, the rapid final phase was accompanied by numerous flares and CMEs. Simultaneously, the entire area of complicated magnetic field patterns on the Sun which, in the phase of peak activity, occupied as much as half of the solar surface, also disintegrated during this declining phase.

Global distribution and the depth of sources The regularities in the longitudinal distribution and the persistence in the same longitude interval of many activity complexes suggests they were anchored to a rigidly rotating subsurface source of magnetic flux, not affected by differential rotation, and operating with maximum power just before, and through much of the complex's final phase. However, we have also noted

them on Personation

significant changes on the local scale: possible local strenghtening, or even induction of new magnetic flux, due to strong local motions (Bumba et al. 1993; 1995a; 1996b; etc.). But at some point before, or during the final period of maximum activity, the complex seems to have become disconnected with this subsurface source, or the source itself changed, weakened, or disappeared.

Involvement of the convection On magnetic maps of different kinde, the investigation of the dynamics of rebuilding the magnetic field during its complex development indicates that it is due to the successive appearance, restructularization, and disappearance of large, characteristic, nearly elliptical magnetic field structures, whose origin is very probably in convection (Bumba 1987a, b). Their evolution, if compared with the longitudinal shift of active longitudes, is retrograde, i. e. in the direction of diminishing heliographic longitudes. At the same time, these patterns function evidently as one of the main agents in the global reconstruction of the background magnetic field, together with the global redistribution of activity in the solar zone of activity.

The development of the activity complex can also be clearly observed on spectroheliograms of the K line of CaII. First of all, the ionized calcium spectroheliograms show that the investigated complex sometimes developed almost in a region in which several rotations ago the evolution of a similar complex went through its final stage (e.g. Bumba et al., 1996a). The new complex in the same area therefore means a practical renewal of the complex's activity. The spectroheliograms indicate that some of the emission seems to be organized by convection into circular or elliptical patterns. And because of this influence, the new complex appears to evolve from the crossings of these structures, more active when crossing closer to the equator. The new individual active regions then appear further and further away from the place of their first appearance, but at quantized distances, equal roughly to the diameter of the structures. At later stages, the emission diffuses from the originally well-defined patterns, and these in turn lose their forms.

The elliptical structures mentioned, visible best on Stanford Observatory synoptic magnetic charts and on the ionized calcium spectroheliograms, again seem to demonstrate that the process of continuous restructuralization of the solar global magnetic field, in which the development of activity complexes represents well-defined phases, witnesses the important role convection plays therein, and simultaneously in the evolution of the solar magnetic field and activity.

Complexes of activity during the last two cycle minima Even during the transitional phase between the old and new eleven-year cycle of solar activity, at least during the last two minima, we have observed the same pattern of appearance and formation of activity complexes: they are mutually longitudinally dependent both in the old and new cycles, and their isolated magnetic bodies, well visible on the solar surface (we refer to them as "magnetic bubbles") have all the features of an activity complex, as defined in Section 2. They grew successively, they have a life time of many rotations, their boundaries shift at the same rate of about 100 msec⁻¹, and on the Stanford synoptic maps they have elliptical forms: briefly, morphologically they really remind one of a large convective bubble emerging in the photospheric layer.

Coronal holes - final stages of series of activity complexes evolution The final stages of the evolution of the 1982 activity complex (Bumba et a., 1998), paralleled by the evolution of large-scale magnetic fields studied during 1991 and 1992 (Bumba et al. 1995a), were interesting. In these cases, the disintegration of a large-scale magnetic complex led to the formation of a magnetically open region over the areas of formerly strong activity. A large polar coronal hole penetrated the area of the former activity complex and replaced it. From this we conclude that the development of a large coronal hole is a global process depending on the evolution of the global magnetic field, due to the successive formation of individual elements of the activity cycle. In addition, the evidence of this study for the rigid rotation of magnetic boundaries of active-region complexes during the final stages of their evolution suggests "preparation" of the rigid boundaries of large coronal holes that penetrate into low latitudes in the declining phase of the solar cycle. It should also be noted that the rigidly rotating pivot lines and pivot points appeared to be associated with emerging flux regions and with the strengthening of this flux by other processes (Bumba et al. 1995a, 1998).

We also note there is evidence that the final opening of the magnetic field lines into interplanetery space in the regions studied occurred well before their disconnection from the source of the new flux, and possibly, even before the energetic event that announced the peak phase of activity.

4. Conclusions

Thus, the activity complexes highly probably represent basic structural elements of the eleven-year solar activity cycle. They play the role of specific units of solar activity in the hierarchy of solar activity patterns, temporaly much longer (around one year) and spatially much more extensive (a part of the solar activity zone) than a single active region. They combine the family of active regions physically interconnected at least by their origin. During the development of a complex, we see the effect of this impulse of solar activity in the whole volume of the solar atmosphere, in which successively, subject to certain rules, a number of individual active regions evolves, reaching their maximum quickly in terms of numbers, as well as importances, with continually increasing area they cover, then to decline slowly with possible postmaximum oscillations of activity (Bumba & Howard 1965a, b).

Due to the concentration of activity into certain intervals of heliographic longitudes, the complexes of activity often occur several times repeatedly in almost the same area of the solar surface, forming time series. An evolutionary process of very complicated and complex magnetic structures then occupies a substantial fraction of the solar atmosphere's volume. Its evolution exhibits a progressive increase, mostly lasting more than one year, in the number and size of its active regions, and above all, in the complexity of its magnetic field topology, according to the rule discovered by Mme Martres (1968): the closer the new region in space and time to the older region, the more complicated and active the whole new formation. The phase of its peak activity lasts usually one or two rotations. The largest flares, coronal mass ejections, etc., occue during this maximum phase. After this, the magnetic field becomes greatly simplified over this entire area, with the lines of force opening into interplanetary space, forming a large coronal hole in its final stages.

Thus, the appearance of coronal holes seems to be bound to the latest stages of magnetic, as well as photospheric, chromospheric and coronal activity of these elements of solar activity, lasting about two years, inclusive of the duration of the coronal hole. The holes represent, at least in the vicinity of the equator, or in the main activity zone, the last evolutionary phases of several large, successively developed, long-living complexes of activity, displaying at this stage a specific magnetic situation in the form of widely extended magnetically unipolar regions, built up step by step in a long-lasting process from the remnants of old magnetic fields of all active regions which occurred during the lifetime of the complex within it.

Consequently, the formation of a coronal hole is a global process, resulting from a general trend in the evolution of solar activity in the given phase of the cycle. Let us add that equatorial and polar coronal holes are very closely linked together (Bumba, 1991; Bumba and Gesztelyi, 1988a, b).

From the identification of pivot lines and pivot points for the rotation of the main boundary of the complex of activity (Bumba at al., 1998), we conclude that the subphotospheric source of its magnetic flux rotates as a rigid body for at least four rotations prior to the phase of maximum activity. During this final, most energetic phase, either the connection with the underlying source of flux was severed, or the source itself has changed. On energetic grounds, a considerable emergence or induction of new flux probably took place during the numerous strong flares that occurred within the complex before its destruction.

The complete "life cycle" of the activity complex underscores the fundamental importance of large-scale subsurface processes for the generation, emergence, transformation and dissipation of the global magnetic field. It provides further insight into the relative rates at which activity builds up and then rapidly dissipates. Since a similar life cycle was observed in detail during several eleven-year cycles, an anologous development of stellar activity complexes might be expected, given a similar temporal and spatial organization of activity, on other solar-like stars.

Acknowledgments

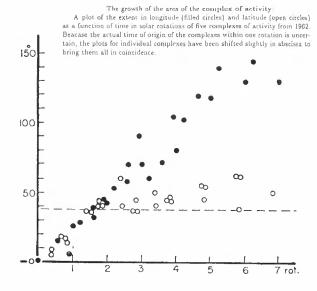
We would like to acknowledge the support of this work by Grant A 3003903 of the Grant Agency of the Academy of Sciences of the Czech Republic.

References

- Bumba V., 1972, Solar Wind, C. P. Sonett, P. J. Coleman, J. M. Wilcox (eds.), NASA, Washington, 151
- Bumba V., 1973a, b, World Data Center A for Solar-Terrestrial Physics, Report UAG-28 Part I, 43; 155
- Bumba V., 1982, Space Sci. Reviews 32, 229
- Bumba V., 1987a, Bull. Astron. Inst. Czechosl. 38, 92
- Bumba V., 1987b, Solar Phys. 110, 51
- Bumba V. and Gesztelyi L. 1988 a, b, Bull. Astron. Inst. Czechosl. 39, 1; 86
- Bumba V. and Hejna L. 1991, Bull. Astron. Inst. Czechosl. 42, 76
- Bumba V. and Howard R. 1965a, b, Astrophys. J. 141, 1492; 1502
- Bumba V. and Klvaňa M. 1997, Solar Phys. 173,111
- Bumba V. and Sýkora J., 1972, Bull. Astron. Inst. Czechosl. 23, 85
- Bumba V. and Sýkora J., 1974, Coronal Disturbances, G. Newkirk, J. (ed.) D. Reidel Publ. Comp., Dordrecht, 73
- Bumba V., Garcia A. and Jordan S., 1998, A&A, 329, 1138
- Bumba V., Garcia A. and Klvaňa M., 2000a, b, accepted in Solar
- Phys.
- Bumba V., Hejna L. and Gesztelyi L., 1987, Publ. of the Astron. Inst. of the Czechosl. Acad. Of Sci. No. 66, Ondřejov, 129
- Bumba V., Klvaňa M. and Kálmán B. 1996a, Astron. Astrophys. Suppl. Ser. 118, 35
- Bumba V., Klvaňa M. and Kálmán B. 1995b, A&A Suppl Ser. 109, 355
- Bumba V., Křivský L. and Sýkora J., 1972, Bull. Astron. Inst. Czechosl. 23, 85
- Bumba V., Klvaňa M., Kálmán B. and Györi L. 1993, A&A, 276, 193

Martres M. J., 1968, Structure and Development of Solar Active Regions (Ed. K. O. Kiepenheier, D. Reidel Publ. Co., Dordrecht, 25

Jordan S., Garcia A., Bumba V., 1997, Solar Phys. 173, 359



LINE-DEPTH AND $\mathrm{T}_{\mathrm{EFF}}$ VARIATIONS WITH THE SOLAR CYCLE DUE TO POSSIBLE

SIZE-CHANGES OF PHOTOSPHERIC GRANULATION

B. Caccin., V. Penza

¹Dipartimento di Fisica, Università di Roma "Tor Vergata", via della Ricerca Scientifica 1, I-00133 Roma, Italia. <u>caccin@roma2.infn.it</u>, penza@roma2.infn.it

ABSTRACT

We explore, with a highly simplified model of a convective cell, the dependence on the cell's size L of the line-depth ratios used by Gray & Livingston (1997a, 1997b) as indicators of $T_{\rm eff}$ variations with the solar cycle. Values of $\Delta L/L$ from current estimates of granular size variations (-5% from minimum to maximum of sunspot cycle) give non negligible effects on continuum intensity (-0.13%) and line-depth ratios (-0.2%) at disk center as compared with the observed variations ($\Delta T_{\rm eff} \approx +1.5$ K, if measured variations of the total irradiance are totally ascribed to $\Delta T_{\rm eff}$; disk-integrated line depth ratios + 0.4%).

1. INTRODUCTION

As soon as the variability of the total irradiance was measured by the ACRIM experiment on SMM, it was proposed that significant dips were produced when a large sunspot group passed disk center (Willson and Hudson, 1981) and that positive excursions were produced when large active areas were near the solar limb (Oster, Schatten, Sofia, 1982). Successively, when the 11 years variation was observed, Foukal and Lean (1988) proposed that also the magnetic network contributed to the total irradiance. The effect of all these variations were calibrated to best reproduce the trend of the total irradiance observed over the solar activity cycle and these empirically obtained calibrations were subsequently used to infer the variations of the total irradiance over the past 300 plus years (cf. Lean, 1997). On estimating the contributions of spots, faculae and network to the total irradiance, the old procedure has been essentially one of curve fitting. The reason for this was that measurements for these features were difficult to make, and thus not available. To solve this problem the Precision Solar Photometric Telescopes (PSPTs) were designed, and, since then, measurements carried out with them and with other instruments have provided

real values for these contributions (cf. Ermolli et al., 2000). What all these measurements appear to show is that, while they explain most of the observed variation of the total irradiance, they do not seem to explain it all. In fact the major shortcoming of most of the early work on solar variability has been the assumption that active regions and network should explain all of the solar variability, and that these features were superposed to an otherwise constant background.

When we consider the Sun as a star, we must be aware that its global structure may change as a consequence of variations of the magnetic field both in the solar interior, where the dynamo process operates, and on the surface, where the activity modifies the boundary conditions. This possibility is confirmed by the observed variations of the frequency spectrum of solar oscillations.

These changes have been successfully reproduced with exploratory models as a consequence of the structural effects of a variable dynamo field in the solar interior (Lydon and Sofia, 1995; Lydon, Guenther and Sofia, 1996). A solid prediction of these models is that, when the structure changes, all the global solar parameters (radius, $T_{\rm eff}$, luminosity) also change in very specific ways. Therefore, to uniquely identify the physical nature of the changes, it is necessary to simultaneously observe all those parameters to insure their self-consistency. Finally, the entire scenario must be confirmed by helioseismological studies.

2. MEASUREMENTS OF T_{eff} FROM LINE-DEPTHS

An attempt to evaluate possible T_{eff} variations with the 11 years cycle has been made by Gray and Livingston (1997a, 1997b) from the monitoring observations of temperature sensitive lines performed at Kitt Peak over the years 1978-1992.

To avoid the uncertainties of previously adopted, model-based calibrations, they made new *ad hoc* observations of the same lines using the Moon and a sequence of stars bracketing the Sun in T_{eff} (\approx 300 K) to derive an empirical calibration. Of course, in this way,

Proc. 1st Solar & Space Weather Euroconference, 'The Solar Cycle and Terrestrial Climate', Santa Cruz de Tenerife, Tenerife, Spain, 25-29 September 2000 (ESA SP-463, December 2000)

only modifications of the atmospheric stratification of the same kind of those occurring along the main sequence can be properly taken into account and, as recognized by the same authors, that might not be a complete description of the changes that actually occur in the Sun during its magnetic cycle.

With the three lines listed below, they formed the two central-depth ratios D_C/D_{Fe} and D_C/D_{Ti} , which are independent from many instrumental errors. The analysis was very careful and seems to have removed, for the first time, many subtle systematic errors present in the solar data. The T_{eff} sensitivity was given in the form $\delta T_{eff} = C \, \delta r/r$, where $\delta r/r$ is the variation of either the C/Fe or the C/Ti ratio and C=346 or C=468 respectively; the estimated error on δT_{eff} was a fraction of I K. According to the authors, the spectral lines used are not directly affected by the presence of faculae or unresolved magnetic fields (sunspots should give a negligible contribution to integrated-disk spectra), however we do not consider their arguments really conclusive.

When applied to solar data, the T_{eff} variations obtained from both line ratios reproduced fairly well the whole observed variations of the total irradiance S, if variations of the solar radius were neglected ($\delta S/S = 4 \delta T_{eff}/T_{eff}$). If we could believe in this result, no room would be left for an additional effect due to the balance of bright and dark magnetic regions.

A theoretical calibration of the same line ratios was attempted by Caccin and Staro (1998) and by Caccin et al. (1998) with Kurucz (CD-ROM No. 19) photospheric models. In selecting the grid of Teff values, we kept gravity, microturbulence and mixing length constant and equal, respectively, to 4.5 in log scale, 2 km/s and 1.25. The results obtained were C=629 for C/Fe and C=942 for C/Ti. They are both about twice the empirical values and the discrepancy might be mainly due to the behaviour of the C line, which is formed deep enough to feel the atmospheric region where the $T(\tau)$ structure is determined by convection. This explanation is corroborated by the fact that the sensitivity of other line ratios, formed in higher layers and empirically calibrated by Gray but not used in solar observations, is instead well reproduced by theoretical calculations (Caccin & Staro, 1998). In addition to that, a variation of the convective efficiency, obtained by a $\approx 20\%$ increase of the mixing length α , would sensibly affect theoretical calculations, by changing the temperature slope in the deeper layers were the C line is formed. Unfortunately, there is no easy way to include simultaneous perturbations of T_{eff} and α in our calibration procedure evaluating their combined effect along the main sequence.

As it is, the theoretical calibration described above gives values in excess with respect to the observed variations of the total irradiance variation with the solar cycle, making the problem even worse than in the case of the empirical one Hovewer, we do not believe that onedimensional calculations with plane parallel atmospheres are adequate for the purpose of calibrating solar variations of T_{eff} . However, we do not believe that one-dimensional calculations with plane parallel atmospheres are adequate for the purpose of calibrating solar variations of T_{eff} . We will show below, with simple estimates based on exploratory models, that neglecting the presence of horizontal inhomogeneities may be incorrect or even misleading.

In particular, we will assume that the size of photospheric granules might be reduced by 5% from minimum to maximum of the sunspot cycle, as suggested by some observations (cf. Müller & Roudier, 1984) and we will vary, by the same amount, the size of the convective cells in an average plane-parallel model atmosphere which remains constant. This will have non negligible effects both on continuum intensity and on line profiles.

3. THE GRANULATION MODEL

To mimic the effects of granulation on the emergent intensity, we consider a periodic x-y tesselation of a 0-th order plane-parallel, hydrostatic atmosphere with square cells of a single size L.

The perturbation is represented by a tridimensional velocity field and the associated thermodynamic perturbations.

The value of L is then varied, as a free parameter, to estimate the effect of its variation on the emergent intensity.

3.1 <u>0-th Order Model</u>

We got the following analytic approximation of $\rho(z)$ from the table of Kurucz's theoretical model of the solar atmosphere, then derived P(z) and T(z) from the condition of hydrostatic equilibrium and the gas equation of state (with μ =1.32):

$$\rho_0(z) = \rho_{00} \frac{e^{z/H}}{1 + e^{z/H}}$$

where H=100 km.

3.2 Perturbed Model

We adopted, for momentum density ρV , a simple analytic expression already used by Nordlund (1982), for exploratory purposes, satisfying to linearized equation of continuity:

$$\begin{cases} V_{1v} = V_{10} \frac{e^{(\alpha - \beta)z} + e^{\alpha z}}{kH_{\alpha}} \sin(kx) \\ V_{1y} = V_{10} \frac{-(e^{(\alpha - \beta)z} + e^{\alpha z})}{kH_{\alpha}} \sin(ky) \\ V_{1z} = V_{10} \left(e^{(\alpha - \beta)z} + e^{\alpha z} \right) (\cos(kx) + \cos(ky)) \end{cases}$$

where $\beta = 1/H$, $\alpha = 1/H$, ($\alpha \approx 2\beta$) and the dependence on the cell size is hidden within k, since $k = 2\pi/L$.

The relative perturbations of thermodynamic quantities satisfy linearized Navier-Stokes equations (P and ρ) and the state equation (T).

4.CALCULATION OF THE EMERGENT INTENSITY

Given the atmospheric model, we computed for any given line of sight the emergent intensity, in the line and in the continuum, by solving numerically the radiative transfer equation (RTE). In this way nonlinearities in the RTE are taken into full account.

4.1 The source function and opacity

For the source function we take the familiar formula:

$$S = \frac{\sigma}{\pi}T^4$$

Instead, for the continuum opacity we choose the following analitic form, deriving from a fit over Kurucz's model:

$$K_{\ell^*} = K_0 \left(\frac{\rho}{\rho_0}\right)^a e^{bP/P_0}$$

with a=0.5 and b=3.5.

In the line opacity expression we used the Saha-Boltzmann's equation, where for the electronic pressure we put $P_c = P_{c0}P^{0.5}T^{11.5}$, from a suitable fit of Kurucz's data)

Only the thermal gaussian profile (without micro- or macro-turbulence) was considered for all lines.

4.2 Emergent Intensity

We calculated the emergent intensity (continuum and lines) at the disk center, for any line of sight on a suitable x-y grid, with the following formulas:

$$I_{C}(x, y) = \int_{-\infty}^{t} S(x, y, z) \chi_{C}(x, y, z) e^{-z_{C}(x, y, z)} dz$$

$$I_{T}(x, y, v) = \int_{-\infty}^{t} S(x, y, z) \chi_{C}(x, y, z) [1 + \eta(x, y, z, v)] e^{-z(x, y, z, v)} dz$$
where $\eta(x, y, z, v) = \frac{K_{T}(x, y, z, v)}{K_{C}(x, y, z)}$

The computed intensities have then been averaged over the whole cell. The lines chosen are those of Gray & Livingston (1997a, 1997b): C1 (5380.32 Å), Fel (5379.586 Å) and Till (5381.020 Å). The atomic data are the same used by Caccin and Staro (1998).

5. RESULTS AND CONCLUSIONS

The first result that we want to report is the growth of the continuum intensity emergent at the disk center I_c with the cell-size L (fig.1).

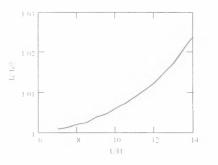


Fig. 1 I_{t} (in units of the unperturbed value $I_{t(0)}$ vs. the the cell-size I_{t} (in units of II).

In particular, for a variation $\delta L/L \approx 0.05$ around L/H=10 we obtain $\delta I/I\approx 0.0013$; the corresponding value of δT_R obtained from the relation $\delta I/I=4 \ \delta T_R/T_R$, which can be a considerable overestimate of δT_{eff} , is 1.8 K or 2.1 K if we take a linear fit of the curve over the whole range shown in the fig.1.

Since L is minimum at sunspot maximum, we infer that either a modification of the average atmospheric structure or the effect of magnetic structures must overcompensate the deficit due to the "pluridimensional" effects considered here to reproduce the observed excess of about 1.5 K. Although our estimate is very crude, it shows that "pluridimensional" effects have to be carefully computed and taken into account. Also the line depth D grows with L for all of the three lines we studied (fig. 2):

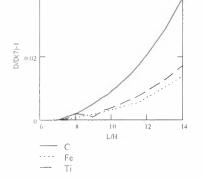


Fig. 2 Relative variations of lines depht vs. L/H

The largest variation is that of the C line, which feels more than the others the effects of perturbations because it forms in deeper layers. The ratios D_C/D_{Fe} and D_C/D_{Ti} are very similar to each other (fig. 3) and, calculating $\delta r/r$ from linear or parabolic fits, we obtain that the C/Fe ratio is slightly more sensitive to cell-size variations, as obtained by Gray & Livingston for T_{eff} sensitivity.

In any case it appears very unlikely, at present, that total irradiance variations might be ascribed to a single effect as it has often been done in the past.

REFERENCES

- 1.Caccin, B., Staro, F., 1998, *Themis Workshop on Radiative transfer and inversion codes*, p.81.
- 2.Caccin, B., Staro, F., Gomez, M. T., 1998, *Mem. S.A.It.* 69, 595.
- 3.Ermolli et al., 2000, poster paper at this conference
- 4.Gray, D.F., Livingston, W.C., 1997a, *Astrophys. J.* 474, 798.
- 5.Gray, D.F., Livingston, W.C., 1997b, Astrophys. J. 474, 802.
- 6. Foukal, Lean., 1988, Astrophys. J. 328, 347.
- 7. Lean J. 1997, Ann. Rev. Astron. Astrophys. 35, 33
- Lydon, Guenther, Sofia, 1996, Astrophys. J. Lett. 456, 127
- 9. Lydon, Sofia, 1995, Astrophys. J. Suppl. 101, 357
- 10.Müller, R., Roudier, Th., 1984, Solar Phys. 94, 33.
- 11.Nordlund, Å., 1982, Astron & Astrophys. J. 107, 1.
- 12.Oster, Schatten & Sofia, 1982, Astrophys. J. 256, 768.
- 13. Willson, Hudson, 1981, Astrophys. J. 244, 185.

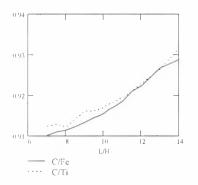


Fig. 3 D_C/D_{Fe} and D_C/D_{Ti} Vs. L/H

From a linear fit over the whole range, we get $\delta r/r \approx 0.002$ for $\delta L/L \approx 0.05$; again the sign of the variation is opposite to the observed one ($\delta r/r \approx 0.004$, positive from minimum to maximum of 11-yr cycle).

Although the numerical results obtained in the present paper must be considered only as preliminary estimates, we can conclude that the calibration of Gray & Livingston cannot be applied without problems to derive solar cycle variations of $T_{\rm eff}$ and that more realistic models of photospheric granulation and of its variation with the 11 years cycle must be employed to understand the physics of global variations at the Sun surface.

GRAVITATIONAL ENERGY OF SOLAR OSCILLATIONS AND CLIMATIC CHANGES

D.K.Callebaut¹, V.I.Makarov², A.G.Tlatov²

¹Physics Department, UIA, University of Antwerp, B-2610, Belgium, ²Pulkovo Astronomical Observatory, 196140, Saint Petersburg, Russia

ABSTRACT

The gravitational energy associated with variations in the radius of the Sun is huge: with a relative change of 1/2000 (the estimated difference between maximum and minimum solar activity) and taking only the convection zone to expand, corresponds to about 2 10^{34} J, which is 1/10 of the total rotational energy of the Sun. Non-radial oscillations with a tiny nonlinearity can still yield energies comparable to or larger than the total magnetic energy of a full sunspot cycle or three or four orders more than the luminosity of the Sun, but that is not sufficient to account for the changes of the temperature on Earth. The expansion of the upper layers of the convection zone, however, may directly or indirectly affect the climate and the biological aspects on the Earth. Moreover this suits a qualitative explanation why the Sun expands during a minimum of the magnetic activity.

Key words: Maunder minimum, sunspot activity, gravitational energy

1. INTRODUCTION

The total brightness of the Sun, B, has been monitored by the spacecraft radiometers of NASA since 1978, Lee et al. (1995). It was discovered that the brightness of the Sun varies by an amount $\Delta B/B \approx 10^{-3}$ during the 11-year cycle. Monitoring the solar-type stars shows that this is normal behaviour. There is much evidence in the solar and climate records to support the hypothesis that our Sun has a influence on Earth's climate, Reid (1987). The phenomena related to the Maunder Minimum attract more and more attention, in particular because some of them throw some light on the solar cycle itself Callebaut & Makarov (1992); Makarov & Callebaut (1999) and its possible effects on climate and biological aspects on the Earth. Moreover, although very few sunspots occur during a grand minimum like the Maunder minimum, some magnetic activity continues as revealed from ice cores from the Artic and Antartic, Beer et al. (1999) and the references therein or from radio-carbon measurements, Kocharov et al. (1995). The effect on the temperature on the Earth is very intriguing as the Maunder Minimum corresponds to a little ice age. In the 17th century painters canvassed skaters on the frozen

rivers of Flanders (Belgium) while those rivers did not freeze anymore or not to the same extent. (The pollution prevented it too during this century). The pollution prevented it too during this century). Chinese and in particular the Korean Imperial Annals mention a drastic increase of calamities (floods, etc.) during that period, Yi (1995). Ribes & Nesme-Ribes (1993) gave a careful analysis of the French astronomical observations during the Maunder Minimum. In particular they indicated that the solar diameter increased by about 7 parts in 2000. The relative variation of the solar diameter from a maximum to a minimum of the solar cycle is about 1/2000only, Brown (1991); Wittman et al. (1993); Vasilyev & Makarov (1996). Callebaut (1977) has drawn long ago the attention to the huge gravitational energies associated with small variations in diameter. Here we attempt to correlate the change in diameter with the change in gravitational energy and thus in radiated energy and consequently with a change in temperature on Earth. Moreover a qualitative explanation for the relation between magnetic activity and solar diameter is proposed.

2. GRAVITATIONAL ENERGY ASSOCIATED WITH RADIAL OSCILLATIONS

2.1. Calculation for homogeneous sphere.

The gravitational energy associated with a homogeneous sphere of radius R and mass M is Chandrasekhar (1939):

$$E_{gh} = \frac{-3GM^2}{5R}$$

where approximately $G = 6.67 \ 10^{-11} \ \text{m}^3/\text{s}^2\text{kg}$ and for the Sun $M = 2 \ 10^{30} \ \text{kg}$ and $R = 7 \ 10^8 \text{m}$ (SI units). With a change in radius ΔR is associated a change in energy:

$$\Delta E_{gh} = \frac{3}{5} \frac{GM^2 \Delta R}{R^2} = -E_{gh} \frac{\Delta R}{R}.$$

Part of this is used the change the internal energy, the other part increases or decreases the radiated energy. We have to a good approximation that the change in radiated energy is given by:

$$\Delta E_r = \frac{3\gamma - 4}{3(\gamma - 1)} \Delta E_g.$$

Proc. 1st Solar & Space Weather Euroconference, 'The Solar Cycle and Terrestrial Climate', Santa Cruz de Tenerife, Tenerife, Spain, 25-29 September 2000 (ESA SP-463, December 2000)

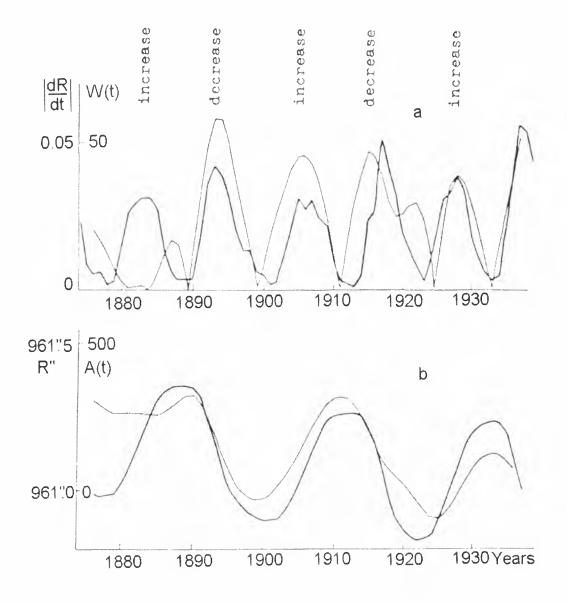


Figure 1. (a) The relationship between the temporal variations of Wolf numbers, W(t) (thick curve) and the temporal variations of the module of the solar radius derivative, |dR/dt| (thin curve) according to the Italian and Greenwich observations. (b) The temporal variations of the $A(t) = \sum_{min}^{t} W(t) + C$, (thick curve) and the average smoothed data set for the solar radius (thin curve). It is clear seen that the variations of the solar radius and Wolf number indices coincide with good precision during more than four solar cycles, (Vasilyev and Makarov, 1996).

Here γ is the ratio of the specific heats and is for a star between 4/3 and 5/3. Using 5/3 yields that half of the gravitational change goes in radiation. The (extreme) limit $\gamma = 4/3$ would yield no radiation at all from the gravitational energy. Ribes & Nesme-Ribes (1993) indicate $\Delta R/R = 7/1950$ for the Maunder Minimum. Present day measurements give about seven times less for the difference between minimum and maximum of a solar cycle. We use this value $\Delta R/R = 1/2000$ in the following. There results: $E_{gh} = 2.3 \ 10^{41}$ J and $\Delta E_{gh} = 1.1 \ 10^{38}$ J. The change is gigantic, nearly 12 orders of magnitude more than the solar luminosity.

2.2. Estimation for an non-homogeneous sphere.

Suppose we put all the mass of the Sun inside a homogeneous sphere of half its radius and use again

the same relative change in radius: 1/2000. Then the value for E_{gh} and ΔE_{gh} is doubled. For the Sun we have that the mass inside half its radius is still 0.96 of the total mass. This is barely less than in our hypothetical consideration; so the values given in subsection 2.1 essentially double. If we put all the mass inside 0.4R, then the energies given in subsection 2.1 are multiplied by 2.5, but the real mass inside 0.4R is 0.9M. Hence the given values by the homogeneous model may in reality still be multiplied by a factor 3 or so to account for the inhomogeneity. The stronger the concentration towards the center, the greater E_g and ΔE_g , where we drop the index h for the non homogeneous case. However the main point is that the change in energy associated with the variation in radius is so huge that clearly a more realistic model has to be considered.

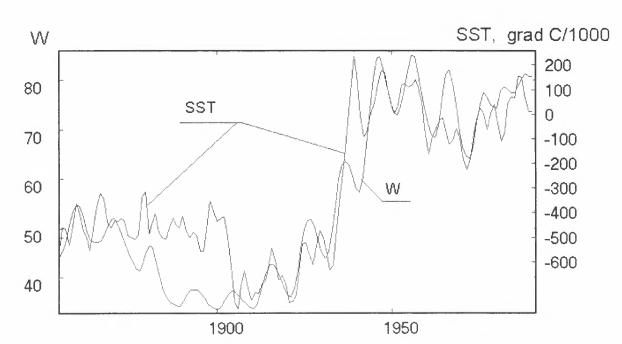


Figure 2. Correlation between global sce-surface temperature and solar activity. SST and W continuous curves represent the run of sce-surface temperature and Wolf numbers for the period 1861-1995 average over 25 years. It is clear seen that the Earth's climate responds to variations of the Sun's magnetic activity. A general warming of the Earth's climate began at the beginning of the twentieth century.

2.3. Calculation if only the convection zone is lifted over ΔR . With the following values: $\Delta R = R/2000 = 3.5 \ 10^5 \text{ m}, \ g_{\odot} = 280 \text{ m/s}^2$ for the gravitational acceleration at the solar surface, $M_{CZ} = 3 \ 10^{-3} M = 6 \ 10^{27} \text{ kg}$ for the mass of the convection zone, we obtain

$$\Delta E_{CZ} = M_{CZ} g_{\odot} \Delta R = 6 \ 10^{35} \text{J}.$$

which is already 200 times less than the result of section 2.1, but still huge: it is 3 times the rotational energy of the Sun. Still much too much for a reasonable model.

2.4. Calculation if only the upper part of the convection zone is lifted over ΔR . We estimated the mass above r > 0.9R to be 1.3 10^{26} kg. Thus $\Delta E(r \ge 0.9R) = 1.3 \ 10^{34}$ J, which is already 10 000 times less than 2.1 and about 0.06 of the rotational energy, but it is still huge.

2.5. Calculation if the convection zone expands only

We have:

$$g_{CZ}(r) = GM/r^2 = \frac{GM}{R^2} \frac{1}{(r/R)^2} = 280/r'^2 \text{m/s}^2,$$

$$h(r) = \frac{(r'-0.7)3,510^5}{0.3} \text{m}, r' = r/R \text{ and}$$

$$\Delta E_{e,r} = 4\pi R^3 \int_{0.7}^1 \rho_{0.7} \exp\left(-ar + 0.7a\right) g_{CZ}(r)h(r)r^2 dr$$

Here we made an exponential approximation for the density for the relevant interval with $\rho_{0,7} = 50 \text{kg/m}^3$

and a = 17. The result is $\Delta E_{ex} = 2.3 \ 10^{34}$ J, which is one tenth of the rotational energy of the Sun. Taking half of it for the radiation corresponds to about a year of the solar output, which should be spread over some 5 to 6 years of a minimum of activity. Probably only the upper layers of the convection zone expand, so that the figure is still reduced by two orders of magnitude.

3. GRAVITATIONAL ENERGY ASSOCIATED WITH NON-RADIAL OSCILLATIONS

As non-radial oscillations are half an expulsion and half a depression the corresponding gravitational changes roughly compensate: only the nonlinearity may yield a net contribution. Some non-radial oscillations have amplitudes of 1 km. Assume that the difference in amplitude between a depression and an expulsion is 1 m, i.e. $\Delta R/R = 10^8/7$ or $3 \ 10^{-6}$ of the value used above. We have to take only half of the solar surface (or less if the oscillation doesn't extend over the whole Sun) and another factor 1/2 for the time average. Adapting the results from section 2.5. we obtain: 2.3 10^{34} 3 $10^{-6}/2 \times 2 = 1.7 \ 10^{28}$ J which is about 40 times the solar luminosity. Taking half of this value as a decrease in radiation means a negligible decrease during a solar minimum (about 5.5 years) with respect to a maximum. This result has to be considered with caution: 1. One meter difference due to nonlinearity is a rough estimate: it may be 10 times more or 10 times less. 2. There are thousands of simultaneous non-radial oscillations, however most of them have smaller amplitudes. 3. If the non-radial oscillations are responsible at all for the expansion. why should there be less non-radial oscillations during a solar maximum than during a minimum or during a Maunder Minimum? If this would turn out to be the case that would be an important physical feature which needs explanation. Taking 1000 times the value (a somewhat extreme situation) and taking it fully as radiation loss yields $1.7 \ 10^{31}$ J. This is only one part in 4000 of the solar radiation during 5.5 years. This is 6 times lower than the value $15/10\ 000$ which Beer et al. (1999) mention according to their references. Non-radial oscillations are probably only a marginal effect in the energy considerations here.

4. TEMPERATURE EFFECT

With an expansion ΔR corresponds a change in (surface) temperature. Using Lane's theorem for a homothetic expansion Chandrasekhar (1939) yields

$$\frac{-\Delta T}{T} = \frac{\Delta R}{R} = \frac{1}{2000}.$$

As the luminosity L is proportional to R^2T^4 we have

$$\frac{\Delta L}{L} = \frac{2\Delta T}{T} = \frac{1}{1000}$$

Hence the associate temperature change for the Earth (surface temperature 300 K essentially due to solar radiation) would be $\frac{300K}{1000} = 0.3K$, which seems to suit rather well the value mentioned by Beer et al. (1999). However we have argued in our calculations above that the expansion of the upper region of the convection zone only can easily account for the energy requirement. If we use a region of 0.1R thick, than the relative change in thickness is 10 times larger and the change for the temperature on Earth would be 3K, which is drastically too much. However we should take the whole energy transport mechanism into account. According to Ribes & Nesme-Ribes (1993) $\Delta R/R = 7/2000$ during the Maunder Mini-mum. The corresponding changes for the temperature on Earth should be 7 times larger and, as the Maunder Minimum lasted more than 70 years, so that effects of delay are much smaller than in the case of the 5.5 years between maximum and minimum activity, the effect would have been much more drastic than actually experienced.

5. ANTI-CORRELATION BETWEEN EXPANSION AND MAGNETIC ACTIVITY

When magnetic fields are generated they make the flux tubes expand and by buoyancy force help the eddies to rise. Thus the transport of heat is increased, resulting in more radiation. When few magnetic fields are generated the opposite happens: less energy transport, less radiation and the consequent accumulation of part of the thermal energy in gravitational energy. It seems plausible that the upper layers of the convection zone are most affected by this, in agreement with the calculations in section 2., showing that only a thin layer of the convection zone has to expand to account for the required energy.

6. CONCLUSION

Our calculations show that a small increase in the solar radius may absorb tremendous amounts of energies at the expense of the internal energy and the radiated energy. The resulting values are clearly much too large in view of the temperature variations estimated on Earth. However if only a thin layer at the surface of the convection zone expands then the energies may accommodate. Moreover this suits a qualitative explanation of the increase of the solar radius when little magnetic activity is present. Non-radial oscillations probably contribute only a minor fraction to the variations in the temperature on Earth.

7. ACKNOWLEDGMENTS

One of us (V.I.M) is grateful to the organizers of the First SOLSPA - Euroconference "The Solar Cycle and Terrestrial Climate" held in Santa Cruz, Tenerife (Spain) from 25th to 29th September 2000, for financial support. This work was partially supported by the grants: RFBR 00-02-96019.

REFERENCES

- Beer, J., Tobias, S., Weiss, N., 1999, Solar Phys., 181, 237
- Brown, T.M., 1991, in (eds) Sonett, C.P. et al. The Sun in Time, University of Arizona, Tucson
- Callebaut, D.K., 1977, Solar Phys., 51, 271
- Callebaut, D.K., Makarov, V.I., 1992, Solar Phys., 141, 381
- Chandrasekhar, S., 1939, An Introduction to the Study of Stellar Structure, Dover ed., 1957.
- Kocharov, G.E., Ostryakov, V.M., Peristykh, A.N., Vasil'ev, V.A., 1995, Solar Phys., 159, 381.
- Lee, R.B., Gibson, M.A., Wilson, R.S., Thomas, S.J., 1995, J.Geophys. Res., 100, 1667-1675
- Makarov, V.I. and Callebaut, D.K., 1999, in (ed.) A.Wilson, Proc. 9th European Meeting on Solar Physics, "Magnetic Field and Solar Processes", Florence, Italy, 117
- Reid, G.C., 1987, Nature, 328, No.6310, 273
- Ribes, J.C., Nesme-Ribes E., 1993, Astron. Ap., 276, 549.
- Vasilyev, O.B., Makarov, V.I., 1996, Solar Phys. 163, 249
- Wittman, A.D., Alge, E., Bianda, M., 1993, Solar Phys. 145, 205
- Yi Tae-jin, 1995, 18th Int. Congress of Historical Sciences, Montreal, Canada.

HYDROGEN AND HELIUM NUCLEI OF GALACTIC ORIGIN IN THE INNER HELIOSPHERE

L. del Peral¹, R. Gómez-Herrero¹, M. D. Rodríguez-Frías¹, J. Sequeiros ¹, H. Kunow², and R. Müller-Mellin²

¹Departamento de Física. Universidad de Alcalá. Spain ²Institut für Experimentelle und Angewandte Physik. Universität Kiel, D-24118 Kiel, Germany

ABSTRACT

The differential energy spectra of Hydrogen and Helium isotopes in the energy range 4-50 MeV/n are also presented. The ⁴He population is found to be mainly of anomalous origin.

Key words: Cosmic rays: abundances; cosmic rays: general; interplanetary medium; interstelar: matter; cosmic rays: anomalous component..

1. INTRODUCTION.

Since the SOHO¹ launch the 2^{nd} December 1995, the Electron-Proton-Helium INstrument (EPHIN) has been collecting protons and alpha particles from its halo orbit, around the L1 Lagragian point at 1.5 million kilometers from Earth. From this position outside the Earth magnetosphere the fluxes of those particles are not affected by the Earth magnetic field.

EPHIN sensor (Figure 1) is a stack of six cylindrical solid state silicon detectors, surrounded by a plastic scintillator acting as veto detector for background noise reduction. The two first thinner detectors are divided in six sectors to allow a rough trajectory determination and particle range corrections, which improve isotopic discrimination for light nuclei. The energy range for electrons is 0.150 to 10 MeV and for protons and Helium nuclei from 4 to 53 MeV/n. The EPHIN geometrical factor of 5.1 $cm^2 sr$ can be reduced by a factor of 24 either automatically or by telecommand to allow high counting rates without significant dead time losses. The sensor axis points in the nominal direction of the interplanetary magnetic field at 1 AU, 45° west of the spacecraft Sun line. A detailed description of the sensor can be found in Müller-Mellin et al. (1995).

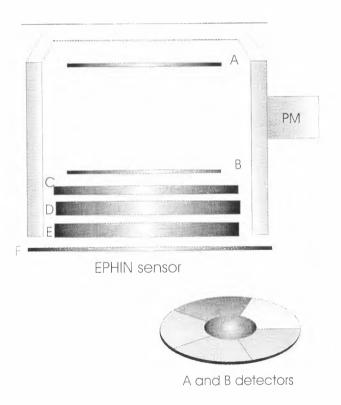


Figure 1. EPHIN (Electron Proton Helium INstrument) scheme. Detectors A and B are sectioned into six sectors.

¹SOHO is an ESA-NASA collaboration

Proc. 1st Solar & Space Weather Euroconference. 'The Solar Cycle and Terrestrial Climate', Santa Cruz de Tenerife, Tenerife, Spain, 25-29 September 2000 (ESA SP-463, December 2000)

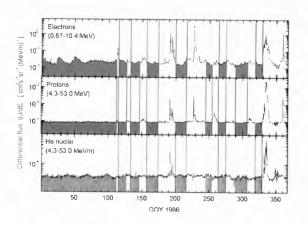


Figure 2. Particle flux measured by EPHIN during 1996. The shaded areas have been discarded as corresponding to solar events and not to quiet time periods.

2. DATA SELECTION AND ANALYSIS

The data analyzed in this work correspond to quiet time periods occurred during 1996 where the solar minimum of the 22nd solar cycle took place. During these periods no solar events are present and the particle populations are either of interplanetary or galactic origin. A total of 217 days have been analyzed. In Figure 2 the differential fluxes for electrons (0.15-10.4 MeV), Hydrogen (4.3-53.0 MeV/n) and Helium (4.3-53.0 MeV/n), detected by EPHIN during 1996 are shown. The shaded areas present solar origin events, therefore they have been rejected from the analysis of the quiet time periods. The electron intensity-time profile shows a 27 day recurrence characteristic of quiet time jovian electrons.

3. GALACTIC HYDROGEN IN THE HELIOSPHERE

The differential energy spectrum of protons has contribution from two particle populations of different origin. The dominant population at high energies (E > 10 MeV) comes from interstellar cosmic rays, which undertakes solar modulation, providing information on the diffusion and transport parameters of cosmic rays in their journey through the Heliosphere. At energies above a few GeV/n the spectrum is essentially of galactic origin with a 2.6 spectral index. This high energy component is not affected by modulation as the Larmor's radius of these particles are larger than the dimensions of the Heliosphere.

A second contribution at low energies (E< 10 MeV) is of solar and heliospheric origin, which in quiet time periods is not dominant. This population presents a power law in energy with high spectral index, $\gamma_{SEP} \sim 4$.

Still a third component of protons can be seen only

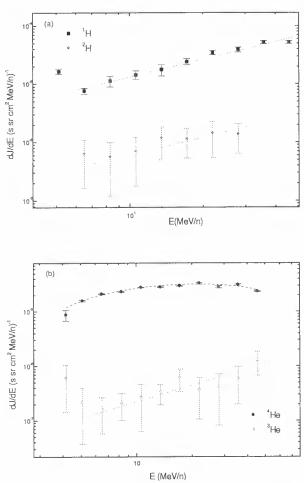


Figure 3. a) Proton and deuterium spectra and the corresponding fitted curves. b) ${}^{3}He$ and ${}^{4}He$ spectra and the corresponding fitted curves.

during quiet time periods and it is composed of the cosmic radiation anomalous component. This proton component is not negligible at energies of the order of a few hundred MeV/n. Anyway, as these energies are above EPHIN detection capability, this component has not been taken into account in the data analyzed in this work.

Figure 3 (a) shows the energy differential spectrum of protons in the energy range 4-50 MeV/n measured by EPHIN during the selected quiet time periods (Table 1). The hidrogen energy spectrum has been fitted to a linear law of the form:

$$j_H(E) = j_{gcr}E\tag{1}$$

reflecting the contribution of the modulated galactic cosmic radiation in the energy interval covered by EPHIN. The j_{gcr} factor is expressed in particle flux units $(\text{cm}^2 \text{s sr MeV/n})^{-1}$. The solar events rejection has allowed us to obtain a purely galactic spectrum as shown in Figure 3 (a).

Deuterium is found in solar abundance determination in a so low rate that is not expected to be seen in the flux detected by EPHIN. Consequently the deuterium observed during quiet time periods is assumed to be of galactic origin (Figure 3 (a)). Galactic deuterium is produced in the spallation reactions that take place during transport of cosmic rays from their sources to the local interstellar medium. When they enter the Heliosphere the low energy tail of the spectrum (< 1 GeV/n) is affected by solar modulation producing a linear spectrum in energy in the range 4-50 MeV/n, similar to what is observed in the modulated cosmic radiation. Due to its low abundance it is difficult to eliminate the background, which produces larger uncertainties than in the case of protons. Figure 3 (a) shows the fit performed on the differential spectrum of deuterium.

4. HELIUM POPULATION

Two Helium isotopes, ³He and ⁴He, have been detected by EPHIN onboard SOHO. ³He is produced in the so call "³He rich solar flares" but its main contribution comes from the spallation products of more massive cosmic ray ions. The ³He spectrum (Figure 3 (b)) is similar to that of deuterium, although with larger uncertainties than proton spectrum presents.

The ⁴He differential energy spectrum, in the energy range detected by EPHIN, is nearly flat with a maximum at 20.4 MeV/n, as can be seen in Figure 3 (b). This behavior is due to the dominant contribution of the anomalous component at these energies. ⁴He nuclei are assumed to enter the Heliosphere in neutral form so that they are not affected by heliospheric modulation, but in getting closer to the Sun they are ionized by UV radiation and drug out again by the solar wind towards the Solar Wind Termination Shock (SWTS) at about 90 AU. This shock accelerates again the ions towards the Sun being detected by EPHIN at 1 AU. Steemberg and Moraal (1996, 1999) have computed the spectrum at the SWTS assuming a spherical symmetry shock at 90 AU, they have obtained for the non relativistic part of the spectrum, the following expression:

$$j_{SWTS} = j_{ac} \left(\frac{E}{E_c}\right)^{1-q/2} \exp\left[-b \left(\frac{E}{E_c}\right)^a\right]$$
(2)

where E_c is the cutoff kinetic energy per nucleon and the j_{ac} factor is the contribution of the anomalous cosmic rays to the SWTS differential spectrum. Coefficients $a = 0.689\gamma + 1.34$ and $b = -0.083\gamma + 0.272$ with γ spectral index of the radial diffusion mean free path inside the shock, and the q factor depends on the strength of the SWTS. In this work we have assumed a radial diffusion mean free path inside the shock $\gamma = 1$ as sugested by Steemberg and Moraal (1999) for the SWTS.

Assuming a linear dependence of the diffusion coefficient with the radial distance from the Sun, of the form (??)

$$\kappa(r,R) = \frac{\kappa_0 \beta r (1+\kappa_s^2) R^2}{1+(\kappa_s R)^2} \tag{3}$$

where $\kappa_0 = 3.1 \ 10^{21} \ cm^2 s^{-1}$, $\kappa_s = 1.51$, R is the magnetic rigidity of ions in GV units, r is the radial distance to the Sun in AU and $\beta = v/c$ is Lorentz's factor.

The transport equation (Longair, 1981) gives us the relation between two values of the particle intensity at two different positions:

$$j_{He} = j_{SWTS} \exp\left[-\int_{r_s}^{r_{SWTS}} \frac{Cv_{sw}}{\kappa(r,R)} dr\right]$$
(4)

where j_{Hc} is the differential flux observed by EPHIN at 0.9 AU, C is the Compton-getting factor, r_s is the radial distance of the SOHO spacecraft and r_{SWTS} is the radial distance of the SWTS that we have assumed as 90 AU.

Substituting the diffusion coefficient in (3) and performing the integration in the r variable, we obtain the following expression for the ⁴He flux :

$$j_{He} = j_{SWTS} \exp\left[-\eta \frac{E_0 + \kappa_s^2 E}{E^{3/2}}\right]$$
(5)

$$\eta = \eta_0 C v_{sw} \ln\left(\frac{r_{SWTS}}{r_s}\right) \tag{6}$$

where $\eta_0 = 3.2 \cdot 10^{-3} (\text{MeV/n})^{1/2} (\text{km/s})^{-1}$. $v_{sw} = 450 \text{ km/s}$ the solar wind velocity at 90 AU and C is the Compton-getting factor.

Figure 3 (b) shows the ⁴He spectrum obtained and the fit of the relation (5) to the obtained energy spectrum. In Table 1 the fit parameters obtained are listed.

5. CONCLUSIONS

The quiet time periods differential energy spectrum for protons and deuterium depends linearly on energy (see equation (11)) in the energy interval of the EPHIN sensor. The j_{ger} scale factor is $(1.33 \pm 0.05) \ 10^{-6} \ (\text{cm}^2 \text{ s sr MeV})^{-1}$ for protons and $(6.1 \pm 0.5) \ 10^{-8} \ (\text{cm}^2 \text{ s sr MeV})^{-1}$ for deuterium. The abundance ratio obtained is $^1\text{H}/^2\text{H} = 21.8$ which means that about a 4.5 % of Hydrogen is in the form of Deuterium.

The energy spectrum profile for ³He also indicates the galactic origin of this helium isotope. The fit performed to equation (11) has given a value of $j_{gcr} = (2.2 \pm 0.2) \ 10^{-8} \ (\text{cm}^2 \text{ s sr MeV/n})^{-1}$ corresponding to abundance ratios ³He/²He = 0.3606 and ³He/¹H = 0.0165. The ratio with ⁴He change with

	⁴ He	³ He	$^{2}\mathrm{H}$	$^{1}\mathrm{H}$
Ĵgcr		$2.2 \pm 0.2 \cdot 10^{-8}$	$6.1 \pm 0.5 \cdot 10^{-8}$	$1.33 \pm 0.05 \cdot 10^{-6}$
Ĵac	$5\pm1\cdot10^{-5}$			
q	2.36 ± 0.14			
$E_c \; ({\rm MeV/n})$	32 ± 2			
$n ({\rm MeV/n})^{1/2}$	$5.5 \pm 0.2 \cdot 10^{-2}$			

Table 1. Differential energy spectra fit parameters of Hydrogen and Helium isotopes j_{gcr} and j_{ac} are given in $(cm^2 \ s \ sr \ MeV)^{-1}$.

energy as the two spectral shapes are quite different due to the different origin of both isotopes.

The ⁴He spectrum fitted parameters obtained give us information about the origin of the anomalous ⁴He. The scale factor of $5 \cdot 10^{-5}$ (cm² s sr MeV/n)⁻¹ obtained is 500 times higher that those expected from the interstellar abundances. The kinetic energy cutoff obtained of 32 MeV/n make us to think that all the ⁴He convected to the SWTS to be accelerated arrive fully ionized due to the energy cutoff obtained corresponds to a mass-charge ratio of 2 for a fixed $\gamma = 1$ (Steemberg and Moraal, 1999). From the q parameter we can deduce a strong SWTS with a 3.7 compresion ratio that generates a hard spectrum with 2.36 spectral index, and assuming a solar wind velocity of 450 km/s at the SWTS (Köhnlein, 1996) we can obtain a interstellar wind velocity of 122 km/s in a solar coordenate system assuming a static SWTS. The shock temperature (Steemberg and Moraal, 1999) can be obtained as $T_{SWTS} \sim 4.6 \cdot 10^6$ K. From the η parameter we obtain a compton-getting factor of $C = 8.29 \cdot 10^{-3}$ meaning that the adiabatic deceleration in propagation is important and can not be assume as negligible.

ACKNOWLEDGEMENTS

This work has been supported by the Comisión Interministerial de Ciencia y Tecnología (CICYT) of Spain, grant ESP97-1776. R. Gómez-Herrero is indebted with the University of Alcalá for a predoctoral grant.

REFERENCES

- Köhnlein, W., 1996, Solar Physics, 169, 209-213.
- Longair, 1981, in *High Energy Astrophysics*, Cambridge University Press.
- Müller-Mellin, R. et al., 1995, *Solar Physics*, 162, 483-504.
- Steemberg, C. D. and H. Moraal, 1996, Astrophysical J., 463, 776-783.
- Steemberg, C. D. and H. Moraal, 1999, Journal of Geophysical Research, 104-A11, 24879-24884.

- Stone, E. C. and A. C. Cummings, 1999, Procc. of the 9th International Solar Wind Conference, Ed.
 S. R. Habbal, R. Esser, J. V. Hollweg and P. A. Isenberg. AIP Proceedings, Vol. 471, 201–204.
- R. Gómez-Herrero et al., 2000, Solar Physics 194, 405–413.

THE SOLAR DYNAMO: FLUX PUMPING BY STRATIFIED CONVECTION

S.B.F. Dorch¹ and Å. Nordlund²

¹ The Royal Swedish Academy of Sciences, Stockholm Observatory, SE-13336 Saltsjöbaden

tel: +46 8-163357 / fax: +46 8-164228 e-mail: dorch@astro.su.se

 2 The Niels Bohr Institute for Astron., Physics and Geophys., Juliane Maries Vej 30, DK-2100 Copenhagen Ø

tel: +45 35325968 / fax: +45 35325989

e-mail: aake@astro.ku.dk

ABSTRACT

A longstanding issue in the theory of the solar dy-namo is the "flux storage problem" i.e. the problem of explaining how the magnetic field may be kept within the solar convection zone long enough for the dynamo to replenish it. We present results from numerical 3-D MHD simulations of deep solar-like magneto-convection (both with and without open upper boundary conditions) that show that by the very nature of stratified over-turning convection, magnetic flux of a considerable strength may be 'pumped' downwards and kept in the lower part of the solar convection zone. As a consequence even a formally super-equipartition magnetic field may be effectively stored in and below the solar convection zone thereby rendering the flux storage problem obsolete.

Key words: solar dynamo; magnetic fields; convection.

1. INTRODUCTION

It is generally agreed that solar bipolar active regions are the surface manifestations of a strong toroidal flux system that is generated and anchored deep be-low the surface of the Sun: Toroidal magnetic strands in the form of flux loops ascend through the convection zone because of their buoyancy and the on the average adiabatic and super-adiabatic stratification. The much weaker poloidal field is assumed to be gencrated in the convection zone from the toroidal field by a cyclonic effect.

In the context of mean field dynamos, the mechanism that takes care of transporting the poloidal field back to the region where the toroidal field is thought to be generated, is often assumed to be a diffusive coupling of the regions where the ω -effect and the cyclonic α -effect operate (e.g. Parker 1993). Additionally, meridional circulation may also couple the

two regions, if it has the right amplitude and sense of direction (Choudhuri & Dikpati 1995), but it is not well observed. The modeling by diffusive coupling of the regions is somewhat unsatisfactory since it relies on a rather ad hoc approach.

The question of how the poloidal field may return to the region where the generation of the toroidal field supposedly takes place is related to the "flux storage problem" and the generally assumed solution to this problem: Any magnetic field located in the convection zone will escape because of its buoyancy, but magnetic flux may be stored in the stably stratified region below the convection zone; i.e., in the so-called undershoot layer. In the scenario of the "flux storage problem" the convection zone is considered to be a passive one-dimensional medium while the magnetic fields are treated as 1-D solid objects that move in it.

Dorch 1998 and Dorch & Nordlund 2000 show, however, that a competition may occur between the drag of descending plasma and the buoyancy of the magnetic field embedded in the plasma: In the following we aim at illustrating how the interaction of magnetic fields and solar-like stratified over-turning convection and differential rotation may render the "flux storage problem" obsolete.

2. MODEL SCENARIO

The model of the Sun is a "local Cartesian box" model of a convection region sandwiched between two stable layers. In order to avoid problems associated with the large ratio between thermal and dynamical time scales, the model has a much higher luminosity than the Sun, and all variables are scaled accordingly.

The full resistive and compressible MHD-equations are solved using the staggered mesh method by Galsgaard and others (e.g. Galsgaard & Nordlund 1997, Nordlund & Stein 1989 and 1994): The code uses a finite difference staggered mesh with 6th order derivative operators. 5th order centering operators and a

Proc. 1st Solar & Space Weather Euroconference, "The Solar Cycle and Terrestrial Climate", Santa Cruz de Tenerife, Tenerife, Spain, 25-29 September 2000 (ESA SP-463, December 2000)

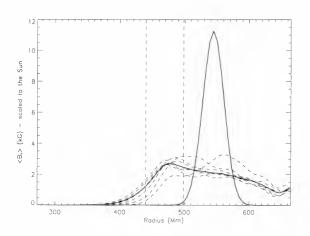


Figure 1. The horizontally averaged poloidal magnetic field as a function of radius for 7 different times (simulation [A]): t = 0 (initial field – solid curve), 3.3, 6.5, 9.8, 13.0, 16.3 (thin dashed curves), and 19.5 (solid curve) turn-over times. The approximate bottom and top of the undershoot layer are indicated by two vertical dashed lines.

3rd order time-stepping routine. Viscous and magnetic diffusive terms are quenched in regions with smooth variations to reduce the diffusion of wellresolved structures. Typical magnetic Reynolds numbers in non-smooth regions are of the order of a few hundred, while they can be much larger in large-scale smooth regions.

In the Sun envelope convection is essentially driven by surface cooling. To model this situation, without having to include all layers up to the surface a simple expression for a thing isothermal cooling layer at the upper boundary of the model was used.

Both simulations with closed and open upper boundaries were performed. In order to implement a stable open upper boundary a buffer zone was allocated where the magnetic field is dragged out of the buffer zone. This layer is far below the real boundary of the solar convection zone.

The hydrodynamic part of the initial condition is a snapshot from a well developed stage of a numerical model of solar-like undershooting convection. The model has a high degree of stratification with a density contrast of roughly $5 \, 10^3$ in the convection zone. The thickness of the undershoot layer in the model is much larger than the helioseismological upper limits (see e.g. Christensen-Dalsgaard 1995) because the (unscaled) convective velocities are larger due to the enhanced energy flux. Scaling the extension of the undershoot layer in proportion to the velocity the resulting thickness falls well within the upper limits from observations.

In the "flux pumping" simulations the initial condition for the magnetic field is given by a unidirectional (henceforth "poloidal") sheet that is placed in the middle of the convection zone. The sheet is initially in a state of isentropic pressure equilibrium with the surroundings and characterized by its initial plasma β .

In the simulations with rotation, background differential rotation and the Coriolis force are included with the angular frequency given by a fit to the observed solar angular frequency (from Dziembowski et al. 1989).

3. FLUX PUMPING

Several simulations with varying initial magnetic field strengths, numerical resolutions, and upper boundary conditions were performed (see Table 1). First, results from simulations without rotational effects are discussed and then results from a simulation including latitudinal shear are reported.

Table 1. Summary of five simulations of the "pumping effect".

No.	Plasma β	Dimensions	Boundary	Rotation
A	2×10^3	78×64^2	Closed	None
В	2×10^{3}	63×64^{2}	Open	None
С	200	63×64^{2}	Open	None
D	20	63×64^2	Open	None
E	2×10^{3}	69×135^2	Open	Solar-like

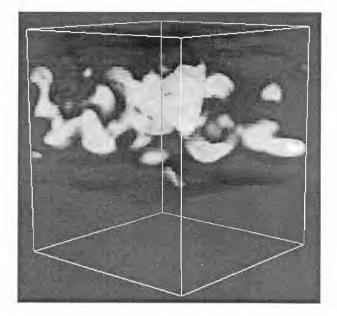


Figure 2. A 3-D rendering of the magnetic field at an instant in simulation [A] (see Table 1). A color version of this figure may be found at — http://www.astro.su.se/~dorch/.

Figure 1 shows the horizontally averaged field at 7 equidistant instants of time for simulation [A]: The poloidal sheet is spread out, and the distribution of poloidal magnetic flux settles to a characteristic distribution. The highest (horizontally averaged) poloidal flux density occurs in the overshoot layer, and in these particular simulations a significant fraction of the total flux also resides there. In the real Sun, this fraction may be expected to be much smaller, because the real undershoot layer is much thinner. Given the shape of the distribution, with no particular enhancement in the undershoot layer, it is likely the Sun has a correspondingly smooth distribution, with the majority of the poloidal flux residing inside the convection zone. Figure 2 shows a rendering of the magnetic field at an instants in time for simulation [A]: the magnetic field more or less fills the whole volume of the convection zone and penetrates into the stable layer below.

The "pumping effect" described in the above takes place because of the topology of the over-turning stratified convection: Of all the fluid parcels threaded by magnetic field lines about half are initially ascending. However, because of the stratification, most of the ascending fluid parcels must over-turn and descend and most of these keep descending down to the bottom of the convection zone (Stein & Nordlund 1989). The fluid parcels drag the threading field lines along and hence an appreciable fraction of the field is transported downwards. Fragments of the field that are caught in ascending flows are advected upwards. In the simulations with an open upper boundary some of these fragments escape through the top of the computational domain and flux is systematically lost: Figure 3 shows the average poloidal field strength for simulations with an open upper boundary (simulations [B], [C] and [D]). The relative reduc-tion in the poloidal flux by the escape of magnetic structures through the upper boundary does not depend much on the field strength. for strengths up to several times formal equipartition values.

The flux loss in the models with an open upper boundary is, however, strongly exaggerated in comparison to the Sun. The real solar flux loss may be expected to be significantly smaller than in the models with open upper boundaries discussed here: Much of the weak ascending flux must over-turn rather than reach the solar surface since it is embedded in a fluid of which only a tiny fraction reaches the solar surface. Note that the magnetic field considered is weak and incoherent and does not have sufficient buoyancy to overcome the drag of the fluid motions.

In what follows, results are presented for a particular simulation that includes shear and the Coriolis force (simulation [E] in Table 1): After an initial transient process where the differential rotation establishes itself and the over-turning convection distorts and pumps downward the poloidal sheet, the system enters a well-developed state, where the magnetic field displays the structure of the differential rotation.

When the background rotation profile is fully attained by the fluid, the toroidal magnetic field begins to increase linearly, with the rate of increase given by the latitudinal shear and the poloidal field strength. The structure of the magnetic field directly reflects the latitudinal dependence of the background azimuthal velocity field as a result of the latitudinal shear (see Fig. 4). The "center of gravity" of the magnetic field is above the bottom of the convection zone.

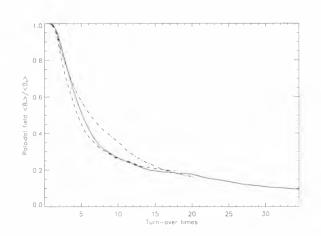


Figure 3. The normalized average poloidal field strength as function of time in turn-over times for the simulations with an open upper boundary condition: (simulation [B]dashed curve, simulation [C] solid curve and simulation [D] dashed-dotted curve).



Figure 4. Rendering of strong magnetic field lines to visualize the (four, because of the horizontal periodicity of the imposed rotation) toroidal flux streets in simulation [E].

As the initial poloidal sheet fragments while being wound up, toroidal flux structures leave the convection zone through the open upper boundary. Fig. 5 illustrates the feasibility of a field-reversal mechanism suggested by van Ballegooijen (1995, private communication): Subsurface connections between the following and the leading polarity of two adjacent emerging structures may become tilted in the sense opposite to the "normal" tilt (Fig. 5). Caught by the differential rotation, these reversed tilts will lead to an unwinding and reversal of the poloidal field.

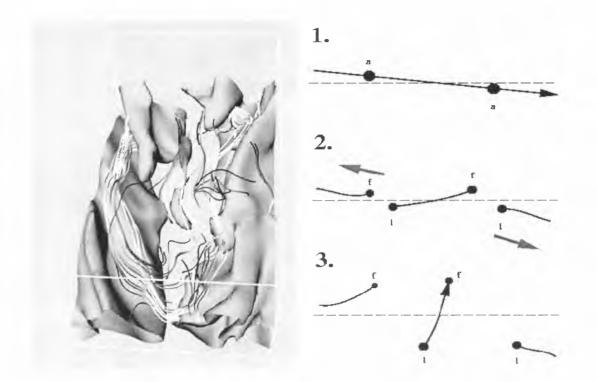


Figure 5. Left: A view of one forth of the box zoomed in on two of the toroidal flux streets: A flux structure is emerging through the top and moved across the equator (simulation [E]). Right: Schematic illustration of a field-reversal mechanism.

4. CONCLUSIONS

Stratified convection induces a strong tendency to transport magnetic flux downwards. However, unless an open upper boundary is placed sufficiently close to the actual solar surface, i.e. at sufficiently low density, there may be an exaggerated loss of flux through the open boundary as flux is carried around by the over-turning convection. The transport properties (both the downwards transport and the surface flux loss) are quite robust and field strengths well in excess of formal equipartition are needed to change the distribution and rates significantly. While magnetic flux indeed is pumped into the undershoot layer, the center of gravity of the magnetic field is above the bottom of the convection zone.

Where does this leave the "storage problem"? The toroidal magnetic field in the simulations peak at several tens of kG (scaled to the Sun). The peak field strengths occur near the bottom but still inside the convection zone. It is likely that emerging flux regions form when buoyancy finally becomes dominant, and this might occurs at field strengths of the order of 100 kG. Because of numerical limitations we have not studied that process with the current series of simulations.

ACKNOWLEDGMENTS

Computing time at the UNI•C computing center was provided by the Danish Natural Science Research Council. SBFD acknowledges support through an EC-TMR grant to the European Solar Magnetometry Network.

REFERENCES

- Choudhuri, A.R. and Dikpati, M. (1995): A&A, 303, L29
- Christensen-Dalsgaard, J., Monteiro, M.J.P.F.G. and Thompson, M.J. (1995): MNRAS, 276, 283
- Dorch, S.B.F. (1998): Ph.D. Thesis, Copenhagen University, 59
- Dorch, S.B.F. and Nordlund, Å. (2000): A&A, in press
- Dziembowski, W.A., Goode, P.R. and Libbrecht, K.G. (1989): ApJ, 337, L53
- Galsgaard, K. and Nordlund, Å. (1997): Journ. Geoph. Res., 102, 219
- Nordlund, Å., Galsgaard, K. and Stein, R.F. (1994): In R.J. Rutten, C.J. Schrijver (eds.), Solar Surface Magnetic Fields NATO ASI Series, 433
- Parker, E.N. (1993): ApJ, 408, 707
- Stein, R.F. and Nordlund, Å. (1989): ApJ, 342, L95

INVESTIGATING THE VERTICAL STRUCTURE OF THE SOLAR GRANULATION WITH THE SODIUM $\rm D_2$ LINE

M. T. Eibe¹, Th. Roudier², P. Mein¹, and M. Faurobert³

¹Observatoire de Paris, Section de Meudon, DASOP, F-92195 Meudon Principal Cedex, France ²Laboratoire d'Astrophysique de Toulouse, Observatoire Midi-Pyrénées, 14 avenue E. Belin, 31400 Toulouse, France ³Observatoire de la Côte d'Azur, BP 4229, F-06304 Nice Cedex 04, France

ABSTRACT

We present a method to estimate temperature and velocity at different heights in the solar photosphere from fluctuations of intensity and Doppler velocity measured at several positions in the sodium D_2 line profile. Line intensity variations due to small perturbations of temperature and velocity occurring at particular depths in the atmosphere were investigated with the non-LTE radiative transfer code MULTI. The result was used to calculate so-called response functions. As an example we present an application of our method to solar granulation data obtained with MSDP spectroscopy.

The granulation fluctuations (intensity, dynamics) over the solar cycle may reflect a probable interaction between the convection zone and the magnetic field at the global scale of the Sun or possibly to a local interaction between granules and magnetic flux tubes. The variation of the solar granulation, and more particularly of the exploding granule dynamics, provides a direct insight into the change of physical properties in the upper convection zone.

I. INTRODUCTION

Multichannel Subtractive Double Pass (MSDP) spectrograms allow to measure the profile of one or several spectral lines at every point in the two-dimensional field of view. Observed line profiles result from the relative, wavelength-dependent contributions of different atmospheric layers. If those contributions are well determined, one can then in principle extract information on the variation with depth of physical conditions from fluctuations of intensity and velocity measured at different parts of the profile.

The NaID resonance doublet (5890,5896 Å)is particularly interesting for photospheric diagnostics since its extended wings allow to obtain information from a wide range of heights in the solar photosphere. A method to estimate the vertical structure of temperature and velocity from the observed profiles of the D lines have been developed. In this poster we present main results concerning the D_2 line using an example with solar granulation data.

High-spatial resolution images of the solar surface in the visible part of the spectrum show granulation as a continually changing cellular pattern. Nowadays, granulation is known to originate from convection in the photosphere and its basic properties are quite well understood. Numerous works at present are devoted to obtain quantitative information about the dynamical and thermal structure of granules, taking advantage from latest advances in solar instrumentation. Results are of great interest for evaluation of theoretical models of solar granulation.

2. METHOD

The sensitivity of the NaID₂ line profile to fluctuations of temperature and velocity at different layers was investigated through the numerical calculation of theoretical profiles with the non-LTE radiative transfer code MULTI (Carlsson 1986). We used the VAL C (Vernazza et al. 1981) mean quiet-sun model atmosphere as a reference. which was then perturbed by introducing small amplitude disturbances of temperature and velocity. Resulting profiles led to the calculation of so-called Response Functions (hereafter, RFs). RFs describe the effect that perturbations of a given physical parameter have in the emergent line intensity. They were first defined by Mein (1971) and have since then become extensively used in inversion techniques (Beckers & Milkey 1975: Canfield 1976: Caccin et al. 1977: Ruiz Cobo & del Toro Iniesta 1992: Bellot Rubio et al. 1997). RFs of the D₂ line have been obtained before for temperature and pressure fluctuations under LTE conditions (Kneer & Nolte 1994, Krieg et al. 1999).

Temperature and Velocity RFs of the D_2 line profile calculated as explained above are shown in Figure 1. The wavelength scale in the x axis covers only one side of the profile, for the sake of clarity. But one should keep in mind that RFs are symmetric with respect to the axis

Proc. 1st Solar & Space Weather Euroconference, 'The Solar Cycle and Terrestrial Climate', Santa Cruz de Tenerife, Tenerife, Spain, 25-29 September 2000 (ESA SP-463, December 2000)

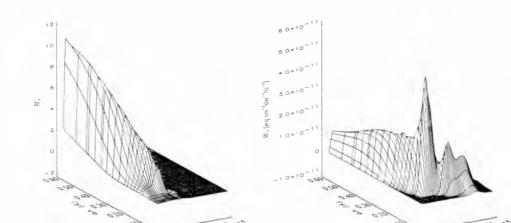


Figure 1. RFs of the NaID₂ for temperature (left) and for velocity (right). The 'x' axis of wavelength position with respect to the line centre covers only one half of the profile, for clarity. Depth is indicated in the 'y' axis as $\log m$, where m is column mass in gcm^{-2} (see text).

 $\Delta \lambda = 0$. The depth scale (axis y) is given in log m units. where m is the column mass in gcm^{-2} . In general, velocity RFs (RF_V) are seen to extend over a wider range of heights than temperature RFs (RF_T). With RF_V one can obtain information for heights up to log $m \sim -2.8$ (geometrical height of 900 km) whereas RF_T become negligible above log m = -2 (~650 km). The maximum contribution is found for $\Delta \lambda = 0.108$ Å at heights close to log m = -0.5 (~290 km).

The mapping between given wavelength positions in the D_2 line profile and atmospheric height levels is then established through the barycenters of the RFs obtained for those wavelengths. The method performance has been tested with several theoretical models of perturbations and non-linear effects have been investigated. The agreement is good provided that perturbations are small as it is required for a linear treatment to be valid. A more detailed description will be published in a future paper.

3. ANALYSIS OF DATA

Analysis of solar granulation data with the RFs presented above allowed to recover information about the evolution of exploding granules through the photosphere. A complete investigation was carried out by Roudier et al. (2000) and Espagnet et al. (1995). For a more detailed description we refer the reader to those works.

The time series consists of 64 2D spectrograms in the Na I D₂ line covering a quiet area of the solar surface. The effective field of view after images processing is $172'' \times 8''$. The total duration of the sequence is 16 min, with consecutive frames separated by 15 s. The 5-min oscillations were filtered out as part of the reduction process.

We present results from the most representative example among the nine exploding granules that were detected in the field of view. Observations allowed to trace them dur-

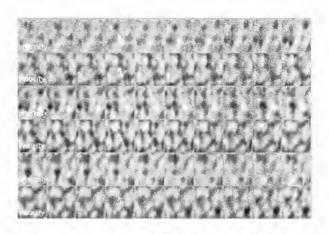


Figure 2. Evolution of a exploding granule as seen in maps of intensity and velocity fluctuations during the time series of observations. Intensity and velocity frames are placed in alternatively rows with time running from left to right. The position of the exploding granule is indicated by arrows. Consecutive frames are separated by 15 s, each one covering a field of view of $6.9'' \times 7.7''$ (see text). Bright elements in the velocity frames correspond to upwards (positive) velocities and dark areas are for downflow (negative) velocities.

ing most of their lifetime. Intensity and Doppler velocity fluctuations for every point of the field were calculated at ten different positions in the D₂ line profile, as described in Espagnet et al. (1995). An example of the twodimensional maps for intensity and velocity fluctuations obtained at $\Delta \lambda = 0.144$ Å and $\Delta \lambda = 0.288$ Å, respectively, is shown in Figure 2. RFs for those wavelengths yield as most representative heights those of 202 km in the case of temperature (intensity) and 170 km in the case of velocity. Brightest and darkest areas in the velocity frames correspond to Doppler velocities of -0.7 and 0.6 km s⁻¹, respectively. We have applied the method described above to derive the height variation of local disturbances of temperature and velocity in the photosphere at every time during the series.

The height variation of temperature fluctuations derived for selected frames during the sequence is shown in Figure 3 (*left panel*). An absolute maximum of $\Delta T/T$ is always found in the low photosphere, followed by an approximately linear decrease with height in the immediate overlying layers up to ~175 km. The maximum amplitude as well as the slope (absolute value) of the following decay are seen to increase progressively before the explosion. Approximately 1 min after the explosion the absolute maximum is reduced by half. A reversal of temperature is clearly seen at about 150 km in the atmosphere all the time before explosion. After explosion, $\Delta T/T$ remains negative at almost all heights.

The temporal evolution of velocity at different heights can be seen in Figure 3 (*right panel*). Contrary to what is found for temperature fluctuations, the height variation of velocity in the low photosphere would not be consistent with a linear model of perturbations. The largest velocity perturbations tend to occur at heights around 150 km in the mean photosphere during the entire lifetime of the granule. Decay after maximum is generally smoother than in the case of temperature. Only around explosion time we see a sharper decrease of velocity with height in the immediate layers above maximum. On the other hand, velocity disturbances are always positive. By the time of explosion the absolute maximum shows an increase of 70% over its initial value. After a time interval of 4.5 min, the maximum amplitude goes back to half its value. Effects in the velocity structure due to granule explosion seem to persist for a longer time than they are seen in temperature.

4. CONCLUSIONS

In this work we have calculated Response Functions of the Na I D₂ resonance line profile to temperature and velocity disturbances in the solar photosphere. It is found that they probe quite different layers in the atmosphere, with RF₁, extending over larger heights than RF_T. On this basis we have developed a method to estimate the vertical structure of temperature and velocity from the observed D₂ line intensity at several wavelengths.

By way of illustration, we used an example with a time series of MSDP spectrograms to study the height variation of solar granulation. The temporal evolution of exploding granules in temperature and velocity was investigated. We conclude that granulation velocities are seen to penetrate higher in the atmosphere than the associated temperature disturbances. The birth of granules is accompanied by a temperature increase and strong upflows at some levels. The maximum of velocity fluctuations is always located at about 150 km in the mean photosphere. followed by a progressive decay. In the case of temperature, however, the maximum is always found in the low photosphere. Effects due to explosion are seen for both velocity and temperature as a change in their gradients with height. After explosion, the velocity structure is recovered in a longer time scale than that for temperature.

ACKNOWLEDGMENTS

We would like to thank Ch. Coutard, R. Hellier, F. Colson and the Pic du Midi staff for technical assistance during observations. Photometric measurements were done with the microdensitometer "M.A.M.A." of the Institut National des Sciences de L'Univers in Paris. M.T.E. acknowledges financial support from IAC/INSU through a post-doctoral grant.

REFERENCES

- Beckers, J.M., Milkey, R.,W., 1975, Solar Physics 43, 289
- Bellot Rubio, L.R., Ruiz Cobo, B., Collados, M., 1997, ApJ, 478, L45
- Caccin, B., Gomez, M.T., Marmolino, C., Severino, G., 1977, A&A 54, 227

Canfield, R.C., 1976, Solar Physics 50, 239

- Carlsson, M., 1986. A Computer Program for Solving Multi-Level Non-LTE Radiative Transfer Problems in Moving or Static Atmospheres, Report No. 33, Upsalla Astronomical Observatory
- Espagnet, O., Muller, R., Roudier, T., Mein, N., Mein, P., 1995, A&AS 109, 79

Kneer, F., Nolte, U., 1994, A&A 286, 309

- Krieg, J.M., Wunnenberg, M., Kneer, F., Koschinsky, M., Ritter, C., 1999, A&A 343, 983
- Mein, P., 1971, Solar Physics 20.3
- Roudier, T., Eibe, M.T., Malherbe, J.M., Rieutord, M., Mein, P., Mein, N., Faurobert, M., 2000, in preparation
- Ruiz Cobo, B., del Toro Iniesta, J.C., 1992, ApJ 488, 462
- Vernazza, J.E., Avrett, E.H., Loeser, R., 1981, ApJS 45, 635

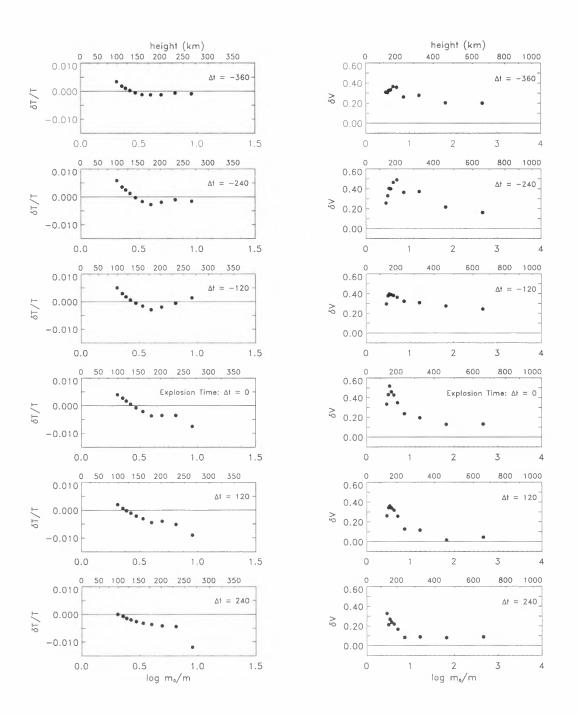


Figure 3. Temporal evolution of temperature (left) and velocity (right) disturbances in the centre of the exploding granule as estimated from the measured fluctuations of line intensity and Doppler velocity. The interval of time with respect to explosion (in seconds) is annotated in each plot.

THE MAGNETIC NETWORK CONTRIBUTION TO LONG-TERM IRRADIANCE VARIATIONS

I. Ermolli¹, F.Berrilli² and A. Florio²

¹ Osservatorio Astronomico di Roma, Viale del Parco Mellini 84, 00136 Roma, Italia tel: +39 0635347056 / fax: +39 0635347802 e-mail:ilaria@oarhp1.rm.astro.it

² Università degli Studi di Roma "Tor Vergata", Viale della Ricerca Scientifica, 00133 Roma, Italia tel: +39 06372594430 / fax: +39 062023507 e-mail:name@roma2.infn.it.it

ABSTRACT

We studied the average properties of the network pattern in the photosphere and chromosphere by analyzing the full-disk near simultaneous CaII K, blue and red continuum images daily obtained with the Rome-PSPT telescope.

We described the temporal variation of these properties from July 1997 to August 2000 during the ascending phase of Solar Cycle 23.

By the direct measurements of the brightness contrast and disk coverage for the network regions we estimated the network contribution to long-term irradiance variations. We estimated that the contribution to total solar irradiance (TSI) due to the spatial fluctuations of effective temperature of the Sun associated to the photospheric network is about 10^{-4} . By the measured temporal variation of the network properties, we evaluated a change of the network contribution to TSI of order $3x10^{-4}$ over the cycle. This value is close to the 0.1% increase in TSI measured during the last two solar cycles.

INTRODUCTION

The radiative output of the Sun is modulated by solar activity (Willson et al. 1986; Foukal and Lean 1986, 1988; Hudson 1988) as an effect of the appearance of dark and bright magnetic structures on the solar disk. While some attempts were made to model both the contribution of active magnetic regions, i.e. dark spot and bright faculae, using different approaches and proxies (Chapman and Meyer 1986, Steinegger et al. 1996, Worden et al. 1998, Fligge et al. 1998, Fontenla et al. 1999) the determination and modeling of the quiet network contribution is still lacking and currently represents one of the major problems in irradiance studies. In fact, the empirical models developed taking into account the combined influence of active magnetic features on solar irradiance were able to explain about 95% of the variance recorded over the past two decades on total solar irradiance (TSI) measurements (Lean 1997, Frohlich 1999). The amplitude of the network contribution to the irradiance measured has been only evaluated to be sufficient to fulfill the variance recorded (Foukal, Harvey and Hill 1991), but are still lacking both a precise measure of its amplitude and a modeling of it. Both these tasks are required to get clear to what extent the remaining discrepancy between the variance measured and that modeled is due to shortcoming in the models, uncertainties in the data or possible effects of solar variability mechanisms not connected to magnetic regions.

In this paper we present the first result of an estimate for the quiet network contribution to TSI based on direct measurements both of the photospheric contrast and of the disk coverage for network and internetwork regions. These regions were identified with an automated procedure on sub-arrays extracted from full-disk near simultaneous Ca II K (393.3 nm) and continuum images (409.4 nm and 607.2 nm) obtained with the PSPT telescope at the Rome Observatory (Coulter and Kuhn, 1994; Ermolli et al. 1998a, Ermolli et al., 1998b).

NETWORK IDENTIFICATION

The network pattern was identified on the Call K images by applying an up-grated version of the procedures described in Berrilli et al. (1998) and Florio and Berrilli (1998).

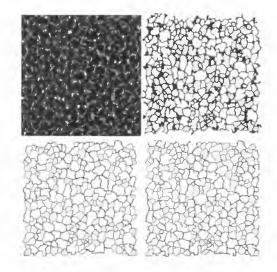


Figure | An example of the three different network identifications (clockwise: SKC, SKP, SKE) performed by the algorithms applied to 256x256 Call K sub-arrays analyzed.

313

Proc. 1st Solar & Space Weather Euroconference, 'The Solar Cycle and Terrestrial Climate', Santa Cruz de Tenerife, Tenerife, Spain, 25-29 September 2000 (ESA SP-463, December 2000).

These use skeletonizing algorithms (taking into account intensity information in the image) to identify the pattern that verify a threefold definition (SKE, SKP, SKC (figure 1).

The pattern identified in the CaII K images were used to trace the corresponding photospheric features in the near simultaneous continuum images (figure 2).

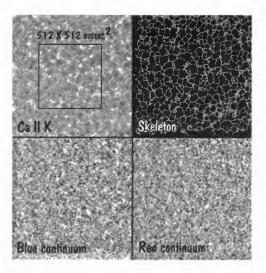


Figure 2 An example of the sub-arrays analyzed.

The procedures were applied both to ≈ 200 full-disk (1kx1k) and to ≈ 1400 sub-arrays images (128x128, 256x256 pixels centered on the solar disk).

IMAGE ANALYSIS

We evaluated the average network contrast at the disk center both in the chromosphere (C_K) and in the photosphere (C_B, C_R) , by computing the average intensity C_{net} of the pixels pointed out by the identified patterns with respect to the mean intensity of the whole image C_{med} .

We also evaluated the network disk coverage α by the percentage ratio of the area of the identified network pattern to respect to the total area of the analyzed image. We corrected the calibrated images analyzed for solar rotation and scale image. Bright active regions and their remnants were masked using intensity threshold and geometric connection criteria. The limb-darkening was corrected by computing circularly symmetric mean values on the full-disk images, while an FFT filtering was applied on sub-arrays.

AVERAGE PROPERTIES

We analyzed the full-disk images acquired from January 1998 to June 1999 to evaluate average properties of the network pattern over the whole disk. The center to limb variation of the network contrast in the photosphere is shown in figure 3.

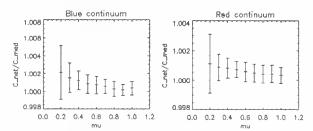


Figure 3 Center to limb variation of the network contrast in the photosphere. Bars represent the standard deviation of the values of each bin. These variations were obtained by the analysis of the images acquired from January 1998 to June 1999.

The results obtained evaluating the average properties at the disk center for the network pattern, as defined by the three different identifications already mentioned, are summarized the result obtained in the following table.

	SKC	SKP	SKE
CK	1.029±0.003	1.024±0.003	1.025±0.003
Св	1.0012 ± 0.0003	1.0010±0.0002	1.0011±0.0003
C_R	1.0005 ± 0.0002	1.0004 ± 0.0001	1.0004 ± 0.0001
α	0.26±0.02	0.15±0.01	0.14±0.01

THE NETWORK IN TIME

We analyzed the whole sample of very quiet 128x128 sub-arrays extracted at the disk center of the full-disk available images to study temporal variations of the network properties. By this analysis we found that the chromospheric quiet network properties do not show significant variations (figure 4) during the ascending phase of Solar Cycle 23, from July 1997 to August 2000.

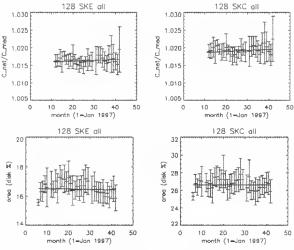


Figure 4 Results obtained by the analysis of the full sample of the very quiet 128x128 CaII K sub-arrays extracted at the disk center. Bars represent the variation of the values respect the monthly mean. The result of a weighted fit is also shown.

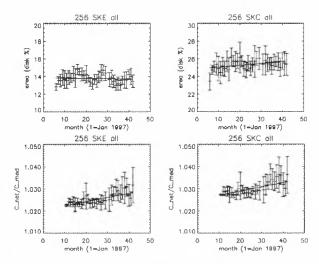


Figure 5 Results obtained by the analysis of the full sample of 256x256 CaII K sub-arrays extracted at the disk center. These sub-arrays include active latitudes. Bars represent the variation of the values respect the monthly mean. The result of a weighted fit is also shown.

However, by the analysis of the whole sample of 256x256 sub-arrays extracted by the full-disk images that include active latitudes with enhanced network regions, we found an increase of the network disk coverage (3%) and contrast (<1%) over the same period (3 years). This increase, even outlined by the full-disk images analysis, disappears by considering sub-samples of very quiet 256x256 sub-arrays.

In particular, table 2 summarize the variation of the average network properties resulted from the analysis of the full-disk images (obtained on 1998, 1999, 2000, July and August), for the SKC network identification.

	1998	2000	Δ
CK	1.027±0.004	1.031±0.004	+0.4
CB	1.0004 ± 0.0002	1.003±0.0001	+0.3%
CR	1.0004 ± 0.0001	1.002±0.0002	+0.2%
α	0.32±0.001	0.33±0.001	+1%

It is worth noting that these results were even outlined by the independent analysis performed on Rome-PSPT CaII K full disk images described in the contribution by Fofi et al. in this issue.

NETWORK CONTRIBUTION TO TOTAL IRRADIANCE

We assumed that the continuum intensity variations are produced by a change in the brightness temperature of the corresponding parts of the Sun surface.

The brightness temperature evaluated by the results of our image analysis are summarized below (assuming Tquiet=5780 K)

	1998	2000
blue	Tn=5780.4±0.2 K	Tn=5783.0±0.1 K
red	Tn=5780.7±0.1 K	Tn=5782.8±0.3 K

Then describing the solar irradiance flux by

$$F_{TOT}^{\lambda} = (1 - \alpha)B(\lambda, T_{Sun}) + \alpha B(\lambda, T_N)$$

we derived the network relative contribution to the total irradiance

$$\frac{\Delta S}{S} \approx \frac{4\alpha \delta T_{eff}}{T_{Sun}}$$

Assuming the change of network properties resulted from the analysis of Rome-PSPT images, we evaluated a change of the network contribution to total solar irradiance over the cycle of order 3×10^{-4}

$$\left(\frac{\Delta S}{S}\right)_{MIN} \approx 1.7 \times 10^4 \qquad \left(\frac{\Delta S}{S}\right)_{MAX} \approx 5 \times 10^4 \\ \left(\frac{\Delta S}{S}\right)_{MAX} - \left(\frac{\Delta S}{S}\right)_{MIN} \approx 3 \times 10^4$$

This result is close to the 0.1% increase in total solar irradiance measured during the last two solar cycles.

CONCLUSIONS

We studied the average properties of the network pattern in the photosphere and chromosphere by analyzing the near full-disk simultaneous CaII K, blue and red continuum images daily obtained with the Rome-PSPT telescope.

We described the temporal variation of these properties from July 1997 to August 2000 during the ascending phase of Solar Cycle 23.

We found the chromospheric quiet network properties do not show significant variations during the ascending phase of Solar Cycle 23, from July 1997 to August 2000.

We reported an increase of the chromospheric enhanced network disk coverage (3%) and contrast (<1%) over the 3 years analyzed.

We estimated the contribution to TSI due to the spatial fluctuations of effective temperature of the Sun associated to the photospheric network is about 10^{-4} .

By assuming the obtained results, we evaluated a change of the network contribution to TSI of order

 $3x10^{-4}$ over the cycle. This result is close to the 0.1% increase in TSI measured during the last two solar cycles.

BIBLIOGRAPHY

Berrilli, F., Florio, A., Ermolli, I.,1998, Solar Physics, 180, 29

Chapman, G.A., and Meyer, A.D., 1986, Solar Physics, 103, 21

Coulter, R.L., Kuhn, J.F. 1994, in: Active Region Evolution: Comparing Models with Observations, ASP Conference Series, Vol. 68, K.S. Balasubramaniam and G.W. Simon (Eds.)

Ermolli, I., Fofi, M., Bernacchia, C., Berrilli, F., Caccin, B., Egidi, A., Florio, A., 1998, Solar Physics, 177, 1

Ermolli, I., Fofi, M., Torelli, M., 1998, Mem SAIt., vol. 69, 587

Fligge, M., Solanki, S.K., Unruh, Y.C., Frohlich, C., Wehrli, Ch., 1998, A&A, 335, 709

Florio A. and Berrilli, F. 1998, Mem SAIt., vol. 69, 655

Fontenla, J., White, O.R., Fox, P.A., Avrett, E.H.,

Kurucz, R.L., 1999, ApJ, 518, 480

Foukal, P. and Lean, J., 1986, ApJ, 302, 826 Foukal, P. and Lean, J., 1988, ApJ, 328, 347

Foukal, P., Harvey, K. and Hill, F., 1991, ApJ, 383, L89

Frohlich, C., 1999, IUGG 99

Hudson, H.S., 1988, ARA&A, 26, 473

Lean, J., 1997, ARA&A, 35, 33

Steinegger, M., Brandt, P.N., Haupt, H.F., 1996, A&A, 310, 635

Willson, R.C., Hudson, H.S., Frohlich, C. and Brusa, R., 1986, Science, 211, 708

Worden, J.R., White, O.R., Woods, T.N., 1998, ApJ, 496, 998

THE CONTRIBUTION OF THE MAGNETIC REGIONS TO IRRADIANCE VARIATIONS

M. Fofi, I. Ermolli and M. Centrone

Osservatorio Astronomico di Roma, Viale del Parco Mellini 84, 00136 Roma, Italia phone: +39 0635347056 / fax: +39 0635347802 e-mail: name@oarhp1.rm.astro.it

ABSTRACT

We present photometric indexes and proxies of the solar irradiance computed by the analysis of the fulldisk images obtained with the Rome-PSPT.

The full set of data analyzed consisted of 700 daily images taken at the CaII K and the continua from around the minimum of the Solar Cycle 22 through the current ascending phase of the Solar Cycle 23.

The main purpose of our analysis was the precise identification of the magnetic features on the solar disk and the measure of their spatial and contrast properties. The feature identification was based both on the use of intensity thresholds and on geometric connection criteria.

The computed indexes were compared to the solar total irradiance measured by sensors from space (VIRGO on SOHO) and to some usual proxies of the solar activity (Radio flux, MgII index, Sunspot number).

IMAGE ANALYSIS

The full-disk images analyzed were obtained with the Precision Solar Photometric Telescope PSPT at the Rome Observatory in the framework of the RISE (Radiative Inputs of the Sun to Earth) project. For a detailed description both of the telescope and of the image quality see Coulter and Kuhn (1994), Ermolli et al. (1998a, 1998b).

The analysis was applied to the calibrated (dark current and flat-field response corrected) and contrast (C=I/Iq) images.

IRRADIANCE RECONSTRUCTION

The full set of images available at the Rome-PSPT data archive was used to describe solar irradiance variations over a period spanning several months. This was done by the reconstruction of an irradiance signal based on the computation of photometric indexes PI of magnetic regions identified on the full-disk images analyzed. In particular, the daily PSPT CaII K images were used together with the near-simultaneous PSPT continuum images to compute the indexes for the magnetic active (faculae and spots) and quiet (network) regions. The photometric indexes PI of the different magnetic features f identified on the daily images were calculated following the definition given by Hudson et al. (1982) and Frohlich et al. (1994) :

$$PI_f = \sum_f A_f \mu_f C_f \frac{I(\mu)}{I(1)}$$

taking into account the spatial (Area A_f, position μ_f) and the photometric (Contrast C_f) properties of the identified photospheric features. The Call K images were used just to trace the facular and network areas. A daily value of the reconstructed irradiance signal was obtained summing up the contributions of all the pixels of the features identified over the disk. The indexes computed for each day give the temporal variation of the reconstructed irradiance signal over the observing period. The reconstructed irradiance variation was compared (figure 1) to the irradiance signal measured from space by SOHO-VIRGO.

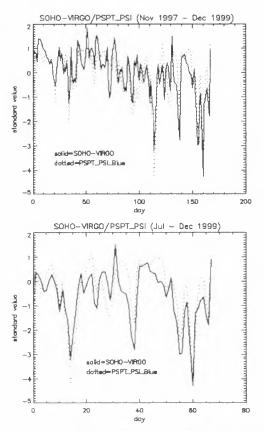


Figure 1: Temporal behavior of the solar irradiance standardized signal measured from space by SOHO VIRGO with superimposed the signal obtained by the Rome-PSPT continuum images for the two periods spanning several months (top: from November 1997 to December 1999, bottom: from July to December 1999).

Proc. 1st Solar & Space Weather Euroconference, 'The Solar Cycle and Terrestrial Climate', Santa Cruz de Tenerife, Tenerife, Spain, 25-29 September 2000 (ESA SP-463, December 2000)

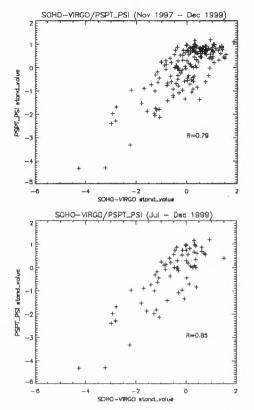


Figure 2 Correlation scatter plot between the daily standardized values of the Rome-PSPT reconstructed irradiance and the solar irradiance values measured from space by SOHO VIRGO instrument for the same periods in figure 1 (top: from November 1997 to December 1999, bottom: from July to December 1999).

We began our reconstruction describing irradiance variations during short periods at recent time, then extending the period length to use the full set of images available at the Rome-PSPT archive, that is images acquired from July 1996 to date. We found that the reconstructed signal fit (R=0.79) the measured irradiance signal for the two year long period from January 1998 to December 1999. For shorter periods (figure 2) the correlation found between the measured and the reconstructed signals increases (R=0.85).

Surprisingly, we found that the correlation between reconstructed and measured irradiance signals is very poor (R < 0.5) for the period spanning the very beginning of Solar Cycle 23, from October 1996 to October 1997 (figure 3). By excluding a change in the nature of the radiative sources of solar irradiance at short time scales and after verification both of the data used and the analysis performed, this result suggested us the existence of problems in the SOHO-VIRGO measurements. As also announced at the SOLSPA 2000 conference by the VIRGO PI, some calibration problems indeed affected the first data obtained by the instrument.

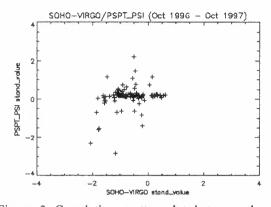


Figure 3 Correlation scatter plot between the daily values of the Rome-PSPT reconstructed irradiance and the solar irradiance values measured from space by SOHO VIRGO instrument for the period from October 1996 to October 1997.

CONTRAST HISTOGRAM PROPERTIES

We applied the contrast histogram properties analysis (Caccin et al. 1998) to all the CaII K images acquired with the Rome-PSPT from July 1996 to August 2000. This analysis can be summarized as follow. At first, active regions were identified on the contrast CaII K images by using both intensity threshold and spatial connection criteria. Then, contrast histograms for the full-disk and the quiet regions (non magnetic and network regions) were computed. The histogram skewness, that is a measure of the asymmetry of a distribution respect to the mean value, shows a clear behavior with the solar cycle (see reference already mentioned). Besides the skewness we extracted indexes connected with the area of non magnetic, quiet and active magnetic regions on the disk.

Figure 4 shows the temporal variation of activity proxies computed by the full-set of images available at the Rome-PSPT data archive. Variations of the disk coverage of both active and quiet regions are plotted, together with the variation of the skewness of full-disk and quiet regions contrast histograms. The latter are modulated by changes on the chromospheric emission of active and quiet regions. As the Rome-PSPT archive cover 48 months of observations daily performed during the whole ascending phase of Solar Cycle 23, the figure clearly shows the occurrence on October 1996 of the activity minimum between Cycles 22 an 23. The figure also clearly shows that the disk coverage of active and quiet magnetic region still grows during the whole period analyzed, while the skewness of full-disk contrast histogram, modulated by changes of the active region chromospheric emission, saturates at the growing of solar activity.

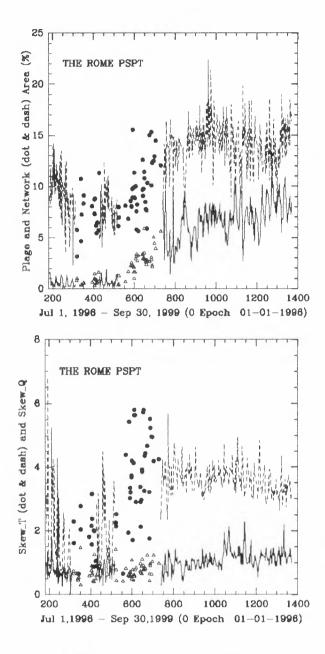


Figure 4 Temporal variation of activity proxies computed from the full-set of images available at the Rome-PSPT data archive. Variations of the disk coverage of both active and quiet regions are plotted, together with the variation of the skewness of full-disk (Skew_T) and quiet (Skew_Q) regions contrast histograms.

This saturation is also evident by comparing among the activity indexes computed from Rome-PSPT Call K images and some usual proxies of solar activity (Radio flux, MgII index, Sunspot number).

The behavior showed in figure 5 suggest a different pattern for chromospheric emission modulating the histogram skewness with respect to the emissions described by the other proxies, in particular the TR and coronal emissions represented by the MgII and the Radio flux indexes. The behavior showed in figure 5 indicates a different pattern for chromospheric emission with respect to those described by the other proxies, in particular the TR and coronal emissions represented by the MgII and the Radio flux indexes.

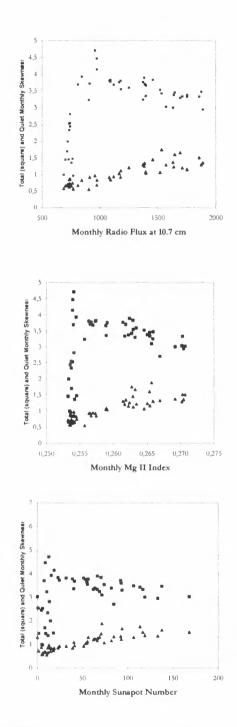


Figure 5 Downward: Correlation scatter plots between the monthly mean values of the histogram skewness activity proxy computed by the full-disk CaII K Rome-PSPT images obtained through the ascending phase of solar cycle 23 and usual proxies of solar activity.

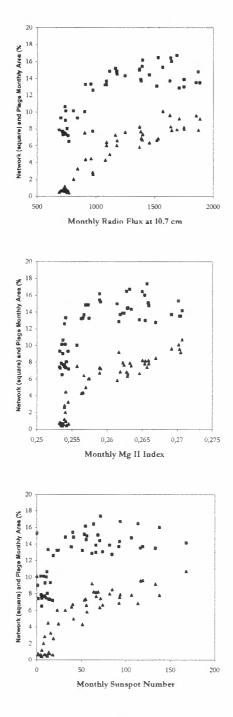


Figure 6 Downward: Correlation scatter plots between the monthly mean values of the area proxy computed by the full-disk CaII K Rome-PSPT images obtained through the ascending phase of solar cycle 23 and usual proxies of solar activity.

In fact the figure 5 points out both the latter emissions increase at the growing of the magnetic region disk coverage, the active region chromospheric emission quickly get a maximum value. This confirms that the TR and coronal emission differ significantly from the chromospheric one and suggests that the difference is due to the sensitivity on the geometry of the magnetic of the magnetic field as well as on the magnetic flux. The change in the rate of the emissions can derive by a different chromospheric sensitivity when compact magnetic regions appear over the disk.

CONCLUSIONS

In this paper we summarized some results obtained studying the magnetic region contribution to solar irradiance variations by the use of full-disk photometric images obtained with the Rome-PSPT from July 1996 to August 2000.

Calculations of solar irradiance based on measured photometric properties extracted from 1998-1999 Rome-PSPT continuum images match SOHO/VIRGO measurements (R=.85), while calculations for 1996-1997 do not fit the SOHO-VIRGO measurements (R<0.5). By excluding a change in the nature of the radiative sources of solar irradiance at short time scales and after verification of the goodness of both the data used and analysis performed, this result suggested us the existence of problems in the SOHO-VIRGO measurements, as recently announced.

The computed skewness of full-disk CaII K intensity histograms show the existence of a well defined non linear relation between chromospheric intensity and the usual indexes of solar activity. A significant positive correlation can be found considering the period around the minimum of Solar Cycle 22, while after minimum a light negative correlation appears. This might indicate the occurrence of a magnetic saturation in the CaII K chromosphere.

BIBLIOGRAPHY

Coulter, R.L., Kuhn, J.F. 1994, ASP 68, 37 Ermolli, I., Fofi, M., Bernacchia, C., Berrilli, F., Caccin, B., Egidi, A. and Florio, A. 1998a, Solar Physics, 177, 1 Ermolli, I., Fofi, M., Torelli, M. and Reardon K. 1998, Mem. SAIt., 69, 587 Frohlich et al., 1994, Solar Physics, 152, 111

Hudson et al., 1982, Solar Physics, 76, 211

IDENTIFICATION OF POTENTIAL SEP ASSOCIATED FLARES FROM **INTERBALL RF15-I HARD X-RAY OBSERVATIONS**

S. Gburek, M. Siarkowski, and J. Sylwester

Space Research Centre, Polish Academy of Sciences, Solar Physics Division Wrocław, Poland*

ABSTRACT

Several times a year large clouds of solar protons and other particles enters Earth environment causing significant disturbances in magnetosphere and atmosphere of our planet. These, often abbreviated as SEP (Solar Energetic Particle) events, may also damage satellites, communication networks, and cause failures of power systems. SEP could be, above all, injurious for humans in space. Hence, prediction of SEPs plays important role in space weather.

A distinctive class of SEPs form events that occur closely after solar flares. Their characteristic is a specific pattern of spectral evolution seen in X-rays. This gives a possibility to construct a SEP prediction algorithm that is based on analysis of solar flares X-ray radiation properties. These algorithms have been already developed and incorporated, but due to the infrequent occurrence of SEPs the spectral properties

collecting telemetric data since 6 August 1995. The RF15-I photometer measures integral solar flux in three soft channels s1, s2, s3 and five hard channels h1, h2, h3, h4, h5. Nominal energy bands, for each channel, are shown in Table 1. Detailed description of the instrument construction, and performance can be found in Sylwester, et al. (2000).

SEP EVENTS IDENTIFICATION in RF15-I RECORDS

Investigation of solar particle emissions and their influence on Earth's environment can be performed using various space-born and ground based data. In particular, measurements from GOES satellites allow to study particle properties from SEP events and to analyse associated parent solar flares in soft X-rays (provided that a given SEP has such a parent flare assigned). The list of SEP events, based on GOES

	raore r.	romman	energy ban	us for m	1.J-1 Cha	inners			
Channel	sl	s2	s3	hl	h2	h3	h4	h5	
Energy range	2 - 3	3 - 5	5 - 8	10 - 15	15 - 30	30 - 60	60 - 120	120 - 240	
[keV]	0.7 - 1.0	1.0-1.7	1.7-2.7*						
*ofter December 1007									

Table 1 Nominal energy hands for RE15-L channels

fafter December 1997.

of their associated flares are still not well understood and need further investigations. Since 1995, a number of SEP events have been observed by RF15-1 soft/hard X-Ray photometer, working on board Interball-Tail satellite. In this contribution we perform inspection of the hard RF15-I X-ray measurements in order to select SEP event records among RF15-I database.

RF15-I INSTRUMENT

RF15-I is a solar photometer-imager, developed in order to investigate solar flares and other active events on the Sun. The instrument, launched aboard INTERBALL-Tail satellite in summer 1995, has been

*email: sg@cbk.pan.wroc.pl

measurements, can be found at the NOAA www site

www.sec.noaa.gov/getftp.cgi?get=/indices/SPE.txt

The list contains information for more than 150 SEPs which occurred between 1976 and 2000. By exploiting GOES observations one can better understand certain specific data patterns present in RF15-I records. Namely, for several periods, signal in RF15-1 hard X-ray channels rises suddenly and holds its high level for many hours. Comparison of RF15-I records with GOES proton flux measurements shows that the observed high signal levels coincide with increased proton fluxes registered by GOES satellites. We have found that at least 10 of them can be identified, in this

Proc. 1st Solar & Space Weather Euroconference, The Solar Cycle and Terrestrial Climate', Santa Cruz de Tenerife, Spain, 25-29 September 2000 (ESA SP-463. December 2000)

way, with SEP events, from NOAA list, attributed to parent flares. Such an identification yields a possibility

(about 03:30 UT) in RF15-I records is deformed near the maximum what is a typical effect for RF15-I

		FLARE	PARTICLE	EVENT			
Year	Maximum (X ray/Opt)	Importance	Location	NOAA SEC Region No.	Start (Day/UT)	Maximum (Day/UT)	Proton Flux (pfu @ >10 MeV)
1995	Oct20/0607	M1/0F	S09W55	7912	Oct20/0825	Oct20/1210	63
1997	Nov04/0558	X2/2B	S14W33	8100	Nov04/0830	Nov04/1120	72
1998 1998 1998 1998	Apr20/1021 May06/0809 Sep23/0713 Sep30/1350	M1/EPL X2/1N M7/3B M2/2N	S43W90 S11W65 N18E09 N23W81	8194 8210 8340 8340	Apr20/1400 May06/0845 Sep25/0010 Sep30/1520	Apr21/1205 May06/0945 Sep25/0130 Oct01/0025	1700 210 44 1200
1999 1999	May3/0602 Jun04/0703	M4/N2 M3/2B	N15E32 N17W69	8525 8552	May05/1820 Jun04/0925	May05/1955 Jun04/1055	14 64
2000 2000 2000 2000 2000	Feb17/2035 Apr04/1541 Jun06/1525 Jun10/1702 Jul22/1134	M1/2N C9/2F X2/3B M5/3B M3/2N	S29E07 N16W66 N20E18 N22/W38 N14/W56	8872 8933 9026 9026 9085	Feb18/1130 Apr04/2055 Jun07/1335 Jun10/1805 Jul22/1320	Feb18/1215 Apr05/0930 Jun08/0940 Jun10/2045 Jul22/1405	13 55 84 46 17

Table 2. List of SEP events identified in RF15-I records

of determining SEP associated flare characteristics and analyse their time evolution in a wide X-ray energy range covered by RF15-I measurements. Determined flare characteristics could be later used to construct SEP events prediction algorithms (Sylwester 1995, Garcia 1998). In Table 2 we show SEP events we have identified in RF15-I records. For two of them we present a comparison of RF15-I and GOES particle fluxes below. Basic plasma characteristics for parent flares for 20 April 98, 30 September 98 and 4 Jun 99 events are analysed in details by J. Sylwester (see the parallel contribution).

RF15-I SEP MEASUREMENS

As an example of our SEP events observations let us consider RF15-I X-ray records for the event on 22 July 2000, shown in Fig. 1. Characteristic RF15-I signal pattern, clearly visible in h3, h4 and h5 hard channels, starts at about noon, just after the flare of GOES importance M3.7, which reached maximum at 11:34 (seen in soft X-rays). The high RF15-I signal level is associated with increased GOES proton fluxes. Similar pattern of RF15-I and GOES signal time behaviour is observed on 9 May 1998 event, shown in Fig. 2 (our second example). This time, however, the flare signal

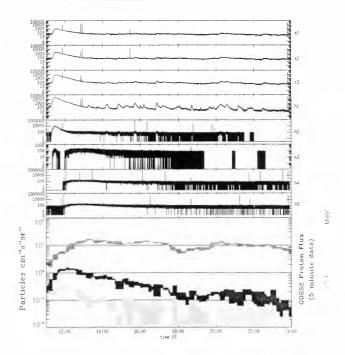


Fig. 1. RF15-I X-ray signal (eight upper panels) compared with GOES records for SEP event on 22 July 2000. Characteristic particle signal pattern starts at about 12:00 UT. GOES 5-minute average proton fluxes for energies >10MeV, >50MeV, >100MeV are shown below.

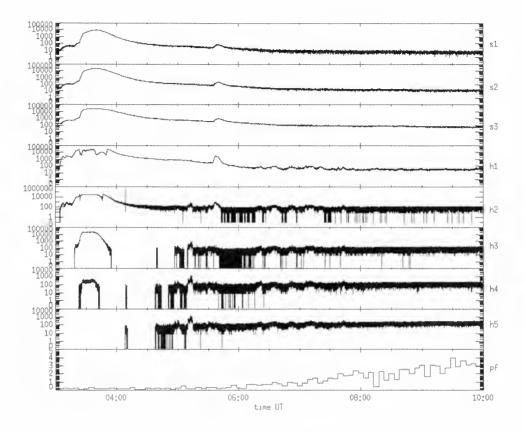


Fig. 2. A comparison of RF15-1 X-ray records with GOES proton fluxes for SEP event on 9 May 1998. GOES 5-minute average proton flux for energies >10 MeV is shown in the lowest panel. RF15-1 and GOES measurements exhibit similar time behaviour as, for previously discussed, 4 November 1997 and 6 May 1998 events.

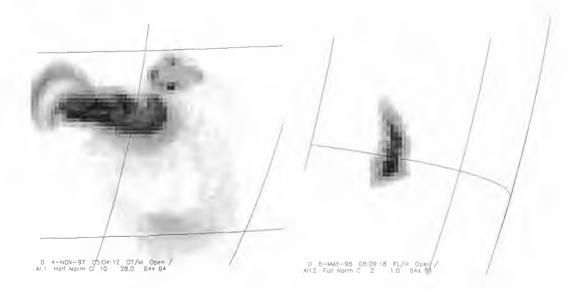


Fig3. SXT images for SEP associated flares on 4 November 1997 (left panel) and 6 May 1998 events (right panel).

observations of big flares. For example, the count rate level from large flares (i.e. above M5-M6 of GOES class) exceeds the capacity of counters (set at 32000 and 64000 hits per integration time in particular channels). This causes counter wrapping, sometimes

many-fold. Recently, we have developed software to regain original flare X-ray profiles from these wrapped measurements. We have also inspected SXT data for SEP events listed in Table 2. It appears that the parent flares for SEPs occur in various magnetic loop

configurations as seen in SXT images. SXT frames for 6 May 1998 and 4 November 1997 events are shown in Fig. 3.

CONCLUSIONS

We show that characteristic signal patterns, seen in RF15-I measurements after certain solar flares, occur simultaneously with increased particle fluxes measured by GOES satellites.

By inspecting SXT images for 1997 November 4 and 1998 May 6 events, we show also that occurrence of SEPs does not depend evidently on magnetic loop system configuration of their parent flares, except that it may be quite complicated higher up in the corona.

AKNOWLEDGEMENT

This work has been possible thanks to the grant 2.P03D.024.17 of Polish Committee for Scientific Research.

REFERENCES

Garcia, H. A., Farnik, F., Kiplinger, A. L. Hard x-ray spectroscopy for proton flare prediction. In: *Missions to the Sun II.* - Washington, Society of Photo-Optical Instrumentation Engineers 1998. - S. 211-216. Siarkowski, M., Sylwester, J., Gburek, S. et al, Review Of Rf15-I X-Ray Photometer Observations, ESA SP Series (SP-448) p. 877-882, 1999. Sylwester, B., Sylwester, J., Garcia H., Thermodynamic Signatures of Proton Flares, JOSO Annual Report, p. 161, 1995. Sylwester, J., Farnik, F., Likin, O. et al, Solar Soft/Hard X-ray Photometer-Imager aboard the INTERBALL-Tail Probe, Solar Physics, in print (2000).

COMPARISON BETWEEN GRADUAL AND IMPULSIVE SOLAR ENERGETIC PARTICLE EVENTS DETECTED BY EPHIN/SOHO^{*} EXPERIMENT

R. Gómez-Herrero¹, M.D. Rodríguez Frías¹, L. del Peral¹, J. Sequeiros¹, R. Müller-Mellin², H. Kunow²

¹Departamento de Física, Universidad de Alcalá, Spain ²Institut für Experimentelle und Angewandte Physik, Universität Kiel, D-24118 Kiel, Germany

ABSTRACT

This work is a preliminary study of 18 Solar Energetic Particle (SEP) events detected by EPHIN/SOHO during 1996, 1997 and 1998. Differential fluxes of electrons, protons and helium nuclei are presented for each event. Differential energy spectra and spectral temporal evolution for protons and ⁴He nuclei have been studied, and abundance ratios of e/p, ⁴He/p and ³He/⁴He have been determined using pulse-height analysed data. Most of the events presented here can be classified as impulsive or gradual events, but some of them have mixed features and cannot be clearly classified in one of these two categories.

1. INTRODUCTION

The studied events have been selected among more than 60 solar energetic particle events registered by EPHIN sensor during 1996, 1997 and 1998. These events have a wide variety of observational features (composition, spectra, duration, etc), and there is an adequate sample of the differences that can be found studying SEP events. Nevertheless, most of the events can be classified in two broad categories: impulsive and gradual events. Observational characteristics of these two categories have been widely described by many authors (Mason et al. 1986, Reames et al. 1997, Reames 1999). Gradual events show large increases in particle fluxes, they are commonly associated with CMEs and interplanetary shock waves, they are long duration (several days) events, and the composition is similar to solar wind and corona. Impulsive events are characterised by low particle fluxes, short duration. heavy ions and ³He enrichment, and they are commonly associated to impulsive X-ray flares.

2. OBSERVATIONS

The observations were carried out with EPHIN instrument, aboard SOHO spacecraft, located in an halo orbit centered at the inner Lagrange point, outside Earth's magnetosphere. EPHIN (Electron Proton and Helium Instrument) is a multi-element array of solid state detectors designed to detect Hydrogen and Helium isotopes in the energy range 4.3-53 MeV/n, and electrons in the energy range 0.15-10 MeV (see Müller-Mellin et al. 1995, for a detailed description). Particles detected by EPHIN can be identified using ΔE vs E

method, and it is possible to obtain accurate ¹H and ⁴He spectra. Isotopic resolution of the instrument is high enough to discriminate ¹H, ²H, ³He and ⁴He isotopes, and ³He-rich events can be easily identified when ³He/⁴He ratio reaches values greater than 0.1 approximately (fig 1).

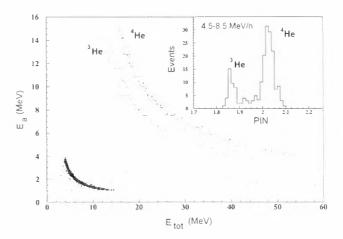


Figure 1. ΔE vs E plot for Nov 26, 1997 event. Vertical incidence counts has been selected. Top right corner shows the isotopic discrimination achieved for ³He and ⁴He using these data (PIN = $((MZ^2)/2)^{1/3}$.

Events presented in this work happened between July 1996 and May 1998. The first half of this period showed relatively quiet particle fluxes, corresponding to solar activity minimum. During the second half of this period, solar activity increased gradually, corresponding to the rising phase of 23rd solar cycle, and extremely large SEP events (Nov 97 and Apr 98) were detected.

The start and end times of individual events have been identified using proton differential flux (4.3-7.8 MeV). These two times delimit the temporal period studied for each event. Particle fluxes, global spectra of ¹H and ⁴He corrected from galactic background, temporal spectral evolution, and isotopic composition have been determined for all the events in order to obtain observational parameters to classify them as impulsive or gradual events. Some of the experimental parameters obtained for the 18 studied events are listed in table 1.

^{*}SOHO is an ESA-NASA collaboration

Proc. 1st Solar & Space Weather Euroconference, 'The Solar Cycle and Terrestrial Climate', Santa Cruz de Tenerife, Tenerife, Spain, 25-29 September 2000 (ESA SP-463, December 2000)

Table 1. Experimental parameters obtained for the 18 events presented in this work. From left to right: Spectral index for protons, spectral index for Helium 4 nuclei, abundance ratios, and time interval studied. Energy ranges for abundance ratios calculation is 4.5-8.5 MeV/n for 1 H, 4 He and 3 He, and 0.25-4.25 MeV for electrons. The time interval studied approximately coincides with the event duration for low energy protons, although can be smaller than the whole event if the end has been truncated.

		$\gamma_{\mathbf{p}}$	Yee	e/ ¹ H	⁴ He/ ¹ H	³ He/ ⁴ He	Δt^{-} (days)
Jul 9	9, 1996	-3.13	-2.65	399.7	0.139	0.01	3.1
Jul 12	2, 1996	-3.91	-3.66	348.2	0.155	0.03	2.04
Aug 13	3, 1996	-1.74	-	516.9	0.010		3.71
Nov 25	5, 1996	-5.33	-	382.0	0.050	_	1.75
Nov 26	5, 1996	-3.46	-3.74	121.8	0.113	0.01	1.78
Nov 28	8, 1996	-3.44	-3.53	6.7	0.023	<0.01	9.16
Dec 24	1, 1996	-2.33	-	96.0	0.005	_	2.97
Apr 1	1, 1997	-1.95	-2.46	88.5	0.021	<0.03	6.25
Apr 7	7, 1997	-2.65	-2.85	10.3	0.008	<0.01	10.31
Aug 10	0, 1997	-3.33	-3.39	657.6	0.284	0.28	1.66
Sep 17	7, 1997	-3.01	-3.00	526.8	0.155	0.18	2.65
Sep 20), 1997	-3.57	-3.22	44.6	0.034	0.04	3.22
Sep 24	1, 1997	-1.48	-	181.0	0.015	_	7.65
Nov 4	1, 1997	-2.02	-2.16	25.9	0.022	<0.01	2.26
Nov 6	5, 1997	-1.80	-1.92	107.9	0.022	<0.03	7.43
Nov 28	8, 1997	-2.33	-2.73	152.3	0.144	0.317	1.12
Apr 20	0, 1998	-1.16	-1.85	352.4	0.048	<0.01	9.58
May 27	7, 1998	-4.79	-3.45	37.0	0.013	0.04	3.41

3. RESULTS AND DISCUSSION

After data analysis, six events have been classified as impulsive: July 9 1996, July 12 1996, November 26 1996, August 10 1997, September 17 1997, and November 28 1997. The most relevant observational features found in these events are:

- Event duration is less than 4 days
- There is no significant acceleration of protons beyond 25 MeV
- High electron content: in all cases e(0.25-4.25 MeV)/p(4.5-8.5 MeV) ratio reaches values greater than 100
- High ⁴He content: in all cases ⁴He(4.5-8.5 MeV)/p(4.5-8.5 MeV) ratio reaches values greater than 0.1
- Most of the events have ³He(4.5-8.5 MeV)/⁴He(4.5-8.5 MeV) ratio greater than 0.01. In some cases this ratio is particularly high (>0.1).
- In general, they have associated neither CMEs nor interplanetary shock waves
- Proton and ⁴He spectra are relatively soft ($\gamma_p < -3.0$, except for Nov 28 1997 event)

Seven events have been classified as gradual: November 28 1996, April 1 1997, April 7 1997, September 24 1997, November 4 1997, November 6 1997, and April 20 1998. These events are characterised by:

• The event duration is greater than five days, exceeding 10 days in some cases.

- Protons are accelerated beyond 25 MeV
- Electron content is, in general, lower than that of impulsive events. Although, Some events have high electron abundance (April 20, 1998)
- ⁴He/¹H ratio is close to coronal and solar wind value. (typically between 0.02 and 0.05). In some events slight helium acceleration is observed and the ratio becomes lower
- ³He can not be seen appreciably above background
- Most of them have associated CMEs, and interplanetary shock waves (although in some cases it has not been possible to find any associated shock). In some cases shock passage can be seen as transient hardening of spectral index, followed by long periods of invariant spectrum
- Proton and ⁴He spectra are hard ($\gamma_p > -3.0$, except for Nov 28 1996 event)

November 25 1996, December 24 1997, September 20 1997 and May 27, 1998 events have mixed features, although the first one seems to be more impulsive and the last three ones more gradual events. August 13 1996 event, probably associated to a eruption in the back side of the sun (Torsti et al, 1999), shows some peculiarities and it has not been classified.

Figure 2 shows the results obtained for a typical gradual event (November 6, 1997) and a typical impulsive event (November 28, 1997). Figure 3 shows the temporal evolution of spectra for November 6 event

November 6, 1997 (Gradual event)

Time interval studied: 310.49-317.92

c(0.25-4.25 MeV)/p(4.5-8.5 MeV) = 107.9 ${}^{4}\text{He}(4.5-8.5 \text{ MeV}/n)/p (4.5-8.5 \text{ MeV}) = 0.022$ ${}^{3}\text{He}(4.5-8.5 \text{ MeV}/n)/{}^{4}\text{He}(4.5-8.5 \text{ MeV}/n) < 0.03$

November 26, 1997 (Impulsive event)

Time interval studied; 332.56-333.68

c(0.25-4.25 MeV)/p(4.5-8.5 MeV) = 152.3 ${}^{4}\text{He}(4.5-8.5 \text{ MeV/n})/p (4.5-8.5 \text{ MeV}) = 0.144$ ${}^{3}\text{He}(4.5-8.5 \text{ MeV/n})/{}^{4}\text{He}(4.5-8.5 \text{ MeV/n}) = 0.317$

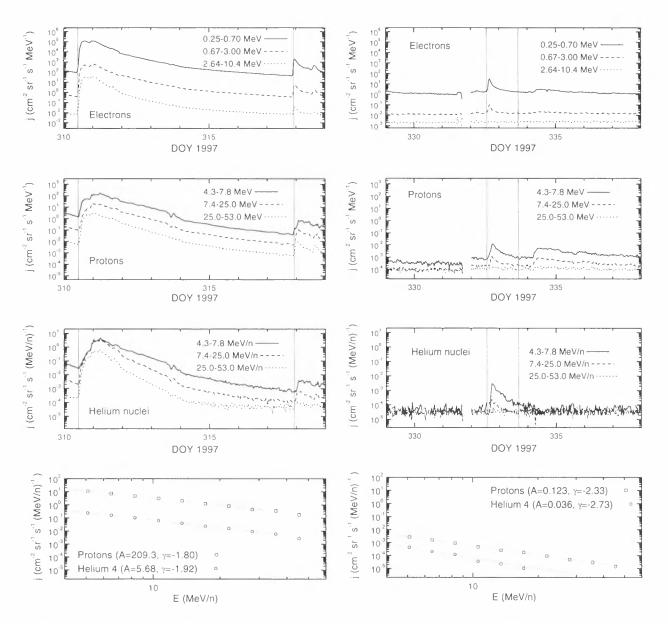


Figure 2. Abundance ratios, differential fluxes and spectra for November 6, 1997 gradual event and November 26, 1997 impulsive, ³He-rich event. November 6 event is very energetic, with strong acceleration of p and He beyond 50 MeV/n and e beyond 10 MeV. It is associated with a 2B/X9.4 flare at 310:11:49 UT, \$18W63 (NOAA 8100) followed by a CME ejected at 310:12:10 UT. A magnetic cloud ejected during Nov 4 CME passed by spacecraft between days 311.2-312.5. This MC was preceded by a strong IP shock at 310.9, other shocks passed at 313.4 and 313.9. Nov 26 event is less energetic, there is not appreciable acceleration of p and ⁴He beyond 25 MeV/n. There is not a clear candidate for this event, possibly it is associated with a 2B/X2.6 flare at 331:12:59 UT, N17E63 (NOAA 8113). However, bad magnetic connection is not frequent for impulsive events because of their low particle fluxes.

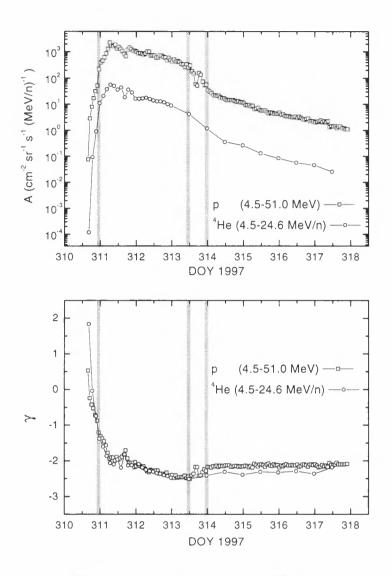


Figure 3. Temporal evolution of the power law AE^{γ} fit parameters for protons and helium 4 nuclei spectra in November 6, 1997 gradual event. Vertical lines mark shocks passages. Spectral invariance can be appreciated for the late stages of the event.

ACKNOWLEDGEMENTS

The authors acknowledge the use of the WIND/MFI and WIND/SWE data in the magnetic structure interpretation involved in this publication.

This work has been supported by the Spanish Comisión Interministerial de Ciencia y Tecnología (CICYT), ref. ESP 97-1776.

Raúl Gómez-Herrero is indebted to the Universidad de Alcalá for a pre-doctoral grant.

REFERENCES

Mason et al 1986, ApJ 303, 849-860.

Reames D.V. et al 1997, ApJ 483, 515.

- Reames D.V. 1999 Space Science Reviews Vol 90 413-491
- Müller-Mellin et al 1995, Solar Physics 162, 483. Torsti et al, 1999, JGR 104.9903T.

GALAXY-SUN-EARTH RELATIONS. THE DYNAMO OF THE EARTH, AND THE ORIGIN OF THE MAGNETIC FIELD OF STARS, PLANETS, SATELLITES, AND OTHER PLANETARY OBJECTS

Giovanni P. Gregori

IFA (CNR), via Fosso del Cavaliere 100, 00133 Roma (Italy)

tel. +39 06 4993 4321; fax +39 06 20 660 291; e-mail: gregori@ifa.rm.cnr.it

Magnetic fields ought to be a frequent feature in the universe, originated by dynamos within stars, planets, satellites, and, maybe (although in terms of simple induced electric currents and/or of permanent magnetised sources) within asteroids, meteorites, and/or comets. The problem can be tackled in terms of a few different kinds of dynamos, all of which seem to apply in different case histories and are distinguished depending

- (i) on whether their respective constituents have either a large or a small electrical conductivity σ ,
- (ii) on their respective prime energy supply,
- *(iii)* on what mechanism is operative for releasing their power, and
- (*iv*) on whether one can apply the quasistationary approximation (QS) or not, i.e. on whether $div \mathbf{i} = 0$ or not.

Comparing different dynamos

Quasi- stationarity		Characte		Comments	Application	s	
NO div $\mathbf{j}(t) \neq 0$		Presently gene standard o	Larmor's and Elsasser's	Sun, stars, Earth, planets, satellites			
*	DYNAMO TYPE	CONSTITUENTS	ELECTRICAL CONDUCTIVITY	USER NETWORK			
	Туре І	Wires	$\sigma \sim \infty$	YES	Engineering dynamos	Power lines network None	
YES div $\mathbf{j}(t) = 0$	Type II	Wires	$\sigma \sim \infty$	NO	Biermann's blocking		
	Type III a	3D j- distribution	σ~∞	NO	Biermann's blocking (+ thermo- nuclear breaking)	Sun stars	
	Type III b	3D j- distribution	$\sigma \sim \infty$	NO	Biermann's blocking (no breaking)	Earth planets satellites	?
	Type IV	3D j- distribution			Tide-drivenPlanets, sTide-drivenEardynamo(~1% ma~99% Jo		ic,

A star dynamo was modelled (without QS) since 1920 by Larmor, and in 1946 it was generalised and adapted to the Earth by Elsasser.

When referring to any given planetary object, provided that it has a fluid portion in its interior and be subject to a tide, an alternative general mechanism ought to exist by which the tidal pull breeds a dynamo. Such a general configuration (with QS) ought to be a frequent feature in the universe. Maybe, it could also apply to the Earth, and in such a case the origin both of the magnetic field and of the (unexplained) endogenous energy of the Earth could be much simpler than it has been generally believed.

The presently standard MHD dynamo does not assume QS, being appropriate in a star where thermonuclear reactions can imply non-null concentration of electric charge. The alternative kind of dynamo here considered ought to apply to a planet, much like e.g. to the Earth, or to some other case history in the universe, that has a solid inner core, and a solid thick outer layer (composed e.g. altogether of mantle, lithosphere, and crust). In between them, a fluid outer core has negligible viscosity. Moreover, some external body, such as e.g. a satellite, or the central star provided that the planet be reasonably close to it, originates a tide.

The tidal interaction reduces planet's spin and is applied to radial layers, like in an onion. The computed tidal torque on every such layer implies a torque on the inner core negligible compared to outer layer's. In the case that the planet has an external fluid ocean, the tidal deformation and torque is even larger, and applies only on the outer layer. The spin of the

Proc. 1st Solar & Space Weather Euroconference, 'The Solar Cycle and Terrestrial Climate', Santa Cruz de Tenerife, Tenerife, Spain, 25-29 September 2000 (ESA SP-463, December 2000)

outer layer is thus much reduced compared to inner core's. Since large σ are involved, this is a dynamo.

A stellar dynamo presumes a high σ , likewise the analogous standard geodynamo. Since no agreed explanation is known for the endogenous energy of the Earth, and since the power required for the geodynamo is negligible compared to other endogenous phenomena, it is generally claimed that the electric currents **j**'s of the dynamo flow in regions of high σ , by which no concern arises about its energy sustaining. Such a guess, however, has two ultimate drawbacks.

First, every **j**-loop must expand as much as possible, until it encounters some region of low σ , where it unavoidably decays. Hence, one should speculate about some unrealistic barrier in order to forbid such outward expansion.

Second, whenever no user network is connected to a dynamo, its magnetic energy continuously increases, hence also the forces in between its constituents, by which the system results to be completely blocked (in 1939 Biermann applied this argument while studying sunspot cooling). The Earth should thus be rigid, and maybe it would be even impossible to get seismological evidence of its fluid outer core. Otherwise, some energy source, equivalent to star's thermonuclear, ought to overwhelm such a blocking. Such a drawback strictly holds only provided that QS can be applied (although, maybe, it holds also in some more general case).

- *"Type I*" dynamo deals with usual engineering devices that supply power lines.
- "*Type IP*" implies full blocking, recalling Biermann's.
- "Type III" looks, apart QS, much like the standard MHD stellar or Earth's dynamo although maybe, on special circumstances, some conclusions could be almost independent of QS. A crucial difference is the distinction between "type IIIa" and "type IIIb" depending on whether there is, or not, respectively, some overwhelming endogenous energy capable of breaking Biermann's blocking. That is, in the case of the Sun or of a star thermonuclear energy disrupts blocking. "Type IIIa" is almost the same as a standard star's model. "Type IIIb" should be (perhaps) much similar to Elsasser's geodynamo, although it appears difficult to justify why it is not blocked by Biermann's.
- "Type IV" dynamo is the concern of the present proposal. It has a finite σ , and in the case of the Earth it can be shown to imply a low performance (~1%), while the remaining ~99% breeds the endogenous energy budget of the Earth. It works under very general conditions, that appear likely to occur frequently in the universe.

One substantial difference between standard and tide-driven dynamos deals with the superrotation of the inner core. In standard geodynamo $\sim 0.1-3$ ° year⁻¹

is reported, while the tide-driven dynamo implies (order of magnitude) $\sim 10^3 \circ day^{-1}$. Such superrotation can be tested by observations, in terms of a stroboscopic effect by means of standard ground-based geomagnetic records, and also by a suitable reinterpretation the presently claimed seismological evidence for such a superrotation.

Another difference is concerned with the fact that the Earth can no more be considered as a slowly cooling planet, rather in terms of some comparatively very rapid energy accumulation, and time-delayed energy release, much like in a car battery. This is one of the most surprising inferences, seemingly an unavoidable observational requirement.

Science is the search for truth, made of ideas, eventually wrong and to be rebutted after check by observations. The ultimate basic understanding could hardly progress without new ideas. Emphasis ought to be focused on unexplained and/or unprecedented observations.

The present study was formerly originated for interpreting Lowes' (1974) and Nevanlinna's (1987) evidence about the spatial spectrum of the geomagnetic field, and for fitting it with the available information on deep Earth's interior, based either on seismology or on e.m. induction. This required consideration, as a first order approximation, of some abstraction and approximation. In this way, almost inadvertently, an entire unprecedented model Earth was obtained. Every progressive inference was derived after careful consideration of observations, searching for an interpretation conforming as much as possible with the generally accepted standards. But, sometimes this led to totally unexpected conclusions.

Such a multidisciplinary approach had been impossible without the inputs from several specialists of different disciplines (it is impossible to acknowledge here all of them).

For over a decade the situation remained almost in stand-by, because on one side reference had to made to standard geodynamo, and on the other hand the former attempt at providing an explanation for unexplained observations led to some opposite conclusions. The missing ring (QS distinction) closed the logical chain.

The final resulting picture is shown in figure 1, where the palaeohistory of the Earth, of its climate, geodynamics, volcanisms, etc. fit into an apparently well co-ordinated interpretation, where Galaxy - Sun -Earth relations can be explained in terms of the galactic control on solar phenomena, that controls Earth's dynamo and endogenous energy budget, volcanism and gas exhalation, atmospheric chemistry and climate. All other planetary objects (including Moon's and Mars' palaeohistory, except Venus) fit into such a scheme.

Whether wrong or correct, it contains several unprecedented ideas, by which previously unexplained observations can be interpreted, or even must be expected. Whether it is a coincidence or not, it appears worthwhile to consider it, even for proving where and how it is eventually wrong.

Such a model is not the result of a speculation. Rather it derives from subsequent refinements while interpreting otherwise unexplained observations. If somebody affords in interpreting them in terms of other or previous models, every proposal shall be welcome.

Several inferences of the present study derive from QS, although several conclusions could eventually result to be independent of QS. If such an Earth model is akin to reality, the σ of the medium, and the prime (tidal) driving mechanism, are such that the time scales allow for electric charges to redistribute and neutralise, and thus ensure QS. The same applies to every planet or satellite. In contrast, a star is certainly much different, dominated by thermonuclear processes. Therefore, the tide-driven dynamo for the Earth is not ruled out by the impossibility of applying QS.

Several facts seem to support such tide-driven model, beginning from an unprecedented justification for the entire energy budget of the Earth, through Lowes' and Nevanlinna's and their fit with seismological and e.m. induction evidence, through inner core's superrotation derived from ground-based geomagnetic records, and the apparent time variation of the inner core radius, through solar modulation of volcanism, through the interpretation of the large igneous provinces (*LIP*) and the output from Hawaii's hot spot, through field reversals (*FR*) excursions, their correlation with cosmic rays and with the encounters with interstellar matter, palaeoclimatology, etc.

All this could obviously be only a coincidence. However, until one finds some specific effect that is in clear contradiction with such tide-driven dynamo, it cannot be simply ruled out, only because it does not conform with the presently generally agreed models.

A short conclusion

• The dilemma is between the standard geodynamo (similar to "*type IIIb*") and "*type IV*".

The standard geodynamo has a high σ , it requires a small total amount of energy, and the system is almost blocked, including even its own convection within the outer core. Motions occur only by the limited amount needed for generating the tiny Joule heating dissipated by its **j**'s. Two major difficulties are concerned with the former trigger of the α - ω effect, and with the strict need for electric insulation of the region of very large σ in order to forbid the **j**'s to leak outward. Inner core's superrotation is $\sim 0.1^{\circ}-3^{\circ}$ year⁻¹. Excursions and *FR*'s are of endogenous origin. The dynamo has no recognised, either direct or indirect, connection with other endogenous phenomena, the prime mover of which remains a difficult puzzle. The tide-driven dynamo is concerned with **j**'s that flow within a medium of low σ , and ~99% of its energy is dispersed as Joule's heating that supplies the endogenous energy of the Earth (or almost all of it). Inner core's superrotation is (order of magnitude) ~ $10^3 \circ day^{-1}$. Excursions and *FR*'s are the effect that *must* be expected when the heliosphere is compressed into Earth's orbit.

Several observations appear to support the tide-driven model. It is possible to envisage a decisive tests by a data handling of standard geomagnetic records, by which the westward drift can be treated as an aliasing effect (much like the wheels of a chariot observed in a movie).

- There are three kinds of objects in the universe.
 - A) Stars have a large endogenous energy source, and fully ionised constituents. Fluid motion continuously disrupts the system, as well as every regular dynamo. Their B displays a pattern fluctuating in space and time, typically like the Sun.
 - B) Planetary objects with their own dynamo ought to be comparatively frequent in the universe. Every one must be expected to have a dynamo provided that

(i) it has different parts de-coupled with respect to each other

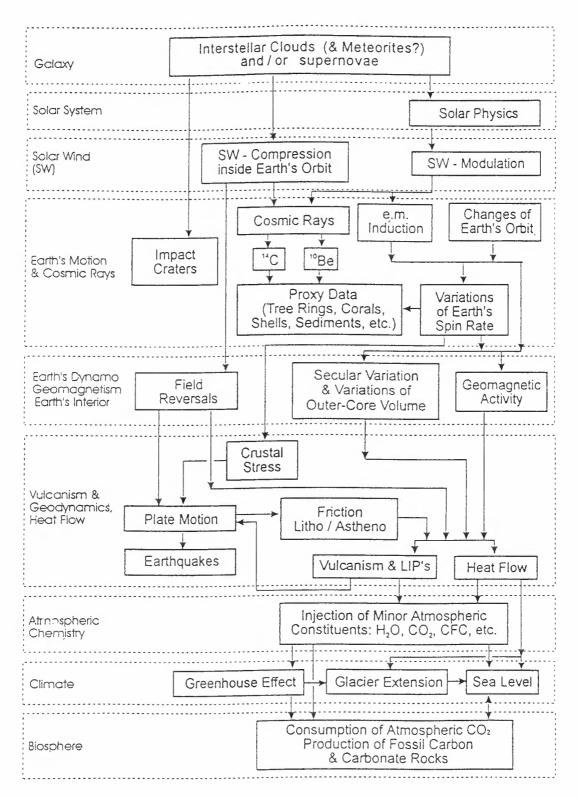
- (ii) it is subject to a tide, and
- (*iii*) it has a finite internal σ .

If $\sigma = \infty$ all of its parts result to be strongly coupled with each other (Biermann's argument). The **B** of a planetary object is regular and almost steady, mainly dipolar. Excursions and FR's are easily derived as a response to the interaction of the solar (or stellar) system with a cloud of interstellar matter. The relative tilt of planetary dipole's and spin's axis depends on the state of the solar (or stellar) wind at the time of the reestablishment of the B of the planet. Owing to Cowling's theorem, the dipole axis should always be significantly non-aligned with spin's. The steadiness of the dynamo of the planet, and its survival in time (unlike it happened e.g. to the Moon or to Mars) depends on the size and internal structure of the planet (owing to this reason the Earth never exhausted its dynamo, and its associated effects, including life survival). The propagation mechanism is explained in Gregori (1993, PEPI, 77, 39-).

C) Asteroids, comets, meteorites are solid and cold objects and have no dynamo. Sometimes they could have a B either (i) by permanent magnetisation, or (ii) by induced j's.

The second possibility applies to every asteroids, comets, or meteorites that eventually is electrically conducting (at least within its outermost layer, such as carbon or dirty ice in comets). It experiences e.m. induction by the **B** that is either transported by the solar (or stellar) wind, or generated by some intense dynamo of some close-by planet. In principle, such induced \mathbf{j} 's, whenever the σ is adequately large, originate a **B**, hence also a magnetosphere. Whenever observable and tracked by some observations

(e.g. perhaps by a cometary coma), such a magnetosphere ought to display specific features vs. its distance either from the Sun (or central star) or from other planetary objects having their own **B**. Whenever such a speculation can be eventually applied to a few comets, they could be cheep natural probes for sounding interplanetary space.



3-D TOMOGRAPHY OF THE SOLAR PHOTOSPHERE

A. Hanslmeier¹, A. Kučera², J. Rybák², and H. Wöhl³

¹Institut für Geophysik, Astrophysik und Meteorologie, Graz, Austria ²Astron. Inst., Slovak. Acad. of. Sciences, Tatranská Lominica, Slovakia ³Kiepenheuer Institut für Sonnenphysik, Freiburg, Germany

ABSTRACT

We analyze the behaviour of solar photospheric granular motions using 2-D scans in different sepctral lines. The location of acoustic flux is investigated by a comparison of enhanced full width at half maximum variations with granular motions.

Key words: The Sun, convection.

1. INTRODUCTION

Dynamical motions in the solar photosphere and their propagation and time evolution are crucial for the understanding of various processes of solar activity and heating of upper layers. However, it is extremely difficult to obtain high quality data. We present an analysis from recent observations from the VTT (Observatorio del Teide) with the newly installed XEDAR cameras. In order to obtain a 2-d spectrogram, the Sun was scanned over an area of 20 arcsec by 50 scans. Thus a time series of 8 images separarted by a 130 s interval could be studied. Using lines of different line formation heights we obtain information about the vertical structure and motions of the evolving elements.

A comparison between previous observational results and theoretical 2-d simulations can be found in Gadun et al, 2000. The influence of oscillations on convective structures is discussed in detail in Rast (2000), where further references can be found.

2. DATA

The data were taken with the 70 cm VTT at the Observatorio del Teide in Izana, Tenerife. A more detailed description of this telescope can be found in Schröter et al. (1985). We obtained during an observing campaign in 1999 time series of two dimensional spectral scans, where the spatial sampling interval was $\delta x = 0.4''$ and the total number of spectral

exposures was 50. Thus an area of 20" was scanned. The time step between two successive images was 2.5 s. Thus one 2-d scan lasted for slightly more than 2 minutes. The spectrograms contained the two FeI lines:

- Fe I at 630.1508 nm and $W_{\lambda} = 127 \text{ mÅ}$, EP = 816 eV and $g_{eff} = 1.6$, estimated line core formation height 378 km (Gadun et al 2000).
- Fe I at 630.2499 nm and $W_{\lambda} = 83 mA$, EP = 816 eV and $g_{eff} = 2.5$, estimated line core formation height 270 km (Gadun et al, 2000).

From these data the following spectral parameters were calculated after applying the usual image reduction procedures:

- continuum intensity
- central line residual intensity
- line center velocity
- full width at half maximum fwhm

In the next paragraph this time series of 8 images each separated by 130 s is analyzed in order to investigate the evolution of the solar photospheric fine structures.

3. RESULTS

We present the results for the evolution of the correlation of spectral parameters between a) two subsequent images in the time series (full line) and b) between the first image of the time series and the following ones.

The data calculated for the highest originating line I (h=378 km) are given by Fig. 1. In Fig. 2 the same kind of data is given for the deeper forming line II

Proc. 1st Solar & Space Weather Euroconference. 'The Solar Cycle and Terrestrial Climate', Santa Cruz de Tenerife, Tenerife, Spain, 25-29 September 2000 (ESA SP-463, December 2000)

(h =270 km). It is clearly seen that the most pronounced difference is in the behaviour of the fwhm. For the deeper forming line the correlation between subsequent images remains constant at a moderate value of 0.50; however the correlation drops down very quickly between the first image and the other images in the time series. For the highest line the correlation for the fwhm values is lower (correlation coefficient ~ 0.40) and the decay between the first image and the other images is lower for the correlations. The correlations between residual intensities are higher for the lower forming line.

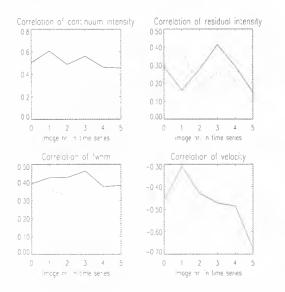


Figure 1. Correlation coefficients for line I, h=378 km; full line: between subsequent images of the time series, dotted line: between the first image of the time series and the subsequent images

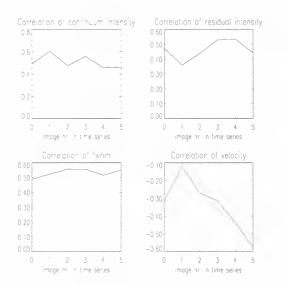


Figure 2. Correlation coefficients for line II, h=270 km; full line: between subsequent images of the time series, dotted line: between the first image of the time series and the subsequent images

In Fig. 3 examples of the evolution of the line parameters are given. The time interval between the images is 130 s. We give two images for each line

parameter separately for line I and line II. The continuum variations for both lines are add at the top of the figure for comparison.

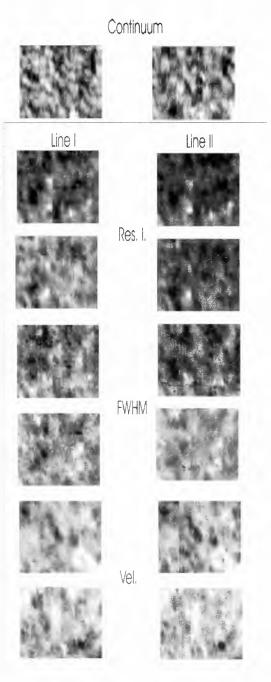


Figure 3. Examples of the variation of different line parameters: the time step between the two images is 130 s

In order to follow the variation of the full width at half maximum values we calculated for each image the corresponding mean value of that parameter. Then we denoted all values of this image that were above the mean value by a positive number and the other values by 0. The results are shown in Fig. 4

In Fig. 5 we show a kind of correlation between the continuum intensity and the fwhm. For each image the mean continuum intensity and the mean fwhm was calculated. In the Fig. 5 bright denotes

areas where the continuum intensity is $\langle \bar{I} \rangle$ and the full width at half maximum is $\langle fw\bar{h}m$. Thus we can see if turbulent motions are associated with integranular areas and follow their evolution.

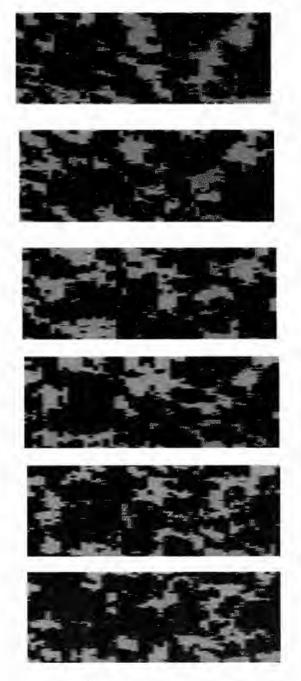


Figure 5. Correlation between continuum intensity and fwhm. Bright points denote areas where the continuum intensity is below the mean value of each image and the fwhm is above the mean value : the time step between the images is 130 s

4. CONCLUSIONS

The evolution of granular/intergranular structures can be clearly seen when comparing the images of continuum intensity. This is illustrated by the top images in Fig. 3. The variation of the other line pa-

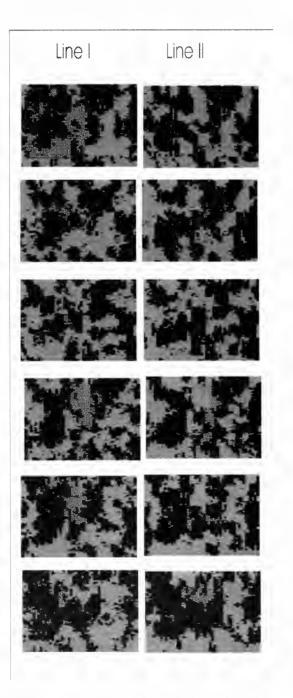


Figure 4. Variation of the fwhm; the values above the mean value are marked grey, the other values dark: the time step between the images is 130 s

rameters is demonstrated by comparing two different images that are separated by the scanning intervall (130 s). By comparing the two lines (line I in the left column and line II in the right column) we can state that for velocity, full width at half maximum and residual intensity variations the images are very similar thus there does not exist a vertical gradient in the evolution of these parameters. However, for the full width at half maximum variations there seems to exist more features for the higher forming line II. This line paramater also behaves differently when regarding the correlationcoefficients. It decays more slowly between the first image and the other images in the case of the higher forming line I (compare Fig. 1 with Fig 2.).

An explanation for such a behaviour could be that in the higher photospheric layers regions of enhanced turbulence are more persistent than in the layer 100 km deeper (h=270 km for line II).

In the analysis here we give only two examples for the illustration. A similar behaviour was found for the other data.

Also the residual intensity correlation behaves similar. The correlation is higher for the deeper forming line as has to be expected. However, the correlation bewteen the first images and the subsequent images nearly remains constant. This indicates persistent temperature fields at these layers. Such a behaviour was not found for the velocity. The correlation rapidly decays between the first image and the subsequent ones.

This can be explained by the breakdwon of the correlation between temperature and velocity fields in the higher photosphere. The structure of the high photosphere was studied in Hanslmeier et al, 2000.

ACKNOWLEDGMENTS

A. H. thanks the 'Austrian Fonds zur Förderung der wissenschaftlichen Forschung' for supporting these investigations. A. K and J. R. acknowledge the grant VEGA 2/7229/20 and the Austrian and Slovak Academy of Sciences.

REFERENCES

- Gadun, A.S., Hanslmeier, A., Kučera, A., Rybák, J., Wöhl, H., 2000, A&A, in press
- Hanslmeier, A., Kučera, A., Rybák, J., Wöhl, H., Neunteufel, B., 2000, A&A, 356,308
- Rast, M, 2000, in The dynamic Sun, eds. A. Hanslmeier and M. Messerotti, Kluwer
- Schröter, E.H., Soltau, D., Wiehr, E., 1985, Vistas in Astronomy, 28, 519

VARIABILITY OF THE CR/XBG-L RELATIONSHIP DURING THE SOLAR CYCLE EVOLUTION

Maria Jakimiec¹, Anna Antalová², and Marisa Storini³

¹Astronomical Institute, University of Wroclaw, Kopernika 11, 51–622 Wroclaw. Poland ²Institute of Experimental Physics, Slovak Academy of Sciences, Watsonova 47, 043-53 Košice. The Slovak Republic

³IFSI/CNR, Area di Ricerca Roma-Tor Vergata, Via del Fosso del Cavaliere, 100 - 00133 Roma, Italy ³Raggi Cosmici - Dip. di Fisica - Università Roma Tre, Via della Vasca Navale. 84 - 00146 Roma, Italy

ABSTRACT

The cross-correlation analysis of the daily data has been undertaken to obtain quantitative information on the relationship between the Calgary intensity of the nucleonic component of galactic cosmic rays (CR) and the logarithmic transformed solar soft X-ray background (XBG-L). The investigated period, from July 1968 to June 1996, was divided into 28 sequences (each of the twelve-month duration). The CR/XBG-L cross-correlation functions (ccf-s) were computed from the basic undetrended (d_i) . detrended (t_i) , the running mean $c_i(n)$, and the residual $r_i(n)$ data sequences, where n = 3, 7, 15, 27 day and i = 1, ..., 28. The used time lag ranges between - 2 and + 60 days. An average lag of about 5 days is needed to obtain the best CR-XBG-L correlation coefficients. The performed cross-correlation analyses between the galactic CR intensities and the solar XBG-L on daily basis suggest that ccf-s are closely related with the dynamical component of the solar activity working throughout the 11-year (sunspot) cycle.

1. DATA SETS AND TREATMENT

The aim of this long-term investigation (e.g. Storini, Antalová, and Jakimiec, 1995; Jakimiec, Antalová and Storini, 1999, 2000 and references therein) is to clarify the relation existing between the short- and mediumterm CR variability and the one of the solar soft X-ray background (XBG). In this briefly report we continue the study using the following parameters:

i) The daily Calgary neutron monitor records. Geographic coordinates for Calgary neutron monitor are: N 51°.1 W 114°.1. 1128 m a. s. l. and about 1 GV is the cutoff-rigidity (see Venkatesan et al., 1989). Data are normalized to the May 1965 average (i.e. 285554 counts/h = 100% level). The gaps in CR data were filled considering data from other appropriate neutron monitors. Hence, some small differences can be found when results of the present paper are compared with those reported in Jakimiec, Antalová and Storini (1999). ii) The daily logarithmic transformed XBG flux (XBG-L). According to Donnelly, Grubb and Cowley (1977) as well as Donnelly and Puga (1990), the daily XBG values can be used to describe the solar corona as a whole entity and to follow its evolution during the entire solar activity cycle (the so-called 11-year cycle). The XBG data from March 1968 to February 1973 are taken from Solar Geophysical Data (SGD, 602 / part II). The XBG data for the period February 1973 - April 1983 were derived by us using a scanning procedure of the 5-minute full-sun soft X-ray (0.1-0.8 nm) profiles as reported in detail by Jakimiec. Antalová and Storini (2000). The XBG data from April 1983 - December 1993 those from SGD (594 / part II). The XBG data from January 1994 - June 1996 were regularly published in SGD series. All the XBG fluxes were transformed into the logarithmic scale (XBG-L). We remember that XBG values are evaluated in units of $10^{-8} W \, m^{-2}$ (i.e., our unit for XBG corresponds to the GOES A1 class level).

Data treatment For every original data sequence d_1 (i = 1, ..., 28), we estimated the linear trend and computed the detrended sequences. To investigate the response of the CR modulation to the medium- (27 and 15 days) and short-time (7 and 3 days) solar XBG fluctuations the running mean and the residual sequences were also evaluated (see Figure 1 for a summary of the sequence build-up). Hence, in our analysis we used the detrended $-t_i$, running mean $-c_i(n)$ and the residual $r_i(n)$ sequences. The complete data set for July 1968-June 1996, was divided into the 28 subsets of the 12month each. The $c_i(n)$ of both parameters (XBG and CR) allowed us to remove the spurious fluctuations and to take into account parameter variabilities related to a scale longer than the appropriate the running-mean points (ndays). On the other hand, fluctuations shorter than ndays can be analysed using the $r_i(n)$. The complete set of ccf-plots for the July 1968 - June 1986 period (i.e., for solar activity cycles 20 and 21) are reported by Storini, Jakimiec and Antalová (2000), while relevant numerical results of the cc-analyses are shown in Table 1. We notice that the best CR/XBG-L anticorrelation values were found for the $c_i(15)$. For completeness the ccf-s of the detrended sequences are illustrated in Figure 2.

Proc. 1st Solar & Space Weather Euroconference, 'The Solar Cycle and Terrestrial Climate', Santa Cruz de Tenerife, Tenerife, Spain, 25-29 September 2000 (ESA SP-463, December 2000)

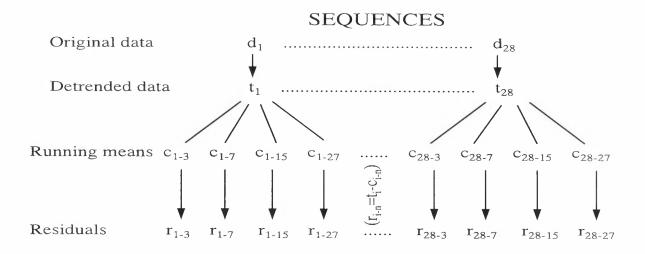


Figure 1. Summary of the sequence build up.

Table 1. The 1-st minimum values of the CR/XBG-L ccf-s calculated from the daily detrended (t_i) , the 15-day running mean $-c_i(15)$ and the 15-day residual $-c_i(15)$ sequences are followed by the corresponding lag (in days). The statistically significant values are less than -0.20. The 1-st minimum of ccf-s has the lags from 1 to 10 days and the 2-nd minimum from 11 to 50 days. N - stay for the noisy-like ccf; M - the strong 1-st minimum of $c_i(15)$, m - the faint 1-st minimum; B - the very broad ccf, b - faint blend of the first and the second minimum. The daily mean values of CR and XBG are given in the 5-th and 6-th rows.

i years	l 68/69	2 69/70	3 70/71	4 71/72	5 72/73	6 73/74	7 74/75	8 75/76	9 76/77	10 77/78
t_i $c_i(15)$ $r_i(15)$ type CR XBG	-0.28/3 N 86.2 105	+ +0.26/6 N 86.6 111	-0.48/4 -0.73/4 -0.21/4 M 89.3 87	-0.32/3 -0.53/2 - Mb 96.1 49	-0.43/8 -0.67/9 - Mb 96.0 37	- - mb 98.4 44	-0.25/3 -0.37/4 - m 96.0 34	-0.35/10 -0.55/8 - M 96.7 26	- - 97.1 19	-0.24/3 95.7 96
i years	11 78/79	12 79/80	13 80/81	14 81/82	15 82/83	16 83/84	17 84/85	18 85/86	19 86/87	20 87/88
t_i $c_i(15)$ $r_i(15)$ type CR XBG	- + -0.21/4 N 91.5 182	-0.38/5 -0.43/5 - m 88.7 233	-0.47/8 -0.66/9 -0.21/5 MB 86.2 268	-0.36/3 -0.43/3 - Mb 87.3 325	-0.50/3 -0.63/3 -0.21/3 MB 82.6 220	-0.23/8 -0.23/9 -0.21/7 mB 88.5 77	- -0.33/5 m 92.2 14	-0.50/6 -0.57/7 -0.26/5 MB 97.1 15	-0.48/10 -0.61/10 MB 98.2 7	- N 93.1 27
i years	21 88/89	22 89/90	23 90/91	24 91/92	25 92/93	26 93/94	27 94/95	28 95/96		
t_i $c_i(15)$ $r_i(15)$ type CR XBG	-0.29/3 -0.24/2 -0.21/4 m 85.5 122	-0.45/8 -0.65/7 	- N 81.1 127	- + -0.30/4 m 84.3 107	-0.28/3 N 93.2 41	+ - N 94.4 14	+ + N 96.5 7	- N 98.1 2		

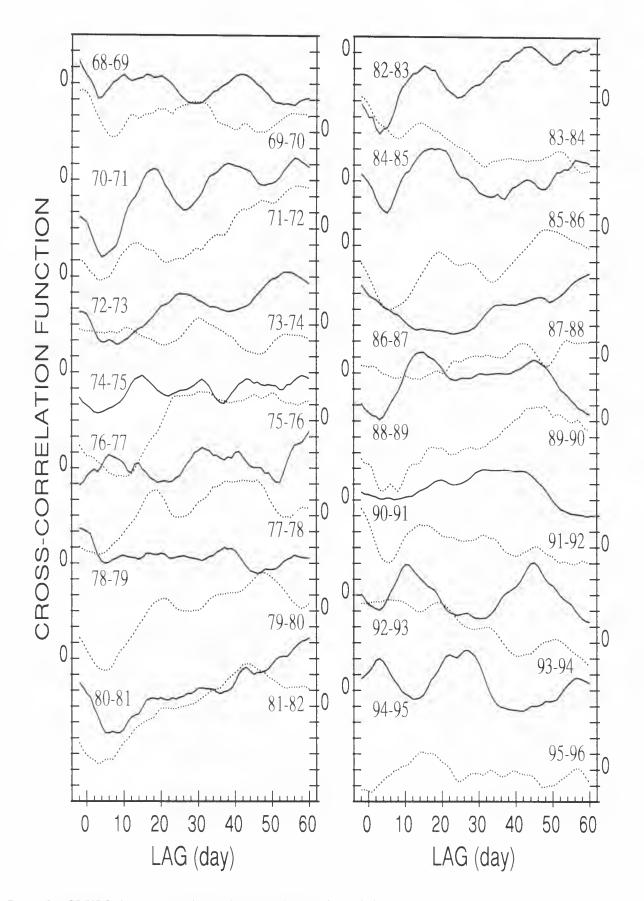


Figure 2. CR/XBG-L cross-correlation functions for the detrended t_i daily sequences, where the short-, as well as medium-term fluctuations are present. Left panel shows results for sequences from July 1, (1967 + i) to June 30, (1968 + i), being i = 1, 2, ..., 14. and right panel illustrates those for i = 15, 16, ..., 28.

2. RESULTS OF THE CR/XBG-L CROSS-CORRELATION ANALYSIS

The advantage of the cc-analysed here performed using running-means is the possibility of obtaining the time delay in days of the CR response to the solar variability, what is not possible to derive using monthly averages of the involved parameters. From the reported results we can state that the changes in the shape of CR/XBG-L cc-functions reflect the solar cycle evolution and that the best CR/XBG-L anticorrelation appears for $c_i(15)$. Moreover:

• Statistically significant CR/XBG-L anticorrelation for a CR time delay (lag) smaller than 10 days exits in 15 t_i subsets from the whole 28 subset here investigated. We notice that during sunspot cycle 22 (after the 89/90 subset) there is no stable lag between both parameters. The mean value of the CR lag is around 5 days, which is in good agreement with the lag found in the past by Storini, Antalová and Jakimiec (1995). It is worth mentioning that similar lags were in the past obtained not only analyzing galactic cosmic ray intensities (Iucci et al. 1979), but also flare occurrence (Dodson and Hedeman, 1972 and Křivský, 1972) and solar proton fluxes (Sarris et al. 1984). Moreover, this result is also emerging from multi-spacecraft measurements of CMEs (Reames, 1994) through the interplanetary protons (accelerated by CME shocks).

• The most significant ccf-shape changes are related to the best lag occurrence. The ccf-s with a lag in the range of 1–10 days (the 1–st minimum of ccf-s) are very frequent in *the onset of the decay phase* of the solar cycles. There are also ccf-s with dual minimum (where the 1–st minimum is comparable to the 2–nd minimum, with a lag around the synodic recurrence: 27–days and 1.5 synodic rotation: around 40–days). Such broad ccf-s are typical for the late interval of the decreasing phases of the solar activity cycles.

• The changes in degree of the anticorrelation are remarkable. The best CR-XBG anticorrelation is found in the subsets preceding and following the maximum activity phases (i.e., the 70/71, 71/72, 72/73, 80/81, 86/87, 89/90 subsets). As expected, there is a good correspondence between the recovery of the CR modulation and the low level of XBG (Table 1) for all the analyzed cycles.

• The subsets around the solar cycle maximum are characterized by a high activity level in a large heliolatitudinal range (3D – heliosphere, see Storini and Hofer, 1999). Small values of the ccf-s (i.e. statistically unsignificant values) are obtained using the 68/69, 69/70 and the premaximum 78/79 subset, as well as the 90/91 and 91/92 subsets. On the other hand, in the other subsets located around solar cycle maxima (the 79/80, 80/81 as well as in 88/89 and 89/90), the short-term anticorrelation is well depicted, what is very different behaviour comparing 'o earlier discussed maximum cycle subsets. Clearly, much more work is needed to get a better understanding of the CR modulation during the maximum phases of sunspot cycles.

• The decay phases of the 20-th, the 21-st and the 22nd cycles are characterized by solar activity phenomena occurring towards the solar heliomagnetic equator and we found that the the decay phases for two consecutive cycles (n. 20 and 21) are not similar: namely the 2-nd minima (with lags greater than 10 days) occurring in the 81/82 – 86/87 subsets are stronger than in the 1973 –1976 years. During the descending phase of the 21-st cycle, the residual data subsets give statistically significant cc-values. It implies that during the period July 1981–June 1986 the CR/XBG-L relation is partly determined by the short-term fluctuations, what is not true for the period July 1973–June 1978.

ACKNOWLEDGEMENTS

This research was performed within the CNR/PAN Agreement for the years 1997-1999 and is partly supported by the KBN Grant of the Wroclaw University (1007/S/IA/2000) and the Slovak VEGA Grant 2/5137/20. The IFSI/CNR and PNRA/MURST grants are also acknowledged for enduring studies related to Solar-Terrestrial Relations. A. Antalová thanks the warm hospitality of the Instituto de Astrofisíca de Canarias during the 1-st SOLSPA Euroconference and expresses her gratitude to European Union for financial support.

REFERENCES

- Donnelly, R. F., Grubb, R.N. and Cowley, F.C., 1977, NOAA Techn. Memorandum ERL SEL-48, Boulder
- Dodson, H. W. and Hedeman, E. R., 1972, Solar Activity and Predictions, eds. P.S. McIntosh and M. Dryer. The MIT Press, Boston, 19
- Donnelly, R. F. and Puga, L.C., 1990, Solar Phys. 130, 369
- Iucci, N., Parisi, M., Storini, M. and Villoresi, G., 1979, Il Nuovo Cimento 2C, 1
- Jakimiec, M., Antalová, A. and Storini. M., 1999. Solar Phys. 189, 373
- Jakimiec, M., Antalová, A. and Storini M., 2000, Contr. Astron. Obs. Skalnaté Pleso 30, 75
- Křivský, L., 1972, Solar Activity and Predictions, eds. P.S. McIntosh and M. Dryer, The MIT Press, Boston, 389
- Reames, D. V., 1994, ESA SP-373, ESTEC, Noordwijk, The Netherlands, 107
- Sarris, E.T., Anagnostopoulos, G.C. and Trochoutsos, P.C., 1984, Solar Physics 93, 195
- Solar Geophysical Data (ed. H. E. Coffey), 1968–1996, Parts I and II
- Storini, M., Antalová, A. and Jakimiec, M., 1995, J. Geomagn. Geoelectr. 47, 1085
- Storini, M. and Hofer, M.Y., 1999, ESA SP-448, Volume 2, ESTEC, Noordwijk, The Netherlands, 889
- Storini, M., Jakimiec, M. and Antalová, A., 2000. Report CNR/IFSI, Roma, in press
- Venkatesan, D., Mathews, T., Graumann, H. and Sharman, P., 1989, in Calgary Cosmic Ray Intensity Records (Super neutron Monitor), 3

P-MODE FREQUENCY SHIFT AS SOLAR ACTIVITY INDEX

Sebastián J. Jiménez-Reyes^{1,2}, Thierry Corbard¹, Pere L. Pallé², and Steve Tomczyk¹

¹High Altitude Observatory, NCAR, PO Box 3000, Boulder, CO 80307 USA

²Instituto de Astrofísica de Canarias, E-38701, La Laguna, Tenerife, Spain

ABSTRACT

We present an analysis of the frequency shift and the even terms of the frequency splitting coefficients carried out using six years of LOWL data, starting in 1994. The temporal variations, and their dependences with the frequency and degree are addressed. In agreement with previous analysis, we show that these parameters are very sensitive to the solar cycle. This opens new perspectives for the studies of the solar structure and magnetic fields variations.

1. INTRODUCTION

The solar magnetic field pattern progress with time following a quasi-cycle with a period close to 22 years, known as the solar cycle. This phenomenon has fascinated humans for centuries since it also affects different terrestrial phenomena like the climate or radio communications. Although, the solar cycle has been studied for many years from the theoretical and observational point of view, it is not well understood yet. For instance, there are still open questions about the strength and the location of the magnetic field associated with to the solar dynamo. The development of helioseismology has been a revolution in Solar Physics. We have been able to address important questions like the internal rotation and structure of the Sun. During the last cycle, the frequency shifts of solar *p*-modes, have also been shown to be very well correlated with the solar activity indices and therefore helioseismology can also help our understanding of the processes at the origin of solar magnetic cycle.

The first report about the frequency shift was given by Woodard and Noyes (1985) using ACRIM observations. They found that few modes with degrees ℓ =0 and 1 presented a change in the central frequency of 0.42 ± 0.14 μ Hz. For intermediate and high degree *p*-modes, Duvall et al. (1988) and afterward Libbrecht and Woodard (1990) have also found a shift, always very well correlated with the solar cycle changes.

We will first give the most important points in the analysis of the LOWL data. A short description of the fitting method used to measure the mode parameters is given in the next section. Then, we will show our results about the central frequency and even splitting-coefficients changes.

2. DATA ANALYSIS AND RESULTS

The raw data consist in full disk solar Doppler images, which have been collected by LOWL instrument. This experiment is based on a Magneto-Optical Filter and has demonstrated its high sensitivity to the solar oscillations. The data were analyzed using the LOWL pipeline which has recently been improved (Jiménez-Reyes 2000). The images are first calibrated and then a spherical harmonic decomposition is performed in order to create time series for degrees from ℓ =5 to 99. Finally, a Fast Fourier Transform is applied to the time series.

The spherical harmonics are not orthogonal over the observed area, limited to one hemisphere. Therefore, the modes cannot be totally isolated and some correlations between different (ℓ, m) spectra exist. Historically, the statistic of the power spectra has been assumed to be as χ^2 with 2 degrees of freedom. However, this assumption is not correct when the spectra are not independent. Recently, important improvements have been achieved in the fitting techniques to be applied to observations made using instruments with spatial resolution (Schou 1992, Appourchaux et al. 1998). The real and the imaginary part of the Fourier Transform follow a multi-normal distribution which is described by a covariance matrix. The likelihood function under these assumptions can be written as:

$$S(\vec{a}) = \sum_{i=1}^{N} \log |E(\vec{a}, \nu_i)| + y^T(\nu_i)E(\vec{a}, \nu_i)y(\nu_i)$$
(1)

where $y(\nu_i)$ corresponds to the Fourier Transform and $E(\vec{a}, \nu_i)$ is the covariance matrix calculated by:

$$E_{nm}(\vec{a},\nu_i) = \sum_{m'=-\ell}^{\ell} C_{nm'} C_{mm'} v_{m'}(\vec{a},\nu_i) + B_{nm}$$
(2)

where C is the leakage matrix which represents the correlation between modes with different m (m-leakage),

Proc. 1st Solar & Space Weather Euroconference, 'The Solar Cycle and Terrestrial Climate', Santa Cruz de Tenerife, Tenerife, Spain, 25-29 September 2000 (ESA SP-463, December 2000)

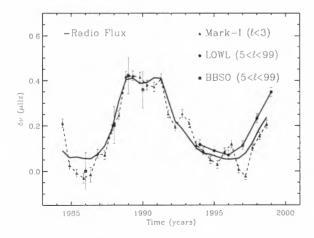
whereas B is the noise covariance matrix which gives information about the noise correlation between spectra. $v(\vec{a}, \nu)$ is the variance and it is given by a simple Lorentzian profile defined by the parameters \vec{a} that we are trying to infer using a maximum likelihood method. The shift between m-components is given by:

$$\nu_{n\ell m} = \nu_{n\ell} + \sum_{i=1}^{n_{coef}} a_i(n,\ell) P_i^{\ell}(m)$$
(3)

where $P_i^{\ell}(m)$ are orthogonal polynomials normalized such that $P_i^{\ell}(\ell) = \ell$ (Schou et al. 1994, App. A). The odd *a*-coefficients are induced by the internal rotation into the solar interior while the even terms are mainly related to effects of second order due to the rotation, the presence of magnetic fields or any departure from spherical symmetry.

The distance between modes with the same order n and with $\Delta \ell = \pm 1$ get closer and closer at high degrees leading to a leakage of the modes (ℓ -leakage). This problem arises at lower degree in the case of observations from just one station, due to the existence of the sidelobes as a result of the modulation of one day in the signal. That is particular important for those modes where $\nu/L \approx 31 \mu$ Hz. In order to reduce the systematic errors an extra covariance matrix is added to take into account the presence of spurious modes which can be close to the target mode. Nevertheless, we have seen that the systematic errors are specially important in the odd acoefficients and not in the even ones.

At high degree, the numerical evaluation of the likelihood function get slow, mainly because of the large dimensions of the covariance matrix. Therefore, we use just the main diagonal of the covariance matrix. We have checked that this is indeed a very good approximation for high degrees.



3. FREQUENCY SHIFT

Figure 1. Time variation of the integrated frequency shift.

Figure 1 shows the temporal variation of the integrated frequency shift for frequencies between 2 and 3.5 mHz. For comparison, the figure includes the same calculations using the BBSO data (squares). Mark-I instrument has

been measuring the solar oscillation for more than 20 years. This instrument observes the Sun like a star, so the information is limited to low degrees ($\ell \leq 3$). Recently, the database has been re-analyzed (Jiménez-Reyes 2000) over a much wider time interval than before. We have calculated the yearly frequency shift every six months for the last 15 years. All the results are very well correlated with the changes in the solar activity cycle denoted on Figure 1 by the best linear fit between the radio flux and the results from Mark-I. The amplitude of these changes are, for low degrees, close to 0.4μ Hz, peak-to-peak, and the correlation with the radio flux variations is close to 1.

The temporal variations of the central frequency are expected to change with both frequency and degree. Earlier works (Libbrecht & Woodard, 1990) have shown a strong variation with the frequency, the frequency shift being null at ~ 2 mHz and increasing at higher frequency. The ℓ -dependence has been found to be more weak.

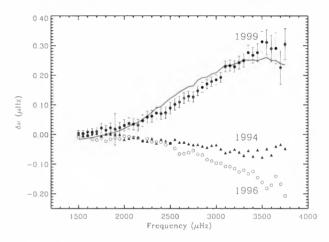


Figure 2. Frequency dependence of the frequency shift for three years. The error bars have been shown just for one year for clarity. The solid line represents the best linear fit of the inverse mode mass to the 1999 observations.

Figure 2 shows the variation of the frequency shift averaged over ℓ for three selected years. The reference is the mean over the six years of data. The last minimum of the solar cycle happened in 1996, whereas 1999 represents the year with higher level of solar activity in our database. As we can see, the frequency dependence is very clear, mainly between 1996 and 1999. The inverse mode mass has been calculated using the model of Morel et al. (1997). It has been averaged in the same way as the results shown in Figure 2. The solid line over the points corresponding to 1999 represents the best linear fit to the inverse mode mass. The observed frequency shift exhibits almost the same frequency dependence than the inverse mode mass. However, there are still some differences which can be seen also in the analysis of the GONG data (Howe et al. 1999). This may or not be significant but it is interesting to notice that both results present the same fluctuations around the inverse mode mass curve.

The ℓ -dependence has been also calculated and plotted in Figure 3. Again, we have selected the same years than in the last figure and the reference is the mean over the six years. The dependence with the degree is maximum for 1999 with a difference of about 0.1μ Hz between $\ell = 0$

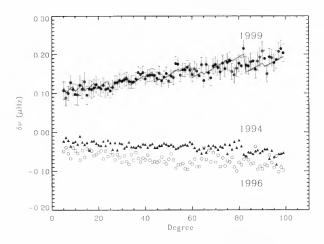


Figure 3. *l-dependence of the frequency shifts for three different years. The solid line through the results corresponding to 1999, denotes the best linear fit to the inverse mode mass.*

and $\ell = 99$. The inverse mode mass, averaged in the same way than the observations, is shown in the figure, scaled to the best linear fit using the results corresponding to 1999. The solid line follows remarkably well the frequency shift.

The variations of the frequency shift have been studied, assuming a linear relationship with the solar activity indices.

The solar indices used here are:

(i) the sunspot number, R_I ;

(ii) the integrated radio flux at 10.7 cm, F_{10} (both obtained from the Solar Geophysical Data);

(iii) the Kitt Peak magnetic index (KPMI) extracted from the Kitt Peak full disk magnetograms (Harvey 1984);

(iv) the Mount Wilson index also called Magnetic Plage Strength Index, MPSI (Ulrich et al. 1991);

 (\mathbf{v}) the equivalent width of HeI 10830Å averaged over the whole solar disk using data from Kitt Peak observatory and

(vi) the Total Solar Irradiance, TSI (Fröhlich, C. & Lean, J., 1998).

The results shown in Tab. 1 are very similar to those obtained recently by Howe et al. (1999) and Bhatnagar et al. (1999) from GONG observations.

Table 1. Results of the weighted linear least-squares fits for the frequency shifts as a function of different solar indices.

arees.		
Index	Intercept (µHz)	Slope
R _I	-0.0314±0.0070	0.0031 ± 0.0001^{a}
F_{10}	-0.2245 ± 0.0131	0.0032 ± 0.0001^{b}
KPMI	-0.2203 ± 0.0191	0.0317 ± 0.0018^{c}
MPSI	-0.0168 ± 0.0063	0.1604 ± 0.0068^d
He	-0.5286 ± 0.0416	0.0114 ± 0.0008^{e}
TSI	-363.4905 ± 52.6823	0.2662 ± 0.0386^{f}

a: μ Hz: b: μ Hz/(10⁻²² J/s/m²/H): c.d: μ Hz G⁻¹: c: μ Hz mÅ⁻¹: f: μ Hz W⁻¹m²

4. THE EVEN A-COEFFICIENTS

The even terms are expected to change with the frequency. Therefore, they were ℓ -averaged over short regions in frequency, as we did with the frequency shift. The results for two selected years, (1996 in the bottom and 1999 in the top) are shown in Figure 5. The even *a*-coefficients are close to zero in 1996, when the solar cycle reached the last minimum. However, a big change can be seen in 1999, following again the same frequency dependence than the inverse mode mass. Again, there is a clear fluctuation of a_2 around the inverse mode mass curve. Nevertheless this may not be significant as it stays within the error bars.

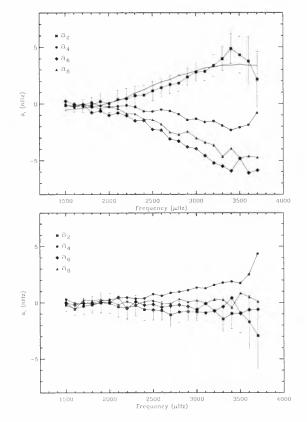


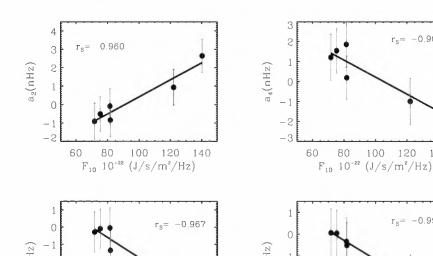
Figure 5. Frequency dependence of the even acoefficients for two different years, 1996 (bottom) and 1999 (top).

The time-variation of the solar cycle does not affect only the central frequency. The changes in the even *a*coefficients demonstrate that, whatever is the perturbation leading to these variations, it depends on the latitude.

We have integrated the even terms for each one of the time series. The resulting values are shown in Figure 4 against the radio flux calculated over the same period. The straight line represents the best linear fit of both quantities.

5. CONCLUSION

We have analyzed six years of LOWL data from 1994 to the end of 1999 in order to parameterize the variation of



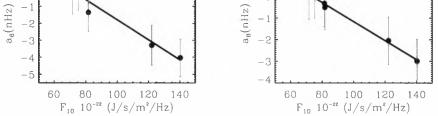


Figure 4. Variation of the integrated even a-coefficients against the radio flux at 10.7.cm. The solid line shows the best linear fit.

the frequency shift and the even a-coefficients.

In summary, the acoustic central frequency presents a variation which is very well correlated with the solar cycle. The integrated amplitude of this variation, peak-topeak, is close to 0.4μ Hz. This variation is however a function of both the frequency and the degree, and these dependences can be well fitted by the inverse of the mode mass.

In addition, the even a-coefficients present a significant change with the solar cycle, very well correlated with the solar indices. Moreover, as for the frequency shift, these changes increase with the frequency. The results agree very well with earlier studies (Libbrecht and Woodard, 1990) carried out at the beginning of the last solar cycle.

LOWL instrument has been recently updated and a new instrument has been developed and installed at the Observatorio del Teide (Tenerife), leading to a new network called Experiment for Coordinated Helioseismic Observations (ECHO). ECHO is intended to continue observing for a complete solar cycle allowing us to better track the origin of the solar activity cycle.

6. ACKNOWLEDGMENTS

We are extremely thankful to Mausumi Dikpati for useful discussions and additional comments. S.J. Jiménez-Reyes and T. Corbard are very thankful to the organizers of the meeting for providing financial support. T. Corbard acknowledge support from NASA grant S-92678-F.

REFERENCES

 $r_s = -0.906$

140

 $r_s = -0.997$

- Appourchaux, A., Gizon, L. and Rabello-Soares, M.C., 1998, A&A,132,107.
- Bhatnagar, A., Kiran Jain and Thipathy, S.C., 1999, ApJ, 521,885.
- Duvall, T. L., Jr., Harvey, J. W., Libbrecht, K. G., Popp, B. D. and Pomerantz, M., 1988, ApJ, 324, 1158.
- Fröhlich, C. and Lean, J., 1998 in "The Suns Total Irradiance: Cycles, Trends and Related Climate Change Uncertainties since 1978, Geophys.Res.Let., 25, 4377-4380.
- Harvey, J. W. 1984, in Workshop on Solar Irradiance Variations on Active Region Timescales, ed. B. La Bonte, G. Chapman, H. Hudson, & R.C. Wilson (NASA CP-2310; Washington: NASA), 197.
- Howe, R., Komm, R. and Hill, F. ApJ, 524, 1084.
- Jiménez-Reyes S.J., 2000, Ph.D. dissertation, La Laguna University (in progress).
- Jiménez-Reyes S.J., Régulo, C., Pallé P.L. and Roca Corté T., 1998, A&A, 329,1119.
- Libbrecht, K. G. and Woodard, M. F. 1990, Nat, 345, 779.
- Morel, P., Provost, J. and Berthomieu, G., 1997, A&A,327,349.
- Régulo, C., Jiménez, A., Pallé, P. L., Hernández, F. P. and Roca Cortés, T., 1994, ApJ, 434,384.
- Schou, J., Cristensen-Dalsgaard, J. and Thompson, M. J., 1994, ApJ, 433, 389.
- Schou, J., 1992: Ph. D. thesis, On the analysis of heliosismic data, Aarhus Iniversity, Aarhus.
- Ulrich, R. K., 1991, Adv. Space Res., 11(4), 217.
- Woodard, M. F. and Noyes, R. W., 1985, Nat, 318, 449.

VARIATION OF 3 GHz DAILY RADIO FLUX DURING THE YEARS 1995-2000

K. Jiřička, M. Karlický and H. Mészárosová

Astronomical Institute, CZ-25165 Ondřejov, Czech Republic e-mail: radio@asu.cas.cz

ABSTRACT

The 3 GHz daily solar radio flux observed by the Ondřejov radiometer in 1995-2000 is presented and compared with the 2.8 GHz DRAO observations. As expected a high correlation between them was found. Then using the cross-correlation methods the 3 GHz radio flux variations were compared with the sunspot number and soft X-ray background flux (GOES 8) indices. During the 1996 minimum and during the rising phase of the solar cycle 23 two trends in the evolution of the cross-correlation coefficients were recognized: a) the cross-correlation coefficients between the 3 GHz radio flux and sunspot number are increasing and the time shift maxima are in the interval from 0 to -1 day, showing that the the radio flux is delayed after the sunspot evolution, and on the other hand, b) the cross-correlation coefficients between the 3 GHz radio flux and X-ray flux is decreasing. Furthermore, the time maxima shift is changed from positive to negative value (-1 day in 2000). The results obtained are shortly discussed.

Key words: solar cycle; radio flux; sunspot numbers; soft X-ray background flux.

1. INTRODUCTION

Long-lasting (days, months, years) solar activity is concentrated in active regions. It is closely connected with their evolution, especially with their magnetic field (Bumba and Howard, 1965, Gaizauskas et al., 1983, De Toma et al., 2000). The activity is reflected differently in various layers of the solar atmosphere. Depending on the method of observations various indices of the solar activity were defined. Thus, at the photosphere, chromosphere, and corona the daily values of the sunspot number, CaII flocculae, and slowly varying component of the soft X-ray and radio fluxes on various frequencies are used (Karlický, 1997, NOAA Boulder Space Weather Center).

In this paper the authors' objective is to study statistically, using cross-correlation methods, the time series of the radio fluxes observed by the 3 GHz Ondřejov radiometer and by the 2.8 GHz DRAO radiometer, and the time series of the sunspot number and the soft X-ray background flux observed by the GOES 8 spacecraft in the period from June 1, 1995 till June 30, 2000. This period covers the minimum of the solar activity (1996) and the rising phase of solar cycle 23.

2. ONDŘEJOV 3 GHz RADIOMETER

For the solar radio observations at 3 GHz we use in Ondřejov a Dicke-type radiometer (Jiřička, 1992) with ultra low noise pre-amplifier at the front end. The antenna is formed by a broad-band thick horizontal dipole mounted in the focus of a 3 m parabolic dish. The data are in digital form (12 bits) with 10 ms time resolution. The instrument is fully automated, running every day from sunrise to sunset. Originally only radio events were archived, but since 1995 also whole day data with 1 s time resolution are recorded and archived. The daily mean solar radio flux data used in this article are determined from quiet parts of these 1 s resolution daily records, it is after removal of intervals with solar radio flares.

3. DATA

For comparison and correlation analysis we use the following four types of solar indices, representing the solar activity:

- Ondřejov 3.0 GHz radio flux daily means (www.sunkl.asu.cas.cz/~radio)
- DRAO 2.8 GHz radio flux daily means (www.drao.nrc.ca/icarus/www/daily.html)
- SIDC daily sunspot numbers (*sidc.oma.be/DATA/DAILYSSN/dailyssn.html*)
- GOES soft X-ray background flux daily means (www.sel.noaa.gov/Data/solar.html)

Proc. 1st Solar & Space Weather Euroconference, 'The Solar Cycle and Terrestrial Climate', Santa Cruz de Tenerife, Tenerife, Spain, 25-29 September 2000 (ESA SP-463, December 2000)

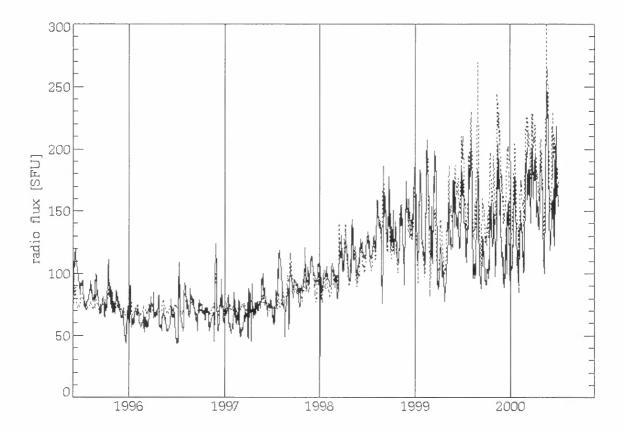


Figure 1. Comparison of the 3 GHz (solid line) and 2.8 GHz (dashed line) daily radio fluxes observed by the Ondřejov and DRAO radiometers in the 1995-2000 period.

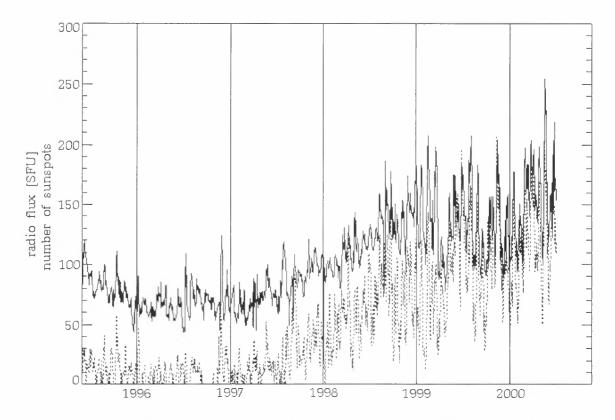


Figure 2. Comparison of the 3 GHz radio flux (solid line) and the time profile of the daily sunspot number (dashed line).

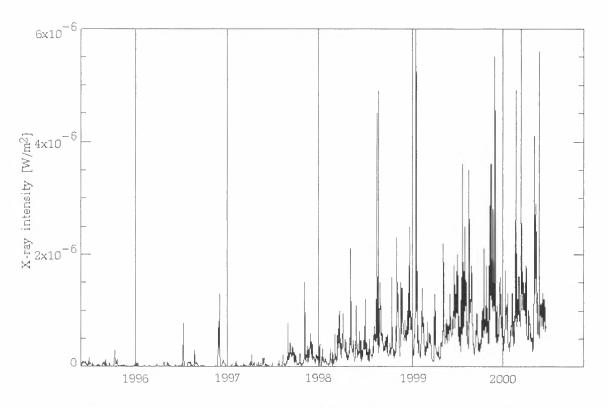


Figure 3. The time profile of the daily soft X-ray background flux (GOES 8).

4. STATISTICAL ANALYSIS

For comparison of statistical properties of analyzed time series we use cross-correlation method, which gives the measure of association between the time series under study.

We use the standard formulae for linear crosscorrelation coefficients r_k (Press at al., 1986)

$$r_{k} = \frac{\sum_{i} (x_{i} - \bar{x}) (y_{i-k} - \bar{y})}{\sqrt{\sum_{i} (x_{i} - \bar{x})^{2}} \sqrt{\sum_{i} (y_{i} - \bar{y})^{2}}}$$
(1)

where k denotes the time shift and \bar{x} and \bar{y} denote the means of time series x_i and y_i , respectively.

We computed cross-correlation coefficients for both the whole analyzed interval 1995-2000 as well as cross-correlation coefficients for individual years.

5. RESULTS

The 3 GHz daily radio fluxes observed by the Ondřejov radiometer in the period from June 1, 1995 till June 30, 2000 are presented in Figure 1. They are compared with that of the 2.8 GHz radio fluxes observed by the DRAO radiometer. As expected the high correlation coefficient for the whole studied interval was found: 0.892. Then the 3 GHz radio flux variations were studied in comparison with the

sunspot numbers and soft X-ray background flux observed by the GOES 8 satellite. The methods of the cross-correlation coefficients were used. The whole time period was divided into years and corresponding cross-correlation coefficients were determined (Table 1 and 2). From these coefficients two interesting trends were recognized:

- a) the cross-correlation coefficients between the 3 GHz radio flux and sunspot number are increasing in the 1995-2000 period; the time shift maxima are in the interval from 0 to -1 day, showing that the the radio flux is delayed after the sunspot evolution,
- b) the cross-correlation coefficients between the 3 GHz radio flux and X-ray flux is decreasing. Furthermore, from the asymmetry of the cross-correlation maxima (see asterisks in Table 1 and 2, which express the second highest values of cross-correlation coefficients in specific years) it was found that the time maxima shifts are changed from positive to negative values (-1 day in the year 2000).

6. DISCUSSION AND CONCLUSIONS

During the 1995-2000 years, i.e. during the 1996 minimum and rising phase of the solar cycle 23 the correlation coefficients between the 3 GHz radio flux and sunspot numbers are increasing and between the 3 GHz radio flux and soft X-ray background flux are

Table 1. The cross-correlation coefficients between the 3 GHz Ondřejov radio fluxes and sunspot numbers for individual years and different time shifts. The bold values correspond to the cross-correlation coefficient's maximum and the underlined values correspond to its second highest value.

Time shift (days)	-2	-1	0	1	2
year 1995	0.439	0.491	0.503	0.467	0.421
year 1996	0.495	0.553	<u>0.530</u>	0.458	0.35
year 1997	0.544	0.574	0.586	0.559	0.528
year 1998	0.690	0.715	<u>0.707</u>	0.666	0.605
year 1999	0.580	0.630	0.634	0.586	0.501
year 2000	0.733	0.820	0.850	0.806	0.715

Table 2. The cross-correlation coefficients between the 3 GHz Ondřejov radio fluxes and soft X-ray background flux (GOES 8) for individual years and different time shifts. The bold values correspond to the cross-correlation coefficient's maximum and the underlined values correspond to its second highest value.

Time shift (days)	-2	-1	0	1	2
year 1995	0.525	0.591	0.610	0.593	0.560
year 1996	0.367	0.474	0.520	0.484	0.453
year 1997	0.474	0.511	0.525	0.489	0.445
year 1998	0.380	<u>0.492</u>	0.508	0.455	0.397
year 1999	0.376	0.422	0.425	0.389	0.358
year 2000	0.480	0.496	0.481	0.391	0.297

decreasing. It can be explained by the fact that a role of the slowly component of the 3 GHz radio emission from active regions is increasing with the solar cycle activity rise. Probably, at the solar activity minimum the 3 GHz slowly component is generated on the low intensity level from extended regions which are not closely connected with small isolated active regions. Moreover, the magnetic field evolution (expressed through the sunspot numbers) precedes the slowly component of the radio emission in the interval less than 1 day. On the other hand, the crosscorrelation coefficient decrease found for the 3 GHz radio and X-ray fluxes could be connected with thermal sources of different temperatures or by the presence of the non-thermal components in different proportions in the radio and X-ray fluxes. The same reasons can be considered also for an explanation of the time shift maxima change.

ACKNOWLEDGEMENTS

This work was supported by the key projects K1-003-601 and K1-043-601, as well as grants S1003006 and A3003707 of the Academy of Sciences of the Czech Republic and grant GACR 205/00/1726.

REFERENCES

- Bumba, V., Howard, R. 1965, ApJ, 141, 1502
- De Toma, G., White, O.R., Harvey K.L. 2000, ApJ, 529, 1101
- Gaizauskas, V., Harvey, K.L., Harvey, J.W., Zwann, C. 1983, ApJ, 265, 1056
- Jiřička, K. 1992, Publications of the Astronomical Institute of the Czechoslovak Academy of Sciences No. 81, pp. 1-3
- Karlický, M. 1997, Bull. Astron. Inst. Czechosl., 28, 200
- Press, W., Flannery, B., Teukolsky, S., Vetterling W. 1986, Numerical Recipes, Cambridge University Press, pp. 484-488

ON MEASUREMENTS OF RAPID VARIATIONS IN SOLAR FLARE OPTICAL RADIATION

P. Kotrč

Astronomical Institute, Academy of Sciences of the Czech Republic, 251 65 Ondřejov, Czech Republic

ABSTRACT

Solar flares and eruptive prominences are especially in early phases accompanied by changes in output radiation related to their development. Even with the increasing role of space-borne device observations, ground-based telescope data are still important in the solar flare research. At the Multichannel Flare Spectrograph we use several CCD video-cameras for simultaneous detection both the H α filtergrams and the spectrum in several diagnostically important lines as H α , H β and CaII 8542 Å. Hereafter we summarize an experience of active phenomena observations performed with high temporal resolution oriented for study of rapid variations in the optical radiation. Using individual examples f data we discuss some problems related both the observation technique and an importance of other types of complementary data.

Key words: solar flares; eruptive prominence; $H\alpha$, X-ray and radio spectra: Doppler velocities; particle beam flux; shock waves: linear polarization.

1. INTRODUCTION

Solar flares make possible to study plasma in very extremal conditions that can not be performed in any technical laboratory. Especially high temperature, high ionization of atoms of chemical species. extremely low densities of plasma, large amounts of the released energy, huge geometrical scales and duration lasting up to hours constitute the basic frame of physical conditions for the most sizable energetic processes in the solar atmosphere. During the hightemperature flaring process (as shown e.g. by Svestka et al., 1992), the energy accumulated in electric currents and corresponding magnetic field is rapidly transformed into the plasma heating, plasma movements with shock waves, acceleration of particles and radiation ranged from gamma-rays up to radio waves. It is generally accepted that individual mechanisms of the flare plasma heating can not be considered as stable phenomena. Recent observations in the hard X-rays and radio-wave passband found series of short-lasting, subsecond spikes. These fast variations of radiation are explained as a direct consequence of impulsive heating of the solar plasma via superthermal charged elementary particles. Particle beams are believed to be one of the most probable

mechanisms of solar flare energy propagation from the corona into lower chromospheric layers. It concerns beams of electrons or protons that propagate with velocity of about 0.1 - 0.3 c and then they are suddenly decelerated in lower and denser plasma lay-Such a process may produce bremsstrahlung ers. with resulting hard X-ray emission and simultaneously an intensive heating of chromospheric plasma occurs. As a consequence, a density and temperature increase is produced in these atmospheric layers, accompanied by a strong radiation in optical regions, mainly in spectral lines of the Balmer series. Time dependent non-LTE simulations of the pulse particle beam heating the solar atmosphere were performed by Heinzel and Karlický (1992). The resulted Ha intensities exhibit unexpected decrease during pulse beam atmosphere heating. However, such an effect has not been observed yet. Up to the present time. the dynamics of the plasma was mainly studied on longer time-scales, by several order longer than characteristic times of the pulse heating of the plasma by means of the superthermal electron beams (Dennis et al, 1986). One can expect also subsecond-lasting variations of optical radiation. These fast variations can be detected in the spectral line of H α and in other lines in the optical region. The response of the chromosphere to the pulse beam heating is considered to be localized in space. Spatial spectral line variations due to suprathermal electron beams can be estimated as about 5 arcsec (Canfield and Gunkler, 1985). Velocity analysis seems to be a very important aspect to distinguish between various mechanisms of flare processes. If large plasma velocities occur, this high velocity or explosive evaporation can be caused by non-thermal electrons accelerated during the primary energy release (Antonucci et al. 1984). In addition, beams of accelerated particles have to result into occurrence of linearly polarized radiation. Therefore, observations of the linear polarization of hydrogen line emission from the upper chromosphere during solar flares could allow the monitoring of the energy transport mechanisms in the flaring atmosphere (Hénoux, 1991, Vogt a Hénoux, 1996). From the analysis of the degree of polarization and of the azimuth of the polarization plane within the emission core of the hydrogen H α line it was inferred that during solar flares, beams of low energy protons. formed in the upper corona and propagating within flare loops, are responsible for the transport of energy into the upper chromosphere. This conclusion is based on the property of protons not to lose their directivity while passing through the diluted medium on their way to the chromosphere. Analysis of the

Proc. 1st Solar & Space Weather Euroconference, 'The Solar Cycle and Terrestrial Climate', Santa Cruz de Tenerife, Tenerife, Spain, 25-29 September 2000 (ESA SP-463, December 2000)

linear polarization both in the H α and H β Balmer series lines in a solar flare by the method providing the linear polarization along the line profile at various selected places was performed by Firstova and Kotrč (1987).. The simultaneous observation of both the polarized and unpolarized line profiles brings additional information about the source of energy deposit and the origin of the observed polarization and helps to avoid pertubations of the polarization signal due to the Doppler shift. Moreover, one can suppose that the processes connected to the particle beam interaction with the plasma can be rather short-lasting. Therefore, occurrence of the polarized radiation can be also substantially limited in time.

2. OBSERVATIONS

As a matter of fact, this short lasting process can have a character of pulsations (Heinzel and Karlický, 1992). To detect it, one should use telescope and spectrograph with a good angular and spectral resolution fitted to the light detectors working at very short exposure time and having a high (subsecond) temporal resolution. The Ondřejov Multichannel Flare Spectrograph described by Valníček et al. (1959), see Fig. 1, enables a simultaneous detection of several diagnostically important lines. It is a

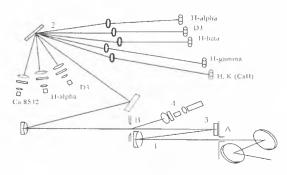


Figure 1. Schema of the Multichannel Flare Spectrograph.

substantial point that it has a large light power at a very good spectral resolution (120 000 in the second order). Recently, this spectrograph was modernized substantially (Kotrč et al. 1993). The device is supplemented by CCD videocameras working on the image sampling frequency 25 images/second. Exposure time can vary from $1/10\ 000$ to 1/50 s. In the period from 1993 we started to analyse problems of fast processes in spectra and $H\alpha$ filtrogramms monitored by a system of videocameras. In addition, we used both the radio data of the recently improved Ondřejov radiotelescopes (Karlický et al, 1992) and the registration of X-ray data from the GRO BATSE experiment. For future we also rely on the scheduled HESSI and the just starting Czech-American experiment HXRS on board of the American satellite MTI to obtain unique sets of complementary data for our observations. As one of the most important aims is to observe expected responses of high-velocity particle beams in the optical and spectral data and compare them to other solar data we use a comparable time scale and an exact time of the observation. Therefore, it is important that the time scale of all spectral and video data is fixed to the time standard DCF-77. The time information as well as other auxiliary data is implemented to the videosignal and is displayed on the monitor. Hardware and software means were recently improved and they are also used to control the coeloestat movements and to evaluate the heliographic coordinates of the selected position on the slit. This fact is very important for precise identification of especially weak objects marked as targets of observation during various international observation campaigns we are involved in. We are able to use the Multichannel Flare Spectrograph for observation at any time when the weather is favourable. As a result we have observed lots of active phenomena (see our data archive with examples of maim interesting objects of the day available at http://www.asu.cas.cz/pkotrc/archive.html).

3. SOLAR FLARES

During all the period of the described project, many interesting flare phenomena were observed and good spectra and filtergrams were obtained. One of the most interesting flare observation was that of the September, 23, 1998. The Solar Geophysical Data reported that the flare was observed in the NOAA 8340 from 06:44 UT till 10:09 UT at the heliographic coordinates W09, N18. The Ondřejov Multichannel Flare Spectrograph observed the flare for several hours from the early beginning to its complete disappearance and the optical H α filtergrams and spectra were registered with the video frequency 25 pictures per second, see Figures 2 and 3.

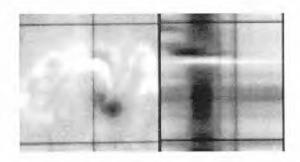


Figure 2. Ha slit-jaw and spectrum taken on Sept., 23, 1998 at 06:51:06 UT.

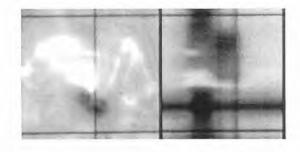


Figure 3. H α slit-jaw and spectrum taken on Sept., 23, 1998 at 06:56:48 UT.

There were reported two BATSE events (5205, 5206, see BATSE) during the flare duration. The begin-

ning of the flare well correlates with the hard X-ray BATSE effect No. 5205. The 0.8-2.0 GHz radio spectrographs detected bursts from 06:47-07:31 UT. At the beginning of this phenomenon three slowly positively drifting components followed by a continuum were recorded). Later on the radio noise storm at lower frequencies occurred. Unfortunately, no SOHO data were available for that flare. We processed Ha spectra from various parts of the flare. Two interesting H α spectra with a position of the spectrograph slit (vertical line) and two hairs (the horizontal lines) are shown in the Figures 2 and 3. They display spectral patterns typical for the beginning phase of the flare with very broad and shifted emission and ab-sorption lines. There are distinguished regions with dark absorption features in the central part of the flare. However, while in Figure 2 taken before the radio bursts. one can see the absorption feature shifted towards left (Heinzel et al, 1994), the Figure 3 taken just after the radio bursts shows a might absorption shifted towards red (longer wavelengths). That means a complete change of the prevailing movement of the absorbing plasma cloud occurred in the time when the radio bursts were detected. Just at these periods we looked for the evidence of the optical intensity rapid variations.

4. SEARCH FOR CHROMOSPHERIC RESPONSE OF THE PARTICLE BEAMS

The flare Ha spectra registered with a video frequency were digitized into an 8 bit dynamical scale. They were calibrated both in intensity and the wavelength scale. A semiautomatic off-line regime procedure controlling the video tape recorder was developed. It compared subsequent H α slit-jaw images and searched for short lasting excesses of radiation exceeding over an error limit in each pixel of the entire flaring region. The slit scanning regime over the flaring region determined individual blocks of data for their off-line processing. For preliminary searching we choose these time periods that are simultaneous with hard X-ray bursts as registered by BATSE experiment. For further analysis of obtained spectra and filtergrams it was necessary to transform the analog signal into a digital form. In order to gain maximum of information from such relatively high temporal resolution an analysing software controlling Panasonic video recorder and the DIPIX P360F frame grabber was developed. Supposing that spectral line flare intensity variations have their counterpart in filtergram flare intensity variations, data reduction is performed by an analysis of changes in filtergram flare intensity in subsequent frames. The intensity variations are searched in a small preselected region only, just around a slit position. Possible optical counterparts displayed at the slit-jaw filtergrams were chosen according to their intensity concentration into spatially small regions and to the time intervals of the BATSE events. Temporal variations of the H α intensities both in the line core and the wings are plotted in Fig. 4. However. up to now, no possible optical counterpart of the two effects which BATSE registered during the flare has been found in the preliminary searching. We think that such fundamental problems of successful observations and data analysis will be definitely solved using the planned HESSI experiment and we should like to continue our efforts

to find the optical counterparts of the particle beam.

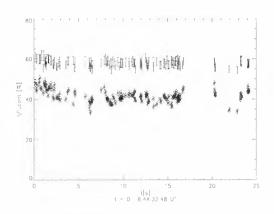


Figure 4. Temporal variations of $H\alpha$ measured intensity in a selected point at the flaring region. Intensities are plotted with error bars and normalized to local continuum; + corresponds to line center, \diamond corresponds to line wings.

5. ERUPTIVE PROMINENCE ON MAY 15, 2000

Just recently a dynamic eruptive prominence with rapid structural and intensity changes was observed at the NE limb and its eruption was observed in details by the Ondřejov H α patrol telescope shortly after a solar flare in its vicinity (Karlický et al, 2000), see Figure 5. A large circular symmetric structure with high velocities was detected in the H α spectrum.

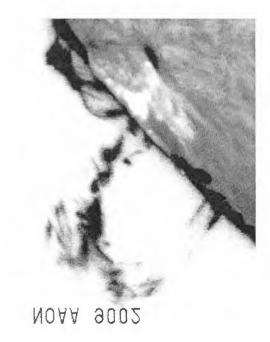


Figure 5. Negative + positive $H\alpha$ prominence and flare images at 09:07:04 and 08:54:15 UT, respectively.

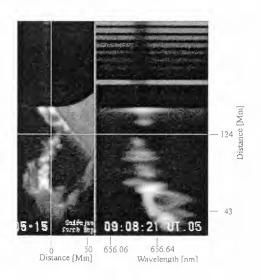


Figure 6. The H α eruptive prominence on May 15, 2000 slit-jaw and spectrum at 09:08:21 UT.

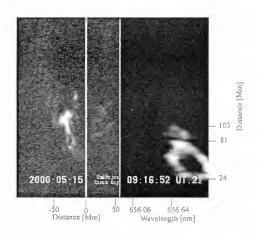


Figure 7. An almost symmetric high velocity structure was observed in the $H\alpha$ eruptive prominence on May 15, 2000 slit-jaw and spectrum at 09:16:52 UT.

6. CONCLUSIONS

As the search for optical counterparts of X-ray and radio bursts is a rather technical difficult task, first attempts to find an undoubted manifestation of accelerated particle beam in the optical radiation using a semiautomatic searching in video data were performed without positive results. Obtained temporal line intensities are mainly influenced by errors in spatial resolution due to bad seeing conditions and perhaps due to some problems in the method of spectra analysis, especially in errors in setting the reference point for the coordinate system. We will continue this effort both in the data of this flare, the eruptive prominence and other observations using also the methods of spectropolarimetry. We also believe that the high temporal X-ray solar photometry at the experiment HXRS at the MDI satellite and the HESSI images and other important complementary data will help to solve the problem soon.

ACKNOWLEDGMENTS

The author acknowledges the support of the Grant No. 205/00/1726 of the Grant Agency of the Czech Republic and Grant Agency of the Academy of Sciences of the Czech Republic via grant No. A3003707, and the Key - Project of the Academy of Sciences of the Czech Republic K1-003-601. Substantial help of Ms. J. Kašparová and Mr. Yu. Kuprjakov is highly appreciated.

REFERENCES

- Antonucci, E., Gabriel, A. and Dennis, B.: 1984, Astrophys. J. 287, 917
- Canfield, R. C. and Gunkler, T. A.: 1985, Astrophys. J. 417, 760
- Dennis B. R., Orwig L. E. a Kiplinger A. L.: 1986, Rapid Fluctuations in Solar Flares, NASA Conf. Publ. 2449
- Firstova, N. M. and Kotrč, P.: 1987, Bull. Astron. Inst. Czechosl. 38, 257
- Heinzel P.: 1991, Solar Phys. 135, 65
- Heinzel, P. and Karlický, M.: 1992a, in Eruptive Solar Flares, Proc. of the IAU Coll. 133, eds. B.V. Jackson, M. Machado and Z. Švestka, Lecture Notes in Physics, Springer-Verlag
- Heinzel, P. and Karlický, M.: 1992b, in Proc. of the First SOHO Workshop, eds. A. Poland and J.T. Mariska, ESA SP-348, 237
- Heinzel, P., Karlický, M., Kotrč, P. and Švestka Z.: Solar Phys., 152, 393
- Hénoux, J.-C.: 1991, Solar Polarimetry, Proceedings of the Eleventh National Solar Observatory Sacramento Peak Summer Workshop, p. 285
- Karlický, M., Tlamicha, A., Jiřička, K., Aurass, H. and Zlobec, P.: 1992, Hvar Obs. Bull. 16, 23
- Karlický M.: 1997, Space Sci. Rev., 81, 143
- Karlický M., Kotrč P. and Kuprjakov Yu. A.: 2000, Solar Phys., submitted
- Kotrč, P., Heinzel, P. and Knížek M.: 1993, JOSO Annual Report 1992, ed. A. v. Alvensleben, 114
- Kotrč P.: 1997, Hvar Obs. Bull. 21, 97
- Vogt, E. and Hénoux, J.-C.: 1996, Solar Phys. 194, 345
- Švestka, Z.: 1976, Solar Flares, D. Reidel Publ. Co., Dordrecht

PHASE RELATIONS BETWEEN CHROMOSPHERIC AND TRANSITION REGION OSCILLATIONS

J.M.Krijger¹, W. Curdt², P. Heinzel³, and W.Schmidt⁴

¹Sterrekundig Instituut, Postbus 80 000, NL-3508 TA Utrecht, The Netherlands
 ¹Tel: 31(0)302535225 Fax: 31(0)302535201 e-mail: krijger@astro.uu.nl
 ²Max-Planck-Institut für Aeronomic, D-37191 Katlenburg-Lindau, Germany
 ³Astronomical Institute, Academy of Sciences of the Czech Republic, CZ-25165 Ondřejov, Czech Republic
 ⁴Kiepenheuer-Institut für Sonnenphysik, D-79104 Freiburg, Germany

ABSTRACT

We present results from combined TRACE and VTT observations for H1 L_{α}. Ca II K and the 170, 160, 155 nm TRACE continua, showing oscillatory patterns in bright network and internetwork regions of the quiet Sun near disk centre. All data were spatially and temporally co-aligned. Temporal behaviour and phase relations of these co-spatial data are discussed.

Key words: Sun:atmosphere, oscillations.

1. INTRODUCTION

The Transition Region and Coronal Explorer (TRACE) was launched on April 1, 1998 into Sunsynchronous orbit. It images the Sun at characteristic temperatures between 10^4 K and 10^7 K by sequentially selecting different spectral passbands to feed a 1024 px×1024 CCD camera with 0.5 arcsec pixels (366 km/px on the Sun) that covers nearly 10% of the solar disk. Details are given by Handy et al. (1999a).

In this paper we use image sequences taken through the extreme-ultraviolet TRACE passbands centered at $\lambda = 121.6$ nm, 170.0 nm, 160.0 nm, and 155.0 nm to study quiet-Sun oscillations in the atmospheric domains from which solar radiation emerges in these passbands. In standard models of the solar atmosphere such as VAL C of Vernazza, Avrett & Loeser (1973, 1976, 1981) and FALC of Fontenla et al. (1993), the disk-center intensity at 121.6 nm emerges from the "transition region", the 170.0 nm from the "upper photosphere", the 155.0 nm radiation from the "lower chromosphere", and the 160. nm radiation from the "temperature minimum region", where the temperature minimum at h = 500 km above continuum optical depth $\tau_{500} = 1$ at $\lambda = 500.0$ nm defines the transition from photosphere to chromosphere (see the formation panels in Fig. 36 of Vernazza et al. (1981)).

This and somewhat higher atmospheric regimes are accessible to groundbased observation and has been studied extensively using the cores of strong absorption lines and the CaII K_{2V} and H_{2V} inner-wing emission peaks.

In order to explore the relations between the oscillatory behaviour at these atmospheric levels . some studies focussed on coordinated observations with SOHO, TRACE and GBO (Ground-Based Observatories). e.g. by Steffens et al. (1997). The present contribution shows first results of a coordinated SOHO/TRACE/VTT/GCT campaign which took place in May 1999 and had similar objectives.

We carried out an observing campaign in the frame of the SOHO-TRACE-GBO programme JOP 95 with simultaneous observations in H1 Lyman lines and continuum, the Ca11 K line (intensity oscillations) and a magnetically sensitive Fe1 line (Stokes polarimetry), and, in addition TRACE H1 L_{α} images are also included. The campaign and involvement of individual instruments and some first results are described in Curdt et al. (1999) We present and discuss some more results here (TRACE and VTT data only).

2. OBSERVATIONS

Three runs of JOP 95 were performed between 4 and 9 May 1999.

The TRACE instrument took an H₁ L_{α} time series during the morning observing time of the German Solar telescopes on Tenerife (VTT, GCT).

On all occasions, a quiet-Sun site near disk centre had been selected as target and the solar rotation

Proc. 1st Solar & Space Weather Euroconference, 'The Solar Cycle and Terrestrial Climate', Santa Cruz de Tenerife, Tenerife, Spain, 25-29 September 2000 (ESA SP-463, December 2000)

had been compensated by the instruments. Because of excellent weather conditions on Tenerife on May 8, we selected the data taken on this day for our first analysis. More details for these observations can be found in Curdt et al. (1999).

2.1. VTT TIME SERIES IN THE Call K LINE

At the 70 cm Vacuum Tower Telescope (VTT) on Tenerife sequences of Ca II K filtergrams were taken between 07:39–10:57 on May 8. A Lyot filter centered on the K_{2v} emission peak near the core of the Ca II 393.3 nm line, with an FWHM of 0.06 nm was used. Data were recorded on a 16 bit 1024 × 1024 pixel CCD camera operated in 512 × 512 summing mode. The image scale was 0."366/pixel and the useable field of view was about 150" × 150". The cadence of the observations was 6 s, with an integration time of 0.25 s. Seeing conditions were good during this observation.

2.2. TRACE OBSERVATIONS

From 08:10–12:58, TRACE collected a time series of 121.6, 155.0, 160.0 and 170.0 nm band images with \approx 40 s cadence. The FOV was 128 × 320", with 0."5 pixels (1" resolution). Standard procedures were employed for decompression, flatfield and dark signal correction of the data. The 121.6 nm images also contain significant leakage of UV continuum in the 150.0–170.0 nm region along with L_{α} emission; a subtraction technique has been developed to provide a cleaner estimate of L_{α}(Handy et al. (1999b)).

3. CO-ALIGNMENT

For this first analysis only the data between 08:10-08:58 was used as the TRACE FOV jumped (for, at this moment, unknown reasons) at 08:58. The 121.6 nm images however do not start before 8:20. All Call and TRACE data was corrected for solar/earth rotation and satellite/telescope jitter by aligning each frame to the first frame of the time series, which given the short duration of the observation (only the data during the overlapping times was used) does not introduce any errors. The different TRACE passbands were co-aligned by cross-correlating their respective average image. We converted the Call data to TRACE resolution and co-aligned the averaged images through crosscorrelation. All alignments are accurate to within sub-pixels resolution. Finally a subfield from all overlapping data was taken.

From the aligned TRACE 121.6 nm and 160.0 nm images a L_{α} estimate was constructed (Handy et al. (1999b)). In this analysis we use the following naming-convention: 121.6 nm for the contaminated images and L_{α} for a cleaned construct.

4. PHASE RELATIONS

Having thus 5 independent (and a 6th constructed) datasets we investigated the phase relations between signals which would correspond to different atmospheric layers.

We take a x - t slice at a given X (or Y) position. For each x - t slice we determine the time-offset with the x - t slice from the same X (or Y) position from another dataset and repeat this for all X and Y positions. This gives us a scatter plot of time-offsets per dataset combination. After binning this scatter plot we fitted a curve consisting of 5 Gaussian profiles to this data. The reason for using multiple Gaussians will be explained later.

The found phase shifts were corrected for nonsimultaneous sampling of the different datasets by subtracting the average difference between times of exposures.

The above process was repeated for the network and the internetwork by using adjacent (inter)network patches instead of the entire X or Y-range.

Some results are included in table 1.

5. DISCUSSION

According to table 1 the TRACE 160.0 nm passband shows the same morphology and temporal evolution as CaII (as earlier shown by Rutten et al. (1999)): they are in phase, within the uncertainty.

In all passbands the difference between network and internetwork is small (zero within error). Other current work however shows many differences between these regions. A more detailed Fourier analysis is currently being done to confirm these results.

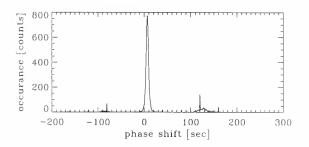


Figure 1. Histogram of phase shifts (in sec) for L_{α} -160.0 nm combination Most phase shifts are around zero as a result of the 160.0 nm signal correlating with itself in the L_{α} construct. The sharp peaks around -80 and 120 sec are also possibly due to this effect. Note, the broad bump around 125 sec which is the most likely solar phase shift between L_{α} and 160.0 nm

Table 1. Phase relations and their 1 σ - uncertainty (in sec) between different wavelength combinations for the entire field (all). network (nw) and internetwork(in) from cross-correlation of x - t data sets. The '2' in the L_{α} -160 set indicates the second peak. Positive shifts mean that second signal arrives later then the first signal. Δt_{total} is the derived phase shift between the combination of passbands (derived by adding with Δt_{cross} and $\Delta t_{sampling}$) with σ_{total} the uncertainty in this number. Δt_{cross} and σ_{cross} give the same information derived from crosscorrelating the data (and fitting a Gaussian to the resulting histogram) and $\Delta t_{sampling}$ and $\sigma_{sampling}$ give the average time difference between the moments of image-taking. N_{Gauss}/N_{total} is a measure of the certainty of the fit by the Gaussian by dividing the number of counts in the fitted Gauss curve by the total number of counts.

Passband	NW/IN	Δt_{total}	σ_{total}	Δt_{cross}	σ_{cross}	$\Delta t_{sampling}$	$\sigma_{sampling}$	N_{Gauss}/N_{total}
170-160	all	2.75	0.92	5.93	0.80	-3.18	().47	0.93
170 160	ΠW	2.40	1.29	5.58	1.21	-3.18	0.47	0.96
170 - 160	in	2.79	1.07	5.97	0.96	-3.18	().47	0.93
160 - 155	all	1.16	1.06	6.22	0.95	-5.06	().47	0.92
160 - 155	1117.	1.06	1.56	6.12	0.49	-5.06	0.47	0.97
160-155	all	1.23	1.25	6.29	1.16	-5.06	().47	0.94
Ca 11-160	all	0.13	4.34	0.19	3.96	-0.06	1.77	0.24
Ca II=160	nw	-0.56	4.40	-0.50	4.03	-0.06	1.77	0.19
Ca II-160	in	0.86	5.26	0.92	4.95	-().()6	1.77	0.24
121.6-160	all	-3.97	1.84	4.60	1.82	-8.57	0.31	0.92
121.6-160	nw	-4.45	2.88	4.12	2.86	-8.57	0.31	0.96
121.6-160	in	-3.84	2.14	4.73	2.12	-8.57	0.31	0.93
$L_{\alpha} = 160$	all	-1.50	2.67	7.07	2.65	-8.57	0.31	0.68
L _o 160	all 2	111.63	0.31	120.19	0.04	-8.57	0.31	0.02
$L_{0} = 160$	11W	-2.32	4.10	6.25	4.09	-8.57	0.31	0.66
L_{α} 160	nw 2	111.63	0.31	120.20	0.03	-8.57	().31	0.01
L_{α} =160	in	-1.64	3.15	6.93	3.14	-8.57	0.31	().6()
L_{α} 160	in 2	111.62	0.31	120.19	0.04	-8.57	0.31	0.01

The L_{o} -160.0 nm combination is the main reason for fitting multiple Gaussians. Figure 1 shows that the spread is clearly non-uniform and cannot be fitted with a single Gaussian curve.

Two Gaussians stand out from the noise level. The large central Gaussians is the result from the construction method of the L_{α} channel (a linear combination of 121.6 and 160.0 nm) and is the alignment of the 160.0 nm channel with itself in the construct. More interesting is the appearance of the second Gaussian at ≈ 112 sec. which looks like a downward propegating wave with an average chromospheric sound speed of ≈ 14 km/sec (with a difference of ≈ 1500 km between the formation heights of L_{α} and 160.0 nm (Vernazza et al. (1973)). However further analysis is needed to confirm this result.

6. CONCLUSIONS AND OUTLOOK

We have demonstrated here that the L_{α} oscillations are correlated to chromospheric (160.0 nm) oscillations. Also we have provided more proof of the strong correlation between Ca II K and TRACE 160.0 nm channel. We want to emphasize that the results presented here are preliminary, and much more work has to be done. Also, the interpretation of our observation is still in its initial phase.

Future work will include fourier analysis and also different SOHO Lymann line and longer time series.

ACKNOWLEDGEMENTS

J.M.Krijger would like to thank the Leids Kerkhoven-Bosscha Fonds and the Max-Planck-Institut für Aeronomic for financial support making this analysis possible. P.Heinzel acknowledges the support of MPAE during his visit and of the grand A3003902 of GA AVČR.

REFERENCES

- Curdt W., Heinzel P., Schmidt W., et al., 1999. in 9th European Meeting on Solar Physics: Magnetic Fields and Solar Processes (ESA SP-448), p. 177
- Fontenla J. M., Avrett E. H., Loeser R., 1993, ApJ 406, 319

- Handy B. N., Acton L. W., Kankelborg C. C., et al., 1999a, Solar Phys. 187, 229
- Handy B. N., Tarbell T. D., Wolfson C. J., et al., 1999b, Solar Phys. 190, 351
- Rutten R. J., de Pontieu B., Lites B. W., 1999, in T. R. Rimmele, K. S. Balasubramaniam, R. R. Radick (eds.), High Resolution Solar Physics: Theory, Observations, and Techniques, Proc. 19th NSO/Sacramento Peak Summer Workshop, ASP Conf. Ser., Vol. 183, p. 383
- Steffens S., Deubner F.-L., Fleck B., et al., 1997, in B. Schmieder, J. C. del Toro Iniesta, M. Vázquez (eds.), Advances in the physics of sunspots, Proc. First Adv. in Solar Physics Euroconf., ASP Conf. Ser., Vol. 118, p. 284
- Vernazza J. E., Avrett E. H., Loeser R., 1973, ApJ 184, 605
- Vernazza J. E., Avrett E. H., Loeser R., 1976, ApJ 30, 1
- Vernazza J. E., Avrett E. H., Loeser R., 1981, ApJ 45, 635

FE I AND CA II K LINES IN QUIET AND ACTIVE REGIONS

A. Kučera¹, K. Brčeková¹, A. Hanslmeier², J. Rybák¹, and H. Wöhl³

¹Astronomical Institute of the Slovak Academy of Sciences, SK-05960 Tatranská Lomnica, Slovak Republic ²Institut für Geophysik, Astrophysik und Meteorologie, Universitätsplatz 5, A-8010 Graz, Austria ³Kiepenheuer-Institut für Sonnenphysik, Schöneckstr. 6, D-79104 Freiburg, Germany

ABSTRACT

We investigated Fe I (557.6 nm and 522.5 nm) and Ca II K lines in active and quiet regions. The line intensity ratios and velocities were compared in quiet (disc center) region, plage and subflare. Using correlations of line center intensity and velocity fluctuations along the slit we estimate appropriate layers of the photosphere which are affected by the subflare. Difference between quiet and 'flaring' photosphere is discussed.

Key words: Spectral lines; photosphere; flare.

1. INTRODUCTION

Spectra of the solar atmosphere, obtained with high spatial and spectral resolution are good tool for diagnostics of fine differences of the physical conditions of the solar atmosphere. It is important to select suitable set of lines in order to investigate properly dynamic and magnetic characteristics of the atmosphere in the chosen levels. Such set of lines, then serve for theoretical calculations of the physical models of all types of the solar activity. This contribution is a part of long-duration project of investigation of the dynamic parameters of the solar atmosphere in different types of the solar activity. Determination of the spectral characteristics and investigation of their statistical behaviour is the first step of such analysis. The aim of this paper is to compare spectral characteristics of two photospheric lines, Fe I 557.6 nm (dynamic line), Fe I 522.5 nm (magnetic line) and one chromospheric line Ca II K 393.3 nm, in quiet and active atmosphere after solar cycle minimum, in vear 1993.

2. OBSERVATIONS

The data were taken on Vacuum Tower Telescope (VTT), (Schröter et al., 1985, Soltau, 1989), at Observatório del Teide, Tenerife, on June 1, 1993. Vve

observed in three spectral regions. More than 1000 spectra in all three regions were taken including the calibration spectra for flatfielding. The relevant parameters for the observed spectral lines are given in Tables 1, 2 and 3. Both Fe I lines are formed at the same height in the photosphere ($\sim 300 \text{ km}$) but the Fe I 557.6 nm is dynamic line and the second one Fe I 522.5 nm is magnetically sensitive line with $g_{eff} = 2.5$. For information about chromosphere, we add Ca II K line to the set of the two Fe I lines. The inner wings of the Ca II K line should form at the same height as the centers of the Fe I lines.

For this work we have selected three sets of spectra (three lines in each) for typical quiet region, plage and subflare (see Table 2.) The three lines in one set were taken simultaneously, i.e. the start of exposure was the same. The spectra were recorded with CCD cameras of 1024 x 1024 pixels with binning 2. Thus the resulted spectra are of 512 x 512 pixels. The resolution in spatial direction is 0.17" per pixel. The dispersion in wavelength direction is given in Table 3. The width of the spectrograph slit was 150 μ m. The spectra were stored on exabyte tape in on-line regime. Simultaneous slit-jaw images in Ca II K and H_{α} lines were recorded on video tape. There is shown one set of spectra together with slit-jaw images in Figure 1.

3. DATA REDUCTION

The data were reduced using IDL software including the IDL KIS LIB - library of IDL programs at Kiepenheuer-Institut für Sonnenphysik, Freiburg. Standard procedures were applied (dark current subtraction, precise flatfielding, and FFT profiles restoration) in the reduction process. For our analysis we calculated the following spectral characteristics:

- $-I_c$ continuum intensity;
- $-I_o$ line center intensity;
- $-v_D$ Doppler shift velocity (in Fe I lines only);
- bisectors (in Fe I lines only);

Proc. 1st Solar & Space Weather Euroconference, 'The Solar Cycle and Terrestrial Climate', Santa Cruz de Tenerife, Tenerife, Spain, 25-29 September 2000 (ESA SP-463, December 2000)

	1.000	TC I. OPCCOID	mico citara	0001100100	
line	wavelength [nm]	eqv. width [mÅ]	multiplet	excit. pot. [eV]	Lande factor g_{eff}
Fe I	557.6	113	686	3.43	0.0
Fe I	522.5	68	1	0.11	2.5
Ca II K	393.3	20253	1	3.2	1.17

Table 1. Spectral lines characteristics

			Table 2. Spectr	a finally used	
n:	line [nm]	time [UT]	exposure time [s]	location on the disk μ	activity
1	$393.3 \\ 557.6 \\ 522.5$	08:01:01 08:01:01 08:01:01	2.0 0.2 0.2	$egin{array}{ll} \mu &= 1 \ \mu &= 1 \ \mu &= 1 \end{array}$	quiet region quiet region quiet region
2	$393.3 \\ 557.6 \\ 522.5$	08:28:31 08:28:31 08:28:31	2.0 0.2 0.2	$\begin{array}{l} 0.97 > \mu > 0.77 \\ 0.97 > \mu > 0.77 \\ 0.97 > \mu > 0.77 \\ 0.97 > \mu > 0.77 \end{array}$	plage plage plage
3	$393.3 \\ 557.6 \\ 522.5$	08:12:48 08:12:48 08:12:48	2.0 0.2 0.2	$\begin{array}{l} 1 > \mu > 0.97 \\ 1 > \mu > 0.97 \\ 1 > \mu > 0.97 \\ 1 > \mu > 0.97 \end{array}$	subflare subflare subflare

Before that, an influence of the atmospheric refraction on the spectra was eliminated. For this, we rotated the spectrograph tank of the VTT before the observations to have the slit in appropriate angle to keep the effect of the refraction along the slit only. The resulted shift of spectra between the 'violet' and 'green' spectral regions in 'y' direction (along the slit) was then calculated using the correlations between intensity fluctuations along the slit in the centers of the Fe I lines and in the wing of the Ca II K line. We have found the best correlation with shifts of these intensity fluctuations 11 pixels between Ca II K (wing) and Fe I 557.5 nm (line center) and 9 pixels for the Ca II K and Fe I 522.5 nm. The intensity fluctuations are demonstrated in Figure 2 and the correlations are shown in Figure 3. After the coaligment of all three spectra according to the estimated shifts, we calculated the spectral characteristics for every scan (row) in the particular spectrum. There are 413 scans (rows) in the finally reduced spectra. It represents a spatial region of 70.21" along the slit.

Table 3. Dispersion of the spectral regions

line	dispersion per 1 pixel [10 ⁻³ nm]
Fe I 557.6	0.3476 3
Fe I 522.5	0.3672
Ca II K 393.3	0.2578

4. RESULTS

First, we have estimated ratios of the Fe I and Ca II K line central intensities. They are shown in Figure 4. Using the method described by Kučera et al. (1998) we have calculated autocorrelations of the shifts of Fe I lines (Fig.5). Line center shifts fluctuations along the slit were correlated with bisector fluctuations along the slit. Let us explain the idea. If the center of line and also the wings of the line are formed at almost the same height in the atmosphere, the shifts of both line center and bisectors should be identical. The correlation of such shift fluctuations along the slit will be high. If the center of line is formed in different conditions than the wings, the correlation will be weak (for details see Kučera et al., 1998).

5. DISCUSSION

The ratios of the I_o (Fig.4) reflect mainly the temperature and density situation in the atmosphere. There is no coupling, as expected, between photosphere and chromosphere in quiet region. No reflection of higher intensities of Fe I lines acts in Ca II K line center. Contrary to that, plageous atmosphere is characterized by reaction of the Ca II K line intensities to the changes in the Fe I line center ones. More, the intensities are generally shifted to higher values. This indicate hotter photosphere and some coupling of the photosphere and chromosphere even for those layers, in which the lines are formed. Different situation pays for Figure 4 - subflare. Here we



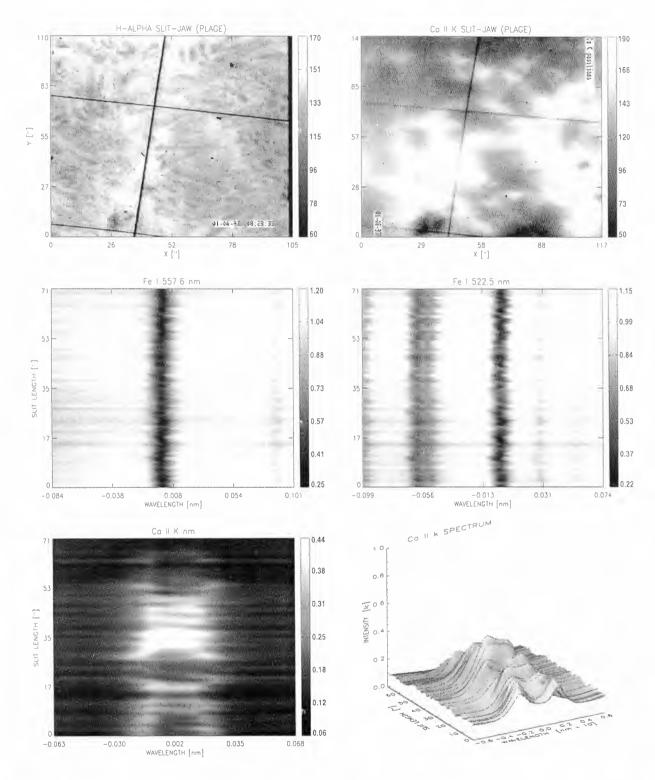


Figure 1. An example of the spectral set observed in plage including two slit-jaw images, three spectra. and 3D plot of intensities of the Ca II K spectrum.

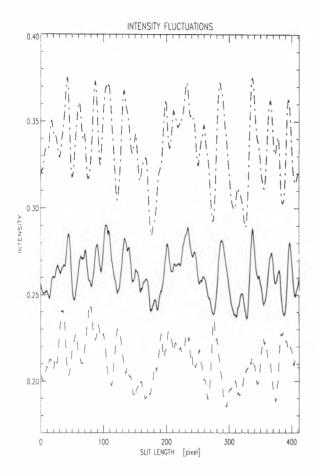


Figure 2. Intensity fluctuations along the slit in centers of Fe I 557.6 nm (full line), Fe I 522.5 nm (dotdashed line) and Ca II K 393.3 nm line wing (dashed line). The lines in figure are artificially shifted for better resolution.

met several types of behaviour of the intensity ratios:

a) High rise of Ca II K intensity without reaction in Fe I lines;

b) High rise of Fe I intensities without reaction in Ca II K line;

c) intermediate behaviour between types a) and b);

Such situation could support the idea, that the energy of the flaring plasma penetrate deeper to the photospheric layers in very structured isolated bent bunches. Therefore we can see enhanced intensities in Ca II K line but at the same position on the slit there is no activity in photospheric Fe I lines and vice versa.

The autocorrelation of the fluctuations of the line shifts in Fe I lines (Fig.5) indicate also changes mainly between quiet and flaring photosphere. While the differences in correlations for quiet and plageous atmospheres are rather small, the differences for subflare and quiet region and for subflare and plage are dramatic. In both panels of Figure 5 we can see rapid departures of autocorrelations if we go out from the

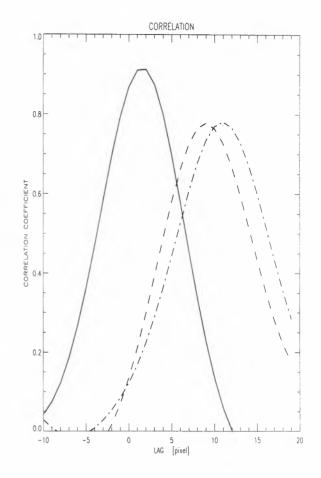


Figure 3. Correlations between the intensity fluctuations shown in Figure 2. Full line stays for $\langle Fe I$ 556.7, Fe I 522.5>, dashed line for $\langle Fe I$ 522.5, Ca II K> and dot-dashed line is for $\langle Fe I$ 557.6, Ca II K > correlations.

centers of lines to the wings. The departure is higher for magnetic Fe I 522.5 nm line. The behaviour of the autocorrelations in flaring photosphere exhibits that centers of both Fe I lines are here formed in higher hotter plasma comparing to the situation in quiet region. The Fe I 522.5 nm line is additionally affected by the magnetic field which is presented in the active region.

To describe the behaviour of the investigated parts of the photosphere it is necessary to model them for every particular case (quiet, plage, subflare). This is the aim of our near future work using the SIR code (Cobo, 1998) developed at Instituto de Astrofisica de Canarias.

ACKNOWLEDGMENTS

A.H. thanks the 'Austrian Fonds zur Förderung der wissenschaflichen Forschung' for support. A.H., A.K and J.R acknowledge the Grant VEGA 2/7229/20 and the Austrian and Slovak Academy of Sciences.

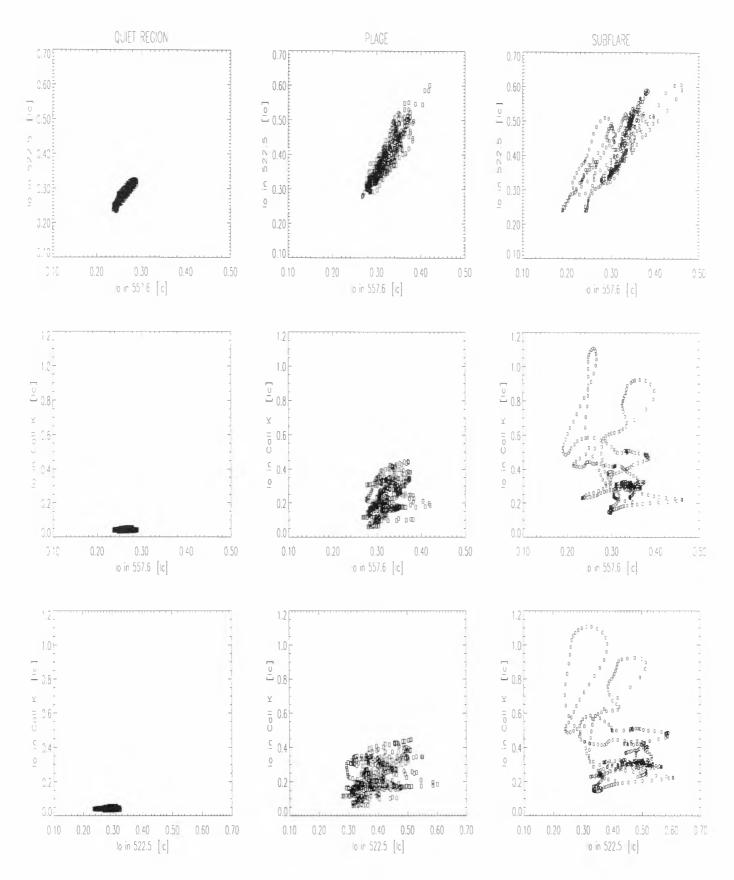


Figure 4. Line intensity ratios of the Fe I and Ca II K lines in all three (quiet, plage. subflare) investigated regions.



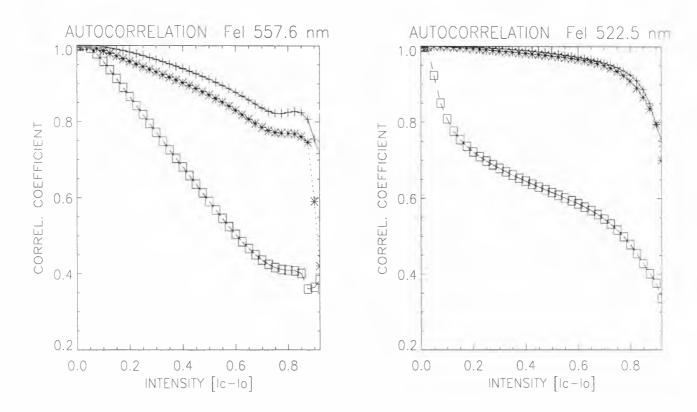


Figure 5. Autocorrelations of the line center shifts (v_{λ}) and wing shifts (bisectors) of the two Fe I line along the slit. The intensity [Ic -Io] means the line intensity depression. The crosses symbolize quiet region, the stars stay for plage and the squares pays for subflare.

REFERENCES

Cobo B.R., 1998, Ap&SS 263, 331

- Kučera A., Balthasar H., Rybák J., Wöhl H., 1998, A&A 332. 1069
- Schröter E.H., Soltau D., Wiehr E., 1985, Vistas in Astronomy 28, 519
- Soltau D., 1989, in: High Spatial Resolution Solar Observations, ed. O.von der Lühe, National Solar Observatory, Sacramento Peak, Sunspot, p.3

RADIO EMISSION OF SOLAR CHROMOSPHERE AT MILLIMETER WAVELENGTHS

Maria A. Loukitcheva and Valery G. Nagnibeda

St-Petersburg University Astronomical Institute 198504, Bibliotechnaya pl., 2, St-Petersburg, Russia tel/fax: (+7 812) 428 7129, e-mail: loukmas@hotmail.com, vnag@vnag.usr.pu.ru

ABSTRACT

Investigation of solar radio emission at millimeter wavelengths provides simple diagnostics of physical conditions in the solar chromosphere. In this paper we present the results of long-term ground-based observations of solar chromosphere at millimeter wavelengths. We analyze observational characteristics of the Quiet Sun and their evolution during the solar cycle and compare them with theoretical calculations derived from present-day models based on UV and optic data.

1. INTRODUCTION

Observations of the Quiet Sun have several aspects in solar physics. These include studies of the solar atmosphere, heating mechanisms and solar cycle variations. The radio emission of the Quiet Sun is the sum of the optically thick chromosphere emission and the overlying optically thin corona. For wavelengths below several centimeters (frequencies above several hundred megahertz) the coronal contribution into the emission becomes negligible and one measures the chromosphere temperature at the optical depth of unity that concrete wavelength. Thus having at multifrequency millimeter observations of the Ouiet Sun brightness temperature one can obtain the temperature and the emission measure in the chromosphere. Data derived from radio observations serve as a powerful tool for testing chromospheric models on the basis of radio results. The following discussion is restricted to the millimeter part of the quiet solar spectrum and its interpretation.

2. THE MILLIMETER SPECTRUM OF THE QUIET SUN

The brightness temperature at the center of the disk $T_b^c(\lambda)$ has been measured by many authors during the last 50 years as was reviewed by Fuerst (1979), Nagnibeda and Piotrovich (1987), Fedoseev and Chernyshev (1998). However, the spectrum has not yet been established with the required accuracy. At the wavelengths under consideration the highest possible accuracy is provided by three methods: the "artificial Moon" method (2-3%), the standard antenna method (4%) and method based on the comparison with the

temperature of the new Moon (up to 5%). In two first methods due to the using of antennas with not narrow beams, the brightness temperature is averaged over the entire solar disk thus requiring special analysis of the contribution of the S-component. The latter method makes it possible to reduce the data obtained with different antenna beams to the center of the disk but strongly depends on the choice of the Moon's reference spectrum (the present-day reference spectrum can be found in Fedoseev and Chernyshev (1998)).

For our investigations we considered the millimeter experimental data from the above reviews completed with the submillimeter data of Lindsey *et. al.* (1995), the centimeter data of Zirin *et. al.* (1991). We included the experimental data obtained after the reviews were published – Bastian *et. al.* (1996), Urpo *et. al.* (1987), Efanov *et. al.* (1980). At the wavelength $\lambda = 3.4$ mm the central brightness temperatures were obtained by our group with the radiotelescope RT-7.5 of MSTU (Russia) using the method based on the new Moon reference spectrum (see, e.g., Nagnibeda and Piotrovich, 1994).

Multifrequency observations of the Quiet Sun brightness temperatures disclose scatter in the independent measurements (Fig. 1). The scatter can be referred to solar variability (see below), the difficulty in establishing of a precise reference spectrum and the fact that as a rule observations are made at a single wavelength with instruments with different angular resolution. Still at present many experimental data are obtained with angular resolution of about 1-4 arc min, therefore the Quiet Sun radiation represents the average emission of an inhomogeneous solar atmosphere. At longer centimeter wavelengths the Quiet Sun spectrum with high angular resolution was obtained by Zirin *et. al.* (1991) (Fig. 2).

The scatter in the independent measurements of different years and of different solar cycle phases led us to the idea of the investigation of the dependence between the Quiet Sun brightness temperatures and the solar cycle phases. The results of such investigation and their analysis are presented in the next sections.

Proc. 1st Solar & Space Weather Euroconference. 'The Solar Cycle and Terrestrial Climate', Santa Cruz de Tenerife, Tenerife, Spain, 25-29 September 2000 (ESA SP-463, December 2000)

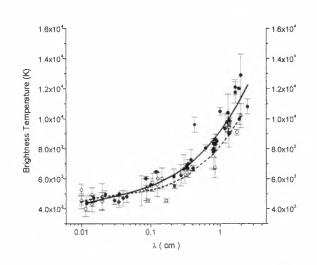


Fig. 1. - Observed brightness temperatures as a function of λ and its polynomial fit. Hollow circles and the dashed curve represents the data for the sunspot minimum phase, solid circles and the straight line - for the sunspot maximum phase. For the references to the experimental data see the text above.

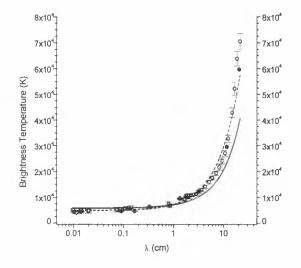


Fig. 2. – Combined mm and cm observed brightness temperatures as a function of λ for the sunspot minimum - hollow circles. Solid line represents the approximation with parameters taken from Piddington (1954), dashed line – the approximation with the parameters obtained in this work. Solid circles – cm observed brightness temperatures near solar minimum taken from Medar (2000).

3. THE QUIET SUN AT MILLIMETER WAVELENGTHS AND THE SOLAR CYCLE

The radio emission from the Sun consists of a semipermanent part referring to thermal radiation and a

superimposed variable part. The former is considered to change only slowly and slightly during the solar cycle and is called the emission of the Quiet Sun or Bcomponent. The variable part is composed partly of slowly varying component (S-component) of thermal origin and partly of non-thermal sporadic radiation. The first cyclic variations in the Quiet Sun spectrum and the Quiet Sun level at radio wavelengths were derived from the solar observations in the 19th solar cycle (Zheleznyakov, 1964). Several investigations were carried out to explore this phenomena (Piddington, 1954). The reason for the difference in the brightness temperatures of the Quiet Sun for different solar cycle phases can be seen in the fact, that in the period near sunspot maximum the measurements of the central brightness of the basic stable radiation are complicated by the presence of superimposed active components, particularly the S-component which is associated with sunspot and plage activity. This active component is very difficult to separate from the quiet B-component because the sunspot component is not proportional to the sunspot area and the contribution of decaying spots into the radio emission is decreasing much more slowly than their area does. The investigations of the cyclic brightness variations in the 8-32 cm range based on the data obtained with radio telescopes RATAN-600 (SAO, Russia) and Pulkovo radio telescope (Pulkovo, Russia) were presented by Borovik (1994). It was obtained that the emission measure of the coronal layers changes up to 40% during the solar cycle. At shorter wavelengths the difference up to 10-15% between the Quiet Sun brightness in different solar cycle phases was reported on the wavelength λ =3.2 cm (Zieba and Gula (1976)).

It is considered that for the wavelengths below 3 cm the dependence between the Quiet Sun brightness and the solar cycle is absent and $T_b^{c}(\lambda)$ is permanent during the solar cycle (see Borovik (1994)). In our investigations we have separated the experimental data obtained at the time near sunspot maximum and near solar minimum. The results can be seen in the Figures 1, 2, 3, 4. In spite of the given scatter in experimental data the difference in the obtained brightness temperature spectra for the sunspot maximum phase and the sunspot minimum phase is clearly seen. It can not be accounted for the incorrect separating of the sunspot associated component and the Quiet Sun component, because special investigations has shown that at millimeter wavelengths the sunspot component does not contribute significantly into the total radio emission (Loukitcheva and Nagnibeda, 1999).

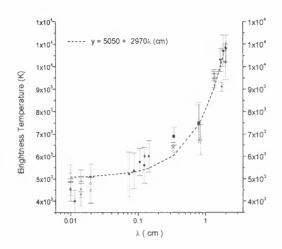


Fig. 3.- Observed brightness temperatures as a function of λ for the sunspot minimum and its fitting by a linear function with experimental errors as weights.

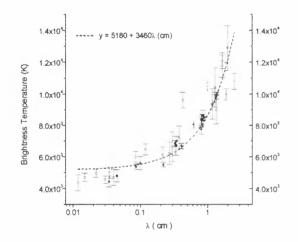


Fig. 3.- Observed brightness temperatures as a function of λ for the sunspot maximum and its fitting by a linear function with experimental errors as weights.

4. ANALYSIS OF THE MILLIMETER SPECTRA

Several empirical forms for the approximation of the brightness temperature spectrum $T_b{}^c(\lambda)$ at radio wavelengths are in use by different authors. One of the first and basic empirical approximations was obtained by Piddington (1954) in the following form:

$$T_b^{\ c}(v) = a + b \cdot v^{-1} + c \cdot v^{-2} \tag{1},$$

where *a*, *b* and *c* are constants found from the experimental data. Since that it has become generally accepted to treat $T_b^c(\lambda)$ in terms of a two component atmosphere with chromosphere contribution $(a + b \cdot v^{-l})$ and the coronal contribution $(c \cdot v^{-2})$. For millimeter wavelengths the chromospheric contribution exceeds considerably over the coronal contribution and this fact

provides a basis for investigating the chromosphere conditions from mm data. But the question is in what form to look for the chromospheric contribution into the brightness temperature. According to Piddington's approach the chromospheric $T_b^{\ c}(\lambda)$ is a linear function of the wavelength λ and then the electron temperature distribution in the chromosphere is expressed by:

$$T_e(\alpha) = a + b \cdot (\pi \cdot \alpha)^{-1/2}$$
(2),
where $\alpha = 0.07 \cdot_z \int^{c_0} N_e^2 \cdot T_e^{-3/2} dz.$

This does not itself constitute a model chromosphere but it may be used to test any model against the radio data. For deriving the coefficients a, b, c from the experimental data for the sunspot minimum we completed the mm data with the cm spectrum obtained by Zirin *et. al.* (1991) (Fig. 2). The experimental data we used in the investigation may be represented by equation (1), where now $a = 4885 \pm 200$, $b = 7.4 \cdot 10^{13}$, $c = 1.55 \cdot 10^{20}$. Then the chromospheric N_e-T_e relationship, which is a criterion for testing sunspot minimum models, becomes the following:

$$T_e(\alpha) = (4885 \pm 200) + 1.58 \cdot 10^{14} \cdot \{z^{f_0} N_e^2 \cdot T_e^{-3/2} dz \}^{-1/2}$$

We used this equation to test several atmosphere models (e.g. FAL model for the Quiet Sun (C) (Fontenla *et. al.*, 1993)) and obtained no coincidence between the model distributions of parameters and derived from the experimental millimeter data (for corresponding $T_b^{c}(\lambda)$ see Fig. 5).

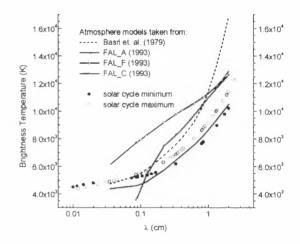


Fig. 5. – Calculated mm $T_b^c(\lambda)$ on the basis of FAL models (Fontenla *et. al.* (1993)), Basri et. al. (1979) model and linear approximations for observed $T_b^c(\lambda)$ for different phases of the solar cycle.

Fedoseev and Chernyshev (1998) used a linear law to reproduce their brightness temperatures at 0.87 - 8.86 mm as follows:

$$T_b^c(\lambda) = 5126(\pm 157) + 3720(\pm 290) \cdot \lambda(cm).$$

Using experimental data errors as weights we recalculated the coefficients on the basis of the data in the range 0.01-2.0 cm and got different values for the sunspot minimum condition and for the sunspot maximum condition. They were the following:

 $T_b^c(\lambda) = 5050(\pm 200) + 2970(\pm 175) \cdot \lambda(cm)$ for the minimum of the solar cycle and

 $T_b^c(\lambda) = 5180(\pm 155) + 3460(\pm 180) \cdot \lambda(cm)$ for the maximum.

It is seen that the coefficient values of Fedoseev and Chernyshev (1998), that were derived in the range of 0.87-8.86 mm, are close to our coefficients for the condition of the sunspot maximum.

The changes in the coefficients during the solar cycle may be interpreted in different ways. Assuming a linear law to reproduce $T_b^c(\lambda)$ we conclude that during the solar cycle the slope in the linear approximation changes significantly. This fact can be explained in terms of corresponding changes in chromosphere conditions (electron density or electron temperature). But any concrete conclusions about chromosphere variations with solar cycle should be made after considering different classes of functions to represent chromosphere contribution into the brightness temperature. Actual chromosphere is an opaque layer with a small temperature gradient and its contribution into the brightness temperature is far from the linear law. We consider that further investigations are needed in this direction.

5. RESULTS

On the basis of the analysis of the Quiet Sun brightness temperatures in the range 0.01-2.0 cm it was obtained that $T_b^{\,\,c}(\lambda)$ varies with the solar cycle phase. Assuming a linear law to reproduce $T_b^{\,\,c}(\lambda)$ the slope in the linear approximation changes significantly during the solar cycle.

The difference between $T_b^c(\lambda)$ during the sunspot minimum and $T_b^c(\lambda)$ during the sunspot maximum can not be accounted for the incorrect determination the Quiet Sun at the sunspot maximum phase.

We consider that a possible reason for cycle variations in T_b^c (λ) at millimeter wavelengths can be in corresponding changes in chromosphere conditions during the solar cycle (electron density or electron temperature) but further investigation is strongly required.

 $T_b^c(\lambda)$ for millimeter wavelengths with an assumption about the form of chromosphere and corona contributions into the brightness temperature can be used as a criterion for testing sunspot minimum models.

ACKNOWLEDGEMENTS

This work was partly supported by Russian scientific programs "Astronomy" (grant 1.5.2.2) and "Integration" (project AO107-2.1/2000).

REFERENCES

Basri, G.S., Linsky, J.L., Bartoe, J.-D.F., Brueckner, G., Van Hoosier M.E.: 1979, *ApJ*, 230, 924.

Bastian, T.S., Dulk, G.A., Leblanc, Y.: 1996, ApJ, 473, 539.

Borovik V.N.: 1994, *Lecture Notes in Physics*, 432, 185. Efanov, V.A., Moiseev, L.G., Nesterov, N.S., Stewart, R.T.: 1980, in M.R. Kundu and T.E. Gergely (eds.) *Radio Physics of the Sun*, 141.

Fedoseev, L.I., Chernyshev, V.I.: 1998, Astronomy Reports, 42, 105.

Fontenla, J. M.; Avrett, E. H.; Loeser, R.:, 1993, *ApJ*, 406, 319.

Fuerst E.: 1979, in M.R. Kundu and T.E. Gergely (eds.) Radio Physics of the Sun, 25.

Lindsey, C., Kopp, G.: 1995, ApJ, 453, 517.

Loukitcheva M.A., Nagnibeda V.G.: 1999, in J.-C. Vial and B. Kaldeich-Schuermann (eds.) *Plasma Dynamics* and Diagnostics in the Solar Transition Region and Corona, 450.

Medar, V.G.: 2000, *PhD Thesis*, Pulkovo observatory. Nagnibeda, V.G., Piotrovich, V.V.: 1987, *Trudy AO LGU*, 51, 5 (*in Russian*).

Nagnibeda, V.G., Piotrovich, V.V.: 1994, Sol. Phys., 152, 175.

Piddington J.H.: 1954, ApJ, 119, 531.

Urpo, S., Hildebrandt J., Krueger A.: 1987, Sol. Phys., 112, 119.

Zheleznyakov, V.V.: 1964, Radio Emission of the Sun and Planets, M., Nauka (in Russian).

Zieba S., Gula R.: 1976, Acta Astronomica, 26, 55.

Zirin H., Baumert B.M., Hurford G.J.: 1991, ApJ, 370, 779.

POLAR ACTIVITY AND MAGNETIC FIELD REVERSAL IN CURRENT SOLAR CYCLE 23

V.I.Makarov¹, V.V.Makarova¹, A.G.Tlatov¹, D.K.Callebaut², K.R.Sivaraman³

¹Pulkovo Astronomical Observatory, 196140, Saint Petersburg, Russia, ²Physics Department, UIA, University of Antwerp, B-2610, Belgium, ³Indian Institute of Astrophysics, Bangalore, 560034.India

ABSTRACT

Global solar cycle is considered as a manifestation of 3 types magnetic activity: polar, sunspot and largescale magnetic field cycles. We present polar activity cycle at the latitudes more than 40° marked by the white light polar faculae, bright magnetic regions according to SOHO/MDI, Nobeyama radio-data and magnetic neutral lines. We note that polar activity cycle is not dependent on sunspot activity. It is expected that polar magnetic field reversal in cycle 23 will be over in the late 2000.

Key words: global solar cycle: polar activity; sunspots; large-scale magnetic field.

1. INTRODUCTION

In early papers (Makarov (1984); Makarov & Sivaraman (1989): Callebaut & Makarov (1992); Makarov & Makarova (1996)) we clearly demonstrated that the global photospheric magnetic activity consists of three components: the high latitude and the low latitude components with the large-scale magnetic field at all latitudes. The high latitude component is represented by the corona emission, polar faculae and the ephemeral active regions, which makes its appearance after the polar reversal and is characterized by the polar faculae "butterfly" diagram. The second component is represented by the sunspots that appear when the first component is already at its peak. The third component is determined by the distribution of unipolar magnetic regions which are evident on magnetograms. In previous paper (Makarov & Tlatov (1999) we clearly demonstrated that the large-scale magnetic fields are primary regarding the sunspot magnetic fields and they do not result from the dispersal and transport of old active region magnetic fluxes. The recognition that the polar faculae is an important component of the global cycle is gaining strength as more and more observations on these structures accrue (Makarov & Sivaraman (1990); Makarov & Makarova (1996)). They possess kilo Gauss fields. Homan et al. (1998). The polar faculae have been identified in the broad band granulation frames of the Pulkovo Stratoscope flights (spatial resolution $\approx 0.24 arcsec$) and are seen to be made up of a conglomeration of a few structures in the size range of 200 - 400 km, Makarov et al. (1999). Two types of the "butterfly" diagrams, obviously, are connected with two different gradient of the inner solar rotation in the tachocline. This layer is likely to be the place where the solar dynamo operates (Goode et al. (1991); Thompson et al. (1996); Kosovichev et al. (1997))

Another aspect pertains to the large-scale magnetic fields and their poleward migration. Babcock (1959) showed that a magnetic field reversal at the poles took place in the middle of the solar cycle 19 (1955-1965). The subsequent reversals were monitored by Howard (1974). Makarov & Sivaraman (1983) demonstrated that these reversals can also be observed by monitoring the migration of the filament bands on the H-alpha synoptic charts and showed the excellent agreement between the polar reversals pattern obtained from the filament bands and those from the magnetograms. Following this, they worked out the epoch of polar field reversals over a period of nearly 12 solar cycles (1880-1980). Makarov & Sivaraman (1989). In this paper we describe the types solar activity, the zone structure and polar magnetic field reversal in cycle 23.

2. OBSERVATIONAL DATA

Observational data on polar activity and the migration of magnetic fields were obtained from SOHO/MD1 magnetograph. Kislovodsk white light polar faculae data set. H-alpha synoptic charts (Soln. Dann., 1978-2000) and Nobeyama radio data set.

3. RESULTS

In Figure 1 we show the position of the mean latitude of the filament bands in solar cycle 18-23. At the minimum of activity in 1995, the zone boundaries of the polemost filament bands designated by $\Theta_{N,2m}$ and $\Theta_{S,2m}$ in the N and S hemispheres and shown by filled circles in Figure 1 were located at latitudes

Proc. 1st Solar & Space Weather Euroconference. The Solar Cycle and Terrestrial Clunate', Santa Cruz de Tenerife, Tenerife, Spain, 25-29 September 2000 (ESA SP-463, December 2000)

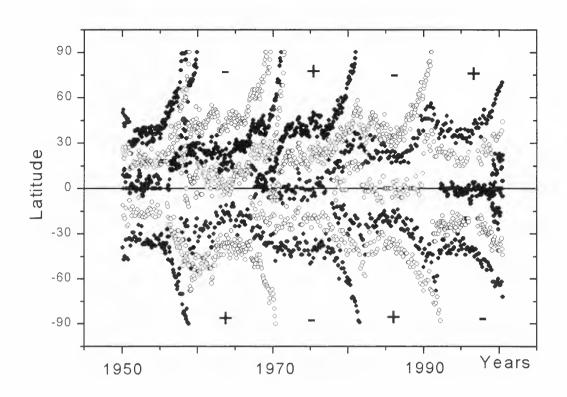


Figure 1. Migration trajectories of magnetic neutral lines of the large-scale magnetic fields derived from H-alpha synoptic charts in the N and S hemispheres for the period 1950-2000. In the north, filled circles represent the neutral line trajectory with the opposite polarities on either of its sides in the order (+/-) and open circles represent the trajectory of the neutral line with polarities on either of its sides in the order (-/+). In the south it is in the reverse order.

 $\Theta_{N,2m} = 36^{\circ}$ and $\Theta_{S,2m} = 39^{\circ}$. The next lower filament bands designated by $\Theta_{N,1m}$ and $\Theta_{S,1m}$ in the N and S hemispheres and were located at latitudes $\Theta_{N,1m} = 18^{\circ}$ and $\Theta_{S,1m} = 22^{\circ}$. During the years of minimum spot activity, the polar faculae were present at latitudes $\approx 50^{\circ}$ and higher in the N and S hemispheres and the filament bands remained more or less steady at the latitudes they have already reached, Figures 2. Although the polar reversal took place in 1991 the migration towards the poles started only by 1996 (with a speed of $V_{pw} \approx 3ms^{-1}$) when the sunspot activity picked up at the middle latitudes. By 2000.6 (rotation no. 1964) these zone boundaries migrated polewards in the Northern hemisphere to locations $\Theta_{N,2m} = 75^{\circ}$ and $\Theta_{N,1m} = 44^{\circ}$ and to locations in the Southern hemisphere $\Theta_{S,2m} = 72^{\circ}$ and $\Theta_{S,1m} = 44^{\circ}$. In addition, two more zonal boundaries formed at latitudes $\Theta_{N,0m} = 22^{\circ}$ and $\Theta_{S,0m} = -19^{\circ}$.

One interesting feature in Figure 1 is the formation of a new low latitude zone at the beginning of each cycle close to the equator. This would imply that the magnetic field reversal takes place close to the equator at the beginning of the cycle continuing through the years of minimum. This is an indication of the flux cancellation by the fragmented flux from spots very close to the equator which are the last vestiges of the cycle. Another feature seen in Figure 1 is that when the sunspot activity reaches its peak, the polemost filament bands at the latitudes $\approx (45^\circ - 50^\circ)$ suddenly accelerate with almost a ten fold increase in speed in their poleward migration (accelerates from $3 ms^{-1}$ up to about $30 ms^{-1}$) and reach the poles in about 3 years causing the polar field reversal. The fil-

ament bands below the polemost ones also commence their poleward journey synchronously and proceed almost at the same high speed as the polemost filament bands. But if the sunspot activity subsides by the time they reach the latitudes $\pm 45^{\circ}$, then these filament bands abruptly stop their poleward journey and either remain at the latitude they already are or at times tend to move towards the equator at very low speeds for a short period and stay at that latitude. This is what happens in a single fold reversal.

Whereas in a three fold reversal, the filament bands just below the polemost ones also reach latitudes $\pm (45^{\circ} - 50^{\circ})$, while the sunspot activity is still in progress and so they proceed poleward with the same high speed as the pole most ones and reach the poles and this is followed by the third filament band too causing the final reversal of the three fold reversal process. The three fold reversal seems to be generally a characteristic of cycles with high and persistent sunspot activity, if not it ends up in a single fold reversal. These situations raise questions about the role of the meridional motions in transporting the fields towards the poles. Why does the meridional circulation become effective only with the rapid rise in solar activity and not during the years of minimum? None of the filament bands show any sign of poleward journey during the years of solar minimum. As soon as the sunspot activity picks up, the filament starts the poleward journey with a speed of $V_{pw} \approx 3ms^{-1}$ and when the activity reaches high levels, it accelerates to $V_{pw} \approx 30 m s^{-1}$. This may mean that either the meridional flows are weaker during the years of minimum or there are no significant flux in the sunspot

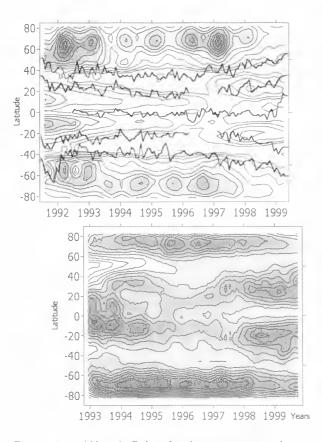


Figure 2. (Above) Polar faculae, sunspot and magnetic neutral line cycles according to Kislovodsk observations. The zone boundaries of the polemost filament bands distinguish high-latitude activity cycle at the Northern and Sounhern hemispheres. (Below) Polar activity and sunspot cycles according to Nobeyama radio observations. Active regions with T > 11700K were selected.

belt (due to the paucity of sunspots during the years of deep minimum) to be transported although the meridional flows are present all the time with no significant cycle related changes. Although the latter possibility would seem more realistic and consistent with the modest dynamical concepts of flows on the solar surface we cannot rule out the possibility of a cycle dependence which according to Snodgrass & Dailey (1996) is rather complex but does not disagree with our results.

On the other hand in our study if there are no magnetic tracers available to be transported we would not perceive any motion although it might be present all the time. We have seen that only when the spot activity has picked up, the polemost filaments cross the $\pm 45^{\circ}$ latitudes with accelerated speeds and cause the reversal. While, if the sunspot activity has subsided by the time the filament band just below the polemost one reaches the $(45^{\circ} - 50^{\circ})$ latitude position then, it does not proceed further but hovers around the 45° latitude belt until the sunspot activity of the next cycle builds up. This indicates that the remnant flux from decaying active regions that still remain on the surface (even after cancellation, submerging etc) do not constitute a body of flux sufficient to effect further cancellation and hence the neutral line does not shift towards the poles. This neutral line (now the polemost one) seems to wait for the activity of the next cycle to build up to start its poleward jour-

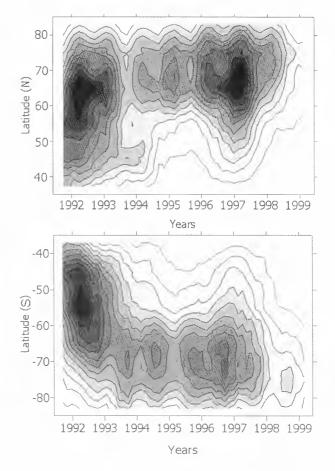


Figure 3. Polar faculae "batterfly" diagram for cycle 23 during 1991-1999. It is clear seen that the zone of appearance of the polar faculae starts at $50^{\circ} - 70^{\circ}$ and then migrates to $60^{\circ} - 80^{\circ}$ after the polar magnetic field reversal.

ney. Also the $\pm(45^{\circ} - 50^{\circ})$ belt seems to act like a boundary where the decision whether the filament band will proceed poleward or stay stagnant takes place. Thus the poleward migration of the neutral lines seems to depend very sensitively on the sunspot activity, Makarov & Callebaut (1999).

It is clear seen that the zone of appearance of the polar faculae starts at $50^{\circ} - 70^{\circ}$ and then migrates to $60^{\circ} - 80^{\circ}$ after the polar magnetic field reversal. Figure 3. The large fluctuations in the latitude of the lower boundary of the polar faculae is seen very clearly to be episodic like the episodic emergence of sunspots from the interior. But these fluctuations are not shown by the neutral lines. They seem to remain more or less at the same latitude waiting for sunspot activity to build up and for the sunspot flux to arrive from lower latitudes.

4. CONCLUSION

We have presented the polar activity cycle and magnetic field reversal pattern for cycle 23. Figures 1-3. It is expected that polar magnetic field reversal in cycle 23 will be over in the late 2000. Latitude time distribution of the magnetic fields "+" and "-" polarities according to SOHO/MDI data set confirms the

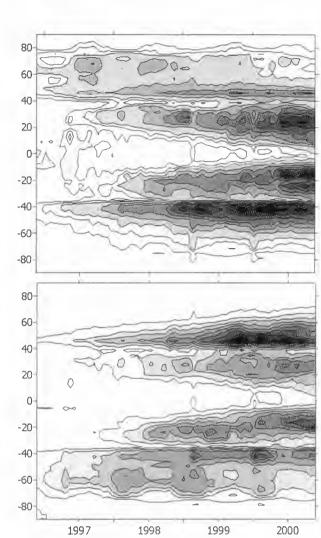


Figure 4. Latitude-time distribution of the magnetic fields of "+" (above) and "-" polarities (below) according to SOHO/MDI data set. This pattern clearly demonstrated the global photospheric magnetic activity that consists of two components: the high latitude and the low latitude components.

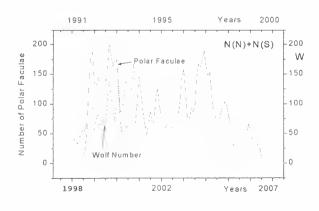


Figure 5. N(N)+N(S): Time-variation of the number polar faculae for 1991-1999 and Wolf number for 1997-2000. A shift time T is 6.8 yrs.

zone structure of magnetic field, Figure 4. It is clear seen the "calm forties" and two types solar activity that are divided by its. There is a meaningful correlation between the number of polar faculae and the sunspot numbers of the next cycle, Figure 5.

5. ACKNOWLEDGMENTS

One of us (M.V.I.) is grateful to the organizers of the First SOLSPA - Euroconference "The Solar Cycle and Terrestrial Climate" held in Santa Cruz, Tenerife (Spain) from 25th to 29th September 2000, for financial support. This work was partially supported by the grants: RFBR 99-02-16200, 00-02-16355, INTAS 97-1088 and NRA 98-OSS-08.

REFERENCES

- Babcock, H.D., 1959, Ap.J., 130, 364
- Callebaut, D.K., Makarov, V.I., 1992, Solar Phys., 141, 381
- Goode, P. R., Dziembowski, W. A., Korzennik, S. G., Rhodes, E.J., 1991, Ap. J., 367, 649
- Homann, T., Kneer, F., Makarov, V.I., 1998, Solar Phys., 175, 81
- Howard, R., 1974, Solar Phys. 38, 283
- Kosovichev, A.G., Schou, J., Scherrer, P.H., the SOHO Team, 1997, in (Eds) Fleck, B., Svestka, Z. "The first results from SOHO", 43
- Makarov, V.I., Sivaraman, K.R., 1983, Solar Phys., 85, 227
- Makarov, V.I., 1984, Solar Phys., 93, 393
- Makarov, V.I., Sivaraman, K.R., 1989, Solar Phys., 119, 35
- Makarov, V.I., Sivaraman, K.R., 1990, in (ed) J.O.Stenflo, Solar Photosphere: Structure, Convection, and Magnetic fields, IAU Symp., 138, 281
- Makarov, V.I., Makarova, V.V., 1996. Solar Phys., 163, 267
- Makarov, V.I. and Callebaut, D.K., 1999, in (ed.) A.Wilson, Proc. 9th European Meeting on Solar Physics, "Magnetic Field and Solar Processes", Florence, Italy, 117
- Makarov, V.I. and Tlatov A.G., 1999, in (ed.) A.Wilson, Proc. 9th European Meeting on Solar Physics, "Magnetic Field and Solar Processes", Florence, Italy, 125
- Makarov, V.I., Okunev, O.V., Pravdjuk, L.M. Kneer, F., 1999, in (eds.) A.Antalova; H.Balthasar; and A.Kucera, Annual Report 1998, Joint Organisation for Solar Observations, 151
- Snodgrass, H.B., Dailey, S.B., 1996, Solar Phys. 163, 21
- Soln.Dann., 1978-1999, "Solnechnye Dannye Bull.", Saint Petersburg, Pulkovo.
- Thompson, M.J., Toomre, J., the GONG Team, 1996, Science, 272, 1300

SOLAR ACTIVITY LEVEL ON THE ASCENDING PHASE OF THE SOLAR CYCLE 23

G. Maris, M.-D. Popescu, A. Oncica, A.-C. Donea

Astronomical Institute of the Romanian Academy St. Cutitul de Argint 5, RO-75212 Bucharest 28, Romania Fax: +40 1 337.33.89; tel.: +40 1 335 80 10 E-mail: gmaris@roastro.astro.ro

ABSTRACT

We investigate the statistical behavior of sunspot. X-ray flares, coronal mass ejections, solar proton events during the ascending phase of the solar cycle 23 (1996 - 2000). The time distribution of these phenomena and the heliographic distribution for some of them are considered. A short notification of their influences in geomagnetic field is done. The comparison of the results with the corresponding phases of the previous cycles (nos. 21 - 22) is made.

1. SOLAR CYCLE 23: THE FORECAST AND THE OBSERVATIONS

According to sunspot relative number (smoothed), the SC 23 minimum was in May 1996 with a value of 8.0. According to the number of days without any sunspot the cycle's minimum appeared in October 1996 (26 spotless

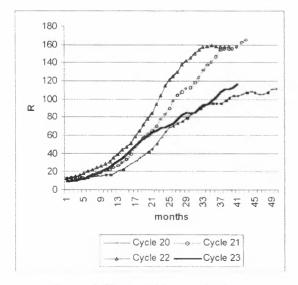


Figure 1. The monthly smoothed sunspot relative number for SC 20-23

days) when the observed monthly R was 1.8. Solar cycle 23 was originally predicted to reach a magnitude comparable with those of the solar cycle 21.

The figure 1 presents the monthly values of the Wolf smoothed number according to the SIDC's values on the ascending phases of solar cycles 20 - 23. During the first 16 months of the current cycle 23, the R values were higher than the cycle 21 ones. After the 24^{th} month from the minimum, the R values follow the trend of the SC 20. It means the solar cycle 23 might be a long and not a high cycle, just like cycle 20. The ascending phase of the current cycle begins in September 1997.

The first active region of the solar cycle 23 appeared on May 1996, just in the minimum phase. This appearance produced very late in comparison with the previous cycles when the first active region of the new ones appeared on the first half of descending phase. This late appearance might be an information about a slow amplification of the new cycle's toroidal magnetic field underneath the convective zone. This fact, could it give any information about the level of the new cycle? Further studies are necessary to investigate such cases. The active region of the 23rd SC became predominant in comparison with the old ones of the 22nd SC after February 1997. The total number of the active regions during the ascending phase of the 23rd SC is considerably smaller in comparison with that registered in the previous cycles. 21 and 22 (Ishkov, 2000). Contrary, the number of the coronal holes is increasing from the SC 21 to SC 23 (see Table 1). The coronal holes seem to appear casier into a less perturbed corona lying above the photosphere with fewer active regions.

Table 1. The number of the active regions (AR) and coronal holes (CII) during the first 48 months of the SC 21 - 23

Phenomenon	SC 21	SC 22	SC 23
AR	1771	1490	1059
СН	>142	165	301

Proc. 1st Solar & Space Weather Euroconference, 'The Solar Cycle and Terrestrial Climate', Santa Cruz de Tenerife, Tenerife, Spain, 25-29 September 2000 (ESA SP-463, December 2000)

The sunspot groups of the 23^{rd} SC are smaller and less complex than usually and they are evolving slower than normal. Many of them are longer-lived than the sunspot groups on the ascending phase in other cycles. These properties prove a more stability of the active regions; that may be due to a weaker circulation in the solar convective zone (Ishkov, 2000).

2. THE OCCURRENCE OF SOLAR FLARES DURING 1996 – 2000

Flare activity is less important than in cycles 20, 21 and 22. according to data published recently in the NOAA Solar-Geophysical Reports. This is consistent with the average qualities of the sunspot groups. The total number of the optical and X-ray solar flares as well as the solar flare with geomagnetic consequences during the ascending phase of the 23^{rd} SC is considerably smaller than the those registered during the same period in previous solar cycles (20 - 22) (Ishkov 2000).

Solar flares create a massive electromagnetic explosion in the upper solar atmosphere. It is expected that the site where the particles are accelerated be dominated. for the X-type solar flares, by strong shocks. The shocks going downwards towards the photosphere produce the "sunquakes". Solar flares are the most variable seismic phenomena. They produce "sunquakes" (Kosovichev and Zarkova, 1998) which are quantified with "egression power maps" (Donea et al., 1999) revealing the

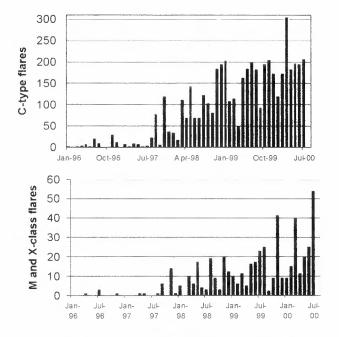


Figure 2. The monthly distribution of the X-ray flares (C-class – the upper panel, M and X-class – the underneath panel)

dimension of the acoustic source involved in the flare explosion. This phenomena was for the first time observed in 1996 July 9, in NOAA AR 7978, during the time when the Sun was at activity minimum. The solar flares that may produce "sunquakes" are the most powerful ones, that classified as X or M solar type. We shall emphasize on the X-ray solar flares registered during the interval 1996 – 2000.

The representation of the number of the C. M and X-type solar flares (no./months) during the period January 1996–July 2000 can be seen in the figure 3. For both types of X-ray flare. C-type and M+X-type. the high flare activity after November 1999 could be remarked. The highest C-type X-ray flare took place in March 2000. Three maxima are revealing for the M and X-class of X-ray flares in November 1999, March and July 2000. the last one being the highest.

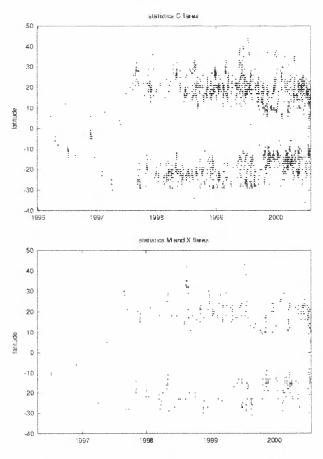


Figure 3. The Butterfly Diagram of the X-ray flares (C-class – the upper panel, M and X-class – the underneath panel)

The heliographic distributions of the X-ray flares is presented in the figure 3 (the Butterfly diagram). separately for the C-class and for the (M and X)-class. It

is worth to draw attention on the high latitude X-ray flares of more than 40° north: in 1999 – for C-class and, in 1998 and 1999 for M and X-class, respectively. We have calculated the yearly north – south asymmetry of this distribution by the ratio:

A= (N-S)/(N+S).

N and S are the annual flare numbers observed in northern and southern solar hemisphere, respectively. The result is shown in the figure 4. The Northern Hemisphere is dominating in X-flare occurrence during the ascending phase of the 23^{rd} SC. Verma (1987) found that asymmetrics in all phenomena prevailed in the north during SC 19 and 20 and in the south in SC 21. The southern preference was shown by the total number of solar flares during the 1987 – 1991 period of the 22^{nd} SC (Mariş et al., 1993). Schmieder et all. (2000) found a southern dominance for the X-ray solar flare during the

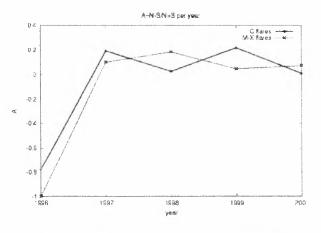


Figure 4. The yearly values of the North-South asymmetry of the X-ray flares

period 1987 – 1992 (an important interval of the 22^{nd} SC). These aspects of the north – south asymmetry could suggest a 22 years dominance of one hemisphere's flare activity.

3. CORONAL MASS EJECTIONS AND OTHER ENERGETIC SOLAR PHENOMENA

Coronal Mass Ejections (CME) occur, like other phenomena of solar activity, with a variable frequency during the 11-years solar cycle. It was estimated, from the data of the 22nd SC, that the Sun emitted about 3.5 CMEs/day near solar maximum and only about 0.1 CMEs/day near solar activity minimum (Gosling, 1993). The SOHO data will improve certainly the CME's statistics for the current cycle.

CMEs, the most spectacular manifestations of solar activity, are propelling outward into interplanetary space a huge quantity of solar material (about 10^{16} g). The

CMEs are linked with other solar activity and their connections with geomagnetic events are now recognized. In this end we are considered here the statistics of the CMEs in comparison with that of Solar Proton Events (SPE) affecting the Earth environment (http://ngdc.noaa.gov/STP/SOLAR_DATA).

SPEs suppose solar energetic particles accelerated above solar active regions from the available coronal material during solar flares. In this respect, of their particles' origin, the CMEs and SPEs have a common point. From the SC 19 – 22 data, it appears that the majority of SPEs occur from the second to the eight years after sunspot minimum (Shea and Smart. 1989). The figure 5 presents the monthly number of CMEs and SPEs registered since 1996.

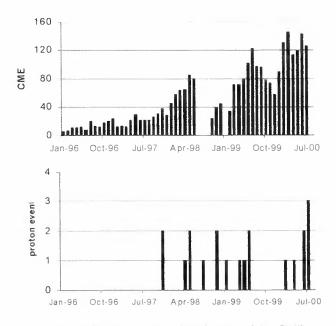


Figure 5. The monthly distribution of the CMEs and SPEs (the upper and the underneath panel, respectively)

As Shea and Smart (1992) notified, the SPEs occurred in "sequences of activity". Such sequences may be due to multiple particle events associated with multiple flares from the same active regions or, to different regions on the Sun producing a bulk of solar particles.

The CMEs may be also considered as appearing in "sequences of activity". So, it could be remarked the sequences centered on May 1997. May 1998. July 1999. March and July 2000. Some of these sequences are coincident with the SPEs' ones (May 1998. July 1999 and July 2000). The statistics of the CMEs associated with SPEs during the 1979 – 1985 period (Mariş et al. 1992), reveled the high CMEs' parameters: velocity

between 600 and 1000 km/s; large span (more than 90°); long distance of propagation (more than 6 R_{\odot}). Such association of solar events is very geoeffective more than 85% are followed by some geomagnetic event.

4. GEOMAGNETIC ACTIVITY

Geomagnetic activity can have a devastating effect on the spacecraft operating in the near-Earth space, on the communication systems relying upon the high-latitude ionosphere, and on a wide variety of human groundbased technological systems.

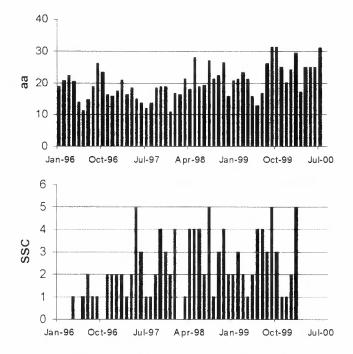


Figure 6. The monthly mean value of the aa geomagnetic index (upper panel) and the monthly number of SSC (underneath panel)

The figure 6 presents the geomagnetic activity level by the monthly mean values of the aa-index and the monthly number of the sudden storm commencements (SSC). The monthly distribution of the SSCs' number presents the same appearance in "sequences". So, it could be remarked the high activity in May 1997, April – June 1998, June – October 1999, and February 1999. The majority of these sequences are coincident with the CMEs and SPEs' high activity.

5. CONCLUSIONS

The general trend in recent solar cycle is toward a medium sunspot activity and longer duration cycle. like SC 20. The SC 19 was the largest in recorded history and SC 22 was the third largest. The SC 21 lasted 10 years

and 3 months while cycle 22 lasted only 9 years and 8 months. The longest cycle in the recent history of solar activity was cycle 20 that lasted 11 years and 7 months. The 22-year solar cycle must be considered as a "physical unit" of the solar activity taking into account the magnetic properties of the sunspot and the mean solar magnetic field evolution. The 22-year "unit" consists of two 11-year solar cycle, a even – odd pair. Gnevyshev and Ohl, in 1948, indicated that the odd 11-years sunspot cycles should be mightier than previous even solar cycle. Since SC 23 is an odd numbered cycle it must be extremely high, according to the Gnevyshev and Ohl's rule. However, the current cycle evolution does not abide by this rule.

The dramatic variability from one cycle to the next in the sunspot records shows the difficulty in making empirical predictions of solar activity.

ACKNOWLEDGEMENTS

Two of us (G. M. and M.-D. P.) are grateful to the organizers of the First SOLSPA Euroconference for financial support to attend the meeting.

REFERENCES

Donea, A.C., Braun D., and Lindsey C., 1999, Ap. J., 513, L143

Gosling, J.T., 1992, Bull. Am. Phys. Soc., 37, 1466

- Ishkov, V.N., 2000, JENAM Poster Session
- Kosovichev. A. G., Zharkova, V. V., 1998, Nature, 393, 317
- Mariş, G., Pojoga, S., and Dinulescu S., 1992, in: Fischer S. and Vandras M. (eds.). Proc. of the First SOLTIP Symposium. Astron. Inst. Of the Czechoslovak Acad. Sci., p. 131

Mariş, G., Dinulescu, S., and Dumitrache, C., 1993, Rom, Astr. J., 3, 105

Schmieder, B., Li, K.J., and Li, Q.S., 2000, this volume.

Shea, M.A., Smart, D.F., 1989, J. Spacecraft and Rockets, 26, 403

Shea. M.A., Smart, D.F., 1992, Radiocarbon, 34, 255

Verma, V.K., 1987, Solar Physics, 114, 185

PRESENTATION OF FIRST RESULTS FROM MULTI-SPECTRAL SOLAR PATROL SYSTEM AND THEIR COMPARING WITH SOME WORLD DATA

Eva Marková, Marcel Bělík, Jan Klimeš, sr., Jan Klimeš, jr. Observatory Úpice, 542 32 Úpice, Czech Republic markovae@mbox.vol.cz, marcel belik@yahoo.com, sunarchiv@volny.cz

ABSTRACT

The multi-spectral solar patrol system in Úpice observatory start the observation of the Sun in H-alpha, Call-K and white light in August '98. At the paper some interesting events are presented and supplemented with some other world data.

INTRODUCTION

Observation of the Sun in the different spectral ranges from terrestrial observations plays important role in solar research, even in actual "satellite epoch". These data complement satellite data and they guarantee uninterrupted series of observation in the case of failure of satellite. Moreover, the great advantage of terrestrial observation is relatively low cost of obtained data, as well as the flexibility of experiment settings and easy possibility of modernizing of experiment. Very big handicap of terrestrial observation consists in the strong dependence on the weather condition.

HISTORY OF SOLAR OBSERVATION ON OBSERVATORY ÚPICE

Observation of the solar activity on Observatory Úpice ($16^{\circ}0'43,5$ ''E, $50^{\circ}30'26,6$ ''N, 416 m above sea level) started in March 1964. At that time only observation on frequency 29,5 MHz (CN) was carried. Observation on another frequencies started little later – 27,5 kHz (SEA) in March 1965 and 32,8 MHz (CN) in 1972. The radio data are published on Solar Geophysical Data from 1972 (SGD, 1972-2000). The patrol observation in Halpha line was performed during 1966 - 1974. All the data obtained during above-mentioned time range of H-alpha patrol observation are stored on 36 mm black and white film (full disc and details). These data are complemented by daily charts of solar photosphere. During the 1974 – 1998 the observation on H-alpha line was interrupted due the big financial and technical troubles connected with repair of H-alpha filter. All the optical parts of solar telescope was reconstructed and modernized. Moreover, the Call-K filter, white-light and the next "spectral" part of the telescope were added (Klimeš et al., 1999).

At present time, the radio data are orderly published in SGD. Moreover, they are monthly published on www pages of Observatory Úpice: www.trutnov.vol.cz/obsupice/radio. The data from H-alpha and Call-K lines, as well as the pictures of photosphere are daily published on www pages: www.trutnov.vol.cz/obsupice/halfa.

THE FIRST SIGNIFICANT RESULTS

a) THE APRIL 15TH, 2000 FLARE PHENOMENA

Very interesting solar flare was observed by rebuilt "multi-spectral solar patrol system" on April 15th, 2000. SF level flare had occurred in active region NOAA 8955, with maximum at 10:18 UT. This feature emitted X-emission of middle level M4 importance. The proton emission was not detected. This active region was the source of the next faint flares (SGD, 2000).

All these events was observed in H-alpha and CAII-K lines and in CN (33 MHz) and SEA (27 kHz) frequencies (fig. 1 and 2). Moreover, the detection of X-ray emission from GOES 8 is shown on fig. 1 (http://www.sec.noaa.gov/).

b) THE MAY 15TH, 2000 FLARE PHENOMENA

On May 15th, 2000 the next interesting flare phenomena was observed. The prominence situated on eastern limb of the quiet solar disc come to move off due the under-limb flare at 8:35 UT (fig. 3). Subsequently, the solar flare located near north-eastern limb was activated. This flare further accelerated moving of mentioned

Proc. 1st Solar & Space Weather Euroconference, 'The Solar Cycle and Terrestrial Climate', Santa Cruz de Tenerife, Tenerife, Spain, 25-29 September 2000 (ESA SP-463, December 2000)

prominence and at the same time eruption filaments took up (fig. 4a, b). Sequential shock wave, expanding through the solar disc, activated the next solar flare at western part of solar disc. All flare events were observed on SEA (Sudden Enhancement of Atmospherics) registration on Observatory Úpice. On fig. 5 a, b one can see the pictures of violent CME observed at 9:42 and 10:42 UT on LASCO 3 coronograph on SOHO satellite (http://sohodata.nascom.nasa.gov). All above mentioned events are clearly visible on animation composed from Observatory Úpice and LASCO pictures. We can to see clear spatial and time continuation of violent CME on discussed flare event.

CONCLUSIONS

Both described phenomena are a part of wide collection of observations, obtained on Observatory Úpice from 1998. The rebuilt and modernized "multi-spectral solar patrol system" produce every sunny day series of pictures and video sequences in H-alpha, CaII-K and whitelight. The one picture in every line is placed on www pages as soon as possible. Moreover, it is prepared the digitalization of pictures in H-alpha, obtained during 1966 – 1974. All these digitized "old" pictures will be placed on www pages.

REFERENCES

- Klimeš, J., jr, Bělík, M., Klimeš, J., sr., Marková,
 E.: Simultaneous Observation of the Sun in White-light, H-alpha, Ca and Radio Waves on Observatory Úpice, 1999, Proc. of the 8th SOHO Workshop, Paris, France, 22-25 June 1999 (ESA SP-446, October 1999)
- Solar Geophysical Data, Part I,II, 1997-2000, NOAA Boulder USA
- http://mesola.obspm.fr/nancay2d.html http://sohodata.nascom.nasa.gov http://www.sec.noaa.gov/

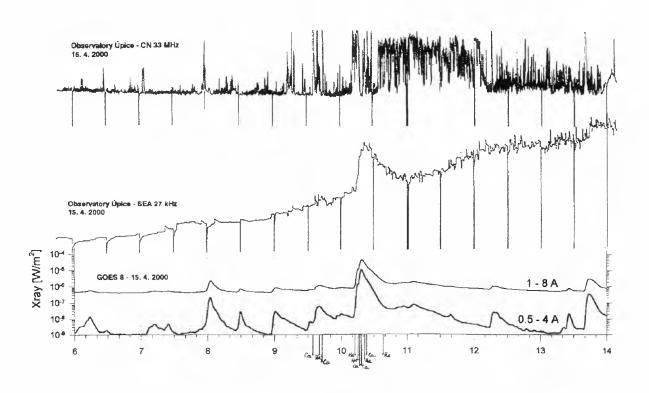


Fig. 1: Registration SEA 27 kHz, CN 33 MHz (Úpice) and X-emission on GOES 8 (15.4.2000)

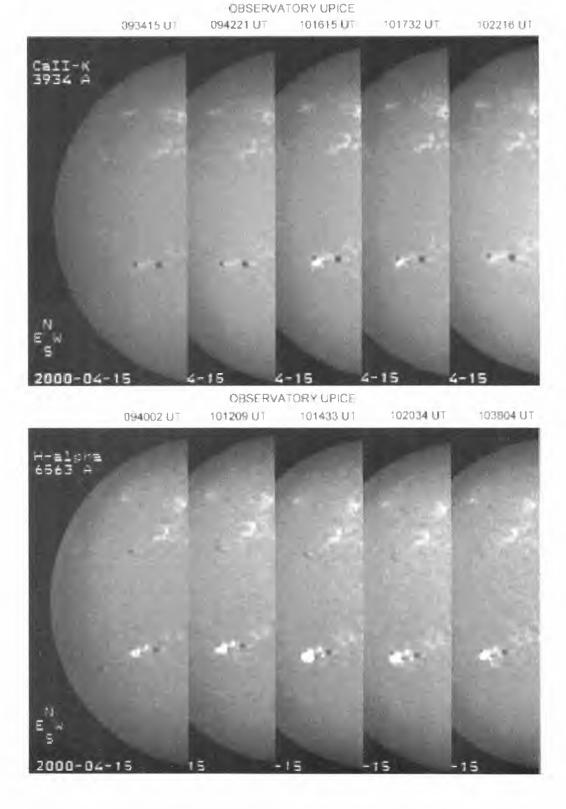


Fig.2: Sequence of snapshots in H-alpha a Call-K (Úpice) from April 15th, 2000

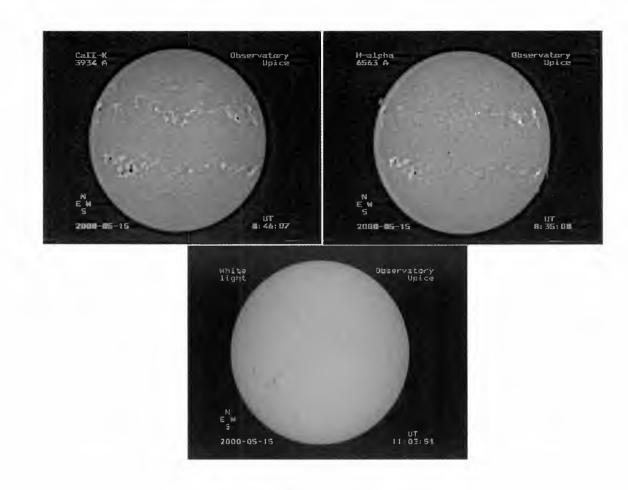


Fig.3: Situation on solar disc in H-alpha, CaII-K a WL on May 15th, 2000

H - alpha (6563A)	15.5.2000	OBSERVATORY ÚPICE
-------------------	-----------	-------------------



Fig.4a: Sequence of snapshot in H-alpha (Úpice) on May 15th, 2000

15.5.2000

OBSERVATORY ÚPICE



White light 110351 UT
White light
110351 UT
White light
110351 UT

Fig. 4b: Sequence of snapshot in Call-K (Úpice) on May 15th, 2000

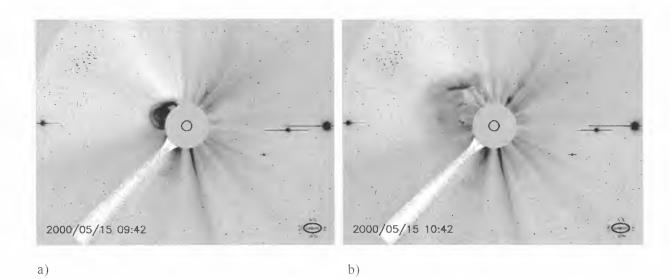


Fig. 5a, b: Lasco3 pictures (SOHO) obtained at 09:42 UT (a) and at 10:42 UT (b) (SOHO is a project of international cooperation between ESA and NASA)

LOCAL AND GLOBAL MAGNETIC OSCILLATIONS IN THE PHOTOSPHERE

P.F. Moretti¹, A. Cacciani², A. Hanslmeier³, M. Messerotti⁴, and W. Otruba⁵

¹Osservatorio Astronomico di Capodimonte, Via Moiarello 16, 80131 Napoli, Italy, moretti@na.astro.it

²Department of Physics, University of Rome La Sapienza, Italy

³Institut für Geophysik, Astrophysik und Meteorologie, Graz, Austria

⁴Osservatorio Astronomico di Trieste, Italy

⁵Sonnenobservatorium Kanzelhöhe, Austria

ABSTRACT

The solar influence on the terrestial climate is typically associated to changes during the solar cycle. that is at timescales of years and more. In fact, the variability seems to be related to the magnetic activity. Nevertheless, the dynamic of the magnetic field is still not well understood. The characteristics of the processes acting at higher temporal frequencies (such as flares etc.) are clearly a signature of the long term magnetic changes and their investigation supports the understanding of the energy relaxing in the interplanetary space. Four hour fulldisk magnetograms (with a 4 arcsec/pix resolution) obtained in the Sodium D-lines have been analyzed pixel-bypixel (locally) and in the $\ell - \nu$ diagram (globally). The magnetic oscillation have been detected at different frequencies and identified on the solar disk. Some oscillations have been correlated to the $H\alpha$ bright points as the signature of the magnetic reconnection and subsequent plasma out-flow.

1. INTRODUCTION

The solar magnetic field has been thought almost stationary for centuries. The 22 year cycle has usually been considered the only relevant change in the magnetism related to the dynamo process. A more complete understanding of the processes that lead to the solar cycle changes and the heating of the corona asks for further observations of the dynamic small scale magnetic structures of the Sun. Indeed, the measure of low and small magnetic fluxes and its interpretation in terms of magnetic field is not a trivial task. Most of the knowledge of the fast evolving magnetic structures is carried by indirect observations in the radio or in the Fraunhofer lines formed in the chromosphere, where the magnetic energy dominates. Data are often in disagreement when finding spatial and temporal correlation between Ca K bright points, magnetic field, Uv jets ecc. (Cook, Rutten and Hoekzema, 1996, Hoekzema. Rutten and Cook, 1997, Lites, Rutten and Berger, 1999) In the photosphere, the magnetic field fluctuations have been primarily framed in the research of the magneto-acoustic waves in spots (Lites, 1992, Lites et al. 1998, Horn et al., 1997, Cacciani et al., 1998, Ruedi et al., 1998). and recently in the quiet sun (Ulrich, 1996). Anyway, it seems reasonable that the magnetic field anchored to the base of the convective zone and dominated by the plasma motions up to the photosphere, is closely related to the chromospheric network behavior and the scenarios should match each other.

Transition region explosive events have been correlated to magnetic cancellation as a consequence of the relaxed magnetic ropes upward expansion (Chae et al., 1998), but these cancellations are difficult to localize due to their small scales (1"). In the framework of the solar five-minute oscillations and their origin, the seismic flux has been found to be related to downflows in the intergranular lanes (Goode et al., 1998, Espagnet et al., 1996). This phenomenum has been invoked to explain the solar "background" in the intensity (I) velocity (V) phase difference spectra (Skartlien and Rast, 2000) but no observational evidences of the relation between the magnetic flux and the downflows have been found yet. On the other hand, some observational evidences seem to attribute the inhibition of the p-modes power by the magnetic activity: velocity local seismology in magnetic regions has proofed the absorption of the pmodes power at low frequencies and its enhancement at the highers (Braun and Lindsey, 1999). A possible explanation of this apparent contradiction could be attributed to the presence of distinct processes involving the magnetic and the kinetic energy: the generation of the solar oscillations by continuous jets of plasma triggered by the magnetic reconnections and the interaction of the velocity field with the established, long term variable, magnetic field. In this paper we present the characteristic of the full-disk magnetic oscillations in a day at the beginning of 1998. The results are similar for different days in that period of the solar cycle.

Proc. 1st Solar & Space Weather Euroconference, 'The Solar Cycle and Terrestrial Climate', Santa Cruz de Tenerife, Tenerife, Spain 25-29 September 2000 (ESA SP-463, December 2000)

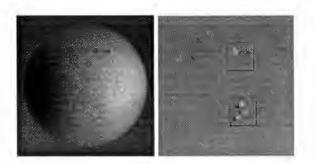


Figure 1. a dopplergram (left) and a magnetogram (right) obtained on 30 January 1998 at Kanzelhöhe. The upper frame in the magnetogram limits the selection shown in figure 2.

2. THE DATA ANALYSIS

The data consist of two sets of simultaneous dopplergrams and magnetograms obtained with a sodium Magneto-Optical Filter (MOF) at Kanzelhöhe on 30 january 1998. The images have been acquired every minute and 256 minutes have been selected for the analysis. The spatial resolution is 4.3 arcsec/pix.

All the images have been calibrated (Moretti & the MOF Development Group, 2000) and registered. The full-disk data have been treated locally (pixel-by-pixel) and globally (using the spherical harmonics decomposition) to obtain the power distribution on the disk and the $\ell - \nu$ diagram. The dayly trend has been removed in the pixel-by-pixel time-series using a polynomial fit, while a differential filter has been used in the spherical harmonics decomposition. The final spectra have been corrected for the filtering of the data.

Let us consider what a $\ell - \nu$ diagram is : the velocity (or whatever other signal) is filtered by some masks and the coefficients of its decomposition in these masks are displayed.

In seismology, these coefficients are related to a global resonance but they still are the contributions to the signal, in a particular spatial scale and at a particular frequency. The modes are the components you need to explain a particular configuration in time of the distribution of the velocity on the solar surface. When the velocity and intensity oscillations are treated locally, their trait is different as the mixing with the local phenomena and their characteristic distributions on the disk is not washed out by a filter as the spherical harmonics do.

The local analysis uses a three-dimensional representation, as the distribution on the disk (in x,y) has to be visualized in function of the frequency (ν). In fact, the images time-series are pixel-by-pixel fast fourier transformed (FFT) and the power and phase difference maps are obtained. This kind of analysis permits to investigate the distribution on the disk of the oscillating power and phase but cannot intrinsically achieve a high frequency resolution. In fact, long time-series would produce a spatial average because of the solar rotation and of the evolution of the structures on the solar surface. The granules and supergranules have time-scales of 10 minutes and hours with dimensions of 1'' and tenths of arcseconds respectively. The structures would lose their identity after a lifetime and a compromise has to be reached not to wash out anything but the rotation.

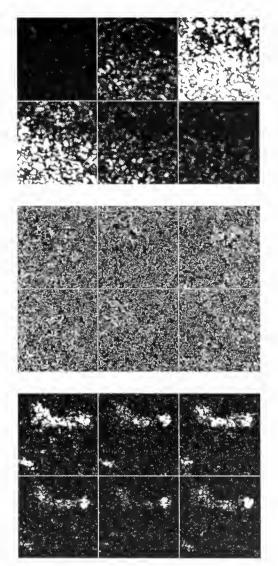


Figure 2. The velocity power (top), the V-B phase difference (center) and the longitudinal magnetic power (bottom) for the selected upper area in figure 1 at 0.91, 2.47, 3.16, 3.78, 4.88, 5.53 mHz (from top left to bottom right). The black to white scales are: for the velocity power from 0 to 200 $(m/s)^2$, for the phase from -180 to +180 degrees, for the magnetic power from 0 to 0.4 G^2 .

As a consequence, the temporal resolution we get is limited by an observing run of few hours. Nevertheless, it is really useful to perform this analysis since it relates the oscillations to the local phenomena. often considered independent of them. In order to evaluate the contribution of the convection to the signal, a $\ell - \nu$ diagram should be produced in any case, as the distinction between the oscillations and the convection results much easier. In our case the convection contribution is negligible in comparison to the five-minute component.

3. THE RESULTS

The power and V-B phase difference maps have been obtained. Some samples are shown in figure 2 for a selection shown in figure 1. The power spectra for a plage and spot region are also displayed in figure 3. The phase difference changes along the frequency domain and depends strongly on the spatial resolution. Any estimate, averaged in frequency or space, would give misleading values (Ulrich, 1996).

The $\ell - \nu$ diagrams have been produced for more data sets of 256 minutes in January 1998 and using two different software packages to decompose the images into the spherical harmonics: the GRASP managed by the GONG group and the OAC package.

The main differences between the results regard the ℓ dependence of the spectra and will be discussed elsewhere. All the diagrams have been corrected for the differential and sync filters applied to the data (figure 4). Nevertheless, some general traits are common:

1) the magnetic diagram does not reproduce the velocity diagram (where the p-modes ridges dominate). 2) the magnetic spectra show two bumps at the five and three-minute bands (figure 5). The first point is confirmed by the local analysis, where the pixelby-pixel magnetic spectra do not mimic the velocity power, that is the crosstalk can be considered at a lower order of magnitude in the magnetic regions. The second point is also shown in the local analysis in correspondence of the magnetic structures (see figure 3). We remark that the presence of the threeminute bump in the $\ell - \nu$ magnetic spectra does not imply a global rensponse of the solar cavity (likewise in the p-modes) but can be reproduced by a broad spatial distribution of local sources on the surface (as irregular shaped plages etc.). This can be also seen in the increase of the power in correspondence of the typical spatial scales of the plages and spots present at those days.

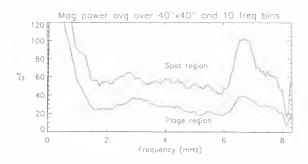


Figure 3. The local magnetic power for a spot region and a plage region of approximately $40^{\circ} \times 40^{\circ}$. The five and three-minute bumps are visible.

In order to investigate the general behavior of the power distribution at different spatial scales, the ℓ dependence of the magnetic power $\Delta B^2(\ell)$ (hereafter ΔB^2) obtained as the average over the frequency ν of the $\ell - \nu$ diagram has been performed. We rely

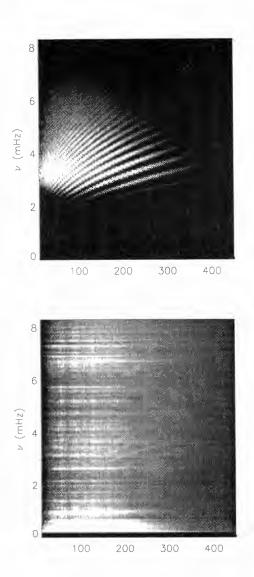


Figure 4. The $\ell - \nu$ diagrams for the velocity (top) and longitudinal magnetic field (bottom). They have been obtained from 256 images acquired each minute. The displayed magnetic diagram has been corrected for the differential and sync filters. The software has been provided by M. Oliviero of the OAC.

on the results shown in figure 6, obtained using the OAC package developed by M. Oliviero.

We adopt the following approach to give a possible interpretation of the results: let us assume that, at the formation layer of the sodium D lines, ΔB^2 is mainly driven by the convective and oscillatory motions. We treat the solar atmosphere as an electric circuit. We used a CR and a RLC to reproduce ΔB^2 as ouput when ΔV^2 is chosen as input. A dissipative process in a simple resistor circuit can be also used by using the RLC transmission as the resistor's ℓ dependence, but its physical interpretation is different. The CR circuit can not explain an increase in the high- ℓ values as measured. Indeed, the RLC parameters can be tuned in order to match the results. A 1/LC=160000 ($\ell = 400$) and R/L=100 have been introduced to obtain an output the most similar

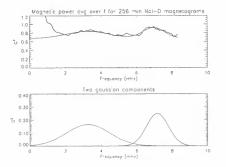


Figure 5. Top: the $\ell - \nu$ diagram averaged over ℓ . The smooth line is a fit containing the two gaussian components shown in the bottom panel added to a bias equal to 0.67 G^2 .

to the ΔB^2 . This implies the presence of a magnetic structure at lenghtscales of the order of 10000 Km to produce that resonance filter (that is approx. 10 arcsec at disk center). The spatial resolution of the data is limited to 4 arcsec/pix (ℓ max measured=460) and higher resolution data with full-disk configuration are needed to confirm this conclusion.

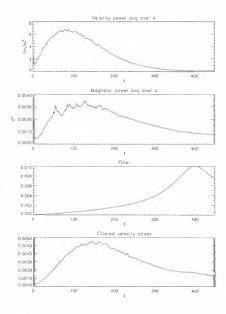


Figure 6. From top to bottom: 1) the velocity $\ell - \nu$ diagram averaged over ν . 2) The magnetic $\ell - \nu$ diagram averaged over ν . 3) A RLC filter with $1/LC = \ell^2 = 160000$ and R/L=100. 4) The velocity power shown in the first panel as transmitted through the RLC filter in the third panel (this curve should reproduce the magnetic power shown in the second panel).

4. CONCLUSIONS

The magnetic oscillations have been detected. The local analysis suggests a careful interpretation of the results when the data are analyzed to obtain the velocity-magnetic phase difference (V-B) values. In fact, the V-B strongly depends on the spatial resolution and on the frequency.

The magnetic oscillations have been correlated to the $H\alpha$ bright points (Moretti et al., 2000). The $\ell - \nu$ diagrams have been obtained using two different software packages. The $\ell - \nu$ diagram for the magnetic signal shows two bumps at the three and five-minute bands. The same bumps are visible in the spot and plage regions with the local analysis. The possible crosstalk between velocity and magnetic field can not reproduce the trait of the spectra.

The ℓ dependence of the power spectra have been preliminary interpreted to invoke the presence of a resonant spatial scale peaked at approximately 10000 Km.

Higher spatial resolution data are needed to confirm these results.

REFERENCES

-Braun, D.C, Lindsey, C., 1999, Astrophys. J., 513.

- -Chae, J, wang, H., Lee, C., Goode, P.R., Schouhle, U., 1998, Astrophys. J., 497, L109
- -Cacciani, A., Di Martino, V., Jefferies, S.M., Moretti, P.F., 1998, ESA Sp-418, 617
- -Cacciani, A., Hanslmeier, A., Messerotti, M., Moretti, P.F., Otruba, W., Pettauer, Th., 1997,
- Motions in the Solar Atmosphere, A. Hanslmeier & M. Messerotti eds., Kluwer Academic publ., 297
- -Cook, J.W., Rutten, R.J., Hoekzema, N.M., 1996, Astrophys. J., 470, 647
- -Espagnet, O., Muller, R., Rouder, Th., Mein, N., Malherbe, J.M., 1996, *Astron. & Astrophys.*, **313**, 297
- -Goode, P.R., Strous, L.H., Rimmele, T.R., Stebbins, R.T., 1998, *Astrophys. J.*, 495, L27
- -Haber, D.A., Toomre, J. Hill, F., Gough, D., 1988, in Seismology of the Sun and Sun-like Stars, E.J. Rolfe eds., ESA SP-286, 301
- -Hoekzema, N.M., Rutten, R.J., Cook, J.W., 1997, Astrophys. J., 474, 518
- -Horn, T., Staude, J., Landgraf, V., 1997, Solar Phys., 172, 69
- -Lites, B.W., 1992, in Sunspots: Theory and Observations, J.H. Thomas and N.O. Weiss (eds.), Kluwer, 261
- -Lites, B.W., Thomas, J.H., Bogdan, T.J., Cally, P.S., 1998, Astrophys. J., 497, 464
- -Lites, B.W., Rutten, R.J., Berger, T.E., 1999, Astrophys. J., 517, 1013L
- -Moretti, P.F., and the MOF Development Group, 2000, *Solar Phys.*, in press
- -Moretti, P.F., Cacciani, A., Hanslmeier, A., Messerotti, Otruba, W., Warmuth, A., 2000, *Dynamics of the Sun*, A. Hanslmeier & M. Messerotti eds., Kluwer Academic publ., in press

-Ruedi, I., Solanki, S.K., Stenflo, J.O., Tarbell, T., Sherrer, P.H., 1998, Astron. & Astrophys., **335**, L97 -Skartlien and Rast, 2000, Astrophys. J., **535**, 464 -Ulrich, R.K., 1996, Astrophys. J., **465**, 436

SOLAR ROTATION AND ACTIVITY CYCLE

Zadig MOURADIAN^a. Roméo BOCCHIA^b, Christian BOTTON^b ^a Observatoire de Paris-Meudon, 92195 Meudon CEDEX, France zadig.mouradian@obspm.fr ^b Observatoire de Bordeaux, Avenue Pierre Semirot, 33270 Floirac, France

Abstract

We give the results of measurements of the rotation period detected at 10.7 cm radio emission between 1947 and 1999. The average period for synodic rotation is 26.65 days, which becomes 26.2 at activity maximum and to 27.0 at minimum. The rotation rate grows and decreases during the solar cycle.

Abridged version[‡]

In order to investigate the Sun's rotation during the solar activity cycle, we used the radio emission at 10.7 cm (2800 MHz), which originates in the low corona. This is a good indicator of solar activity, integrate over the solar disk. Observations are obtained by Dominion Radio Astrophysical Observatory survey, started in late 1946 and is still continuing and offers the best data set for our purpose.

Figure 1 gives an example of radio flux data (www.drao.nrc.ca/icarus/). where it can be seen that a periodic slowly varying component is superimposed on a background radiation. The periodic signal is due to active region emissions, which cluster mainly around active longitudes.

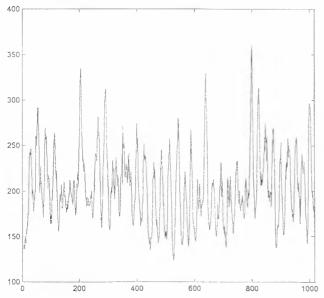


Figure 1. The absolute radio flux at 10.7 cm, from November 23, 1988 to September 5, 1991, including the activity maximum of cycle 22. In abscissa Julian Days.

For each time interval (Δt) , we counted the number (n) of periods and obtained the periodicity of the solar

rotation $P_{syn} = \Delta t/n$ in days. Figure 2a shows the variation of synodic period (P_{syn}), over five solar cycles, i.e. cycles 18 to 22. This is a periodic function of 11 years which can be compared to the solar activity index. the Annual Mean of Sunspot Number in figure 2b. The two functions are anti-correlated and, at the maximum of activity. the solar surface angular rotation speed (14.73 °/d = 2.975 m rad/s = 473 nHz) is higher (shorter period) than during the minimum of activity (14.32 °/d = 2.893m rad/s = 460 nHz). The table gives the extreme values of solar activity indices. synodic rotation period, the sidereal rotation angular velocity and, for the last two cycles, the solar half diameter variation (Laclare et al., 1996). The last column gives the average values of studied cycles.

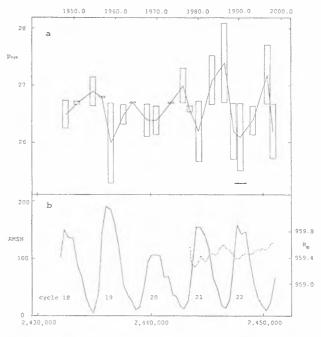


Figure 2. This figure sketch the period from 5 November 1946 to 9 July 1999 (cycles 18 to 23). a) shows the variation of the rotation synodic period in function of Julian Days. b) variation of Annual Mean of Sunspots Number (AMSN) and of the solar radius (dotted line).

Our measurements confirm indirectly the results of Ribes et al. (1987), who note that during the Maunder minimum (1645 to 1715) the solar diameter was larger and the rotation speed lower.

Activity	Solar Cycle	18	19	20	21	22	Average
		Jan. 1944	Feb. 1954	Aug. 1964	Aug. 1976	Jul. 1986	_
		Jan. 1954	Jul. 1964	Jul. 1976	June 1986	Oct. 1996	
	Rotation period 1 (d)	26,5	26.0	26.4	26.2	26.1	26.2
Maximum	Angular velocity 2 (°/d)	14.57	14.83	14.62	14.73	14.77	14.73
	Annual Mean Sunspot Number	151.5	190.2	105.5	155.4	157.6	152.0
	Solar half-diameter (arc sec)				959.27	959.36	959.325
	Rotation period ¹ (d)	26.9	26.7	27.0	27.4	27.2	27.0
Minimum	Angular velocity 2 (°/d)	14.37	14.47	14.32	14.12	14.22	14.32
	Annual Mean Sunspot Number	4.4	10.2	12.6	13.4	8.6	9.8
	Solar half-diameter (arc sec)				959.60	959.55	959.575

¹ Synodic rotation period ² Sidereal rotation rate

References:

- Laclare F., Dalmas C., Coin J.P., Irbah A., 1996. Measurements and variations of the solar diameter, *Sol. Phys.*, **166**, 211-229
- Ribes E., Ribes, J.-C., Barthalot, R., 1987.Evidence for a larger Sun with a slower rotation during the seventeen century: *Nature*, **326**, 52-55

‡ Comprehensive version: *Compte Rendu de l'Académie des Sciences de Paris* 2000, vol. 1 Sér. IV, p. 353-358. An extensive article is in progress.

PERSISTENT 22-YEAR CYCLE IN SUNSPOT ACTIVITY: EVIDENCE FOR A RELIC SOLAR MAGNETIC FIELD

K. Mursula¹, I. G. Usoskin¹^{*} and G. A. Kovaltsov²

¹ Dept. of Physical Sciences, P.O.Box 3000, FIN-90014 University of Oulu, Finland phone/fax: +358-8-5531378/5531287, email: kalevi.nursula@oulu.fi. ilya.usoskin@oulu.fi

² Ioffe Physical-Techical Institute, Politekhnicheskaya 26, 194021 St.Petersburg. Russia phone/fax: +7-812-2479167/2471017, email: gcna.kovaltsov@pop.ioffc.rssi.ru

Abstract

We use the recently presented group sunspot number series to show that a persistent 22-year cyclicity exists in sunspot activity throughout the entire period of about 400 years of direct sunspot observations. The amplitude of this cyclicity is about 10% of the present sunspot activity level. A 22-year cyclicity in sunspot activity is naturally produced by the 22-year magnetic polarity cycle in the presence of a relic dipole magnetic field. Accordingly, a persistent 22-year cyclicity in sunspot activity gives strong evidence for the existence of such a relic magnetic field in the Sun. The stable phase and the roughly constant amplitude of this cyclicity during times of very different sunspot activity level strongly support this interpretation.

1 INTRODUCTION

Magnetic activity in the Sun is determined by the dynamo mechanism [Babcock, 1961]. However, a weak relic magnetic field may exist in the Sun's interior since its formation [Cowling, 1945]. Sonett [1982, 1983] tried to find a signature of such a relic field in sunspot activity. Assigning a negative sign to odd solar cycles, he fitted the Wolf sunspot series with a model consisting of two harmonics with periods of 22 and 90 years, and found a small negative offset in the running mean of the model during the last 150 years. He suggested that such an offset gives evidence for a relic solar field. However, his results for the earlier period from the 18th century to mid-19th century were not conclusive since the offset changed sign in late 1700's. Because of this reason. Sonett's results, and the implied evidence for a relic magnetic field remained rather unconvincing. More recently, Bravo & Stewart [1995] studied the difference in the Sun's polar coronal field during subsequent minima, claiming evidence for an inclined dipole

relic field. However, the available data covered only two solar cycle minima which is insufficient to allow a statistically significant conclusion [Boruta, 1996].

has been argued [Levy & Bover, 1982. 11 Boyer & Levy, 1984] that the solar dynamo with its 22-year magnetic polarity (Hale) cycle must result, in the presence of a dipole relic field, in a 22-year cyclicity of sunspot activity. Accordingly, a 22-year cyclicity in sunspot activity would provide compelling experimental evidence for the existence of a relic field in the Sun. However, no convincing evidence for such a cyclicity has been found in sunspot activity when using the famous Wolf sunspot series. This is probably because of the rather poor quality of Wolf sunspot data before mid-19th century [Hoyt & Schatten, 1998. Wilson, 1998. Letfus, 1999]. and because of the large long-term variations of sunspot activity level (the secular Gleissberg cycle), The poor quality of Wolf sunspot data is also a likely reason for the inconclusive results by Sonett [1983] for the early times.

Here we perform a detailed analysis of the 22-year cyclicity using the new group sunspot numbers (GSN). The GSN series, depicted in Fig. 1a, includes all known archival records of sunspots starting from the observations of G. Galilei in 1610, and gives a more correct measure of early sunspot activity than the Wolf sunspot numbers [[Hoyt & Schatten, 1998]. Contrary to Sonett [1982, 1983], we do not fit the data to any model but rather analyze the raw sunspot data directly.

2 22-YEAR CYCLICITY IN SUNSPOT ACTIVITY

An empirical Gnevyshev-Ohl (G-O) rule [Gnevyshev & Ohl, 1948] orders the sunspot cycles to even-odd pairs so that the intensity (sum of sunspot numbers over a cycle) of the odd cycle of a pair exceeds that of the preceding even cycle. However,

^{&#}x27;on leave from loffe Phys -Tech Inst., St.Petersburg, Russia

Proc. 1st Solar & Space Weather Euroconference. 'The Solar Cycle and Terrestrial Climate'. Santa Cruz de Tenerife. Tenerife. Spain, 25-29 September 2000 (ESA SP-463. December 2000)



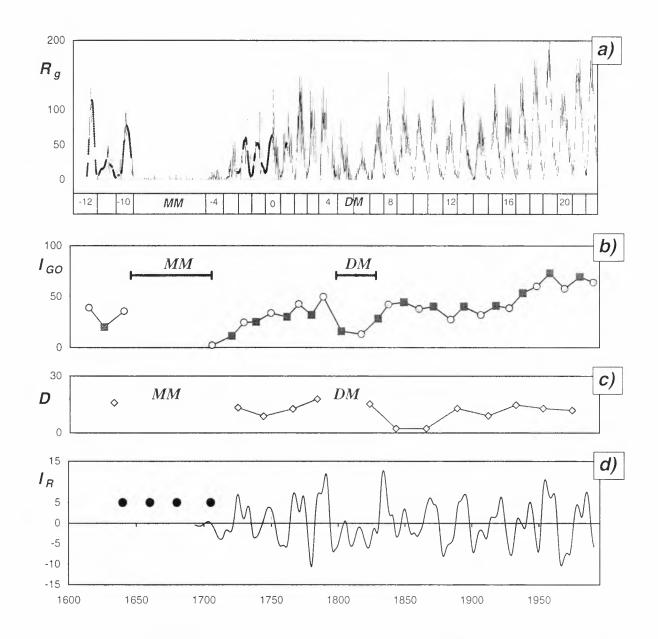


Figure 1: (a) Monthly group sunspot number series R_g (thin line) with interpolated gaps (sections of thick line). Sunspot cycle numbers are shown in the lower panel together with the location of the Maunder (MM) and Dalton (DM) minima. (b) Sunspot cycle intensities I_{GO} (see Eq. (1)) for odd (grey squares) and even (open circles) sunspot cycles. (c) Intensity differences D between the two sunspot cycles forming a G-O pair. (d) Running standardized and 11-year averaged GSN series I_R (see Eq. (3)). The times of the 22-year cycle maxima before and during the Maunder minimum [Usoskin et al., 2000] are noted by black circles.

the G-O rule in the Wolf sunspot series is only valid since solar cycle 10 and fails for cycle pairs 4-5 and 8-9 [Gnevyshev & Ohl, 1948, Vitinsky et al., 1986, Wilson, 1988. Storini & Sykora, 1997]. In analogy with [Gnevyshev & Ohl, 1948], we define the intensity $I_{GO}(k)$ of the sunspot cycle number k as the normalized sum of sunspot numbers over the cycle:

$$I_{GO}(k) = \frac{1}{132} \sum_{j=J(k)}^{J(k+1)-1} R_g(j),$$
(1)

where $R_q(j)$ is the GSN value for the month number jand J(k) is the month starting cycle k. (As cycle minima we use here the minima of the running 12-month average [Mursula & Ulich, 1998].) The 11-year cycle length (132 months) is used as a normalization factor. The monthly GSN series has some gaps until the end of 18th century. Most data gaps are rather short, but a few gaps are longer than one year. The longest data gap of 27 months was during cycle 0. The data gaps were interpolated using a fit to a binomial curve with a window length of 41 months. The interpolation method was tested with an artificial series (noised 11year sinusoid with gaps), yielding an accuracy better than 5% even for the longest gaps. The $I_{GO}(k)$ series. depicted in Fig. 1b, allows to examine the validity of the G-O rule in the GSN series. Starting from cycle 6. each even cycle (including cycle 8) is followed by a more intense odd cycle, verifying the G-O rule in the GSN series since the Dalton minimum in 1790-1830. Before the Dalton minimum, the G-O rule is also valid in a phase-reversed form whereby an odd cycle is followed by a more intense even cycle. Note that this phasereversed G-O rule applies even for the time before the Maunder minimum which occurred from 1645 to 1715. (Noting that the time difference between the last maximum in 1639-1640 before the deep minimum, and the first maximum in 1705 after it, was roughly six 11-year cycles, we have numbered the three cycles before the minimum as -12, -11 and -10). As a quantitative measure of the G-O rule we have depicted in Fig. 1c the difforence $D(k) = I_{GO}(k+1) - I_{GO}(k)$ between the intensities of the two cycles forming a pair. These differences are roughly constant, about 10-20, throughout most of the GSN interval, including D(-11), the only value before the Maunder minimum. It is important to note that the D(k)-values do not correlate with sunspot activity. The correlation coefficient between D(k)-values and average pair intensities $((I_{GO}(k) + I_{GO}(k+1))/2)$ is -0.09 ± 0.25 for solar cycles -4 to 21.

Note that in 1830-1930 and 1950-1990, when cycle intensities remained roughly constant (see Fig. 1b), the odd cycles were more intense than either of the two neighboring even cycles. Similarly, in 1740-1790 the even cycles were larger than the two neighboring

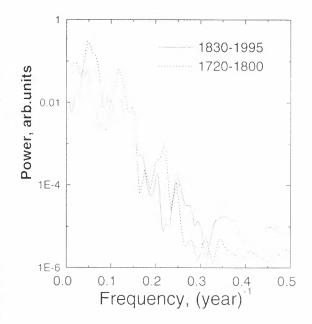


Figure 2: FFT power spectra of the $I_R(i)$ -series before the Maunder minimum (1720-1800) and after it (1830-1996).

odd cycles. This behaviour suggests that a 22-year periodicity in cycle intensity is the underlying pattern behind the G-O rule. However, the visibility of the 22-year cyclicity is hidden at times when the sunspot activity level is rapidly changing, e.g., during the recovery of activity after the Maunder minimum, around the Dalton minimum and at the start of the recent high cycles in 1940's. During these times the G-O rule is valid only in the fixed order of cycle pairs. Therefore, in order to examine the existence of the 22-year periodicity in cycle intensity in more detail we standardized [Jenkins & Watts, 1969] the monthly GSN series by subtracting the long-term (30-year) trend:

$$U_g(i) = R_g(i) - \frac{1}{361} \sum_{j=-180}^{180} R_g(i+j)$$
(2)

and suppressed the dominant 11-year Schwabe cycle by calculating the running 11-year average intensity $I_R(i)$:

$$I_{R}(i) = \frac{1}{132} \left(\sum_{j=-65}^{65} U_{g}(i+j) + \frac{1}{2} U_{g}(i\pm 66) \right)$$
(3)

The $I_R(i)$ -series (see Fig. 1d) shows a persistent 22year cyclicity both between the Maunder and Dalton minima and since the Dalton minimum. The FFT power spectra of these two parts of the $I_R(i)$ series are shown in Fig. 2 separately. The confidence level [Jenkins & Watts, 1969] of the 22-year peak in

the power spectrum of $I_R(i)$ -series is 0.99 for 1720-1800 and better than 0.9999 for 1830-1996. (Note that some power from the Schwabe cycle still remains in the $I_R(i)$ - series forming the second peak with a period slightly less than 10 years.) In agreement with results obtained above for the discrete series (see Fig. 1c), the peak-to-peak amplitude of the 22-year cyclicity in Fig. 1d is roughly constant and about 10-20, corresponding to approximately 10% of the amplitude of recent solar cycles. Also, the correlation coefficient between the monthly $I_R(i)$ -series and the monthly GSN series is roughly zero $(0.05 \pm 0.04 \text{ and } 0.07 \pm 0.07 \text{ for } 1830$ -1996 and 1720-1790, respectively), implying that the 22-year cyclicity is independent of the overall sunspot activity level. We have shown recently that during the Maunder minimum, when the Schwabe cycle was strongly suppressed, the remaining, seemingly sporadic sunspot activity still shows a significant 22-year periodicity [Usoskin et al., 2000]. Accordingly, a persistent 22-year cycle exists in sunspot activity throughout the whole time interval of nearly 400 years of direct solar observations. The sunspot maxima during the Maunder minimum [Usoskin et al., 2000] occur in phase with the maxima of the 22-year cyclicity before and after the minimum (see Fig. 1d). Moreover, the times of maxima of the $I_R(i)$ -series roughly correspond to even cycles before and to odd cycles after the Dalton minimum (see Figs. 1b and 1d), in agreement with the suggested phase reversal in the G-O rule at the Dalton minimum. The 22-year cyclicity was not clearly visible during the Dalton minimum. However, the two maxima in the $I_R(i)$ -series around the Dalton minimum are separated by about 43 years, implying that the 22-year cyclicity has no sizeable phase change around the Dalton minimum. Therefore, the phase reversal in the G-O rule is not related to the 22-year cyclicity but, most likely, to the known phase catastrophe (e.g. [Vitinsky et al., 1986, Kremliovsky, 1994]) of the Schwabe cycle in the beginning of the Dalton minimum.

3 DISCUSSION AND CON-CLUSIONS

The idea of a weak dipole relic solar magnetic field gives a natural explanation for the observed 22-year cyclicity. A relic field can, due to the high conductivity in the solar interior, survive in the Sun for a very long time, even over time scales comparable to the solar age [Cowling, 1945]. Due to a strong amplification by the dynamo fluid motions in the convection zone, such a weak constant field can interact with the poloidal/toroidal dynamo field and hence play a considerable role in the formation of a sunspot cycle [Levy & Boyer, 1982, Boyer & Levy, 1984]. The total magnetic field in the convection layer is enhanced when the dynamo field has a favorable orientation with respect to the relic field, and suppressed during the next sunspot cycle which has an opposite magnetic orientation in accordance with the Hale law. Thus, a constant relic field leads to cyclicity in sunspot activity with the period of the magnetic polarity cycle.

Concluding, we have shown that a persistent 22-year cyclicity indeed exists in sunspot activity throughout the whole time interval of about 400 years of direct solar observations. The 22-year cyclicity in sunspot activity is naturally produced by the 22-year magnetic Hale cycle in the presence of a relic dipole magnetic field. Accordingly, the detected 22-year cyclicity in sunspot activity gives strong evidence for the existence of such a relic magnetic field in the Sun. The stable phase and the roughly constant amplitude of this cyclicity during times of very different sunspot activity level strongly support this interpretation.

Acknowledgements. The financial support by the Academy of Finland is gratefully acknowledged. We appreciate the electronic service of NOAA for an easy access to sunspot data.

References

- Babcock, H. W., 1961, ApJ, 133, 572.
- Boruta N., 1996, ApJ, 458, 832.
- Boyer, D., Levy, E. H., 1984, ApJ, 277, 848.
- Bravo, S., Stewart, G., 1995, ApJ, 446, 431.
- Cliver, E. W., Boriakoff, V., Bounar, K. H., 1999, J. Geophys. Res., 101(A12), 27091.
- Cowling, T. G., 1945, Mon. Not. R. Astron.Soc., 105, 166.
- Gnevyshev, M. N., Ohl, A. I., 1948, Astron.Zh., 25(1), 18
- (in Russian).
- Hoyt, D. V., Schatten, K., 1998, Solar Phys., 179, 189.
- Jenkins, G. M., Watts, D. G., Spectral Analysis and Its Applications, Holden-Day, San Francisco, 1969.
- Jokipii, J. R., Levy, E. V., 1977, ApJ, 213, L85.
- Kremliovsky, M. N., 1994, Solar Phys., 151. 351
- Letfus, V., 1999, Solar Phys., 184, 201.
- Levy, E. H., Boyer, D., 1982, ApJ Lett., 254, L19.
- Mursula, K., Ulich, T., 1998, Geophys. Res.Lett., 25, 1837.
- Richardson, I. G., Cane, H. V., Wibberenz, G., 1999, J.
- Geophys.Res., 104(A6), 12549.
- Sonett, C. P., 1982, Geophys. Res. Lett., 9, 1313.
- Sonett, C. P., 1983, Nature, 306, 670.
- Storini, M., Sykora, J., 1997, Solar Phys., 176, 417.
- Usoskin, I. G., Mursula, K., Kovaltsov, G. A. 2000, A&A, 354, L33.
- Vitinsky, Yu. I., Kopecky, M., Kuklin, G.V. Statistics of Sunspot Formation Activity (in Russian). Nauka. Moscow, 1986.
- Wilson, R. M. 1988, Solar Phys., 117, 269.
- Wilson, R. M. 1998, Solar Phys., 182, 217.

LONG-TERM NORTH-SOUTH ASYMMETRY IN SOLAR WIND SPEED: EVIDENCE FOR A NEW TYPE OF CENTURY-SCALE SOLAR OSCILLATION

K. Mursula¹, and B. Zieger^{2*}

¹ Dept. of Physical Sciences, P.O.Box 3000, FIN-90014 University of Oulu, Finland phone/fax: +358-8-5531378/5531287, email: kalevi.mursula@oulu.fi

> ² Danish Space Research Institute, Copenhagen, Denmark phone/fax: +45-35-325781/362475, email: *zieger@dsri.dk*

Abstract

A very similar annual variation in solar wind speed and in geomagnetic activity was recently found around all the four solar cycle minima covered by direct SW observations since mid-1960's. We have shown earlier that the phase of this annual variation reverses with the Sun's polarity reversal, depicting a new form of 22-year periodicity. The annual variation results from a small north-south asymmetry in SW speed distribution where the minimum speed region is shifted toward the northern magnetic hemisphere. Here we study the very long-term evolution of the annual variation using early registrations of geomagnetic activity. We find a significant annual variation during the high-activity solar cycles in mid-19th century and since 1930's. Most interestingly, the SW speed asymmetry in mid-19th century was opposite to the present asymmetry, i.e., the minimum speed region was then shifted toward the southern magnetic hemisphere. This change of asymmetry suggests for a possible new form of century-scale oscillation in the north-south asymmetry of the Sun. We explain the asymmetry in terms of a relic magnetic field dislocated slightly in the north-south direction from the heliographic equator. The change in the asymmetry would result from the century-scale northsouth oscillation of the location of the relic field across the ecliptic.

1 Introduction

Annual variation in geomagnetic activity (GA) and auroral occurrence was found in several studies over the last decades [see, e.g., *Fraser-Smith*, 1972; *Delouis and Mayaud*, 1975; *Silverman and Shapiro*, 1983; *Gonzalez et al.*, 1993]. The annual variation in GA is manifested

as a difference between the two semiannual maxima close to the Spring and Fall equinoxes [Mcyer, 1972; Münch, 1972; Triskova, 1989].

Annual variation is also known in solar wind (SW) speed, temperature and density [Bolton, 1990; Paularena et al., 1995; Szabo et al., 1996]. Szabo et al. [1996] showed that annual variation in SW speed is strongest around solar minima. In a recent study [Zieger and Mursula, 1998; to be called P1] we found that the phase of annual variation in SW speed (and in GA) reverses from one solar minimum to another such that a stronger solar wind is found when the Earth is at the highest northern heliographic latitudes (in September) during negative helicity minima and at the highest southern latitudes (in March) during positive minima. This implies a north-south asymmetric SW speed distribution across the heliographic equator such that the minimum speed region during solar minima is displaced towards the northern magnetic hemisphere. The alternating phase depicts a new form of 22-year cyclicity and excludes earlier explanations proposed for annual variation in SW speed such as internal solar variation. According to P1, the annual variation results from the Earth's annual passage through an asymmetric SW speed distribution. As discussed in P1, several observations find evidence for a north-south asymmetry in SW speed distribution. in agreement with the alternating phase of the annual variation [Hundhausen, 1971; Zhao and Hundhausen. 1983; Crooker et al., 1997].

In P1 we verified that SW speed and geomagnetic activity depict a very similar annual variation during the whole period of direct SW observations including the four last solar minima. Here we use this correlation to study the annual variation and the related north-south asymmetry in SW speed distribution before the time of direct SW measurements using the very early registrations of geomagnetic activity from mid-19th century onwards.

^{*}permanently at Geodetic and Geophysical Research Institute, Sopron, Hungary

Proc. 1st Solar & Space Weather Euroconference, 'The Solar Cycle and Terrestrial Climate', Santa Cruz de Tenerife, Tenerife, Spain 25-29 September 2000 (ESA SP-463, December 2000)

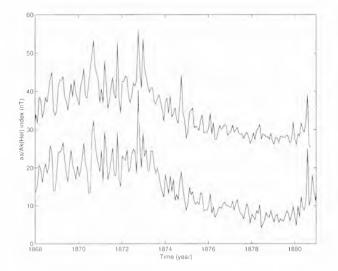


Figure 1: The Ak(Hel) index (upper curve) and the aa index (lower curve) forming the extended aa index. plotted over the common time interval from 1868 to 1881. The Ak(Hel) curve is shifted by 20 nT upward with respect to the aa index for better visibility.

2 Long-Term Annual Variation

We use two geomagnetic indices, the aa index [Mayaud, 1973] and the Ak(Hel) index [Nevanlinna and Ketola, 1993] which were adjusted to form the longest uniform index of global geomagnetic activity [Nevanlinna and Kataja, 1993], now extending over nearly 15 solar cycles. In Figure 1 we show the 27-day averages of these two indices for the overlapping time interval 1868-1880. There is an excellent correlation between the 27-day averages of the two indices with correlation coefficient r=0.95. We extended the aa index to the earlier time interval (1844-1867) covered by the Ak(Hel) index using the best fitting linear regression between the two indices aa= 1.03^* Ak(Hel)+1.27.

We study the annual variation in GA using a similar procedure as in P1. We designed a finite impulse response band pass filter (see Figure 2) with a pass band of one year \pm 5 % following the Parks-McClellan optimization procedure [see e.g. MATLAB, 1994] and filtered the 27-day averaged indices. The filter is flat in the pass band and attenuates the signal by 70 dB in the stop band. The middle panel of Figure 3 displays the filtered annual variation of the extended aa index as an intensity map where one year is depicted along the vertical axis so as to demonstrate the phase of the annual variation. White (black) scale represents a large positive (negative) value of annual variation, while light gray denotes a small amplitude. In the bottom panel of Fig. 3 we reproduce the annual variation of the SW speed from P1, showing the alternation of the annual phase from Spring in positive helicity minima to Fall in negative minima. The same pattern is seen in the aa

Figure 2: The time (upper panel) and frequency (lower panel) characteristics of the optimum filter used to extract the annual variation.

index during the overlapping time. Fig. 3 also includes the monthly sunspot numbers (top panel) with helicity signs denoted, and vertical lines marking the time two years after the sunspot maximum. This time is close to the average time of reversal of polar magnetic fields in the Sun.

Fig. 3 shows that since 1930's there was a significant annual variation in GA with phase (maximum) in Spring during positive helicity minima and in Fall during negative minima. This extends the interval studied in P1 and shows that a significant north-south asymmetry persisted at least during the last 7 solar cycles. Accordingly, during the last 70 years the region of minimum SW speed was consistently shifted toward the northern magnetic hemisphere.

It is interesting to note that the time interval of a sizable annual variation since 1930's coincides with the interval of recent high-activity solar cycles. On the other hand, around the turn of the century, during lowactivity cycles, the annual variation was weaker. Even earlier, in mid-1800's, again during more active cycles. we find a strong annual variation with maxima alternating systematically between Spring and Fall from one solar minimum to another. However, most interestingly, the Fall maxima occurred during the two positive helicity minima included in this time interval and the Spring maxima during the negative helicity minimum. This is opposite to the Spring-Fall asymmetry observed during the last 7 solar cycles and implies an opposite shift of the SW speed distribution toward a southern magnetic hemisphere during these early cycles in mid-1800's.

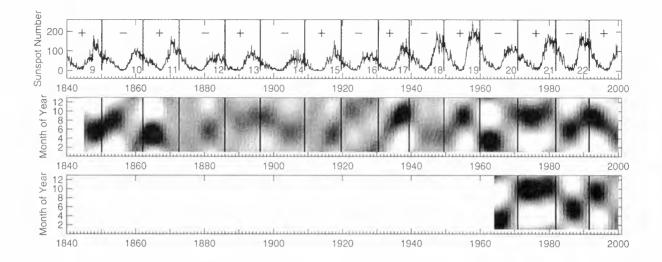


Figure 3: Monthly sunspot numbers with magnetic helicities noted by + and - signs (top panel). Filtered annual variation of the extended as index in 1845-1999 (middle panel), and the solar wind speed in 1964-1999 (bottom panel) in the same intensity coding. The scale of the code (the largest amplitude of annual variation) extends from -3.5nT to +3.5nT for the as index and from -25 km/s to +25km/s for the solar wind speed. Vertical lines denote the approximate time of polarity reversal two years after official sunspot maximum.

3 Discussion

In Fig. 3 we have noted the approximate times of solar polarity reversal which occur typically two years after sunspot maxima. However, deviations exist to this rule and, thus, these times should only be considered indicative. E.g., during solar cycle 19, the two-year interval during which the reversal took place (see, e.g., *Makarov and Sivaraman*, [1986]) already ended two years after sunspot maximum, i.e., at the time noted in Fig. 3. On the other hand, during the two previous cycles, the reversal interval only started at the noted time and lasted 2-3 years. Accordingly, the annual variation with a Fall maximum which occurred exceptionally late in cycle 18 indeed corresponds to the helicity of the previous minimum, in accordance with the above explanation.

The pattern of an oscillating phase of annual variation breaks down during the low-activity cycles around the turn of the century. This happens first around 1880 with the start of low-activity cycles when the annual phase remained in Fall during two consecutive solar minima with opposite helicity. A similar break in the oscillating pattern took place between 1900's and 1910's, when the phase again remained in Fall after polarity reversal, and also later, with the start of highactivity cycles, when the Spring phase in 1920's did not reverse but prevailed during the next solar minimum with opposite helicity in 1930's. Triskova [1989] also found the alternating Spring-Fall asymmetry in GA during the last few solar cycles but claimed only one phase break in the oscillating pattern between 1910's and 1920's. On the contrary, we find a regular phase change from Fall to Spring between these two periods

with opposite helicity.

Although the annual variation during low-activity cycles is quite weak we note that the phase of annual variation was mostly fairly close to Spring or Fall, supporting the view that the annual variation indeed reflects the evolution of the north-south asymmetry in SW speed even at this time. A break in the oscillating phase of annual variation between two subsequent solar minima with opposite helicities would imply that the SW speed distribution changed its asymmetry between the two solar minima. The asymmetry is found to change three times during the 155-year interval studied in this paper. Note that one of these changes occurred at the end of high-activity cycles in 1870's, one at the start of current high-activity cycles in 1930's and one during the low-activity cycles. A definite proof of the change in the SW speed asymmetry during the studied interval is obtained by the oppositely oscillating annual phase between mid-1800's and the latest high-activity cycles. At these times the annual variation was large and the phase changed consistently with the polarity reversals of the Sun. Accordingly, we find that the SW speed distribution was, from the start of the extended aa index until 1870's, clearly asymmetric and shifted toward the southern magnetic hemisphere. During the low-activity cycles from 1880's to 1920's. the asymmetry was rather small and was fluctuating between magnetic north and south. Finally, with the start of high-activity cycles, a fixed asymmetry with a shift towards the northern magnetic hemisphere was established.

Since the north-south asymmetry in SW speed is related to the heliomagnetic (not heliographic) hemispheres and oscillates in concert with the 22-year magnetic (Hale) cycle, it must be related to dynamo mechanism and the generation of magnetic field deep in the convection layer. Moreover, it implies an asymmetry in magnetic flux generation between the two halves of the magnetic cycle. Such an asymmetry in flux generation can occur, e.g., if there is a relic magnetic field in the Sun [Cowling, 1945; Sonett, 1982; 1983]. Recently, Mursula and Usoskin [2000] have found a persistent 22year cyclicity in sunspot activity, giving strong support for the existence of a relic field directed toward southern heliographic hemisphere. Also, in order to explain the present dominance of the southern magnetic hemisphere, the relic field must be located asymmetrically across the heliographic equator. If the relic is shifted northward of the heliographic equator, it would imply a larger flux in the southern solar hemisphere than in the northern hemisphere during positive helicity cycles. and vice versa during negative helicity cycles, leading to the observed dominance of the southern heliomagnetic hemisphere.

The observed change from the magnetically southward directed asymmetry in mid-1800's to the magnetically northward asymmetry since 1930's suggests that the location of the solar relic field is oscillating between the northern and southern (heliographic) hemispheres. Although we can not exactly determine the period of this oscillation with present observations, it must be at least some 200 years because the maximum southward asymmetry is not later than 1860 and the maximum northward asymmetry not earlier than 1960. Accordingly, the period is longer than, e.g., the 80-100-year Gleissberg cycle *Gleissberg* [1944] in sunspot activity. and probably also longer than the 178.8-year periodicity in solar motion [it Jose, 1965; it Landscheidt, 1999].

4 Conclusions

We use very long-term observations of geomagnetic activity to study the north-south asymmetry in the location of the minimum solar wind speed region. This asymmetry is found to be related to the solar magnetic field and causes the annual variation in geomagnetic activity and solar wind speed, as well as the oscillation of annual phase. We find a strong annual variation. and thus a significant north-south asymmetry, during the high-activity cycles in mid-19th century and since 1930's. Interestingly, while the solar wind distribution is shifted toward the northern magnetic hemisphere since 1930's, it was opposite in mid-1800's, i.e., directed toward the southern magnetic hemisphere. The observed change in this asymmetry between mid-1800's and presently implies a new form of century-scale oscillation in the north-south asymmetry of solar magnetic activity. We suggest that the observed solar wind asymmetry related to solar magnetic cycle is produced

by a relic magnetic field in the solar convection layer which is located slightly asymmetrically across the heliographic equator. The century-scale oscillation in the asymmetry could be due to the north-south oscillation of the location of the relic field.

Acknowledgements. We acknowledge the financial support by the Academy of Finland and the Danish Research Council.

References

Bolton, S., Geophys. Res. Lett., 17, 37-40, 1990.

- Cowling, T. G., Mon. Not. Roy. Astron. Soc., 105, 167, 1945.
- Crooker, N. U., A. J. Lazarus, J. L. Phillips, J. T. Steinberg, A. Szabo, R. P. Lepping, and E. J. Smith, J. Geophys. Res., 102, 4673, 1997.
- Delouis. H., and P. N. Mayaud, J. Geophys. Res., 80, 4681, 1975.
- Fraser-Smith. A. C., J. Geophys. Res., 77, 4209, 1972.
- Gleissberg. W., J. Geophys. Res., 49, 243-244, 1944.
- Gonzalez, A. L. C., W. D. Gonzalez, S. L. G. Dutra, and B. T. Tsurutani, J. Geophys. Res., 98, 9215, 1993.
- Hundhausen, A. J., S. J. Bame, and M. D. Montgomery, J. Geophys. Res., 76, 5145, 1971.
- Jose, P. D., Astron. J., 70, 193-200, 1965.
- Landscheidt, T., Sol. Phys., 189, 415-426, 1999.
- MATLAB. Signal Processing Toolbox for Use with Matlab. pp. 1(64)-2(175), MathWorks, Inc., Natick, Mass., USA. 1994.
- Makarov, V. I., and K. R. Sivaraman, Bull. Solnechnye Dannye 9, 64, 1986 (in Russian).
- Mayaud, P. N., in IAGA Bull., 33, Int. Union of Geod. and Geophys., Paris, 1973.
- Meyer, J., J. Geophys. Res., 77, 3566, 1972.
- Mursula, K., I. Usoskin, and G. Kovaltsov, Persistent 22year cycle in sunspot activity: Evidence for a relic solar magnetic field, accepted to Sol. Phys., 2000.
- Münch, J. W., Planet. Space Sci., 20, 225, 1972.
- Nevanlinna, H. and E. Kataja, Geophys. Res. Lett., 20, 2703, 1993.
- Nevanlinna, H. and A. Ketola, Geophysical Publications, 33, Finnish Meteorological Institute, 1993.
- Paularena, K. I., A. Szabo, and J. D. Richardson, Geophys. Res. Lett., 22, 3001, 1995.
- Silverman, S. M., and R. Shapiro, J. Geophys. Res., 88, 6310, 1983.
- Sonett, C. P., Geophys. Res. Lett., 9, 1313-1316, 1982.
- Sonett. C. P., Nature, 306, 670-672, 1983.
- Szabo, A., R. P. Lepping, J. H. King, K. I. Paularena, and J. D. Richardson, in Proceedings of Solar Wind 8, ed. by D. Winterhalter, J. Gosling, S. Habal, W. Kurth, and M. Neugebauer, AIP Press, Dana Point, CA, USA, 1996, p. 399.
- Triskova, L., J. Atm. Terrestr. Phys., 51, 111-118, 1989.
- Zhao, X.-P., and A. J. Hundhausen, J. Geophys. Res., 88, 451, 1983.
- Zieger, B., and K. Mursula, Geophys. Res. Lett., 25, 841-844, 1998; correction of editorial errors in Geophys. Res. Lett., 25, 2653, 1998.

AN EXAMPLE OF ISOLATED ACTIVE REGION ENERGY EVOLUTION: NOAA AR 7978

A. Ortiz¹, V. Domingo^{1,2}, B. Sanahuja^{1,2}, and L. Sánchez³

¹Dept. Astronomia i Meteorologia, Universitat de Barcelona, E-08028 Barcelona, Spain, +34-93-4021122, fax +34-93-4021133, aortiz@am.ub.es

²Institut d'Estudis Espacials de Catalunya, E-08034 Barcelona, Spain

³ESA/Space Science Dept. at NASA/GSFC, Greenbelt, MD, U.S.A.

ABSTRACT

The facular contribution to solar irradiance variations on the short time scale is studied by analysing a simple case of an isolated active region, NOAA AR 7978, during the minimum of 1996. We focus on the relationship between the temporal evolution of the active region surface magnetic field, its physical characteristics and the total facular energy emission, using VIRGO/SOHO and MDI/SOHO data sets.

Key words: solar variability; facular excess; energy spectrum.

1. INTRODUCTION

Solar irradiance variations on the short time scale are due to the presence and evolution of sunspots and faculae over the solar disk, and probably to smaller features of the magnetic field (Foukal & Lean, 1986; Solanki, 1994; Frölich & Lean, 1998).

The observation of a single active region (AR) during 1996, that was the only source of irradiance variations during four months, is a unique opportunity to study the relation between the evolution of the excess radiance of the active center and the evolution of its associated magnetic field. We present an example of observation and analysis of the irradiance from this single AR using data from the VIRGO and MDI instruments on board SOHO.

2. DATA AND OBSERVATIONS

We have used the following MDI (Scherrer et al., 1995) and VIRGO (Fröhlich et al., 1995) data:

- Full disk line-of-sight longitudinal magnetograms and full disk images in the intensity continuum at 676.8 nm (1024x1024).

- Total solar irradiance measured by the radiometers.
- Spectral irradiance by the SPMs at 402, 500 and 862 nm.
- Spectral radiance at 500 nm, by the LOI telescope.

During the 1996 minimum, a new center of magnetic activity emerged on Carrington Rotation (CR) 1911. This center developed into a new region that was still well visible on CR 1916. Rotations 1913, 1914 and 1915 were particularly sunspot free. We used these CRs to determine the evolution of the facular contribution.

Figure 1 presents an ensemble of MDI/SOHO magnetograms, from CR 1911 to CR 1916, each centered in the AR. The smooth ageing of the region from one rotation to the next is clearly seen, as well as that its extent grows with time. The AR contains sunspots and faculae; one small sunspot is still visible in CR 1913 but it has already vanished in CR 1914.

3. TOTAL FACULAR EMISSION EVOLUTION

We have focused our analysis in the facular region and its associated excess of irradiance.

Histograms in figure 2 show the evolution with Carrington rotations of the magnetic field distribution. In figures 1 and 2 we see that: the AR has a smaller extent when it is younger (see figure 1) and has the highest magnetic field values (CR 1911, 1912 and 1913; figure 2). These CRs are dominated by sunspots (very small in CR 1913). As the active region becomes older, magnetic field values become lower and faculae start dominating. At the same time, the AR grows in extent.

Proc. 1st Solar & Space Weather Euroconference, 'The Solar Cycle and Terrestrial Climate', Santa Cruz de Tenerife, Tenerife, Spain 25-29 September 2000 (ESA SP-463, December 2000)

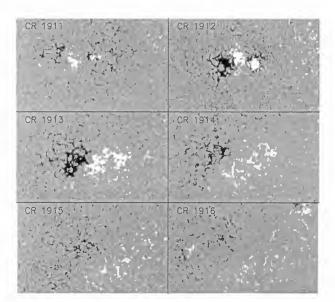


Figure 1. Solar magnetograms obtained by MDI showing the evolution of the studied AR, NOAA 7978, which emerged on CR 1911 (July 1996) and lasted until November 1996.

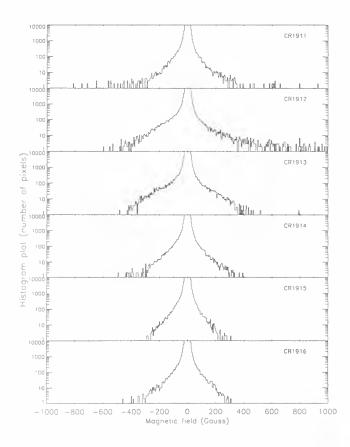


Figure 2. Evolution of the distribution of the magnetic field from magnetograms obtained when the AR was near the Central Meridian. For clarity, the number of pixels has been cut at 10^4 .

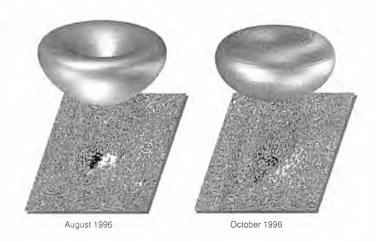


Figure 3. 3-dimensional rendering of the fit to the angular distribution of the excess irradiance emitted by the AR at 500 nm at two stages of its development. The brightening of the facular region is more uniform at the latter stage. The surfaces under the distributions are MDI magnetograms.

We have tried to reproduce the center to limb variation of the facular contribution to irradiance fluctuations by fitting phenomenological models to the corresponding angular distributions. Specifically, we have fitted the excess irradiance with respect to the heliocentric angle; the functional dependence assumed is:

$$I(\mu) = \mu(a + b\mu + c\mu^2) \tag{1}$$

where $\mu = \cos(\theta)$, theta is the heliocentric angle and a, b and c are the limb brightening parameters (Chapman et al., 1992). Rotating these curves, and assuming that the region emits the radiation in cylindrical symmetry around the vertical to the surface, we obtain a display of the excess facular emission in all directions.

Figure 3 shows that the angular distribution becomes less limb-brightened as the region becomes older and larger in extent.

In figure 1 we see how the AR spreads out from CR 1913 through 1916. To evaluate the effect of the AR ageing we have developed the concept of active region extent. We use two variables; first is the number of pixels of the AR with magnetic field intensity > 30 G, 3σ above the noise level in the MDI magnetograms (NB in figure 4). Second variable is the AR surface in millionths of solar hemisphere (SAR in figure 4).

NB and SAR reflect the evolution of the AR: the magnetic field present in the region decays while its extent grows with time.

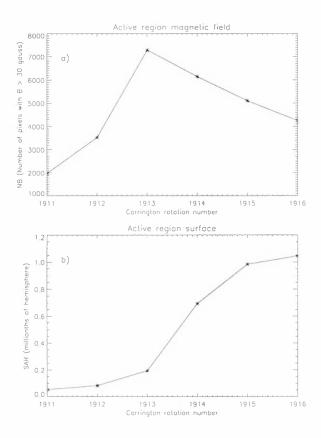


Figure 4. Magnetic evolution of the AR: a) number of AR pixels with B > 30 G (NB); b) magnetic region surface (SAR).

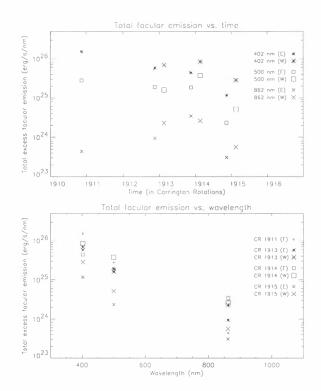


Figure 5. Temporal (top) and spectral (bottom) evolution of the total facular emission, for CRs 1913, 1914 and 1915

Figure 5 shows the temporal (top) and spectral (bottom) evolution of the total facular emission, i.e. in all directions, for CRs 1913, 1914 and 1915 (faculae dominated), though a small sunspot contribution is present in CR 1913. E and W mean the East and West disk passages of the AR. The behaviour of the excess irradiance during CRs 1913 and 1914 is quite similar, while CR 1915 shows a decrease probably due to the enlargement of the region as it gets older. The greatest excess occurs at the shortest wavelength (402 nm). The wavelength dependence of the total facular emission observed in this example is stronger than the one deduced from the contrast wavelength dependence elsewhere (Chapman & McGuire, 1977; Lawrence, 1988; Unruh et al., 1999).

4. CONCLUSIONS

We have characterised the evolution of the magnetic region by studying the equivalent extent and the number of pixels with a magnetic field value above a given threshold.

A simple model has been used for the total facular emission of the sample region, showing again a relationship with the evolution of the associated magnetic field. A strong dependence of the total excess irradiance with wavelength is found.

REFERENCES

- Foukal, P.J. & J. Lean, Astrophys. J. 328, 1986, 347
- Solanki, S.K., The Sun as a Variable Star: Solar and Stellar Irradiance Variations, IAU Colloquium 143, 1994
- Fröhlich, C. & J. Lean, GRL 25, 1998, 4377
- Scherrer, P.H. et al., Sol. Phys. 162, 1995, 129
- Fröhlich, C. et al., Sol. Phys. 162, 1995, 101
- Chapman, G.A. et al., JGR 97, 1992, 8211
- Chapman, G.A. & T. McGuire, Astrophys. J 217, 1977, 657
- Lawrence, J.K, Sol. Phys. 116, 1988, 17
- Unruh, Y.C, Solanki, S.K. & Fligge, M., A&A 345, 1999, 635

ON THE CONTRAST OF FACULAE AND SMALL MAGNETIC FEATURES

A. Ortiz¹, S.K. Solanki³, M. Fligge⁴, V. Domingo^{1,2}, and B. Sanahuja^{1,2}

¹Dept. Astronomia i Meteorologia, Universitat de Barcelona, E-08028 Barcelona, Spain, +34-93-4021122, fax +34-93-4021133, aortiz@am.ub.es

²Institut d'Estudis Espacials de Catalunya, E-08034 Barcelona, Spain

³Max-Planck-Institut für Aeronomie, 37191 Katlenburg-Lindau, Germany,

solanki@linmpi.mpg.de

⁴Institute of Astronomy, ETH-Zentrum, CH-8092 Zürich, Switzerland, fligge@astro.phys.ethz.ch

ABSTRACT

Sunspots, faculae and the magnetic network contribute to solar irradiance variations. The contribution due to faculae and the network is important for understanding solar irradiance variations, but suffers from considerable uncertainty. We focus our study on the faculae and the network which produce an increase in the irradiance. Data from the Michelson Doppler Interferometer (MDI) are employed. Starting from the surface distribution of the solar magnetic field we build a mask to detect bright features and study their contrast dependence on limb angle and magnetic field. By sorting the magnetic field strength into different bins we can distinguish between different associated bright features. We find that the contrast of active region faculae and the network exhibits different centre to limb variations, implying that they need to be treated separately when reconstructing variations of the total solar irradiance.

Key words: solar activity; irradiance variations; faculae; network.

1. INTRODUCTION

There is increasing evidence that the solar surface magnetic field is the most important driver of solar irradiance variations on time scales of days up to the solar activity cycle length (Fligge & Solanki, 2000). The photospheric magnetic field is bundled into discrete elements (flux tubes) whose diameter ranges from a hundred kilometers to several thousand. The brightness signature of these magnetic features is a strong function of their limb angle and their size (the large sunspots are dark while small flux tubes are generally bright) (Solanki, 1993). Our knowledge of the brightness of small scale magnetic features (groups of which form faculae and the network) is very incomplete (e.g. Solanki, 1994). We focus our study of the contrast dependence of faculae and the (enhanced) network on limb angle and magnetic field because:

- their contribution is important when modelling irradiance variations on time scales of years, but is not well known,
- it can be used as a test for flux tube models (Spruit, 1976; Deinzer et al., 1984a,b; Knölker & Schüssler, 1988),
- previous measurements usually have not distinguished features by magnetic flux, with a few exceptions. See Topka et al. (1992) and Topka et al. (1997) for examples.

In our analysis we use data from the MDI instrument (Scherrer et al., 1995) on the SOHO spacecraft; their main characteristics are:

- their continuity and uniformity (no seeing fluctuations),
- data from the magnetograms have a low noise level.
- the characteristics of the instrument and the data are well known.

2. DATA AND ANALYSIS PROCEDURE

We have used MDI/SOHO full disk magnetograms and continuum intensity images taken at $\lambda = 676.8$ nm for the period February to October, 1999. Intensity has been corrected for limb-darkening effects as suggested by Neckel & Labs (1994). The employed

Proc. 1st Solar & Space Weather Euroconference, 'The Solar Cycle and Terrestrial Climate', Santa Cruz de Tenerife, Tenerife, Spain, 25-29 September 2000 (ESA SP-463, December 2000)

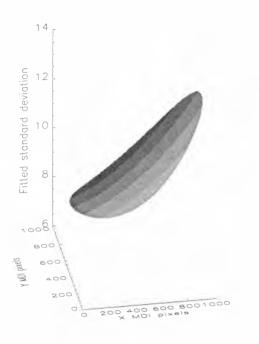


Figure 1. Standard deviation of the 5-minute averaged MDI magnetograms.

magnetograms are averages over 20 single magnetograms (taken at a cadence of 1 per minute). Intensities are standard 1-minute images; these images have been rotated to co-align with the corresponding average magnetogram. Care has been taken to use intensity images obtained as close in time to the magnetograms as possible. In almost all cases the two types of images were recorded within 30 minutes of each other. Therefore, features over the solar disk superpose on both the magnetogram and the intensity image.

We have carefully determined the noise level of MDI magnetograms and continuum images as a function of position. The standard deviation for the magnetic signal has been calculated using a running 100x100 pixel box over the solar disk, with the exception of the limbs. A surface is then fitted to the result and extrapolated to the whole solar disk. The resulting noise level shows an increase towards the SW limb probably due to velocity signal leakage. Figure 1 shows the calculated standard deviation $(1 \sigma_{mag})$ for the 5-minute averaged magnetograms. The procedure to determine the standard deviation and average of the quiet Sun intensity is similar.

Bright magnetic features are identified by setting a threshold of $3\sigma_{mag}$ for magnetic activity (≈ 18 G) and $3\sigma_{Iqs}$ below the average intensity to avoid sunspots. Using both thresholds we build a mask of the contrast of bright features for each day. In each pixel, the contrast C_{fac} is defined as:

$$C_{fac}(x,y) = \frac{I(x,y) - I_{qs}(x,y)}{I_{qs}(x,y)},$$
 (1)

where the subscript qs means the quiet Sun.

Pixels above the thresholds for each selected day are put together into a vector of about 6 10^5 elements, which gives good statistics of the facular and network behaviour. Contrasts, as well as limb angle $\mu = \cos(\theta)$ and magnetic flux are calculated for each point.

3. RESULTS

Figure 2 shows an example of the contrast mask mentioned above for October 12, 1999. The magnetogram (top) and continuum image (middle) show the activity present on the solar disk. The mask (bottom) shows the detected bright features. For example, sunspots near the NE limb are not evident in the mask, although it takes into account the faculae surrounding those sunspots. Smaller features belonging to the network are also pinpointed outside of the active regions.

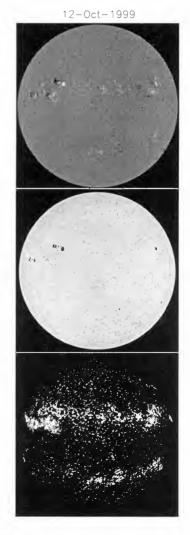


Figure 2. Top: averaged MDI magnetogram; middle: MDI intensity image; bottom: contrast mask for October 12, 1999.

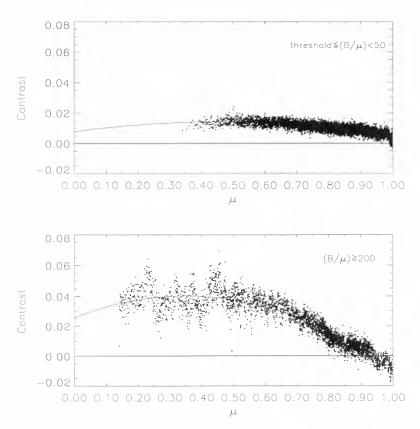


Figure 3. Facular and network contrast as a function of μ for low (top) and high (bottom) magnetic fields.

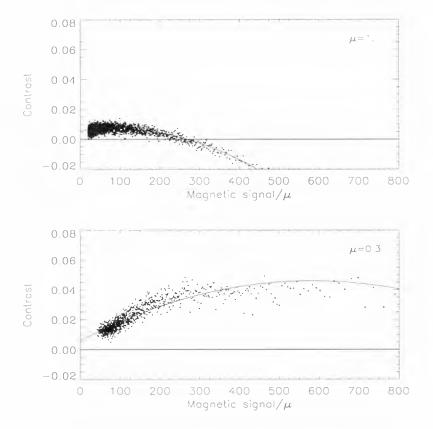


Figure 4. Contrast of "bright" features (contrast > -0.02) as a function of B/μ for $\mu = 1$ (top) and $\mu = 0.3$ (bottom).

We present the contrast dependence on μ , for different bins of B/μ , and on B/μ , for different positions on the solar disk. Representing B/μ takes account of the foreshortening effects that cause the magnetic signal to decrease to the level of the background noise at the very limb (even if regions with strong magnetic field are present). Finally, to represent this amount of data they are binned into groups of 40 pixels before plotting.

The B/μ values are binned in five intervals that range from threshold level (≈ 18 G) to more than 200 G. In figure 3 we present the contrast as a function of μ , for both the lowest and highest B/μ intervals. A second order polynomial has been fitted to guide the eye and a line indicating $C_{fac} = 0$ has been added for clarity.

There are clear differences between the behaviour of the contrast in both cases, one showing features with the lowest magnetic flux per pixel (top), probably the network, the other showing features with the highest magnetic signal (bottom), probably faculae. Clearly, features within the network show a low and almost constant contrast compared to that shown by active region faculae which have a very pronounced center-to-limb variation (CLV). Note also the negative contrast around disk center seen for faculae, that becomes positive when looking at the network.

Figure 4 shows the contrast dependence on B/μ , for positions at disk center (μ =1) and at the limb (μ =0.3). The fits are also second degree polynomials. The contrast at the limb is considerably higher than at disk centre. At the limb, higher contrasts are associated with higher magnetic fields, whereas at μ =1 faculae with high fields appear dark, as in Figure 3.

4. CONCLUSIONS

The magnetic network provides an important contribution to irradiance variations that has to be taken into account in irradiance models. By binning into different magnetic fields we can distinguish between different associated bright features. The contrast of active region faculae and of the network exhibits different CLV, implying that they need to be treated separately when reconstructing variations of the total solar irradiance.

Stronger magnetogram signals (corresponding to wider flux tubes on average, see Grossmann-Doerth et al., 1994) appear dark at disk centre, but very bright at the limbs, while the weakest signals (narrowest flux tubes) are equally visible at disk centre and at the limb. This result is in good agreement with the observational results of Topka et al. (1997) and with the predictions of theoretical flux-tube models (Deinzer et al., 1984a,b; Knölker et al., 1988; Knölker & Schüssler, 1988) if there is a distribution of fluxtube sizes present on the Sun. The advantage of the present investigation relative to that of Topka et al. (1997) is that by using full disk MDI data we have a result for a well-defined spatial resolution, so that any models derived on the basis of these results can be directly used for reconstructing total and spectral solar irradiance measered by VIRGO (Fröhlich et al., 1995) without further adjustment.

REFERENCES

- Deinzer et al., 1984a, Astron. Astrophys. 139, 426.
- Deinzer et al., 1984b, Astron. Astrophys. 139, 435.
- Fligge M., Solanki S.K., 2000, J. Astrophys. Astr., in press.
- Fröhlich, C. et al., Sol. Phys. 162, 1995, 101
- Grossmann-Doerth et al., 1994, Astron. Astrophys. 285, 648.
- Knölker M., Schüssler M., 1988, Astron. Astrophys. 202, 275.
- Knölker M. et al., 1988, Astron. Astrophys. 194, 257.
- Neckel H, Labs D., 1994, Solar Phys. 153, 91.
- Scherrer P. et al., 1995, Solar Phys. 162, 129.
- Solanki S.K., 1993, Space Sci. Rev. 61, 1.
- Solanki S.K., 1994, in *The Sun as a Variable Star:* Solar and Stellar Irradiance Variations, (ed. J.M. Pap, C. Fröhlich, H. Hudson and S.K. Solanki), Cambridge Univ. Press IAU Coll. 143, p. 226
- Spruit H.C., 1976, Solar Phys. 50, 269.
- Topka et al., 1992, Astrophys. J. 396, 351.
- Topka et al., 1997, Astrophys. J. 484, 479.

EFFECTS OF HYSTERESIS OF SOME SOLAR INDICES DURING THE PAST THREE SOLAR CYCLES 20, 21 AND 22

A. Özgüç¹, T. Ataç¹, and A. Antalová²

¹Boğaziçi University, Kandilli Observatory and Earthquake Research Institute, Çengelköy, Istanbul, Turkey ²Astronomical Institute of the Slovak Academy of Sciences, 059 60 Tatranská Lomnica, The Slovak Republic

ABSTRACT

We show smoothed time series of some solar activity indicators exhibit significant solar cycle dependent differences in their relative variations during the past three solar cycles 20, 21 and 22. The shapes and the directions of these differences vary from cycle to cycle. This study is a continuation of the previous hysteresis effect studies performed by A.Ö. and T.A. We expand upon previous work by including some new indices of solar activity such as the 10.7 cm radio flux (F 10) and the relative sunspot number.

Key words: sun; solar cycles; solar activity; hysteresis.

I. INTRODUCTION

Some recent works suggest that certain pair of the solar activity indices show hysteresis, e.g., solar cycle dependent differences in their relative variations (Özgüç & Ataç, 2001; Bachman & White, 1994; Harvey, 1992). The shapes and the directions of these differences vary from cycle to cycle. Bachman & White, in particular, express confidence that hysteresis is a real phenomenon, not a result of instrumental effects, and estimate lag times of activity indices compared to the sunspot number, however, some of their measured delay times can be significantly larger than the short-time delays associated with the rotational modulation of enhanced solar activity. Some other authors go a step further to show the hysteresis between oscillation frequency and activity indicators (Moreno-Insetis & Solanki, 2000; Tripathy et al., 2000; Jiménez-Reyes, 1998).

In the present paper, we expand upon the above work to show that hysteresis is present among many pairs of activity indices during solar cycles 20, 21 and 22. For this purpose we choose the flare index (FI), the relative sunspot numbers (SSN), the coronal index (CI), and the daily radio flux at 10.7 cm (F10) as the indicators of solar activity. Although hysteresis shapes amongst several indices have been shown in the past (Bachman & White, 1994), this is the first time that such relations are seen in flare index for three successive cycles.

2. SOLAR ACTIVITY INDEX DATA SETS

The solar activity indicators we used in this study are as follows:

- The flare index. It is of value as a measure of the short-lived activity on the Sun. The daily sums of the index for the northern and the southern hemispheres and for the total surface are divided by the total time of observation of that day. Because the time coverage of flare observations is not always complete during a day (sometimes 75% or 90%), it is corrected by dividing by the total time of observations of that day to place the daily sum of the flare index on a common 24-hour period (Ataç & Özgüç, 1998).
- The relative sunspot number. This is an index of the activity of the entire visible disk of the Sun calculated at the World Data Center A in Boulder, Colorado using daily observations from the network of contributing observers. This index is considered to be consistent with the original Zürich sunspot number since 1848 (mcKinnon, 1987).
- The coronal activity index. This is derived by Rybanský et al. (1994) from the measurements of the total energy emitted by the Sun's outermost atmospheric layer (the corona) at a wavelength of 530.3 nm. It gives a radiant energy emitted by the entire visible corona within Fe XIV spectral line. Lomnický Štit in The Slovak Republic served as the reference station for calculating the index.
- The daily solar radio flux values. These are derived from the daily measurements of the integrated emission from the solar disc at 2800 MHz (10.7 cm wavelength) which have been made by the NRC of Canada since 1947. The flux values are expressed in solar flux units $(1s. f.u. = 10^{-22} Wm^{-2} Hz^{-1})$ and originate in the chromosphere and corona. The characteristics of the observations are rewieved by Covington (1969).

Proc. 1st Solar & Space Weather Euroconference, 'The Solar Cycle and Terrestrial Climate', Santa Cruz de Tenerife, Tenerife, Spain, 25-29 September 2000 (ESA SP-463, December 2000)

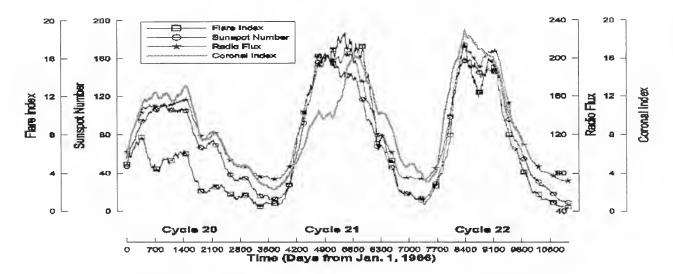


Figure 1. Plots of smoothed time series of FI, SSN, F10 and CI. Each plot is drawn with 365-day running means for three successive cycles 20, 21 and 22.

3. ANALYSIS

Figure 1 shows how the activity indicators we used exhibit variations during the successive three cycles. We choose flare index to be the abscissa of all plots in figures except Figure 1, in order to display the effects of hysteresis most clearly. We perform the 365-day running means using only common days of data to produce smoother hysteresis patterns for three successive cycles 20, 21 and 22. The plotted curve in Figure 2 clearly exhibits a hysteresis: The flare index does not follow the same path in the rising and falling parts of the three solar cycles when plotted against the coronal index. Line styles of the individual plots are the same in all the three figures (Figures 2-4). The thicker sections of the curves with the symbols

Table 1. Position differences between the ascending and the descending branches of the three cycles.

	CI	SSN	F10
Cycle 20	Negative	Negative	Negative
Cycle 21	Negative	Positive	Positive
Cycle 22	Positive	Negative	Negative

correspond to the rising parts of the cycles (e.g., flare index increasing with time). Arrows indicate the direction of time. The saturation effects are seen in all the plots at the extreme phases. The most interesting finding in Figure 2 is the separations (width of the hysteresis) between the two branches for each cycle. These separations are very large for cycle 20 and 21 but not so large for cycle 22. We can observe the same hysteresis phenomenon when we draw the plots for SSN and F10 versus FI (Figures 3 and 4). The separations between the two paths for each cycle are small but larger than the error limits. The error bars at the top left corner of each figure indicate 1σ values of that plot. The hysteresis is the same for the three indicators for cycle 20. The hysteresis cycles

shown in Figures 2 - 4 will be said to have *positive* circulation sense when the flare index is smaller in the rising half of the cycle (clockwise circulation of the hysteresis). Similarly, we will say that the inclination of a cycle is *positive* (or that it is *forward inclined*) if the plot of that cycle moves the clockwise direction if we assume that the position of the cycle 20 as a base in that figure; otherwise the inclination will be called *negative* (and the cycle will be said to be *backward inclined*). All the indices we used shown in figures have negative circulation sense for cycle 20. SSN and F10 have positive circulation sense, however CI has negative one for cycle 21 and this cycle is

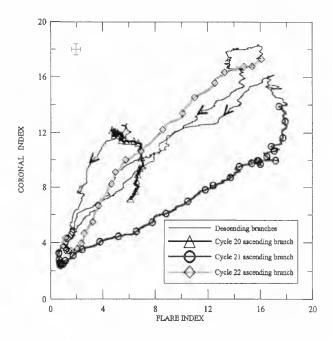


Figure 2. Scatterplots showing the hysteresis phenomenon for the coronal index versus flare index for three successive cycles (20, 21 and 22). The thick lines with the different symbols drawn with 365-day running means, show the ascending branches and the thin lines are the descending branches. Arrows indicate the direction of time.

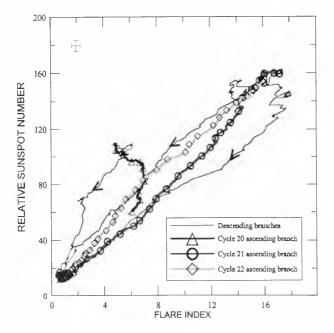


Figure 3. Scatterplot drawn with 365-day running means, shows the hysteresis during the past three solar cycles (20, 21 and 22) between the relative sunspot number and the flare index.

forward inclined while cycle 22 is backward inclined. CI has positive circulation sense and SSN and F10 have negative ones for cycle 22. This circulation senses are show in Table 1.

4. DISCUSSION

The choise of activity indicator versus flare index may strongly influence the resulting hysteresis in a given cycle. For example for cycle 20, the circulation senses are negative for all the indices; however for cycle 21, the circulation sense is negative only for CI. The width differences of the hysteresis for each index are very significant from cycle to cycle. Bachman & White (1994) estimated lag times for all possible pairs of indices by offsetting one index in time untill the hysteresis curve collapses into roughly a straight line. However we could not estimate lag times for the pairs of indices. Because the shape and the width of the hysteresis vary from cycle to cycle (e.g., for one cycle lag time to be found 40 days and for the next cycle is it found 180 days). The difference between the two cycles is, however, unexpected. Recently some authors have shown that a hysteresis exists between the p-mode frequency shifts and the activity indicators but they investigated for only cycle 22 (Jiménez-Reyes, et al., 1998; Moreno-Insetis & Solanki, 2000; Tripathy, et al., 2000). The sign of the inclination of hysteresis varies from one cycle to the next. Figures 2 - 4 show how the inclination varies for the different indices for the successive three cycles (20, 21 and 22). To summarise, although hysteresis warrants serious consideration as a possible long-term feature of solar activity but the shape and width differences between the three cycles are, however, unexpected. The circulation sense and the inclination of cycle need more detailed investigations.

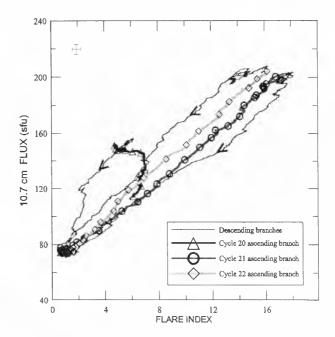


Figure 4. Scatterplots showing the hysteresis phenomenon for the radio flux versus flare index for three successive cycles (20, 21 and 22).

ACKNOWLEDGMENTS

This work was supported by Boğaziçi University Research Fund by the project of 00T101.

REFERENCES

- Ataç, T. & Özgüç, A., 1998, Solar Phys. 180, 397
- Bachman, K. T. & White, O. R., 1994, Solar Phys. 150, 347
- Covington, E. A., 1969, JRASC, 63, 125
- Harvey, K., 1992 in Proc. Workshop on the Solar Electromagnetic Radiation Study for Solar Cycle 22, R. F. Donnelly (ed.), p. 113
- Jiménez-Reyes, S. J., Régulo, C., Pallé, P. L. & Roca Cortés, T., 1998, A&A, 329, 1119
- McKinnon, J. A. 1987, Sunspot Numbers: 16101985, UAG-95, (Boulder: NOAA)
- Moreno-Insetis, F. & Solanki, S. K., 2000, MNRAS, 313, 411
- Özgüç, A. & Ataç, T., 2001, Recent Insights into the Physics of the Sun and Heliosphere, ASP Conf. Ser., P. Brekke, B. Fleck & J. B. Gurman (eds.) in press.
- Rybanský, M., Rušin, V., Gaspar, P. & Altrock, C. R., 1994, Solar Phys. 152, 487
- Scherrer, H. P., Wilcox, M.J., Svalgaard, L., et al., 1977, Solar Phys. 54, 353
- Tripathy, S. C., Kumar, B., Jain, K., & Bhatnagar, A. 2000, J. Astrophys. Astr. in press

GRANULAR EVOLUTION FROM 2D(X,T)-SLICES AND FROM TRACKING GRANULES

W. Poetzi¹, A. Hanslmeier¹, and P.N. Brandt²

¹IGAM, Graz, Austria ²KIS, Freiburg i. Br., Germany

ABSTRACT

The evolution of granules can be investigated in various ways, two of them have been selected for this paper. The first method makes use of 2 dimensional slices of the data set containing granulation images with one spatial and one time dimension. In these slices the evolution can be seen very clearly. The second method tracks individual granules from one image to the next. With these methodes we want to find automatically different types of granules, like exploding granules, merging granules, or granules that fade away. In combination with velocity fields (divergence patterns) we also want to show the relation between exploding granules and mesogranules.

Key words: sun;granulation;mesogranulation.

1. INTRODUCTION

The Russian astronomer Alexis Hansky (1870 – 1908) used a conventional astrograph and an enlarging camera for high-resolution photography of the solar disk. He tried to get sequences of granulation photographs separated by short time intervals in order to study the changes in the granules with time. Although his attempts were only partially successful, he derived an estimate of about 5 minutes for the mean lifetime of the granules.

With better instruments and better data aquisition these measurements have been improved and a lot of questions arose. The evolution of the individual granules did not behave in a simple manner. The lifetime measurements (e.g. Bray & Loughhead (1984), Deubner et al. (1978), Mehltretter (1978), Alissandrakis et al. (1987)) have been done with some restrictions, the birth and death of granules had to be defined. Mehltretter (1978) found that merging granules have shorter lifetimes and granules that dissolve live longer. Kawaguchi (1980) found a relation between the size of the granules and their birth. Hirzberger et al. (1999) investigated the evolution of granules and defined several different types of granules; he obtained 30.2% fragmenting, 15.9% dissolving, and 52.9% merging granules - the selection of the types was done manually.

2. OUR DATA

The data were obtained by G. W. Simon, P. N. Brandt, and R. A. Shine (Simon et al. (1994)) on 5th of June 1993 at the Swedish Solar Observatory on La Palma. A total of more than 3700 images (2 images per 21 sec) at a wavelength of 468 ± 5 nm with very high quality have been obtained in 11 hours. The corrected and reduced images had a size of 64×64 arcsec (8 pixels/arcsec) including apodised borders (5%) and the length of the series was about 8.75 hours (1500 images, the better one of each image pair was taken). 76% of the images have a contrast better than 8%.

3. METHODS

3.1. Space-Time Slices

Space time slices are 2 dimensional sections through a 3 dimensional data set in the time direction, i.e. the resulting data set has one time and one spatial dimension. The simplest way is just to use one row or column of each image and put them together in ascending time. In our case we used a row in the center of our images. The resulting image has then the dimensions 64" x 8.75 hours (512 x 1500 pixel).

Such an image (as Fig. 1) shows very clearly the evolution of the granules that are intersected, it even seems to be the case that there are granules that can be followed through the whole time series.

The next step is to distinguish between granular and intergranular regions, this is done by a simple unsharp masking procedure. The unsharp masking is applied line by line so that only a spatial smoothing is performed. In order to find the granular type the geometrical granular centers in each line are marked.

By this procedure granules are defined as structures with (x, t) coordinates, they are temporal cross-sections at a fixed location. Events such as fragmenting, merging, or fading away can happen more than once per granule. In Fig 2 one can see that a granule can have branches upwards and downwards, the upward branches are fragmenting events, the downward branches are merging events, and each *dead end* is a fading away event.

Proc. 1st Solar & Space Weather Euroconference, 'The Solar Cycle and Terrestrial Climate', Santa Cruz de Tenerife, Tenerife, Spain, 25-29 September 2000 (ESA SP-463, December 2000)

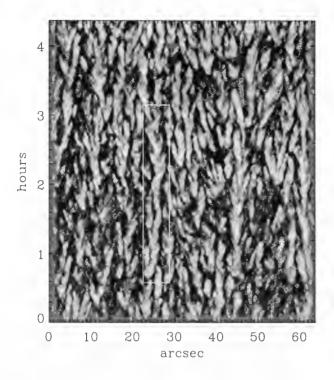
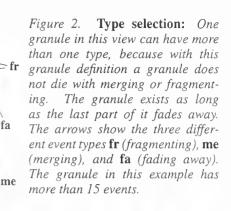


Figure 1. Space time slice image: Granules are represented by bright ridges. In the white rectangle the evolution of a single granule can be seen, it is not clear of which type it is: it splits up, merges, and seems to explode in the upper part.

The type of the granule events is then detected by counting the number of centers and interpreting the change of this number. A merging happens when the number of centers decreases and the pixel after the last centers is not intergranular. A fragmenting event occurs when the number of centers increases. If the number of centers decreases it has also be checked if the following pixel is intergranular, which will lead to a fading away event. A hole, which is an intergranular region inside a granulum, consists of a fragmenting and a merging event, this can also be wrong if the granulum is only ring-like or ushaped. In Fig. 2 we show how the types are selected in principle. Exploding granules are only detected in the fragmenting type of granules – a cross section through an exploding granule shows in most cases more than one center (e.g. if it is ring-like a cross section will show 2 granules, except the section is tangential). Not all exploding granules are detected in this way, but they are larger in size than other granules and therefore they are more likeley to be detected. The detection of exploding granules is done by calculating the mean velocity of the expanding branches in our granule. If a threshold velocity of 2 km/s is set 4.2% of all events are exploding events, with 3.0 km/s only 2.0 % are remaining.

3.2. Tracking Granules

In this method granules are tracked forward in time from one image to the next. At first granules have to be separated from the intergranular regions, this is done with a Fourier filter described in Roudier & Muller (1986).



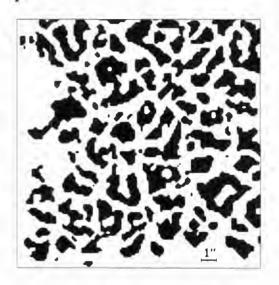


Figure 3. Subimage with identified granules: Granules are separated from intergranular regions by a Fourier filtering technique. Granules touching the borders of the image are cut away (left and bottom), they are also affected by the apodizing, which decreases the image contrast down to 0 at the borders. Granules smaller than 4 pixels are not taken into account.

The FWHM of the filter is for our case 1.54 arcsec and the position is 0.33 to 1.87 arcsec (i.e. structures with a size of 0.33 up to 1.87 arcsec are enhanced, smaller or larger structures become fainter). After a convolution of the image with this filter an intensity threshold value has to be determined, above which a pixel is a granular pixel, see Fig. 3. This threshold value lies normally a little bit above the mean value in order to separate more granules (in my case I used 1% above the mean).

It is also possible to use other methods for separating granules from intergranular regions, such as segmentation (Strous (1995); Roudier et al. (1999)), unsharp masking (see above), or applying a Laplace Filter and determine the inflection points, which are then defined as granular borders.

The separated granules have then to be identified and each granule gets its own number (color). Then for each granule the subsequent granules are searched until following happens:

• The granule splits up into 2 or more parts $\longrightarrow frag$ -

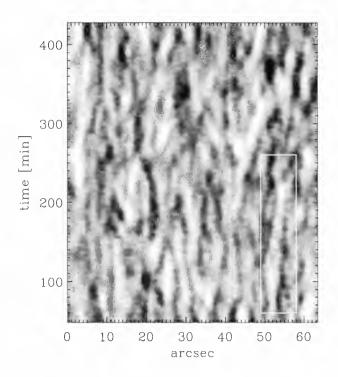


Figure 4. Space-time slice of divergence: The divergence was integrated over 20 minutes (= 57 images), then a column of each divergence image was taken and plotted. The bright ridges are the upflow regions (mesogranules ?), from this image their size seems to be about >5", their lifetime somewhere between 50 and 150 minutes and they show horizontal motions - from the mesogranule in the white rectangle one can derive a velocity of about 0.5 km/s.

menting.

- The granule disappears \longrightarrow fading away.
- The granule shows none of the above mentioned evolutions, then the image before is used and it is tested, whether there are two granules merging → *merging*, or not. In the latter case the granule is not taken for the statistics.

As can be seen in Fig. 3, there are granules missing, that lie at the borders, therefore only granules are taken into account, that are definitely inside the image (all pixel are more than 4 arcsec away from the borders).

3.3. Mesogranules

In order to make the mesogranulation visible, November et al. (1981) averaged velocity images in Fe 1, Mg 1, and Ca 11 lines over about 1 hour. They averaged them at different resolutions (1", 3", and 9"), the best images of the mesogranular pattern were obtained by subtracting the 9" averaged supergranular pattern from the 1" averaged velocity images. As a result they got a cellular pattern of 5 to 10 Mm in size.

Our mesogranulation images were produced by the following method: The displacement vectors between each

	fr		m			
granule tracking method						
Rel. Num. (%)	52.9	19.7	27.4			
Mean Dia.	1.94"	0.35"	1.84"			
Mean diverg.	0.000 -0.01		-0.004			
space-time-slice method						
Rel. Num.	35.7 (4.2)	46.5	17.8			
Mean diverg.	-0.023 (-0.006)	0.004	-0.025			
Hirzberger et al.	30.2	15.9	52.9			
Mehltretter	50	20	30			

Table 1. Granule types and divergence: The relative numbers for the different types: (fr) fragmenting, (fa) fading, (m) merging, exploding are put into brackets. The mean diameter depends on the type, but the mean divergence is nearly the same for all types.

pair of images in our time series were calculated with the Local Correlation Technique method using a Gaussian window of 1.35 and of 67. Then the difference between the 67 and the 1.35 velocities have been taken in order to remove the supergranular background. In the temporal direction a moving average over 20 minutes (57 images) is applied. If from each of these divergence images only one column is taken (always at the same spatial position) and combined to a space-time slice, an image as shown in Fig. 4 is obtained. The plot shows dark and bright ridges corresponding to downflow and upflow regions, respectively. The bright upflow regions can be interpreted as mesogranules.

4. RESULTS

When detecting the granular types, also the position of each granule has to be stored, the position is defined by all granule pixels and the time, when the event happens. Table 1 shows the number obtained with the two different methods and a comparison with two other authors. The two methods produce more or less completely different results, especially the number of granules that fade away is enormous for the space-time-slice method. The values of the tracking method are in relatively good agreement with Hirzberger et al. (1999), who obtained their results manually, but they investigated only 481 granules whereas we had 49819. The mean divergence of the granule positions are nearly 0 (the maximum possible divergence values are $\pm 5 \cdot 10^{-3} s^{-1}$) with a standard deviation of 1.3. The number of positive divergence values is nearly the same as that of the negative ones.

The excess plots in Fig. 5 show the following: In the upper left panel one can see that the mean divergence is negative, and additionally the whole histogram is not symmetric. There are more small negative divergence values then small positive ones, but more large positive divergence values then large negative ones. The fragmenting and the merging types show nearly the same underlying velocity field, they are lying on positive divergence regions. The fading away granules show the opposite behavior, they have a strong depression in positive divergence values (down to -30%).

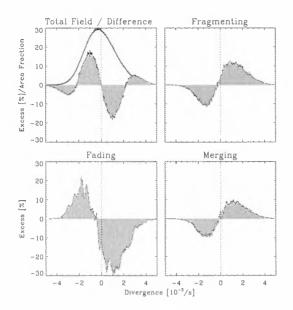


Figure 5. Divergence Excess: The difference between the histograms of the divergence at locations of the different granular types and of the divergence of the total field (= excess). In the first plot the excess is plotted as the difference between the negative and the positive histogram axis.

5. DISCUSSION

Table 1 and Fig. 5 show a completely different result. This is mainly due to the mean divergence of the total field, which is negative. But the field is not only negative it is also asymmetrical, which tells us something about the upflows and downflows. The excess is positive for large divergence values, which means that upflows are faster, and the downflows seem to be slower, because there excess is positive for small divergence values. Fragmenting granules are expected to be at locations where the matter expands and the granules split up therefore, this implies a positive underlying divergence field, which is the case. But also merging granules show the same behavior, that means that granules mainly merge when they are expanding and not when they are pushed together. Granules that fade away should show that they are located at downflow regions, which can be seen clearly in Fig. 5, because the excess is much higher for negative divergence values than for positive.

The difference in the relative numbers in table 1 between the different authors has a relatively simple reason: The relative number depends strongly on the way how these events are counted, Hirzberger et al. followed a granule as long until an event happened, we only looked into the next or the preceeding image, in our routine most of the granules did not show any event. We found merging granules by a backward search, i.e. we looked for fragmenting granules in a negative time direction, in this case granules that merge do only count for one granule, otherwise one would get more than twice as much merging granules, since there are always 2 or more granules that are necessary for a merging event. If we take this into account we get following relative numbers: fragmenting < 41%, fading < 15%, and merging > 44%, which is not far away from the result of Hirzberger et al. who had obtained their values manually.

Using space-time slices is affected with the problem of velocities perpendicular to the slices, i.e. in an x - t slice the y velocities are not taken into account. Due to this perpendicular velocity field a lot of granules seem to fade away because they leave the slice and move into the neighor slice. The x - t slice show at a first glance very clearly the granular evolution, but in this form they cannot really be used for investigating the temporal behavior of the granulation.

These results are not in coincidence with Straus et al. (1992), who could not find a dividing line between granulation and mesogranulation. An additional test with different averaging times of the mesogranular field lead to the same results which is contradictionary to Rieutord et al. (2000), who showed that it is possible to generate different mesogranule properties by various averaging techniques and scales.

In the future we also want to separate exploding granules with the tracking method, and see if their behavior is more linked to the mesogranular field than that of the fragmenting granules.

This project is supported by the Austrian Science Fund Nr. P 13 308.

REFERENCES

- Alissandrakis C.E., Dialetis D., Tsiropoula G., 1987, Astron. Astrophys., 174, 275
- Bray R.J., Loughhead R.E., 1984, The solar granulation, Cambridge University Press
- Deubner F.L., Durrant C., Stix M., Schröter E.H. (eds.), 1978, Small Scale Motions on the Sun, vol. 179 of Mitteilungen des Kiepenheuer Instituts
- Hirzberger J., Bonet J.A., Vázquez M., Hanslmeier A., Apr. 1999, ApJ, 515, 441
- Kawaguchi I., Mar. 1980, sp, 65, 207
- Mehltretter J.P., 1978, Astron. Astrophys., 62, 311
- November L.J., Toomre J., Gebbie K.B., 1981, Astrophys. J., 245, L123
- Rieutord M., Roudier T., Malherbe J.M., Rincon F., May 2000, Astron. Astrophys., 357, 1063
- Roudier T., Muller R., 1986, Sol. Phys., 107, 11
- Roudier T., Rieutord M., Malherbe J.M., Vigneau J., Sep. 1999, Astron. Astrophys., 349, 301
- Simon G.W., Brandt P.N., November L.J., Scharmer G.B., Shine R.A., 1994, Solar Surface Magnetism, 261–270
- Straus T., Deubner F.L., Fleck B., Mar. 1992, Astron. Astrophys., 256, 652
- Strous L.H., 1995, Fourth SOHO Workshop: Helioseismology, 213–217

BEHAVIOUR OF THE COSMIC IONS CHARGE STATE UNDER ACCELERATION IN THEIR SOURCES

M. D. Rodríguez-Frías¹, L. del Peral¹, and J. Pérez-Peraza²

¹Departamento de Física. Universidad de Alcalá, E-28871 Alcalá de Henares, Madrid, Spain. ²Instituto de Geofísica, U. N. A. M., 04510 - C. U., México D. F., México.

ABSTRACT

We have fully developed a computational model (ES-CAPE) to follow the behaviour of the mean charge state of ions in Solar Energetic Particle (SEP) events while are accelerated. Our model takes into account explicitly the 2nd-order Fermi-type stochastic acceleration under a magnetohydrodynamic turbulence. We have found that the mean ionic charge states are strongly dependent on plasma parameters as source temperature or density and on acceleration parameters as efficiency or the time scales for acceleration. Our model finds a systematic increase of the ionic charge states with energy for all the ions studied. This energy dependence differs between ions, but in the energy range of observations affects mainly to heavy ions.

Key words: Cosmic rays: particle acceleration; cosmic rays: solar energetic particles..

1. INTRODUCTION.

The calculation of the mean charge states of various ion stages of abundant elements is the first step in understanding and modelling the X-ray emission from hot astrophysical plasmas such as stellar coronae. The charge state enhancement of different species over the solar values shows that there are parameters on which the amount of emission of any element depends, as for example the effective charge, the ion rigidity, the source confinement time... Moreover, the fractional effective charge behaviour directly affects models that attempt to explain the abundance variations. As we will show later the mean ionization states should be a valuable tool for studies of the possible sources at the acceleration site of these ions, but also for how the acceleration mechanism may affect particles with different rigidity.

Our nearest astrophysical plasmas are the solar corona and the solar wind. Particle acceleration in these plasmas has been stated from UV, RX and Solar Energetic Particle (SEP) measurements. Nowadays, it is well assumed a rough division of the SEP events into Gradual Solar Energetic Particle (GSEP) events and Impulsive Solar Energetic Particle (ISEP) events. ISEP events are compatible with high charge states for Fe ions $(q \sim 20)$ and most of the ions lighter than Si appear fully stripped. From these observations, a common plasma source temperature of $T \sim 10^7$ K has been assumed for these events. GSEP events are characterized by lower Fe charge states $(q \sim 11 - 15)$ and most of the ions have charge states typical of an equilibrium temperature $T \sim 2 \ 10^6 \ {\rm K}$ for the plasma source. Moreover it has been stated that ISEP events are dominated by particles accelerated low in the corona by stochastic acceleration, while GSEP events are dominated by particles accelerated by CME-driven shocks. For a more quantitative approach see (Pérez-Peraza, 1998).

New direct measurements of SEP ionic charge states, with high sensitivity of the new instrumentation have been obtained rencently, in particular from ACE (Cohen et al., 1999), (Mobius et al., 1999) and SAM-PEX (Leske, 1999), (Mazur et al., 1999). These new experiments have provided charge states information in a wider energy range, even up to 60 MeV/n, and for single SEPs, instead of the event averages provided by earlier measurements. Anyway up to now they have mainly reported on ionic charge state distributions of GSEP, while those from ISEP have been scarce, mainly due to the low ion statistic in this kind of events. We hope in a nearly future to have accurated charge state measurements from ISEP to check the range of validitity of our model.

We have foccused our study on 12 astrophysically abundant elements (C, N, O, Ne, Na, Mg, Al, Si, S, Ca, Fe, Ni) and we have covered a very wide energy range, from the thermal equilibrium up to 1 GeV/n. As source plasma, we are interested in the solar flares, regions of low- β , hot ($T = 10^7$ K) plasma with high density ($n = 10^9 \text{ cm}^{-3}$), short magnetic confinement times ($\tau = 0.01 - 10$ s), high magnetic field (B=100 G) and high Alfvén speed. To model the projectil behaviour under acceleration, the source has been modelled as a plasma of protons and free electrons.

Proc. 1st Solar & Space Weather Euroconference. 'The Solar Cycle and Terrestrial Climate'. Santa Cruz de Tenerife. Tenerife. Spain. 25-29 September 2000 (ESA SP-463, December 2000)

2. EFFECTIVE CHARGE BEHAVIOUR UNDER STOCHASTIC ACCELERATION

Energized ions travelling inside a plasma at velocity v may undergo two charge exchange processes. They can capture or lose electrons while they interact with the ambient plasma. Therefore the following processes have to be cosidered: electron ionization, autoionization after electron excitation, radiative recombination and dielectronic recombination. For a detailed description see Rodríguez-Frías et al. (2000). Moreover, these energized ions lose energy due to Coulomb collisions with the electrons of the medium, where the Bethe-Bloch equation gives the energy loss rate due to ionization. Therefore the charge state distribution of the projectiles have been obtained by the interaction of the ion projectil with the free plasma electrons, while ion-ion interactions have been neglected.

Here, our analysis is focussed on projectil ions accelerated from the background thermal matter, in a way that their initial velocities and charge states correspond to that of the thermal plasma. For the thermal charge states, q_{th} , we merely rely in calculations based on astrophysical plasma ionization fractions given by Arnaud and Rothenflug (1985) and updated for Fe ions Arnaud and Raymond (1992), as tables of equilibrium ionization of plasma ions for coronal conditions.

If the acceleration mechanism at the source site is not taken into account, the energy loss contribution will bring the particle to thermalize. Nevertheless, when an acceleration mechanism is present, it will transfer energy to the given particle at a rate that for stochastic acceleration by the fast MHD mode is (Gallegos-Cruz and Pérez-Peraza, 1995):

$$\left(\frac{dE}{dt}\right)_{acc} = \left(\frac{4}{3}\right)\alpha(E^2 + 2mc^2E)^{1/2} \qquad (1)$$

where m is the ion mass, c is the light speed, E is the projectil kinetic energy and α (s^{-1}) is the efficiency of the acceleration mechanism involved. The α parameter depends on the specific MHD turbulence, the wave number, the total turbulent energy density and the magnetic energy density, and can roughly be taken as a time-independent and energy-independent parameter (Pérez-Peraza and Gallegos-Cruz, 1994).

Once the gain energy rate due to acceleration is higher than that accounting for losses, the ion is accelerated from the thermal matter, starting with an averaged thermal effective charge q_{th} . While the ion is accelerated, the effective charge state, q^* , evolves iteratively in each acceleration step, according to the equation:

$$q^* = q_0 + n_t t_a \Delta q_i \int_0^c [\sigma_{ioniz}(v)] v f(v) dv \quad (2)$$
$$-n_t t_a \Delta q_c \int_0^c [\sigma_{capture}(v)] v f(v) dv$$

where q_0 is the effective charge of the ion at the beginning of each acceleration step in electron charge units (for the first acceleration step $q_0 = q_{th}$), Δq_i and Δq_c are the average charge exchange in each ionization and capture process respectively, f(v) is the plasma electron distribution which is a Maxwellian function in the rest frame of the source plasma, σ_{ioniz} is the total cross section for electron loss, $\sigma_{capture}$ is the total cross section for electron capture and t_a is the time spent in each acceleration step, obtained from (1) (Rodríguez-Frías et al., 2000).

Concerning propagation effects and additional acceleration in the interplanetary medium, we have assumed they do not affect significatively the charge state distributions obtained, due to the rather low density of the interplanetary plasma.

3. RESULTS AND DISCUSSION

To show how the efficiency of the acceleration mechanism affects the charge state behaviour, we have plotted in Figure 1 the fractional charge states of Fe ions versus the kinetic energy of the ion. In Figure 1(a) we have taken as input parameters a source temperature and density number of $T = 10^7$ K and $n = 10^9 \ cm^{-3}$ respectively. These are the source parameters of ISEP events inferred from experimental measurements, where Fe charge states from q =18.11 - 19.66 were reported (Mobius et al., 1999). We have considered three acceleration efficiencies, and as it can be seen in Figure 1(a), in all cases our model predicts Fe charge states higher than experimental ones, as can be seen in Table 1. The mean charge states may either be enhanced or depressed, depending on the acceleration efficiency of the acceleration mechanism involved. Under $\alpha = 0.01 \ s^{-1}$ and $\alpha = 0.05 \ s^{-1}$ Fe ions appear full stripped at $E \sim 1$ MeV, the energy scales of experimental observations. Only under more efficient stochastic acceleration, $\alpha = 0.1 \ s^{-1}$, Fe ions remain partially ionized, anyway the charge state they preserve is higher than observations. Therefore we have tried in Figure 1(b) a lower source temperature $T = 8 \ 10^6$ K. Again the fractional effective charge q/Z remains lower than 1 for $\alpha = 0.1 \ s^{-1}$ but higher than the experimental values (Table 1). Our model reproduces the experimental Fe charge states reported for ISEP events under the source parameters $T = 8 \ 10^6 \ \mathrm{K}$ and $n = 5 \ 10^8 \ cm^{-3}$, presented in Figure 1(c) and an $\alpha = 0.1 \ s^{-1}$ for the acceleration efficiency. Table 1 gives the numerical values obtained for the mean Fe charge states.

From X-ray and γ -ray data for solar flares one can conclude that particle acceleration timescale is about several seconds. Therefore to reproduce experimental charge state values, the values predicted by our model have to be consistent with this temporal scale. Figures 2(a), 2(b) and 2(c) present the time profiles of Fe charge states under different source conditions and stochastic acceleration efficiencies. The temporal range of seconds should give the charge interval compatible with experimental values. Table 1 presents our model estimations of the time scale needed to achieve the Fe charge states obtained. We have found that these acceleration times are consistent with solar flare observations.

Once we have analyzed the Fe charge state behaviour, we have found that the source parameters that give Fe charge states consistent with experimental observations are $T = 8 \ 10^6$ K and n = $5 \ 10^8 \ cm^{-3}$. Therefore we have obtained the ionic charge states for Ni, Ca, Ar, S, Si, Al, Mg, Na and Ne. From Arnaud and Rothenflug results (Arnaud and Rothenflug, 1985) C, N and O have q/Z = 1 at these source temperatures and then keep their charge state during all the acceleration process. Figure 3 presents the ionic charge state behaviour for these ions in the energy range $(5 \ 10^4 - 7 \ 10^7) \ eV/n$. Here the mean charge states have been modelled under $T = 8 \ 10^6$ K and $n = 5 \ 10^8 \ cm^{-3}$. The ionic charge states show dependence on kinetic energy of the projectil under acceleration for all the ions studied. This energy dependence on the mean charge states is confined to a narrow and low energy range for ions up to Si, that mainly become full stripped at energies around 1 MeV/n, and to broaden out with the increase of energy for S, Ar, Ca, Fe and Ni, that remain in high ionization states at energies higher than 1 MeV/n. That is in accordance with ISEP measurements where all elements up to Si are fully ionized (Luhn and Hovestadt, 1987).

It is usually assumed that the charge state of cosmic rays corresponds to the ionization equilibrium of the plasma where they undergo acceleration. That is how experimentalists have found, for example, a rough consistency of GSEP ionization states with quiet coronal source temperatures, T=(1.5-3) 10^6 K. What we attemp to demonstrate with our model is that the acceleration mechanism involved, modifies the equilibrium charge states of projectiles under stochastic acceleration, to higher ionization states. Therefore the source temperature inferred from charge states observations should be lightly overestimated.

ACKNOWLEDGEMENTS

This work has been supported by the Universidad de Alcalá project ref. E019/2000.

REFERENCES

- Arnaud M. and Rothenflug R., 1985, Astron. Astrophys. Suppl. Ser, 60, 425-457.
- Arnaud M. and Raymond J., 1992, Ap. J., 398, 394-406.
- Cohen C. M. S. et al., 1999, Geophys. Res. Lett. 26, 149-152.

- Gallegos-Cruz A. and Pérez-Peraza J., 1995, *Ap. J.*, 446, 400-420.
- Luhn A. et al., 1985, Proc. 19th International Cosmic Ray Conference, 4, 241-244.
- Luhn A. and Hovestadt D., 1987, *Ap. J.*, 317, 852-857.
- Mazur J. E. et al., 1999, Geophys. Res. Lett. 26, 173-176.
- Mobius E., et al., 1999, *Geophys. Res. Lett.* 26, 145-148.
- Pérez-Peraza J. and Gallegos-Cruz A., 1994, Ap. J. Supp., 90 669-682.
- Pérez-Peraza J., 1998, Rayos Cósmicos 98. Proc 16th ECRS, eds J. Medina, L. del Peral, M. D. Rodríguez-Frías and J. Rodríguez-Pacheco. Alcalá de Henares: Servicio de Publicaciones de la Universidad de Alcalá, 97-112.
- Rodríguez-Frías M. D., del Peral L. and Pérez-Peraza J., 2000, J. Phys. G: Nucl. Part. Phys, 26, 259-264.

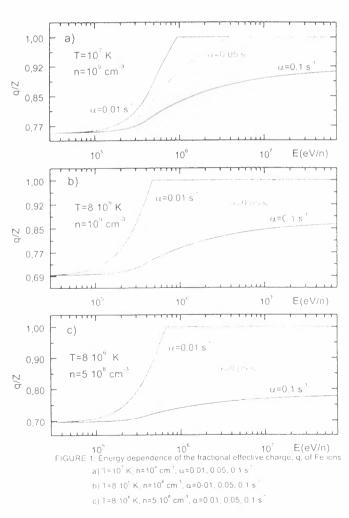


Table 1. Mean Fe charge states, q, in a source of temperature T and density number n, under an acceleration efficiency α . t_a is the acceleration time that spends the ion to reach a charge state q.

T(K)	$n(cm^{-3})$	$\alpha(s^{-1})$	E(MeV/n)	q	$t_a(s)$
107	10 ⁹	0.01	>1	26.0	1.9
		0.05	2	25.0	1.3
		0.05	50	26.0	1.8
		0.1	2	22.3	0.7
		0.1	50	23.6	3.3
-8.10^{6}	10^{9}	0.01	>0.5	26.0	3.2
		0.05	2	23.8	1.3
		0.05	50	26.0	3.5
		0.1	2	21.0	0.7
		0.1	50	22.3	3.4
$8 10^6$	$5 \ 10^8$	0.01	>0.7	26.0	3.8
		0.05	2	21.0	1.3
		0.05	50	22.3	6.7
		0.1	2	19.5	0.6
		0.1	50	20.1	2.2

Table 2. Ionic mean charge states, q, for different kinetic energies and acceleration times, in a source of $T = 8 \ 10^6 \ K$ and $n = 5 \ 10^8 \ cm^{-3}$, under an acceleration efficiency $\alpha = 0.1 \ s^{-1}$. t_a is the acceleration time that spends the ion to reach a charge state q.

	E=2 MeV/n		E=50 MeV/n		
Ion	q	t_a (s)	q	t_a (s)	
Ni	21.5	0.6	22.1	2.4	
Fe	19.5	().7	20.1	2.0	
Ca	18.9	().6	19.6	2.6	
Ar	17.2	().6	17.8	2.4	
S	15.4	0.6	16.0	3.0	
Si	13.7	0.6	1.1.()	1.1	
AL	13.0	().6	13.0	0.6	
Mg	12.0	().4	12.0	().4	
Na	11.0	().3	11.0	0.3	
Ne	10.0	().2	10.0	0.2	
()	8.0	0.0	8.0	0.0	
N	7.0	0.0	7.0	0.0	
С	6.0	().()	6.0	().()	

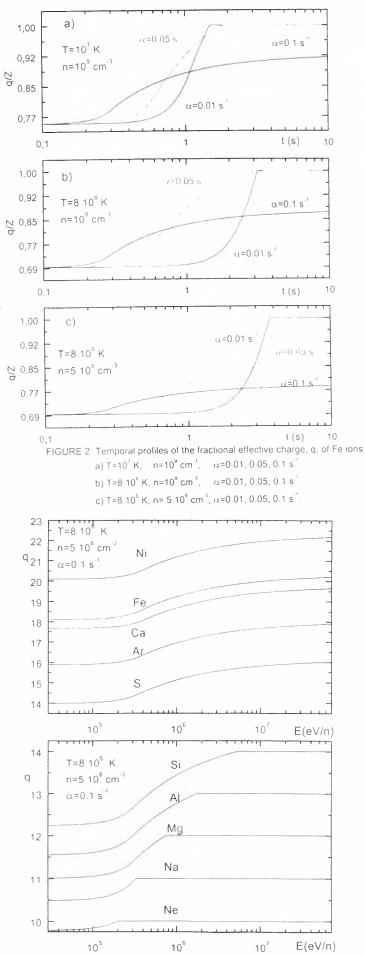


FIGURE 3: Mean charge states, q_i of Ni, Fe, Ca, Ar, S, S' Al, Ma, Na and Ne vs projectil kinetic energy $E(\cdot (eV/n))$

OBSERVATION WITH EPHIN/SOHO OF ELECTRON DURING QUIET TIME PERIODS

M. D. Rodríguez-Frías¹, R. Gómez-Herrero¹, L. del Peral¹, J. Sequeiros¹, R. Müller-Mellin², and H. Kunow²

¹Departamento de Física. Universidad de Alcalá, Spain ²Institut für Experimentelle und Angewandte Physik. Universität Kiel, D-24118 Kiel, Germany

ABSTRACT

The electron spectrum in the energy range 150 keV to 10 MeV, measured by EPHIN sensor onboard SOHO¹ observatory during 1996 quiet time periods, is presented. The results show that the dominant electron population is of jovian origin. The spectral indexes obtained range from 1.5 to 1.7 depending on heliospheric modulation. In this work an estimation of the emission intensity of electrons from the jovian magnetosphere is also obtained. Recurrence of jovians electrons at the middle of 1996 during poor Earth-Jupiter magnetic connection have been observed.

Key words: Cosmic rays; Jovian electrons; solar quiet times; interplanetary medium .

1. INTRODUCTION.

Since the SOHO launch the 2^{nd} December 1995, the Electron-Proton-Helium INstrument (EPHIN) has been collecting protons and alpha particles from its halo orbit, around the L1 Lagragian point at 1.5 million kilometers from Earth. From this position outside the Earth magnetosphere the fluxes of those particles are not affected by the Earth magnetic field.

EPHIN sensor is a stack of six cylindrical solid state silicon detectors, surrounded by a plastic scintillator acting as veto detector for background noise reduction. The two first thinner detectors are divided in six sectors to allow a rough trajectory determination and particle range corrections, which improve isotopic discrimination for light nuclei. The energy range for electrons is 0.150 to 10 MeV and for protons and Helium nuclei from 4 to 53 MeV/n. The EPHIN geometrical factor of $5.1 \text{ cm}^2 \text{sr}$ can be reduced by a factor of 24 either automatically or by telecommand to allow high counting rates without significant dead time losses. The sensor axis points in the nominal direction of the interplanetary magnetic field at 1 AU,

¹SOHO is an ESA-NASA collaboration

45° west of the spacecraft Sun line. A detailed description of the sensor can be found in (Müller-Mellin et al., 1995).

2. DATA SELECTION AND ANALYSIS

The data analyzed in this work correspond to 217 days of quiet time periods occurred during 1996 where the solar minimum of the 22nd solar cycle took place. During these periods no solar events are present and the particle populations are either of interplanetary or galactic origin.

The EPHIN sensor response has been simulated for electrons in the energy range 0.15 to 10 MeV and for Hidrogen and Helium isotopes from 4 to 53 MeV/n, using the Monte Carlo code GEANT (v. 3.21) (Brun et al., 1996). To simulate the jovian differential energy spectrum for electrons, considered the dominant contribution, a power law with $\gamma = 1.5$ spectral index has been used, while for ions a lineal fit, representative of the galactic cosmic radiation has been implemented.

3. QUIET TIME ELECTRON POPULATION

Solar flares, geomagnetic explosions and Jupiter magnetosphere are the dominant interplanetary electrons sources in the inner heliosphere in the energy range 0.2 to 25 MeV. Solar flares electrons are observed as sudden and intense increases in the intensity of energetic electrons in the interplanetary medium in connection with solar flare occurrences. Jovian electrons follow the interplanetary magnetic field lines, so that their intensities observed near Earth fluctuate depending on magnetic connection between Earth and Jupiter, with a 13 months periodicity.

While proton spectra are dominated by solar cycle variations, electron intensities do not show a significant variation due to solar modulation. Differences in the intensity variation of both particle species are

Proc. 1st Solar & Space Weather Euroconference, 'The Solar Cycle and Terrestrial Climate', Santa Cruz de Tenerife, Tenerife, Spain 25-29 September 2000 (ESA SP-463, December 2000)

due to different heliospheric regions crossed. Protons come from interstellar space and cross through the complete heliosphere to reach 1 AU. Meanwhile electrons are generated in the inner solar system, mainly in the jovian magnetosphere and in solar flares. The apparent lack of solar modulation of jovian electrons in contrast with the modulation of galactic protons and energetic electrons, is consistent with measurement of radial gradients of cosmic rays showing that during solar activity maximum, modulation takes place mainly at distances over 31 AU (McKibben, 1985).

As a consequence of the continuous expansion of solar wind, electrons undertake adiabatic deceleration in their transport through the interplanetary medium. Parker [1966] showed that the particle energy losses due to adiabatic expansion of solar wind can be expressed as:

$$\frac{dE}{dt} = -\frac{\alpha}{3} \left(\nabla \cdot \mathbf{v}_{sw} \right) E \tag{1}$$

being v_{sw} the solar wind velocity, E the kinetic energy of the particle and $\alpha = \frac{E+2m_ec^2}{E+m_ec^2}$, where m_e is the electron rest mass.

Integrating along the particle trajectory, the kinetic energy variation of the particle during propagation can be obtained by:

$$E_{Earth} = E_{Jupiter} \exp\left(-\frac{\alpha}{3} \int \nabla \cdot \mathbf{v}_{sw} dt\right) \qquad (2)$$

which implies a shift in the energy axis of the jovian electron energy spectrum, while the spectral shape remains unchanged during propagation. At energies between 0.2 and 25 MeV the jovian electron intensity is dominant over the interplanetary electron flux observed at 1 AU during quiet time periods (McKibben, 1985); consequently the spectral profile detected by EPHIN at 0.9 AU should reflect the electron spectrum originated in the jovian magnetosphere.

The electron intensity temporal profile shows a 13 months modulation period due to the synodical variation in the Earth-Jupiter magnetic connection. It is observed as a gradual increases in the electron flux during 5 or 6 months and it recurred after 13 months. The year started with a good magnetic connection and it was diminishing up to approximately the middle of the year, when the magnetic connection started again to recover, to end the year with a good magnetic connection again.

The convection-diffusion transport model is based in the Fokker-Plank equation (Parker, 1963):

$$\frac{\partial n_e}{\partial t} = \nabla \cdot (\mathcal{K} \nabla n_e - n_e \mathbf{v}_{sw}) + \frac{1}{3} \left(\nabla \cdot \mathbf{v}_{sw} \right) \frac{\partial}{\partial E} (\alpha n_e E)$$
(3)

where $n_e(r, E, t)$ is the electron differential density and \mathcal{K} is the diffusion tensor. Assuming that the jovian atmosphere behaves as a point source which continuously inject electrons per unit time of kinetic

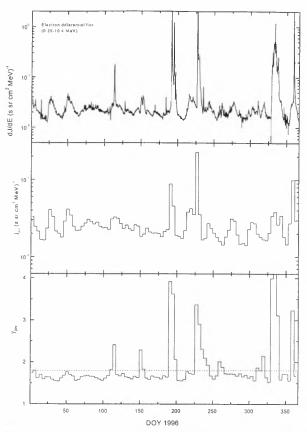


Figure 1. Fitting of the electron fluxes to expression (9), in 5 days time intervals. Temporal evolution of the j_{jov} and γ_{jov} fitted parameters.

energy E, following an injection spectrum $Q(E) = Q_0 E^{-\gamma_{jov}}$ with γ_{jov} the spectral index of the jovian electrons, and assuming a constant and diagonal diffusion tensor of eigenvalues $K_x = 7 \cdot 10^{20} \ cm^2 s^{-1}$, $K_y = 5 \cdot 10^{22} \ cm^2 s^{-1}$ and $K_z = 5 \cdot 10^{19} \ cm^2 s^{-1}$. Conlon (1978) and Chenette (1980) have obtained a stationary solution for the differential electron energy spectrum, as follows:

$$j_e(X, Y, Z, E) = \frac{cQ_0 E^{-\gamma_{jov}}}{4\pi H} \exp\left[2D(F - G)\right] \quad (4)$$

being (X, Y, Z) the spacecraft position in the archimedian coordinate system of the Parker spiral centered at the Jupiter position. The Y and Z transverse coordinates may be considered negligibles in comparison to X, that follows the magnetic field lines direction. The D, F, G, and H parameters are given by the following expressions (Chenette, 1980):

$$F = \frac{v_{sw}}{2K_x^{1/2}} \tag{5}$$

$$D = \frac{X}{2K_x^{1/2}}$$
(6)

$$G = \left[F^2 + \frac{2}{3}(\gamma - 1)\frac{v_{sw}}{r_s}\right]^{1/2}$$
(7)

$$H = 8\pi D (K_x K_y K_z)^{1/2}$$
 (8)

being r_s the SOHO radial distance from the Sun. This stationary solution agrees with observations both in solar activity maximum and minimum.

J

For temporal scale of days, the variations in temporal profiles of electron intensities requires to take into account the changes observed in the interplanetary medium in order to obtain a more realistic solution. For instance, CIR's should be considered as barriers to the electron propagation, as the compression of solar wind produces a reduced diffusion perpendicular to the direction of the magnetic field vector. Therefore, when a CIR is interposed between Jupiter and Earth, the propagation of jovian electrons across the average direction of the interplanetary magnetic field is suppressed. The jovian electron flux observed at Earth should be a minimum from the time a CIR passes Earth until that CIR passes Jupiter. Inmediately thereafter, the jovian electron flux at Earth should begin to increase. This behaviour is found with a periodicity of 27 days during 5 or 6 months.

dJ/dE (s sr cm² MeV)¹

10

10

SOHO/EPHIN electrons

Day 26, 1996 (minimum jovian flux) Day 21, 1996 (maximum jovian flux)

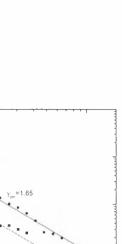
As we have already stated, during solar quiet time periods the dominant electron population in the energy range from 0.2 to 25 MeV is of jovian origin. The jovian electron abundance is 50 times higher than galactic electrons at these energies. The electron spectrum obtained with 4 days time interval has being fitted by a power law of the form:

$$j_e(E) = j_{jov} E^{-\gamma_{jov}} \tag{9}$$

$$j_{jov} = \frac{cQ_0}{4\pi H} \exp[2D(F-G)]$$
 (10)

Figure 1 shows the temporal evolution of the fitting parameters obtained. It is observed that the spectral indexes remain between 1.5 and 1.7 except for solar origin events where the index exceedes values of 2.0. This feature is intended to be used for event identification of solar origin. It can also be observed the typical recurrence of 27 days solar modulation. This recurrence is more clearly observed from the temporal evolution of the j_{jov} parameter (Figure 1).

Figure 2 shows the electron differential spectrum obtained by normalization of pulse-height data recorded by the EPHIN electron counters. The electron spectrum of 26 January 1996 is shown in Figure 2(a). It is remarkable the increase of the 27 days modulation intensity of jovian electrons, which present a spectral index $\gamma_{jov} = 1.65$ in perfect agreement with the expected spectrum of jovian electrons (Table 1). Overimposed in the same figure the electron spectrum during the minimun flux of the same period (DOY 21-1996) with a spectral index $\gamma_{jov} = 1.51$, is shown. The only difference between both spectra is in the j_{jov} factor, which depends on the transport conditions of the interplanetary electrons and does not depend on the source (Jupiter) conditions. Figure 2 (b) shows the differential energy spectrum during a SEP event with DOY 21 1996. It is observed that the SEP event produces electrons in the energy range 0.15 to 2 MeV, while the electron highest energy are of jovian origin. Figure 2 (c) shows the electron global spectrum during the solar quiet time period analyzed. A total of 217 days have been recorded which provides a statistically significant data collection that allow us to



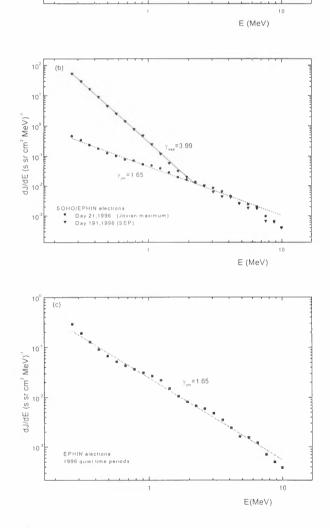


Figure 2. Comparison of electron spectra during the three time intervals of Table 2. a) During minimum and maximum jovian flux. b) Superposition of spectra for a SEP event and maximum jovian flux. c) Electrons quiet time global differential energy spectrum

Table 1. Parameters from $j_e = j_{jov}E^{-\gamma_{jov}}$ fitted to the electron differential energy spectra (Figure 5). j_{jov} is given in $(cm^2 \ s \ sr \ MeV)^{-1}$

	DOY	jjov	γ_{jov}
minimum	021	$(1.5 \pm 0.1) \cdot 10^{-2}$	1.51 ± 0.06
maximum	026	$(4.5 \pm 0.2) \cdot 10^{-2}$	1.65 ± 0.04
SEP event	191	$(2.9 \pm 0.1) \cdot 10^{-1}$	3.99 ± 0.03
total spectrum		$(2.4 \pm 0.1) \cdot 10^{-2}$	1.65 ± 0.05

obtain the averaged spectrum with quiet good precision. Table 1 shows the results obtained for the different fitting performed on the selected periods. The electron emission intensity obtained from the differential energy spectra, averaged over the complete time interval selected, of the jovian magnetosphere is $Q_0 = 3 \cdot 10^{25}$ electrons s⁻¹ MeV⁻¹.

4. IV. CONCLUSIONS

The quiet time energy spectra for electrons (0.15-10 MeV) in the inner heliosphere at 0.9 A.U has been presented.

The electron population shows three components according to their different origin. The main component, with a spectral index of 1.65, corresponds to jovian electrons. This spectral value is in good agreement with the value of 1.7 found in literature. Moreover, we have obtained a $3 \cdot 10^{25}$ electrons s⁻¹ MeV⁻¹ value for the emission intensity Q_0 of the jovian magnetosphere in good agreement with expectation (Eraker, 1982). A Fourier analysis has shown the existence of two main periodicities, one of 26.76 days an the other of 13 months. The shortest one corresponds to the modulation produced by solar rotation, and it has an amplitude of $1.5 \cdot 10^{-2}$ (cm² s sr MeV)⁻¹ and the longest one is due to the relative position of Jupiter and Earth and their magnetic connection. The maximum intensities are observed at the beginning and at the end of the year and the minimum at about the middle of the year. The amplitude of this modulation is $0.5 \cdot 10^{-2} (\text{cm}^2 \text{ s sr MeV})^{-1}$. During the worst magnetic connection between Earth and Jupiter, toward the middle of the year, an increase in the electron flux has been observed. As it has been shown in Figure 1, the spectral shape of this flux seems to match with those of jovian origin although the observation conditions of these electrons are not favorable.

The comparison of the electron spectra measured during maximum and minimum fluxes shows that their spectral indexes are practically the same and in good agreement with the values expected for the jovian magnetosphere (Figure 2 (a)). The modulation has an effect on the electron intensity detected near Earth but it does not alter significantly the spectral shape which is a signature of the source.

The other two type of observed events (Figure 1) have spectral indexes considerably higher. Some

events have spectral indexes of the order of 4 indicating their solar origin and being clearly correlated to solar flares. Others show spectral indexes in the range 2 to 3 with a change in slope, which indicates a mixed solar and interplanetary origin, as shown in Figure 2 (b) for two particular dates.

ACKNOWLEDGEMENTS

This work has been supported by the Comisión Interministerial de Ciencia y Tecnología (CICYT) of Spain, grant ESP97-1776. R. Gómez-Herrero is indebted with the University of Alcalá for a predoctoral grant.

REFERENCES

- Brun, R. et al., 1996, *GEANT 3.21*,. CERN Data Handling Division.
- Chenette, D. L., 1980, Journal of Geophysical Research, 85-A5, 2243-2256.
- Conlon, T. F., 1978, Journal of Geophysical Research, 83-A2, 541-552.
- Eraker, J. H., 1982, Ap. J. 257, 862-880.
- McKibben, Pyle and Simpson, 1985, NASA Goddard Space Flight Center, Proce 19 Int. Cosmic Ray Conference, 5, 206-209.
- Müller-Mellin, R. et al., 1995, Solar Physics, 162, 483-504.
- Parker, E. N, 1966, Planet Space Sci., 14, 371-375.
- Parker, E. N., 1963, in *Interplanetary dynamical processes*, New York, Interscience Publishers.

THE INTERMITTENCY OF THE SOLAR INTERMEDIATE-TERM PERIODICITY (1969-1998)

Ján Rybák¹, Anna Antalová¹, and Marisa Storini²

¹Astronomical Institute, Slovak Academy of Sciences, 059 60 Tatranská Lomnica. The Slovak Republic
 ²IFSI/CNR, Area di Ricerca Roma-Tor Vergata, Via del Fosso del Cavaliere, 100 - 00133 Roma, Italy
 ²Raggi Cosmici - Dip. di Fisica - Università Roma Tre Via della Vasca Navale, 84 - 00146 Roma, Italy

ABSTRACT

Wavelet transform has been used for the time-frequency decomposition of solar data series through the last three solar cycles (the 20-th, the 21-st and the 22-nd), on daily basis, for the following parameters: the non-flare full-disk soft X-ray background (XBG), the daily solar LDE-type flare index (LDE) and the daily impulsive-type flare index (IMP). From the wavelet analysis we can distinguish the existence of discrete impulses of the intermediate-term periodicities (IP) during the 1969-1998 year interval. The impulses were determined in the following years: 1981.0, 1982.7, 1990.0, 1991.6. It is very likely, that obtained impulsive episodes indicate those time intervals, in which the continuing eruption of the new solar magnetic flux existed.

1. INTRODUCTION

The structure of the 11-year cycle depends on intermediate-term variations of the Sun. Our knowledge of intermediate-term periodicities (IPs) is mainly based on the analysis of sunspot data (see references reported by Antalová, 1999). The existence of the continuous IPs were theoretically predicted from the oscillationconvection model of the Sun (Wolff, 1974, 1983, 1992). From the IPs, two of them are dominant: the 155- and 323-days (Lean and Brueckner, 1989; Cane, Richardson and von Rosenvinge, 1998). SOHO/MDI and GONG helioseismic data (Komm, Howe and Hill, 2000) reveals other very important period around 1.3 year (about 474 days), which they located at the bottom of the convective zone of the Sun. Going to intermittency, we note, that Ballester. Oliver and Baudin (1999) stated the disappearance of 150-day sunspot periodicity during the minima of all modern 11-year solar cycles (No.1 - No.22). During the maxima of the 21-st and the 22-nd solar cycles, Antalová (1999), from Fourier analysis, displayed the different amplitudes in the occurrence of IPs in the solar soft X-ray data. The intermittent character of 150-d_/ periodicity during the maximum of the 21-st cycle was presented in cosmic rays by Bazilevskaya et al. (1998). Kudela et al. (1999). Bouwer (1992) for full-disk soft X-ray background (XBG), from the analysis of August 1975 – October 1986 interval found that 150–day periodicity had two maxima: the 1-st in August 1980 and the 2-nd in September 1982.

The aim of this paper is to investigate the intermittency of the intermediate-term periodicities during 1969–1998 years, on the basis of the solar soft X-ray data. From prior papers we know, that IPs are related to the solar cycle maximum. Data sets available allow us to study *in detail* temporal variations of the occurrence IPs during solar cycle maximum. The question arises if IPs are preferred in certain part of solar cycle maximum. The data sets are given in Section 2. Wavelet transform used for the timefrequency decomposition of the studied solar SXR data series is given in Section 3. Main results are summarized in Section 4.

2. THE DATA SETS

The temporal profiles of our data are shown in Figure 1. The analysis was performed on the following SXR parameters:

(a) the non-flare full-disk soft X-ray background – **XBG**. from the 1–8 Å GOES measurements, as published in *Solar Geophysical Data*. XBG here analyzed is given in units of $10^{-8}Wm^{-2}$. The detailed description of construction of homogeneous XBG data sequence is given in Jakimiec, Antalová and Storini (2000) and references therein.

(b) the LDE-type flare index – LDE, computed from the 5-minute averages of GOES-flux, from all long lasting (LDE-type) GOES soft X-ray flares, with duration exceeding 2 hours above the quiet SXR GOES level by weighting the SXR flare-classes (in units of 10^{-6} W/m²). The daily flare indices (FI-LDE) were investigated by Landi and Storini (1997) as well as Landi et al. (1998) in connection with the occurrence of non-recurrent geomagnetic storms, as proxy data of the coronal activity of the Sun, in years 1969–1974.

(c) the impulsive flare index – IMP, which is computed by us, in the same way as LDE index, for the flares which duration in SXR is shorter than 2 hours.

Proc. 1st Solar & Space Weather Euroconference, 'The Solar Cycle and Terrestrial Climate', Santa Cruz de Tenerife, Tenerife, Spain, 25-29 September 2000 (ESA SP-463, December 2000)

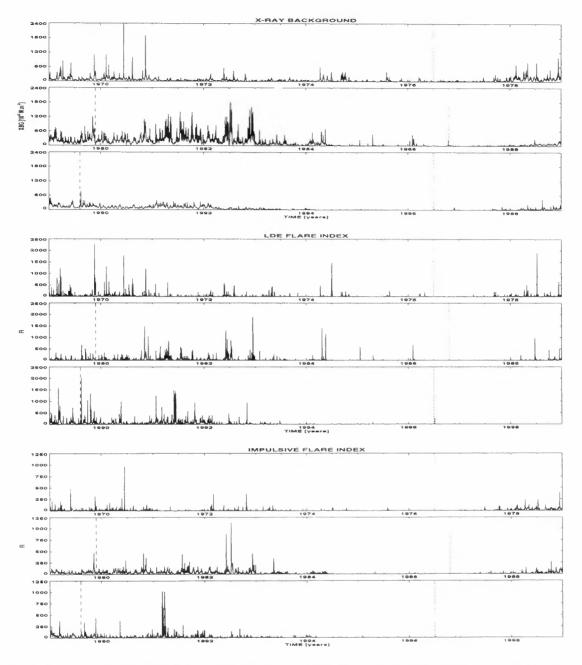


Figure 1. Time series of the daily values of XBG (the upper panel), LDE-type flare index (the middle panel) and IMP flare index of impulsive flares (the bottom panel). The solar activity cycle maxima and minima are signed by dashed and dotted vertical lines respectively.

3. METHOD OF PROCESSING

The wavelet transform (WT) – suitable tool for the analysis of the non-stationary time series (e.g., Daubechies, 1990, Kumar and Foufoula-Georgiou, 1997) was used in this study. The Morlet wavelet – a plane sine wave of amplitude windowed in time by a Gaussian function – has been selected to search for power at different frequencies over the whole length of the series.

The WT computational algorithm of Torrence and Compo (1998) with a convenient set of scales in the period range 16-1024 days and the scale resolution 48 scales per octave was used for calculation of the WT

power spectra (WPS). The global wavelet spectrum (Torrence and Compo, 1998) has estimated the background mean power spectrum against which the significance of the local wavelet power spectrum features has been tested.

4. RESULTS AND CONCLUSIONS

Intermediate-term periods found in the wavelet global power spectrum analysis are given in Table 1. The WPS of XBG, LDE and IMP flare indices are illustrated in Figure 2. The carried out wavelet power spectrum analysis has shown the following results and conclusions:

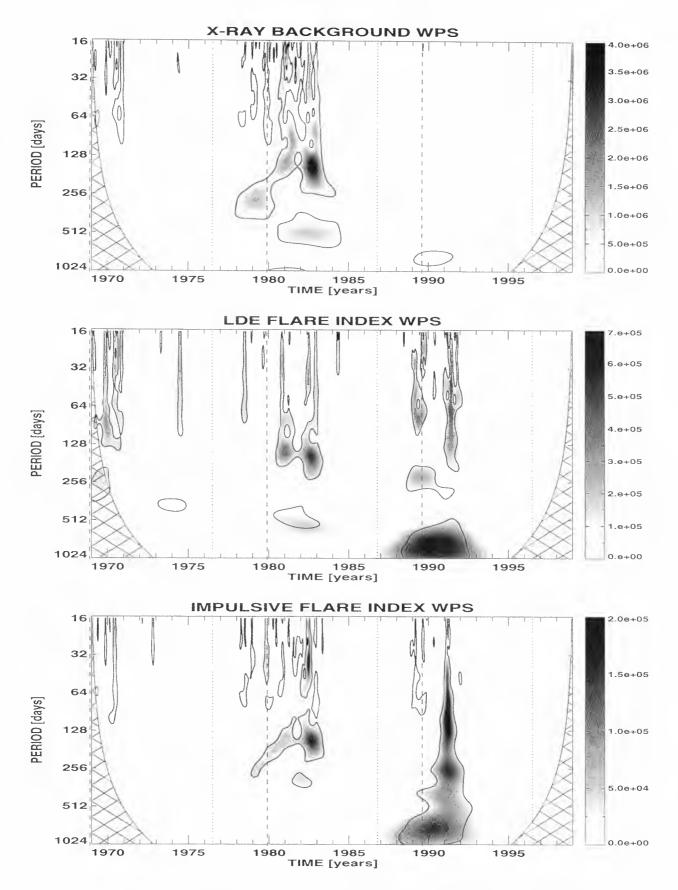


Figure 2. The wavelet power spectra (WPS) of the XGB, LDE and IMP flare index data series. The time spacing parameter of the series is 1 day, the scale resolution is 48 scales per octave. The thick solid curve stem for the 95% confidence level of the spectrum. The coin of incidence is marked by the cross-hatched regions. The solar activity cycle maxima and minima are signed by dashed and dotted vertical lines respectively according to the Wolf's sunspot index.

Table 1. The wavelet global power spectrum analysis of soft X-ray parameters. Periods are given in days. In head-line are given expected periods, from the 27-day synodic recurrence as well as from Wolff's g-beats (Wolff, 1974). Our results from wavelet global power spectrum are given in the three soft X-ray parameter rows. LTstay for Long Term periods.

IP(days)	27-	80-	155-	270-	323-	LT-
SXR :						
XBG	28	83	155		301	568
LDE	31	80	146	223		850
IMP	38	83	157	268		810

The gap in WPS during the maximum epoch of the last two cycles: The wavelet power spectra of all three SXR parameters display the gaps in the occurrence of IPs during the maximum epoch of the last two solar cycles. We obtained dual peaks, the first peak in the premaximum and the second peak in the post-maximum years. As is shown in WPS, the second peak is much stronger, comparing to the first one of the same cycle. This result is consistent with Bazilevskaya et al. (1998) and Kudela et al. (1999) statements.

The dual-peak in the 22-nd solar cycle: In the WPS of solar soft X-ray parameters there is a valley during the maximum of the 22-nd solar cycle, which is similar to structures presented by Feminella and Storini (1997) as well as Massetti and Storini (1998). The valley is called **the Gnevyshev gap** by the Rome Cosmic Ray Group (e.g. Storini and Pase, 1995). The dual-peak maximum of the 11-year solar activity cycle (Gnevyshev, 1977 and references therein) is well indicated, when intense coronal and/or long-lasting activity events are considered.

Relationship between solar activity and the heliomagnetic field: As was shown by Ataç and Özgüç (1998) the first 1989 peak was higher than the second one (1991) for all solar parameters, which they analyzed. One of the most remarkable differences is, that total magnetic flux had the stronger 1991 peak than 1989 one (Mendoza et al., 1999 and Storini et al., 1999). Bao and Zhang (1998) obtained in the magnetic helicity the same temporal profiles (the first peak in 1989 is smaller than the second peak in 1991 year). Our WPS result of the stronger occurrence of IP periodicities in 1991 comparing to 1989 year coincides very well with the magnetic field behaviour. This similarity in temporal evolution gives a promising chain to understand the origin of the Gnevyshev gap and its role in the solar activity cycle.

ACKNOWLEDGMENTS

This contribution was carried out within the scope of the Slovak VEGA Grant 2/7229/20. A. Antalová thanks the warm hospitality of the Instituto de Astrofisíca de Canarias during the 1-st SOLSPA Euroconference and expresses her gratitude to European Union for financial support. The IFSI/CNR and PNRA/MURST grants are acknowledged for endoring studied related to SolarTerrestrial relations. The computations were performed using the modified wavelet software, original of which was provided by C. Torrence and G. Compo (Program in Atmospheric and Oceanic Sciences, University of Colorado, Boulder, U.S.A.) available at URL: paos.colorado.edu/research/wavelets/.

REFERENCES

- Antalová, A., 1999, Proc. of the 9-th European Meeting on Solar Physics, ESA SP-448, 743
- Ataç, T. and Özgüç, A., 1998, Solar Phys., 180, 397
- Ballester, J.L., Oliver, R. and Baudin, F., 1999, Astrophys. J. 522, L153
- Bao, S.D. and Zhang H.Q., 1998, JOSO AR '97, 132
- Bazilevskaya, G.A., Krainev, M.B., Makhmutov, V.S, Sladkova, A.I., Storini, M. and Flückiger, E., 1998, in Proc. 16-th ECRS, Alcala, Spain, 83
- Bouwer, S.D., 1992, Solar Phys. 142, 365
- Cane, H.V., Richardson, I.G. and von Rosenvinge, T.T., 1998, Geophys. Research Letters 25, 4437
- Daubechies, I., 1990, *IEEE Transactions on Information Theory* 36, 961
- Feminella, F. and Storini, M., 1997, Astron. Astrophys., 322, 311
- Gnevyshev, M.N., 1977, Solar Phys. 51, 175
- Jakimiec, M., Antalová, A. and Storini M., 2000, Contr. Astron. Obs. Skalnaté Pleso 30, 75
- Komm, R., Howe, R. and Hill, F., 2000, in these Proc.
- Kudela, K., Yasue, S., Munakata, K. and Bobik, P., 1999, 26-th ICRC, Vol. 7, 163
- Kumar, P. and Foufoula-Georgiou, E., 1997, *Reviews of Geophysics* 35, 385
- Landi, R., Moreno, G., Storini, M. and Antalová, A., 1998, J. Geophys. Res. 103, 20553
- Landi, R. and Storini, M., 1997, Rep. CNR/IFSI-97-12, Frascati, Italy
- Lean, J.L. and Brueckner, G.E., 1989, Astrophys. J. 337, 568
- Massetti, S. and Storini, M., 1998, Report CNR/IFSI-98-01, Roma - Italy
- Mendoza, B., Lara, A., Maravilla, D. and Valdés–Galicia, J.F., 1999, Solar Phys. 185, 405
- Solar Geophysical Data, 1969 1976, Parts I and II; 1994, No. 602, part II
- Storini, M. and Pase, S., 1995, STEP GBRSC News 5, Special issue, 255
- Storini, M., Feminella, F., Antalová, A. and Massetti, S., 1999, JOSO Annual Report 1998, 153
- Torrence, C. and Compo, G.P., 1998, Bulletin of the American Meteorological Society 79, 61
- Wolff, C.L., 1974, Astrophys. J. 193, 721
- Wolff, C.L., 1983, Astrophys. J. 264, 667
- Wolff, C.L., 1992, Solar Phys. 142, 187

N-S VARIATION OF THE X-RAY FLARE NUMBER DURING THE SOLAR CYCLE 22

B.Schmieder¹, K.J.Li², Q.S.Li²

¹ Observatoire de Paris, Section Meudon, 92195 Meudon Principal Cedex ² Yunnan Observatory, Kunming, China

Abstract The X-ray flare events of class larger than M ocurring between April. 1, 1987 and December 30, 1992 and listed in SGD (Solar Geophysical Data) have been statiscally analysed. During this period of maximum activity of the 22nd solar cycle, the annual number of flare events is larger in the southern hemisphere than in the northern hemisphere. The N-S asymmetry with the dominance of the southern hemisphere, already studied for the number of spots, really exist for the flare events. The solar cycle 22 seems to have the same behaviour than the cycle 21 in respect to the N-S asymmetry.

1. Introduction

Solar activity indications do not occur evenly on the solar disk. It is well known that many types of solar phenomena exhibit some N-S asymmetry distribution such as optical flare events. relative sunspot numbers, sunspot areas, sunspot magnetic classes, sudden disappearances of solar filaments, type II radio bursts, white-light flares, gamma-ray bursts, hard X-ray bursts, events of coronal mass ejection. and X-ray flares. Although the existence of N-S asymmetry in solar activity is generally well established, that is not so well interpreted (Carbonell, Oliver & Ballester 1993). Garcia (1990) studied the N-S asymmetry of large flares based on X ray observations from GOES satellites during solar cycles 20 and 21. He shows that the spatial distribution of flares varies with an solar cycle such as that the preponderance of flares occurs in the North in the early part of the cycle and moves south as the cycle progress. We are doing a similar analysis for the solar cycle 22.

2. Statistical Analysis

The data used in this paper come from the table of the X-ray $M \ge 1$ flares (Li & Zhang 1994), extracted from the SGD (Solar Geophysical Data) in the time interval of 1 April 1987 to 30 December 1992 corre-

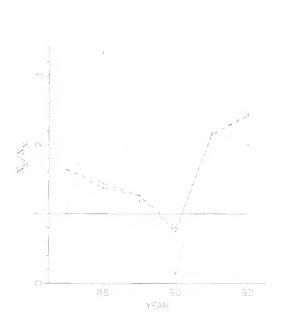


Figure 1. The annual number ratio of the flare events in the southern hemisphere (N_S) to those in the northern hemisphere (N_N) . All flare events of M & X classes are considered in the dashed curve, those of M class in the dashed and dotted curve, and those of X class in the dotted curve

Proc. 1st Solar & Space Weather Euroconference. 'The Solar Cycle and Terrestrial Climate'. Santa Cruz de Tenerife. Tenerife. Spain 25-29 September 2000 (ESA SP-463. December 2000)

	$No_{(S,M)}$	No.(S.X)	No.(N,M)	No.(N,X)	No.(E,M)	No.(E,X)	$No_{(W,M)}$	No.(W,X)	** total
*1987	18	0	11	0	12	0	17	0	29
1988	111	10	81	3	112	3	80	10	205
1989	347	32	274	27	325	29	296	30	680
1990	121	2	151	[-]	142	11	130	5	288
1991	398	37	186	17	298	36	286	18	638
1992	142	8	58	-4	80	1	120	11	212
total	1137	89	761	65	969	80	929	74	

Table1. Number of $M \ge 1$ X-ray flares during the period of 1987 to 1992

* The flare events are summed up into the numbers of this row only from 1 April 1987 . ** Number in this column corresponds to the number of the flare events of each year, the half of the sum $\sum No$. of the corresponding row.

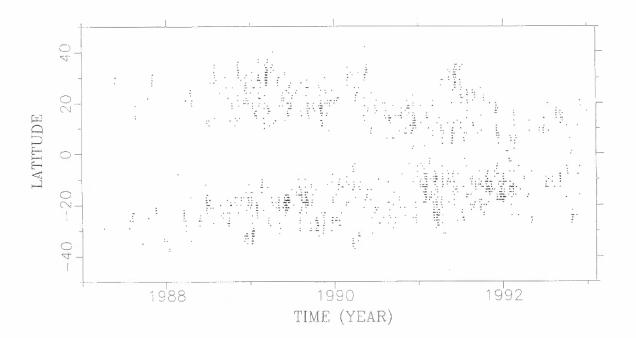


Figure 2. Distribution of X-ray $M \ge 1$ flares from 1987 to 1992, with respect to heliographic latitude.

sponding to the maximum period of the 22nd solar cycle (Li et al. 1998).

Table 1 gives the number of the flares classified by hemisphere and by X-ray class.

Fig. 1 gives the annual number ratio of the flare events in the southern hemisphere (N_S) to those in the northern hemisphere (N_N) . There is no flare of X class to occur in 1987, here we let the value N_S/N_N of this year equal to 1 for the flares of X class. The ratio of the total number of the flare events in the southern hemisphere to that in the northern hemisphere is 1.49 for M class, 1.37 for X class. 1.48 for M&X class.

To be sure that this result cannot be obtained purely by chance we check by using probability lqws and compute what would be the ratio of flares in the southern hemisphere to those of northen hemisphere that would be expected by chance. The probability to get class M+X events occuring in the southern hemisphere is $\sim 10^{-8}$. to get class X events is 0.026. These probabilities are less than 5% so our results are significant. They are complimentary to several ones recently published (Oliver and Ballester 1994. Atac and Ozgue 1996). The heliographic latitude distribution shows in Figure 2 that at the beginning of the 22nd solar cycle, the X-ray M > 1 flares occurred in the relatively hight latitudes (above 20°), then, as the cycle progressed, there was an obvious shift in the statistical centroid of position to the lower latitudes. the majority of the flare events occurred in the latitudes 8^0 and 35^0 . Only 2 flares occurred in the latitudes over 40° . The distribution of flares is comparable to the sunspot distribution.

3. Conclusion

In the present study we have found that the N-S asymmetry really existed for the flare events with the dominance of the southern hemisphere. The solar cycle 22 seems to have the same behaviour than the cycle 21 in respect of the N-S asymmetry. Verma (1987) who was working on 3 solar cycles 19.20 and 21 with different indicators found that asymmetries in all phenomena prevailed in the north during cycles 19 and 20 and in the south in cycle 21. This would indicate that superimposed on the well observed periodicities of 11. 22 years a much longer cycle of unknown duration does exist.

The relationship between flare distribution and sunspot ditribution lead to think that flares are originated in active regions anchored deep in the convection zone, may be at the boundary of giant cells. So there is, may be, a relationship between the asymmetries and convective giant cells. A global convection pattern was recently discovered by analysing the data of MDI aboard SOHO (Kosovitchev 1997) and large convection rolls parallel to the equator were suspected. The existence of such rolls could be related to the work of Ribes et al. (1993) using filaments as tracers. They show that the number of such convective rolls changes according to the phase of the solar cycle and this change could be responsible of the transfer of the polarity from one hemisphere to the other one. That gives a new view on the solar dynamo phenomena.

Bibliography

Atac T. & Ozgue A., 1996. Solar Phys., 166, 201

Carbonell M., Oliver R. & Ballester J. L., 1993, Astron. and Astrophys., 274, 497

Garcia H.A. 1990. Solar Phys., 127, 185

Kosovitchev A.G., 1997, IAU Colloquium in Kyoto. 1997

Li K.J., Schmieder B., Li Q.S. 1998, Astron. and Astrophys. Suppl., 131, 99

Li Qiusha & Zhang Bairong, 1994, Publications of Yunnan Observatory, 54, 1

Oliver R. & Ballester J. L., 1994, Solar Phys., 152, 481

Ribes J.R., Ferreira E.N., Mein P. 1993, Astron. and Astrophys., 274, 563

Verma V. K., 1987, Solar Phys., 114, 185

MID-TERM RADIANCE VARIATION OF FAR-ULTRAVIOLET EMISSION LINES FROM QUIET-SUN AREAS

Udo Schühle¹, Jörg Hollandt², Anuschka Pauluhn³, Klaus Wilhelm¹

 ¹⁾ Max-Planck-Institut für Aeronomie, D-37191 Katlenburg-Lindau, Germany tel:+49-5556-979-458/fax:+49-5556-979-6458/e-mail:schuehle@linmpi.mpg.de
 ²⁾ Physikalisch-Technische Bundesanstalt,D-10587 Berlin, Germany
 ³⁾ INTEC Bern and Institute of Astronomy, ETH-Zentrum, CH-8092 Zürich, Switzerland

ABSTRACT

The Solar Ultraviolet Measurements of Emitted Radiation (SUMER) spectrograph on the Solar and Heliospheric Observatory (SOHO) has been used to measure solar radiances of far- and extreme-ultraviolet emission lines of quiet-Sun areas from March 1996 until June 2000. The measurements allow us to derive the trends of the radiance of the quiet Sun near the centre of the solar disk during the time of the ascending phase of the present sunspot cycle. We have measured the radiance of the emission lines He I 584Å, Mg X 609Å and 624Å, N v 1238Å, Fe xii 1242Å, Ne viii 770Å, and the hydrogen Lyman continuum at 880Å until June 1998 when observations with SOHO were interrupted. All lines show an increasing trend during this period of the ascending phase of the present solar activity cycle. We characterise the effects of the loss and recovery of the SOHO spacecraft in 1998 on the radiometric calibration of the SUMER instrument and extend the radiance measurements through July 2000. The extended measurements show that the increasing trend has continued.

INTRODUCTION

The variation of solar irradiance in the extreme ultraviolet, which goes along with the solar activity cycle, is known to be very strong (Hall et al. 1969), but has not been measured for many spectral lines (Tobiska, et al. 1998, Woods et al., 1998). Accordingly, the detailed variation of the EUV irradiance is not well understood (Lean, 1991).

The solar irradiance in the ultraviolet and its variability is of fundamental importance due to its effect on the upper atmosphere of the Earth. In several spectral lines in the UV and EUV, the irradiance has been measured by the SUMER spectrograph (Solar Measurements of Emitted Radiation) on the Solar and Heliospheric observatory (SOHO) during 1996 and 1997 (Wilhelm et al., 1998 and 2000). From the spatially resolved images of the Sun, the contributions of active and coronal hole regions could be obtained, that contribute to the variation of the irradiance of spectral lines. These results provide important input parameters for models of the solar irradiance spectrum (Fontenla et al., 1999) and the EUV irradiance variability based on the contrast ratio of different regions on the solar disk. In addition it was possible to measure the detailed centre-to-limb variations of the radiance in these emission lines. To understand the variability of solar irradiance it is also necessary to know whether the quiet-Sun is affected by the solar activity cycle. In particular, it is unclear whether the variability of the irradiance of the Sun can be modelled by active region and plage area contributions alone or is also due to a global change of the quiet-Sun radiance introduced by the varying activity during a sunspot cycle.

We have measured the radiance of selected EUV emission lines with the SUMER spectrograph on SOHO from March 1996 to June 1998 and extended measurements until July 2000. The data obtained only from quiet-Sun areas, measured close to the centre of the solar disk, revealed an increasing trend of the radiance that seems to go along with the sunspot cycle (Schühle, 2000a).

The measurement of long-term radiance is particularly difficult because of stability uncertainties of instrument responsivity due to degradation of optics and detectors in space (Steward et al., 1989). The careful tracking of the instrument responsivity changes during the mission is of paramount importance for the evaluation of longterm trends. This has been accomplished by these measurements which have been repeated on a regular basis. Based on the condition that the radiance of the quiet-Sun does not decrease during this period of the sunspot cycle, we have shown that the responsivity of the SUMER instrument had not degraded during launch and the first year of the SOHO mission (Schühle et al., 1998). Contrary, continued measurements showed an increasing trend of the radiance of the lines. The measurements can thus be used to derive mid-term variations of the radiance of the observed spectral lines. However, during the accidental loss and the recovery of the SOHO spacecraft in 1998 the instruments suffered changes in their responsivity. We try to evaluate these changes in order to maintain the radiometric capabilities and, in particular, to follow-up these long-term trends of the quiet-Sun radiance.

Proc. 1st Solar & Space Weather Euroconference, 'The Solar Cycle and Terrestrial Climate', Santa Cruz de Tenerife, Fenerife, Spain, 25-29 September 2000 (ESA SP-463, December 2000)

OBSERVATIONS AND DATA CALIBRATION

Five emission lines had been selected that have repeatedly been observed in quiet-Sun areas near the disk centre. The lines measured during the observing sequence are He I 584 Å, Mg X 609 Å and 624 Å, Ne VIII 770 Å, N V 1238 Å. To exclude any contributions from active or bright regions, an area close to disk centre was always selected that was devoid any solar activity by referring to the He II 304 Å images of the Extreme-Ultraviolet Imaging Telescope (EIT) of SOHO. An area of 60" x 300" was registered by a raster scan of the telescope with a step size of 0.76" in eastwest direction. After September 1996 the raster scan mode was given up, and instead the slit was kept at a fixed position, letting only the solar image drift across the slit by the solar rotation. Each line was registered for 21 minutes, taking 80 exposures of 16 seconds. The area sampled by solar rotation was 3.5" x 300". So the area sampled was much smaller, and thus the sample of the chromospheric network structure was only marginally representative, when the raster scan was not invoked. This causes a greater scatter of the data points, but nevertheless, the size of this area warranted that always a part of chromospheric network and cells was sampled. Recently, in August 1999, the raster scan mode was resumed temporarily so that a few raster images could be acquired again.

An additional set of measurements was obtained by an observing sequence of the hydrogen Lyman continuum, performed independently but with similar regularity. In these observations a spectral window of 40 Å of the hydrogen Lyman continuum at 880 Å was sampled for three hours at a quiet-Sun area, corresponding to a raster scan area of about 30" x 300".

The radiometric responsivity of the SUMER instrument has been calibrated with both detectors before flight using a transfer standard source which itself had been calibrated against the primary radiometric source standard BESSY I (Hollandt et al. 1996). This laboratory calibration established the responsivity of the instrument at a set of wavelengths provided by the transfer source. By the fact that none of the observed lines presented in this communication showed any decline of intensity, we verified that the instrument responsivity was stable during the mission time (Schühle et al. 2000b) until the SOHO accident occurred, when the nominal spacecraft attitude was lost for three months. After the recovery of SOHO in November 1998, a change of responsivity of SUMER was noticed. Anticipating that the radiometric calibration can be re-established after the accident, these measurements have been continued after instruments from SOHO had been recovered. The data before and after the SOHO accident have been fitted by a linear least squares fit and, assuming that the trends would be unchanged, a "sensitivity loss factor" was derived for each line measured.

RESULTS AND DISCUSSION

We determined for each measurement the average radiance in the observed area. From 5 March 1996 to 7 July 2000 we have made 39 observations. A summary of the data is presented in Figure 1. Here we show the uncorrected data measured for each line in the entire time period starting well before the minimum of the sunspot activity between solar cycles 22 and 23. The time has been divided (indicated by vertical lines) into three periods that have been fitted separately: Before solar minimum, after solar minimum but before the SOHO accident, and after.

After the recovery from the SOHO accident both detectors have been used alternately. Thus we can exclude any variation due to changes of response of one detector. In order to re-establish the calibration after the SOHO accident, the trends of the radiances before and after the accident have been fitted separately as shown in Figure 1, and correction factors for the change of responsivity have been determined. The loss factors derived by this procedure are 26% for He I 584 Å, 28% for Mg x 609 and 624 Å, 34% for Ne VIII 770 Å, 39% for N v 1238 Å lines, and 29% for H I Lyman continuum.

After applying the post-recovery corrections we plot the evolution of the radiances in Figure 2. From a linear least squares fit to these data we can derive the amount of radiance change observed during the time period after the solar minimum: 25% for He I 584 Å, 16% for Ne VIII 770 Å, 53% for Mg x 609 Å, 86% for Mg x 624 Å, 83% for N v 1238 Å line, and 44% for the H I Lyman continuum at 880 Å.

The scatter of data points is quite large. The uncertainty levels of the radiometric calibration were 15 % (1s) for the A detector (Wilhelm et al. 1997) and 20 % (1s) for the B detector (Schühle et al. 2000b). After the SOHO accident we estimate a 40 % uncertainty when the corrections for the loss of responsivity have been applied. The scatter of the results, however, is larger due to variation of the radiance inside the sampled area. This has been proven by a comparison with data measured in co-registration by the CDS (Coronal Diagnostics Spectrometer) instrument on SOHO. The data where both instruments have captured the same target areas at the same wavelengths agree on the absolute scale within the uncertainty margins given by both instruments. In particular the variations of these lines are in phase for both instruments (Pauluhn et al. 1999). Thus the scatter of data is not instrumental and would perhaps be reduced if a larger area were sampled.

However, we cannot exclude entirely any systematic drift. Particularly the difference between the two Mg x lines, which originate strictly from the same plasma, may be due to a blend contribution hidden inside either line profile.

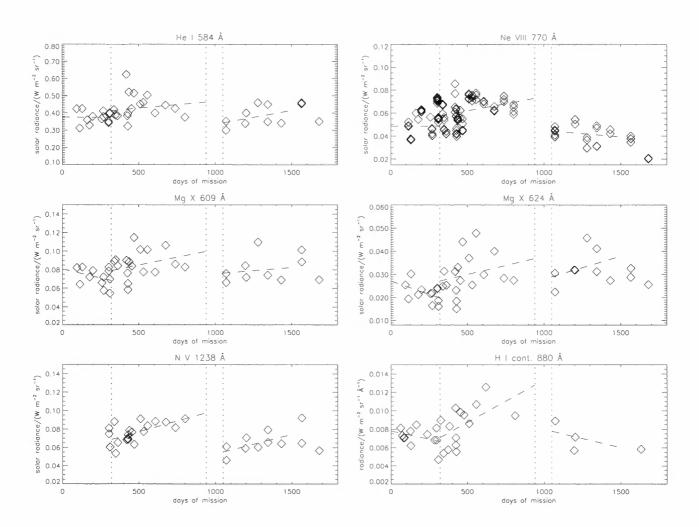


Figure 1: Radiances of the lines He I 584 Å, Ne VIII 770 Å, Mg x 609 Å and 624 Å, N v 1238 Å, and the H I Lyman continuum at 880 Å measured at quiet-Sun areas between 5 March 1996 and 7 July 2000. The time period is divided into three zones: Before solar minimum, after solar minimum but before the SOHO accident, and after. A linear least squares fit was applied to each data set.

We conclude that the radiances of the lines of He, Mg^{9+} , Ne^{7+} , N^{4+} , and the hydrogen Lyman continuum which originate in the transition region and the lower corona, show an increase in quiet-Sun areas that seems to be associated with the solar activity cycle. This result implies that the variation of the irradiance from the full Sun cannot simply be modelled by the number of active regions and plage areas visible on the solar disk and their variation throughout the solar cycle. Instead, there is an additional contribution to the variability from the quiet Sun.

We must stress that the scatter of data points is much higher than photon counting statistics and is entirely of solar origin, as a result of the limited size of the sampled area. Also, as we approach the maximum of the solar activity cycle, it becomes more difficult to select regions on the solar disk that are not influenced by active regions nearby, and the term "quiet Sun" may become questionable. We must notice also that the maintenance of the radiometric calibration over such a long period is a difficult task, and any error in this procedure will influence these results. It is therefore extremely valuable to have such observations from several independent instruments on SOHO. A joint evaluation of the data from SUMER, UVCS, and CDS instruments is underway.

ACKNOWLEDGEMENTS

SUMER is financially supported by DLR, CNES, NASA, and the ESA PRODEX programme (Swiss contribution). SOHO is a mission of international cooperation between ESA and NASA.

REFERENCES

Fontenla, J., White, O. R., Fox, P. A, Avrett, E. H., Kurucz, R. L., Astrophys. J., 518, 480, 1999.

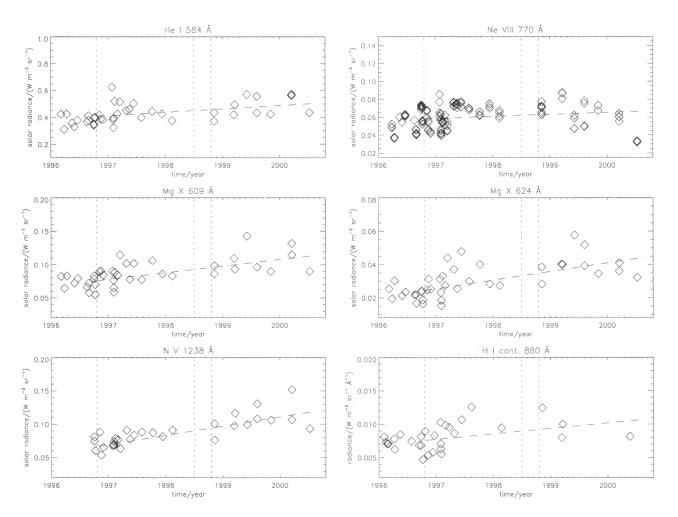


Figure 2 : Radiances of the lines shown in Figure 1 scaled over one decade for better comparability of their variation. A linear least squares fit was applied to each data set after solar minimum. The SOHO accident period in 1998 falls between the vertical dashed lines, and data after that period have been treated with the correction factors given in the text.

- Hall, L. A., Higgins, J. E., Chagnon, C. W., and Hinteregger, H. E., J. Geophys. Res., 74, 4181, 1969.
- Hollandt, J., Schühle, U., Paustian, W., Curdt, W., Kühne, M., Wende, B., and Wilhelm, K., Appl. Opt., 35, 5125, 1996.
- Lean, J., Rev. Geophys., 29,4, 505, 1991.
- Pauluhn, A., Rüedi, I., Solanki, S. K., Lang, J., Pike, C. D., Schühle, U., Thompson, W. T., Huber, M. C. E., Appl. Opt., 38, 7035, 1999.
- Schühle, U., Brekke, P., Curdt, W., Hollandt, J., Lemaire, P., and Wilhelm, K., Appl. Opt., 37, 2646, 1998.
- Schühle, U., Wilhelm, K., Hollandt, J., Lemaire, P., Pauluhn, A., Astron. Astrophys. 354, L71, 2000a.
- Schühle, U., Curdt, W., Hollandt, J., Feldman, U., Lemaire, P., and Wilhelm, K., Appl. Opt., 39, 418, 2000b,

- Steward, T. B., Arnold, G. S., Hall, F., Marten, H. D., Report SD-TR-89-45, The Aerospace Corporation, El Segundo, California, 1989.
- Tobiska, W. K., Eparvier, F. G., Sol. Phys., 177, 147, 1998.
- Wilhelm, K., Lemaire, P., Feldman, U., Hollandt, J., Schühle, U., and Curdt, W., Appl. Opt., 36, 6416, 1997.
- Wilhelm, K., Lemaire, P., Dammasch, I. E., Hollandt, J., Schühle, U., Curdt, W., Kucera, T., Hassler, D. M., and Huber, M. C. E., Astron. Astrophys., 334, 685, 1998.
- Wilhelm, K., Lemaire, P., Dammasch, I. E., Hollandt, J., Schühle, U., Curdt, W., Kucera, T., Hassler, D. M., and Huber, M. C. E., Phys. Chem. Earth (C), 25,5-6, 389, 2000.
- Woods, T. N., Rottman, G. J., Bailey, S. M., Solomon, S. C., and Worden, J. R., Solar Phys., 177, 133, 1998.

ANALYSIS OF THREE SEP ASSOCIATED FLARES

J. Sylwester, B. Sylwester, M. Siarkowski and S. Gburek

Space Research Centre, Polish Academy of Sciences, 51-662 Wroclaw, Kopernika 11, Poland *

ABSTRACT

We present examples of analysis of physical conditions in flares followed by SEP events recorded in vicinity of Earth. The data we used consist of *Yohkoh* SXT images and broad-band photometric observations of the soft and hard X-ray solar fluxes obtained using the RF15-I Photometer-Imager aboard *INTERBALL-Tail* satellite.

Key words: solar physics; flares; SEP events

1. INTRODUCTION

The aim of present research is to study physical conditions in a set of well observed flares which have been followed by SEP disturbance reaching the Earth vicinity. As data sets which have been used for the analysis of flaring plasma conditions we have chosen:

- Yohkoh SXT images obtained with All2 and Bel19 filters
- RF15-I broad-band measurements of the soft and hard X-ray solar flux

These two data sets allow to study both the spacial distribution of soft X-ray plasma characteristics from the images and the conditions in the plasma component responsible for presence of harder part of the X-ray spectra. This component is usually fast varying and needs observations frequent in time.

We selected for the analysis three SEP - associated flares which have been well observed by both *Yohkoh* SXT and *INTERBALL-Tail* RF15-I instruments. The basics of the physical analysis performed are explained in the next Section. The characteristic of the selected flares are described in more detail in dedicated further Sections. We present maps showing the evolution of emission measure and temperature within the flare as well as related distributions of socalled quasi- differential emission measure (QDEM).

Present study represents a first phase of the larger programme which may lead towards identifying possible differences of distribution of physical conditions for SEP-associated and NOT- associated flares. There are earlier papers by Kiplinger (1995), Sylwester, Sylwester and Garcia (1995) and Garcia (2000) indicating that such differences may exist indeed.

Results of the present study for SEP associated flares will be next intercompared with similar results performed for events which were not accompanied by following particle events observed in Earth vicinity.

2. DATA ANALYSIS

At first the temperature (T) and emission measure (EM) maps have been constructed adopting an isothermal approximation. The filter ratio technique for Al12 and Be119 deconvolved images has been used. The images $(64 \times 64 \text{ pixels})$ have been deconvolved using ANDRIL algorithm (Sylwester and Sylwester, 1998, 1999). The deconvolution removed the image blurring due to the instrument point spread function and increased numerically the spatial resolution of the images down to 1 arc sec. As a result of deconvolution we obtained corresponding sequences of images of 320×320 subpixels, where 1 subpixel is of $\sim 0.5 \operatorname{arcsec} \times \sim 0.5 \operatorname{arcsec}$ size. The deconvolved images have been carefully coaligned to within the fraction of arcsec. In order to present statistically significant maps of (T) and (EM), as the first step of analysis, the common regions on Al12 and Be119 images have been selected with the statistics good enough. For analysed flares the value of 20 DN/subpixel i.e. about 500 DN/pixel has been chosen. The common region is delimited by light thin line in the Figures 1, 3 and 5. For each subpixel located inside this boundary the temperature and emission measure have been derived using isothermal approximation. Next, based on the temperature and emission measure maps the corresponding "quasi" differential emission measure distributions (QDEM) have been constructed. The QDEM histograms have been constructed according to the following recipe:

- The subpixels have been identified where the temperature falls into $(T, T + \Delta T)$ range.
- The emission measures for elements assigned to appropriate temperature have been summed.
- Corresponding emitting volume has been estimated based on the assumption of the symmetry (i.e. the depth of the emitting region has been taken as square root of the area).

^{*}e-mail: js@cbk.pan.wroc.pl

Proc. 1st Solar & Space Weather Euroconterence, 'The Solar Cycle and Terrestrial Climate', Santa Cruz de Tenerite, Tenerite, Spain, 25-29 September 2000 (ESA SP-463, December 2000)

• The average density of the plasma has been determined from the emission measure and the volume $(N = \sqrt{(EM/V)})$.

The average temperatures for the entire region have been estimated based on the ratio of area-integrated Bell9 and All2 rates. The average T values are indicated in the bottom panel of Figs 1, 3 and 5.

The results of described analysis are discussed in the following Sections.

3. 20 APRIL 1998 Flare

This M1.4 flare (max at 10:21 UT) most probably occurred in behind the western limb active region (NO AA 8194). Therefore it has not been observed/classified in H α . Flare X-ray emission has been characterised by a symmetrical rise and decay in hard X-rays and smooth long duration decay in the softer range (see RF15-I light curves). The Sun was rather quiet many hours before the investigated event with only two active regions identified on the northern hemisphere.

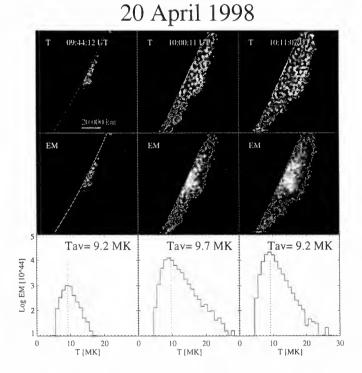


Figure 1. Spatial distribution of main thermodynamic parameters for two moments during the rise phase (the first and second columns) and for the maximum of GOES light curve (the third column) for the flare on 20 April 1998. Maps of temperature and emission measure are presented in the first and second rows respectively. The wiggly white line delimits the common region for Al12 and Be119 images where the signal is statistically significant. The bottom row shows corresponding "quasi" differential emission measure distributions. See the text for explanation.

In Figure 1, the basic thermodynamic parameters for the 20 April 1998 flare are displayed. The parameters shown correspond to two moments during the rise

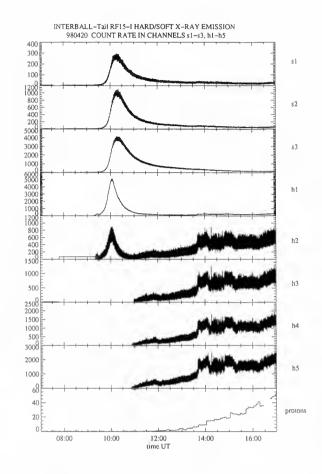


Figure 2. The variations of the soft and hard X-ray solar radiation level as observed by RF15-I (8 top panels). The fluence of protons with $E \ge 10$ MeV from GOES-8 (5 min averages) is plotted in the bottom panel for the comparison. The RF energy bands are as follows: s1: 0.7 - 1.0 keV; s2: 1.0 - 1.7 keV; s3: 1.7 - 2.7 keV, h1: 10 - 15 keV; h2: 15 - 30 keV; h3: 30 - 60 keV; h4: 60 -120 keV; h5: 120 - 240 keV. Letters s and h correspond to proportional and scintillation detectors respectively.

phase (the first and second column) and to the maximum (third column) of *GOES* light curve. The two instants presented are separated by about 15 min and 11 min (from their predecessors) respectively. The emitting plasma is concentrated in small kernels. The temperature and the emission measure distribution is very dynamic during the flare rise phase. By taking into account results of all the tests of the refined deconvolution and coalignment procedures, we believe this variations represent real changes of plasma conditions within the flaring region.

It is seen from Figure 1 that the bulk of plasma is characterised by the relatively high temperature around 10 MK. This temperature is nearly constant for all three times presented in spite of the fact that the morphology of the region changed substantially during this period. The corresponding (not indicated) average densities are not very high and account for 2.8, 1.7 and 1.8 in units of 10^{10} (per cm³) respectively. The QDEM histograms presented in the bottom row reveal that the total emission measure increases during the rise phase and the high temperature tails with temperature above 20 MK are pronounced. This tails are also present during the decay phase. The low temperature cut-off in QDEM distribution is of instrumental origin, as only the plasma with temperatures higher than ~ 5 MK can be probed based on analysis of the Be119/Al12 ratios.

4. 30 SEPTEMBER 1998 FLARE

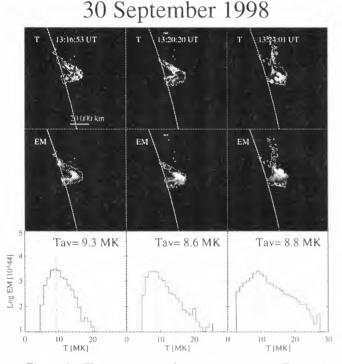


Figure 3. The same type of presentation as in Figure 1. The selected times correspond to three instants during the flare rise phase.

This flare (max at 13:50 UT) occurred in the active region NOAA 8340 situated just at the western solar limb. The Sun was moderately active during the day before the event. The X-ray class of this event was M2 (GOES) and 2N (H α). The flare was pronounced in X-ray radiation with an impulsive rise and smooth decay.

In Figure 3 we present temperature and emission The frames shown correspond to measure maps. the flare rise phase. The patterns are separated by 4 min. The morphology of this event resembles a loop like structure consisting of many small kernels. This event has been quite dynamic throughout the rise phase as can be followed in the Figure. The quasi differential emission measure distribution for selected times reveals presence of the high temperature tails. These tails evolve fast during the rise phase (no plasma with T_{i20} MK is seen on the first QDEM histogram and quite noticeable amount is present 7 min later). The average plasma density (for presented period) is around 4.0 in units of 10^{10} (per cm^3). Plasma density and the average temperature do not change substantially during the period shown in the Figure.

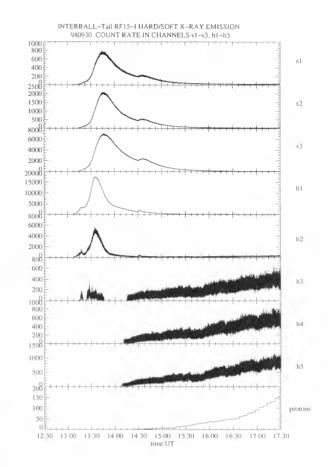


Figure 4. The same as in Fig. 2 for 30 September 1998 event.

5. 4 JUNE 1999 FLARE

This flare took place in the active region close to the western limb (NOAA 8552). The solar disc was very spotted during this day and 13 active regions can be distinguished on the visible hemisphere. The flare of interest was the most important X-ray event analysed in this contribution (M3.9). Also it was very bright as seen in H α (2B). This flare differs in comparison to previous ones in its X-ray characteristics. Although it was also characterised by rather impulsive rise its decay phase was also relatively short in comparison. The Al12 and Be119 SXT images for this flare have been available during the decay phase only. The maps of temperature and emission measure distributions displayed in the upper and middle panels in Figure 5 are separated in time by about 2 min. They correspond to times during flare decay phase. The lowest panel shows the corresponding quasi differential emission measure distributions (QDEM). The average temperatures and the total emission measures for individual times do not change substantially during presented period. The corresponding plasma density is about 3.3 in units of 10^{10} $(per cm^{3})$. The high temperature tails (T > 20 MK)seen on QDEM histograms are pronounced and are seen to vary within a short time interval shown.

4 June 1999

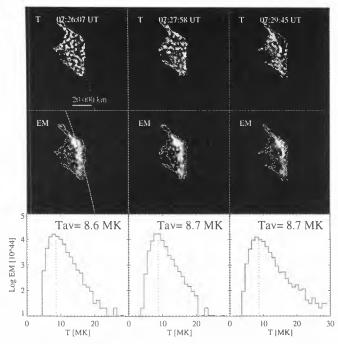


Figure 5. The same as in Figure 1, except that the results correspond to decay phase (SXT data were not available for the rise phase).

6. CONCLUSIONS

We present basic characteristics of the flaring plasma including maps of the temperature and emission measure distribution for three flares which were associated with the following SEP particle events. The flare physical characteristics have been derived using the soft and hard X-ray observations obtained from SXT images *Yohkoh* and RF15-I on *Interball-Tail* satellites. We have noticed that:

- All considered flares appear to be quite extended in X-rays.
- Substantial reconfiguration of coronal structures took place possibly related with the SEP accompanied flare.
- Plasma appears to be localized in a net of emitting kernels.
- Temperature distribution of the plasma is powerlaw above the average temperature with the tail extending up to 30 MK later during the rise phase. These tails are present also later-on during flare decay indicating for continuous heating.
- Early during flare rise presence of significant amount of super-hot plasma (at 40 80 MK range) can be deduced based on the isothermal analysis of RF15-I h2/h1 flux ratio.

ACKNOWLEDGMENTS

This work has been possible due to the Grant: Organisation of Magnetic Fields in the Corona 2.P03D.024.17 of Polish Committee for Scientific Research.

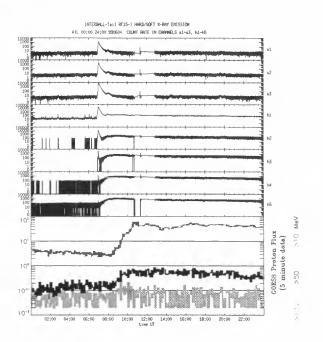


Figure 6. The same as in Fig. 2 but for 4 June 1999 event. In addition to E > 10 MeV, the E > 50 MeV and E > 100 MeV proton flux variations are shown in the two bottom panels.

REFERENCES

- Garcia, H, 2000, Astrophys. J., 241, 197
- Kiplinger, A.L., 1995, Astrophys. J., 453, 973
- Sylwester, J. and Sylwester, B., 1998, Acta Astron., 48, 519
- Sylwester, J. and Sylwester, B., 1999, Acta Astron., 49, 189
- Sylwester, B., Sylwester, J., and Garcia, H.A., 1995, JOSO Annual Report, ed. M. Saniga, 161

EUV IRRADIANCE VARIATIONS MEASURED WITH THE SOHO CORONAL DIAGNOSTIC SPECTROMETER

William T. Thompson¹ and Pål Brekke²

¹Emergent IT, Inc., NASA Goddard Space Flight Center, Code 682.3, Greenbelt, MD 20771, USA ²ESA Space Science Department, NASA Goddard Space Flight Center, Code 682.3, Greenbelt, MD 20771, USA

ABSTRACT

The Coronal Diagnostic Spectrometer aboard the Solar and Heliospheric Observatory observes the solar EUV spectrum in two bands between 308-379 Å and 513-633 Å. The full Sun irradiance can be measured by rastering the instrument over the solar disk. Measurements of the solar irradiance have been made starting 25 March 1997 and continuing to the present, ranging from very quiet to very active Sun. These measurements are the only current EUV spectral irradiance measurements taken on a regular basis. As well as irradiance values, the most recent observations also provide moderate resolution solar images to help quantify the important sources of the irradiance variability. The dependence of individual spectral lines on the solar cycle is presented, spanning the temperature range from 3×10^4 K to 2.7×10^6 K. The important spectral lines of He II and Si XI at 304 Å are observed in second order and separated. The high spectral resolution of these measurements, combined with the coverage of a significant proportion of the solar cycle, provide a unique dataset for understanding solar variability in the EUV. In addition, these data are important input for interpreting data from broadband and lower resolution irradiance monitors, such as the SOHO SEM and TIMED.

Key words: EUV; Irradiance; SOHO; CDS.

1. THE OBSERVATIONS

The Normal Incidence Spectrometer (NIS) of the SOHO Coronal Diagnostic Spectrometer (CDS) observes spatially resolved spectra in two bands, NIS-1: 308–379 Å, and NIS-2: 513–633 Å. A special observing program allows the full-Sun irradiance to be measured by rastering over the entire Sun. A full scan takes approximately 13 hours, and is performed on a roughly monthly basis. Figure 1 shows representative full-Sun NIS spectra. The spectral resolution varies from 0.3 to 0.6 Å, allowing the separation of

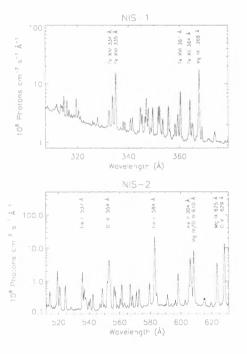


Figure 1. Representative CDS full-Sun irradiance spectra in the two wavelength bands. A selection of prominent lines are identified. Irradiances from 154 separate spectral lines have been extracted. The apparent continuum component is actually due to offband scattering in the spectrometer.

closely spaced lines. For example, the Si XI line at 303.3 Å can be clearly separated from the He II line at 303.7 Å (both seen in second order).

Full disk irradiances have been measured with CDS starting on 25 March 1997, when the Sun was close to solar minimum ($F_{10.7} = 70$). A total of 7 irradiance measurements were made up through the summer of 1998, during which time the level of solar activity increased substantially ($F_{10.7} = 104$). The irradiances of a total of 154 separate spectral lines have been extracted from these data for each observation date, with corresponding emission temperatures ranging from 3×10^4 K (He I) to 2.7×10^6 K (Fe XVI), with good coverage over that temperature range. Figure 2

Proc. 1st Solar & Space Weather Euroconference, 'The Solar Cycle and Terrestrial Climate', Santa Cruz de Tenerife, Tenerife, Spain, 25-29 September 2000 (ESA SP-463, December 2000)

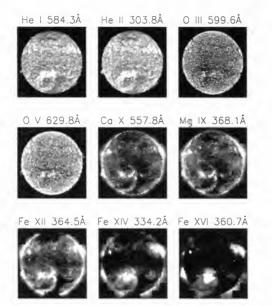


Figure 2. Monochromatic images of a representative sample of spectral lines. ranging in formation temperature from 3×10^4 K to 2.7×10^6 K, taken on 23 April 1998.

shows monochromatic images of the Sun in selected lines from the CDS irradiance data.

In the summer of 1998. just a day after one of the CDS irradiance measurements, pointing control of the SOHO spacecraft was lost for several months. After SOHO was recovered in the fall of 1998, regular observations of the full-Sun irradiance were resumed. The accident caused changes in the spectral line shapes, and some closely spaced lines which were previously treated separately are now treated as blends in the post-recovery data. Also, some faint lines which could previously be measured had to be dropped. Because of these two effects, the total number of lines analyzed in the post-recovery data was reduced to 106.

Figure 3 shows the measured irradiance from the Mg X line at 625 Å as a function of time. Also shown is the $F_{10.7}$ radio flux for comparison. There are still some issues to be worked out regarding the calibration of the post-recovery data. Therefore, we will only consider the pre-accident data for the remainder of this report.

2. CALIBRATION

The calibration used for the CDS NIS measurements are based on two sounding rocket underflights. Coordinated observations of the solar irradiance were made on 15 May 1997, together with the EUV Grating Spectrometer (EGS) instrument aboard a NASA/LASP sounding rocket. The EGS is a prototype instrument for the upcoming NASA Thermosphere Ionosphere Mesosphere Energetic Dynamics

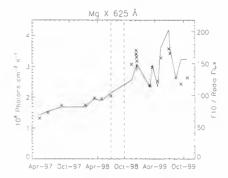


Figure 3. Solar irradiance from the Mg X line at 625 Å (X symbols) as a function of time. Also shown is the $F_{10.7}$ radio flux (solid line) for comparison. The vertical dashed lines represent the temporary loss and subsequent recovery of SOHO pointing control.

(TIMED) mission. The highly precise calibration of the EGS instrument (8–10%), combined with the coincident CDS observations of the irradiance allows a calibration curve to be derived for the CDS instrument. These data provided a calibration for the entire NIS-2 band, and the area of the NIS-1 band around the strong Mg IX line at 368 Å. Extracting a calibration for the rest of NIS-1 was complicated by the lower spectral resolution of the EGS, and the dense spacing of lines in NIS-1, although a rough calibration curve could be derived.

Measurements of the solar radiance of an active region target with another sounding rocket underflight extended the calibration to the remainder of the NIS-1 wavelength band. The Solar Extreme-ultraviolet Research Telescope and Spectrograph was launched on 18 November 1997. During the flight, both the SERTS and CDS instruments were co-pointed at the same target. The SERTS measurements covered most of the NIS-1 wavelength range, up to 354 Å. By combining the SERTS measurements with the EGS measurements at 368 Å, a complete NIS-1 calibration curve could be derived.

Both sounding rocket measurements also provided a measurement of the CDS second-order efficiency at 2×304 Å which were in excellent agreement with each other.

Additional corrections are applied to the data for burn-in effects on the detector. Loss of sensitivity from the two narrow slits are measured directly by using a special $90'' \times 240''$ "movie" slit. Loss in sensitivity from the occasional use of this wider "movie" slit is estimated from regular observations of He I 584 Å emission from the quiet Sun.

3. COMPARISON WITH EUV MODELS

Figure 4 shows the variation of a number of selected emission lines with time. One sees that the irradiances of the chromospheric lines change only slightly

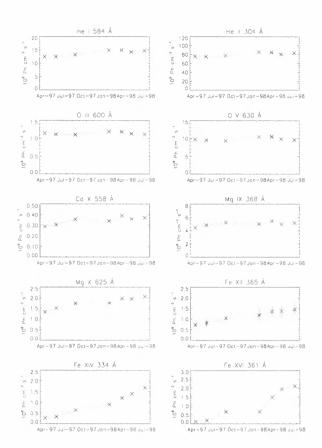


Figure 4. Variation in the irradiances of selected lines with time. The chromospheric lines change only slightly, while coronal irradiances steadily increase with the rise in the solar cycle.

with time, while the coronal irradiances steadily increase with the rise in the solar cycle. For the lines with the highest formation temperatures, the irradiances vary by as much as an order of magnitude.

We compared our results against four standard models for the EUV irradiance:

- Hinteregger: (Hinteregger et al. 1981) In general, the model predicts lower irradiances for NIS-1, and higher irradiances for NIS-2, by as much as a factor of two. These results are consistent with those of Woods et al. (1998).
- **EUVAC:** (Richards et al. 1994) More successful at predicting the observed He I 584 Å emission, but still overestimates other parts of the NIS-2 spectrum. in particular the O V 629 Å line. The NIS-1 spectrum, as in the Hinteregger model, is underestimated compared to the measurements. Because the EUVAC model (as well the EUV97 model below) consists of a combination of broadband and line components, detailed aspects of the spectrum are not reproduced by the model.
- **EUV97:** (Tobiska & Eparvier 1998) Also tends to underestimate the quiet-Sun NIS-1 spectrum, but is more successful when solar activity is higher. The NIS-2 spectrum is in general

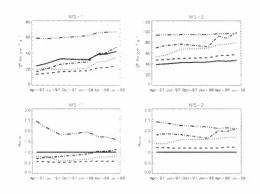


Figure 5. Comparison of the total integrated irradiance in each wavelength band measured with CDS (solid) against the Hinteregger (dot), EUVAC (dash), EUV97 (dot-dash), and SOLAR2000 (dot-dot-dot-dash) models. In the upper two panels are shown the total integrated irradiances in the two NIS wavelength bands. In the lower two panels are the ratios of the models to the measurements. NIS-1 is dominated by coronal lines, while NIS-2 is dominated by chromospheric and transition-region lines.

overestimated-by about a factor of two for the stronger lines.

SOLAR2000: (Eparvier 2000) Tends to overestimate the quiet-Sun NIS-1 spectrum, but is more successful when solar activity is higher. The behavior for NIS-2 is similar to the EUV97 model.

The primary purpose of the above models is to predict the total integrated EUV flux. A fairer comparison, then, is between the measured and predicted integrated intensities, rather than the detailed spectra. Figure 5 shows the total integrated flux in the two wavelength bands against the model predictions, as a function of time. The NIS-1 band is dominated by coronal lines, and the NIS-2 band is dominated by chromospheric and transition-region lines.

Of the four models, the EUVAC model matches best the temporal variation in both wavelength bands, although it's too low for NIS-1, and too high for NIS-2. It's also the closest to the measured irradiance in the NIS-2 band. In NIS-1, the closest match is the EUV97 model, but only for high levels of solar activity. For low solar activity, the Hinteregger model is slightly better.

4. COMPARISON WITH OTHER INSTRUMENTS

In Figure 6 we show a comparison of the irradiance of lines with similar formation temperature, O III from CDS and C IV from SOLSTICE. In general, there's good correspondence between the two. However, the different timescales on which the data are taken do affect the comparison. It may also be that the CDS data do not rise as much as the SOLSTICE data.

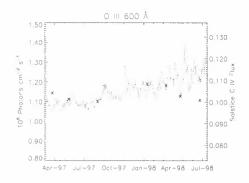


Figure 6. Comparison of CDS measurements of the O III line at 600 Å (symbols) to the C IV irradiance as measured by SOLSTICE (dotted lines). SOL-STICE data courtesy Barry Knapp.

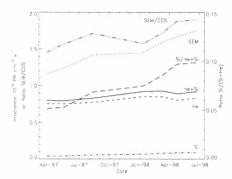


Figure 7. Comparison of the CDS irradiance measurements in the two second-order lines of He II and Si XI at 304 Å (solid) to the broadband measurements by the SEM instrument (dot). The ratio of the SEM to the CDS measurements is shown by the dot-dot-dot-dash line. The individual contributions of the He II (short dash) and Si XI (dot-dash) components are shown, as well as the steadily rising ratio of Si XI component to the total (long dash).

Figure 7 shows a comparison of the second order He II/Si XI 304 Å to the Solar EUV Monitor (SEM) instrument on SOHO. The ratio of the SEM to the CDS measurements shows that these two lines contribute about half of the SEM signal. There's also a slow rise in the ratio, which may either be due to increased contribution from coronal lines in the SEM bandpass, or loss of sensitivity in CDS.

5. CONCLUSIONS

We have demonstrated that the CDS instrument can be used to measure the EUV irradiance in 154 separate spectral lines. Observations over a period of several years allow the characterization of the temporal behavior of spectral lines as a function of formation temperature. These data serve as a useful check on irradiance models based on proxy measurements such as the $F_{10.7}$ radio flux, and demonstrate that revisions are needed in the current models. Future work will extend this analysis to the postrecovery data, after finalizing the calibration for this period.

ACKNOWLEDGMENTS

We would like to thank Barry Knapp for providing the SOLSTICE data, Kent Tobiska for help with the EUV97 model software and for providing the SO-LAR2000 model calculations, and Tom Woods for providing software for the Hinteregger and EUVAC models.

This work was supported by NASA grant NAS5-32350.

REFERENCES

- Eparvier F., 2000, private communication
- Hinteregger H.E., Fukui K., Gilson B.R., 1981, Geophys. Res. Letters, 8, 1147
- Richards P.G., Fennelly J.A., Torr D.G., 1994, J. Geophys. Res., 99, 8981
- Tobiska W.K., Eparvier F.G., 1998, Solar Phys., 177, 147
- Woods T.N., Rottman G.J., Bailey S.M., Solomon S.C., 1998, Solar Phys., 177, 133

TILT ANGLE VARIATION THROUGH THE 14TH SUNSPOT CYCLE

L. Tóth and O. Gerlei

Heliophysical Observatory of the Hungarian Academy of Sciences, H-4010 Debrecen, P.O.B. 30. Hungary Tel/fax: +36 52-437-343 e-mail: tothla@tigris.klte.hu / otto@fenyi.sci.klte.hu

ABSTRACT

The tilt angle variation of bipolar magnetic regions (BMRs) in space and time is a probable indicator of large-scale properties of magnetic field distribution, the dynamo process and different influences effected on rising flux tube. Such an investigations have been made in several cases but without distinction of markedly aligned sunspot groups to others. In cases of that kind a great number of long term datasets are required. We have a long-term series of photosphere drawings from 1880 to 1919 (Fényi 1919). With the help of these daily observations the data of Greenwich Photo-Heliographic Results (GPHR) have been analysed to study the orientation angles of BMRs through the 14th sunspot cycle. We have investigated the tilt angle distribution and the variation of tilt angle as a function of latitude and time. Our work differs from any of the previous investigations to the studied sunspot cycle, data sets and applied evaluation procedure. Despite all this it has even confirmed the Coriolis force hypothesis.

INTRODUCTION

The Joy's law as it was shown by Hale et al. (1919) states that BMRs are inclined to the latitudinal line, with the preceding spot (p-spot) of the BMR closer and the following spot (f-spot) away from the equator as well as the tilt angle increasing with latitude.

It is believed that the origin of solar magnetic field is in the dynamo operating in a stable layer at the base of the convection zone. BMRs originate in the strands of magnetic flux, which may come out of this stable layer and would rise through the convection zone. According to dynamo models (Parker 1955; Babcock 1961; Leighton 1964,1969) a poloidal field emerges from and turns into toroidal because of differential rotation. If the tilt was caused by this winding it should then decrease at given latitude as the field lines are stretched further with the progress of the solar cycle. However, this has not been clearly observed yet.

The solution for this problem is to take Coriolis force into account that can twist the ascending flux loops (Schmidt 1968) so that it finally emerges at the surface with a tilt to the local latitudinal line. Although this latitudinal dependence of tilt, called "Joy's Law", has been studied in several cases (Wang 1989, 1991; Howard 1990, 1992, 1996; Sivaraman 1999) we have performed a new one on the basis of different sunspot cycle, data sets and applied evaluation procedure. We carried it out in order to strengthen the Coriolis force hypothesis or got some knew results.

METHOD OF INVESTIGATION

In our case there was no magnetic field information available for studied sunspot groups. It follows that we could identify an active region (AR) as a BMR if the pand f-parts of it were separable well. On the other hand, it was fortunate because of it has given a colation of several complicating factors too.

For the same reasons only those ARs were taken into account that longitudinal co-ordinates were not farther from the central meridian than 60°. The abovementioned selections of suitable ARs for years from 1901 to 1913 were made on the basis of photosphere observations of Fényi at al. (1919). It has meant 685 selected groups in 3756 different cases.

The tilt angle calculation of selected ARs was based on data of GPHR. This angle is by convention positive for ARs that p-spots are equatorward and negative if poleward. The calculation was made in three different ways:

- At first we calculated the area weighted positions of p and f parts of the given AR. Following this the tangent of orientation angle was given by ΔB/[(Δl)cosB] (Howard 1990). Where ΔB is the difference in solar latitude between the p and f parts of AR, and Δl is the similar difference in solar longitude.
- Secondly we calculated the tilt angle as the bend of a straight line fitted by least-squares method to the points of AR.
- And finally we calculated the tilt angle as the bend of a straight line fitted by area weighted leastsquares method to the points of AR.

The comparison of these three methods has shown negligible difference among them and finally we applied the third one with estimated errors.

Proc. 1st Solar & Space Weather Euroconference. 'The Solar Cycle and Terrestrial Climate', Santa Cruz de Tenerife, Tenerife, Spain, 25-29 September 2000 (ESA SP-463, December 2000)

RESULTS

The distribution of axial tilt angles over 5° increments of tilt angle is shown and compared with other results (Sivaraman 1999) in figure 1.

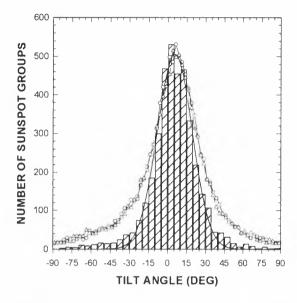


Figure 1: The distribution of axial tilt angles. (Explanation is in the text.)

The striped columns show our results that are based on selected groups (from 1901 to 1913 as stated above) and the solid line is the Gaussian least-squares fit to it. The open circles represent the Kodaikanal (1906-1987) while triangles the Mount Wilson data (1917-1985) (Sivaraman 1999) normalised to our results.

These last results are practically the same. But not in our case where due to the selection of ARs the peak is more narrow then the others and follow Gaussian distribution fairly well. The peak position of this fitted Gaussian curve is compared with other results in table 1.

Table 1: Different values of "averaged" tilt angles.

The mean o	f tilt angles	The peak position of the fitted Gaussian curve
Howard 1996	Sivaraman 1999	Our result
4.28(19)°	4.2°	5.502(2)°

More information is obtainable from the tilt angle distribution as a function of latitude that gives practically the "Joy's Law" (table 2. and figure 2.). The notation of figure 2. is quite the same with the previous one. The striped columns show our results are based on selected groups (stated above) and the solid line is the weighted least-squares fit of equation 1. to our data. The open circles represent the Kodaikanal while triangles the Mount Wilson data (Sivaraman 1999).

Table 2:	The	tilt	angle	as	а	function	of	latitude.	Our
work (in	degre	ee)							

Latitude region	Averaged tilt angle over the given intervals of latitude
0-5°	0.2(1.7)°
5-10°	2.5(1.1)°
10-15°	3.2(1.0)°
15-20°	6.3(1.0)°
20-25°	9.1(1.4)°
25- 30°	8.1(4.8)°
30-35°	0.1(5.2)°

Our results agree well within error bars with previous ones. The one of the striking differences is at higher latitudes (up to 20°) where our results are larger then the others. The another difference is in the zone $30^{\circ}-35^{\circ}$ because of the small number of ARs there, nevertheless it corresponds within error bars too.

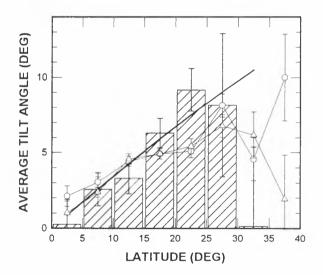


Figure 2: The distribution of tilt angles as a function of latitude averaged over 5° intervals. (Explanation is in the text.)

As we stated above if the tilt is caused by the winding of magnetic field it should then decrease at given latitude as the field lines are stretched further with the progress of the solar cycle. In the hope that if we could get a fine allusion of this, we investigated the averaged tilt angles over 5° intervals of latitude and a year interval of time too through the 14th sunspot cycle. Since it didn't bring the required results the presentation of relevant figures are unnecessary.

On the other hand, this failure is favourable to Coriolis force hypothesis. There is a simple theoretical model for role of Coriolis force in the tilts of BMRs by D'Silva et al. (1992) (see equation 1). Where $\Omega = 2.8 \times 10^{-6} \text{ s}^{-1}$ is the average rotational frequency of the Sun, (t) is the rise time of the flux tube and (Θ_{em}) is the angular distance from the pole. This equation was fitted to our data by weighted least-squares method.

$$\gamma = \tan^{-1}(\tan(\Omega t)\cos(\Theta_{em})) \tag{1}$$

The result of this calculation for the rise time of flux tube from the basis of convection zone is $1.18(12)*10^5$ second. The rising velocity may be taken to be $v=R_{\odot}/3t=1.97(19)$ km/s, since the depth of the convection zone is about $R_{\odot}/3=2.32*10^5$ km. And this value is the same in order of measured upward velocities of granules (~1 km/s) and umbral dots (~3 km/s) (Bray 1984) that is an unambiguous confirmation of the Coriolis force hypothesis.

CONCLUSIONS

First of all on the basis of this work we can claim that the Greenwich Photo-Heliographic Results together with other historical datasets is a well usable catalogue nowadays too, and the selection of aligned active regions was lead to the reduction of errors allowed better determination of average tilt angle.

Furthermore, our investigation is in line with others and it has shown that there is no clear time dependency of tilt angle. It means that it is not necessary to take the role of the winding of magnetic field lines into account during the explanation of tilt angle of active regions.

Our tilt angle distribution values as a function of latitude agree well with others, and to take the Coriolis force into account provides us with a possibility to determine the typical rising velocity of magnetic flux tube. And this agrees well with other observations, that is a confirmation of the Coriolis force hypothesis.

ACKNOWLEDGEMENT

This work was supported by the Hungarian National Science Found (OTKA: F030957)

REFERENCES

- Babcock H.W., 1961, ApJ 133, 572
- Bray R.J., Loughhead R.E., Durrant C.J., 1984, The Solar Granulation, Second edition, Cramridge University Press, p93
- D'Silva S., Choudhuri A.R., 1992, Astron. Astrophys. 272,621
- Fényi Gy., 1919, Photosphere Drawings from 1880 to 1919, http://fenyi.sci.klte.hu

- Hale G.E., Ellerman F., Nicolson S.B., Joy A.H., 1919, Apj 49,153
- Howard R.F., 1990, Sol. Phys. 132, 49
- Howard R.F., 1992, Sol. Phys. 137, 205
- Howard R.F., 1996, Sol. Phys. 169, 293
- Leighton R.B., 1964, ApJ 140, 1547
- Leighton R.B., 1969, ApJ 156, 1
- Parker E.N., 1955, ApJ 122, 293
- Sivaraman K.R., Gupta S.S., Howard R.F., 1999, Sol. Phys. 189, 69
- Schmidt H.U., 1968, in Kiepenheuer K.O. (ed.) Sructure and Development of Solar Active Regions. Proc. IAU Symp. 35, 95
- Wang Y.M., Sheely N.R., 1989, Sol. Phys. 124, 81
- Wang Y.M., Sheely N.R., 1991, ApJ 375, 761

STUDY OF CHROMOSPHERIC Ca II CLOUD-LIKE STRUCTURES

K. Tziotziou¹, P. Heinzel², P. Mein¹, and N. Mein¹

¹Observatoire de Paris, Section de Meudon, DASOP, F-92195 Meudon Principal Cedex, France tel:+33-1-45077798 / fax:+33-1-45077959 e-mail:Kostas.Tziotziou@obspm.fr

²Astronomical Institute, Academy of Sciences of the Czech Republic, CZ-25165 Ondřejov, Czech Republic e-mail:pheinzel@sunkl.asu.cas.cz

ABSTRACT

We present an inversion method to estimate the temperature, electronic density, microturbulence, velocity and emission measure of chromospheric cloud like features observed in the 8542 Å Call line. The method involves the computation of a large grid of Ca II models using a multi-level non-LTE transfer code. We compute the necessary photoionization rates by first solving the non-LTE hydrogen case and then we proceed to the calculation of the Ca II line depth-dependent mean intensity inside an isolated, isothermal cloud laying above the photosphere. The inversion of observed profiles with the grid of computed synthetic Ca II profiles is performed with a searching and matching χ^2 algorithm which is followed by an interpolating algorithm permitting a more accurate determination of the aforementioned parameters. We apply the results to a filament observed with the MSDP instrument on VTT (Tenerife) and discuss through an error analysis the accuracy of the method in determining the physical parameters of the filament. We furthermore compare the results with a corresponding H α investigation and discuss future extensions of the inversion technique. The determination of the physical parameters of dark cloudlike structures around active regions is crucial to the understanding of the temporal and spatial evolution of such regions and their connection to the solar cycle.

INTRODUCTION

Solar spectral inversion codes that take into account the formation of chromospheric lines under conditions of non local thermodynamic equilibrium (non-LTE) are a powerful diagnostic tool for obtaining information from observed line spectra.

Synthetic profile calculations with multilevel non-LTE transfer codes are usually either based to the linearization or the preconditioning approach. The first approach on which the MULTI code by Carlsson (1986) is based, linearizes all the necessary multilevel transfer equations by neglecting second and higher order terms in the perturbed equations. The preconditioning approach linearizes the original non-linear equations by choosing some quantities from a previous iteration and using an approximate relationship for the radiation field. The latter is used in the one-dimensional multilevel transfer code MALI by Heinzel (1995). The MALI approach has been recently used by Molowny-Horas et al. (1999) - hereafter MH -

for the non-LTE inversion of a chromospheric $H\alpha$ cloudlike filament. Cloud models have been successful for the study of several chromospheric features like filaments, arch filaments and mottles.

In this paper we are interested in the non-LTE formation of the Ca II 8542 Å line in chromospheric cloud-like features. We construct with MALI a large grid of models and afterwards apply the non-LTE Ca II inversion procedure to the same filament that MH studied in H α to obtain valuable information about inversion in different spectral lines.

MALI PROFILE CALCULATIONS

A thorough description of the MALI code and its boundary conditions is given in Mein N. et al. (1996), Heinzel et al. (1999) and MH. The application to Ca II is worked out in Mein et al. (2000). The cloud-like filament is represented by an isothermal horizontal 1D slab which lays above the solar surface and moves as a whole with a bulk velocity. The input parameters for the synthetic profile calculations are temperature, electron density, microturbulent velocity, macroscopic bulk velocity, geometrical thickness, height above the solar surface and the incident solar radiation.

We first solve the non-LTE problem for hydrogen in order to compute the radiation field in Lyman lines and the continuum used for the evaluation of the CaII photoionization rates and then we proceed to the Ca II non-LTE calculations. We consider a five level plus continuum Ca II model. We refer the reader to Shine & Linsky (1974) for a summary of the Ca II atomic level structure, transition rates, level broadening parameters and photoionization rates used in the MALI code. The incident solar radiation field is a compilation of various observations made by Gorshkov et al. (1996). The infrared Call lines are computed with complete frequency redistribution (CRD). The computed non-LTE level populations as a function of the line-center optical depth are used to evaluate the Ca II line source function. The formal solution of the radiation transfer equation along the line of sight is then numerically calculated where the optical depth τ_{λ} is expressed by a Doppler-shifted Gaussian profile. The grid of input parameters for the Call MALI synthetic profile calculations is presented in Table 1.

An analysis of the Ca II synthetic profiles for the case of a static $V = 0 \text{ km s}^{-1}$ cloud shows that:

Proc. 1st Solar & Space Weather Euroconference, 'The Solar Cycle and Terrestrial Climate', Santa Cruz de Tenerife, Tenerife, Spain, 25-29 September 2000 (ESA SP-463, December 2000)

Parameter	Range	No of points
$V ({\rm kms^{-1}})$	-5 - 5	3
$N_{\rm e}~({\rm cm}^{-3})$	$2 \times 10^{10} - 1 \times 10^{11}$	9
T (K)	6000 - 11000	11
Z (km)	1000 - 5000	5
$\xi_{\rm t}$ (km s ⁻¹)	3 – 9	7
Height (km)	20000	1

Table 1. Parameters used for the calculation of the grid. The total number of computed MALI models is $3 \times 9 \times 11$ $\times 5 \times 7 = 10395$. Since the source function is symmetric to negative and positive velocities only the three positive points are calculated for parameter V.

- An increase in temperature T gives brighter Ca II intensities near the center of the line as a direct result of the increase of the rate of collisions with temperature. Moreover, since the optical thickness of the cloud decreases with increasing temperature we see more background radiation due to the lower line center opacity.
- An increase of microturbulence causes a considerable broadening of the profile and thus a decrease of the line center opacity. As a consequence, we see more background radiation.
- There is a strong dependence of intensity on electron density N_e (see Fig. 1). For low temperatures with increasing N_e the Ca II line center intensity goes through a minimum before increasing again while for high temperatures the line center intensity is monotonically decreasing within the range of used densities. For low temperatures an increase of N_e leads initially to an increase of the optical thickness of the cloud and thus absorption until N_e reaches a high enough value for collisions to dominate and thus give rise to emission. However, as temperature increases Ca II starts ionizing to Ca III. As a consequence for high temperatures larger electronic densities N_e are needed in order for Ca II to start emitting.
- As Z increases the Ca II line intensities decrease since the optical thickness of the cloud increases making it less transparent to the incident radiation.

Since ambiguities can occur in the inversion for large uncertainties in the observed profiles, the number of variables is reduced to four by collapsing Z and N_e into a new single parameter, the emission measure Q, defined as $N_e^2 Z$.

THE INVERSION PROCEDURE

The comparison of the observed line profile $I_{\mathrm{fil},\lambda_i}$ with each of the grid model profiles $I_{\lambda_i}(V, T, \xi_t, Q)$ is done by a minimizing χ^2 function given by

$$\chi^2 = \sum_{i=1}^{N} \left[\frac{I_{\text{fil},\lambda_i}}{I_{\text{bg},\lambda_i}} - \frac{I_{\lambda_i}(V,T,\xi_t,Q)}{I_{\text{tab},\lambda_i}} \right]^2 \tag{1}$$

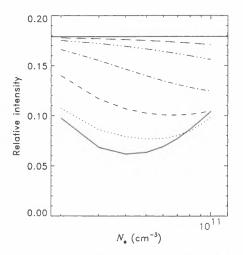


Figure 1. Intensity of the Ca II line center in relative units as a function of electronic density N_e for V = 0 km s⁻¹, Z = 5000 kmand $\xi_t = 9$ km s⁻¹. The curves from bottom to top correspond to T = 6000, 6500, 7500, 8500, 9500and 10500 K. The horizontal solid line corresponds to the Ca II background line center intensity.

where I_{bg,λ_i} and I_{tab,λ_i} are the observed and tabulated background profiles, λ_i refers to the wavelength positions used in the line profile and N is the number of these positions which in our case is equal to five. Since this χ^2 procedure gives the minimum at the resolution of the grid's mesh, a more accurate determination of the parameters is further achieved by a parabolic interpolation which takes into account the nearby grid mesh points of the minimum.

We apply the procedure to a filament observed with the MSDP instrument of the German VTT at the Observatorio del Teide on September 25th, 1996 (see Fig. 2). The calibration of the observed and grid calculated profiles is done by comparing the observed and tabulated background profiles I_{bg,λ_i} and I_{tab,λ_i} . and calculating a proportionality factor K which satisfies that $I_{bg,\lambda_i} = K \cdot I_{tab,\lambda_i}$ for all *i*'s. The calibration gives a difference of the observed and the tabulated profile which is always less than 2% and can be attributed to instrumental or observational reasons.

We have inverted a total of 4009 Ca II profiles from the filament region that have a maximum contrast (compared to the background profile) lower than 0.95 excluding thus all border points where the filament is extremely optically thin and we may be observing the background. A first qualitative look of the inversion maps (Fig. 2) shows that the darker center of the filament seems to have lower temperatures than its borders which is in agreement with the results obtained for H α by MH. We also roughly recognize the same velocity structures seen for Haand although there is no clear pattern the filament borders seem to have higher values of microturbulence. However, there is no trend at all in the distribution of emission measure Q which is in contrast with the H α inversion where Q increases from the border towards the center of the filament.

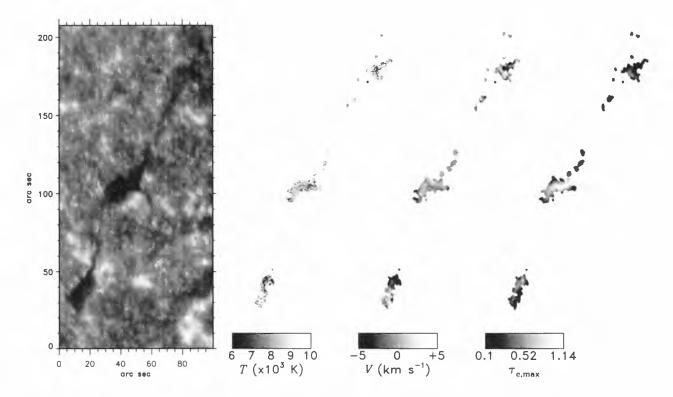


Figure 2. The observed filament and maps of temperature (T), velocity (V) and maximum line-center optical depth $\tau_{c,max}$ according to the inversion of filament Ca II profiles. Negative and positive velocities correspond to velocities towards and away from the observer. Only points within the filament that have a contrast profile in Ca II less than 0.95 are considered.

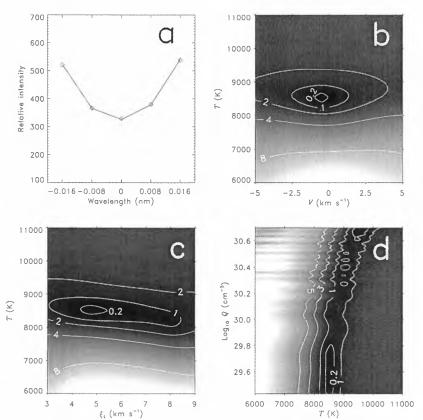
A direct comparison of the inverted parameter values for Ca II and for $H\alpha$ at every point in the filament is usually not possible because of the different formation depths for $H\alpha$ and Ca II within the filament as well as to the different refraction indices of the two lines in Earth's atmosphere. However a statistical analysis of the results for the two lines, reveals that:

- The Ca II temperature distribution peaks around 8500 K and then drops dramatically for higher temperatures. This is expected since Ca II is mostly dominant for low temperatures and dramatically drops for higher temperatures where the formation of Ca III is more favorable. The H α distribution has no clear equivalent peak in temperature and the filament seems to be on average cooler. The different behaviour is explained by the fact that the Ca II line is collision dominated and hence much more sensitive to temperature compared to H α which is photoionization dominated.
- The Ca II microturbulence distribution shows a peak around 5 km s⁻¹. Since temperature is well defined by the Ca II inversion it leads to a better definition of the microturbulence from the profile width which depends on temperature and microturbulence. The coupling of temperature and microturbulence is stronger in the case of H α which is a much lighter element than Ca IIand as a result there are several couples of values for temperature and microturbulence that correspond to a specific H α line width.

• The velocity distribution of Ca II is almost Gaussian like while the equivalent velocity distribution for $H\alpha$ shows an excess of blue shifted velocities (filament moving upwards). However, we should take into account that for the optically thiner Ca II where the optical thickness is on average less that one, velocity structures of the background play an important role for the velocity determination in the filament itself.

The uniqueness and precision of the inversion procedure can be checked by exploring the whole parameter space. In Fig. 3 we present for an observed filament profile plane cuts of the 4-dimensional χ distribution. They show that temperature is always well defined and that the inversion gives only one solution within the range of parameters and defines quite accurately the global minimum of the χ distribution for velocity, temperature and microturbulence. It fails however to define Q since small fluctuations of temperature result to a wide range of values for Q, contrary to the case of H α where the emission measure is always well defined. As MH demonstrated there is a clear relationship between the integrated $H\alpha$ intensity emitted by the slab itself and Q while the corresponding Ca II one shows no correlation at all, something related to the different nature of the two lines. The almost unique correlation found for $H\alpha$ means that for a given Q, the integrated intensity is almost insensitive to kinetic temperature. The reason is that $H\alpha$ is photoionization dominated line. The Call line is, on the other hand, coupled to kinetic temperature via collisions.





corresponding MALI grid profile (solid line) that minimizes the χ^2 function. The inverted parameters values are: V = 0.51 km s⁻¹, $\xi_t = 5.29$ km s⁻¹, T =8617 K and log Q = 29.53. V – T cut (b), ξ_t - T cut (c) and T – Q cut (d) through the χ^2 distribution for the profile presented in (a). Darker tones reveal lower χ^2 values and the contours denote intensity differences between the observed and the MALI grid profiles normalized in units of 1% of the nearby Ca II continuum.

Figure 3. (a) An observed Ca II profile (diamonds) from the filament and the

The calculation of the standard deviation for each of our inverted parameters (V, T, ξ_t, Q) by considering all solutions with an intensity which is within 2% of the observed profile intensity gives an average standard deviation value of 0.45 km s⁻¹ for velocity, 0.61 km s⁻¹ for microturbulence, 918 K for temperature and 1.75×10^{30} cm⁻⁵ for emission measure. Even for such a large error the average standard deviation is quite low for velocity, microturbulence and temperature but very high, comparable to the actual range of values, for emission measure.

A parameter that can always be inverted is the maximum line-center optical depth $\tau_{c,max}$. which is proportional to the line-center absorption coefficient. The latter depends on the lower level population, microturbulence and temperature. The lower level population is strongly coupled with N_e and T. As ξ_t increases the values of $\tau_{c,max}$ slightly decrease. The inversion shows (see Fig. 2) that $\tau_{c,max}$ is generally higher in the center of the filament than its borders which is in absolute agreement with previous observations.

DISCUSSION

The inversion strategy for the Ca II filament with the use of a grid of models permits a quick and quite accurate search for the best fit to a large amount of observational data. Future investigations in Ca II should probably include a grid extended to lower densities and also consider a filling factor for the filament. The inversion of velocity suggests that a more careful consideration of the background intensity should be taken into account. Since the background in Ca II is quite structured below cloud-like features, as Fig. 2 clearly shows, that influences the optically thin observed Ca II profiles by introducing modifications to the line profile through different illumination conditions and possible Doppler shifts existing to the incident radiation profiles. A future extension of the inversion code will include the incident radiation as a free parameter, something that should definitely lead to a more accurate determination of the actual velocity structure within cloud-like features. An extension of the grid to higher velocities combined with the inclusion of incident radiation as an input parameter would enable the investigation of a wide range of chromospheric cloud-like features apart from filaments.

REFERENCES

- Carlsson, M., 1986, A Computed Program for Solving Multi-level Non-LTE Radiative Transfer Problems in Moving or Static Atmospheres, Upsala Astronomical Observatory Report No.33
- Gorshkov A.B., Heinzel P., Vial J.-C., 1996, unpublished
- Heinzel P., 1995, A&A 299, 563
- Heinzel P., Mein N., Mein P., 1999, A&A 346, 322
- Mein N., Mein P., Heinzel P., et al., 1996, A&A 309, 275
- Mein P., Briand C., Heinzel P., Mein N., 2000, A&A 355, 1146
- Molowny-Horas R., Heinzel P., Mein P., Mein N., 1999, A&A 345, 618
- Shine R.A., Linsky J.L., 1974, Solar Phys. 39, 49

REGULAR AND RANDOM COMPONENTS OF SUNSPOT ACTIVITY DURING ACTIVE SUN AND GREAT MINIMA: MODEL SIMULATION

I. G. Usoskin¹^{*} K. Mursula¹, and G. A. Kovaltsov²

¹ Dept. of Physical Sciences, P.O.Box 3000, FIN-90014 University of Oulu. Finland

phone/fax: +358-8-5531378/5531287, email: lya.usoskin@oulu.fi, kalem.mursula@oulu.fi

 2 Ioffe Physical-Techical Institute, Politekhnicheskaya 26, 194021 St. Petersburg, Russia

phone/fax: +7-812-2479167/2471017. email: gena.kovaltsov@pop.coffe.rssi.ru

Abstract. We model sunspot production during the two different modes of sunspot activity (the normal activity level and great minima), using the idea of a threshold-like mechanism [Ruzmaikin, 1997]. The model includes a dynamo field, a constant relic field of the Sun and a random field. This model describes the main features of sunspot activity both during normal activity times (dominant 11-year cycle and weak 22year cycle) and during the Maunder minimum (sparse sunspot occurrence with 22-year cycle) with the same model parameters, only varying the dynamo amplitude. The relic field must be about 3-10 % of the dynamo field in normal activity times.

INTRODUCTION

Time evolution of sunspot activity (SA) is of great interest for solar physics, since it reflects processes in the solar convection zone. The main feature of SA is its 11-year cycle due to the action of the dynamo mechanism. This 11-year cyclicity is modulated by the long-term secular Gleissberg cycle. (For a review see, e.g., Wilson [1994]; Vitinsky [1965].) Recently, a weak persistent 22-year cyclicity, associated with a dipole relic solar magnetic field [Cowling, 1945], has been found in SA [Mursula et al., 2000]. Sometimes SA is dramatically suppressed, forming great minima. The most recent was the Maunder minimum in 1645-1715 [Eddy, 1976]. SA series contains also a random component which is larger than observational uncertainties. Earlier it was common to describe SA as a multiharmonic process with some fundamental harmonics (see, e.g., [Sonett. 1983, Vitinsky, 1965] and references therein. Since early 1990's, SA was considered as low-dimensional deterministic chaos due to a strange attractor. (e.g., [Ostryakov & Usoskin, 1990, Mundt et al., 1991]). However, this approach was criticized because the analyzed data set is too short [Carbonell et al., 1993] and disturbed by filtering [Price et al., 1992]. While the majority of earlier papers were concentrated on either regular or random components, some papers studied both components [Sonett, 1982, Ruzmaikin, 1997, 1998]. They studied SA only during normal SA times. However, it has been suggested that the dynamo can be in a quite different mode during great minima (e.g., [Sokoloff & Nesme-Ribes, 1994, Schmitt et al., 1996]). Correspondingly, the relation between regular and random component can be different for great minima and normal SA.

Here we present a unified model of sunspot production, which describes both modes of SA. The magnetic field in the bottom of the convection zone is considered to be a superposition of a regular and random components, and sunspots occur if this total field exceeds a buoyancy threshold [Ruzmaikin, 1997, 1998]. This model includes also a solar relic magnetic field [Cowling, 1945, Sonett, 1982] Pudovkin & Benevolenskaya, 1984]. whose signature was found recently in SA [Mursula et al., 2000]. 11, relic field can, due to amplification by the dynamo mechanism, play a significant role in sunspot occurrence [Bover & Levy, 1984, Bornta, 1996].

PROPERTIES OF SA

As index of SA we used the group sunspot number (GSN) series [Hovt & Schatten, 1998] which covers the period since 1610 including the period of the Maunder minimum (MM) in 1645-1715, and is

Proc. 1st Solar & Space Weather Euroconference, 'The Solar Cycle and Terrestrial Climate', Santa Cruz de Tenerife, Tenerife, Spain, 25-29 September 2000 (ESA SP-463, December 2000)

^{&#}x27;on leave from loffe Phys.-Tech.Inst., St.Petersburg, Russia

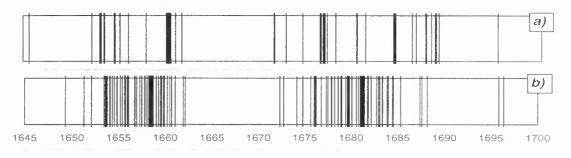


Figure 1: Days with sunspots during the deep Maunder minimum. a) actual recorded days with sunspots (GSN series); b) a sample of simulation for $B_o = 0.05$, $\sigma_o = 3$, $A_{11} = 0.03$.

more correct and homogeneous than the Wolf series [Hoyt & Schatten, 1998, Letfus, 1999]. Time behaviour of SA during MM was significantly different from normal SA. Therefore, we studied the great mininuum separately from normal SA.

Main features of sunspot activity during the *Maunder minimum* in 1645-1715 are as follows:

- 1. Sunspots occurred seldom ($\approx 2\%$ of days) [Hoyt & Schatten, 1996].
- Daily sunspot occurrence was clustered in two major groups in 1652-1662 and 1672-1689, implying for a dominant 22-year cyclicity during MM [Usoskin et al., 2000].

The main features of SA during *normal solar activity* periods are:

- 1. The 11-year cyclicity is the most significant feature. The ratio between 12-month smoothed sunspot maxima and minima is about 10-200.
- Monthly GSN values fluctuate randomly around the running average SA profile. The normalized fluctuations have Gaussian distribution implying for a correlated noise (e.g., [Oliver & Ballester, 1996].
- 3. There is a persistent, roughly constant 22year cycle in sunspot activity at about 20% level of present sunspot cycle intensity level [Mursula et al., 2000].

THE SIMULATION MODEL

Following [Ruzmaikin, 1997, 1998], we suggest that if the total magnetic field in the dynamo layer of the convection zone exceeds the buoyancy threshold, sunspots occur. The total field consists of a regular field and randomly fluctuating field generated by random motions [Ruzmaikin, 1998]:

$$B_{tot} = B_{reg} + b. \tag{1}$$

The regular field is below the threshold in the framework of the mean-field $\alpha - \Omega$ dynamo theories, and therefore the random *b*-field is important to exceed the threshold ([Ruzmaikin, 1998] and references therein).

In our model, B_{reg} contains a constant relic field B_o and the dynamo field in the form of a 22-year sinusoid (Hale cycle) with amplitude A_{11} :

$$B_{reg}(t) = B_o + A_{11} \cdot \sin(\pi \cdot t/T_{11}), \qquad (2)$$

Since the random component of SA is correlated noise, we assume that the momentary variance of the random field, $\sigma(t)$, is proportional to the regular component of SA at the moment [Ostryakov & Usoskin, 1990a], $\sigma(t) = \sigma_o + |B_{reg}(t)|$. We assumed the exponential probability distribution function of the random field, $p(b) \propto exp(-|b|/\sigma)$ [Ruzmaikin, 1998]. We have studied also the Gaussian distribution $p(b) \propto exp(-b^2/\sigma^2)$ Here we show results only for the exponential case and discuss both cases later.

SIMULATION RESULTS

We numerically simulated SA separately for normal activity and great minimum. For each day t, the value of b was generated by a pseudo-random number generator. If the simulated $|B_{tot}|$ (Eq. 1) exceeds the threshold ($|B_{tot}| > B_{th}$), sunspots occurred. The number of sunspots was proportional to ($|B_{tot}| - B_{th}$). Values of the field are in arbitrary units, with the value of the threshold, B_{th} , chosen to be unity.

The Maunder minimum

Since the 11-year component of SA was very weak during MM, we assume that A_{11} was small during MM. A sample simulation shows (Fig. 1b) the time behaviour

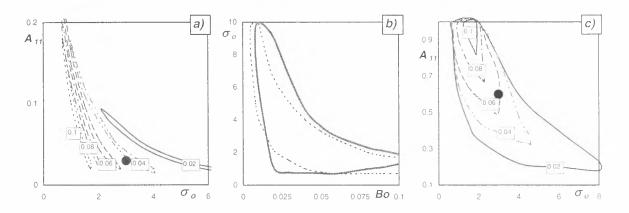


Figure 2: Area of possible values of model parameters. a) A_{11} vs. σ_o for the great minimum. Value of B_{c} is fixed (as shown in boxes). The solid circle denotes values of parameters used for sample simulations shown in Fig. 1b. b) σ_o vs. B_o for all A_{11} . The allowed area is between the two solid curves for the normal SA times, and between the two dashed curves for the Maunder minimum. c) A_{11} vs. σ_o for the normal sanspot activity times. Value of B_o is fixed (as shown in boxes). The solid circle denotes values of parameters used for sample simulations shown in Fig. 3b.

similar to that of the actual sunspot occurrence. We made 10^4 simulation sets for the 20088 days of the deep MM in 1645-1699. In order to study the range of possible values of model parameters we used two constraints.

Constraint I. Correspondingly to the 369 (out of 20088) days with reported sunspots during the deep MM, the number of simulated sunspot days was constrained be 369 ± 57 .

Constraint II. There were long spotless periods in 1645-1652, 1662-1672 and 1690-1699 (Fig. 1a). We require that these statistically significant spotless periods should exist in the simulated series, i.e., not more than one sunspot day per year is allowed for these intervals.

Using these constraints we found areas of possible values of the model parameters for the great minimum mode (Fig. 2a). For a fixed B_o , the allowed area of A_{11} vs. σ_o is prolonged but narrow. The area of all possible values of σ_o and B_o (for all values of A_{11}) is shown in Figs. 2b.

Normal activity level

In order to study the range of possible parameter values for normal activity times, we also used two constraints:

Constraint I concerns the empirical G-O rule [Gnevyshev & Ohl, 1948]. saying that the sum of sunspot numbers over an odd cycle exceeds that of the preceding even cycle. We require that "odd" cycles are 10-30 % more intense than "even" cycles.

Constraint II limits the ratio of 12-month averaged maximum to minimum intensities of a cycle to be 10-200.

The relation between A_{11} and σ_{σ} for fixed B, is shown in Fig. 2c. The area of possible values of σ_{σ} and B_{σ} for all values of A_{11} is shown in Fig. 2b. A sample of simulation is shown in Fig. 3b. There is a good similarity with the actual GSN data (Fig. 3a) for the period of fairly constant SA level (solar cycles 9-13). We simulated 1000 11-year solar cycles. The length of simulated cycles varied from 9.5 to 12.5 years, and the cycle amplitude varied within 100-200 arbitrary units. The G-O rule is valid throughout the entire simulated series. The normalized noise of the simulated series is Gaussian giving additional support to our approach.

DISCUSSION AND CONCLUSIONS

Our model can reproduce all the main features of SA during both great minima and normal activity times. The range of possible values of B_o and σ_o is essentially similar for these two different modes of SA (Fig. 2b). The model reproduces SA behaviour for the two modes of SA with the same values of B_o and σ_o only changing A_{11} . The dynamo can be significantly suppressed during great minima while both the relic field and random component remain unchanged. While the random component of SA plays a major role during MM, the regular component is more important during normal SA times, leading to the 11-year cyclic behaviour of SA. The presence of a fluctuating field is necessary to exceed the buoyancy threshold even in the latter mode.

In the framework of the model, the amplitude of the dynamo field, A_{11} , should be not less than 20% of the

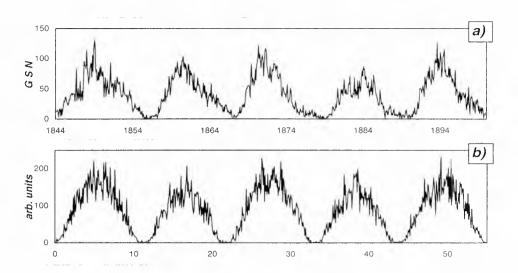


Figure 3: Sunspot activity: a) actual monthly group sunspot numbers for the period of roughly constant SA level: b) a sample of the monthly simulated SA for $A_{11} = 0.6$, $B_o = 0.05$, $\sigma_o = 3$.

threshold level during normal SA times, in agreement with the theoretical expectations [Ruzmaikin, 1998]. For MM, the value of A_{11} is much smaller, 0.03-0.1. This implies that the dynamo was greatly suppressed during MM but had to be non-zero.

The value of the relic field, B_o , is small but non-zero, varying from 0.01 to ≤ 0.1 , which is about 2-10% of the dynamo field. This value of B_o leads to a dominant 22-year cycle in SA during MM and to a weak but persistent 22-year variation during normal SA times.

Concluding, we have shown that the main features of SA throughout the entire period of direct solar observations, including the two different different SA modes (normal and great minimum), can be reproduced by a unified model assuming a dynamo field, a weak constant relic field, and a randomly fluctuating field. This also supports the recent result [Mursula et al., 2000] that the 22-year cyclicity in SA is due to the action of the magnetic 22-year cycle of the dynamo field in the presence of a weak constant (relic) magnetic dipole in the convection zone.

References

- Boruta, N.: 1996, Astrophys.J., 458, 832.
- Boyer, D.W., and Levy, E.H.: 1984, *Astrophys.J.*, **277**, 848. Carbonell, M., R. Oliver, J.L. Ballester: 1993, *As*-
- tron.Astrophys., 274, 497. Cowling, T.G.: 1945, Mon.Not.Roy.Astron.Soc., 105, 167.
- Eddy, J.A.: 1976, Solar Phys., 192, 1189.
- Gnevyshev, M.N., Ohl, A.I.: 1948, Astron. Zh., 25(1), 18.

- Hoyt, D.V., Schatten, K.H.: 1996, Solar Phys., 165, 181 Hoyt, D.V., Schatten, K.H.: 1998, Solar Phys., 181, 491.
- Letfus, V.: 1999, Solar Phys., 184, 201.
- Mundt, M.D., Maguire II, H.W.B., Chase, R.P.: 1991, J.Geophys. Res., 96(2), 1705.
- Mursula, K., Usoskin, I.G., Kovaltsov, G.A.: 2000. Sol. Phys., (accepted).
- Oliver, R., J.L. Ballester: 1996, Solar Phys., 169, 215
- Ostryakov, V.M., I.G. Usoskin: 1990, Solar Phys., 127, 405.
- Ostryakov, V.M., I.G. Usoskin. 1990a, Sov. Tech. Phys. Lett., 16(9), 658.
- Price, C.P., D. Prichard, and E.A. Hogenson: 1992. *J.Gcophys.Rcs*, 97(A12), 19113.
- Pudovkin, M. I., E. E. Benevolenskaya: 1984. Source intron., 28, 458.
- Ribes, J.C., Nesme-Ribes, E.: 1993, Astron. Astrophus. 276, 549.
- Ruzmaikin, A.: 1997, Astron. Astrophys., 319. L13.
- Ruzmaikin, A.: 1998, Solar Phys., 181, 1.
- Schmitt, D.: Schüssler, M., and Ferriz-Mas. A.: 1996. Astron. Astrophys.. 311, L1.
- Sokoloff. D., Nesme-Ribes.E.: 1994. Astron. Astrophys., 288, 293.
- Sonett. C.P: 1982, Geophys. Res. Lett., 9, 1313.
- Sonett. C.P: 1983, Nature, 306, 670
- Usoskin, I.G., Mursula, K., Kovaltsov, G.A = 2000. Astron. Astrophys., 354, L33.
- Vitinsky, Yu. I.: 1965, *Solar Activity Forecosting*, Israel Program for Scientific Translations, Jerusalem.
- Wilson, P.R.: 1994, Solar and Stellar Activity Cycles. Cambridge University Press, Cambridge.

WHAT CAN WE LEARN STUDYING LONG-TERM MAGNETIC EVOLUTION OF SOLAR ACTIVE REGIONS?

L. van Driel-Gesztelyi^{1,2,3}, Zs. Kövári². M. López-Fuentes⁴, C.H. Mandrini⁴, P. Démoulin¹

¹ Observatoire de Paris, DASOP, 92195 Meudon Cedex, France
 ² Konkoly Observatory. 1525 Budapest, Pf. 67, Hungary
 ³ MSSL, University College London, UK
 ⁴ IAFE-CONICET, CC.67, Suc.28, 1428 Buenos Aires, Argentina

Abstract

Using Kitt Peak and SOHO/MDI magnetograms we follow the development of the magnetic fields of two active regions (ARs) from their birth throughout their decay for 4 and 6 solar rotations in the periods of October 1995-January 1996 (NOAA 7912) and July-December 1996 (NOAA 7978). From the photospheric motions of the opposite magnetic polarities of these two bipoles we deduce the sub-photospheric geometry of the flux tubes forming them.

We find that NOAA 7912, which was a non-Hale (reversed magnetic polarity) region, rotated about 180° during three months, and became a normally oriented AR. We show that this rotation was not caused by the solar differential rotation but by a severely kinked shape of the flux tube forming this AR. The deformation of the flux tube was caused by external forces i.e. a vortex in the convective zone while the flux was emerging through it and not by the kink instability due to strong magnetic twist.

A very different long-term magnetic evolution was seen of NOAA 7978 revealing a more simple flux tube geometry. During the first five days of vigorous flux emergence we saw a minor rotation of the bipole. Using magnetic extrapolations we found that in this case the rotation detected in the line-of-sight magnetic field was simply due to the presence of inherent currents. We show that during the ensuing months the deformation of the dispersing magnetic fields of this AR was entirely due to the differential rotation. We conclude that NOAA 7978, like the majority of ARs, was formed by the emergence of an ordinary Ω loop.

1. INTRODUCTION

It is widely accepted that bipolar active regions (ARs) are the manifestations of the emergence of buoyant magnetic flux tubes, the so-called Ω -loops

(Zwaan 1987). The flux tubes are formed at the bottom of the convection zone (Parker 1993), rise due to their buoyancy and eventually break through the photosphere.

Sunspots, and in general magnetic field concentrations, appear at the intersection of flux tubes with the photosphere. Emerging flux tubes can reveal their 3-D geometry through the surface motion patterns of the opposite polarity magnetic counterparts.

Let us assume a planar symmetric flux tube which is rising through the photosphere. The resulting bipolar spot pair should move in diametrically opposite directions and the divergent motion of the (p) and (f)spots should appear symmetric as well. Such symmetric diametrically opposite motions are very rare. The well-known fact that the preceding (p) spots of bipoles move faster westward than the following (f) spots move eastward can be related to a systematic eastward tilt (E-W inclination) of the emerging flux tubes as was proposed by van Driel-Gesztelyi & Petrovay (1990). Simulations of the buoyant rise of flux tubes throughout the convection zone clearly show the appearance of such eastward tilt indeed (Moreno-Insertis, Caligari & Schüssler, 1994; Caligari, Moreno-Insertis & Schüssler, 1995). It has been shown by the above authors that the conservation of angular momentum leads to a retardation of the rising loop, with respect to its anchored feet resulting in an eastward tilt.

It has been a long-standing question what is the cause of more complex, non-diametrically opposite sunspot proper motions. Tanaka (1991), van Driel-Gesztelyi & Leka (1994), Leka *et al.* (1996) proposed that such can be caused by flux tubes emerging with an inherent twist. Above a critical level of twist, kink instability of the flux tube develops. A kinked flux tube is not a planar feature and its emergence may lead to the formation of bipoles with high axial tilt angles (Weart, 1972), and even reversed polarity ARs (Tanaka, 1991).

Normally, flux emergence is considered to be a pro-

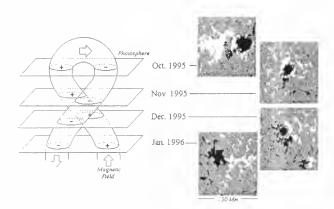


Figure 1. The right panel shows a series of magnetic maps of AR NOAA 7912 tak n during consecutive solar rotations around the times of central meridian passage. In the left panel there is a sketch of the magn tic flux tube as deduced from the observations. The horizontal planes correspond to the approximate position of the photosphere at the times of the magnetograms shown in the magnetograms (after López-Fuentes et al, 2000).

cess which is completed in a few (on average five) days. After that the total magnetic flux does not increase any more. However, we show here that the actual emergence of the flux tube does not necessarily cease after the first five days, but rise of the flux tube may still continue for several months while the magnetic flux is getting dispersed. Following the displacement pattern of opposite polarity magnetic fields in active regions for several months can reveal the large-scale 3-D geometry of flux tubes. The deviation from the planar Ω loop geometry may indicate intrinsic twist, but, as another possibility, deformation of the flux tube can also be caused by external vortices in the convective zone acting on the ascending flux tube. We show such long-term magnetic evolution of two ARs revealing drastically different subphotospheric geometries of their flux tubes.

2. DATA

We follow the development of the magnetic fields of two active regions (ARs) from their birth throughout their decay for 4 and 6 solar rotations in the periods of October 1995-January 1996 (NOAA 7912) and July-December 1996 (NOAA 7978), using Kitt Peak and SOHO/MDI magnetograms, respectively.

3. LARGE-SCALE KINKED LOOP

We find that NOAA 7912, which was a non-Hale (reversed magnetic polarity) region (van Driel-Gesztelyi et al. 2000), rotated about 180° during three

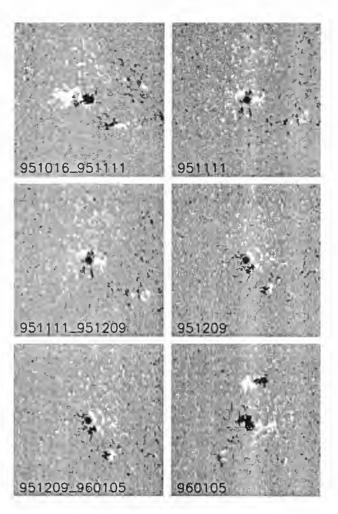


Figure 2. Magnetic maps rotated with differential rotation to the time of the next map, i.e. with a full solar rotation. Substantial differences are present between the observed and the rotated maps, indicating that the changes in the surface magnetic distribution pattern were caused by something else than the differential rotation. Comparing e.g. the map observed on 11 Nov.1995 (right top panel) to the one rotated to the next rotation (left middle panel) we find hardly any difference meaning that the differential rotation played no role in deforming this active region. months, and became a normally oriented AR (Fig. 1; López-Fuentes et al., 2000). Magnetic maps rotated with differential rotation to the time of the next map, i.e. with a full solar rotation, show hardly any change between the observed and rotated images (Fig. 2). This means that the differential rotation played no role in deforming this active region. On the other hand, the consecutive observed maps show substantial changes in the appearance of the AR, indicating the presence of a severely deformed flux tube.

We investigated the origin of the unusual photospheric evolution of the AR, and we ruled out the possibility that it was due to the kink instability caused by strong currents. We extrapolated the photospheric magnetic field in the linear force-free approximation and chose the α parameter matching our extrapolations ($\alpha = 0.03 \text{ Mm}^{-1}$) with Yohkoh/SXT images of the coronal loops. We found that the direction of currents detected would cause a kink of the flux tube opposite than observed, i.e. the writhe and the internal twist of the flux tube forming this AR were of opposite signs. Furthermore, the strength of the currents was much too low to form such a severe kink. We conclude that the kink of the flux tube was caused by external forces (vortices) while emerging through the convection zone. The interaction with vortex motions deformed the flux tube. The creation of a negative writhe introduced a positive twist due to helicity conservation. For more details see López-Fuentes et al., (2000).

4. A SIMPLE Ω -LOOP

A very different long-term magnetic evolution was seen of NOAA 7978 revealing a much more simple flux tube geometry. During the first five days of vigorous flux emergence we saw a minor rotation of the bipole and through magnetic extrapolations we found that the magnetic field emerged with currents (van Driel-Gesztelyi et al, 1999; Mandrini et al., 2000). However, in this case the rotation detec.ted in the line-of-sight magnetic field was much smaller. There was a second flux emergence in the AR with a relatively high tilt angle which mimicked a reversed rotation of the bipole. However, during the ensuing months the change in orientation of this dispersing bipole was entirely due to the differential rotation. Rotating observed magnetic maps (with a differential rotation function) to the epoch of the next central meridian passage creates, within the uncertainty of such simple test, the same tilt of the neutral line as it was really observed (Fig. 3). NOAA 7978 had no large-scale deformation of its flux tube: it was a mildly twisted normal Ω loop. Such simple Ω -shaped flux tube geomety characterizes the majority of flux tubes forming ARs, while the kinked geometry appears in (at most) a few percents of all ARs (López-Fuentes et al, 2001).

ACKNOWLEDGMENTS

We thank the SOHO/MDI consortium and NSO/Kitt Peak Observatory for the magnetograms used in the paper. For rotating the magnetograms we used the MAPPING functions of the SOHO IDL software package written by D. Zarro. L.v.D.G. and Zs.K. were supported by the Hungarian Government grants OTKA T-026165, T032846, a grant by the Hungarian Space Office (TP 096/2000) and the Hungarian-French intergovernmental S & T cooperation programme. M.L.F, C.H.M. and P.D. acknowledge financial support from ECOS (France) and ANPCYT (Argentina) through their cooperative science program (A97U01).

REFERENCES

- Caligari, P., Moreno-Insertis, F.,& Schüssler, M., 1995, ApJ, 441, 886
- López Fuentes M.C., Démoulin P., Mandrini C.H., & van Driel-Gesztelyi, L., 2000, ApJ, 544, in press
- López Fuentes M.C., Démoulin P., & Mandrini C.H., 2001, in preparation
- Mandrini, C.H., van Driel-Gesztelyi, L., Thompson, B., Plunkett, S., Démoulin, P., & Aulanier, G., 2000, Geofísica Internacional, 39, No. 1, 73
- Leka, K.D., Canfield, R.C., McClymont, A.N., & van Driel-Gesztelyi, L., 1996, ApJ 462, 547
- Moreno-Insertis, F., Caligari, P., & Schüssler, M.: 1994, Solar Phys. 153, 449
- Parker, E.N. 1993, ApJ 408, 707
- Tanaka, K., 1991, Solar Phys., 136, 133
- van Driel-Gesztelyi, L.,& Petrovay K., 1990. Solar Phys., 126, 285
- van Driel-Gesztelyi, L., & Leka, K.D., 1994, in K.S. Balasubramaniam and G.W. Simon (eds): Solar Active Region Evolution: Comparing Models with Observations, ASP Conference Series 68, 138.
- van Driel-Gesztelyi, L., Mandrini, C.H., Thompson, B., Plunkett, S., Aulanier, G., Démoulin, P., Schmieder, B., & DeForest, C., 1999, in B. Schmieder, A. Hofmann, & J. Staude, Proc. 3rd ASPE: Magnetic Fields and Oscillations, ASP Conf. Ser., 184, 302.
- van Driel-Gesztelyi, L., Manoharan, P.K., Démoulin, P., Aulanier, G., Mandrini, C.H., López-Fuentes, M., Schmieder, B., Orlando, S., Thompson, B., & Plunkett, S., 2000, JASTP, 62/16, 1437.
- Weart, S., 1972. ApJ, 177, 271.
- Zwaan 1987, Ann. Rev. A&A, 25, 83

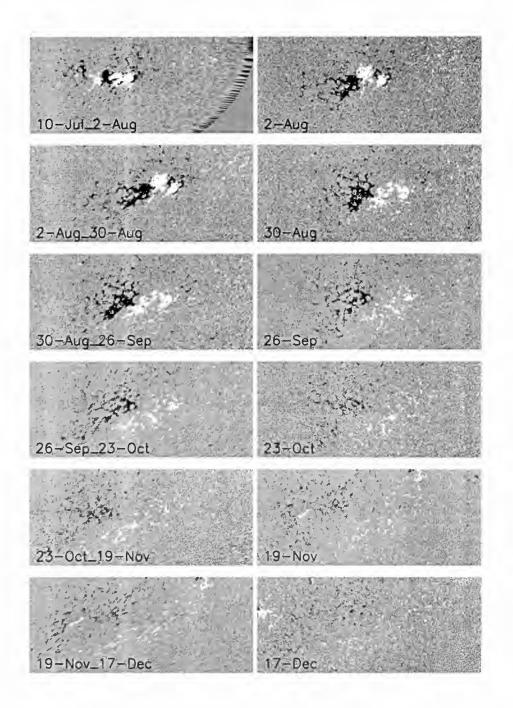


Figure 3. The evolution of the magnetic surface pattern of AR 7978 were caused by (i) tilted secondary flux emergence in the second rotation (ii) purely diffusion and the differential rotation after that. Rotating differentially observed magnetic maps to the epoch of the next central meridian passage creates (within the uncertainties of such experiment) the same tilt of the neutral line as it was really observed. This AR underwent no large-scale deformation of its flux tube: it was a mildly twisted normal Ω loop.

AUTOMATIC IMAGE SEGMENTATION AND FEATURE DETECTION IN SOLAR FULL-DISK IMAGES

A. Veronig¹, M. Steinegger², W. Otruba³, A. Hanslmeier¹, M. Messerotti⁴, M. Temmer¹, G. Brunner¹, and S. Gonzi¹

¹Institute of Geophysics, Astrophysics and Meteorology, University of Graz, A-8010 Graz, Austria ²Big Bear Solar Observatory, New Yersey Institute of Technology, CA 92314-9672, USA ³Solar Observatory Kanzelhöhe, A-9521 Treffen, Austria ⁴Trieste Astronomical Observatory, I-34131 Trieste, Italy

ABSTRACT

At Kanzelhöhe Solar Observatory, Austria, a solar activity monitoring and flare alerting system is under development, which will be based on the parametrization of solar flare activity using photometric and magnetic full-disk images of the Sun obtained simultaneously with high time cadence. An important step in this project is the automatic image segmentation and feature detection of solar activity phenomena related to the occurrence of solar flares. In a first step we have developed a procedure for automatically detecting the onset and describing the evolution of flares in H α full-disk images.

Key words: solar flares; solar activity monitoring; image processing; image analysis.

1. INTRODUCTION

Solar flares are the most energetic phenomena related to solar activity. Due to high energetic particles produced by flare events on the Sun, which interact with the interplanetary medium and the terrestrial environment, flares are a main source for the variations of space weather, thus being able to produce severe effects on Earth. Therefore, a continuous monitoring of solar activity, which is the trigger of space weather variations, is required. Moreover, to minimize damages of space-borne and ground-based technological systems as well as to prevent risks for biological systems, reliable flare alerting and forecasting systems are desirable.

At Kanzelhöhe Solar Observatory (KSO), which is affiliated to the Institute of Geophysics, Astrophysics and Meteorology at the Graz University, Austria, a solar activity monitoring and flare alerting system is under development (see Steinegger et al., 1999a,b). The observing facilities at KSO provide us with the opportunity of obtaining photometric full-disk images of the photosphere and chromosphere simultaneously with full-disk magnetograms and dopplergrams with high time cadence. A description of the KSO observing facilities and their characteristics can be found in Messerotti et al. (1999).

A key point for a flare alerting system is the automatic detection of the onset of a flare and the extraction of features which can act as indicators for future flare activity. In order to make the leap from the rather simple activity monitoring to the more complex flare detection and alerting, a real-time analysis of the data is necessary. In the present paper we describe a procedure, which automatically and in quasi real-time performs a segmentation of $H\alpha$ full-disk images with respect to flare activity, and moreover analyzes the evolution of the detected flares.

2. ANALYSIS

2.1. Objectives and Requirements

The main objectives are the automatic flare detection and flare identification. On the one hand, the real-time detection of $H\alpha$ flares may be used for flare alerts, which, e.g., can be made accessible to the community via the World Wide Web. On the other hand, the detection of the onset of a flare can act as trigger for an enhanced high time cadence observing mode (of the order of seconds) for various observing instruments at KSO, which enables to study the evolution of an ongoing flare at different wavelengths with an exceptional high time resolution. The flare identification includes the extraction of relevant flare parameters, such as position, area, brightness, etc. The analysis of the time evolution of these parameters yields a global description of a flare, moreover such parameters are directly related to the flare importance and brightness class.

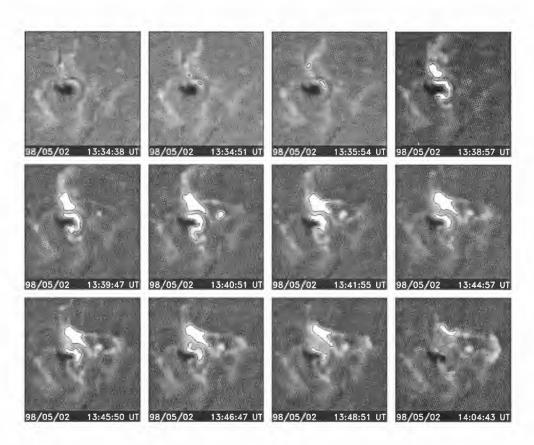


Figure 1. Time evolution of the May 2, 1998 flare. The black contour lines outline the flare area, determined by the automatic algorithm.

The analysis software has to fulfill three crucial requirements: It must be fast, automatic and robust. For the continuous solar activity monitoring at KSO the data acquisition rate of the $H\alpha$ imaging system will be one minute, which has turned out to be a reasonable time cadence with respect to solar flare monitoring (see the statistical analysis by Temmer et al., 2000). This means that the data analysis per $H\alpha$ image is restricted to a maximum of one minute. Moreover, the analysis must be performed fully automatically, i.e. without any visual inspection and/or modification. Finally, the analysis procedure is expected to be robust. On the one hand it must avoid artifacts caused by degraded images (due to bad seeing conditions for instance), on the other hand it must be independent of the specific flare parameters (e.g., faint vs. bright flares).

2.2. Image Preprocessing

Before the actual processing and analysis can be performed, the images must be preprocessed (for fundamentals on image processing and analysis see, e.g., the textbooks of Gonzales & Woods, 1992; Jähne, 1997; Sonka et al., 1999). This comprises the removal of effects caused by non-uniform illumination and of the center-to-limb variation (CLV). Moreover, a criterion has to be applied to reject degraded images from further analysis.

For the determination of the disk center and radius,

we apply a median filter with a large mask to the $H\alpha$ images. This non-linear filter has the effect, that active regions are smeared but the limb is kept sharp. An edge enhancement of the filtered image, e.g., by application of a Sobel operator, yields strong intensities only at the solar limb. After thresholding the edge enhanced image, a least squares circle fit is applied, which gives the solar center and radius.

The corrections of large scale asymmetries in the images are performed by a method developed by K. Burlov-Vasiljev at KIS Freiburg, Germany. This method splits the solar disk into concentric rings and fits polynomials to these. Since on large scales the disk is supposed to be radially symmetric, the polynomials give the image distortion similar to a Fourier decomposition. Combining the polynomials of the rings, this method yields also the CLV of the sun. In order to save computing time, the corrections are calculated from the downsized image, interpolated afterwards and applied to the original image. This procedure is justified by the fact that both corrections, asymmetries and CLV, are global ones.

The further steps of image processing and analysis are only applied to images, which pass a quality criterion, in order to avoid artifacts due to image degradations. The quality criterion we use is based on the standard deviation of the intensity histogram of the already corrected image. Around the mean value the histogram is expected to be normally distributed, and image degradations result in a broadening of the histogram.

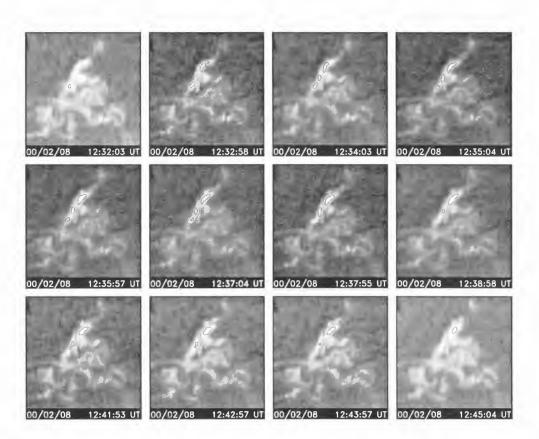


Figure 2. Time evolution of the February 8, 2000 flare. The black contour lines outline the flare area, determined by the automatic algorithm.

2.3. Image Processing

A crucial step in image processing, since it strongly determines the outcome of the subsequent analysis, is the image segmentation, i.e. the subdivision of an image into its constituent parts. In the frame of the present flare detection and alerting system, we restrict the segmentation process only to flare regions.

Two kinds of segmentation methods can be distinguished, region based and edge based ones. Region based segmentation methods, such as thresholding, region growing, region splitting, etc., make use of the property of similarity of a region, whereas edge based methods utilize discontinuities of image properties at region borders.

For the segmentation of possible flare regions from $H\alpha$ full-disk images, we apply a combination of region and edge based methods. The flare detection is performed by an intensity threshold, chosen as > 2 times the quiet sun level. For the determination of the flaring area, a region growing algorithm is used, which starts at seed points with high intensity values. The region growing stops if the intensity is too low, i.e. less than two times the quiet sun level, or if a region border is encountered.

For this purpose an advanced edge detection technique is needed. We use the *Canny edge detector* (Canny, 1983; 1986), which is optimized with respect to three main goals, the edge detection, the edge localization, and the one-response to edges. The basic steps of the Canny edge detector are the convolution of the image with the derivative of a Gaussian mask, which yields the edge enhanced image; the application of a non-maximum suppression, i.e. edge pixels that are not local maxima are removed; a hysteresis thresholding, which utilizes a combination of a high threshold T_H and a low threshold T_L : Any edge pixel with an intensity value higher than T_H is presumed to be an edge pixel, and all connected pixels with a value higher than T_L are also selected as edge pixels. Finally, in addition to the Canny edge detector we apply an edge tracing algorithm in order to achieve closed edges, defining different image regions.

3. RESULTS

We have applied the flare detection procedure to several time series of H α images, taken from the data archive of the Kanzelhöhe Solar Observatory. The time cadence of the observations was of the order of one minute.

Figures 1 and 2 demonstrate the outcome of the flare detection procedure for two sample events. The black contour lines indicate the borders of the flare regions, as determined by the automatic procedure. Figure 1 illustrates the results for the May 2, 1998 flare of class 3b, which reveals a great variation in its morphological evolution, representing a developed

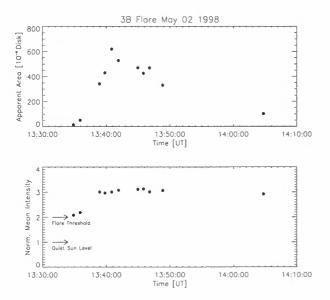


Figure 3. Time evolution of the flare area (top panel) and its mean intensity normalized to the quiet sun level (bottom panel). The end of the flare was not captured.

two-ribbon flare. Due to bad seeing conditions several images were rejected, particularly at the decaying phase of the flare. The Sf flare of February 8, 2000 shows little morphological evolution.

In Figures 3 and 4 the time evolution of the flare area and the mean intensity of the flare regions are plotted. Such information can be easily extracted from the segmented flare regions. The first and the last dots in the plots mark the onset and the end of the flare, except for the May 2, 1998 flare, where the end could not be captured due to clouds. Note the significant differences in the time evolution of the flare area and the different brightness levels for the two sample events.

4. CONCLUSIONS

We have presented a procedure, developed with the aim of automatically and in quasi real-time detecting and identifying solar flares in H α full-disk images. The application of the procedure to time series of H α images from the Kanzelhöhe data archive reveals that the flare regions are appropriately detected and segmented. Moreover, the method works independently with respect to the kind of flare occurring (small vs. large size, faint vs. bright). This is a crucial requirement of the system, which, e.g., cannot be achieved by simple segmentation techniques based on thresholding.

ACKNOWLEDGEMENTS

A.V., A.H., M.T., G.B. and S.G. gratefully acknowledge the support by the Austrian *Fonds*

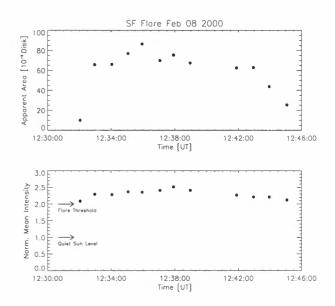


Figure 4. Time evolution of the flare area (top panel) and its mean intensity normalized to the quiet sun level (bottom panel).

zur Förderung der wissenschaftlichen Forschung (FWF grant P13655-PHY). M.S. acknowledges the support of the Österreichische Nationalbank (Jubiläumsfondsprojekt 7722). M.M. acknowledges the support by MURST and ASI.

REFERENCES

- Canny J.F., 1983, Technical Report AI-TR-720, MIT, Artificial Intelligence Laboratory, Cambridge, MA
- Canny J.F., 1986, IEEE Transactions on Pattern Analysis and Machine Intelligence 8(6), 679
- Gonzales R.C., Woods R.E., 1992, Digital Image Processing, Addison-Wesley Publishing Company
- Jähne B., 1997, Digital Image Processing: Concepts, Algorithms, and Scientific Applications, 4th ed., Springer Verlag
- Messerotti M., Otruba W., Warmuth A., Cacciani A., Moretti P.F., Hanslmeier A., Steinegger M., 1999, in Proceedings of the ESA Workshop on Space Weather, ESA WPP-155, 312
- Sonka M., Hlavac H., Boyle R., 1999, Image Processing, Analysis, and Machine Vision, 2nd ed., PWS Publishing
- Steinegger M., Veronig A., Hanslmeier A., Messerotti M., Otruba W., 1999a, Proceedings of the 12th Cambridge Workshop on Cool Stars, Stellar Systems and the Sun, submitted
- Steinegger M., Veronig A., Hanslmeier A., Messerotti M., Otruba W., 1999b, in The Dynamic Sun, A. Hanslmeier and M. Messerotti (eds.), Kluwer Academic Publishers, Dordrecht, submitted
- Temmer M., Veronig A., Hanslmeier A., Steinegger M., Brunner G., Gonzi S., Otruba W., Messerotti M., 2000, Hvar Obs. Bull., submitted

ON THE CORRELATION BETWEEN THE ORIENTATION OF MOVING MAGNETIC FEATURES AND THE LARGE-SCALE TWIST OF SUNSPOTS

V. B. Yurchyshyn^{1,2}, Haimin Wang¹, Philip R. Goode¹

¹Big Bear Solar Observatory, New Jersey Institute of Technology, Big Bear City, CA 92314, USA, *e-mail* vayur@bbso.njit.edu
²Crimean Astrophysical Observatory, 334413, Nauchny, Crimea, Ukraine

ABSTRACT

We present new results on the nature of moving magnetic features (MMFs) deduced from Big Bear Solar Observatory observations of the longitudinal magnetic fields of two large solar spots. MMFs are small magnetic bipoles that move outward, across the moat, of an eroding sunspot. Distinct from previous studies, we find that MMFs are not randomly oriented. To wit, in 23 out of 28 (82%) MMFs pairs, the magnetic element with the polarity of the sunspot was located farther from the sunspot. Furthermore, there is a correlation between the orientation of the bipole and that of the twist in a sunspot. For the two nearly round sunpots we studied, we find that the bipoles are rotated counterclockwise in the case of a clockwise twisted sunspot and clockwise for a spot with counterclockwise twist. We also find a correlation between the orientation of MMFs bipole and the amount of twist in the spot. The MMF bipoles around the highly twisted sunspot are oriented nearly tangential to the edge of the sunspot; while in the slightly twisted sunspot the bipoles are oriented nearly radially, so that they point back to the spot.

Key words: Sun: magnetic fields, moving magnetic features, moat flow

1. INTRODUCTION

The magnetic fields outside a sunspot appear discontinuous, while the large area around the spot displays a variety of mass flows. Moving Magnetic Features (MMFs) are regarded as small magnetic elements which are carried away from the sunspot to the periphery by plasma flows (Vrabec 1971; Harvey and Harvey 1973; Muller and Mena 1987; Brickhouse and LaBonte 1988; Lee 1992). A complete list of all known properties of MMFs was compiled by Ryutova et al. (1997).

Mayer et al. (1974) reviewed the possible orientations in which a magnetic tube can be taken away from a sunspot. The model by Harvey and Harvey (1973) suggests that magnetic flux is removed from the sunspot at the photospheric level (Figure 1a). This would produce pairs of MMFs in which magnetic elements of opposite polarity to the sunspot tend to be formed farther out. An alternative possibility, depicted in Figure 1 b, was suggested by Wilson (1973). In latter case, the magnetic flux tube is detached from the main bundle of tubes well below the surface (at depths of about 12,000km). The detached tubes turbulently float to the surface developing twists and kinks (Ryutova et al. 1997) which then are seen as MMFs. Significantly, orientation of the MMFs bipoles in Wilson's model is exactly the opposite: magnetic elements of opposite polarity to the sunspot will tend to be formed close to the sunspot. Therefore, high resolution observations of longitudinal magnetic field can easily delineate between the models. At present, there is no solid observational evidence on MMF bipole orientation that would favor one or another model. However, Mayer (1974) and Ryutova et al. (1997) showed some evidence that the inner footpoint of the MMF bipoles share the sunspot's polarity, which marginally supports the model of Harvey and Harvey (1973).

To distinguish between existing models, one needs to know exactly how MMFs appear on the solar disk and their subsequent evolution, as well. We focus here on several observational facts which are relevant to the theoretical models of MMFs. In Section 2, we present new information on MMFs derived from Big Bear Solar Observatory (BBSO) videomagnetograms and compare our findings to existing theoretical models. In Section 3, discussion and a short summary is presented.

2. OBSERVATION AND RESULTS

The data are observations of the longitudinal magnetic field of two large sunspots (AR NOAA 8375 and AR NOAA 8525) which were obtained at BBSO on 1998 November 4 and 1999 May 05, respectively. During the observations, the sunspots were located near the central meridian (AR NOAA 8375

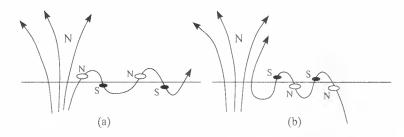


Figure 1. Proposed models for the MMFs. 9a) the detached field line at the photospheric level (harvey and harvey, 1973); (b) the detached field line at deep photospheric levels (Wilson 1973).

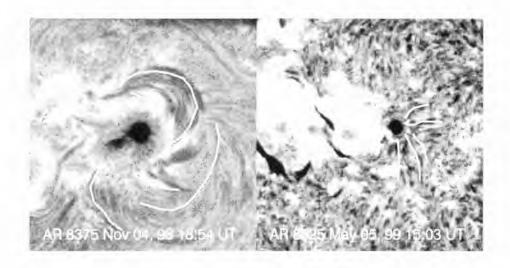


Figure 2. Two chromospheric $H\alpha$ images of AR NOAA 8375 and AR 8525 taken at Big Bear Solar Observatory. Left frame is a high resolution image and right frame is an enlarged part of a full-disk $H\alpha$ image. The solid white lines in both panels re-inforce the apparent direction of the field.

- N18W06 and AR NOAA 8525 - N18E02). Line-ofsight magnetograms were obtained by the 25-cm refractor with a pixel resolution of 0".6. Both sunspots were surrounded by intense, nearly radial moat flows. Diameters of the moat annuli were about 70", in the south-north direction, which is twice as large as the diameter of the penumbra. $H\alpha$ images indicate that the sunspot in AR NOAA 8375 was rotated in a clockwise direction (positive helicity), while dark filaments and fibrils in an AR NOAA 8525 indicate that the sunspot had a weak, but noticeable counterclockwise twist (negative helicity, Figure 2). Figure 3 shows two magnetograms taken on 1998 November 4 with a time interval of approximately one hour. The magnetic configuration includes three different structures: the N polarity sunspot, the moat boundary circumscribing the sunspot on the west and the moat flow transporting magnetic flux from the sunspot to the moat boundary. Figure 4 shows the N polarity sunspot surrounded by the moat flow observed on May 5, 1999. We observed the origination of the MMFs pairs at the penumbral boundary. Most of the MMFs appeared in closely spaced pairs of oppositepolarity magnetic elements. Usually, the magnetic element of sunspot polarity came out first and only then, the second magnetic element of the opposite polarity appeared on the scene. Frequently magnetic elements in a pair were not equally visible: opposite (to the sunspot) polarity element was often observed as a loose and weak magnetic structure. A 6hour movie made of the longitudinal magnetograms clearly illustrated that the moving magnetic features originated at the penumbral boundary and migrate outside through the moat.

In Figures 3 and 4 a total of 28 MMF pairs are encircled and numerated. Each pair was reliably defined by two successive magnetograms. To avoid an ambiguity in the measurements of the orientation of MMFs bipole, we selected only well-isolated MMFs pairs. Table 1 shows angles ϕ of axes of MMFs bipoles in reference to the radial direction. ϕ is defined as a smallest angle measured in direction from N polarity element to the sunspot radius and is a positive number when the measurement is made in the counter-clockwise direction (see Figure 5 for definition of ϕ).

First, we find no evidence that the inner footpoint of the MMFs pair shares the sunspot polarity as it was guessed earlier (Meyer et al. 1974, Ryutova et al. 1997). In fact, in 23 out of 28 MMFs pairs (82%), the magnetic element with the sunspot's polarity was located farther from the sunspot ($|\phi|$ is greater than 90°).

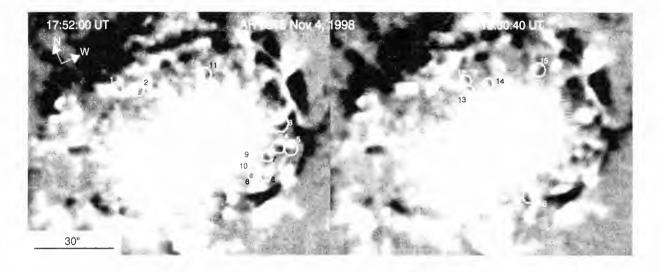


Figure 3. Two longitudinal magnetic field images of AR NOAA 8375 taken on November 4, 1998 at Big Bear Solar Observatory. White is north polarity magnetic field. Clearly defined pairs of MMFs are marked with circles and numbered.

Table 1. Orientation of MMFs pair	Table	1. C)rienta	ation	of	MMFs	pairs
-----------------------------------	-------	------	---------	-------	----	------	-------

Bipole]	2	3	4	5	6		8	9	10	11	12	13	14	15	16
\$\$375	138	138	135	78	102	102	95	92	93	93	90	93	30	99	78	125
ϕ_{8525}	-135	-135	-130	-130	-112	30	160	-155	168	-70	-165	150				

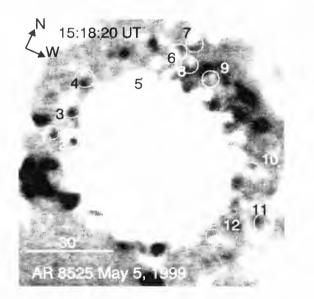


Figure 4. Image of longitudinal magnetic field of AR NOAA 8525 taken on May 5, 1999.

Second, MMFs bipoles do not seem to be randomly oriented. Orientation of the MMFs bipole is related to the large-scale twist of the sunspot. In each MMFs pair, the magnetic element of the sunspotpolarity has a preferable position in the pair: it is located on the left side, if we look at the pair from the center of the sunspot with clockwise twist. and on the right side in the case of counterclockwise twist (see also Figure 5). A careful study of the sequence of magnetograms showed that the orientation of bipoles remains the same throughout the lifetime of the bipoles. The only notable and significant changes in orientation were related to the break-up of the bipoles. The picture we deduce from the date is shown in Figure 5.

Third, we find that the deviation $\beta = 180^{\circ} - \langle \phi \rangle$ (angle β measured in counter-clockwise direction is positive) of bipole axes from the radial direction is correlated with the amount of helicity (twist) in the sunspot. The amount of helicity can be estimated by calculation of 2D current helicity maps (Abramenko et al. 1996) or by comparison of parameter α of linear force-free field with $H\alpha$ pattern around the sunspot (Seehafer 1990; Pevtsov et al. 1995). Unfortunately, we were not able to use these methods, for we lack vector magnetograms for the ARs under study. However, reliable qualitative estimations of the amount of current helicity can be done using the $H\alpha$ images of the active regions. Penumbral filaments and chromospheric fibrils in the vicinity of sunspots show a hemisphere-dependent predominant sense of curvature. The degree of the curvature is related to the amount of helicity in the sunspot. Thus, clockwise rotational motions of the N polarity spot would generate a vortex structure with a positive helicity. In our case, BBSO H α images of AR 8375 revealed that the leading sunspot had strong positive helicity and deviation β_{8375} was 81° (see also Figure 2).

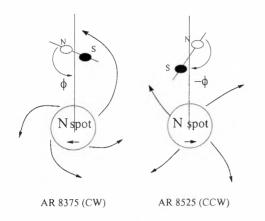


Figure 5. Definition of an ϕ .

At the same time, the sunspot in AR 8525 showed a very weak, but noticeable amount of negative helicity (counter-clockwise twist) and $\beta_{8525} = -51^{\circ}$. This might imply that a sunspot without large-scale twist would have all its MMFs bipoles oriented along the sunspot radius.

3. CONCLUSIONS AND DISCUSSION

We presented high resolution observations of the longitudinal magnetic field in a sunspot area. We learned new specific properties of MMFs in the sunspot moat.

- 1. MMF bipoles are not randomly oriented. In 23 out of 28 (82%) MMfs pairs, the magnetic element with the sunspot's polarity has a preferred position in the pair: it is located farther from the sunspot and a bipole is rotated counter-clockwise when the sunspot is twisted clockwise, and vice versa.
- 2. There seems to be a link between amount of rotation of the MMFs bipole, and amount of twist in the sunspot. Bipoles around the sunspot with strong twist oriented nearly perpendicular to the sunspot radius, while bipoles of slightly twisted sunspot are oriented mostly parallel to the radius.
- 3. The magnetic element of the same polarity as the sunspot comes out first, and the magnetic element of the opposite polarity appears second to form the MMFs bipolar pair. We found no evidence that the inner foot of a MMFs pair shares the sunspot polarity.
- 4. The majority of MMFs pairs consist of a stronger and compact magnetic element with the polarity of the sunspot, and a weaker and diffuse magnetic element of opposite polarity.

Loop models proposed by Wilson (1986) and Spruit, Title and Ballegooijen (1987) assume that MMFs are formed by closed detached loops which are separated and, hence, are randomly oriented. This model is inconsistent with the observed preferred orientation of the MMFs pairs.

Another possibility is that the magnetic flux is detached from the main flux bundle at the surface as suggested in the model of Harvey and Harvey (1973). MMFs would appear in pairs with the magnetic polarity of the sunspot being located closer to the sunspot, which contradicts our data.

Ryutova et al. (1997) proposed that non-linear coupling of flux and plasma flows leads to formation of a stable soliton-like kink along the magnetic flux. Numerical simulations show that the kink travels with a precisely defined speed and it has precisely defined width and amplitude. The orientation of the kink soliton is uniquely defined by the sign and the amount of helicity in the magnetic flux tube. Applying their results to the observed properties of MMF they found a reasonable qualitative and quantitative agreement, however, the model seems to fail to explain the diffuse structure of the second magnetic element in a MMFs pair. According to Ryutova et al. (1997) both elements in MMFs pair are clearly seen in the simulations.

In the case of strong positive helicity, a soliton-like kink would be seen at the photospheric level as MMFs pairs in which, the magnetic element to the left shares the sunspot magnetic polarity. If we assume that the kink occurs in the configuration suggested by Wilson (1973), then the closest magnetic element in the model will have the same polarity as the closest element in an observed MMFs pair, but it will be positioned to the left of the radius of a sunspot, which does not correspond to the observed result (see Fig. 1). We suggest, that strong subsurface outflow outside of a sunspot (Hulburt and Rucklidge 1999) can rotate a detached magnetic flux and, thus, affect the orientation of a MMFs pair as well as its asymmetry.

REFERENCES

- Abramenko, V.I., Wang T.J., and Yurchishin, V.B. 1996, Solar Phys., 168, 75
- Brickhouse, N.S., and LaBonte, B.J. 1988, Solar Phys., 43
- Harvey, K., and Harvey, J. 1973, Solar Phys., 28, 61 Lee, J.W. 1992, Solar Phys., 139, 267
- Mayer, F., Schmidt, H.U., Weiss, N.O., and Wilson, P.R. 1974, Mon. Not. R. Astr. Soc., 169, 35
- Muller, R., and Mena, B. 1987, Solar Phys., 112, 259
- Ryutova, M., Shine, R., Title, A., and Sakai, J.I. 1997, ApJ, 492, 402
- Seehafer, N. 1990, Solar Phys., 125, 219
- Spruit, H.C., Title, A.M., and van Ballegooijen, A.A. 1987, Solar Phys., 110, 115
- Vrabec, D. 1971, in IAU Symp. 43, Solar Magnetic Fields, ed. R. Howard (Dordrecht: Reidel), 329
- Wilson, P.R. 1973, Solar Phys., 32, 435
- Wilson, P.R. 1986, Solar Phys., 106, 1

MAGNETIC TOPOLOGY IN NOVEMBER 5, 1998 TWO-RIBBON FLARE AS INFERRED FROM GROUND-BASED OBSERVATIONS AND LINEAR FORCE-FREE FIELD MODELING

V. B. Yurchyshyn^{1,2}, H. Wang¹, J. Qiu¹, P. R. Goode¹, V. I. Abramenko²

¹Big Bear Solar Observatory, New Jersey Institute of Technology, Big Bear City, CA 92314, USA, tel: 1-(909)-866-5791/fax: 1-(909)-866-4240; *e-mail* vayur@bbso.njit.edu ²Crimean Astrophysical Observatory, 334413, Nauchny, Crimea, Ukraine

ABSTRACT

We analyzed the 3D structure of the linear forcefree magnetic field. A longitudinal magnetogram of the AR NOAA 8375 has been used as the photospheric boundary condition. Nov 5, 1998 2B/M8.4 two-ribbon flare can be explained in the framework of quadrupolar reconnection theory: the interaction of two closed magnetic loops which have a small spatial angle. The revealed magnetic configuration allows us to understand the observed location and evolution of the flare ribbons and the additional energy released during the gradual phase of the flare, as well. Besides, reconnection of closed magnetic loops can logically explain the connection between a two-ribbon flare and a giant X-ray post-flare arch which usually is observed after the flare onset. We emphasize that unlike the Kopp and Pneuman configuration, the model discussed here, doesn't necessarily need destabilization and opening of the magnetic field.

Key words: Sun: flares, magnetic field, linear force-free field modeling

1. INTRODUCTION

It is generally accepted that a two-ribbon flare (TRF) is due to a reconnection process which happens in previously open magnetic field (Sturrock 1968, Hirayama 1974, Kopp and Pneuman 1976). It suggests that rising prominences and/or fast expanding coronal loops are trigger of the TRF. After the filament destabilization and eruption, the stretched magnetic field lines become open and reconnect. This process is accompanied by type III and IV radio bursts.

On the other hand, it has also been shown that there is no direct link between filament eruption and TRF (Forbes 1992). Out of 16 studied two-ribbon flares with pre-existing dark filament, in 10 cases filaments erupted and 5 filaments remained undisturbed (Hirayama 1974). In an earlier study by Smith and Ramsey (1964), about half of the major flares were found to be associated with active region filaments and preceded by their sudden eruption.

Any flare model must explain not only how and where magnetic energy is released, but also a location (shape?) and a topological link between all flare ribbons and remote brightenings seen in the course of a two ribbon flare.

The Hard X-ray Imaging Spectrometer aboard the SMM mission discovered extensive post-flare coronal arches (Švestka et al., 1982). The arches appeared to be connected to the occurence of two-ribbon flares. Simberová et al. (1993) also showed that a giant post-flare arch was formed by interactions of large-scale loops present above the flaring active region. This result doesn't seem to support the Kopp and Pneuman (1976) model which invokes the reconnection of the open magnetic field lines. To the contrary, the co-existence of a giant X-ray post-flare arch and a post-flare loops system can be a sign of a single reconnection event in a simple magnetic system of closed coronal loops.

For the famous, well-studied May 16, 1981 tworibbon flare, Vršnak et al. (1987) established that the site of energy release was located at the loop top in a closed magnetic configuration. They also conjectured that, in the studied flare, a process of driven reconnection between neighboring loops took place.

Many studies have shown that chromospheric H α kernels were found to be on the intersection of the separatrices (surfaces that separate volumes of different magnetic connectivity) with the photosphere. But only relatively few ones studied in detail the magnetic topology in two-ribbon flares (Gorbachev and Somov 1988, Demoulin et al., 1994a, Mandrini et al., 1995, Yurchishin 1997). Both the magnetic configuration and the H α brightenings are found to be qualitatively different and more complex than ones proposed in models with open magnetic field. They concluded that the flares under consideration result from the interaction of closed large-scale magnetic structures, and not from an internal instability happening within a twisted flux tube.

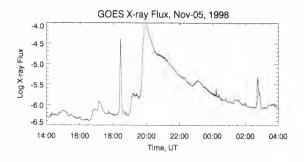


Figure 1. GOES X-ray time profile of November 5, 1998 flare.

2. OBSERVATIONAL DATA AND MAGNETIC FIELD RECONSTRUCTION

BBSO observations completely covered the Nov 5, 1998 flare which occurred in AR NOAA 8375 (Yurchyshyn et al. 2000). We also used the Al1 filter YOHKOH soft X-ray data.

Figure 1 shows GOES soft X-ray 1-8 Å flux plot of the

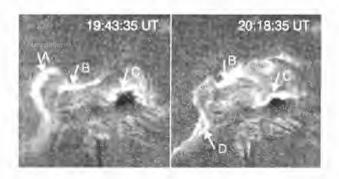


Figure 2. H α images of the two-ribbon flare. The field of view is 200 by 200 arcsec.

flare as a function of time. It is interesting to note that the two-ribbon flare was not provoked by filament eruption, in fact, no filament was present in this AR. Figures 2 and 3 show H α images obtained at the center and at the red wing of the spectral line. The post-flare loop system connected flare ribbons *B* and *C* and showed apparent growth.

To reconstruct coronal magnetic field we used a numerical method for the LFFF calculation proposed by Abramenko and Yurchishin (1996). We used the BBSO line-of-sight magnetogram as the photospheric boundary condition. The magnetogram was recorded at 18:18 UT, before the flare onset. We obtained a set of numerical solutions with different α parameter and then, using high resolution BBSO H α images as well as soft X-ray images from YOHKOH we chose the numerical solution ($\alpha = 0.013 \text{ arcsec}^{-1}$) which best fits the observed magnetic configuration before the flare.

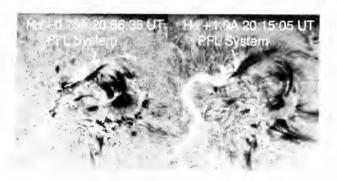


Figure 3. $H\alpha$ off-band images of the two-ribbon flare.

3. RESULTS

We used a simple method which allowed us to define magnetic links between the flare ribbons in this two-ribbon flare. First, we calculated, the lines of force which originate within the leading spot. Then, considering each line, we located both its footpoints. Doing so, we could distinguish three different magnetic flux tubes. All the lines of force which originate in the area marked with *a* have their ends at the flare ribbon marked with *B* (line 1, Figure 4). All the field-lines starting from the area *b* ended at the flare

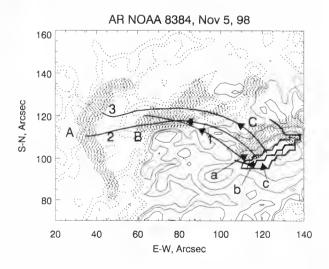


Figure 4. Location of $H\alpha$ flare ribbons (dashed area) superposed on a contour map of the longitudinal magnetic field (solid lines - N polarity, dashed - S polarity). Contours levels are 100, 200, 400, 800 G. Solid lines 1, 2, 3 denote calculated field-lines ($\alpha = 0.013 arcsec^{-1}$) connecting the areas a and b with the flare ribbons A and B.

ribbon A (lines 2, 3, Figure 4) while field-lines coming



Figure 5. $H\alpha + 0.75 \text{ Å}$ image taken at 20:56:35 UT. Dark loops at upper right – growing post-flare loops system (PFL). Solid lines denote calculated field-lines connecting the area b with the flare ribbon A. Dashed lines – calculated field lines ($\alpha = 0.013 \text{ arcsec}^{-1}$) which connect the area c with the flare ribbon D.

out from the area c went south-eastward and ended at the H α brightening D (Figure 5). Any two closest magnetic field lines originated correspondingly in areas a and b, nearby to the border between them, have their second ends separated and rooted in different distant magnetic elements of northern polarity. Thus, the boundaries of these a, b, c areas are the intersection of separatrices with the photosphere. In other words, following the definition by Demoulin et al. (1996), these boundaries are places where a drastic change in the field-line linkage occurs. Discontinuities in the field-line linkage at the boundary are at the origin of the formation of current sheets. It has been found that observed flare kernels are located at these discontinuities (Demoulin et al., 1996 and references therein). Our calculation show that in case of the Nov 5, 1998 flare, H α brightenings are also located at places where rapid changes in the fieldlinkage above the photosphere take place. According to this, we are able to clear up the magnetic configuration in the two-ribbon flare as well as indicate magnetic fluxes which took part in energy release process.

We suggest that there were at least two large-scale events of energy release. The first and major energy release event happened about 19:35 UT (Figure 1). The H α image taken at 19:43:35 UT (Figure 2) shows three well developed flare ribbons also marked on Figure 5 with letters A, B, C. We suppose that this energy release was due to the reconnection of two magnetic fluxes during which the connectivity of magnetic field was exchanged between four loop footpoints without a significant change in the longitudi-



Figure 6. Greyscale $H\alpha + 0.75$ Å image overlapped by a soft X-ray YOHKOH image shows the magnetic configuration after the flare. The resultion configuration consists of the low-laying post-flare loops system (dark loops) and the overlaying giant X-ray post-flare arch. The crosses denote the hottest parts of H α and X-ray loops and might locate the site of the reconnection.

nal field. Analysis of the longitudinal magnetograms supports this theoretical assumption since no largescale magnetic flux cancellations at, or around, the flare site were observed. The first magnetic flux is represented by a line 1 which connects the area a and the flare ribbon *B* and shown in Figure 4. The second one is magnetic flux which leaves the leading sunspot in the area b and goes to the flare ribbon A (lines of 2. 3). The reconnection will create new magnetic loops systems. The first one, the H α post-flare loop system connects the area b and the flare ribbon B (Figure 4). while the second one, a large scale loop system, connects the area a and the flare ribbon A. This largescale loop might corresponds to a well-known giant X-ray post-flare arch (Švestka et al., 1982). Figure 6 shows the off-band $H\alpha$ image (the same as in Figure 3) with an overlapped SXT/YOHKOH image. One clearly sees the presence of both the low-lying $H\alpha$ post-flare loop system (dark loops) and the overlaying hot X-ray giant coronal arch (a white loop with contours at the right top corner). The H α loop are located just below the hot X-ray loop with their top being almost tangential. The post flare loop system connects the leading sunspot and the flare ribbon Band the large scale X-ray arch has its footpoints at the sunspot and the flare ribbon A. This kind of magnetic connection corresponds to that predicted by the model.

Both, the post flare loops system and the giant X-ray post-flare arch exhibit apparent growth (Poletto

and Švestka 1992, Schmieder et al., 1995) as the flare is in progress. Thus, due to the evolution of newly formed loops, a disturbance of the pre-existing overlaying magnetic field will take place. This, in turn, might provoke the subsequent reconnection of the newly formed loops with the loops system which connects the area c and the flare ribbon D (Figure 5). If we are correct, this second-step reconnection should start a bit later than the main phase of the energy release. This might be seen in $H\alpha$ images taken at 19:43 UT and 20:29 UT (Figure 2). One may see that when the eastern ribbon (marked with A in Figures 2) has faded, the south-east ribbon (marked with D) became brighter. Also, according to SGD (Figure 1), at 20:30 UT, after the X-ray flux reached its maximum, the GOES light curve has broken its gradual decrease and has formed plateau which might imply that an additional source of energy has turned on. This second reconnection event creates a new loop system connecting the area c with the flare ribbon \hat{A} and b with D (Figure 5) and explains the evolutin aof the flare ribbons.

4. DISCUSSION AND CONCLUSION

As inferred from LFFF modeling, the two-ribbon flare was a product of multiple reconnection process between interacting loops which make a small angle in space. The calculations explore only the largescale magnetic field structure in the AR. However, taking into account a possible filamentation of the solar magnetic field, this flare could be considered as a superposition of many small-scale reconnection events. In this case, one would expect a variety of angles between small-scale magnetic fluxes which would bring up the additional energy for the flare (Anschwanden et al., 1999). Another possible scenario is that the self-organized criticality model could be realized with the avalanche process of small-scale energy releases (Lu and Hamilton 1991).

The magnetic configuration, revealed here, naturally explains the location and the shape of the flare ribbons, the location of the post flare loop system, as well as the magnetic connection between the H α brightenings. Multiple magnetic reconnection also allows us to explain the evolution of the flare ribbons and the additional energy release during the gradual phase of the flare. The interaction of closed magnetic loops in two-ribbon flare can also explain the origin of the giant X-ray coronal arch observed after the two ribbon flare onset (Švestka et al., 1982). This result also meets the Šimberova et al. (1993)'s conclusion that the giant arch is the result of progressive reconnection of elementary flux tubes of two (or more) interacting loops.

We would like to emphasize that unlike the Kopp&Pneuman configuration, the model discussed here does not necessarily need destabilization and eruption of the active region filament. The filament eruption, even if it accompanies a two-ribbon flare, could be a one of many equal possibilities to trigger a solar flare.

REFERENCES

- Abramenko, V.I., and Yurchishin, V.B. 1996, Solar Phys., 168, 47.
- Aschwanden, M.J., Kosugi, T., Hanaoka, Y., Nishino, M., and Melrose, D.B. 1999, ApJ, accepted.
- Demoulin, P., Mandrini, C.H., Rovira, M.G., Henoux, J.-C., and Machado, M.E. 1994a, Solar. Phys., 150, 221.
- Demoulin, P., Henoux, J.C., Priest, E.R., and Mandrini, C.H. 1996, A&A 308, 643.
- Forbes, T.G., 1992, in Lecture Notes in Physics: Eruptive Solar Flares, ed. Z. Švestka, B.V. Jackson, and M.E. Machado, 79
- Gorbachev, V.S., and Somov, B.V. 1988, Solar Phys., 117, 77.
- Hirayama, T. 1974, Solar Phys., 34, 323.
- Kopp, R.A., and Pneuman, G.W. 1976, Solar. Phys., 50, 85.
- Lu, E.T., and Hamilton R.J.:1991, ApJ, 380, L89.
- Mandrini, C.H., Demoulin, P., Rovira, M.G., de La Beaujardière, and Henoux J.-C. 1995, A&A, 303, 927.
- Ogir, M.B. 1967, Bull. Crimean Astrophys. Obs., 37, 94.
- Poletto, G., and Švestka, Z.F. 1992, Solar Phys., 138, 189.
- Schmieder, B., Heinzel, P., Wiik, J. E., Lemen, J., Anwar, B., Kotrc, P., and Hiei, E. 1995, Solar Phys., 156, 337.
- Šimberova, S., Karlicky, M., and Švestka, Z. 1993, Solar Phys., 146, 343.
- Smith, S.F. and Ramsey, H.E. 1964, Z. Astrophys. 60, 1.
- Sturrock, P.A., 1968, in IAU Symp. 35: Structure and Development of Solar Active Regions, ed. K.O. Kiepenheuer, 471.
- Švestka, Z., Stewart, R.T, Hoyng, P., van Tend, W., Acton, L.W., Gabriel, A.H., Rapley, C.G., and 8 coauthors: 1982, Solar Phys., 75, 305.
- Vršnak, B., Ruždjak, V., Messerotti, M., and Zlobec, P. 1987, Solar Phys., 111, 23.
- Yurchishin, V.B. 1997, Kinematics Phys. Celest. Bod., 13, N6, 33.

ANALYSIS OF THE SOLAR MAGNETIC DIPOLE REVERSAL DURING THE CURRENT SOLAR CYCLE

A. N. Zhukov, I. S. Veselovsky

Institute of Nuclear Physics, Moscow State University, Moscow, 119899 Russia phone 7-095-939-1298; fax 7-095-939-3553; e-mail anz2@dec1.npi.msu.su

ABSTRACT

We analyze the behaviour of the solar magnetic dipole moment during the current 23rd solar cycle (in 1998 – 2000). The magnetic dipole vector was determined via analysis of the coronal magnetic field data by Wilcox Solar Observatory, taking the dipole coefficients from the expansion of the coronal magnetic field in multipoles at the source surface located at 2.5 solar radii. An attempt is undertaken to investigate the motions of the magnetic poles of the Sun (i. e. the poles of its central dipole). During the years of solar activity minimum the dipole lies close to the rotational axis of the Sun. During the rising phase of activity cycle the reversal of the dipole vector takes place. Some implications on the problem of active longitudes are obtained.

I. INTRODUCTION

The solar coronal magnetic field plays very important, if not dominant, role in organizing the coronal plasma, both in large and small scale structures. However, it is still very difficult to perform direct measurements of the magnetic field in the corona. Several models (e. g. Mikić and Linker 1995) were developed in order to calculate the coronal field on the base of the photospheric magnetic field synoptic charts, which are recorded for a long time (e. g. Hoeksema 1991). A force-free extrapolation of the photospheric field produces the coronal field, which becomes radial beyond the source surface. Between the photosphere and the source surface the magnetic field could be written as a sum of different multipole components (Hoeksema 1986).

The temporal behaviour of the solar magnetic field expresses prominent 22-year cycle which is well-known for a long time. During the maximum activity years the large-scale magnetic field of the Sun changes its polarity. The details of this process (which is believed to be governed by some dynamo mechanism under the photosphere) are still not completely known. The leading role belongs to the dipole component, which naturally describes the large-scale field and dominates over the higher-order multipoles on large distances. The dipole component of the solar magnetic field is also very important in the heliosphere, where, along with the heliospheric current sheet, it determines the large-scale interplanetary magnetic field (Veselovsky 1996).

In the present paper we make an attempt to investigate the large-scale coronal magnetic field reversal process during the current 23rd solar cycle.

2. RESULTS

It is the dipole component what determines the largest scales of the coronal magnetic field, so we investigate the behaviour of the solar magnetic dipole vector during the current activity cycle.

The vector of the central magnetic dipole moment was determined through the analyses of coronal magnetic field data by Wilcox Solar Observatory. Taking the coefficients g_{10} , g_{11} and h_{11} from the expansion of the coronal magnetic field in multipoles at 2.5 solar radii (which correspond to the perpendicular to the ecliptic plane, earthward and sky-plane components of the dipole moment vector), we can calculate the dipole value as

$$\mu = (g_{10}^2 + g_{11}^2 + h_{11}^2)^{1/2} r_1^3.$$
⁽²⁾

where $r_1 = 2.5$ solar radii is the source surface location. Taking the ratio of different components and the absolute value, we can deduce the polar and azimuthal inclination angles θ and φ of the magnetic dipole vector in respect to the solar rotational axis.

We performed these calculations for the period from January 8, 1998 to July 17, 2000. The plot of the variations of the dipole field value $(g_{10}^2 + g_{11}^2 + h_{11}^2)^{1/2}$, which is equivalent to the solar magnetic dipole, is presented in Fig. 1. In Fig. 2 the dependence of the polar inclination angle θ is shown as a function of time. The reversal of the magnetic dipole took place in July – August, 1999 (days 550 – 600). Several temporal reversals also could be seen. Comparing Fig. 1 and Fig.

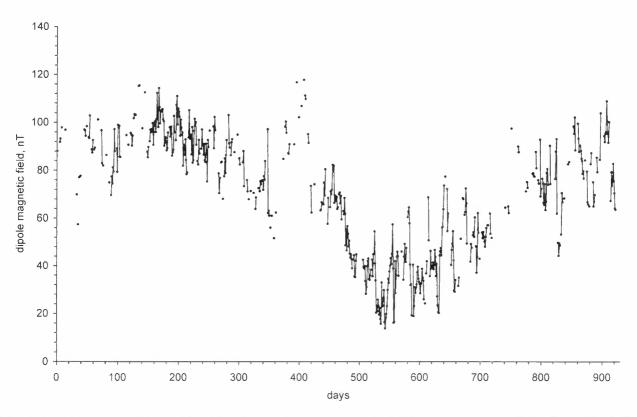


Figure 1. The time variations of the solar dipole magnetic field value at the source surface (2.5 solar radii) during January 8, 1998 – July 17, 2000.

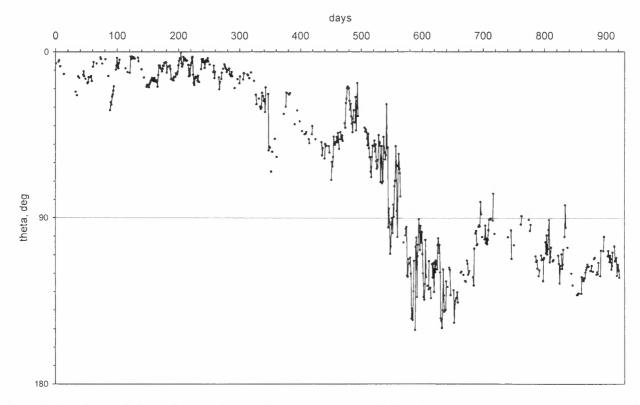


Figure 2. The time variations of the polar inclination angle θ of the solar magnetic dipole vector during January 8, 1998 – July 17, 2000.

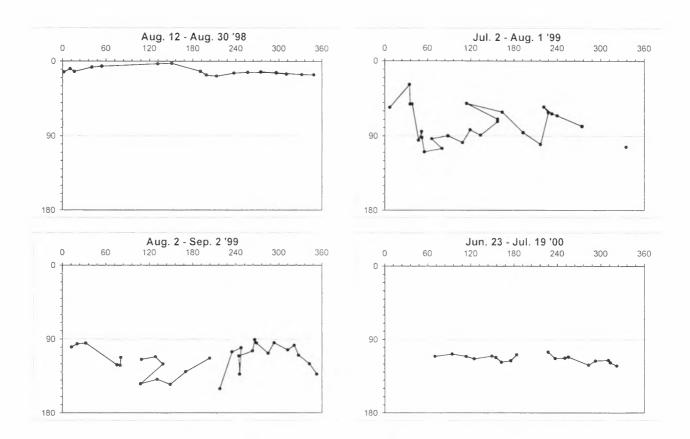


Figure 3. Typical maps showing the motions of the solar northern magnetic pole. On the horizontal axis: the azimuthal inclination angle φ of the solar magnetic dipole in respect to its rotational axis, on the vertical axis: the polar inclination angle θ . Scales in degrees. $\varphi = \theta$ corresponds to the Sun – Earth direction: φ increases counterclockwise if one looks from the solar north.

2, we can conclude that during the polarity reversal process the strength of the dipole field decreases.

We have also calculated the dependence of the polar inclination angle θ on the azimuthal one φ for the whole considered time interval. Such calculations for shorter period of time in 1999 were reported in the paper by Veselovsky et. al (1999). In Fig. 3 we present several typical maps showing full rotations of the magnetic dipole vector during different phases of activity cycle. It could be seen that during the minimum activity years or early growth phase (in 1998) the polar inclination angle θ is close to zero, i. e. the magnetic pole is situated near the heliographic pole. Then, while the activity grows, the motions of the magnetic pole become more irregular, the dipole vector approaches the equator plane $(\theta = 90^{\circ})$ and crosses it (in July – August, 1999). Unfortunately, the lack of data does not permit us to follow the reversal process more closely. After the reversal the magnetic dipole moves towards the southern pole (in 2000).

We then determined the Carrington longitude of the northern magnetic pole as a sum of the central meridian Carrington longitude and the azimuthal angle φ . Its dependence on time is shown in Fig. 4. This plot shows the magnetic pole longitudinal motions when the solar rotation is subtracted. We note that when the magnetic pole is situated at high latitudes, these calculations are not sufficiently exact because of the differential rotation of the Sun. However, the most interesting near-equator motions of the magnetic pole (after day 550) are calculated accurately enough.

During the low activity period the magnetic pole drifts on the solar surface, sometimes in the direction coinciding with the solar rotation, sometimes in the opposite direction. However, near the time of the polarity reversal the magnetic pole Carrington longitude is situated between 140° and 270°. Moreover, all the reversals (temporary and main) take place in the Carrington longitude range between 200° and 250°. These longitudes (with the magnetic field increased relatively to the dipole field near the magnetic equator) could be considered as «active» in this respect, although

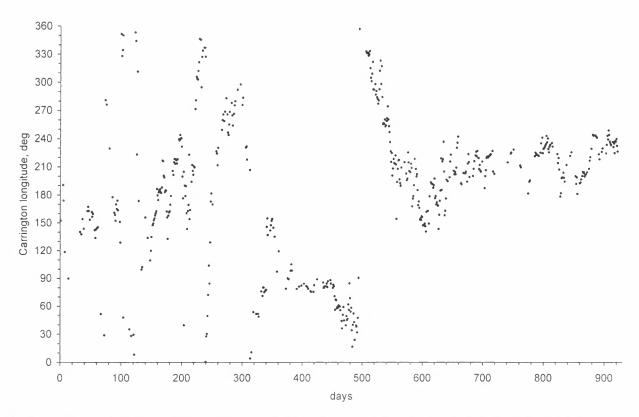


Figure 4. The time variations of the Carrington longitude of the northern solar magnetic pole during January 8, 1998 – July 17, 2000.

the investigated period is too short for reliable determination of active longitudes. We also note, that during this time the antipodal region of active longitudes $(20^{\circ} - 70^{\circ})$ should exist on the opposite side of the Sun near the southern magnetic pole.

4. CONCLUSIONS

Investigating the variations of the magnetic dipole vector during the current 23rd solar cycle (in January, 1998 – July, 2000) we found that:

 during the epoch of activity minimum and early growth phase the magnetic dipole of the Sun is situated close to its rotational axis;

• during the raising phase of the solar activity cycle the reversal of the magnetic dipole takes place, during the current cycle it happened in July – August, 1999;

• the reversal of the dipole is not instantaneous: the temporal reversals occurred before and after the main reversal;

• the value of the magnetic dipole decreased in the period of time close to the polarity reversal;

• all the reversals (main and temporal) occurred in the range of Carrington longitudes of about $200\degree - 250\degree$.

ACKNOWLEDGEMENTS

The authors are grateful to J. T. Hoeksema (Wilcox Solar Observatory) for the coronal magnetic field harmonic coefficients. A. N. Zhukov is acknowledged to the organizers of the meeting for providing resources to attend the conference.

REFERENCES

Hoeksema J. T., 1986, WDC-A Report UAG-94.

Hoeksema J. T., 1991, Tech. Rep. CSSA-ASTRO-91-01, Center for Space Science and Astronomy, Stanford University, Calif.

Mikić Z., Linker J. A., 1995, in: Solar Wind Eight. Proceedings of the Eighth International Solar Wind Conference, AIP Conference Proceedings 382, Woodbury, New York, p. 104.

Veselovsky I. S., 1996, Geomagn. Aeronomy, 36, p. 1.

Veselovsky I. S., Zhukov A. N., Panassenko O. A., Koutchmy S., 1999, Rom. Astron. J., Vol. 9, Supplement. p. 29. **Poster Papers**

The Terrestrial Record of Solar Variability

COHERENCY BETWEEN SOLAR ACTIVITY AND METEOROLOGICAL PARAMETERS AT 11 YEAR PERIOD

D. Altadill, J.J. Curto, L.R. Gaya-Piqué, J.G. Solé and J.M. Torta

Observatori de l'Ebre. CSIC-URL. Horta Alta 38, 43520, Roquetes, Spain. Tel: +34 977-500-511 / fax: +34 977-504-660 Corresponding author e-mail: ebre.daltadill@readysoft.es

ABSTRACT

The historical records of temperature and rainfall at Ebre Observatory (40.8° N, 0.5° E) and the relative sunspot numbers have been used to study the possible influence of the 11-year solar cycle over the meteorological parameters. Spectral and crosscorrelation analysis have been applied in order to find such a relationship. The yearly averaged maximum temperature displays a period near 11 years, while the yearly averaged minimum temperature and yearly rainfall values do not present any significant peak about that period. It has been obtained that the 11-year solar cycle and the 11-year oscillation found in the maximum temperature are coherent, practically in phase. Moreover, an 11-year oscillation is found to be significant in the cross-correlation between the solar activity data and maximum temperature. The results show a possible relation of the 11-year solar activity cycle on the maximum temperature data used here.

INTRODUCTION

During the last few decades, several studies have been developed to determine the relation between solar activity and climate changes (for instance Friis-Christensen and Svensmark, 1997 and references therein). Some of them have been centered on the influence of solar activity cycles, mainly the wellknown 11-year period cycle, over global meteorological records or from selected places over the world.

The purpose of this work is to look for possible influence of the 11-year solar activity cycle on meteorological parameters. Although the total solar irradiance is a better indicator of solar activity when searching Sun-Climate relationships, we chose the relative sunspot numbers as indicator of solar activity because we study long term series. The results obtained are only applicable to this series, and no global conclusions can be extracted.

DATA AND METHODOLOGY

In order to carry out this study, we used the temperature and rainfall data recorded at Ebre Observatory (40.8° N, 0.5° E) from 1905 to 1999. These time series have been extended up to 1880 with the meteorological records carried out in a previous meteorological station less than 2 km far from the actual position of the observatory. From the daily temperature records, we obtained yearly averages of

the daily variation and studied their extrema, hereafter Tmax and Tmin. The yearly rainfall values were obtained from the daily rainfall records. Moreover, we have studied the yearly rainfall at Valencia (39.48° N, 359.62° E) from 1864 to 1994 (Almarza et al., 1996), in order to contrast it with the data from Ebre observatory. The solar activity data that we used in this study were the yearly averages of the relative sunspot numbers (SSN) provided by the Solar-Terrestrial Physics Division of the NOOA. The temperature and solar activity data are presented in figure 1.

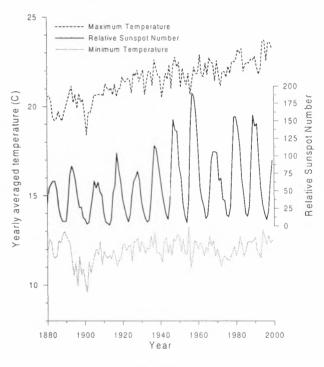


Figure 1

We used statistical methods based on high spectral resolution harmonic analysis (see Vitinsky et al., 1986 for details) in order to obtain the spectral characteristics of the temperature and rainfall variations probably related to the 11-year solar cycle. We also used cross-spectral analysis to seek for the coherency between the above-mentioned variations and from the magnitudes linked with it we used an estimation of the squared coherency and phase spectra but avoiding to filter the spectrum (Bloomfield, 1976). Moreover, cross-correlation analysis was used to evaluate the possible influence of the 11-year solar cycle on the meteorological parameters.

Proc. 1st Solar & Space Weather Euroconference, 'The Solar Cycle and Terrestrial Climate', Santa Cruz de Tenerife, Tenerife, Spain, 25-29 September 2000 (ESA SP-463, December 2000)

RESULTS

Figure 2 shows the averaged amplitude spectra corresponding to the SSN, Tmax and Tmin. The spectra have been obtained from 21 time intervals with duration of 80 years and shifted from one to each other by 2 years. The initial year of the first interval was 1880, and the ending year of the last interval was 1999. In this figure we clearly observe the 11-year solar cycle in the SSN. Such 11-year oscillation activity is also observed in Tmax data but with lower amplitude than oscillations with periods of 7.5, 14 and 17.5 years. These spectral peaks are also observed in Tmin, but no peak with period near 11-year is observed in Tmin. The 17.5-year peak could be attributed to the cycle of regression of the lunar nodes (Currie, 1981). We are not able to explain the possible origin of the other peaks.

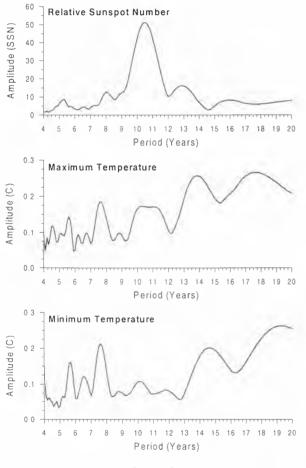


Figure 2

Figure 3 shows the squared coherency and phase spectra between the SSN and Tmax (left) and Tmin (right). To obtain this figure we have used the same spectral windows as in figure 2. It is noticeable the large coherency between the SSN and Tmax at near 11-year period. Moreover, the phase spectrum shows phase stability for the harmonics near such oscillation activity. This figure shows also large coherency between SSN and Tmin. However, the phase stability is not as clear as in the previous results.

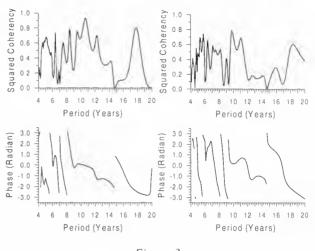


Figure 3

Figure 4 shows the dynamic amplitude spectra corresponding to SSN (top), Tmax (middle) and Tmin (bottom). The plots were obtained using spectral windows of 63-year time length shifted by 1 year from one to each other. Only those harmonics having a probability of existence larger than 90% were taken into account, the others were set to have zero amplitude. It is interesting the slowly change of the dominant period of the 11-year solar cycle as observed from SSN, decreasing from 11.1-year in the early 10's to 10.5 in the 40's and increasing to 10.8 in the late 60's. This result probably reflects the well-known Gleissberg period. The 11-year cycle shows an intermittent presence in Tmax, being most persistent from the late 40's to the late 60's, when the 11-year solar cycle has the largest amplitude in the SSN. No significant presence of the 11-year cycle is observed in the Tmin data.

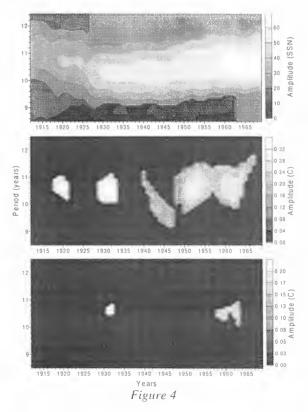


Figure 5 shows the results of cross-correlation functions between SSN and temperatures. The 0.99 and 0.95 confidence levels of correlation are plotted to confirm the statistical significance of the 11-year solar cycle on the meteorological parameters. We clearly observe the oscillations in the cross-correlation functions with a period near 11 years in analysis, SSN vs. Tmax and SSN vs. Tmin. However, only the former displays consecutive maxima above the 0.99 confidence level, particularly 4 recurrences.

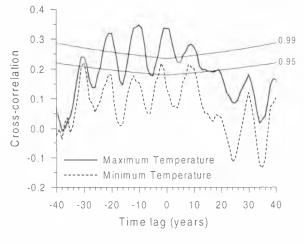


Figure 5

We made the same analysis for the rainfall data and we found that the 11-year solar cycle is not sensitive in such data. Figure 6 was obtained in the same way as figure 4. We observe that practically there is no significant 11-year oscillation in the rainfall records at Ebre Observatory, and the dominant period observed from data at Valencia is outside of the periodic range of the 11-year solar cycle. Moreover, the results of cross-correlation analysis show no consecutive peaks rising the confidence levels (Figure 7).

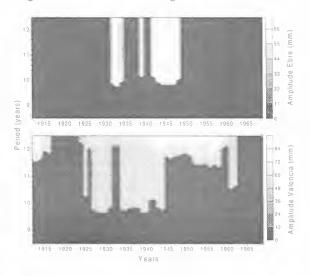
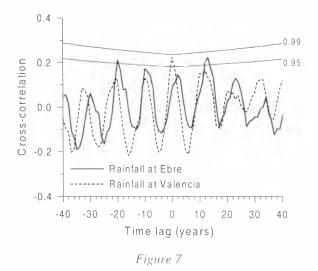


Figure 6



We performed the same type of analyses by using monthly mean values in the aforementioned time series, and the results we found are qualitatively indistinguishable from those obtained with yearly values.

CONCLUDING REMARKS

All the results presented here lead to the conclusion that the maximum temperature data recorded in the vicinity of the Ebre Observatory is sensitive to the 11-year solar cycle, being more stable in the second half of the time series when the solar cycle is most energetic. Another interesting fact is that the 11-year oscillation is practically in phase between SSN and Tmax (figures 3 and 5). However, the cross-correlation maximum at a time lag of -9 years is larger than that at 1 year. This fact may be related with the 22-year solar cycle, essentially due to the fact that, although the well-known Gnevyshev-Ohl rule is applicable in the SSN considered here, the solar cycle 18 (1945 – 1954) is most active than cycle 17 (1934 – 1944).

REFERENCES

- Almarza C., López J.A. and Flores C. (1996): Homogeneidad y variabilidad de los registros históricos de precipitación de España. Publicación A-143 del Instituto Nacional de Meteorología, Ministerio de Medio Ambiente, Madrid.
- Bloomfield P. (1976): Fourier analysis of time series: an introduction. John Wiley, NY.
- Currie, R.G. (1981): Evidence for 18.6 year M_× signal in temperature and drought conditions in North America since AD 1800. *Journal of Geophysical Research*, Vol. 86, pp. 11055-11064.
- Friis-Christensen E. and Svensmark H. (1997): What do we really know about the Sun-Climate connection? *Advances in Space Research*. Vol. 20, No. 4/5, pp. 913-921.
- Vitinsky Y. I., Kopecky M. and Kuklin G. (1986): Statistics of sunspot-creating activity (in Russian). Nauka, Moscow.

ON SOLAR-TERRESTRIAL CORRELATION STUDIES: PITFALLS AND REAL SIGNALS

Rasmus E. Benestad

The Norwegian Meteorological Institute, PO Box 0313, Oslo, Norway (rasmus.benestad@dnmi.no)

ABSTRACT

Hypotheses proposing that variations in Sun's activity account for most of the observed global warming on Earth have recently received some attention. Friis-Christensen & Lassen (1991) found an apparent match between the sunspot cycle length (SSCL) and the northern terrestrial hemispheric temperature. More objective methods are used to search for a real solar activity signal in Earth's climatic record, and the relationships between solar activity proxies and global mean temperature are re-examined in order to quantify the relationship between the terrestrial temperature and solar activity. High correlation between the sunspots and the terrestrial global mean temperature is found for non-detrended data, but similar analysis on detrended data indicates a weak solar-terrestrial connection. The results from this study contradict the hypothesis that most of the recent warming is due to the solar activity. Predictions of terrestrial temperature with linear regression models based on the Wolf number (R_z) have limited skill.

Key words: statistical analysis, statistical inference, prediction.

1. INTRODUCTION

There have been speculations whether the sunspots affect our climate for more than 100 years, but still there seems to be no firm conclusion about which role the sunspots play for the terrestrial climate. *Helland-Hansen & Nansen* (1920) and others made claims about relationships between the solar activity and various temperature series, whereas sceptics, such as *Monin* (1972), later refuted such hypotheses. Since then, more observations with higher quality have been gathered, and the advent of the electronic computers has made it possible to apply sophisticated analytical tests to these data.

There have recently been published a number of papers which have reported relationships between the sunspot data and the terrestrial surface temperature. This paper re-examines some of these studies and highlights a number of grave mistakes made when applying inappropriate statistical methods to test hypothesised relationships.

The sunspots are from Greenwich Observatory, and the SSCL is the time between two consecutive minima and maxima respectively. This estimate is associated with typical errors of 4-5 months, but was chosen because it gives more data points than the Median method (*Mursula & Ulich*, 1998). The temperature records are from Univ. East Anglia, CRU.

This paper discusses the presence of long-term trends and contamination from external factors that have not been eliminated, filtering of epochs, using inappropriate null distribution for statistical inference, alternative and more robust ways of estimating correlation statistics, the correlation between the hemispheres, and using sunspots for prediction of the global mean temperature.

2. TRENDS

Regression and correlation analysis can be biased by the presence of long-term trends in the record (Benestad, 1999). One common mistake is to apply correlation and regression analysis to series which contain long-term trends if it is not known a priori that these are part of the signal. Such trends may bias the analysis by for instance inflating the correlation scores if these trends are caused by external factors. It is often wise to detrend the data (here the least-squares fit linear trend has been subtracted) in order to reduce such biases. Detrending can be justified in terms of a simple mathematical model: let y = mx + c [1], $y = y_{dt} + y_{tm}$, $x = x_{dt} + x_{tm}$, and y_{tm} be contain the mean of y as well as the best-fit linear trend. Let y_{dt} be the detrended part of y, with zero mean. Equation 1 implies that $(y_{dt} + y_{tm}) = m(x_{dt} + x_{tm}) + c$, or $y_{dt} = mx_{dt} - (y_{tm} - x_{tm} - c)$ [2]. If the linear trends in x and y are related (not influenced by external factors), then the expression parentheses in Equation

2 equals zero and we are left with $y_{dt} = mx_{dt}$ [3], which relate short-term excursions in x with shortterm variations in y. If, on the other hand, the trends are influenced by external factors, then the non-detrended analysis will be biased by these. It is less likely that short term variations are correlated by chance than slow trends because the former have more degrees of freedom. An example of the inflation of the correlation score by non-zero long-term trends can be seen in Fig. 1a: The correlation scores for the non-detrended records of SSCL and 61-month and 121-month low-passed filtered (Gaussian) R_z are shown in Table 1 and are for the non-detrended analyses -0.45 and 0.79 respectively, whereas for the detrended series these test statistics are -0.17 and 0.52. These are similar to the cross-validation correlation scores reported by Benestad (1999). The main difference between this study and the former is that a longer time record is used here (1862-1985, as opposed to 1904-1985 in Benestad (1999)).

3. FILTERING OF THE EPOCHS

The SSCL can be found by identifying the maxima and/or minima of the sunspot number (Fig. 1b) or by wavelet analysis. There have in the past been attempts to filter the SSCL curve (Friis-Christensen & Lassen, 1991): if there is no sound physical reason for this, such filtering may corrupt the data. On the one hand, a reconstruction of the times of sunspot maxima and minima using a filtered curve will give a squeezed and stretched version of the original one, and the timing of the maxima/minima will be shifted. The timing of the maxima and minima can be reconstructed from the SSCL curves, and using smoothed SSCL records gives a shift in the timing of the maximum and minima (marked with '+'and 'o' in Fig. 1b). On the other hand, the filtering will introduce a non-linear transform where cycles before/after long adjacent epochs have equal influence on a given cycle as those before/after short adjacent epochs.

4. HOW TO ESTIMATE CONFIDENCE INTERVALS?

Often statistical tests do not make sense without some confidence interval: Can the null hypothesis be rejected? The estimation of such confidence intervals require much careful thought. It is important that the test is objective and that in principle any outcome is equally probable: the null distribution must be appropriate for the particular case. Monte Carlo (MC) tests are often used for testing the null hypothesis using many random processes that mimic the behaviour of the processes in question. But, how should one deal with the long-term trends? Fig 2a-b show the distribution plots for two MC tests for the same data series, but with the difference that the data had been detrended prior to the analysis in a) and the observed trends were added to the surrogate data in b). The null-distribution in panel b) is biased towards negative values compared to the distribution for detrended series. The addition of random trends tends to increase the spread of the null-distribution (not shown). The unbiased 5% MC confidence limit is ≈ 0.48 for SSCL and 0.54 for R_z .

The significance estimates of the Pearson correlation r for two series with a few number of N independent (subsampled, defined midway between minima and maxima respectively) data points can also be found from (*Press* et al., 1989, p.533):

$$t = r\sqrt{\frac{(N-2)}{(1-r^2)}}.$$
 [4]

If n is the length of the data record and ρ_1 is the maximum autocorrelation of the two series, then N can be estimated by taking $N \approx n(1-\rho_1)/(1+\rho_1)$ (*Wilks*, 1995, p.127). The test statistic t is distributed according to a t-distribution:

$$f(t;N) = \frac{1}{\sqrt{N\pi}} \frac{\Gamma[(N+1)/2]}{\Gamma[N+1]} (1 + t^2/N)^{-(N+1)/2}.$$

All test statistics in Fig. 1a indicate insignificant relationships at the 5% level according to Eq. 4, which is also confirmed by the MC test. These confidence measures are only "rule-of-thumb" estimates. The p-value in the regressional analysis is estimated according to standard ANOVA procedure.

5. ALTERNATIVES TO PEARSON CORRELATION

Other alternatives to the correlation analysis include the more robust Spearman rank correlation and correlation between the tendencies (let $z=x_n - x_{(n-1)}$). Long-term trends carry little weight in the latter method. Spearman rank correlation scores for detrended SSCL and R_z respectively: -0.07 and 0.60 (P-values estimated from *Sneyers* (1990) eq. 1.4.2.1 (4)). The rank correlations indicate lower scores for SSCL and higher for R_z than the Pearson correlation scores. The correlation analysis for the differentiated series are 0.06 and 0.17 respectively. The Wolf number is more correlated with the terrestrial temperature than the SSCL.

6. CORRELATION BETWEEN THE HEMISPHERIC MEAN TEMPERATURES: A SIGN OF EXTERNAL FORCING?

Sometimes the correlation between the two (detrended) hemispheric mean temperatures have been interpreted as evidence of external (solar) forcing (e.g. Hoyt & Schatten (1993)). Equatorial climate variations, such as ENSO which is a result of oceanatmosphere coupling and not solar activity, affect the temperatures in both hemispheres. Hence, there may be more than one explanation for inter-hemispheric correlation/coherence. It is easy to demonstrate from coupled ocean-atmosphere general circulation model results that the mean temperature of the two hemispheres are correlated. The model integration shown in Fig.2 was integrated without information on the solar activity. The correlation can be explained in terms of large-scale equatorial anomalies.

7. USING SUNSPOTS FOR THE PREDICTION OF THE GLOBAL MEAN TEMPERATURE

The ultimate test of solar-terrestrial relationships is to use the solar data to make predictions for the future. Ordinary linear regression can be used for making empirical predictions schemes. The global mean temperature and sunspot data for an early period have been used to calibrate the linear regression model (Fig 3), and the same model has been used to make predictions for more recent temperature not used in the model calibration. The model coefficients and the predictions fluctuate greatly with the number of data points when only the early data is used for model calibration, which is a sign of a poor fit (poor data quality?). Models based on more than 16 points can account for up to 40% of the variance and the regression p-value is down to 3%. Predictions with univariate models suggest no skill for SSCL-based models, but the R_z models give similar results as the bivariate model. Further experiments replacing the global mean temperature with northern hemispheric mean temperature produce similar results. Both detrended and non-detrended analyses are shown.

8. CONCLUSIONS

One of the main points made in this paper is that all external factors that can influence or "contaminate" the tests must be eliminated or accounted for in order to arrive at valid conclusions. It is also important to stress that the tests must be appropriate and objective, so that any outcome is in principle equally probable and the test is not predisposed. Although the signals are weak, these results suggest that we cannot entirely reject the hypotheses proposing a connection between sunspots and the terrestrial temperature. The SSCL and terrestrial temperature are not related.

REFERENCES

Benestad, R.E. 1999. Solar Activity and Global Sea Surface Temperatures. Astronomy & Geophysics,

Table 1. Correlation scores (in %) between the global mean temperature and proxy solar activity data with corresponding p-values given in parentheses (%). The rows show statistics for non-detrended data, y, detrended data, y_{dt} , differenced data. z. and Spearman rank correlation.

	61-month	low-pass	121-month	low-pass
	SSCL	R_z	SSCL	R_z
y	-41 (31)	31 (45)	-45 (39)	79 (06)
Ydı	-10 (80)	14 (73)	-17 (75)	52 (31)
z	-07 (87)	10 (81)	06 (92)	17 (79)
rank	-01 (99)	26 (52)	-07 (90)	60 (19)

40(June), 14-17.

- Friis-Christensen, E., & Lassen, K. 1991. Length of the solar cycle: an indicator of solar activity closely associated with climate. *Science*, **254**, 698.
- Helland-Hansen, B., & Nansen, F. 1920. Temperature variations in the North Atlantic ocean and in the atmosphere. Smithsonian miscelleneous collections, vol. 70, no. 4.
- Hoyt, D.V., & Schatten, K.H. 1993. A Discussion of Plausible Solar Irradiance Variations 1700-1992. Journal of Geophysical Research, 18, 18,895-18,906.
- Monin, A.S. 1972. Weather Forecasting as a Problem in Physics. The MIT Press. English translation from Russian.
- Mursula, K., & Ulich. T. 1998. A New Method to determine the Solar Cycle Length. *Geophys. Res. Lett.*, **25**, 1837-1840.
- Press, W.H., Flannery, B.P., Teukolsky, S.A., & Vetterling, W.T. 1989. Numerical Recipes in Pascal. Cambridge University Press.
- Sneyers, R. 1990. On statistical analysis of series of observations. Technical note 143. WMO.
- Wilks, D.S. 1995. Statistical Methods in the Atmospheric Sciences. Orlando, Florida, USA: Academic Press.

ACKNOWLEDGMENTS

This work was supported by the Norwegian Meteorological Institute.

9. FIGURES

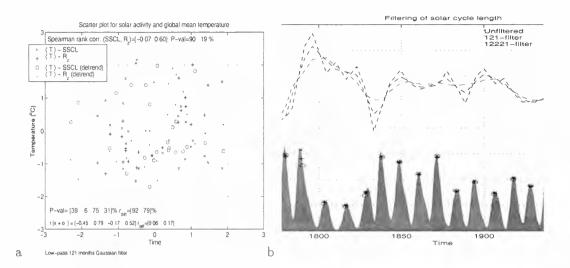


Figure 1. a) Scatter plot between the global mean temperature and non-detrended and detrended sunspot data. b) The Wolf number (histogram), estimate of the SSCL (black dashed curve), and low-pass filtered versions of this. The symbols 'x', '+' and 'o' mark reconstructed times of maxima using unfiltered and two filtered SSCL records.

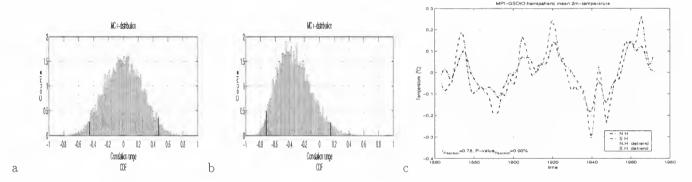


Figure 2. The null-distribution of two MC tests on SSCL and $\langle T \rangle$: a) where the series have zero long-term trend, and b) where all the time series have deterministic trends. c) Correlation between the two hemispheric mean temperatures from ECHAM4 GSDIO.

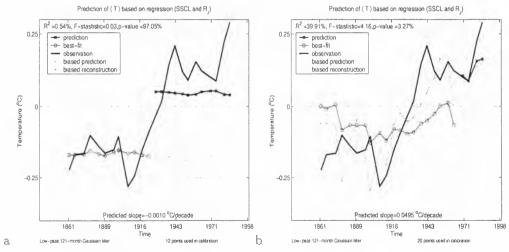


Figure 3. Prediction studies using linear bivariate least-squares best-fit models calibrated with the first 12 (a) and 20 (b) data points and using the remaining points for validation. R^2 , F-ratio and p-value are based on the calibration period.

THE 11 YEAR SOLAR CYCLE AND THE MODERN INCREASE IN THE δ^{13} C OF PLANKTONIC FORAMINIFERA OF A SHALLOW-WATER MEDITERRANEAN SEA CORE (590-1979)

G. Cini Castagnoli¹, G. Bonino², C. Taricco³ and S.M. Bernasconi⁴

^{1.2.3} Istituto di Fisica Generale dell'Universita' and Istituto di Cosmogeofisica del C.N.R., C.so Fiume, 4, 10133, Torino, Italy

¹+39-011-6306809, Cini@icg.to.infn.it, ²+39-011-6306808, Bonino@ph.unito.it,

³+39-011-6306812, Taricco@icg.to.infn.it,

⁴ Geology Institute, ETH-Zentrum, Sonneggstrasse 5, 8092 Zurich, Switzerland,

+41-1-6323693, Stefano@ethz.ch

ABSTRACT

In this paper we discuss the $\delta^{13}C$ profile of Globigerinoides ruber measured in the GT90/3 shallowwater Ionian sea core, spanning the time interval 590-1979 AD. The most important features revealed in this profile are: i) the 11-y cycle, determined at high confidence level, ii) an increase of -0.4% from 650 (Dark Age) to 1050 AD (Medieval Optimum) and iii) a Modern Increase (MI) of -0.3% from 1770 to 1940 AD. We show that in order to explain the $\delta^{13}C$ 11y amplitude variation (0.08 %) measured in our core, we must introduce an atmospheric effect amplifying the illumination cycle, expected from the solar Hy irradiance variation (0.1%). This effect can be found in a change of cloud coverage paced by the solar cycle, according to the mechanism proposed by Svensmark and Friis-Christensen (1997).

Cloud cover changes are here proposed also to interpret the MI of the last century. An observed decreasing trend in rainy days of about 11% at the site of the core deposition could account for about 2/3 of the MI.

INTRODUCTION

In the last few years, our research activity has been mainly devoted to the study of climatic change in the past centuries through the measurements of oxygen and carbon isotopic ratios in the planktonic for G. ruber deposited in shallow water Ionian sea sediments (Cini Castagnoli et al., 1999a, 1999b, 2000a). In these papers, using different spectral methods, we have shown the imprint in the time series of the variability of the solar output. In fact, the 11-year component is identified in the records at high significance level by Monte Carlo-Singular Spectrum Analysis (MC-SSA; Allen, 1992; Allen and Smith, 1996; Dettinger et al. 1995; Ghil and Taricco, 1997). An evidence for a 22 y-cycle in the δ^{18} O series has also been reported (Cini Castagnoli et al., 2000b). Recently we have prolonged the δ^{13} C profile down to 590 AD and we have shown the presence (beside the 11-year signal) of 2 centennial cycles (100 and 200 years) (Cini Castagnoli et al., 2000c). The centennial and the decadal components have the same amplitude (peak-to-trough) of 0.08%. A comparison between the δ^{13} C profile and the historical aurorae series (600-1500 AD) shows that the δ^{13} C long term variations are at least partially of solar origin undergoing similar long-term modulations as those of the aurorae time series, induced by the solar-wind interactions with the geomagnetic field.

In this paper we focus attention on the amplitude of the δ^{13} C Modern Increase (MI) from 1770 to 1940 and we compare it to the amplitudes of other variations recorded in the series and in particular to that of the 11 year cycle.

EXPERIMENTAL PROCEDURE

The core GT90/3 is one of the cores we took during different campaigns from the Gallipoli terrace (Gulf of Taranto, Puglia, Italy). The extraction site of this core $(39^{\circ}45'5''N, 17^{\circ}53'3''E)$ is at a water depth of 174 m. We have demonstrated the uniform stratigraphy of the platform and we have obtained an accurate dating, using the following methods:

1) *Radiometric methods* were applied in the upper part of the cores (Cini Castagnoli et al., 1990; Bonino et al., 1993), indicating that in this terrace 1 cm of sediment is deposited in 15.5 years. This high sedimentation rate allows to obtain a high temporal resolution.

2) Tephroanalysis methods. Owing to the position of the site with respect to the volcanic Campanian area, westerly winds bring into the sediment the ashes of the eruptions (clinopyroxenes of clear volcanic origin characterized by skeletal morphology and sector zoning). These markers can be used to test down core the sedimentation rate, obtained by radiometric methods in the upper part. A record of the eruptions is found in the written historical documents all throughout the last two millennia, since roman times. The first historical eruption is the Vesuvius explosion of the year 79 AD, which destroyed the city of Pompei. With the help of other 21 volcanic markers, the sedimentation rate s was found to be quite constant along the cores and uniform throughout the whole platform in the last two millennia, $s=(0.0645\pm0.0007)$ cm y⁻¹. The depth scale was therefore transformed in a very accurate time scale, tested with an accuracy better than 1%.

In order to measure isotopic ratios in foraminifera G.ruber of the core, we sampled it at 2.5 mm in a continuous sequence. Samples of about 5 g of sediment were soaked in 5% Calgon solution over night then treated in 10% H₂O₂ to remove any residual organic material, subsequently washed with distilled water jet through a sieve (150 µm). The fraction >150 µm was kept and oven-dried at 50°C. G. ruber were picked up under microscope. For each sample, 20-30 specimens of G.ruber were selected for the isotopic determination. The stable isotope measurements were performed using а VG-PRISM mass spectrometer fitted with an automated ISOCARB preparation device. Analitical precision based on internal standards was better than 0.1%c. Calibration of the mass spectrometer to VPDB scale was done using NBS19 and NBS18 carbonate standards.

RESULTS AND DISCUSSION

In order to confirm the uniform stratigrafy of the Gallipoli terrace and to verify the reproducibility of δ^{13} C measurements, we have measured δ^{13} C also in 33 samples from the top of an other core (GT91/1) taken from the same platform at a water depth of 250 m (39°59′25′N, 17°45′52′E). In figure 1 the δ^{13} C profiles of the GT90/3 core (dashed curve) and of the GT91/1 core (solid curve) are shown.

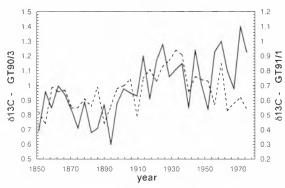


Figure 1: $\delta^{\prime 3}C$ in two cores extracted from the Gallipoli terrace.

Although the mean values of the two profiles are different, the two cores being taken 30 km apart one from the other and at different water depths (Cini Castagnoli et al., 1993), we note that the δ^{13} C relative variations are the same.

It is commonly accepted that $\delta^{13}C$ variations in the shells of symbiontic foraminifera mainly record the effects of symbiont density and of photosynthetic activity at the time of their growth. Therefore the signal is of climatic nature. Experiments performed in vitro on *G. sacculifer* (unfortunately not on *G. ruber*) show that there is a relationship between the illumination level of the specimens and their $\delta^{13}C$ (Spero e Lea, 1993). In a linear approxymation, it can be expressed as:

(1)
$$\Delta \delta^{13} C = 0.02 \Delta I (\Delta \delta^{13} C \text{ in } \%, \Delta I \text{ in } W/m^2).$$

However other factors which may contribute to the formation of the carbon isotope signal cannot be ruled out (Russel and Spero, 2000).

In figure 2, 359 δ^{13} C values (590-1979 AD; light curve) are shown as a function of time with a time resolution of 3.87 years, corresponding to a sampling interval of 2.5 mm.

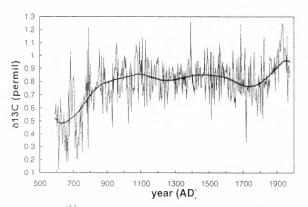


Figure 2: $\delta^{I3}C$ profile of the GT90/3 core (light curve) and the SSA-reconstructed trend (heavy curve).

Superposed on the original profile we show the SSAreconstructed trend (RCs 1,2,3; heavy curve). MC-SSA analysis (Cini Castagnoli et al, in preparation) suggests that δ^{13} C series consists at 95% confidence level of a) a trend, including a 200 year component (RCs 1, 2, 3), b) a periodic component of 11.3 y (RCs 8, 9), c) a periodic component of 100 y (RCs 4, 5 and 6, 7), d) AR(1) noise. We note that the trend shows an increase 0.4‰ from 650 (Dark Age) to 1050 AD (Medieval Optimum) and a Modern Increase (MI) of 0.3‰ from 1770 to 1940 AD. The MI is comparable in shape to the natural one occurring at the transition from the Dark Age to the Medieval Optimum.

In order to calibrate the δ^{13} C curve in terms of variations of the solar irradiance, we may tentatively relate the average 0.08% $\delta^{13}C$ 11-y peak-to-trough amplitude variation (described by RCs 8, 9) to the direct effect of the 0.1% variation of the solar irradiance measured in space in the last two solar cycles by high accuracy radiometers (Froehlich and Lean, 1998). In doing so, we realise immediately that the small direct solar forcing does not verify the proposed experimental relationship between illumination and $\Delta\delta^{13}C.$ In fact the change of illumination at sea level in our site of 0.15 W/m² (Cini Castagnoli et al., 2000c), due to the 0.1% solar irradiance variation, would produce a $\delta^{13}C$ change of 0.003%, smaller by more than one order of magnitude with respect to the observed one. Therefore an amplification factor for the illumination change must exist. This can be found in a change of cloud coverage paced by the solar cycle. Svensmark and Friis-Christensen (1997) suggested that global cloud cover correlates closely with the galactic cosmic ray intensity, which varies with the sunspot cycle. More clouds, less

illumination and lower δ^{13} C. Over a sunspot cycle, the absolute variation of global cloud cover was found to be about 3% on an average total cloud coverage of about 65% (Svensmark, 1998). A more recent analysis (Svensmark, this SOLSPA meeting) indicates that it is the low altitude cloud fraction (below about 3.2 km) that gives the significant correlation with the changes of the cosmic ray flux. The absolute variation in low cloud cover is of about 2% over a solar cycle. In a recent proposal of the CLOUD collaboration at CERN for a study of the link between cosmic rays and clouds, with a cloud chamber at the CERNPS (Kirkby, this SOLSPA meeting), the effects of the observed absolute variation of cloud cover on the Earth's radiation budget are discussed. Estimates from the Earth's Radiation Budget Experiment (ERBE) (Hartmann, 1993) indicate that low clouds, 26.6% of the total global fraction of the Earth's surface cover (63.3%), produce a net cooling due to the dominance of the increased albedo of short wave solar radiation of -20.2 W/m². The short waves control the photosynthetic processes, originating our signal. The variation paced by the solar cycle would therefore produce a peak-to-trough change in the illumination at the sea level of 1.5 W/m² (2% * 20.2Wm²/26.6%).

The corresponding variation in δ^{13} C expected by (1) should therefore be 0.03%c. This is of the same order of magnitude of the measured value. This favours the hypothesis that the direct effect of the solar irradiation variation has to be amplified by concomitant atmospheric effects.

The long term changes of the last century will now be discussed in terms of the decrease in cloud cover observed over the same area in the last century. A decrease in cloud coverage has been observed from 1875 to 1975 in the region in which we took the core. The meteorologist De Giorgi has collected an accurate homogeneous archive of rainfall data from 1875 to 1921 in Lecee (Puglia). In the paper of Mangia et al. (1991) those data have been integrated up to 1980 by using data taken in Bari. A decrese of annual rainy days (with rainfall >0.2 mm) of about 11% between 1875 and 1980 has been reported. In figure 3 we compare the δ^{13} C data (dashed line) with the number of rainy days per year (solid line).

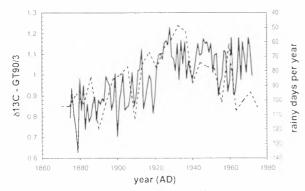


Figure 3: Dashed line: modern $\delta^{3}C$ increase; solid line: decrease of rainy days per year.

We note that the rainy days decrease of 30 days per year, i.e. of -11%, is concomitant with the $\delta^{13}C$ MI of -0.3%c.

The Apulian observations are confirmed by other evidences. Buffoni et al. (1999) have analysed the precipitation in Italy from 1833 to 1996. On a yearly basis a decreasing trend in precipitation of the order of 10% has been found statistically significant. Furthermore Russo et al. (2000) have observed in the long running time series of rainy days over Genova a decrease of about 10% between 1833 and 1992 with an unvarying negative tendency throughout the whole period.

Therefore the experimental decrease in our area of about 11% of rainy days between 1875 and 1980 can be used for interpreting the carbon isotope effect. Assuming that a rainy day corresponds to a whole day with low cloud coverage, we can evaluate an increase of irradiation in the last century of 20.2*11%/26.6%=8.4 W/m² over our site during the δ^{13} C modern increase of about 0.3%. From (1), this change in illumination gives an increase of 0.2% in $\delta^{13}C$. We can conclude that the $\delta^{13}C$ data, together with the cloudiness evidence and the in-vitro experiments on foraminifera, support the view that cloud cover decrease accounts for about 2/3 of the MI during the last century at the site of the core deposition. Other factors influencing the carbon isotopic fractionation effect cannot be ruled out and may account for -30% of the signal.

ACKNOWLEDGMENTS

We thank Prof. C. Castagnoli for his support and discussions and A. Romero for continuous technical assistance.

This work was supported by MURST-Co-fin 98.

REFERENCES

- Allen M.R. (1992): Interactions between the atmosphere and oceans on timescales of weeks to years. PhD Thesis, Clarendon Laboratory, Oxford.
- Allen M.R. and Smith L.A. (1996): Monte Carlo SSA: detecting irregular oscillations in the presence of coloured noise, J. Clim., Vol. 9, p.3373, 1996.
- Bonino G., Cini Castagnoli G., Callegari E. and Zhu G.M. (1993): Radiometric and tephroanalysis dating of Recent Ionian Sea cores, *Nuovo Cimento*, Vol.C16, pp.155-161, 1993.
- Buffoni L., Maugeri M. and Nanni T. (1999): Precipitation in Italy from 1833 to 1996. *Teor. Appl. Climatol.*, Vol.63, pp.33-40, 1999.
- Cini Castagnoli G., Bonino G., Caprioglio F., Provenzale A., Serio M. and Zhu G.M. (1990): The carbonate profile of two recent Ionian sea cores: evidence that the sedimentation rate is constant over the last Millennia, *Geophys.Res.Lett*, Vol.17, pp.1937-1940, 1990.
- Cini Castagnoli G., Bonino G. and Taricco C. (1993):

Cronologia dei sedimenti marini costali e fenomeni cosmogeofisici negli ultimi 5000 anni, *Nuovo Cimento*, Vol.C16, pp.795-806, 1993.

- Cini Castagnoli G., Bernasconi S.M., Bonino G., Della Monica P., Taricco C. (1999a): 700 year record of the 11 year solar cycle by planktonic foraminifera of a shallow water Mediterranean core, *Adv. Space Res.*, Vol.24, pp.233-236, 1999.
- Cini Castagnoli G., Bernasconi S.M., Bonino G., Della Monica P. and Taricco C. (1999b): Solar activity in the last millennium recorded in the δ^{18} O profile of planktonic foraminifera of a shallow water Ionian sea core, *Sol. Phys.*, Vol. 188, pp.191-202, 1999.
- Cini Castagnoli G., Bonino G., Taricco C. (2000a): Long term solar-terrestrial records from sediments: carbon isotopes in planktonic foraminifera during the last millennium, *J.of Atm. And Solar-Terr. Phys.*, in press, 2000.
- Cini Castagnoli G, Bonino G. and Taricco C. (2000b): 22 year cycle in the planktonic δ^{18} O of a shallowwater Ionian sea core, *Nuovo Cimento*, Vol.C23, pp.449-452, 2000.
- Cini Castagnoli G, Bonino G., Taricco C. and Bernasconi S.M. (2000c): Solar radiation variability in the last 1500 years recorded in the carbon isotope ratio of a Mediterranean sea core, *Adv. Space Res.*, in press, 2000.
- Dettinger M.D., Ghil M., Strong C.M., Weibel W. and Yiou P. (1995): Software expedites singularspectrum analysis of noisy time serie, *EOS Trans.* AGU, Vol.76, p.12, 1995.
- Froehlich C. and Lean J. (1998): The Sun's total irradiance: cycles, trends and related climate change uncertainties since 1976, *Geophys.Res. Lett.*, Vol.25, pp. 4377-4380, 1998.
- Ghil M. and Taricco C. (1997): Advanced spectralanalysis methods, in Past and Present Variability of the Solar-terrestrial System: Measurement, Data Analysis and Theoretical Models, Proc. of the Int. School of Physics E.Fermi, Varenna, 1996, Course CXXXIII, edited by G.Cini Castagnoli and A.Provenzale (IOS Press, Amsterdam), pp.137-159, 1997.
- Hartmann D.L. (1993): Radiative effects of clouds on Earth's climate, in Aerosol-cloud-climate interactions, *Int. Geophys. Series*, Vol.54, p. 151, P.V.Hobbs ed., Academic Press Inc., S.Diego, 1993.
- Mangia C., De Sanctis L.V., Ruggiero L., Zito G., Zuanni F. (1991): Un secolo di precipitazioni piovose a Lecce, 4th Workshop Progetto strategico: Clima, ambiente e territorio nel mezzogiorno, ISIATA-CNR, Lecce, pp.153-161, 1991.
- Russel A.D. and Spero H.J. (2000): Field examination of the oceanic carbonate ion effect on stable isotopes in planktonic foraminifera, *Paleoceanography*, Vol.15, no.1, pp.43-52, 2000.

- Russo G., Eva C., Palau C., Caneva A. and Sacchini A. (2000): Nuovo Cimento, Vol.C23, pp.39-52, 2000.
- Spero H.J. and Lea D.W. (1993): Intraspecific stable isotope variability in the planktonic foraminifera Globigerinoides sacculifer: Results from laboratory experiments, *Mar. Micropaleontol.*, Vol.22, pp.221-234, 1993.
- Svensmark H. and Friis-Christensen E. (1997): Variation of cosmic ray flux and global cloud coverage- a missing link in solar-climate relationships, J.Atmos.Sol.Terr.Phys., Vol.59, pp.1225-1232, 1997.
- Svensmark H. (1998): Influence of cosmic rays on Earth's climate, *Phys.Rev.Lett.*, Vol.81, pp.5027-5030, 1998.

THE LONG-TERM SOLAR CYCLICITY (210 AND 90 YEARS) AND VARIATION OF THE GLOBAL TERRESTRIAL AIR TEMPERATURES SINCE 1868

V.A.Dergachev¹ and O.M.Raspopov²

¹Ioffe Physico-Technical Institute, Russian Academy of Sciences Politekhnicheskaya 26, 194021 St.Petersburg, Russia tel: + 7 812-247-9981 / fax: +7 812-247-1017 / e-mail: v.dergachev@pop.ioffe.rssi.ru ²St.Petersburg Branch of Institute of Terrestrial Magnetism, Ionosphere and Radiowaves Propagation, RAS Muchnoy per. 2, P.O. Box 188, 194023 St.-Petersburg, Russia tel: +7 812-552-8500 / fax: +7 812-310-5035 / e-mail: oleg@omr.izmi.ras.spb.ru

ABSTRACT

A quantitative analysis of the long-term variations of solar activity, total solar irradiance and terrestrial air temperature are presented. The analysis of changes in sunspot records, auroral intensity, $^{14}\mathrm{C}$ and $^{10}\mathrm{Be}$ levels in the Earth's atmosphere and other proxy data shows evidence of ~210- and ~90- year periodicities. A large number of investigations have been dedicated to this problem. It is established that there are numerous statistical similarities among a variety of solar indices and climate data on multiple temporal and spatial scales. Recently obtained data concerning the evolution of the Sun's open magnetic flux, the solar irradiation and modulation of galactic cosmic rays (GCR) show the existence the long-term variations of "solar constant" and intensity of GCR. The changes of the average surface temperature of the Earth for the last 150 years show the good correlation with long-term trend of solar activity, taking into account the solar cyclic variations of the ~210- and ~90-year periods. Thus the significant part of the increasing of the Earth's surface temperature during the last 100 years may be related to the long-term cyclicity in the Sun's processes. From this point of view, supposing the existence of 210- and 90- year periodicities in long-term variation of solar activity and solar irradiation as well as in modulation of GCR, it is possible to explain main features in global temperature changes.

INTRODUCTION

The fundamental source of all energy in the Earth's climatic system is the Sun. Thus, variations in solar output and solar activity may provide a means for radiative forcing of climatic changes. The influence of solar activity on climate remains one of the most important problems of solar-terrestrial physics. The data recently obtained have shown the existence of long-term changes of the solar magnetic fields and related to its changes of the solar irradiation and solar activity (Lockwood et al.,1999; Wang et al., 2000; Lockwood and Stamper, 1999; Soon et al., 2000). The value of the long-term changes of solar irradiation is significantly greater than that recorded by satellites during the 11year solar cycle (Lockwood and Stamper, 1999). Soon et al. (2000) have shown that variations of solar coronal hole area related to structure of the solar magnetic fields correlate well with variations of lower troposphere This correlation demonstrates the temperatures. existence of indirect action of solar activity on the terrestrial climate through galactic and solar cosmic-ray action on the optical properties and radiation balance of the terrestrial atmosphere. The estimation made by Lockwood and Stamper (1999) demonstrated that the long-term variations of solar irradiation play а

significant role for solar forcing on terrestrial climate change as also suggested by number of other studies (Lean et al., 1995; Cliver et al., 1998) The results mentioned above demonstrate actuality of detailed analyses of the long-term periodicity and trends of solar activity in the past and especially for the last 100 - 150years. This is important for estimation of the problem of long-term climatic changes in the future and for analysis of natural and anthropogenic ("greenhouse effect") contribution on climate changes. We have centered attention on a manifestation of the long-term solar cyclicity (mainly 210 years) in different natural archives and its relation to climatic changes.

210-YEAR SOLAR CYCLE IN HISTORICAL CHRONICS

A direct indication of long-term solar activity may be provided only by sunspots observed by instrumental methods and spots visible on the Sun's disc in the pretelescopic periods. As it is established by the satellite measurements the sunspot periods are accompanied by periodic variations in the solar luminosity. The investigation of long-term cyclicity in solar variability may be inferred from historical observations of both sunspots and auroras, reports of which extend back more than two millennia.

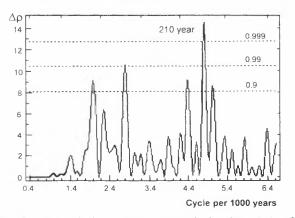
The behavior of solar activity in the past is based on the different catalogue of non-telescopic sunspot observations. Wittman and Xu (1988) have studied cyclic variations of solar activity from a catalogue of naked-eye sunspots covering the period 165 BC to 1986 AD. In power spectra they extract significant peaks at periods of 8.4, 10.0, 11.1, 12.2, 56.0 and 92.5 years. They pointed out that 92.5-year period correspond to the Gleissberg cycle, which manifests itself in an amplitude modulation of the 11-year cycle. Xu (1990) reviewed many historical materials of solar observations in ancient China, transformed descriptive sunspot records into a numerical time series and obtained the detailed power spectrum of long-term variations of solar activity over 2000 years. It appeared that the 210-year cycle has the largest significance in the power spectrum. Nagovitsin (2000), using the Wittman and Xu catalogue of naked-eye sunspots, received four time series that characterize the different side of solar activity in the past. He established some pronounced peaks at periods of 11, 90, 200, 400 years.

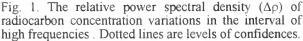
Power spectral analysis of historical auroral data from 450 AD to 1450 AD, carried out by Feynman (1988), show a strong line at 88.4 ± 0.7 years verifying the existence of the Gleissberg cycle in auroras during that 1000 years. The minima in sunspot amplitude and

auroral frequency occurred at about 1901 and 1811. There is no direct evidence of changes in solar irradiance during the Holocene. However, we do know that some characteristics of the Sun's output did change during the Holocene on the century time scale. Historical evidence shows that the scope of sunspots has varied markedly, occurring on a number of occasions during the past thousand years. The Maunder minimum of the 17^{th} century is the most recent and well known of these. This sunspot minimum are also associated with periods of enhanced 14 C production rate in the Earth's atmosphere.

210-YEAR CYCLE IN NATURAL ARCHIVES

Evidence of solar variability on the century time scales during the Holocene in the atmospheric ¹⁴C variations is indisputable and this type of solar variability must be considered to be a permanent feature of the Sun's behavior. Global-scale climate fluctuations of the Little Ice Age type appear to be associated with these concentration anomalies. This implies that significant irradiance variations occur in parallel with the solar fluctuations responsible for the ¹⁴C anomalies. This link has been examined previously by a number authors, e.g. Damon et al. (1978); Neftel et al. (1981). Suess (1973) was the first who derived a dominant ~200-year line in early ¹⁴C concentration data from tree rings of known date. This cycle was noisy and was not at first accepted by other investigators, although later its reality was generally agreed. Subsequently, a number of investigators, using different spectral methods of analysis of radiocarbon concentration over the long time scale, estimated the value of this period from 202 to 210 years. Raisbeck et al. (1990) extracted the ~200-year in "Be concentration from core from South Pole. Vasiliev and Dergachev (1995) demonstrates the very high significance of the 210-year period that was displayed in radiocarbon time series (Figure 1).





The isotopes ¹⁴C and ¹⁰Be are produced by similar physical interactions of cosmic radiation with the nuclei in the Earth's atmosphere but their geochemical pathways to the ground are very different. It allows to attribute the 210-year period to modulation of cosmic ray flux by the solar variability with this period. It will be noted that the historical records of sunspots and discovery minima of solar activity are in agreement with

the ${}^{14}C$ and ${}^{10}Be$ data in showing the existence of ~ 210 -year period.

There are a number of new investigations that suggest statistically significant ~210-year cyclicity in various natural archives. The regular 206-year wave was traced by Castagnoli et al. (1990) in the thermoluminescence profile of a recent sea sediment core. Evidence of the 210-and 90-year periodicity was shown also in variation of acidity in Greenland Crete ice core data (Shumilov et al., 2000). This variations of acidity relate to variations of atmospheric aerosols generated by galactic cosmic rays (GCR). Correlation coefficient between variations of Wolf number and acidity background is rather high (r=-0.8). So, aerosol background variations are in phase with cosmic ray intensity changes, and the maximal amount of aerosols would be created during minima of solar activity. Comparison of the results of the spectral analysis of the δ^{18} O from Greenland GRIP ice core, the ⁴C concentration from German oak chronology, and the German varves chronology for the Holocene recently was carried out by Schlüter (1999). The strong ~210year line is traced in the all mentioned above Earth's archives. Important result was obtained by Roig et al. (2000). They showed the evidence of ~210 year periodicity in tree-ring growth around 50,000 years BP from subfossil trees from Pelluco, Seno de Revoncavi, Chile.

Sonett and Suess (1984) showed a convincing correlation between variations of cosmic ray-produced ¹⁴C activity of the CO₂ in the terrestrial atmosphere during the past millennia and annual growth ring widths for bristlecone wood from Campito Mountain in eastern California (3384 m). The relative power spectral densities for the ¹⁴C concentration and growth of ring widths demonstrated that both time series contain cyclic features, in particular a prominent spectral line of about 210 year. The appearance of the 210-year period in the ¹⁴C data. repeated in the tree-ring data, strongly supports the arguments that this solar-based signal is reflected in the growth rate of wood in the bristlecone pines. It will be noted that although time series examined are statistically non-stationary the ~210-year line is strong over the entire period.

THE SURFACE TEMPERATURE RECORD

It is well known that the predictions of future climate based predominantly on the record of temperature derived from terrestrial weather stations. There are temperature profiles of a smoothed averaged annual global time series of the many individual land and sea estimates surface temperature records with of uncertainty defined by different methods, e.g., Jones et al. (1977). Most of the temperature rises occurred since ~1910 up to ~1940, the temperature also rises from \sim 1975 up to now, the most temperature decrease took place since ~1945 to ~1975. Since the late of 19th century up to now the increase in global surface temperatures is in the range about $0.6\pm0.2^{\circ}$ C. The linear trend in surface temperature over the period 1979-1989 is about 0.15°C. As will be shown below, the pronounced different phases in the observed temperature changes during the considered time interval can be explained taking into account the long-term variability in solar activity and solar irradiance.

DISCUSSION

In situ satellite observations suggest that there may be a solar effect on surface temperature due solar variability on a decadal time scale. These observations show that at periods of higher solar variability the whole troposphere and the lower stratosphere become warmer as a result of the increasing total solar irradiance. Statistical investigations suggest that solar effect may have contributed substantially to global surface temperature changes on decadal to century time scales. A climatic effect caused by total solar irradiance variations may become more effective when its impact lasts longer. Variations in the total solar irradiance can be monitored by changes in solar cycle length, sunspot structure and others indirect data. By studying the effect of the changes of solar irradiance with periods of 11(22). 80-90 and 210 years on the atmosphere from historic and proxy records, we may hope to come to a better understanding of the Earth's atmosphere and how it responds to changing of total solar irradiance.

The rise of solar magnetic flux from 1901 up to now (Lockwood et al., 1999) is a significant indication for the century time scale variations of total solar irradiance. From a linear relationship between magnetic flux and the total solar irradiance they have evaluated the value of the rise of the total solar irradiance during 1901-1995 as 1.65 ± 0.23 Wm⁻². So it may be expected that an effective action of total solar irradiance is undergone to considerable change taking into account the Maunder and Gleissberg modes of solar activity. When we takes the midpoint of the Maunder minimum of solar activity at approximately 1690-1700 AD, the next minimum of the 210-year solar cycle occured near 1900 AD, since then the solar irradiance is increased. Each of these pronounced minima of solar activity coincided with coolings. When the peaks of the Maunder and Gleissberg modes were connected by an enveloping curve, we obtained some complicated trend of the enhanced solar variability, which remains to be continued during a few years of new century (Fig. 2). Dergachev and Raspopov (2000)

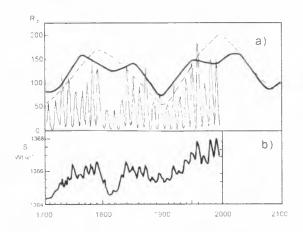


Fig. 2. Changes in time of: (a) solar activity: R_z is the sunspot number, the broken curve shows the 210-year cycle of solar activity and the thick curve shows the lineal combination of 90- and 210-year cycles of solar activity: (b) the reconstructed total solar irradiation (Lean et al., 1995).

To produce a quantity proportional to the envelope of the solar cycle, we smooth the time series of sunspot number by taking an 11-year running mean. The same procedure was carried out for the most recent time series of solar irradiance, geomagnetic aa-indices and global average SST. Figure 3 shows 11-year running means of a) solar irradiance, b) sunspot number, c) aaindices and d) global average SST anomalies. There is an obvious long-term trend in all time series.

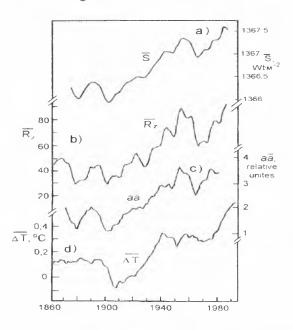


Fig. 3. Long-term changes of 11-year running averages of: (a) the total solar irradiation (Lockwood and Stamper, 1999); (b) the sunspot number; (c) the geomagnetic aa-index; (d) the anomalies of the surface temperature of the Earth.

Although these four curves are somewhat distinguished. they have enough points of similarity to arrive at a conclusion on the existence of a causal relationship between them. All curves have minima near 1900-1910 AD and maxima near 1950-1960 AD. All curve have the same increase between 1910 and 1950 AD and the decrease between 1960 and 1980 AD. The key features of the global SST curve and the variation in the solar irradiance, sunspot numbers and aa-indices, shown in this Figure, agree with the combined long-term trend of solar activity (Fig. 2). taking into account the cyclic variations of the ~90- and 210-year periods. In such case, we can draw an conclusion that the solar irradiance might vary in phase with the long-term trend of the solar activity and global average SST variations are responded on the long-term change of solar irradiance. As shown by these figures, changes in total solar irradiance are the major driver of climate change in the 20th century and earlier. These results suggest that a substantial part of the low-frequency temperature variability appear to be related to variations in external forcing. The proposed mechanism explains the general changes that have been observed during the 20th century and also explains the past few hundred years of climate records.

As the last minimum of the large-scale 2400-year cycle associated with cold epoch was during the Little Ice Age, the next Little Ice Age would be expected only in a

too distant future. At present we are concerning with the increasing trend of the 2400-year cycle and we will temperature increase. observe only Thus, the modulation of the sunspot cycle over 210 years in combination with of the Glaissberg cycle might be expected to have a larger effect on climate than the 11year period. The synchronism of these four time series opens a possibility of long term forecasts.

CONCLUSIONS

Existence of ~ 210- and 90-year solar periodicity in climatic signals obtained from tree-ring growth data, sea sediments, varves, ice core δ^{18} O, aerosol record etc. shows that solar irradiance and input of solar energy to the Earth might be varied with the long-term variations and trends of the solar activity.

The changes of the average surface temperature of the Earth for the last 150 years show the good correlation with long-term trend of solar activity, taking into account the solar cyclic variations of the ~210- and ~90 year periods. Thus the significant part of the increasing of the Earth's surface temperature during last 100 years may be related to the long-term cyclicity in the Sun's processes.

ACKNOWLRDGEMENT

This work was supported by the RFBR (grant 00-05-64921) and by EC (INTAS grant 97-31008 and INCO-COPERNICUS grant "EXTRATERRESTRIAL").

REFERENCES

- Castagnoli, G. C., Bonino, G., Provenzale, A. and Serio, (1990): On the presence of regular M periodicities in the thermoluminescence profile of a recent sea sediment core. Phil. Trans. R. Soc. London, Vol. A330, pp. 481-486. Cliver, E., Boriakoff, V. and Bounar, K. H. (1998):
- Geomagnetic activity and the solar wind using the Maunder minimum. Geophysical Research Letters, Vol. 25, p. 897-900.
- Damon, P.E., Lerman, J.C. and Long, A. (1978): Temporal fluctuations of atmospheric ¹⁴C: causal factors and implications. Annual Rev. Earth Planet. Sci. Vol. 6, pp. 357-494.
- Dergachev, V.A. and Raspopov, O.M. (2000): Longterm processes on the Sun determining tendency of the solar irradiation and the Earth's surface temperature changes. Geomagnetism and Aeronomy, Vol. 40, No. 3, pp. 9-14.
- Feynman, J. (1988): Solar, geomagnetic and auroral variations observed in historical data. In F.R.Stephenson and A.W.Wolfendale (eds.) Secular Solar and Geomagnetic Variations in the Last 10,000 years, Kluwer Academic Publishers, pp. 141-159.
- Jones, P.D., Osborn, T.J. and Briffa, K.R. (1997): Estimating sampling errors in large-scale temperature averages. J.Climate, Vol. 10, pp. 2548-2568.
- J., Beer, L., and Bredley, R. (1995): Lean, Reconstruction of solar irradiance since 1610:

implications for climate change. Geophysical Research Letters, Vol. 22, pp. 3195-3198.

- Lockwood, M. and Stamper, R. (1999): Long-term driftof the coronal source magnetic flux and the total solar irradiance. Geophysical Research Letters, Vol. 26, pp. 2461-2464.
- Lockwood, M., Stamper, R. and Wild, M. N. (1999): A doubling of the Sun's coronal magnetic field during the last 100 years. Nature, Vol. 399, pp.437-439
- Neftel, A., Oeschger, H. and Suess, H.E. (1981): Secular non-random variations of cosmogenic carbon-14 in the terrestrial atmosphere. Earth Planet. Sci. Letters, Vol. 56, pp. 127-147.
- Nagovitsin, Yu.A. (2000): Solar activity of two millennia: "Sun's Service" in China of the Ancient and Middle Ages. Geomagnetism and aeronomy. Vol. 40 (in press).
- Raisbeck, G. M., Yiou, F., Jouzel, J and Petit, J. R. (1990): ¹⁰Be and δ^2 H in polar ice cores as a probe of the solar variability's influence on climate. Phil. Trans. R. Soc. London, V. A330, pp. 463-470.
- Roig, F. A., Le-Quesne, C., Boninsega, J. A., Lara, A., Grudd, H., Briffa, K., Jones, P and Villgran, C. (2000): A 1,229-year tree-ring record from late Pleistocene in Southern Chile. Book of Abstract of International Conference on Dendrochronology for the Third Millennium, Mendoza, Argentina, Publ. IANIGLA-CONICET, p. 109.
- Schlüter, A.-D. (1999): Vergleichende Analyse paläoklimatologischer Proxydaten fur das Holozän. Diplomarbeit, Meteorologischen Institut der Freien Universität Berlin, 87 p. Shumilov, O.I., Kasatkina, E. A., Raspopov, O. M. and
- Turunen E. (2000): Combined influence of solar and volcanic activity on climate in the past. Geomagnetism and Aeronomy, (in press. Soon, W., Baliunas, S, Posmentier, E. S. and Okeke, P
- (2000): Variations of solar coronal hole area and terrestrial lower tropospheric air temperature from 1979 to mid-1998: astronomical forcing ofchange in the Earth's climate? New Astronomy, Vol. 4, pp.563-579.
- Sonett, C. P. and Suess, H. E.(1984): Correlation of bristlecone pine ring widths with atmospheric ⁴C variations: a climate-Sun relation. *Nature*, V. 307, pp. 141-143.
- Suess, H.E. (1973): Natural radiocarbon. Endeavour,
- Vol. 32, pp. 34-38. Vasiliev, S. S. and Dergachev, V.A. (1995): A change of natural radiocarbon level in the Earth's atmosphere and the geomagnetic field Geomagnetism and Aeronomy, Vol. 35, No. 5, 147-151.
- Wang, Y.-M., Lean, J. and Sheeley, N. R., Jr. (2000): The long-term variation of the Sun's open magnetic flux. Geophysical Research Letters, Vol. 27, pp. 505-508.
- Wittman, A.D. and Xu, Z. (1987): A catalog of nontelescopic sunspot observations. Astronomy and Astrophysics. Suppl. Ser. Vol. 70, pp. 83-94.
- Xu, Zhentao (1990): Solar observations in ancient China and solar variability. *Phil. Trans. R. Soc. London.* Vol. A330, pp. 513-515.

LONG-TERM VARIABILITY OF SOLAR ACTIVITY DURING THE HOLOCENE

V.A.Dergachev¹, O.M.Raspopov² and S.S.Vasiliev¹

¹Ioffe Physico-Technical Institute, Russian Academy of Sciences Politekhnicheskaya 26. 194021 St.Petersburg, Russia tel: + 7 812-247-9981 / fax: +7 812-247-1017

e-mail: v.dergachev@pop.ioffe.rssi.ru / sergey.vasiliev@pop.ioffe.rssi.ru ²St.Petersburg Branch of Institute of Terrestrial Magnetism, Ionosphere and Radiowaves Propagation, RAS Muchnoy per. 2, P.O. Box 188, 194023 St.-Petersburg, Russia tel: +7 812-552-8500 / fax: +7 812-310-5035 / e-mail: <u>oleg@omr.izmi.ras.spb.ru</u>

ABSTRACT

Spectral analysis of long series of the radiocarbon concentration in tree-rings for the Holocene has shown the existence of a number of spectral maxima. However, the some harmonics features are not independent. We resolve a number of periods: 2400. 940, 720, 570, 420, 360, 230, 210, 190 years applying the methods of analysis on the non-stationary time series, as the frequency-time method and bi-spectral analysis, to the radiocarbon concentration during the last 8.000 years. The long period of about 2400 years in this time series is more pronounced. Analysis shows that the periods of 210, 420, and 720 years are primary and related to solar activity. Besides the amplitudes of primary periods are modulated by the 2400-year period. The periods of 190, 230, 360, 570, and 940 years are a result of generation of combinative frequencies by interaction of the 2400 year oscillation and oscillation with other primary periods.

INTRODUCTION

The most reliable and detailed information about changes of solar activity and cosmic ray flux is based on direct observations. The cosmic ray flux, observed in the upper atmosphere of the Earth, varies with changes in solar activity. A significant correlation between the cosmic-ray flux modulation and the 11-year sunspot cycle was established by Pomerantz and Duggal (1974). The solar activity has a maximum during the period of sunspot number maximum but cosmic ray fluxes have the lowers level at the same time. During intervals of low sunspot activity a larger galactic cosmic-ray flux arrives in the upper atmosphere.

Annual global ¹⁴C production, as calculated from observed neutron fluxes, varies with the 11-year solar cycle (O'Brien, 1979). It was established, e.g., Stuiver and Quay (1980), that a variable solar modulation of the cosmic ray flux causes cosmogenic ¹⁴C to change on a decadal to century time scales. Sunspot, auroral and ¹⁰Be data suggest that decadal and century type ¹⁴C fluctuations are also primarily influenced by the Sun. The history of fluctuations of cosmogenic ¹⁴C and ¹⁰Be can be derived from their concentration in tree-rings and ice cores, correspondingly.

High-precision measurements were carried out to analyze of the radiocarbon concentration in tree rings of well-known ages to study causes of changes in atmospheric ¹⁴C concentration in the past. This work was done in different laboratories over the world during last 25 years. Many measurements have been made, both of continuous annual series of tree-ring samples, covering time scale from decades to hundreds of years, and of continuous samples of decadal or bidecadal rings, spanning several millennia, e.g., Stuiver and Becker (1986): Stuiver and Becker (1993). ¹⁴C measurements show three types of fluctuations: shortterm (years to several decades); medium-term (decades to several hundreds of years) and long-term (thousands of years). These fluctuations are characterized by a different amplitude of changes in the ¹⁴C concentration: from fractions of a percentage to ~10%. The same pattern can be traced in the ¹⁰Be concentration from ice cores, e.g., Finkel and Nishizumi (1997).

It is able to draw important conclusions about the ¹⁴C activity level in wood samples of known age by examining ¹⁴C concentration. One can observe the physical manifestation of approximately 210- and 2400-year cycles (Dergachev and Chistyakov, 1995) in the relative deviations of the ¹⁴C concentration in high-precision ¹⁴C measurements of dendrochronologically dated wood samples. The mathematical manifestation of these cycles can be obtained by applying statistical techniques of time series analysis. Houtermans (1971) was a pioncer in revealing the most long 2400-year cycle in unequally spaced ¹⁴C data by statistical methods. After Houtermans (1971) this large-scale cycle was borne out by analyzing the spectral characteristics of the high precision ¹⁴C data with different techniques of time series analysis (e.g., Suess, 1980; Damon and Linick, 1986; Hood and Jirikowic (1991).

The high amplitude variations in the cosmogenic ¹⁴C and ¹⁰Be during the last millenium correlate well with Wolf, Spörer, Maunder and Dalton solar minima. Thus it possible to explain the periodicity in ¹⁴C concentration as result of solar forcing. The goal of the present work is to study the nature of different spectral maxima of ¹⁴C concentration during the Holocene. We tried to select the maxima which relate to the basic periodicity of solat activity and maxima which have other nature.

THE CYCLIC FLUCTUATIONS OF ¹⁴C RECORDS

In our study we used of high-precision 14 C series from 6.000 BC till 1950 AD in dendro-chronologically dated

490

wood samples (Stuiver and Becker, 1993) for investigation of the cyclic fluctuations in14C concentration. The average standard deviation for sets of data is about 0.2-0.3 percent. The resulting ¹⁴C time sequence represents a monotonous long-term change of the relative radiocarbon concentration (Δ^{14} C) modulated by short-. medium, and long-term fluctuations. This fluctuations are quasi-periodic with the periods from tens till thousand years. In order for study the peculiarities of fine structure in ¹⁴C time series, it is necessary to remove the monotonous long-term trend from the initial data. Figure 1 shows the $\Delta^{14}C_D$ sequence, which is the result of subtraction of the trend from the initial ¹⁴C time sequence of Stuiver and Becker (1993).

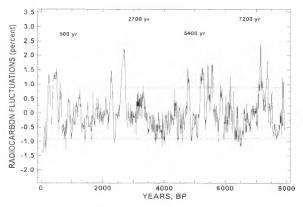


Fig. 1. The time series of $\Delta^{14}C_D$ after subtraction of the long-term trend. The dotted lines are located on the levels of triple experimental error (3 σ). Four pronounced intervals in excess of 3 σ level marked by the vertical dotted lines.

One can observe that peaks above the level of 3σ may by seen to be approximately 500, 2700, 5400, and 7200 years ago. These extrema represent the large-scale changes of radiocarbon concentration during the last 8000 years and relate ton several high amplitudes in $\Delta^{14}C_D$ of the Maunder mode of solar minimum during the Holocene. It is significant that these events in $\Delta^{14}C_D$ coincide with cold epochs revealed by Schmidt and Gruhle (1988) in dendroclimatic data. as well as with glacier expansions shown, e.g., by Rothlisberger (1986). The epochs of $\Delta^{14}C_D$ fluctuations with high amplitude recur through approximately 2200 years.

This non-stationary $\Delta^{14}C_D$ sequence was examined by Vasiliev and and Dergachev (1998), using different types of spectral analyses. The power spectrum of the $\Delta^{r_4}C_D$ concentration is shown in Figure 2. The power spectrum in Figure 2 shows a very strong line with the period of ~ 2400 years, having the amplitude substantially exceeding the amplitudes of other lines in the spectrum. This component with period of ~2400 years is the principle component of super-long changes in the temporal $\Delta^{14}C_{\rm D}$ sequence. The low-frequency filtration in a vicinity of this period allows to find maxima of long-term changes of the radiocarbon concentration. Such filtration was carried out by (1998). and Dergachev Vasiliev The result demonstrated that the location of maxima of 2400-years oscillation coincide with $\Delta^{14}C_D$ maxima shown in the Figure 1.

Vasiliev and Dergachev (1998) have analyzed distribution of the $\Delta^{14}C_D$ oscillation (Figure 2) for

different frequencies by using the multiple filtration method (Dziewonski et al., 1969) during the Holocene. As it follows from this analysis the amplitude of $\Delta^{14}C_D$ series cyclically varies in time and the amplitude changes are synchronous in the wide frequency band. It turns out that the epochs of $\Delta^{14}C_{\text{D}}$ fluctuations with high amplitude are recurred through 2300-2500 years . It means that the amplitude of $\Delta^{14}C_{\text{D}}$ are modulated by principal periodicity of 2400-years in different This long-period amplitude frequency ranges. modulation was revealed before by Sonett (1984) only for the ~210-year period in radiocarbon concentration variations. In accordance with our results. the ~2400year change of the amplitude takes place also in the other harmonics extracted in this $\Delta^{14}C_D$ sequence (Figure 2). It should be noted that the amplitude of lines in radiocarbon power spectra arises with the increase of a period.

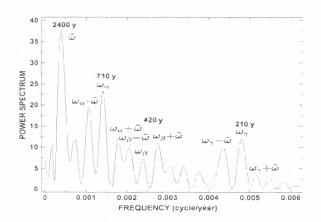


Fig. 2. The power spectrum of the $\Delta^{14}C_D$ series. The horizontal axis is marked by frequency, on vertical axis there is shown the normalized power spectral density. A number denotes the period (years) of primary spectral components. A greek symbol shows the frequency of primary and side lines (see table 1).

BI-SPECTRUM OF $\Delta^{14}C_D$ SEQUENCE

The more detailed study of the interrelation between the \sim 2400-year variation and other secular components in the temporal $\Delta^{14}C_D$ sequence can be made by the use of bi-spectral analysis (as the review, see King, 1996). The bi-spectral method is applied to the analysis of non-linear processes and complex interactions in geophysical data. The bi-spectrum is calculated by means of Fourier transformation of the autocovariation function of the second order, depending on two shifts.

The procedures of bi-spectral method in many respect is analogous with the routine spectral analysis. The bispectrum may be considered as a function of two frequencies. ω_x and ω_y . From properties of bi-spectrum follows that if the data involve harmonics with the frequency ω modulated by frequency ϖ , the analysis must reveal maxima of two-dimensional spectral density P(ω_x , ω_y). Figure 3 shows the projection of twodimensional spectral density P(ω_x , ω_y) on the plane (ω_x , ω_y). The dark areas in the plot correspond to local maxima of spectral density. The symmetry of the left and right part of the spectrogram is well seen. Because of symmetry it is enough to analyze the part of spectrogram in the sector bounded by lines S1 and S2.

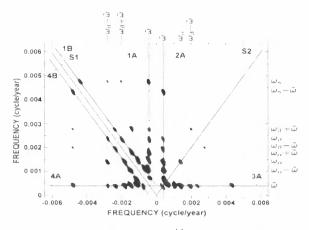


Fig. 3. The bi-spectrum of the $\Delta^{14}C_D$ series. A dark spot designates peak top. The lines marked as S1 and S2 are the symmetry axes of left side ($\omega_x < 0$) and right side ($\omega_x > 0$) correspondingly. The position of vertical lines 1A and 2A with tops located on them is defined by the 2400-year period.

This Figure shows two vertical lines, marked as 1A and 2A, with projections of peak tops on them. The ω_x location of these vertical lines correspond to the period of ~2400 years. Moreover, the inclined line 1B located above the left axis of symmetry S1 with the vertical offset. corresponding to the period of ~2400 years is of interest. In addition to it. Figure 3 represents curves 4A. 3A and 4B, which are mirrors in relation to 1A, 2A and 1B. The fact that the projection of peak tops are located on these lines, it is the evidence of monotonous change of amplitude of the primary harmonics forming the spectrum of temporal $\Delta^{14}C_D$ variations. The period of monotonous changes is equal to the ~2400 years. By analyzing bi-spectrum there had been derived the primary harmonics ω_{α} , ω_{β} and ω_{γ} in power spectrum (Table 1).

Table 1. Results of the bi-spectral analysis of a $\Delta^{14}C_D$ series. The periods are given in the years.

Period	2400	940	710	570	500
Status	ធ	$\omega^{\alpha} - \omega$	ωα	ωα+ϖ	ω _β -ϖ
Period	420	360	230	210	190
Status	ωβ	$\omega_{\beta} + \overline{\omega}$	ω, -ω	ωγ	ω _γ +ϖ

Due to the effect of modulation there are some images of primary harmonics ω_{α} , ω_{β} , ω_{γ} on the bispectral diagram. For instance, for the frequency ω_{α} we can see the spots $(-\overline{\omega}, \omega_{\alpha})$ and $(-\overline{\omega}, \omega_{\alpha}+\overline{\omega})$ on the line 1A, the spots $(\overline{\omega}, \omega_{\alpha})$ and $(\overline{\omega}, \omega_{\alpha}-\overline{\omega})$ on the line 2A, and the spots $(-\omega_{\alpha} + \overline{\omega}, \omega_{\alpha})$ and $(-\omega_{\alpha}, \omega_{\alpha}+\overline{\omega})$ on the line 1B. It will be noted that the part of spots is not designated due to weakness of the spectral line with frequency $\omega_{\gamma} + \overline{\omega}$. The existence and the location of mentioned peak tops on the bispectrogram demonstrates the existence of the mechanism of ~2400-year modulation of the atmospheric radiocarbon concentration.

NATURE OF ~2400-YEAR MODULATION

It is possible to consider three sources of \sim 2400-year modulation of the radiocarbon concentration: solar activity, change of carbon dioxide transfer between the atmosphere and ocean (climatic influence) and variations in the dipole magnetic moment with the period of \sim 2400 years.

In works of Elsasser. Ney and Winckler (1956); O'Brien (1979) the mechanism of effect of the geomagnetic field on radiocarbon production rate is grounded and described. The number of produced atoms ¹⁴C is proportional to $\mu(t)^{0.52}$, where $\mu(t)$ is the magnetic dipole moment of the Earth. Damon and Linick (1986) analyzed the possibility to explain the change of amplitude of 210-year carcon cycle from this point of view. However, according to archaeomagnetic and palaeomagnetic data for the value of the Earth's dipole magnetic moment does not provide sufficient fluctuations with this period (Damon and Sonett, 1992).

The scenario of possible climatic effect on amplitude variations of the radiocarbon concentration was considered by Vasiliev. Dergachev and Raspopov (1999). The amplitude of 2400-year cyclical wave in the $\Delta^{14}C_D$ as a result of climatic effect on exchangeable processes in carbon system was estimated. We used the three-reservoir model of exchangeable carbon with parameters from work of Damon. Lerman and Long (1978) and the relationship between changes of the temperature and concentration $\delta^{18}O$ (Salamatin et al., 1998) It appears that the relative amplitude of radiocarbon concentration change is in agreement with changes of temperature.

There are numerous palaeoclimatic data, which confirm the cyclic character of climate change with duration of about 2400 year. The results of study by Dansgaard et al. (1984) of the content of the δ^{18} O in the Greenland ice cores have demonstrated the existence of the ~2500year period of climatic nature. The ~2400-year period was found by Pestiaux (1988) in $\delta^{18}O$ concentration of ice cores and in foraminifera from oceanic core. As a result of carried out of the dendroclimatic investigation by Schmidt and Gruhle (1988), it has become distinctly that the Little Ice Age (1500-1800 AD) preceded the cold Hallstattzeit epoch. 750 - 400 BC, and the latest – earlier cold epoch, 3200 – 2800 BC. The position of all three epochs coincides with the epochs of high amplitude in changes of $\Delta^{14}C_D$. Investigations of average temperature extrema of the Atlantic water (Arabadji, 1986) have allowed to reach a conclusion about existence, in particular, temperature minima. having a place 400, 2800 and 5100 years BP. Recently. Finkel and Nishizumi (1997) found a good correlation between the observed millennial-scale variations in the concentration of radiocarbon and ¹⁰Be during the Holocene. The authors interpret the changes in ¹⁰Be concentration as a climatic effect

The solar as the source of excitation of ~2400-year cycle, was considered by Hood and Jiricowic (1990). As during the Holocene there is a close relation between the increase of amplitude fluctuations in $\Delta^{14}C_D$ and the climatic coolings through every ~2400 years and these coolings coincide with pronounced minima in solar activity, the 2400-year fluctuation in carbon reservoir may be caused by solar variability. It seems likely that the regularity of strong climatic changes may be a consequence of solar forcing. The climatic system is very sensitive even to small variations in solar activity.

CONCLUSION

The spectral temporal spectral and bi-spectral analysis were carried out for the high-precision data on

radiocarbon concentration in the Earth's atmosphere for the past 8000 years. It is shown that the amplitude of large-scale fluctuations varies by cyclically. The period of this cycle is about 2300-2500 years. The bi-spectral analysis of data has demonstrated the existence of amplitude modulation. The period of basic modulating component is ~2400 year. As a result of bi-spectral analysis the classification of lines observed in power spectrum is made. In addition to the modulating component, three basic lines, α , β and γ are determined, which have periods respectively 710, 420 and 210 years. The periods of 190, 230, 360, 570, and 940 years which also exist in the $\Delta^{14}C_D$ spectrum are result of generation of combinative frequencies by interaction of the 2400-year oscillation and oscillation with other basic periods. The spectrum contain also the second harmonic (1200 years) of modulating component. The presence at power spectrum of the first and the second harmonics of modulating component (2400 years) and also splitting of ground lines $(\alpha, \beta, \text{ and } \gamma)$ by these harmonics demonstrates that use the modern methods of spectral analyses like bi-spectral method produce more fundamental understanding the physical nature of radiocarbon periodicity during the Holocene. The nature of ~2400-year periodicity is discussed as result of solar forcing.

ACKNOWLEDGEMENTS

We are grateful to EC for supporting of this work under INTAS program (Grant No. 97-31008), and INCO-COPERNICUS (project EXTRATERRESTRIAL), and to RFBR (Grant 00-05-64921).

REFERENCES

- Arabadji, M.S. (1986): In Interior of Light-Blue
- Continent, Moscow, Nedra, 142pp. Damon, P.E. and Linick, T.W. (1986): Geomagnetic-heliomagnetic modulation of atmospheric radiocarbon production. Radiocarbon, Vol. 28, No. 2A, pp. 266-278.
- Damon, P.E., Long, A. and Grey, D.C. (1966): Fluctuation of atmospheric ¹⁴C during the last six millennia, J. Geophysical Research, 7, 1055-1063
- Damon, P.E. and Sonett, C.P. (1992): Solar and terrestrial components of the atmospheric ¹⁴C variation spectrum, In C.P. Sonett, M.S. Giampapa, M.S. Mathews (eds.) The Sun in Time, Tucson, University of Arizona Press, pp. 360-388.
- Dansgaard, W. et al. (1984): North Atlantic climate oscillations revealed by deep Greenland ice core, In J.E. Hansen and T.Takahashi (eds.) Climate Processes and Climate Sensitivity. Washington, D.C., American Geophysical Union, pp. 288-298.
- Dergachev, V. and Chistyakov, V. (1995): Cosmogenic radiocarbon and cyclical natural processes. Radiocarbon, Vol. 37, No. 2, pp. 417-424. Dziewonski, K., Bloch, S. and Landisman, M.A.
- (1969): A technique for the analysis of the transient seismic signals. Bulletin of the Seismological Society of America, Vol. 59, pp. 427-444
- Elsasser, W., Ney, E.P. and Winckler, J.R. (1956):

Nature, Vol. 178, pp. 1226-1227. L.L. and linkowie V

- Hood, L.L. and Jirikowic, J.L. (1990): Recurring variations of probable solar origin in the atmospheric ¹⁴C time record. *Geophysical Research Letters*. Vol. 17, pp. 85-90.
- Houtermans, J.C. (1971): Geophysical interpretation of Bristlecone pine radiocarbon measurements using a method of Fourier analysis of unequally spaced data. Ph. D. Thesis, Univ. of Bern.
- O'Brien, K.(1979): Secular variations in the production rate of cosmogenic isotopes in the Earth's atmosphere. J. Geophysical Research, Vol. 84, pp. 423-431. T. (1996).
- T (1996): Quantifying non-linearity and geometry in time series of climate. *Quaternary* King. Science Reviews, Vol. 15, pp. 247-266.
- Finkel, R.C. and Nishizumi, K. (1997): Berillium 10 concentrations in the Greenland ice sheet project 2 ice core from 3-40 ka. J. Geophysical Research, Vol. 102, No. C12, pp. 26,699-26,706.
- Pestiaux, P., Berger, A. and Duplessy, J.C. (1988): Paleoclimatic variability at frequencies ranging from 1 cycle per 10,000 years to 1 cycle per 1,000 years: Evidence for nonlinear behavior of the climate system. Climatic Change. Vol. 12, No. 1, pp. 9-37
- Pomerantz, M.A. and Duggal, S.P. (1974): The Sun and cosmic rays. Rev. Geophys. Space Physics, Vol. 12, pp. 343-376.
- Rothlisberger, F. (1986): 10 000 Jahre Gletschergeschichte der Erde. Aarau: Verlag Sauerlande.
- Salamatin, A.N. et al. (1998): Ice age dating and paleothermometer calibration based on isotope and temperature profiles from deep boreholes at Vostok Station (East Antarctica). J. Geophysical
- Research, Vol. 103, pp. 8963-8978. Schmidt, B. and Gruhle, W. (1988): Radiokohlenstoffgehalt und dendrochronologie. Naturwissenschaftliche Rundschau, Vol. 5, pp. 177-182.
- Sonett, C.P. (1984): Very long solar periods and radiocarbon record. *Rev. Geophys. Space Physics*, Vol. 22, No. 3, pp. 239-254. Stuiver, M. and Becker B. (1986): High-precision
- decadal calibration of the radiocarbon time scale, AD 1950-2500 BC. Radiocarbon. Vol. 28. No. 2B. pp. 863-910.
- Stuiver M. and Becker, B. (1993): High-precision decadal calibration of the radiocarbon time scale, AD 1950-6000 BC. Radiocarbon, Vol. 35. No. 1, pp. 35-65.
- Stuiver, M. and Quay, P.D. (1980): Changes in atmospheric carbon-14 attributed to a variable Sun. Science, Vol. 207, No. 4426, pp.11-19.
- Suess, H.E. (1980): The radiocarbon record in tree rings of the last 8000 years. Radiocarbon, Vol. 22, No. 2, pp. 200-209.
- Vasiliev, S.S. and Dergachev, V.A. (1998): A change of natural radiocarbon level in the Earth's atmosphere over the past 8000 years as a consequence of solar activity, geomagnetic field and climatic factors: 2400-year cycle. Biofizika, Vol. 43, No.4, pp. 681-688 (in Russian).
- Vasiliev, S.S., Dergachev, V.A. and Raspopov, O.M. (1999): The sources of large-scale variations of the radiocarbon concentration in the Earth's atmosphere. Geomagnetism and Aeronomy. Vol. 39, No. 6, pp. 80-89.

THE 1940'S TEMPERATURE DECREASE IN LOCATIONS OF ARGENTINA

Teresita Heredia⁽¹⁾, Nieves Ortiz de Adler⁽¹⁾ and Ana G. Elías^(1,2)

⁽¹⁾Laboratorio de Física de la Atmósfera – Departamento de Física

Facultad de Ciencias Exactas y Tecnología – Universidad Nacional de Tucumán (UNT)

⁽²⁾Departamento de Ecología – Facultad de Agronomía y Zootecnia – (UNT)

Avenida Independencia 1800 – (4000) Tucumán – Argentina - tel/fax: 54 381 4364596

-the redia @herrera.unt.edu.ar/adler @arnet.com.ar/aelias @herrera.unt.edu.ar/aelias @herrera.unt.ed

ABSTRACT

Southern Hemisphere (SH) Temperature time series corresponding to argentine meteorological stations located between 22° and 26° S latitude, and at altitudes between 400 m and 3000 m above sea level, are analyzed. The environmental conditions are also different ranging from industrialized to unpolluted regions. The stations and periods are La Quiaca (1911–1991), Salta (1901-1991) and Tucumán (1856–1999)

The Anomaly of the annual mean Temperature, TA (deviation from the mean calculated over the complete data set) shows a trend to decrease for the period 1940-1970. The 1940's cooling is unexpected according to the Global Warming theory. For this period, it should not be expected changes in the increasing trend of temperature responding to an increasing greenhouse gases concentration since the 19th century, when the industrial epoch began.

The annual mean temperature have decreased 0.4, 1.1 and 1.2°C for La Quiaca. Salta and Tucumán respectively, since 1940 to 1970.

TA for each series analyzed correlates with SCL (Solar Cycle Length is the interval between successive sunspots maximum or minimum). Temperature decrease agrees with a SCL increase. Being the correlation coefficients 0.90 for La Quiaca and Salta and 0.80 for Tucumán over 1940-1970.

Each station analyzed behaves like Northern Hemisphere Land air Temperature Anomaly (NHLTA). At least in the period analyzed the variation of the argentine stations temperature appears to have been modulated by the varying solar activity as represented by SCL. An expected contribution to the greenhouse effect due to anthropogenic sources seems to be less dominant in 1940-1970 temperature records compared to solar influences.

INTRODUCTION

For many years it has been considered the possibility that changes in the sun may affect weather and climate on Earth. Many studies tried to correlate solar activity and meteorological parameters. Historically observations of solar activity were restricted to sunspot number and it was not clear its physical connection to meteorological factors. Friis-Christensen and Lassen (1991) correlated solar activity reflected by SCL and Northern Hemisphere Land air Temperature Anomaly (NHLTA). They found that the long-term variation of NHLTA is negatively correlated with the long-term variation of solar activity during the interval of available temperature records from 1861 to 1989. NHLTA shows a trend to increase except in the interval 1940–1970 for which there is a cooling in coincidence with SCL increasing. Their result have attracted attention in the debate related to the climate change because it would be seen as a proof that global warming is more influenced by solar activity variations than by greenhouse gases.

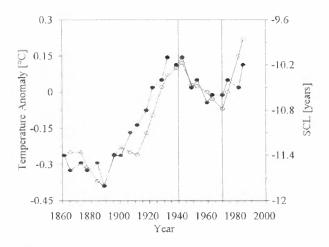


Figure 1. Northern Hemisphere Land air Temperature Anomaly (filled circle), and Solar Cycle Length, (empty circle) assigned to the central year of each cycle.

In Figure 1 it can be observed that NHLTA shows a surprising cooling over the period 1940-1970 unexpected according to the Global Warming theory by Greenhouse gases enhancement. For this period, it should not be expected changes in the increasing trend of temperature responding to an increasing greenhouse effect since the 19th century, when the industrial epoch began

The aim of this work is to search if in other temperature series the 1940-1970 cooling is observed.

Proc. 1st Solar & Space Weather Euroconference, The Solar Cycle and Terrestrial Climate', Santa Cruz de Tenerife, Tenerife, Spain, 25-29 September 2000 (ESA SP-463, December 2000)

The monthly mean temperature data used in this work, was obtained at the Laboratory of the National Climatic Data Center of the NOAA (National Oceanic and Atmospheric Administration) where all the quality and homogeneity testing was done with temperature time series.

Mean annual land air temperature has been used to calculate the anomaly of temperature.

Data of three meteorological argentine stations located at different geophysical and environmental conditions, are considered:

La Quiaca (22.1S, 65.6W); 3459 masl - Rural Salta (24.8S, 65.5W); 1221 masl - Urban Tucumán (26.8S, 65.1W); 450 masl- Urban

SOLAR CYCLE LENGTH

Solar activity is far from being constant. One of its periodicities is the varying number of sunspot (R_z). The length of a sunspot period from minimum to minimum as well as from maximum to maximum is known as the Solar Cycle Length (SCL). A SCL is described as an 11-year period but the actual length varies between 8 and 17 years (Friis-Christensen and Lassen 1991,1992) in such a way that short solar cycles implies high activity levels while long solar cycles are associated to low activity levels. This solar parameter has a longterm periodicity of about 80-90 years, the Gleissberg cycle. The length of the solar cycle may be disturbed by accidental variations and a low-pass filter is applied to the SCL series in order to remove short variations. This filter is a moving average with weight 1, 2, 2, 2, 1. In this work, SCL smoothed series were used.

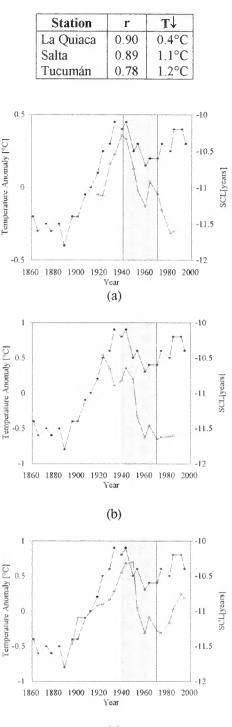
RESULTS

In order to determine the association between TA and the long-term solar variation, the mean value of TA for each solar cycle was calculated.

In Figure 2, TA and SCL have been drawn for the three stations here analyzed.

During the period 1940-1970 TA varies in the range $(-0.1 \text{ to } 0.3)^{\circ}$ C for La Quiaca, $-(0.5 \text{ to } 0.6)^{\circ}$ C for Salta, and $(-0.5 \text{ to } 0.7)^{\circ}$ C for Tucumán. Although TA range of variation is different from station to station, its behavior is quite similar in all the cases. The difference in TA range of variation is attributable to the different conditions of the meteorological stations.

The correlation coefficient (r) between TA and SCL for period 1940-1970, and temperature decrease $(T\downarrow)$ for each station are the following:



(C)

Figure 2: Solar Cycle Length, SCL, in years (filled circle), Temperature Anomaly value in °C (empty circle) for each solar cycle and assigned to the central year of each cycle for the stations: (a) La Quiaca; (b) Salta; (c) Tucumán.

Although each station is located at different elevations and environmental and geophysical conditions, the cooling around the 1940's, observed clearly in all of them, is very similar (Figure 3).

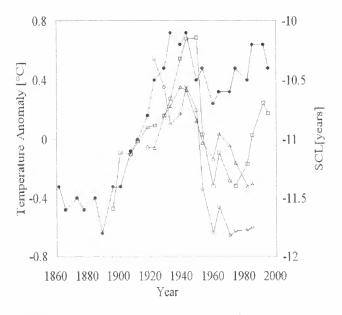


Figure 3: Temperature Anomaly of La Quiaca (empty triangle), Salta (empty circle), Tucumán (empty square) and SCL (filled circle).

The TA behavior of SH stations, where land/ocean relationship is different than in the NH, agrees with the NHLTA behavior.

The 1940's cooling, between 0.4°C and 1.2°C, is unexpected according to the global warming theory by greenhouse gases enhancement. For this period, it should not be expected changes in the increasing trend of temperature responding to an increasing greenhouse effect since the 19th century, when the industrial epoch began.

In the pre-industrial epoch, before 1850, the concentration of greenhouse gases seems to have remained almost constant, but since then, it has been monotonically increasing (Tsonis and Elsner, 1989; Mann et al., 1998; Victor, 1998). In figure 4 it can be noticed the steep increase in CO_2 atmospheric content -one of the greenhouse gases- during the period 1958-1988, and it is assumed that the upward trend will continue in the future. Due to the warming effects of the greenhouse gases, a continue rise in temperature is expected.

A possible cause of land air temperature decrease is volcanic eruptions. A large volcanic eruption injects large amounts of SO_2 into the lower stratosphere, which is converted into H_2SO_4 aerosols with a typical lifetime of 2-3 years. The most obvious impact is to scatter some of the incoming radiation producing cooling at the Earth's surface that lasts for about two years (Mao and Robok, 1998).

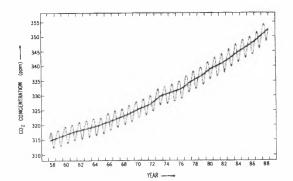


Figure 4: Atmospheric CO_2 concentration, measured at Mauna Loa Observatory, Hawaii (19.5°N, 155°W) between 1958 and 1988 (after Peixoto and Oort, 1992). Thick solid line was fitted to the monthly data showing the annual trend. The trend at Mauna Loa is generally accepted be representative of the global trend.

In the period 1940-1970 the only strong volcanic eruption was the Agung (8.5°S, 115.5E) in 1963 with 800 DVI (Dust Veil Index is a numerical index that quantifies the impact of volcanic eruption's release of dust and aerosols over the years following the event). The close volcanic eruptions were Novarupta in 1912 with 150 DVI and Santa Elena in 1980 with 100 DVI. So, volcanic eruptions would not be enough to explain the decrease observed in temperature.

During the period analyzed, temperature long-term behavior follows SCL variations, in such a way that the temperature decreases when SCL increases in spite of the enhancement of the greenhouse gases occurred during this period. Temperature behavior seems to be more affected by solar influences than by environmental, geographical or anthropogenic ones.

REFERENCES

- Friis-Christensen, E. and K. Lassen: Length of the solar cycle: an indicator of solar activity closely associated with climate; *Science*, 254, 698-700, (1991)
- Friis-Christensen, E. and K. Lassen: Global temperature variations and a possible association with solar activity variations. Scientific Report 92-3, Danish Meteorological Institute, (1992)
- Mann, M.E., R. S. Bradley and M.K. Hughes: Globalscale temperature patterns and climate forcing over the past six centuries, Nature, 392, 779-187, (1989)
- Mao, J. and A. Robok: Surface air temperature simulations by AMIP General Circulation Models: Volcanic and ENSO signals and systematic errors, Jour. of Climate, 11, 1538-1552, (1998)
- Peixoto, J.P. and A.H. Oort: Physics of Climate, American Inst. of Physics Press, U.S., 520 pp., (1992)
- Tsonis, A.A. and J.B. Elsner: Testing the global warming hypothesis, Geophys. Res. Lett., 16, 137-140, (1989)
- Victor, D.G.: Strategies for cutting carbon, Nature, 395, 837-838, (1998)

SOLAR WIND NEAR EARTH: INDICATOR OF VARIATIONS IN GLOBAL TEMPERATURE

Theodor Landscheidt

Schroeter Institute for Research in Cycles of Solar Activity, 11227 Cabot Trail, Belle Côte, Nova Scotia B0E 1C0, Canada Tel. (902) 235-2281. E-mail: theodor.landscheidt@ns.sympatico.ca.

Abstract. Near-Earth variations in the solar wind, measured by the geomagnetic *aa* index since 1868, are closely correlated with global temperature (r = 0.96; $P < 10^{-7}$). Geomagnetic activity leads temperature by 4 to 8 years. Allowing for this temperature lag, an outstanding *aa* peak around 1990 could explain the high global temperature in 1998. After 1990 the geomagnetic aa data show a steep decline comparable to the decrease between 1955 and 1967, followed by falling temperatures from 1961 through 1973 in spite of growing anthropogenic CO₂ emissions. This points to decreasing global temperature during the next 10 years.

Introduction

The total magnetic flux leaving the Sun, dragged out by the solar wind, has risen by a factor of 2.3 since 1901 (Lockwood et al., 1999). Concomitantly, global temperature has increased by 0.5° C. The energy in the solar flux is transferred to the near-Earth environment by magnetic reconnection and directly into the atmosphere by charged particles. There are indications that this energy has meteorological effects within days after solar eruptions which generate highspeed streams in the solar wind (Roberts and Olson, 1973; King, 1974; Stolov and Shapiro, 1974; Schuurmans, 1979; Prohaska and Willett, 1983; Neubauer, 1983; Bucha, 1983; Herman and Goldberg, 1985; Tinsley, 1996). As there is a linear relationship between magnetic flux and solar irradiance, the 130% rise in the Sun's magnetic flux since 1901 indicates a rise in the average total solar irradiance of 1.65 W m⁻² (Lockwood and Stamper, 1999). The respective radiative forcing in the atmosphere is 0.29 W m⁻², corresponding to 0.23° C at a moderate climate sensitivity of 0.8° C/W m⁻². This increase of 0.23° C potentially accounts for nearly half of the change in the Earth's global temperature over the same period. Charged particles and indirect solar wind effects make a strong additional contribution.

Svensmark and Friis-Christensen (1997) have shown that global cloud cover, observed by satellites, is linked to the strength of galactic cosmic rays modulated by the solar wind (r = 0.95). This effect, attributed to cloud seeding by ionized secondary particles (Pruppacher and Klett, 1997), induced a change in cloud cover by more than 3% within 3 1/2 years. The corresponding change in radiative forcing is in the range 0.8 to1.7 W m⁻². This is significant, as the total radiative forcing by CO₂ accumulated in the atmosphere since pre-industrial times is about 1.5 W m⁻². Measurements of cosmic ray flux registering myons instead of neutrons go back to 1937. When Svensmark (1998) compared these data with temperature in the Northern Hemisphere, his results were corroborated. Short-term observations confirm the connection. Forbush decreases - sudden deep drops in cosmic ray flux within 2 days after energetic solar eruptions - coincide with local shrinking of cloud cover by 3% (Pudovkin and Veretenenko (1995). In the long run, climate would not be affected if the amplitude of the indirect solar wind effect on clouds did not change. The strength of the solar wind, however, has increased by a factor of 2.3 since 1901.

Direct and indirect effects, taken together, point to a dominant role of solar activity in climate change. Accordingly, many of the recent publications in the field of solarterrestrial relationships range the Sun's contribution between 50 and 100 % (Friis-Christensen and Lassen, 1991; Lean et al., 1995; Lau and Weng, 1995; Landscheidt, 1995; Soon et al., 1996; Svensmark and Friis-Christensen, 1997; Reid, 1997; White et al., 1997; Svensmark, 1998; Cliver et al. 1998 a, b; Labitzke, 1999).

Correlation analysis

The strongest contributors to the solar wind intensity are energetic solar eruptions (coronal mass ejections, flares, and eruptive prominences) which create the highest velocities in the solar wind and shock waves that compress and intensify magnetic fields in the solar wind plasma. Coronal holes have a similar effect. So it suggests itself to investigate whether periods of strong plasma ejections on the Sun are connected with temperature on Earth. Not all strong eruptions have an impact on the near-Earth environment. The effect at Earth depends on the

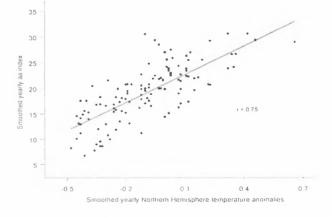


Figure 1. Scatter plot of yearly means of the geomagnetic *aa* index and Northern Hemisphere land air and sea surface temperature anomalies 1868-1998. The *aa* data are shifted to offset a 6-year lag of temperature. The slope of the regression line and the aggregation of the slightly smoothed data around the straight line fit indicate a close correlation (r = 0.75) which is highly significant ($P < 10^{-7}$).

heliographic position of the eruptions and conditions in interplanetary space. Indices of geomagnetic disturbances measure the response to those eruptions that actually affect the Earth. Mayaud's *aa* index of geomagnetic activity (Mayaud, 1973; Coffey, 1958-1999) is homogeneous and covers the long period 1868 to present. So I compared it with temperature. The correlation between temperature and the length of the 11-year sunspot cycle, established by Friis-Christensen and Lassen (1991), only covers land air temperature. Hence I selected a time series that combines Northern Hemisphere land air temperature anomalies (Jones, 1994) with sea surface temperature anomalies (Parker et al., 1995). A scatter plot of the raw yearly data shows a promising positive correlation between *aa* and temperature (r = 0.48).

If there were a causal connection, temperature should lag the aa index. So I computed the correlation coefficients for different lags and found that the correlation reaches a maximum when temperature lags aa by 6 years. The scatter plot in Fig. 1 is based on aa data that were shifted by 6 years to offset the temperature lag. The data were subjected to three-point smoothing. The least-squares linear fit line indicates a strong correlation (r = 0.75) which explains 56% of the variance. This correlation is highly significant. After the shift, the record of yearly means is reduced from 131 to 125 data points as the data lost by shifting cannot be replaced. Three-point smoothing, applied once, reduces the number of independent data to 42. Autocorrelation within the two time series is taken into consideration by diminishing the number of the degrees of freedom (Schönwiese, 1985) to 35. The t method (Chambers, 1952) yields t = 6.7. The rejection of the null hypothesis is justified at a high level of significance: $P = 9 \cdot 10^{-8}$. The *t*-test can be applied as both of the time series are close to a normal distribution. Spearman's parameterfree rank correlation coefficient yields the same level of significance. Randomization tests (Edgington, 1995) and bootstrap resampling confirm this result.

The Trellis graph in Fig. 2 shows how the correlation presented in Fig. 1 varies with different aa values. The respective subclass of aa values is indicated at the top of the different panels. The shaded rectangles represent the width of the respective class and its subrange within the total aa range. Consistently, the weakest aa values between 6.8 and 12.9 (bottom left) show no correlation with temperature at all, whereas the highest values between 25.6 and 30.6 (top right) indicate the strongest correlation. The Trellis graph also demonstrates how the correlation develops over time. The strongest correlation concentrates on the period from 1955 through present. This is in contradiction to assertions in the literature (Tett et al., 1999) that there was only a negligible effect of solar activity on temperature in the second half of the century and especially in the two last decades.

The correlation between temperature and solar cycle length, established by Friis-Christensen and Lassen (1991),

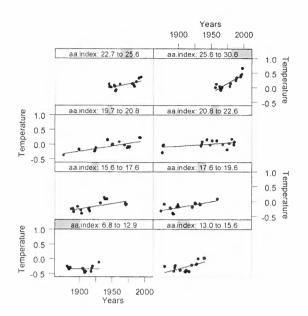


Figure 2. Trellis graph of the data presented in Fig. 1. The panels show scatter plots for different classes of *aa*. Shaded rectangles indicate the width of the respective class and its location within the total *aa* range. The weakest *aa* values (6.8 - 12.9) show no correlation with temperature in a period around 1900. The highest *aa* values (25.6 - 30.6) display the strongest correlation covering the period 1955 - 1998.

covers only the Northern Hemisphere. There is also no clear indication of solar activity, the presumed cause, leading temperature, the effect. This is also true of a correlation between decadal *aa* data and temperature found by Cliver et al. (1998 a) which otherwise corroborates the result presented here, though on a much lower level of significance, as it is solely based on 7 independent data points. The result in Fig. 3 is not exposed to such objections. The vertical axis on the left measures yearly global

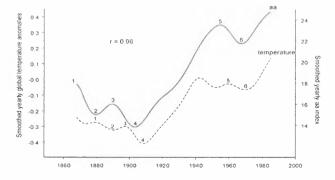


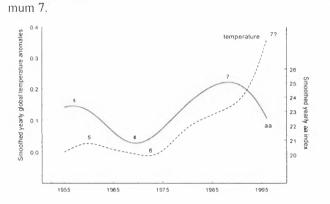
Figure 3. The solid curve shows the aa index of geomagnetic activity, the dashed curve a combination of global land air and sea surface temperature anomalies. The yearly data were subjected to repeated three-point smoothing. Temperature lags aa by 4 to 8 years, but follows the undulations of the aa curve. The connection between the leading aa extrema and the following temperature extrema is highlighted by identical numbers. A disturbance of the correlation around 1940 points to exceptional internal forcing.

surface temperature anomalies combining land and marine records (Jones, 1994; Parker et al., 1995). The axis of ordinates on the right indicates the original yearly aa index without any offset. The original data were subjected to repeated three-point smoothing. These strongly smoothed data, covering 1868 - 1985, show a very close correlation between geomagnetic activity, driven by high-speed plasma streams in the solar wind, and global land and sea surface temperatures (r = 0.96). This correlation explains 92% of the variance. As this result is based on the data that have already been shown to be highly significant, it can be considered valid. Temperature lags aa on the average by 6 years. The lag varies from 4 to 8 years. The related extrema in the two curves are marked by identical numbers. The temperature curve follows the undulations of the aa curve. There is only one exception. After 1942 temperature did no longer follow the ascent of aa and formed a shallow trough not emerging in the aa curve. An explanation could be that between 1942 and 1952 the steepest rise in volcanic activity since 1860 was observed (Simkin et al., 1981).

The lag of the temperature data suggests that some of the excess energy linked to solar activity is stored and accumulated in the climate system by processes taking years. The thermal inertia of oceans may offer an explanation. White et al. (1997) have shown how the oceans respond to excess insolation caused by solar forcing and why there is a lag of several years depending on the length of the involved cycles of solar activity. According to Wigley (1988) an 80-year cycle of irradiance would yield an atmospheric temperature response with a lag of 7 to 9 years. The secular cycle of solar activity, modulating the intensity of the 11-year cycle, has a mean length of 80 - 90 years.

Long-range forecast of global temperature

The presented results suggest that future change in global temperature may be read from the leading *aa* data. Fig. 4 shows the repeatedly smoothed yearly global land and sea surface temperature anomalies and *aa* values after 1985. Around 1990 the *aa* curve reached the highest maximum since the beginning of the record in 1868. This *aa* maximum is marked by the number 7. Allowing for a lag of 8 years, the corresponding maximum 7 of global temperature could have occurred in 1998 with the highest temperature measured since the establishment of regular meteorological services.



global cooling during the decade after temperature maxi-

Figure 4. Extension of the data in Fig. 3. The *aa* curve reaches its highest maximum, marked by number 7, around 1990. After 1990 the *aa* data show a steep decline. Allowing for a lag of 8 years, a maximum in the curve of global temperature could have occurred around 1998. This was the year with the highest temperature observed since the establishment of international meteorological services. In 1999 the temperature was considerably lower, especially in the Southern Hemisphere. This relationship points to global cooling for at least 10 years.

Actually the global temperature in 1999 was much lower than in 1998, especially in the Southern Hemisphere. Satellites observed negative anomalies. As the investigated relationship seems to be solid, we should see falling temperatures at least during the next ten years. The decline in the *aa* curve after maximum 7 is steeper than after maximum 5. So global temperature should fall at a faster rate than after temperatur maximum 5.

Anthropogenic CO_2 contributions should not be an obstacle to such decrease, as temperatures were falling from the early sixties through the early seventies in spite of the fast rise of anthropogenic CO_2 emissions. The increase in surface temperature from 1910 to 1940 was steeper and smoother than in the current warming phase though the rate of anthropogenic emissions at that time was only 10% of the present rate. In view of insufficient data, lacking knowledge of complex feedback processes in the climate system, and controversial hypotheses the outcome of the forecast experiment should contribute to answering the question to which degree solar activity and human greenhouse gas contributions force global temperature.

500

Energy problems

Willis (1976) has calculated that the solar wind energy flux is less than one millionth of the Sun's electromagnetic power deposited near Earth. However, this estimation is based on the total cross-sectional area of the globe. It does not take into account that the solar wind energy may preferentially penetrate into areas smaller than the total disk where it can dominate other energy sources. Herman and Goldberg (1978) have shown that the solar wind energy concentrates on a narrow circumpolar latitude belt near the auroral zone. Taking additionally into account the slant incidence of the Sun's radiant flux, they calculated that the available power of the solar wind would reach 20% of the Sun's electomagnetic energy flux. If Svensmark could show in detail in his laboratory experiments, planned in cooperation with CERN, how galactic cosmic rays, regulated by the solar wind, affect cloud development, we would even have to concede that the energy of starlight is sufficient to affect climate. Cosmic rays and starlight inject nearly the same amount of energy into the atmosphere.

References

- Bucha, V., 1983: Direct relations between solar activity and atmospheric circulation. Stud. Geophys. Geod. 27, 19-45.
- Chambers, E. G., 1952: Statistical Calculation. University Press Cambridge, 61.
- Cliver, E. W., Boriakoff, V., Feynman, J., 1998 a: Solar variability and climate change: Geomagnetic *aa* index and global surface temperature. Geophys. Res. Lett. 25, 1035-1038.
- Cliver, E. W., Boriakoff, V. Bounar, K. H., 1998 b: Geomagnetic activity and the solar wind during the Maunder minimum. Geophys. Res. Lett. 25, 897-900.
- Coffey, H. E. (Ed.), 1958-1999: Solar-Geophysical-Data. National Geophysical Data Center, Boulder, 1958-1999.
- Edgington, E. S., 1995; Randomization tests, Marcel Dekker, New York, Basel, Hong Kong.
- Friis-Christensen, E., Lassen, K., 1991: Length of the solar cycle: an indicator of solar activity closely associated with climate. Science 254, 698-700.
- Herman, J. R., Goldberg, R. A., 1985: Sun, Weather, and Climate. Dover, New York, 43.
- Jones P. D., 1994: Hemispheric surface air temperature variations: a reanalysis and an update to 1993. J. Climate 7, 1794-1802.
- King, J. W., 1974: Weather and the Earth's magnetic field. Nature 247, 131-134.
- Labitzke, K. G., 1999: The Stratosphere. Springer, Berlin-Heidelberg-New York, 147. Landscheidt, T., 1995: Global Warming or Little Ice Age? In: Finkl, C. W., Ed.:
- Holocene cycles. J. Coastal Res., Special Issue No. 17, 371-382. Lau, K. M., Weng, H., 1995: Climate signal detection using wavelet transform. Bull.
- American Meteorol. Soc. 76, 2391-2402. Lean, J., Beer, J., Bradley, R., 1995: Reconstruction of solar irradiance since 1610:
- implications for climate change. Geophys. Res. Lett, 22, 3195-3198. Lockwood, M., Stamper, R., 1999: Long-term drift of the coronal source magnetic flux
- and the total solar irradiance. Geophys. Res. Lett. 26, 2461.
- Lockwood, R., Stamper, R., Wild, M. N., 1999: A doubling of the Sun's coronal magnetic field during the past 100 years. Nature 399, 437-439.

- Mayaud, P. N., 1973: A Hundred Year Series of Geomagnetic Data. IUGG Publications Office, Paris.
- Mecherikunnel, A. T., Kyle, H. L., Lee, R. B., 1990: Solar constant data from Earth radiation budget measurements. In: Schatten, K., Arking, A. (Eds.): Climate Impact of Solar Variability. National Aeronautics and Space Administration, Greenbelt, 309-313.
- Neubauer, L., 1983: Sudden stratospheric warmings correlated with sudden commencements and solar proton events. In: McCormac, B. M. (Ed.): Weather and Climate Responses to Solar Variations. Colorado Associated University Press, Boulder, 395-397.
- Parker, D. E., Folland, C. K., Jackson, M., 1995: Marine surface temperature: observed variations and data requirements. Climatic Change 31, 559-600.
- Prohaska, J. T., Willett, H. C., 1983: Dominant modes of relationships between temperature and geomagnetic activity. In: McCormac, B. M. (Ed.): Weather and Climate Responses to Solar Variations. Colorado Associated University Press, Boulder, 489-494.
- Pruppacher, H. R., Klett, J.D., 1997: Microphysics of Clouds and Precipitation. Kluwer Academic Publishers.
- Pudvokin, M., Veretenenko, S., 1995: Cloudiness decreases associated with Forbushdecreases of galactic cosmic rays. J. Atmos. Terr. Phys. 57, 1349-1355.
- Reid, G. C., 1997: Solar forcing of global climate change since the mid-17th century. Climatic Change 37, 391-405.
- Roberts, W. O., Olson, R. H., 1973: New evidence for effects of variable solar corpuscular emission on the weather. Rev. Geophys Space Phys. 11, 731-74.
- Schönwiese, C. D., 1985: Statistical Practice for Meteorologists and Geophysicists.Borntraeger, Berlin-Stuttgart, 173.
- Schuurmans, C. J. E., 1979: Effects of solar flares on the atmospheric circulation. In: Mc Cormac, B. M., Seliga, T. A. (Eds.) Solar-Terrestrial Influences on Weather and Climate. Reidel, Dordrecht, 105-118.
- Simkin, T., Siebert, L., McClelland, L., Bridge, D., Newhall, C., Latter, J. H., 1981: Volcanoes of the World. Hutchinson Ross, Stroudsburg, 25.
- Soon, W. H., Posmentier, E. S., Baliunas, S. L., 1996: Inference of solar irradiance variability from terrestrial temperature changes, 1880-1993. Astrophys. J. 472, 891-902.
- Stolov, H. L., Shapiro, R., 1974: Investigation of the responses of the general circulation at 700 mb to solar geomagnetic disturbance, J. Geophys. Res. 79, 2161-2170.
- Svensmark, H., 1998; Influence of cosmic rays on Earth's climate, Phys. Rev. Lett. 81, 5027-5030.
- Svensmark, H., Friis-Christensen, E., 1997: Variation of cosmic ray flux and cloud coverage: a missing link in solar-climate relationships. J. Atmosph. Sol. Terr. Phys. 59, 1225-1232.
- Tett, S. F. B., Stott, P. A., Allen, M. R., Ingram, W. J., Mitchell, J. F. B., 1999: Causes of twentieth-century temperature change near the Earth's surface. Nature 399, 569-572.
- Tinsley, B. A., 1996. Correlations of atmospheric dynamics with solar wind induced changes of air-Earth current density into cloud tops. J. Geophys. Res. 101, 29,701-29,714.
- White, W. B., Lean, J., Cayan, D. R., Dettinger, M. D., 1997: Response of global upper ocean temperature to changing solar irradiance. J. Geophys. Res. 102, 3255-3266.
- Wigley, T. M. L., 1988: The climate of the past 10,000 years and the role of the Sun. In:Stephenson, F. R., Wolfendale, A. W. (Eds.), Secular Solar and Geomagnetic Variations in the Last 10,000 Years. Kluwer, Dordrecht.
- Willis, D. M., 1976: The energetics of Sun-weather relationships: magnetospheric processes. J. Atm. Terr. Phys. 38, 685-698.
- Willson, R. C., 1997: Total solar irradiance trend during solar cycles 21 and 22. Science 277, 1963-1965.

CHARACTERISTICS OF INTENSE GEOMAGNETIC STORMS AND THEIR RELATION TO SOLAR ACTIVE PHENOMENA

C.H. Mandrini¹, S. Dasso^{2,3}, D. Gómez^{1,3}

¹ Instituto de Astronomía y Física del Espacio, CONICET-UBA, CC.67, Suc.28, 1428 Buenos Aires, Argentina, e-mail: mandrini@iafe.uba.ar

² Instituto de Física del Plasma, CONICET-FCEyN/UBA, Buenos Aires, Argentina

³ Physics Department, FCEyN/UBA, Buenos Aires, Argentina

ABSTRACT

We perform a statistical study of the decay times for the recovery phase of the 300 most intense magnetic storms, that occurred between Jan. 1, 1957, and Dec. 31, 1998. Statistically representative values for the decay time (τ) are obtained by averaging the most reliable τ values, which result from applying a least square method to the Dst index time series during each recovery phase. The Dst index in the decaying stage of the storm has been systematically fitted with an exponential function and a very good correlation has been obtained for most of the storms. A mean value of $\tau \sim 14 \pm 4$ hs has been obtained. Using the data set in this study and the facility of web access to the GOES satellite data since 1986, we selected a set of storms (from 1986 to 1998), having $Dst_{min} < -200$ nT, and investigated their solar origin. We present preliminary results of a more detailed correlation analysis based on longer time scales.

Key words: geomagnetic storms; solar flares; space weather.

1. INTRODUCTION

Magnetic storms are characterized by a sudden enhancement of the ring electric current circulating around the Earth. This current is mainly transported by protons, oxygen ions and electrons (in the 10-300 keV energy range), and is located between 2 to 7 Earth radii (see González et al. 1994 and references therein). When the interplanetary magnetic field hits the Earth bowshock with a southward orientation, a reconnection process can take place. As a result, energetic particles coming from the Sun as part of the solar wind are free to enter to the magnetosphere and, after a period of storage, part of these particles are injected into the ring current system. The ring current index Dst was introduced as a measure of the ring current magnetic field.

Variations of the *Dst* index during magnetic storms are found to display a direct relationship with the energy stored in the ring current, which is given by

$$Dst(t)/B_0 = 2E(t)/(3E_m)$$

where B_0 is the average equatorial surface field, E(t) is the total energy of the ring current, and E_m is the total magnetic energy of the geomagnetic field. The temporal variation of the ring current energy is related to the injection of charged particles from the magnetotail and also to the energy losses. A simple relationship describing this energy balance is given by,

$$\frac{d}{dt}E(t) = U(t) - E(t)/\tau$$

where U(t) is the rate of energy input and τ is the decay time. The main energy losses of the ring current are given by the following processes: (1) charge exchange, (2) Coulomb scattering and (3) resonant interactions with plasmons (González et al. 1994). Each of these processes depends rather strongly on several properties of the particles, such as their pitch angle, ion energy, composition and location in the radiation belt. The energy decay time (τ) in the ring current is, therefore, the end result of a rather complex combination of all these effects.

One of the first estimates for the ring current decay time (τ) was reported by Burton et al. (1975), where a typical value of τ of the order of 7 hs with a rather large uncertainty was obtained. Many attempts have been done to estimate τ from then on. A summary of previous studies can be found in the review of Feldstein (1992), where a large dispersion among estimates by different authors (for different sets of storms) can be observed. Within this framework, we have decided to perform a statistical study of the recovery phase for a large number of intense storms. Our statistical study involves 300 recovery phases corresponding to the most intense magnetic storms $(Dst_{min} < -100 \text{ nT})$ that occurred from Jan 1, 1957 to Dec 31, 1998. With this goal in mind, we have made the following working hypotheses: (1) once the decay phase starts, energy injection is negligible (i.e. $U(t) \approx 0$), (2) the value of τ is constant and (3) the *Dst* index represents the magnetic perturbations induced by the ring current. According to these hypotheses, for any given storm the *Dst* index will decay exponentially like

$$Dst(t) = Dst(t=0) \quad \exp[-t/\tau] \tag{1}$$

where t = 0 corresponds to the peak of activity.

Although we are aware of the fact that our hypotheses are probably too simplistic, they allow us to use the same technique for the whole dataset. However, we want to stress that a large fraction of the storms are consistent with these assumptions. In Section 2 we outline the procedure adopted for our statistical analysis and we present our results. Section 3 outlines the preliminary results of a work in which we intend to look for the connection between nonrecurrent storms and solar events, as done by Landi et al. (1998), but covering a different period of time. Section 4 lists our conclusions.

2. RING CURRENT DECAY RATES: FITTING PROCEDURE AND RESULTS

We develope a numerical procedure to recognize intense magnetic storms (i.e. $Dst_{min} < -100 \text{ nT}$) and to fit their decay times. We use the Dst series with a time resolution of one hour, this series was obtained from the NOAA NGDC Solar Terrestrial Physics Division datasets (ftp://ftp.ngdc.noaa.gov/STP/).

We define the starting time $(t_{s,i})$ of each storm (labeled as i), as the time in which the Dst value from

the main phase crosses down a threshold value defined as $Dst^* = -100$ nT. In a similar fashion, during the recovery phase, we define the final time of an intense storm $(t_{f,i})$ when the Dst crosses again Dst^* . The Dst peak for each event $(Dst_{min,i})$ is the minimum value in the time interval $t_{s,i} \leq t \leq t_{f,i}$. We call $t_{M,i}$ to the time corresponding to the peak value. In this way we construct sub-series containing the Dst data for each intense event, finding a total of 300 sub-series in the analysed period.

We consider the 10 Dst values after Dst_{min} , corresponding to the first 10 hours of the recovery phase. That is to say, we obtain 300 new sub-series with 10 elements, Dst_{ij} (i = 1, 2, ..., 300; j = 1, 2, ..., 10).The decay time is estimated by fitting the value of τ_i for each of the 300 recovery phases, assuming an exponential decay according to Eqn. (1). These τ_i are computed using a standard least-square linear procedure. We assume a linear dependence between y = log(-Dst) and the time t elapsed from $t_{M,i}$ (i.e. $y = A - t/\tau$, according to Eqn. (1)). The fitting method is carried out in two successive steps. In a first step, a fit is done for every storm without considering errors in the measured Dst. The result of this procedure is a first order estimate for the decay time $(\tau_{1,i})$ as well as for A $(A_{1,i})$. Then, using the original series Dst_{ij} , $\tau_{1,i}$ and $A_{1,i}$, we compute $\Delta D_{ij} = |Dst_{ij} + exp(A_{1,i})exp(-t_j/\tau_{1,i})|$. Using the new series, ΔD_{ij} , we perform a second standard linear least square fit considering uncertainties for Dst_{ij} . Thus, we obtain a better estimation for τ_i and its uncertainty $\Delta \tau_i$. From inspection of the 300 events, we find that $\approx 50\%$ are in good agreement with an exponential decay, as shown in Fig. 1.

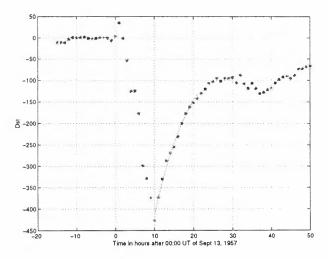


Figure 1. Dst values for the storm on Sep. 13, 1957.

A histogram of the number of storms for different linear cross correlation coefficients (r_i) , shows that ~ 67% of the events have |r| > 0.9. Almost 80% of the events have |r| > 0.8 and 26% (i.e. 77 storms) display an excellent correlation, |r| > 0.97. Considering only these last 77 cases, we have obtained a mean value for the decay time, $\tau = 14.0 \pm 4.0$ hs (see Fig. 2). Note that, for very intense storms $(Dst_{min} < -250 \text{ nT}), \tau$ decreases with the intensity of the storm. The life time of ions due to the charge exchange process is inverse to their velocities (Daglis et al. 1999) and the abundance of O^+ (absolute and relative) increases during the occurrence of intense storms (Daglis 1997). We suggest that the trend discussed above might correspond to a combination of a higher energy level and a higher abundance of O^+ in the ring current.

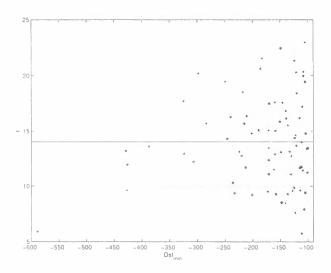


Figure 2. Decay time as a function of the intensity of the storm for r < -0.97. The continuous line (dash-dotted) corresponds to the mean value (standard deviation).

Fig. 3 shows the τ_i values (with their error bars) obtained for the 200 events with r < -0.9. Stars in this figure correspond to storms having $Dst_{min} < -200$ nT (44 events), while dots mark the rest of the events. We find that when the value of r becomes closer to -1, values of τ_i do not converge to a unique value, quite the contrary they spread over a wide range between 6 and 23 hs. Notice that the error bars in Fig. 3 are significantly lower (~ 0.1-1 hs in most cases) than the above mentioned standard deviation. This indicates that the decay time characterizing the recovery phase of any given storm is an intrinsic property of that particular event, rather than a universal constant. The continous line in Fig. 3 shows the partial average decay time as the thresh503

old value for r is changed. For qualities worse than $r \sim -0.97$, a monotonic increase of this partial average time is observed. This trend indicates that those events, which cannot be cleanly fitted by exponentials, display recovery phases which are rather extended in time, perhaps connected to the presence of a sustained source of injection or perhaps due to the combination of multiple decay times. However, this curve also indicates that this trend is negligible for quality fittings better than $r \approx -0.97$.

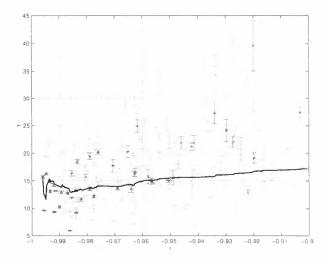


Figure 3. Decay time as a function of the fitting quality. The continuous line indicates the partial average decay time for storms with quality better than r (see text).

The histogram shown in Fig. 4 considers all the storms with r < -0.97, classifying them according to their decay time. Overlaid, we show (continuous line) the result of a moving average smoothing procedure with a very narrow bin size. This average is performed by convolving the histogram counts with a triangular function with a base of 4.2 hs. This smoothed curve displays three peaks, a main peak at ~ 9.5 hs and two secondary peaks at ~ 13.1 and ~ 20 hs. This result suggests the existence of three groups of storms characterized by different decay times. These differences might be caused by a combination of different levels of injected energy and/or populations of O^+ and H^+ at different altitudes (Smith and Bewtra 1978).

3. CONNECTION WITH SOLAR ACTIVITY

In the last years the solar origin of geomagnetic storms has been the subject of a long debate (see eg. Kosugi and Shibata 1997, Hudson 1997). After

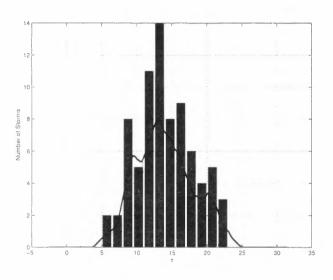


Figure 4. A histogram of the number of storms vs. the decay time. The thick line shows an average convolving the histogram with a triangular function (see text).

the work of Gosling (1993) the "solar flare myth" (which considers a cause-effect link between major solar flares and nonrecurrent perturbations of the geomagnetic field) was partially abandoned. It was then proposed that such storms had their origin in fast coronal mass ejections (CMEs). However, a long list of examples (based on analysis of individual events or statistical studies) is showing a link between long duration flare events (LDEs) and CMEs (see eg. van Driel-Gesztelyi et al. 2000, Landi et al. 1998). In this spirit, we selected a set of storms (15 events), having $Dst_{min} < -200$ nT, and confronted it to the GOES five minutes data base (http://sec.noaa.gov/Data/goes.html), from 1986 to 1998, and to the reports published in the corresponding numbers of Solar Geophysical Data. Taking a lag time of 5 days between the peak of the storm and the GOES time series, we find that an LDE (temporal duration > 1.5 hs) occurred at a solar longitude (latitude) of less than 30 deg. W or E (N or S) for all but one of the storms. Besides, considering all the events, 45% were associated with type II-IV radio bursts and $\approx 22\%$ with type IV bursts (on this topic see the work by Cane 1997).

4. CONCLUSIONS

The simple scenario of an exponential decay to describe the recovery phase of geomagnetic storms seems appropriate for more than half of the 300 studied cases (considering r < 0.9). However, it is also apparent that geomagnetic storms are rather complex phenomena, since: $\approx 40\%$ of the cases cannot be described by this scenario and, for those which can be considered as exponentially decaying, the associated decay time is different for different storms and also does not seem to remain constant as the recovery phase progresses (as found when extending the fitting time to 20 and 30 hs after Dst_{min}).

The results discussed in Section 3 seem to indicate that LDEs, accompanied by type 4 radio emission, are effective to perturb the geomagnetic field, as found by Landi et al. (1998).

Acknowledgements: This work was supported by the Univ. of Buenos Aires (grants UBACyT TX065/98 and TX032/98) and by CONICET. C.H.M. and D.G. are members of the Carrera del Investigador Científico (CONICET) and S.D. is a research fellow of CONICET. C.H.M. acknowledges finantial support from Paris Observatory, Meudon, to attend this meeting.

REFERENCES

- Burton, R.K., McPherron, R.L. & Russell, C.T. 1975, JGR 80, 4204
- Cane, H.V. in Coronal Mass Ejections, eds. N. Crooker, J.A. Joselyn & J. Feynman 1997, Geophys. Monograph 99 (AGU), 205
- Daglis I.A. 1997, in Magnetic Storms, eds. B.T. Tsurutani, W.D. González, Y. Kamide & J.K. Arballo, Geophys. Monograph 98 (AGU), 407
- Daglis I.A., Thorne, R.M., Baumjohann, W. & Orsini, S. 1999, Rev. of Geophys. 37, 407
- Feldstein, Y.I. 1992, Space Sci. Rev. 59, 83
- González W.D. et al. 1994, JGR 99, 5771
- Gosling, J.T. 1993, JGR 98, 18949
- Hudson H.S. 1997, in Magnetic Storms, eds. B.T. Tsurutani, W.D. González, Y. Kamide & J.K. Arballo, Geophys. Monograph 98 (AGU), 35
- Kosugi, T. & Shibata, K. 1997, in Magnetic Storms, eds. B.T. Tsurutani, W.D. González, Y. Kamide & J.K. Arballo, Geophys. Monograph 98 (AGU), 21
- Landi, R., Moreno, G., Storini, M. & Anatalová, A. 1998, JGR 103, 20553
- Smith, P.H. & Bewtra, N.K. 1978, Space Sci. Rev. 22, 301
- van Driel-Gesztelyi, L. et al. 2000, JASTP, in press.

A POSSIBLE ORIGIN OF LONG-TERM GLOBAL CIRCULATION VARIATIONS AND 1920-1940 YEARS WARMING

V. Mordvinov, E. Tikhomolov, and A. Karakhanian

Institute of Solar-Terrestrial Physics SD RAS664033, P.O. Box 4026, Irkutsk, Russia e-mail: v_mordv@iszf.irk.ru

ABSTRACT

During the 1920-1940 years warming weather regimes changed in certain order. The order appears as the result of the modulation of the flows by a large-scale disturbance moved in the direction opposite to the Earth's rotation and twice revolved around the Earth from early 1910s to 1950s. We discuss whether this feature could be a consequence of decrease in the period of solar cycles during this time interval.

1. INTRODUCTION

Short-term climate fluctuations (of the order of 20-30 years) attract attention because of the next reasons:

- climate changes, which are believed to be a result of greenhouse effect, occur approximately on this time scale;
- their time-scale is close to the period of variations of solar activity, that is considered after paper of Friis-Christensen and Lassen (1991) as one of the main sources of climate variability.

It would be very important to separate these two factors: natural and antropogenic, because they are different in view of long-term variability. Variations of solar activity are cyclic. But technogenic changes will increase in time.

The main feature of long-term variations of mean North hemisphere temperature in 1920-1940 was warming coincided in time with period of relatively short solar cycles. After 1940 temperature began to decrease, but in 70th the increase in temperature continued. In order to find the reasons for temperature increase in the first half of 20th century it is necessary to study the features of general circulation of the atmosphere (GCA) in this time interval. In regard of high variability of synoptic processes, this problem seems very complicated. For its solution one of the typization systems of weather regimes could be used.

At least two systems, namely Vangengeim-Girs and Dzerdzeevsky systems had got wide acceptance and are used in super-long-term forecasts (Dzerdzeevsky, 1975; Girs, 1974). Vangengeim-Girs system is based on the 850 mb and 700 mb geopotential height fields and is aimed to extract long waves in free atmosphere. Dzerdzeevsky tipization is of much more details and is based on localisation of leading air flow directions by the use of sea-level pressure maps. Because these flows are in accordance with positions and orientations of free atmosphere long waves, tipizations could compliment each other. In what follows we'll use, basically, Dzerdzeevsky typization.

2. DZERDZEEVSKY TYPIZATION SCHEMA

Dzerdzeevsky system consists of 13 basic typical schemas of **elementary circt 'ation mechanisms** (ECM) in North hemisphere. Regimes differ from each other by the number of polar air injections tracks or north-eastward tracks of south cyclones. They are united into 4 groups:

- 1. Zonal circulation. There are no polar injections tracks, 2 or 3 tracks of south cyclones injections. Types of ECM are 1 and 2.
- 2. Break down of zonal flows. There are 1 polar injection track, and from 1 to 3 tracks of south cyclones injections. Types of ECM are 3-7.
- 3. Meridional north circulation. There are from 2 to 4 of polar injection tracks, and from 2 to 4 south cyclones tracks. Types of ECM are 8-12.
- 4. Meridional south circulation. There are no polar injections tracks, and from 2 to 4 tracks of south cyclones injections, penetrating into polar region. Type of ECM is 13.

Each type of ECM is divided into subtypes differed by direction of polar air injections and tracks of south cyclones. The total number of subtypes is 41. The reality of types of ECM was the subject of a number of researches. The independent testing showed that likelihood of non-random change of ECM is very high and is not lower than 95%.

For studying the long-term variations of circulation in the North hemisphere as a whole all ECM were united into groups of "zonal" and "meridional" circulation forms. For time interval from 1899 to 1978 three circulation epochs were revealed with dominance of "meridional" (1899~1915, 1951~1978) and "zonal"

(1916~1950) forms of circulations. These definitions are enclosed in quotes, because they do not correspond correctly to definition of zonal and meridional circulation, specifically "zonal" forms consist of ECM with one blocking. We think it would be better to call this group as a group of cyclonic processes in which the injections of south cyclones and activity of arctic fronts suppress the development of polar anticyclone and lead to decrease of quantity of polar air injections. Correspondingly, the group of "meridional" forms is a group of anticyclonic circulation processes with welldeveloped polar anticyclone and increased number of polar air injections. Note that the new interpretation is also rather conditional: in the frame of such definition it would be better to include ECM of 13th type into group of cyclonic processes because its feature is the cyclone at pole (C-A system). Such inclusion was made in first papers of Dzerdzeevsky. But then such classification was rejected.

3. CIRCULATION EPOCHS

Unfortunately, in this schema the key to understanding of reasons for changes of circulation regimes and circulation epochs was not suggested. From our point of view some illuminating features could be lost in classification of ECM, when types are united into groups.

During our analysis of frequencies of "zonal" and "meridional" forms of ECM the doubts appear on the correctness of specifying the epochs. Only with a big portion of arbitrariness one can consider the second epoch of meridional circulation similar to first. In both cases an increase in frequencies of meridional forms took place, but during the second epoch this increase was not compensated by corresponding decrease in frequency of zonal forms. Before the beginning of 50th years the total number of ECM of all types always was constant, oscillations occurred as a result of redistribution of quantity of ECM of first and second group. But since the middle of 50th the total number of ECM increased. In Dzerdzeevsky system it happened because of increasing frequency of "meridional" forms and in a C-A system it occurred because of increasing frequency of ECM of both groups.

4. THE MOST FREQUENT ECM

In order to specify the circulation types that are responsible for increase of total number of ECM we analysed the changes in time of frequencies of all types of winter and summer ECM.

The most noticeable result is an increase of 12 and 13 ECM types frequencies from the second half of 40^{th} years (i.e. during transition to second epoch of meridional circulation). In the first epoch of meridional circulation 12^{th} type of ECM was seen fewer, especially

in winter. An increase of frequency of 13th type says about total increase of cyclonic character of the hemisphere, first of all, in high-latitude zone. Along with increase of ECM of 12th type, it says most likely about instability of circulation in polar region, fast change of south cyclonic and polar injections. It corresponds to total increase of quantity of ECM mentioned above. Possibly, in 50th not a repeat of meridional circulation epoch took place but transition of ECM into some new state. Change of relationship between types of ECM of the same group indicates the difference in character of circulation in first and second "meridional" circulation epoch. During the first and second epoch in winter, respectively, the 5th (polar injections into Asia) and 7th (polar injections into America) type of "meridional" circulation dominated. Thus epochs differ from each other by a degree of development of anticyclonic centres of actions in Atlantic-Euro-Asian and Pacific-American sectors.

Our analysis shows that increase in frequency of 13th type of ECM, at least, partially is caused by replacement of some zonal ECM. This suggestion is supported by observation in C-A system of one additional variation in summer in 50th that coincided in time with awaiting next pulse of "zonal" ECM forms increase. In some degree it supports the inclusion of 13th ECM type into group of "zonal" circulation. Possibly the replacement of some zonal ECM occurred as a consequence of methodical reasons as well, because the identification of 13th type of ECM became possible only after drift of USSR polar station SP-1 in 1937.

Many questions appear also while analysing epoch of "zonal" circulation. There is a strong seasonal dependence of ECM variations. Both in winter and in summer variations have a form of two consequent pulses, but character of pulses is different. In winter and in summer first pulse is caused by intensification of, respectively, "meridional" and "zonal" circulation. Moreover, summer variations are longer than winter ones and they begin later. In more details the seasonal dependence of ECM dynamics was studied by Dzerdzeevsky (1975). Six seasons were specified, namely, winter, summer, spring, autumn, pre-spring, and pre-winter. In all cases variations are different, and not only amplitudes but periods of oscillations as well. An open question is what are the reasons of these differences and can we unite all these variations into one epoch taking as the base the average characteristics.

5. ECM VARIATIONS ARE THE RESULT OF THE WAVE WITH 18 YEAR PERIOD

Analysis of integral characteristics does not answer on appearing questions, but variations of types and subtypes of ECM, ordered in some specific row, permit to suppose a hypothesis which can explain the features of ECM variations during "zonal" circulation epoch. Figure 1 shows graphics of ECM frequencies in such a way that it is possible to reveal the order of development of variations. For convenience of visual analysis graphics are shifted along ordinate axis and smoothed on several points. Upper and lower figures show graphics of ECM, respectively, in summer and in winter. Graphics for summer are smoothed on 4 points. but for winter on 2 points because length of variations in summer is slightly larger than in winter. Graphics show numbers of corresponding types and subtypes in summer or in winter. In the right part of the figure the directions of polar injections corresponding to these ECM are depicted. Initially we depicted graphics for all subtypes of ECM, but then were forced to unite some subtypes, because their frequencies was insufficient for extraction of variations. For summer period we united subtypes of groups 2 and 7 and for winter types 1,5,7. We did not also show frequencies for those types and subtypes, which were observed relatively rarely, namely, 8, 9, 10, 12a, 12g.

The results of sorting of graphics appeared very unexpected. Variations of ECM frequencies had a form

of disturbance that moved to the west and during 35 years twice revolved around the Earth. Especially apparently the motion of disturbance is seen in graphics of change of "zonal" ECM types in summer period. The direction of polar air injections changed in the next sequence: polar injections into Atlantic, then into America, Pacific Ocean and Asia. When disturbance moved in the west hemisphere the number of pure "zonal" ECM of type 2 increased, and frequencies of "meridional" types decreased. When disturbance moved in East hemisphere "zonal" circulation types were replaced by "meridional" that had in summer and in winter, respectively, two and three main tracks. In winter the main polar injections corresponded to mean climate position of pressure crest, that linked Siberian and American anticyclones across Arctic. The third polar injection had tendency to move along longitude in western direction, likely, lags behind the main disturbance. In summer period the increases in frequencies of meridional circulation types were longer than in winter and finally decayed after moving of disturbance into western hemisphere.

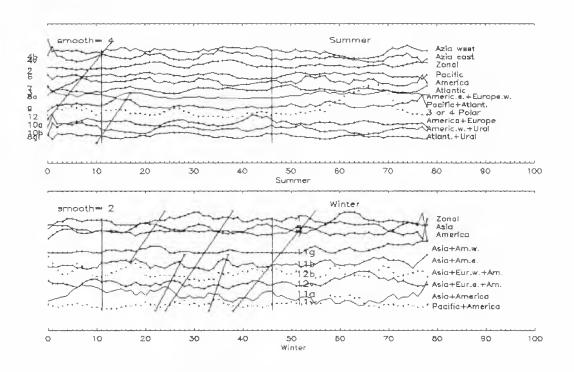


Figure 1: Smoothed graphics of summer and winter ECM frequencies, constructed with due account of directions of polar injections.

Unfortunately, synoptic maps at the beginning of 20 century were not of high quality, so to determine time of appearance of disturbance by the use of graphics of ECM frequencies is, in practice, impossible. The motion of disturbance is clearly seen from the instance of time,

determined by Dzerdzeevsky as a beginning of "zonal" circulation epoch, and disappearance of disturbance occurred, likely, at the instance of time of its finish. One can suppose that these events were connected and appearance of disturbance became the source (or result) of increase, on an average, of "zonal" circulation and increase of mean temperature in North hemisphere during first half of 20^{th} century. Break down of the wave, in its turn, gave rise to global restructuring of ECM in 50^{th} years and to decrease in temperature (or was its consequence).

6. CAN IT BE THE SOLAR INFLUENCE ?

In the frame of our idealised schema the reason for change of subtypes of ECM is the drift in western direction of the axis of main polar injections, and transition from one form of circulation to another was caused by interaction of disturbance with continental and ocean areas. In Asia the disturbance initialised the development of "meridional" forms of circulations, and above oceans and America of "zonal" types. Extrapolating on later period one can suppose that warming in 70th-90th years was also connected with appearance of such kind of disturbance. Indirect proof of this supposition is substantial difference of spatial structure of temperature and pressure anomaly fields during first and second phase of warming in 1977-1988 and 1989-1994 years, that were revealed by Volodin and Galin (1999). The difference is so substantial that anomaly fields are well described by orthogonal functions. Authors suggested two different mechanisms of warming: in 1977-1988 as a result of increase of sea surface temperature (SST) in tropics, and in 1989-1994 years as a result of decrease in ozone concentration in lower stratosphere. Such division seems not very logic although it is supported by calculations. In the frame of our model a drift of disturbance can cause the difference in spatial structure.

Keeping in mind that period of revolution is approximately of 18 years, quasiorthogonaity of pressure and temperature field anomalies during first and second phase of warming is explained by shift of disturbance approximately on 180 degrees. Considering high correlation of mean temperature in North hemisphere and SST in tropics, one can suggest that mechanism of pumping of disturbance has heat nature and is connected with anomalies of ocean circulations. This conclusion is very important for understanding of nature of ECM dynamics during last decades.

Of course, the simplicity of the suggested model is relative. In atmosphere and ocean the inter-annual, decadal and centennial variations of climate characteristic are known, but mechanisms of their development and connections at global scale are studied very poor. To some extent study of long-term variations of ocean circulation replaced the searches of external sources of climate variations among which the best known were variations of solar activity. Researches of Friis-Christensen and Lassen (1991) reanimated the interest to solar-terrestrial relationships. But they limited themselves by analysis of mean climate characteristics.

With higher spatial resolution specific structure of global atmosphere circulation variations in the first half of 20th century is revealed. This structure looks like the modulation of zonal and meridional circulation forms by a wave-like disturbance that slowly moved in westward direction. We speculate, that the interaction of "disturbance" with surface gave rise to change of circulation forms, and then to temperature changes. We know that during considered period of time solar cycles were shorter. Possibly transition of the Sun to another, short cycle period regime could trigger the development of such terrestrial waves. Mechanism of triggering and support of such waves is unknown at present. Probably under some conditions terrestrial atmosphere becomes unstable to excitation of specific largest-scale wave; this wave controls excitation of smaller-scale vortical flows and is supported through the mechanism of interaction with them. One of such kind of mechanism was studied in our previous paper (Tikhomolov, 1996) and gave very promising results for interpretation of a number of effects. Investigation of possibility of application of this mechanism to the terrestrial atmosphere is the next step of our researches.

REFERENCES

- Friis-Christensen E. and Lassen K. (1991): Length of solar cycle: An indicator of solar activity closely associated with climate. *Science*, Vol. 254, p. 698.
- Dzerdzeevsky B.L. (1975): The global circulation of Atmosphere and climate. M.: Nauka, p. 285.
- Girs A.A. (1974): Macrocirculation method of longterm meteorology. L.: Gidrometeoizdat, p. 485.
- Volodin E.M., Galin V.Ya. (1999): About interpretation of winter warming on continents of North hemisphere in 1977-1994. *Meteorologiya i* gidrologiya, No. 1, p.20.
- Tikhomolov E. (1996): Short-scale convection and long-scale deformational-unstable Rossby wave in a rotating fluid layer heated from below. *Physics of Fluids*, V.8, issue 12, p. 3329.

SOLAR VARIABILITY ASSOCIATED TO IONOSPHERIC, STRATOSPHERIC AND TROPOSPHERIC PARAMETERS

Nieves Ortiz de Adler⁽¹⁾ and Ana G. Elías^(1,2)

(1) Laboratorio de Física de la Atmósfera – Departamento de Física Facultad de Ciencias Exactas y Tecnología – Universidad Nacional de Tucumán ⁽²⁾Departamento de Ecología – Facultad de Agronomía y Zootecnia Universidad Nacional de Tucumán Avenida Independencia 1800 – (4000) Tucumán – Argentina email: adler@arnet.com.ar / aelias@herrera.unt.edu.ar

ABSTRACT

In this work the solar cycle length, *SCL*, is used as a proxy of long-term changes in solar radiation, and it is associated to ionospheric, stratospheric and tropospheric parameters. These parameters are the maximum ionospheric electron density, Nmax, the global lower stratospheric temperature, LST, and the tropospheric temperature TT. The anomaly of Nmax, LST and TT (*NmaxA*, *LSTA*, and *TTA*, respectively) are highly correlated to SCL, with a correlation coefficient greater than 0.7 with a 95% significant level. The solar variability then could be the responsible for the long-term modulation observed in the atmospheric parameters here analyzed.

SOLAR CYCLE LENGTH

It is well known that solar activity is not constant. One of its periodicities is of approximately 11 years whose most obvious aspect is the cycle of the sunspot number, Rz. The length of the sunspot period from minimum to minimum as well as from maximum from to maximum, is known as the solar cycle length, SCL.

SCL has varied between 8 and 17 years (since sunspot number record exists, around 1500) (Friis-Christensen and Lassen, 1991; 1992; 1993), in such a way that short solar cycles implies high activity levels, while long solar cycles are characteristics of low activity levels. This solar parameter has a long-term periodicity of around 80-90 years called the Gleissberg cycle.

Usually the Gleissberg low-pass filter is applied to the SCL series in order to remove short period variations of an accidental character. This filter consists of a moving average with weight 1, 2, 2, 2, 1. The SCL smoothed series, which can be seen in figure 1, was used in this work.

ATMOSPHERIC PARAMETERS

Maximum ionospheric electron density, Nmax - measured around 300 km height

Based on ionospheric data during solar cycles previous to cycle 21, it has been established that Rz have a linear

correlation with the maximum electron density, Nmax:

Nmax = a
$$Rz + b$$
, a and b constants (1)

In this work, in order to appreciate the Nmax association to SCL, the effects of Rz (which explain around 80% of Nmax variability) has been filtered, estimating the Nmax anomaly, *NmaxA*, through

$$NmaxA = Nmax - Nmax'$$
 (2)

being Nmax the experimental value and Nmax' the one estimated with equation (1).

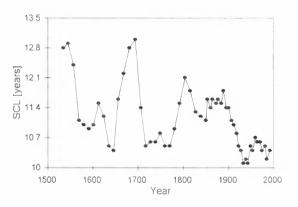


Figure I: Solar Cycle Length in years smoothed with the Gleissberg low-pass filter.

Annual Nmax data, measured at 12 LT, from the following four ionospheric stations and periods have been analyzed: Slough (51.15N, 0.6W) (1935-1995), Manila (14.7N, 121.1E) (1865-1993), Tucumán (29.6S, 294.6E) (1957-1986), and Christchurch (43.6S, 172.8E) (1957-1984).

Figure 2 shows mean values of NmaxA for each solar cycle, together with SCL. The correlation coefficient between them is greater than 0.80 in all the cases, with a 95% significance level, stating a high linear association.

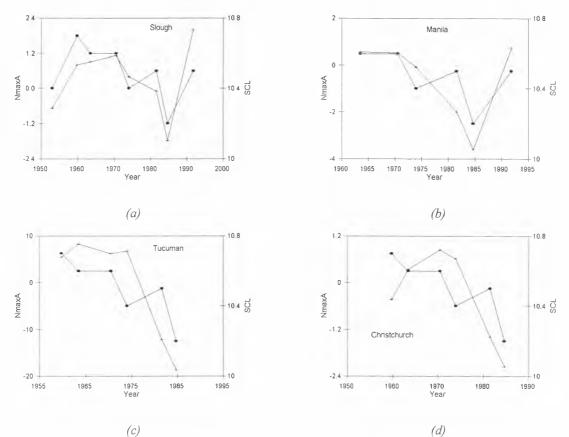


Figure 2. Solar cycle length, SCL, in years (filled circle) assigned to the central year of each cycle and NmaxA $(x \ 10^4 \text{ cm}^3)$ mean values (plus sign) for each solar cycle for (a) Slough, (b) Manila, (c) Tucuman and (d) Christchurch.

Global Lower Stratospheric Temperature- LST .measured around 30 km height

The global monthly LST of the period 1979 to 1999 was analyzed. The LST anomaly, *LSTA*, was computed as the difference between LST and the mean of the 1982-1991 base period.

The solar radiation mainly involved in stratospheric heating is the 200-300 nm spectral range, UV. The 10-102.6 nm range of the solar EUV radiation is the primary cause of ion production in the ionosphere. Although UV and EUV originates in different sun regions, their variations resemble each other (Donnelly et al., 1986). Since the period length of the LST record is not enough to estimate a significant statistical association between LSTA and SCL, this association could be analyzed through NmaxA, assuming that both parameters are linearly related to the solar radiation in the UV and EUV ranges.

Figure 3 shows LSTA monthly values together with NmaxA. The correlation coefficient is higher than 0.90 with a 99% significance level. It can be deduced then that if NmaxA is associated to SCL, then LSTA could also be related to this solar parameter.

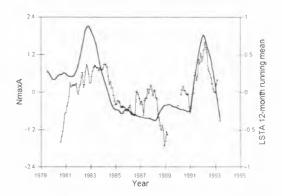


Figure 3: LSTA (°C) after a 12-month moving average (enhanced line) and monthly values of NmaxA for Manila (plus sign).

Tropospheric Temperature- TT.- measured at land surface

The annual mean temperature obtained from the mean daily temperature record of San Miguel de Tucuman

(29.6S, 294.6W at 481 m above sea level), has been analyzed in this work. This record is one of the longest time series in Argentina, covering the period 1889-1998. The deviation from the mean temperature of the complete period 1889-1998 has been considered here, and it was called Tucuman Temperature Anomaly, TTA.

This temperature data has been controlled with consistency and homogeneity tests (Minetti, 1991). To test the randomness of the TTA series, the cumulative periodogram was estimated (Durbin, 1969; Harvey, 1993). From it the existence of low frequency oscillations is deduced. In fact, the spectrum of TTA (Harvey, 1993), shows a significant peak at a period around 100 years.

In order to determine the association between this long term periodicity in TTA and SCL, the mean value of TTA for each solar cycle was calculated. In figure 4, TTA and SCL curves have been drawn. A close association can be noted, confirmed by a the correlation between them which results 0.71 at a 99% significance level.

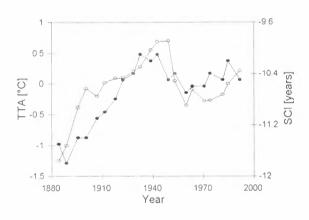


Figure 4. Solar cycle length, SCL, in years (filled circles) and TTA value for each solar cycle (empty circle).

DISCUSSION AND CONCLUSIONS

There is a close association between SCL and the atmospheric parameters Nmax, LST and TT.

In figure 5 it has been drawn, together with TTA, NmaxA and SCL, the Northern Hemisphere land temperature anomaly analyzed by Friis-Christensen and Lassen (1991) who reported that solar variability, measured by SCL, explain its variability since 1860. It can be noticed that the three curves have a similar behavior to that of SCL.

TTA, measured at a Southern Hemisphere location,

behaves in the long-term like the Northern Hemisphere does, supporting in this way, the results of Friis-Christensen and Lassen (1991).

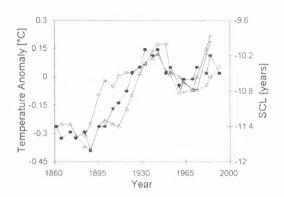


Figure 5: Northern Hemisphere temperature anomaly (empty triangle), TTA (empty circle), NmaxA (plus sign) -mean values for each solar cycle and assigned to the central year of each cycle- and SCL (filled circle).

It seems then, that solar activity modulates the longterm temperature variation observed in Tucuman.

Special attention deserves the important decrease from 1945 to 1970. For this period, it should not be expected changes in the increasing trend of temperature responding to an increasing greenhouse effect since the 19th century, when the industrial epoch began.

In the pre-industrial epoch, before 1850, the concentration of greenhouse gases seems to have remained almost constant, but since then, it has been monotonically increasing (Tsonis and Elsner, 1989; Mann et al., 1998; Victor, 1998). CO_2 atmospheric content -one of the greenhouse gases- has a steep increase during the period 1958-1988, and it is assumed that the upward trend will continue in the future. Due to the warming effects of the greenhouse gases, a continue rise in temperature is expected.

The unexpected temperature decrease during 1945-1970, suggests that solar activity seems to be more dominant than the greenhouse effect, in the long-term temperature behavior.

Nmax presents the same behavior that SCL including the decrease during 1945-1970. It is not expected over this parameter, measured around 300 km height, noticeable effects due to changes in lower regions of the atmosphere, for example a cooling of the thermosphere after an increase in greenhouse gases (Rishbeth, 1990). The changes observed in Nmax, seems to be due to solar effects only.

The time variation of LSTA is similar to that of NmaxA, suggesting that the stratosphere also responds solar long-term variations.

REFERENCES

- Donnelly, R. F., H. E. Hinteregger, and D. F. Heath, Temporal variations of solar EUV, UV and 10,830-A radiations, *J. Geophys. Res.* 91, 5567-5578, (1986)
- Durbin, J., Tests for serial correlation in regression analysis based on the periodogram of least-squares residuals, *Biometrika* 56, 1-15, (1969)
- Friis-Christensen, E. and K. Lassen, Length of the Solar Cycle: An Indicator of Solar activity Closely Associated with Climate, *Science* 254, 698-700, (1991)
- Friis-Christensen, E. and K. Lassen, *Global Temperature Variations and a Possible Association with Solar Activity Variations*, Scientific Report 92-3, Danish Meteorological Institute, Copenhagen, 8 pp, (1992)
- Friis-Christensen, E. and K. Lassen, Two and a Half Centuries of Solar Activity Variations and a Possible Association with Global Temperature, Scientific

Report 93-4, Danish Meteorological Institute, Copenhagen, 19 pp, (1993)

- Harvey, A.C., *Time Series Models*, Harvester Wheatsheaf, London, 307 pp, (1993)
- Mann, M.E., R.S. Bradley and M.K. Hughes, Globalscale temperature patterns and climate forcing over the past six xenturies, *Nature* 392, 779-787, (1998)
- Minetti, J. L., Estudio de las singularidades climáticas en series de temperaturas del Noroeste argentino (Climatic singularities study of North-west Argentine temperature series). Ph.D. Thesis. Atmospheric Sciences Department. University of Buenos Aires, Argentina.
- Tsonis, A.A. and J.B. Elsner, Testing the Global Warming Hypothesis, *Geophys.Res.Lett*, 16, 137-140, 1989.
- Victor, D.G., Strategies for cutting carbon, *Nature* 395, 837-838, (1998)
- Rishbeth, H., A greenhouse effect in the ionosphere, *Planet Space Sci.* 38, 945-948, (1990)

ABRUPT CLIMATE CHANGE AROUND 2700-2800 YEARS BP AS AN EXAMPLE OF EXISTENCE OF 2400 YEAR PERIODICITY IN SOLAR ACTIVITY AND SOLAR VARIABILITY

O.M.Raspopov, O.I.Shumilov^{1,2}, V.A.Dergachev³, B. van Geel⁴, N.-A.Mörner⁵, J. van der Plicht⁶ and H.Renssen⁷

1St.Petersburg Branch of Institute of Terrestrial Magnetism, Ionosphere and Radiowaves Propagation, RAS Muchnoy per. 2, P.O. Box 188, 194023 St.-Petersburg, Russia

tel: +7 812-552-8500 / fax: +7 812-310-5035 / e-mail: oleg@omr.izmi.ras.spb.ru

²Polar Geophysical Institute, Russian Academy of Sciences

tel: +7 81555-78201 / e-mail: oleg@pgi-ksc.murmansk.su

³Ioffe Physico-Technical Institute, Russian Academy of Sciences

Politekhnicheskaya 26, 194021 St.Petersburg, Russia

tel: + 7 812-247-9981 / fax: +7 812-247-1017 / e-mail: v.dergachev@pop.ioffe.rssi.ru /

⁴Centre for Geo-ecological Research, Faculty of Science, University of Amsterdam,

P.O.Box 94062, 1090 GB Amsterdam, The Netherlands.

tel: +31 20-525-7664 / fax: +31 20-525-7878 / e-mail: vanGeel@bio.uva.nl

⁵Paleogeophysics & Geodynamics, Stockholm University

SE 106 91 Stockholm, Sweden

tel: +46 (0)8-790-6771 / fax: +46 (0)8-790-6777 /e-mail: morner@pog.su.se

⁶Centre for Isotope Research, Radiocarbon Laboratory, Groningen University

Nijenborgh 4, 9747 AG Groningen, the Netherlands

tel: +3150-363-4760 / fax: +3150-363-4738 / e-mail plicht@phys.rug.nl

⁷The Netherlands Centre for Geo-ecological Research. Free University,

Amsterdam. The Netherlands.

ABSTRACT

One of well-known climate cooling events took place during the Little Ice Age, in the epoch of Wolf, Spörer, Maunder and Dalton minima of solar activity. It is experimentally documented that periods of decreased solar activity, as reconstructed with ¹⁴C and ¹⁰Be data in samples of known age, coincide with climatic change. A sharp rise in the ${}^{14}C$ concentration in the atmosphere, which occurred around 850 calendar years BC in the northern hemisphere, was contemporaneous with indications for an abrupt climate changes from relatively warm and continental to cooler and wetter conditions. Moreover, a ~2400-year periodicity in the development of the most sharp climatic variations was recorded. This periodicity is consistent with long-term secular solar activity fluctuations. Analysis of the geophysical situation has shown that in time interval from 2800 BP to 2600 BP a unique combination of external factors (solar activity, cosmic ray enhancement and geomagnetic field fast changes) took place which together forced abrupt climate change.

INTRODUCTION

The reconstruction of features of climatic changes has been greatly aided by historical documents, tree-ring width variations, pollen records, ice cores, glacier fluctuations, lake level records and so on. In the northern hemisphere, climatic data of high resolution for the Holocene exist in documentary record tree rings, lake and peat sediments. Historical evidence indicates that during the sharp cooling which happened relatively recent, from about AD1400 to about AD1990 (the Little Ice Age), global temperature is lowered by 1-2 °C, e.g., Dansgaard et al. (1993). The Little Ice Age coincides with the epoch of Wolf, Spörer , Maunder and Dalton minima in solar activity and with an significant increase of amplitude variations in the ¹⁴C concentration in the Earth's atmosphere, e.g., Stuiver and Quay (1980); Dergachev and Chistyakov (1995). As the Little Ice Age has the best geographic monitoring, this allows make some generalizations to other such oscillations. We present evidence for the next climatic cooling event, in the vicinity of 750-850 BC using mainly historical and proxy data and discuss the possible causes of the event (geophysical aspects). The examination of such oscillations may contribute to a greater understanding of the climate and the solar activity as the possible cause of climatic changes.

THE ABRUPT CLIMATE CHANGE AROUND 2700 BP

Evidence for climatic cooling in the northern hemisphere around 850 BC was found by Kilian et al. (1995) and Van Geel et al. (1996), from studying peat deposits. The sharp climatic cooling in this period can be also obtained from the examination of parameters of ring growth of long tree-rings chronologies. According to data presented by Becker and Kromer (1993) ring growth anomalies in the German oak occurred near this period. Becker et al.

¹⁸⁴²⁰⁰ Apatity Murmansk region, Russia.

(1985) published dendrochronological data from lakeside villages in the north Alps. They got the conclusion that no new villages were built for about half a millenium after 850 BC. The analysis of variations of tree-ring growth of the bristlecone pine (Campio Mountains) also indicates the cooling climate conditions around 2700 BP (Jacoby, 1997).

Palynological records of lake sediments in Cameroon (Reynaud-Farrera et al., 1996; Maley and Brenac, 1996) indicate a sudden forest retreat around 2700 BP. Using sediments from two sites in tropical Africa, Gasse and van Campo (1994) reconstructed the hydrological balance of lakes in Ethiopia and Ghana. From the result obtained it may be deduced that the manifestation of the large scale arid oscillation of climate in the vicinity of about 400 (period of Little Ice Age) and 3000 BP.

Van Geel et al. (1996, 1998), reviewing palynological, geological and archaeological evidence, concluded that global abrupt climate change occurred around 2700 BP. Climate in middle latitudes of the Northern Hemisphere (Europe, North America, Japan) and the Southern Hemisphere (New Zealand, South America) changed to colder and wetter conditions, and in the tropics (Africa, Caribbean) to drier conditions. Climate changed to dry conditions, related to world-wide changes of the atmospheric circulation.

EVIDENCE FROM THE PAST SOLAR AND GEOPHYSICAL FORCING OF CLIMATE CHANGE

The important peculiarity of climate change around 2700 BP is the synchronous sharp increase of cosmic ray fluxes recorded as an increase of the concentration of the cosmogenic isotope ¹⁴C (Δ^{14} C) in tree-rings (Fig. 1). An increase of ¹⁰Be record in ice core (Beer et al., 1988) was also found around this time.

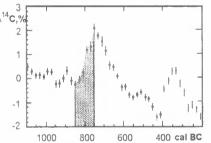


Figure 1. Δ^{14} C for the period between 1000 to 200 calendar years BC (after Stuiver et al., 1993). The abrupt rise of Δ^{14} C around 800 BC coincides with the phase of palaeoecological, geological and archaeological evidence for climate change (vertical hatching).

There is an increasing amount of evidence for the time interval from 3000 to 2000 BP that major climate changes correspond with variations in cosmic ray intensity, modulated by the changing intensity of solar wind. In the temperate zones of the Northern and Southern Hemisphere, the periods of increasing cosmic ray fluxes were characterized by a lowering of temperatures and by an increase of effective precipitation. At the same time there was a change to aridity in tropic regions, e.g., Gasse and van Campo (1994). An explanation for the climate changes, making the wet-dry contrast between the temperate zones and the tropics understandable, is given by Van Geel and Renssen (1998), see also van Geel et al. (1998). In that explanation the influence of changing UV intensity (important part of the relatively small changes in solar radiation) and the related changes in the production of ozone may play an important role (Haigh, 1994; 1996).

Two physical reasons can be responsible for long-term variations (tens of years and more) of cosmic ray fluxes in the Earth atmosphere: the action of solar activity variations on galactic cosmic ray fluxes, and changes of the dipole moment of the Earth's magnetic field.

Recent works, e.g. Vasiliev et al. (1997) showed that the large maxima of 2300-2400-year periodicity in atmospheric ¹⁴C concentrations may be caused by long-term decreases in solar activity and may be related to cooling climatic periods with Alpine glacier expansions shown (Denton and Karlen, 1973; Rothlisberger, 1986) and sharp reductions of the Caspian Sea level (Karpychev, 1994). The abrupt climate change around 2700 BP is one of the events in this series of cool intervals.

However, it was not only the decrease of solar activity that caused the increasing cosmic ray fluxes around 2700 BP. Around this time a geomagnetic excursion named "Sterno-Etruria" was recorded (Ransom, 1973). Around 2800 BP large variations of the direction of the geomagnetic dipole were observed (Kochegura, 1992). Two times the inclination (I) moved from positive (around 60°) to 0 or negative values (around $10-20^{\circ}$). Based on archaeomagnetic data from Georgia (Caucasus), Burlatskaya and Chelidze (1990) found that the strength of the geomagnetic field was reduced by 2 to 2.5 times around 2800 BP. A reduction by 3-4 times of the value of the geomagnetic dipole moment would lead to a sharp increase of cosmic ray penetration into the middle and low latitude atmosphere which would strongly enlarge the total value of cosmic ray fluxes on a global scale.

SUN'S ACTION, COSMIC RAYS AND CLIMATE

Experimental data discussed above show a close relation between the sharp increase of cosmic ray fluxes and the abrupt climate change around 2700 BP. Nearly the same situation was observed around the Wolf, Spörer, Maunder and Dalton minima of solar activity: a sharp increase of cosmic ray fluxes occurred during one of the coldest phases of the Little Ice Age.

An explanation of the physical effects of cosmic ray fluxes (modulated by solar activity and geomagnetic dipole changes) on climate and meteoparameters was given by Pudovkin and Raspopov (1992), and by Raspopov et al. (1998a). They studied the physical mechanisms (effects of galactic and solar cosmic ray fluxes penetrating into the stratosphere and troposphere and causing physical-chemical reactions) and concluded that optical parameters and the radiation balance of the atmosphere change under influence of varying cosmic ray fluxes (Fig. 2).

Experimental data indicate that the intensity of galactic cosmic ray fluxes change by several percents during

geomagnetic storms (Forbush decrease). During the 11years solar cycle the change of galactic cosmic ray fluxes

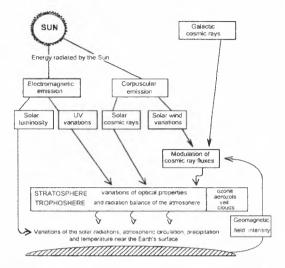


Figure 2. Scheme of the action of solar activity and the changes of geomagnetic field intensity on the climate and meteoparameters.

can be about 10 % on the Earth surface and even about 50% in the stratosphere. Larger changes in cosmic ray intensity will have taken place during long-term cycles of solar activity, for example during the Maunder minimum or during geomagnetic excursions.

Recent experimental data support the proposed physical mechanism. These data demonstrate the change of ozone layer density, the development of cloudiness, the formation of an aerosol layer in the stratosphere and an atmospheric veil during the increase of cosmic ray fluxes in the stratosphere and decrease of the temperature in the stratosphere, e.g., Dmitriev and Lomakina (1977); Shumilov et al. (1992; 1996); Stephenson and Scourfield (1992); Kodama et al. (1992), Svensmark and Friis-Christensen (1997). The data mentioned above concerning the changes of optical and thermodynamical properties of the atmosphere related to cosmic ray flux variations in the atmosphere permitted, e.g. Raspopov et al. (1997a; 1997b; 1998b) to estimate the possible decrease of the Earth surface temperature during the Maunder minimum of solar activity. This estimation gave the value of $\sim 0.6-0.7$ °C, that corresponds with the temperature change really observed. The proposed physical mechanism explains the physical link between the solar cycle length (indicative for solar activity which modulates galactic cosmic ray intensity) and the global Earth's surface temperature (Friis-Christensen and Lassen, 1991). At the same time the proposed mechanism explains changes of the Earth's surface temperature during excursions, inversions, and sharp variations of the geomagnetic field intensity (Raspopov et al., 1998b; Petrova and Raspopov, 1998).

We emphasise that during the deep minimum of solar activity around 2700 BP, the flux of solar radiation to the Earth surface was reduced; not only because of the change the atmospheric opacity due the action of cosmic rays, but also because of the reduction of the total solar irradiation. In addition, the reduction of the geomagnetic dipole value related to the geomagnetic excursion caused an increase of cosmic ray fluxes which was most effective in the middle and equatorial latitudes. As a consequence, during the geomagnetic excursion the dynamics and circulation of the equatorial and middle latitude atmosphere probably was strongly affected. Possibly this is the reason of dryness in equatorial Africa at the time discussed. In addition (van Geel et al., 1998; van Geel and Renssen, 1998), a reduction of solar UV, and related changes in ozone production, with worldwide effects on atmospheric circulation patterns may have played a role.

CONCLUSIONS

Palaeo-records indicate that the increase of cosmic ray fluxes around 2700 BP, which relate to 2400-year perid icity of solar activity, was accompanied by global climate cooling. The analysis of the geophysical situation shows that around 2700 BP a unique combination of externals factors (reduced solar activity and solar irradiation, cosmic ray enhancement, and a geomagnetic excursion) occurred, which together caused this climate change. Recent experimental data demonstrate the influence of cosmic rays on optical properties and on the radiation balance of the atmosphere. Cosmic ray enhancement leads to a global temperature decrease. We conclude that the sudden temperature decrease recorded around 2700 BP was caused by the combined effects of the above mentioned geophysical factors. These factors together caused the solar radiation decrease near the Earth surface and thus created conditions for the sudden and sharp climate cooling as shown in the palaeorecords.

ACKNOWLEDGEMENTS

This work was supported by the RFBR (grant 00-05-64921) and by EC (INTAS grant 97-31008 and INCO-COPERNICUS grant "EXTRATERRESTRIAL").

REFERENCES

- Becker, B., Billamboz, A., Egger, H., Gassmann, P., Orcel, A., Orcel, C. and Ruoff, U. (1985): Dendrochronologie in der Ur- and Frühgeschichte. *Antiqua*, Vol. 11, pp. 1-68.
- Becker, B. and Kromer, B. (1993): The continental treering record - absolute chronology, ¹⁴C calibration and climate change at 11 ka. *Palaeogeography*, *Palaeoclimatology*, *Palaeoecology*, Vol. 103, pp. 67-71.
- Beer, J., Siegenthaler, U., Bonani, G., Finkel, R.C., Oeschger, H., Suter, M. and Wölfli, W. (1988): Information on past solar activity and geomagnetism from ¹⁰Be in the Camp Century ice core. *Nature*, Vol. 331, pp. 675-678.
- Burlatskaya, S.P. and Chelidze, Z.A. (1990): The changes of geomagnetic field in Georgia during the last 1500 years BC. *Izvestiya Academii Nauk* USSR, Physics the Earth, No 7, pp. 84-93 (in Russian).
- Dansgaard, W., Johnsen, S.J., Clausen, H.B., Dahl-Jensen, D., Gundestrup, N.S., Hammer, C.U., Hvidberg, C.S., Steffensen, J.P., Sveinbjornsdottir, A.E., Jouzel, J. and Bond, G. (1993): Evidence for general instability of past climate from a 250-kyr ice core record. *Nature*, Vol. 364. pp. 218-220.

- Denton, G.H. and Karlen, W. (1973): Holocene climatic variations – their pattern and possible cause. *Quaternary Research*, Vol. 3, pp. 155-205. Dergachev, V. and Chistyakov, V. (1995): Cosmogenic
- radiocarbon and cyclical natural processes. Radiocarbon, Vol. 37, No. 2. pp. 417-424.
- Dmitriev, A.A. and Lomakina, E.Ju. (1977): Cloudiness and solar X-ray emission. In L.R.Rakipova (ed.) Solar Activity Effects in the Lower Atmosphere Hydrometeoizdat, Leningrad, pp. 70-75 (in Russian).
- Friis-Christensen, E. and Lassen, K. (1991): Length of the solar cycle: an indicator of solar activity closely associated with climate. Science, 254: 698-700.
- Gasse, F. and Vaaan Campo, E. (1994): Abrupt post-glacial climate events in West Asia and North Africa monsoon domains. Earth and Planetary Science Letters. Vol. 126, pp. 435-456.
- Haigh, J. D. (1994): The role of stratospheric ozone in modulating the solar radiative forcing of climate. Nature, Vol. 370, pp. 544-546.
- Haigh, J. D. (1996): The impact of solar variability on climate. Science, Vol. 272, pp. 981-984, 1996.
- Jacoby, G. (1997): personal communication. Karpychev, Ju.A. (1994): The periodicity of the level of the Caspian Sea on the data of radiocarbon analysis of Newcaspian sediments. Vodnye resursy, Vol. 21, No. 4, pp. 415-421 (in Russian).
- Kilian, M.R., van der Plicht, J. and van Geel, B. (1995): Dating raised bogs: new aspects of AMS ¹⁴C wiggle matching, a reservoir effect and climate change. Quaternary Science Review, Vol. 14, pp. 959-966.
- Kochegura, V.V. (1992): Use the Paleomagnetic Methods for Geological Mapping of Sea Shelf, St.-Petersburg, 144 pp. (in Russian.).
- Kodama, M., Kohmo, T., and Kanzawa, H. (1992): Stratospheric sudden cooling after solar proton event over Syowa Station, Antarctica, J. Geomagnetism and Geoelectricity, Vol. 44, pp. 361-366.
- Maley, J. and Brenac, P. (1998): Vegetation dynamics, palaeoenvironments and climatic changes in the forest of western Cameroon during the last 28,000 years BP. Review of Palaebotany and Palynology, Vol. 99, pp. 157-187.
- Petrova, G.N. and Raspopov, O.M. (1998): The link of changes in the geomagnetic moment and palaeoclimate for the last 12,000 years. Geomagnetism and Aeronomy., Vol. 38, No. 5, pp. 141-150.
- Pudovkin, M.I. and Raspopov, O.M. (1992): The mechanism of action of solar activity on the state of lower atmosphere and meteorological parameters. Geomagnetism and Aeronomy, Vol. 32, pp. 593-608 (English ed.).
- Ransom, C.J. (1973): Magnetism and archeology, Nature, Vol. 242, No. 5399, pp. 218-219.
- Raspopov, O.M., Shumilov, O.I., Kasatkina, E.A., Jacoby, G., and Dergachev, V.A. (1997a). The cosmic ray influence on cloudy and aerosol layers of the Earth and connection of solar cycle lengths to global surface temperature. Ioffe Physical-Technical Institute, St.-Petersburg, Report 1694, 21 pp. Raspopov, O.M.,
- Shumilov, O.I., Kasatkina, E.A., Dergachev, V.V., and Creer, K.M. (1997b):

Impact of cosmic ray flux variations caused by change in geomagnetic dipole moment on climate variability. Ioffe Physical-Technical Institute, St.-Petersburg, Report. 1693, 42 pp.

- Raspopov, O.M., Shumilov, O.I., and Kasatkina, E.A. (1998a): Cosmic rays and connection between solar cycle and global temperature. Biophysics,
- Vol. 43, No. 5, pp. 902-908. Raspopov, O.M., Shumilov, O.I., Kasatkina, E.A., Petrova, G.N., Dergachev, V.A., Creer, K. (1998b): Connection between the changes of geomagnetic field intensity and climate changes in the Holocene. Annales Geophysicae, Suppl. I to Vol. 16, pp. C22.
- Reynaud-Farrera, I., Maley, J and Wirmann, D. (1996): Vegetation et climat dans les forets du Sud-Quest Cameroun depuis 4770 ans BP: analyse pollinque des sédiments du Lac Ossa. Comptes Rendus de l'Académie des Sciences Paris, Vol. 322, pp. 749-755.
- Rothlisberger F. (1986): 10 000 Jahre Gletschergeschichte der Erde. Aarau: Verlag Sauerlande.
- Shumilov, O.I., Henriksen, K., Raspopov, O.M., and Kasatkina, E.A. (1992): Arctic ozone abundance and solar proton events, Geophysical Research Letters. Vol. 19, pp. 1647-1650.
- Shumilov, O.I., Kasatkina, E.A., Henriksen, K. and Vashenyuk, E.V. (1996): Enhancement of stratospheric aerosols after solar proton event. Annales Geophysicaes, Vol. 14, pp. 1119-1123.
- Stephenson, J.A.E. and Scourfield, M.W.J. (1992): Ozone depletion over the polar caps caused by solar proton, Geophysical Research Letters, Vol. 12, pp. 2425-2428.
- Stuiver, M. and Quay, P.D. (1980): Changes in atmospheric carbon-14 attributed to a variable Sun. Science, Vol. 207, No. 4426, pp.11-19.
- Stuiver, M., Long, A. and Kra, R.S. (1993): Calibration 1993. Radiocarbon, Vol.35, pp. 215-230.
- Svensmark, H. and Friis-Christensen, E. (1997): Variation of cosmic ray flux and global cloud coverage: A missing link in solar-climate relationship, J. Atmospheric and Solar-Terrestrial Physics, Vol. 59, pp. 1225-1232.
- Van Geel, B., Suurman, J., and Waterbolk, H.T. (1996): Archaeological and palaeoecological indication of an abrupt climate change in The Netherlands, and evidence for climatological teleconnection around 2650 BP. J Quaternary Science, Vol. 11, pp. 451-460.
- Van Geel, B. and Rensen, H. (1998): Abrupt climate change around 2650 BP in North-West Europe: evidence for telleconnections and a tentative explanation. In A.Issar and N.Brown (eds.), Water, Environment and Society in Times of Climatic Change. Dordrecht: Kluver, Proceedings of Sede Boker Workshop.
- Vasiliev, S.S., Dergachev, V.A. and Chistyakov, V.F. (1997): ~2400-year cycle detection in natural radiocarbon level in the atmosphere and the sensitivity of human behaviour to the large-scale climatic changes. Radiocarbon and Archaeology, No. 2, pp., 13-35 (in Russian), St.Petersburg, Institute of the History of Material Culture.

35-YEAR CLIMATIC BRUCKNER CYCLE – SOLAR CONTROL OF CLIMATE VARIABILITY?

O.M.Raspopov¹, O.I.Shumilov^{1,2}, E.A.Kasatkina^{1,2}, E.Turunen³, M.Lindholm⁴

¹St.Petersburg Branch of Institute of Terrestrial Magnetism, Ionosphere and Radiowaves Propagation, RAS Muchnoy per. 2, P.O. Box 188, 194023 St.-Petersburg, Russia

tel: +7 812-552-8500 / fax: +7 812-310-5035 / e-mail: oleg@omr.izmi.ras.spb.ru

²Polar Geophysical Institute, Russian Academy of Sciences, 184200 Apatity Murmansk region, Russia,

tel: +7 81555-78201 / e-mail: oleg@pgi-ksc.murmansk.su

³ Sodankyla Geophysical Observatory, FIN-99600 Sodankyla, Finland

⁴ University of Joensuu, FIN-80101, Finland

ABSTRACT

The effect of solar activity and variability on climatic processes during the last 300 years has been studied by analyzing the tree-ring growth at the northern timber line at Kola Peninsula (Russia) and in Scandinavia (Finnish Lapland). It has been shown that there is a good correlation between the solar activity periodicity (22 and 90 years) and cyclicity of climatic processes whose indicator is the tree-ring growth. The tree-ring growth is also the evidence of variability in climatic processes with periods of about 33 and 18 years. Climatic cyclicity with a period of about 35 years is known as the Brückner cycle. In the paper the physical interpretation of generation of the climatic Brückner cycle as resulting from the nonlinear effect of solar activity on atmospheric conditions is given.

INTRODUCTION

The data obtained in recent years point to the existence of long-term variations in solar irradiation associated with changes in the structure of solar magnetic fields [Lockwood and Stamper, 1999]. Soon et al. [2000] have shown that there is a close connection between the solar activity manifesting itself in changes of the size of solar coronal holes and such climatic parameter as variation in surface temperatures. Dergachev and Raspopov [2000] have demonstrated that variation in mean surface temperatures in the Northern hemisphere is subjected to the influence of the 90 and 210-year solar cycles. These studies, and also a number of other works [Lean et al., 1995; Friis-Christensen and Lassen, 1991; Pudovkin and Raspopov, 1992; Pudovkin and Veretenenko, 1996; Svensmark and Friis-Christensen, 1997; Svensmark, 1999; Shumilov et al., 1996; Raspopov et al., 1998; Tinsly, 1996] have given evidence for a strong effect exerted by solar activity and variability on climatic conditions on the Earth. This effect manifests itself in the most pronounced fashion for the periodicity of solar processes of about 20 years and more.

The physical nature of the effect of solar activity and variability on climatic changes can be interpreted both in the context of variations in solar irradiation in the process of solar activity evolution [Lean et al., 1995; Lockwood and Stamper, 1999] and in the context of the influence of solar rays on the atmosphere [Ney, 1959; Pudovkin and Raspopov, 1992; Shumilov et al., 1996; Raspopov et al., 1998; van Geel et al., 1999; Svensmark, 1999; Soon et al., 2000]. However, irrespective of the physical mechanism of the influence of solar activity and variability on climatic processes, this effect cannot be linear because of a complex structure of the atmosphere-ocean interaction, specific features of atmospheric circulation, etc.

The goal of this work was to obtain experimental data confirming the nonlinear character of the effect of solar activity and variability on climatic conditions by analyzing long-term dendrochronological data series of increases in tree-ring width near the northern timber line at the north-west of Russia (Kola Peninsula) and Scandinavia.

EXPERIMENTAL DATA

Analysis of the dendrochronological data reveals that the most pronounced climatic response is observed in the rings of the trees growing in critical climatic conditions, i.e., at high-elevation and high-latitude timber lines. For the investigations, the northern timber line region (pine) at Kola Peninsula in the Tuloma river valley $(\Phi=68,8^{\circ}N, \lambda=32,8^{\circ}W)$ was chosen. This region has a flat relief, and climatic conditions throughout the year are influenced by the warm Gulf Stream. As a consequence, the region has a good wetness in summer months, which creates favorable conditions for growth of trees in spite of the fact that the region is in polar latitudes. The presence of 250-350-year old trees confirms this. A good wetness of the region suggests that the main factor regulating the tree-ring growth here are temperature conditions, which, in principle, is typical of trees growing in the northern timber line regions [Jacoby and D'Arrigo, 1989; Briffa et al., 1992]. It is important to note that the Tuloma region is close to Northern Finland, whose climatic conditions are similar, where Siren [1961] carried out dendrochronological studies by using the tree-ring growth data for Lapland from 1180 to 1960 for latitudes $68 - 70^{\circ}$ N.

Fig. 1 shows mean annual tree-ring widths (in mm) for pine in the Tuloma valley region for 1629 – 1974. For

the analysis, core samples of 10 trees with the age of more than 300 years [Lovelius, 1979] were used. The samples were employed to determine the tree-ring growth for each of the trees, and then the mean for the whole series was found. The data were smoothed by a 5year running average. This representation of the data was used to exclude the annual meteorological variability and to demonstrate more clearly long-term variations in

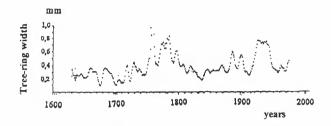


Figure 1. Tree-ring width (Pine) at the Northern timberline at Kola Peninsula, Tuloma River Valley (Φ =68.8° N, λ =32.8° W). A running mean filter of 5 years was used to smooth the data.

tree-ring growth. Variations in tree-ring growth with periods of ~20-30 years and ~ 80-90 years can be easily seen in Fig.1. It is also evident that the largest width of tree rings and, hence, highest summer temperatures at Kola Peninsula took place in ~ 1760 – 1780 and in 1940 – 1950, and the minimum width of tree rings (and temperature) were observed in 1770 – 1780 and ~ 1840. This is in good agreement with the temperature behavior in the Northern hemisphere in the past reconstructed from the data on tree-ring widths in Northern America [Jacoby and D'Arrigo, 1989]. A pronounced minimum around 1815 –1816 is well seen as well. This temperature minimum has a global character and is typically attributed to eruption of the Tamboro volcano in 1815 r. [Jones et al., 1995].

Thus the data on pine ring growth at the northern timberline at Kola Peninsula contain palaeoclimatic information consistent with the general trends in climatic variations at high latitudes of the Northern hemisphere during the last centuries.

Fig.2a shows the results of spectral analysis of temporal variations in ring widths of pine in the Tuloma valley for the period from 1629 to 1974; Fig.2b presents the results of spectral analysis of tree-ring growth for Finnish Lapland from 1463 to 1960 [Siren, 1961]. It is obvious that the two spectra nearly coincide, which points to identical changes in climatic conditions in the north of Scandinavia and at Kola Peninsula during the last 400 -500 years. The spectral density is seen to peak at periods ~ 11, 23, and 88 - 90 years corresponding to the periodicity in solar activity. In addition, the spectral density distribution has maxima at ~ 30 - 33 and ~ 18years. Periodicity in climatic phenomena with a period of about 30 –35 years was for the fist time revealed in 1890 by Brückner [1890] and was called the Brückner cycle. At first Brückner found the fundamental period of climatic oscillations equal to 34.8 ± 0.7 years. Later

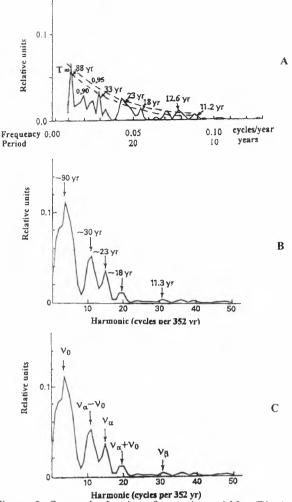


Figure 2. Spectral density of tree-ring width (Pine) at Kola Peninsula (a) and Finnish Lapland (b), and distribution of frequencies of variation in the tree-ring width corresponding to periodicities in solar activity $(v_0, v_{\alpha}, v_{\beta})$ and their combinatory frequencies $(v_{\alpha}-v_0 \text{ and } v_{\alpha}+v_0)$ in Finnish Lapland (c). Dotted lines on curve (a) are confidential levels (0.9 and 0.95).

convincing experimental evidence for such a periodicity in climatic processes was obtained, and detailed analysis extended the Brückner cycle from 30 to 45 years [Sazonov, 1979]. The 18-year periodicity in climatic processes is typically interpreted in the context of the effect of lunar tides [O'Brien and Currie, 1993].

DISCUSSION

Spectral analysis of dendrochronological series for the north of Kola the spectra, the climatic Brückner cycle also manifests Peninsula and Finnish Lapland (Fig. 2) shows that external factors (solar activity, lunar tides) efficiently affect climatic processes at high latitudes. In The spectra the climatic Brückner cycle also manifest itself. Note that the physical nature of this cycle has not been explained so far.

As noted above, the effect of solar activity and variability on climatic processes cannot be linear on the

global scale because of a number of factors, such as a large inertia of the atmosphere-ocean system, a complicated structure of atmospheric circulation, difference in the albedo of the water surface and land, etc. Let us examine the structure of the spectra shown in Fig.2 from the point of view of the nonlinearity of the effect of solar activity and variability on the atmosphere. In case of a nonlinear process, oscillations multiple to basic periods of solar activity are bound to arise in the system (Gleissberg cycle – $T_1=1/v_1=88-90$ years, Hale cycle – $T_2=1/v_2=22$ years, Schwabe cycle $T_3=1/v_3=11$ years) [Damon et al., 1989]. In addition, combinatory frequencies given by the relation $v=mv_1+nv_2$, where m and *n* integers, can be generated [Burroughs, 1994]. Analysis of dendrochronological and other climatic data for different regions of the Earth, including temperature measurements records in Sr.Petersburg, Stockholm, and Trondheim [Pudovkin and Lyubchich, 1989; Ol', 1969] has revealed a stronger effect of 22 and 90-year solar cycles compared with 11-year cycles. Therefore, it can be expected that combinatory frequencies and harmonics resulting from Gleissberg and Hale cycles will appear in the spectra of natural processes. In this case Gleissberg and Hale cycles can generate such combinatory frequencies as $v_{-}=v_{2}-v_{1}=1/T_{2}-1/T_{1}=0.034$ and $v_{+}=$ $v_2 + v_1 = 1/T_2 + 1/T_1 = 0.057.$

These frequencies correspond to oscillation periods $T_{-} = 29.4$ years and $T_{-} = 17.5$ years. Since the length of solar cycles also varies, which is due to physical processes on the Sun, combinatory frequencies can cause periods in the range ~ 30-35 and ~ 17-18 years. Just these periods are present in the power spectra in Fig. 2. From this point of view the Brückner cycle in climatic processes can be interpreted as a result of the nonlinear effect of solar activity and variability on atmospheric processes. Variability of climatic conditions with a period of ~ 18 years requires further consideration aimed at separation of the effects of solar activity and lunar tides on climatic parameters

This physical interpretation of the reasons for the Brückner cycle implies that Brücker cycle can manifest itself on the global scale. This hypothesis in supported by analysis of palaeoclimatic data from different regions of the Earth. Schlueter [1999]. having performed spectral analysis of the δ^{18} O content in ice cores in Greenland and radiocarbon concentration in tree rings and thickness of lake varves in Germany for the Holocene period, found peaks at periods ~ 90, 20 -21 and ~ 33 years in all data series. Wang et al. [2000] analyzed the content of nitrates in ice at the Plateau of Tibet for 900 - 1900 and discovered periodic changes in nitrate concentration following the solar activity periodicity and also Brückner cycle. Spectral analysis revealed periods of 10.3, 22.9. 31.3 and 88.1 years. Cyclicity in climatic processes with a period of $\sim 30 - 35$ years was found in changes in the Saima Lake level in Finland [Sazonov, 1979]. There is a 31-year periodicity in the Kaspian sea level [Bagrov. 1963] and a 30-year periodicity in river flow at northwest of Russia. including basins of the Ladoga and

Onega lakes and areas adjacent to Ural [Zeretskaya et al., 1992].

An important feature of the Bruckner cycle consisting in the presence of two frequency bands with periods centered around 30 and 45 years was revealed by Sazonov [1979]. The author [Sazonov, 1979] emphasized that the attempts to find the 33-year cycle in solar activity failed and drew attention to the fact that short periods (T~ 30 years) were observed during the epochs with a high solar activity level, and long cycles (T~ 45 years) are typical of a low solar activity level. This result confirms the idea that the physical nature of the Brückner cycle is the result of the nonlinear effect of solar activity on climatic processes. Indeed, under conditions of a low solar activity and, hence, small or even nearly zero amplitude of the 11 and 22-year cyclicity, as in the Maunder minimum period, generation of combinatory frequencies of the type of $1/v = 1/v_1 \pm 1/v_2$ $1/v_2$ (with periods of ~ 18 and 30 years in our case) are not to be appreciable, and the nonlinear effect of solar activity must manifest itself in generation of harmonics of the 90-year cycle, which was actually observed. A 45year periodicity is the second harmonic of the 90-year cycle. An increasing amplitude of the 11 and 22-year solar cycles gives rise to a corresponding growth in the amplitude of combinatory frequencies with periods of ~ 30 and 18 years, and their effect on climatic processes becomes dominating over that of the 2-nd harmonic of the 90-year cycle.

CONCLUSIONS

The effect of solar activity on climatic processes during the last 300 years has been studied by using long-term dendrochronological series of tree-ring growth near the northern timber-line at Kola Peninsula and Northern Scandinavia. It has been shown that cyclicity of climatic processes correlates well with the solar activity periods (T \approx 22 and 90 years). and also with the periods corresponding to combinatory frequencies (T \approx 30-33 and 18 years) of 22- and 90-year solar periodicity.

The obtained results allow us to physically interpret the climatic Brückner cycle (T $\sim 30-35$ and ~ 45 years) as a result of the nonlinear effect of solar activity on atmospheric processes. Climatic variability with a period of ~ 18 years can be interpreted in the context of both the nonlinear effect of solar activity and the effect of periodicity in lunar tides on the climate.

ACKNOWLEDGEMENT

We are grateful to EC for supporting of this work under INTAS program (Project 31008) and INCO-COPERNICUS (Project EXTRATERRESTRIAL). and to Russian Foundation for Basic Research (Grant 00-05-64921).

REFERENCES

Bagrov, N.A. (1963): About oscillation of not-sink

lakes. Meteorology and Hydrology, No 6, pp. 41-46.

- Briffa, K.R., Jones, P.D., and Schweingruber, F. (1992) Tree-ring reconstruction of summer temperature patterns across western North America since 1600. J. of Climate, Vol. 5. pp. 735-754. Brückner, E. (1890): Klimaschwankungen seit 1700. Vol. 5. pp. 735-754.
- Geographische Abhandlungen, Vol. 14. 325 p.
- Weather Cycles. Real or Burroughs, W.J.(1994): imaginary? Cambrige: University Press. 207 p.
- Damon, P.E., and Jirikowic, J. (1992): The Sun as a lowfrequency harmonic oscillator. Radiocarbon ... Vol. 34. pp. 199-205.
- Dergachev, V.A., and Raspopov, O.M. (2000): Longterm processes on the Sun detemining tendency of the solar irradiation and the Earth's surface temperature changes. Geomagnetism and Aeronomy, Vol.40. No 3. pp.9-14.
- Friis-Christensen, E., and Lassen, K. (1991): Length of the solar cycle: A indicator of solar activity closely associated with climate. Science, Vol. 254. pp. 698-700.
- Jacoby, G.C., and D'Arrigo, R. (1989): Reconstructed Northern Hemisphere annual temperature since 1671 based on high-latitude tree-ring data from North America. Climate change, Vol. 14. pp. 39-59.
- Jones, P.D., Briffa, K.F., and Schweingruber, F. (1995): Tree-ring evidence of the widespread effect of explosive volcanic erruption. Geoph. Res. Lett., Vol. 22. pp.1333-1336.
- Lean, J., Beer, L., and Bredley, R. (1995): Reconstruction of solar irradiance since 1610: implications for climate change. Geophys. Res. Lett., Vol. 22. pp. 3195-3198.
- Lockwood, M., and Stamper, R. (1999): Long-term drift of the coronal source magnetic flux and the total solar irradiance. Geophys. Res. Lett., Vol. 26. pp.2461-2464.
- Lovelius, N. V. (1979): Variability of tree growth. Lenigrad, Nauka, 231 p.
- Ney, E.P. (1959): Cosmic radiation and weather. Nature, Vol. 183. pp. 451-452.
- O'Brien, D.P., and Currie, R. (1993): Observation of The 18.6-year cycle of air pressure and a theoretical model to explain certain aspects of this signal Climate Dynamics, Vol. 6. pp.287-298.
- Ol', A.I., (1969): 22-years cycle of solar activity in climate. Reports AANII, Vol. 289. Leningrad. Hydrometeoizdat. pp. 116-120.
- Pudovkin, M. I., and Lubchich, A.A. (1989): The manifistation of solar and magnetic activity variations in air temperatures at Leningrad. Geomagnetism and Aeronomy, Vol. 29, 359-363.
- Pudovkin, M. I., and Raspopov, O. M. (1992): The mechanism of action of solar activity on state of the lower atmosphere and meteorological Geomagnetism and Aeronomy, parameters.

(English Edition), Vol. 32. No 5. pp. 593-608.

- Pudovkin, M.I., and Veretenenko, S. (1996): Variations of the cosmic ray as one of the possible links between the solar activity and the lower atmosphere. Adv. Space. Res., Vol. 17. No 11. pp. (11)161-(11)164.
- Raspopov, O.M., Shumilov, O.I., and Kasatkina, E.A. (1998): Cosmic rays as a main factor of solar activity influence on climatic and atmospheric processes. Biophysics, Vol. 45, No 5. pp.721-726.
- Sazonov, B.I. (1979): Brückner cycle of droughts. In: Criterions and characteristics of droughts phenomena in USSR, Hydrometeoizdat, Leningrad, pp. 82-92.
- Vergleichene Schlüter, A.-D. (1999): Analyse Proxydaten fur das Paläoklimatologischer Diplomarbeit. Meteorologischen Holozän. der Freien Universität Berlin. Institute 87 p.
- Shumilov, O.I., Kasatkina, E.A., Henriksen, K. and Vashenyuk, E. V. (1996): Enhancement of stratospheric aerosols after solar proton event. Annales Geophysicaes, Vol. 14, pp. 1119-1123,
- Siren, G. (1961): Skogsgranstallen som indicator for klimatfluktuationerna I norra Fennoskandien under historisk tid. Communicationes Inst. Forestalis Fenniae, Vol. 54. p. 2.
- Soon, W., Baliunas, S., Postmentier, E.S., and Okeke, P. (2000): Variations of coronal hole area and terrestrial lower tropospheric air temperature from 1979 to mid-1998: astronomical forcing of change in the Earth's climate? New Astronomy, Vol. 4. pp. 563-579
- Svensmark, H. and Friis-Christensen, E. (1997): Variation of cosmic ray flux and global cloud coverage: A missing link in solar-climate relationship, J. Atmospheric and Solar-Terrestrial Physics, Vol. 59, pp. 1225-1232,
- Svensmark, H. (1998): Influence of cosmic rays n Earth's climate. Phys. Rev. Lett., Vol. 81. pp. 5027-5030
- Tinsley, B.A. (1996): Solar wind modulation of the global electric circuit and the apparent effect on cloud micriphysics, latent heat release, and tropospheric dynamics. J. Geomagn. Geoelectr., Vol. 48. pp. 165-175.
- Van Geel, B., Raspopov, O., Renssen, H., van der Plicht, J., Dergachev, V., and Meijer, H. A. J. (1999): The role of solar forcing upone climate change. Quarternary Sci. Rev., Vol. 18. pp. 331-338.
- Wang, N., Yao, T., and Thompson, L.G. (2000): Nitrate concentration in the Guliya ice core and solar activity. PAGES Newsletter, Vol. 8. No 2. p. 11
- Zaretskaya, I.P., Lobasenko, G.V., Rumyantsev, V.A., Ptitsina, N.G., and Tyasto, M.I. (1992): The variability of river flow depending on solar activity cycles. Biophysics, Vol. 37, pp. 517-533.

PHYSICAL INTERPRETATION OF SOLAR CYCLE LENGTH CONNECTION TO GLOBAL SURFACE TEMPERATURES

O.I. Shumilov^{1,2}, O.M. Raspopov^{1,2}, E.A. Kasatkina^{1,2}, G. Jacoby³, V.A. Dergachev⁴, and M.Lindholm⁵

¹Polar Geophysical Institute of RAS, P.O. Box 162, 184200 Apatity, Murmansk region, Russia tcl.: +7 81555-79-284 / fax: +7 81555-30-925 / c-mail: <u>olcg@aprec.ru</u>

² St.-Petersburg Filial of IZMIRAN, P.O. Box 181, 191023 St.-Petersburg, Russia tel.: +7 812-310-50-31 / fax.: +7 812-310-50-35 / e-mail: <u>oleg@omr.izmi.ras.spb.ru</u>

³ Tree-Ring Laboratory, Lamont-Doherty Earth Observatory, 61 Route 9 W, Palisades, New York 10964, USA tel.: +914 365-8616 / fax.: +914 365-8152 / e-mail: <u>druid@ldco.columbia.edu</u>

⁴ Ioffe Physical-Technical Institute of RAS, St.-Petersburg, Russia ⁵ University of Joensuu, FIN-80101, Finland

ABSTRACT

Possible physical interpretation of connection between solar cycle length (SCL) and temperature anomalies are discussed. It is shown that as a rule shorter cycles are the more intensive ones. During more intensive cycles one can observe solar radiation increase and decrease of galactic cosmic ray influence on cloud formation. Both, direct and non-direct effects of solar activity are additive and lead to temperature enhancement. So, the shorter cycles could be the warmer ones. It is demonstrated that temperature response to cycle length changes are different for periods 1705-1810 and 1900-1990, and equal $\sim 0.03^{\circ}/yr$ and $0.4^{\circ}/yr$ correspondingly, and practically absent for period 1810-1890.

SCL-parameter reflects only tendency: shorter (and more powerful) cycles are connected to warmer climate and could hardly be used for numerical estimates of solar influence on the climate.

INTRODUCTION

Physical interpretation of well-known excellent correlation between Solar Cycle Length (SCL) and Northern Hemisphere temperature (Δ T) why the connection shown by Friis-Christensen and Lassen (1991) is still far from complete understanding on account that SCL is not the causal factor influencing global temperatures. More over in work by Damon and Peristykh (1999) and Laut and Gundermann (2000) is the serious critics concerning results obtained by Friis-Christensen and Lassen (1991). Damon and Peristykh (1999) concluded that in the last century the temperature increase is connected in general to green-house effect and solar activity action was not more than 25%.

However neither in Damon and Peristykh (1999) work, not in the work by Laut and Gundermann (2000) there is no interpretation why the connection between SCL and ΔT rather well expressed in industrial epoch. Besides till present time there was not any attempt to give possible physical interpretation of connection between SCL and ΔT . The main aim of the present paper is discussion about possible physical interpretation of connection between SCL and variation of global temperature ΔT . Such interpretation probably may be based on the connection between SCL and solar cycle intensity: as a rule the shorter cycles are the more intensive ones.

RELATION BETWEEN SOLAR CYCLE LENGTH AND SOLAR CYCLE INTENSITY

Bray (1965) was the first, who noted the tendency that the shorter solar cycles are the more intensive. In more common form this tendency may be expressed by the equation (Chistyakov, 1997):

$$W_m = (377.9 \pm 64.5) - (24.959 \pm 58) \cdot L \tag{1}$$

where L is cycle length and W_m is the maximum sunspot number for the same cycle.

This equation can be used for comparison mean values W_m and L for 10 and more cycles. Unfortunately, it expresses rather weak correlation between W_m and L on long time scale. See, for example, Fig.1, where it is shown dependence between W_m and L for period 1705.5 – 1989.6 (time of cycle maximum) on W_m and L data from (Chistyakov, 1997). So, L is simply proxy measure of level of solar activity influencing on the climate. The dependence of temperature variations ΔT from SCL which is shown in (Friis-Christensen and Lassen, 1991) demonstrates the situation: the more active the Sun (and more shorter solar cycle) reflect to the higher Earth temperatures.

DISCUSSION

Two main agents connected to solar activity and influenced the climate are:

1. Level of solar radiation, because experimental data prove that integral value of total radiation changes on 0.1-0.15% from maxima to minima of 11-year cycle of solar activity (Frolich and Lean, 1998; Willson and Hudson, 1991). Estimates of solar radiation longer trend

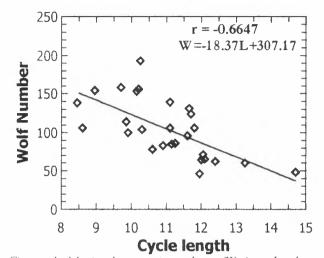


Figure 1. Maximal sunspot numbers (Wm) and solar cycle lengths (L) for 1705.5-1989.6, unfiltered data (Chistyakov, 1997).

on increase of activity of the Sun expressed in mean coronal source field over interval 1901-1995, give rise of total solar irradiation of $\Delta I = 1.65 \pm 0.23$ W·m⁻² (Lockwood and Stamper, 1999).

2. The second agent probably acting on the climate are galactic cosmic ray variations (Pudovkin and Raspopov, 1992: Shumilov et al., 1996; Svensmark and Friis-Christensen, 1997; Raspopov et al., 1998; van Geel et al., 1999). Changes of solar activity lead to changes of galactic cosmic ray intensity penetrating into the atmosphere. It was shown on some experimental data and model calculations that galactic (GCR) and episodic solar cosmic rays (SCR) can create additional aerosol clouds stimulating lower cloudiness creation in the atmosphere, which partly block solar radiation input to the surface that leads in turn to some decrease of the ground temperatures (Palle Bago and Butler, 2000). Taking into account the pronounced cyclic variations of GCR intensity (this variation is about 40% from min to max in cycles at the 18 km altitude), then the linear dependence between mean surface temperature departures (ΔT) and sunspot number W takes place (Raspopov et al., 1998):

$$\Delta T = 0.0031W - 0.57$$
 (2)

It is very important that effect of solar radiation change and effects of cosmic rays under changes of solar activity add each other. Actually, for example, under solar activity decrease the solar radiation also decreases, and cosmic ray intensity increases. The last leads to increases of aerosol layer density (Shumilov et al, 1996) and intensification of cloudiness formation (Svensmark and Friis-Christensen, 1997; Palle Bago and Butler, 2000) that in turn to decrease the solar radiation input to the Earth surface.

Let we consider the behavior of SCL proxy climate parameter for longer period outside period of instrumental temperature observations used in paper of Friis-Christensen and Lassen (1991), where it was obtained that excellent correlation between SCL and global temperature changes. For comparison we used: filtered (1-2-2-2-1) SCL data (SCL meanings were taken from (Chistyakov, 1997), multiproxy smoothed (Mann et al., 1998) data and land-sea instrumental smoothed temperature data (Jones et al., 1998).

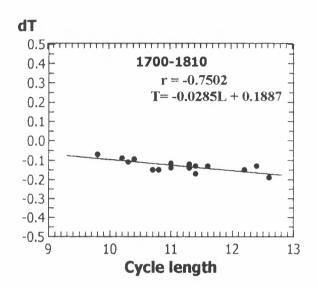
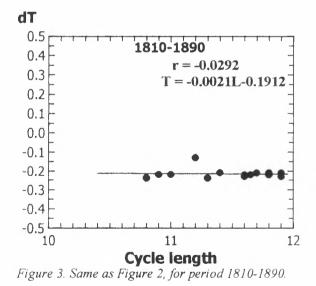


Figure 2. Annual smoothed multiproxy temperatures (Mann et al., 1998) plotted against filtered (12221) sunspot lengths (Chistyakov, 1997) for period 1700-1810.



In Figs.2,3,4 it is shown the dependence between the temperatures and SCL for periods: 1700-1810, 1810-1900, 1900-1990. The intervals were choosen taking into account the following reasons:

1. We cannot exclude the possible influence on the climate the very powerful Tambora volcanic eruption in 1815.

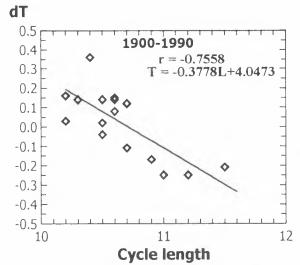


Figure 4. Annual smoothed land-sea instrumental data of Northern Hemisphere temperature variations (Jones et al., 1998) and filtered (12221) sunspot lengths (Chistvakov, 1997) for period 1900-1990.

- 2. We used the last interval in which Friis-Christensen and Lassen (1991) got excellent correlation between SCL and ΔT .
- 3. From 1900 year the strong rise of the global temperature was connected to green-house effect.
- 4. The first and the third intervals coincide with 210year maximum of solar activity. The intensity of 210-year cycle (the de Vries cycle) is 2-4 times more than that of 90-year ones (the Gleissberg cycle) (Dergachev, 1995).

From comparison of Figs.2-4 it can be concluded:

- A) SCL as climate parameter "works" not always, but around enhanced periods of long-term solar activity variations (possibly maximum of 210-year cycle) (Fig. 5). The alternative interpretation of this efficiency might have been distorted by other (nonsolar) physical reasons. For example, Tambora cruption in 1815 was the most powerful eruption for the last 22.000 years and could have led to rather shurt-time volcanic signal.
- B) The response of temperature to SCL was different from the first and third intervals: ~0.03°/yr and $0.4^{\circ}/yr$.

The interpretation of the last conclusion seems to be rather indefinite. The stronger response may be connected to green-house effect influence. But the presence of temperature minimum in 1950-1970 years (which coincides with 90-year solar cycle minimum) demonstrates the compatible influence of solar factor on the climate even on the ground of well-pronounced green-house effect (Fig. 5). On the other hand, SCL parameter is determined from-11-year Wolf number cycle parameter and cannot reflect all sides of solar activity. For example, level of solar radiation is more strongly connected to coronal source magnetic flux (Lockwood and Stamper, 1999). Long-term trend of coronal magnetic flux is not obviously connected to SCL determined from 11-year cycle parameters. In reality some discrepancy between annual means trend of the coronal source magnetic flux and smoothed sunspot numbet is seen from Fig.6 in (Lockwood and Stamper, 1999). The very good connection between solar coronal hole area and global tropospheric temperature anomaly has obtained by Soon et al. (2000).

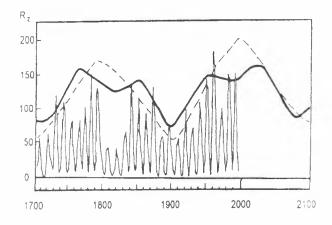


Figure 5. Temporal variations of solar activity for the last 300 years: R_{z} is the sunspot number; the broken line shows the 210-year cycle of solar activity; the thick one shows the linear combination of 90- and 210-year solar activity cycles.

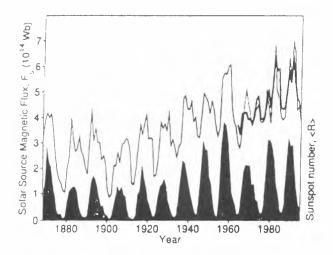


Figure 6. Annual means of coronal source magnetic flux and sunspot numbers (Lockwood and Stamper, 1999).

CONCLUSIONS

Physical connection between solar cycle length (SCL) and variation of global temperature (ΔT) could be based on relation between intensity of solar cycles an its duration: shorter (and more powerful) cycles are connected through pronounced solar radiation and effects of galactic cosmic rays on the cloudiness (and acrosols) to warmer climate. However the connection between SCL and temperature variation ΔT one have to considers only as a some tendency because not only solar cycle (and Wolf numbers) may determine the solar radiation level and the solar activity level in general. Relation coefficients between SCL and ΔT variations may as well depend on long-term variation of solar activity (the 2400-year, the Gleissberg, the de Viere cycles and etc.), and also on action other external factors (volcanic activity, green-house effect and etc.). We have to take into account that last century period coincides with epoch of 2400- and 210-year solar activity cycles enhancement.

ACKNOWLEDGEMENT

We are grateful to EC for supporting of this work under INTAS program (Project 31008) and INCO-COPERNICUS (Project EXTRATERRESTRIAL), and to Russian Foundation for Basic Research (Grant 00-05-64921).

REFERENCES

- Bray, J.R. (1965): Forest growth and glacier chronology in North-West North America in relation to solar activity. *Nature*, Vol. 205, pp. 440-443.
- Chistyakov, V.F. (1997): Solar cycles and climate oscillations, Dalnauka, Vladivostok (in Russian).
- Damon, P.E. and Peristykh, A. (1999): Solar cycle Length and 20th century Northern Hemisphere warming: Revisited. *Geophys. Res. Lett.*, Vol.26, pp. 2469-2472.
- Dergachev, V.A. (1995): On large-scale solar modulation of cosmogenic radiocarbon formation rate in the Earth atmosphere. *Izvestya RAS. Physics*, Vol. 59, pp. 53-62 (in Russian).
- Friis-Christensen, E. and Lassen, K. (1991): Length of the solar cycle: an indicator of solar activity closely associated with climate. *Science*, Vol. 245, pp. 698-700.
- Frolich, C. and Lean, J. (1998): The Sun's total irradiance: Cycles, trends and related climate change uncertainties. *Geophys. Res. Lett.*, Vol. 25, pp. 4377-4380.
- Jones, P.D., Parker, D.E., Osborn, T.J., and Briffa K.R. (1998): Global and hemispheric temperature anomalies – land and marine instrumental records. *Trends: a compendium of data on Global Change*, CDIAC, ORNL, Oak Ridge.
- Laut, P. and Gundermann, J. (2000): Is there a correlation between solar cycle lengths an

terrestrial temperatures? Old claims and new results. The Solar Cycle and Terrestrial Climate, I SOLSPA Euroconference, Programme and Abstracts. Tenerife, Spain. p.65.

- Lockwood, M. and Stamper, R. (1999): Long-term drift of the coronal source magnetic flux and the total solar irradiance. *Geophys. Research Lett.*, V. 26, pp. 2461-2464.
- Mann, M.E., Bradley, R.S., and Hughes, M.K. (1998): Global-scale temperature patterns and climate forcing over the past six centuries. *Nature*, Vol. 392, pp. 779-787.
- Palle Bago, E. and Butler, C.J. (2000): The influence of cosmic rays on terrestrial clouds and global warming. Astronomy & Geophysics, Vol. 41. pp.4.18-4.22.
- Pudovkin, M.I. and Raspopov, O.M. (1992): Mechanism of solar activity influence the low atmosphere state and meteoparameters. *Geomagnetism and aeronomy*, Vol. 32, pp. 1-10 (in Russian).
- Raspopov, O.M., Shumilov, O.I. and Kasatkina, E.A. (1998): Cosmic rays as main factor of influence of solar variability on climatic and atmospheric parameters. *Biophysics*, Vol. 43, pp. 902-908.
- Shumilov, O.I., Kasatkina, E.A., Henriksen, K., and Vashenyuk, E.V. (1996): Enhancement of sstratospheric aerosols after solar proton event. Ann. Geophysicae. Vol. 14, pp. 1119-1124.
- Soon, W., Baliunas, S., Posmentier, E.S., and Okeke, P. (2000): Variation of solar coronal hole area and terrestrial lower tropospheric air temperature from 1979 to mid-1998: astronomical forcing of change in earth's climate? New Astronomy, Vol. 4. Pp. 563-579.
- Svensmarjk, H. and Friis-Christensen, E. (1997): Variation of cosmic ray flux and global cloud coverage: A missing link in solar-climate relationship. J. Atmos. Sol.-Terrestr. Phys., Vol. 59, pp. 1225-1232.
- van Geel, B., Raspopov, O.M., Renssen, H., van der Plicht, J., Dergachev, V.A., and Meijer, H.A.J. (1999): The role of solar forcing upon climate change. *Quaternery Science Reviews*. V. 18, pp.331-336.
- Willson, R.C. and Hudson, H.S. (1991): The Sun's luminosity over a complete solar cycle. *Nature*, Vol. 351, pp. 42-44.

DIFFERENCES IN THE ZONAL BEHAVIOUR OF SOLAR ACTIVITY ARE RELEVANT FOR THE SOLAR-TERRESTRIAL RELATIONS

J. Sýkora¹, O. G. Badalyan², and M. Storini³

¹Astronomical Institute, 05960 Tatranská Lomnica, Slovak Republic; sykora@ta3.sk ²IZMIRAN, 142190 Troitsk, Russia; badalyan@izmiran.troitsk.ru; obridko@solter.troitsk.ru ³IFSI/CNR, Via del Fosso del Cavaliere 100, 00133 Roma, Italy; storini@fis.uniroma3.it

ABSTRACT

It is undoubtedly valuable to explore the space distribution and time evolution of different solar activity phenomena when trying to understand better the quality and quantity of their responses in the heliosphere. By the phenomenon of coronal green line brightness we demonstrate that the dynamics of this line radiation, as recorded especially within the zone of middle solar latitudes, may represent a source of relevant information to achieve the goal.

Key words: solar emission corona; solar cycle; solarterrestrial relations.

1. INTRODUCTION

Solar corona represents a highly rarefied and fully ionized conductive plasma. Its time and space organizations are extremely sensitive to the structure and intensity of the solar magnetic field and, in fact, characterized by a pronounced anisotropy of the instantaneous state of this field. Indeed, such a largescale coronal inhomogeneities as are the streamers, condensations, coronal holes, polar rays, loops, voids, etc., all they are caused and outlined by a discrete magnetic field distribution in the solar atmosphere. The above structures come from the so-called whitelight corona originating from the scattering of photospheric photons by the free electrons present in the coronal medium.

Similarly, the long-term and large-scale distributions of the solar emission corona brightness are not isotropic, as well. They specifically reflect evolution of the global solar magnetism during the solar cycles. At the same time, the E-corona represents the only component of the coronal radiation which arises out of true emission by the coronal ions. The mentioned discrete coronal distributions are manifested both in the heliographic longitude and in the heliographic latitude and contribute to the variabilities and periodicities found in the general solar activity.

Intensity of the coronal green line Fe XIV 530.3 nm (CGL, in the next) represents a very proper index of solar activity. It is because CGL radiation is proportional to the density and temperature of the medium where this line originates. The regular daily patrol measurements of the CGL intensity are now carried out for more than half a century by a small network of the high-altitude coronal observatories. We have transformed all the accessible data to a common photometric scale and the digitized database was created. More details about the reduction of data and the structure of database can be found. e.g., in Sýkora (1992a).

The data on CGL intensity is available for each 5° of solar latitude. Therefore, we are able to analyse the course of brightness at different latitudes, within arbitrary latitudinal zones, solar hemispheres or, over the Sun as a star. We prefer to cut the Sun to, at least, five latitudinal zones: one equatorial and the polar and middle-latitude zones at both the hemispheres. In fact, we found the global coronal indices improperly characterizing the solar activity, smoothing many important details.

Some results indicating a particular role of the middle-latitude zones (in our interpretation covering most often $\pm 20^{\circ} - 50^{\circ}$ of latitude) in relation to the 22-year solar magnetic cyclicity and the long-term cosmic ray modulation, including existence of the dynamic and quasi-stationary components in this modulation, were already published (Storini and Sýkora. 1997; Storini et al., 1997). The green corona low brightness regions (alias coronal holes), identified inside the middle-latitude zones, were found well correlated with the increased geactivity (Sýkora, 1992b).

We are sorry do not concern here with the interesting longitudinal distributions of the CGL brightness, displaying a long-lasting persistence of coronal activ-

Proc. 1st Solar & Space Weather Euroconference, 'The Solar Cycle and Terrestrial Climate', Santa Cruz de Tenerife, Tenerife, Spain, 25-29 September 2000 (ESA SP-463, December 2000)

526

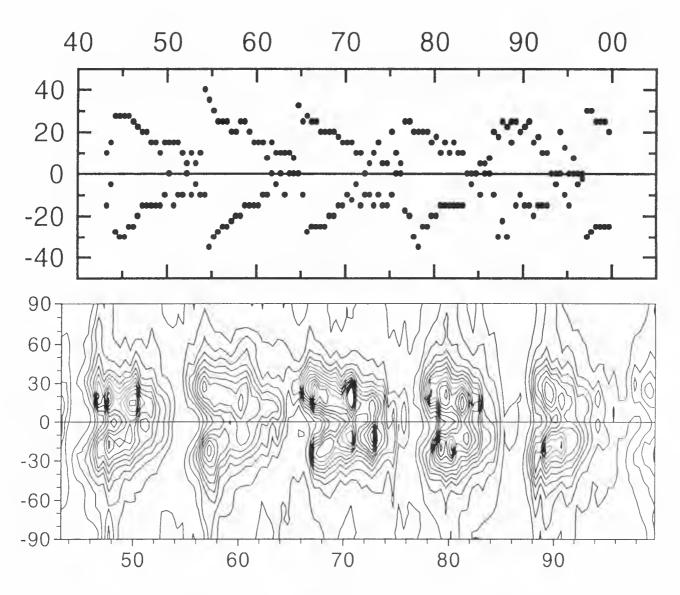


Figure 1. Time-latitude distribution of the CGL intensity during the last five solar cycles and a gradual cyclic relocation of the brightnes maximum (cf. coronal activity). The isophotes are drawn with step of 10 absolute coronal units (a.c.u.) and range from 10 to 140 a.c.u. in this figure. (We appologize for the difference in the horizontal scales on both the panels.)

ity in the discrete intervals of heliographic longitudes and allowing to assume two modes (rigid and differential) in the rotation of the solar corona (Sýkora, 1994, and the references therein).

2. A SAMPLE OF THE RESULTS OBTAINED

The time-latitude distribution of the CGL intensity (the half-yearly averaged data was used in this case) is plotted in the lower panel of Figure 1. Clearly non-uniform distribution of the coronal brightness is displayed both over the solar latitudes and during the solar cycles. Some impulses (maxima) in the coronal activity may be well distinguished. they are, probably. modulated by the generally accepted quasi-biennial oscillations in solar activity. The upper panel of Figure 1 shows a gradul shift of the brightness maximum from the higher latitudes down to the equator (Spörer's law). There is indication on the relation between the height of the sunspot cycle and the highest latitude at which the coronal maximum is situated at the beginning of a given cycle.

Monthly averaged CGL intensities, as plotted in five panels of Figure 2, demonstrate quite a small contribution of the extensive polar zones $\pm 60^{\circ} - 90^{\circ}$ to the total CGL brightness. This is because the polar regions are most often covered by coronal holes which with their reduced density and temperature are not favourable for the CGL excitation. Conversely, the green corona low brightness regions are good proxy of coronal holes (Sýkora, 1992b; Sýkora et al., 2000). Except of that, the polar zones manifest a strongly supressed variability of the CGL brightness during the solar cycles. The last finding is well seen also in Figure 3 where the maximum and minimum half-

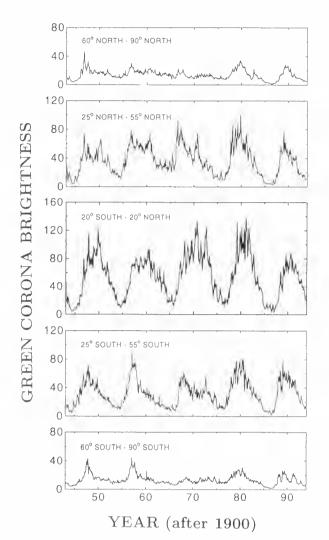


Figure 2. Monthly averaged CGL intensities plotted for the chosen latitudinal zones manifest very small contribution of the extensive polar zones to the total CGL brightness of the Sun.

yearly means are drawn separately for the equatorial, middle and polar zones. It is worth noticing that the largest variability of coronal brightness (proportional to the size of the shadowed area) is typical for the middle-latitude zones at both solar hemispheres.

A specific behaviour of exactly these zones is oncemore shown in Figure 4. When the total green line (TGI) intensity is compared with the sunspot number curve ($\mathbb{R}_{\mathbb{Z}}/2$) the correlation is not very good as for the heights of the cycles. On the other hand, this correlation is much better when the coronal brightness is normalized to the brightness of the middlelatitude zones (the lower panel of Figure 4). However, in this case the coronal cycle is substantially shifted back in time.

The mentioned peculiarity is even better visible in Figure 5 and we seriously emphasize this quality. The courses of the CGL brightness during activity cycles are presented separately for the equatorial and

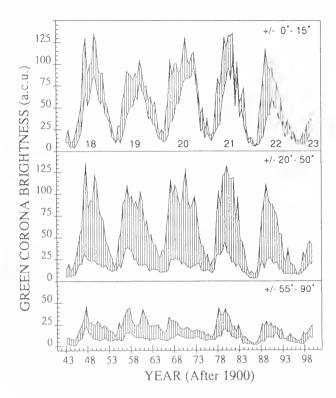


Figure 3. Course of the maximum and minimum CGL brightness within the different zones of the Sun convince oneself on the largest dynamics in activity of the middle latitude zones.

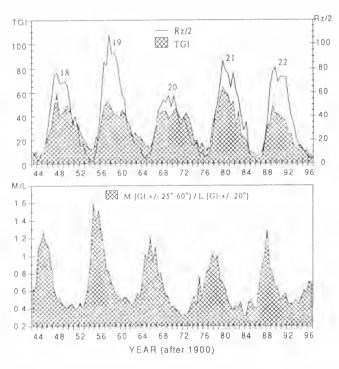


Figure 4. Comparison of the sunspot and CGL activity cycles indicates a peculiar role of the middlelatitude zone.

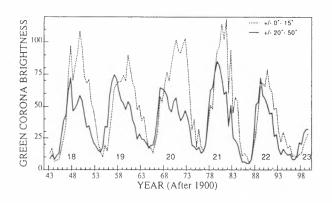


Figure 5. The course of the CGL solar cycles is considerably different when comparing two solar zones.

middle-latitude zones. Surprisingly, the maxima of the CGL brightness middle-latitude curve occur for some 2–5 years earlier in comparison with those in the equatorial curve. This fact need not be omitted and ignored.

The solar corona undoubtedly reflects the MHD processes in the lower layers of the Sun and, subsequently, it mediates governing of the processes taking place in the heliosphere. Therefore, the last finding, together with the other properties described in this contribution, drive us to recommed more frequent investigations of solar activity and its responses in the heliosphere by dividing the Sun into the particular latitudinal zones. Consideration of the different phases in the solar cycle separately could be fruitful, as well. In both the approaches, more relevant results may be expected in comparison with the studies based on the analysis of the whole Sun indices only.

ACKNOWLEDGMENTS

The authors greatly appreciate the support of the VEGA Grant 02/5007/98 of the Slovak Academy of Sciences, the Grant No. 99-02-18346 of the Russian Foundation for Basic Research and the 1998–99 Grant of the National Antarctic Program of Italy.

REFERENCES

- Storini M., Pase S., Sýkora J., et al., 1997, Solar Phys. 172, 317
- Storini M., Sýkora J., 1997, Solar Phys. 176, 417
- Sýkora J., 1992a, Contrib. Astron. Obs. Skalnaté Pleso 22, 55
- Sýkora J., 1992b, Solar Phys. 140, 379
- Sýkora J., 1994, Adv. Space Res. 14, (4)73
- Sýkora J., Badalyan O.G., Obridko V.N., 2000, in this volume

RELATIONSHIPS BETWEEN IONOSPHERIC DISTURBANCES AND CHANGES OF SEA LEVEL PRESSURE OVER THE ARCTIC

L. Tóth and S. Szegedi

Heliophysical Observatory of the Hungarian Academy of Sciences, H-4010 Debrecen, P.O.B. 30. Hungary Tel/fax: +36 52-437-343, e-mail: tothla@tigris.klte.hu

Department of Meteorology, University of Debrecen, H-4010 Debrecen, P.O.B. 13. Hungary Tel: +36 52-512-900/2366, Fax: +36 52-512-927, e-mail: szegedis@tigris.klte.hu

ABSTRACT

Large amounts of energy are absorbed in the atmosphere around the polar cap during geomagnetic disturbances connected to solar activity that may indirectly influence meteorological processes in the troposphere. For the examination of the phenomenon mentioned above the localization of the energy absorption is necessary. A possible way is the observation of the upper atmosphere in UV-light or in X-ray generated by showers of energetic electrons. Due to the higher energy the last one yields more compact excited areas that makes better position determination possible. Therefore in the present work an attempt is made to trace relationships between ionospheric disturbances detectable in the X-ray region and trends of changes of sea level pressure (SLP) over the Arctic. It was found that the effect can be stronger or weaker depending on the initial conditions. If there is a strong and stable surface high or low-pressure system under the area activated in X-ray the influence will be very weak. If the disturbance takes place over a weaker surface high or low-pressure system the effect is stronger. It may deepen the low if SLP is stagnating or decreasing. It may slow down the increase of SLP when the low is weakening or a high-pressure ridge is developing.

INTRODUCTION

During geomagnetic disturbances caused by solar activities large amounts of energy are absorbed in the atmosphere, which may have an indirect effect on meteorological processes in the troposphere. One of the possible reasons is that the charged particles due to solar activity penetrate into the auroral zones and generate an electric jet current in the lower ionosphere. In the polar cap this current may induce variable magnetic fields in the lover atmosphere, which produces conductivity electric currents. These vortex currents are one of the possible sources of the heating of atmosphere, which causes the air masses to expand. The variations of the temperature in the atmosphere may produce a meridional pressure profile, which may cause a change of the zonal circulation. This has been supported by several works showing a slight change in the air pressure connected to geomagnetic activities caused by solar events (Mustel 1966, 1972; Shchuka 1969; Shuurmans et al. 1969, 1979; Roberts et al. 1973; King 1974; Smirnov 1996; Bochnicek 1998; Pudovkin 1998; etc). Special interest is in the fact that the places of this energy feedings are mainly in the auroral zone that is approximately coinciding with the zone of the planetary waves from where the mid-latitude cyclones originate.

For this reason in this paper an attempt is made to find relationships between the location of disturbances of the ionosphere detectable in the X-ray region and changes of SLP over the Arctic.

METHOD OF INVESTIGATION

In our work the changes of SLP under the center of areas of twenty-four different ionospheric X-ray events were analyzed between 11 January and 27 February 2000. The time pattern of the observed X-ray events ($e_{1.24}$) related to the geomagnetic disturbances is seen in figure 1.

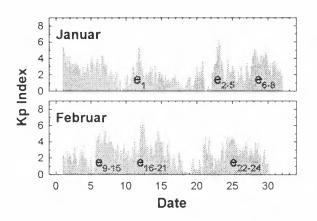


Figure 1: Geomagnetic Activity Indices during the winter of year 2000 (see ref. NOAA) connected to the examined X-ray disturbance events (e_{1-24}) of the ionosphere.

Proc. 1st Solar & Space Weather Euroconference, 'The Solar Cycle and Terrestrial Climate'. Santa Cruz de Tenerife, Tenerife, Spain. 25-29 September 2000 (ESA SP-463, December 2000)

Two main considerations in view were kept in the course of the selection of the studied time period. First of all we have chosen a term that is around the solar activity maximum, when the number of different ionospheric disturbances originated from solar events are sufficient but they still do not in overlap with each other. On the other hand, the winter period is favourable because that time the Arctic and the planetary waves along the edge of the polar cap are free of disturbances caused by solar irradiation (Serrze 1993)

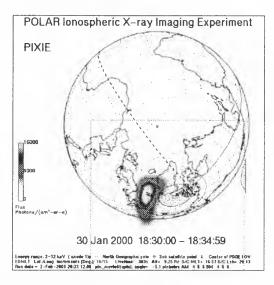


Figure 2: An observation (the case of e_8) of Polar Ionospheric X-ray Imaging Experiment (PIXIE).

To localize the ionospheric disturbances images of Polar Ionospheric X-ray Imaging Experiment (see ref. PIXIE, figure 2.) were applied while changes of SLP over the North polar areas were analyzed using the surface atmospheric pressure analysis charts of the Canadian Meteorological Centre (see ref. CMC).

Despite the fact that in similar investigations the 500 hpa geopotential height analysis charts are generally used we applied SLP maps because of their higher space and time resolution. First the size and co-ordinates of the centre of areas of ionospheric disturbances projected onto the surface of the Earth had been determined. Then the changes of atmospheric pressure in the centres and the time derivatives of them were calculated by interpolation on the base of the surface isobar charts before, during and after the ionospheric disturbances. Synoptic events like cyclone development under the areas of ionospheric disturbances have been taken into consideration as well.

RESULTS

The expected changes of pressure at the surface of the Earth have appeared to be similar to have been observed. Namely, the heating of the atmosphere under the place of the ionospheric disturbance observed in X-

ray in our cases usually caused an observable decreasing of SLP. Clear examples of this phenomenon are shown in figure 3. The disturbance may deepen the low if the SLP is stagnating (case of e_2 in figure 3.) or decreasing (case of e_1 in figure 3.). It may slow down or turn back the increase of SLP when the low is weakening or a high-pressure ridge is developing (case of e_8 in figure 3.).

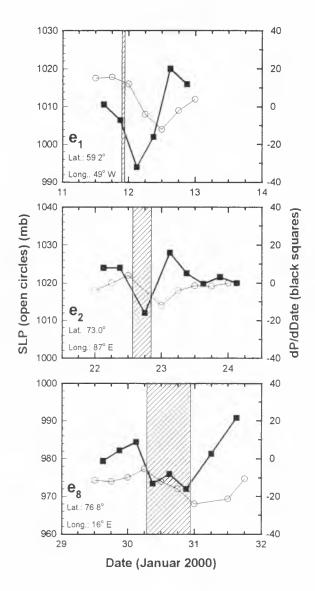


Figure 3: The changes of sea level pressure (SLP) as the function of time (open circles) and the time derivative of it (black squares) at the term of an ionospheric disturbance. The duration of the given ionospheric disturbance event $(e_{1,2,8})$ observed in X-ray region is shown by stripped area.

The only exceptions in the course of our investigation were in the cases of e_{9-14} events where two large and relatively stable low-pressure systems with a strong high-pressure ridge between them covered the Arctic. These were such large and strong formations that

processes connected to geomagnetic disturbances were unable to produce considerable decreases in the SLP (figure 4.).

However, an interesting effect appeared in these stagnating SLP areas between the surface high and low pressure systems called the "polar front" that is the most sensitive area from the point of view of development of mid-latitude cyclones (Parker 2000). The heating of the atmosphere during geomagnetic disturbances may create or stop waves of SLP (with a period of ~12 hours in our cases) at a given location (figure 4.) which affects the position of the "polar front".

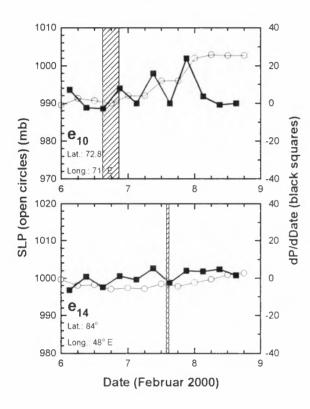


Figure 4: Possible connection between ionospheric disturbances and the fluctuations of SLP at a given point of the polar front. (Notation is the same as in figure 3.)

And the impacts of the heating by energy absorbed in the atmosphere around the "polar front" are different depending on the initial conditions. If the change induced by geomagnetic disturbances in the atmospheric pressure is in phase with the trends of the 12 hour waves at the given point it may strengthen that (case e_{10} in figure 4). If it is in anti-phase it may weaken or even extinguish the 12 hour waves (e_{14} in figure 4).

CONCLUSIONS

Our results support the hypothesis that energy absorbed in the lover atmosphere during ionospheric disturbances that affects on thermodynamic processes in the troposphere causing characteristic patterns of SLP. Furthermore these processes are in coincidence in time and space with ionospheric disturbances detected in the X-ray region. These impacts cannot trigger large-scale meteorological processes like cyclogenesis alone, but can strengthen or weaken the development of tropospheric processes.

ACKNOWLEDGEMENT

The authors thank the PIXIE and David Chenette for their support with observations.

REFERENCES

- Bochnicek J., Hejda P., Bucha V., Pycha J. (1998): Ann. Geophysicae, 17, 925
- CMC, Canadian Meteorological Centre. Operational Analysis Charts and Bulletins, (http://www.cmc.ec.gc.ca/cmc/htmls/analysis.ht ml)
- King J.W. (1974): Naturem 247, 131
- Mustel E.R. (1966) Soviet astr. 10, 288
- Mustel E.R. (1972): U.S.S.R. Acad. Sci. Astron. Counc. Publ. No. 24.
- NOAA (2000) Solar-Geophysical Data prompt reports. 667, 146 and 668, 162
- Parker D.J. (2000): Frontal Theory. in: Weather.55, 120
- PIXIE, Polar Ionospheric X-ray Imaging Experiment (http://pixie.spasci.com/)
- Pudovkin M.I., Morozova A.L. (1998): Journal of Atmospheric and Solar-Terrestrial Physics 60,1729
- Roberts W.O., Olson R.H (1973): J. Atmos. Sci. 30, 135
- Shchuka T.I., 1969, Trudy AANII 289, 74
- Serrze M.C., Box J.E., Bary R.G., Walsh J. E. (1993): Meteorol. Atmos. Phys. 51, 147.
- Shuurmans C.J.E., Oort A.H. (1969): Pure App. Geophys. 75, 233
- Shuurmans C.J.E. (1979): Solar-Terrestrial Influence on Weather and Climate, eds: McCormack B.M., Seliga T.A. (Reidel, Dordrecht), 105
- Smirnov R.V. (1996): Solar Drivers of Interplanetary and Terrestrial Disturbances, APS Conference Series, 95, 481

Poster Papers

Non-Solar Sources of Climate Change

EVOLUTION OF EARLY HOMINIDS IN THE CONTEXT OF CLIMATE CHANGES DURING THE PLIO-PLEISTOCENE

Ekaterina Y. Bulygina¹ & Josep Gibert Clols²

¹ Moscow State University, Biology Faculty, Anthropology Department, Vorobiovy Gory, Moscow, Russia; e-mail: ebulygin@yahoo.com

² Institut de Paleontologia M.Crusafont, Carrer Escola Industrial 23, 08201 Sabadell, Spain. Fax: 0034 93727664, e-mail orce-palacio@ctv.es

ABSTRACT

Climatic changes caused by astronomic cycles have had a considerable impact on the Earth's biosphere. The evolution of Hominids represents one of the examples of a biotic answer to such changes. It would be wrong to attribute evolution and extinction solely to the shifts of climate. Ecological inter and intraspecific relationships as well as development of culture by later hominids should of course also be taken into account while interpreting evolutionary events.

INTRODUCCTION

Climatic changes on the Earth have been partly attributed to alterations in the insolation of its surface due to the so-called Milancovich variations in the eccentricity of the Earth's orbit, the obliquity of its rotational axis and precessional changes (Willson et al., 2000). These cycles have caused the large scale expansion and retreat of ice at the poles of the Earth thus directly changing climatic conditions in high latitudes. It has been also argued that ice expansion at the poles caused considerable climatic shifts in lower latitudes due to a fall of the sea level and increase of aridity. Corresponding records have been received on foraminifers sediment on the sea bed. This data have reflected alterations in the atmosphere temperature because of the fact that the concentration of ¹⁸O in sea sediments is higher during cold periods when ¹⁶O concentrates in the snow. The isotopic curve (Shakleton et al., 1995; Opdyke et al, 1995) demonstrates global climatic changes during the last several million years. These changes correlate with the eustatic curve recording alterations in the sea level (modified from Haq et al., 1988).

The pollen record demonstrates that expansion of ice sheets at the poles during cooling reflected in a shift of floristic assemblages towards the equator and, in lower latitudes, the substitution of rainforests by savannahs. These climatic shifts also correlate with drops in sea level during the cold glacial periods. Interglacial periods correspond to rises in the sea level and expansion of rain forests to the north (Suc et al., 1983). Following pollen records one could expect that climatic changes have direct impact on all biological organisms. However, as it is pointed out by R. Foley (1984), the biological community has a complex organisation maintained by many idiosyncratic interactions. Most of the events in biological communities, including extinction and speciation, arise from, or are dependent upon, these interactions. R. Foley argues that the named inter and intraspecific interactions form the major cause of evolution of species. Nevertheless, faunal records confirm that climatic changes coincide with migration, extinction and speciation of organisms, which was shown by E.Vrba (1995) for African bovids. It may be expected that the evolution of hominids has also been affected by climatic alterations.

OUT OF AFRICA

The first record of hominids remains is from Africa and dated of 4 - 4.2 Ma. Hominid species developed and existed within the African continent for the next several million years. The first migrations of hominids out of African cradle are recorded by findings in Georgia (Dmanisi, 1.7 Ma), Spain 1.4 Ma (Orce, and Cueva Victoria) and Java (1.9Ma). Later migrations of hominids are reflected in Asian and European findings starting at about 1 Ma.

The period of existence of hominid genus spans a number of major climatic events in Africa. According to isotopic records, a period between 5.45 - 4 Ma is characterised by a warm interglacial climate with a number of positive temperature excursions. The warmest Pliocene temperatures were established at 4-3.4 Ma. A considerable climatic shift occurred at the second part of the Gauss epoch when cold temperatures started to prevail, marking the beginning of glaciation in the Northern Hemisphere (3-2.5 Ma). The glacial stages within the next, Matuyama, epoch have a frequency of 40 thousand years (in phase with the changes of the Earth's axis). However, further forward in time, between the Jamarillo and the top of Brunhes epochs (about 1 Ma), the 100 kyr frequency of major glaciation began due to an increase in glacial ice cover (Opdyke, 1995).

Proc. 1st Solar & Space Weather Euroconference, 'The Solar Cycle and Terrestrial Climate', Santa Cruz de Tenerife, Tenerife, Spain, 25-29 September 2000 (ESA SP-463, December 2000)



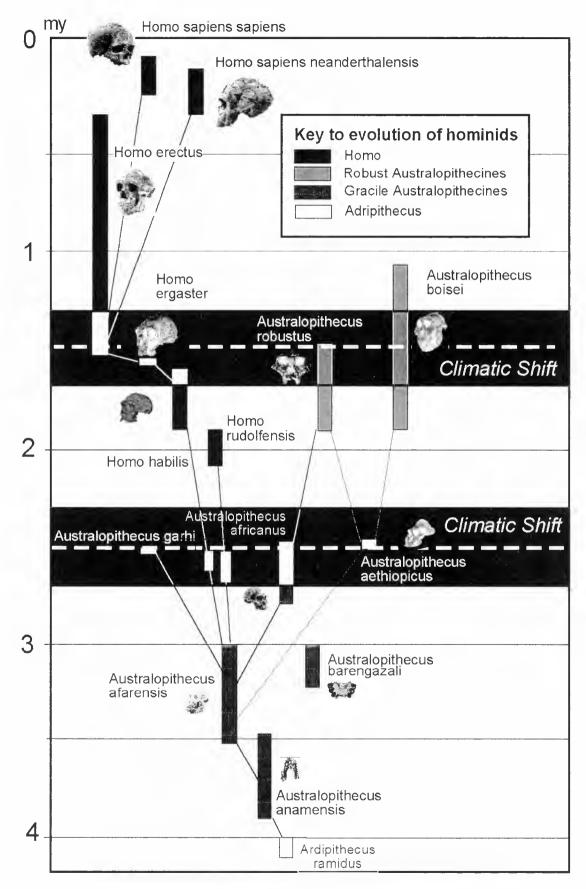


Figure 1: evolutionary three with indication of two important periods of climatic shift which affect human evolution. First one occurs at 3-2.4 million years ago when appeared the first species oh Homo and Rubust austrolopithecines. The second important event occurs 1 million years ago when austrolopithecides disappear persisting only Homo thanks to the development of culture.

CLIMATIC EVENT AT 3-2.5Ma

The climatic event of 3-2.5 Ma in Africa is particularly interesting from the point of view of hominid evolution. This time approximately marks the extinction of the earliest species of gracile Australopithecines and the appearance of robust Australopithecines and the first representatives of genus Homo. There are a number of studies on the alterations in mammalian paleofauna in accordance with climatic changes. One specific case has been studied by Wesselman (1995) in Omo formation (3.0 -1.9 Ma) on rodents. It appears that global climatic changes caused significant migrations of rodents. It has been demonstrated that species of closed tropical forest, mesic savannah and woodland dominated Omoassociations of rodents at 2.95 Ma. However, at 2.34 Ma, local biota changed to domination of dry savannah and arid steppe species. These result correspond with the general picture of global climatic change in Africa from warmer and wetter to a colder and drier environment. Other groups of mammals, such as bovines (Harris & Shipman, 1988; Vrba, 1995), hippotamids (Gèze, 1985) and suids (Cooke, 1985) where also affected by the climate changes of this period. During this time, Equids colonised Africa following the savannah expansion, whereas Hipparion became extinct as the less adapted genus.

It can be noted that the expansion of savannah and the reduction of rain forest determined extinction of gracile australopithecines (*A. africanus, A. garhi*), and appearance of both - genus Homo and robust Australopithecines (*A. aethiopicus*). These new hominids have probably appeared as an answer to the new biotop. However the more complicated ecological relationship between and within species might have also accounted for the result.

CLIMATIC SHIFT AT 1-0-9Ma

The following important climatic change of 1-0.9 Ma coincided with the extinction of the robust Australopithecines. However, it did not obviously affected a more progressive group of hominids: *Homo erectus* (Figure 1). This species is known for the first expansion out of Africa and as well as for a more elaborated stone culture than its predecessors. The expansion of *Homo erectus* occurred during the glacial period in the Northern hemisphere and the drop in the sea level. This event could have directly enabled *Homo erectus* to surpass intercontinental barriers.

CONCLUSIONS

Climate changes coincide with and may be one of the causes of the species evolution. It can be seen during the first steps of human evolution between 4 and 1 million years. Two major cooling events, caused by

astronomic cycles and expansion of earth pole ice sheets, happened during this time. They had a substantial impact on distribution and evolution of biological species, including hominids. It appears that Homo species became more sustainable to climatic changes with acquisition of more elaborated culture. The development of the latter could have permitted *Homo erectus* to survive in colder environments and expand beyond the African continent.

ACKNOWLEDGEMENTS

To Luis Gibert Beotas, Carles Ferràndez, Emma La Salle and Escuela-Taller "Orce Patrimonio de la Humanidad"

REFERENCES

- Cooke, H.B.S. (1985) Plio-Pleistocene Suidae in relation to African hominid deposits. In: LÈnvironnement Des Hominidès au Plio-Plèistocène. Foundation Singer-Polignac et Masson. Paris, New York, Barcelona, Milan, Mexico, Sao Paolo.
- Foley, R. (1984) Putting people into perspective: an introduction to community evolution and ecology. In: Hominid evolution and community ecology. (ed. Foley, R.) Academic press. London, Orlando, San Diego, San Francisco, New York, Toronto, Montreal, Sydney, Tokyo, Sao Paolo: 1-20.
- Gèze, R. (1985) Rèpartition palèoècologique et relations phylogènìtiques des Hippopotamidae (Mammalia, Artiodactyla) du Nèogene d'Afrique Orientale. In: LÈnvironnement Des Hominidès au Plio-Plèistocène. Foundation Singer-Polignac et Masson. Paris, New York, Barcelona, Milan, Mexico, Sao Paolo: 81-100.
- Haq, B.U., Hardebol, J. & Vail, P (1988). Mesozoic and Cenozoic Chronostratigraphy and Eustatic Cycles. In: Sea-Level changes, an integrated approach. C.K. Wilgus, B.S. Hastings, C.G. Wagoner (eds.) Soc. Econ. Paleont. Mineral., Spec. Pub. 42: 71-108.
- Opdyke, D.N. (1995) Mammalian Migration and Climate over the last Seven Million Years. In: Paleoclimatic Evolution with emphasis on Human Origins. Yale University Press, New Haven, Connecticut:109-114.
- Shakleton, N. J., (1995) Data on the evolution of Pliocene climatic variability. In: Paleoclimatic Evolution with emphasis on Human Origins. Yale University Press, New Haven, Connecticut: 242-248.
- Shipman, P. and Harris, W.K. (1988). Evolutionary History of the "Robust" Australopithecine. Audisme D. Cruyter. New York: 115-120.
- Suc, J.P. and Zagwijn, W.H. (1983). Plio-Pleistocene

Correlations between the North-western Mediterranean Region and North-western Europe according to Recent Biostratigraphic and Paleoclimatic data. Boreas, 12; 153-166.

- Vrba, E.S., (1995) On the connections between paleoclimate and evolution. In: Paleoclimatic Evolution with emphasis on Human Origins. Yale University Press, New Haven, Connecticut: 24-48.
- Vrba, E.S., (1995) The fossil record of African Antelopes (Mammalia, Bovidae) in relation to human evolution and paleoclimate. In:

Paleoclimatic Evolution with emphasis on Human Origins. Yale University Press, New Haven, Connecticut: 385-424.

- Wesselman, B.H., (1995) Of Mice and Almost-Men:
 Regional paleoecology and Human Evolution in the Turkana Basin. In: Paleoclimatic Evolution with emphasis on Human Origins. Yale University Press, New Haven, Connecticut: 356-368.
- Wilson R.C.L., Drury S.A., Chapman J.L. (2000) The great ice age climate changes and life. Routledge. The open University. London and New York. 267p.

CO2 CONTINUOUS MEASUREMENTS AT THE IZAÑA GAW STATION

Pilar Rípodas and Ramón Ramos

Observatorio Atmosférico de Izaña, Instituto Nacional de Meteorología, La Marina, 20, 38071 Santa Cruz de Tenerife, SPAIN, pripodas@inm.es

ABSTRACT

 CO_2 is the most important greenhouse gas in the atmosphere after H₂O. The CO₂ in situ continuous measurements at Izaña Observatory (Instituto Nacional de Meteorología, Tenerife, SPAIN) in the period June 1984-May 1999 are presented. The Observatory is located in a privileged place for monitoring the free troposphere, especially in the night period. A NDIR (Non Disperse Infrared Analyser) SIEMENS ULTRAMAT-3 is used, registering a CO₂ mean value every 10 minutes. The 10-minute error is constrained to 0.1 ppmv since 1994 (to 0.2 ppmv before this date). The mean trend observed in the period is 1.6 ppmv/year. This trend has been increasing in the last years after a minimum in 1990, in May 1999 the trend is 2.7 ppmv/year. CO₂ shows a seasonal cycle with amplitude of 7.8 ppmv, the maximum occurs at the beginning of May and the minimum in the middle of September. A comparison between the INM and NOAA CO2 programs at Izaña reveals a good agreement between discrete samples (NOAA) and in situ measurements (INM). The mean difference (one sigma) is 0.12 ± 0.63 ppmv.

Key words: Carbon Dioxide; greenhouse effect; climate change.

1. INTRODUCTION

The Izaña Observatory is located at 28⁰18'N, 16⁰29'W on the island of Tenerife (Canary Islands) at 2367 m a.s.l.. The station has been running since June 1984 (Schmitt et al., 1988), as a result of an international agreement between the governments of Spain and the Federal Republic of Germany. At present it is operated by the Spanish Weather Service (Instituto Nacional de Meteorología).

There is generally a strong and persistent subsidence inversion over this region with the top located at about 1200 m in summer and about 1800 m in winter. The Observatory normally lies above the top of the inversion layer although it some times reaches the station under certain synoptic conditions. This is why Izaña is considered a very good station for representative atmospheric measurements of the free troposphere.

Only during daytime hours this background condition of the station is broken by the effects of local winds. Due to differential heating and orography, a mountain breeze is established. During daytime hours upward winds bring to the Observatory air from the lower belt of pine forest that is between the Observatory and the top of the inversion layer, producing lower CO_2 values. During the night a catabatic regime (descending air) reinforces the "background" condition at the Observatory.

Izaña station participates in the Global Atmospheric Watch (GAW) programme from the World Meteorological Organization (WMO). This programme promotes systematic and reliable observation of the global environment in the atmosphere.

Among others, Izaña contributes to the GAW programme with continuous measurements of one of the most important greenhouse effect gases, CO_2 . In this paper the CO_2 time series (June 1984-May 1999) is presented.

2. INSTRUMENTATION

There is a NDIR SIEMENS ULTRAMAT-3 at the station for the CO_2 measurements. The general air inlet is at 13 m above ground. A cool trap $(-65^{\circ}C)$ is used to dry the sample.

Three levels of standard gases are used (primary, secondary and working tanks). The working tanks are used in the routine measurements to calibrate the ambient air measurements every 3 hours. The working tanks are calibrated against the secondary tanks, and the secondary ones against the primary tanks. At the moment ten SIO (SCRIPPS INSTITUTION OF OCEANOGRAPHY) tanks with CO₂ concentrations ranging from 330 to 400 ppmv and calibrated in the WMO-93 scale are used as the station primary tanks.

For ambient air measurements a mean value and a standard deviation is registered every 10 minutes. For more details see Rípodas et al. (1999).

Proc. 1st Solar & Space Weather Euroconference, 'The Solar Cycle and Terrestrial Climate', Santa Cruz de Tenerife, Tenerife, Spain, 25-29 September 2000 (ESA SP-463, December 2000)

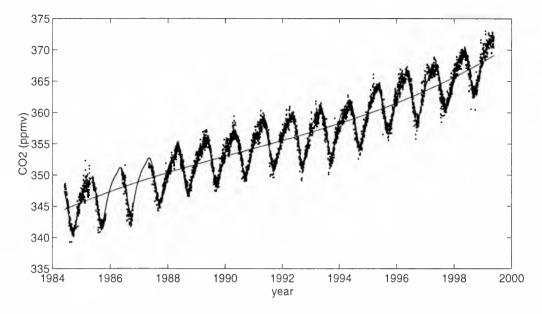


Figure 1. Daily mean night CO_2 time series at Izaña.

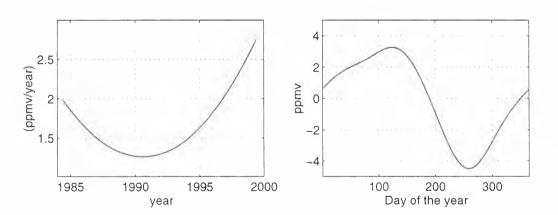


Figure 2. Left graph: CO₂ increasing ratio through the years. Right graph: CO₂ annual cycle at Izaña.

3. DATA QUALITY CONTROL

New software has been written to evaluate the calibrations and the ambient air measurements. Several improvements have been introduced: a quadratic fit is now possible for the calibration evaluation, taking into account the non-linearity of the instrument, and several criteria have been introduced to select good quality ambient air data (Rípodas et al., 1999).

All the calibrations and data since 1995 have been reevaluated with the new software. For data before January 1, 1995, only data that departs considerably from the other data has been removed.

A test called "the third gas test" is used to evaluate the consistency of the whole instrumental and calibration system. The CO_2 concentration of one of the three working tanks is calculated against the other two working tanks and against the secondary tanks. Then the differences between both calibrations are calculated.

The results of this test has been improving with years and it can be said that since 1994 the CO_2 measurements error is constrained to 0.1 ppmv (parts per million in volume). Before this date the error is constrained to 0.2 ppmv (Rípodas et al., 1999).

Finally, to be sure of avoiding the local winds effect and obtain CO_2 representative measurements of the free troposphere, only night data (from 20 hours to 8 hours) must be considered (Navascués & Rus , 1991; Cuevas et al. , 1991; Rípodas et al. , 1999).

4. IZAÑA DAILY MEAN NIGHT CO₂ TIME SERIES

Daily mean night CO_2 values have been calculated for the period June 1984-May 1999. The main features of this time series are analyzed in this section. The time series has been fitted to the following function:

$$f(t) = a_0 + a_1 t + a_2 t^2 + a_3 t^3 + + \sum_{k=1}^{4} [b_{2k-1} sin(2\pi kt) + b_{2k} cos(2\pi kt)] \quad (1)$$

where t is the time in years since January 1, 1984. The standard deviation (STD) of data and the fitted function are 7.17 ppmv and 7.11 ppmv respectively. The residuals are normal distributed with STD=0.93 ppmv. The fitted function explains 98% of data variability.

In Figure 1 the daily mean night CO_2 time series can be seen. The fitted function and the polynomial part of it are drawn in the same figure.

The derivative of the polynomial part of the equation 1 represents the CO_2 increasing rate evolution through the years (Figure 2 left). The mean trend observed in the data is 1.6 ppmv/year. At the beginning of the measurements (June 1984) the trend was 2.0 ppmv/year. It has been decreasing through the years till August 1990 with a minimum of 1.3 ppmv/year. After this date it has been increasing rapidly and in May 1999 the trend is 2.7 ppmv/year. The amplitude of the seasonal cycle (Figure 2 right) is 7.8 ppmv. The maximum is 3.3 ppmv above the mean value and occurs at the beginning of May. The minimum is 4.5 ppmv below the mean value and occurs in the middle of September.

5. COMPARISON BETWEEN INM DATA AND NOAA DATA

The NOAA CMDL (National Oceanic and Atmospheric Administration. Climate Monitoring and Diagnostics Laboratory) cooperative air sampling network is an international effort which includes regular discrete samples from the 4 NOAA CMDL baseline observatories, cooperative fixed sites, and commercial ships. Air samples are collected weekly from a globally distributed network of sites. Samples are analyzed for CO_2 , CH_4 , CO, H_2 , N_2O , and SF_6 ; and for the stable isotopes of CO_2 and CH_4 . Measurement data are used to identify long-term trends, seasonal variability, and spatial distribution of carbon cycle gases.

Izaña Observatory is a cooperative station to the NOAA CMDL programme. The INM CO_2 continuous measurements are an invaluable quality control tool when they are compared with weekly discrete samples from the NOAA programme at Izaña.

A comparison between INM and NOAA CO_2 measurements for the period November 1991- February 1999 has been realized. In Figure 3 the CO_2 INM values are represented against the CO_2 NOAA values. The histogram of the differences NOAA - INM CO_2 values is also represented.

The mean difference (one sigma) is 0.12 ± 0.63 ppmv.

6. DATA BASES

The INM CO₂ data is submitted regularly to the World Meteorological Organitation Word Data Centre for Greenhouse Gases in Tokio,Japan (http://gaw.kishou.go.jp/wdcgg.html).

The INM also contributes with the CO_2 data to the CADIP-CO2 (Cooperative Atmospheric Data Integration Project for Carbon Dioxide) product GLOBALVIEW-CO2, (2000).

7. CONCLUSIONS

The 10-minute CO_2 record error at Izaña is constrained to 0.1 ppmv (0.2 ppmv before 1994). The mean CO_2 trend at Izaña (1984-1999) is 1.6 ppmv/year. It has been increasing in the last years and is 2.7 ppmv/year in May 1999. The CO_2 seasonal cycle amplitude is 7.8 ppmv (maximum in May and minimum in September).

A comparison between the INM and NOAA CO₂ programs at Izaña reveals a good agreement between

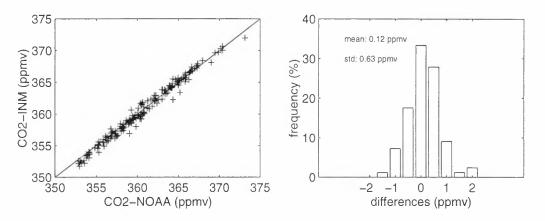


Figure 3. Left graph: CO_2 INM values against CO_2 NOAA values (November 1991- February 1999). Right graph: Histogram of differences NOAA - INM CO_2 values.

discrete samples (NOAA) and in situ measurements (INM). The mean difference (one sigma) is 0.12 ± 0.63 ppmv.

ACKNOWLEDGMENTS

The authors thank all the people that, at present and in the past, have contributed to the beginning and maintenance of the CO_2 measurements at Izaña.

REFERENCES

- Schmitt, R., Schreiber, B., Levin, I., 1988, Effects of long-range transport on atmospheric trace constituents at the baseline station Tenerife (Canary Islands), Journal of Atmospheric Chemistry 7, 335-351.
- Cuevas, E., Díaz, A., Martín, F., Atmospheric Carbon Dioxide at Izaña BAPMON Observatory, Canary Islands, 1984-90, Proceedingsof 19th NATO-CCMS International Technical Meeting on Air Pollution Modelling and its Application, Greece, 1991.
- Navascués, B., Rus, C., Carbon Dioxide observations at Izaña baseline station, Tenerife (Canary Islands) 1984-1988, Tellus, 43B, 118-125.
- Rípodas, P., Ramos, R., Cuevas, E., Calbet, X., 1999, 1984-1999 CO2 continuous measurements at Izaña (Tenerife). Relationship between the CO2 short-term variability and the latitude origin of air masses. Report of the "WMO 10th CO₂ experts meeting", Stockholm, 1999.
- GLOBALVIEW-CO2: Cooperative Atmospheric Data Integration Project - Carbon Dioxide. CD-ROM, NOAA/CMDL, Boulder, Colorado. [Also available on Internet via anonymous FTP to ftp.cmdl.noaa.gov, Path: ccg/co2/GLOBALVIEW], 2000.

ATMOSPHERIC AEROSOLS CREATED BY VARING COSMIC RAY ACTIVITY – ONE OF THE KEY FACTORS OF NON-DIRECT SOLAR FORCING OF CLIMATE

O.I. Shumilov^{1,2}, O.M. Raspopov^{1,2}, E.A. Kasatkina^{1,2}, V.A. Turjansky¹, V.A. Dergachev³ and N.S. Prokhorov¹

¹ Polar Geophysical Institute of RAS, P.O. Box 162, 184200 Apatity, Murmansk region, Russia tel.: +7 81555-79-284 / fax: +7 81555-30-925 / e-mail: <u>oleg@aprec.ru</u>

² St.-Petersburg Filial of IZMIRAN, P.O. Box 181, 191023 St.-Petersburg, Russia tel.: +7 812-310-50-31 / fax.: +7 812-310-50-35 / e-mail: <u>oleg@omr.izmi.ras.spb.ru</u>

³ Ioffe Physical-Technical Institute of RAS, 194021 St.-Petersburg, Russia tel.: +7 812-247-99-81 / fax.: +7 812-247-10-17 / e-mail: dergach@crld.ioffe.rssi.ru

ABSTRACT

In this paper results of model calculations and measurements of atmospheric parameter changes after several GLEs (Ground Level Enhancements) of Solar Proton Events (SPE) are presented. We have got on lidar high-latitude measurements that after 16 February 1984 GLE event the increase of R(H) (backscattering ratio) at 17 km altitude reached 40%. The model calculations of CN (condensation nuclei) profile, which can be served as centers of sulfate aerosol and Polar Stratospheric Cloud (PSC) formation, demonstrate good coincidence with above-mentioned experimental data. Besides, after other GLE event (2 May 1998) we measured considerable increase of NO₂ (nitrogen dioxide) column of incident solar protons in polar region. All these data support the idea that aerosols created by galactic and solar cosmic rays may be one of the key factors in non-direct solar forcing mechanism influencing climate variability. These aerosols can block input of solar radiation to the Earth taking part in creation of additional cloudiness.

INTRODUCTION

In a series of papers Dreschhoff and Zeller (1986; 1990;

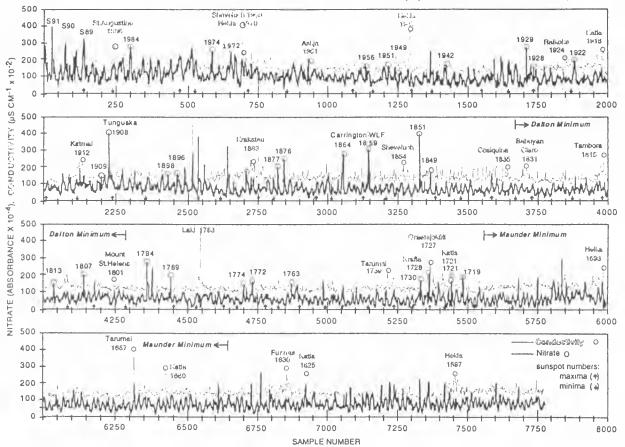


Figure 1: Nitrate and conductivity record from the central Greenland ice sheet (Zeller and Dreschhoff, 1995).

Proc. 1st Solar & Space Weather Euroconference, "The Solar Cycle and Terrestrial Climate", Santa Cruz de Tenerife, Tenerife, Spain, 25-29 September 2000 (ESA SP-463, December 2000)

1995) demonstrated that during many SPEs pronounced increases of sulfate and nitrate anions took place in polar ice. Figure 1 taken from (Zeller and Dreschhoff, 1995) shows variations of nitrate and sulfate abundance in 415-year Greenland ice core record. According to their results several nitrate anomalies coincide with major solar proton events, and in turn large sulfate peaks reflect powerful volcanic eruptions (Laki, 1783; Tambora, 1815; Krakatau, 1883; Pinatubo, 1991). Signatures above some nitrate peaks (see figure 1) mark hagh-energy (E>450 MeV) Solar Proton Events of GLE type detected at the surface by neutron monitors during the last fifty years (Shea and Smart, 1993): February 1956; November 1960-July 1961; August 1972; February 1984; September-October 1989, May 1990). Three events (August 1972, September-October 1989, May 1990) caused considerable NO (nitrogen oxide) enhancement and ozone decrease in the stratosphere (Heath et al., 1977; Jackman et al., 1980; Zadorozhny et al., 1992; Shumilov et al., 1992). During May 1990 GLEs for the first time ozone total content depletions up to 20% (ozone "miniholes") have been detected in Arctic (Shumilov et al., 1992). Another GLE of February 1984 led to aerosol enhancement at 17 km height detected by lidar installed at Verhnetulomsky obs. (68.6°N, 31.8°E) (Shumilov et al., 1996; Kasatkina et al., 1999).

Here we compare experimental results and model calculations reported in our previous papers concerning changes of atmospheric parameters after GLEs and results presented in papers of Dreschhoff and Zeller (1986, 1990; 1995). Results of high-latitude NO₂ column measurements during recent GLE of 2 May 1998 are also performed.

EFFECT OF SOLAR PROTON EVENT ON THE MIDDLE ATMOSPHERE

Solar energetic protons penetrated into the Earth atmosphere cause ionization and dissociation of nitrogen and oxygen generating NO:

$$N(^{2}D) + O_{2} \rightarrow NO + O$$
 (1)

An increase of atmospheric NO concentration results in an enhancement of NO $_2$, HNO $_3$:

$$NO + O_3 \rightarrow NO_2 + O_2 \tag{2}$$

During polar night HNO₃ (nitric acid) can be removed the gas phase leading to condensation and PSC formation with following precipitation in polar ice.

In figure 2 NO altitude distribution calculated for three large GLEs (4 August 1972, 21-24 May 1990, and 2 May 1998) are shown. In calculations the equation for the ionization rate q(h) (cm⁻³ s⁻¹) at altitude h was used (Shumilov et al., 1995):

q(h) =
$$(2\pi K/Q) \int_{0}^{\infty} D(E) \cdot E_{i}(E) dE$$
 (3),

where $E_1(E)$ is the energy loss in the i-th altitude slab in MeV, D(E) is the differential energy spectrum of incident protons in cm⁻¹s⁻¹sr⁻¹MeV⁻¹, Q=35eV is the energy for one ion-electron pair production, and K is an anisotropy coefficient. The production of NO is assumed to be proportional to the ion production rate with a coefficient of 1.25 (Jackman et al., 1980).

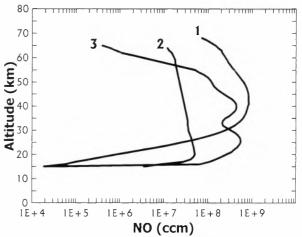


Figure 2: Altitude profiles of NO distribution after solar proton penetration calculated for 4 August 1972 GLE-1, 21-27 May 1990 GLEs-2, 2 May 1998 GLE-3.

It is clearly seen from the figure 2 that May 1990 and May 1998 GLEs are powerful enough to cause nitrate spikes in ice core records, as it was observed in case 4 August 1972 event (see figure 1). As it was mentioned above May 1990 GLEs initiated ozone "minihole" creation in Arctic (Shumilov et al., 1992; 1995).

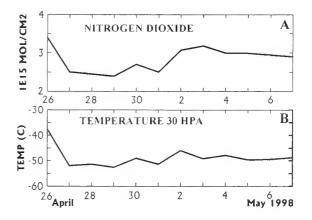


Figure 3: (A) Observations of NO₂ column performed at Murmansk from 26 April until 7 May, 1998; (B) Temperature at 30 hPa (24 km).

During the 2 May 1998 GLE event NO₂ total column was measured by zenith viewing spectrometer (435-453 nm) at high latitudes (Murmansk: 68.3° N, 33.1° E; geomagnetic latitude – 63.4°). Results of measurements

variations of temperature at 30 hPa that seem to coincide with NO₂ changes (Goutail et al., 1994). This coincidence is clearly seen in figure 3 encluding period since 2 May 1998, when a continuous NO₂ increase can be observed in spite of the temperature decrease. Such NO₂ behaviour allows us to assume it to be caused by incident solar protons.

MECHANISM OF AEROSOL ENHANCEMENT CAUSED BY INCIDENT SOLAR PROTONS

An ordinary gas-phase photochemical theory could not explain ozone "minihole" and nitrate spikes in ice core creation during solar proton events. So, the following scheme (including heterogeneous chemistry) was suggested (Shumilov et al., 1995):

an increase of incident solar protons \rightarrow increase of ionization in the stratosphere \rightarrow increase of NOx and HOx \rightarrow preliminary decrease of stratospheric ozone \rightarrow decrease of stratospheric temperature (or increase of spatial electric charge in the stratosphere, or increase of ion nucleation) \rightarrow formation of stratospheric aerosol clouds (sometimes, PSCs) \rightarrow ozone destruction through heterogeneous reactions.

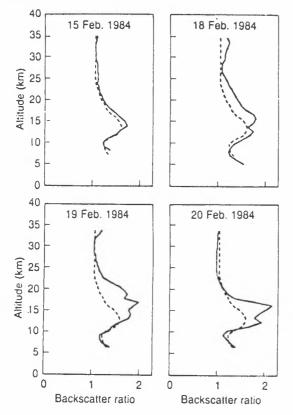


Figure 4: The vertical profiles of scattering ratio R(H), l=694.3 nm taken on 15, 18, 19, and 20 February 1984 at Verhnetulomski observatory (Shumilov et al., 1996). Dashed curves give the quiet day level averaged for previousfive undisturbed days.

This mechanism has been supported later both experimentally and theoretically (Shumilov et al., 1996; Kasatkina et al., 1999). In figure 4 high-latitude lidar measurements of aerosol backscattering ratio R(H) during 16 February 1984 GLE are shown (Shumilov et al., 1996). Measurements were made by lidar installed at Verhnetulomsky obs., Murmansk region (68.6°N, 31.8°E). It is seen aerosol backscattering increase at 18 February 1984 between 15 and 25 km altitude. This GLE event seems to be connected with 1984 nitrate spike in ice core record (see figure 1).

DISCUSSION AND CONCLUSIONS

Note that it should be cold enough (below -72°C) for nitrate PSC creation and nitrate anomalies in ice core record appearance. Shumilov et al. (1996) and Kasatkina et al. (1999) developed a model and present calculations based on ion nucleation mechanism with sulfate aerosol creation that can be formed at higher temperatures in stratosphere (-30°C). The indirect evidence is performed in figure 1, where one can see that some sulfate peaks are not correspond to volcanic eruptions and coincide with nitrate anomalies. Another support was reported by Shumilov et al. (2000, this issue), where it is shown that sulfate acidity record in polar ice reflects behind volcanic eruptions also galactic cosmic ray variations modulated by solar activity.

Taking into account the similarity of mechanism of ozone "minihole" and nitrate spike in ice core formation the similar conditions of their creation should be expected. Actually nitrate spikes and ozone "miniholes" relevant to maior GLEs have been detected in Antarctic ice also showing a prominent North-South asymmetry in their appearance (Zeller et al., 1986; Dreschhoff and Zeller, 1990; Kasatkina et al., 1998). In local winter and early spring, when meteorological conditions are favorable (low temperatures, large humidity etc.) the probability of these phenomena increases. For example, the amplitude of nitrate spike in Antarctic ice relevant to 4 August 1972 GLE (Zeller et al., 1986) is higher in comparison with Arctic one (see figure 1). In case of ozone "miniholes" caused by GLEs the effect of N/S asymmetry is more appeared (they are created only inside one polar cap and simultaneously absent in other). Another common feature is an auroral footprint by nitrate in Antarctic snow (Dreschhoff and Zeller, 1990) and distribution of ozone "miniholes" created by solar protons along auroral oval border (Kasatkina et al., 1998). This property is explained by peculiarities of solar proton penetration to polar caps (zones surrounded by auroral oval), where geomagnetic field lines are open into space and do not prevent a free access of incident particles.

In conclusion, we may argue that nitrate and sulfate contents in polar ice core along with cosmogenic isotopes (14 C and 10 Be) can be used as indicators of solar forcing of climate in the Past.

ACKNOWLEDGEMENT

This work was supported by Russian Academy of

Sciences (RFBS Grant 98-05-03791 and 00-05-64921) and EC (INCO-COPERNICUS Grant ERB IC 15 CT 980123 and INTAS grant 97-31008).

REFERENCES

- Dreschhoff G. and Zeller E. (1990): Evidence of individual solar proton events in Antarctic snow. *Solar Physics*, Vol. 127, pp. 333-346, 1990.
- Gountail F., Pommereau J.P., Sarkissian A., Kyro E. and Dorokhov V. (1994): Total nitrogen dioxide at the Arctic polar circle since 1990. *Geophysical Research Letters*, Vol. 21, No. 13, pp. 1371-1374, 1994.
- Heath D.F., Krueger A.J. and Crutzen P.J. (1977): Solar proton event: influence on stratospheric ozone. *Science*, V. 197, No. 4063, pp. 886-889, 1997.
- Jackman C.H., Frederick J.E. and Stolarsky R.S. (1980): Production of odd nitrogen in the startosphere and mesosphere: an intercomparison of source strengths. J. Geophysical Research, Vol. 85, No. C12, pp. 7495-7505. 1980.
- Kasatkina E.A., Shumilov O.I., Raspopov O.M. and Henriksen K. (1998): Ozone "miniholes" created by solar protons inside the Northern and Southern polar caps. *Geomagnetism and aeronomy (in Russian)*, Vol. 38, No. 2, pp. 30-36. 1998.
- Kasatkina E.A., Shumilov O.I. and Vashenyuk E.V. (1999): Corpuscular solar activity as a source of aerosols in the atmosphere. *Cosmic Research (in Russian)*, Vol. 37, No. 2, pp. 163-167, 1999.
- Shea M.A. and Smart D.F. (1993): Significant proton events of solar cycle 22 and a comparison with

events of previous solar cycles. Advances Space Research, Vol. 13, No. 9, pp. 439-442. 1993.

- Shumilov O.I., Henriksen K., Raspopov O.M. and Kasatkina E.A. (1992): Arctic ozone abundance and solar proton events. *Geophysical Research Letters*, V. 19, No. 16, pp. 1647-1650. 1992.
- Shumilov O.I., Kasatkina E.A., Henriksen K. and Raspopov O.M. (1995): Ozone "miniholes" initiated by energetic solar protons. J. Atmospheric and Terrestrial Physics, V. 57, No. 6, pp. 665-671. 1995.
- Shumilov O.I., Kasatkina E.A., Henriksen K. and Vashenyuk E.V. (1996): Enhancement of stratospheric aerosols after solar proton event. Annales Geophysicae, V. 14, pp. 1119-1123. 1996.
- Zadorozhny A.M., Kikhtenko V.N., Kokin G.A., Raspopov O.M., Shumilov O.I., Tuchkov G.A., Tyasto M.I., Chizhov A.F., Shtyrkov O.V., Kasatkina E.A., Vashenyuk E.V. (1992): The reaction of the middle atmosphere to solar proton events in October 1989. *Geomagnetism and Aeronomy*, V. 32, No. 2, pp. 184-190. 1992.
- Zeller E.J., Dreschhoff G.A.M. and Laird C.M. (1986): Nitrate flux on the Ross ice shelf, Antarctica and its relation to solar cosmic rays. *Geophysical Research Letters*, V. 13, No. 12, pp. 1264-1267. 1986.
- Zeller E.J. and Dreschhoff G.A.M. (1995): Anomalous nitrate concentrations in polar ice cores – do they result from solar particle injections into the polar atmosphere? *Geophysical Research Letters*, V. 22, No. 18, pp. 2521-2524. 1995.

INFLUENCE OF COSMIC RAY INTENSITY MODULATED BY SOLAR ACTIVITY AND VOLCANIC ERUPTIONS ON THE CLIMATE

O.I. Shumilov^{1,2}, E.A. Kasatkina^{1,2}, O.M. Raspopov^{1,2}, E. Turunen³, G. Jacoby⁴ and N.-A. Morner⁵

¹ Polar Geophysical Institute of RAS, P.O. Box 162, 184200 Apatity, Murmansk region, Russia tel.: +7 81555-79-284 / fax: +7 81555-30-925 / e-mail: <u>oleg@aprec.ru</u>

² St.-Petersburg Filial of IZMIRAN, P.O. Box 181, 191023 St.-Petersburg, Russia

tel.: +7 812-310-50-31 / fax.: +7 812-310-50-35 / e-mail: <u>oleg@omr.izmi.ras.spb.ru</u>

³ Sodankyla Geophysical Observatory, FIN-99600 Sodankyla, Finland tel.: +358 16-619-837 / fax.: +358 16-619-875 / e-mail: esa@sgo.fi

⁴ Tree-Ring Laboratory, Lamont-Doherty Earth Observatory, 61 Route 9 W, Palisades, New York 10964, USA tel.: +914 365-8616 / fax.: +914 365-8152 / e-mail: <u>druid@ldeo.columbia.edu</u>

⁵ Department of Paleogeophysics and Geodynamics, Stockholm University, SE-106 91 Stockholm, Sweden tel.: +46 08-790-67-71 / fax.: +46 08-790-67-77 / e-mail: morner@pog.su.se

ABSTRACT

The influence of cosmic rays modulated by solar variability and volcanic activity on the aerosol layer is considered. For analysis the Crete (Greenland) acidity ice core record (Crowley et al., 1993) have been used. It was obtained a high correlation between sunspot numbers and acidity background variations that seem to support the mechanism suggested by authors earlier about the cosmic ray influence on climate and global temperatures through aerosol concentration changes. Results of analysis have shown that the acidity ice core index (with exception of volcanic activity) is suitable for demonstration of cosmic ray influence on climate in the Past.

INTRODUCTION

Correlation between climate and volcanism is rather weak (r=-0.23) according to recent data (Crowley et al., 1993). However, the strong volcanic events did influence on the climate. For example, it was noted on dendrochronological data that the coldest temperature since 1600 occur in 1601 in western United States and in 1641 in Fennoscandia (Briffa et al., 1992). These dates seem to correlate with the eruption in Huaynapatina in Peru (1600) and Awu in Indonesia (1641) (Crowley et al., 1992). The Tambora eruption (1815) peak is also prominent in tree ring records from Eastern Canada and Western Europe (Jacoby and D'Arrigo, 1989; Briffa et al., 1993). Note, however, that climate cooling began several years earlier than Tambora eruption (Jacoby and D'Arrigo, 1989). Some authors (Thompson et al., 1986; Dai et al., 1991; Jones et al., 1995) to be sure in the connection between volcanism and climate suggested the existence of unknown volcanic eruption about 6 years preceding Tambora one. Extremely strong eruption of Toba in Sumatra (about 75000 BP) also was apparently followed the initiation of climate cooling (Rampino et al., 1979).

Several models considering such external climate forcings as solar activity, volcanos and anthropogenic greenhouse gases have been developed during last two decades (Gilliland et al., 1984; Hansen and Lacis, 1990; Reid, 1991; Lean et al., 1995). All these models consider stratospheric aerosol enhancement as a consequence of volcanic eruptions and anthropogenic activity (Gilliland et al., 1984; Hansen and Lacis, 1990; Bertrand et al., 1984; Hansen and Lacis, 1990; Bertrand et al., 1999). On the other side, the possible impact of solar variability on climate has been estimated only through solar irradiance variations (Reid, 1991; Lean et al., 1995). However, the amplitude of solar irradiance variation over a 11-year solar cycle is about 0.1% and seems not to be the only reason of climate changes.

MECHANISM OF SOLAR FORCING OF CLIMATE

Recently it was shown (both experimentally and numerically) that high-energy solar protons during powerful solar proton events of Ground Level Event (GLE) type can increase aerosol concentration in the atmosphere (Shumilov et al., 1996). Taking into account that GLE-type solar proton events and galacic cosmicm rays are identical in their physical nature the physical mechanism of cosmogenic forcing of global temperature and climate has been proposed. According to this mechanism suggested cosmic rays modulated by solar variability cause periodic variations in aerosol concentration leading to global temperature changes (Shumilov et al., 1998).

On the base of the above mentioned mechanism it was obtained the regression relation between temperature changes ΔT and sunspot numbers W (Shumilov et al., 1998):

$$\Delta T = 0.0031W - 0.57 \tag{1},$$

where ΔT and W are 10-year averaged values. To obtain this equation a proxy records of cosmogenic isotope ¹⁰ Be and δO ¹⁸ derived from Greenland ice cores

Proc. 1st Solar & Space Weather Euroconference, 'The Solar Cycle and Terrestrial Climate', Santa Cruz de Tenerife, Tenerife, Spain, 25-29 September 2000 (ESA SP-463, December 2000)

have been used. Note that this equation describe the influence of the general (solar and cosmic) «signal» on the surface temperature including variations of solar irradiation depending on the solar activity. It is connected to the fact that closed to the solar maxima the solar irradiation increases and during the same period lack of aerosols created by cosmic rays would increase the input of the solar energy to the Earth atmosphere and to the surface. This will lead to the positive climatic cumulative effects. During solar minima the effects would be negative ones.

Equation (1) is very similar to another one obtained as a regression relation between 11-year averaged Northern hemisphere temperature departures dT and the envelope of the 11-year sunspot number curve derived by simply connecting the successive Wolf number maxima (r=0.7):

$$dT = 0.0039W - 0.55 \tag{2}$$

This equation was obtained using instrumental Northern hemisphere temperature records (Jones and Bradley, 1992) and results reported by (Reid, 1991).

COMBINED INFLUENCE OF SOLAR AND VOLCANIC ACTIVITY ON CLIMATE

In this paper some experimental data supporting the mechanism proposed are shown, and another factor (volcanic eruptions) influencing the global temperature is considered. We have tried to separate the climatic influence of these different agents using the Crete (Greenland) ice core acidity record (Crowley et al., 1993).

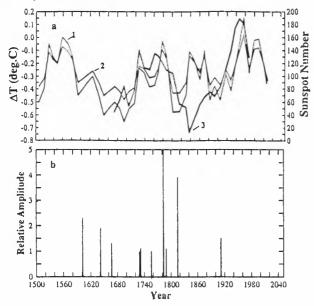


Figure 1: a) Maximum sunspot number envelope for the period 1500-1990 (1), calculated global temperature departures (2) and Northern Hemisphere 10-year averaged temperature departures (3) (Jacoby and D'Arrigo, 1989).

Fig.1a shows the envelope of 11-year sunspot number cycles, global temperature departures ΔT calculated with help (1), and 11-year averaged Northern Hemisphere temperature variations derived from tree ring data for the period 1500-1980 (Jacoby and D'Arrigo, 1989). For estimation of ΔT variations during the period XV-XVI centuries the data of sunspot maximum number restored by Schove (1955) were used. It is seen from the Fig.1a that a rather good correlation exists between model and experimental temperatures (curves 2 and 3) with exception the period since 1810 (some years before Tambora eruption). For comparison in Fig.1b the volcanic eruptions with more than 1 µEH /kg amplitudes taken from the list of Crowley et al. (1993) are shown for the period 1600-1973. These data have been obtained from the Crete (Greenland) ice core acidity record (Crowley et al., 1993). It is clearly seen from Figs.1a,b that the largest differences between model and experimental temperature data are observed after the greatest volcanic eruption of Tambora (1815). This eruption really influenced the climate (Briffa et al., 1998). Influence of another most famous eruption of Laki (1783) was comparatively weaker on account of its pollution influence was restricted to the troposphere so that cooling effect was local (ref. 18). It is seen from the Fig1b that the date of Laki eruption was closed to the maximum of solar activity, and in this case volcanic forcing should be compensated by solar forcing of climate.

On account of the cooling effect began 5 years before the Tambora eruption whole this cold period could not be connected to volcanic activity. Even if we attract for interpretation the unknown eruption, because of its moderate intensity (Dai et al., 1991). For understanding the discrepancy we try to call on the influence of cosmic rays and other cosmophysical factors on the Earth aerosol layer.

Hammer et al. (1980) suggested using of sulphuric acid signal detected through electrical conductivity measurements on ice cores to identify volcanic eruptions. Ice core acidity index is now ordinary used as indicator of volcanic activity in the Past (Crowley et al., 1993). In contrast to sporadic volcanic eruptions the cosmic agents (GCR) «work» permanently and should influence on ice core acidity background through atmospheric aerosol variations. Taking into account the above-mentioned mechanism we consider this index to reflect also the variations GCR intensity. In Fig.2 variations of Wolf number and acidity background (without volcanic eruptions) taken from Crete ice core data (Crowley et al., 1993) are shown. Correlation coefficient between these two indexes is rather high (r=-0.8). Negative sign of correlation coefficient reflects the fact that the GCR intensity variations show an inverse relation to the sunspot number. So, aerosol background variations are in phase with cosmic ray intensity changes, and the maximal amount of aerosols would be created during minima of solar activity. Some

experimental support of this result was reported by Svensmark and Friis-Christensen (1997), who showed using satellite data that variations cloudiness are correlated with ones of cosmic ray flux. Fig.2 shows that ice core acidity index seems to be suitable for demonstration of cosmic ray activity influence on the climate in the Past.

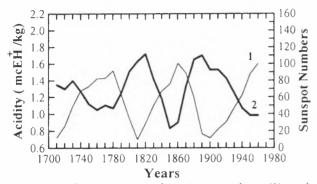


Figure 2: 20-year averaged sunspot numbers (1) and acidity background record taken from Crete ice core (Crowley et al., 1993) (2).

Note the problem of connection between solar and volcanic activity is rather complicated. This question includes the set of positive and negative feedback connections. May be this feedbacks especially positive ones, are responsible for rather long-time influence of prominent volcanic eruptions on the climate. Because if in case of the most powerful Tambora eruption, we take into account only simple summing up of both cosmogenic and volcanic climate forcing signals in the stratosphere in attempt to understand influence of Tambora eruption on the climate for period (1810-1840), then we meet many difficulties. The main one is that volcanic aerosols exist in the stratosphere not more than 7 years (Barbera and Self, 1978). (In case of Tambora eruption the aerosols exist about 3 years). That is the direct immediate influence of the eruption should have been finished not late than in 1820. However, the supposed influence lasted at least till 1840 according to Fig.1. But we have to remember that Tambora eruption was the most powerful one for about the last 20000 years (Rampino et al., 1979). So, that we cannot exclude impact of very powerful eruptions would differ from ordinary ones, and climatic response can last, connected to some feedback connections for more than several years. The same conclusions were made in the report (Briffa et al., 1998), where it was shown that cluster of eruptions seems to lead to cooling on decadial and multi-decadial time scales as it was in XVI-XVII centuries.

The bulk effect of volcanic clusters seems to cause the same, as in Tambora case, rather long influence on the climate. The similar situation with some probability could have been realized in case of Toba eruption – the greatest explosive event for the last 2 million years: 13-15 times more powerful than Tambora one. The eruption seemed to initiate catastrophic cooling and new Ice Age at 75000 BP (Rampino et al., 1979).

CONCLUSIONS

Finally, the influence of both solar and cosmogenic factors can be expressed in the next scheme (Fig.3).

SOLAR AND COSMIC FORCING AGENTS

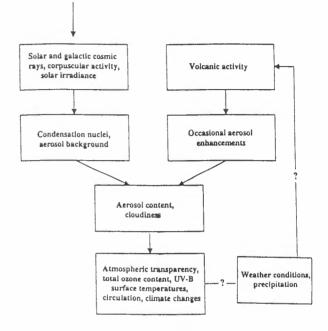


Figure 3: The scheme of combined (cosmic and volcanic) forcing of the climate.

Some increase of the volcanic activity during solar minima might be connected to basic state of the atmosphere. Solar flares are believed to cause changes in atmospheric circulation patterns that abruptly alter the Earth's spin (Schothers, 1989). The resulting jolt probably triggers small earthquakes which may temporarily relieve some stress in volcanic magma chambers, thereby weakening or even aborting large eruptions (Schothers, 1989). From the other side the increased precipitation during solar minima might stimulate eruption (Rampino et al., 1979). This feedback connection impressed by arrow in the scheme (see Fig.3). This scheme may be useful, because till present the investigators try to apply climate forcing of volcanos and other agents (in our case solar and cosmogenic ones) separately. However, as it was shown (see Fig.1) the combined consideration of both (cosmophysical and volcanic) agents gives the better coincidence with experiment.

It was shown that the background ice core acidity record can be used for manifestation of cosmic ray influence on aerosol background and climate in the Past. And only combine consideration of volcanic and cosmic agent influence on the climate could explain the Past temperature variations. High correlation coefficient between background acidity ice core data and solar activity proves the existence of solar (galactic cosmic ray) influence on the Earth aerosol layer. All attempts to connect acidity ice core (aerosol) data only to volcanic activity seem to be incorrect and the influence of cosmic ray (and other cosmophysical and solar agents) on acidity backcground should be taken into account.

ACKNOWLEDGEMENT

This work was supported by Russian Academy of Sciences (RFFI Grant 98-05-03791 and 00-05-64921) and by EC (INCO-COPERNICUS Grant ERB IC 15 CT 980123 and INTAS grant97-31008).

REFERENCES

- Barbera, J. and Self, S. (1978): New volcanic eruption and temperature records: evaluation for the period 1755-present. *EOS Transact*, Vol. 59, p. 294.
- Bertrand, C., van Ypersele, J.-P., and Berger A. (1999): Volcanic and solar impacts on climate since 1700. *Clim. Dyn.*, Vol. 15, pp. 355-367.
 Briffa, K.R., Jones, P.D., Bartholin, T.S., Eckstein, D.,
- Briffa, K.R., Jones, P.D., Bartholin, T.S., Eckstein, D., Schweingruber, F.H., Karlen, W., Zetterberg, P., and Eronen, M. (1992): Fennoscandian summers from AD 500: Temperature changes on short and long timescales. *Clim. Dynam.*, Vol. 7, pp. 111-119.
- Briffa, K.R., Jones, P.D. Schweingruber, F.H., and Osborn, T.J. (1998): Influence of volcanic Eruptions on Northern Hemisphere summer Temperature over the past 600 years. *Nature*, Vol. 393, pp. 450-454.
- Crowley, T.J., Criste, T.A., and Smith, N.R. (1993): Reassesment of Crete (Greenland) ice core acidity/volcanism link to climate change. *Geophys. Res. Lett.*, Vol. 20, pp. 209-212.
 Dai, J., Mosley-Thompson, E., and Thompson, L.G.
- Dai, J., Mosley-Thompson, E., and Thompson, L.G. (1991): Ice core evidence for an explosive tropical volcanic eruption 6 years preceeding Tambora. J. Geophys. Res., Vol. 96, pp. 17361-17366.
- Gilliland, R.L. and Schneider, S.H. (1984): Volcanic, CO₂, and solar forcing of Northern and Southern Hemisphere surface air temperatures. *Nature*, Vol. 310, pp. 38-41.
- Hammer, C.U., Clausen, H.B., and Dansgaard, W. (1980): Greenland ice sheet evidence of postglacial volcanism and its climatic impact. *Nature*, Vol. 288, pp. 230-235.
- Hansen, J.E. and Lacis, A.A. (1990): Sun and dust versus greenhouse gases: an assessment of their relative roles in global climate change.

Nature, Vol. 346, pp. 713-719.

Jacoby, G.C. and D'Arrigo, R.D. (1989): Reconstructed Northern Hemisphere temperature departures. *Clim. Change.*, Vol. 14, pp. 39-59.

- Jones, P. D. and Bradley, R. S. (1992): Climatic variations in the longest instrumental records. In *Climate since A.D. 1500* (eds. Bradley, R.S. and Jones, P.D.) Routledge, London, pp. 246-268.
- Jones, P. D., Briffa, K. R., and Schweingruber, F. H. (1995): Tree-ring evidence of the widespread effects of explosive volcanic eruptions. *Geophys. Res. Lett.*, Vol. 22, pp. 1333-1336.
- Lean, J., Beer, J., and Bradley, R. (1995): Reconstruction of solar irradiance since 1610: Implications for climate change. *Geophys. Res. Lett.*, Vol. 22, pp. 3195-3198.
- Pyle, D.M. (1998): How did the summer go? *Nature*, Vol. 393, pp. 415-417.
- Rampino, M.R., Self, S., and Fairbridge, R.W. (1979): Can rapid climatic change cause volcanic eruptions. *Science*, Vol. 206, pp. 826-829.
- Reid, G.C. (1991): Solar total irradiance variations and the global sea surface temperature record. J. Geophys. Res., Vol. 96, pp. 2835-2844.
 Schothers, R.B. (1989): Volcanic eruptions and solar
- Schothers, R.B. (1989): Volcanic eruptions and solar activity. J. Geophys. Res., Vol. 94, pp. 17371-17381.
- Schove, D.J. (1955): The sunspot cycle, BD 649 to AD 2000. J. Geophys. Res., Vol. 60, pp.127-146.
- Shumilov, O.I., Kasatkina, E. A., Henriksen, K, and Vashenyuk, E.V. (1996): Enhancement of stratospheric aerosols after solar proton event. Annal. Geophys., Vol. 14, pp. 1119-1123.
- Shumilov, O.I., Raspopov, O.M., Kasatkina, E.A., and Dergachev, V. A. (1998): Global temperature changes and solar cycles. In Proc. from the Fourth Ny-Alesund Seminar, Ravello, Italy, p. 105.
- Svensmark, H., and Friis-Christensen, E. (1997): Variation of cosmic ray flux and global cloud coverage – a missing link in Solarclimate relationships. J. Atmos. Terr. Phys., Vol. 59, pp. 1225-1232.
- Thompson, L.G., Mosley-Thompson, E., Dansgaard. W., and Grootes, P.M. (1986): The Little Ice Age as recorded in the Stratigraphy of the tropical Quelccaya ice cap. *Science*, Vol. 234, pp. 361-364.

551

ESTIMATION OF A "CLEAR" SKY ATMOSPHERE USING GROUND AND SATELLITE MEASUREMENTS OF THE SOLAR RADIATION

G. Tsiropoula^{*1} and Ath. Argiriou^{$\dagger 2$}

¹Institute of Space Applications and Remote Sensing ²Institute of Environmental Research and Sustainable Development

Abstract

Values of VIRGO/SOHO extraterrestrial solar radiation and global radiation on a horizontal surface measured by a pyranometer installed at the P. Penteli (near Athens, Greece) Meteorological Station $(l = 23^{\circ}E, \phi = 38^{\circ}N)$, height above sea level = 500 m) are used to estimate a clear sky atmosphere. The estimation is based on the model proposed by ASHRAE (American Society of Heating, Refrigerating and Air Conditioning Engineers). This knowledge is a fundamental input for General and/or Regional Circulation models and for surface radiative energy budget studies.

Key words: solar irradiance; clear sky atmosphere.

1. INTRODUCTION

The influence of the solar radiative output to the terrestrial atmosphere is a critical element in the overall understanding of our climate system. It is now well established that this output is not constant. Direct measurements of the total solar irradiance from space-born instruments which exist since 1978 reveal the existence of an 11-year cycle upon which are often superimposed larger, short-term changes of 27 days directly related to the photospheric manifestations of solar activity (Fröhlich et al. 1998). The effects of the Sun's variability are evident in a variety of physical and chemical processes in the upper earth's atmosphere and in several meteorological parameters (Tsiropoula, 2000). Variations in solar radiation must, therefore, be measured continuously and considered as a possible cause of climate change, among a number of other possible causes.

[†]e-mail: thanos@astro.noa.gr,

National Observatory of Athens, 15236 P. Penteli, Greece The solar radiation arriving at the Earth's surface is not the same to that emitted by the Sun, since it interacts with the Earth's atmosphere. This interaction results to its attenuation and also to the modification of its spectral composition. Thus this radiation is subject to atmospheric scattering by air molecules, water and dust, and atmospheric absorption by O_3 , H_20 , CO_2 etc. and clouds. To study these different processes, accurate measurements and comparison of the incoming broadband solar irradiance outside the atmosphere to the irradiance measured at the surface are essential.

In this work measurements of the total solar irradiance (TSI) obtained by the experiment VIRGO on-board SOHO and a pyranometer measuring the global radiation at a selected site on the Earth's surface were used. Since the solar input to the lower atmosphere is strongly affected by the state of cloudiness, decreasing with the cloud amount, information about the presence or absence of clouds and their effect on the shortwave irradiance as measured at surface is higly desirable for surface radiative energy budget studies. One measure of the presence or absence of clouds is obtained by the continuous comparison between measured irradiance to clear (i.e. cloudless) sky irradiance. We use the model proposed by ASHRAE (American Society of Heating, Refrigerating and Air Conditioning Engineers, 1995) to estimate, in a first step, a clear sky atmosphere for September 1997 at the ground instrument site, and to separate cloudy and cloud-free situations.

2. SATELLITE AND GROUND-BASED MEASUREMEN'TS

The average amount of radiant solar energy integrated over all wavelengths, hence total irradiance per unit time per unit area reaching the top of the atmosphere at the earth's mean distance from the Sun, is traditionally called "solar constant", although it is now clear that it varies on all time scales from minutes to decades.

The incoming TSI data set was gathered by the

Proc. 1th Solar & Space Weather Euroconference, 'The Solar Cycle and Terrestrial Climate', Santa Cruz de Tenerife, Tenerife, Spain, 25-29 September 2000 (ESA SP-463, December 2000)

e-mail: georgia@space.noa.gr

VIRGO experiment on-board SOHO. The VIRGO experiment measures the TSI with two absolute radiometers (DIARAD and PMO6) (Fröhlich et al. 1997). VIRGO's continuous sampling (since 18 January 1996) and improved determination of the degradation (Anklin et al. 1998) yield reliable time series of the TSI, probably the best available to date.

Pyranometers have been used for many years to measure broadband surface incoming solar irradiance and give data that are necessary for surface energy budget, cloud forcing and satellite validation research. For the needs of the present work one minute averages of global horizontal irradiance were used. These readings come from a Kipp and Zonen CM11 pyranometer. The sensor is interrogated every 30 seconds. Hourly averages were produced, based on one-minute averages.

The solar activity effects on the radiation input were investigated at one station located at geographic latitude $\phi = 38^{\circ}N$ and altitude A=500 m. A period from September 1 to September 30, 1997, was selected for the present analysis. Hourly means of irradiance measurements from VIRGO and the pyranometer were used (Fig. 1 and Fig. 2a). The irradiance dip in Fig. 1 is due to the passage of sunspots on the solar disk.

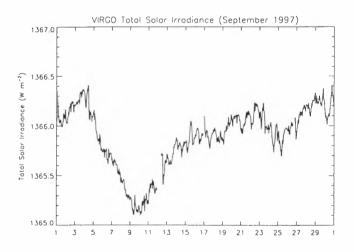


Figure 1. Total Solar Irradiance variations during September 1997 as measured by VIRGO on-board SOHO. The dip in the TSI is due to the passage of sunspots on the solar disk.

3. RESULTS

Apart from the variation of the solar radiation due to the solar activity, at any given location the radiation arriving on the TOA depends primarily on (a) the angle of the Sun above the horizon (zenith angle) and (b) the length of time the TOA is exposed to the Sun; in addition solar radiation arriving at the surface of the Earth depends on the atmospheric conditions.

Thus the TSI on a horizontal surface at the TOA at any time following the diurnal cycle at the site where ground measurements are available would be:

$$G_h = G_{ext} (1 + 0.033 \cos \frac{360n}{365}) \cos \theta_z \qquad (1)$$

where G_{ext} the extraterrestrial radiation measurements given by VIRGO, *n* the day of the year, θ_z the zenith angle e.g. the angle between the vertical and the line to the Sun given by the equation:

$$\cos\theta_z = \cos\phi\cos\delta\cos\omega + \sin\phi\sin\delta \qquad (2)$$

In the above equation ϕ is the geographic latitude, ω the hour angle, e.g. the angular displacement of the Sun east or west of the local meridian due to rotation of the Earth on its axis at 15° per hour, noon zero, morning negative, and δ the declination of the Sun given by the equation:

$$\delta = 23.45 \sin(360 \frac{284 + n}{365}) \tag{3}$$

Fig. 2 shows the hourly averages of the extraterrestrial radiation measured by VIRGO/SOHO allowed to follow the diurnal cycle above the site under consideration for September 1997 (Fig. 2 (left)) and the global radiation at the surface as measured by the pyranometer Kipp and Zonnen CK11 (Fig. 2 (right)). The daily averages are also overplotted. Note that the values plotted in Fig. 2 correspond to dayilight hours only. The effect of the sunspot is nomore apparent on the irradiances which means that the primary factor that determines the magnitude of the incoming radiation at the TOA is the solar zenith angle. The effects of the atmosphere in scattering and absorbing radiation depend on atmospheric conditions and air mass and thus are not constant with time. It is useful to define a standard "clear" sky and calculate the radiation which would be received on a horizontal surface under these standard conditions. To do this we follow the model proposed by ASHRAE. This method estimates the beam radiation taking into account zenith angles. According to this method hourly values of the clear sky beam radiation, I_{bc} , on a horizontal surface are given by:

$$I_{bc} = G_h \exp\left(-B/\cos\theta_z\right) \tag{4}$$

where B is a factor to allow for changes of the incoming solar radiation due to the presence of the atmosphere. Hourly values of the clear sky diffuse radiation are estimated can be done from the relation:

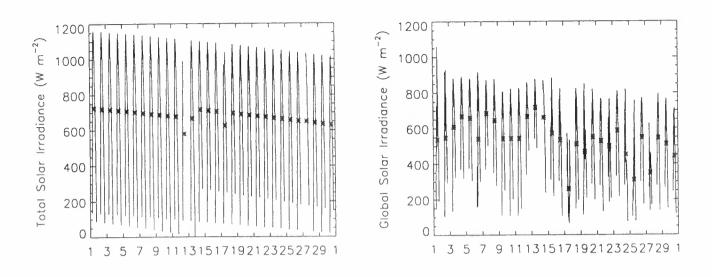


Figure 2. Left. Time series of the Total Solar Irradiance outside the atmosphere following the diurnal cycle during September 1997. Right global radiation on Earth as measured by a pyranometer at the P. Penteli Meteorological Station. These data are hourly averages. Daily averages (denoted by *) are also overplotted.

$$I_{dc} = C I_{bc} \tag{5}$$

C depends on the relative humidity and the presence of different particles in the atmosphere. B and C are given by the empirical relations:

$$B = \sum_{i=1}^{4} b_i n^i \tag{6}$$

$$C = \sum_{i=1}^{4} c_i n^i \tag{7}$$

 b_i , c_i are constants n the day of the year (Kouremenos et al. 1991). Finally, the clear sky horizontal global radiation is obtained by the sum of the beam and the diffuse radiations (Fig. 3 (left)).

We use the ratio $g = I_{meas}/I_{calc}$, where I_{meas} , I_{calc} are the hourly values of the measured and the calculated global irradiance respectively, to describe the modification of the cloudless sky irradiance due to the presence of clouds. Thus clear sky conditions produce ratio values of near unity, while deviations from unity are due primarily to the influence of the clouds that may be in the upper atmosphere and not always visible (Fig. 3 (right)). As can be seen from Fig. 3 (right) cloudy days which have lower g (e.g. the 17^{th} , 25^{th} and 27^{th} of September) show also lower global irradiance daily averages (Fig. 2 (right)).

4. DISCUSSION

Accurate data of the Earth's surface radiation budget are urgently needed to improve our understanding of the dynamics of the atmosphere used for detailed climatological analysis. A useful information on this subject is a distinction between clear and cloudy sky situations. To date it is still not well established how much solar energy is absorbed within the Earth's atmosphere. In particular, it is not well known what portion of the solar energy is absorbed in the cloudy and the cloud-free atmosphere, respectively. In this context long-term monitoring of surface radiation is very important together with additional information on cloudiness to allow for the separation between cloud-free and cloudy situations.

In this work we used space and ground measurements of the solar radiation and a model proposed by ASHRAE (1995) to define a clear sky atmosphere. We continuously compared the measured global irradiance to the calculated clear sky irradiance at the same moment and define conditions at the ground instrument site. The method was applied, in a first step, to September 1997 measurements. In a subsequent work the method used for the clear sky detection will be verified using both longer-term data series and images obtained by NOAA satellites from the ground reception station at P. Penteli which will help to clearly identify cloudless or cloudy situations.

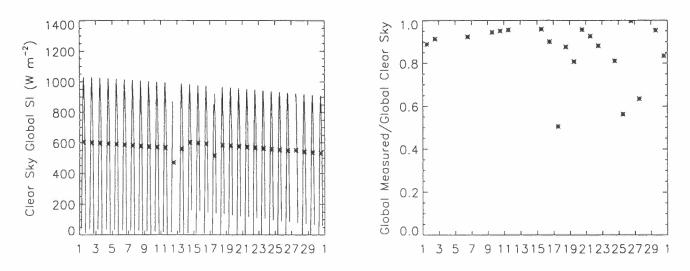


Figure 3. Left Hourly values of the calculated clear sky global radiation. Right Ratio of the measured to the calculated global radiation (* denote daily averages).

Acknowledgments

The authors are grateful to the VIRGO team for providing the TSI dataset. The version used is the 2.5t.

References

- Anklin M., Fröhlich C., Finsterle W., et al., 1999, Metrologia, 35, 686
- American Society of Heating, Refrigerating and Air Conditioning Engineers (ASHRAE), HVAC Applications Handbook, 1995, Atlanta, GA
- Fröhlich C., Crommelynck D., Wehrli C., et al., 1997, Solar Phys. 175, 267
- Fröhlich C. and Lean J., 1998, IAU Symposium 185: New Eyes to See inside the Sun and Stars, F.L. Deubner (ed.), Kluwer Academic Publ, Dordrecht, The Netherlands, 89-102
- Kouremenos D., Antonopoulos K., Dimocritou F., 1991, Thermal flow of structural elements for airconditioning systems in Greece, Foibos, Greece (in greek)
- Tsiropoula G., 2000, J. Atmos. Solar Terrestr. Phys, submitted

MOON DYNAMICS AND CLIMATE PREDICTION

A. Ulla¹, J. A. Belmonte², and P. Thejll³

¹Departamento de Física Aplicada, Universidade de Vigo, E-36200 Vigo (Spain). fax: +34 986812556; ulla@uvigo.es
 ²Instituto de Astrofísica de Canarias, E-38200 La Laguna, Tenerife (Spain). fax: +34 922605210; jba@ll.iac.es
 ³ Danmarks Meteorologiske Institut, DK-2100 København Ø (Denmark). fax: +45 39157460; thejll@dmi.dk

ABSTRACT

Historically, the Moon has been related to rain by several ancient cultures, using our satellite in different ways like a weather forecast. For example, a common belief in the Mediterranean is that the direction of the horns of the Moon at certain times is a good forecast of a rainy or dry period. Also, we have found some predictive practices (*Cabañuelas* in Spanish), following a cycle of 19 years -very close to the 18.6 year regression cycle of the lunar nodes.

Until now, scientists have not in general pursued or found physical reasons to sustain these beliefs. However, the position of the horns of the Moon (up or bent) at a certain epoch is highly dependent on the 18.6 yr cycle of regression of the lunar nodes. In this cycle, the Moon suffers a 10 degree change of declination of its extreme position (lunastice or standstills), meaning that the tidal peak within a certain ocean or sea can vary as much as 10 degrees of latitude within one cycle.

Consequently, this cycle, and its harmonics at 9.3 & 4.7 years, could be related to periodic climate changes. In this work we present attempts to detect such periodicities in local climate series for the Canary Islands. We also present results of spatiotemporal analysis of the the atmospheric circulation on the Northern Hemisphere to show which major circulation factors determine the weather on the Canary islands.

Key words: Moon; Weather.

1. INTRODUCTION

Several ancient cultures, as documented so far (Belmonte & Sanz de Lara, 2000), have been using the Earth's satellite in different manners like a weather forecast. The historical tradition for a link between the Moon and climate probably stands along all the Mediterranean since it can be found already in Hesiod (Greece, IX B.C.). For example, a common belief



Figure 1. The Horns of the Moon: "Luna derecha agua no echa". Francisco Méndez, Frontera (Hierro), August 31st, 2000.

is that the direction of the horns of the Moon at a certain novilunium, specially the autumnal and winter ones, is a good forecast of a rainy or dry period (horns up, dry weather; horns bent, wet weather). In the Canary Islands this tradition has been alive in all the islands until today and, in particular, in the island of El Hierro -the "World's End" until the XV Century- there is a special class of men in charge of this type of observations: the "perlos" (pearls) (Figure 1).

The anthropologist Alicia Navarro found the reference "RULE TO KNOW THE FERTILITY OF YEARS WITH THE "AVERO"" shown in Table 1,

Proc 1st Solar & Space Weather Euroconference, 'The Solar Cycle and Terrestrial Climate', Santa Cruz de Tenerife, Tenerife, Spain, 25-29 September 2000 (ESA SP-463, December 2000)

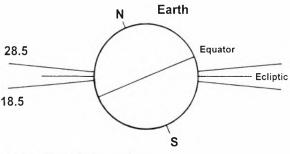
yr nr.	year	prediction
1	1862	Normally Fine
2	1863	Bad, Worst
3	1864	So, so
4	1865	Excellent
5	1966	Very bad, less than 2
6	1867	Regular
7	1868	Excellent
8	1869	The least of the worse
9	1870	Excellent as 4
10	1871	Extremely bad
11	1872	So, so
12	1873	Good, better than 1
13	1874	Worse
14	1875	Some fine
15	1876	More excellent than 4
16	1877	Extremely bad
17	1878	The least of the best
18	1879	Good
19	1880	As bad as 8

Table 1. RULE TO KNOW THE FERTILITY OFYEARS WITH THE "AVERO".

from XIX century sources of the Canarian island of Fuerteventura. This sort of weather predictive practices, known as Cabañuelas in Spanish, is very common in the popular tradition. However, this one is exceptional for its long duration and periodicity, 19 years, which oblige us to think of a possible relationship to some of the lunar cycles. If we apply the prediction to the cycle of rainfall in Betancuria (the ancient island capital) for the period 1967-1975, we obtain a percentage of good hits of 74%, which is higher than the randomly expected 50% (Belmonte & Sanz de Lara, 2000). Another common weather forecast practice relates to the tide of the night of Saint John, a very important festivity in the Canary Islands. If the tide is "llena" (full), a good year can be expected, while if it is "vacia" (empty) drought will come.

2. PHYSICAL MEANING?

In general, and to our knowledge, no scientific reasons have been proposed so far to sustain these traditional beliefs relating "Moon and Weather". However, the position of the Moon horns (up or bent) at a certain epoch is determined by the Moon declination which varies with the 18.6 year cycle of regression of the lunar nodes (Figure 2). When the Moon is at the maximum declination (rising at major lunastices), it has a declination interval of \pm 28.5 degrees while in the minor lunastice, the declination is \pm 18.5. That is, during the cycle the Moon suffers a 10 degree



TIDAL PEAK AT MAXIMUM & MINIMUM LUNAR DECLINATION

Figure 2. Tidal peak at maximum & minimum lunar declination: For example, if at a certain moment the tidal peak is at the latitude of the Canary Islands (28.5N), 9.3 years later, at a similar moment, this peak will be at the latitude of Cabo Verde (18.5N). In the Caribbean Sea, origin of the Gulf Stream, the variation is from the coast of New Orleans to the southern shores of Jamaica. Consequently, we believe that this cycle, and its harmonics at 9.3 & 4.7 years, may be related to periodic climate changes (as demonstrated for instance in the level of the Nile floods, Currie 1987) due to the most probable Moon tidal influence on local, and perhaps general, ocean streams.

change of declination which in turn means that the position of the tidal peaks within a certain ocean or sea of the water geoid can vary as much as 10 degrees of latitude in 18.6 years. Also, Moon phases and Sun positions repeat more or less in a period of 19 years (the Methonic Cycle).

It is conceivable that such a large variation in latitude could influence the tides regime, in particular at certain Globe positions, and, consequently, the ocean flows which in turn may affect climate phenomena like the ENSO or the NAO. In particular, in the North Atlantic, at the latitudes where the NAO exerts its influence, we are dealing with differences of latitude from Newfoundland to Southern Greenland, locations in front of the coast of Terranova, very near Nova Scotia which is the place with the largest tides in the World. On the other hand, any phenomena associated to the 10 degrees of declination variation, due to the N & S symmetry of the Moon movement in one sidereal cycle, should have periods of, not only 18.6, but also 9.3 and, specially, 4.7 years because the variation of the tide peak position happens 4 times in 18.6 years, two coming and two going.

In looking for these periods in climatic registers, Currie (1987) suggests that predictions of the Nile floods from this 19 year cycle are possible. The 19-year cycle is not the second harmonic of the solar 11 year cycle. Other climatic variations, such as precipitation in the U.S., do also show periodicities at 11.1

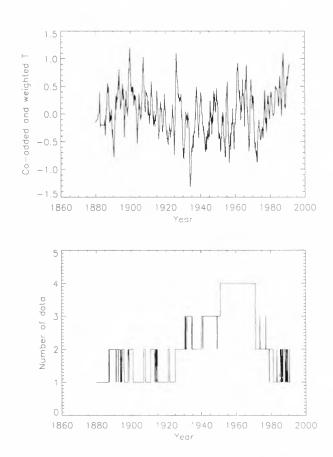


Figure 3. Temperature time series for the Canary Islands (upper panel) and data coverage (lower panel).

and 18.8 years, together with smaller evidence for a periodicity at 9.1 years (second harmonic of the latter). From barometric data in Japan, former USSR, southern Europe, southern Africa and South America, O'Brien & Currie (1993) find air pressure variations with periods near 18.6 yr, which can attain amplitudes as high as 0.9 mb. They identify them as induced by the luni-solar nodal tide component and invoke several theoretical coupling mechanisms to explain some of their properties on sub-continental scales.

3. THE DATA

Several overlapping temperature series from the Canary Islands have been combined into one long continuous time series (Figure 3, upper panel; lower panel: the data coverage), using a technique adapted from dendrochronology (Osborne et al., 1997). As can be seen, the temperature is rising from 1970 onwards, like for the rest of the Northern Hemisphere (NH), while it falls in the period 1900-1940, a time when the rest of the NH was warming. Multi-Taper Frequency Analysis of the data series, in Figure 4, shows that low-frequency power is evident in the bands of interest: there is significant spectral power near 18 or 19 years, together with a suggestion of the bi-decadal signal.

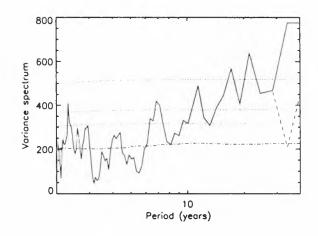


Figure 4. MultiTaper Frequency Analysis of the data series in Figure 3. Vertical dotted lines are plotted at 17, 18, 19 and 22 years. The horizontal dotted lines show confidence levels between 90% (lowermost) and 99% (uppermost).

This analysis is accompanied by a composite map of the air surface pressure on the Northern Hemisphere, given the temperatures on the Canary Islands in the period 1948-1990 (Figure 5). The map was made by subtracting the map of mean surface air pressure during times of NEGATIVE temperature anomalies in the Canaries from the map of mean surface air pressure during times of POSITIVE temperature anomalies. This difference is shown in the figure contour lines, spaced at one mb distances. Negative pressures are shown as dashed contours and positive ones as solid lines, with 0 as a heavy contour. Grey areas show the statistically significant areas. determined by a Monte Carlo technique. Looking at the map it is clear that the geostrophic wind will be from the South over the Canaries, consistent with the temperatures, when they are larger than average, and from the North when the temperatures are less than average. This map looks very much like the leading mode of the NAO circulation over the Atlantic, suggesting that an important part of the climate over the Canaries is controlled by the NAO.

4. CONCLUSIONS

A possible physical link between the position of the Moon horns at a certain novilunium, as determined by the Moon declination within the 18.6 year regression cycle of lunar nodes, and the rainy or dry nature of the following year on the Canary Islands. is explored in this work. While the idea is well documented for several ancient cultures which use the Moon as a weather forecast, the 18.6 yr period itself has also been reported in the analysis of various climate data series. In particular, we show its detection in a long temperature series for the Canary Islands and combine the study with a composite map of the air surface pressure on the N.H. We find that the importance of the NAO can not be neglected and

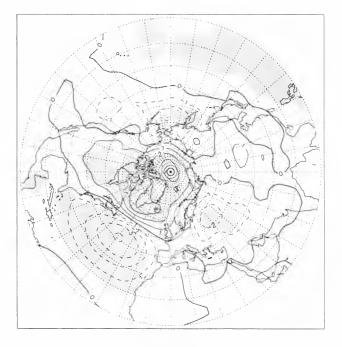


Figure 5. Composite map of the air surface pressure on the Northern Hemisphere, given the temperatures on the Canary Islands in the period 1948-1990.

intend to investigate whether the NAO is expressing the 18.6 year cycle or is a factor in addition to this possible external mechanism, both from the theoretical and observational sides. Rain gauge measurements and various climate proxies of the Mediterranean area will be investigated.

ACKNOWLEDGMENTS

This work was partly supported by the Spanish Ministerio de Educacion y Cultura under Project DGESIC PB97-1435-C02-02, and the Danish Climate Centre.

REFERENCES

Belmonte J.A., Sanz de Lara M. El Cielo de los Majos. Editorial La mareta. La Laguna. 2000.

Currie R.G. 1993. International Journal of climatology 13, 31-50.

O'Brien, D.P., Currie, R.G., Observations of the 18.6-year cycle of air pressure and a theoretical model to explain certain aspects of this signal. Climate Dynamics, 8, 287-298. 1993.

Osborne, T.J., Briffa, K.R., Jones, P.D., Adjusting variance for sample-size in tree-ring chronologies and other regional mean timeseries, Dendrochronologia, vol. 15, pp.89-99, 1997. Joint Organisation for Solar Observations (JOSO)

JOSO

Data Handling in Solar and Geophysical Research

SOLAR AND GEOPHYSICAL DATABASES: THE TILES OF A PLANETARY META-ARCHIVE

Mauro Messerotti

Trieste Astronomical Observatory, Via G.B. Tiepolo 11, 34131 Trieste, Italy

ABSTRACT

In the frame of solar-terrestrial physics and the related space weather applications, a brief overview is given on the available resources to access solar, interplanetary, geospace and geophysical data with special emphasis on the creation of a Solar-Terrestrial Data Planetary Meta-Archive (STDPMA) to exploit their full potentialities as a huge, inhomogeneous, distributed dataset in a user-transparent way by means of the new technologies in database management and user interface design.

Key words: data base; meta-archive; space weather.

1. INTRODUCTION

Current ground-based and space-based instrumentation produces a continuous flow of data, which feeds the existing datasets at a nonlinear rate and extends the data amount according to power laws.

Nowadays a scientific user faces with a great number of inhomogeneous datasets, usually organized in geographically distributed archives with limited remote access, limited data query capabilities and non-existent cross-search resources due to the scarce coordination in archive virtual linking all over the world. This situation makes difficult an efficient multi-band, multi-disciplinary data mining and prevents the use of the whole data information content. Hence an advanced approach in archive extension, linking and interfacing is needed wherever multiband and multi-instrument data are to be crosssearched and cross-analyzed as it is the rule, e.g., in solar, solar-terrestrial and terrestrial physics.

In this frame, the aim of this work is to briefly review the present status of existing and planned data mining resources with special attention to possible future developments. In particular, scientific motivations for the advancement in data archiving technologies are considered in Section 2. A brief review of some relevant solar-terrestrial data portals is given in Section 3. The requirements of a Solar-Terrestrial Data Planetary Meta-Archive and the conclusions are presented in Section 4.

2. ADVANCEMENTS IN DATA ARCHIVING: MOTIVATIONS AND PROJECTS

A huge amount of space- and ground-based data is acquired on a daily basis and stored in existing archives, challenging the available storage capacity, as its typical unit of measurement on an annual basis is now the Terabyte (10^{12} bytes) .

The problem in dealing with such enormous data amounts is twofold, as both *data storage* and *data management* play a fundamental complementary role. Both technologies are under continuous development, which progresses in parallel, even if the former involves experimentation in the science of materials, whereas the latter in software architecture.

In fact, on one hand, new technologies and new media promise efficient, reliable and low-cost solutions by means of an increase in pointwise information density both via new materials and writing/reading modes, as well as by using spatial (e.g., holographic) techniques (see, e.g., Messerotti, 1999), which can, in principle, provide storage media with fast access times and capacities higher by orders of magnitude with respect to current ones. On the other hand, the data management software technology is suitable to be further extended to cope with the new needs and in the following we will concentrate on this aspect.

From the raw datum to the most advanced metaarchive, the *data organization* occurs in physical and logical *hierarchical categories* of increasing complexity. Raw data are organized in records and set of records in files, which characterize specific data series. A set of data series originates a specific dataset, a set of datasets forms a database, and a set of databases an archive (we prefer such a terminology, even if in the literature the terms database and archive are often used as synonyms). Finally, a set of archives can be linked in a meta-archive.

At the basic level, data catalogs are generated and

Proc. 1st Solar & Space Weather Euroconference, 'The Solar Cycle and Terrestrial Climate', Santa Cruz de Tenerife, Tenerife, Spain, 25-29 September 2000 (ESA SP-463, December 2000)

updated to describe the archive content. At an operational, more refined level, the *data information content* is indexed via *selected descriptors* and arranged in *interconnected tables* via refined software tools named Relational Data Base Management Systems (RDBMS), which make easier complex queries on the data via a standard query meta-language, the SQL (Structured Query Language).

The power of an archive for a specific research is given by the following features: (a) completeness in datasets relevant to the research; (b) easiness in access; (c) power in data search; (d) speed in data retrieval.

Most of the above requirements are satisfied in modern archives thanks to the availability of fast hardware and refined software technologies. In fact, user-friendly access is achieved via World-Wide Web (WWW) Graphical User Interfaces (GUI) or Telnet sessions, data search occurs via HTML forms in a user-transparent way and data request and retrieval can occur via HTML and FTP protocols respectively. These general architectural guidelines were used in the development of many solar archives, such as, e.g., the ARchive of THEMIS (Reardon et al., 1997) with excellent results in terms of usability.

Notwithstanding that, the key point becomes today point (a), i.e. the completeness in datasets relevant to a specific research. In fact, current research in specific topics like Solar-Terrestrial Physics and Space Weather relies on a multi-disciplinary, i.e. multi-instrument multi-band approach (Crosby, 2000). Most of current archives are dedicated to just one ground-based instrument or to the set of instruments, which pertains to a spacecraft, and sometimes they act as portals towards other remote archives but only at the connection level, i.e., no cross-search over geographically distributed datasets is made available.

This is a serious limitation imposed to research, as many data are available in independent, remotely distributed archives, but they are not searchable through a common unified interface, which represents a fundamental tool in remote collaborative research work as well (Messerotti et al., 2000).

To overcome such a limitation and in consideration of the synergetic action of the SOHO archive, the Whole Sun Catalog (WSC) project has been conceived (Sanchez-Duarte et al., 1997; Dimitoglou et al., 1998). In brief, the WSC, managed by an RDBMS and accessible via a WWW GUI, in its initial development phase, should represent a mean to search in a catalog of observations, which builds up via the daily submission of a standard log form by the participating observing facilities. It can therefore be considered as a searchable catalog of catalogs, which, upon a specific query, provides a list of available data for the date(s)/time(s) from the same or different instruments, one or more wavelengths, specific time and spectral resolution(s), etc., but indicating only the location of the related repositories and relying on their local resources for data retrieval, e.g., via FTP.

The WSC project considers also an advanced extension in a second phase after the testing of the first one, specifically the implementation of the *distributed database technology* and the *spatial database extensions*. As RDBMS's are scalable, they allow table replication among geographically distributed archives and the creation of a common catalog, which virtually links them at the data information level but keeps their physical management independent. This provides a search tool for data with specified features over different remote datasets and a way to transparently retrieve data, which are incorporated into the WSC archive itself via the spatial database extensions.

Recently a new project with even more advanced goals was conceived, i.e., the Virtual Solar Observatory (VSO) detailed in Hill (2000). As a metaarchive, VSO is designed to match all the mentioned requirements with an additional feature, which is *data analysis*. This means that the final scientific user will be able to search, access and analyze the requested solar data via a common WWW GUI in a transparent way, independently of their location and with a valuable spin-off in terms of productivity, besides a substantial extension in data mining capabilities.

3. SOLAR AND GEOPHYSICAL PORTALS

When the WWW became an established technology in information management over Internet, many solar data resources started to be developed (Messerotti, 1995) as also international organization sites, e.g. the Joint Organization for Solar Observations (JOSO) WWW server (Messerotti. 1996; Messerotti and Veronig, 1998). Soon the number of solar, solar-terrestrial and terrestrial WWW data resources increased exponentially in number, making difficult the search for a specific resource. Hence

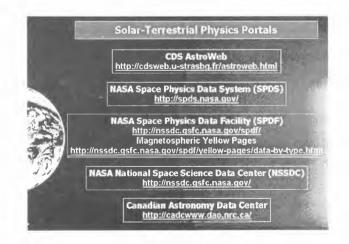


Figure 1. Some relevant portals in Solar, Solar-Terrestrial and Terrestrial Physics.

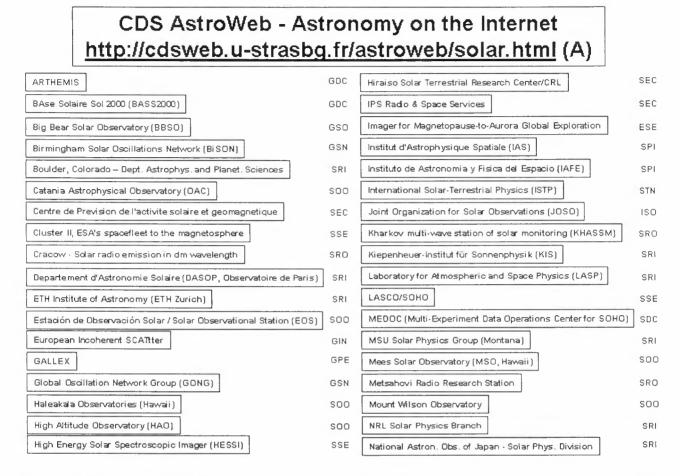


Figure 2. First part of the list of hyperlinks made available by the CDS AstroWeb portal under the heading "Solar". In this picture non-professional sites are not shown. Site typology acronyms mean respectively: EDC (Earth Data Center), ESE (Earth Space Experiment), GDC (Ground-Based Data Center), GIN (Ground-Based Ionospheric Network), GPE (Ground-Based Particle Experiment), GSN (Ground-Based Solar Network), GSO (Ground-Based Solar Observatory), ISO (International Solar Organization), NSO (National Solar Organization), SDC (Space Data Center), SEC (Space Environment Center), SOO (Solar Optical Observatory), SPI (Space Research Institute), SRI (Solar Research Institute), SRO (Solar Radio Observatory), SSE (Solar Space Experiment), STN (Solar-Terrestrial Network).

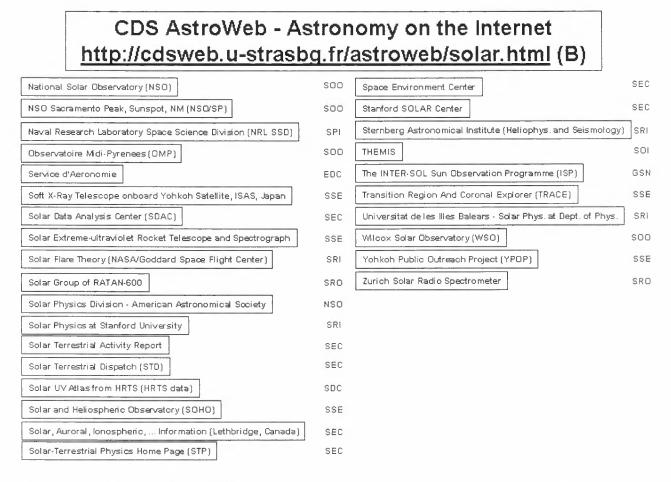


Figure 3. Second part of the list of hyperlinks made available by the CDS AstroWeb portal under the heading "Solar". In this picture non-professional sites are not shown. Site typology acronyms mean respectively: EDC (Earth Data Center), ESE (Earth Space Experiment), GDC (Ground-Based Data Center), GIN (Ground-Based Ionospheric Network), GPE (Ground-Based Particle Experiment), GSN (Ground-Based Solar Network), GSO (Ground-Based Solar Observatory), ISO (International Solar Organization), NSO (National Solar Organization), SDC (Space Data Center), SEC (Space Environment Center), SOO (Solar Optical Observatory), SPI (Space Research Institute), SRI (Solar Research Institute), SRO (Solar Radio Observatory), SSE (Solar Space Experiment), STN (Solar-Terrestrial Network).

some *portals* were developed, i.e., WWW sites acting as a unique central gateway to a set of hyperlinked resources.

To give an idea about the enormous amount of information distributed over the network and the intrinsic difficulty in identifying and managing it. it is sufficient to mention some major portals in Solar, Solar-Terrestrial and Space Physics, which are very rich in links and embedded facilities, such as (Figure 1): the CDS AstroWeb [http://cdsweb.u-strasbg.fr/astroweb/solar.html], the NASA Space Physics Data Svstem (SPDS) [http://spds.nasa.gov/], NASA the Space Physics Data Facility (SPDF) [http://nssdc.gsfc.nasa.gov/spdf/] with the Magnetospheric Yellow Pages [http://nssdc.gsfc.nasa.gov/spdf/yellow-pages/databy-type.html], the NASA National Space Science Data Center (NSSDC) [http://nssdc.gsfc.nasa.gov/] and the Canadian Astronomy Data Center [http://cadcwww.dao.nrc.ca/]. Most known WWW resources in the mentioned fields are indexed and reachable through these portals and each of them, in turn, points to the same or similar resources. This makes the hyperlinking a very complex and non-optimized graph, which negatively biases the success in specific data searching and results in the typical responses of the generic search engines with thousands of entries with hundreds of repeated items.

As an example of the variety of data sources and general resources, we tried to index the items provided by the CDS AstroWeb under the heading "Solar" after discarding all the non-professional organizations for an easier categorization. CDS provides the hyperlink to 64 professional organizations (Figures 2 and 3) in the following 17 categories: EDC (Earth Data Center), ESE (Earth Space Experiment), GDC (Ground-Based Data Center), GIN (G-B Ionospheric Network), GPE (G-B Particle Experiment), GSN (G-B Solar Network), GSO (G-B Solar Observatory), ISO (International Solar Organization), NSO (National Solar Organization), SDC (Space Data Center), SEC (Space Environment Center), SOO (Solar Optical Observatory), SPI (Space Research Institute), SRI (Solar Research Institute), SRO (Solar Radio Observatory), SSE (Solar Space Experiment), STN (Solar-Terrestrial Network). The related distribution in typologies by disciplinary affinity provides the following results in terms of number of entries:

- General typology (Figure 4)
 - 37 Ground-Based Solar
 - 13 Ground-Based Solar-Terrestrial
 - 14 Space-Based Solar-Terrestrial
- Ground-Based data (Figure 5)
 - 02 GDC
 - 01 GSO
 - 03 GSN

- 12 SRI
- 11 SOO
- 05 SRO
- 01 GPE
- 01 NSO
- 01 ISO
- Solar-Terrestrial data (Figure 6)
 - 10 SEC
 - 01 STN
 - 01 EDC
 - 01 GIN
- Space data (Figure 7)
 - 02 SDC
 - 08 SSE
 - 03 SPI
 - 01 ESE

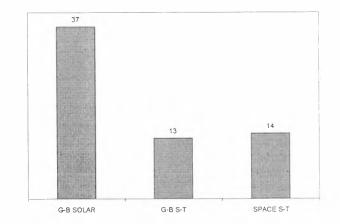


Figure 4. General site typology according to data sources: Ground-Based Solar Data, Ground-Based Solar-Terrestrial Data, Space-Based Solar-Terrestrial Data.

4. A SOLAR-TERRESTRIAL DATA PLANETARY META-ARCHIVE

Today's physical modelling stringently needs a common unified, user-friendly interface for *multiwavelength data search, data display and data analysis.* Especially applications like Space Weather are intrinsically multi-disciplinary, as it requires multi-event modelling over solar, space and earth datasets with the largest coverage possible of observed phenomena. In particular, events' prediction needs to operate cross-searches over different archives, perform statistical analyses and have real-time data available at a glance. As reviewed in previous sections, some major Solar-Terrestrial Data Portals exist, but they are inadequate to match the above requirements. as: (a) mainly resource indexing is available; (b) few

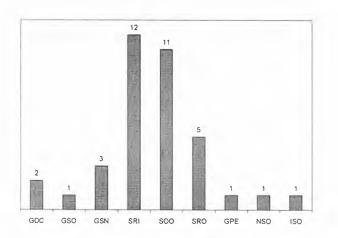


Figure 5. Specific subtypologies for Ground-Based Solar Data sites (see text).

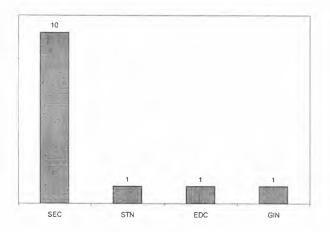


Figure 6. Specific subtypologies for Solar-Terrestrial Data sites (see text).

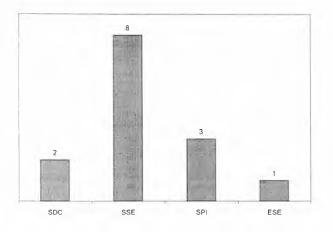


Figure 7. Specific subtypologies for Space-Based Solar-Terrestrial Data sites (see text).

resources partially allow complex, distributed data searching over limited subsets of databases; (c) very few resources partially allow data analysis on inhomogeneous datasets. Therefore a Solar-Terrestrial Data Planetary Meta-Archive (STDPMA) is needed to exploit the full scientific potentialities of multiwavelength modelling in Solar-Terrestrial Physics by: (a) indexing observational resources; (b) indexing theoretical resources; (c) allowing user-transparent data access to distributed datasets all over the world; (d) allowing complex data searching, retrieval and analysis via a simplified common GUI. In principle, present data archiving technologies allow the achievement of such goals, but a global coordination and collaboration must be established among the participating data providers, archive scientists and final scientific users, which is difficult to obtain on a so large scale. Last but not least the allocation of proper financial resources by the participating organizations is a must for a full success of the initiative. Despite its complexity, we are convinced that the scientific community should start considering the STDMPA as a feasible project, worthwhile doing when considering the benefits in terms of improved modelling. In this light, the WSO and VSO projects can represent the initial tiles of STDPMA and act as operational test-beds for it.

ACKNOWLEDGMENTS

The Italian Ministry for University and Research (MURST) and the Italian Space Agency (ASI) are acknowledged for the financial support to this work.

REFERENCES

- Crosby N., 2000, these proceedings
- Dimitoglou G., Mendiboure C., Reardon K., Sanchez-Duarte L., 1998, ASP Conf. Ser. 155, 297
- Hill F., 2000, these proceedings
- Messerotti M., 1995, JOSO Annual Report 1994, M. Saniga (ed.), Astron. Inst. Slovak Acad. of Sci., Tatranska Lomnica, Slovakia, 134
- Messerotti M., 1996, JOSO Annual Report 1995, M. Saniga (ed.), Astron. Inst. Slovak Acad. of Sci., Tatranska Lomnica, Slovakia, 81
- Messerotti M., 1997, ASP Conf. Ser. 118, 390
- Messerotti M., Veronig A., 1998, ASP Conf. Ser. 155, 287
- Messerotti M., 1999, ESA SP Series 448, 271
- Messerotti M., Otruba W., Hanslmeier A., 2000, Proc. SPIE 4011, 11
- Reardon K., Severino G., Cauzzi G., Gomez M.T., Straus T., Russo G., Smaldone L.A., Marmolino C., 1997, ASP Conf. Ser. 118, 398
- Sanchez-Duarte L., Fleck B., Bentley R., 1997, ASP Conf. Ser. 118, 382

THE VIRTUAL SOLAR OBSERVATORY CONCEPT

Frank Hill

National Solar Observatory PO Box 26732, Tucson AZ 85726-6732 USA Phone: +1-520-318-8138 Fax: +1-520-318-8278 E-Mail: <u>fhill@noao.edu</u>

ABSTRACT

The continuing development of the Internet as a research tool has sparked new interest in the development of networked astronomical databases and analysis tools. In this paper, I outline a concept for a Virtual Solar Observatory (VSO), a set of data archives and analysis tools distributed in physical location at sites that already host such systems. The technical concepts of the VSO include federated distributed archiving, an adaptive metadata thesaurus, a single unified intuitive GUI, context-based searches, and distributed computing. Potential analysis tools include content-based searches, visual programming tools, and visualization packages. The development of a VSO would greatly facilitate solar physics research since a user would no longer need to have detailed knowledge of all solar archive sites.

1. INTRODUCTION

The VSO concept outlines a software environment for searching, obtaining and analyzing data from archives of solar data that are distributed at many different observatories around the world. This "observatory" is virtual since it exists only on the Internet, not as a physical structure. As a research tool, the VSO would enable a new field of correlative statistical solar physics in which large-scale comparative studies spanning many dimensions and data sources could be carried out. While many such comparative solar studies are carried out today (observational studies in recent issues of Solar Physics consider an average of 4-5 data sets), much larger comparisons are not feasible due to the shear logistical obstacle of simply finding the data. This task requires the user to learn what archives exist, where they are, what data they contain, and the details of the file naming convention and access methods. The substantial effort expended for this process results in most users accessing only a few archives in their careers.

The idea of combining solar archives into a unified system was first proposed by Sanchéz-Duarte et al. (1997), and further discussed by Dimitoglou et al. 1998. The VSO has been briefly described by Hill (2000). Individual solar archives have been discussed by Hill et al., (2000), Reardon et al. (1998), Sanchéz-Duarte (1999), and Roudier and Mahlerbe (1997).

Several avenues of solar research would be accelerated by a VSO. These areas include:

- Space weather, which would greatly benefit from more reliable and detailed knowledge of the solar surface signature of an imminent CME. This requires correlating time series of coronal images, filament positions, and surface quantities such as vector magnetic fields and x-ray emission in several wavelengths.
- The structure of a sunspot atmosphere, which is still poorly understood. A composite data set of vector magnetic field maps, space-based UV spectra, and temporal sequences of EUV images could yield a more complete description of the density, magnetic field, velocity, and turbulence with height above sunspots.
- The mechanism by which sunspots block solar energy, thus creating fluctuations in the solar irradiance. is poorly understood. Observations of the surface vector magnetic field and the spatial intensity distribution in several wavelengths are needed for comparisons with theory.
- The statistics of active region life cycles are not known. Such a study requires multi-day time series of surface magnetic field, Doppler velocity, and intensity in several wavelengths.
- The statistical evolution of the solar granulation properties over the course of an 11-year solar activity cycle has only been sparsely sampled. A consistently sampled study could reveal clues about the long-term behavior of the underlying near-surface flow field as well as provide insight into the driving and damping mechanisms of the solar oscillations. This problem requires multiyear time series of surface magnetic field, Doppler velocity, and intensity in several wavelengths.
- The subsurface structure of active regions is beginning to be probed by local helioseismology, in which subsurface properties are determined in small patches rather than globally averaged. These results must be placed in context, which requires both surface magnetic field measurements and time series of the Doppler velocity. This technique may eventually be able to locate active regions

Proc. 1st Solar & Space Weather Euroconference, 'The Solar Cycle and Terrestrial Climate', Santa Cruz de Tenerife, Tenerife, Spain, 25-29 September 2000 (ESA SP-463, December 2000)

before they emerge on the surface, which would be useful for space weather predictions.

- The solar wind is believed to originate near the boundaries of coronal holes where the solar magnetic field is open to interplanetary space. However, the details of the physical process that accelerates the wind are still unknown. Research on this question requires images that show the location of coronal holes at either x-ray or infrared wavelengths in conjunction with data on solar wind speed, and surface quantities.
- A long-standing mystery is the heating of the outer solar atmosphere. It is now known that substantial areas of the atmosphere are actually much cooler than the surface. Unraveling the complex thermodynamic and energy budget of the solar atmosphere requires the spatial and temporal correlation of observations in the infrared, visible, and UV with magnetic and velocity fields at different heights above the solar surface.

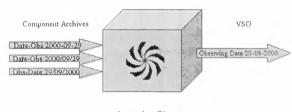
2. TECHNICAL COMPONENTS

The VSO technical concept includes the federation of distributed solar archives, an adaptive metadata thesaurus, a single unified intuitive GUI, context-based searches, and distributed computing.

Federating distributed solar archives means linking together a number of archives that are located at different physical sites into a larger, more uniform system. A user would then need only access a single web site from which the entire set of component archives could be searched. This basic VSO functionality is schematically illustrated in figure 1.



Figure 1: Schematic of basic VSO functionality. The user submits a data request to the VSO, which can either translate the query into the form appropriate for Archive 1, or search a VSO catalog for the file location in Archive 2. These archives return their data to the VSO, which then collates it and returns it to the user. An adaptive metadata thesaurus is a method to reconcile the myriad of definitions of common data descriptors. An example that is likely to be familiar to most users of solar data is the formatting of the date an observation was obtained. Figure 2 schematically shows the thesaurus in action as it learns that three common forms of the FITS header keyword DATE-OBS are equivalent to the more intuitive "Observing Date". In figure 3, the thesaurus is translating the user's input back into the format specific for the component archives. The thesaurus is essentially a lookup table that is updated when a new archive is added to the VSO, or when an archive revises its metadata format.



Learning Phase

Figure 2: The learning phase of the adaptive metadata thesaurus, a program that is taught to recognize synonyms for common data descriptors. In the example here, the thesaurus is learning that three common forms of the FITS keyword for the observation date are equivalent to a more intuitive term.

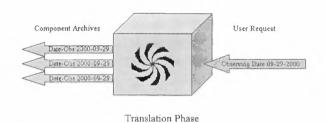


Figure 3: Here the thesaurus is translating the user's input into the specific format required to query a particular component archive.

The graphical user interface (GUI) is a critical component of the VSO. The GUI is the component through which the user will interact with the VSO, and it must be simple, intuitive, and easy to use. Many solar archives currently require the user to be an expert in specific details such as file naming conventions, experiment numbers, etc. The VSO GUI will not require this expert knowledge, but must provide

M. 9			6		謎	A
Back Forward	Reload	Home Search Netscape Print	Security	Shop	Stop	
		on file:/home/hill/nvo/toolb	html			/ CI What's Relate
		specification:				anaanaand.
-		value)		description	
name	type				110 AN 000 01 A 01 A 0 A A A A A A A A A A A A A A A A A	(a. e. (b
l_start	Real	1082	starting	waveleng	th, e.g. 6350	ees - Hees - Heel Hilling - Jeffers - Jeffers all Hilling
stop	Real	1084	ending	ending wavelength, e.g. 6370		
_resolution	Real		spectra	spectral sampling, e.g. 0.1		
l units	Ang	nm m Mev Ghz cm^-1 Sel	ect units		en el compositor i arre de la decoration en en en el compositor en el compositor en el compositor en el compos	
cinporta si						
emporal s	ecificati	on:				
					1	elee line anna a la la construction de la construction de la construction de la construction de la construction
name	type	value			descrip	e an lane a bellen (lant) e te at lane (at lane) bellen til an at laner (at lane
name		value 2000.05.01.00.00.00	starting	time: YY	descript 7Y.MM.DD.HH.	e an them a letter that the letter of the the letter that the the second s
name t_start	type					e an them a letter that the letter of the the letter that the the second s
name t_start t_stop	type	2000.05.01.00.00.00	ending	ime; defa	YY.MM.DD.HH.	e an them a letter that the letter of the the letter that the the second s
name t_start t_stop t_resolution	type Time Time	2000.05.01.00.00.00 2000.05.31.23.59.59	ending t	time; defa al resolutio	(Y.MM.DD.HH. alt: current time on sec min	MM.SS
name t_start t_stop t_resolution t_cadence	type Time Time Real	2000.05.01.00.00.00 2000.05.31.23.59.59 60	ending t tempor	time; defa al resolutio al cadenco	YY.MM.DD.HH. alt: current time on sec min c sec min o	MM.SS day year
name t_start t_stop t_resolution t_cadence t_window	type Time Time Real Real	2000.05.01.00.00.00 2000.05.31.23.59.59 60 60	ending t tempor tempor	time; defa al resolutio al cadenco al window	YY.MM.DD.HH. alt: current time on sec min c sec min o	MM.SS day year day year lay year
name t_start t_stop t_resolution t_cadence t_window	type Time Time Real Real Real	2000.05.01.00.00.00 2000.05.31.23.59.59 60 60 1440	ending t tempor tempor	time; defa al resolutio al cadenco al window	YY.MM.DD.HH. alt: current time on sec min e sec min sec (mnin d	MM.SS day year day year lay year
	type Time Time Real Real Real Real	2000.05.01.00.00.00 2000.05.31.23.59.59 60 60 1440	ending t tempor tempor	time; defa al resolutio al cadenco al window	YY.MM.DD.HH. alt: current time on sec min e sec min sec (mnin d	MM.SS day year day year lay year
name t_start t_stop t_resolution t_cadence t_window t_fill Clear temporal	type Time Time Real Real Real	2000.05.01.00.00.00 2000.05.31.23.59.59 60 60 1440	ending t tempor tempor tempor	time; defa al resolutio al cadenco al window ld for acco	YY.MM.DD.HH. alt: current time on sec min e sec min sec (mnin d	MM.SS day year day year lay year
name t_start t_stop t_resolution t_cadence t_window t_fill Clear temporal Example: If you	type Time Time Real Real Real Real	2000.05.01.00.00.00 2000.05.31.23.59.59 60 60 1440 0.95	ending t tempor tempor tempor thresho	time; defa al resolutio al cadenco al window ld for acco	YY.MM.DD.HH. alt: current time on sec min e sec min sec (mnin d	MM.SS day year day year lay year
name t_start t_stop t_resolution t_cadence t_window t_fill Clear temporal Example: If you	type Time Time Real Real Real Real	2000.05.01.00.00.00 2000.05.31.23.59.59 60 60 1440 0.95 nutes of data with 10-second resolu	ending t tempor tempor tempor thresho	time; defa al resolutio al cadenco al window ld for acco	YY.MM.DD.HH. alt: current time on sec min e sec min sec (mnin d	MM.SS day year day year lay year

Figure 4: One menu in a possible design of the VSO user interface. This screen allows the user to specify the spectral and temporal characteristics of the data.

flexible ways for the user to specify the data that he is searching for.

A portion of one possible design of the VSO GUI is shown in figure 4. The user is provided menus from which data sources, observed quantities (i.e. magnetic field, intensity, Doppler velocity, etc.), and dimensions can be chosen. Other menus allow the specification of spectral, temporal, and spatial characteristics, and finally provide the user with some control over the platforms that will process the request. After the data has been selected and the VSO has performed the search, the user will be provided with quick look thumbnail images of the data that meet the search criteria. An example design of the search results screen is shown in Figure 5. The user will be provided with check boxes to select individual images, or to obtain the entire set of offered data. Alternatively, graphical displays could be employed to further refine the data selection. Finally, the user will choose a data delivery method.

2 2 3	1 2	M	k 💰	(i)				1.50
lack Forward Reload	Home Search	Netscape Pri	nt Security	Shop	Stop			
Internet 🗂 Lookup 🗋	1 New&Cool							
🖉 Bookmarks 🎄 Loca	ation: [file_/hom	e/hill/nvo/tool	out.html				/ 🕼 What's	Relate
					VS0	1		

Results of Search ID 0009875 for user F. Hill on 11 June 2000 1742 GMT

Thumbnail	Data Source	Data Type	Date
	NSO Digital Library	KPVT He I 1083-nm SHG	14 May 2000
	NSO Digital Library	KPVT He I 1083–nm Coronal Hole Drawing	14 May 2000
	NSO Digital Library	KPVT Fe I 868.8—nm Magnetogram	14 May 2000
	Stanford SSC	MDI Ni I 676.8—nm Dopplergrar	ns 14 May 2000
00006	Stanford SSC	MDI Ni 1 676.8—nm Magnetograms	14 May 2000
	NASA/GSFC/SDAC	SOHO EIT He II 30.4-nm Spectroheliogram	14 May 2000
100%			1 34 34 10 G

Figure 5: One possible display of the results of a VSO search.

Currently, the VSO interface design is a series of large menus either on separate pages or on a single page. This will most likely be replaced by a sleeker "PC"-style single-screen design with a large workspace surrounded by tool bars and pull-down menus. The workspace would display the search results as well as provide an area for interactive data analysis and visualization tools. The VSO would also include context-based searches. In contrast to RDBMS queries on tables of metadata obtained from image headers, context-based searches use quantities directly calculated from the data. This allows much more complex scientific queries such as "Which images had a magnetic field between 500 and 1000 G in the northern hemisphere between latitudes 30 and 40° during 1984?"

Context-based searches are usually expensive computationally. Thus, the VSO will require distributed computing for efficient operation. This is shown schematically in figure 6. A user submits a context-based query, which is sent by the VSO to an archive. This archive, in turn, distributes the computational load between itself, other component archive systems of the VSO, and the central VSO server. After the search is completed, the results are sent back to the VSO server, which collates the data and returns the results to the user.

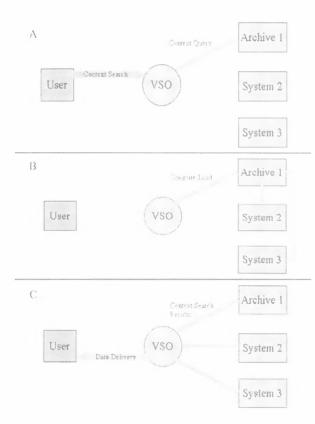


Figure 6: The essential steps in the distribution of the compute load for a VSO context-based search. Panel A: The user submits a context search request to the VSO, which sends the query to the relevant archive. Panel B: The archive sends part of the computing task to two other systems, and the VSO server. Panel C: The results are sent back to the VSO server, which collates the results and sends the results back to the user.

Other VSO components will include analysis software, data visualization tools, a visual programming interface, and a usage tracking system. The combination of the analysis and graphics packages with the search capabilities of the VSO will create a powerful new tool for solar research. The usage tracking is essential for measuring the overall impact on the VSO on solar physics.

While the implementation details remain to be determined, it is likely that the VSO will be written in a platform-dependent language such as Java or JavaScript. The user interface could also be written in Java (Scholl et al. 1999). Java-based solutions are attractive because of their portability, but security concerns will need to be addressed. It is also likely that the structure of the central VSO catalog will incorporate XML.

3. COMPONENT ARCHIVES

There are roughly a dozen major solar archives currently maintained on the Internet. These archives are prime candidates for inclusion in the VSO, and contain about 102 TB of data. The archives are located at:

- The NSO Digital Library (data from the KPVT, GONG, and SOLIS)
- NASA/GSFC SDAC, (SMM, Yohkoh, etc)
- SOHO
- The Stanford University SSSC (SOI/MDI, TON, Wilcox Solar Observatory)
- The TRACE archive at Lockheed
- Montana State University
- UCLA/Mt. Wilson 150-ft Tower
- USC/Mt. Wilson 60-ft Tower
- BBSO/NJIT
- HESSI
- ARTHEMIS
- BASS2000
- HAO
- CSUN/SFO

The archive list above is preliminary; the VSO is intended to be easily expandable so that additional archives can be simply incorporated without requiring substantial resources.

4. MANAGEMENT CONCEPT

The linking of distributed archives is more effective than the construction of a large centralized data center since the expertise required to fully exploit the data resides with the groups that designed, built, and used the instruments to collect the data. These groups are by far the most qualified to maintain and update their own data sets. Similarly, the people responsible for the data will best manage the VSO. Thus, the VSO management concept includes a board comprised of data users and representatives (such as scientists, information technologists) from each component archive. This will give the solar physics community substantial influence over the development of the VSO. In addition, a small top-level group (Project Director, Scientist, and Manager) will provide the point of contact with funding agencies. The community will be further involved by making the Project Scientist a rotating position filled by archive representatives.

The technical development of the VSO will be shared among the community as well. It is hoped that each archive would obtain resources to provide programming support both for integration of a particular archive, and for the overall VSO system implementation

5. CONCLUSION

The VSO is a community-based research tool combining distributed solar archives and analysis packages into a unified system. This would increase the efficiency of performing solar research, and would enable a new era of statistical correlative solar physics. This should produce new results in several areas of inquiry, including space weather, helioseismology, coronal heating, active region evolution, irradiance variations, solar wind origins, and sunspot structure.

ACKNOWLEDGMENTS

The National Solar Observatory is operated by AURA, Inc. under a cooperative agreement with the National Science Foundation.

REFERENCES

Dimitoglou, G., Mendiboure, C., Reardon, K., Sanchéz-Duarte, L. 1998, in ASP Conf. Ser. Vol. 155, 2nd Advances in Solar Physics Euroconference: Three-Dimensional Structure of Solar Active Regions, ed. C. E. Alissandrakis & B. Schmieder (San Francisco: ASP), 297

Hill, F. 2000, in ASP Conf Ser., Virtual Observatories of the Future. (San Francisco: ASP), in press.

Hill, F., Erdwurm, W., Branston, D., McGraw, R. 2000, J. Atmospheric and Solar-Terrestrial Physics, in press.

Reardon, K., Severino, G., Cauzzi, G., Gomez, M. T., Straus, T., Russo, G., Smaldone, L. A., Marmolino, C. 1997, in ASP Conf. Ser. Vol. 118, 1st Advances in Solar Physics Euroconference: Advances in Physics of Sunspots, ed. B. Schmieder, J. C. del Toro Iniesta, & M. Vazquez (San Francisco: ASP), 398

Roudier, Th., Malherbe, J. M., 1997, in Forum THEMIS: Science with THEMIS, ed. N. Mein & S.Sahal-Brèchot (Paris: Obs. de Paris), 45

Sanchéz-Duarte, L. 1999, in 9th European Meeting on Solar Physics: Magnetic Fields and Solar Processes, ed. A. Wilson (Norwijk: ESA SP-448), 269.

Sanchéz-Duarte, L., Fleck, B., Bentley, R. 1997, in ASP Conf. Ser. Vol. 118, 1st Advances in Solar Physics Euroconference: Advances in Physics of Sunspots, ed. B. Schmieder, J. C. del Toro Iniesta, & M. Vazquez (San Francisco: ASP), 382.

Scholl, I., Girard, Y., & Bykowski, A. 1999, in ASP Conf Ser. Vol. 172, Astronomical Data Analysis Software and Systems VIII, ed. D. M. Mehringer, R. L. Plante, & D. A. Roberts (San Francisco: ASP), 253.

SPACE WEATHER USER REQUIREMENTS OF SOLAR DATA

N. B. Crosby

International Space University, Strasbourg Central Campus - Parc d'Innovation, Boulevard Gonthier d'Andernach, 67400 Illkirch-Graffenstaden, France

ABSTRACT

Space weather is an interdisciplinary field, especially from the scientific point-of-view and demands data from all parts of geo-space. Of utmost importance it requires constant monitoring of the Sun, relying on both space-borne and ground-based observations. The question of data handling in this respect requires a complex yet as simple as possible approach.

In the above context, the requirements of solar data for space weather related issues will be addressed in this paper having the user in mind. Emphasis will be made on the point that the data centers must have a clear understanding of what the users actually need as information. This will be illustrated by showing examples of various space weather induced effects and looking at the physical phenomena that caused them. It shall be stressed that the time required to avoid these unwanted effects is an important factor in defining the type of solar data necessary to forecast the above phenomena. Hence a fundamental need is that better communication between the user and solar community must be aimed at.

Key words: space weather; Sun; solar data.

1. INTRODUCTION TO SPACE WEATHER

Technological systems are becoming more sensitive to the space environment and the sending out of humans to space more of a standard routine. Therefore it is clear that one must be able to monitor the space environment continuously, the aim being to avoid unwanted space weather induced effects. This can only be accomplished if one has reliable data that describes this forever changing space environment (on all time and spatial scales) - better known as "space weather".

In simple terms space weather refers to how solar activity may have unwanted effects on technological systems and human activity. Our local space weather is thus a consequence of the behaviour of the Sun, the nature of Earth's magnetic field and atmosphere, and our location in the solar system.

The U.S. National Space Weather Program (NSWP) defines "space weather" as conditions on the sun and in the solar wind, magneto-sphere, ionosphere, and thermosphere that can influence the performance and reliability of space-borne and ground-based technological systems and can endanger human life or health (see http://www.ofcm.gov/nswp-sp/text/a-cover.htm and http://www.geo.nsf.gov/atm/nswp/nswp.htm).

Solar Terrestrial Physics (STP) research and space weather are closely linked, but the main difference is that space weather is an application-oriented discipline and addresses the needs of users. It should be emphasised though that basic research in the field of STP is necessary for space weather applications. The main differences between STP and space weather are summarised in Table 1 (Koskinen and Pulkkinen, 1998). Note that whereas STP research uses observations on all timescales, continuous monitoring is essential for space weather services and this ofcourse includes the monitoring of the Sun. In fact the Sun can be said to be the driver of space weather. But space weather is much more than understanding the physical processes that occur on the Sun. It also implies understanding how the various physical phenomena cross interplanetary space and how the magnetosphere, ionosphere and the Earth's atmosphere respond to the never ending changing Sun. The main question is how to work with such a complex environment in the most concise way.

During the "The ESA Workshop on Space Weather" (ESTEC, Noordwijk, The Netherlands, 11-13 November 1998), the working group "Forecasting Space Weather - Scientific Road Map", hereby referred to as "the working group", considered what would be needed as operational models, observations, theoretical breakthrough during the next 2-5 years in Europe, to accomplish just that. The working group formulated seven questions that they then discussed during a morning session (Crosby et al., 1999). These questions will be covered in this paper emphasising results concerning solar observations. The working group will be identified when the results originate

Proc. 1st Solar & Space Weather Euroconference, 'The Solar Cycle and Terrestrial Climate', Santa Cruz de Tenerife. Tenerife. Spain, 25-29 September 2000 (ESA SP-463, December 2000)

	Space Weather	Solar-Terrestrial Physics
Users	Application-Oriented	Basic Research
Required Observations	Continuous Monitoring	Scientific Observations
Products	Service Products	Scientific Products

Table 1. Space weather compared to Solar-Terrestrial Physics

directly from their discussion. Below are the seven questions that the working group formulated:

- Who are the potential users/customers for our statement of work?
- What are the most important effects of space weather conditions on spacecraft and ground based systems?
- What are the space weather phenomena that cause these effects?
- When, how far ahead, and how accurate do we want to predict these phenomena?
- What is required in Solar-Terrestrial Physics to predict space weather?
- How can we establish reliable prediction techniques?
- Which funding services can be envisaged to finance these services?

In Section 2 of this paper, the first 6 questions will be addressed, using case studies to illustrate the difference in the types of solar observations that are needed. The final section will cover question 7 and shall conclude by emphasising the necessity of communication between the solar community and the potential user community.

2. THE IMPORTANCE OF SOLAR DATA FOR SPACE WEATHER FORECASTING

Potential users of space weather facilities are numerous; basically, everybody is in some way directly/indirectly a user. It is these different users of space weather products that help define the various space weather effects that are observed, thereafter defining what observations are needed to help prevent these effects happening in the first place. The user community has interest in effects observed on Earth all the way to where the farthest spacecraft is at the moment.

2.1. Space Weather Effects and Solar Observations

The technological user community has interests for both space and Earth purposes, many of which are inter-connected. For example, spacecraft problems may cause disturbances in transmission to Earth and as a consequence affect our daily life on Earth. Spacecraft operators need reliable predictions of events that can cause anomalies or failures in order to schedule operations or take protective action. Potential ground based customers include powerline companies, oil companies and telecommunications industry. Astronauts are the most well known biological users, but also crew/passengers on airlines especially on polar routes are potential users. For more information on the various space weather users/induced effects see Daly et al. 1996 and Lanzerotti et al. 1997.

As mentioned previously solar activity can be said to be the driver of space weather. Therefore it is very important that one is able to predict phenomena such as coronal mass ejections (CMEs), solar flares, and solar energetic particle events. In the future it will be the users of space weather forecasting centers that must set the requirements for the time scales and precision of the predictions. This shall be illustrated by the following two examples, the first addressing time scales of minutes whereas the second refers to longer time scales.

It is not possible to predict the exact occurrence, intensity or duration of solar protons events, and consequently mission planning on both a short-term and a long-term basis can be problematic. Short-term forecasts are necessary for any tasks requiring extravehicular activity and the operation of radiationsensitive detectors. Real-time observation of the Sun can provide useful warning of solar event activity. For example a 50 MeV proton can arrive from the Sun in less than 25 min. Thus a warning time for solar proton events from a flare observation is very short and there is instead a need to be able to predict the events that can produce them.

On the other hand a CME may reach Earth in 3 to 4

days. Once a CME is observed there is time to take protective measures. Here instead the main problem is that it is not yet possible to predict whether an observed CME will hit the Earth or not and how geoeffective it will be until it has reached the L1 point. From there the CME moves to the magnetopause in about one hour. From the first effects at the magnetopause it takes some tens of minutes before the damaging effects have propagated to the various regions of geospace.

2.2. Using Solar Data for Space Weather Prediction

From the above two examples it is clear, that establishing an easy-to-use reliable prediction tool is not a simple matter. Spacecraft such as Yohkoh, SOHO, Ulysses, TRACE, ACE, etc. are providing us with a wealth of information concerning the physics of the Sun. Also future solar missions (e.g. STEREO, Solar Orbiter) will provide us with many of the essential parameters that are necessary to obtain realistic models of the structure of the corona and heliosphere, and for the first time it will become possible to directly observe solar disturbances from the Sun to the Earth (Bothmer, 1999). Furthermore missions such as STEREO will help in the understanding of the onset, structure and evolution of CMEs.

Space weather research is an interdisciplinary science which strongly enhances the links in the chain of physical processes between the Sun (interior, corona, solar wind,) and the Earth's magnetosphere, ionosphere, etc.. The working group emphasized that databases for space weather applications must include continuous monitoring of the ionosphere, radiation belts, solar wind and especially the Sun. They also concluded that long data series for all fields (ground-based and space-borne) are necessary and rapid dissemination of the data is vital. Data must be made available in real-time not only on the spacecraft, but also in the relevant data centers. To accomplish this the working group emphasized that a fleet of satellites (elliptical, geo-stationary, polar and heliocentric), along with ground-based observations be defined.

The working group concluded that in order to measure progress in establishing reliable prediction techniques, an evaluation process has to be defined to regularly compare current prediction accuracies with older methods. Especially, one must see if the models are getting better in predicting the phenomena that may produce space weather induced effects.

3. THE FUTURE OF SOLAR DATA IN RELATION TO SPACE WEATHER

Where will the money come from to do all the above? This was the question that the working group did not have time to discuss. There are actually two points that are relevant to this topic: 1.) Who will fund the space weather data centers (observations and models), and 2.) Who will pay when a space weather event is not predicted or wrongly predicted?

The first question depends on whether the space weather center is for example governmental and/or private, and whether it is on national or international (collaboration between many countries) level. It is suggested that proposals for solar missions should continue to emphasise space weather application as an important issue.

Factors such as revenue loss, damage to equipment, loss of customer confidence, degraded service, cost of deferred maintenance, cost of augmented staffing are all important key issues when it comes down to the second question (http://www.sec.noaa.gov/). Imagine if a space weather event is predicted and does not happen - who will cover the financial loss of the shutdown of e.g. technical utilities? On the other hand if the event happens, a spacecraft may be "saved", thus avoiding a big financial loss. Space weather events are becoming more and more of interest from the insurance point-of-view.

Conclusions of the working group indicated that observers and modellers have much to contribute in the space weather arena in the new millennium. Having now entered this millennium one can state that this conclusion is indeed more true than ever, especially for the solar community.

REFERENCES

- Bothmer, V., 1999, in Proceedings from the ESA Workshop on Space Weather, ESA-WPP-155, 117
- Crosby, N., Toivanen, P., Heynderickx, D., et al., 1999, in Proceedings from the ESA Workshop on Space Weather, ESA-WPP-155, 521
- Daly, E., Hilgers, A., Drolshagen, G., et al., 1996, in Proceedings from the Symposium on Environment Modelling for Space-Based Applications, ESA-SP-392, 15
- Koskinen, H., Pulkkinen, T., 1998, State of the art of space weather modelling and proposed ESA strategy, Technical Note SPEE-WP310-TN-1.2, Finnish Meteorological Institute
- Lanzerotti, L., Thomson, D., and Maclennan, C.: 1997, Bell Labs Technical Journal, summer issue

JOSO

Meeting on the 1999 Solar Eclipse

THE TECONet PROJECT ONE YEAR AFTER TOTALITY

F. Clette and J.-R. Gabryl

Observatoire Royal de Belgique, B-1180 Bruxelles, Belgium

ABSTRACT

The TECONet99 campaign (Trans-European Coronal Observing Network) initiated by the JOSO, succesfully acquired polarimetric images of the corona during the August 11, 1999 total solar eclipse. 15 stations, out of a total of 28, collected photographic or CCD images from many sites distributed along the totality band, from France to Iran. Using a common observing technique, they formed a time-lapse sequence spanning a duration of about 1h 30min. We present here a summary of this international eclipse campaign, and we describe the data processing techniques, as well as the current results. Electron density distributions were computed up to $2.5 R_{\odot}$, and show an abnormally steep radial density gradient. The subsequent cross-analysis with the EIT experiment on SOHO, and the study of temporal changes in the corona during the eclipse will also be outlined, although no major transient (CME) occured during the eclipse.

Key words: Sun; corona; solar eclipses; polarimetry.

1. INTRODUCTION: the TECONet concept

In the special context of the European total solar eclipse of August 11, 1999, a Trans European Coronal Observing Network (TECONet) was set up in 1998 to take advantage of the exceptionally high number of potential amateur and professional observers (Clette 1999). Although some participating teams used advanced computer-controlled cameras, the TECONet concept was based on the use of a common observing technique: white-light polarimetry, which required only fairly simple instrumentation. It was thus open to anyone with the necessary observing skills, either individual amateur astronomers or professionnal solar physicists with limited funding. Therefore, the participants used their own telescopes and had to build some of the special mechanical components (rotating filter holder) using their own resources. Only film and polarizing filters were provided by the network coordinator, as these special items were essential to ensure the homogeneity of all photographic data.

In a way, this campaign was a special scaled-up version of the Belgian coronal polarimetry program, which started in 1973 and has now gathered data during 7 total eclipses spanning two solar cycles (Gabryl et al. 1999). TECONet thus relied on an extensive experience, but represented an unprecedented challenge, as many more stations were participating and had to produce useful data in unison, without any direct personal contact or joint training. Such an initiative was in fact possible only through the extensive use of Internet, which allowed the exchange of innumerable messages and questions, as well as technical drawings and sometimes images. The Internet platform also helped a lot in recruiting observers, by making a wide public aware of this project, even in distant countries.

In this paper, we present the current status of the ongoing analysis effort, as well as first key results based on a subset of the huge image collection produced by TECONet.

2. The observing campaign

By using many observing stations distributed in longitude along the totality band, as was possible for the 1999 eclipse, one can of course avoid the detrimental consequences of bad weather conditions. However, the primary advantage is to allow a continuous monitoring of the solar corona over durations much longer than the 2 minutes of totality at one site. Changes to the rotational parallax or true intrinsic evolutions can thus be studied (dynamic events, flows, coronal mass ejections). Although this kind of time series can now be obtained by space-borne instruments. ground-based white-light images provide an independant absolute calibration, as well as direct measurements of electron densities. For that reason, a joint observing program with the LASCO and El'I coronal imagers on SOHO was submitted and executed.

More fundamentally, well-calibrated polarimetric images allow the separation of the K-corona from other non-solar components and the direct determination of the density of free electrons, a basic parameter for models of the solar atmosphere. The purpose of TECONet was thus to go beyond qualitative studies of coronal evolution (motion tracking) by measuring variations of the electron density in evolving magnetic structures. A key aspect of this campaign was thus to ensure a good data homogeneity by imposing instrumental requirements (Table 1) and a common observing procedure.

Proc. 1st Solar & Space Weather Euroconference, 'The Solar Cycle and Terrestrial Climate', Santa Cruz de Tenerife, Tenerife, Spain, 25-29 September 2000 (ESA SP-463, December 2000)

(T) 1 1	4	T	
Table	1.	Instrumental	requirements

Detector	B&W photography, CCD camera
Bandpass	broadband, white-light
Field of view	1.0-1.15 to 2.5-4.0 $ m R_{\odot}$
Spatial resolution	10 arcsec or better
Polarimetry	- linear polarizing filter on indexed rotating mount - either focal-plane sheet filter or full-aperture glass filter
Calibration	- laboratory pre-exposures of a step density scale - when possible, step exposures of the photosphere outside totality using a neutral filter of known density

Table 2. Eclipse film digitization using the NIKON LS-2000 film scanner

S-2000 film_scanner	
Intensity resolution	12 bits (4096 levels)
Scanning resolution	10 microns/pixel
Raw angular resolution	3.5 arcsec
Scanning dimensions	2592 x 3894 pixels
File size	19 Megabytes
Number of digitized images	$14 \ge 27 = 378$
Total data volume	7 Gigabytes

On eclipse day, there were finally 30 observing sites run by observers from 16 different nationalities. About half of the 28 participating teams collected good image sets. Although unfavourable weather conditions ruined observations in Western Europe, the successful observing sites were fairly evenly distributed along the totality band, from France to Iran. More details about the outcome of this observing campaign and a full list of the participants can be found in Clette & Gabryl (1999).

Hundreds of photographic and CCD images were finaly collected. These images are currently being processed at the Royal Observatory of Belgium (ROB) according to a standard procedure outlined below. Although this huge task is not yet completed, some preliminary results were derived for a few reference stations and from a first comparison with simultaneous extreme-ultraviolet images from EIT.

3. Data processing

After the development and digitization of photographic films, the data analysis procedure has been organized in four successive steps:

- 1. pre-processing and cosmetic corrections
- 2. polarization maps for each station
- 3. multi-station intercomparison: cross-calibrations, dynamical studies
- 4. modeling of the electron density distribution

Film digitization and processing step #1 are now almost completed, while steps #2 and #4 have been carried out only for 3 primary stations.

3.1. Data collection and film handling

All exposed films were collected at the ROB in Brussels, together with the corresponding observing reports. The same Kodak Tmax 400 emulsion was

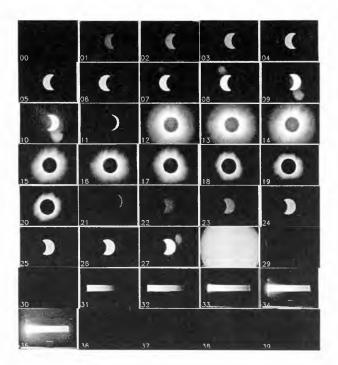


Figure 1. Mosaic of all scanned images produced by a single photographic station (Ramnicu-Valcea, Romania; ROB). It contains 3 polarimetric sequences of the corona (exposures: 1/2, 1/8, 1/30 s), as well as several series of calibration images.

used by all stations. This film was choosen for its good sensitivity and wide dynamic range. All films were processed by us at ROB using the same standard procedure. All films had then to be digitized. For this operation, the ROB purchased a NIKON LS-2000 film scanner. This option made the scanning task fast and flexible, while ensuring a photometric quality that was appropriate for the purpose (Table 2).

Each film contains 2 or 3 polarization sequences made at 3 different exposures, to cover the 1 to 1000 intensity range present in the corona (Fig. 1). They are scanned together with calibration exposures (partially eclipsed photosphere, laboratory density scales), which then allows to correct the instrumental response (film, scanner), as well as variations of the local sky transparency and of the film development (gamma variations). An additional flat-field exposure gives the correction of the radial vignetting function.

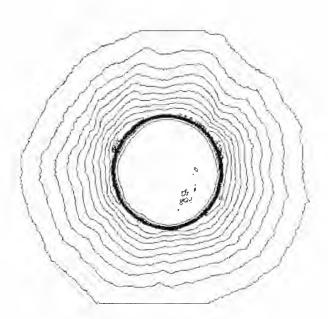


Figure 2. Total brightness deduced from our reference photographic experiment. The intensity scaling is logarithmic with a factor of 2 between two successive contours. The outermost contours corresponds to $2 \times 10^{-8} \text{ B}_{\odot}$.

3.2. Processing of single-station data sets

Both the CCD and photographic images were coregistered and corrected for the detector response. The proper registration was achieved by a crosscorrelation method applied to the lunar limb, followed by the compensation of the relative Moon-Sun motion. In addition, CCD images were further corrected for dark current, the flat-field, and some blooming artifacts.

In the next step, we computed the total intensity $I_{\rm K}$, polarized brightness $pI_{\rm K}$, degree of polarization p and angle of linear polarization, from each individual sequence. The latter contained a minimum of 3 images (angular step: 60°). In some cases like the computer-driven camera used by the ROB team (Clette et al. 1999), up to 10 sequences of 12 images (angular step: 15°) were obtained, in order to improve the precision by using a least-square method. Based on the corresponding photospheric images and the solar filter factor, the intensities are finally converted into absolute units $(10^{-6} \, {\rm B}_{\odot})$. Series of different exposures can then be combined to provide a full coverage of the corona from about 1.1 to 3 ${\rm R}_{\odot}$.

4. Polarized brightness and structure of the 1999 corona

Up to now, we started our analysis with CCD and photographic data from the Belgian team located in Ramnicu-Valcea (Romania), that are of excellent quality and will serve as the network reference. Polarization maps from the CCD experiment can be found in Clette et al. (1999), and the corresponding contour maps from the photographic experiment are shown in Figures 2 and 3. Both sets lead to consistent photometric results, but a significant discrep-

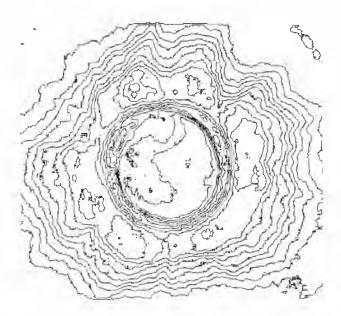


Figure 3. Polarization p_{K+F} deduced from our reference photographic experiment. Contours are given in steps of 5%, starting from 15% (outermost contour).

ancy is observed for the degree of polarization, which is systematically lower in the CCD data. The analysis of another good photographic image set from Iran (T. Mirtorabi) allows us to conclude that CCD-based polarizations are indeed biased. This is probably attributable to a spurious near-infrared response of the CCD (infrared-cutoff filter). This effect does not influence the intensity calibration and can in fact be modeled and compensated. We are now conducting specific laboratory measurements to solve this problem.

Both in total intensity and polarized brightness, the August 1999 corona has a very symmetrical shape, and is thus rather typical of a maximum-activity morphology. The polarization degree reaches 50 to 60% all around the Sun, with even a local maximum of 65% near the North pole (PA 26.9°). However, there are no large coronal streamers extending far from the limb, beyond about $2 R_{\odot}$. Strongly non-radial streamers were emerging from the North-East limb, close to the pole.

Finally, regarding dynamical phenomena in the corona, the results a more limited. Indeed, no major eruptive event took place in the 2-hour time interval of the eclipse observations, except for small outflowing disturbances in the Eastern sector of the corona. A major coronal mass ejection (CME) actually occured, but only 10 hours after the eclipse (at 22h UT), near the North-West limb. However, in this particular region, a prominence and a thin low-contrast magnetic arcade are detected in the TECONet data. They might show some evolution, and could thus justify a more careful study of possible CME precursors. This question will be the focus of future work.



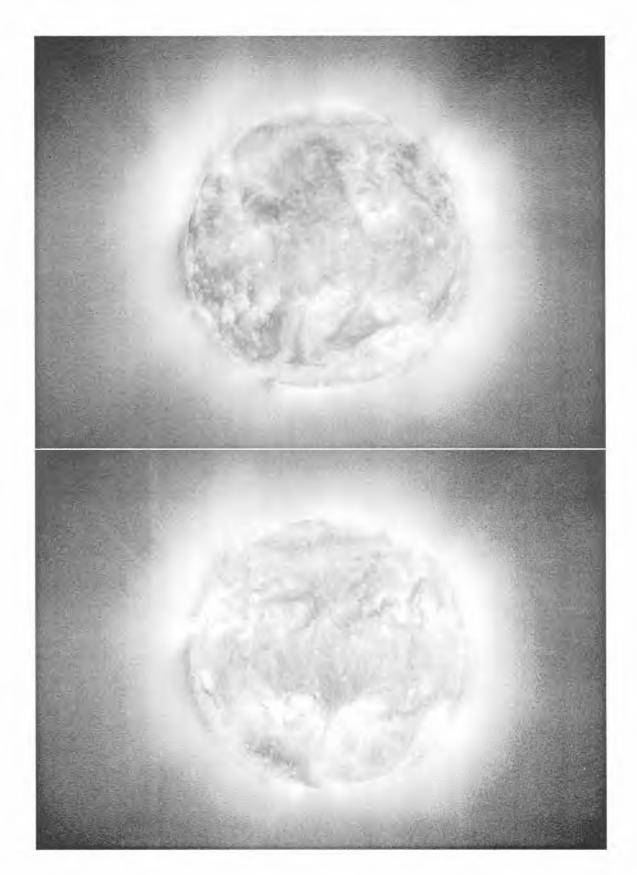


Figure 4. Composite images obtained by merging in the central part (disc and low corona) an extreme-ultraviolet image from the EIT experiment on SOHO (Fe XII line, 195 Å) with a photographic image of the extended white-light corona made by a TECONet station (Station: ROB, Ramnicu-Valcea, Romania, 11h 02min 30s UT). The top image uses an EIT image taken simultaneously with the eclipse (11/08/1999, 11h 08min 16s UT), while the bottom image includes an EIT image made half a solar rotation before the eclipse and mirror reversed (29/07/1999, 13h 13min 16s UT). Correspondances can be identified between eclipse features and structures on the whole solar surface: for example, the thin threads fanning out from the bright region in the North-East quadrant are actually rooted on a far-side active region.

5. EIT-eclipse composite images

By using the EIT images of the on-disc EUV corona taken simultaneously by the EIT experiment, it becomes possible to disentangle the spatial distribution of magnetic structures seen sideways above the Moon's limb in eclipse pictures. Some ambiguities due to the projection of an optically thin atmosphere on the plane of the sky can then be removed. As a first experiment, we merged an EIT image taken in the FeXII emission line (195 Å) at the time of maximum eclipse with a single photographic image from the ROB camera placed in Romania. As the emissivity in the coronal emission line is proportional to the square of the electron density (collisionally dominated transition), we took the square root of the EIT intensities. This should then give a radial distribution proportional to the visible light resulting from the Thomson scattering by coronal free electrons. Despite the inevitable approximations (e.g. different spatial weightings along the line of sight), the resulting composite image in Figure 4 (top) demonstrates that this procedure results in a very good seamless transition between those complementary images. It now becomes possible to trace magnetic features (threads, rays, dark and bright ridges) detected in the outer corona in eclipse images to field lines and local arcades observed on the solar disk in EUV light, i.e. down to their footpoints at the base of the corona.

Moreover, we can now create an equivalent composite, but with an EIT image taken half a solar rotation before or after the eclipse, and mirror reversed to properly match the orientation (Fig. 4, bottom). Correspondances can then be indentified in the same way with surface features located on the far side of the Sun at the time of the eclipse. A first examination of these composites immediately shows that most of the solar activity was concentrated on the invisible far side of the Sun. Therefore, many streamers and threads seen above the limb are connected to active regions or plages on the far side. Those results are encouraging as matching features (even small and thin ones) can still be found despite the 13-day delay, even for a very active Sun which evolves quickly over its whole surface. This technique can still be improved, and we will soon introduce the correction of the EIT sensor aging (source of the dark-ring artifact just outside the limb) and use the computed polarized-brightness image instead of a single raw image.

5.1. Global electron density distribution

In order to derive a global electron density distribution, we used the photographic data from the ROB station in Romania and we derived the polarized brightness $pI_{\rm K}$ by substracting the F-corona intensity distribution from Saito (Saito 1970). We then implemented an axisymmetrical model that was already applied with success to CCD data from previous eclipses in 1991,1994 and 1998 (Gabryl et al. 1998, Gabryl et al. 1999). In that model, we determine the radial and angular parameters of an analytical solution in two successive and independant steps by a least-square procedure. We can freely choose the orientation of the symmetry axis, and we decided to align it on the global dipolar heliospheric magnetic field. As in addition, the latitudinal dependancy is expressed in terms of Legendre polynomials, two independant models are then calculated for the "East" and "West" hemispheres.

Now, considering the radial electron density distribution in various polar angles, we find particularly high densities near the limb in almost all regions $(2 \times 10^9 \,\mathrm{e/cm^3})$, i.e. about one order of magnitude higher than in the 1998 eclipse data), but this density enhancement seems to be absent higher up. This is well illustrated in the plots of Figure 5, where some radial density profiles are compared with other radial density distributions along typical coronal structures. This measurement confirms quantitatively the initial observation that no major streamers were seen extending beyond 2.5 R_{\odot} . This results in an exception-nally strong radial density gradient.

If the observed electron density gradient is interpreted by assuming the hydrostatic equilibrium (usually, a very good approximation in coronal streamers), the density scale height and the corresponding hydrostatic temperatures are abnormally low (8.5 to 9.0×10^5 K). This is apparently in contradiction with the high activity level prevailing at that time, when temperatures are expected to be in the range 1 to 2×10^6 K.

6. Conclusions

Overall, we can conclude from this first exploration of the TECONet data that we succeeded in producing a coherent polarimetric data set spanning a duration of about 1h 30min. This might well be the first successfull attempt to overcome past deficiencies like incompatible observing procedures, the disparity of detectors or the absence of an absolute calibration. Furthermore, the abundance of redundant polarization data available in this case will help to improve the accuracy of the combined results by bringing a better understanding of errors and biases affecting the calibration of eclipse images acquired at single sites.

Considering now the current science products, our most surprising result is certainly the particularly steep radial electron density gradient found everywhere in this corona. Such a gradient is probably too high to be interpreted simply in terms of an hydrostatic equilibrium. In that case, which process could induce this global departure from hydrostatic conditions? In coming months, the analysis will partly concentrate on that issue.

By accurately fitting the EIT images to the whitelight ground-based images, we also show that whitelight images of the K corona can be merged seamlessly with on-disk EUV images. This opens the new perspective of tracing magnetic fields over their full extent, from their footpoints on the disk out to 3 solar radii, removing ambiguities. It also indicates that such cross-analyses can be more than just morphological (image "pasting") and become quantitative (cross-checking of two independant measurements of the electron density).

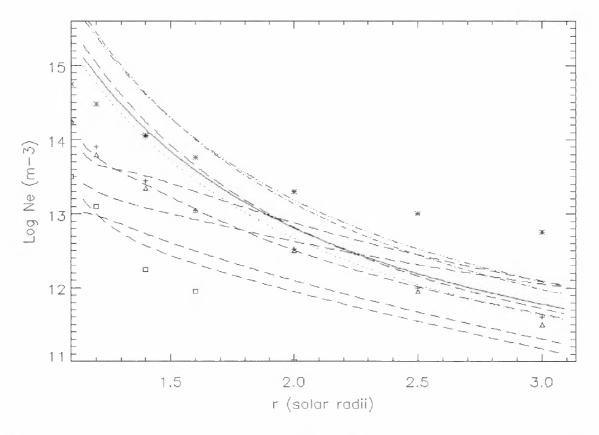


Figure 5. Radial density distributions along some typical features in the August 1999 corona (West limb): latitude 90° (solid), 65° (long dash), 20° (dash dotted), -30° (dash 3 dots) and -70° (dotted). As a comparison, we include the distributions for some radial structures in the February 1998 eclipse (dashed). Symbols correspond to the average reference profiles derived by Koutchmy (1992) for a streamer (*), a polar hole (square) and the equatorial region (+ and triangle). Note the high densities at the base of the corona, and the steep radial density gradient.

Although no major eruptive event was captured over the duration of the ground-based eclipse observations, TECONet images might provide insight about precursors of a large coronal mass ejection that went off 10 hours later. So, new questions arise and will probably remain open until the massive processing work of the full TECONet data set is completed. Anyway, this eclipse again showed us how difficult it still is nowadays to predict exactly how the corona will look like, up to the last second before totality.

ACKNOWLEDGMENTS

The authors wishes to thank all participants who, by their dedication and their careful measurements, made this project possible. We also would like to thank the ROB, in the person of his Director, Prof. Paul Pâquet, for putting the institute's resources at our disposal for the practical organization of the network.

REFERENCES

Clette, F. 1999, in "Solar Magnetic Fields and Oscillations", eds. B. Schmieder, A. Hofmann & J. Staude, 3rd ASPE, Astron. Soc. Pac. Confer. Series, Vol. 184, 339

- Clette, F., Cugnon, P., Gabryl, J.-R. 1999, Contrib. Astron. Obs. Skalnate Pleso, Vol.28, N° 3, 251
- Clette, F., Gabryl, J.-R. 1999, in "Magnetic Fields and Solar Processes", ESA, SP-448, 1273
- Gabryl, J.-R., Cugnon, P., Lamy, P.1998, in "Three-Dimensional structure of solar active regions". eds. C.E. Alissandrakis & B. Schmieder, Astron. Soc. Pac. Conf. Series, Vol. 155, 361
- Gabryl, J.-R., Cugnon, P., Clette, F. 1999, Contrib. Astron. Obs. Skalnate Pleso, Vol.28, N° 3, 216
- Koutchmy, S. 1992, Institut d'Astrophysique de Paris, Pré-publication, N° 404 (partim. Allen, C., "Astrophysical Quantities", 3rd edition)
- Saito, K. 1970, Ann. Tokyo Astron. Obs., Second Ser., 12, 53

COMPARISON OF CORONAL STRUCTURES 11.8.1999 ON THE LONG OBSERVATION BASE

M. Bělík¹, E. Marková², E. Brandejsová³, J. Kučera⁴, J. Kareš⁵, M. Švanda⁶

¹ObservatoryÚpice, U lipek 160, 542 32 Úpice, Czech Republic, marcel_belik@yahoo.com

²ObservatoryÚpice, U lipek 160, 542 32 Úpice, Czech Republic, markovae@mbox.vol.cz ³VUT Brno, nimrodel@email.cz

⁴West-Czech part of Czech Astronomical Society, Rokycany, Czech republic

⁵Author. lab. of ionize emission metrology, Olomouc, jaroslav kares@volny.cz

⁶Charles University, Ke Karlovu 3, 121 16 Praha 2, svanda@asu.cas.cz

ABSTRACT

Observation of total solar eclipse obtained along the path of totality allows to study both fast and slow changes of white-light corona structures. These types of changes, as well as CME, slow moving of plasma, oscilations and so on reflect dynamics of photospheric and chromospheric activity caused by convection of magnetic fields. It is shown that structure changes in the individual formations. especially in coronal streamers could be occurred. By comparison of obtained pictures the speeds of moving of disturbances 100-200 km/s was found.

INTRODUCTION

The 1999 "European" eclipse had a great opportunity to organize the multi-station observation of total solar eclipse along the entire totality band. After the last successful eclipse observations performed by Observatory Úpice we had an idea to employ this opportunity and organize two-station observation.

Moreover, plenty of Czech amateur astronomers, some Czech observatories and any other people asked us to coordinate "'99 eclipse Czech observational campaign", or to help them with preparing of their experiments. Then we decide to spread our program about their observation and make real multi-station observation. This circumstance allows collect the unique data obtained with the same or very similar telescopes, the same exposure times and the same types of films. These data make possibility to register some changes in solar corona during the time (approx. 120 min) of totality band crossing the Europe (Marková and Bělík, 1999).

EQUIPMENT AND OBSERVATIONS

In this paper the first results obtained from three observation places are presented. The first observation group was located in town Grandvilliers (France, 49,667N, 1,933E), the second one was near Balaton Lake (Hungary, 46,5N, 17,5E), the third one was in Pitesci (Romania, 45,5N, 24,47E). All three groups was equipped by the same, or similar (MTO1100/100, telescopes Rubinnar 1000/100, lens objective 300/4,5). All pictures were made on the same type of film (Kodak Royal 200 ASA) with the same exposures (1/1000 - 2s). All the films was developed at the same laboratory and at the same developer. Finally, the films were digitized at the same scanner with maximal resolution of 2000 DPL

RESULTS

As Parker (1988) has suggested, the solar corona is heated by nanoflares. One may suppose that their responses should be observed as faint brightness excess in chosen coronal structures, especially in the thin extended streamers.

We have tried to find these faint brightness changes in the center axes of chosen streamers (fig. 1). The long helmet streamers were scanned along radial axes to find course of

Proc. 1st Solar & Space Weather Euroconference, 'The Solar Cycle and Terrestrial Climate', Santa Cruz de Tenerife, Tenerife, Spain, 25-29 September 2000 (ESA SP-463, December 2000)

density downtrend. This process was repeated on different pictures and on gentle different "axes" of one and the same streamer to eliminate irregularities caused by impurities and faults on the pictures.

a) 345° streamer:

This streamer is situated in polar solar region, which shows only faint solar activity (Solar Data Analysis Center, 2000). On the west-side of this streamer the violent coronal hole is situated. We found possible "brightness candidates" in this streamer: 1,12 Ro on France snapshots (sign. F in the next), 1,45 Ro on Hungary pictures (H in the next) and 1,55 Ro, respectively 1,62 Ro on Romania pictures (R in the next). All radial scans are shown on fig. 2. The time diference is 1720 s (F-H) and 840 s (H-R). The corresponding speeds of irregularity moving along the streamer are 133 km/s (F-H) and 93 km/s, respectively 141 km/s (H-R).

b) 235° streamer:

This streamer is situated in region, which shows little enhanced activity. In this streamer only very faint brightness were found: 1,35 and 1,61 Ro (F), 1,54 and 1,71 Ro (H) and 1,5, 1,74 and 1,95 Ro (R). All radial scans are shown on fig. 3. It is very complicated to identify correlations between individual irregularities. We can only with very big insurance determine the speeds on 77 or 146 km/s (F-H) and 198 km/s (H-R).

c) 120° streamer:

This streamer is situated above active region No. 8665, which shows rather strong activity (Mees Solar Observatory, 2000). In this streamer we can detect brightness changes at 1,42 Ro (F), 1,85 Ro (H) and 2,07 Ro (R). All radial scans are shown on fig. 4. The speeds are 174 and 182 km/s.

d) 60° streamer:

This streamer is situated above arising active regions No. 8667 and 8668. In this streamer were found next possible events: 1,26 Ro (F), 1,33, 1,35 and 1,58 Ro (H) and 1,5, 1,72 and

1,95 Ro (R). All radial scans are shown on fig. 5. If we suppose the relations of events 1,26(F), 1,58(H) and 1,72(R) Ro, the corresponding speeds are 129 km/s (F-H) and 116 km/s (H-R).

DISCUSSION

Optimal condition over total solar eclipses offers an opportunity to observe structural changes in the white-light corona (Zirker et al., 1992). Observations made at different sites along the eclipse path provide a possibility to study both the slow and fast changes in the solar corona. Photometric analysis shows that there could be another type of changes in the same type of coronal structure, especially in helmet streamers. These changes, preliminary called as "waves", have been detected in some helmet streamers during 1999 eclipse. Providing that these enhancements, detected at different heights in the streamer, are the same, we have estimated a speed of their propagation of 77-198 km/s. These values are in agreement with the our results obtained during the total solar eclipses on Oktober 24, 1995 and November 3, 1994 (Bělík et al., 1999).

CONCLUSION

We have tried to detect the possibility of small-scale manifestation, as result of nanoflares or other dynamic processes, in the brightness in coronal streamers observed during total solar eclipses. Koutchmy (1994) proposed that probably all white-light corona is in dynamic state at sub-arcsec resolution.

Irregularities in the brightness along the helmet streamers are very faint and they could by lightly interchanged with errors caused by digitize process, impurities, film inhomogenities and some more faults. As we sad earlier, this fault possibilities were minimized.

Nevertheless, we are in opinion that almost all detected events could be realistic and they could be an another type of phenomena showing that the white-light corona is in dynamic state.

REFERENCES

Bělík, M., Marková, E., Rušin, V., Šmelcer,
L.: 1999, Manifestation Of 'Shock Waves' In Coronal Streamers, Proc. 9th European Meeting on Solar Physics, 'Magnetic Fields and Solar Processes', Florence, Italy, 12-18 September 1999 (ESA SP-448), 225

Koutchmy, S.: 1994, Adv. Space Res., Vol. 14, No. 4, pp. (4)29-(4)39

Mees Solar Observatory, Haleakala, Hawaii

http://www.solar.ifa.hawaii.edu/mees.htm

- Parker, E.N.: 1988, Nanoflares and the Solar X-ray corona, Astroph. K., 330, 474
- Rušin, V., Minarovjech, M.: 1994, IAU Coll.
 144 "Solar Coronal Structures", V. Rušin,
 P. Heinzel and J.-C. Vial (eds), VEDA
 Bratislava, pp. 487-490
- Solar Data Analysis Center, NASA Goddard Space Flight Center, Greenbelt, Maryland USA, http://umbra.nascom.nasa.gov
- Solar Geophysical Data, Part 1, Part 2, 1999, NOAA Boulder USA

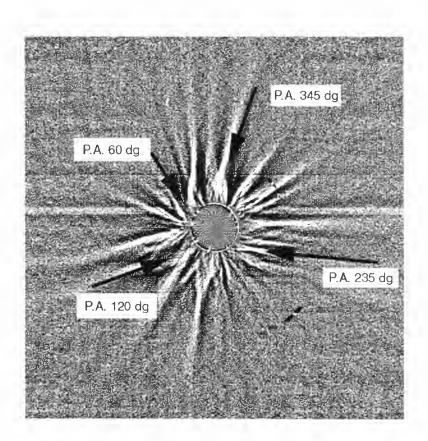


Fig.1: Position of chosen helmet streamers



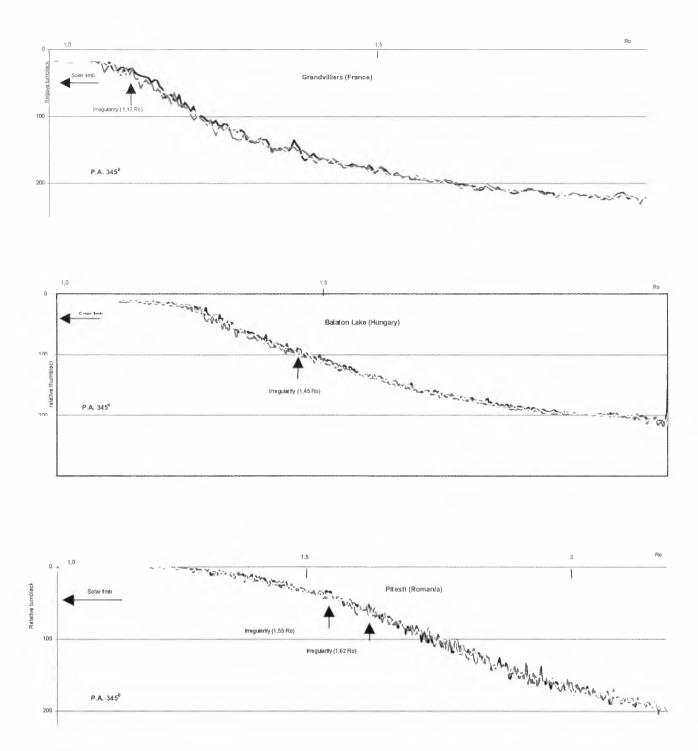
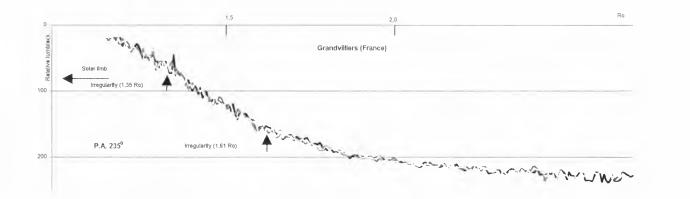
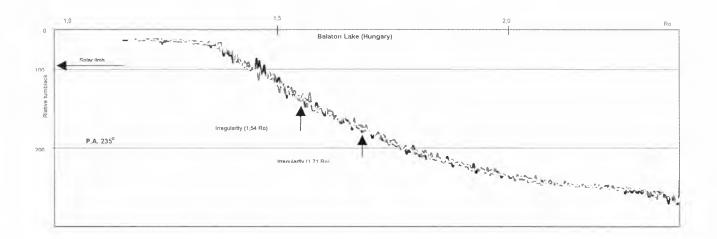


Fig. 2: Radial scan along streamer at P.A. 345°





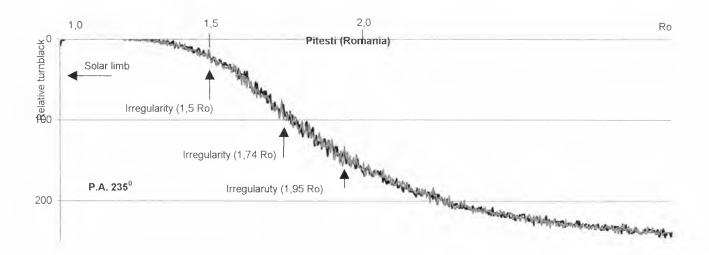


Fig. 3: Radial scan along streamer at P.A. 235°

591

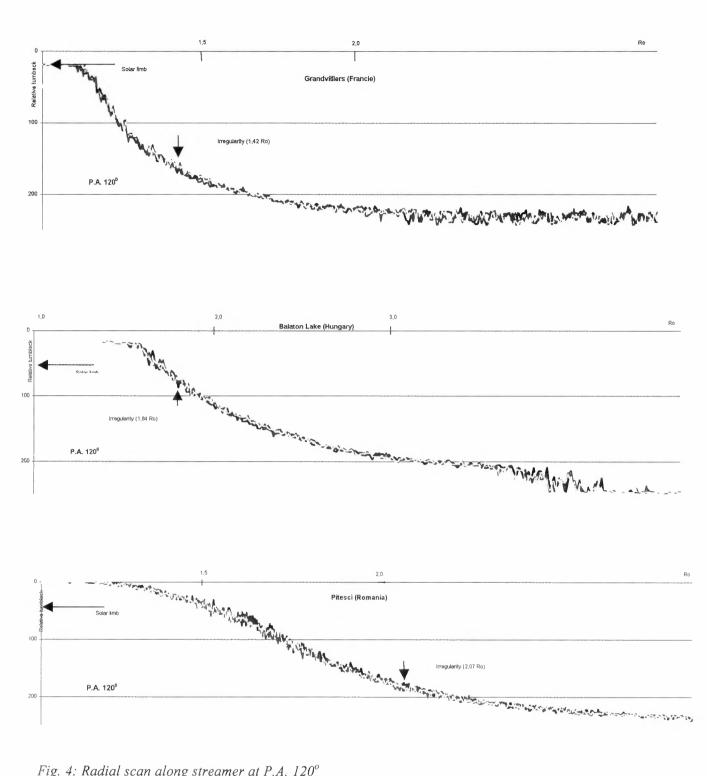
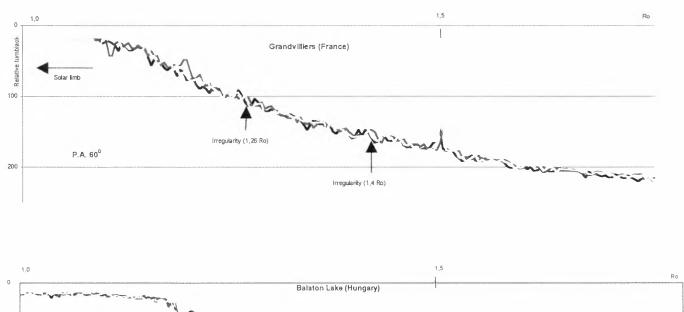
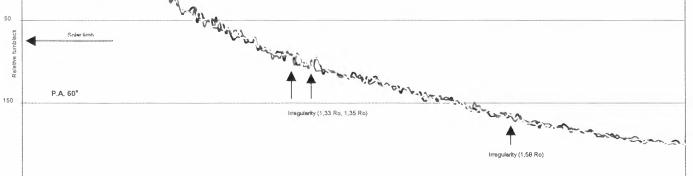


Fig. 4: Radial scan along streamer at P.A. 120°

592





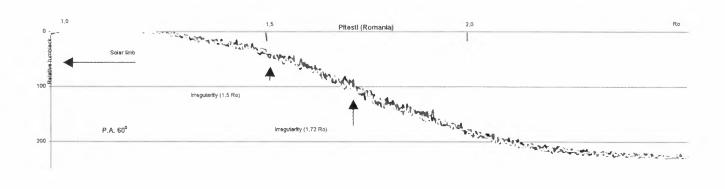


Fig. 5: Radial scan along streamer at P.A. 60°

593

RADIO POLARIMETRIC OBSERVATIONS OF THE 11 AUGUST 1999 SOLAR ECLIPSE VIA THE TRIESTE SOLAR RADIO SYSTEM

M. Messerotti, P. Zlobec, and S. Padovan

Trieste Astronomical Observatory, Via G.B. Tiepolo 11, 34131 Trieste, Italy

ABSTRACT

The Trieste Solar Radio System (TSRS) was used to perform radio polarimetric observations of the partial occultation of the radio Sun in the m-dm band at fixed frequencies (237, 327, 408, 610, 1420 MHz) during the 11 August 1999 solar eclipse. By comparing the theoretical eclipse curve of the optical disk with the observed radio ones for the LH and RH polarization components respectively, it was possible to derive an estimation of the radii of the radio disk at the different frequencies to construct theoretical radio eclipse curves. The comparison of the observed and theoretical radio eclipse curves is discussed with respect to the possible presence of solar radio sources.

Key words: solar eclipse; radio occultation; radio source.

1. INTRODUCTION

The observation of solar eclipses in the radio domain can allow to increase the spatial resolution of the instrumental set by means of the knife edge effect originated by the lunar limb during its passage over the solar disk. Moreover, such scans of solar radio sources provide details on their location and spatial morphology even when large beam antennas are used, see, e.g., the review by Messerotti (1997). The Trieste Solar Radio System is a set of two multichannel solar radio polarimeters, operating at 237, 327, 408, 610 MHz with a 10 m parabolic antenna and at 1420, 2695 MHz with a 3 m parabolic antenna respectively, operated by the Trieste Astronomical Observatory (Italy) at the Basovizza Observing Station. The TSRS has limited spatial resolution, but very high time resolution (routinely 1 ms at all channels) and accurate circular polarization measurements (Messerotti et al., 2000). It has been used to observe the 11 August 1999 solar eclipse in the attempt to estimate the radius of the radio disk at each observing frequency and to locate possible existing radio sources. Section 2 describes the Sun's activity level. The TSRS observations are detailed in Section 3 and the data processing scheme in Section 4. The radio eclipse curves are presented in Section 5 and the estimated radio radii in Section 6. The occultation of radio sources is discussed in Section 7 and the conclusions are summarized in Section 8.

2. SOLAR ACTIVITY ON 11 AUGUST 1999



Figure 1. H_{α} synoptic filtergram taken on 11 August 1999 at the Kanzelhöhe Solar Observatory (Austria).

Although in the maximum phase of the present cycle, which is expected to peak in 2000-2001, the activity level was quite low on 11 August 1999. Only three active regions were visible on the solar disk: one located in the southern hemisphere in the proximity of the central meridian and the others near the eastern and the western limb respectively (Figure 1) with no prominent magnetic topology and a limited number of spots. Therefore very weak, mainly unpolarized activity was detected in the radio band as well.

Proc. 1st Solar & Space Weather Euroconference, 'The Solar Cycle and Terrestrial Climate', Santa Cruz de Tenerife, Tenerife, Spain, 25-29 September 2000 (ESA SP-463, December 2000)

3. THE RADIO OBSERVATIONS IN TRIESTE

The circumstances of the solar eclipse for the date and different locations all over the world are detailed in Espenak & Anderson (1997). The Basovizza observing station is located at longitude $13^{\circ}52'34''E$, latitude $45^{\circ}38'37''N$ and 403 m a.s.l. and the related local circumstances of the partial eclipse are reported in Table 1.

Table 1. Topocentric eclipse circumstances.

09:19:22.9 UT 10:43:25.9 UT 12:07:55.6 UT
$02^h \ 48^m \ 32^s.7$
0.953

The considerable eclipse magnitude, i.e. the fraction of the solar diameter covered by the Moon at maximum occultation, and the Moon/Sun radius ratio for the date (1.028), made such eclipse an interesting event for the detection of possible radio sources.

For the whole event duration, the TSRS was operated in disk tracking mode and the flux density and polarization data were acquired with a sampling rate of 1000 Hz at 237, 327, 408, 610 and 1420 MHz, as the 2695 MHz receiver was under maintenance. Unfortunately, the 610 MHz channel was made unusable due to strong TV broadcast interferences, so that only four frequency channel (237, 327, 408, 1420 MHz) data were used in the present analysis. As the lunar disk passage occurred over a long time span, only low time resolution (1 s averaged) data were considered. Finally, the unpolarized character of the observed emissions allowed us to limit the analysis to the Left-handed Circular Polarization (LCP) channel for each frequency.

The normalized LCP radio recordings are shown in Figure 2. The background is essentially unpolarized at all frequencies, but a very weak type I burst activity shows a stronger Left-Handed (LH) polarization before the eclipse start at 237 MHz, the preferred frequency for noise storms of which type I bursts are the impulsive component, and decreases both in intensity and in occurrence frequency at 327 and 408 MHz. At 237 MHz the total flux density is about 11 solar flux units (sfu). This indicates the quite weak character of the emission when compared with the typical quiet Sun level at this frequency, which is about 8 sfu. Therefore the activity contributed only by 2 or 3 sfu over the background during that day.

Some weak, short-living man-made interferences are mixed with solar activity and visible also at the time of eclipse maximum, when most of the Sun is oc-

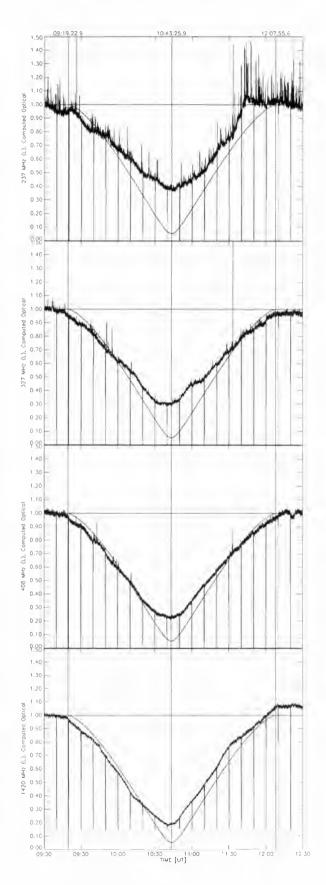


Figure 2. Normalized LCP radio flux density time profiles for each receiving frequency and the related optical eclipse curve. The eclipse start, maximum and end times are identified by vertical markers.

597

culted, more prominently in the RCP 327 MHz channel. Hence we focused our attention on the LCP channel only.

4. DATA PROCESSING SCHEME

We computed the theoretical solar eclipse curve in the visible domain by assuming an optical solar radius $R_{\odot} = 0^{\circ}.2630$ and a lunar radius $R_{Moon} = 0^{\circ}.2704$. The photometric curve was derived as the time evolution of the normalized solar disk visible area resulting from the relative motion of the covering Moon in a Sun-centered ecliptic reference frame, whose high accuracy ephemeris were computed by means of the Horizons On-Line Ephemeris System made accessible by the Jet Propulsion Laboratory (JPL) at the URL http://ssd.jpl.nasa.gov/horizons.html.

The observed solar eclipse curves in the radio domain at each frequency in the LCP channel were then compared with the theoretical optical one (Figure 2). By assuming an uniform radio emission, we estimated a corresponding *effective radio radius*, i.e., the effective radius of the solar radio disk for each frequency, from the difference in the minima of the observed radio and the theoretical optical eclipse curves.

Based on the estimated radio radii, we derived the *effective radio occultation curves* for each frequency and compared them with the observed radio ones (Figure 3) to detect possible features indicative of the occultation of localized radio sources.

5. RADIO ECLIPSE CURVES

The working hypothesis that the solar radio brightness is uniform is a zero order approximation, as we already stressed in Section 3 that at least one source of type I bursts was present, but is not unreasonable due to the very low intensity of the source itself, which should only cause a modest asymmetry in the photometric barycenter. Moreover, one must take into account as well that at radio frequencies the limb edge is by no means as sharp as the optical one.

It comes immediately evident from a comparison of the observed radio and the computed optical curves (Figure 2) that the radio occultation minimum is less deep than the optical one, which demonstrates that the radio radius is larger than the optical one, as expected. Moreover, the difference becomes larger as the observing frequency decreases, which is due to the fact that lower frequencies are originated higher up in the corona in plasma shells with progressively larger radii. This is also indicated by the presence of a flat plateau in the radio minima of the correspondent radio eclipse curves presented in Figure 3. In fact, they are larger at lower frequencies, which

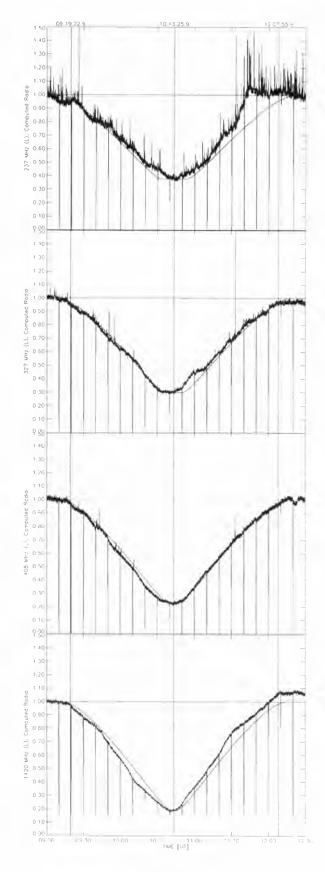


Figure 3. Normalized LCP radio flux density time profiles and the related radio eclipse curves computed according to the estimated radio radio. The eclipse start, maximum and end times are identified by vertical markers.

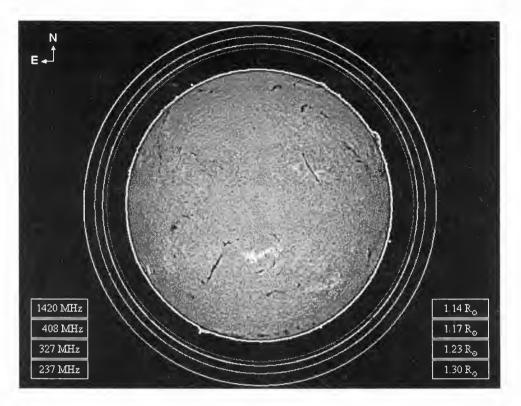


Figure 4. Estimated effective radio radii for each observing frequency of the TSRS.

is typically observed, e.g. in the photometry of binary stars, when the occulting body (in such case, the Moon) is much smaller then the eclipsed one (i.e. the radio corona).

A further evident feature in Figure 2 is the time shift of the radio minima with respect to the optical one, more pronounced at higher frequencies, i.e. the radio eclipse anticipated the optical one. This effect can be ascribed to the presence of an active region that was occulted just at the eclipse start and was therefore located at the western solar limb, as discussed later in Section 7.

6. ESTIMATED EFFECTIVE RADIO RADII

Under the above assumptions, we derived the values reported in Table 2 for the effective radio radii, which are also presented in graphical form in Figure 4 with respect to the optical H_{α} disk.

The estimated radio radii are physically consistent, if one takes into account both the typical smoothness of the radio limb and the presence of a radio source at the western limb as well as an increased coronal electron density with a steep gradient, derived from optical observations along the totality path in the frame of the TECONet 99 campaign (Clette, 2000), which can explain the presence of denser plasma layers with higher critical frequencies higher up in the corona with respect to unperturbed conditions. In fact, the reported values are comparable with the ones generally assumed in the literature for the height above the photosphere of an active region, see, e.g., Kai, Melrose and Suzuki (1985) and references therein. As a comparison, the occultation of a radio source observed in Trieste at 239 MHz during the 20 May 1966 solar eclipse provided a lower limit of 0.24 solar radii for its height above the photosphere (Abrami et al., 1967).

Table 2. Optical and effective radio radii of the Sun.

	[°]	$[R_{\odot}]$	λ [cm]	ν [MHz]
Moon's radius	0.2704	1.028	vis.	vis.
Sun's radius	0.2630	1.000	vis.	vis.
Sun's radius	$0.2996 \\ 0.3077 \\ 0.3228 \\ 0.3428$	$1.139 \\ 1.170 \\ 1.227 \\ 1.303$	$21.1 \\ 73.5 \\ 91.7 \\ 126.6$	1420 408 327 237

7. RADIO SOURCE OCCULTATION

Any consideration on possible radio source occultation can more appropriately come from the comparison of the observed and estimated radio eclipse curves (Figure 3) and, in particular, more precisely from the difference curves, obtained by subtracting the observed from the computed radio eclipse ones (not shown here for conciseness).

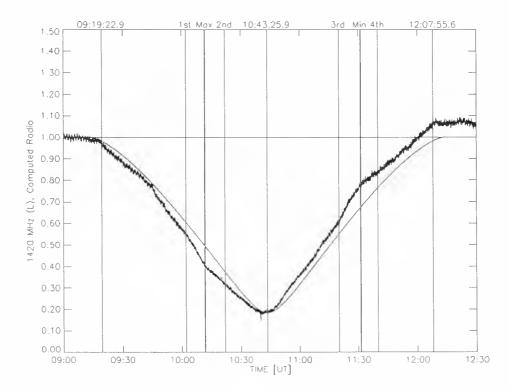


Figure 5. Occultation of the radio source at 1420 MHz. Relevant times are identified by vertical markers.

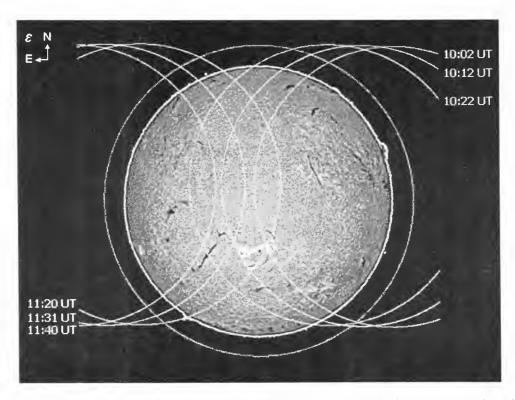


Figure 6. Occultation of a radio source at 1420 MHz depicted by the lunar limb positions at the relevant times.

A noise storm activity enhancement is observable at lower frequencies, i.e. both in the 237 and in the 327 MHz LCP channels, before and after the eclipse maximum (Figure 3). In particular, the storm continuum and the impulsive type I component are more pronounced at 237 MHz from 11:10 to 12:20 UT and show an increase from 11:33 to 12:10 UT. During this time span the eastern limb was occulted and therefore the source of such radio emission was located in the proximity of the western limb. The polarization of the type I activity is the same both before and after the eclipse maximum and this suggests that it was originated in the same source.

Type I activity is never observed at 1420 MHz, so that here it does not mask other possible underlying activity as it does at lower frequencies. In fact, the 1420 MHz radio eclipse curve (Figure 5) and the correspondent difference curve (not shown) evidentiate a negative bump in the decreasing branch before the eclipse maximum and a positive bump of the same duration in the increasing branch after it. This indicates the presence of a localized source on the solar disk near the central meridian. In fact, the times (Table 3) characterizing the start and the minimum of the negative bump are associated respectively with the first contact of the lunar limb with the radio source and the occultation of its maximum emission region in the southern hemisphere. The times, which identify the start, maximum and end of the positive bump, indicate the uncovering of the radio source by the lunar disk. A graphical representation of such occultation is shown in Figure 6, where the positions of the lunar limb at the relevant times specified in Table 3 are superimposed to the H_{α} filtergram oriented in the ecliptic (ϵ) reference frame. A reasonable spatial correspondence between the radio and the optical active region is evident, especially if one takes into account that the coronal radio source is larger than the optical active region and that the presence of the observed peak emission subsource can significantly modify the symmetry of the radio isophote topology with respect to the radial direction above the optical

Table 3. Approximate occultation times of a radio source located near the central meridian as derived from the eclipse curve observed at 1420 MHz.

1^{st} contact	10:02 UT
Occultation of maximum	10:12 UT
2^{nd} contact	10:22 UT
3^{rd} contact	11:20 UT
Uncovering of maximum	11:31 UT
4^{th} contact	11:40 UT

active region. Due to the weakness of the observed radio activity, which decreases the signal-to-noise ratio, no further detailed analysis of the radio source fine structure in the spatial domain was possible.

8. CONCLUSIONS

The 11 August 1999 solar eclipse was observed in the radio domain by means of the Trieste Solar Radio System with limited spatial resolution. The radio eclipse curves at 237, 327, 408 and 1420 MHz were compared with the computed optical eclipse one to derive the correspondent radii of the solar corona at each frequency under the hypothesis of uniform radio brightness. The estimated effective radio radii (1.14 at 1420 MHz, 1.17 at 408 MHz, 1.23 at 327 MHz and 1.30 at 237 MHz) are consistent with those reported in the literature and with the increased electron density distribution determined by optical measurements in the totality path as well. Based on the derived effective radio radii, radio eclipse curves were computed to be compared with the observed ones in the search for radio source occultations. A noise storm source was observed most prominently at 237 MHz and its impulsive component also at 327 and 408 MHz, which exhibited a slight LH polarization, whereas the other weak activity was unpolarized at all frequencies. A detailed analysis at 1420 MHz resulted in the identification of a radio source located near the central meridian, but no spatial fine structure could be derived.

ACKNOWLEDGMENTS

The Italian Ministry for University and Research (MURST) and the Italian Space Agency (ASI) are gratefully acknowledged for the partial financial support to this work and the TSRS.

REFERENCES

- Abrami A., Cester B., Zlobec P., 1967, in Atti X Convegno SAIt, 11
- Clette F., these proceedings
- Espenak F., Anderson J., 1997, NASA Reference Publication 1398
- Kai K., Melrose D.B., Suzuki S., 1985, in Solar Radiophysics, D.J. McLean and N.R. Labrum (eds.), Cambridge University Press, 422
- Messerotti M., 1997, in *Theoretical and Observational Problems Related to Solar Eclipses*, Kluwer Academic Publishers, 59
- Messerotti M., Zlobec P., Padovan S., 2000, Mem. S.A.It., (in press)

Adrian Oncica

Astronomical Institute of the Romanian Academy Cutitul de Argint 5, RO-75212, Bucuresti 28, Romania Fax: +40 1 337.33.89; tel.: +40 1 336 36 87 e-mail: adrian@roastro.astro.ro

Abstract:

The observation of the total solar eclipse of August 11, 1999 at Bucharest was aimed at finding the (lack of) evidence of small (arcsecond) scale radio structures in the solar atmosphere ([1] Oncica 1997a and the references within). The method was borrowed and adapted from lunar occultation measurement of extragalactic radio sources ([2] Hazard 1976). The transit of the Moon's limb over the Solar disk was observed for 3h30m (9h20mUT - 12h50mUT), more than the duration of the eclipse (2h47m19s from 9h41m25sUT to 12h28m44sUT). Some global evidence of the Fresnel diffraction pattern was found. The coincidence with the occultation of particular solar structures as observed in other spectral regions is analyzed.

The Instruments

The observation was carried out with a low noise $(T_z=35K)$ microwave receiver in a wide (B=2GHz) bandwidth configuration. The measured system temperature was nevertheless much higher ($T_{sys}=320K$). The receiver was placed at the focus of an equatorial mounted (D=2m) dish. The measured antenna lobe (HPBW=2°.7) was twice the theoretical one. The radio equipment and its parameters was described in an earlier paper ([3] Buiculescu et.al. 1997)

The down converted signal, square law detected and low pass filtered (at 50kHz), was sampled at 10ms (Nyquist rate) and fed to a 14 bit D/A converter ([4] Oncica 1998) For the visual control the same signal was send to a strip chart recorder also.

The eclipse circumstances for Bucharest were (in UT):

1 st Contact	09h41m24s9
2 nd Contact	11h05m47s7
Maximum	11h06m58s.9
3 rd Contact	11h08m10s0
4 th Contact	12h28m43s6

Due to some technical problems the total effective observation time used for analysis was of only 3h21m40s. Due to some technical problems some 5min. Each of data at both ends of the eclipse were discarded (see figure 1).

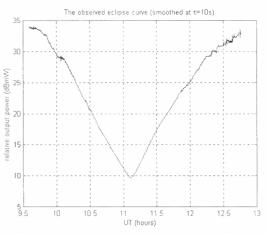


Figure 1: The eclipse curve (smoothed at 10s)

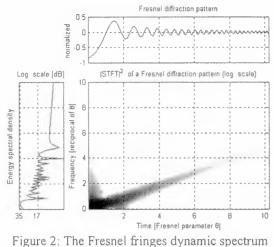
The Principle

The main idea behind the experiment was to use the transit of the Moon's limb over the solar disk to generate a Fresnel diffraction pattern for solar radio structures smaller than the first Fresnel fringe *if such structures do exist* ([5] Oncica 1997b and the references within).

The main parameter is the angular size of the first Fresnel zone (θ =1.2arcsec at 2.6cm). The transit of the Moon over the solar disk translates the angular pattern into the time domain at 2^s.8/arcsec.

The data analysis was aimed to detect the characteristic, chirp like, linear drift in frequency of the signal generated by the time evolution of the Fresnel fringe rate (see figure 2).

The feature must appear around 0.5Hz (at immersion) and fade away around 0.3Hz. At emmersion the spectral pattern is reversed both in time and in frequency. Lower frequencies are allowed for non-central contact.



rigute 2. The riesher hinges dynamic spectru

The Observations

Using the standard spectral analysis of the full 3h22m data record an obvious spectral feature in the 0.35-0.45Hz range is easily observable (see figure 3). This was <u>the only</u> spectral feature of the entire eclipse curve and is indicates that *something may happen* as expected.

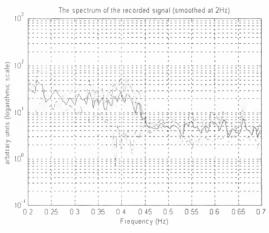


Figure 3: The full eclipse curve spectrum

For a more elaborate insight the Joint Time-Frequency Analysis (JTF) was used. This method allows for localization both in time and frequency of a particular feature. Its objective was to test for the chirp like behavior of the spectral feature around 0.4Hz at a particular moment that is to be correlated with the lunar occultation of a solar structure as seen in some other wavelength range.

Although in this analysis the noise is a real nuisance the large frequency bandwidth (2GHz, allowed by the slow chirp rate) and long integration time (0.5s, allowed by the slow fringe rate) brought a quality factor of 3.2×10^4 for a resolution of 10mK (!).

The full data set was split in intervals of 256s each and tested for the linear chirp. This has to be descending at the 1^{st} contact and ascending at the 4^{th} contact.

Five JTF features resembled to the expected linear chirp rate of the Fresnel like signal (see figures 4, 5, and 6).

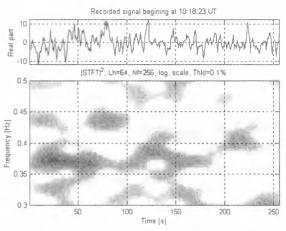


Figure 4: Descending chirp at T+20s and T+125s

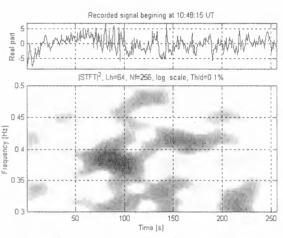


Figure 5: Descending chirp at T+80s

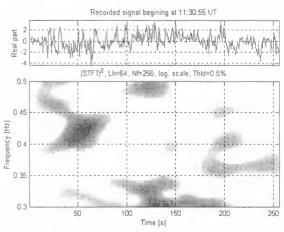


Figure 6: Ascending chirp at T+50s

Three other features. more fuzzy than faint, may be considered as candidates.(see figures 7, and 8).

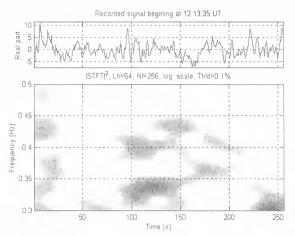
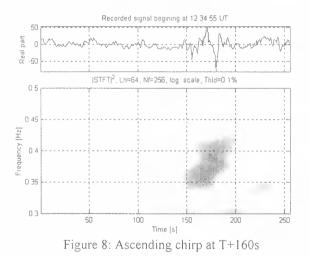


Figure 7: Ascending chirp at T+110s





To see if these chirp-like features in the dynamic spectrum can be considered as a signature of the occultation of some solar atmospheric structure we choose to use the soft X-ray image of the Sun as seem by Yohkoh at 14h42mUT (see figure 9). North is up.

The features at 10h19m in figure 4 correspond with the 1st contact with the most important active region on the solar disk (near the center SSE). The features at 10h50m in figure 5 correspond with the 1st contact with the loops near the SW solar limb.

The feature at 11h30m in figure 6 corresponds with the 4th contact of *the same* active region as in figure 4 (near center SSE). The same stands for figure 7 at 12h13, which corresponds to the 4th contact of the same loop, near the SW solar limb. The feature in figure 8 at 12h38m may rise some question as it takes place some 3min. after the optical end of the eclipse. Nevertheless

the Moon's limb is only R/10 high in the large loops over the NE solar limb

Conclusion

Even if the significance of these results may be a matter of debates the author is confidant based on three arguments. The first is the prominent and almost singular spectral peak around 0.4 Hz. The second is obvious characteristic linear drift of the five JTFA features. The third argument is the slight coincidence between the time occurrence of that chirp like features and the moments of contact for some solar active regions as observed in other spectral ranges. This last argument needs further work to be enforced.





Figure 9: Yohkoh soft X-ray image of the Sun (From Kiepeheuer Institut fur Sonnen Physsik website)

Bibliography

- Oncica A. 1997a: "Relevant Radio Observation During a Total Solar Eclipse", in: Z. Mouradian and M. Stavinschi (eds): NATO Advanced Research Workshop, May 1-5, 1996, Sinaia, Romania, NATO ASI Series C, vol 494, p.219-222, Kluwer Academic Publ, 1997.
- Hazard C. 1976: "Lunar Occultation Measurements", in Meeks M. L. (ed): *Methods in Experimental Physics*, vol.12, *Astrophysics*, part C: *Radio Observations*, Academic Press, 1976, p.92-117.

- Buiculescu V., Buiculescu O., Oncica A. 1997: "Radioastronomy Receivers for Solar Observations", *IEEE CAS'97 Proceedings of the* 20th International Semiconductor Conference, Oct.5-8. 1997, Sinaia, Romania, vol.2, p.609-612.
- Oncica A. 1998: "Data Acquisition System for Digitally Controlled Solar Radio Observations", *IEEE CAS'98 Proceedings of the 21st International Semiconductor Conference*, Oct.9-12. 1998, Sinaia, Romania, vol.2, p.623-626.
- Oncica A. 1997b: "A Radio Observation Project for the 1999 Solar Eclipse", in: Z. Mouradian and M. Stavinschi (eds): NATO Advanced Research Workshop, May 1-5, 1996, Sinaia, Romania, NATO ASI Series C, vol 494, p.235-238, Kluwer Academic Publ, 1997.

JOSO

Meeting on Observing Techniques and Recent Instrumental Development in Solar Physics

IBIS: A PURELY INTERFEROMETRIC INSTRUMENT FOR SOLAR BIDIMENSIONAL SPECTROSCOPY

Cavallini F.¹, Berrilli F.², Cantarano S.², and Egidi A.²

¹Osservatorio Astrofisico di Arcetri, I-50125 Firenze, Italy ²Dipartimento di Fisica, Università degli Studi di Roma "Tor Vergata", I-00133 Roma, Italy

ABSTRACT

In October 1999 started in Arcetri the construction of IBIS (Interferometric BIdimensional Spectrometer), a new instrument for solar bidimensional spectroscopy.

When completed in 2002, this instrument will allow to take monochromatic images of the solar surface on a large spectral range and on a large field of view, with high spectral, spatial and temporal resolution. These characteristics will make IBIS a poweful solar spectrometer, well suited for new generation telescopes such as THEMIS.

Key words: Sun; instrumentation; spectrographs; interferometers.

1. INTRODUCTION

Both theoretical and observational results suggest that observations with high spectral, spatial and temporal resolution are necessary to the comprehension of solar phenomena relevant to solve basic problems in stellar atmospheres.

On the other hand, the three-dimensional relationships between pressure, temperature, velocity and magnetic field, describing the state of the plasma in different solar structures, can only be investigated by narrow-band bidimensional spectroscopy.

For this reason, at the end of 1996, the Italian Panoramic Monochromator (IPM) (Cavallini, 1998) has been installed at THEMIS, where, from April 1997, it is operative and at the disposal of all observers.

This instrument suffers, however, of some limitations, as low transparence and slow wavelength positioning.

Drawing therefore from the experience acquired with the construction of IPM, a new instrument with improved characteristics has been designed and it is now under construction in Arcetri. It will be built with the contribution of the Arcetri Astrophysical Observatory, the Department of Astronomy and Space Science of the Florence University, and the Department of Physics of the Rome "Tor Vergata" University.

2. THE ITALIAN PANORAMIC MONOCHROMATOR

Let us consider firstly the more relevant instrumental characteristics of IPM (Tab. 1):

1 - High spectral resolving power. $\mathcal{R} = \lambda/\Delta\lambda = 260\ 000 - 270\ 000;$

2 - High wavelength stability.

The maximum drift of the instrumental profile is $\leq 10 \text{ m s}^{-1}$ on 10 h;

3 - Small useful spectral range.

IPM is essentially formed by a Fabry-Perot interferometer, used in telecentric mounting, in series with a Universal Birefringent Filter (UBF) (Beckers, 1971, 1972), used as *order sorter*, namely to isolate only one order of the interferometer. To be suitably used to this purpose, UBF demands however a very long calibration procedure, which, for the moment, has been performed on only 6 spectral ranges, 5 of which of astrophysical interest. This limits the useful spectral range, which in principle extends from 4600 Å up to 6800 Å, to $\simeq 200$ Å;

4 - Small field of view.

The present field of view (51" in diameter) is too small for some applications as, for example, to study active regions;

5 - Long exposure time \implies Low spatial resolution.

Mainly due to UBF, the overall transparence is low: from 0.7 % at H_{β} (4861 Å) to 2.0 % at H_{α} (6563 Å), imposing a mean exposure time of about 200 – 300 ms, too long to freeze the seeing. As a consequence, while IPM has been designed to completely exploit the spatial resolution allowed by the telescope

Proc. 1st Solar & Space Weather Euroconference. 'The Solar Cycle and Terrestrial Climate', Santa Cruz de Tenerife, Spain, 25-29 September 2000 (ESA SP-463, December 2000)

($\simeq 0.2$ " for THEMIS), due to the long exposure time, the spatial resolution is lowered by the seeing effects;

6 - Low acquisition rate \implies Low temporal resolution.

UBF is formed by nine crystal groups (Lyot elements) the rotation of which around the optical axis allows the passband wavelength positioning. The tuning is mechanically performed (nine steps motors and shaftings), preventing short setting times. Moreover, as the angular rotations necessary to set the passband to the demanded wavelength depend on the start configuration, the setting time is not constant and can vary from $\simeq 0.1$ s up to $\simeq 1$ s. This implies that, if sequences of images taken at equal time intervals are desired, a minimum wavelength setting time of 1 s must be used. For this reason, and due to the long exposure time, also using high speed CCD cameras, as those recently installed at IPM (March 2000), the acquisition rate cannot be higher than \simeq $0.7 \text{ frames s}^{-1}$.

Among the instrumental characteristics detailed above, the high spatial resolution certainly is the most demanding one, not readly obtainable with ground-based observations. Two metods are used to correct the seeing effects limiting the spatial resolution in solar observations: adaptive optics and the phase diversity tecnique (Löfdahl & Scharmer, 1994; Tritschler et al., 1997). However, while the use of adaptive optics is limited, for the present, to small fields of view (about $10" \times 10"$), phase diversity does not suffer of this limitation. On the other hand, phase diversity requires that two images of the same solar region (one on focus and another out of focus of a known amount) are simultaneously taken with a very short exposure time (less than $\simeq 40 \text{ ms}$), in order to freeze the seeing. The post facto analysis of the two images allows then to find and to correct the effects of the atmosferic wavefront on the observed field of view.

The short exposure times required by this method impose therefore a very high instrumental throughput and, for this reason, all the results so far obtained are limited to data acquired with broad-band filters, devoid of any spectral information.

Concluding, therefore, a high transparence is required to an instrument which is able to take monochromatic images of the solar surface with high spectral and spatial resolution on a large field of view.

3. THE INTERFEROMETRIC BIDIMENSIONAL SPECTROMETER

Starting from the previous considerations, a new instrument has been therefore designed to overcome all the limitations imposed by IPM, mainly due to the use of UBF to isolate one order of the interferometer.

On the other hand, the same result can be also obtained, as known, by using a narrow-band interference filter in tandem with a series of interferometers with suitable spacings. This solution, already adopted in the past (Mack et al., 1963; McNutt, 1965; Stoner, 1966; Ramsay et al., 1970; Loughhead et al., 1978; Bray, 1988), did not obtain, however, good results, mainly due to the difficulty in securing the correct tuning between different interferometers.

This problem has been solved however (Hicks et al., 1976), thanks to the progresses in controlling spacing and parallelism of the interferometer plates.

So IBIS is essentially formed by two Fabry-Perot interferometers and a narrow-band interference filter mounted in series. The adopted interferometers are two Queensgate (Mod. ET50), piezo-scanned and capacity servo-controlled, with a clear diameter of 50 mm, a maximum flatness error for each plate of $\lambda/150$ (after coating), and a very short wavelength setting time (few ms).

The interferometers are used in classic mounting and in axial-mode, that allows higher spectral resolution and secures the same shape of the instrumental profile on all the points of the final image plane.

The ratio between the spacings of the two interferometers has been choosen so to produce the minimum amount of parasitic light (defined as the ratio between the flux outside the instrumental profile, and the flux within it). Finally, the two spacings and the coating reflectivity have been selected as the better compromise between parasitic light, spectral resolution and overall transparence.

The principal optical path is formed by four lenses: the two interferometers are mounted in series between the third and the fourth of them. The first three lenses successively collimate the field stop, placed in a secondary focus of the telescope, and the pupil, producing an image of the latter compatible with the clear diameter of the interferometers. The forth lens, followed by a suitable optics, finally forms, on two identical CCD cameras, two monochromatic images of the selected solar area, one on focus and another out of focus, to be used for the *phase diversity* procedure.

Between the two Fabry-Perot, a filter wheel carries a set of narrow-band interference filters (FWHM = 3 Å or 5 Å, depending on wavelength) with the double aim of isolating the instrumental profile and of reducing the ghost images produced by inter-reflections between the two interferometers. Narrow-band interference filters have a peak transparence of $\simeq 30\%$, while the intensity of ghost images is $\simeq 10\%$ of the principal one (that simply transmitted). Due to the filter, therefore, the resulting intensity of ghost images is lowered to $\simeq 1\%$. This allows the use of the interferometers in axial-mode, avoiding the unwanted effects produced by their tilt, essentially consisting in a different shape of the instrumental profile in different points of the final image plane.

Moreover, a beamsplitter, placed between the first and the second lens, draws a small amount of the

	IPM	IBIS
Wavelength range	4600 Å – 6800 Å	5800 Å – 8600 Å
Calibrated ranges	5184 Å (Mg b1), 5380 Å (C I), 5576 Å (Fe I), 5890 Å (Na D2), 6438 Å (Cd red line), 6563 Å (H $_{\alpha}$)	No calibration is necessary
Full Width at Half Maximum (FWHM)	17 mÅ – 26 mÅ	21 mÅ – 42 mÅ
Spectral resolving power $(\lambda/\Delta\lambda)$	$260\ 000\ -\ 270\ 000$	205 000 - 320 000
Wavelength drift	\leq 10 $\rm ms^{-1}$ on 10 h	\leq 10 ms ⁻¹ on 10 h
Field of view (circular)	51"	80"
Transparence	$0.7\% - 2.0 \ \% \ ({ m H}_eta - { m H}_lpha)$	10.0 % - 16.2 %
Exposure time $(S/N \ge 100)$	200 – 300 ms	$\leq 20 \text{ ms}$
Wavelength setting time	1 s	$\simeq 1.5~{\rm ms}$
Acquisition rate	$\simeq 0.7 {\rm ~frames~s^{-1}}$	$\simeq 5 \text{ frames s}^{-1}$

Table 1. Comparison between IPM and IBIS characteristics

incoming radiation ($\simeq 0.25$ %), which then passes through a second set of broad-band interference filters (FWHM = 50 Å), centered at the same peak wavelength of the previous ones. A suitable optics finally forms on a third CCD camera a *white* light image, on the same scale of the monochromatic ones. The three CCD cameras then simultaneously take one *white* light and two monochromatic images of the same selected solar area.

The high transparence of the whole system (see later) allows very short exposure times and hence the reconstruction of the seeing modified wavefront by means of the *phase diversity* tecnique, applied to the monochromatic images. These images can be therefore corrected for the seeing effects, achieving a spatial resolution near the diffraction limit of the telescope.

The adopted CCD cameras are three high speed (5 MHz) Pentamax of Princeton Instruments, with a Kodak CAF-1400 detector with 1317×1035 pixels.

Some secondary optical paths are then necessary to allow the instrumental set-up. In particular:

1 - Tuning: the radiation emitted by a continuos source can be injected in the principal optical path to find the initial tuning conditions for the two interferometers;

2 - Parallelism: the radiation emitted by a frequency stabilized He-Ne laser can be injected in the principal optical path to verify and to adjust the parallelism of the two interferometer plates;

3 - Orthogonality: two pellicle beam splitters can be inserted on the plane of the image formed by the second lens and before it to verify and to adjust the orthogonality between each interferometer and the optical axis.

Many instrumental components are provided with actuators for a remote positioning, while four TV cameras allow to verify the correctness of the operations.

A fifth TV camera continuously shows the selected solar region to monitor the solar and atmospheric conditions.

The more relevant instrumental characteristics of IBIS can be finally summarized as follows (Tab. 1):

1 - High spectral resolving power. $\mathcal{R} = \lambda/\Delta\lambda = 205\ 000\ (at\ 8600\ \text{\AA}) - 320\ 000\ (at\ 7000\ \text{\AA});$

2 - High wavelength stability. The maximum drift of the instrumental profile is \leq 10 m s^{-1} on 10 h;

3 - Large useful spectral range. The useful spectral range covers 2800 Å (5800 Å - 8600 Å), without any limitation (if the required interference filters are available); 4 - Large field of view.

The field of view (80" in diameter) is large enough to study also active regions;

5 - Short exposure time \implies High spatial resolution.

The instrumental transparence (10% - 16%) is large enough to allow exposure times of 5 - 20 ms (S/N ≥ 100 on the solar continuum, in the THEMIS situation). The seeing can be therefore frozen and the images can be corrected *post facto* for the wavefront distortion (*phase diversity*), achieving a spatial resolution near the theoretic limit of the telescope;

6 - High acquisition rate \implies High temporal resolution.

A test performed by using a high speed CCD camera (Princeton Instruments Mod. Pentamax with CCD Kodak KAF-1400) showed that, for a frame of 512×512 pixels (1024×1024 binned ×2) and a dynamic range of 12 bits, the acquisition time, including exposure (20 ms), reading and storing, amounts to $\simeq 200$ ms. Since the wavelength positioning time of the two interferometers is negligible (some ms), an acquisition rate of 5 frames s⁻¹ can be expected.

4. CONCLUSIONS

The characteristics detailed above (high spectral, spatial and temporal resolution, very high wavelength stability, large useful spectral range and large field of view) make IBIS a nearly ideal instrument for solar bidimensional spectroscopy. When completed in 2002 and installed at THEMIS, it will be a powerful instrument for solar research, suitable to be successfully used for a wide range of scientific projects.

REFERENCES

Bray R.J., 1988, LEST Tech. Rep., 35

Cavallini F., 1998, A&ASS 128, 589

Hicks T.R., Reay N.K., Stephens C.L., 1976, A&A 51, 367

Löfdahl M., Scharmer G., 1994, A&ASS 107, 243

Loughhead R.E., Bray R.J., Brown N., 1978, Appl. Opt. 17, 415

Mack J.E., McNutt D.P., Roesler F.L., Chabbal R., 1963, Appl. Opt. 2, 873

McNutt D.P., 1965, J. Opt. Soc. Am. 55, 288

Ramsay J.V., Kobler H., Mugridge E.G.V., 1970, Solar Phys. 12, 492

Stoner J.O., 1966, J. Opt. Soc. Am. 56, 370

Tritschler A., Schmidt W., Knölker M., 1997, ASP Conf. Series Vol. 118, 170

SOLAR MAGNETOMETRY WITH THE DUTCH OPEN TELESCOPE

R.J. Rutten, R.H. Hammerschlag, P. Sütterlin, F.C.M. Bettonvil, E.B.J. van der Zalm

Sterrekundig Instituut, Postbus 80 000, NL-3508 TA Utrecht, The Netherlands telephone: 31-30-2535200, telefax: 31-30-2535201; website http://dot.astro.uu.nl email: R.J.Rutten/R.H.Hammerschlag/P.Suetterlin/F.C.M.Bettonvil/E.B.J.vanderZalm@astro.uu.nl

ABSTRACT

The Dutch Open Telescope (DOT) has become operational at the Roque de los Muchachos Observatory on La Palma. The first image sequences taken with this innovative telescope demonstrate its capability for tomographic high-resolution imaging of the magnetic topology of the solar atmosphere up to the transition region over the large field of view permitted by consistent speckle restoration. We review the science needs for such imaging and describe the DOT solution to the problems posed by the earth atmosphere and the solar physics niche filled by the DOT.

Keywords: solar telescopes, solar atmosphere, solar magnetism, speckle reconstruction.

1. INTRODUCTION

This meeting connects solar physics with the terrestrial climate. One back-reaction aspect of the latter on the former is that terrestrial weather, in particular the "atmospheric seeing" which characterizes the amount of image deterioration caused by the earth's atmosphere, is of great importance in setting the angular resolution of groundbased solar telescopes. Achieving high angular resolution over long durations in many spectral diagnostics is a prime quest of solar physics because many of its key problems are dominated by magnetism while the solar magnetic field is structured into very slender tubes and loops. The latter harbor important processes especially in the outer solar atmosphere where magnetic pressure dominates gas pressure, but mapping them and measuring their properties requires higher resolution than achieved sofar due to the spoiling by the earth's atmosphere. The quest is to obtain high angular resolution not just in the brief glimpses permitted by the best seeing at the best sites, but consistently over long duration. At present, this goal comes in reach with the advent of adaptive optics. The Dutch Open Telescope described here relies on an alternative technique to get rid of the degradation by the earth's atmosphere: consistent high-volume speckle restoration. Its advantage is that it produces image restoration to the diffraction limit over the whole field of view of the telescope.

In this contribution we briefly review the reasons why high angular resolution is so important to solar physics and describe how the new and innovative Dutch Open Telescope (DOT) fills this need by speckle-restored multi-wavelength imaging. This presentation is in rather general terms in view of the mixed audience at this conference. More detailed DOT presentations were given at the 20th NSO/Sac Peak Summer Workshop and will appear in the ASP Conference Series (editor M. Sigwarth). An excellent recent monograph on solar (and stellar) magnetism that is suited as introduction to scientists from outside the field (such as climatologists) is *Solar* and Stellar Magnetic Activity by Schrijver & Zwaan (2000).

2. HIGH RESOLUTION SOLAR PHYSICS

Figure 1 updates a figure printed in older ESA proceedings (Rutten 1993). The update consists of tilting the dotted groundbased resolution limit to vertical. The image-restoration revolution, whether through adaptive optics or speckle reconstruction, will permit groundbased registration of solar scenes at about 100 km resolution over durations as long as the sun shines (or round the clock with roundthe-earth networks). The tilt change implies a much better grasp on sunspot umbrae and penumbrae, "magnetic grains" which mark individual fluxtubes away from active regions, and prominences. These are all magnetically dominated structures that are rather ill-understood. The phenomena more to the left in Fig. 1 are mostly gasdynamical in nature and are generally much better understood, in particular the granulation (turbulent convection) and the 5-min oscillation (global p-mode oscillations). The MHD paradigms (capitalized in Fig.1) are applied elsewhere in astrophysics (e.g., to explain accretion disksaround magnetic white dwarfs and neutron stars and the AB Dor and Be star phenomena), but they depend on high-resolution solar physics for elaboration. Likewise, the sun-climate connection requires identification of the way in which the sun modulates its irradiance and wind, i.e., to understand the activity cycle. The major cycle components, active regions and magnetic network, are made up of the slender MHD configurations called fibrils and fluxtubes. Studying solar cycle properties entails trying to understand these basic building blocks of magnetism in the solar atmosphere at their intrinsic scales and their pattern evolutions over long durations. The currently achieved tilting of the groundbased limit in Fig.1 therefore represents a major breakthrough in solar astrophysics.

3. TOMOGRAPHIC SOLAR PHYSICS

Another requirement in solar physics is a holistic approach, as exemplified by the SOHO mission ("from the solar interior to the outer heliosphere").

Proc. 1st Solar & Space Weather Euroconference, 'The Solar Cycle and Terrestrial Climate', Santa Cruz de Tenerife, Tenerife, Spain, 25-29 September 2000 (ESA SP-463, December 2000)

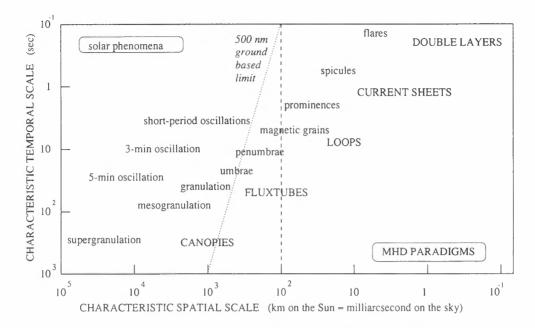


Figure 1: Spacetime characteristics of solar phenomena (small print) and solar-inspired paradigms of magnetohydrodynamics (capitals). The dotted groundbased limit corresponds to the best "seeing" of the earth's atmosphere which even at the best sites permits subarcsecond resolution only over brief duration. The limit now tilts to the dashed vertical line set by aperture diffraction, thanks to the advent of adaptive optics and speckle restoration. The latter technique is exploited at the DOT.

In optical solar magnetometry, one aspect is the need to sample the solar atmosphere at different heights simultaneously. The reason is that the solar atmosphere changes dramatically between different regimes and presents drastically different scenes to the terrestrial observer at different wavelengths.

The solar photosphere, defined as the layer where the bulk of the electromagnetic radiation escapes as visible light (a dramatic transition from nearequilibrium photon enclosure, killing off the subsurface convection into the shallow pancake pattern called granulation) is also the layer where magnetic fields take over from gas dynamics in dictating the structuring and in supplying the key processes, and it is also the outermost layer where the sun may be regarded as spherical in zero-order approximation. The chromosphere is magnetically split into network and internetwork in quiet regions and is very finely structured above active regions. The transition to the corona consists of tiny fibrils with much variation in length, inclination, and ordering. The closed-field parts of the corona outside coronal holes are made up of bundles of very thin coronal loops. Yet unidentified processes supply energy to the gas in these loops, reaching a balance against cooling by X-ray photon losses at temperatures of 1–2 million K.

The loops are magnetically anchored (in unknown fashion) to the strong-field fluxtubes that break out of the photosphere and respond dynamically on a wide variety of timescales to the footpoint forcing. These magnetic connections between very disparate regimes, from gas dynamics via magnetohydrodynamics to plasma physics and from LTE radiation enclosure to X-ray photon drain, require simultaneous study of structures, processes and radiation in the photosphere, chromosphere, transition region and corona.

4. PROXY MAGNETOMETRY

The Dutch Open Telescope $(DOT)^1$ relies on "proxy" magnetometry, *i.e.*, using the intensity encoding imposed by magnetic structures to portray the topology and evolution of the magnetic field. The chief optical diagnostics are the G band, CaII K, and H α . Higher up, the coronal topology is best sampled in soft-X ray lines such as the FeIX, FeX line pair at 171 nm used by the TRACE mission² to produce vivid movies of coronal field evolution. Obviously, holistic solar tomography requires combining groundbased observing and space observing — a tactic frequently followed in current solar physics, for example in the multi-telescope campaigns of the European Solar Magnetometry Network (ESMN)³.

4.1 G band: photospheric topology

The G band around 430.5 nm (a 1 nm piece of spectrum filled with lines of the CH molecule, the name was given by Fraunhofer) has been found to be the best diagnostic to chart the location and evolution of magnetic fluxtubes in the deep photosphere because these appear on high-resolution G-band filtergrams as bright points (Fig. 2). Standard fluxtube models explain this from the "hot wall" effect (Spruit 1976, Spruit & Zwaan 1981): the tube is relatively empty because the inside magnetic pressure balances the outside gas pressure, and so it acts as a viewing

¹DOT: http://dot.astro.uu.nl

²TRACE: http://vestige.lmsal.com/TRACE

³ESMN: http://www.astro.uu.nl/~rutten/tmr

tube through which radiation escapes from layers below the outside surface, with the hot tube walls producing brighter emission than the surroundings. In the G band this contrast is enhanced because the CH molecules dissociate in the fluxtube so that the many dark CH lines in the G band vanish and the tube gas gains even more transparency compared to the outside gas than at other wavelengths.

The intrinsic sharpness of the photospheric fluxtubes is very high because they are very thin and the G-band photons are emitted thermally and are not much spread by scattering on their way out. At 100 km resolution most resulting G-band bright points are not resolved, but at least they are identifiable so that they can be located and traced in time. At somewhat lower resolution (say 0.5 arcsec) they vanish because they are mostly located within dark intergranular lanes so that smearing by atmospheric seeing cancels bright against dark (Title & Berger 1996).

4.2 CaII K: chromospheric topology

The CaII K line is the strongest Fraunhofer line and samples the chromosphere at about 1000 km above the white-light surface. At this height, the magnetic network is enhanced by yet unidentified heating processes so that the CaII K line-center intensity (at about 0.1 nm bandwidth) provides an excellent magnetogram proxy (but unsigned). This fact has been exploited extensively in gauging the magnetic activity of sun-like stars (reviewed extensively by Schrijver & Zwaan 2000).

The sharpness of CaII K images is intrinsically less than for the G band, partially because the line photons are scattered considerably on their way out before their final escape towards the observer, and partially because the fluxtubes expand and merge with height. The same regime and the same patterning are also sampled by imaging in the near-UV continua, but the state of the art (160 nm and 170 nm passbands of the TRACE mission) does not yet reach the intrinsic angular resolution nor the resolution obtained at groundbased telescopes.

4.3 H α : transition region topology

The Balmer H α line comes from the most abundant element but is much less strong than CaII K in the solar spectrum because its lower-level n = 2 population has very low weight in the Boltzmann population partitioning over the hydrogen energy levels. Nevertheless, its high excitation energy causes this line to respond to gas at high temperature so that it maps low-lying fibrils in the transition regime between chromosphere and corona if these are sufficiently dense.

This transition regime has often been modeled as a spherical shell between the 8000 K chromosphere and the 2 million K corona, but a high-resolution H α movie immediately shows the fallacy of such modeling by displaying a mass of fibrils with no semblance of sphericity. The "moss" phenomenon discovered with TRACE indicates that 2 million-K plasma actually descends down to between the H α fibrils in plage (Berger et al. 1999).

Using H α as magnetograph proxy to derive the field topology from the observed fibrils is not straightforward because the latter harbor length-wise flows that modulate the apparent fibril contrast through substantial Dopplershifts. The resulting mix of brightness and Dopplershift variations requires full profile modeling, so that filtergrams must be taken at a number of wavelengths and interpreted through inversions based on sophisticated radiative transfer modeling.

The intrinsic H α resolution can be exceedingly high because the fibrils may be effectively or even optically thin, imposing their scale on the emergent radiation without transfer smearing. This is particularly the case in filaments and prominences (the latter are filaments seen off-limb where the background radiation along the line of sight vanishes). These amazing structures, keeping very cool gas up in the hot corona and persisting very long, are rich sources of MHD physics. They probably consist of very thin magnetic fibrils in complex topologies that are best encoded in H α radiation.

5. DUTCH OPEN TELESCOPE

The DOT is located at the Roque de los Muchachos Observatory on La Palma which is one of the best sites known worldwide for high-resolution solar imaging. The La Palma seeing can be superb, especially when the oceanic trade wind blows strongly upslope from the North. The photographs in Fig. 3 illustrate that the DOT adheres to its name in being open, a design which capitalizes on the strong-wind good seeing by firstly not upsetting the laminar character of the trade wind (open transparent tower), secondly by relying on mirror and telescope flushing by the same wind to avoid internal seeing. Solar heating of the prime focus structure is avoided by reflecting most of the image away with a mirror that is watercooled to ambient temperature. The DOT design departs radically from all other high-resolution solar telescopes, which all employ telescope evacuation to avoid internal turbulence. The excellent image quality achieved by the DOT (Fig. 2 and assorted movies at http://dot.astro.uu.nl) attest to the success of the open principle.

One potential problem of an open telescope that relies on wind flushing is shake by wind buffeting. The DOT has an extraordinary stiff structure and sophisticated self-aligning gear trains that avoid telescope pivoting under variable wind loads. The DOT support tower is not stiff but permits platform motions only parallel to the platform, without the pivoting that would represent pointing errors when observing the sun (a source at infinity).

The DOT enclosure is a fold-away clamshell canopy of stiff fabric on heavy steel ribs. It can be closed in very strong winds and should withstand hurri-

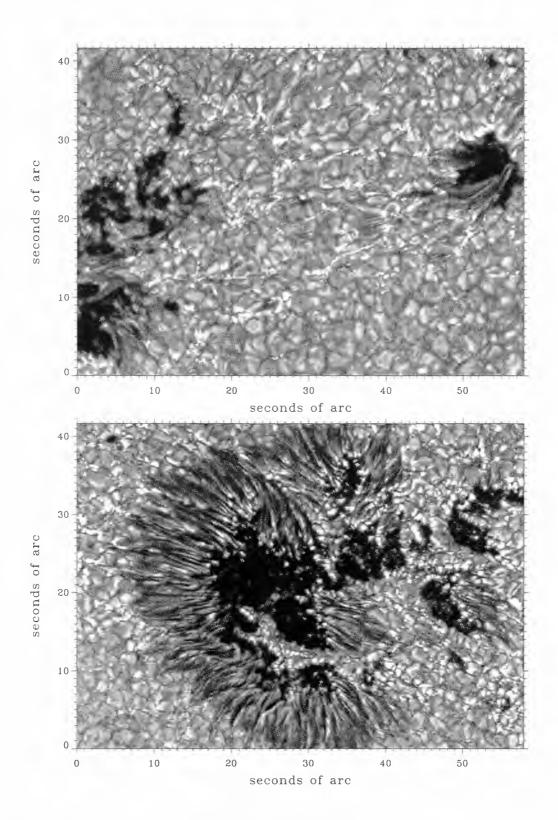


Figure 2: Speckle-restored G band images taken with the DOT on 1999 October 21 (top) and 23 (bottom). The upper image is part of a one-hour movie of which each frame resulted from speckle reconstruction using 60 video exposures from the initial analog DOT camera digitized at s bits. The quality of the G band as high-resolution diagnostic of the photospheric magnetic field topology is well exhibit d: all bright grains in the intergranular lanes between the two sunspots correspond to strong-field fluxtubes that jut through the surface like angler's floats. The full movie is available at http://dot.astro.uu.nl and vividly displays the rapid evolution of the fluxtube patterning, with some tubes traveling fast from left to right and others the other way (rather as if pulled along by subsurface trout) The lower image shows a similarly complex scene including a larger sunspot.

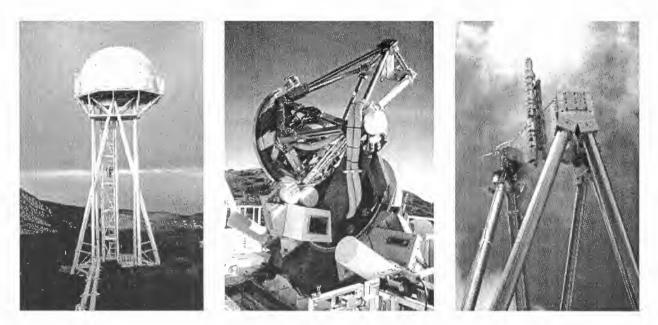


Figure 3: The Dutch Open Telescope at the Roque de Los Muchachos Observatory on La Palma. First panel: DOT with clamshell dome closed. The open tower is 15 m high. The pipelines in the foreground connect the DOT to the Swedish solar telescope building from which the DOT is operated, with fiber-optic links for image transport. North is to the right. Middle panel: DOT pointed towards the sun. The parallactic mount has large and heavy gears to avoid windshake since good seeing often correlates with strong wind on La Palma. The wind also flushes the primary mirror (45 cm diameter) which sits left of the two hoses. Righthand panel: initial prime focus instrumentation. The steel struts support imaging equipment that in this 1999 photograph consisted only of the slender tube at center, containing a water-cooled field stop (a 2 mm hole in a tilted mirror) which transmits only a 3 arcmin field and reflects the rest of the prime-focus image away: and re-imaging optics. G-band filter and a simple analog video camera of which the output is digitized at only 8 bits. At present, the DOT is being equipped with a new 10-bit digital five-camera system and multiple-wavelength optics that will mostly be mounted besides the incoming beam.

cane wind loads — and has done so the past winters. The coated fabric also tends to resist ice deposition, otherwise a major problem at the Canary Island mountain summits where undercooled fogs often cause heavy upwind icicle growth.

The DOT is currently being equipped with a multiwavelength multi-camera imaging system, using five digital CCD cameras to obtain speckle-restored images in the G band, the center of the CaII K line, and a rapidly switched narrow passband in H α using a birefringent Lyot filter on loan from the Canadian Research Council. Another tunable birefringent filter on loan from colleagues at Irkutsk will probably be installed to obtain Dopplergrams (velocity maps) using the narrow BaII 4554 resonance line. The cameras will be operated synchronously in speckle mode (many-frame bursts at fast cadence) and provide a four times larger field of view than the one in Fig. 2.

6. SPECKLE RESTORATION

The DOT is located at an excellent site which provides the good seeing at strong wind combination that is needed to make the wind-flushed open telescope principle work. The DOT doesn't spoil the good seeing there by virtue of its open structure. Nevertheless, the site and the open principle do not suffice to tilt the groundbased limit to the vertical as in Fig. 1. Excellent seeing not only occurs fairly rare even at La Palma, but it also comes intermittently. Thus, the remaining atmospheric deterioration of the image quality limits the frequency and the duration of high-resolution image taking severely. The DOT answer to this problem is to consistently apply speckle reconstruction to all image acquisition. This sets the DOT apart from the atmospheric restoration programs elsewhere which rely on adaptive optics. Both techniques require at least moderate seeing quality because the solar scene should yet contain sufficient angular structure to permit gauging the atmospheric wavefront deformations. The gain is that moderate seeing occurs far more frequently as well as far more consistently over long durations.

Speckle reconstruction through the speckle masking technique is a well-established technique also in solar physics (Weigelt 1977, Weigelt & Wirnitzer 1983, de Boer & Kneer 1992) but has not been applied at the scale on which the DOT will employ it, generating up to 500 Gbyte of speckle data per observing day. This data stream implies that the (very small) DOT team will be swamped, but the hope is that in the near future parallel processing of the speckle data can be realized to obtain fast, perhaps near-real time, reduction.

The major advantage of the choice for speckle reconstruction over adaptive optics is that it delivers diffraction-limited resolution of 0.2 arcsec over the whole field of view set by the camera chip size, 130×100 arcsec² for the new DOT cameras. The alternative, adaptive optics, delivers full correction only for the central isoplanatic patch of about 5×5 arcsec² instead of the many hundred patches restored at the DOT. Multiconjugate adaptive optics (Beckers 1989) may solve this problem eventually, but not soon.

The reason that adaptive optics is intensely pursued at many other solar telescopes is that speckle reconstruction gives out at larger aperture because the speckle coding signal diminishes, and that adaptive optics permits feeding spectrometer slits with a stabilized image and so permits the long exposure times needed for spectropolarimetry at high spectral resolution and large signal-to-noise as required for precise Stokes vector mapping. Similar signal-tonoise problems may arise for the narrow-band imaging through the tunable $H\alpha$ and BaII 4554 filters at the DOT (or for future Fabry Perot instruments at the DOT), but these are solvable using the twochannel speckle restoration technique of Keller & von der Lühe (1992) in which synchronous wide-band speckle bursts define a deconvolution operator for the narrow-band speckle frames.

7. DOT NICHE AND PROSPECTS

With its new five-camera system and its large-volume speckle data-acquisition system, the DOT will be the first solar telescope with the capability to provide long-duration image sequences at the telescope diffraction limit (0.2 arcsec) that map the magnetic topology over a sizable field $(130 \times 100 \text{ arcsec}^2)$ in tomographic fashion, simultaneously for the photosphere (G band), chromosphere (CaII K) and low transition region (tuned $H\alpha$). Obviously, this capability fills a niche in solar physics concerning the horizontal topology and vertical structure of solar magnetic fields. It is also obvious that such tomographic high-resolution imaging will be desirable as context information to high-resolution spectropolarimetry at other telescopes employing adaptive optics, and to coronal field mapping using X-ray image sequences from space.

Whether the DOT will actually fill this niche is primarily a question of funding. The DOT team is very small (just the author list to this contribution) and the DOT finances are insecure. The current funding ends by the end of 2001. The DOT future therefore hinges on the first campaigns with the new multiwavelength imaging system. In a wider context, the future of solar physics at Utrecht rides on the outcome as well.

8. DOT SPINOFF

The success of the DOT in obtaining superb image sequences (Fig. 2) even with the very simple initial analog camera (Fig. 3) has demonstrated the validity of the open concept. This demonstration and the advent of adaptive optics together open the way for much larger solar telescopes. Vacuum reflectors and refractors are limited to about 1 m diameter because the entrance window or lens cannot be much larger when thin, or causes resolution deterioration

from imperfections in the glass volume when thick. The success of the open principle is therefore very good news. In addition, adaptive optics now permits restoration of the atmospheric degradation beyond the aperture limit at which speckle reconstruction (and phase-diverse reconstruction, or a mixture) work well. Thus, the future for high-resolution observing of the sun from the ground has become rosy. Two major new telescope projects exploit these advances. The German GREGOR⁴ project aims to refurbish the Gregory-Coudé telescope at Izaña (Tenerife) with a new open feed on the top of the building, weather-protected by an upsized copy of the DOT clamshell canopy. The US solar physics community led by the National Solar Observatory is embarking on the ATST⁵, currently targeted as an open telescope with 4 m diameter. Its roadmap advertises the DOT as technology example.

Acknowledgement. The DOT project is funded by Utrecht University, the Netherlands Graduate School for Astronomy NOVA and the Netherlands Organization for Scientific Research NWO. The DOT team enjoys hospitality at the Swedish solar telescope building in close cooperation within the European Solar Magnetometry Network funded by the EC under TMR contract ERBFMRXCT98019. The DOT was built by the workshops of the Sterrekundig Instituut Utrecht and the Faculty of Physics and Astronomy of Utrecht University and the Central Workshop of Delft University. The new DOT data acquisition system is built by the Instrumentele Groep Fysica at Utrecht.

REFERENCES

- Beckers J. M., 1989, in R. J. Rutten, G. Severino (eds.), Solar and Stellar Granulation, NATO ASI Series C 263, Kluwer, Dordrecht, p. 43
- Berger T. E., De Pontieu B., Schrijver C. J., Title A. M., 1999, ApJ 519, L97
- de Boer C. R., Kneer F., 1992, A&A 264, L24
- Keller C. U., von der Lühe O., 1992, A&A 261, 321
- Rutten R. J., 1993, in C. Mattok (ed.), Targets for Space-Based Interferometry, Proc. ESA Coll. (Beaulieu), ESA SP-354, ESA Publ. Div., ES-TEC, Noordwijk, p. 163
- Schrijver C. J., Zwaan C., 2000, Solar and Stellar Magnetic Activity, Cambridge Univ. Press, Cambridge, UK
- Spruit H. C., 1976, Solar Phys. 50, 269
- Spruit H. C., Zwaan C., 1981, Solar Phys. 70, 207
- Title A. M., Berger T. E., 1996, ApJ 463, 797
- Weigelt G., Wirnitzer B., 1983, Optics Lett. 8, 389
- Weigelt G. P., 1977, Opt. Comm. 21, 55

⁴GREGOR: http://www.kis.uni-freiburg.de/GREGOR ⁵ATST: http://www.sunspot.noao.edu/ATST

THE NEW GLOBAL HIGH–RESOLUTION H α NETWORK: FIRST OBSERVATIONS AND FIRST RESULTS

M. Steinegger¹, C. Denker¹, P. R. Goode¹, W. H. Marquette¹, J. Varsik¹, H. Wang¹, W. Otruba², H. Freislich², A. Hanslmeier³, G. Luo⁴, D. Chen⁴, and Q. Zhang⁴

¹Big Bear Solar Observatory, NJIT, 40386 North Shore Lane, Big Bear City, CA 92314, U.S.A.

²Kanzelhöhe Solar Observatory, A–9521 Treffen, Austria

³Institute of Geophysics, Astrophysics, and Meteorology, Universitätsplatz 5, A-8010 Graz, Austria

⁴Yunnan Astronomical Observatory, P. O. Box 110, Kunming 650011, P. R. China

ABSTRACT

A new global network for high-resolution $H\alpha$ full-disk observations of the sun has been established at the Big Bear Solar Observatory (U.S.A.), the Kanzelhöhe Solar Observatory (Austria), and the Yunnan Astronomical Observatory (China). Each of the three stations have a $2K \times 2K$ pixel CCD detector available to monitor the sun with a spatial resolution of 1 arcsec per pixel and a cadence of at least 1 image per minute. We will implement automatic detection routines for flare and filament eruptions. These routines can automatically trigger even higher cadence observations. Having high-cadence data from three observing stations will enable us to accurately track solar rotation rates as determined by local correlation and feature tracking techniques. This includes, e.g., tracking over several days the proper motion of active regions. High-cadence H α data with high spatial resolution allow us to study in detail the correlations between coronal mass ejections and the solar surface activity. The new network also represents an important tool for correlative studies between ground-based and space observations, as well as for improving the reliability of current space weather predictions.

Key words: solar activity; space weather; full-disk observations; flare monitoring.

1. INTRODUCTION

While full-disk observations in the spectral line of H α (λ 656.3 nm) obtained at a single observing site can contribute to important solar research, for several reasons it is necessary to monitor the sun round-the-clock. The most severe problem for single station observations is the inevitable night-time gap. Many interesting and important chromospheric phenomena, such as flares or filament eruptions, occur during the night so that they are missed and lost at a single observing station. Round-the-clock

full-disk observations with high spatial resolution and high cadence performed by a dedicated network of H α telescopes distributed around the globe can continuously follow the evolution of active regions and monitor every flare and filament eruption occuring on the visible solar hemisphere. Observing the sun continuously in H α is not only important for solar physics, but also for space weather research. As triggers of space weather variations, chromospheric features such as flares and filament eruptions and the associated coronal mass ejections, have a direct impact on the solar terrestrial environment. Uninterrupted high cadence H α observations are therefore important for monitoring and forecasting both solar activity and space weather.

To overcome the limitations of single observing sites and to enable the continuous monitoring of the solar chromosphere with fast and large format CCD cameras, the new global high-resolution H α network has been established between Big Bear Solar Observatory (BBSO) in the U.S.A., Kanzelhöhe Solar Observatory (KSO) in Austria, and Yunnan Astronomical Observatory (YNAO) in China.

2. NETWORK SITES AND INSTRUMENTS

BBSO has a long tradition in obtaining synoptic fulldisk observations of the sun in H α (Denker et al., 1999). The same applies to KSO, where high-cadence full-disk H α data are obtained since more than 25 years (Otruba, 1999). The characteristics of the H α imaging systems operated at each of the network's sites are summarized in Table 1. At each observatory a $2K \times 2K$ pixel CCD camera is in operation, allowing to obtain full-disk H α images with a resolution of 1 arcsec per pixel and a cadence of at least 1 image per minute. In case of a rapid solar activity change, this cadence can be increased to a rate of several images per minute. All cameras use the same Kodak KAF-4200 sensor, which is essential for obtaining a homogeneous and consistent data set.

Proc. 1st Solar & Space Weather Euroconference, 'The Solar Cycle and Terrestrial Climate', Santa Cruz de Tenerife, Tenerife, Spain, 25-29 September 2000 (ESA SP-463, December 2000)

<i>Table 1. Characteristics of the full-disk H</i> α <i>imaging sys-</i>
tems at Big Bear Solar Observatory (BBSO), Kanzelhöhe
Solar Observatory (KSO), and Yunnan Astronomical Ob-
servatory (YNAO). Both BBSO and KSO use an Apogee
KX4 CCD camerae, whereas YNAO operates a Kodak
Megaplus CCD camera. All cameras use a Kodak KAF-
4200 sensor. The meanings of the symbols and abbrevi-
ations are the following: geographical longitude (ϕ) and
<i>latitude</i> (β), <i>elevation</i> (<i>h</i>), <i>telescope aperture</i> (\otimes), <i>filter</i>
bandpass ($\Delta \lambda$), tunable filter range (FR), number of pix-
els (PN) , pixel size (PS) , and dynamic range (DR) .

	BBSO	KSO	YNAO
ϕ	$+116^{\circ}54.9'$	$-13^{\circ}54.4'$	$-102^{\circ}47.4'$
β	$+34^{\circ}15.2'$	$+46^{\circ}40.7'$	$+25^{\circ}01.5'$
h	2067 m	1526 m	1940 m
\oslash	15 cm	10 cm	18 cm
$\Delta\lambda$	0.05 nm	0.07 nm	0.05 nm
FR	$\pm 0.10 \text{ nm}$	$\pm 0.30 \text{ nm}$	$\pm 0.06 \text{ nm}$
PN	$2K \times 2K$	$2K \times 2K$	$2\mathrm{K} imes 2\mathrm{K}$
PS	$9 imes9\ \mu\mathrm{m}^2$	$9 imes9\ \mu\mathrm{m}^2$	$9 imes9\ \mu\mathrm{m}^2$
DR	14 bit	14 bit	8 bit

The largest time difference between the network sites is about 9.4 hours between BBSO and YNAO. The difference between BBSO and KSO is about 8.7 hours and that between YNAO and KSO about 5.9 hours. During the summer, each station can observe 12 hours on clear days. Therefore, during the summer months and good weather, there is no night-time gap. In winter, when each station is expected to operate 8 hours, the BBSO/YNAO gap will be about 1.4 hours and the BBSO/KSO gap about 0.7 hours. However, these short gaps are no real limitation because although occacionally a flare can be missed in winter time, we are still able to record the pre- and postflare evolution with high temporal resolution. Moreover, we do not intend to use the network data for FFT analysis, as it is the case with the GONG network and therefore such short data gaps are negligible. Based on long-term weather records of the three stations, we anticipate a 70% duty cycle in summers and 60% in winters.

3. DATA PRODUCTS

All data obtained by the network are processed in exactly the same way in order to produce a homogeneous data set. After correcting for dark current and flat-field, the average quiet sun limb darkening function is subtracted to obtain contrast-enhanced H α images. A detailed description of this data calibration can be found in Denker et al. (1999). Figure 1 shows one such high-resolution full-disk H α image obtained by the network. This particular image was observed at BBSO on June 6, 2000, at 15:42 UT with the 15 cm Singer full-disk telescope. Please note the uniform contrast throughout the whole disk, which facilitates the detection of chromospheric features like plages, filaments, and prominences. The first network observations have been obtained in March 2000 at BBSO, KSO, and YNAO. Since then we have been able to constantly improve the quality of the data. In Figure 2 we present a recent set of network data observed on August 23, 2000.

The central data archive of the network resides at BBSO, where the most recent network observations can be accessed through the World Wide Web (http://www.bbso.njit.edu/Research/Halpha/). Since the amount of high-cadence data (about 5 GB per day and per site on an average observing day) does not allow an instantaneous transfer by internet, the data from KSO and YNAO are sent on a regular basis to BBSO on exabyte and DLT tapes. At BBSO all network data are included into the recently upgraded archiving system (ftp://ftp.bbso.njit.edu/Archive/).

Besides high-cadence contrast-enhanced H α images of unique quality and resolution, we are going to provide lists with the positions and characteristics of all flares and filament disappearances, as well as lists with all new flux emergences observed on the sun.

4. SCIENTIFIC OBJECTIVES

In combination with space and ground-based observations, $H\alpha$ full-disk observations of high temporal and spatial resolution have been proven to be a key diagnostic for determining the magnetic field topology between the photosphere, chromosphere, transition region, and corona. We believe that large format CCD cameras and advanced image processing techniques provide a unique opportunity for studies with full-disk $H\alpha$ data. Among the scientific objectives of the new network are the following:

Feature Identification and Feature Tracking: Local correlation and feature tracking is used to determine global (differential rotation) and local flow fields (flows in active regions and filaments) from full-disk data. Discontinuities in currently available time sequences severely inhibits the accurate measurement of these flow fields.

Flare Monitoring: High-resolution $H\alpha$ images with 24 hours high-cadence coverage are essential to identify all the flares on the visible hemisphere of the sun and to derive a detailed picture of flare evolution and the underlying physical processes.

Filament Eruptions and Coronal Mass Ejections: Round-the-clock high-resolution full-disk H α data are extremely important for studying the correlation between filament disappearances and CMEs and for understanding their possible driving mechanisms. Figure 1 is an excellent example of how ground based observations and space observations can supplement each other for studying correlations between the various activity phenomena.

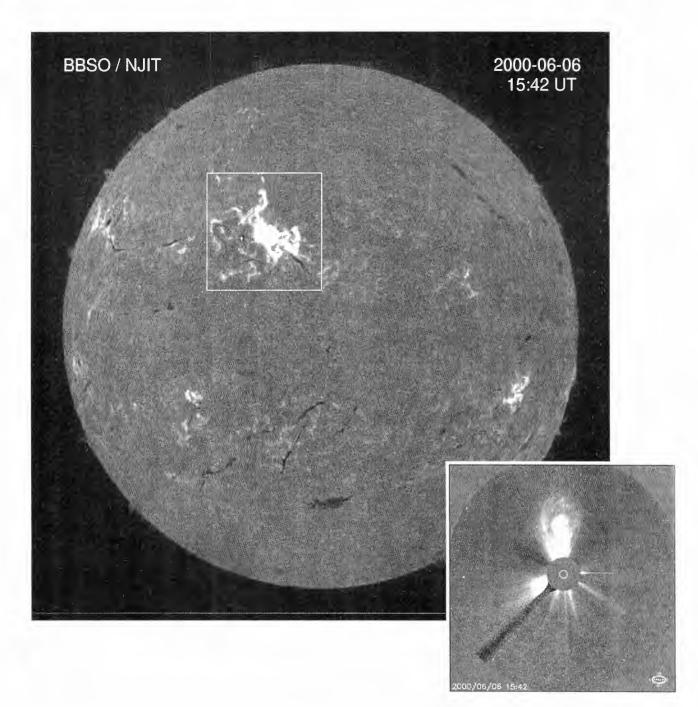


Figure 1. Contrast–enhanced full–disk $H\alpha$ image ($2K \times 2K$ pixel) obtained after correcting for dark current and flatfield, and after subtracting the average center–to–limb variation of the quiet sun. This image was recorded with Big Bear Solar Observatory's 15 cm Singer full–disk telescope on June 6, 2000, at 15:42 UT during the eruption of an X2.3 flare in NOAA 9026. This flare, whose position is marked by the white box (400×400 pixel), started at 14:48 UT and was associated with a halo CME and a severe magnetic storm. The inset in the lower right corner shows this magnificent CME on a SOHO/LASCO C3 image recorded at the same time, although the contrast of the halo is quite weak.

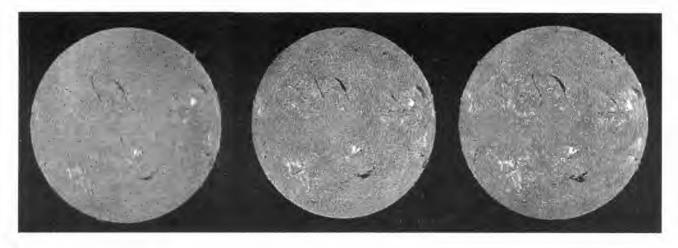


Figure 2. This series of contrast–enhanced H α images was obtained on August 23, 2000, at Yunnan Astronomical Observatory (03:11 UT, left), Kanzelhöhe Solar Observatory (06:37 UT, center), and Big Bear Solar Observatory (15:46 UT, right). Note the evolution of the filament in the southern hemisphere within only a few hours.

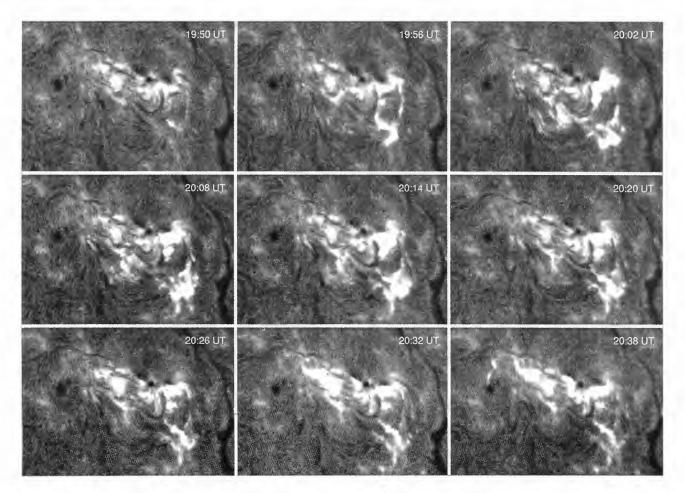


Figure 3. Temporal evolution of the M1.9 flare which erupted on July 10, 2000, at 20:05 UT (time of maximum X-ray flux measured by GOES) in the active region NOAA 9070. The frames are 300×210 pixel subframes of $2K \times 2K$ high-resolution full-disk H α images. The flare is located in the lower right corner of the active region. Only every sixth image of the actual observed 1 minute cadence data is shown.

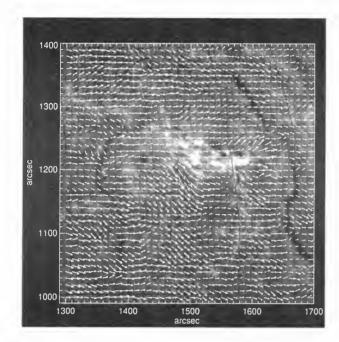


Figure 4. Average flow field around the M1.9 flare shown in Figure 3 derived by local correlation tracking (LCT) from 110 H α images obtained before the flare started to erupt (18:00 – 19:50 UT). Solar north is on the top and east on the left of the image.

Mini–Filaments: The energy release and mass ejections of erupting mini–filaments are of particular importance, since both can contribute to coronal heating and solar wind acceleration (Wang et al., 2000). With high– cadence and high–contrast H α data, the spatial distribution of mini–filaments is easy to measure and their detailed evolution can be studied.

Support of Space-Based Observations: The SOHO (Domingo et al., 1995) and TRACE (Schrijver et al., 1996) space missions are supported by supplying H α data from BBSO and KSO. By having available high cadence round-the-clock observations from three different sites, we are able to offer even more complete and homogeneous data sets for correlative studies with data obtained in space. Of special interest in this respect is the upcoming HESSI (Holman et al., 1997) mission which will be devoted to solar flare research. High quality H α data obtained simultaneously with the X- and γ -ray data from HESSI will be an essential tool to reveal the physics behind solar flare eruptions. Since HESSI will provide full-disk observations, continuous solar full-disk data obtained from the ground are vitally important.

Support of Ground–Based Observations: The data and aims of the new H α network are similar to those of the ISOON project (Neidig et al., 1997), which however is still not fully operational. Data from our network will be available to ISOON for closing data gaps and supplementing their observations. Additionally, our data analysis and forecasting tools can be adopted by ISOON. The Max Millennium Program (Canfield, 1999) and its coordinated observing campaigns will also profit from the availability of high–cadence and high–resolution network observations.

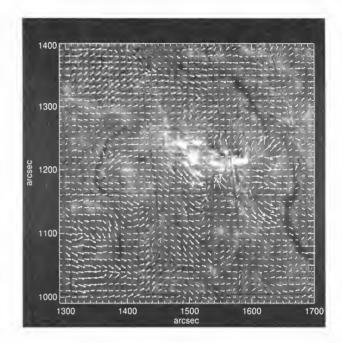


Figure 5. Flow field obtained by LCT from 75 frames observed during the flaring phase (19:50 - 21:15 UT).

Solar Activity and Space Weather Forecasting: Based on the detailed structure of the active regions monitored with high-cadence, we will predict the probability of flaring and filament eruptions. The automatic detection of filament and flare eruptions will extend the forecast times for space weather predictions.

5. PRELIMINARY RESULTS: FLOW FIELDS AROUND A FLARE

Although the network is in operation for only a few months and considering the fact that the first weeks after its installation have been mainly devoted to extensive testing and improving of the imaging and data archiving systems, we have already compiled a large amount of high quality contrast-enhanced full-disk data. One of the first questions which we try to answer with this material is, how the dynamics of the chromosphere is changing before and during a flare event. It is a well known fact that the proper motion of bipolar sunspot groups lead to shearing of the associated magnetic field lines, which in turn can trigger flares (see, e.g., Li et al., 1999: Raman et al., 1998; Wang et al., 1991). Additionally, the various components of a flare exhibit a pronounced dynamic behaviour during the flaring phase (for an overview see Martin, 1989). If there is a typical pattern in the motions around an active region observed in H α , it can be used as a precursor for flaring activity. There have been only a few attempts to address this problem, but with data of lower quality and resolution (e.g., Gutermuth, 1999).

For a first preliminary analysis we selected a flare which erupted in active region NOAA 9070 on July 10, 2000.

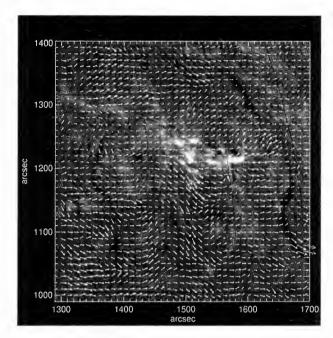


Figure 6. Flow field obtained by LCT from 80 frames observed after the flaring phase (21:15 - 22:35 UT).

In Figure 3 the temporal evolution of this M1.9 flare is shown, which reached the maximum of its X-ray emission at 20:05 UT as measured by the GOES satellite. A $600'' \times 600''$ subframe around NOAA 9070 is used to derive the average flow field by local correlation tracking from a 4.5 hour time series of calibrated high-cadence full-disk data. In each subframe the displacement between subsequent exposures is calculated for a grid of 60×60 evenly spaced points. The resulting displacement maps are converted into velocities and the average flow fields for the pre-flare, flaring, and post-flare phases are computed.

The first qualitative results of this analysis are shown in Figures 4 to 6. The displayed flow fields $(400'' \times 400'')$ around the active region) are represented by white arrows superimposed on the images and the lengths of the arrows denote the magnitude of the motions in arbitrary units. A comparison of these figures yields the following results: (a) The flow field is clearly changing between the different flare phases. (b) Before the flare erupts (Figure 4), there exists a strong southwest-ward flow at the southern edge of NOAA 9070. From the western edge of the active region, flows are moving outwards. No motions of the nearby filament can be detected. (c) In Figure 5 the dynamics of the flare eruption leads to an increased radial motion away from the western edge, whereas the flow around the southern part has weakened. Additionally, the lower part of the filament starts moving to the west. (d) During the post-flare phase (Figure 6), the flows around NOAA 9070 have slowed down noticeably, whereas the motion of the lower portion of the filament has clearly increased.

These preliminary findings are a promising hint for using the changes in the flow fields around active regions as a precursor for flaring activity, in addition to other parameters like, e.g., area, intensity, and complexity. In continuation of this work we will perform a detailed statistical analysis of a representative sample of flares of different structure, size, and evolution.

6. CONCLUSIONS

The new global H α network enables us to monitor the chromosphere of the sun continuously with high spatial resolution (1 arcsec per pixel) and high cadence (1 exposure per minute). The calibrated full-disk images available from the network are unique in quality and resolution. The availability of these data is essential for a variety of important scientific research projects, relevant for both solar physics and space weather.

ACKNOWLEDGMENTS

This work is supported by NSF under grants ATM-0076602, ATM-9714796, and ATM-9903515, by NASA under grants NAG5-4919, NAG5-7350, and NAG5-7085, and by ONR under grant N00014-97-1-1037. The SOHO/LASCO image used in this paper is produced by a consortium of the Naval Research Laboratory (USA), Max-Planck-Institut für Aeronomie (Germany), Laboratoire d'Astronomie (France), and the University of Birmingham (UK). SOHO is a project of international cooperation between ESA and NASA.

REFERENCES

Canfield R. C., 1999, AAS, 194, 8006

Denker C., Johannesson A., Marquette W. H., Goode P. R., Wang H., Zirin H., 1999, Solar Physics 184, 87

Domingo V., Fleck B., and Poland A. I., 1995, Solar Physics 162, 1

Goode P. R., Wang H., Marquette W. H., and Denker C., 2000, Solar Physics, in press

Gutermuth R. A., 1999, AAS 195, 10706

Holman G. D., and 18 co-authors, 1997, AAS 191, 7416

Li W., Lee C. Y., Chae J., Wang J., Goode P. R., Wang H., and Ai G., 1999, in Proceedings of the Ninth European Meeting on Solar Physics, ESA SP-448, 169

Martin S. F., 1989, Solar Physics 121, 215

Neidig D., and 10 co-authors, 1997, SPD 29, 0224

Otruba W., 1999, ASP Conference Series 184, 314

Raman K. S., Selvendran R., and Thiagarajan R., 1998, Solar Physics 180, 331

Schrijver C., and 13 co-authors, 1996, AAS, 188, 6704

Wang H., Tang F., Zirin H., and Guoxiang A., 1991, Astrophysical Journal 380, 282

Wang, H., and 7 co-authors, 2000, Astrophysical Journal 530, 1071

RECENT DEVELOPMENTS IN SOLAR INSTRUMENTATION AT THE INSTITUTO DE ASTROFÍSICA DE CANARIAS

I. Rodríguez Hidalgo¹

¹Instituto de Astrofísica de Canarias, La Laguna, Tenerife, Spain

ABSTRACT

This contribution corresponds to the report presented within the Meeting on Observing Techniques and Recent Instrumental Developments in Solar Physics.

The main advances in solar instrumentation during the past year at the Instituto de Astrofísica de Canarias (IAC) are reviewed. They concern with the upgrading of facilities for the Vacuum Newton Telescope (VNT) of the Observatorio del Teide (OT, Tenerife), and two last-generation full Stokes Polarimeters based on Ferroelectric Liquid Crystals (FLCs): LPSP (La Palma Stokes Polarimeter, first light in September 1998), for visible wavelengths, installed at the Swedish Vacuum Solar Telescope (SVST) of the Observatorio del Roque de Los Muchachos (ORM, La Palma), and TIP (Tenerife Infrared Polarimeter, first light in July 1998) for the near IR range, presently working at the Vacuum Tower Telescope (VTT) of the OT. Both instruments have been designed and developed at the IAC, in collaboration with the Royal Swedish Academy of Sciences and the Kiepenheuer Institut für Sonnenphysik, respectively.

Key words: solar instrumentation; visible photometry; infrared photometry; visible spectropolarimetry; infrared spectropolarimetry.

1. Upgrading of the Vacuum Newton Telescope

The VNT@OT operates now fully dedicated to the development of two long-term observing programs related to the solar cycle:

(i) Modeling of the variation of the solar irradiance. The aim is to fit the irradiance variations measured from space borne radiometers to ground-based measurements of parameters such like brightness and areas of magnetic regions in the Sun.

For this purpose, full disc images are taken on a daily basis since 1996. Obtaining full disc images requires a small refractor (7 cm of diameter, 100 cm of focal length) attached to the main tube of the VNT, sharing the tracking of the Sun. Several filters are available: three broad-band (blue, green, red), G band, and two Call K (10 and 3 Å half-width).

One example of a full disc image in the G band can be seen in Fig. 1.

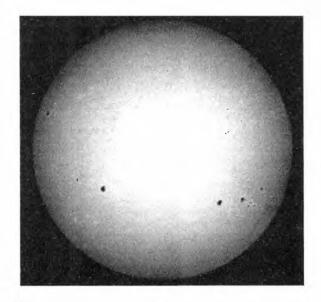


Figure 1. Full disc image in the G band taken with the VNT@OT

(ii) Variation of the infrared contrast in sunspots. The goal of this program is to verify, using new generation instruments, the variation of the sunspot contrast with the solar cycle, in wavelengths around 1.6 μ m, detected in the late sixties and early seventies (Albretgsen & Matlby 1978, 1981).

For this purpose, a IR detector (SU128-1.7 RT, 128×128 px of $60 \times 60 \ \mu$ m) placed at the focal plane of the telescope (scale: 0^{''}.22/pixel) takes images covering an ample range of sunspot sizes, positions on the disc, and phases along the activity cycle.

Two IR images (1.6 μ m) of sunspots and pores are shown in Fig. 2.

Proc. 1st Solar & Space Weather Euroconference, 'The Solar Cycle and Terrestrial Climate', Santa Cruz de Tenerife, Tenerife, Spain, 25-29 September 2000 (ESA SP-463, December 2000)



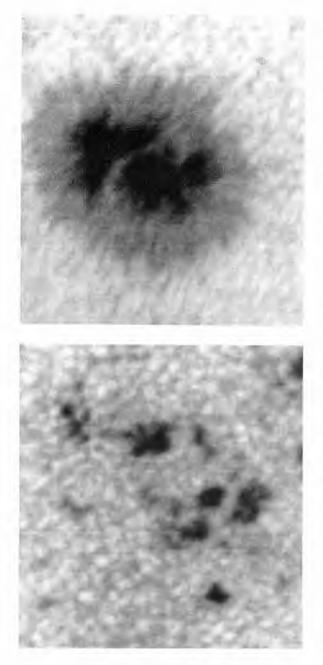


Figure 2. IR images at 1.6 μ m of sunspots and pores.

2. Visible and IR Polarimeters for the Canarian Observatories

These two analysers measure all 4 Stokes parameters almost simultaneously using a modulation scheme based on FLCs. Four images corresponding to 4 different states of the FLCs are needed to measure the whole Stokes vector, and a number of exposures for each of those states can be added to improve the S/N ratio. Details about these instruments can be found in Collados (1999) and Martínez Pillet et al. (1999).

Line spectra, time series of spectra, and twodimensional maps of Stokes I, Q, U, and V can be obtained with LPSP and TIP, by scanning the spatial direction perpendicular to the slit with the aid of available Correlation Trackers. 2.1. La Palma Stokes Polarimeter

The nominal wavelength (λ_0) of LPSP@ORM is 6300 Å. The detector used is a CHIL-CCD camera with 755×242 px of 8.5 μ m×19.75 μ m (spatial×spectral direction).

A field of view is $60'' \times 60''$ can be scanned in about 30 minutes. The spectral range at λ_0 is 4.3 Å, with a pixel size of $0''.157 \times 17.95$ mÅ.

Maps of the four Stokes parameters for a sunspot with a light bridge, and one example of slit spectra for a spatial point in the bridge can be seen in Fig. 3.

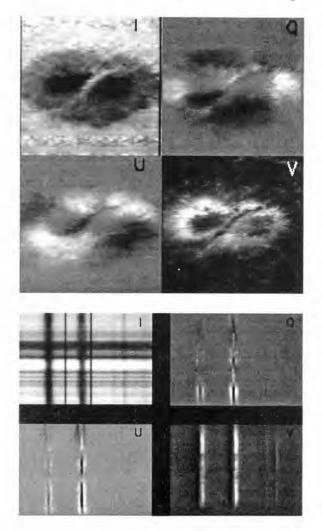


Figure 3. Maps of Stokes I, Q, U, and V corresponding to a sunspot. Spectra of the 6301 and 6302 Å FeI lines for a spatial point in the light bridge are also shown.

During this last year, two observing campaigns have been carried out to observe the four Stokes parameters at the solar limb for lines which are sensitive to scattering and Hanle effect.

In addition, LPSP has made a coordinate campaign with SOHO/MDI to provide a calibration of MDI magnetograms.

Finally, LPSP will be adapted to the New Swedish Solar Tower. The calcite beam-splitter should be changed due to the F/# two times smaller. An upgraded CCD and communication with the new image stabilisation system are also considered.

2.2. Tenerife Infrared Polarimeter

TIP@OT has been designed for a wavelength range from 1 to 2.3 μ m. Presently, a pair of FLCs is installed, valid for the H band (1.5 to 1.8 μ m, λ_0 =1.56 μ m). TIP uses a NICMOS-3 IR detector, with 256×256 px of 40 μ m×40 μ m.

A field of view is $40'' \times 40''$ can be scanned at steps of 0^{''}.4, in about 10 minutes. The spectral range at λ_0 is 7.4 Å, with a pixel size of 0^{''}.37×29 mÅ.

Four observational campaigns of different groups have been scheduled and succesfully carried out during this year within this spectral range. In particular, temporal series of 2D maps have been obtained last July for the first time. Fig. 4 shows a series of Stokes I and V maps of a quiet region at disc centre, lasting by about 1.5 hours.

A new pair of FLCs for the 1 μ m region have already been tested at the laboratory and the telescope. Nevertheless, their use is still restricted to the 1.13 to 1.23 μ m spectral range, due to problems with overlapping of diffraction orders, which are presently under study.

The new filter for 1.08 μ m, which includes the Hei 1.0830 μ m line, has been received during the Euroconference. The first tests at the telescope have been carried out by the end of September 2000.

Although FLCs sensitive to the 2μ m region are available and have been tested at the laboratory, this wavelength is not accessible for the moment, because the beam-splitter has null transmission in that band. The most plausible explanation is that one of the two crossed calcites absorbs the ordinary beam, and the other one absorbs the extraordinary beam. This is coherent with a paper by Oliva et al. (1997).

REFERENCES

Albretgsen, F. & Matlby, P. 1978, Nature, 274, 41

- Albretgsen, F. & Matlby, P. 1981, Solar Phys., 74, 147
- Collados, M. 1999, in 3rd Advances in Solar Physics Euroconference: Solar magnetic fields and oscillations (eds.) Schmieder, B., Hoffmann, A. & Staude, J., ASP Conf. Series 184, 3
- Martínez Pillet, V., Collados, M., Sánchez Almeida, J., González, V., Cruz-López, A., Manescau, A., Joven, E., Páez, E., Díaz, J.J., Feeney, O., & Sánchez, V. 1999, in *High Resolution Solar Physics: Theory, Observations and Techniques*, 19th NSO/Sacramento Peak Summer Workshop, (eds.) Rimmele, T. & Balasubramaniam, K.S., ASP Conf. Series 183, 264
- Oliva, E., Gennari, S., Vanzi, L., Caruso, A., & Ciofini, M. 1997, A&AS, 123, 589

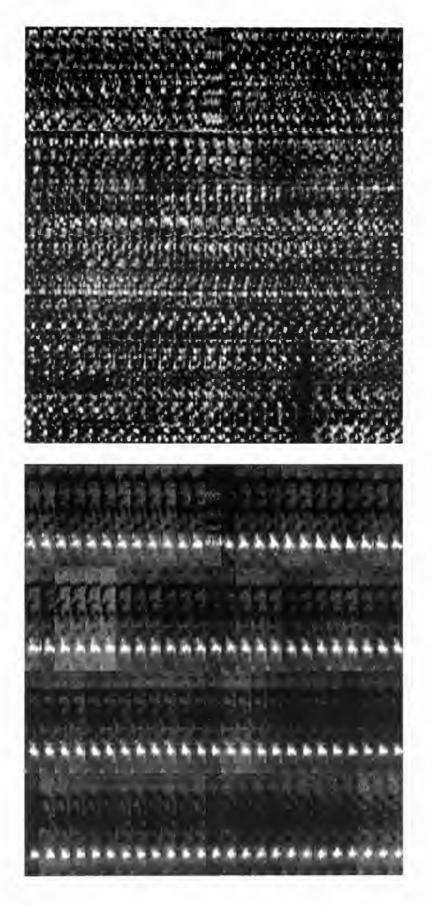


Figure 4. Time series (about 1.5 hours) of Stokes I and V maps corresponding to a quiet region at disc centre, obtained with TIP + CT at the VTT@OT on July 25, 2000. Each map consists of 15 adjacent positions of the slit (~ 38'' long), taken at steps of ~0''.4. The time step between two adjacent positions is about 1 min.

JOSO

Annual JOSO Meeting

GREGOR: A 1.5 M TELESCOPE FOR SOLAR RESEARCH

Oskar von der Lühe¹, Wolfgang Schmidt¹, Dirk Soltau¹, Franz Kneer², and Jürgen Staude³

¹Kiepenheuer-Institut für Sonnenphysik, Schöneckstr. 6, 79104 Freiburg, Germany
 ²Universitäts-Sternwarte Göttingen, Geismarlandstraße 11, 37083 Göttingen, Germany
 ³Astrophysikalisches Institut Potsdam, Telegrafenberg, 14473 Potsdam, Germany

ABSTRACT

GREGOR is a high resolution solar telescope with an aperture of 1.5 meter which will be equipped with an adaptive optics system. It is designed for highprecision measurements of the magnetic field and the plasma motion in the solar photosphere and chromosphere with a resolution of 70 km on the Sun. The focal plane instrumentation will include a high resolution filter spectrometer and a polarimetric spectrograph for the visible and the near-UV spectral range. GREGOR will replace the Gregory coudé telescope at the Observatorio del Teide on Tenerife.

1. INTRODUCTION

A new generation of large aperture telescopes is needed to understand the small-scale physical processes in the the solar atmosphere. These occur at spatial scales of 100 km and below and often involve very short time scales. Only a large aperture can collect enough flux within a short enough time to study the processes with sufficient photometric and polarimetric precision. An aperture which significantly exceeds the apertures of today's solar telescopes can actually resolve their structure.

GREGOR will be a Gregorian telescope – hence the name – with an aperture of 1.5 meter. It is designed for high precision polarimetric measurements. It will replace the 45 cm Gregory Coudé telescope at the Teide Observatory on Tenerife (Fig 1), which will be retired after 40 years of service. the existing building will be reused except for the dome. GREGOR will make use of modern technology and telescope design principles. Besides offering unprecedented scientific potential to its users, it will also serve as a test bed of new technologies of even larger ground-based solar telescopes.

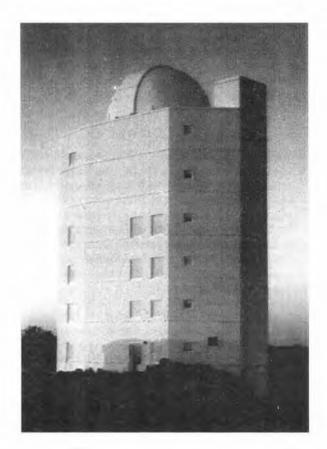


Figure 1. The Gregory Coudé telescope at the Teide Observatory.

Proc. 1st Solar & Space Weather Euroconference, 'The Solar Cycle and Terrestrial Climate', Santa Cruz de Tenerife, Tenerife, Spain, 25-29 September 2000 (ESA SP-463, December 2000)

2. SCIENTIFIC OBJECTIVES

The magnetic activity of the Sun plays a dominant role in virtually all processes in the solar atmosphere. It is responsible for the energy balance of the outer atmosphere, it causes the activity cycle and the concomitant variability of the solar luminosity, and it produces most of the sometimes spectacular phenomena like sunspots, prominences, flares and coronal mass ejections. Theoretical studies and numerical computations suggest that much of the interaction between the solar plasma and the magnetic field occurs on very small spatial scales of about 70 km on the Sun, corresponding to an angle of 0.1 arcsec. It is therefore important to have a large enough telescope which can resolve such small details. In addition, a large aperture is needed to achieve the photometric accuracy and sensitivity needed for a quantitative physical understanding of the solar magnetic field.

Topics which will be addressed by GREGOR include:

- Emergence, evolution and disappearance of magnetic flux in the solar photosphere: Magnetic flux appears at the solar surface as dipoles with a variety of sizes, from large spots to small magnetic elements. The total flux of the Sun is replaced within 2 or 3 days. Since the magnetic flux does not constantly increase, a mechanism for flux disappearance must exist. The corresponding processes occur on the scale of the smallest magnetic elements.
- Energy budget of sunspots: The strong magnetic field of a sunspot blocks the convective energy transport to the solar surface. This blocking effect qualitatively explains the presence of cool sunspots, but the sunspot temperature is much higher as one would expect from complete suppression of convective energy transport. Smallscale phenomena, like umbral dots or penumbral grains are likely to provide the observed heat flux in a sunspot.
- *Chromosphere:* The bright points at the boundaries and the interior of the supergranulation cells play a key role for the heating and the dynamics of the chromosphere. The size of and the wave motion in these structures need to be measured with high photometric precision and sufficient spatial resolution.

3. CHARACTERISTICS OF GREGOR

GREGOR will be located at the top of the building which currently houses the Gregory coudé telescope (GCT) and its spectograph (fig 1). The GCT will be removed and the top of the building will be refurbished. Fig 2 shows the new telescope mounted in an alt-az configuration. The telescope tube consists of an open Serrurrier truss which supports the main

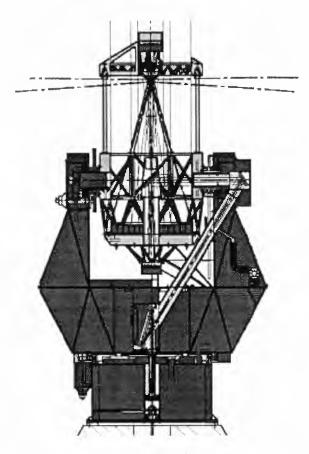


Figure 2. Sketch of GREGOR. Mount structure: blue, telescope tube: yellow, optical elements: red.

mirror cell, the top ring / secondary mirror assembly with a primary field stop, and a tertiary mirror assembly behind the primary mirror. A coudé train directs the sunlight through the mount structure to the fixed scientific foci in two observing areas underneath the telescope.

The entire telescope will be made light-weighted, which, despite the considerably larger aperture, can be supported by the building. The open concept makes an open dome necessary to avoid dome seeing. We presently consider a dome which is of the same design and slightly bigger than the one of the Dutch open telescope (DOT, Rutten et al. 1999) on La Palma. During operation the dome will be complutely folded down, allowing the air to flow freely through the telescope.

Wind buffeting will be minimized by a stiff mechanical design and a retractable wind shield. We currently investigate CO_2 cleaning of the mirrors for controlling contamination by the dust conditions which occur every now and then on the Canaries. A lightweight telescope implies lightweight optics; an open telescope implies strict thermal control of the telescope structure and the mirror surfaces to avoid internal and mirror seeing. We intend to address these problems with new materials for the optics as described in the following sections.

3.1. Optical Configuration

The optical design is a 3-mirror configuration where the first two mirrors form a classical Gregorian telescope (Fig 3). The design is very similar to that of the LEST telescope (Engvold et al. 1990), and has inherited much of its features. The first three mirrors (M1, M2 and M3) are curved to provide imaging. The primary mirror M1 is an f/1.75 paraboloid. A cooled field stop at the prime focus (F1) directs most of the sunlight sideways and transmits a field of view of 300 arcsec, of which the central 180 arcsec are unvignetted. There is a secondary focus (F2) near the center of the telescope tube where polarisation optics and a removable field lens will be placed. The field lens produces a pupil image suitable for adaptive optics further down the light path. Focusing of the telescope is achieved by an axial translation of M3.

A folding flat (M4) directs the light towards the coudé train and to the scientific focal plane (F3) in the observing room below the telescope. The coudé train is accomodated within the mount structure which also gives room for an optical bench with adaptive optics near its central part. The two folding mirrors M6 and M7 at the center of the fork are located near a 110 mm diameter image of the pupil and will be used for fast guiding and adaptive optics. A folding flat M8 directs the light horizontally towards the science focus. M8 can be removed to let the light pass through the floor into the room below. The effective focal length is 75 m and the final f/50 focal plane can be directed towards two laboratories in the two stories below the telescope.

The absence of vacuum windows makes the entire infrared spectral regime accessible, including the thermal IR Johnson N and Q bands at $10\mu m$ and $20\mu m$. as soon as the field lens is removed from the optical path. The adaptive optics will not be required at these wavelengths.

3.2. Lightweight Technology

The current concept includes lightweighted silicon carbide (SiC) as the material of choice for the first three mirror blanks. This results in an estimated weight of about 150 kg for the 1.5 meter primary. SiC has a thermal conductivity which is about 100 times that of conventional glass ceramics and which results in excellent thermodynamic stability and a very homogeneous mirror temperature. This property is crucial for a precise control of the air temperature fluctuations in front of the mirror surface. the main cause of internal seeing of an open telescope. The primary absorbs about 170 W when the telescope is pointed to the Sun. This heat will be disposed of by active cooling of the mirror from the back side, maintaining its temperature close to the ambient.

Since large SiC optics are still challenging today's

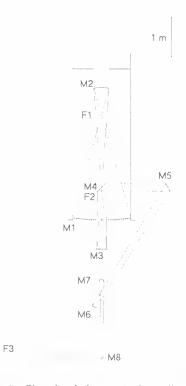


Figure 3. Sketch of the optical configuration.

technology, we are conductung a development program with the German industry. Fig 4 shows the back side of the lightweighted prototype of the tertiary mirror M3, with which the feasibility of stable, polishable surface layers on large SiC blanks could be demonstrated. The 36 cm diameter blank weighs 2.5 kg. We are now starting the development of the primary mirror.

The lightweight mirrors considerably reduce the overall weight of the telescope. This increases the lowest resonance frequency and the stiffness of the mount structure, thus reducing its sensitivity to wind-induced vibrations.

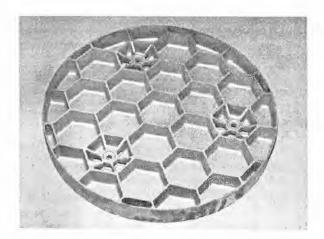


Figure 4. Back side of the M3 prototype, showing the lightweight structure.

3.3. Adaptive Optics

Adaptive optics (AO) is essential for high resolution observations from the ground, and the only way to reconcile the conflicting requirements on spatial, spectral and temporal resolution and photometric precision. In the current concept, GREGOR will be equipped with a "first-level" AO system which will be capable of compensating 64 degrees of freedom (about 150 actuators) with a closed-loop frequency of 150 Hz. Such a system would achieve a Strehl ratio of better than 0.5 for about 20 % of the time under the atmospheric conditions at Izaña.

A Hartmann-Shack wavefront sensor measures the deformed wavefront near the science focus. The linear terms of the deformation will be fed back to a long range tip-tilt mirror to remove the major part of the error. The low-frequency part of the terms corresponding to Seidel coma and spherical aberration will be used to control the alignment of M2 with respect to M1 in three translational degrees of freedom. The low-frequency part of the focus term will control the axial position of M3, which will also be used for focusing.

3.4. Focal-plane instruments

Focal plane instruments will be installed in the present observing room and in the spectrograph room of the GCT, which comprise the two topmost floors of the building. A sketch of the upper floor with the telescope at the center and fixed optical benches with instruments is shown in fig 5. M8 will be rotated to direct the light to the desired table.

GREGOR will be equipped with a high-resolution Fabry-Perot filter spectrometer and a polarimetric spectrograph for the visible and near-UV wavelength range. Both instruments will be installed in the top floor. The existing Czerny-Turner spectrograph in the room below will be remodeled to be used with the new telescope.

4. CONCLUSIONS

GREGOR combines several important goals for observational solar astronomy in Germany in an ideal fashion. Most important is the access to a first class observing facility which represents a major step in scientific potential compared to current solar telescopes. This is accomplished by the large collecting area and spatial resolution in combination with the adaptive optics system and the excellent site. Another important aspect is the application of new technology to improve solar telescopes, which could serve as an example for future large solar telescope projects.

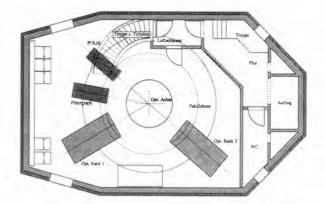


Figure 5. Horizontal cross section of the top observing floor. The round structure near the center is the lower part of the telescope mount at the level of M8. Several optical benches accomodate post focus instruments.

ACKNOWLEDGEMENTS

Many concepts which were developed for LEST found their way into the GREGOR design. We owe to the scientists and engineers who devoted their time and ideas to LEST, most notably to its project director Oddbjørn Engvold. Torben Andersen and Mette Owner-Pedersen did a great job in supporting the optical and mechanical design, and in helping us with many difficult decisions.

REFERENCES

- Engvold, O., Andersen, T. (Eds.) 1990, LEST Design, LEST Foundation Design Report
- Rutten, R., Hammerschlag, R. H., Bettonvil, F. C.
 M. 1999, in *Solar and Stellar Activity*, C. J. Butler,
 J. G. Doyle (Eds.), ASP Conf. Ser. 158, 57-60.

Poster Papers

JOSO Meetings

LONG-TERM OBSERVATIONS OF SOLAR ACTIVE REGIONS AT THE VNT

J.A. Bonet, R. Casas, C. Giammanco, V. Martínez Pillet, and M. Vázquez

Instituto de Astrofísica de Canarias, E-38200 La Laguna, Spain

ABSTRACT

A long-term programme of observations at the Vacuum Newton Telescope is described. It consist of two main parts: 1) full-disc observations in six different filters to determine the different contributions of magnetic structures (sunspots, plages and network) to the solar irradiance fluctuations and 2) a study of the variation of the IR contrast of sunspots with the solar cycle.

I. INTRODUCTION

The Vacuum Newton Telescope (VNT) was installed at a pre-existing solar tower at the Observatorio del Teide, Tenerife, on 1972 June 17. Designed and constructed by the Fraunhofer Institute (now Kiepenheuer Institute, Freiburg, Germany), it had previously been used in sitetesting campaigns in the Mediterranean area and after some improvements (evacuation and a new mounting) it was transferred to Tenerife for testing the promising characteristics of the Canarian Observatories for solar observations.

In the seventies, this telescope was almost exclusively dedicated to site-testing campaigns that culminated in a comparative analysis between the Roque de los Muchachos (La Palma) and Teide (Tenerife) Observatories in 1979 (Brandt & Wöhl, 1982). Mattig & Casanovas (1975) and Vázquez (1987, 1991) report on the instrumentation existing during these periods and the main scientific results achieved.

When starting the operation of other solar telescopes in the Canaries (VTT, GCT, SVST and THEMIS) we considered that the full dedication of the VNT to long-term observing programmes would optimally fit its performance. Consequently, we are presently running on the VNT two scientific programmes which are described below. One of these programmes requires an additional instrument-the Full Disk Images (FDI) telescope-that has been attached to the main telescope sharing the tracking of the Sun (see Figure 1).

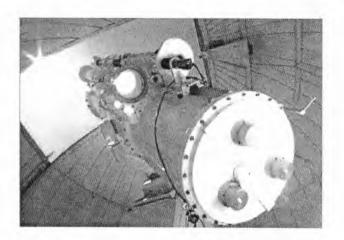


Figure 1. Vacuum Newton Telescope (VNT) operating at Observatorio del Teide (Tenerife). The main mirror has an aperture of 40 cm and a focal length of 3 m. A secondary magnification system gives an effective focal length of 37.5 m (image scale = 5.5''/mm). The evacuated tube is closed by a BK7 entrance window of diameter 50 cm. The FDI telescope can be seen riding on the upper part of the VNT.

2. SIMULATION OF VARIATIONS IN SOLAR IRRADIANCE (PROGRAMME 1)

The variation of irradiance with the solar cycle has been measured by space borne radiometers since 1980 (see, for example, Vázquez, 1999; White, 2001, these proceedings). However, information covering longer periods in the past are crucial for comparison with climatic records, and consequently simulations of the solar irradiance variation for these periods are needed. These simulations can be derived only from fits of the current irradiance variations to ground-based measurements of parameters such as brightness and areas of magnetic regions on the Sun, which have been monitored for many years now.

As the solar radiometers integrate spatially the information over the entire solar disc, images including the full disc are accordingly needed for a reliable measurement of the above mentioned parameters (see examples in Figures 2 and 3).

Proc. 1st Solar & Space Weather Euroconference, 'The Solar Cycle and Terrestrial Climate', Santa Cruz de Tenerife, Tenerife, Spain, 25-29 September 2000 (ESA SP-463, December 2000)

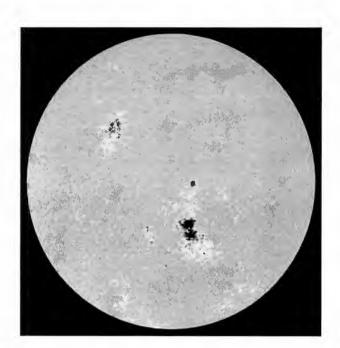


Figure 2. Solar disc at λ 393.3 nm (Ca II K), fwhm=1.5 nm, corrected for limb-darkening. The image was recorded with the FDI telescope described in the text, on 2000 September 22.

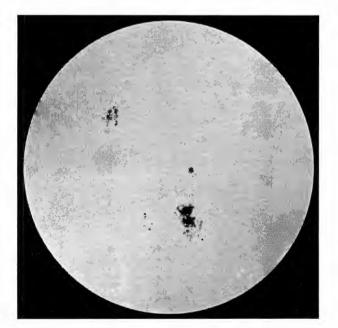


Figure 3. Solar disc at λ 425.0 nm, fwhm=15 nm, corrected for limb-darkening. The image was recorded with the FDI telescope on 2000 September 22.

2.1. The FDI telescope

For the purpose of recording full-disc solar images, in 1996 we coupled to the main telescope a small refractor of aperture 68 mm and focal length 600 mm. The telescope was equipped with a CCD videocamera (PULNIX) operating at a rate of 25 frames/s and a frame-grabber, giving a pixel size of 5". A system of cross-polarizers allowed fine tunning of the light level, and the images were taken in the interferential filters listed in Table 1.

Table 1. F	Filters c	perating	on the	FDI	telescope
------------	-----------	----------	--------	-----	-----------

Wavelength (nm)	FWHM (nm)	Colour
425.0	15.0	blue
520.0	15.0	green
630.0	20.0	red
430.8	1.1	G-band
393.3	1.5	Ca II K
393.3	0.3	Ca II K

Focusing, tuning of cross-polarizers and filter selection were remote-controlled by motors, and the best images within an optional period were selected and recorded by the SAIS (System for Automatic Image Selection). All these devices for image acquisition were developed at the IAC. Images were collected on a daily basis from 1996 to 1998, and in 1999 the system was updated as follows:

- The former FDI telescope was replaced by a larger refractor of aperture 70 mm and focal length 1000 mm.
- The videocamera was substituted by an 8-bit CCD camera (DALSA) 1024 \times 1024 pix, operating at a rate of 40 images/s, and with a pixel size of 12 μ m.
- A new version of the System for Automatic Image Selection, SAIS-II, adapted to the new framegrabber and including more capabilities, was implemented.

Figure 4 shows a sketch of the new FDI telescope and the equipment attached to it. The combination of the new camera and new optical configuration produces a final pixel size of 2.475". Significant effort has also been made to improve the software for reduction of data mainly as far as the flatfield correction is concerned. The latter is based on the paper by Kuhn, Lin & Loranz (1991).

3. VARIATION IN IR BRIGHTNESS WITH THE SOLAR CYCLE (PROGRAMME 2)

During the late sixties and early seventies the Oslo group (Maltby and collaborators) carried out systematic observations of sunspot contrast with a pinhole photometer in a

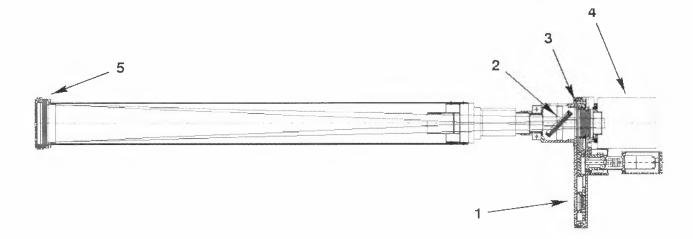


Figure 4. Sketch of the FDI telescope: 1) wheel housing the interferential filters; 2) a beam-splitter to deflect energy outside the telescope; 3) cross-polarizers to modify the light level incident on the chip; 4) an 8-bit CCD camera (DALSA) 1024×1024 pix, and 5) a holder for diaphragms and/or neutral density filters.

wavelength range from the visible to IR. One of the highlights of their work was the detection of variability in the sunspot contrast during the solar cycle at two wavelength ranges centred on 1.6 and 2.2 μ m (Albretgsen & Maltby, 1978, 1981).

Several interpretations of this variability have been offered (e.g. Schüssler, 1980; Yoshimura, 1983). However, these observational results need urgent confirmation with more powerful instrumentation. With this purpose in March 1999 we started an observing programme at $\lambda 1.6$ μ m, in an attempt to get an adequate coverage of sunspot sizes, positions on the disc and phases during the solar cycle.

3.1. Instrumentation

For the IR programme the main telescope (40 cm aperture and 37.5 m effective focal length) is used. Images are taken with a SbIn detector from Sensors Unlimited, 128 pix square with a pixel size of 40 μ m, which corresponds to 0.22"/pixel in the focal plane.

The image acquisition is performed using the SAIS-II, which is also switched to operate with the IR camera. The small field of view included in the chip of the camera means that large sunspots have to be mosaicked. To overcome this drawback very efficient and user-friendly software has been developed to assemble post facto the different regions of a large sunspot (see Figure 5).

Our aim is shortly to modify the secondary optics of the Newton in order to reduce the latter's effective focal length by a factor of 2 so that the field of view is twice as large. Also in the new version, the focusing mechanism and the device to interchange neutral density filters will be motorized to be remote controlled.

A code has been developed to flatfield the images and to determine in a quick and routine way the brightness, area and histogram of umbrae and penumbrae so that statistical analysis of a large sample of sunspots is made possi-

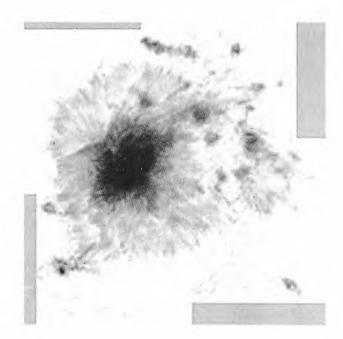


Figure 5. Example of the results achieved with the code developed for assembling frames including different sunspot sub-fields. In this case four frames have been assembled. The image corresponds to a sunspot in $\lambda 1.6$ µm (2000 August 10).

3.2. Aerosols and stray-light

Stray-light, of both instrumental and atmospheric origin, is one of the most notable disturbing factors in the correct determination of sunspot contrast. Although its influence decreases with increasing wavelength it is still noticeable at IR.

In the first phase of our observing programme, we are taking daily IR images of the solar limb to estimate its degradation and from this infer the shape of the spread function that will be used in the stray-light correction.

In a second phase of the programme we will use aureola measurements out to a distance of 1 solar radius for a more complete determination of the spread function. The records of aureolas will be performed with a pinhole photometer at several wavelengths in the visible to establish their dependence on λ and subsequently extrapolate to the IR (1.6 μ m) using an aerosol model by González Jorge et al. (1998).

ACKNOWLEDGEMENTS

We thank the large team of observers who have participated in the observing programme (C. Abajas, L. Chinarro, M. Dovrinčic, A. Gómez, J. Licandro, S. López, A. Pimienta, and K. Puschmann). We are grateful to the personnel of the IAC's Instrumentation Division who developed the existing instrumentation (A. Díaz, F. Gago, A. García, E. Joven, R. López, J.L. Rasilla, and M. Reyes). This project has been partially financed by the Spanish DGESIC under grant 95-0028.

REFERENCES

Albretgsen F., and Maltby P., 1978, Nature 274, 41

- Albretgsen F., and Maltby P., 1981, Solar Physics 71, 269
- Brandt, P.N., and Wöhl, H., 1982, Astronomy and Astrophysics 109, 77
- González Jorge, H., Martínez Pillet, V., Vázquez, M., Pallé, P., Mc Govern, F., and Raes, F., 1998, New Astronomy Reviews 42, 515–520
- Kuhn, J.R., Lin, H., and Loranz, D., 1991, Publications of the Astronomical Society of the Pacific **103**, 1097– 1108
- Mattig, W., and Casanovas, J., 1975, JOSO Annual Report 1975
- Schüssler, M., 1980, Nature 288, 150
- Vázquez, M., 1987, in The Role of Fine-scale Magnetic Fields on the Structure of the Solar Atmosphere, E.H. Schröter, M. Vázquez, A. Wyller (eds.), Cambridge University Press, p. 370.

- Vázquez, M., 1991, Astrophysical Letters & Communications 28, 113-130
- Vázquez, M., 1999, in Motions in the Solar Photosphere, A. Hanslmeier, M. Messerotti (eds.), Kluwer Academic Publishers, p. 169.

White, O.R., 2001, these proceedings

Yoshimura, H., 1983, Solar Physics 87, 251

SOLAR PATROL AT CATANIA ASTROPHYSICAL OBSERVATORY

L.Contarino¹, P.Romano¹, M.Ternullo², R.A.Zappalà¹, and F.Zuccarello¹

¹Dipartimento di Fisica e Astronomia - Università di Catania, Città Universitaria, Via S.Sofia 78 - Catania

²Osservatorio Astrofisico di Catania - Città Universitaria, Via S.Sofia 78 - Catania

ABSTRACT

A synthetic description of solar observations carried out at Catania Astrophysical Observatory in the optical range is given. More precisely, the Catania Astrophysical Observatory history, the instrument characteristics, the data obtained by reduction of images, the data distribution list, the international cooperations and the main research topics are reported.

Key words: Solar Optical Observations: Photosphere; Chromosphere.

1. HISTORICAL INTRODUCTION

Optical observations of the solar photosphere and chromosphere have been carried out at Catania Astrophysical Observatory since 1880, year of its foundation.

In 1906 Annibale Riccò (1844-1919) started the regular program of solar patrol in the H α of H and K of Ca II lines in the old seat of Catania Astrophysical Observatory (fig. 1(a)). Visual observations of sunspots and rapid evolution phenomena made since the first years of observations are keepen in our archives (see figg. 2 (a) and 3 (a)).

In 1910, in cooperation with G. Hale, he carried out the first observations with a spectroheliograph on the Mt. Etna at 3000 meters above see level.

Solar observations were carried out with a certain continuity also during the world wars.

In 1955 Mario G. Fracastoro organized the move of all the instruments for solar observations in the present seat situated at the Città Universitaria (fig. 1 (b)).

Due to the acquired experience and competences, to the quality of operating instruments, to the good seeing and to its geographycal position, since 1970 Catania Astrophysical Observatory has taken part in the International Program MONSEE (Monitoring of the Sun-Earth Environment) for systematic observation and data exchange in solar-terrestrial research activities. The MONSEE program operates under the auspices of the Scientific Committee on Solar Terrestrial physics (SCOSTEP) of the International Council of the Scientific Unions (ICSU).

Between several international cooperations, we would like to mention the one which took place in 1973 with the ATM project of the Skylab mission (Italy-ASE cooperation). Catania Astrophysical Observatory, besides than beeing involved as a scientific partner during the phase of the instruments planning, also played the following roles during the manned mission: first, in alerting the astronauts when a flare was taking place, not to risk going outside the vehicle during the high energetic bombardment following the event, and second in indicating the most interesting regions where the ATM telescope had to be pointed.

Moreover, besides than the historical background, we would like to stress that all the researchers involved in Solar Physics in Catania have always intended the work of sistematic observation of solar activity to be a fundamental reasearch, also devoted to a continuous improving and testing of instruments and technologies and to the formation of new experimental researchers in the field of Astrophysics.

Moreover, the acquisition of data in the optical range, besides than beeing an invaluable inheritance for future generations, has been and will be unreplaceable to deepen solar physics topics together with space observations.

2. INSTRUMENTS

At present, the instruments used for solar observations are inside the Catania Astrophysical Observatory (lat= 37° 31' 4".2 N, long= 1h 00m 17.4s E. h= 193 m asl).

The program for the observations is performed by means of an equatorial spar which includes three instruments:

- a) Cook refractor, used to make daily drawings of pores and sunspots from visual observation;
- b) 150 mm refractor (focal length of 230 cm) with a H α Lyot-filter (bendwidth of 0.25 or 0.50 .4) and a 1024 × 1024 (24.6 × 24.6) CCD array (in

Proc. 1st Solar & Space Weather Euroconference. The Solar Cycle and Terrestrial Climate'. Santa Cruz de Tenerife. Tenerife. Spain. 25-29 September 2000 (ESA SP-463, December 2000)

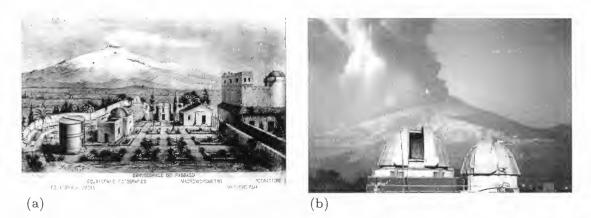


Figure 1. (a) The Catania Astrophysical Observatory at the beginning of the last century; (b) the domes containing the instruments for solar observation in the present seat at the Cittá Universitaria.

patrol mode the camera can take images every 40 sec);

c) 150 mm refractor feeding a H α Halle-filter for limb observations.

The program performed by means of these instruments includes : daily drawings of sunspots and pores by projection of the Sun image (fig. 2 (b)); digital image acquisitions (every 15 minutes) in the H_{α} line center and wings, besides than the monitoring of transient phenomena, like active prominences (fig. 3 (b)) and flares (fig. 4).

3. DATA REDUCTION AND DISTRIBUTION

Each day, one white light and one H_{α} image (fig. 5) are available on the official Web site of the Catania Astrophysical Observatory.

Moreover, from observations we deduce the following data :

- Sunspots: latitude, longitude, Carrington longitude, type according to Zurich classification, sunspots number, pores number, projected area in millionths of the solar hemisphere;
- Hα faculae : latitude, longitude, Carrington longitude, compactness, projected area in millionths of the solar hemisphere;
- Hα flares : time of beginning, time of maximum, time of end, latitude, longitude, projected area in millionths of the solar hemisphere, maximum intensity referred to the local undisturbed chromosphere;
- Hα quiescent prominences : latitude, longitude, height in arc seconds, area in Prominence Area Units (U.P.);
- Hα active prominences : latitude, longitude, time of beginning, time of end, importance according to standard international rules.

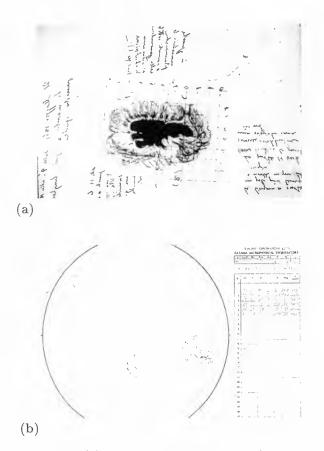


Figure 2. (a) Example of the drawing of a sunspot made in 1865; (b) drawing of sunspots and pores (on the left) and table containing data for each sunspot group (on the right (20 September 2000)).

These data are regularly distributed to the following Observatories : Boulder, Moscow, Freiburg, Meudon, SIDC Bruxelles, Cracow, Bologna, Trieste. During the period 1967-1995 all the reduced data were yearly published in a Bulletin (Ternullo, 1990a). Data since 1995 to date, will be soon distributed by means of our web pages.

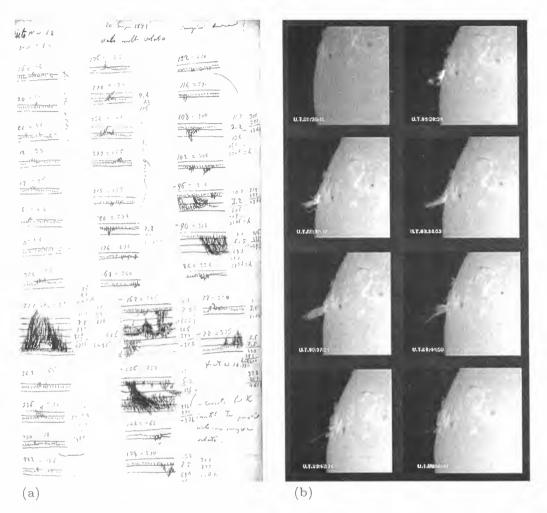


Figure 3. (a) Example of a chromospheric prominence drawing made in Catania in 1881; (b) example of a BSL observed with $H\alpha$ Zeiss filter (03 December 1999 - 11 N 80 E (O.A.C.)).

4. RESEARCH ACTIVITY AND FUTURE DEVELOPMENTS

Research activity carried out at Catania Astrophysical Observatory in the field of solar physics mainly concerns the following topics :

- determination of the photospheric angular velocity by tracers (Zappalà and Zuccarello, 1991). (Ternullo, 1990b);
- study of the interaction between photospheric tracers and plasma (Zuccarello,1993);
- determination of the variability of the solar differential rotation as a function of the phase of the activity cycle (Paternò et al.,1991, Zappalà and Zuccarello,2000):
- maintainance of the solar dynamo (Belvedere et al.,1991);
- static loops modelling (Van den Oord & Zuccarello,1996):
- mechanisms of storage of magnetic energy in coronal loops (Zuccarello et al.,1987, Zappalà and Zuccarello,1989);

- diagnostics of plasma in the transition region and corona (Ventura and Spadaro,1999):
- study of transients by means of a comparative analysis between ground-based and satellite images (Zuccarello and Romano,1999, Zuccarello et al.,2000);
- Sun-Earth connection.

As to the last point, we would like to stress that sistematic observations of solar phenomena is necessary for the comprehension of mechanisms which cause sudden variations in the heliosphere where the Earth is dipped.

The Sun is in fact the source of the solar wind : a flow of gases that streams towards the Earth at speeds more than 500 km per second. Disturbances in the solar wind shake the Earth's magnetic energy and provide energy to the radiation belts. Moreover, regions on the surface of the Sun often flare-up and give off ultraviolet light and x-rays that heat up the Earth's upper atmosphere. This Space Weather can change the orbits of satellites and shorten mission lifetimes. As we become more dependent upon satellites in space we increasengly feel the effects of space weather and need to predict it.

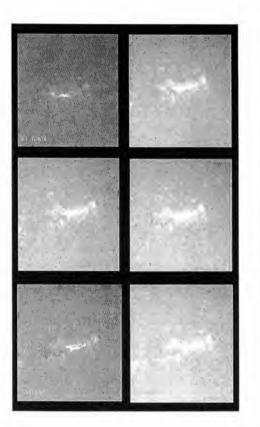
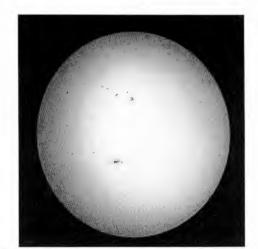


Figure 4. Example of a two ribbon flare observed at the line center of the $H\alpha$ line (19 November 1999 - 16 N 28 W (O.A.C.)).

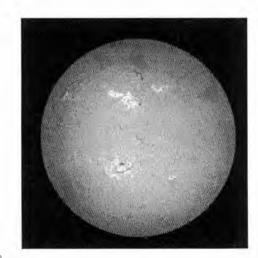
In the framework of this question, thanks to the compentences of the Catania solar physics group and to the metheorologic conditions which ensure good seeing for more than 350 days per year, the Catania Astrophysical Observatory, is strongly involved in the Space Weather Program.

REFERENCES

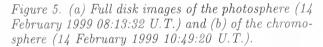
- Belvedere, G., Proctor, M.R.E., Lanzafame, G., Lecture Notes in Physics, 380, 237, 1991
- Paternò, L., Spadaro, D., Zappalà, R.A., Zuccarello, F., A&A, 252, 337, 1991
- Ternullo, M., Solar Observations made at Catania Astrophysical Observatory during 1990, 177, ISSN 1120-8430, 1990a
- Ternullo, M., Solar Phys., 127, 29, 1990b
- Van den Oord, G.H.J., Zuccarello, F., Stellar Surface Structure, K.G. Strassmeier and J.L. Linsky eds., 433, 1996
- Ventura, R., Spadaro, D., A&A, 341, 264, 1999
- Zappalà, R.A., Zuccarello, F., A&A, 214, 369, 1989
- Zappalà, R.A., Zuccarello, F., A&A, 242, 480, 1991
- Zappalà, R.A., Zuccarello, F., A&A, submitted, 2000
- Zuccarello, F., Burm, H., Kuperus M., Raadu, M., Spicer, D.S., A&A, 180, 218, 1987
- Zuccarello, F., A&A, 272, 587, 1993



(a)







- Zuccarello, F., Romano, P., Proc. 9th European Meeting on Solar Physics (ESA SP-448; Florence, Italy), 907, 1999
- Zuccarello, F., Contarino, L., Romano, P., Solar Phys, submitted, 2000

OPTIMAL WINDOWS TO DETERMINE SOLAR GRANULATION IMAGE QUALITY

C. Giammanco

Instituto de Astrofísica de Canarias, E-38205 La Laguna, Spain

ABSTRACT

Information theory can help us to determine an optimal window (Giammanco, 2000) for image analysis; therefore, the size of the window is a good estimator of image quality. The Optimal Window Method (OWM) is sensitive to the size of the structure present in the image and indicates features that are more or less smeared out.

1. THE OPTIMAL WINDOW METHOD

We define the quality of an image according to the amount of detail that can be seen in it. In this way the quality of a flatfield image containing no detail is made equal to 0 and the quality of any other image is given by a suitable definition of its distance from the flatfield image.

For this purpose, we divide the whole image into $p \times p$ windows and denote by n_p the number of windows that are not "flat" out of the total of N_p windows obtained (of course n_p and N_p depend, for a given image, on the width, p, of the windows). Information theory suggests that the optimal value, p_o , corresponds to the maximum of the entropy:

$$S_p = r_p \cdot \ln_2(r_p) - (1 - r_p) \cdot \ln_2(1 - r_p), \quad (1)$$

where $r_p = n_p/N_p$, and we can use p_o as a quality parameter of the image (when p_o increases, the image worsens). We must emphasize that p_o is not the resolution in pixels, although it is related to it; a possible calibration is under study.

This method appears to be more suitable than that previously used, based on image contrast (Collados & Vázquez, 1987), (Ricort et al., 1981), because the quality of each image is now mainly determined by the presence of small structures, while the contrast can be significantly influenced by large-scale variation.

To prove this we present two images of granulation in Figure 1; the time delay between them is about 7 minutes. Their quality have been evaluated by the popular contrast method and by the OWM. The results are conflicting: the contrast method gives the image in Figure \mathbf{b}), which is

better than simple visual analysis; the OWM gives the image in Figure **a**).

The corresponding quality maps are on the right of each figure. Note the large black areas in the map of image \mathbf{b} , which appear darker and contribute to the contrast but are of poor quality.

2. CONCLUSIONS

A method of determining the quality of granulation images has been presented that can be applied in other astrophysical contexts.

Its characteristics are that very different images can be compared with them, and they provide a quality map of image and a parameter that can be related to the spatial resolution (after calibration).

The method is useful for following the time evolution of instrument performance and choosing the best images of a large time series. The quality maps may be useful for optimizing image restoration software and compressing images by a factor p without loss of information.

ACKNOWLEDGMENTS

This work is based on observation obtained with the IPM (Cavallini, 1998) mounted on the THEMIS-CNRS/INSU-CNR telescope at the Spanish Observatorio del Teide (Tenerife) of the Instituto de Astrofísica de Canarias.

REFERENCES

Ricort et al. :1981, Solar Phys., 69, 223

Collados, M., Vázquez, M.: Astron. Astrophys., 180, 223

Giammanco, C.: A& AS., in press

Cavallini, F.: 1998 A&AS 128,589.

Proc. 1st Solar & Space Weather Euroconference, 'The Solar Cycle and Terrestrial Climate', Santa Cruz de Tenerife, Tenerife, Spain, 25-29 September 2000 (ESA SP-463, December 2000)

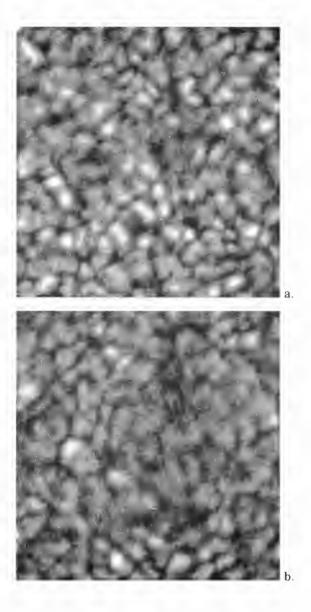


Figure 1. The images of different quality classes: **a**) contrast = 4.4%, $p_0 = 6$, **b**) contrast = 5%, $p_0 = 8$. The indications given by the two quality parameters are opposite. The contrast method gives image **b**) as the best, while it is apparent from visual inspection that image **b**) has better resolution.



Figure 2. Quality maps of the images shown in Figure 1. The images were divided in 6×6 windows, corresponding to the optimum width for image **a**). The detailed windows are given in white, "flat" windows in black. Note the presence in **b**) of a large black region which, nevertheless, contributes significantly to the higher contrast of **b**) with respect to **a**).

STANDARDIZED COORDINATE SYSTEMS FOR SOLAR IMAGE DATA

William T. Thompson

Emergent IT, Inc., NASA Goddard Space Flight Center, Code 682.3. Greenbelt, MD 20771, USA

ABSTRACT

The current state of describing the coordinates of solar image data is chaotic, and does not take into account the most recent developments in the coordinate systems for astronomy in general, especially as related to FITS files. A set of formal systems for describing the coordinates of solar image data is proposed. These systems build on current practice in applying coordinates to solar image data. Both heliographic and heliocentric coordinates are discussed. A distinction is also drawn between heliocentric and helioprojective coordinates, where the latter takes the observer's exact geometry into account. The extension of these coordinate systems to observations made from non-terrestial viewpoints. such as STEREO and Solar Probe, is discussed. A formal system for incorporation of these coordinates into FITS files, based on the FITS World Coordinate System, is described.

Key words: Solar; Coordinates.

1. INTRODUCTION

Solar research is becoming ever increasing more sophisticated. Advances in solar instrumentation have led to increases in spatial resolution, and will continue to do so. Future space missions will view the Sun from different perspectives than the current view from ground-based observatories, or satellites in Earth orbit. Both of these advances will require more careful attention to the coordinate systems used for solar image data. In fact, some taste of this has already occured with the Solar and Heliospheric Observatory (SOHO) satellite, which views the Sun from the inner Lagrange point between the Earth and the Sun. The Sun appears approximately 1% bigger from SOHO than it does from the Earth, requiring adjustment whenever SOHO images are compared with data from ground-based observatories, or satellites in low Earth orbit, such as Yohkoh.

Although there is widespread agreement on the coordinate systems to be used for interplanetary space (Russell, 1971; Hapgood, 1992), no formal structure exists for solar image coordinates, except for the wellestablished heliographic coordinate system. In particular, there is no agreement on how these coordinates should appear in FITS headers, with potential confusion when data from one observatory is compared to data from another. Therefore, I have put together a draft proposal to outline the various possible coordinate systems which may be used for solar image data, and to show how these coordinate systems relate to the World Coordinate System (WCS) formalism used in FITS files. In this proposal, attention is given to current practice within the solar imaging community.

With solar imaging instrumentation now planned for spacecraft which will operate at large distances away from the Earth-Sun line, consideration must also be given as to how the viewpoint of the instrument should be taken into account in the coordinate system. This is also discussed in the proposed

There is not enough space here to outline the full proposal, which is available from

However, the basic outline of the proposal will be given here.

2. THE COORDINATE SYSTEMS

Three main classes of coordinate systems are considered. The first is the well known heliographic system of solar latitude and longitude, illustrated in Figure 1. This class includes both Stonyhurst and Carrington varieties.

The next class is heliocentric coordinate systems, with three orthogonal axes x, y, and z, measured in physical units (e.g. kilometers or solar radii), and centered on the Sun. There are a number of well-established heliocentric coordinate systems used in space physics (Hapgood 1992). Examples include Heliocentric Aries Ecliptic (HAE), Heliocentric Earth Ecliptic (HEE), and Heliocentric Earth

Proc. 1st Solar & Space Weather Euroconference, 'The Solar Cycle and Terrestrial Climate', Santa Cruz de Tenerife, Tenerife, Spain, 25-29 September 2000 (ESA SP-463, December 2000)

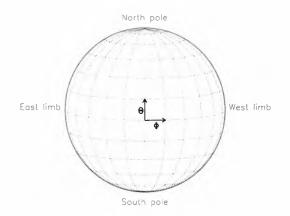


Figure 1. A diagram of the Sun, showing lines of constant heliographic longitude and latitude on the solar disk. The origin of the coordinate system is at the intersection of the solar equator and the (terrestrial) observer's central meridian. This representation is also known as a Stonyhurst grid.

Equatorial (HEEQ). However, the heliocentric systems considered here are aligned to have one axis (z)oriented along the Sun-observer line, so that the xand y axes correspond to positions on a solar image.

The third class replaces the heliocentric positions with their angular equivalents, and is given the name helioprojective. Such a coordinate system is actually observer-centric, and the distance from the observer forms the third dimension of the system. For a terrestrial observer, we would call this a geocentric coordinate system; however, non-terrestrial viewpoints will also be allowed. Both the formal and informal relationships between the heliocentric and helioprojective coordinate systems are considered in the full proposal. In the formal definition, they are related by spherical trigonometry. Informally, the relationship between a heliocentric position and a helioprojective angle in degrees is simply

$$x \approx D_{\odot}(\frac{\pi}{180^{\circ}})\theta_x$$

where D_{\odot} is the distance to the Sun.

Both heliocentric and helioprojective coordinates can be expressed in two subcategories. The Cartesian subcategory, illustrated in Figure 2 expresses coordinates as distances along the east-west and southnorth axes. For example, this subcategory has been extensively used in the planning and cataloging of SOHO observations. On the other hand, the Radial subcategory, shown in Figure 3, consists of a radial distance and a position angle, and is commonly used with coronagraph data.

3. THE WORLD COORDINATE SYSTEM

So far, I have not discussed how to incorporate these coordinate systems into FITS files. It was decided to make use of the World Coordinate System

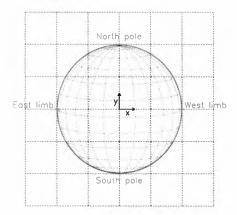


Figure 2. A diagram of the Sun, with lines of constant heliocentric-cartesian position (x, y) overlayed. The z axis points out of the page. For helioprojectivecartesian coordinates, the spatial positions (x, y) are replaced by the angles (θ_x, θ_y) , and the coordinate z is replaced by the distance d from the observer. In the formal definition of helioprojective-cartesian coordinates, the angle θ_x acts like a longitude, and θ_y acts like a latitude. In the small-angle approximation, however, they differ from (x, y) only by a simple scaling factor.

(WCS) (Greisen and Calabretta, 2000; Calabretta and Greisen, 2000) for this purpose, for the following reasons:

- It is the emerging standard in the FITS world for annotating the coordinates of data arrays (including non-spatial axes).
- It resolves the ambiguities inherit in the original FITS coordinate scheme (Wells et al. 1981).
- It explicitly handles spherical coordinates, which is useful both for properly handling the perspective of the data, and also for heliographic coordinates.
- It allows multiple coordinate systems to be associated with the same data. For example, one can provide coordinates in both a heliographic and helioprojective system for the same data set.

The WCS labels for the solar imaging coordinates discussed earlier are given in Table 3. Using the WCS does involve some changes in the FITS coordinates keywords, outlined in Table 2. However, I will also consider how solar coordinates can be expressed in the older system.

There is not enough space here to illustrate how all these different coordinate systems can be incorporated into a FITS header. Instead, I will concentrate on the simplest and most commonly used coordinate system, namely helioprojective-cartesian. Figure 4 shows a sample header for a hypothetical instrument with a plate scale of 3.6 arcsec/pixel, observing from 1 A.U. The detector is a 1024×1024 CCD, with the

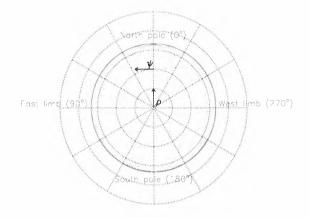


Figure 3. A diagram of the Sun demonstrating heliocentric-radial coordinates, with lines of constant impact parameter ρ and position angle ψ overlayed. The value of ψ at each of the four compass points is also shown. The z axis points out of the page. For helioprojective-radial coordinates, the distance ρ is replaced by the angle θ_{ρ} , and the coordinate z is replaced by the distance d from the observer. However, because of the requirements of the WCS, the quantity which appears in the FITS headers is $\delta_{\rho} = \theta_{\rho} - 90^{\circ}$, so that disk center is one of the poles of this spherical coordinate system.

Sun centered in the CCD, and the solar north pole pointing straight up on the detector.

Figure 4. Sample FITS header, demonstrating helioprojective-cartesian coordinates.

SIMPLE	= T /Simple FITS file
	1
BITPIX	= -32 /Real*4 (Floating point)
NAXIS	= 2 /Two-dimensional image
NAXIS1	= 1024 /# of pixels per column
NAXIS2	= 1024 /# of pixels per row
CTYPE1	= 'HPLN-TAN' /Axis labels (Theta_X)
CTYPE2	= 'HPLT-TAN' / (Theta_Y)
CRPIX1	= 512.5 /Ref. is center of CCD
CRPIX2	= 512.5 /
CUNIT1	= 'arcsec ' /Angles in arcsec
CUNIT2	= 'arcsec ' /
CD1_1	= 3.6 /Plate scale in arcsec
CD2_2	= 3.6 /
CRVAL1	= 0.0 /Ref.pix. is Sun center
CRVAL2	= 0.0 /
CRVAL1	= 0.0 /Ref.pix. is Sun center

One of the strengths of the WCS is its ability to handle different map projections. For example, an image of the Sun in helioprojective-cartesian coordinates is most likely to be expressed in something known as the gnomic or TAN projection, in which the pixels are spaced as the tangent of the anglular positions, rather than directly as the angles themselves. Almost all solar imaging instruments have optics which produce an image in the TAN projection. This is why the labels HPLN and HPLT are always shown here fol-

Table 1. World Coordinate System axis labels (CTYPEi values) for the various coordinate systems, where d is the distance from the observer, D_{\odot} is the distance to Sun center, and ζ is the helioprojective analog of the heliocentric coordinate z.

Coordinate system				
Variables WCS labels				
Heliographic coordinates				
Θ, Φ, r HGLT-AZP, HGLN-AZP, HECF	ł			
Carrington coordinates				
Θ, Φ_C, r CRLT-AZP, CRLN-AZP, HECH	{			
Heliocentric-cartesian				
x,y,z SOLX, SOLY, SOLZ				
Heliocentric-radial				
$ ho,\psi,z$ Soli, HCPA, Solz				
Helioprojective-cartesian				
θ_x, θ_y, d HPLN-TAN, HPLT-TAN, DIST	ſ			
Helioprojective-radial				
$\delta_ ho,\psi,d$ HRLN-TAN, HRLT-TAN, DIST	F			
Additional parameters				
$h=r-R_{\odot}$ HECH				
D_{\odot} DSUN				
$\zeta = D_{\odot} - d$ HPRZ				

lowed by the letters -TAN, because that is the map projection of these data. (Similarly, the heliographic coordinates of the same image would be in the perspective zenithal projection, represented by -AZP.)

However, the spherical coordinate map projection capabilities of the World Coordinate System offer a large amount of flexibility in dealing with data which are not cast in straightforward cartesian terms. With the appropriate map projections, one can handle not only images, but also synoptic maps in the heliographic system, and maps of the corona in radial distance and position angle.

Table 2. Comparison of the FITS coordinate keywords in the old and new system, for helioprojectivecartesian coordinates. The only differences are the usage of the CD_{j-i} matrix, and the CTYPEi labels. Although the WCS makes CDELTi and CROTAi obsolete, their inclusion is recommended for backwards compatibility.

Keyword	Original	WCS		
CRPIXi	Exactly the same in both			
CRVALi	Exactly the same in both			
CDELTi	Spacing	Obsolete		
CROTAi	Rotation	Obsolete		
$ ext{CD} j_i$	Not used	Replaces CDELT <i>i</i> , CROTA <i>i</i>		
CUNIT <i>i</i>	Exac	tly the same in both		
CTYPEi	SOLARX	HPLN-TAN		
	SOLARY	HPLT-TAN		

4. OBSERVER'S POSITION

To support non-terrestrial viewpoints, such as the upcoming STEREO mission, a mechanism is needed for specifying the observer's position. In the proposed system, this is handled in the following manner:

- Observer's position specified by using FITS keywords formed by taking four-letter WCS code, followed by the characters "_OBS".
- Recommended keywords are DSUN_OBS, HGLN_OBS, HGLT_OBS, e.g.

DSUN_OBS=	1.507E+11	/Dista	ance ((m)
HGLN_OBS=	0.0	/Obs.	long.	(deg)
HGLT_OBS=	7.25	/Obs.	lat.	(deg)

- Space physics coordinate systems can also be used, e.g. HEQX_OBS, HEQY_OBS, HEQZ_OBS for Heliocentric Earth Equatorial coordinates.
- If the keywords for observer's position are omitted, then an Earth-based (or low Earth orbit) observation is assumed.

One extra consideration for non-terrestrial viewpoints is that I suggest that the prime meridian of the non-Cartesian heliographic coordinate system be defined to always include the sub-Earth point. That way, observers with different viewpoints will still measure the same heliographic coordinates. Thus, for a terrestrial observer, the central meridian on the disk will always represent $\Phi = 0$, while it will take on other values for non-terrestrial observers.

5. THE CURRENT FITS COORDINATE SYSTEM

Over the last few years, a standard has been developing for solar image coordinates in FITS files, using the older CDELT*i*, CROTA*i* keywords rather than the newer WCS formalism with a CDj_{-i} transformation matrix. This system has the following characteristics:

- The coordinate axes correspond to Figure 2.
- The coordinate axis labels vary, or are omitted, but are typically SOLARX, SOLARY, as used by the SOHO project.
- The coordinates are expressed in arcseconds. However, no map projections are explicitly given, and the distinction between heliocentric and helioprojective coordinates is glossed over.

Since the positions are not true angles, but vary as the tangent, this system is really helioprojectivecartesian in the TAN projection. More details on how older FITS systems can be incorporated into the WCS-based system are given in the full text of the proposal.

Although I encourage the eventual adoption of the WCS, the above system can be used for data which don't require the full WCS formalism. Even with the WCS, I recommend including CDELT*i* and CROTA*i* for backwards compatibility.

6. CONCLUSIONS

I have presented a standardized coordinate system which is precise, rigorous, and comprehensive. Heliographic, heliocentric (distance), and helioprojective (angular) coordinates are all treated. The proposed system builds on current standards, and extends them for the needs of future missions, such as STEREO and Solar Probe. It incorporates the emerging World Coordinate System standard for rigor, and for the flexibility needed to encompass all possible coordinate representations. However, many current FITS files are incorporated as a special subset of the helioprojective-cartesian system in the TAN projection.

Only an outline of the proposed coordinate system is given here. The full text of the proposal can be found at

ACKNOWLEDGEMENTS

This work was supported by NASA grant NAS5-32350.

REFERENCES

- Calabretta M., Greisen E.W., 2000, Astron. Astrophys., to be submitted
- Greisen E.W., Calabretta M., 2000, Astron. Astrophys., to be submitted
- Hapgood M.A., 1992, Planet. Space Sci., 40, 711
- Russell C.T., 1971, Cosmic Electrodynamics, 2, 184
- Wells D.C., Greisen E.W., Harten R.H., 1981, Astron. Astrophys. Supp., 44, 363

Participants List

Abramenko, Valentina Crimean Astrophysical Observatory 334413 Nauchny 14 Crimea Ukraine

aviabbso.njit.edu/aviacrao.crimea.ua

Alexander, Pedro Universidad de Buenos Aires Dpto Física, Facultad de Ciencias Exactas y Naturales 1428 Buenos Aires Argentina

peter@df.uba.ar

Alves Da Cunha. Rita Joao Portuguese Institute for Water (Inag) Av. Almirante Gago Coutinho. 30 1000 Lisboa Portugal

mintaka@mail.telepac.pt

Ambroz, Pavel Astronomical Institute Academy of Science CZ-251-65 Ondrejov Czech Republic

pambroz a asu.cas.cz

Anker-Nilssen, Peter Centre For Energy & Environment Norwegian School of Management P.O. Box 580 N-1302 Sandvika Norway

per.anker-nilssen a bi.no

Antalova, Anna Astronomical Institute Slovak Academy of Sciences SK-05960 Tatranska Lomnica Slovak Republic

antalova a ta3.sk

Arpe, Klaus MMP für Meteorologie Bundesstrasse 55 D-20146 Hamburg Germany

arpe a dkrz.de

Baudin, Frederic Institute D'Sstrophysique Spatiale, Bat 121 Campus D'Orsay F-91405 Orsay Cedex France

baudin@medoc-ias.u-psud.fr

Beer, Juerg EAWAG Ueberlandstrasse 133 Postfach 611 CH-8600 Duebendorf Switzerland

beer a eawag.ch

Belik, Marcel Observatory Upice P.O. Box 8 CZ-542 32 Upice Czech Republic

marcel_belik a yahoo.com

Bellot Rubio. Luis Instituto de Astrofísica de Canarias C/ Via Lactea S/N E-38200 La Laguna Spain

Ibellot a Il.iac.es

Belmonte, Juan Antonio Instituto de Astrofísica de Canarias C/ Via Lactea S/N E-38200 La Laguna Spain

jba/a/ll.iac.es

Benestad, Rasmus E. Norwegian Meteorological Institute Climate Division P.O. Box 43 Blindern N-0313 Oslo Norway

rasmus.benestad a dnmi.no

Berger, André Inst. D'Astronomie et de Géophysique G. Lemaître 2 Chemin Du Cyclotron B-1348 Luovain La Neuve Belgium

berger a astr.uel.ac.be

Berrilli, Francesco Università Di Roma "Tor Vergata" Dpto. di Fisica V. Le Ricerca Scientifica S/N I-00133 Roma Italy

berrilli@roma2.infn.it

Bonet. Jose Antonio Instituto de Astrofísica de Canarias C/ Via Lactea S/N E-38200 La Laguna Spain

jab@ll.iac.es

Boulyguina, Ekaterina Lomonosov Moscow State University Anthropology Dpt. Moscow Tsvetnoy Blvd. 25/3 Moscow 103051 Russia

ebulygin@yahoo.com

Brandt, Peter Kiepenheuer Institut Schoeneckstr 6 D-79104 Freiburg Germany

pnb@kis.uni-freiburg.de

Brekke, Paal NASA Goddard Space Flight Center Mail Code 682.3, Bld. 26, Room G-1 Greenbelt MD 20771 USA

pbrekke@esa.nascom.nasa.gov

Briand, Carine THEMIS IAC, Via Lactea, S/N E-38205 La Laguna Spain

cbriand@ll.iac.es

Bumba, Vaclav Astronomical Institute Academy of Science Fricova 237 CZ-251 65 Ondrejov Czech Republic

bumba@asu.cas.cz

Butler, C John Armagh Observatory College Hill Bt61 9dg Armagh Northern Ireland

cjb@star.arm.ac.uk

Caccin, Bruno Universitá di Roma "Tor Vergata" Dipartamento di Fisica V. Della Ricerca Scientifica, 1 I-00133 Roma Italy

caccin@roma2.infn.it

Calbet Alvarez, Xavier Observatorio Atmosferico de Izaña C/ La Marina, 20 Santa Cruz de Tenerife Spain

xcalbet@inm.es

Caldeira. Kenneth Lawrence Livermore National Lab. Livermore CA 94550 USA

kenc@llnl.gov / common1@llnl.gov

Calder, Nigel 26 Boundary Road Crawley W. Sussex RH10 2BT UK

nc@windstream.demon.co.uk

Casas, Ricard Agrupació Astronomica de Sabadell Olot, 2 E-08203 Sabadell, Barcelona Spain

ricardcasas@wanadoo.es

Cauzzi, Gianna Osservatorio Astrofísico di Arcetri Largo Enrico Fermi 5 I-50125 Firenze Italy

gcauzzi@arcetri.astro.it

Centrone, Mauro Università di Roma "Tor Vergata" Osservatorio Astronomico di Roma Viale Del Parco Mellini. 84 I-00136 Rome Italy

centrone@oarhp1.rm.astro.it

Ceppatelli, Guido Instituto de Astrofisica de Canarias C/ Via Lactea S/N E-38200 La Laguna Spain

compta@ll.iac.es

Chanin, Marie-Luise Service d'Aeronomie du CNRS B.P. 3 F-91370 Verrieres Le Buisson Cedex France

chanin@aerov.jussieu.fr

Christy, John R. University of Alabama in Huntsville Earth System Science Center Huntsville AL 35899 USA

christy@atmos.uah.edu

Cini Castagnoli, Giuliana Universita di Torino Dipartimento di Fisica Generale Via P. Giuria I I-10125 Torino Italy

cini@icg.to.infn.it

Clette, Frederic Observatoire Royal de Belgique Av. Circulaire, 3 B-1180 Bruxelles Belgium

fred@oma.be

Corbard, Thierry High Altitude Observatory, NCAR 3450 Michell Lane, PO Box 3000 Boulder CO 80307-3000 USA

corbard@ucar.edu

Cornish, Monique R. University of Auckland School Of Enviromental & Marine Sciences Private Bag 92019 Auckland New Zealand

m.cornish@auckland.ac.nz

Crosby, Norma International Space University Strasbourg Central Campus Bld. Gonthier d'Andernach F-67400 Illkirch, Graffenstaden France

ncrosby@wanadoo.fr

Cugnet, David Service d'Aeronomie du CNRS B.P. 3 F-91370 Verrieres Le Buisson Cedex France

luc.dame@aerov.jussieu.fr

Curto Subirats, Juan Jose Observatori de l'Ebre E-43520 Roquetes Spain

ebre.jjcurto@readysoft.es

Davies. Stephen European Commission DG Research, SDME 4/49 Rue de la Loi / Wetstraat 200 B-1049 Brussels Belgium

stephen.davies@cec.eu.int

De Toma, Giuliana Univ. of Colorado at Boulder Lab. for Atmospheric and Space Physics 1234 Innovation Drive Boulder CO 80303 USA

detoma@lasp.colorado.edu

Del Peral, Luis Departamento de Física, Facultad de Ciencias Universidad de Alcalá, Campus Universitario Ctra de Barcelona km 33.600 E 28871 Alcalá de Henares Madrid Spain

luis.delperal@alcala.es

Domingo Codoñer, Vicente Universidad de Barcelona Dept. Astronomia y Meteorologia Avda Diagonal, 647, Planta 7 E-08028 Barcelona Spain

vicente@am.ub.es

Dorch, Bertil Stockholm Observatory Dept of Astronomy S-13336 Saltsjöbaden Sweden

dorch@astro.su.se

Eff-Darwich, Antonio Instituto de Astrofísica de Canarias C/ Via Lactea S/N E-38200 La Laguna Spain

adarwich@ll.iac.es

Eibe, Teresa Observatoire de Paris (DASOP) Dasop 5 Place Janssen F-92195 Meudon Cedex Principal France

eibe@mesopa.obspm.fr

Ermolli, Ilaria Osservatorio Astronomico di Roma Viale Del Parco Mellini, 86 I-00136 Rome Italy

ilaria@oarhp1.rm.astro.it

Estupiñan Lopez, Jose Antonio Universidad De Las Palmas De G.C. Carr. Almatriche 101 Las Palmas de Gran Canaria Spain

jael2@arrakis.es

Ferriz Mas, Antonio University of Oulu Dept of Physical Sciences, Astronomy Div. P.O. Box 3000 FIN-90014 Oulu Finland

aferriz a sun3.oulu.fi

Fleck, Bernhard NASA Goddard Space Flight Center ESA Space Science Dept, Mailcode 682.3 Greenbelt MD 20771 USA

bfleck@esa.nascom.nasa.gov

Fligge, Marcel Inst. of Astronomy, ETH Zürich ETH-Zentrum CH-8092 Zürich Switzerland

fligge@astro.phys.ethz.ch

Fofi, Massimo Osservatorio Astronomico di Roma Viale Del Parco Mellini. 86 I-00136 Rome Italy

fofi@oarhp1.rm.astro.it

Froehlich. Claus PMOD/WRC Dorfstrasse. 33 CH-7260 Davos Dorf Switzerland

cfrohlich@pmodwrc.ch

Gaya I Pique, Lluis Observatori de l'Ebre Horta Alta, 38 E-43520 Roquetes Spain

ebre.lgava@readysoft.es

Gburek, Szymon Polish Academy of Sciences Space Research Center UI. Kopernika 11 PL-51-662 Wroclaw Poland

sg@cbk.pan.wroc.pl

Giammanco, Corrado Instituto de Astrofísica de Canarias C/ Via Lactea S/N E-38200 La Laguna Spain

corrado all.iac.es

Gibert Beotas, Luis Universidad Politécnica de Cataluña Farinera 2 E-08211 Castellar Barcelona Spain

gbeotas@hotmail.com

Golipour. Manouchehr Weather Action Ltd 90 London Rd London SW9 0NR UK

golipour@hotmail.com

Gonzalez Jorge, Helena Instituto de Astrofísica de Canarias C/ Via Lactea S/N E-38200 La Laguna Spain

hglez@ll.iac.es

Goode. Philip Big Bear Solar Observatory 40386 N. Shore Lane Big Bear City CA 92314 USA

pgoode@bbso.njit.edu

Gregori, Giovanni P. IFA-CNR Via Fosso Del Cavaliere, 100 I-00133 Roma Italy

gregori@ifa.rm.cnr.it

Hanslmeier, Arnold University of Graz Inst Geophys Astrophys & Meteorology Universitaetsplatz, 5 A-8010 Graz Austria

arnold.hanslmeier@kfunigraz.ac.at

Heredia, Teresita del Valle Universidad Nacional de Tucuman Av. Independencia 1800 4000 Tucuman Argentína

theredia@herrera.unt.edu.ar

Hill. David Charles Rutherford Appleton Laboratory Chilton Didcot Oxfordshire OX11 UK

dhill a wobble.ag.rl.ac.uk

Hill, Frank National Solar Observatory P.O. Box 26732 Tuczon AZ 85726 - 6732 USA

fhill@noao.edu

Hochedez, Jean Francois Royal Observatory of Belgium Avenue Circulaire, 3 B1180 Brussels Belgium

hochedez@oma.be

Houghton, Sir John IPCC WGI Hadley Centre, Met Office London Road Bracknell Berks RG12 2SY UK

jthoughton@ipccwg1.demon.co.uk

Jimenez, Antonio Instituto de Astrofísica de Canarias C/ Via Lactea S/N E-38200 La Laguna Spain

ajm@ll.iac.es

Jimenez-Reyes, Sebastian J. High Altitude Observatory NCAR 3450 Michell Lane PO Box 3000 Boulder CO 80307-3000 USA

chano@hao.ucar.edu

Jiricka, Karel Astronomical Institute Academy of Science CZ-251 65 Ondrejov Czech Republic

jiricka@asu.cas.cz

Jones, Philip D. University of East Anglia Climate Research Unit School of Environmental Science Norwich NRr4 7TJ UK

p.jones@uea.ac.uk

Jonsson, Stig Stockholm University Dept. of Physical Geography S-10691 Stockholm Sweden

stig@natgeo.su.se

Kirkby, Jasper CERN CH-1211 Geneva 23 Switzerland

jasper.kirkby@cern.ch

Komm, Rudolf National Solar Observatory P.O. Box 26732 Tucson AZ 85726-6732 USA

komm@noao.edu

Kotrc, Pavel Astronomical Institute Academy of Science CZ 251-65 Ondrejov Czech Republic

pkotrc@asu.cas.cz

Krijger, Thijs Sterrekunding Instituut Utrecht Princetonplein 5 NL-3508 TA Utrecht The Netherlands

j.m.krijger@astro.uu.nl

Kroll, Ron National Solar Observatory P.O. Box 26732 Tucson AZ 85726 - 6732 USA

rkroll@noao.edu

Kucera, Ales Astronomical Institute Slovak Academy Of Sciences SK-05960 Tatranska Lomnica Slovak Republic

akucera@ta3.sk

Labs, Dietrich Landessternwarte Königstuhl Königstuhl 11 D-69117 Heidelberg Germany

d.labs@lsw.uni-heidelberg.de

Landscheidt, Theodor Schröter Institute for Research in Cycles of Solar Activity 11227 Cabot Trail, Beille Cote Nova Scotia, BOE 1CO Canada

theodor.landscheidt@ns.sympatico.ca

Laut, Peter Technical University of Denmark Building 377 DK-2800 Lyngby Denmark

ifakpl@pop.dtu.dk

Leibacher, John National Solar Observatory POB 26732 Tucson AZ-85726 USA

jleibacher@noao.edu

Lockwood, Michael Rutherford Appleton Laboratory World Data Centre C-1 for STP Chilton Didcot OX11 UK

m.lockwood@rl.ac.uk

Loukitcheva, Maria S-Petersburg State University Astronomical Institute Bibliotechnaya Pl., 2 St Petersburg 198904 Russia

loukmas@hotmail.com

Ludmany, Andras Heliophysical Observatory Debrecen P.O. Box 30 H-4010 Debrecen Hungary

ludmany@tigris.klte.hu

Makarov, Valentine I. Pulkovo Astronomical Observatory Pulkovo 196140, St. Petersburg Russia

makarov@gao.spb.ru

Mandrini, Cristina Inst. de Astronomia y Física del Espacio CC.67 Suc.28 1428 Buenos Aires Argentina

mandrini a iafe.uba.ar

Maris, Georgeta Astronomical Institute Str. Cutitul De Argint 5 P.O. Box 28 RO-75212 Bucharest Romania

gmaris a roastro.astro.ro

Markova, Eva Observatory Upice P.O. Box 8 CZ-542 32 Upice Czech Republic

markovae a mbox.vol.cz

Martinez Pillet, Valentin Instituto de Astrofísica de Canarías C/ Via Lactea S/N E-38200 La Laguna Spain

vmp@ll.iac.es

Messerotti, Mauro Osservatorio Astronomico di Trieste Basovizza 302 I-34012 Trieste Italy

messerotti a ts.astro.it

Moreno-Insertis. Fernando Instituto de Astrofísica de Canarias C/ Via Lactea S/N E-38200 La Laguna Spain

fmi@ll.iac.es

Moretti, Pier F. Osservatorio Astron. Di Capodimonte Via Moiarielle, 16 I-80131 Napoli Italy

moretti a cerere.na.astro.it

Mouradian. Zadig Observatoire de Paris-Meudon Place Jules Jansen 5 F-92195 Meudon Cedex France

zadig.mouradian a obspm.fr

Mursula, Kalevi University of Oulu Dept of Physical Sciences P.O. Box 3000 FIN-90014 Finland

kalevi.mursula a oulu.fi

Neubauer, Fritz M. Universität zu Köln Institut für Geophysik & Meteorologie Albertus-Magnus-Platz D-50923 Köln Germany

neubauer a geo.uni-koeln.de

Ogren, John A. NOAA/CMDL 325 Broadway R/CMDLL Boulder CO 80303 USA

jogren a cmdl.noaa.gov

Ortiz Carbonell, Ada Universidad de Barcelona Dept, Astronomia y Meteorologia Avda Diagonal, 647, Planta 7 E-08028 Barcelona Spain

aortiz a am.ub.es

Ortiz De Adler, Nieves Universidad Nacional de Tucuman Quito 2499 (4107) Yerba Buena Tucuman Argentina

adler@arnet.com.ar

Ozguc, Atilla Kandilli Observatory 81220 Cengelkoy Istanbul Turkey

ozguc@boun.edu.tr

Palle Bago, Enric Armagh Observatory College Hill Bt61 9dg Armagh Northern Ireland

Epb@Star.Arm.Ac.Uk

Palle, Pere Lluis Instituto de Astrofísica de Canarias C/ Via Lactea S/N E-38200 La Laguna Spain

corinv@ll.iac.es

Parker, Eugene N. University Of Chicago 1323 Evergreen Road Homewood IL 60430 USA

parker@odysseus.uchicago.edu

Penza, Valentina Universita di Roma "Tor Vergata" Dipartamento di Fisica V Le Ricerca Scientifica S/N I-00133 Roma Italy

penza@roma2.infn.it

Petrovay, Kristof Eötvos University Dept of Astronomy PF. 32 H-1518 Budapest Hungary

kris a innin.elte.hu

Pietropaolo. Ermanno Universita di l'Aquila Dipartamento di Fisica Via Vetoio I-67010 l'Aquila Italy

ermanno@univaq.it

Poetzi, Werner University of Graz Inst Geophys Astrophys & Meteorology Universitaetsplatz 5 A-8010 Graz Austria

werner.poetzi@kfunigraz.ac.at

Popescu, Miruna Daniela Astronomical Institute Str. Cutitul De Argint 5 P.O. Box 28 RO-75212 Bucharest Romania

miruna@roastro.astro.ro

Puschmann, Klaus Instituto de Astrofísica de Canarias C/ Via Lactea S/N E - 38200 La Laguna Spain

klaus@ll.iac.es

Raspopov, Oleg SPBF Izmiran Muchnoy Per. 2 P.O. Box 188 194023 St. Petersburg Russia

Reardon, Kevin Oss. Astron, Capodimonte/Univ, Firenze L.E. Fermi 5 I-50125 Firenze Italy

kreardon a na.astro.it

Ripodas, Pilar Observatorio Atmosferico de Izaña C/ La Marina, 20 Apartado 880 Santa Cruz de Tenerife Spain

pripodas a inm.es

Rodríguez Frías. Dolores Universidad de Alcalá Depto de Fisica Campus Universitario E-28071 Alcala de Henares Spain

dolores.frias@uah.es

Rodríguez Hidalgo. Inés Instituto de Astrofísica de Canarias C/ Via Lactea S/N E-38200 La Laguna Spain

irh all.iac.es

Rodríguez Pacheco, Javier Universidad de Alcala Dpto, de Física Madrid Spain

fsrodriguez@alcala.es

Rodríguez Santana. Angel Universidad de Las Palmas de G.C. Dpto. de Física Campus Universitario Tafira Apdo. 550. Las Palmas de G.C. Spain

angel.rodrigues a fisica.ulpgc.es

Romano, Paolo Universita di Catania Viale Andrea Doria, 6 1-95125 Catania Italy

prom a sunct.ct.astro.it

Romero Campos, Pedro Miguel Observatorio Atmosferico de Izaña C/ La Marina, 20 Santa Cruz de Tenerife Spain

pmiguel a inm.es

Romero, Maria del Carmen Observatorio Atmosferico de Izaña CULa Marina, 20 Santa Cruz de Tenerife Spain

mromero a inm.es

Ruediger. Guenther Astrophysikalisches Institut Potsdam An Der Sternwarte 16 D-14482 Potsdam Germany

gruediger a aip.de

Ruiz Cobo. Basilio Instituto de Astrofísica de Canarias C/ Via Lactea S/N E-38200 La Laguna Spain

brcall.iac.es

Rutten, Robert J. Sterrekundig Instituut Utrecht Postbus 80 000 NL-3508 TA Utrecht The Netherlands

r.j.rutten/a/astro.uu.nl

Sánchez Cuberes, Mónica Instituto de Astrofísica de Canarias C/ Via Lactea S/N E-38200 La Laguna Spain

msanchez all.iac.es

Schmidtke, Gerhard Fraunhofer IPM Heidenhofstr. 8 D-79110 Freiburg Germany

gerhard.schmidtkeaipm.fhg.de

Schmieder, Brigitte Observatoire de Paris-Meudon DASOP 5 Place Janssen F-92195 Meudon Cedex Principal France

schmiede a mesopa.obspm.fr

Schmitt, Juergen Hamburger Sternwarte Universität Hamburg Gojenbergsweg 112 D-21029 Hamburg Germany

jschmitt a hs.uni-hamburg.de

Schober, Hans Josef University of Graz Inst. for Geophysics. Astrophysics & Meteorology A-8010 Graz Austria

schober@email.kfunigraz.ac.at

Schühle, Udo MPI für Aeronomie Max-Planck-Strasse 2 D-37191 Katlenburg-Lindau Germany

schuehle@linmpi.mpg.de

Shaltout, M. A. Mosalam Nat. Res. Inst. of Astron & Geophysics Helwan Cairo Egypt

mamshaltout@frcu.eun.eg

Sofia. Sabatino Yale University Dept of Astronomy P.O. Box 208101 New Haven CT 06520-8101 USA

sofia@astro.yale.edu

Solanki, Sam MPI für Aeronomie Postfach 20 D-37189 Katlenburg-Lindau Germany

solanki@linmpi.mpg.de

Soon. Willie CfA Harvard-Smithsonian 60 Garden Street. MS 16 Cambridge MA 02138 USA

wsoon@cfassp13.harvard.edu

Steinegger, Michael Big Bear Solar Observatory NJIT 40386 North Shore Lane Big Bear City CA 92314 USA

michael a bbso.njit.edu

Suarez, José Manuel Weather Action Ltd. 90 London Rd London SW9 0NR UK

jose@weatheraction.com

Svensmark, Henrik Danish Space Research Institute Juliane Maries Vej 30 DK-2100 Copenhagen OE Denmark

<u>hsv@dsri.dk</u>

Sykora, Julius Astronomical Institute Slovak Academy of Sciences SK-05960 Tatranska Lomnica Slovak Republic

sykora@ta3.sk

Sylwester, Janusz Space Research Centre Polish Academy of Sciences Ul. Kopernika 11 PL-51 622 Wrocław Poland

js@cbk.pan.wroc.pl

Tett, Simon Hadley Centre, The Met. Office London Rd Bracknell Berks RG12 2SY UK

sfbtett@meto.gov.uk

Thompson. William NASA Goddard Space Flight Center Code 682.3 Greenbelt MD 20771 USA

thompson a orpheus.nascom.nasa.gov

Thuillier, Gerard Service d'Aeronomie du CNRS BP 3 F-91371 Verrieres-Le-Buisson France

gerard.thuillier a aerov.jussieu.fr

660

Tikhomolov, Eugene Institute of Solar-Terrestrial Physics SD RAS P.O. Box 4026 664033 Irkutsk Russia

etikhomolov a solar.stanford.edu

Torelli. Maria Osservatorio Astronomico di Roma V. Le Del Parco Mellini 84 I-00136 Roma Italy

torelli a oarhp1.rm.astro.it

Torta Margalef, J. Miguel Observatori de l'Ebre Horta Alta, 38 E-43520 Roquetes Spain

ebre.jmtorta a readysoft.es

Tóth, László Heliophysical Observatory Hungarian Academy of Sciences P.O. Box 30 H-4010 Debrecen Hungary

tothla a tigris.klte.hu

Tsiropoula, Georgia National Observatory of Athens Inst of Space Applications & Remote Sensing Lofos Koufos GR-15236 P. Penteli Greece

georgia a creator.space.noa.gr

Tziotziou, Kostas Observatoire de Paris (DASOP) Dept d'Astronomie Solaire 5 Place Janssen F-92195 Meudon Cedex Principal France

kostas a mesopa.obspm.h

Usoskin, Ilya Sodankyła Geophysical Observatory University of Oulu P.O. Box 3000 FIN-90014 Oulu Finland

ilva.usoskin a oulu.fi

Van Dorland, Robert KNMI P.O. Box 201 NL-3730 AE De Bilt The Netherlands

aad.van.ulden a knmi.nl

Van Driel Gesztelyi, Lidia Observatoire de Paris (DASOP) Dept d'Astronomie Solaire Place Jules Jansen 5 F-92195 Meudon Cedex France

lidia.vandriel@obspm.fr

Van Ulden, Add KNMI P.O. Box 201 NL-3730 AE De Bilt The Netherlands

aad.van.ulden a knmi.nl

Vazquez, Manuel Instituto de Astrofísica de Canarias C/ Via Lactea S/N E-38200 La Laguna Spain

mva a Il.iac.es

Veronig. Astrid University of Graz Institute of Astronomy Universitätsplatz 5 A-8010 Graz Austria

asv a igam.kfunigraz.ac.at

Vogt, Etienne Osservatorio Astron, di Capodimonte Via Moiarielle, 16 1-80131 Napoli Italy

vogt a na.astro.it

Weber, Katja Freie Universitaet Berlin Institut fuer Meteorologie Carl-Heinrich-Becker Weg 6-10 D-12165 Berlin Germany

weber a strat01.met.fu-berlin.de

Wenzler. Thomas Institute of Astronomy. ETH Zentrum SEC Scheuchzerstrasse, 7 CH-8092 Zürich Switzerland

wenzler@astro.phys.ethz.ch

White, O.R. Dick High Altitude Observatory NCAR 3450 Mitchell Lane, PO Box 3000 Boulder CO 80307-3000 USA

orw@hao.ucar.edu/owhite@hubwest.com

White, Warren B. University of California San Diego Scripps Institution of Oceanography 8810 La Jolla Shores Drive CA 92093 - 0230 USA

wbwhite@ucsd.edu/afincham@ucsd.edu

Wilson, Andrew ESA Publications Division ESTEC P.O. Box 299 2200 AG Noordwijk The Netherlands

Andrew.Wilson@esa.int

Wittmann, Axel Universitäets-Sternwarte Göttingen Geismarlandstr 11 D-37083 Göttingen Germany

wittmann@uni-sw.gwdg.de

Woehl, Hubertus Kiepenheuer Institut Schoeneckstr 6 D-79104 Freiburg Germany

hw@kis.uni-freiburg.de

Yerle, Raymond 550 Chemin de la Bâtisse F-31600 Eaunes France

Yurchyshyn, Vasyl Big Bear Solar Observatory 40386 North Shore Lane Big Bear City CA 92314 USA

vayur@bbso.njit.edu

Zhukov, Andrei N. Institute of Nuclear Physics Moscow State University 119899 Moscow Russia

anz2@dec1.npi.msu.su

662

Late Papers

TOTAL SOLAR IRRADIANCE FROM VIRGO ON SOHO

Claus Fröhlich and Wolfgang Finsterle

Physikalisch-Meteorologisches Observatorium Davos, World Radiation Center, 7260 Davos Dorf, Switzerland

ABSTRACT

The long-term changes of the VIRGO radiometers on SoHO have been re-analyzed in detail. The exposure dependent changes can be described for both type of radiometers by a combination of an increase of the sensitivity and a degradation with time which depends on the dose of radiation from the sun. Also an exposure independent increase of the sensitivity has been detected which explains the early increase of the VIRGO TSI which was since the beginning of the measurements a unresolved puzzle.

Key words: Total Solar Irradiance; Solar Radiometry; SoHO/VIRGO.

1. INTRODUCTION

The early increase of the VIRGO total solar irradiance (TSI) shortly after the minimum in 1996 was until recently an unresolved issue (Fröhlich & Lean 1998; Fröhlich 2000). Although this increase was incompatible with the empirical models based on the influence of sunspots, faculae and the network, the former being represented by the photometric sunspot index (PSI, see e.g Fröhlich et al. (1994)) and the later by the MgII index, the core-to-wing ratio of the MgII line (see e.g. Chandra et al. (1995)), there was no obvious reason not to believe the corrections for the long-term behavior of the VIRGO radiometry as proposed by Fröhlich et al. (1997); Anklin et al. (1999); Fröhlich & Anklin (2000). The corrections for the operational radiometers PMO6V-A and DIARAD-L were based on the assumption that changes depend only on the time exposed to solar radiation and thus can be determined by comparing the operational radiometers with the rarely exposed radiometers PMO6V-B and DIARAD-L. Moreover, the DIARAD-R was assumed to be constant, mainly because the DI-ARAD type radiometers showed much less degradation than the PMO6V radiometers. This was a first surprise of SoHO as during e.g. the EURECA mission both types showed a very similar degradation of roughly 1 part-permillion (ppm) per day similar to what other radiometers in space such as ACRIM show. As this increase was definitively not present in the empirical models the obvious conclusion was, that the sun seemed behaving differently than during the minima and early increase towards the maxima before. With increasing solar activity the irradiance achieved levels of the preceding activity maxima well before the maximum was reached. Both, the early increase and the high level before the maximum could obviously be explained by a steady increase of the sensitivity with time of the VIRGO radiometers. A simple linear upward trend of about $1 \text{ mWm}^{-2} \text{d}^{-1}$ up to the time of the SoHO vacations would in a first approach remove most of the problem. An obvious question, however, is what could be the physical reason for this behaviour and why have other radiometers of similar type in space not shown such a behaviour. Definitively the environment on SoHO is extraordinary stable and it was definitively the cleanliest spacecraft ever launched. The cleanliness, however, should not influence the radiometry too much, as cavities are used and exposure dependent changes - although very small - carefully monitored. The high stability of the thermal environment, however, could well result in a yet unobserved behaviour of the radiometers. The principle of these radiometer is based on thermal flux measurements and thus is inherently influenced by changes in the thermal environment at the level of a few parts-permillion.

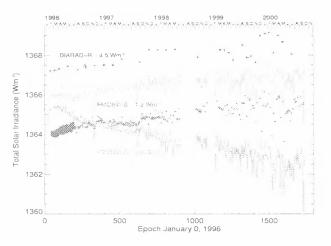


Figure 1. Time-series of the level-1 observations from the VIRGO radiometers PMO6V and DIARAD.

In the following we will describe the investigation of the

Proc. 1st Solar & Space Weather Euroconference. 'The Solar Cycle and Terrestrial Climate'. Santa Cruz de Tenerife, Tenerife, Spain, 25-29 September 2000 (ESA SP-463, December 2000)

VIRGO radiometry which leads to an internally consistent picture of the behaviour although the details of the physical mechanisms are still to be understood. For a description of the principle of electrically calibrated radiometers and more specifically of the VIRGO radiometers we refer to Fröhlich et al. (1995).

2. EXPOSURE DEPENDENT CHANGES

We start with a description of the exposure dependent changes as they can be deduced from comparison of the radiometers with different exposures to the sun. Figure 1 shows the level 1 data as obtained after reducing the raw data to physical units and by applying all a-priori known instrumental effects such as electrical calibration and corrections for the thermal environment and operational corrections for distance and velocity to the sun. These data show a combination of the sun's irradiance variation and instrumental changes. It is also obvious that the two backup instruments show more likely the irradiance changes whereas the operational ones are more influenced by instrumental behaviour. Already at this stage of evaluation the different long-term behaviour of PMO6V and DI-ARAD is very obvious, with the latter showing a much smaller difference between the operational and its backup than the former. Also prominent is the early increase of the PMO6V radiometers during the first few days of exposure. This early increase by about 500 ppm must be an increase in the absorptivity of the black paint in the cavity. However, with a measured reflectivity of the cavity of some 300 ppm still another effect needs to amplify the observed increase. This is most probably related to a decrease of the non-equivalence between electrical and radiative heating. This is due to the radiation reflected onto the side wall of the cavity, from where a certain amount is lost to the environment and not measured by the heat-flux-sensor. Thus radiative heating of the cavity is less efficient than electrical heating, which is called non-equivalence. It is obvious that a decrease of the reflectivity of the paint leads to a proportional decrease in the non-equivalence (less radiation is falling on the sidewall). Assuming a change in reflectivity of the paint by a factor of 2 (e.g. from 0.06 to 0.03) the reflectivity will decrease by 150 ppm; in order to explain the full 500 ppm change the non-equivalence has to decrease by a factor of 2 also, yielding a value of the initial non-equivalence in space of about 700 ppm $(2 \times [500 - 150])$ for the PMO6V radiometers. This value would correspond to a thermal conductivity of something like 4-5 $Wm^{-2}K^{-1}$ if we believe the model calculations for the explanation of the behaviour of the PMO6 radiometers in air where we observe a non-equivalence of 3000 ppm and calculate a conductivity of $\approx 20 \text{ Wm}^{-2}\text{K}^{-1}$ (Fröhlich 1988). Thus the loss of the side-wall would need to have an emissivity $\varepsilon \approx 0.7$ if the energy is transported by radiation only. This is much higher than $\varepsilon \approx 0.1$ which is expected for the actual side wall of the cavity which is gold plated outside and the black inside has a view-factor through the entrance aperture of the cavity of about 7%. Although the amount of the effect lacks a reasonable explanation it is observed not only for the PMO6V radiometers on SoHO, but also for HF on NIMBUS7 (Fröhlich & Lean 1998; Fröhlich

2000) and possibly also for ACRIM-II on UARS which all use the same paint.

To account for changes of the paint we assume a hyperbolic behaviour as function of exposure time. This choice

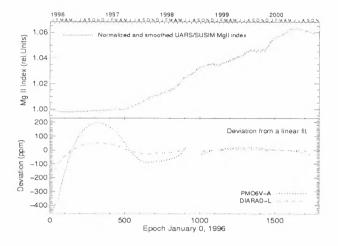


Figure 2. Top panel shows the MgII Index as used for determining the dose and the lower panel shows the result of the analysis of the ratio of the operational and back-up instruments.

is a result of the solution of the differential equation governing a change of the surface properties which in turn reduces the influence of the radiation as a function of the exposure time t_{exp} . The increase $i(t_{exp})$ due to a change in the paint's absorptivity is described by

$$i(t_{\text{exp}}) = a\left(\left(1 + \frac{t_{\text{exp}}}{\tau}\right)^{-b} - 1\right). \tag{1}$$

This function is normalized to zero at $t_{exp} = 0$. The decrease in sensitivity with exposure time $d(t_{exp})$, normally termed as degradation, is assumed to be a decreasing linear function with time which is modulated by the dose of the received radiation weighted with a hyperbolic function in time. For the dose the MgII index from the SUSIM experiment on UARS is used as proxy and the change in sensitivity is described by

$$d(t_{\exp}) = a \int_{0}^{t} (MgII - o) \left(\left(1 + \frac{t_{\exp}}{\tau} \right)^{-b} - 1 \right) dt + ct_{\exp},$$
(2)

with o an offset determining the initial contribution to the slope and c the slope of the linear function; again this function is normalized to zero at $t_{exp} = 0$. For the period before and after the SoHO vacations a reduction factor is introduced to reflect possible changes in the behaviour of the cavities. Also the slope of the linear function is reduced accordingly which could mean that an exponential function would probably better represent the long-term behaviour. But, because of the gap during the SoHO vacations it is difficult to follow the changes

	Exposure dependent Corrections						Exposure independent					
	increase decrease					Corre	ections					
	a	τ	b	0	а	τ	b	С	а	Τ	aafter	offset
	Wm^{-2}	d	-		Wm ⁻²	d	-	$\mathrm{mWm}^{-2}\mathrm{d}^{-1}$	Wm^{-2}	d	-	ppm
PMO6V	1.40	22.22	1.2	0.9879	1.72	885	2.5	6.21	0.693	147.0	0.00087	0
DIARAD	1.27	54.64	0.3	0.9882	1.01	440	2.5	4.12	0.843	430.8	0.0956	275.7

Table 1. Summary of the parameters determined for the long-term changes of the VIRGO radiometers

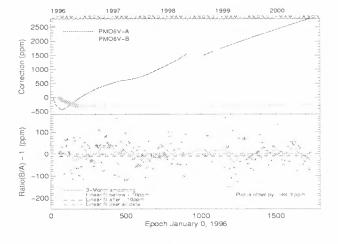


Figure 3. Corrections for PMO6V-A abd B (top panel) and the resulting ratio with the final corrections applied.

accurately. The parameters of these functions are determined for each type of radiometer assuming the same influence on each as a function of their exposure time. In the case of DIARAD-R the total exposure time is not even a day up to now (September 2000) and thus this instrument is assumed to have no exposure dependent change. For PMO6V-B, the exposure time was early in the mission quite important, and reached about 10 days when the cadence was changed from once every 8 hours to about once a week (around May 1996). The parameters are varied in such a way that the standard deviation from a linear fit to the ratio of the back-up to the operational radiometer readings is minimized. The constant c is used to adjust the slope to zero. The result for the dose dependent corrections are shown as deviations from a linear trend in Fig. 2. The final values of the parameters as are listed in Table 1 for the two radiometer types. The ratios of the operational and back-up instruments with the final parameters are shown in Fig. 3 and 4. It is important to note that the dose dependent degradation was essential to achieve this low variation around the straight line (more than a factor of two lower than without). With a final precision of a few tens of ppm this demonstrates also how well it seems to describe the observed degradation. In the case of the DIARAD-L the corrections are such that the degradation at the beginning is masked by an increase in sensitivity as for the PMO6V radiometers, but with a much longer time constant. In parallel with this increase in absolute sensitivity an increase of the relative sensitivity to short-term variations by more than 30% is observed (see below). This was first observed during the passage of an active region without a sunspot in May 1996 as a dif-

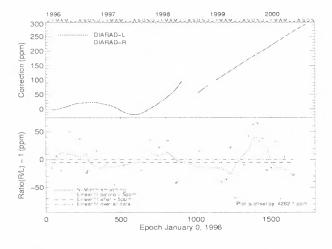


Figure 4. Corrections for DIARAD-L and R (top panel) and the resulting ratio with the final corrections applied.

ference in amplitude between D1ARAD-L and PMO6V-A.

EXPOSURE INDEPENDENT CHANGES

The comparison of the time series of PMO6V-A and DIARAD-L corrected for the exposure dependent changes shows a trend which has to be exposure independent. Obviously, such a trend could never be determined from only one type of radiometer. As stated in the introduction the question is whether this effect can only be observed in a quiet thermal environment like on SoHO and has thus so far never been detected. As a model for this increase in sensitivity we propose an exponential function with a time constant τ and amplitude a; after the SoHO vacations the amplitude is multiplied by a_{after} which corresponds to a shift in time of the exponential function by $\tau \log a_{\rm after}$. Again we minimize the standard deviation from a regression line to the ratio PMO6V-A/DIARAD-L, first by varying the parameters a and τ for the PMO6V-A. In a second step we minimize τ of DIARAD-L and then adjust its a coefficient so that the slope becomes zero. This is done iteratively and the procedure converges to well defined parameters which are listed in Table 1 and shown in Fig. 5. Before the SoHO vacations the situation is straight forward and it converges towards a unique solution, mainly due to the fact that the time constants of the two radiometers are (fortunately) quite different. After the SoHo vacations the fit is done only for the period up to day 1430 when a change in the behaviour is observed (see

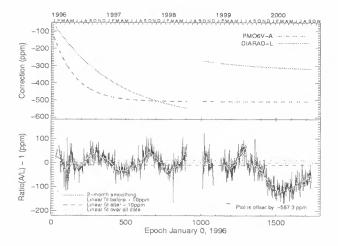


Figure 5. Corrections for the exposure independent behaviour of PMO6V-A and DIARAD-L (top pasnel) and the corrected ratio (lower panel).

below). The minimization works much better than for the full series and the result is quite interesting, as it indicates no change in behaviour after the gap, and the determined a_{after} indicate that the curves just continue from before. It is assumed that the effect starts with the switch-on of the instrument and is due to the slightly higher temperature of the cavity relative to the surroundings. Whether the effect was discontinued over the gap and conforms to the assumption cannot be decided because the effect is already quite small (10% in the case of DIARAD and less than 1% for PMO6V) and its detection marginal. The reason for the effect may again be a change of the nonequivalence through a change in e.g. the emissivity of the side-walls of the cavities (inside and outside). But, as for the early increase, the observed change of 500-600 ppm is larger than what could be expected. For DIARAD-L - and possibly also for PMO6V-A with a smaller amplitude - we need still another effect as it shows a kind of fall-back to a less sensitive mode when it is switched off. After the accidental switch-off of VIRGO in September 1996 this effect is well documented for DIARAD as it starts after switch-on with a sensitivity which is lower by about 200 ppm after the 3-day switch-off. After the SoHO vacations a value of 276 ppm is determined from the ratio to PMO6V-A by assuming that the change is due to DIARAD alone. This sounds reasonable as the Sun has increased during the SoHO vacations and the data from DIARAD are more or less constant over the gap (see Fig. 1). The 1996 event is presently corrected as suggested by the DIARAD team by shifting the data from just after the switch-on until 37 days later by 110 ppm upward, although we would prefer a correction which is consistent with both the events in September 1996 and after the SoHO vacations. As mentioned above there is a further problem encountered after mission day 1430 when the ratio of PMO6V-A/DIARAD-L changes; this coincides with the time when the MgII index increased abruptly (see Fig. 2). Also in Fig. 6 it is obvious that something happened around day 1430. This needs further investigation, and probably some irradiation tests of the black paint used in DIARAD, which has no heritage in long-

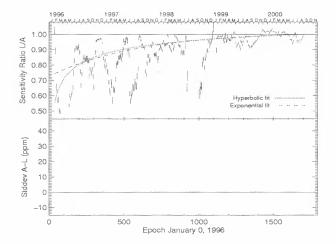


Figure 6. DIARAD sensitivity change as determined by comparing the variability around the mean value with the one of PMO6V-A (top panel). The lower panel shows the difference in standard deviation for the same periods as the sensitivity determinations. The parameters are determined from means over 41 days, shifted by 10 days.

term space radiometry other than on EURECA.

Another interesting observation is the modulation of the ratio with a period of about an year. In the ratio only the difference between the sensitivities of the two instruments is observed. However, the signal in the VIRGO irradiance is of similar magnitude; hence the fact that this signal vanishes after day 1430 may indicate that finally DIARAD has reached a sensitivity similar to the one of PMO6V. All this means that the precision and the sensitivity to the "main" part of the irradiance signal is accurate to only about 0.01% whereas changes of the short-term sensitivity up to that level are still possible. A similar effect was observed by comparison of HF and ACRIM-I during the solar minimum 1985.

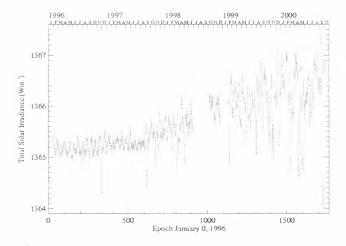
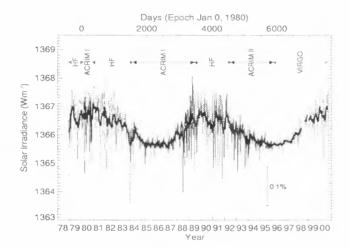


Figure 7. Time-series of the VIRGO *TSI* from February 1996 until September 2000.

4. VIRGO TSI AND COMPOSITE UPDATE

From this analysis a new version (3.50) of the VIRGO TSI can be constructed. The VIRGO irradiance is a composite of the results from the corrected data of DIARAD-L and PMO6V-A. An average of the data from the two radiometers is not a good way to produce the best TSI. The short-term sensitivity change of the DIARAD has to be corrected first, which is possible from the determinations shown in Fig. 6, the exponential curve is used to rise the sensitivity to the same level as PMO6V. This is done until the SoHO vacations and no further corrections are applied afterwards yet. At the beginning of the





mission the PMO6V data are less reliable, partly due to the early increase which cannot be determined very accurately as PMO6V-B was only operative after the major increase of PMO6V-A was over, and partly due to the new type of operation which was needed after the failure of the shutters (Fröhlich et al. 1997). Thus, before mission day 195 the PMO6V data are discarded. During the periods when both radiometers are available the average of PMO6V-A and the short-term corrected DIARAD-L is used. If only one radiometer is available it is multiplied or divided by the average ratio from Fig. 5. For the data after day 1430 the average is taken, although the data are expected to change when the results of a more detailed investigations are available. Figure 7 shows the TSI from February 1996 until September 2000 (Version 3.50); they are also available as daily and hourly values from www.pmodwrc.ch in files with an explaining header and three columns with the VIRGO, PMO6V and DIARAD level-2 values.

With the new VIRGO TSI we have also updated the composite which is shown in Fig. 8 and is also available from the PMOD/WRC web server as version 19. This composite is now compared to the model calibrated over the full period of the composite as described in Fröhlich (1999). The result is shown in Fig. 9 and the onset into the new cycle 23 has no longer the pronounced difference due to the carly increase of the VIRGO radiometry.

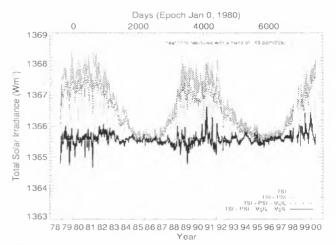


Figure 9. Comparison of the composite with the new VIRGO data with the model composed of *PSI* and a long a short-term MgII index.

5. CONCLUSIONS

The detailed investigation of the behaviour of the VIRGO radiometers allows to determine the long-term changes in an internally consistent and unambiguous way. The most important message is that there are changes which cannot be determined by comparing differently exposed radiometers, because the effects do not dependent on exposure to the sun as detected for the VIRGO radiometers. It is quite possible that this exposure independent behaviour could only be detected in an environment as stable as the one on SoHO. Some of the yet unexplained fluctuations of other space radiometers may be due to such effects, but the substantial changes of the thermal environment do not allow to reach a steady state as on SoHO.

The comparison of the composite with the model shows now reasonable agreement for the increase of TSI towards the maximum of cycle 23.

ACKNOWLEDGMENTS

The authors would like to thank many helpful discussions with and suggestions from George Lawrence, LASP, Boulder, CO. Thanks are extended to the Swiss National Science Foundation for support of the VIRGO Project at PMOD/WRC. These results would not be possible without the continuous efforts of the VIRGO and SoHO teams. SoHO is a cooperative ESA/NASA mission.

REFERENCES

- Anklin M., Fröhlich C., Finsterle W., Crommelynck D.A., Dewitte S., 1999, Metrologia, 35, 686
- Chandra S., Lean J.L., White O.R., et al., 1995, Geophys. Res. Let., 22, 2481

- Fröhlich C., 1988, In: Fox N. (ed.) Optical Radiometry, 73–79, Inst. Phys. Conf. Ser. No. 92, London
- Fröhlich C., 2000, Adv.Space Res., in press
- Fröhlich C., 2000, Space Science Reviews, 94, in press
- Fröhlich C., Anklin M., 2000, Metrologia, 37, in press
- Fröhlich C., Lean J., 1998, Geophys. Res. Let., 25, 4377
- Fröhlich C., Pap J.M., Hudson H.S., 1994, Sol. Phys., 152, 111
- Fröhlich C., Romero J., Roth H., et al., 1995, Sol.Phys., 162, 101
- Fröhlich C., Crommelynck D., Wehrli C., et al., 1997, Sol.Phys., 175, 267

POLAR ICE AS AN ARCHIVE FOR SOLAR CYCLES AND THE TERRESTRIAL CLIMATE

J. Beer

Federal Institute of Environmental Science and Technology, EAWAG, Ch-8600 Dübendorf, Switzerland tel: +41 1 823 51 11 / fax: +41 1 823 52 10, email: beer/c environch

email: <u>beer(a eawag.ch</u>

ABSTRACT

Ice cores represent natural archives that contain information about a large variety of parameters related to climate change and solar variability. Solar variability is recorded in ice through the solar wind induced modulation of the cosmic ray flux. During periods of high solar activity, the cosmic ray flux penetrating into the atmosphere is reduced leading to a smaller production rate of cosmogenic radionuclides such as ¹⁰Be. These nuclides are removed from the atmosphere mainly by wet precipitation and stored partly in ice sheets or glaciers. Since solar activity affects the solar irradiance, reconstruction of cosmogenic nuclides in ice cores also provides information on past solar forcing. Besides solar forcing, ice cores contain additional information about other forcing factors such as greenhouse gases occluded in air bubbles, aerosols, and volcanic ash.

At the same time, ice offers the opportunity to study the response of the climate system to various forms of forcing. A large number of different parameters can be used to derive temperature, precipitation rate, wind speed and others.

The analysis of the cosmogenic nuclides ¹⁰Be, ¹⁴C, and ³⁶Cl reveals not only that solar variability is partly cyclic with periodicities around 11, 90, 205 and possibly more years, but also that extended periods of low solar activity, so called grand minima, often coincide with rapid climate changes.

INTRODUCTION

The Sun is an especially interesting and important object to study for two main reasons. Firstly, the sun is by far the closest star and therefore offers the opportunity to study many details that cannot be resolved on other stars. Secondly, it is the main source of energy on Earth which drives the climate system. Observations during the last decades clearly revealed that the Sun is a variable star. Consequently, its role in climate forcing became an important issue. However, the time scales involved in solar and climate variability significantly exceed the length of observational records which are typically limited to the last few centuries. Therefore, one has to rely on indirect or proxy data which are recovered from natural archives such as ice cores, sediments, tree rings, corals, etc.. The purpose of this paper is to give a short overview on how polar ice cores can be used to learn more about solar cycles and climate changes on time-scales ranging from decades to millennia.

ARCHIVE ICE

Polar ice sheets are formed from snow. The snowflakes grow together to grains which slowly increase in size. Due to the pressure of the overlying new snow layers, the grains become more and more compacted and finally turn into ice. The consequence of this formation process is that the ice not only preserves all the atmospheric constituents such as aerosols and dust, it also contains air bubbles that enable to determine the atmospheric composition and in particular the reconstruction of greenhouse gases in the past. This unique property makes ice the only archive that virtually stores all the climate forcing factors (greenhouse gases, aerosols and volcanic dust, solar irradiance) except internal variability. Ice cores also contain information on the corresponding climate response (temperature. precipitation rate, wind speed, atmospheric circulation). Another important property of ice is that it flows. This can be seen in Fig. 1, which schematically depicts an ice-sheet. The ice slowly flows towards the margin of the ice sheet, where it partly melts and partly breaks up as icebergs. Under steady-state conditions, the ice lost in the ablation area is replaced by snow falling on the accumulation area where new layers are formed continuously. As a consequence of the horizontal movement of the ice, the annual layers become thinner with increasing depth, as indicated in Fig. 1.

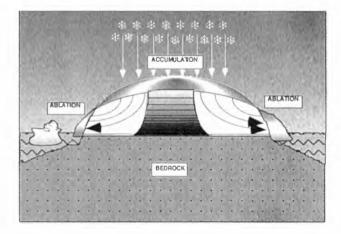


Figure 1: Formation of an ice sheet. The snow falling in the accumulation region turns into ice that slowly flows towards the ablation area where it breaks up into icebergs or melts. As a consequence of the flow characteristics the thickness of annual layers decreases with increasing depth.

Proc. 1st Solar & Space Weather Euroconference, 'The Solar Cycle and Terrestrial Climate', Santa Cruz de Tenerife, Tenerife, Spain, 25-29 September 2000 (ESA SP-463, December 2000)

This leads to another special property of the archive ice. The depth-age relationship is non-linear, which has the advantage that the uppermost part of the core is well resolved and the total time period covered is long (of the order of 10^5 years for polar ice cores). The disadvantage of this non-linear time-scale is, however, that dating ice is difficult and relies strongly on correct modelling of the ice-flow. The main ice sheets are situated in polar regions (Greenland, with a maximum thickness of approx. 3 km and Antarctica, with a thickness of up to 4 km). Smaller ice sheets at lower latitudes can only be found at high altitudes (Andes, Himalaya, Alps) (Thompson, Yao et al. 1997).

There is a steadily growing number of parameters which can be measured in ice cores. It is beyond the scope of this paper to discuss all these parameters. In Table 1, a small selection of those related to climate forcing and climate response is given.

Table 1. Climate parameters measured in ice cores

Parameter	Proxy for
CO ₂	Greenhouse gases
CH_4	Greenhouse gases
SO4	Volcanic eruptions
Ash	Volcanic eruptions
¹⁰ Be, ³⁶ Cl	Solar activity
δ ¹⁸ Ο	Temperature
Borehole temperature	Temperature
Annual layer thickness	Precipitation rate
Dust	Wind speed
Anions / cations	Atmospheric circulation

As an example, δ^{18} O of the GRIP ice core is shown in Fig. 2. δ^{18} O (relative deviation of the 18 O/ 16 O ratio in ice from a standard in ‰) reflects mainly the temperature at which snow is formed.

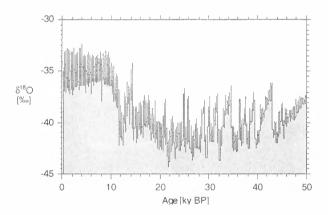


Figure 2: δ^{18} O measured in the GRIP ice core from Greenland. Low values indicate cold climate. During the last 10'000 years the temperature was relatively stable compared to the preceding glacial period.

Fig. 2 shows that during glacial times the temperature in Greenland was characterized by abrupt changes (socalled Dansgaard Oeschger events) of up to 20° C within a few decades. The last 10'000 years, the so-called Holocene, however, looks comparatively stable. The Dansgaard Oeschger events were probably caused by abrupt changes in the ocean circulation, transporting heat to high latitudes. In the following, we concentrate on the question what ice cores can tell us about the history of solar activity and solar irradiance.

RADIONUCLIDES IN ICE

Direct measurements by satellite-based radiometers over the past two decades clearly show that the solar irradiance changes in phase with the magnetic activity (Lean 1997). Models taking into account the positive contribution from faculae and the negative contribution from sunspots explain quite well the changes observed in solar irradiance on time-scales from days to months (see other articles in this volume). With regard to the climatically more relevant time-scales of decades and longer, only little is known. Several attempts were made to reconstruct the increase in solar irradiance from the Maunder minimum (1645 to 1715 A.D.) to the present. The results lay in the range of 0.2 to 0.6% which is considerably more than the observed change of 0.15% from solar minimum to solar maximum during an 11-year cycle (Lean, Beer et al. 1995) (Hoyt and Schatten 1997). Based on observations of solar type stars that exhibit changes in brightness of up to 1%. similar changes in solar irradiance cannot be excluded. An important open question is whether on long timescales, solar irradiance changes are only due to magnetic processes in the photosphere or whether fluctuation in the convective energy transport are involved as well (Yoshimura 1998) (Nesme-Ribes, Ferreira et al. 1994). The magnetic activity manifests itself in many different ways which are all related but differ to some extent. The most famous and longest record is the sunspot record that goes back quite reliably to about 1600, the time of the invention of the telescope. Another proxy of solar activity is the aa-index (Mayaud 1973). It represents fluctuations in the geomagnetic field observed from two antipodal stations. These fluctuations are caused by the interaction of the magnetic field carried by the solar wind with the geomagnetic field. The aa-index goes back to 1868.

Table 2. Some cosmogenic radionuclides and their main properties.

Nuclide	Half-life (years)	Target	Production rate $(atoms cm^{-2} s^{-1})$
¹⁰ Be	$1.5 10^6$	N, O	0.018
¹⁴ C	5730	N, 0	2.0
³⁶ C1	3.01 10 ⁵	Ar	0.0019

The heliosphere interacts not only with the geomagnetic field but also with the cosmic ray particles in the vicinity of the solar system. Solar modulation affects mainly the low energy part of the cosmic ray spectrum. The more active the sun, the lower the cosmic ray flux penetrating into the solar system. The cosmic ray particles (87% protons, 12% helium nuclides, 1% heavier particles) that enter the Earth's atmosphere react with Nitrogen, Oxygen and Argon, producing a cascade of secondary particles. These nuclear processes produce a variety of cosmogenic nuclides such as ¹⁰Be, ¹⁴C and ³⁶Cl. These nuclides are listed in Table 2 together with their main properties.

The physics of the production processes is well understood and therefore the production rate can be calculated for each point in the atmosphere, depending on the heliospheric modulation and the geomagnetic field intensity, provided the involved nuclear crosssections are known (Masarik and Beer 1999). As an example, Fig. 3 shows the dependence of the mean global production rate of ¹⁰Be as a function of solar modulation parameter Φ ($\Phi = 0$: quiet sun, $\Phi = 1'000$: very active sun) and the geomagnetic field intensity B in relative units (B = 1 corresponds to the present field)intensity). As can be seen, the dynamic range between no magnetic field (B = 0), no solar modulation ($\Phi = 0$) and doubled magnetic field (B = 2), very active sun (Φ = 1'000) is about one order of magnitude. Note that the dependencies are non-linear and that production changes by only a factor 3-4 were observed so far.

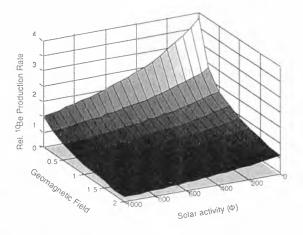


Figure 3: Dependence of the relative mean global "Be production rate on the geomagnetic field intensitiy and the solar activity parameter Φ . The production rate 1 corresponds to a geomagnetic field 1 and a Φ of 550.

The transport of the cosmogenic nuclides produced in the atmosphere is not as well understood as the production processes. ¹⁴C forms CO_2 and exchanges between the main reservoirs of the carbon cycle (atmosphere, ocean, biosphere). ¹⁰Be and ³⁶Cl become attached to aerosols or exist in gaseous form (³⁶Cl). After a mean residence time of 1 to 2 years they are removed from the atmosphere mainly by wet precipitation.

In Polar Regions, the aerosols are removed by the snow that forms the ice sheet. Assuming a production rate of 0.018 ¹⁰Be atoms cm⁻² s⁻¹ (Table 2) and a precipitation rate of 100 cm y⁻¹, a simple calculation reveals a global average ¹⁰Be concentration of approximately 10⁷ atoms per kg of ice. Extremely sensitive detection techniques

are necessary to measure 10⁷ atoms. Due to the long half-life, decay counting is not feasible. However, accelerator mass spectrometry (AMS), using single atom detection is suitable to do the job (Suter, Beer et al. 1989). A known amount of stable ⁹Be (typically 0.5 mg) is added to each sample. This leads to a ¹⁰Be/⁹Be ratio in the range of 10⁻¹³ to 10⁻¹². After extraction of the Be from the water by ion exchange technique, a BeO sample is produced. This sample is put into the ion source of the AMS system and an ion beam is produced and accelerated to high energy (20 MeV) by means of a tandem accelerator. This high energy destroys the molecular background (¹⁰B in the case of ¹⁰Be). In the following, some of the results obtained so far are discussed:

SOLAR CYCLES

Direct observations clearly reveal that part of the solar variability is cyclic. In the following, we will concentrate only on cycles with time scales of years and longer. Cycles with periodicities from centuries to millennia are based on indirect or proxy data. Since these data (e.g. ¹⁰Be, ¹⁴C) represent a complex combination of different signals it is not always possible to unambiguously attribute a cycle to solar variability.

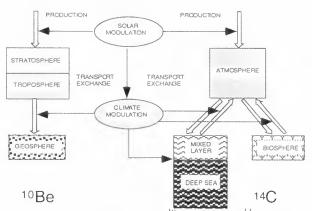


Figure 4: Comparison of the ¹⁰Be and the ¹⁴C system. Solar modulation affects both nuclides in a very similar way. However, climate effects are expected to be different due to the different systems

One way of distinguishing between solar variability induced signals and others is to compare ¹⁰Be and ¹⁴C. Both radionuclides are produced by similar nuclear reactions in the atmosphere. Their respective production rates and its dependence on solar activity can be calculated (Masarik and Beer 1999). However, after production their geochemical behaviour is completely different (Fig. 4).

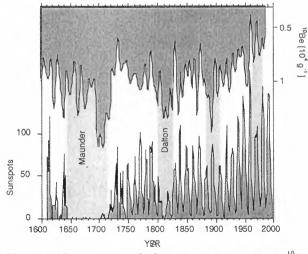
A comparison of the two radionuclide records therefore allows us to distinguish between the production signal caused by solar and geomagnetic modulation and the system signal caused by the climate affecting the transport and the exchange processes between the different reservoirs depicted in Fig. 4.

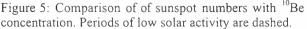
An actual comparison can be made in 2 ways: 1. By an inverse calculation, using the ¹⁴C data to obtain the production rate function that is needed to explain the Δ^{14} C values determined in tree-rings (Δ^{14} C: deviation of the atmospheric ¹⁴C/¹²C ratio from a standard in ‰). 2. By calculating the expected atmospheric Δ^{14} C values assuming that the measured ¹⁰Be concentration in ice reflects exclusively production variations. In both cases, an appropriate carbon cycle model is needed to account for the exchange of CO₂ between atmosphere, biosphere and ocean.

The results from such comparisons indicate that, for the past several millennia, the short-term (decades to centuries) fluctuations in the Δ^{14} C record are mainly due to production variations, most likely caused by solar modulation.

It is important to note that cycles associated with solar activity do not have a fixed periodicity. For example in the case of the sunspot cycle, the periodicity varies between 9 and 17 years. This rises the important question whether the periodicity averaged over longer times stays constant or not (Dicke 1978; Beer, Baumgartner et al. 1994). To answer this question, longer and very precisely dated records of solar activity are needed than are presently available.

The most prominent solar cycle is the 11-y Schwabe cycle discovered by Schwabe in 1843 when analysing his 17 years long sunspot data. In Fig. 5 the sunspot cycle based on sunspot groups (Hoyt and Schatten 1998) is shown for the period 1600-1999 together with the inversely plotted ¹⁰Be concentration measured in the Dye 3 ice core from South Greenland (Beer, Baumgartner et al. 1994).





In view of the fact that sunspot numbers and heliospheric modulation of the ¹⁰Be production rate are different representations of a common cause, the solar activity, the agreement is good. A detailed analysis shows that the ¹⁰Be signal lags behind the sunspot

signal by about 1 year, corresponding to the mean residence of ¹⁰Be in the atmosphere. It is interesting to note that the Schwabe cycle is still present in the ¹⁰Be record during the Maunder minimum (Beer, Tobias et al. 1998).

A 90-year cycle was discussed by Gleissberg when analysing the auroral record (Gleissberg 1965).

The Dye 3 annual ¹⁰Be record going back to 1423 also shows the 90-year Gleissberg cycle (Beer, Joos et al. 1994).

The 205-year DeVries cycle is the most prominent periodicity in the Δ^{14} C record during the Holocene. However, as with other periodicities, its amplitude and periodicity are variable with time. Since the sunspot record is too short to detect the 205-year DeVries cycle, its attribution to solar variability is based on indirect evidence. The agreement between ¹⁰Be and ¹⁴C clearly points to a production origin of this cycle. There is no indication from geomagnetic records so far for a 205-year cycle. On the other hand, the solar minima Maunder, Spoerer and Wolf are spaced at about 200 years.(1700, 1500, 1300 AD.). This and an additional argument further down leads us to the conclusion that the DeVries cycle is indeed a solar cycle.

The DeVries solar cycle is the first solar cycle the existence of which has been proven for a period of 25'000 years. The ¹⁰Be flux from the GRIP ice-core (Summit, Central Greenland) shows a strong DeVries cycle (Wagner, Beer et al. 2001). The band pass filtered data are shown in the upper panel of Fig. 6. In the lower panel, the geomagnetic field intensity is depicted for the same period of time. A comparison of the geomagnetic field intensity with the envelope of the band filter output reveals a relatively high degree of similarity. This is to be expected because calculations show that during periods of low geomagnetic field intensity the production amplitude is enhanced and vice versa.

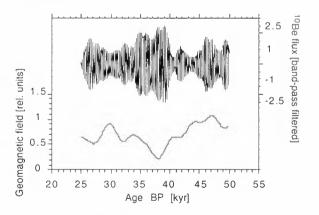


Figure 6: The DeVries 205-year cycle found by bandpass filtering the ¹⁰Be flux data from GRIP for the period 25-50 ky BP. Note that the amplitude of the DeVries cycle is modulated by the geomagnetic field as expected.

Taking into account that a perfect agreement would only be obtained if the solar modulation process had a constant amplitude, which is not the case, the good correlation between the filter output and the geomagnetic field is another argument in favour of a solar origin of the DeVries cycle.

Cycles with longer periodicities (e.g. 1000-2000 years) could not yet be attributed to solar modulation.

SOLAR MINIMA

An especially interesting feature of the sunspot record is the period from 1645 to 1715 A.D. that is characterized by an almost complete absence of sunspots (Fig. 5), the so-called Maunder minimum. Since then, solar activity has steadily grown with the exceptions of a few less pronounced minima: the Dalton minimum (1790-1830) and some weaker minima around 1890 and 1960.

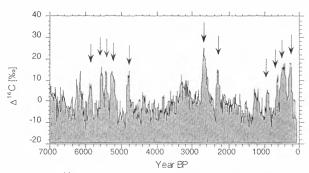


Figure 7: ¹⁴C peaks corresponding to periods of low solar activity and possibly also reduced solar irradiance

Maunder type minima occurred earlier throughout the Holocene and are called grand minima. Since only little is known about these grand minima from direct observations, their occurrence is documented mainly by cosmogenic nuclide records. Fig. 7 shows the detrended Δ^{14} C record (Stuiver, Reimer et al. 1998): The grand minima that correspond to maxima with regard to the cosmogenic nuclide production are marked by arrows. How do we know that these peaks in Δ^{14} C are of solar origin and not caused by climatic effects or geomagnetic modulation? Firstly, the similarity in amplitude and duration of the peaks with the one corresponding to the Maunder minimum points to a common cause. Secondly, it seems rather unlikely that the geomagnetic dipole field exhibits such strong excursions within only approximately a century. Finally, the good agreement between the measured $\Delta^{14}C$ and the calculated $\Delta^{14}C$ based on ¹⁰Be data from ice cores convincingly shows that these peaks are due to production and not climatic effects. This brings us to the last topic, solar forcing and its detection (Beer, Mende et al. 2000).

SOLAR FORCING OF CLIMATE CHANGE

The two main problems related to solar forcing and climate change are:

- 1. The lack of a quantitative solar forcing function. As discussed above, the physical processes responsible for changes in solar irradiance are not yet well understood, especially as far as long-term changes are concerned. All attempts so far are therefore based mainly on various assumptions leading to differences of about a factor of 2. Longer forcing records are based on simple linear regression models (Bard, Raisbeck et al. 2000).
- 2. The response function of the climate system to solar forcing is probably variable in time and not well known. There is an increasing number of experiments with global circulation models (GCM) including solar forcing. However, these model runs do not take into account the change in the spectral energy distribution and its potential effects on the atmosphere (e.g. Ozone). There may be other effects on the atmosphere caused by the interaction of the heliosphere with the magnetosphere and by cosmic rays with the atmosphere which could also contribute to climate change (Tinsley, Brown et al. 1989).

In view of all these uncertainties, the question arises which would be the best strategy to detect solar induced climate changes. One approach is to use the Milankovic forcing that is caused by planetary gravitational effects on the orbital parameters of the earth (Berger, Imbrie et al. 1984). Although only changes of the eccentricity causes changes in the total solar irradiance, the fact that the latitudinal forcing function can be calculated precisely for any time offers the unique opportunity to study the response function on longer time-scales (≥ 10 ky). Another straightforward approach is to search for fingerprints of solar forcing. All we know for sure is that solar irradiance changed in phase with solar activity over the past two Schwabe cycles. It is reasonable to assume that longer solar activity changes are associated with larger changes in solar irradiance (Beer, Mende et al. 2000). Therefore, good candidates for solar forcing effects are solar minima, in particular grand minima. In fact, instrumental temperature records reveal cold events during the minima around 1810, 1890 and 1960 (Fig. 5).

The Maunder and Spoerer minima occurred during the so-called "little ice-age", a period characterized by a general advance of glaciers. The more high-resolution climate records become available, the more evidence is found that abrupt climate changes indeed often coincide with solar minima (Magny 1993; Van Geel and Renssen 1998).

CONCLUSIONS

To fully understand the present variability of the Sun and the terrestrial climate system and even more to make predictions about their future behavior it is inevitable to improve the understanding of their longterm dynamics in the past. For this purpose, natural archives such as polar ice cores provide a wealth of information. Solar variability can be reconstructed by means of cosmogenic radionuclides such as ¹⁰Be and ¹⁴C. The production rates of both nuclides is modulated by the magnetic fields carried by the solar wind. ¹⁰Be

measurements show that solar variability has a cyclic component with periodicities of 11, 90, 205 and possibly more years. However, the relationship between solar activity and solar irradiance is not yet understood in detail.

Ice cores not only contain information on climate forcing, but also on climate response. There is growing evidence that especially periods of low solar activity (grand minima) coincide with periods of rapid climate changes.

ACKNOWLEGMENTS

The author thanks W.Mende, R. Muscheler and G.Wagner for helpful discussions and C. Wedema for typing and correcting the text. This work was financially supported by the Swiss National Science Foundation.

REFERENCES

- Bard, E., G. Raisbeck, et al. (2000). "Solar irradiance during the last 1200 years based on cosmogenic nuclides." Tellus 52B: 985-992.
- Beer, J., S. Baumgartner, et al. (1994). Solar Variability Traced by Cosmogenic Isotopes. The Sun as a Variable Star: Solar and Stellar Irradiance Variations. J. M. Pap, C. Fröhlich, H. S. Hudson and S. K. Solanki. Cambridge, Cambridge University Press: 291-300.
- Beer, J., C. F. Joos, et al. (1994). ¹⁰Be as an indicator of solar variability and climate. The solar engine and its influence on terrestrial atmosphere and climate. E. Nesme-Ribes. Berlin, Springer-Verlag. 1. 25: 221-233.
- Beer, J., W. Mende, et al. (2000). "The role of the Sun in climate forcing." Quat. Sci. Rev. 19(1-5): 403-415.
- Beer, J., S. M. Tobias, et al. (1998). "An active Sun throughout the Maunder minimum." Solar Physics 181: 237-249.
- Berger, A., J. Imbrie, et al., Eds. (1984). Milankovitch and Climate. NATO ASI Series. Dordrecht, D. Reidel Publishing Company.
- Dicke, R. H. (1978). "Is there a chronometer hidden deep in the Sun?" Nature 276: 676-680.Gleissberg, W. (1965). "The eighty-year solar cycle in auroral frequency numbers." J. Br. Astron. Assoc. 75: 227.
- Hoyt, D. V. and K. H. Schatten (1997). The Role of the Sun in Climate Change. New York, Oxford University Press.
- Hoyt, D. V. and K. H. Schatten (1998). "Group sunspot numbers: a new solar activity reconstruction." Solar Physics 179: 189-219.

- Lean, J. (1997). "The sun's variable radiation and its relevance for earth." Annu. Rev. Astron. Astrophys. 35: 33-67.
- Lean, J., J. Beer, et al. (1995). "Reconstruction of solar irradiance since 1610: implications for climate change." Geophysical Research Letters 22(23): 3195-3198.
- Magny, M. (1993). "Solar influences on Holocene climatic changes illustrated by correlations between past lake-level fluctuations and the atmospheric ¹⁴C record." Quaternary Research 40: 1-9.
- Masarik, J. and J. Beer (1999). "Simulation of particle fluxes and cosmogenic nuclide production in the Earth's atmosphere." J. Geophys. Res. 104(D10): 12,099 - 13,012.
- Mayaud, S. N. (1973). "A hundred year series of geomagnetic data 1868-1967, Indices aa, Storm sudden commencements." Bull. Int. Assoc. of Geomagn. and Aeron. 33: 1-251.
- Nesme-Ribes, E., E. N. Ferreira, et al. (1994). "Solar dynamics and its impact on solar irradiance and the terrestrial climate." J. Geophys. Res. 98: 18923-18935.
- Stuiver, M., P. J. Reimer, et al. (1998). "INTCAL98 Radiocarbon age calibration, 24,000-0 cal BP.' Radiocarbon 40(3): 1041-1083.
- Suter, M., J. Beer, et al. (1989). "Advances in AMS at Zurich." Nucl. Instrum. Meth. B40/41: 734-740.
- Thompson, L. G., T. Yao, et al. (1997). "Tropical climate instability: the Last Glacial cycle from a Qinghai-Tibetan ice core." Science 276: 1821-1825.
- Tinsley, B. A., G. M. Brown, et al. (1989). "Solar Variability Influences on Weather and Climate: Possible Connections Through Cosmic Ray Fluxes and Storm Intensification." J. Geophys. Res. 94(D12): 14783-14792.
- Van Geel, B. and H. Renssen (1998). Abrupt climate change around 2,650 BP in North-West Europe: evidence for climatic teleconnections and a tentative explanation. Water, Environment and Society in Tiomes of Climatic Change. A. S. Issar and N. Brown. The Netherlands, Kluwer Academic Publishers: 21-41.
- Wagner, G., J. Beer, et al. (2001). "Presence of the solar de Vries cycle (about205 years) during the last ice age." Geophys. Res. Let. in press.
- Yoshimura, H. (1998). "Role of time-delay concept in understanding mechanism, of total solar irradiance variation and its effect on the climate of the earth." Solar Physics 177: 329-342.

RETRIEVED AEROSOL PARAMETERS NEEDED IN CLIMATE MODEL CALCULATIONS

Helena González Jorge^{1,2}, John A. Ogren³ & Fernando Rosa¹

¹Departamento de Física Fundamental y Experimental, Universidad de La Laguna, Spain (e-mail: hgonzalez@ull.es) ²Instituto de Astrófisica de Canarias, 38200 La Laguna, Tenerife, Spain (e-mail: hgonzalez@iac.es)

³Climate Monitoring and Diagnostic Laboratory, National Oceanic and Atmospheric Administration, 325 Broadway, R/CMDL1, Boulder, Colorado 80303, USA, +1(303)497-6210, fax: +1(303)497-5590, e-mail: jogren@cmdl.noaa.gov

Abstract

Climate model calculations require aerosol properties expressing the fraction of energy scattered in the backward direction, such as the asymmetry factor, the ratio of hemispheric backscattering to total scattering and the upscatter fraction. These parameters can be obtained from the inversion of scattering coefficients using the retrieved size distribution as an intermediate step. The method is described in González Jorge and Ogren (1996). Here we evaluate the approach and its uncertainties applying the method to measurements of aerosol light scattering at Mauna Loa (MLO: Hawaii, USA). The results show that long-term trends of asymmetry factors, hemispheric backscattering to total scattering ratios and upscatter fractions can be obtained from multi-wavelength aerosol scattering coefficients. Multi-wavelength measurements of aerosol light scattering coefficient are available for a variety of locations, some with a 20-year data record. This data base provides an opportunity to estimate typical values of these parameters.

Introduction

The aerosol asymmetry factor. hemispheric backscattering to total scattering ratio and upscatter fraction are key parameters for the recent climate model calculations. The most direct way to obtain the asymmetry factor and the upscatter fraction is by integrating over the aerosol scattering phase function measured with a polar nephelometer, an instrument only found as research versions and not presently commercially available. The hemispheric backscattering to total scattering ratio can be measured with an integrating nephelometer. However this instrument is quite recent and expensive thus hemispheric backscattering coefficients are not included in some data bases. These aerosol properties can be retrieved using the inversion method of King et al. (1978), as shown by Gonzalez Jorge and Ogren (1996) and Gonzalez Jorge and Ogren (in preparation). In both papers the uncertainty statistic analysis has been performed on calculated inversion input data. This is assuming several size distributions an refractive indices and computing the scattering coefficients needed in the inversion. This is a follow on work and the input data are actual data measured at Mauna Loa (Hawaii) in 1988 with an integrating nephelometer. The uncertainty statistical analysis has been performed running the inversion program under different assumptions and quantifying the uncertainty in the retrievals by the differences in the parameters.

This study consisted of the following steps:

1. Uncertainty statistical analysis as in Gonzalez Jorge and Ogren (1996) and Gonzalez Jorge and Ogren (in preparation). The only difference is that the size distributions are similar to the size distributions measured at MLO.

2. Uncertainty statistical analysis calculating the differences in the retrieved parameters obtained under different assumptions in the inversion of scattering coefficients measured at MLO in 1988.

3. Examples of temporal series of Asymmetry factors, upscatter fractions and hemispheric backscattering to total scattering ratio retrieved assuming the most convenient set of assumptions for the inversion method

T 1 1	1	F 12	C	C	
lable	Ι.,	Indices	011	retra	ction

λ (µm)	mp	mAS	mss	
0.45	1.500	1.530	1.432	
0.55	1.525	1.528	1.431	
0.70	1 570	1.526	1.428	
0.85	1.650	1.520	1.426	

* The ammonium sulfate and dust refractive indices are interpolated from the refractive indices reported by Toon et al. (1976) and Patterson (1977), respectively. The sulfuric acid refractive indices are interpolated from the refractive indices reported by Palmer and Williams (1975).

Theory of the tests

Aerosol compositions, size distributions and multiwavelength scattering coefficients have been measured at Mauna Loa. The Ångström exponent (å), which is estimated from multi-wavelength scattering coefficients, can be used as an indicator for changes in the aerosol composition and size distributions. On this basis and according to Clarke and Porter (1991), three Mauna Loa aerosol regimes can be identified. (1) For a < 1 we can assume dust refractive indices; (2) for a > 2we can assume the sulfuric acid refractive indices, and (3) for 1 < a < 2 we can assume the ammonium sulfate refractive indices. Table 1 shows these refractive indices and Table 2 shows six bimodal lognormal distributions that will represent the size distributions measured at MLO.

The inversion algorithm of King et al. (1978), used to retrieve the aerosol size distributions, has been modified to allow the assumptions of wavelength dependent refractive indices and the angular truncation of the nephelometer.

Table 2. Parameters of the number size distributions used to generate the "true" optical properties.

Size distribution	Total number (cm ⁻³)	Mean radius (µm)	Geometric standard deviation
1	(10, 0.005)	(0.1, 0.3)	(1.5, 2.0)
2	(8, 0.05)	(0.1, 0.28)	(1.5, 2.2)
3	(10, 0.05)	(0.1, 0.24)	(1.4, 2.2)
4	(3, 0.6)	(0.12, 0.4)	(1.6, 1.8)
5	(8, 0.6)	(0.1, 0.5)	(1.6, 1.6)
6	(50, 0.1)	(0.08, 0.8)	(1.6, 1.6)

* First and second entry are the accumulation and coarse mode, respectively

* These size distributions have similar shapes to size distributions reported by Clarke and Porter (1991).

We study how uncertainties propagate for:

a. Assumptions of a constant refractive index (m'=cte). This refractive index might be a best assumption for a certain type of aerosol. However, it would not represent the whole aerosol composition picture.

b. Assumptions of a refractive index that only depends on the aerosol composition (m'=m'(a))

c. Assumptions of a wrong refractive index that depends on the Angstrom exponent and on the wavelength $(m'=m'(a, \lambda))$.

We also study how the nephelometer angular trucation can affect the retrievals. Three angular responses can be assumed for the nephelometer: a) Ideal response $(f(\theta)=1)$. b) Step response $(f(\theta)=0)$, for $\theta < 7$ and $\theta > 170$; $f(\theta)=1$, for $7 < \theta < 170$). c) The response measured by Anderson et al. (1996). We will consider only the angular responses (a) and (c).

The sensitivity to particle shape cannot be studied here since Mie theory is being assumed throughout the whole process.

Relative humidity variations lead to particle size and refractive index changes. Therefore changes in RH are somehow studied with changes in the Ångström exponent and in the size distribution.

Tests and results

<u>Step 1</u>. Uncertainty statistical analysis with known size distributions and refractive indices as in Gonzalez Jorge and Ogren (1996; in preparation). We computed "true" scattering coefficients (σ_{so}), asymmetry factors (g), hemispheric to total scattering ratios (σ_{bsp}/σ_{sp}) and upscattering fractions (β_{usp}), assuming the refractive indices with a dependency on wavelength for Ammonium sulfate, Sulfuric Acid and Dust (Table 1) using the size distributions of Table 2. We performed the following tests:

Test 1. Retrieve the aerosol size distribution assuming a

unique refractive index (m'=cte) that is calculated as the aritmetic average of all refractive indices in Table 2. Compute σ_{sp} , g, σ_{bsp}/σ_{sp} and β_{usp} using the retrieved size distributions and m'=cte.

<u>Test 2</u>. Retrieve the aerosol size distribution assuming a constant m'=m'(a) for all λ but depending on the Angstrom exponent. m' is calculated as the aritmetic average of each column in Table 2. Compute σ_{sp} , g, σ_{bsp}/σ_{sp} and β_{usp} using the retrieved size distributions and m'=m'(a).

<u>Test 3</u>. Retrieve the aerosol size distribution assuming a refractive index with a wavelength dependency for each aerosol composition (m'=m(λ , å)). It will be assumed the 3 sets of refractive indices in Table 2 for each "true" aerosol composition. Compute σ_{sp} , g, σ_{bsp}/σ_{sp} and β_{usp} using the retrieved size distributions and m'=m(λ , å). Finally, compare the retrieved parameters in test 1, 2 and

3 with the "true" parameters.

<u>Results.</u> Table 3 shows the average percentage errors and percentage standard deviations in the retrieved parameters of test 1. Since m'=1.506 is closer to the refractive indices for amonium sulfate and dust than for sulfuric acid, sulfuric acid has the largest uncertainties in the retrieved parameters. The hemispheric backscattring to total scattering ratio is the worst retrieval with the uncertainty going for -1% (ammonium sulfate, dust) to 17% (sulfuric acid).

Table 4 shows the average errors and standard deviation in the retrieved parameters of test 2. The assumed refractive indices were m'=1.53 for ammonium sulfate, m'=1.43 for sulfuric acid and m'=1.56 for dust. Again the assumptions of dust or amonium sulfate lead to similar errors in the retrieved parameters, since the refractive indices are almost the same.

Table 5 shows the average errors and standard deviation in the retrieved parameters of test 3. There are not meaningful differences between the uncertainties in the retrievals in both Table 4 and Table 5. In fact, for some cases, assuming a refractive index with a wavelength dependency leads to larger errors than assuming an aritmetic average of the refractive indices for the three wavelengths.

<u>Step 2.</u> Uncertainty statistical analysis performed on the calculated differences in the parameters retrieved from the inversion of actual scattering coefficients data measured at MLO in 1988.

The test cosisted of retrieving the aerosol size distribution and calculate the three parameters making the following assumptions:

A1. A constant m' for all λ and aerosol regimes. m' is calculated as the aritmetic average of all refractive indices in Table 1.

A2. A constant m' for all λ but depending on the Angstrom exponent. m' is calculated as the aritmetic average of each column in Table 1.

A3. m' as a function of λ and aerosol regimes.

A4. Proceed as in 1, but considering $f(\theta)$ measured by Anderson et al. (1996).

A5. Proceed as in 2, but considering $f(\theta)$ measured by Anderson et al. (1996).

A6. Proceed as in 3, but considering $f(\theta)$ measured by Anderson et al. (1996).

Table 3: Percentage average errors and standard deviations in the retrieved parameters for assuming a constant refractive index in the inversion of scattering coefficients.

m	m _D	m _{AS}	m _{SA}
σ _{sp}	(6, 7)	(1, 1)	(.05, 1)
g	(1, 5)	(1, 4)	(-5, 4)
σ_{bsp}/σ_{sp}	(-1, 13)	(-1, 12)	(17, 13)
β _{usp}	(-2, 7)	(-2, 7)	(6, 6)

Table 4: Average errors and standard deviations in the retrieved parameters for assuming the same refractive index for all compositions in the inversion of scattering coefficients. The refractive indices have a dependency on wavelength.

m	σ _{sp}	g	σ_{bsp}/σ_{sp}	β _{usp}	m'
m _D	(-6,7)	(-2,6)	(7,13)	(1,7)	m'D
	(-6,6)	(1,8)	(2,13)	(6,7)	m' _{AS}
	(-6,7)	(6,4)	(-12,12)	(-8,7)	m' _{SA}
	(1,1)	(-2,4)	(7,12)	(2,6)	m' _D
m _{AS}	(-3,1)	(4,6)	(2,11)	(3,6)	m' _{AS}
	(2,1)	(6,5)	(-13,10)	(-8,6)	m' _{SA}
	(.03,1)	(-8,3)	(26,12)	(10,5)	m' _D
m _{SA}	(2,1)	(-6,6)	(21,12)	(8,5)	m' _{AS}
	(2,1)	(-1,5)	(5,12)	(3,6)	m' _{SA}

Table 5: Average errors and standard deviations in the retrieved parameters for assuming a wrong refractive index for all compositions in the inversion of scattering coefficients. The refractive indices have a dependency on wavelength.

m	σ _{sp}	g	$\sigma_{\rm bsp}/\sigma_{\rm sp}$	β _{usp}	m'
m _D	(-5,7)	(-3,7)	(4,17)	(3,9)	m' _D
	(-6,6)	(.2,4)	(2,12)	(-1,7)	m' _{AS}
	(-6,7)	(6,4)	(-12,11)	(-8,6)	m' _{SA}
	(.1,2)	(-3,8)	(3,19)	(3,9)	m' _D
m _{AS}	(3,1)	(2,4)	(1,11)	(6,6)	m' _{AS}
	(3,1)	(6,3)	(-14,10)	(-8,6)	m' _{SA}
	(5,2)	(-11,8)	(29,23)	(14,9)	m'D
m _{SA}	(1,1)	(-6,3)	(20,12)	(8,5)	m' _{AS}
	(-2,1)	(6,3)	(4,12)	(2,6)	m' _{SA}

Results We compare and calculate relative differences among different cases from (A1) to (A6). Tables 6, 7 and 8 show the average percentage difference in the retrieved parameters calculated between running the inversion program under two different sets of assumptions. The average percentage difference is smaller than 2% for the asymmetry factor, 2% for the upscatter fraction and 8% for the hemispheric backscattering to total scattering ratio. The average percentage standard deviation of the percentage difference is smaller than 3% for the asymmetry factor, 5% for the upscatter fraction and 9% for the hemispheric to total scattering ratio. Since the percentage differences are small for all the cases, it is worthless complicating the inversion program by adding detailed assumptions of the aerosol composition.

Step 3. Examples of temporal series of asymmetry factors (Fig. 1), upscatter fractions (Fig. 2) and hemispheric backscattering to total scattering ratio (Fig.

Table 6. Percentage average difference and standard deviation in the retrieved asymptry factor

		4.2	4.7		4.5	47
	AI	AZ	AJ	A4	AS	AO
A1	(.0, .0)	(8, 2.7)	(7, 3.4)	(-1.9, 2.2)	(6, 2.6)	(4, 3.4)
A2	(.7, 2.6)	(.0, .0)	(.1, 1.1)	(-1.0, 2.1)	(.1, .9)	(.2, 1.3)
A3	(.6, 3.4)	(1, 1.2)	(.0, .0)	(-1.1, 3.0)	(.0, 1, 7)	(.2, .8)
A4	(1.8, 2.1)	(.9, 2.2)	(1.0, 2.9)	(.0, .00)	(1.0, 1.8)	(1.1, 2.7)
A5	(.5, 2.5)	(1,9)	(.0, 1.7)	(-1.1, 1.7)	(0,0)	(1,1,4)
A6	(.3, 3.4)	(3, 1.4)	(-,2,8)	(-1.2, 2.8)	(-1, 1.5)	(.0, .0)

Table 7. Percentage average difference and standard deviation in the retrieved upscattering fraction

	A1 A2 A3 A4 A5 A6						
	Al	A2	A3	A4	A5	A6	
A1	(.0, .0)	(1, 2.6)	(7, 4.7)	(1.4, 2.1)	(2, 2.6)	(-1.0,4.9)	
A2	(.0, 2.6)	(.0, .0)	(5, 2,5)	(1.3, 2.7)	(1, 1.1)	(7, 2.8)	
A3	(.5, 4.4)	(.4, 2.3)	(.0, .0)	(1.7, 4.4)	(.3, 2.8)	(2, .9)	
A4	(-1.5,2.3)	(-1.4,2.7)	(-1.9,4.8)	(.0, .0)	(-1.4,2.2)	(-2.1,4.8)	
A5	(.1, 2.6)	(.1, 1.1)	(4, 3.0)	(1.4, 2.1)	(0,0)	(6, 3.0)	
A6	(.7, 4.6)	(.6, 2.6)	(.2, 1.0)	(1.8, 4.4)	(.5, 2.8)	(.0, .0)	

Table 8. Percentage average difference and standard deviation in the retrieved hemispheric backscattering to total scattering ratio

	Al	A2	A3	A4	A5	A6
A1	(.0.00)	(3.7, 7.8)	(3.6, 8.6)	(6.9, 7.0)	(3.7, 7.7)	(3,6, 8.5)
A2	(-4.4, 8.7)	(.0, .0)	(.0, 1.5)	(2.8, 5.1)	(.2, 2.0)	(.2, 1.9)
A3	(-4.5, 9.4)	(.0, 1.5)	(.0, .0)	(2.7, 6.0)	(.1, 3.0)	(.2, 1.8)
A4	(-7.8, 8.3)	(-3.1,5.3)	(-3.2,6.4)	(.0, .0)	(-2.9,4.2)	(-2.9,5.5)
A5	(-4.5, 8.6)	(- 2,2,10)	(2, 3.1)	(2.7, 4.1)	(.0, .0)	(.0.1.9)
A6	(-4.5, 9.3)	(2, 1.9)	(2, .8)	(2.6, 5.2)	(.0, 1.8)	(.0, .0)

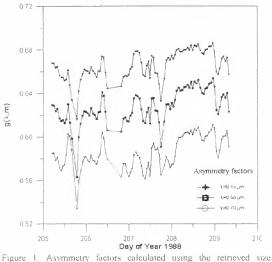


Figure 1_Asymmetry factors calculated using the retrieved size distributions

3) obtained using this method. According to step 2, we have assumed a constant refractive index.

conclusion.

We used the inversion algorithm of King et al to obtain the asymmetry factors, hemispheric backscattering to total scattering ratios and upscatter fractions from scattering coefficients using the retrieved size distributions as an intermediate step. We have done two types of uncertainty analysis:

Step1: Assuming size distributions and refractive indices

for calculating true parameters using Mie theory. From this analysis we conclude that: (1) the largest uncertainties are found for the hemispheric backscattering to total scattering ratio as it was expected from Gonzalez Jorge and Ogren (1996); (2) the smallest uncertainties are obtained in the case of assuming the constant refractive index; (3) it is irelevant to distingush dust event from ammonium sulfate events, using the reported refractive indices of Table 2.

Step 2: Using scattering coefficients measured at Mauna Loa as input data to the inversion program. From this analysis we conclude that the asymmetry factors and upscatter fractions can be obtained assuming a constant refractive index and it is worthless adapting the inversion program to complicate assumptions of the refractive index to retrieve the asymmetry factors and upscatter fractions.

Accordingly we have plotted the retrieved parameters assuming a constant refractive index in Step 3. This figure provides an example of what we can obtain with this method.

The asymmetry factors, hemispheric backscattering to total scattering ratios and upscatter fractions are three needed parameters for climate models calculations.

Scattering coefficients have been measured for many places during long time periods (sometimes more than 20 years long) and inversion procedures allow obtaining the three parameters back in time and for many places, where scattering coefficients (or other multiwavelength optical properties) have been monitored. We intend to retrieve larger temporal series of them for a further analysis.

Acknoledgment

The authors wish to express their gratitude to University of La Laguna (Project 1802260005/2000) for financial support

References

J. R Charlson., S. E. Swartz, J. M. Hales, R. D. Cess, J. A. Coakley, JR, J. E. Hansen and D. J. Hofmann, "Climate forcing by anthropogenic aerosols", Science, 255, 423-430, 1992.

W. J. Wiscombe and G. W. Grams, "The backscattered fraction in two-stream approximations", J. Atmos. Sci., 33, 2440-2451, 1976.

M. D. King, D. M. Byrne, B. M. Herman and J A. Reagan, 1978: Aerosol size distributions obtained by inversion of spectral optical depth measurements. J. Atmos. Sci., 35, 2153-2167.King et al. 1978

H. Gonzalez Jorge and J. A. Ogren, "Sensitivity of retrieved aerosol properties to assumptions", 1996,

H. Gonzalez Jorge and J. A. Ogren, "Uncertainties in aerosol properties retrieved from inversion of nephelometer data". (in preparation)

A. D. Clarke, and J. N. Porter, "Aerosol size distribution, composition, and CO2 backscatter at Mauna Loa Observatory", J. Geophys. Res , 96, No. D3, 5237-5247, 1991

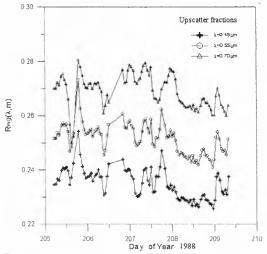


Figure 2: upscatter fractions calculated using the retrieved size distributions.

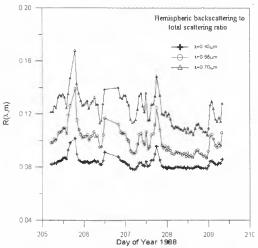


Figure 3: Hemispheric backscattering to total scattering ratios calculated using the retrieved size distributions.

T. L. Andersen, D.S. Covert, S. F. Marshall, M. L. Laucks, R. J. Charlson, R. J. Waggoner, J. A. Ogren, R. Caldow, R. L. Holm, F. R. Quant, G. J. Sem, A. Wiedensohler, N. A. Ahlquist, T. S. Bates, "Performance characteristics of a high-sensitivity three-wavelength, total scatter/backscatter nephelometer", J. Atmos. Oceanic Technol., 13, 967-986, 1996.

O. B. Toon, J. B. Pollack and B. N. Khare, "The optical constants of several atmospheric aerosol species: Ammonium sulfate, aluminum oxide and sodium cloride", J. Geophys. Res., 81, No 33, 5733-5748, 1976 E. M. Patterson, "Atmospheric extinction between 0.55(m and 10.6(m due to soil derived aerosols", Appl. Opt., 16, 2414-2418, 1977.

K. F. Palmer and D. Williams, "Optical constants of sulfuric acid; applications to the clouds of Venus", Appl. Opt., 14 No. 1, 208-219, 1975.

European Space Agency Agence spatiale européenne

Contact: ESA Publications Division ^c/o ESTEC, PO Box 299, 2200 AG Noordwijk, The Netherlands Tel (31) 71 565 3400 - Fox (31) 71 565 5433